Thomas J. Dolan   *Editor*

Magnetic Fusion Technology

Springer

Lecture Notes in Energy

Volume 19

Thomas J. Dolan
Editor

Magnetic Fusion Technology

Co-authors

Jana Brotankova
Lee C. Cadwallader
Alan E. Costley
Denis P. Ivanov
Wallace Manheimer
Mario Merola
Ralph W. Moir
Martin J. Neumann
Alexander Parrish
Lester M. Waganer

 Springer

Editor
Thomas J. Dolan
NPRE Department
University of Illinois
Urbana, IL
USA

Preface

This book is a revision of the technology chapters of *Fusion Research* (Pergamon Press, 1982) by Dolan. The present book covers only magnetic confinement, not inertial confinement, with emphasis on the ITER project (originally called the International Thermonuclear Experimental Reactor), which is under construction in Cadarache, France by an international collaboration, including the People's Republic of China, the European Union, India, Japan, The Republic of Korea, the Russian Federation, and the United States. This book is intended to serve as a textbook for graduate students and advanced undergraduates, and also as a reference book for those working in one area of fusion research to learn about other areas. Each chapter has a summary, objectives, homework problems, references, and review questions. Since the fusion research field suffers from excessive use of abbreviations (EUA) the Appendices provide a List of Abbreviations, in addition to Units Conversions, Constants, Error Function, Vector Relations, Table of Symbols, and Answers to Problems. ITER is mentioned in almost every section, so it is cited sparingly in the Topic Index to avoid overcrowding that entry. Some information, such as thermal stress, appears in more than one place.

Fusion research has suffered from restrictive budgets worldwide, and from cancellation of many successful or planned projects in the USA (EBT-P, FMIT, MFTF-B, TFTR, SSPX, ALCATOR-CMOD, LDX, NCSX,...). It might cost the world ~ 5 G\$ per year for 40 more years to develop fusion energy. This 200 G\$ over 40 years may sound like a large sum, but it is less than the US military spends in 4 months. Although fusion technology is curtailed economically, it is making steady progress towards the goal of safe, clean energy with abundant, inexpensive fuel.

To help improve the next edition please send me your comments on
Errors
Suggested additional paragraphs, figures, tables, and references
Suggested homework problems and solutions.

Thomas J. Dolan
dolantj@illinois.edu

The views and opinions expressed herein do not necessarily reflect those of the ITER Organization.

Acknowledgments

Family name	First name	Chapters
André	Julien	9
Baker	Charles	1, 2, 5, 13
Bird	Mark	1, 3, 4
Boccaccini	Lorenzo	6, 7
Bradshaw	Alex	12
Brandt	Bruce	3, 4
Brotankova	Jana	11
Cadwallader	Lee	12, 13
Chen	Francis	Outline
Cho	Teruji	1, 2, 5, 6, 11, 14
Claessens	Michel	Various
Cohen	Adam	8, 12, 14
Cross	Tim	4
Den Hartog	Daniel	11
Donné	A.	11
El-Guebaly	Laila	6, 12
Fietz	Walter	4

(continued)

Family name	First name	Chapters
Fisch	Nat	5
Forsen	Harold	1, 13
Han	Jung-Hoon	12–14
Huguet	Michel	3, 4, 6, 13
Hwang	Yeong-Sok	7
Ihli	Tomas	6, 7
Ivanov	Denis Petrovich	4
Iwasa	Yukikazu	4
Jiang	Jieqiong	13, 14
Kamendje	Richard	7
Karcher	James	1–6
Kim	Hyuck-Jong	12–14
Kim	Kyung-Jin	HW solutions
Kurnaev	Valery	8
Larbalestier	David	4
Lee	Peter J.	4
Longhurst	Glen	12
Mahdavi	Ali	7
Malang	Siegfried	6
Manheimer	Wally	14
Miller	Ron	13
Minervini	Joseph	4
Mitchell	Neil	12
Moir	Ralph	14
Muraoka	Katsunori	1, 2, 11, 13, 14
Najmabadi	Farrokh	13
Neumann	Martin	9
Overskei	David	Misc.
Parrish	Alexander	All
Pradhan	Subrata	1
Raffray	Rene	7
Raman	Roger	4, 5, 11, 13, 14
Ruzic	David	Li wall
Schneider	Ursula	4, 9, 10
Sen	Abhijit	1
Sharafat	Shahram	7
Sheffield	John	2, 11, 13, 14
Shrestha	Joshi	1, 2
Simonen	Tom	2
Singer	Clifford	5
Stansfield	Barry	1
Stubbins	Jim	8
Swenson	Charles Allen	3
Taylor	Neil	12, 13
Tillack	Mark	6

(continued)

Family name	First name	Chapters
van Oost	Guido	11
Voitsenya	Vladimir	6, 9
Waganer	Les	All
Wang	Xuren	13
Wesson	John	5, 7
Woodruff	Simon	1
Wu	Yican	13
Zakharov	Leonid	7
Zanino	Roberto	1
Zinkle	Steve	8
Zucchetti	Massimo	6, 12

Contents

Chapter 1
Introduction

Thomas J. Dolan and Alexander Parrish

Objectives

After studying this chapter one should understand

Why fusion energy is important
What is required to build a fusion reactor
How the reactor can be built
Fusion research achievements and plans.

1.1 Why Develop Fusion Reactors?

Nuclear fusion reactions power the stars, including our sun. As protons and deuterons are fused into heavier elements at high temperatures, great quantities of energy are released, but the reaction rate is slow enough that the fuel lasts for millions of years. The density and temperature in the solar core are $\sim 1.5 \times 10^5$ kg/m^3 ($\sim 10^{31}$ particles/m^3) and 1.3 keV (15 MK), and the enormous mass of fuel is held together by gravity. About 178,000 TeraWatt (TW) of the solar power is intercepted by the earth, of which much is reflected, reradiated, or absorbed to cause evaporation of water (Fig. 1.1). About 3,000 TW goes into winds, <300 TW into waves, and 80 TW into photosynthesis, producing biomass. The "renewable" energy sources are used for production of electricity and portable fuels, such as hydrogen, which could probably meet mankind's needs. The main advantage of a terrestrial fusion reactor is that it could work independently of wind and weather and be located close to load centers.

T. J. Dolan (✉)
NPRE Department, University of Illinois, Urbana, IL 61801, USA
e-mail: dolantj@illinois.edu

A. Parrish
University of Illinois at Urbana-Champaign, Urbana, IL, USA
e-mail: aparris2@illinois.edu
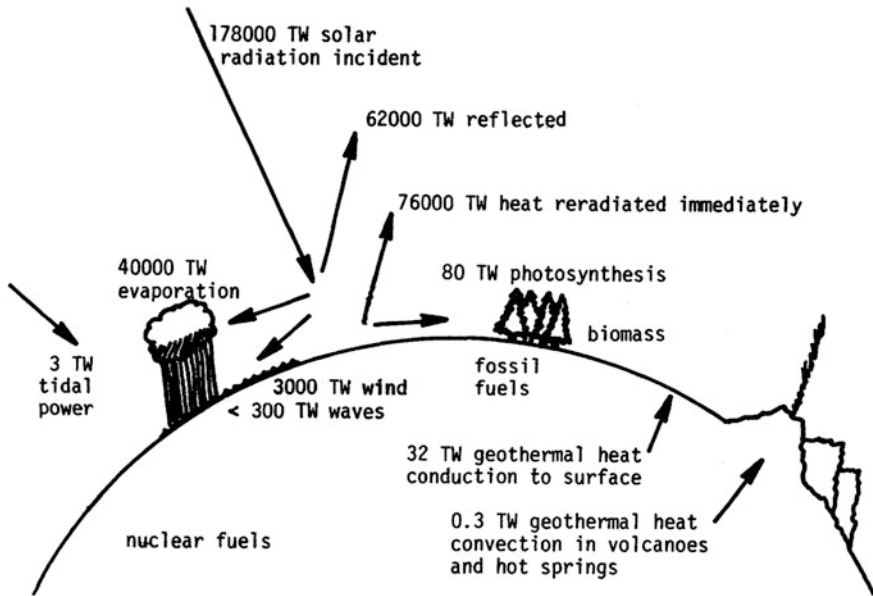
Fig. 1.1 Terrestrial power flows (Dolan 1982)

Its abundant, cheap, easily transportable fuels would avoid the pollution caused by fossil fuels (Ongena and van Oost 2012; Dolan 2012).

While the solar power source remains roughly constant, human demands for energy are growing. This growth is most visible in developing countries, such as China and India.

1.1.1 Energy Demand

Each Joule of food energy produced requires about 8 J of energy input for agriculture, chemicals, transportation, etc. Over 30 % of the cost of the following materials is due to the cost of the energy used in processing them: steel, aluminum, glass, cement, and paper. Thus, countries with a high standard of living consume large amounts of energy, as seen in Fig. 1.2.

Countries above the trend line have inexpensive energy sources or use energy efficiently. For example, Norway and Switzerland have hydroelectric power. Some of the Swiss hydropower is used for pumped storage of French nuclear power.

Developing countries must increase their energy consumption in order to improve their standards of living. This increase plus the growing world population will cause the world energy consumption to rise, as shown in Fig. 1.3.
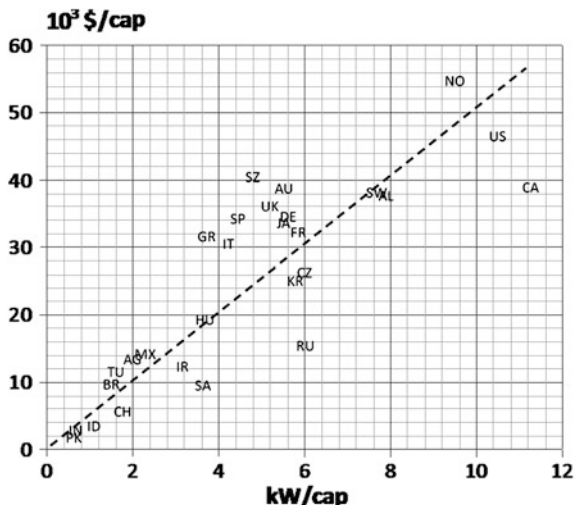
Fig. 1.2 Gross domestic product per capita versus energy consumption per capita for various countries. *AG* Argentina, *AL* Australia, *AU* Austria, *BR* Brazil, *CA* Canada, *CH* China, *CZ* Czech, *DE* Germany, *FR* France, *GR* Greece, *HU* Hungary, *ID* Indonesia, *IN* India, *IR* Iran, *IT* Italy, *JA* Japan, *MX* Mexico, *NO* Norway, *PK* Pakistan, *RU* Russia, *SA* South Africa, *SP* Spain, *SW* Sweden, *SZ* Switzerland, *TU* Turkey, *UK* United Kingdom, *US* USA [The GDP/cap data is from the 2008 CIA World Factbook, and the energy consumption per capita is from the World Resource Institute (2005)]

Fig. 1.3 Total world energy consumption rate (TW) versus year—about 20 TW in 2020 (EIA 2011)
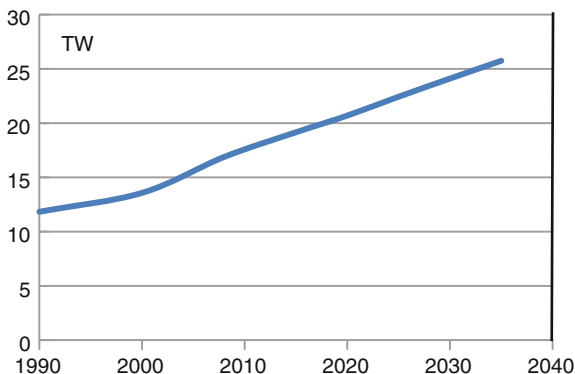
1.1.2 Energy Supply

World energy reserves are summarized in Table 1.1.

The world has about 10^{23} J ($\sim 3{,}000$ TW-years) of fossil fuel reserves that can be economically recovered. Curtailing fossil fuel burning can reduce environmental pollution and prolong the availability of these resources for other uses, such

Table 1.1 Approximate World Energy Estimates

"Reserves" are what can be recovered economically.
"Resources" are greater, but may be much more expensive.
Zetta-Joule (ZJ) = 10^{21} J
1.0 ZJ = 31.7 TW-years
Estimates from various sources differ widely and change yearly.
(Rogner 2012)

Fossil fuels	Reserves ZJ	Resources ZJ
coal & lignite	20	290–440
oil	9	17–23
natural gas	8	50–130
Nuclear fission		
U-238 + U-235	260	1300
Th-232	420	$\sim 3 \times$ Uranium
Nuclear fusion		
lithium in ocean		1.40×10^{10}
lithium on land		1700
deuterium		1.60×10^{10}
Renewable Energy		Technical Potential ZJ/year
biomass		0.16–0.27
geothermal		0.8–1.5
hydro		0.06
solar		62–280
wind		1.3–2.3
ocean		3.2–11

as raw materials for manufacturing (plastics, paints, etc.). Nuclear fission power plants are safe, reliable, and cost-effective for electrical power production, and the fuel supply is adequate for a 1,000 years (The Fukushima accident was caused by emergency cooling systems destruction by a tsunami, which is site-dependent and preventable.). Reprocessing the used fuel and recycling most of it back into the fission reactors can minimize high-level waste disposal requirements, so fission can provide safe, economical energy for many centuries.

The abundance of nuclear fusion fuels (lithium and deuterium) is enormous, and the fuels are inexpensive. Fuel costs from various sources are listed in Table 1.2.

If nuclear fusion could be successfully developed, it would have some advantages over nuclear fission:

Table 1.2 Approximate fuel costs, $/GJ (2009)

Fossil fuels		
Crude oil	10.2	OPEC
Natural gas	5.19	EIA
Coal		Macquarie Group Limited
Thermal	2.6	
Coke	3.82	
Fission fuels		
Uranium		Ux Consulting Company
U-235	0.2	
U-238	0.0014	
Thorium	0.066	Los Alamos National Laboratory
Fusion fuels		
Deuterium	0.15	Sigma-Aldrich Corporation
Lithium	0.038	Sigma-Aldrich Corporation

- No runaway reaction (super criticality) hazard.
- Expensive emergency core cooling systems not required.
- No emergency evacuation plan required for general public.
- No fission products or long-lived high-level radioactive waste (there would still be some lower-level radioactive wastes, such as radioactive steel).
- Possibility of recycling fusion reactor materials (for example reduced activation steel could be recycled after several years of cooling).
- Widespread availability and easy transport of fuels.

Some disadvantages of fusion power plants include high capital cost, radiation damage by 14-MeV neutrons, containment of radioactive tritium, and the need for remote maintenance of the radioactive blanket.

1.2 How Can We Make Fusion Reactors?

Figure 1.4 shows a hypothetical fusion power plant.

The thermonuclear plasma is surrounded by a blanket, shield, and magnet coils. The strong magnetic field provides thermal insulation between the hot plasma (T ~ 100 million Kelvin) and the walls (T ~ 1,000 K). Heat from the fusion reactions is deposited on the walls by conduction, convection, and radiation, and inside the blanket by energetic neutrons. A coolant carries the thermal power to a
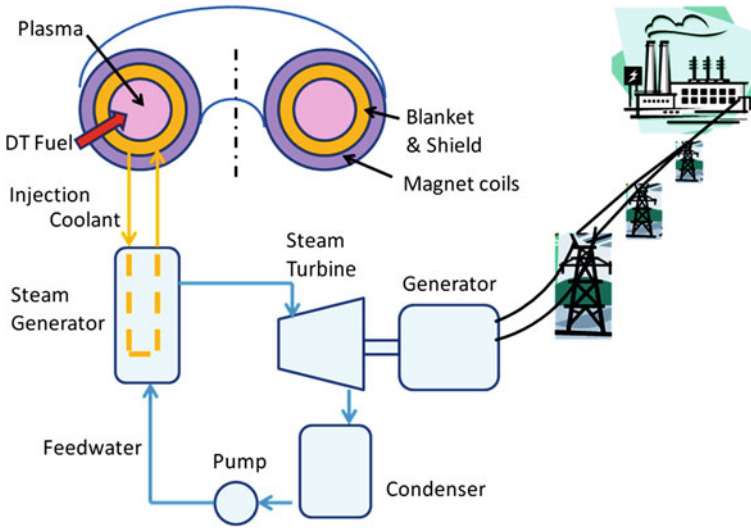
Fig. 1.4 Simplified cutaway view of a fusion reactor connected to a Rankine cycle (steam turbine cycle) to generate electricity. *DT* means "deuterium–tritium"

steam generator, and the steam drives a turbine to turn an electrical power generator. Then steam is condensed, and the feed water is pumped back through the steam generator. This fusion power plant is just like conventional plants that use coal or nuclear fission to generate heat, except that here the heat is generated by nuclear fusion reactions. The power plant components are already well developed, except for the fusion reactor heat source.

1.2.1 Nuclear Energy

Figure 1.5 shows that elements with intermediate mass, such as Fe, have lower mass per nucleon than light elements (H, He), and heavy elements (Pb, U, …). If uranium fissions into lighter elements, the resulting total mass is lower, and the difference is released as energy according to

$$E = \Delta M c^2 \tag{1.1}$$

where ΔM is the change of total mass, and c is the speed of light. If light elements fuse into heavier ones, the resulting total mass is also lower, and energy is released.

Fig. 1.5 Average mass per nucleon (in atomic mass units) versus atomic mass number A, showing a minimum around Fe (A ≈ 56) (Dolan 1982)
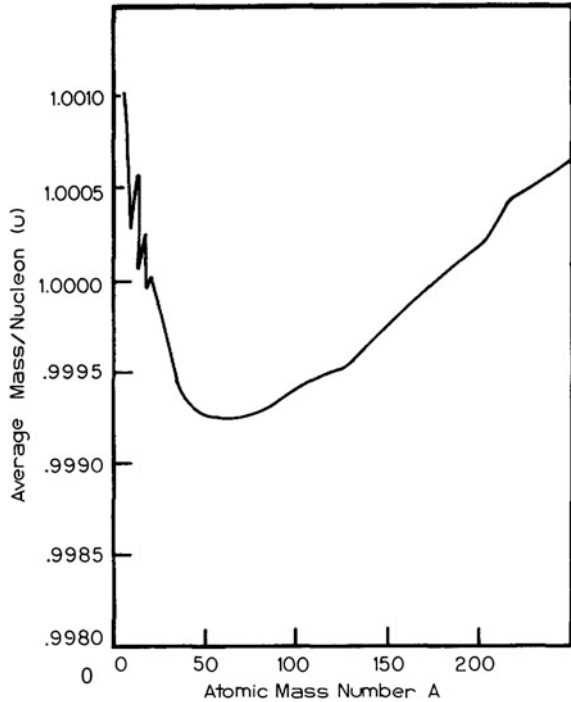
1.2.2 Plasma Heating and Confinement

In order to build a fusion reactor on earth, two conditions must be fulfilled:

- **Heating** the DT fuel to a temperature T $\sim$ 10 keV (120 Million Kelvin). Heating is required because the positive fuel ions repel each other, and they must be heated to high velocities in order to become close enough for the reactions to occur. At high temperatures the fuel becomes a "plasma", meaning a fully ionized gas, a sea of positive ions and negative electrons. Stars, fluorescent lights, welding arcs, flames, explosions, the ionosphere, industrial plasma processing devices, and gaseous lasers are all examples of plasmas. A fusion reactor will be like a miniature sun that is held together by magnetic field pressure instead of by gravity.
- **Confinement** of the heated fuel long enough with sufficient pressure for a few percent of the fusion fuel to "burn". Plasma may be confined by six means:
  - **Solid walls**: Low-temperature plasmas, such as fluorescent lights, may be contained by glass or metal tubes. Solid walls may augment hot plasma confinement in magnetic fields for brief periods of time, but prolonged contact cools the plasma rapidly by heat conduction and may overheat or erode the wall.
  - **Gravity**: Although stellar plasmas, such as the Sun, are confined by gravity, the mass of laboratory plasma is far too low for self-gravitational attraction to be significant.

– **Inertia**: Laser beams or particle beams can compress a small fuel pellet to extremely high density, such as 10^{30} ions/m^3. Inertia limits the expansion rate of the compressed fuel plasma, providing confinement for times ~ 1 ns, which is sufficient for ignition and fusion to occur.

– **Electrostatic fields**: High voltage electrodes can establish positive and negative maxima of the electrostatic potential. Positive potentials repel ions and negative potentials repel electrons. The so-called "inertial electrostatic confinement" (IEC) devices typically use concentric spherical grids biased at high voltages.

– **Magnetic fields**: Magnetic fields can confine plasmas, because the Lorentz force, $\mathbf{F} = q\mathbf{v} \times \mathbf{B}$ (q = charge, $\mathbf{v}$ = velocity, $\mathbf{B}$ = magnetic field), causes electrons and ions to spiral around magnetic field lines. This prohibits them from easily penetrating across the magnetic field. If the magnetic field lines are big circles, as in a torus, then the plasma can, in principle, be well confined, although many phenomena can spoil confinement. This book concentrates on systems for magnetic confinement.

– **Electromagnetic waves**: Radio frequency and microwave fields can confine low pressure plasma well, but enormous power inputs would be required to confine high-pressure plasmas. Electromagnetic waves can also be used to augment magnetic confinement.

1.2.3 Fusion Reactions

The main fusion reactions that could be useful on earth are shown in Table 1.3.

At a plasma pressure of 1 MPa (~ 10 atm) DT fuel can produce a power density of about 6 MW/m^3, while "catalyzed" DD fusion (to be defined in Eq. 1.6) can produce only 0.2 MW/m^3, and other fuels, even lower amounts. Therefore, we focus on DT fuel here.

Tritium has a 12.3 year half-life, so there is little tritium available in nature. Therefore, we will use neutron capture by lithium to produce tritium fuel.

Some symbols in this book have multiple meanings. For example, the symbol T is used to represent tritium, to represent temperature, and to represent the prefix Tera (10^{12}). A Table of Symbols is found in Appendix E.

The natural abundance of deuterium is approximately 1.53×10^{-4} of hydrogen atoms. This fraction varies slightly from one geographical location to another.

1.2.4 Magnetic Confinement

Magnetic fields may be either "open" (Figs. 1.6, 1.7) or "closed" (Fig. 1.8).

A plasma ion starting out near the center of a magnetic mirror would experience a higher magnetic field as it moves toward the magnet coil. In the higher field its rotational velocity component would increase, and its parallel velocity component

Table 1.3 Nuclear reactions of interest

Name	Abbreviation	Reaction (energy, MeV)	Total (MeV)	Energy $(10^{-12}$ J)
DT	$T(d,n)^4He$	$D + T \rightarrow {}^4He(3.54) + n(14.05)$	17.59	2.818
DDn	$D(d,n)^3He$	$D + D \rightarrow {}^3He(0.82) + n(2.45)$	3.27	0.524
DDp	$D(d,p)T$	$D + D \rightarrow T(1.01) + p(3.02)$	4.03	0.646
TT	$T(t,2n)$ ^4He	$T + T \rightarrow n + n + {}^4He$	11.3	1.81
D-^{3}He	$^3He(d,p)$ ^4He	$D + {}^3He \rightarrow {}^4He(3.66) + p(14.6)$	18.3	2.93
p-^{6}Li	$^6Li(p,\alpha)$ ^3He	$^6Li + p \rightarrow {}^4He + {}^3He$	4.02	0.644
p-^{11}B	$^{11}B(p,2\alpha)^4He$	$^{11}B + p \rightarrow 3(^4He)$	8.68	1.39
Reactions for breeding tritium (Natural lithium = 7.42 % ^{6}Li and 92.58 % ^{7}Li)				
n-^{6}Li	$^6Li(n,\alpha)T$	$^6Li + n(thermal) \rightarrow {}^4He(2.05) + T(2.73)$	4.78	0.766
n-^{7}Li	$^7Li(n,n'+\alpha)T$	$^7Li + n(fast) \rightarrow T + {}^4He + n$	−2.47 (endothermic)	−0.396

Numbers in parentheses are approximate energies of reaction products, MeV. The exact energies vary with angle and incident particle energies. The symbols p, d, t, n, and α represent protons, deuterons, tritons, neutrons, and alpha particles (^{4}He), respectively

Fig. 1.6 Simple magnetic "mirror" fields **B** (*top*) and "spindle cusp" fields (*bottom*) produced by bar magnets (*left side*) or by a pair of circular magnet coils carrying currents I (*right side*). Plasma could be confined in the central regions
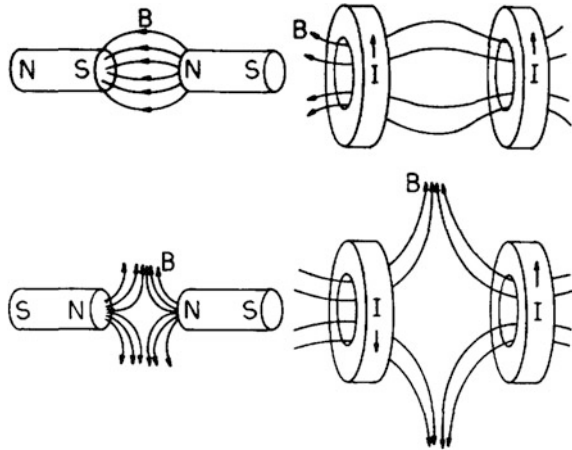
would decrease gradually towards zero, where it would be reflected back towards the center (hence, the name "magnetic mirror"). Ions would tend to oscillate back and forth between high field regions, such as locations a and b in Fig. 1.7. Electrons would also be confined in the same way. Although electrons and ions are reflected by high magnetic fields, those with sufficiently high velocities along the field lines can escape, and confinement is limited by the time it takes for Coulomb collisions to increase their parallel velocities, which makes it unfeasible to achieve energy gain ratios Q > 1 (defined below) in a simple magnetic mirror. The end loss problem can be eliminated by using a closed magnetic field, Fig. 1.8.

A simple toroidal magnetic field like this causes electrons and ions to drift outwards, so they are not well confined (Chen 1984, 2011). If the magnetic field

Fig. 1.7 A simple magnetic mirror (*top*) and axial variation of magnetic field strength (*bottom*)
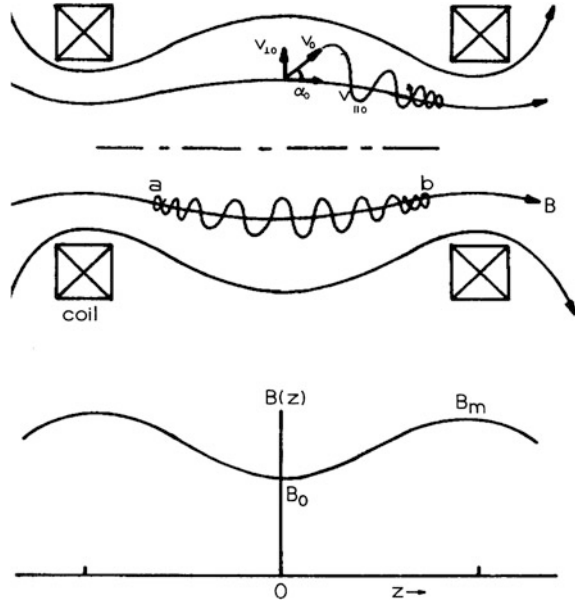
Fig. 1.8 A toroidal magnetic field. The magnet coil currents, I, create a toroidal magnetic field, B_t (*dashed lines*)
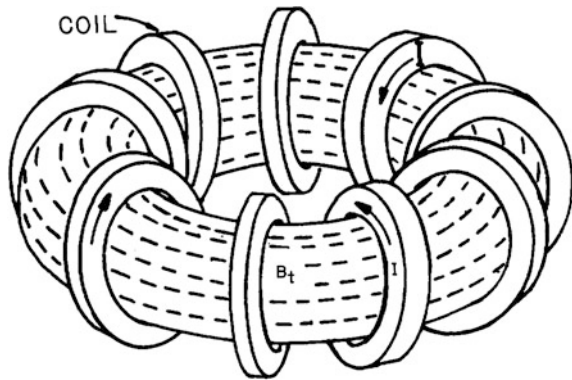
lines are twisted, however, the drift can be neutralized. The twisting can be done in two ways (tokamaks and stellarators):

Tokamaks induce a plasma current in the toroidal direction, which generates a poloidal magnetic field, Fig. 1.9.

Stellarators use helical coils to twist the magnetic field, so that strong toroidal plasma current is not required, and long-term operation is feasible. Figure 1.10 shows a conventional stellarator, comprising both toroidal field coils and helical windings in alternating directions, and a torsatron (or heliotron), which has only helical windings with currents in the same direction.

Fig. 1.9 The toroidal plasma current J induces the poloidal field component B_p. The sum of B_p plus B_t results in the helical magnetic field B (Chen 2011, Fig. 7.17, p. 257)
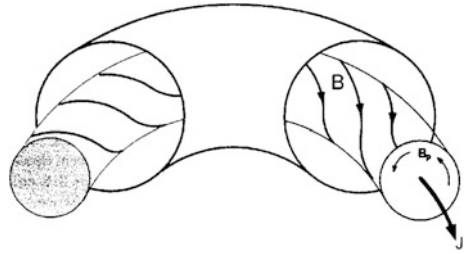
Fig. 1.10 A conventional stellarator (*top*) and a torsatron/heliotron (*bottom*)
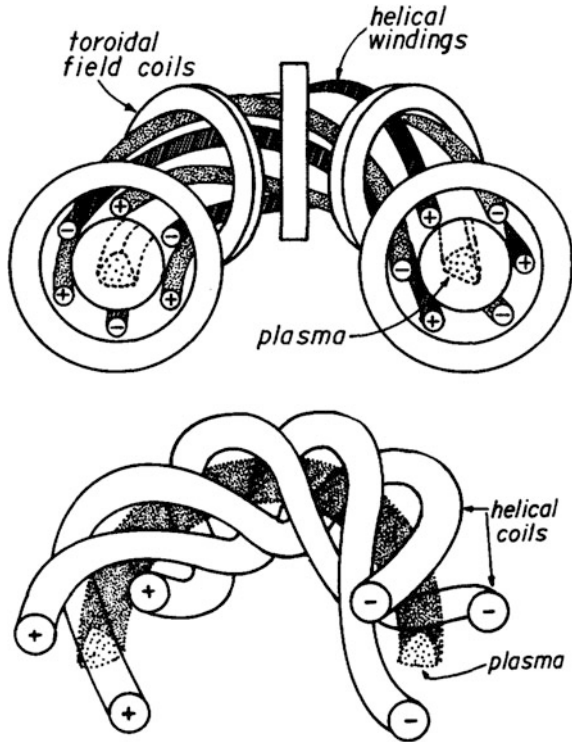
A magnetic field can hold the plasma in equilibrium (force balance). This **plasma equilibrium** must avoid **thermodynamic equilibrium**, where all components tend to arrive at the same temperature, since we need the plasma temperature $T > 10^8$ K (10 keV), while the wall temperature should remain <2,000 K (0.17 eV). The following 7 processes tend to bring the plasma towards the undesirable thermodynamic equilibrium:

- **Plasma flow along B**—in open magnetic systems or in "ergodic" (randomly oriented) magnetic field lines.
- **Plasma Drift** across the magnetic field, caused by electric fields, magnetic field gradients, magnetic field curvature, etc.

- **Heat Transport**—conduction and convection.
- **Radiation losses**—line radiation, bremsstrahlung radiation, and cyclotron radiation.
- **Magnetohydrodynamic (MHD) instabilities**—changes of plasma shape driven by gradients of pressure or current density.
- **Microinstabilities**—interactions of particles and waves that increase heat transport.
- **Charge exchange**—neutralization of hot ions by neutral atoms, allowing their escape.

These mechanisms are discussed in plasma physics texts (Chen 1984, Freidberg 2007, Kikuchi 2012) and will not be explained here. Fusion technology must develop confinement systems that can counteract all 7 loss processes simultaneously, using high-temperature, low-activation materials that can survive in the extreme reactor environment (Chaps. 6, 8).

1.2.5 Energy Gain Ratio Q

The "pressure" of a magnetic field in vacuum is

$$\text{Magnetic field pressure} = B^2/2\mu_o$$

where $\mu_o = 4\pi 10^{-7}$ H/m (H = Henry) is the permeability of free space. Units conversion factors are listed in Appendix A.

For example, a magnetic field B = 1 T (T = Tesla) provides a pressure of 4.0×10^5 Pa, which is roughly 4 atmospheres (Exercise: Check this calculation and verify that the units convert to Pa).

The ratio of plasma pressure to magnetic field pressure is called beta:

$$\beta = p/(B^2/2\mu_o) = 2\mu_o p/B^2 \tag{1.2}$$

High values of beta are good, because they maximize the plasma pressure that can be confined by a given magnetic field. Values of $\beta \sim$ 5–10 % are likely for fusion reactors.

The energy gain ratio, Q, of a pulsed fusion reactor is defined as

$$Q = (\text{fusion energy per pulse}) / (\text{input energy per pulse}).$$

If the reactor operates steady state, then

$$Q = (\text{fusion power}) / (\text{input power}).$$

A simplified analysis assuming parabolic profiles of density and temperature yields the following equation for Q:

$$Q \approx 5(nT\tau) / [5 \times 10^{21} - nT\tau] \tag{1.3}$$

Fig. 1.11 Energy gain ratio versus the "triple product" $nT\tau$
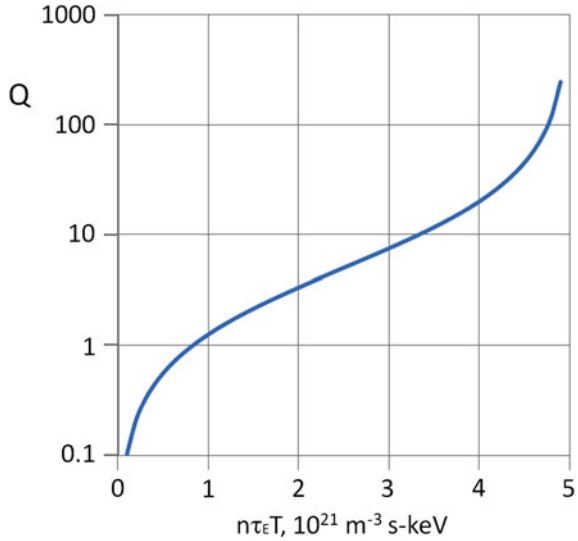
where n = DT fuel ion density (ions/m^3), T = fuel temperature (keV), and τ = energy confinement time (s). This equation, illustrated in Fig. 1.11, ignores the input power needed to sustain the plasma current in a tokamak.

A fusion reactor requires values of the "triple product" $nT\tau > 3 \times 10^{21}$ m^{-3} keV s.

The required triple product value can be accomplished by two general means:

- **Magnetic confinement** fusion: $n \sim 2 \times 10^{20}$ m^{-3}, $T \sim 15$ keV, $\tau \sim 1$ s.
- **Inertial confinement** fusion: $n \sim 2 \times 10^{29}$ m^{-3}, $T \sim 15$ keV, $\tau \sim 1$ ns.

1.2.6 Fusion Power Density

For a monoenergetic ion beam striking a target ion, the reaction rate is proportional to the effective "cross section" area σ of the target, measured in m^2. The reaction rate between monogenetic ions with speed v and density n_1 striking target ions of density n_2 is given by

$$\text{Reaction rate} = n_1 n_2 \sigma v \quad \text{reactions/m}^3 \text{ s.} \tag{1.4}$$

Some values of DT reaction cross sections are listed in Table 1.4.

Usually the ions are not monoenergetic, but are assumed to have Maxwellian velocity distributions characterized by a temperature T. Then the σv must be averaged over the velocity distribution function, and the average value is written $\langle \sigma v \rangle$.

The fusion power densities of a DT plasma (assuming $n_D = n_T = n/2$) and of a DD plasma are given by

$$P_{DT} = (1/4) \, n^2 \langle \sigma v \rangle W_{DT}$$

Table 1.4 DT fusion reaction cross sections, in "barns" versus incident deuteron energy

W (keV)	σ (barn)
0.2	7.15E − 39
0.3	3.90E − 31
0.4	1.53E − 26
0.7	2.42E − 19
1	9.90E − 16
4	1.13E − 06
7	1.51E − 04
10	1.71E − 03
14	1.13E − 02
20	6.00E − 02
26	1.71E − 01
35	4.81E − 01
50	1.40E + 00
65	2.69E + 00
80	3.97E + 00
95	4.79E + 00
104	4.98E + 00
110	5.00E + 00
120	4.88E + 00
135	4.48E + 00
150	4.00E + 00
180	3.10E + 00
220	2.25E + 00
280	1.49E + 00

(1 barn $= 10^{-28}$ m^2)
(Li et al. 2008, Table 3)

$$P_{DD} = (1/2)\ n^2 \langle \sigma v \rangle W_{DD} \qquad (1.5)$$

where $\langle \sigma v \rangle$ is the fusion reaction rate parameter (m^3/s) and $W_{DT} = 17.6$ MeV $= 2.82 \times 10^{-12}$ J per fusion reaction, and $W_{DD} \approx 3.65$ MeV $= 5.85 \times 10^{-13}$ J (average of the two branches in Table 1.3). The factor of ½ is needed to avoid counting the same DD reaction twice (Dolan 1982, Chap. 2).

The two branches of the DD reaction (DDn, DDp) have roughly equal probabilities. If the T and ^{3}He produced by these reactions are reacted with more deuterium, then the net reaction is

$$6D \rightarrow 2H\ +\ 2n\ + 2\left(^4He\right)\ + 43.2\ \text{MeV}. \qquad (1.6)$$
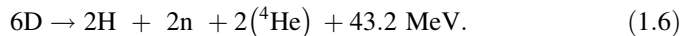
which is 7.2 MeV per deuteron. This is called the "catalyzed DD fuel cycle". The secondary reactions consume the 3He and T rapidly, compared with the slow rate of the primary DD reactions, so the fusion power density is limited by the DD reaction rate. Each primary DD reaction consumes 2 deuterons and leads to the rapid consumption of a third deuteron, so three deuterons are consumed at the DD reaction rate with the release of 21.6 MeV, and $W_{cat} \approx 21.6$ MeV $= 3.46 \times 10^{-12}$ J.

Example Problem 1.1: Energy from water How many deuterium atoms are there in one liter of water, and how much energy could they produce in a catalyzed DD reactor?

The number of water molecules is
N(water) = $\rho N_{av}/M$ = (1.0 g/cm^3) (1,000 cm^3/l) (6.02 × 10^{23} molecules/mole)/ (18 g/mole) = 3.34 × 10^{25} molecules.
Each water molecule contains two hydrogen atoms of which 1.53 × 10^{-4} are deuterium:

$$N(\text{deuterium}) = 2(3.34 \times 10^{25})\,1.53 \times 10^{-4} = 1.02 \times 10^{22} \text{ atoms.}$$

The energy released is

$$W = 1.02 \times 10^{22}(7.2\,\text{MeV})1.60 \times 10^{-13}\,\text{J/MeV} = 1.18 \times 10^{10}\,\text{J} = 11.8\,\text{GJ.}$$

The energy released by burning one liter of gasoline is about 33 MJ, so it would take about 360 l of gasoline to yield as much energy as one liter of water.

Some values of the reaction rate parameter are listed in Table 1.5. At 10 keV the DT reaction rate is almost 100 times greater that the DD reaction rate.
These data are shown graphically in Fig. 1.12.

Table 1.5 DT and DD fusion reaction rate parameters versus temperature

T (keV)	$\langle \sigma v \rangle_{DT}$ (m^3/s)	$\langle \sigma v \rangle_{DD}$ (m^3/s)	$\langle \sigma v \rangle_{D\text{-}3He}$ (m^3/s)
1	5.48E−27	1.52E−28	3.02E−32
1.5	5.89E−26	1.38E−27	1.32E−30
2	2.63E−25	5.42E−27	1.42E−29
3	1.71E−24	2.95E−26	2.75E−28
4	5.58E−24	8.47E−26	1.77E−27
5	1.29E−23	1.77E−25	6.66E−27
6	2.42E−23	3.09E−25	1.83E−26
8	5.94E−23	6.90E−25	7.96E−26
10	1.09E−22	1.21E−24	2.27E−25
15	2.65E−22	2.97E−24	1.27E−24
20	4.24E−22	5.16E−24	3.79E−24
25	5.59E−22	7.60E−24	8.18E−24
30	6.65E−22	1.02E−23	1.45E−23
40	8.03E−22	1.55E−23	3.23E−23
50	8.71E−22	2.08E−23	5.44E−23
60	8.97E−22	2.60E−23	7.82E−23
80	8.90E−22	3.60E−23	1.24E−22
100	8.49E−22	4.55E−23	1.61E−22
150	7.28E−22	6.75E−23	2.20E−22
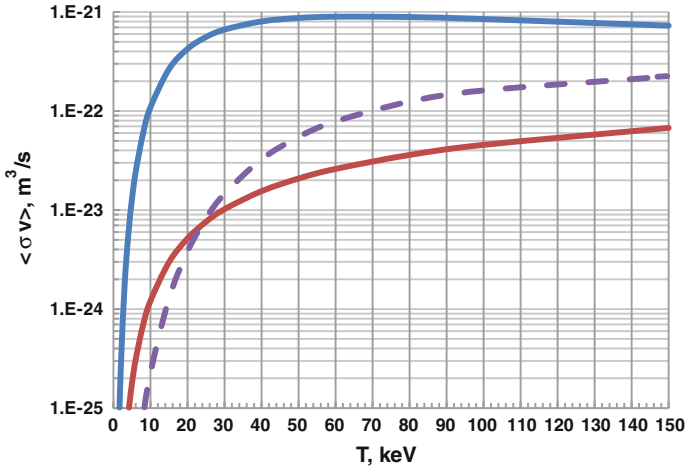
Fig. 1.12 Reaction rate parameters for DT reactions (*upper curve*), DD reactions (*lower curve*), and D-^{3}He reactions (*dashed curve*)

Example Problem 1.2: Fusion power density Estimate the fusion power density and pressure in a DT plasma with $n = 10^{20} \text{ m}^{-3}$ and $T = 20$ keV.

$$P_{DT} = (1/4)n^2\langle\sigma v\rangle W_{DT} = 0.25\left(10^{20} \text{ m}^{-3}\right)^2 4.24 \times 10^{-22} \text{ m}^3/\text{s}\, 2.82 \times 10^{-12} \text{ J}$$
$$= 3.0 \times 10^6 \text{ W/m}^3$$

The plasma pressure $p \approx 2nT = 2 \times 10^{20} \text{ m}^{-3}\, 1.60 \times 10^{-16} \text{ J/keV 20 keV} = 6.4 \times 10^5 \text{ Pa} = 6.3 \text{ atm}$.

A simple formula for the DT fusion reaction rate parameter is

$$\langle\sigma v\rangle \approx 5.1 \times 10^{-22}[\ln(T) - 2.1] \text{ m}^3/\text{s} \tag{1.7}$$

which has ± 6 % accuracy in the range $10 < T < 50$ keV.

The 3.54 MeV alpha particles (^{4}He nuclei) produced by DT fusion reactions can stay in the plasma and heat it up so much that alpha heating alone can sustain the plasma temperature. This self-sustainment, called "ignition", can occur when the triple product is high (when $Q \rightarrow \infty$ in Fig. 1.11).

Plasma Pressure

The optimum temperature for magnetic fusion is the temperature that maximizes the fusion power density (W/m^3) at a given plasma pressure. The total plasma pressure

$$p = \text{(sum of pressures of fuel ions + electrons + impurity ions)}$$
$$p = n_i T_i + n_e T_e + \sum n_z T_z \tag{1.8}$$

where n_i, n_e and n_z are the densities of fuel ions, electrons, and impurities; T_i, T_e and T_z are their temperatures (in units of Joules. 1 keV $= 1.60 \times 10^{-16}$ J); and Σ represents a summation over impurity species z. The impurities could be He, C, O, N, Fe, etc. The plasma will stay quasi-neutral, meaning that it will have equal densities of positive and negative charges. If there are few impurities, then $n_i \approx n_e$, which we will simply call n. If the electron and ion temperatures are equal, then

$$p \approx 2\,nT \tag{1.9}$$

where the temperature must be expressed in Joule to get pressure in Pa. If we solve Eq. (1.9) for n and plug this into Eq. (1.5), the fusion power density is

$$P_{DT} = (1/4)(p/2T)^2 \langle \sigma v \rangle W_{DT} \tag{1.10}$$

For a given plasma pressure the fusion power density is maximized by choosing the temperature where $\langle \sigma v \rangle / T^2$ is maximum.

Example Problem 1.3: Optimum temperature What temperature maximizes the DT fusion power density?

To find the maximum P_{DT}, we make a table of $\langle \sigma v \rangle / T^2$ versus T:

T (keV)	$\langle \sigma v \rangle$ (10^{-22} m³/s)	$\langle \sigma v \rangle / T^2$
5	0.129	0.0052
8	0.594	0.0093
10	1.09	0.0109
15	2.65	0.0118
20	4.24	0.0106
25	5.59	0.0089
30	6.65	0.0074
35	7.45	0.0061
40	8.03	0.0050

Thus, the optimum temperature is around 15 keV, and the fusion power density is

$$P_{DT} \approx 8.1 \times 10^{-6} p^2, \tag{1.11}$$

where p is the plasma pressure in Pa.

For catalyzed DD reactions the optimum is about 20 keV, and the attainable fusion power density is

$$P_{cat} \approx 2 \times 10^{-7} p^2. \tag{1.12}$$

Thus, at the same plasma pressure the DT fuel cycle can attain 40 times the power density of the catalyzed DD fuel cycle.

1.2.7 Reactor Power Balance

A toroidal coordinate system is shown in Fig. 1.13.

The toroidal coordinates are r, ϕ and θ. The angle ϕ measures in the **toroidal direction**, and the angle θ measures in the **poloidal direction**. At the plasma center $R = R_o$. The minor radius at the wall is r = a. The toroidal surface is perpendicular to the toroidal direction, and the poloidal surface is perpendicular to the poloidal direction. Magnetic field components perpendicular to the poloidal surface contribute to **poloidal flux**, and those perpendicular to the toroidal surface contribute to **toroidal flux** (Cylindrical coordinates for this figure would be R, ϕ, Z).

The plasma chamber is surrounded by a blanket and shield of thickness b and toroidal field coils with thickness c, as shown in Fig. 1.14. Current tokamaks are not circular in cross-section, but have a modified "D" shape.

A simplified estimate of the optimum values of a, b, and c from allowable physical parameters can be made as follows (Freidberg 2007).

Each neutron entering the blanket should breed at least one tritium atom, and the fluxes of neutrons and gammas must be attenuated to about 10^{-6} of the unshielded values. With current material properties, the required blanket + shield thickness

$$b \approx 1.2\,\text{m} \qquad (1.13)$$

Fig. 1.13 A toroidal coordinate system, showing the major radius R, minor radius r, toroidal angle ϕ, and poloidal angle θ
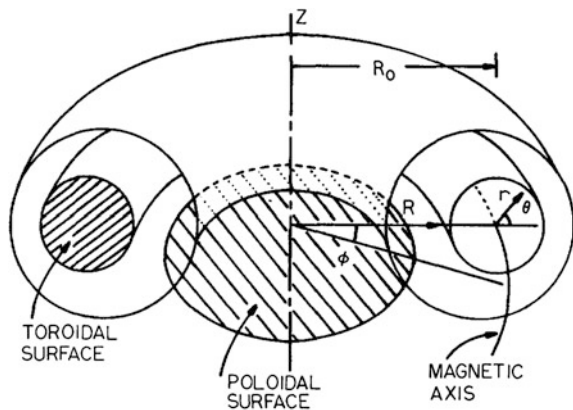
Fig. 1.14 Definitions of R_o plasma major radius, a wall radius, b thickness of blanket + shield, c magnet coil thickness, B_c maximum field at coil
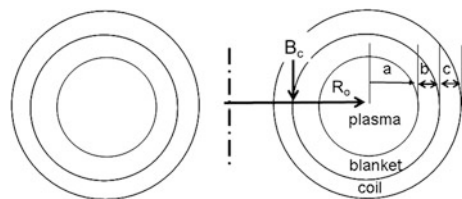
Approximating the torus by a cylinder with length $2\pi R_o$, the plasma volume and surface area are

$$V = 2\pi R_o \pi a^2 \tag{1.14}$$

$$S = 2\pi R_o 2\pi a \tag{1.15}$$

(The above approximations for circular cross sections would vary slightly for elliptical or D-shaped surfaces).

Since neutrons carry 80 % of the DT fusion power, the neutron power flux at the first wall (inner surface of the blanket that is facing the plasma) is

$$P_w = 0.8(\text{fusion power density})V/S \; (W/m^2) \tag{1.16}$$

Assuming that the thermal energy deposited in the blanket is converted into electricity with efficiency η_e and that nuclear reactions in the blanket add about 20 % to the thermal fusion power, the gross electrical power output is

$$P_E = 1.2\eta_e(\text{fusion power density})V \; (W) \tag{1.17}$$

From (1.15–1.18) we find

$$P_E = 3SP_w\eta_e/2 \tag{1.18}$$

The volume of the blanket + shield + coil (assuming circular cross sections) is

$$V_{bc} = 2\pi R_o \pi \left[(a+b+c)^2 - a^2\right] \tag{1.19}$$

To minimize the cost of electricity it is desirable to minimize

$$\begin{aligned}
V_{bc}/P_E &= 2\pi R_o \pi \left[(a+b+c)^2 - a^2\right]/(3SP_w\eta_e/2) \\
&= \left[(a+b+c)^2 - a^2\right]/3\eta_e aP_w
\end{aligned} \tag{1.20}$$

where we have used Eq. (1.16) for S. We can use a force balance to estimate the required coil thickness c in terms of the allowable coil stress σ_{max}. The result is

$$c = 2\xi(a+b)/(1-\xi) \tag{1.21}$$

where

$$\xi = B_c^2/4\mu_o\sigma_{max} \tag{1.22}$$

B_c is the field at the coil (Freidberg 2007). Using $B_c = 13$ T and $\sigma_{max} = 300$ MPa, we find $\xi = 0.112$, and

$$c = 0.252(a+b). \tag{1.23}$$

We insert this value of c into Eq. (1.20), then differentiate it with respect to a, and set the derivative = 0 to find what value of a minimizes V_{bc}/P_E. The result is

$$a = (1+\xi)b/2\xi^{1/2} = 2.0 \; m \tag{1.24}$$

(Freidberg 2007) and

$$c = 0.80 \text{ m}. \tag{1.25}$$

From Eq. (1.16) $S = 80R_o$. Then Eq. (1.19) with $\eta_e \sim 0.4$ and $P_w = 4 \text{ MW/m}^2$ yields

$$P_E \approx 192 \times 10^6 R_o \text{ W} \tag{1.26}$$

If the required electrical power $P_E = 1{,}000$ then the required value of major radius is

$$R_o \approx 5.2 \text{ m}. \tag{1.27}$$

If P_w were only 2 MW/m^2, then $R_o = 10.4$ m, and the reactor would be much bigger and more expensive (Freidberg 2007). This shows the importance of wall materials and cooling systems that can withstand high neutron power fluxes P_w.

In Eq. (2.8) in the next chapter we will see that the toroidal field is given by

$$BR = \mu_o NI/2\pi \tag{1.28}$$

where N = number of toroidal field coils and I = total current in each coil. Thus, BR is constant. Let B_o be the field at the plasma center R_o. The peak field $B_c \sim 13$ T at the coil is at $R_o - a - b$. Therefore,

$$B_o R_o = B_c(R_o - a - b) \tag{1.29}$$

$$B_o = 13(5.2 - 2 - 1.2)/5.2 = 5.0 \text{ T}$$

From Eqs. (1.14) and (1.15), $V/S = a/2$. Then from Eq. (1.16)

$$P_{DT} = P_w S/0.8V = P_w/0.4a = 5 \text{ MW/m}^3. \tag{1.30}$$

From Eq. (1.11)

$$p = \left(P_{DT}/8.1 \times 10^{-6}\right)^{1/2} = 7.86 \times 10^5 \text{ Pa}. \tag{1.31}$$

To confine this plasma then the required value of beta would be

$$\beta = 2\mu_o p/B^2 = 0.079 \tag{1.32}$$

If the plasma confinement system could not achieve this value of beta, then the reactor dimensions would have to be adjusted to satisfy all the requirements. If we want a high Q value from Fig. 1.11 we need at triple product value $nT\tau \approx 5 \times 10^{21}$ m^{-3} keV s. From this the required confinement time is

$$\tau \approx nT\tau/nT = 5 \times 10^{21}/\left(1.7 \times 10^{20} 15\right) = 2 \text{ s} \tag{1.33}$$

The purpose of this exercise is to show how the physical constraints, (neutron cross sections, allowable stress, B_{max}, P_w, and desired P_E) combined with a desire

Table 1.6 Effect of constraints on reactor parameters (based on Freidberg 2007)

Nuclear cross sections	Blanket-shield thickness	$b \approx 1.2$ m
B_{max} and stress limit	Coil thickness	$c \approx 0.8$ m
Cost optimization and η_e	Plasma minor radius	$a \approx 2$ m
Dimensions R_o and a	Plasma volume	$V \approx 410$ m^3
Desired electrical power and P_w	Major radius	$R_o \approx 5.2$ m
Maximization of fusion power density	Optimum temperature	$T = 15$ keV
Fusion power and volume	Fusion power density and plasma pressure	$P_{DT} \approx 5$ MW/m^3 $p \approx 0.8$ MPa
Plasma pressure and temperature	Required plasma density	$n \approx 1.7 \times 10^{20}$ m^{-3}
Plasma pressure and B	Desired value of β	$\beta \approx 8$ %
High-Q triple product	Required value of τ	$\tau \approx 2$ s

to minimize the ratio of V_{bc}/P_E, determine the required dimensions a, b, c, and R_o, plasma parameters, confinement quality β and confinement time τ of a toroidal magnetic fusion reactor. It would be difficult to do better unless we could use a thinner blanket + shield b, a higher coil field B_c and coil stress σ_{max}, a higher neutron wall load P_w, or achieve higher values of η_e, β, or τ. Fusion technology strives to optimize these parameters by clever design and materials development (Table 1.6).

1.2.8 Effect of Impurities

The plasma must remain quasineutral, because slight imbalances of positive and negative charges would result in large voltages (according to the Poisson Equation of electrostatics), which would restore neutrality. For example, if some electrons left, a positive voltage would develop to pull back electrons and push out positive ions. The resulting **Quasineutrality Condition** is

$$n_e = n_H + \sum_z n_z \langle Z \rangle \; \left(m^{-3} \right) \tag{1.34}$$

where n_H = density of hydrogen ions (including deuterium and tritium), n_z = impurity ion densities, $\langle Z \rangle$ = effective charge of impurity species n_z, and the summation is over all impurity species. For example, if carbon is fully ionized $\langle Z \rangle = 6$. (The values of $\langle Z \rangle$ are given as functions of electron temperature in Fig. 11.25.)

Dividing by n_e and rearranging, the hydrogen ion fraction is

$$f_H = 1 - \Sigma f_z \langle Z \rangle \tag{1.35}$$

where $f_H = n_H/n_e$, and $f_z = n_z/n_e$.

Example Problem 1.4: DT Fuel Dilution If a DT plasma contains 4 % of fully stripped oxygen impurity, by how much are the density of the DT fuel and the fusion power density reduced?

From Eq. (1.35) we find $f_H = 1 - 0.04\,(8) = 0.68$.

Since the fusion power density is proportional to n_H^2, it would be reduced to $(0.68)^2 = 46\,\%$ of its value in a pure DT plasma. Thus, it is vital to minimize the accumulation of impurities (In some sections the symbol n_i will represent hydrogen ion density, instead of n_H).

1.2.9 Ignition

A zero-dimensional representation of plasma power balance is

$$\text{Energy gain} = (\text{external heating}) + (\text{alpha heating}) - (\text{convection} + \text{conduction}) - \text{radiation}$$

$$1.5(\partial p/\partial t) = P_{ext} + P_\alpha - 1.5p/\tau_E - P_{rad}$$

$$(1.36)$$

where $P_{ext} = (\text{ohmic} + \text{radio wave} + \text{microwave} + \text{neutral beam injection})$, $P_\alpha = 0.2P_{DT}$ is the alpha heating power density, and τ_E is defined to account for energy losses by convection and conduction.

Using Eqs. (1.10), (1.36) may be written

$$1.5(\partial p/\partial t) = P_{ext} + 0.2(p/4KT)^2\langle\sigma v\rangle W_{DT} - 1.5p/\tau_E - P_{rad} \qquad (1.37)$$

This shows how fast the plasma energy density is increasing or decreasing. If the alpha heating power exceeds the power losses, the plasma can sustain its temperature without external heating, and the external heating may be turned off (unless it is needed to sustain a plasma current). This is the **Ignition Condition**, which may be represented mathematically as

$$0.2(p/4KT)^2\langle\sigma v\rangle W_{DT} \geq 1.5p/\tau_E + (p/2KT)^2\Sigma f_k Q_k \qquad (1.38)$$

where Eq. (11.28) has been used for the radiation term, and Q_k is a "radiation power parameter" (Sect. 11.6). Solving for $p\,\tau_E$ we find

$$p\tau_E \geq 24(KT)^2/(0.2\langle\sigma v\rangle W_{DT} - 4\Sigma f_k Q_k) \qquad (1.39)$$

This quantifies the energy confinement time required to achieve ignition.

Example Problem 1.5: Ignition Condition Consider a DT plasma with T = 15 keV, with 1 % oxygen impurity, $f_{oxy} = n_{oxy}/n_e = 0.01$. Assume $Q_{oxy} = 1.7 \times 10^{-34}$ Wm^3, $Q_H = 2 \times 10^{-36}$ Wm^3. What energy confinement time is required for ignition?

From quasineutrality, $f_H = n_H/n_e = 0.92$. At 15 keV $\langle\sigma v\rangle = 2.65 \times 10^{-22}\,\mathrm{m}^3/\mathrm{s}$. From Eq. (1.39) we find

$$p\tau_E \geq 1.0 \;\mathrm{MPa\,s} \;= 10\,\mathrm{atm\,s}$$

to achieve ignition.

Ignition is desirable, but not absolutely necessary. One could operate a reactor with $Q = 30$ and produce electricity well without ignition.

1.3 What Experiments are Being Conducted?

The main types of magnetic confinement fusion experiments are tokamaks, stellarators, reversed field pinches (RFP), spheromaks, field reversed configurations (FRC), and magnetic mirrors.

1.3.1 Tokamaks

Figure 1.15 shows a simplified diagram of tokamak coils.

The pulsed CS coil induces a high toroidal current in the plasma, which generates a poloidal magnetic field. The combination of the poloidal and toroidal fields gives the resultant magnetic field lines helical shapes, Fig. 1.9. Since the CS coil is pulsed, long-term operation requires the plasma current to be sustained by other non-inductive means, such as by high-power radio waves, microwaves, or neutral beam injection. This input power limits the attainable Q values.

Parameters of some large tokamaks are listed in Table 1.7.
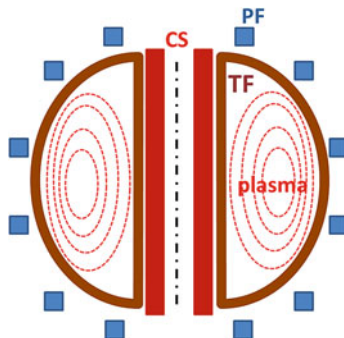
Fig. 1.15 Tokamak coil systems. The D-shaped toroidal field (*TF*) coils provide the toroidal field (as in Fig. 1.8). The central solenoid (*CS*) is pulsed to induce the plasma toroidal current J (as in Fig. 1.9). The poloidal field (*PF*) coils control the plasma shape and position. The *dashed ellipses* represent magnetic flux surfaces of the plasma

Table 1.7 Some large tokamaks

	D III-D	JT-60	JET	ITER
Location	San Diego, USA	Naka, Japan	Culham, UK	Cadarache, France
R_o, m	1.66	3.4	2.96	6.2
a, m	0.67	1	0.96	2.0
B, T	2.2	4.2	4	5.3
Current I, MA	3	5	6	15
Electron cyclotron heating (ECH) MW	6	4	–	20
Ion cyclotron heating (ICH) MW	5	10	12	20
Neutral beam injection (NBI) MW	20	40	24	39
Lower hybrid waves (LH) MW	–	8	7	0
Main achievements	$\beta > 12\ \%$	Long pulses ~ 28 s equivalent Q > 1. Being upgraded	P(DT) = 15 MW Be walls	Expect $Q \sim 10$

R_o and a are defined in Fig. 1.12 (Additional data may be found at www.tokamak.info)

With DT fuel the JET device produced 22 MJ of fusion energy in 4 s (average thermal power of several MW). The ITER experiment (originally called the "International Thermonuclear Experimental Reactor"), is under construction in France.

Tokamaks with low "aspect ratio" R_o/a $\sim$ 1.5 are called "spherical tokamaks". The largest spherical tokamaks are the National Spherical Torus Experiment (NSTX) in the USA and the Meg-Ampere Spherical Tokamak (MAST) in the UK, Fig. 1.16.

Both NSTX and MAST have R_o = 0.85 m, a = 0.65–0.68 m, plasma current > 1 MA, toroidal magnetic field $\approx$ 0.5 T, and several MW of auxiliary heating power. ELM mitigation physics for ITER is an important part of the MAST programme, NSTX has a close-fitting chamber with the coils outside, and MAST has a large chamber with the coils inside. These experiments have demonstrated higher beta values (ratios of plasma pressure to magnetic field pressure) than conventional tokamaks, which usually have higher aspect ratios (R_o/a $\sim$ 2.5 − 5).

1.3.2 Stellarators

The Large Helical Device (LHD) at the National Institute for Fusion Science in Japan is a heliotron with two superconducting windings, shown in Fig. 1.17.

The Wendelstein 7-X stellarator under construction in Greifswald, Germany, has many modular coils, as shown in Fig. 1.18.
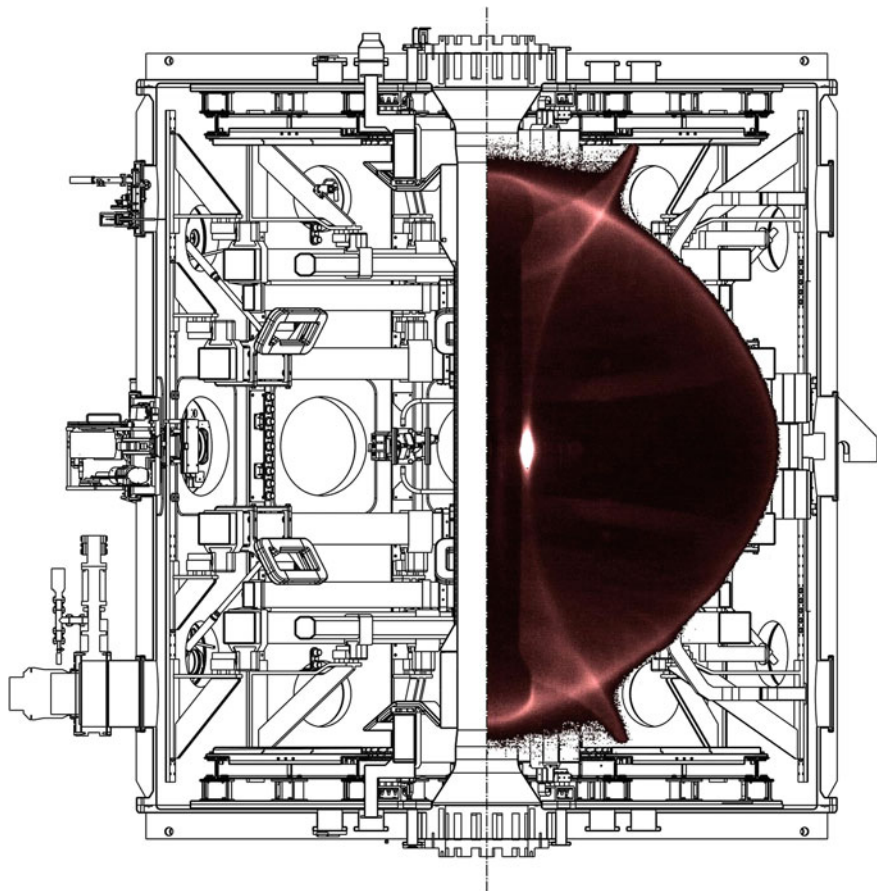
Fig. 1.16 The MAST experiment with an improved divertor and two of the edge localized mode (*ELM*) mitigation coils shown on the *left* (the small rounded rectangles about 45° above and below the midplane). Courtesy of Culham Laboratory, United Kingdom Atomic Energy Authority (UKAEA)

The superconducting magnet coils will be discussed further in Chap. 4. Table 1.8 shows the parameters of these two experiments.

LHD achieved a peak electron density n $\sim$ 5 $\times$ 10^{20} m^{-3}, at T_e = 0.85 keV (Morisaki et al. 2007), and T_i $\sim$ 5 keV at n $\sim$ 2 $\times$ 10^{19} m^{-3} (Yokohama et al. 2008).

In addition to tokamaks and stellarators, other alternative magnetic confinement schemes are being studied, including spheromaks, field reversed configurations, tandem mirrors, pinches, rotating plasmas, magnetized target fusion, and internal rings (Dolan 1982; Braams and Stott 2002; Chen 2011).
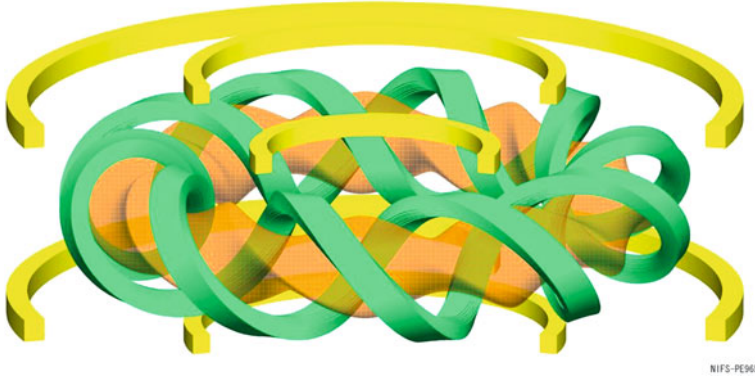
Fig. 1.17 Helical coils (*green*) of LHD with $\ell = 2$ helical coils, m = 10 field periods; vertical field coils (*yellow*); and plasma shape (*orange*). © National Institute for Fusion Science, Toki, Japan

Fig. 1.18 The plasma and modular coils of W 7-X stellarator (Courtesy of Lutz Wegener, Max-Planck Institut für Plasmaforschung, Greifswald, Germany.)
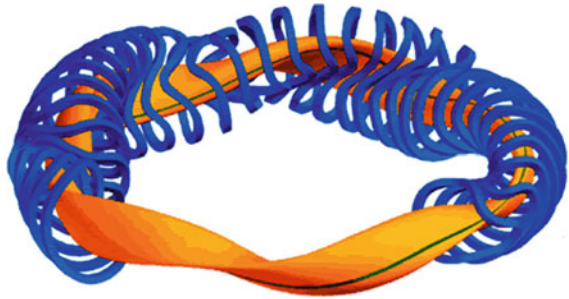
1.3.3 Reversed Field Pinches (RFP)

The toroidal field of a reversed field pinch is positive in the plasma core and negative at the edge, Fig. 1.19.

This causes the direction of the helical field to reverse, Fig. 1.20.

The tokamak requires a strong toroidal field to prevent instabilities. The reversed field pinch can be stable at lower toroidal fields, because the strong gradient of the field produces a strong "magnetic shear" (change of magnetic field direction from one layer to the next) that helps prevent instabilities.

Both RFPs and spheromaks tend towards a "Taylor minimum energy state" characterized by the equation

$$\mu_o \mathbf{J} = \nabla \times \mathbf{B} = k\mathbf{B} \tag{1.40}$$

where k is a constant (Taylor 1984).

The toroidal plasma current produces a poloidal magnetic field. As the plasma moves toward the minimum energy state a "dynamo effect" adjusts the magnetic

Table 1.8 Parameters of LHD and W 7-X

	LHD	W 7-X
Location	Toki, Japan	Greifswald, Germany
R, m	3.5–3.9	5.5
a, m	0.6	0.53
B, T	2–3	3
Number of helical coils	2	50 modular coils
ECH, MW	2	10
NBI, MW	15	5
ICRH, MW	3	3
Pulse length, s	$>10^3$ s at low density	1,800
$nT\tau$ m^{-3}keV s	4.4×10^{19}	Under construction

R_o and a are defined in Figs. 1.10, 1.11

Fig. 1.19 Reversal of the toroidal field direction at the edge of an RFP
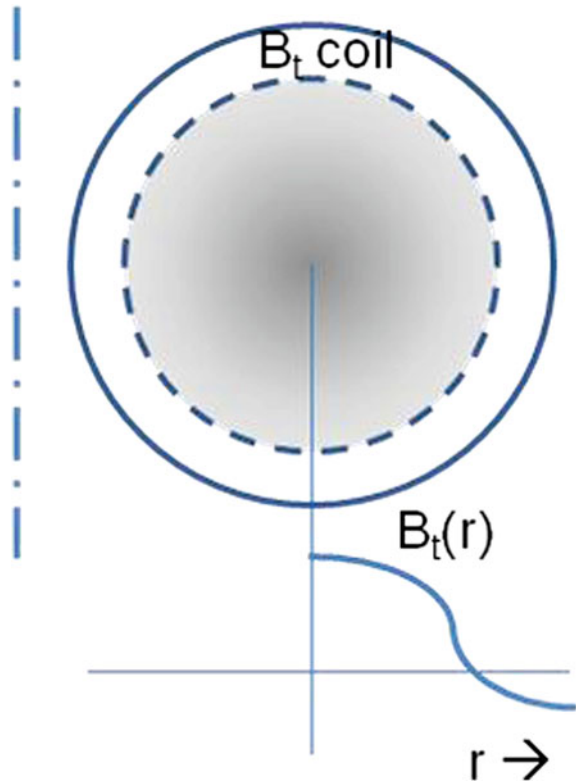
fields to sustain the edge toroidal field reversal, but the dynamo causes turbulence, which limits the energy confinement time. RFP plasmas typically have a turbulent inner region with relative flat density and temperature profiles, a high-shear region that sustains the pressure gradient, and an edge region dominated by atomic collisions and wall interactions.

Fig. 1.20 The helical field lines in an RFP. The spiral on the outside is in the opposite toroidal direction, because the toroidal field is in the opposite direction (Chen 2011, Fig. 10.30)
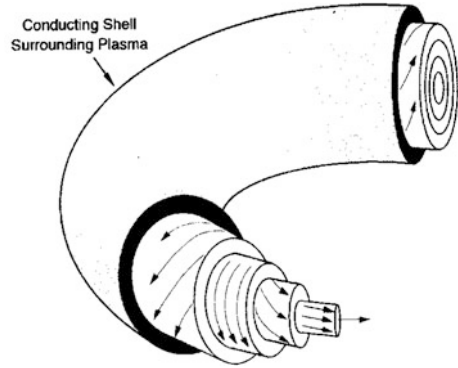
The Reversed Field Experiment RFX experiment in Padua, Italy, with $R = 2$ m, $a = 0.46$ m, has achieved plasma current $I \sim 0.7$ MA, $n_e \sim 6 \times 10^{19}$ m^{-3}, and $T_e \sim 0.25$ keV. The Madison Symmetric Torus (MST) experiment at the University of Wisconsin has achieved $I \sim 0.6$ MA, $T_e \sim T_i \sim 1.5$ keV, $n \sim 10^{19}$ m^{-3} for a duration of 12 ms at $\beta = 0.10$. A maximum beta of $\beta = 0.26$ has been achieved in the MST with a lower current and higher density (Chapman et al. 2010).

1.3.4 Spheromaks

Spheromaks are a naturally stable configuration based on Eq. (1.40). Figure 1.21 shows the magnetic surfaces.

Spheromaks can be produced by a theta pinch (a one-turn coil with high azimuthal current), by pulsed flux cores (circular tubes containing both toroidal and poloidal field coils), and by "helicity injection" (driving current along a magnetic

Fig. 1.21 The magnetic fields of a spheromak. There are no toroidal field coils (Chen 2011, Fig. 10.18)
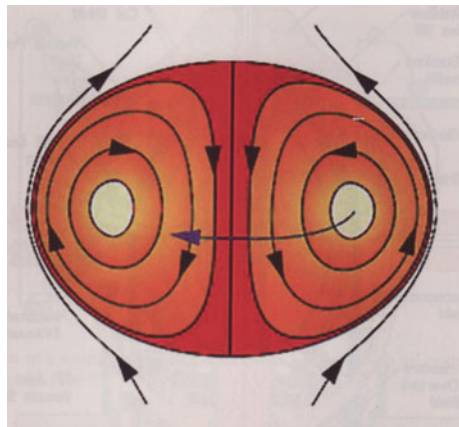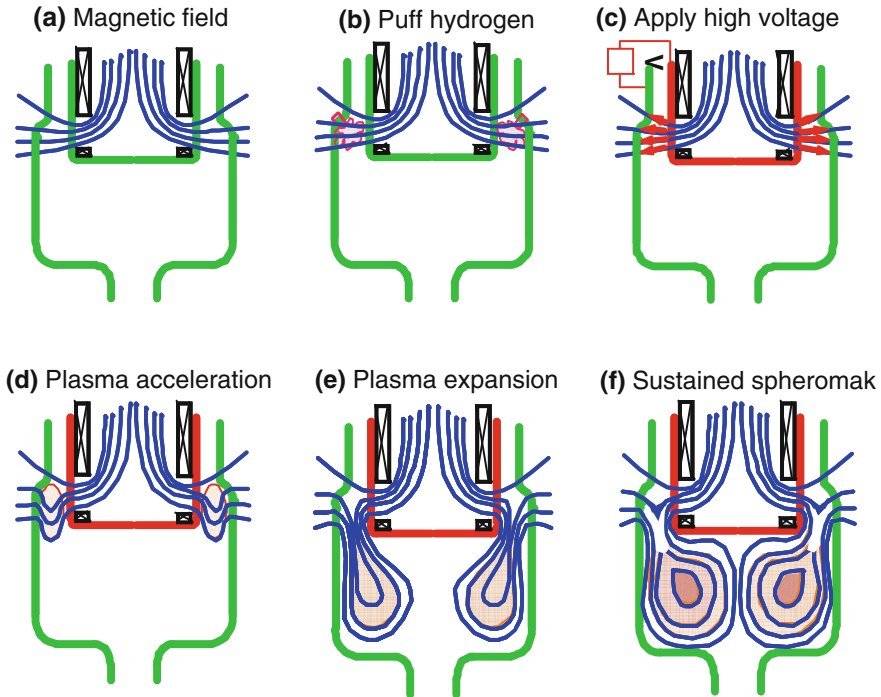
Fig. 1.22 Spheromak formation by a coaxial plasma gun. **a** The magnetic field is established. **b** A puff of gas is admitted by the electrodes. **c** High voltage induces a current along the magnetic field lines. **d** The JxB force pushes the plasma downward. **e** The plasma expands to fill the conducting chamber. **f** The magnetic field lines reconnect to form closed toroidal flux surfaces, and the spheromak plasma decays slowly as the magnetic field diffuses into the flux-conserving shell (usually copper). Courtesy of Lawrence Livermore National Laboratory (LLNL), California

surface in the plasma). Formation by helicity injection using a coaxial plasma gun is illustrated in Fig. 1.22. Section 5.11.8 discusses helicity injection current drive.

The Sustained Spheromak Physics Experiment (SSPX) at LLNL had $R/a = 0.31/0.17$ m, $I_{gun} = 400$–600 kA, $I_{tor} = 600$ kA, $B_p = 0.3$–0.6 T, duration ~ 4 ms, $n \sim 10^{20}$ m^{-3}, $T_e = 300$–500 eV, $\beta \leq 5$ % (Wood et al. 2009). The planned installation of neutral beam heating to extend the current pulse was cancelled by funding cutoff.

The Helicity Injected Torus HIT-SI experiment at the University of Washington produces a small spheromak plasma by magnetic induction in external loops, which helps to avoid contamination by impurities from electrodes. Operating parameters were $a = 0.25$ m, $R_0/a = 1.0$, $I_{tor} = 55$ kA, $I_{inj} = 18$ kA, $n = 2.5 \times 10^{19}$ m^{-3}, $B = 0.044$ T, $T_e = 6$ eV in strong agreement with the theoretical model. A recent breakthrough in this experiment is the discovery of a new current drive method, termed the Imposed Dynamo Current Drive (IDCD). This mechanism eliminates the need for inefficient conventional current drives, such as RF or
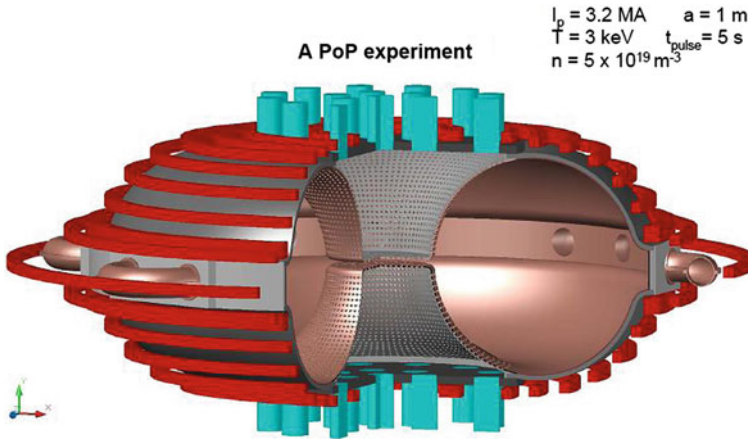
Fig. 1.23 A proof of principle experiment to demonstrate IDCD. Copper tube loops are injectors, and poloidal field coils are shown in *red*. Drawing by John Rogers (Jarboe et al. 2012b)
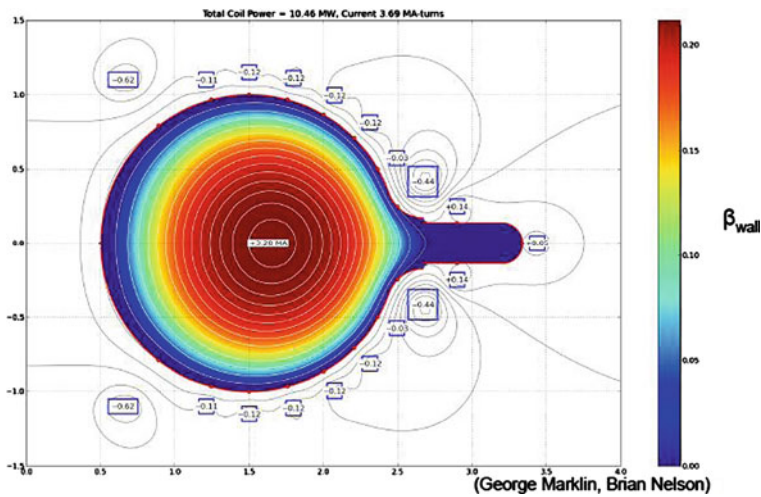
Fig. 1.24 Beta contours of the IDCD experiment relative to the magnetic pressure at the wall. Maximum beta is 16 % (Jarboe et al. 2012b)

neutral beam injection, and would reduce the complexity of a reactor design (Jarboe et al. 2012a). Figures 1.23 and 1.24 show a proposed "Proof of Principle" experiment to demonstrate good confinement.

If successful, this concept could lead to economical fusion power.
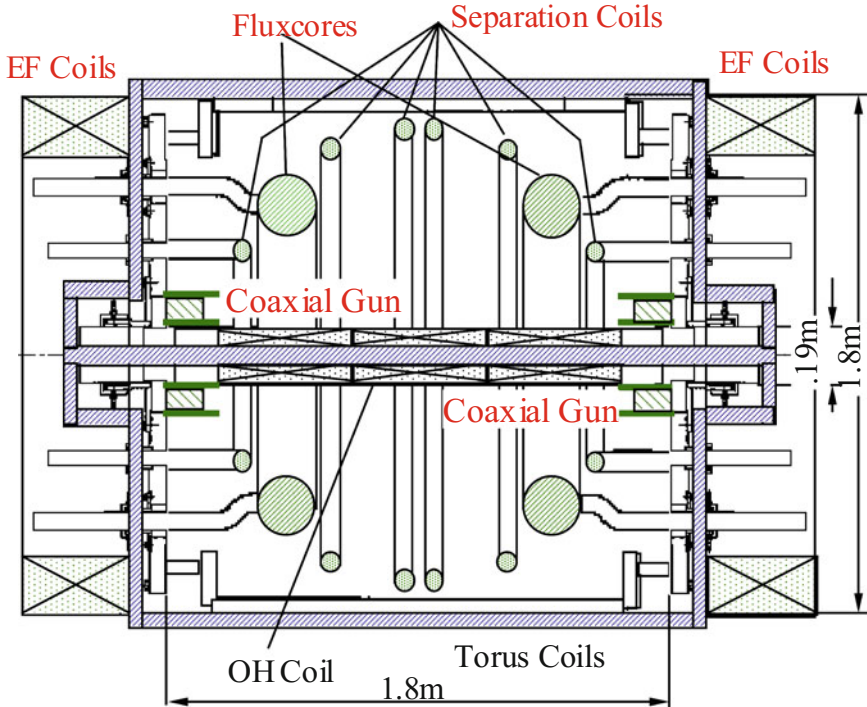
Fig. 1.25 The TS-4 experiment at the University of Tokyo (Courtesy of Y. Ono, University of Tokyo.)

1.3.5 Field Reversed Configurations (FRC)

Field reversed configurations have only poloidal magnetic field. They can be produced by theta pinches, by merging spheromaks with oppositely directed toroidal fields, and by rotating magnetic fields.

The TS-4 device, Fig. 1.25, has R_o = 0.4–0.55 m, R_o/a = 1.2–1.9, toroidal field $B_t \sim$ 0.3–0.5 T, and plasma current up to 300 kA.

It can produce spheromaks, FRCs, RFPs, or spherical tokamaks, depending on how the magnetic fields are actuated. Figure 1.26 shows how two spheromak plasmas can be merged.

The oppositely-directed toroidal fields annihilate each other during merging, and the result is an FRC with a weak or zero toroidal field. The toroidal field annihilation transfers some of the magnetic field energy into ion heating.

Figure 1.27 compares the spheromak and FRC configurations.

Spheromaks and FRCs are naturally stable plasma configurations that do not require a center post or strong external magnetic fields. The experiments so far have been small, so they have not attained high plasma parameters. They must be carefully shaped to avoid instabilities, like tilting, and they tend to have short

Fig. 1.26 Merging of two spheromaks. (Courtesy of Y. Ono, University of Tokyo)
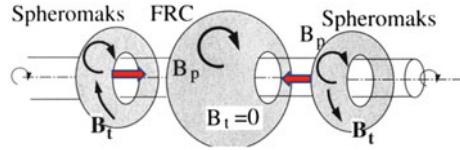
Fig. 1.27 Comparison of spheromak and FRC plasmas (Woodruff et al. 2010)
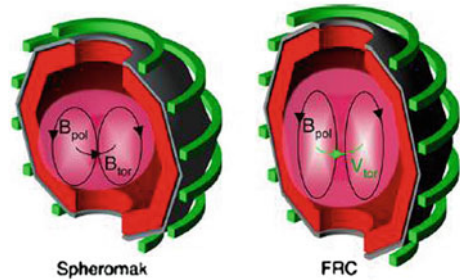
energy confinement times, which may be associated with impurities and turbulence. Larger experiments will be required to test these concepts adequately.

FRC plasmas may be compressed up to ignition temperature using metallic flux conservers that are squeezed by pulsed magnetic fields, by chemical explosives, or by high-pressure fluids. Such "Magnetized Target Fusion" (MTF) experiments are underway in the USA, Canada, and Russia.

General Fusion Company, Canada, will inject a liquid PbLi vortex radially inwards at a velocity up to 2,600 m/s to compress an FRC plasma radius by almost a factor of 10, raising the density to 1.2×10^{26} m^{-3} and temperature to 25 keV (pressure = 470 GPa). The plasma burn will release 700 MJ of energy in 6.9 μs, yielding an energy gain Q = 5.9. Figure 1.28 shows the pistons that force PbLi into the central chamber at high velocities.

Fig. 1.28 Acoustically driven magnetized target fusion. The plasma injector at the top sends an FRC plasma down into the center of the chamber. The pistons drive jets of PbLi radially inwards to compress the plasma (LaBerge 2012)
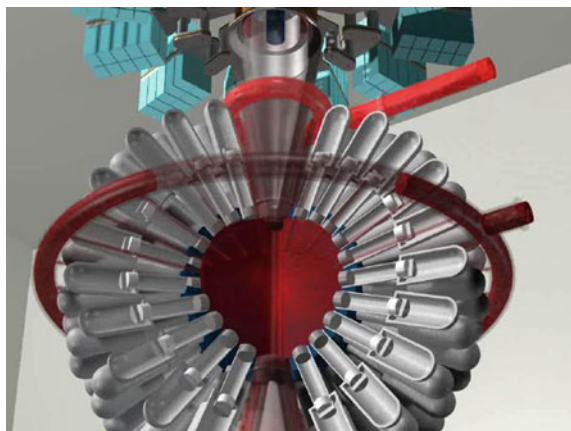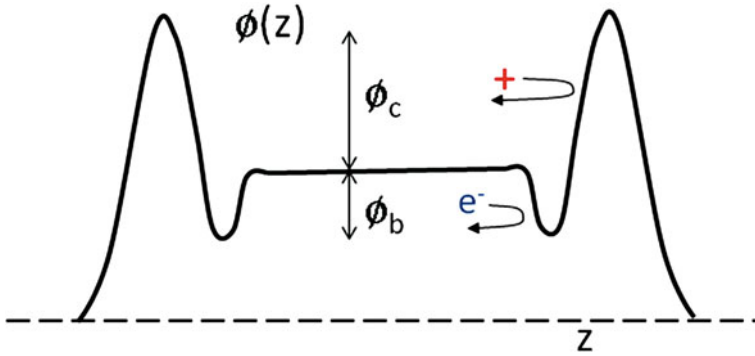
Fig. 1.29 Electrostatic potential versus axial position in a tandem mirror

1.3.6 Magnetic Mirrors

Due to rapid particle loss along the magnetic field lines a simple magnetic mirror can only achieve a power gain ratio $Q \sim 1$, which is inadequate for a power plant. This loss can be reduced by creating an electrostatic potential variation along the magnetic field with hills and valleys, as illustrated in Fig. 1.29.

The positive peaks ϕ_c confine ions in the central cell, and the negative wells ϕ_b confine electrons. The plasma density, temperature and electrostatic potential in tandem mirrors can be controlled by injection of neutral atom beams, by electron cyclotron resonance heating (ECRH), and by radiofrequency (RF) wave heating at selected axial locations. Such electrostatic potential control could make it possible to reduce the required length of a power plant with $Q \sim 10$ from kilometers to less than 200 m. There have been tandem mirror experiments in Japan, Russia, Korea, and the USA. Many ideas for improving mirror performance have been proposed, such as an axisymmetric tandem mirror, but funds for testing them have not been available (Simonen et al. 2008).

In addition to the above concepts, other alternative magnetic confinement schemes are being studied, including internal rings, rotating plasmas, and Z-pinches. Kikuchhi et al. (2012) provide a thorough reference on the physics of fusion research.

1.3.7 Inertial Confinement Fusion

Figure 1.30 illustrates an inertial confinement fusion reactor.

Lasers or heavy ion beams would compress small target pellets (~ 5 mm diameter) containing DT fuel to 1,000 times liquid density, igniting thermonuclear explosions. This would be done several times per second in a large blast chamber to generate neutrons and heat, which could be used to generate electricity, to breed fissile fuel, or to incinerate long-lived radioisotopes in used fission reactor fuel.

Fig. 1.30 An inertial confinement fusion reactor
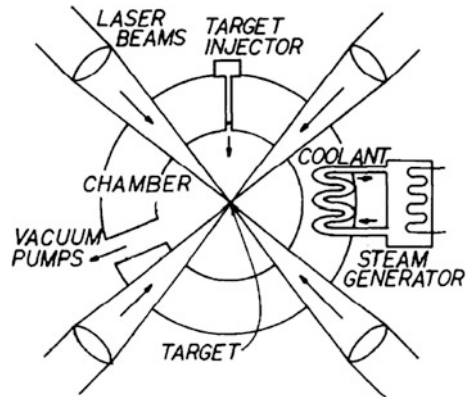
The National Ignition Facility (NIF) in the USA has 192 laser beams producing a total of 1.8 MJ of laser energy. Rayleigh–Taylor instabilities (growing wrinkles on the target shell) can spoil compression, so the target must be very smooth and spherical, and the laser pulses must be precisely aimed and shaped in time. The Laser MegaJoule (LMJ) facility in France and the Institute for Laser Engineering at Osaka University, Japan, are also conducting similar high-power experiments. In 2013 the NIF was close to achieving "break-even" ($Q \geq 1$), meaning that the fusion energy released would exceed the incident laser beam energy. Heavy ion beams could also be used instead of laser beams.

A fuller description of inertial confinement fusion is beyond the scope of this book, except for a brief mention in hybrid reactors, Chap. 14. Additional information can be found in the references (IAEA 1995; Atzeni and Meyer-Ter-Vehn 2004; Theobald et al. 2008; Moses et al. 2009; NAS 2012).

1.4 What has been Accomplished?

The book "Nuclear Fusion—Half a Century of Magnetic Confinement Fusion Research" (Braams and Stott 2002) provides a historical narrative. A few highlights will be cited here.

In the 1920s, Irving Langmuir studied gas discharges and coined the term "plasma". Sir Oliver Lodge noted that fusion of hydrogen into helium might occur in stellar interiors, and these reactions might ultimately be used on earth as energy sources (Lodge 1924; Dolan 1982).

In the 1930s W. H. Bennett derived equations for a plasma pinch, and L. D. Landau predicted collisionless damping of plasma waves by particles with velocities near the wave phase velocity.

In the 1940s a few labs began experiments on plasma confinement, and scientists were considering ways of building fusion reactors, such as a patent by G. P. Thomson and M. Blackman.

In 1950 Oleg Aleksandrovich Lavrentyev, a self-educated Soviet soldier on Sakhalin Island (north of Japan), wrote to Stalin saying that he knew how to make a hydrogen bomb and also a fusion reactor for power generation using electrostatic fields. His letter stimulated Andrei Dmitrievich Sakharov and Igor Yevgenyevich Tamm to consider using magnetic fields for plasma confinement, and Igor V. Kurchatov began the Soviet fusion research program.

In the 1950s, several countries began fusion research experiments, using linear plasma pinches, toroidal pinches, magnetic mirrors, and stellarators. In 1958 the Second United Nations Conference on the Peaceful Uses of Atomic Energy, Geneva, Switzerland, was the first international conference dealing with fusion research, which had previously been classified information in most countries. Most experiments failed, due to plasma impurities and instabilities. The large Model C Stellarator at Princeton had anomalously high plasma energy loss rates consistent with "Bohm diffusion". Reports of thermonuclear neutrons from experiments like the Zeta toroidal pinch in England turned out to be erroneous—the neutrons had resulted from plasma instabilities.

In 1961 Soviet physicist M. S. Ioffe reported a way to stabilize plasma in magnetic mirrors by adding a hexapole magnetic field, but the predicted Q value was still too low for economical power production.

At the Novosibirsk conference in 1968 L. A. Artsimovich announced that the Soviet scientists had achieved $T_e \sim 1$ keV, and $\tau \sim 2$ ms, which far exceeded the Bohm diffusion values, in their T-3 "Tokamak," which is an acronym for the Russian words meaning "toroidal chamber with magnet coils". Then many laboratories around the world began studying tokamaks, and the Princeton Plasma Physics Lab quickly converted its Model C Stellarator into a tokamak.

Since 1970 many countries have built tokamaks, and the world total in 2009 was 205, with about 35 still operating (www.tokamak.info). The achieved fusion triple product values have increased by many orders of magnitude, as shown in Fig. 1.31.

This gradual improvement of the fusion triple product is similar to improvement of semiconductors ("Moore's Law") and high-energy accelerators, as shown in Fig. 1.32. ITER should demonstrate high values of the triple product in about 2027.

The Large Helical Device has achieved beta = 5 % and plasma confinement that is as good as in tokamaks of similar size.
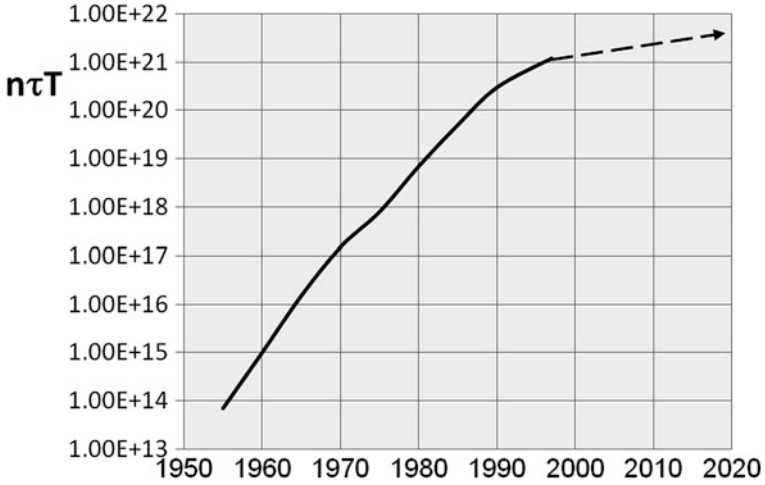
Fig. 1.31 Product $n\tau_E T$ (m^{-3}s-keV) attained by tokamak experiments versus year. The *dashed arrow* points to planned ITER values (Bolt 2007)
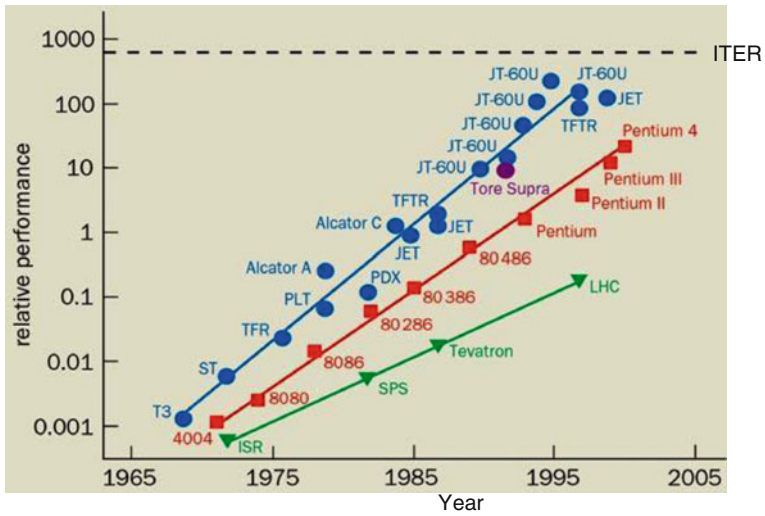
Fig. 1.32 Improvement of fusion triple product, semiconductor electronics, and high energy accelerators (Courtesy of J. B. Lister. Centre de Recherches en Physique des Plasmas, Ecole Polytechnique Federale de Lausanne)

1.5 What are the Future Plans?

1.5.1 International Cooperation

Many fusion research activities involve international cooperation, including

- International journals
- International conferences
- Exchanges of scientists
- Equipment transfers. For example, plasma confinement devices from Russia, Germany, Switzerland, and the USA, have gone to China, Latin America, Korea, and Sweden
- Joint experiments, like ITER and IFMIF (described below).

The International Atomic Energy Agency (IAEA), a United Nations Agency in Vienna, Austria, holds biennial Fusion Energy Conferences attended by over 500 scientists. The IAEA organizes about 5 technical meetings per year on specific topics, such as current drive. It also organizes Coordinated Research Projects lasting about 3 years involving 5–10 countries, and hosts research coordinating meetings for those projects. It publishes many technical documents related to fusion research and provides assistance to developing countries.

The International Energy Agency (IEA), part of the Organization for Economic Cooperation and Development (OECD) in Paris, organizes international cooperation in the following technology areas:

- ASDEX-Upgrade
- Environmental, Safety and Economic Aspects of Fusion Power
- Fusion Materials
- Large Tokamaks
- Nuclear Technology of Fusion Reactors
- Plasma Wall Interaction in TEXTOR
- Reversed Field Pinches
- Spherical Tori
- Stellarator Concept.

1.5.2 ITER

The ITER Project (originally called the "International Thermonuclear Experimental Reactor") was proposed at meetings between French President Francois Mitterrand, Soviet Premier Mikhail Gorbachev, and US President Ronald Reagan in 1985. The Conceptual Design was done by an international team (USSR, Japan, Europe, USA) from 1988 to 1992, followed by the Engineering Design from 1992 to 1998, which was conducted at three different sites (Naka, Japan; Garching, Germany; San Diego, USA). Construction was then deferred, due to financial

Table 1.9 Reduction of ITER parameters

	Ignition 1998	"High-Q" 2005
Q	∞ (Ignition)	10
P_f, MW	1,500	400
Burn, s	1,000	400
R/a, m	8.1/2.8	6.2/2.0
I, MA	21	15
B_ϕ, T	5.7	5.3
# TF coils	20	18 → ripple problem

Courtesy of ITER Organization
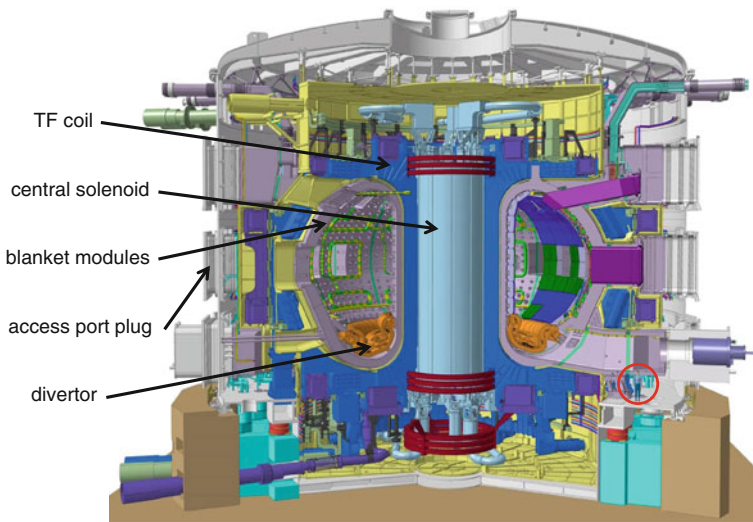
Fig. 1.33 Main components of ITER. A person is shown for scale (in *red circle*). Courtesy of ITER Organization

problems. ITER was redesigned to a smaller size, in order to cut its cost. The reduction of parameters is shown in Table 1.9.

The USA dropped out of the ITER collaboration in 1998, and then rejoined in 2003. China and Korea joined in 2003, and India joined in 2005. Sites for ITER were proposed in Japan, France, Italy, Spain, and Canada. After lengthy negotiations the parties agreed to build it in Cadarache, France. The Director General is Japanese, and each of the other parties has their citizens in upper level management and support positions. Europe is paying about 5/11 of the cost, and each of the other six parties is paying 1/11, including a contingency of up to 10 %.

Figure 1.33 shows the ITER device, now under construction in Cadarache, France.

ITER will be operated in three phases:

- H Phase—studies of plasma control, stability, transport, heat flux, divertor, runaway electrons, electromagnetic loads, diagnostics, etc. Beginning in 2020.
- D Phase—deuterium operations, nuclear reactions, small amounts of tritium, shielding performance.
- DT Phase—full fusion power operation, tritium control, non-inductive, steady-state current drive, long-term burn, blanket module testing, high-heat-flux and neutron fluence testing. Full power operation in about 2027.

Next Step Test Facilities

The International Fusion Materials Irradiation Facility (IFMIF) will produce an intense source of high-energy neutrons by impact of 40 MeV deuteron beams onto a flowing lithium target. This will help qualify various materials for use in fusion reactors. IFMIF is described in Sect. 8.10.

Other facilities, such as a gasdynamic trap neutron source and a component demonstration facility, may also be built.

A Demonstration Power Plant (DEMO) is planned to follow successful operation of ITER. DEMO will generate electrical power, verify tritium breeding and containment estimates, test the capability of tokamaks to operate reliably for extended periods (>80 % availability is desired), and improve estimates of the cost of electricity from fusion.

1.5.3 Power Plant Design Studies

Several countries have done conceptual designs of tokamak fusion power plants. They can probably be built successfully, but the issues of plasma impurities, plasma control, materials, reliability, maintenance, and cost are uncertain. It appears that the cost of electricity from tokamak power plants may be higher than from fission power plants primarily due to higher capital costs. Figure 1.34 shows the ARIES-AT (advanced tokamak) reactor design.

A fusion power plant based on the heliotron concept is illustrated in Fig. 1.35.

Stellarators have the following potential advantages over tokamaks:

- No disruptions
- Current free operation → slower heat loss
- Plasma current drive not required → lower input power, higher Q.

Disadvantages of stellarators include larger size and complex divertor and blanket shapes, which might make maintenance more difficult.

Other types of plasma confinement, such as spheromaks and magnetized target fusion, might achieve lower cost fusion power, but they are more speculative and funding for such alternative concepts has been miniscule.
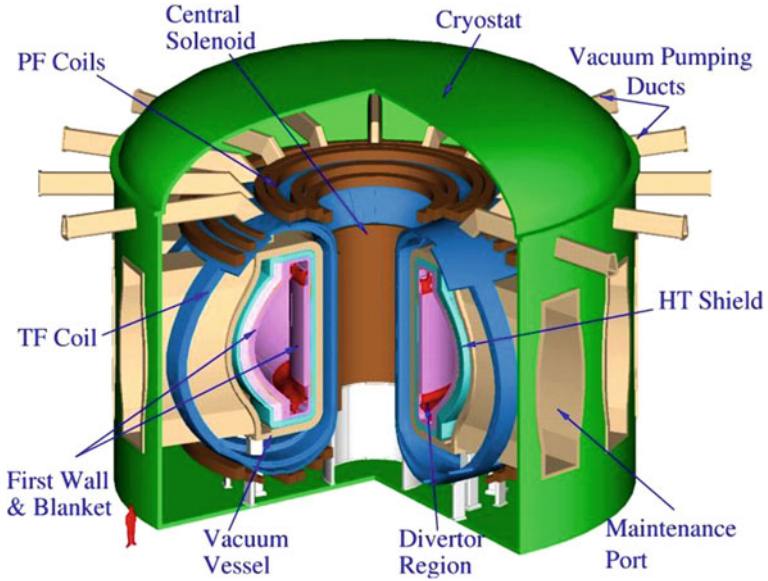
Fig. 1.34 The ARIES-AT fusion reactor. This design incorporates advanced plasma confinement and materials concepts to minimize the cost of electricity. Reprinted from Najmabadi et al. (2006). Copyright 2006, with permission from Elsevier
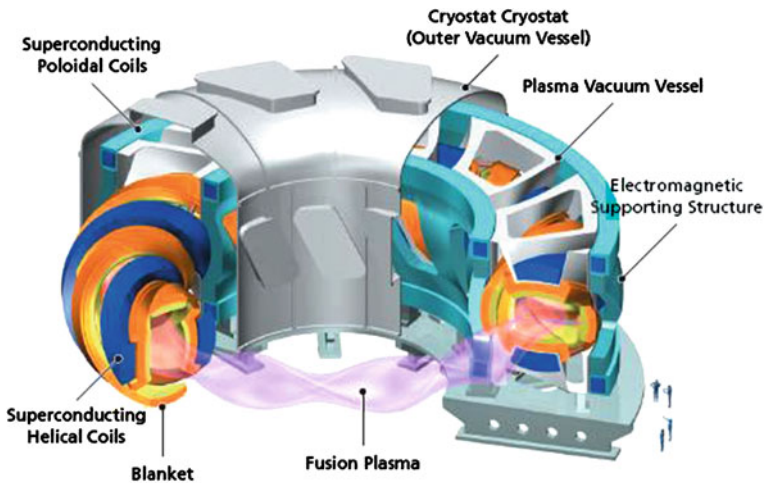
LHD-type fusion energy reactor FFHR2m1

Intensive design activities are being conducted on the LHD-type fusion energy reactor "FFHR" through inter-university collaborations.

Fig. 1.35 A heliotron fusion power plant conceptual design. © National Institute for Fusion Science, Toki, Japan

Fusion power plant economics are dominated by the high capital costs, so the plants will need to operate at full power with high availability. Fusion power has strong **economy of scale**, meaning that the cost of electricity (COE) from a plant with $P_E = 3,000$ MWe would be substantially less than the COE from a plant with $P_E = 1,000$ MWe, so there is an incentive to build them in large sizes. However, the feasible size is limited by many factors, for example the electrical power grid, heat rejection to the environment, desire for redundancy to cope with shutdowns, capital cost funding, and political considerations (Dolan 1993; Sheffield and Waganer 2001).

1.6 Problems

1.1. By looking up the nuclear masses show that the yield of the DT fusion reaction is 17.6 MeV.
1.2. Show that the units of $B^2/2\mu_o$ reduce to Pa.
1.3. Consider a plasma with ion temperature 20 keV and density 2×10^{20} m^{-3}. Compare the fusion power density of a DT plasma (half D, half T) with that of a catalyzed DD plasma at the same density and temperature.
1.4. What is the pressure of the plasma of Problem 1.3? Express the answer in Pa and in atm. If a fusion reactor could confine a plasma at $\beta = 6$ %, what value of B would be required to confine the plasma of the previous problem?
1.5. For the reactor parameters of the example case (Table 1.6, assuming $P_E = 1,000$ MWe), estimate the thermal power of the reactor, the thermal power generated in the plasma, the plasma volume, and the average fusion power density. If the plasma ion temperature is 15 keV, use the fusion power density to estimate the required plasma density and the plasma pressure, assuming no impurities.
1.6. Calculate the temperature that optimizes the DD reaction rate at constant pressure.
1.7. If beta $= 5$ %, what magnetic field would be required to achieve a fusion power density of 1 MW/m^3 with catalyzed DD fuel?

1.7 Review Questions

1. About how many Joule of energy input to agriculture are needed to make one Joule of food energy?
2. About how much power (TW) will the world consume in 2020?
3. What are the advantages and disadvantages of nuclear fusion power compared with nuclear fission power?
4. How can fission and fusion both release nuclear energy?

5. What two conditions must be fulfilled in order to make a fusion reactor?
6. Name 5 means of plasma confinement
7. What will be the primary fuels of a first-generation fusion reactor?
8. If the deuterium from one liter of water were burned in a DD fusion reactor, how much energy would be released, relative to liters of gasoline?
9. Sketch a magnetic mirror and a spindle cusp.
10. What is the difference between plasma equilibrium and thermodynamic equilibrium?
11. What is the pressure of a magnetic field of 1 T, expressed in atmospheres?
12. Define beta and Q.
13. What beta values are considered adequate for fusion reactors?
14. About what value of the triple product is required for a fusion power plant with $Q > 10$?
15. What is the optimum temperature for DT fusion?
16. Define "toroidal angle ϕ" and "poloidal angle θ" with a sketch.
17. What parameters determine the blanket-shield thickness b; the coil thickness c; the plasma minor radius a, and the major radius R_o?
18. Approximately how large are a and I of JET and JT-60?
19. What is a "spherical tokamak", and what is an advantage of this device?
20. How are helical magnetic field lines produced in tokamaks? In stellarators?
21. About how large are a and B in LHD and W7-X ?
22. Sketch B_t versus r in an RFP
23. What does the following equation represent, and what two types of plasma confinement are based on it? $\mu_o \mathbf{J} = \nabla \times \mathbf{B} = k\mathbf{B}$
24. Name two methods for producing FRCs.
25. Sketch the potential versus z in a tandem mirror, and tell how this confines ions and electrons.
26. About how high a value of the triple product has been attained so far by tokamaks?
27. What countries are official partners in ITER?
28. About when will ITER start up? When will it reach full power? Why will it take so long to reach full power?
29. What is IFMIF, and how will it produce neutrons?
30. Name two advantages of stellarators over tokamaks.
31. What values of plasma current, fusion power, and burn time are expected for ITER?
32. Name three factors that limit the attainable economy of scale of fusion power plants.
33. Sketch a torus and label R, R_o, r, a, θ and ϕ.
34. What are the two general classes of particle orbits in tokamaks?

References

Atzeni S, Meyer-Ter-Vehn J (2004) The physics of inertial fusion. Oxford Science Publications

Bolt H (∼2007) Materials for fusion, Sect. 2.9 of European White Book Fig. 2.17. http://www.mpg.de/pdf/europeanWhiteBook/wb_materials_068_113.pd

Braams CM, Stott PE (2002) Nuclear fusion: half a century of magnetic confinement. IOP Bristol, Philadelphia

Chapman BE et al (2010) Generation and confinement of hot ions and electrons in a reversed-field pinch plasma. Plasma Phys Controlled Fusion 52:124048 (14 pages)

Chen FF (1984) Introduction to plasma physics and controlled fusion, Volume 1: Plasma physics, 2nd edn. Plenum Press, New York

Chen FF (2011) An indispensable truth, how fusion power can save the planet. Springer, New York

Dolan TJ (1982) Fusion research. Pergamon Press, New York

Dolan TJ (1993) Fusion power economy of scale. Fusion Technol 24:97–111

Dolan TJ (2012) Nuclear fusion, encyclopedia of sustainability science and technology. Springer, New York

EIA (2011) International Energy Outlook 2011, Report Number: DOE/EIA-0484, Energy Information Administration, US Department of Energy

IAEA (1995) Energy from inertial fusion. International Atomic Energy Agency, Vienna

Freidberg J (2007) Plasma physics and fusion energy. Cambridge University Press, Cambridge

Jarboe TR, Victor BS, Nelson BA, Hansen CJ, Akcay C, Ennis DA, Hicks NK, Hossack AC, Marklin GJ, Smith RJ (2012a) Imposed dynamo current drive. Nucl Fusion 52:083017 (9 pp)

Jarboe TR, Sutherland DA, Akcay C, Golingo R, Hansen CJ, Hossack AC, Marklin GJ, Morgan K, Nelson BA, Raman R, Victor BS, You S (2012b) Facilities needed for the development of economical fusion power, http://www.iccworkshops.org/epr2013/index.php

Kikuchi M, Lackner K, Tran MQ (2012) Fusion physics. International Atomic Energy Agency, Vienna, Austria

LaBerge M (2012) General fusion's acoustic magnetized target fusion. In: 20th American Nuclear Society Topical meeting on the technology of fusion energy, Nashville, TN, USA, Aug 27–31

Li XZ, Wei QM, Liu BA (2008) New simple formula for fusion cross sections of light nuclei. Nucl Fusion 48:125003 (5 pages)

Lodge O (1924) Putting the atom to work. Sci Am (May), pp 306–307, 358–359

Morisaki T et al (2007) Superdense core mode in the large helical device with an internal diffusion barrier. Phys Plasmas 14:056113

Moses EI et al (2009) A sustainable nuclear fuel cycle based on laser inertial fusion energy. Fusion Sci Technol 56:547

Najmabadi F et al (2006) The ARIES-AT advanced tokamak, advanced technology fusion power plant. Fusion Eng Des 80:3–23

NAS (2012) Interim report-status of the study "An Assessment of the Prospects for Inertial Fusion Energy", Committee on the Prospects for Inertial Confinement Fusion Energy Systems; National Research Council of the National Academies, National Academy Press

Ongena J, Van Oost G (2012) Energy for future centuries. Fusion Sci Technol 61:3–16

Rogner HH (2012) World Energy Demand and Supply, IAEA, Vienna, Austria. Accessed at http://www.iaea.org/nuclearenergy/nuclearknowledge/schools/NEM-school/2012/AbuDhabi/PDFs/day1/04_Rogner_World_Energy_D%26S.pdf

Sheffield J, Waganer LM (2001) A study of options for the deployment of large fusion power plants. Fusion Sci Technol 40:1–36

Simonen T, Cohen T, Correll D, Fowler K, Post D, Berk H, Horton W, Hooper EB, Fisch N, Hassam A, Baldwin D, Pearlstein D, Logan G, Turner B, Moir R, Molvik A, Ryutov D, Ivanov AA, Kesner J, Cohen B, McLean H, Tamano T, Tang XZ, Imai T (2008) The axisymmetric tandem

mirror: a magnetic mirror concept game changer—Magnet Mirror Status Study Group, Lawrence Livermore National Laboratory Report LLNL-TR-408176, Oct 24

Taylor JB (1984) Relaxation of toroidal plasma and generation of reverse magnetic fields. Phys Rev Lett 33:1139–l141

Theobald W et al (2008) Initial experiments on the shock ignition inertial confinement fusion concept. Phys Plasmas 15:056306

Wood RD, Hill DN, McLean HS, Hooper EB, Hudson BF, Moller JM, Romero-Talamas CA (2009) Improved magnetic field generation efficiency and higher temperature spheromak plasmas. Nucl Fusion 49:025001 (4 pp)

Woodruff S, Brown M, Hooper EB, Milroy R, Schaffer M (2010) Why compact tori for fusion. J Fusion Energy 29:447–453

Yokohama M et al (2008) Extension of the high temperature regime in the large helical device. Phys Plasmas 15:056111

Chapter 2
Technology Issues

Thomas J. Dolan

Objectives

After reading this chapter one should understand

What technologies are required to build a fusion power plant
What are the main achievements and difficulties in these areas.

2.1 The Issues

The purpose of this chapter is to provide a summary of fusion technology issues that will be covered in the rest of the book. The main technologies of magnetic confinement fusion (MCF) are listed in Table 2.1.

2.2 Magnets

Pulsed magnets energized by capacitor banks have been used for fast pinch experiments. The capacitors can be charged at low input power for minutes, and then discharged suddenly at high power. In effect they amplify the power, but the high power output only lasts for microseconds or milliseconds. They are used for experiments like Z pinches, theta pinches, and plasma focus devices. The central solenoid (CS) coil of a tokamak is pulsed in milliseconds to induce the toroidal plasma current.

Figure 2.1 shows the three coil sets of a tokamak (Fig. 1.14 repeated).

T. J. Dolan (✉)
NPRE Department, University of Illinois, Urbana, IL 61801, USA
e-mail: dolantj@illinois.edu

Table 2.1 Technologies of magnetic confinement fusion

Pulsed and water-cooled magnets
Superconducting magnets
Plasma heating and current drive
First wall, blanket and shield
Power and particle control
Materials issues
Vacuum systems
Cryogenic systems

Fig. 2.1 Tokamak coil systems. The *D-shaped* toroidal field (*TF*) coils provide the toroidal field (as in Fig. 1.8). The central solenoid (*CS*) is pulsed to induce the plasma toroidal current J (Fig. 1.9). The poloidal field (*PF*) coils control the plasma shape and position. *The dashed ellipses* represent magnetic flux surfaces of the plasma
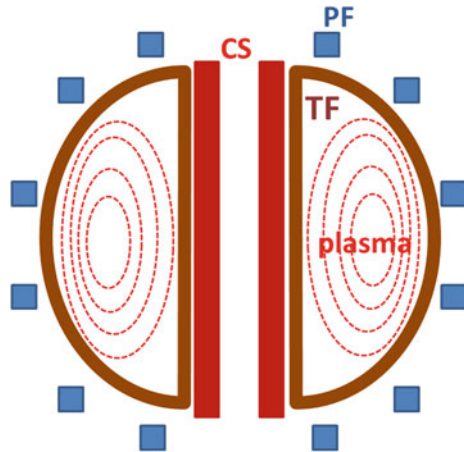
Faraday's Law states that a changing magnetic field induces an electric field:

$$\nabla \times \mathbf{E} = -(\partial B/\partial t) \tag{2.1}$$

The integral form of this equation states that the integral of the electric field around a boundary curve equals the integral of $(\partial B/\partial t)$ over the enclosed surface. (Please see Appendix D for vector relations.)

$$\int d\ell \bullet \mathbf{E} = -\int d\mathbf{S} \bullet (\partial \mathbf{B}/\partial t) \tag{2.2}$$

Consider a CS coil with internal area S, Fig. 2.2.
The electric field induced at radius R by B changing inside S is

$$2\pi RE \approx S(dB/dt) \tag{2.3}$$

If R = 2 m, S = 0.5 m^2, and dB/dt = 10 T/s, then E = 0.4 V/m.
Ampere's law is

$$\nabla \times \mathbf{B} = \mu_o \mathbf{J} + \mu_o \varepsilon_o (\partial \mathbf{E}/\partial t) \tag{2.4}$$

Fig. 2.2 A CS coil with internal area S surrounded by a toroidal plasma at radius R
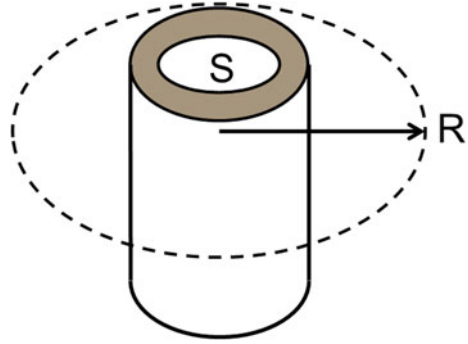
where $\mu_o = 4\pi\ 10^{-7}$ H/m is the permeability of free space and $\varepsilon_o = 8.854 \times 10^{-12}$ F/m is the permittivity of free space. The last term may be neglected, except for very high frequency oscillations. The integral form of this equation is

$$\int d\ell \bullet \mathbf{B} = \mu_o \int d\mathbf{S} \bullet \mathbf{J} \tag{2.5}$$

where $\int d\mathbf{S} \bullet \mathbf{J}$ is the total current I inside the boundary. The azimuthal field B_θ at a radius r from a long, straight wire carrying a current I is

$$2\pi r B_\theta = \mu_o I \tag{2.6}$$

This can be used to estimate the poloidal field around a plasma carrying a toroidal current I. The axial field inside a long straight solenoid with length L carrying a total current I_{tot} is

$$B_z = \mu_o I_{tot}/L \tag{2.7}$$

In a toroidal device, $L \to 2\pi R$, and the toroidal magnetic field at major radius R generated by N toroidal field coils each carrying a current I is

$$B\ = \mu_o NI/2\pi R \tag{2.8}$$

If $N = 20$ coils, $R = 2$ m, and $B = 3$ T, then the required current per coil would be $I = 1.5$ MA. Water-cooled magnets can have current densities in the copper $J \sim 10$ MA/m^2, so the cross sectional area of the copper in each coil would need to be $A_c \sim 0.15$ m^2. If the coil radius $a_c \sim 1$ m, then the volume of copper per coil would be

$$V_c = 2\pi a_c A_c = 0.94 \text{ m}^3 \tag{2.9}$$

(The total volume would be larger to accommodate cooling water channels).

Assuming a copper resistivity of $\eta = 2 \times 10^{-8}$ Ohm-m, the power dissipated in each coil would be

$$P_c = \eta J^2 V_c \sim 1.9 \text{ MW} \tag{2.10}$$

The total power for 20 coils would be 38 MW. This simple example illustrates the fact that very high powers are required for water-cooled copper coils when

fields of several Tesla are required. New large experiments, such as tokamaks and stellarators, use superconducting coils, because the electrical power consumption of ordinary copper coils would be too high.

Researchers are developing superconductors that can carry high current densities in high magnetic fields. Most high-field superconductors operate at T < 10 K and B < 14 T. At higher magnetic fields superconductivity may be lost or the stresses may be too high. Some "high-temperature superconductors" (HTS) can be superconducting at T ~ 80 K, but at lower magnetic fields. However, the HTS materials can produce very high magnetic fields at lower temperatures.

High temperature superconductors are used for current leads into superconducting coils. Superconductors are also used for many applications other than fusion research, including motors, generators, transmission lines, magnetic resonance imaging, and research, so developments in one of these fields may have benefits in others.

Chapter 3 discusses pulsed and water-cooled magnets, and Chap. 4 describes superconducting magnet systems.

2.3 Plasma Heating and Current Drive

Plasma heating can be done by the following methods:

- Ohmic heating
- Plasma compression
- Magnetic induction
- Electromagnetic waves
- Particle beam injection
- Plasma guns.

2.3.1 Ohmic Heating

When a current is pulsed in the CS coil, a toroidal current is induced in the plasma. This is called "inductive current drive". The current density J (A/m^2) flowing through plasma with resistivity η (Ohm-m) generates an ohmic heating power density

$$P_{oh} = \eta J^2 \left(W/m^3\right) \tag{2.11}$$

in the plasma. (Exercise for students: verify that the units are W/m^3). The duration of the current is limited by the magnetic flux (number of Volt-seconds) that can be provided by the CS coil. If the current is to be sustained for longer times, then "non-inductive" current drive is needed.

Since η is proportional to T$^{-3/2}$, at high temperatures η becomes very small, and ohmic heating is unable to heat the plasma adequately.

Plasma compression heating was demonstrated in several tokamaks, but it reduces the plasma volume relative to the magnet coil volume, so it is not currently used in large magnetic confinement fusion devices.

2.3.2 Charged Particle Injection

It is possible to inject electrons or ions along B field lines into an "*open*" magnetic confinement system, shown in Fig. 2.3.

Many of the ions or electrons would simply flow through the plasma and out the other end, but sometimes a plasma instability can trap injected electrons and provide good heating.

It would be difficult to heat a *toroidal* plasma by injecting electrons or ions, because they cannot flow easily across a strong toroidal magnetic field, as can be seen from Fig. 2.4.

Fig. 2.3 *The circular magnet coils* on the *right* produce magnetic fields similar to those of the *bar* magnets on the *left*, namely a magnetic mirror field (*top*) and a magnetic spindle cusp field (*bottom*)
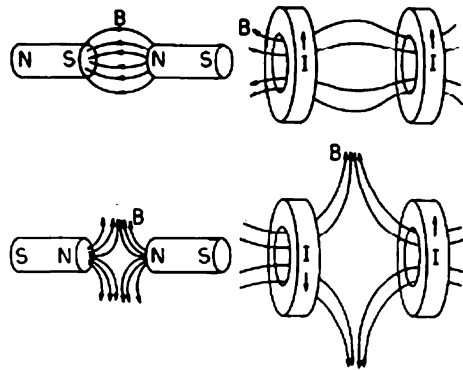
Fig. 2.4 A simple toroidal magnetic field (*dashed lines*) produced by many circular magnet coils. The *curved arrow* represents charged particles coming from the outside that are reflected by the magnetic field
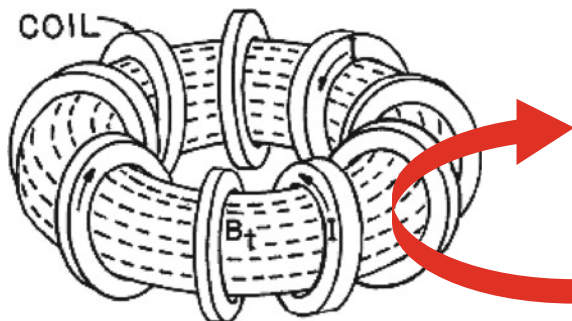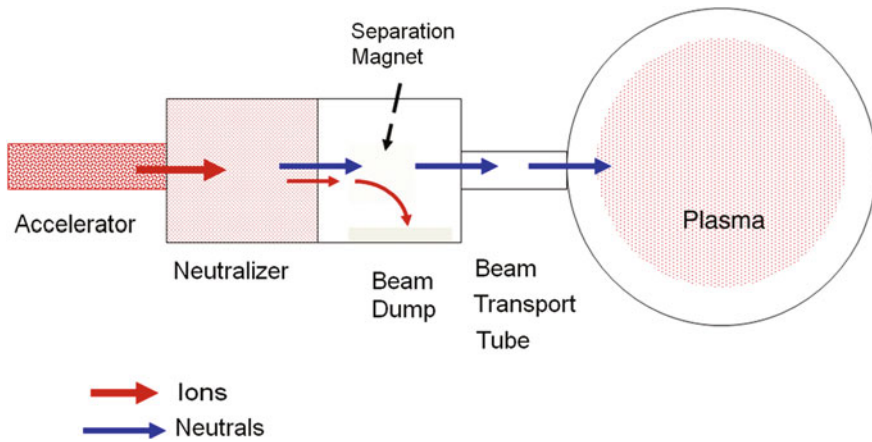
Fig. 2.5 Schematic diagram of a neutral beam injector

2.3.3 Neutral Beam Injection

However, an accelerated ion beam can be neutralized and the neutral atoms can easily cross the magnetic field into the plasma, where they are ionized and trapped.

Figure 2.5 illustrates the main components of a neutral beam injector.

The accelerator has an ion source and high voltage grids to accelerate and focus the ion beam. In a fusion power plant the ions would probably be deuterons or tritons. The beam passes through the neutralizer gas cell, where many of the accelerated ions pick up electrons to become fast neutral atoms. The un-neutralized ions are separated out by a bending magnet and directed into a beam dump. The fast neutral atoms then to pass through the beam transport tube into the hot plasma, where they are ionized and trapped.

Beam energies of 20–50 keV are adequate for small plasmas, but for large high-pressure plasmas, beam energies ~ 1 MeV are required for adequate beam penetration into the plasma core. At high energies negative ions are used, because they are easier to neutralize than positive ions.

In addition to plasma heating, the neutral beams impart momentum to the plasma, which can cause plasma current drive and plasma rotation. Thus, the technology of neutral beam injection (NBI) is very important for tokamaks, such as ITER. Neutral beam injection requires large ports and straight paths for the neutral atoms. Neutrons can stream out from the fusion plasma and make external components radioactive.

2.3.4 Electromagnetic Waves

The "cyclotron frequency" at which electrons and ions spiral around magnetic field lines is

$$\omega_c = qB/m\gamma \quad \text{(radians/s)}$$
$$f_c = w_c/2\pi \quad \text{(Hz)}$$

(2.12)

where m = particle mass (kg), B = magnetic field (T), q is the particle's charge (C) and $\gamma = (1 - v^2/c^2)^{1/2}$. Here we assume, $\gamma = 1$ unless otherwise specified. For example, the electron cyclotron frequency in a field of 1 T is $f_c = 28$ GHz. (Exercise: Verify this value and the units.)

Several types of electromagnetic waves can be used for plasma heating and current drive, including:

- Electron cyclotron resonance (tens to hundreds of GHz)
- Ion cyclotron resonance (tens of MHz)
- Lower hybrid resonance (a few GHz).

These can be tuned to the particle mass and magnetic field region where heating or current drive is needed.

Radio waves require antennas, which can introduce impurities into the plasma. Microwaves can be transmitted through waveguides, with windows separating the plasma chamber from the klystron or magnetron tubes that generate the waves. The windows must be able to transmit high power fluxes with little energy deposition in the windows, which could cause windows to crack. Diamond and sapphire make excellent windows, because of their very high thermal conductivity, but they are expensive.

Engineers have done much work to develop efficient, reliable, high-power generators, transmission lines, windows, and coupling antennas or grills. For example, the provision of 1 MW sources of 170 GHz microwaves that can operate for many seconds is a major technology development program for ITER.

2.3.5 Plasma Guns

Coaxial plasma guns can accelerate plasma blobs to high velocities, pushing through the magnetic field and adding energy and electric current to a plasma. Current drive may be described mathematically as addition of "helicity" to the plasma, where "helicity" is defined in terms of an integral of **A•B** over the plasma volume, **B** is the magnetic field, and **A** is the magnetic vector potential. Plasma heating and current drive are discussed in Chap. 5.

2.4 First Wall, Blanket, and Shield

Figure 2.6 shows the main elements of a fusion reactor blanket and shield.
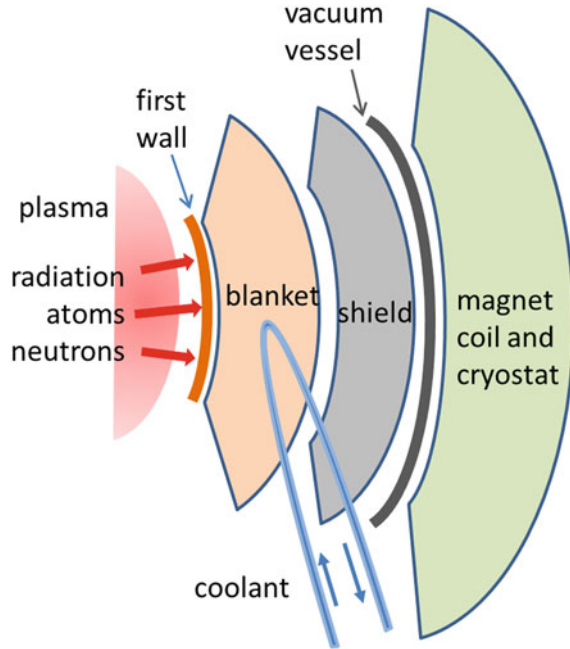
Much of the fusion energy would be absorbed in the first wall- blanket-shield subsystem, and this energy is carried by coolants to a steam generator (to drive a steam turbine and electrical power generator, Rankine cycle) or by gaseous coolant (He, CO_2, …) to a gas turbine/generator (Brayton cycle). There will probably be an intermediate coolant loop between the reactor and the steam generator (or gas turbine) to minimize tritium permeation. The efficiency of converting thermal energy into electricity is always less than the Carnot efficiency

$$\eta_c = (T_h - T_c)/T_h, \tag{2.13}$$

where T_h and T_c are the hot and cold temperatures of the coolant. For example, if $T_h = 800$ K and $T_c = 300$ K, then $\eta_c = 62.5$ %. A typical steam cycle can achieve about 64 % of the Carnot efficiency, which would be about 40 % for this case. Thus, it is important to use structural materials in the first wall, blanket and shield that can operate reliably at high temperatures for years.

The first wall-blanket-shield design must cope with many issues simultaneously

- First wall design issues

  – Access ports
  – High heat flux
  – High neutron flux
  – High temperature operation
  – Degradation due to sputtering, heat, stresses, creep and radiation damage.

- Breeding materials
- Tritium breeding, control, inventory
- Coolants
- Structural materials
- Cooling of first wall, blanket, and shield
- Stresses and loss of properties
- Flow rate and pumping power
- Neutronics calculations, including gamma transport
- Energy conversion methods
- Maintenance scheme, including remote handling of radioactive components
- Hundreds of connections for coolant, plasma heating, tritium control, diagnostics, etc.

The first wall must withstand high fluxes of neutrons and heat, radiation damage, creep, swelling, embrittlement, and stresses, yet operate reliably for several years (Merola 2008).

The blanket region behind the first wall of a fusion power plant will probably contain lithium to multiply neutrons via the endothermic ^{7}Li(n, 2n) reaction and to breed tritium by neutron capture in ^{7}Li and ^{6}Li (Table 1.3). Neutron multiplication can also be done by Be, Pb, and PbLi, which is a potential reactor coolant. On the average each neutron from a DT fusion reaction must breed more than one tritium atom, to sustain the fuel cycle. Since some neutrons are absorbed in other materials (such as structure) without breeding tritium and some are lost, a local tritium breeding ratio (TBR) > 1.1 is needed in the lithium-containing regions of the blanket to produce a net TBR > 1.

A shield outboard of the blanket attenuates neutrons and gamma rays to protect the magnet coils and other systems. The required thickness of a power reactor blanket-shield would probably be in the range 1–1.5 m. Some designs vary this thickness around the torus, using a thinner blanket where the plasma must be close to the coils for good confinement. The shield may be designed to operate at high temperature, to provide structural support for the first wall and blanket, and to last for the lifetime of the plant (~ 60 years).

The majority of the ITER modules will not contain tritium breeding blankets. They will simply contain stainless steel and water to shield the magnet coils from neutrons and gamma rays. It is planned to have some test blanket modules to evaluate their tritium breeding capability. The ITER non-breeding blanket-shield modules are shown in Fig. 2.7.

Each of the 440 ITER blanket-shield modules is comprised of a first wall and a blanket-shield region. Most of the first wall of the main chamber will have
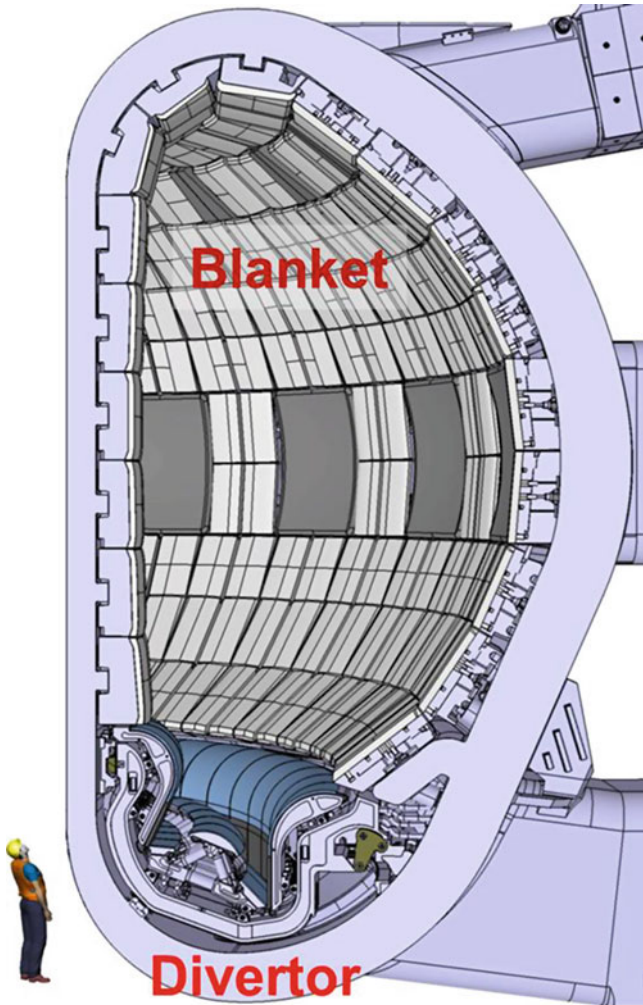
Fig. 2.7 Some of the 440 ITER blanket-shield modules (*rectangular boxes*) and the single-null divertor (the *W-shaped* region at the *bottom*). Courtesy of ITER Organization

beryllium tiles bonded to a copper substrate with stainless steel tubes containing pressurized, low-temperature water coolant, similar to the tiles of Fig. 2.8.

The first wall, blanket, and shield issues are discussed in Chap. 6.
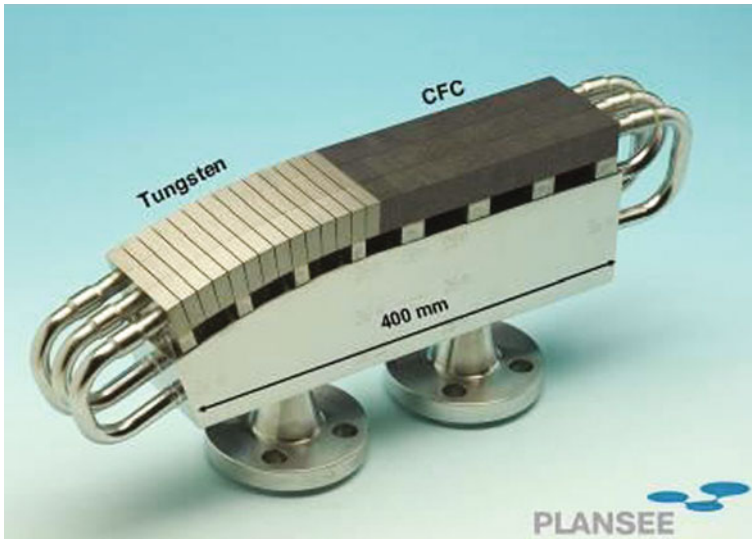
Fig. 2.8 Armor tiles of W and C bonded to copper substrate containing stainless steel coolant tube (Merola 2008)

2.5 Control Systems

The fusion power plant control systems must regulate many processes, including:

- Magnet coils and possible quenches (Chaps. 3, 4)
- Vacuum systems (Chap. 9)
- Cryogenic systems (Chap. 10)
- Plasma density, temperature, fusion power, position, stability, purity (Chap. 7)

  - Plasma diagnostics (Chap. 11)
  - Plasma heating and current drive (Chap. 5)
  - Plasma fueling and gas recycling (Chap. 7)
  - Divertor operation (Chap. 7)

- First wall-blanket-shield heat removal (Chap. 6)
- Tritium flow, recovery from coolant, inventory (Chap. 12)
- Remote handling maintenance systems (Chap. 13)
- Radioactive material inventories (Chap. 13)
- Routine emissions (Chap. 13)
- Accidents (Chap. 13)
- Heat exchangers and steam generators
- Steam turbines and electric generators
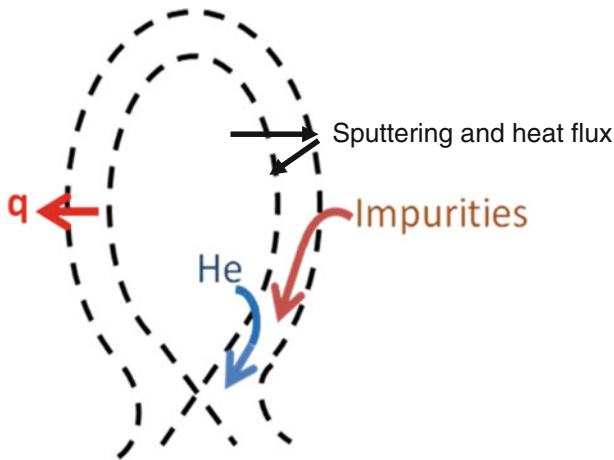
Fig. 2.9 Divertor functions: reduction of heat flux, reduction of sputtering, channeling of helium and sputtered impurities to divertor chamber at the bottom (not shown)

- Electricity switching and distribution.
  The last three systems are common to other types of power plants and will not be discussed in this book.

A "divertor" is a region at the bottom or top of the torus where poloidal magnetic field lines lead plasma to be neutralized and pumped away by vacuum pumps (to be discussed in Chap. 7). The purposes of the divertor are to:

- Reduce the **heat flux** on the first wall of the main chamber by moving much of the heat and particle load to the divertor.
- Reduce **sputtering** by having cooler temperatures near the wall.
- Remove **helium ash** from the outer layers of the plasma, so that it does not build up to high levels and dilute the fuel ion density.
- Prevent **impurity** atoms sputtered from the wall from entering the plasma core.

These are illustrated in Fig. 2.9.
An ITER divertor cassette is shown in Fig. 2.10.
The ITER divertor cassettes are designed for replacement, using a robotic transporter on a removable rail. Other types of magnetic confinement, such as stellarators, will probably also use divertors. Divertor issues are discussed in Chap. 7.
Particles are removed by the divertor and vacuum system and injected by the fueling system and by sputtering.
Plasma fueling may be done by hydrogen gas "puffing", neutral beam injection, solid fuel pellet injection, or other methods.
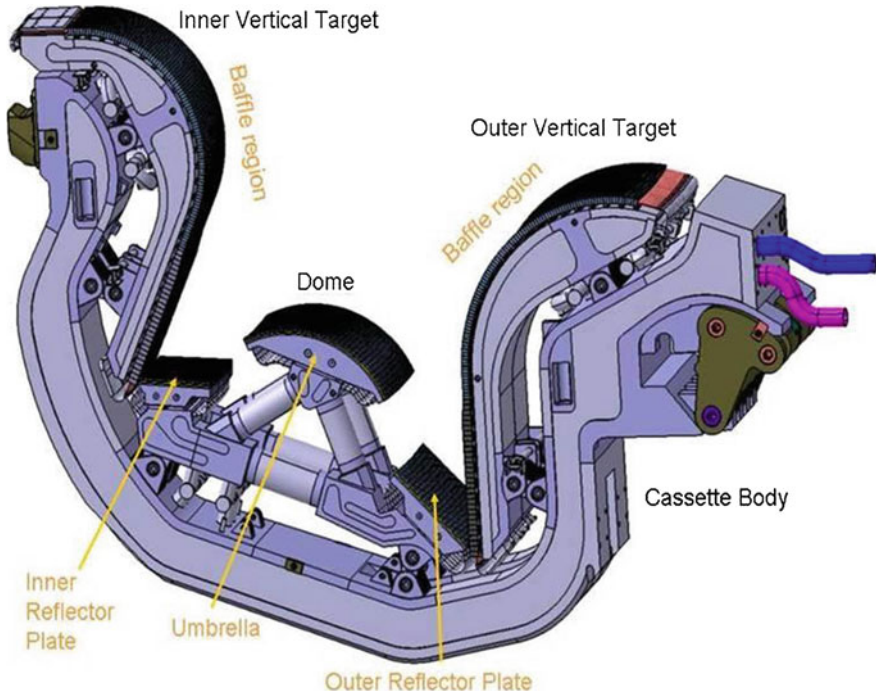
Fig. 2.10 An ITER divertor cassette. The plasma-facing materials in the dome and targets will be water-cooled tiles with tungsten surfaces. Courtesy of ITER Organization

Gas puffing is easiest, but the gas is ionized at the edge of the plasma, the fuel is needed in the plasma core, and the edge density spike may destabilize the plasma. Gas jets injected through nozzles can penetrate slightly better than gas puffs.

Hydrogen atoms adsorbed on the chamber wall or trapped inside the wall may be desorbed during a plasma pulse, causing an additional source of hydrogen ions that may increase the plasma density too much and cause a plasma density limit "disruption" (rapid termination of the tokamak discharge). To avoid excessive hydrogen recycling the walls must be carefully cleaned, heated to about 300 °C to remove most water molecules, and conditioned by preliminary low-density plasma pulses or by coating the walls with special materials, such as titanium or boron. Elastomer (rubber-like) O-rings are not good at high temperatures, so metal gaskets of Cu or Al are widely used.

Plasma blob injection by coaxial plasma guns has been demonstrated in small tokamaks, but for complete fueling of large tokamaks this method would require many rapidly pulsing guns.

NBI can also be used for plasma fueling, but much energy may be expended in accelerating the beam. Therefore, this method limits the attainable Q.

Solid pellets of frozen DT fuel may be injected by a light gas gun or by a rotating arm (like pitching a baseball or cricket ball). Production of the pellets requires a cryogenic system to freeze the DT fuel (T < 20 K).

Control systems are discussed in Chap. 7.

2.6 Materials Issues

Fusion power plants need advanced materials for the first wall, divertor surfaces, coolant tubes and insulators, blanket structure, superconducting magnets, and so on. The materials issues include:

- High temperature operation inside the shield
- Surface erosion by particles and photons
- Plasma chamber dust
- Tritium trapping
- Compatibility of coolant with walls and structure
- Stresses

  – Thermal stress
  – Pressure stress
  – Gravity
  – Cyclic stress and fatigue

- Radiation damage

  – Creep
  – Swelling
  – Embrittlement

- Induced radioactivity
- Hydrogen and helium effects on materials
- Fabrication and durability of superconducting materials
- Lifetime of insulators.

It is desirable for all the reactor components to last the lifetime of the power plant ($\sim$60 years), but the first wall will probably need periodic replacement. It is also desirable to develop advanced materials whose radioactivity decays away to tolerable values in less than 100 years. The leading candidate structural material is reduced activation ferritic or martensitic (RAFM) steel. Silicon carbide composite might be a good candidate for the blanket structure, but it has not been fabricated in large sizes and tested at high temperature under intense neutron irradiation.

Development of materials that can survive 14-MeV neutron bombardment for years will be a challenging problem, especially since no adequate neutron source is yet available. Japan and Europe are collaborating to build the International Fusion

Materials Irradiation Facility (IFMIF), which could test materials under intense neutron irradiation. Chapter 8 deals with Materials Issues.

2.7 Vacuum Systems

Vacuum technology began in the 17th century with experiments on barometers and vacuum pumps by Galileo, Torricelli, Pascal, Von Guericke, and Boyle. In the 20th century industrial development of vacuum tubes for radios, x-ray tubes, oscilloscopes, televisions, radars, and accelerators brought great advances.

Fusion experiments require an ultrahigh vacuum to get rid of impurity atoms that could spoil plasma confinement. ITER will use mainly turbomolecular pumps, roughing pumps, and cryogenic pumps. The technology for vacuum gages, chambers, flanges, valves, windows, and flexible bellows is well developed. Vacuum system designers can calculate conductances of each element, effective pumping speeds, gas flow rates, and the time required to reduce the pressure. The control of tritium is important because of its radioactivity hazard.

Large fusion experiments require complex vacuum systems including all these elements. For example, the ITER vacuum vessel (Fig. 2.11) has many ports for heating, current drive, vacuum pumping, and diagnostics and maintenance.

Elaborate procedures are established for fabricating these large and complex vacuum vessels
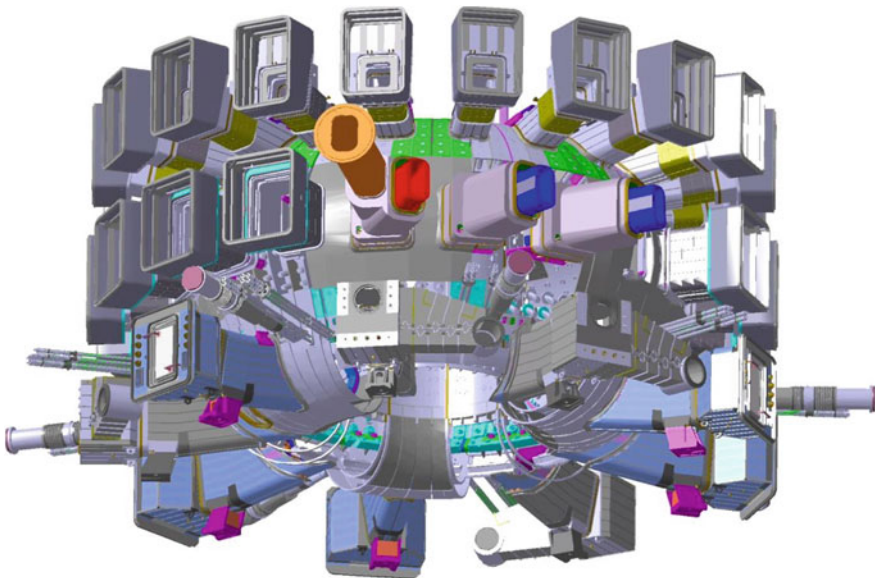
Fig. 2.11 The ITER vacuum vessel ports. Courtesy of ITER Organization

- High quality welding techniques
- Manufacturing components and polishing surfaces to minimize gas trapping
- Cleaning surfaces with degreasing agents, acids or alkalis, deionized water, and alcohol
- Baking the chamber under a vacuum to remove adsorbed water vapor
- Leak testing using a helium gas jet and a mass spectrometer
- Coating the surfaces with special materials, such as lithium, beryllium or boron
- Running low-pressure plasma discharges to further clean the surfaces.

The vacuum chamber for ITER is quite large, as can be seen in Fig. 2.12.
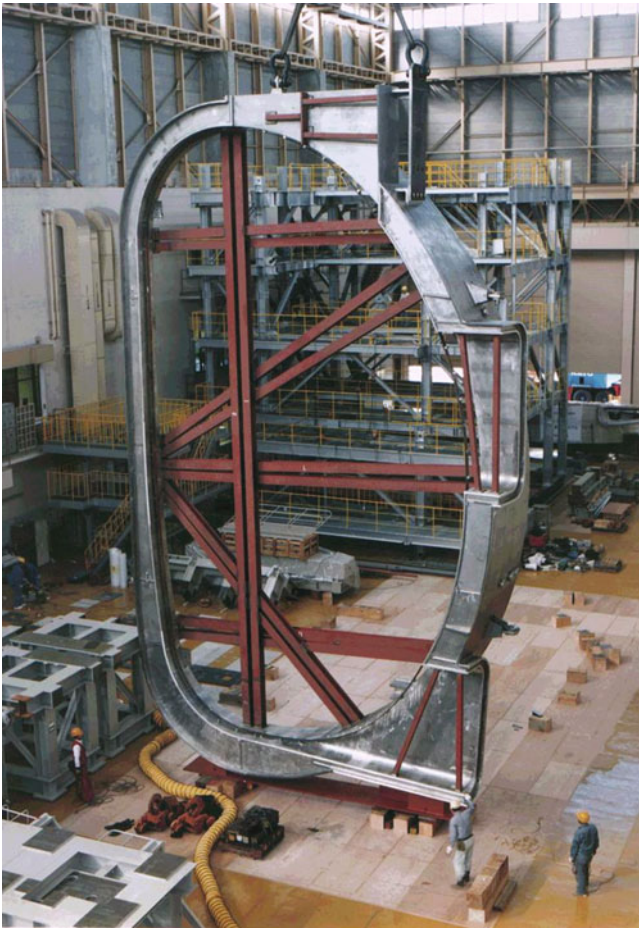
Fig. 2.12 One segment of the ITER vacuum chamber model. Note the person at the *bottom*. Courtesy of ITER Organization

This chamber must be fabricated with great precision, including allowance for dimensional changes due to welds. Vacuum technology is described in Chap. 9.

2.8 Cryogenic Systems

The word "cryo" means "cold", and "genes" means "that which generates", so "cryogenics" deals with systems that produce low temperatures. Cryogenic systems are required for many applications, including:

- Industrial gas production
- Food preservation
- Biomedical applications, such as magnetic resonance imaging
- Bearings
- Electronics
- Motors and generators
- Physics research
- Space technology
- High quality vacuum systems
- Magnets
- Electrical power transmission lines.

Most superconducting applications operate at $T \sim 4$ K (the boiling point of liquid helium), so cryogenic systems are required to maintain that temperature during operation, typically with liquid helium coolant. Liquid nitrogen ($T \sim 77$ K) may also be needed for high temperature superconductors and staged cooling of helium systems.

Materials properties change at low temperatures. Some materials become brittle, such as a banana peel or a flower cooled by liquid nitrogen.

Cryogenic refrigerators were developed by Kapitza in 1934 and Collins in 1947. About 300 W of input power are required to remove 1 W of heat inflow at $T \sim 4$ K. Modern cryogenic refrigerators using multiple stages of cooling and energy dissipation can operate reliably for many months.

Cryogenic engineers can use established practices and databases of materials properties to design reliable systems, taking into account dimensional changes, heat capacities, thermal conductivities, insulation, conduction, convection,

Fig. 2.13 ITER cryostat.
Courtesy of ITER
Organization
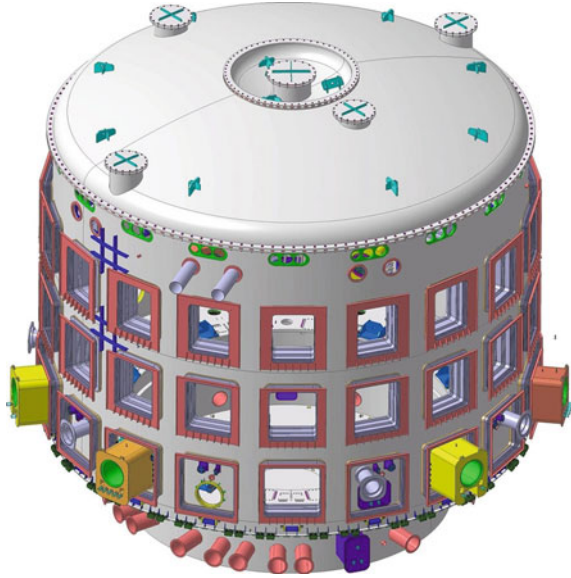
radiation, vapor shielding, flow rates, etc. A large magnet system may take many days to cool down from room temperature to operating temperature.

The massive cryostats surrounding the ITER magnets are shown in Fig. 2.13. Cryogenic systems are discussed in Chap. 10.

2.9 Plasma Diagnostics Systems

Plasma diagnostic systems are needed to measure the following basic plasma parameters (Hutchinson 2002; Hacquin 2008):

A complete four-dimensional space–time mapping of plasma parameters, with spatial resolution of millimeters and accuracies of a few percent, would be desirable, but is not practical to attain at this time. Two or three different techniques may be used for important parameters like electron density and temperature. The agreement of redundant methods provides assurance of their accuracy.

The diagnostic methods may be classified as

- Electric Probes
- Magnetic Probes
- Passive Particle Methods

Table 2.2 Some techniques for measuring electron density

Electron density
Langmuir probe
radiofrequency (RF) conductivity probes
Microwave, far infrared (FIR), and optical interferometers
Microwave cavity resonance
Heavy-ion beam probe
Neutral atom beam probe
Spectroscopy, such as stark broadening
Holographic interferometry
Thomson scattering
Alfven wave and sound wave propagation
Charged particle collectors
Photography

- Active Particle Methods
- Passive Wave Methods
- Active Wave Methods.

Passive methods measure particles or waves emitted by the plasma, and active methods inject particles or waves into the plasma. Table 2.2 illustrates the large variety of methods used for measuring one plasma parameter.

The locations of some ITER diagnostics systems are shown in Fig. 2.14.

Improved plasma diagnostics are continually being developed. The quantity and quality of diagnostics for an experiment are limited by the ports in the chamber, by space around the torus for the instruments, and by the available funds. Plasma diagnostic systems are discussed in Chap. 11.
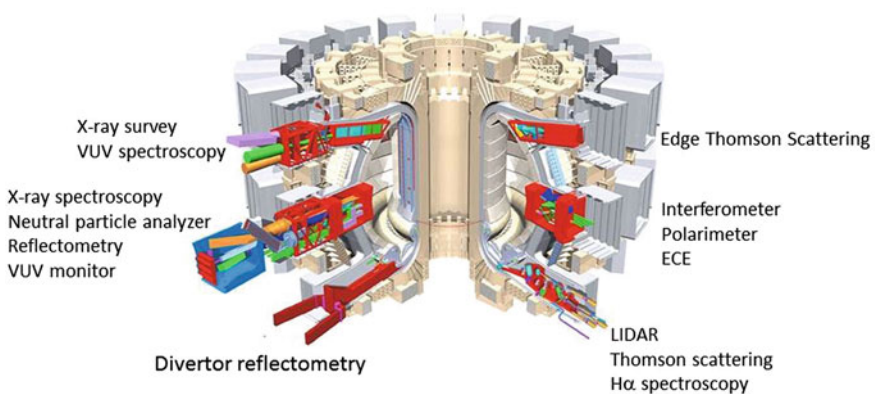
Fig. 2.14 Cutaway view of ITER showing where some diagnostics instruments will be mounted (Hacquin 2008). For simplicity, only a few are labelled. The names will be explained in Chap. 11. Courtesy of ITER Organization

2.10 Safety and Environment

The safety and environmental issues of fusion power include

- Tritium properties, inventory and transport
- Other radioisotope generation and transport
- Routine emissions
- Safety hazards
- Accident scenarios and analyses
- Radiation management approaches
- Materials resources.

Tritium is a radioactive beta emitter, with a half-life of 12.3 years and mean beta energy of about 6 keV. Tritiated water in the human body has a residency half-life of about 10 days, as it is eliminated via sweat, urine, and exhalation. HTO (tritiated water) is more dangerous to humans than gaseous tritium, which disperses more easily and is not so easy to ingest as HTO. The tritium inventory is very difficult to measure and control in a large facility.

Under bombardment by 14 MeV neutrons most structural materials and some coolants will become highly radioactive. The reactor management should calculate the inventories of each radioisotope, manage their safe containment and disposal, ensure that staff are trained in radiation safety, and promote a safety culture in the organization. Special "hot cells" with remote handling equipment will be used to manage the radioactive components.

There will be constant low-level emissions of gases and particulates from the reactor building, usually through a filtered stack. The plant operators will monitor the stack emissions to ensure that they stay within regulatory safe limits. For example, tritium emissions are carefully monitored at CANDU heavy water fission power plants.

Fusion power plant potential safety hazards include

- Fire, such as possible lithium/water reactions
- Explosion (hydrogen)
- Earthquake
- Flood
- People falling from elevated areas
- Electrical shock
- Eye hazards like breaking glass
- Toxic gases
- High magnetic fields
- Magnet quench arcing and pressure

- Severe plasma disruptions
- Structural fatigue and failures
- Exposure to intense electromagnetic waves
- Exposure to ionizing radiation
- Accidental release of tritium
- Accumulation of frozen oxygen in cryogenic systems.

Fusion power plant design studies consider potential accident scenarios, such as rupture of a high-pressure coolant tube, and estimate the possible consequences to the plant, to plant workers, and to the public offsite. It is highly desirable to ensure that no offsite evacuation would be required, even in the case of a severe accident, to gain public acceptance.

The power plant design would include plans for decommissioning, decontamination, and disposal of radioactive materials. Possible shortages of key materials, such as helium and niobium, should be taken into account when planning for deployment of hundreds of fusion power plants.

Safety and environmental issues will be discussed in Chap. 12.

2.11 Power Plant Designs

Power plant design issues include

- Criteria for attractive power plants
- Reliability, availability, and maintenance issues
- Economics estimates
- Fusion-fission hybrids
- Design studies in various countries.

Electric power utility companies have many criteria for selection of power plants to build, including:

- Output of power plant, MWe
- Capital cost per kW
- Cost of electricity, mills/KWh
- Length and rating of required transmission lines to cities and industries
- Size and flexibility of connected grid system
- Location away from areas of high seismic activity and flood danger
- Availability of fuel and its transportation systems (tritium is bred on-site)
- Fuel, operations and maintenance costs
- Feasibility of shipping large components, such as pressure vessels
- Acceptance by local population
- Security requirements and costs

- Availability and reliability of power plant
- Ease and speed of maintenance
- Waste disposal
- Staff numbers, skills, and costs
- Government laws and regulations
- Possible delays due to licensing and opposition.

The availability of fusion power plants is a difficult issue. Current experiments have many equipment failures because they are pushing their performance boundaries, and some components were not designed to be highly reliable or maintainable. This low overall availability of experiments would be unacceptable to utilities. The availability of power plants can be improved by designing and testing highly reliable components and by providing redundant components. The components must be designed for quick efficient repair or replacement. Repair of large power core subsystems, such as the superconducting magnets or vacuum vessel, would be very difficult and time consuming to accomplish, so they should last for the lifetime of the plant. Remote handling will be required for highly radioactive components, such as the first wall and blanket. All power core and hot cell subsystems must be capable of being maintained and replaceable with remote handling equipment.

We calculate the cost of each plant component or subsystem to estimate the total capital cost of the plant. This estimate is escalated according to the assumed interest rate and inflation rate to get an effective annualized capital cost. This is added to the annual cost of the fuel cycle and the operating and maintenance cost, and the sum is divided by the estimated annual net energy output (MWe, including down time for maintenance and equipment failures) to estimate the cost of electricity (COE) in units of cost per kWh for the country of operation (cents/KWh, Yen/kWh, etc.) Design studies for 1,000 MWe fusion power plants, assuming 70 % availability, typically estimate that the COE from fusion power would be higher than the COE from fission or coal plants. This is due mostly to the high capital cost and uncertain availability of the fusion reactors. The fusion fuel costs would be very low, while the operating and maintenance costs could be comparable to those of other power plants. The capital costs might be reduced by more compact designs, or by developing alternative confinement concepts.

Fusion reactors have a strong economy of scale, which means that a 3,000 MWe power plant would have a much lower COE than a 300 MWe plant, but utilities may not wish to build very large power plants (Dolan 1993).

Studies of hypothetical fusion power plants have been done in several countries (Europe, USA, Japan, China, …), and their results are discussed in Chap. 13 (ARIES Team; Dolan et al. 2005).

In addition to electrical power generation, fusion reactors could also be used to

- Produce hydrogen and other fuels for transportation and industry
- Desalinate seawater, which could alleviate water shortages that cause international strife

- Provide heat for industrial processes, such as distillation of alcohol and mining oil shale and tar sands
- "Incinerate" radioactive wastes, which are a major barrier to public acceptance of nuclear fission power plants
- Breed fuel for fission power plants, which could prolong the capability of fission power plants to meet world demand.

2.12 Fusion-Fission Hybrids

Fusion-fission hybrids would use uranium or thorium in the fusion reactor blankets, in addition to lithium. The blanket could be optimized either to produce more heat and electricity from the hybrid plant, to "incinerate" radioactive wastes, or to breed fissile fuel (^{239}Pu or ^{233}U) for use in satellite fission reactors. Such hybrids could improve fusion power economics (Chap. 14).

2.13 Problems

2.1. A central solenoid with area = 0.9 m^2 is pulsed at 8 T/s. What electric field is induced in the plasma at R = 3 m? If the plasma resistivity is twice that of copper, what average current density J is induced in the plasma? (Use E ≈ ηJ) If the plasma minor radius is 0.3 m, estimate the total plasma current.

2.2. A tokamak with R = 1.5 m, coil radius a_c = 0.7 m, is to have B = 2.2 T, provided by 16 copper coils with J = 9 MA/m^2. What are the required current per coil, cross sectional area of each coil, and total power dissipated?

2.3. If the central magnetic field of ITER is 5 T, what wave frequency (MHz) would be needed to heat deuterons there using the ion cyclotron resonance?

2.4. If a steam system can achieve 60 % of the Carnot efficiency and the cold temperature is 30 °C, what hot temperature (K) would be required to achieve a thermal-to-electrical conversion efficiency of 39 %?

2.14 Review Questions

1. What do the parameters in the following equation represent? How is it related to the toroidal field of a tokamak? B = μ_oNI/2πR.
2. What do the parameters in the following equation represent? $P_c = \eta J^2 V_c$.
3. About what temperatures are required for the superconductors used widely now?

4. Name four methods of plasma heating.
5. Sketch a tokamak, showing the toroidal field coils, central solenoid, toroidal field, plasma current, and poloidal field.
6. Why is ohmic heating ineffective at high temperatures?
7. For what type of confinement system could charged particle injection be used? For what type would it not succeed?
8. Sketch a neutral beam injector and explain how it works.
9. What NBI energies would be needed for large plasmas, such as ITER?
10. What frequencies would be good for plasma heating by electromagnetic waves?
11. What do the following equation and its parameters represent? $\eta_c = (T_h - T_c)/T_h$.
12. What materials make good neutron multipliers?
13. What thickness is required for the blanket-shield region?
14. What structural material and coolant are used for most places in ITER?
15. What are the functions of a divertor?
16. What materials are used for plasma-facing components in the ITER divertor?
17. What fueling methods can give good penetration into the plasma?
18. What is the leading candidate structural material for a fusion reactor?
19. What special materials may be used to coat the walls of a tokamak?
20. What does "cryogenics" mean, and why are such systems required for fusion research?
21. About how much power is required to remove 1 W of heat at 4 K?
22. What are the six categories of plasma diagnostic methods?
23. What factors limit the number of diagnostic systems on a large experiment?
24. What are the half-life and mean beta energy of tritium?
25. What materials limitations should be considered when planning for hundreds of fusion reactors?
26. Why would the cost of electricity from fusion power plants probably be higher than from fission or coal power plants?
27. What is "economy of scale"?
28. What are three possible applications of fusion reactors, in addition to generation of electricity?
29. What are possible uses of "fusion-fission hybrids"?

References

ARIES Team, various years. Many fusion reactor design studies are available online, see http://www-ferp.ucsd.edu/ARIES/

Dolan TJ (1993) Fusion power economy of scale. Fusion Technol 24:97–111

Dolan TJ, Yamazaki K, Sagara A (2005) Helical fusion power plant economics studies. Fusion Sci Technol 47:60–72

Hacquin S (2008) Plasma diagnostics in fusion devices, international summer school on fusion technologies, 2–13 Sept 2008, Karlsruhe, Germany

Hutchinson IH (2002) Principles of plasma diagnostics, 2nd edn. Cambridge University Press, Cambridge

Merola M (2008) Overview of the ITER plasma facing components. In: International high heat flux components workshop, La Jolla, CA, 10–12 Dec 2008

Sheffield J (1994) The physics of magnetic fusion reactors. Rev Mod Phys 66:1015–1103

Chapter 3
Pulsed and Water-Cooled Magnets

Thomas J. Dolan

Objectives

After studying this chapter one should understand

How to calculate magnetic fields
The electrical aspects of magnet systems
The mechanical and thermal aspects of magnet systems
How to deal with some coil design issues.

3.1 Magnetic Field Calculations

3.1.1 Background

Since the magnetic rock "lodestone" was discovered near Magnes, Greece (now part of Turkey), the curious phenomena associated with this rock became known as "magnetism". Magnetism first came under intense scientific study in the early nineteenth century. Oersted observed the deflection of a compass needle by a current-carrying wire; Ampere studied the interaction of two current-carrying wires; and Faraday formulated a law of magnetic induction and observed the rotation of polarized light by a magnetic field. Electromagnetic field theory was further developed by Maxwell, who published his famous treatise on electricity and magnetism in the 1870s, and by Heaviside, who put Maxwell's theory into the vector calculus form we use today. Interest in constructing high-field magnets increased around the turn of the century, following Fabry's analysis of high-field, air-cooled solenoids. A water-cooled solenoid, which developed over 5 T and could operate for many minutes, was

T. J. Dolan (✉)
NPRE Department, University of Illinois, Urbana, IL 61801, USA
e-mail: dolantj@illinois.edu

built by Deslandres and Perot in 1914. In the 1920s P. L. Kapitza produced magnetic fields up to 32 T using batteries and motor-generators, and T. F. Wall produced a field of 20 T using a capacitor bank. The volumes of these intense fields were about 0.2–2 cm^3. A field of 10 T was produced at MIT by Bitter in 1939. Higher fields were also produced during this period, but only for a few milliseconds. In 1964 Bitter and Montgomery produced a field of over 20 T with a coil requiring 10 MW of electrical power and about 100 m^3 of cooling water per minute.

Technically, the magnetic field is denoted by H and the magnetic induction or magnetic flux density by **B**, where **B** = μ**H**, and μ is the permeability of the medium. However, in fusion technology **B** is often called the "magnetic field", and this book follows that imprecise terminology.

To confine a reactor plasma with total pressure p in a confinement system characterized by β (Eq. 1.2), the required magnetic induction can be estimated from the equation

$$B^2 = 2\mu_o p/\beta \tag{3.1}$$

where $\mu_o = 4\pi \times 10^{-7}$ H/m is the permittivity of free space. For example, if p = 10^5 Pa (~1 atm) and β = 0.1, then B = 1.6 T. The peak field at the magnet coil conductor is usually significantly larger than the field in the plasma core.

3.1.2 Basic Equations for Calculating B

Let the vector **r** with components (x, y, z) represent the place where we want to calculate the magnetic field, and the vector **r'** with components (x', y', z') represent the location of a differential volume dV through which a current density J flows (Fig. 3.1).

Then the vector

$$\rho = \mathbf{r} - \mathbf{r'}$$

points from dV to the place where we want to calculate the magnetic field, and its length is the distance between these two points. According to the Law of Biot–Savart, the differential magnetic field produced at r by current density **J** flowing through dV is

Fig. 3.1 Definition of coordinates
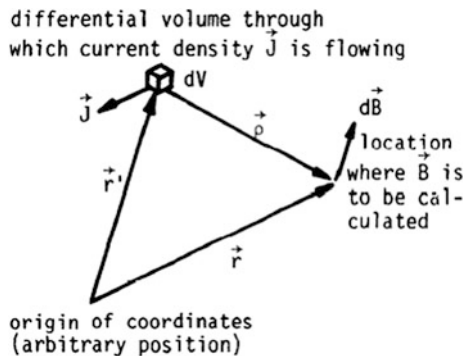
Fig. 3.2 The case of a wire with cross-sectional area dS

for filamentary currents:
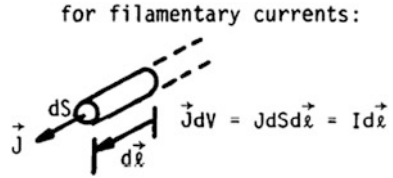
$$d\mathbf{B} = \mu_o dV \mathbf{J} \times \boldsymbol{\rho}/4\pi\rho^3. \tag{3.2}$$

The total magnetic field at **r** is found by integrating over the entire volume where currents are flowing

$$\overrightarrow{B}(r) = \int d\overrightarrow{B} = \frac{\mu_0}{4\pi}\int \frac{dV\,\overrightarrow{J} \times \overrightarrow{\rho}}{\rho^3} \text{ (T)} \quad \textbf{Biot–Savart Law} \tag{3.3}$$

For the case of filamentary currents (thin wires), $\mathbf{J}dV = Id\ell$ (Fig. 3.2) so this equation simplifies to

$$\overrightarrow{B}(r) = \frac{\mu_0 I}{4\pi}\int_{\text{wire}} \frac{d\ell \times \overrightarrow{\rho}}{\rho^3} \text{ (T)} \tag{3.4}$$

where the integration path is along the wire in the direction of current flow.

If magnetic materials, such as plain steel and soft iron, are nearby, the magnetic field will be distorted, and the results of these equations will be inaccurate. In calculating the total magnetic field at a point, the volume of integration should include both the magnet coils and the plasma, since plasma currents can be significant.

For the case in which the currents **J** vary in time, there is a slight delay between the time **J** changes at **r′** and the time when the effect is observed at **r**, but this delay time is negligibly short for cases of interest, and we can use Eq. (3.3) to calculate **B(r**,t) corresponding to **J(r′**, t) as if the "action at a distance" were instantaneous.

For cases in which angular symmetry exists, it is sometimes easier to calculate B from the integral form of **Ampere's Law** (Eq. 2.5), ignoring the ∂E/∂t term

$$\oint d\overrightarrow{\ell} \cdot \overrightarrow{B} = \mu_0 \iint d\overrightarrow{S} \cdot \overrightarrow{J} = \mu_0 I \text{ (enclosed)} \tag{3.5}$$

where dS is integrated over the surface bounded by the closed curve of the line integral. This equation was used in Sect. 2.2 (Please see Appendix D for vector relations).

The magnetic field may also be calculated from

$$\mathbf{B} = \nabla \times \mathbf{A} \tag{3.6}$$

where the magnetic vector potential **A** is defined by

$$\overrightarrow{A} = \frac{\mu_0}{4\pi}\int \frac{dV\,\overrightarrow{J}}{\rho} = \frac{\mu_0 I}{4\pi}\int \frac{d\ell}{\rho} \tag{3.7}$$
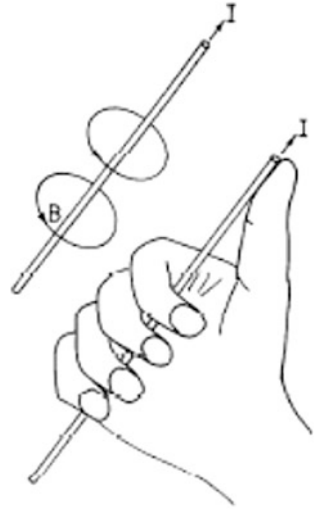
The direction of the magnetic field lines can be determined from the "right hand
rule", shown in Fig. 3.3.

3.1.3 Long Straight Wire

The magnetic field from a straight wire carrying a current I may be found from Eq.
(3.4) using the geometry illustrated in Fig. 3.4.

According to the Biot–Savart Law,

$$
\begin{aligned}
dB &= \frac{\mu_0 I}{4\pi} \frac{d\vec{\ell} \times \vec{\rho}}{\rho^3} = \frac{\mu_0 I}{4\pi} \frac{d\ell \cos\theta}{\rho^2} \\
&= \frac{\mu_0 I}{4\pi} \frac{d(r\tan\theta)\cos\theta}{(r/\cos\theta)^2} = \frac{\mu_0 I}{4\pi r} \cos\theta d\theta
\end{aligned}
\tag{3.8}
$$

since r is a constant. If the ends of the wire subtend angles θ_1 and θ_2, then

$$
\begin{aligned}
B(r) &= \frac{\mu_0 I}{4\pi r} \int_{\theta_1}^{\theta_2} d\theta \cos\theta d\theta \cos\theta \\
&= \frac{\mu_0 I (\sin\theta_2 - \sin\theta_1)}{4\pi r}
\end{aligned}
\tag{3.9}
$$

with the magnetic field lines forming circles around the wire. For the special case
of an infinitely long wire, $\theta_2 = \pi/2$ and $\theta_1 = -\pi/2$, so

Fig. 3.4 Geometry for calculation of the magnetic field of a long straight wire from the Biot–Savart Law
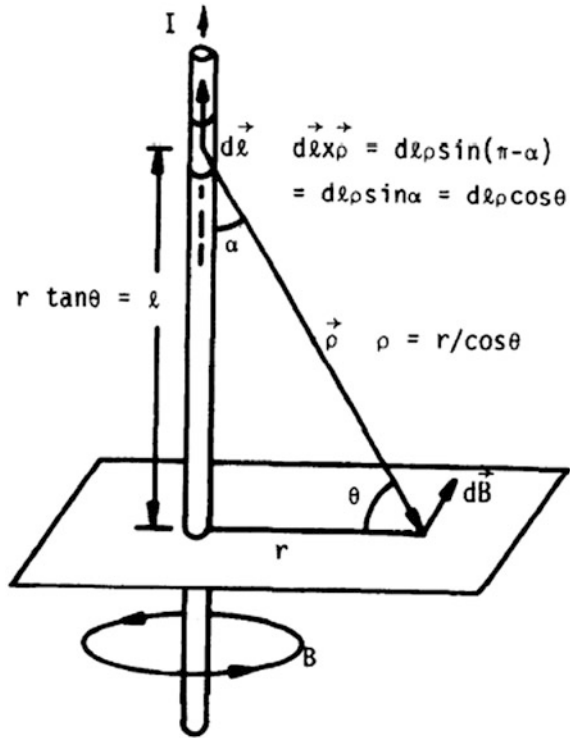
$$B(r) = \mu_o I/2\pi r \qquad (3.10)$$

This result can also be derived from Ampere's Law, as done in Sect. 2.2. The result is the same:

$$2\pi r B(r) = \mu_o I. \qquad (3.11)$$

3.1.4 Toruses (or Tori) and Solenoids

Figure 3.5 shows a torus with a wire coil wrapped around it. The torus is partially cut away to show the integration path for Eq. (3.5).

If the torus has N turns of wire each carrying the same current I, then Ampere's Law reduces to

$$2\pi R B(R) = \mu_0 NI, \quad B(R) = \mu_0 NI/2\pi R \qquad (3.12)$$

For values of R less than the radius where the coils are, there is no enclosed current, and $B(R) = 0$. For values of R outside the outer windings, the currents of the outer windings cancel the currents of the inner windings, the net enclosed
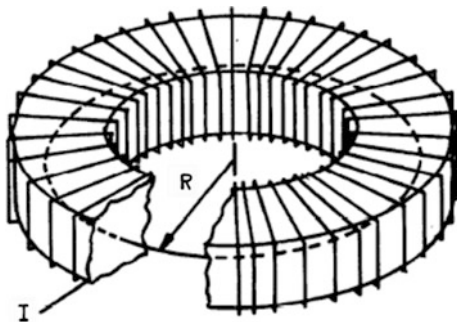
current is again zero, and B(R) = 0. Let L = 2πR. In the limit as the major radius R of the torus becomes infinitely large, its radius of curvature is infinitely large, and each section of the torus is like a section of a straight solenoid. Thus, we can deduce that the field in a long straight solenoid is

$$B = \mu_o(N/L)I \tag{3.13}$$

where N/L is the number of turns per unit length. These results do not depend upon the shape of the cross sections of the torus or solenoid. The accuracy with which an actual toroidal field agrees with Eq. (3.12) depends upon how uniform and closely spaced the toroidal field windings are, and likewise for the solenoid. If there are few windings widely spaced, then better accuracy can be obtained by integrating Eq. (3.4) along the path of the windings.

3.1.5 Circular Loops

In practice, toroidal and solenoidal magnetic fields are often produced by using a set of circular magnet coils. The resultant field may then be calculated by adding the fields of the individual coils, and each coil may be approximated as a set of circular loops. Therefore, the field produced by a circular loop of radius a carrying current I, as shown in Fig. 3.6, is of fundamental importance.

The resultant magnetic field has components in the r and z directions (cylindrical geometry). The Biot–Savart Law cannot be integrated analytically for this case. However, Eq. (3.7) for the vector potential may be expressed in terms of "complete elliptic integrals"

$$
\begin{aligned}
K(k) &\equiv \int_0^{\pi/2} d\theta / (1 - k^2 \sin^2\theta)^{\frac{1}{2}}, \\
E(k) &\equiv \int_0^{\pi/2} d\theta (1 - k^2 \sin^2\theta)^{\frac{1}{2}}
\end{aligned}
\tag{3.14}
$$

Fig. 3.6 Geometry for
calculation of the magnetic
field due to a circular loop of
radius a located in the x–y
plane and carrying a current I
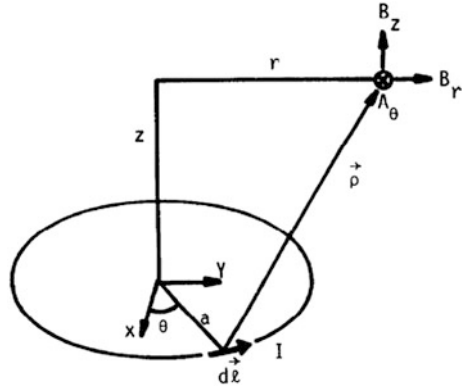
Values of these integrals are given in Table 3.1.

If we let

$$k = \left[\frac{4ra}{z^2 + (r+a)^2} \right]^{\frac{1}{2}} \tag{3.15}$$

then the resulting equation for **A** has only a θ component, given by (Shadowitz 1975).

$$A_\theta = \frac{\mu_0 I a^{1/2}}{2\pi r^{1/2}} \left[\left(\frac{2}{k} - k \right) K(k) - \frac{2}{k} E(k) \right] \tag{3.16}$$

After taking the curl of **A**, the components of **B** are found to be

$$B_r = -\frac{\partial A_\theta}{\partial z} = \frac{\mu_0 I k z}{4\pi (ar^3)^{\frac{1}{2}}} \left[-K(k) + \frac{(1 - 0.5k^2)}{(1 - k^2)} E(k) \right]$$

$$B_z = \frac{1}{r}\frac{\partial}{\partial r} r A_\theta = \frac{\mu_0 I k}{4\pi (ar)^{\frac{1}{2}}} \left[K(k) + \frac{(a+r)k^2 - 2r}{2r(1 - k^2)} E(k) \right] \tag{3.17}$$

The elliptic integrals can be estimated from Table 3.1, computed using the IBM computer subroutine CEL2, or with polynomial approximations from Abramowitz and Stegun (1964). For a point on the axis, the field components can be found by letting $r \to 0$ and using L'Hospital's rule, with the result that $B_r = 0$ and

$$B_z = \frac{\mu_0 I a^2}{2(a^2 + z^2)^{3/2}} \tag{3.18}$$

This result can also be obtained by direct use of Eq. (3.4) with Fig. 3.6 for the case of $r = 0$.

Table 3.1 Complete elliptic integrals

k	K(k)	E(k)	k	K(k)	E(k)	k	K(k)	E(k)
0	1.57080	1.57080	0.34	1.61940	1.52437	0.68	1.82347	1.36934
0.01	1.57084	1.57076	0.35	1.62253	1.52153	0.69	1.83434	1.36258
0.02	1.57095	1.57064	0.36	1.62577	1.51859	0.7	1.84569	1.35566
0.03	1.57115	1.57044	0.37	1.62914	1.51557	0.71	1.85756	1.34858
0.04	1.57143	1.57017	0.38	1.63263	1.51245	0.72	1.86999	1.34132
0.05	1.57178	1.56981	0.39	1.63625	1.50925	0.73	1.88300	1.33389
0.06	1.57221	1.56938	0.4	1.64000	1.50594	0.74	1.89665	1.32628
0.07	1.57273	1.56887	0.41	1.64389	1.50254	0.75	1.91099	1.31847
0.08	1.57332	1.56828	0.42	1.64792	1.49905	0.76	1.92607	1.31047
0.09	1.57399	1.56761	0.43	1.65209	1.49545	0.77	1.94197	1.30227
0.1	1.57475	1.56686	0.44	1.65641	1.49176	0.78	1.95875	1.29385
0.11	1.57558	1.56603	0.45	1.66089	1.48797	0.79	1.97649	1.28522
0.12	1.57650	1.56513	0.46	1.66552	1.48407	0.8	1.99530	1.27635
0.13	1.57750	1.56414	0.47	1.67032	1.48008	0.81	2.01529	1.26724
0.14	1.57858	1.56307	0.48	1.67528	1.47598	0.82	2.03657	1.25788
0.15	1.57975	1.56192	0.49	1.68043	1.47177	0.83	2.05932	1.24824
0.16	1.58100	1.56069	0.5	1.68575	1.46746	0.84	2.08370	1.23833
0.17	1.58233	1.55939	0.51	1.69126	1.46304	0.85	2.10994	1.22811
0.18	1.58376	1.55799	0.52	1.69697	1.45851	0.86	2.13828	1.21757
0.19	1.58527	1.55652	0.53	1.70288	1.45387	0.87	2.16906	1.20669
0.2	1.58687	1.55497	0.54	1.70901	1.44911	0.88	2.20268	1.19544
0.21	1.58856	1.55333	0.55	1.71535	1.44424	0.89	2.23962	1.18379
0.22	1.59034	1.55161	0.56	1.72193	1.43926	0.9	2.28055	1.17170
0.23	1.59221	1.54981	0.57	1.72875	1.43415	0.91	2.32631	1.15913
0.24	1.59418	1.54793	0.58	1.73581	1.42892	0.92	2.37807	1.14602
0.25	1.59624	1.54596	0.59	1.74315	1.42356	0.93	2.43746	1.13232
0.26	1.59840	1.54390	0.6	1.75075	1.41808	0.94	2.50686	1.11792
0.27	1.60066	1.54176	0.61	1.75865	1.41247	0.95	2.59001	1.10272
0.28	1.60302	1.53954	0.62	1.76685	1.40673	0.96	2.69314	1.08655
0.29	1.60548	1.53723	0.63	1.77538	1.40086	0.97	2.82800	1.06915
0.3	1.60805	1.53483	0.64	1.78424	1.39484	0.98	3.02098	1.05009
0.31	1.61072	1.53235	0.65	1.79345	1.38869	0.99	3.35660	1.02848
0.32	1.61350	1.52978	0.66	1.80305	1.38239	1	∞	1.00000
0.33	1.61640	1.52712	0.67	1.81305	1.37594			

Example Problem 3.1: Magnetic field of circular coil A circular coil of radius 0.5 m carries a current of 100 kA. Find the magnetic field 0.4 m from the axis of the coil at a distance of 0.6 m from the plane of the coil.

Here $a = 0.5$, $r = 0.4$, and $z = 0.6$, so $k = 0.827$, $K = 2.052$, $E = 1.251$. Then from Eq. (3.17) we find that $B_r = 0.0025$ T and $B_z = 0.027$ T.

An approximate method for calculating the magnetic fields due to circular coils with rectangular cross section is given in Dolan (1982).
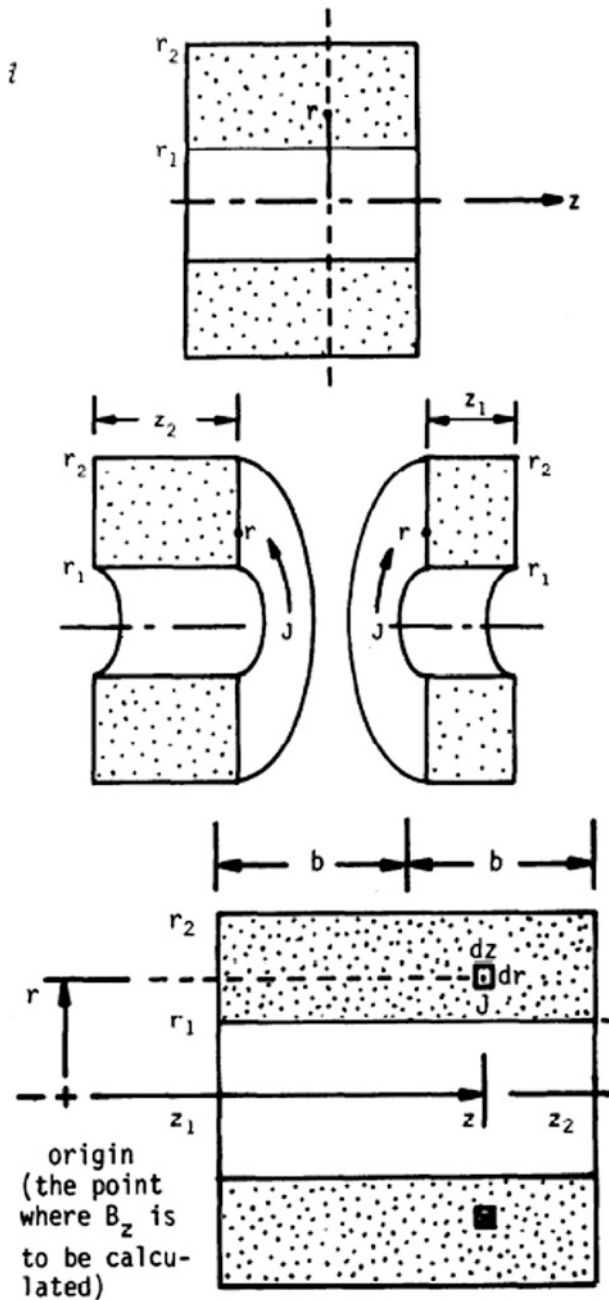
Fig. 3.7 Geometry for finding the axial field in a solenoid. If B_z is to be calculated inside the solenoid, then z_1 will be negative. If B_z is to be found to the right of the solenoid, both z_1 and z_2 will be negative

3.1.6 Axial Field of Solenoid

A simple formula can be derived for the field on the axis of a solenoid, as illustrated in Fig. 3.7.

Replacing I by Jdrdz in Eq. (3.18), we find

$$dB_z = \frac{\mu_0 J drdz\ r^2}{2(r^2 + z^2)^{3/2}} \tag{3.19}$$

The integral of dB_z over the coil area is

$$
\begin{aligned}
B_z &= \frac{\mu_0 J}{2} \int_{r_1}^{r_2} drr^2 \int_{z_1}^{z_2} \frac{dz}{(r^2 + z^2)^{3/2}} \\
&= \frac{\mu_0 J}{2} \left\{ z_2 \ln\left[\frac{r_2 + (r_2^2 + z_2^2)^{\frac{1}{2}}}{r_1 + (r_1^2 + z_2^2)^{\frac{1}{2}}}\right] - z_1 \ln\left[\frac{r_2 + (r_2^2 + z_1^2)^{\frac{1}{2}}}{r_1 + (r_1^2 + z_1^2)^{\frac{1}{2}}}\right] \right\} \quad (T).
\end{aligned}
\tag{3.20}
$$

At the center of the solenoid $z_1 = -b$ and $z_2 = b$, so this reduces to

$$B_z = \mu_0\ Jb \ln\left[\frac{r_2 + (r_2^2 + b^2)^{\frac{1}{2}}}{r_1 + (r_1^2 + b^2)^{\frac{1}{2}}}\right] \quad (T) \tag{3.21}$$

3.1.7 Complex Coil Shapes

Some coils are not circular, however. For example, Yin-Yang coils (in magnetic mirror fusion experiments) and helical windings (stellarators and torsatrons) require the use of computer codes (MAFCO, GAUSS, Opera, Tosca, …). One specifies the coordinates of the coil segments and the locations where the magnetic field is to be calculated. The programs can be directed to follow the path of any given magnetic field line and to print out the coordinates of its trajectory, facilitating magnetic field mapping and ion orbit calculations (Perkins and Brown 1966).

3.2 Coil Forces

Massive structural supports must be provided to sustain the enormous forces produced by interaction of the magnet coil currents with the magnetic field. The basic equation for the differential force on a volume dV of conductor with current density **J** in a magnetic induction **B** is

$$d\overrightarrow{F} = \overrightarrow{J} \times \overrightarrow{B}\ dV \quad (N). \tag{3.22}$$

For thin wires, JdV may again be replaced by Idℓ. The total force on a given volume of conductor is equal to the integral of d**F** over that volume.

3.2.1 Long, Parallel Wires

The case of two long, parallel wires carrying currents I_1 and I_2 is illustrated in Fig. 3.8.

With parallel currents the wires attract each other, and with anti-parallel currents they repel each other, hence, the saying "Like currents attract, unlike currents repel". This rule also holds for the case of two coaxial circular loops. (This is the opposite of the situation for electrostatic charges, where "Like charges repel, unlike charges attract"). Since $B_1 = \mu_o I_1/2\pi r$ the magnitude of the force per unit length on wire 2 is

$$dF/dl = \mu_0 I_1 I_2/2\pi r \quad (N/m) \tag{3.23}$$

The force on wire 1 has the same magnitude.

3.2.2 Coaxial Circular Loops

For the case of two coaxial circular loops with equal radii a in Fig. 3.9, the B_z field produces radial forces on the coils, which create internal stress. However, this does not cause coil motion, since the net force on the coil as a whole is zero.

The radial field B_r produces an axial thrust F_z tending to pull the coils together, if they have co-directional currents, or to push the coils apart, if they have opposite currents. The total force on a coil is
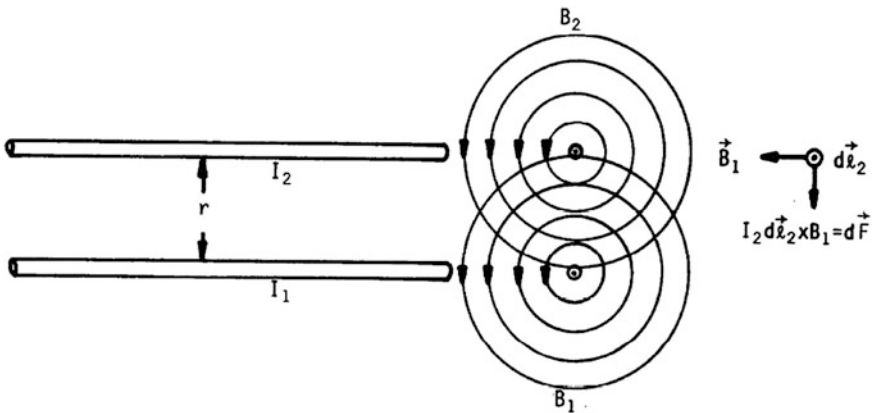
Fig. 3.8 Calculation of forces between two long, parallel wires

Fig. 3.9 Two coaxial circular current loops
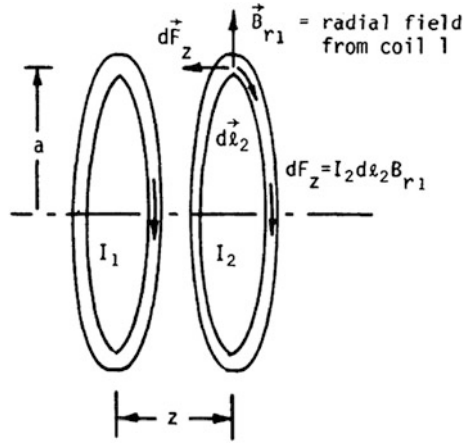
$$F_z = \int dF_z = I_2 B_{r1} \int d\ell_2 = 2\pi a I_2 B_{r1} \quad (N) \tag{3.24}$$

where B_{r1} may be evaluated from Eq. (3.17).

Example Problem 3.2: Force between coils Two coaxial coils with radii $a = 1$ m are separated by $z = 1$ m. If each coil carries a current $I = 1$ MA, find the force between them.

For this case it is found that $k^2 = 0.8$, $k = 0.8944$, $K = 2.257$, and $E = 1.178$. Then $B_r = 0.0697$ T, and $F = 4.38 \times 10^5$ N (98,400 lbs).

3.2.3 Solenoids

The cross section of a long solenoid is illustrated in Fig. 3.10.

Within the coil $r_1 < r < r_2$, and

$$B(r) = B(r_2 - r)/\Delta r \tag{3.25}$$

assuming the current density to be uniform. Using Eq. (3.22), the outward force on the small segment of the free body diagram is found to be

$$F_r = \int_{r_1}^{r_2} dF_r = \int_{r_1}^{r_2} JB \ dv = J \int_{r_1}^{r_2} drr \ d\theta dz \ B(r_2 - r)/\Delta r$$

$$F_r = \frac{JBr_1 \Delta r d\theta dz}{2}\left(1 + \frac{\Delta r}{3r_1}\right) \tag{3.26}$$

where r_2 was eliminated using $r_2 = r_1 + \Delta r$. Since the total coil current $NI = J\Delta rL$, Eq. (3.13) may be written
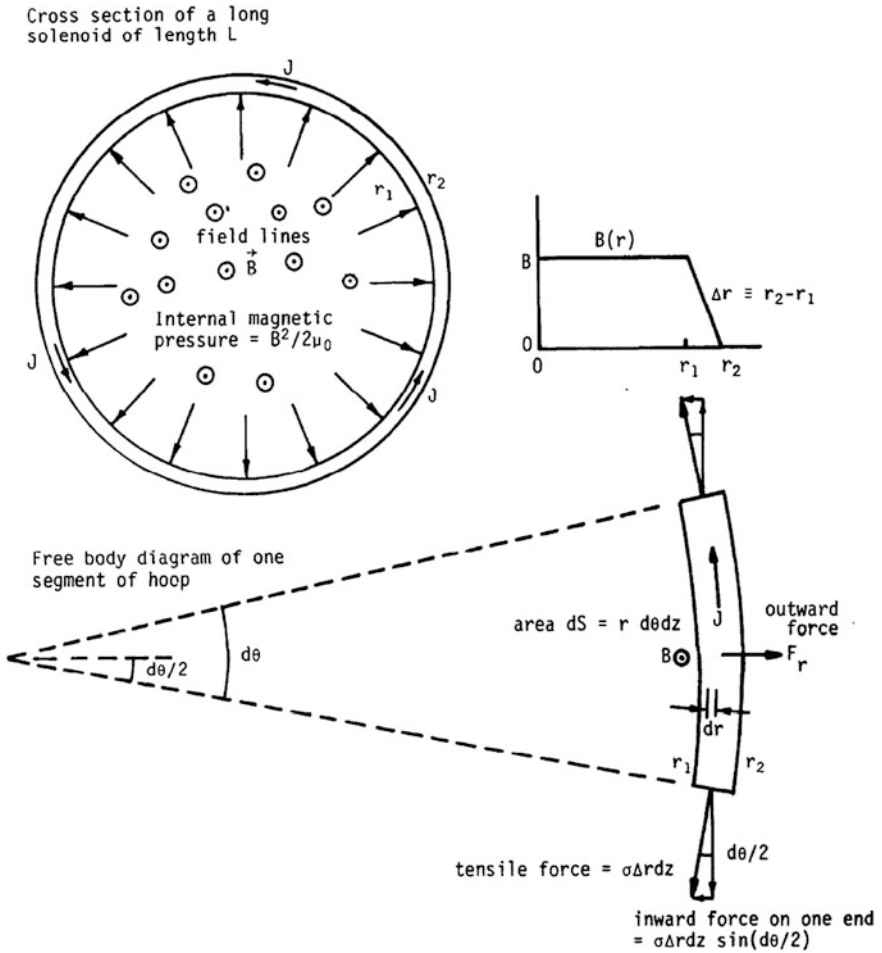
Fig. 3.10 The cross section of a long solenoid, radial variation of B, and free body diagram of one segment of the coil

$$B = \mu_0(N/L)I = \mu_0 J \Delta r \qquad (3.27)$$

If J is eliminated between Eqs. (3.26) and (3.27), the result is

$$F_r = \left(\frac{B^2}{2\mu_0}\right) r_1 d\theta dz (1 + \Delta r/3r_1) \quad (N) \qquad (3.28a)$$

For very small Δr this is equal to the magnetic pressure times the inner surface area. Equating this outward magnetic force to the inward tensile force (Fig. 3.10) we have

$$\left(\frac{B^2}{2\mu_0}\right) r_1 d\theta dz \left(1 + \frac{\Delta r}{3r_1}\right) = 2\sigma\Delta r \ dz \ \sin(d\theta/2) \cong \sigma\Delta r dz d\theta \qquad (3.28b)$$

The resultant average tensile stress is found to be

$$\sigma = (B^2/2\mu_0)\left(\frac{r_1}{\Delta r} + \frac{1}{3}\right) \quad (Pa). \qquad (3.29)$$

For example, if $r_1/\Delta r = 5$ and $B = 10$ T, then $\sigma = 212$ MPa (31,000 psi). This is near the yield stress of copper, which is about 280 MPa (40,000 psi). Nevertheless, these equations can lead to large errors (more than a factor of 10) if the coil is not very thin. A simple alternative estimate of the stress is

$$\sigma \approx JBr_1 \qquad (3.30)$$

which is usually correct within a factor of 2 (Bird 2011).

3.2.4 Force-Reduced Torsatron Coils

Torsatron coils were illustrated in Chap. 1. For a torsatron reactor, the forces on these coils could become enormous, but it is possible to minimize the forces by using a force-reduced coil geometry. The principle of force reduction is illustrated in Fig. 3.11.

Long, straight, parallel conductors with currents in the same direction would have radially inward attractive forces between them. A solenoid, on the other hand, has radially outward magnetic pressure forces. A long straight helix, then, has a combination of the radially inward and radially outward forces. If the pitch of the solenoid is properly chosen, the two radial forces cancel out, resulting in a "force-free" helical winding set.

When the helical windings are bent into a torus, an additional vertical magnetic field is produced, resulting in coil forces. However, by adding a pair of large, circular coils around the outside of the torus to produce an opposite vertical field, the vertical field may be nearly cancelled out, again resulting in low coil forces. In one torsatron reactor design, the resultant coil forces are about 1/30 of what they would be without using the force-reduced geometry. In addition to nullifying the vertical field of the helical coils, the vertical field coils transfer the radial forces to a convenient external structure and greatly reduce stray magnetic fields outside the reactor. (To optimize plasma confinement, it is desirable to shift the magnetic axis outwards a little, which can be accomplished with trim coils producing about 5 % of the vertical field.)

For an $\ell = 3$ configuration, calculations of force-reduction and plasma confinement indicate that the optimum pitch angle is about 42°, and the optimum aspect ratio $R/a_c \sim 7$, where a_c is the minor radius of the helical windings. By careful selection

Fig. 3.11 Conductor configurations around a long, straight cylinder. **a** Rods with parallel currents, **b** A solenoid, **c** Helices. The helix has both the inward forces of the rods and the outward forces of the solenoid
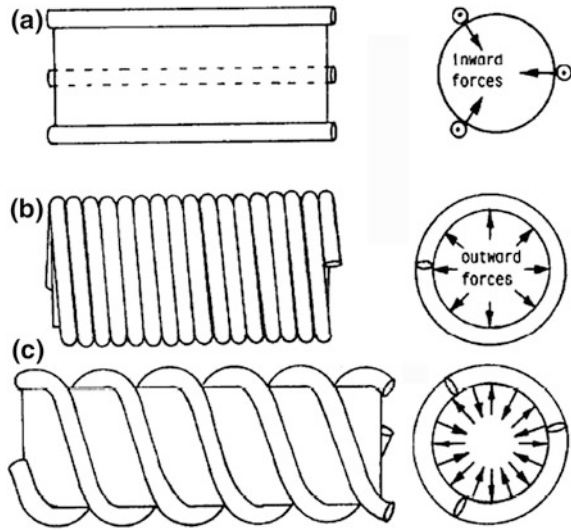
of the number of field periods around the torus, the three helical windings can be connected end to end (electrically in series), so that they all have the same current.

3.3 RLC Circuit Equations

3.3.1 Background

Here R = resistance, L = inductance, and C = capacitance. Pulsed magnet systems consist of energy storage devices, switches, current transmission lines, and coils. Such systems can have higher coil currents and less severe cooling requirements than water-cooled dc magnets. Large capacitor banks (>10 MJ), high voltage switches, and cables have been developed, and ultrahigh fields have been generated using magnetic flux compression in single-shot experiments. Analysis of the circuit equations enables us to determine what values of inductance and capacitance are desirable in order to produce high magnetic fields efficiently.

3.3.2 Circuit Equations

A simple RLC circuit representing a pulsed magnet system is illustrated in Fig. 3.12.

The capacitor C is charged up to a voltage V with the switch S_1 open. Then S_1 is closed at t = 0. The problem is to determine the current I in the circuit as a

Fig. 3.12 A simple RLC
circuit. Here R represents the
total resistance of all
elements in the circuit, such
as the capacitor, switch,
transmission lines, headers,
and magnet coil. L represents
the total inductance of all the
circuit elements
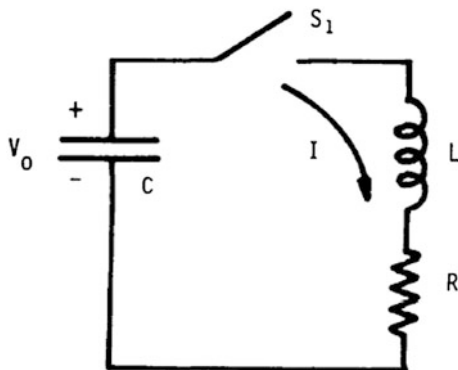
function of time. Then the magnetic field produced by the coil can be calculated approximately using methods from the previous section. If q is the charge on the capacitor, then the voltage across the capacitor is q/C. The voltage drop across the resistance R is R(dq/dt), and the voltage drop across the inductance L is $L(d^2q/dt^2)$, assuming L to be a constant. (In an actual circuit, L will vary, because of phenomena such as plasma diamagnetism. However, a simple estimate of the current can be obtained assuming L to be constant.) By Kirchoff's Law, the sum of the voltages around the circuit is zero, and

$$L(d^2q/dt^2) + R(dq/dt) + q/C = 0 \qquad (3.31)$$

The initial conditions are q = CV, and dq/dt = 0. This linear, homogeneous, second-order differential equation can be solved by using the operator notation D = (d/dt), for which

$$(LD^2 + RD + 1/C)q = 0. \qquad (3.32)$$

The roots of this quadratic equation are

$$D = -a \pm i\omega \qquad (3.33)$$

where a = R/2L and $\omega = [(1/CL) - a^2]^{1/2}$. For pulsed circuits the resistance is kept low, so the quantity in brackets is positive, and the solution is oscillatory. The general solution is therefore

$$q(t) = A_1 e^{-at+i\omega t} + A_2 e^{-at-i\omega t} \qquad (3.34)$$

which may also be expressed in terms of trigonometric functions as

$$q(t) = A_3 e^{-at}\cos\omega t + A_4 e^{-at}\sin\omega t \qquad (3.35)$$

(This method is described in texts on differential equations. The Laplace transform method may also be used to obtain this solution). From the initial condition at $q(0) = cV_o$, we find that $A_3 = CV_o$. From the other initial condition that
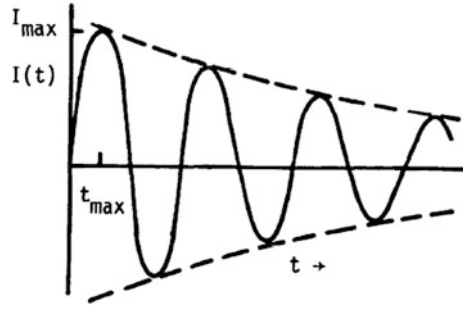
(dq/dt) = 0 at t = 0 we find that $A_4 = aA_3/\omega$. The current is found from $I(t) = -dq/dt$. The result is

$$q(t) = CV_0 e^{-at}(\cos\omega t + (a/\omega)\sin\omega t) \tag{3.36}$$

$$I(t) = (V_0/\omega L)e^{-at}\sin\omega t \tag{3.37}$$

Thus, $I(t)$ is a damped sinusoid (Fig. 3.13).

Setting $dI/dt = 0$ we find the time of maximum current and the maximum current:

$$t_{max} = (1/\omega)\text{Arctan}(\omega/a) \tag{3.38}$$

$$I_{max} = (V_0/\omega L)\exp(-at_{max})\sin(\omega t_{max}) \tag{3.39}$$

If R, L, C, and V_o are known, the t_{max} and I_{max} can be predicted. Conversely, if R and L are unknown, they can be calculated from measured values of t_{max} and I_{max}.

Usually it is desired to have the coil current rise to its maximum value, then stay near that value for as long as possible, instead of oscillating with a damped sinusoid, as shown in Fig. 3.13. If a second switch S_2 is added to the circuit (Fig. 3.14 top), it can be closed when $I = I_{max}$, effectively short-circuiting L_3 at maximum coil current. Then the coil current gradually decays from its peak value with a time constant of $[(L_2 + L_3)/)(R_2 + R_3)]^{1/2}$ (Fig. 3.14 bottom). The switch S_2 is called a "crowbar".

3.3.3 Resistance and Inductance

Usually the parameters of capacitors, cables, and switches are specified by the manufacturer. The dc resistance of conductors in general may be estimated from the equation

Fig. 3.14 *Top* A crowbar switch. R_1 and L_1 are the combined resistance and inductance of the capacitor, switch S_1, and other elements of the C-S_1 circuit. R_2 and L_2 represent the resistance and inductance of the S_2 (crowbar) switch circuit, and R_3 and L_3 refer to the load circuit, including coil, header, transmission lines, etc. *Bottom* Waveform of a crowbarred circuit. The dashed curve would occur if the circuit were not crowbarred. There will also be some ripples (not shown here) on the decay current, due to interaction of energy stored in L_2 and L_3, that may be deleterious in some experiments
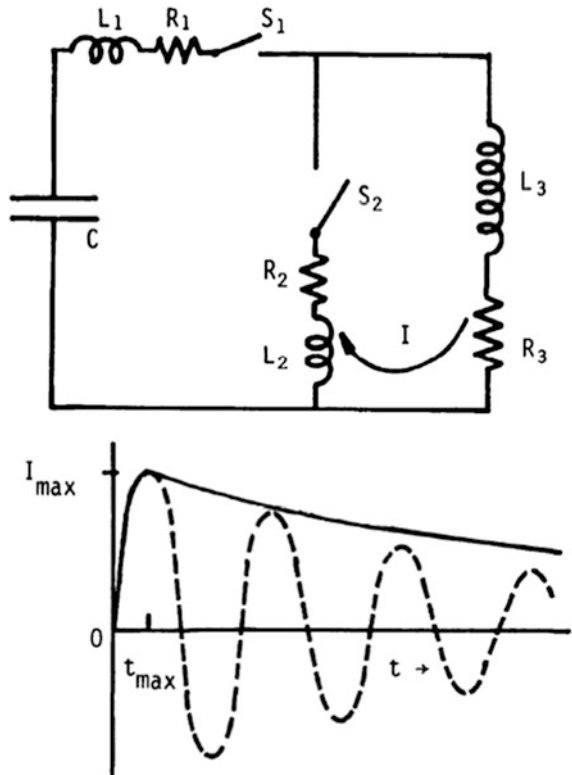
Fig. 3.15 Inductance L (Henry) of a uniform-current–density solenoid with N turns as a function of $\beta = \ell/2r_1$ and $\alpha = r_2/r_1$. From D. B. Montgomery, Reports on Progress in Physics 29, 69–104 (1963) Fig. 4.2, © 1963 The Institute of Physics
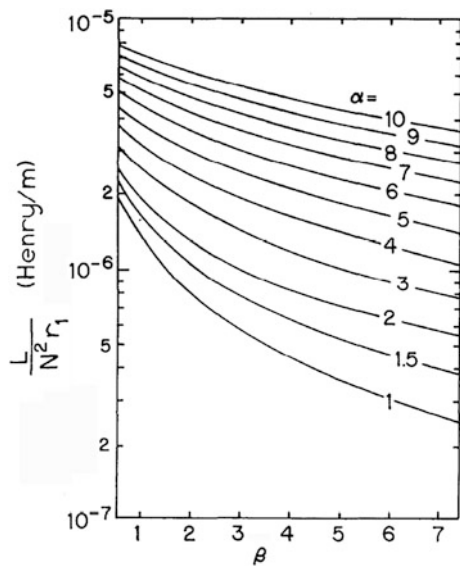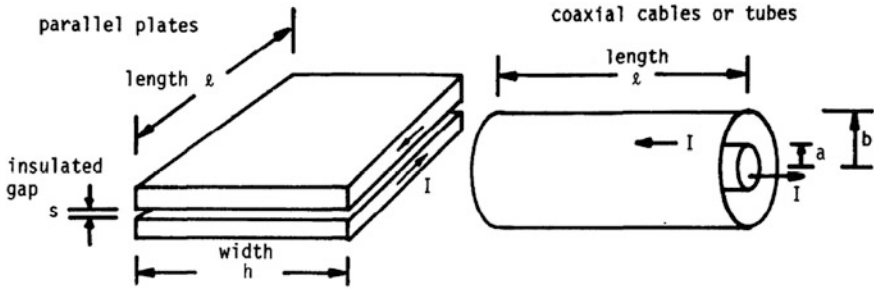
Fig. 3.16 Parameters of parallel plate and coaxial transmission lines

Fig. 3.17 Values of Ksh versus (s/h) for a parallel plate transmission line. If s/h ≪ 1, then Ksh ≈ 1. (Knoepfel 1970 p. 323)
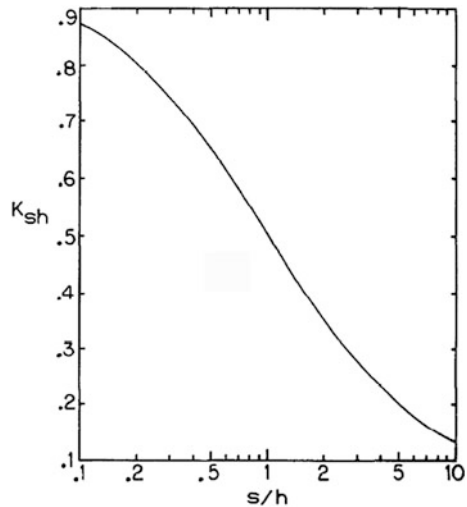
$$R = \int_0^\ell dx\, \eta/S \quad \text{(Ohm)} \tag{3.40}$$

where S = cross sectional area of the conductor (m^2), η = resistivity of the metal (Ohm m), and ℓ = length (m) of the component. However, in pulsed operation the current may be concentrated on the surface, due to the "skin effect" (Sect. 3.3).

The inductance of a uniform-current–density solenoid of length ℓ, inner radius r_1, and outer radius r_2 with N turns can be found from information in Fig. 3.15.

The inductance of parallel plate and coaxial transmission lines are

$$L = \mu_0 s \ell K_{sh}/h \quad \text{(H)} \tag{3.41}$$

$$L = \mu_0 \ell \ln(b/a)/2\pi \quad \text{(H)} \tag{3.42}$$

where the dimensions (m) are defined in Fig. 3.16.

The factor K_{sh} is given in Fig. 3.17 Knoepfel (1970) gives inductances for more complex shapes.

3.4 Distribution of J and B

From "Ohm's Law" and the Maxwell equations it can be shown that J and B obey similar equations:

$$\frac{\partial \overrightarrow{J}}{\partial t} = \nabla^2 \overrightarrow{J}/\sigma\mu \qquad\qquad \sigma = 1/\eta$$
$$\frac{\partial \overrightarrow{B}}{\partial t} = \nabla^2 \overrightarrow{B}/\sigma\mu \tag{3.43}$$

where σ is the conductivity of the medium (A/V-m) and μ is its permeability. These equations are similar to the heat conduction equation

$$\partial T/\partial t = (K/c_v)\nabla^2 T \tag{3.44}$$

in which T = temperature, K = thermal conductivity, and c_v = specific heat. The diffusion of J and B into a conductor is analogous to the diffusion of heat into a solid, and many of the heat conduction solutions can be applied to magnetic field diffusion. For magnetic field diffusion the boundary condition at the edge of the conductor surface varies in time.

Typically, if the magnetic field at the edge of the conductor varies sinusoidally, B = Bo sin(ωt), then the characteristic depth that the magnetic field penetrates into the conductor is called the "skin depth" δ, given by the equation

$$\delta = (2/\mu\sigma\omega)^{\frac{1}{2}} \quad \text{(m)} \tag{3.45}$$

as illustrated in Fig. 3.18 (This is similar to the problem of the earth's surface heating during the day and cooling at night, with the penetration depth of the temperature variations corresponding to the skin depth.) For copper at a frequency of 1 MHz, $\delta \approx 0.07$ mm. (The frequency ω must be expressed in radians/s, not Hz.) Thus, J and B are located in a very thin surface layer at high frequencies.

Order of magnitude estimates of the magnetic field diffusion rates can also be made by approximating the derivatives in Eq. (3.43) as follows:

$$\partial B/\partial t \sim B/\tau$$
$$\nabla^2 B \sim B/l^2 \tag{3.46}$$

where τ and ℓ are the "characteristic diffusion time" and "characteristic diffusion length". Then Eq. (3.43) simplifies to

$$1/\tau \sim 1/\sigma\mu\ell^2 \tag{3.47}$$

Fig. 3.18 Amplitude of a plane electromagnetic wave incident on a metallic conductor. The *dashed curve* shows the exponential decay of the wave amplitude, which occurs over a distance δ, called the "skin depth"
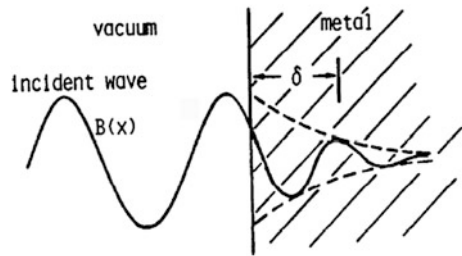
For a given metal we know σ and μ. If we specify a penetration distance ℓ, then we can find the approximate time τ that is required for diffusion. If we specify a time available for diffusion, then we can solve for the distance over which substantial diffusion occurs. For a sinusoidal variation of the boundary condition $\tau \sim 1/\omega$, we find

$$\ell \sim (1/\mu\sigma\omega)^{1/2} \tag{3.48}$$

which is almost the same as Eq. (3.45) for the skin depth.

3.4.1 Single-Turn, High-Field Solenoids

A single-turn solenoid can be simply a thick metal tube with an insulated slot. To sustain the large forces associated with high magnetic fields, the coil may be surrounded by a massive steel block (Fig. 3.19). High-field magnets are described by Kolm et al. (1962); Parkinson and Mulhall (1967); and Turchi (1980).

Fig. 3.19 A single-turn, high-field coil surrounded by a steel block for structural support. From H. Knoepfel, Journal of Physics E: Scientific Instruments 5, 1133–1141 (1972), Fig. 8. © 1972 The Institute of Physics
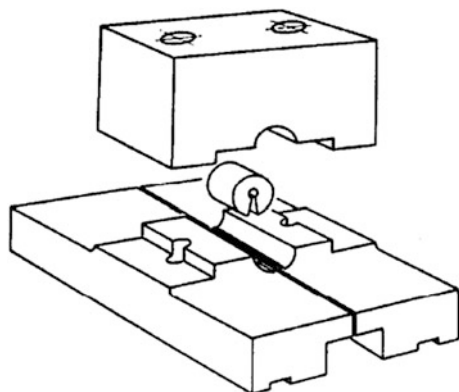
Fig. 3.20 Section through a thick single-turn solenoid, showing the distribution of B and J, as characterized by the skin depth sf. **a** Actual distribution, **b** approximation with three rectangular elements. From H. Knoepfel, Journal of Physics E: Scientific Instruments 5, 1133–1141 (1972), Fig. 2. © 1972 The Institute of Physics
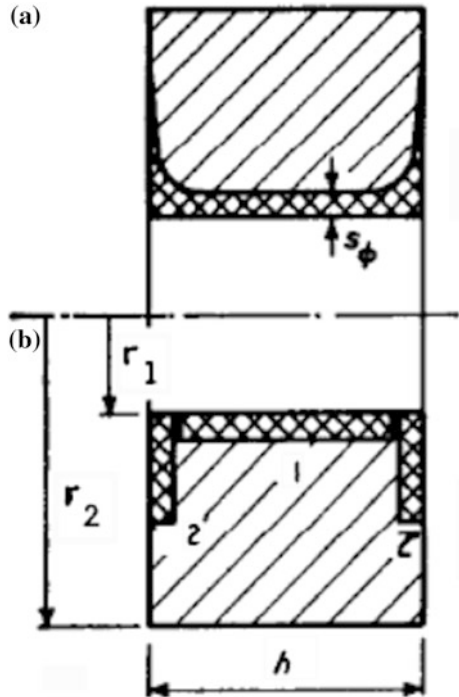
The current density tends to be concentrated radially around the inside of the coil bore and axially near the ends of the coil. We can define a "magnetic flux skin depth" as

$$S_\phi \equiv \frac{\int_0^\infty dx\ B}{B_0}, \tag{3.49}$$

where x is measured inwards from the coil surface and B_o is the magnetic field at the surface. The distribution of s_ϕ is illustrated in Fig. 3.20a. An approximation using three rectangular elements is shown in Fig. 3.20b.

The axial magnetic field distribution may be written

$$B_z(z) = K(z)\mu_0 I/h \tag{3.50}$$

where h = coil length and K(z) describes the spatial variation. Figure 3.21 shows values of K(z) for a few cases. In some cases we can assume that most of the current flows very near the surface.

The attainable B and J are limited by circuit parameters, coil stress, and surface heating. The metals begin to yield at fields

$$B < B_y[(r_2 - r_1)/2r_1]^{1/2} \tag{3.51}$$
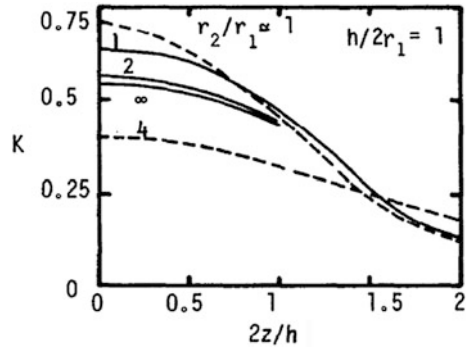
where $B_y \sim 25$ T for Cu, brass, steel, and $B_y \sim 32$ T for Ta. Melting occurs when $B > B_e/\theta^{1/2}$, where $\theta^{1/2} \sim 2$–3 depends on the shape of I(t). For Cu, brass, and steel $B_e = 90$–110 T, and for Ta, $B_e = 137$ T. Other refractory metals, such as Mo, W, and Nb, may also be used for high-field coils, but Mo and W have poor ductility. Since the metal conductivities may decrease with increasing temperature, the diffusion equations (3.43) become nonlinear, especially at high fields and temperatures.

If B is high for a long enough time, the coil may explode. The inner surface of a copper coil expands at a velocity $u \approx 0.15\ B^{3/2}$ (m/s) (valid for $B > 150$ T). Thus, short current rise times ($t_{max} < 2\ \mu s$) are needed for high fields, to produce the field before the coil is destroyed. At lower fields severe stress cracking and fatigue may limit coil life to a few shots (Knoepfel 1970, 1972).

Coil development history is summarized by Bird (2004). Single shot coils have attained $B \sim 2,800$ T, and recoverable coils have attained $B = 85$ T for >150 shots. Coils developing nearly 100 T are under development in the USA, France, Germany, and Japan (Bird 2004, 2011).

3.5 Energy Storage

Energy storage may take the following forms (Chen et al. 2009):

Electrical
Electrostatic (capacitors and supercapacitors)
Magnetic, including superconducting magnetic energy storage (SMES).
Mechanical
Kinetic energy (flywheels)
Potential energy (hydroelectric and compressed air energy storage systems).
Chemical
Electrochemical (lead-acid, nickel metal hydride, lithium ion, and flow-cell batteries, such as zinc bromine and vanadium redox, Metal-Air batteries)

Fuel cells, molten-carbonate fuel cells

thermochemical (solar hydrogen, solar metal, solar ammonia dissociation–recombination and solar methane dissociation–recombination).

Thermal

Low temperature energy storage (Aquiferous cold energy storage, cryogenic energy storage);

High temperature energy storage (sensible heat systems such as steam or hot water accumulators, graphite, hot rocks and concrete, latent heat systems such as phase change materials).

Fusion experiments have mainly used capacitors or motor-generator sets (like flywheel energy storage).

For fast-pulsed fusion experiments, such as theta pinches, the most common form of energy storage is in a capacitor bank. Capacitor banks have the following advantages over other types of energy storage:

- They store *electrical* energy; so conversion from another energy form is not necessary.
- The technology of capacitor banks is very well developed.
- The energy can be released very rapidly, to produce shock heating.

The desirable features for capacitors are:

- Large energy stored per unit volume
- Long lifetime (about 10^6 shots)
- Low self-inductance, to make I_{max} very large

Fig. 3.22 The Scyllac 60 kV, 1.85 μF capacitor. (Kemp 1969)
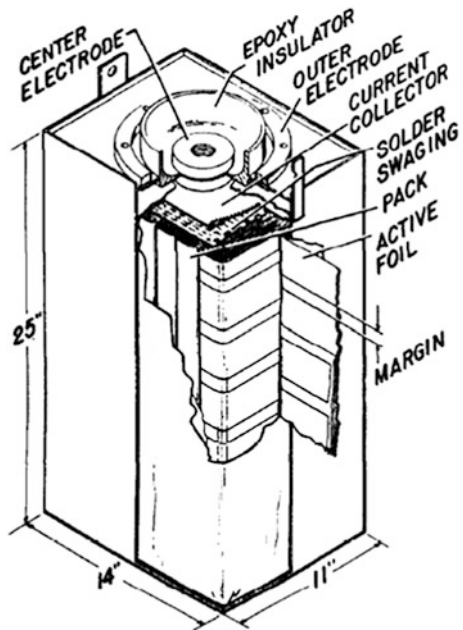
Fig. 3.23 Approximate energy storage system capital costs (1980$) per Joule of electrical energy. *X* is for an optimized flywheel. (From Dolan 1982; Post and Post 1973)
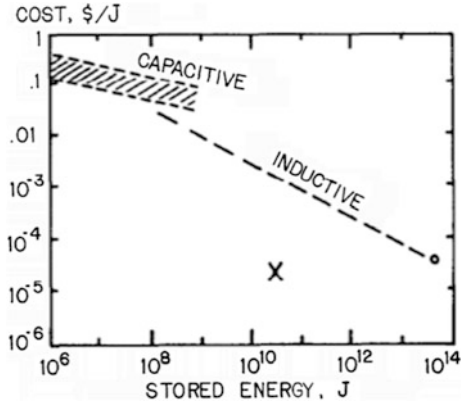
- Low resistance
- Low cost.

The Scyllac bank at Los Alamos National Laboratory could store about 10 MJ at 60 kV. The 60 kV capacitor developed for this bank is shown in Fig. 3.22.

Modern large capacitor banks store several tens of MJ.

At high energies inductive energy storage may be less expensive ($/MJ), but large inductive storage systems have not been used for fusion experiments.

The data of Fig. 3.23 are old, but show roughly how costs scale with energy. Table 3.2 shows more recent costs of energy storage.

Large inductive energy storage systems could have applications for

Table 3.2 Costs of some energy storage systems. Courtesy of Rinat Khaziev (Schoenung 2011; Connolly 2010; Chen et al. 2009)

Type	$/kW	$/kWh[a]	Round-trip efficiency (%)	Remarks
Pb-acid batteries	400	330	80	~1,000 cycles
Li-ion batteries	400	600	85	
Na–S batteries	350	350	75	T > 270 °C
V redox batteries	400–1,800	300–1,000	65–85	10,000 cycles
Capacitors	100–500	300–10,000	95	Low energy density
Flywheel	250–6,000	1,000–5,000	95	>10,000 cycles
Compressed air	400–700	3–10	70	~3 GW planned
Pumped hydro	1,200	75	85	~7 GW planned
Superconducting magnetic	200–500	1,000–10,000	95	Needs cryogenic system
Hydrogen gas	300–1,000	20–50	65–70	Needs fuel cell or similar

[a] 1 kWh = 3.6 MJ

Fig. 3.24 Simplified circuit diagram of an inductive energy storage system for pulsing a current *I* through a magnet coil *L*
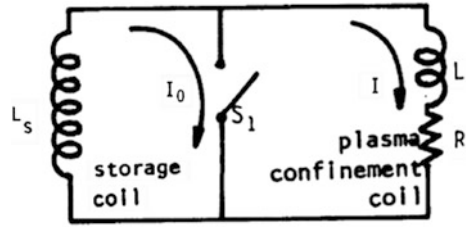
- Smoothing out daily electrical power demand fluctuations
- Preventing instabilities of interconnected electrical power grids
- Providing a "spinning reserve" of power to cope with sudden power source losses
- Smoothing the output of solar and wind electric power stations
- Igniting pulsed fusion reactors, which could require > 100 MJ of stored energy.

A simple inductive energy storage system is shown in Fig. 3.24.

A charging supply (not shown) builds up a high current I_o in the storage inductor L_s with switch S_1 closed. The stored energy is $\frac{1}{2}L_sI_o^2$. When the switch S_1 is opened, a large voltage builds up and forces a current I to flow through the load coil L. Design of the switch S_1 is a major problem. It is difficult to open a switch that is carrying a high current because the current tends to arc across the switch and continue flowing. Switches for this purpose can be fuses designed to melt, thin conductors that explode, vacuum tube interrupters, and superconductors which "go normal" (change from zero resistivity to normal resistivity). For the simple circuit of Fig. 3.24 the fraction of energy transferred to the load coil is

$$\text{transfer efficiency} = \frac{\frac{1}{2}LI_{max}^2}{\frac{1}{2}L_sI_0^2} \leq \frac{L_sL}{(L_s+L)^2}, \tag{3.52}$$

depending on the energy dissipated in R during the switch opening time. This efficiency has a maximum value of 25 % when $L = L_s$. Much higher efficiencies (over 90 %) can be attained by placing a capacitor bank in parallel with switch S_1. For optimum efficiency, the capacitor bank must be able to store half as much energy as the storage inductor. For large systems with slow discharge rates high efficiencies can be achieved without the capacitors. Superconducting energy storage coils will be discussed briefly in Chap. 4.

Other energy storage media are used because of their unique attributes. Batteries have been used to power magnet coils for some fusion experiments. Their relatively high internal resistance makes it difficult to attain very large currents in short pulses, so they are better suited to sustaining moderate currents for many seconds. Batteries tend to wear out after a few thousand heavy discharges and recharges, so they are unsuitable for reactors. Flywheels rotating at high speeds can store energy densities around 0.2 MJ/kg or 500 MJ/m^3. They can be gradually charged up with a motor and then discharged suddenly through a generator to produce a pulse of high current.
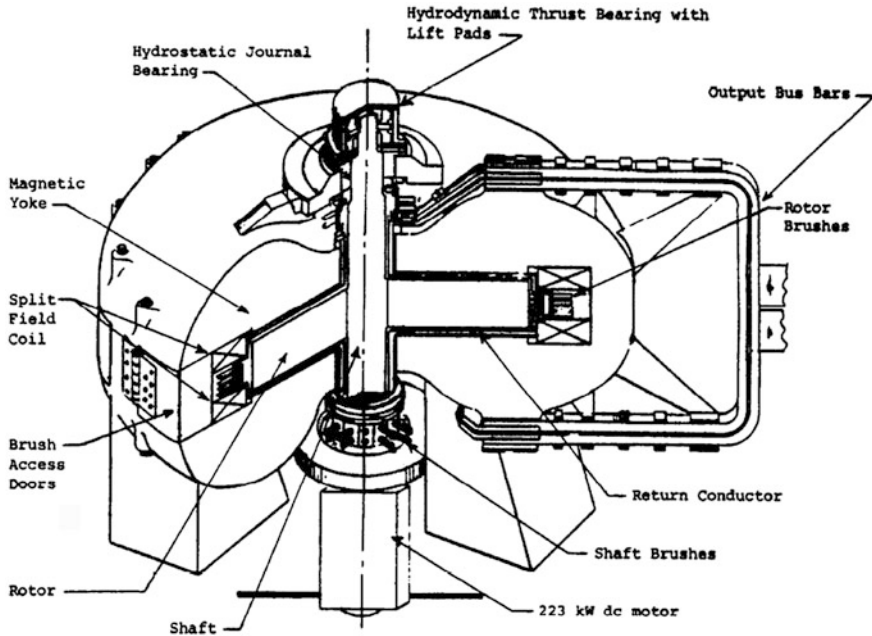
Fig. 3.25 A 50 MJ homopolar generator of the TEXT energy storage system. The rotor turning azimuthally in an axial B field generates a radial electromotive force and drives a current, tapped by brushes on the shaft and rotor. Courtesy of W. F. Weldon, H. G. Rylander, and H. H. Woodson, The Center for Electromechanics, The University of Texas at Austin

Large motor-generator sets have been used by large tokamaks, such as JET, which has two 800-tonne motor-generator sets, each storing up to 2.6 GJ and providing up to 400 MW for magnet coils and heating systems.

Homopolar motor-generators, such as the one shown in Fig. 3.25 are well suited for coupling to flywheels. The rotor is just a conducting disk, which is much simpler than conventional dc generators requiring commutators.

Chemical energy explosives may also be used to compress metal shells, compressing magnetic flux that is trapped inside (Sect. 3.6).

3.6 Switching and Transmission

In order for capacitive energy storage to work efficiently high-voltage switches with precision timing and low-inductance transmission lines are required.

Consider two spherical balls separated by a distance x, as shown in Fig. 3.26, with a high voltage between them.

As the distance x is decreased, the point is finally reached where electrical breakdown occurs, and current jumps across the gap like a lightning bolt. Such

A simple high-
voltage switch actuated by
decreasing the gap between
two electrodes
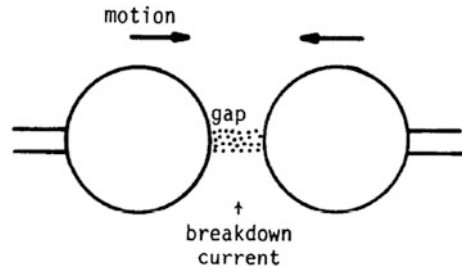
A "spark gap"
high voltage switch.
Breakdown is initiated by
triggering a spark plug near
one electrode
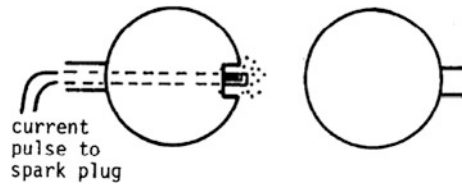
switches might be suitable for fusion experiments if many of them could be fired
quickly and simultaneously, but it is impossible to move the balls fast enough. An
alternative is to put a spark plug in the center of one ball, as shown in Fig. 3.27.

When the spark plug fires, it creates a plasma in the gap, causing breakdown to
occur. In this way the spark gap can be fired electrically with precision timing,
instead of by mechanical motion of the spheres. Further refinements have been
added to improve timing and increase the useable lifetime of the switches. The
spark gap developed for the Scyllac experiment is shown in Fig. 3.28.

It actually consists of two switches, which correspond to switches S_1 and S_2 in
Fig. 3.28. Instead of just two balls, these switches have an additional ring in the
middle to help the switches fire more rapidly. The time lag between firing various
switches, which are supposed to fire simultaneously, is called "jitter". The rms
jitter for the 3,240 spark gaps of the Scyllac primary bank is about 10 ns. When
the current is at its peak, the crowbar switches are triggered, allowing the coil
current to keep flowing with a gradual decay.

Additional explosive switches were developed to aid in crowbarring the dis-
charge. In these switches pulsing a very high current through a thin foil makes it
explode. The explosion squeezes a thin aluminum plate through its insulation to
make a low-resistance contact with the lower collector plate, as shown in
Fig. 3.29.

To obtain very high voltage pulses, capacitors may be charged up in parallel to
about 100 kV, and then rearranged and discharged in series. This technique, called
Marx charging, is illustrated in Fig. 3.30.

When the spark gap switches are closed, they arrange the capacitors in series,
resulting in the total output voltage being the sum of the voltages on the individual
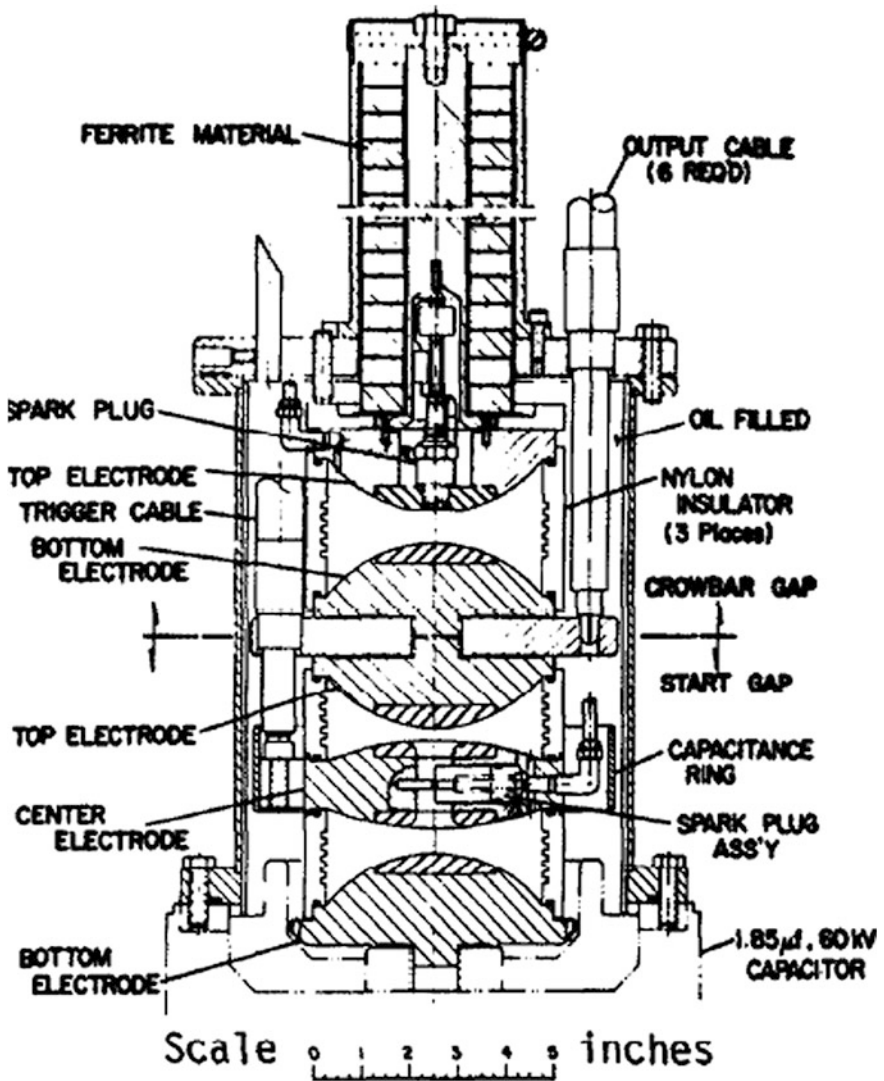
Fig. 3.28 The dual spark gap switch developed for the Scyllac experiment at LANL. (Kemp 1969)
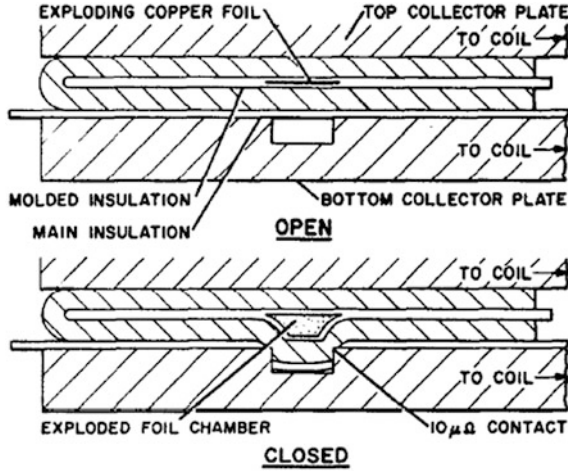
Fig. 3.29 Exploding foil low-resistance crowbar switch developed for the Scyllac experiment. (Kemp 1969)
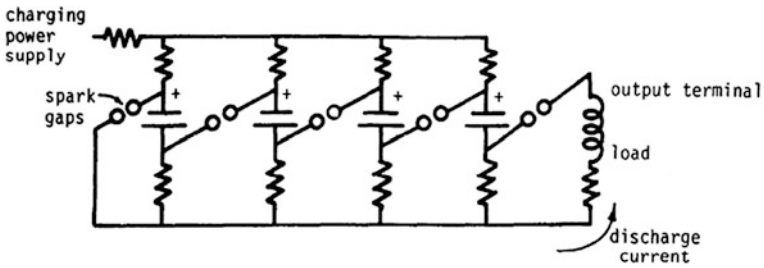
Fig. 3.30 The Marx technique for charging capacitors up to a voltage V_o in parallel, then discharging them in series, so that a voltage NV_o appears across the load, where N is the number of capacitors (N = 4 in this diagram)

Fig. 3.31 The high-voltage coaxial cable developed for the Scyllac experiment. (Kemp 1969)
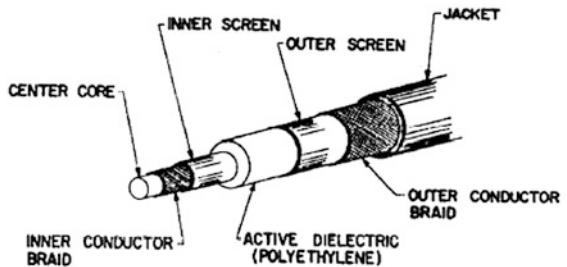
capacitors. Marx charging is used for producing relativistic electron beams and for some magnet coils.

Special low-inductance high-voltage coaxial cables were developed to carry the current from capacitors and switches to the coil header plates. The Scyllac System used around 250 km of the cable shown in Fig. 3.31.

Several layers of braids and screens are used to minimize electric potential gradients and dielectric fatigue, so that the cable can survive over 10^5 pulses without failure. Additional components for high voltage pulsed magnet circuits include collector plates, cable terminations and cartridges where the cables plug into the collector plates, the coils themselves, and protective circuitry to prevent damage to power supplies and capacitors in the event of a misfire.

3.7 Magnetic Flux Compression

Since the magnetic field diffuses comparatively slowly into metallic conductors, it may be compressed by moving the metallic walls inwards. One simple scheme for accomplishing flux compression is illustrated in Fig. 3.32.

A magnetic field is established between two metallic plates by external coils or magnets. Then an explosive charge is detonated around the outside of the metallic plates, driving them together at a high speed. The magnetic field does not have time to penetrate into the metal plates, so it becomes compressed and squeezed through the slot into the circular coil. Now the flux density is very high, on the

Fig. 3.32 The "bellows" type of magnetic flux compression
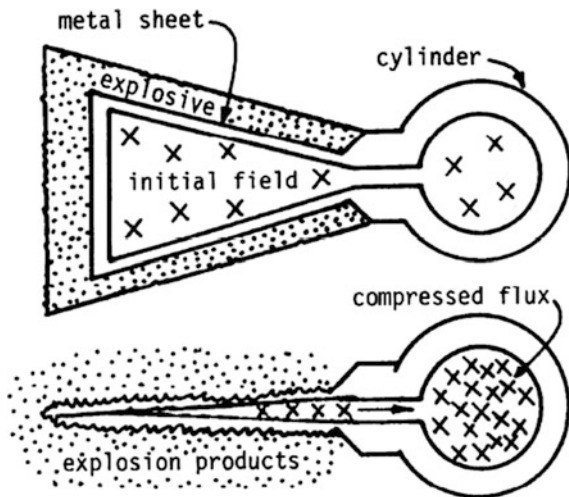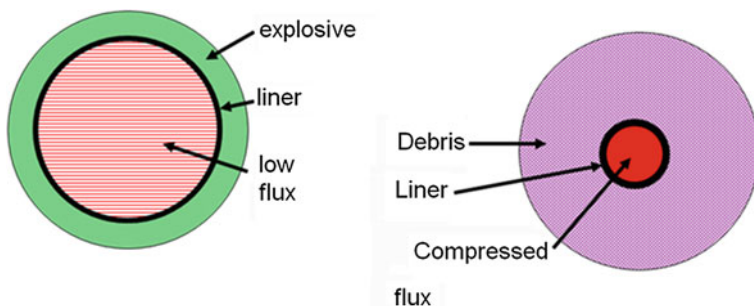
Fig. 3.33 Flux compression by an imploding metallic liner. An external coil (not shown) produces the initial low magnetic flux

order of hundreds of Tesla. Such high fields can be used to compress plasma within the circular coil volume.

An alternative method of flux compression is to use an imploding metallic foil liner inside a coil system, as shown in Fig. 3.33. Fields of 1,000 T have been obtained by flux compression. A liner can be compressed by a rapidly rising magnetic field in the surrounding coil, by chemical explosive, or by a combination of both. Many of the high-field flux concentration experiments only last for one shot, because they self-destruct.

Several fusion reactor schemes have been proposed involving magnetic flux compression, including a fast liner reactor (FLR) and a slow liner driven by compressed gas (LINUS). The FLR would use implosion velocities of about 10^4 m/s, with implosion times on the order of 10 μs. An initial plasma with $n = 10^{24}$ m^{-3}, $T_i = 0.2$ keV, and $B = 5$ T would be compressed up to $n = 10^{27}$ m^{-3}, $T_i = 10$ keV for a burn time of about 1 μs. Difficulties of this scheme include Rayleigh- Taylor instability of the liner, rapid replacement of the liner between shots, production of the initial plasma, high stresses and fatigue failure of structure, and development of electrical insulators that will not fail under such a hostile environment.

3.8 Component Reliability

One of the major problems of pulsed magnet systems is component failure. Even if a given capacitor, switch, or cable has a very low failure probability, such as 10^{-5} per shot, the overall failure probability for a large system with 10,000 components may be unacceptably large. Let $f_j(t)dt$ be the failure probability of item j in the interval dt at time t. The probability that this item will fail between time 0 and time

t is equal to $\int_0^t dt\, f_j(t)$. Therefore, the probability that it will *not* fail during this time period is $\left[1 - \int_0^t dt\, f_j(t)\right]$.

The "failure rate" r_j for item j is defined to be

$$r_j(t) = \frac{\text{failure probability per unit time at time t}}{\text{probability of not failing before time t}}$$
$$= \frac{f_j(t)}{1 - \int_0^t dt\, f_j(t)} \qquad (3.53)$$

In a pulsed plasma device if the current fails in one coil segment, the plasma will be rapidly lost there, and confinement fails. If failure of any one component represents a failure of the entire system, the system is said to be a **series system**. This is like a string of electrical lights wired in series: if one bulb burns out, the whole string goes out. For a series system with N components, the total failure rate is the sum of the individual failure rates r_j.

$$r(t) = \sum_{j=1}^{N} r_j(t) \qquad (3.54)$$

The estimated time to next failure (ETNF) of an entire system is defined to be the reciprocal of the composite failure rate:

$$\text{ETNF} = 1/r(t). \qquad (3.55)$$

For some types of components, the failure rate is generally high for the first group of shots, when manufacturing defects are present. When the defective ones have been eliminated, the failure rate becomes fairly constant for a long time. Then, at very large numbers of shots, the failure rate rises again, because the parts are beginning to wear out. Such a failure rate curve, illustrated in Fig. 3.34, is called a "bathtub curve" because of its shape. This type of failure rate might be expected from new cars, vacuum tubes, capacitors, cables, etc.

Fig. 3.34 The "bathtub" type of failure rate curve
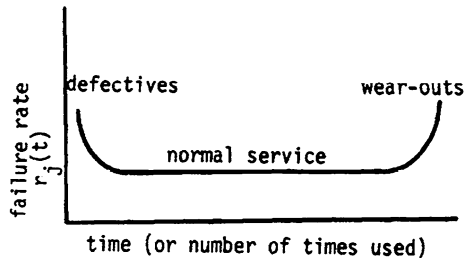
For components with a bathtub failure rate curve, the failure probability along the flat bottom portion of the curve is

$$f_j(t)dt = \lambda_j \exp(-\lambda_j t)dt. \tag{3.56}$$

For this case, it is found from Eq. (3.53) that the failure rate is

$$r_j(t) = \lambda_j = \text{constant} \tag{3.57}$$

For a series system composed of such components, then, the ETNF is

$$\text{ETNF} = \frac{1}{\sum\limits_{j=1}^{N} \lambda_j} \tag{3.58}$$

Example Problem 3.3: Estimated time to next failure Estimate the ETNF for 100 identical capacitors with failure rates $\lambda_j = 10^{-4}$ per shot and 600 identical cables with failure rates $\lambda_j = 2 \times 10^{-4}$ per shot, assuming that all these components are on the flat portion of a bathtub curve.

For this system

$$\text{ETNF} = \frac{1}{100 \left(10^{-4}/\text{shot}\right) + 600 \left(2 \times 10^{-4}/\text{shot}\right)} = 7.7 \text{ shots}$$

For a pulsed reactor operating at one pulse/s, an ETNF of about 3×10^6 s would be needed in order to operate the reactor for a month without a misfire. Therefore, extremely low individual component failure rates would be needed. Such failure analyses may also be applied to other fusion research components, such as laser systems. In some cases the failure rates may not be described by the simple exponential function of Eq. (3.56), and the analysis is more complex (Boicourt 1973). The failure rates of vacuum tube electronics are high. Modern computer-dependent technologies would probably not be feasible without the invention of transistors and integrated circuits, which have much better reliability and smaller size.

Reliability, availability, and maintenance of fusion power plants are discussed further in Sect. 13.2.

3.9 Power and Cooling Requirements

3.9.1 Relation of Magnetic Field to Coil Power

The power dissipated in a differential volume dV by a current density J_c in the metal is

$$dP = \eta J_c^2 dV \quad (W) \tag{3.59}$$

where η is the resistivity of the conductor (Ohm m). For a uniform-current–density solenoid with packing fraction $\lambda = $ (copper volume)/(coil volume) $= V_{cu}/V_{coil}$, the total power required is

$$P = \eta J_{cu}^2 V_{cu} = \eta J_{cu}^2 \lambda V_{coil} = \eta J_{cu}^2 \lambda \pi (r_2^2 - r_1^2) L \tag{3.60}$$

From which

$$J_{cu} = [\, P / \eta \lambda \pi (r_2^2 - r_1^2) L \,]^{1/2} \tag{3.61}$$

From Eq. (3.21)

$$B_z = \mu_o J \, b \, \ln \left\{ \left[r_2 + (r_2^2 + b^2)^{1/2} \right] / \left[r_1 + (r_1^2 + b^2)^{1/2} \right] \right\} \tag{3.62}$$

where $b = L/2$, and the average current density $J = \lambda J_{cu}$. Eliminating J_{cu} between Eqs. (3.61) and (3.62) and defining dimensionless variables $\alpha = r_2/r_1$ and $\beta = L/2r_1$, the result may be expressed in the form

$$B_z = \lambda^{3/2} \mu_o g(\alpha, \beta) \, (P/\eta r_1)^{1/2} \tag{3.63}$$

where

$$g(\alpha, \beta) \equiv \left[\frac{\beta}{2\pi(\alpha^2 - 1)} \right]^{\frac{1}{2}} \ln \left[\frac{\alpha + (\alpha^2 + \beta^2)^{\frac{1}{2}}}{1 + (1 + \beta^2)^{\frac{1}{2}}} \right] \tag{3.64}$$

[This differs from Montgomery (1969). His $G(a,\beta) = (4\pi/10)g(\alpha,\beta)$]. Values of $g(\alpha, \beta)$ are shown in Table 3.3.

For pure, unirradiated copper at temperatures between 270 and 400 K the resistivity is given by

$$\eta = [1.68 + 0.0068(T - 293)] \times 10^{-8} \quad (Ohm\,m) \tag{3.65}$$

Taking $\lambda = 0.9$ and $T = 340$ K, the maximum value of B attainable in a uniform-current–density solenoid with rectangular cross section at g_{max} is found to be

$$B_{max} = 0.0012 \, (P/r_1)^{1/2} \quad (T) \tag{3.66}$$

Example Problem 3.4: Attainable magnetic field A solenoid is to be wound around a 0.2 m diameter bore, and 100 kW are available to power it. What is the maximum magnetic field that can be generated?

Here $r_1 = 0.1$ m. We use $\alpha = 3$, $\beta = 2$, yielding $r_2 = 0.3$ m and $L = 0.4$ m. Then $g = g_{max} = 0.142$. From Eq. 3.66 we find $B_{max} = 1.2$ T.

Example Problem 3.5: Required power We want to produce B = 10 T in a solenoid with inner radius = 2 m. How much power is required?

Table 3.3 The values of g (α, β). The maximum value $g_{max} = 0.1425$ at $\alpha = 3.2$, $\beta = 2$

Alpha	Beta										
	0.2	0.4	0.6	0.8	1	1.4	2	3	4	5	6
1.2	0.0482	0.0651	0.0745	0.0792	0.0810	0.0799	0.0745	0.0652	0.0580	0.0525	0.0483
1.4	0.0604	0.0820	0.0945	0.1014	0.1045	0.1046	0.0987	0.0873	0.0780	0.0708	0.0652
1.6	0.0663	0.0904	0.1048	0.1131	0.1174	0.1189	0.1136	0.1014	0.0911	0.0829	0.0764
1.8	0.0693	0.0948	0.1104	0.1198	0.1250	0.1279	0.1235	0.1114	0.1005	0.0918	0.0847
2	0.0706	0.0969	0.1133	0.1235	0.1295	0.1336	0.1303	0.1188	0.1077	0.0985	0.0911
2.2	0.0711	0.0977	0.1146	0.1254	0.1320	0.1372	0.1351	0.1242	0.1132	0.1039	0.0962
2.4	0.0709	0.0977	0.1149	0.1261	0.1331	0.1393	0.1383	0.1283	0.1175	0.1082	0.1004
2.6	0.0704	0.0971	0.1144	0.1259	0.1334	0.1403	0.1404	0.1314	0.1209	0.1116	0.1038
2.8	0.0697	0.0962	0.1136	0.1253	0.1330	0.1407	0.1417	0.1337	0.1236	0.1144	0.1066
3	0.0687	0.0950	0.1124	0.1242	0.1322	0.1404	0.1423	0.1353	0.1257	0.1167	0.1089
3.2	0.0677	0.0937	0.1110	0.1229	0.1310	0.1398	0.1425	0.1365	0.1274	0.1186	0.1109
3.4	0.0667	0.0924	0.1095	0.1214	0.1297	0.1389	0.1423	0.1372	0.1286	0.1201	0.1125
3.6	0.0656	0.0909	0.1079	0.1199	0.1282	0.1377	0.1418	0.1376	0.1295	0.1213	0.1139
3.8	0.0645	0.0895	0.1063	0.1182	0.1266	0.1364	0.1411	0.1377	0.1302	0.1223	0.1150
4	0.0634	0.0880	0.1047	0.1165	0.1250	0.1350	0.1402	0.1376	0.1306	0.1230	0.1159
4.2	0.0624	0.0866	0.1031	0.1148	0.1233	0.1336	0.1392	0.1373	0.1308	0.1235	0.1166
4.4	0.0613	0.0851	0.1014	0.1131	0.1216	0.1320	0.1380	0.1369	0.1309	0.1239	0.1172
4.6	0.0603	0.0837	0.0998	0.1114	0.1199	0.1304	0.1368	0.1363	0.1308	0.1242	0.1176
4.8	0.0593	0.0824	0.0983	0.1098	0.1182	0.1289	0.1356	0.1356	0.1306	0.1243	0.1180
5	0.0583	0.0810	0.0967	0.1081	0.1165	0.1273	0.1343	0.1349	0.1303	0.1243	0.1182
5.2	0.0573	0.0797	0.0952	0.1065	0.1149	0.1257	0.1330	0.1341	0.1299	0.1242	0.1183
5.4	0.0564	0.0785	0.0937	0.1049	0.1133	0.1241	0.1316	0.1332	0.1295	0.1241	0.1184
5.6	0.0555	0.0772	0.0923	0.1034	0.1117	0.1225	0.1302	0.1323	0.1290	0.1239	0.1184
5.8	0.0546	0.0760	0.0909	0.1019	0.1101	0.1210	0.1289	0.1313	0.1284	0.1236	0.1183
6	0.0537	0.0749	0.0896	0.1004	0.1086	0.1195	0.1275	0.1304	0.1278	0.1232	0.1182

From Eq. 3.66 we find $P = r_1 (B/0.0012)^2 = 139$ MW.

Thus, the required power becomes enormous if water-cooled copper magnets are used in fusion reactor designs with high fields and large coil radii.

The above analysis was restricted to uniform-current–density coils with rectangular cross sections. By varying the current density and coil cross sectional shape, higher values of $g(\alpha, \beta)$ can be obtained. The highest g attainable is about 0.19. The value of B_{max} can also be increased by using cryogenic coolants, such as liquid nitrogen at 77 K, to lower the resistivity temporarily.

3.9.2 Cooling Water

The thermal power removed by the coolant is

$$P = C\rho_m \Delta T(dV/dt) \quad \text{(W)} \tag{3.67}$$

where C is the specific heat of the coolant (J/kg K), ρ_m is its mass density (kg/m^3), dV/dt is its volumetric flow rate (m^3/s), and ΔT is the temperature rise of the
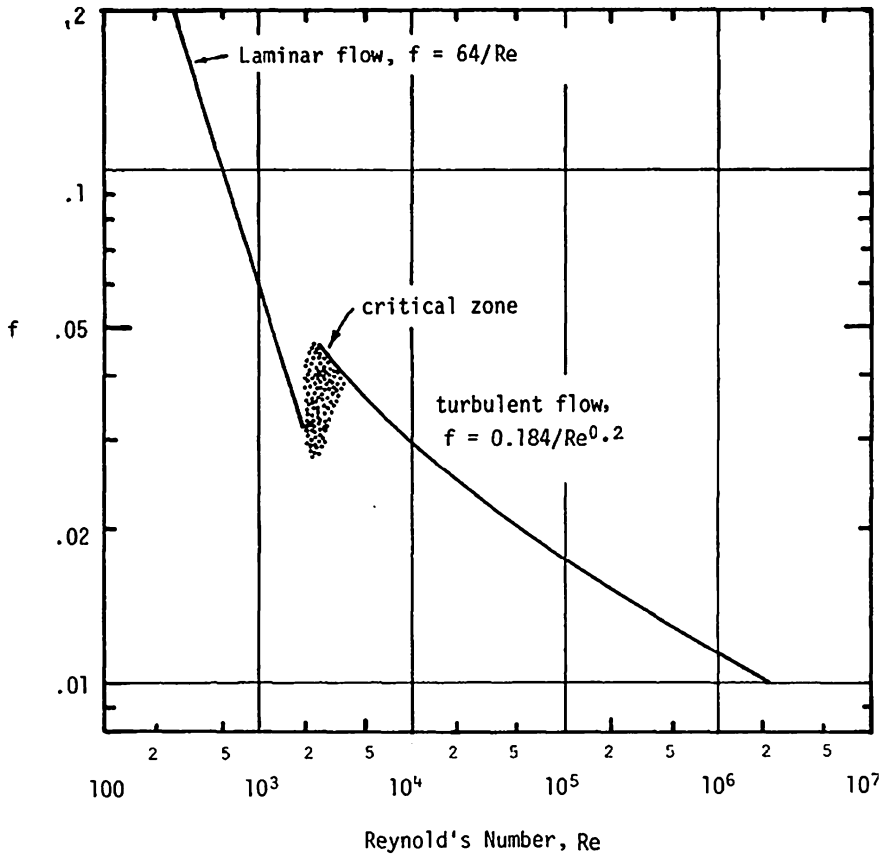
Fig. 3.35 Friction factor f versus Reynold's Number, for smooth tubes. Based on data of M. El-Wakil, Nuclear Heat Transport, Appendix F, Figure F-1, p. 476., © 1978 by the American Nuclear Society, La Grange Park, Illinois

coolant as it passes through the coil. Equating this power removed to the power dissipated determines the required coolant flow rate. The volumetric flow rate is related to the average flow speed v in a given coolant channel by the equation

$$(dV/dt)_{channel} = A_w v \quad (m^3/s) \tag{3.68}$$

where A_w is the cross sectional area of the channel. Cooling water is usually deionized to prevent mineral deposits from clogging channels and decreasing A_w.

The pressure drop of the coolant flowing through a tube of length L, and diameter D depends upon the Reynold's Number

$$Re = Dv\rho_m/\mu \quad (dimensionless) \tag{3.69}$$

where μ is the fluid viscosity (Pa-s). The pressure drop may be written as

$$\Delta p \ = \ fL_c\rho_m v^2/2D \quad (Pa) \tag{3.70}$$

where the "friction factor" f is given as a function of Re in Fig. 3.35.

The pumping power required to produce a pressure rise Δp and flow rate dV/dt is

$$P_c = \Delta p(dV/dt)/\eta_p \quad (W) \tag{3.71}$$

where η_p is the pump efficiency. The most commonly used coolant is water, because of its favorable properties and low cost. The properties of water at 293 K (20 °C) are:

$$
\begin{aligned}
C &= 4182 \text{ J/kg-K} \\
\rho_m &= 998 \text{ kg/m}^3 \\
\mu &= 0.001002 \text{ Pa-s}
\end{aligned}
\tag{3.72}
$$

If an electrically conducting coolant is used, there is an additional pressure drop produced by the interaction of the coolant with the magnetic field.

Example Problem 3.6: Required coolant flow rate and pumping power A 100 kW magnet has 16 coolant passages, each 30 m long and 4.6 mm in diameter, connected in parallel. Find the required coolant flow rate, velocity, pressure drop, and pumping power, assuming a temperature rise of 60 K. For simplicity, ignore the slight variations of C, ρ_m, and μ with temperature, and assume a pump efficiency of 80 %.

From Eq. (3.67) we find dV/dt = 3.99×10^{-4} m^3/s. Then (dV/dt) channel = (dV/dt)/16 = 2.50×10^{-5} m^3/s, and v = 1.50 m/s. From Eq. (3.69) Re = 6,870, f = 0.035. The pressure drop $\Delta p = 2.56 \times 10^5$ Pa (37 psi) and the pumping power is 128 W, Eqs. (3.70) and (3.71).

3.10 Coil Design Considerations

Water-cooled magnet coils require large amounts of electrical power and cooling water. In comparison with superconducting magnets, they offer the following advantages:

- No need for cryogenic insulation and refrigeration
- Can be bolted together for easy disassembly and maintenance
- Little danger from plasma disruption
- Can withstand higher neutron influences.

The use of water-cooled tokamak toroidal field coils is discussed by Kalnavarns and Jassby (1979).

Fig. 3.36 Types of coil windings and coolant flow directions. **a** "Pancake" coils, azimuthal flow, **b** tape-wound, axial flow, **c** disk wound "Bitter" coil, axial flow (through small holes) or radial flow (in grooves). In the Bitter magnet individual copper disks are slit, twisted, and joined to form a spiral, with insulation between adjacent disks
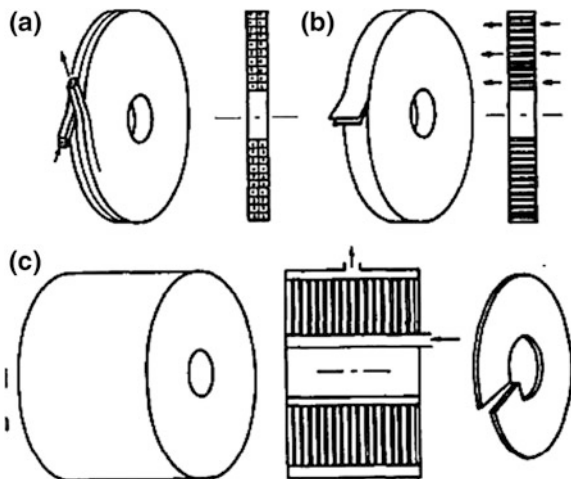
Computer codes, such as FORCE (Henning 1966), are used to calculate the forces at any point in a coil system. Since the toroidal field decreases with major radius, the azimuthal coil stress tends to be greatest at small R. Large toroidal field (TF) coils can be shaped to minimize bending stresses (Gralnick et al. 1979). TF coils shaped like "D"s have lower bending stresses than circular coils. The magnetic forces on TF coils tend to increase the coil radius (tensile strength), to decrease the major radius of the torus (due to attraction between coils), and to flip the coils over (due to interaction with poloidal fields). In designing structural elements to sustain coil forces, stress concentrations, cyclic fatigue, creep, and thermal stress must be taken into account (Chap. 8). Slight deviations of the magnetic field from the desired shape, called field errors, can spoil plasma confinement. To minimize field errors, the following steps are taken:

- Coil winding is done very carefully to achieve the desired shape.
- Coils are aligned with great accuracy.
- Massive coil supports keep coil deflections within tolerable limits (mm).
- The coils may be connected in series electrically, to equalize their currents.
- Stray magnetic fields from current leads and nearby ferrous objects are carefully accounted for.

There are three main types of magnet coil windings: azimuthal coolant flow in hollow-conductor coils, axial current flow in tape-wound coils, and either axial or radial coolant flow in disk-shaped coils (Bitter coils), as illustrated in Fig. 3.36.

Hollow conductors can be cooled by water flowing along the inside of the copper. They are often wound in "pancakes". The coolant in one pancake spirals radially inwards, and then spirals back radially outwards. Epoxy between layers enhances mechanical strength of the coil.

Tape-wound coils are usually cooled by water flowing axially through small slots in the conductor or insulator. Windings are separated by insulation of plastic or synthetic fibers.

Bitter coils, named after Francis Bitter of the National Magnet Laboratory (USA), may be cooled by axial flow through holes drilled through both copper and insulator disks or by radial flow in grooves. Hollow-conductor coils are probably most common, but the highest fields are attained with Bitter coils, because of their higher mechanical strength and shorter coolant flow paths. Bitter coils produce a peak toroidal field (at the coil) up to $B_\phi \sim$ 12 T in the Alcator C Tokamak at MIT. The highest-field DC resistive magnets use Florida-Bitter technology and reach 35 T. Florida-Bitter technology uses axially-cooled disks with elongated cooling holes in a staggered grid to reduce radial force transmission. It is roughly 40 % more efficient than competing technology and is used by 5 of the 6 largest resistive magnet labs in the world (Bird 2011).

3.10.1 Windings

For a given pump pressure and coolant channel size, the attainable volumetric flow rate can be determined for one channel of a coil using Eqs. (3.68) and (3.70). Then, the heat which can be removed per channel is found from Eq. (3.71). If this heat removal power is equated to the heat dissipated per channel $\eta J_c^2 V_{ch}$, where V_{ch} is the copper volume to be cooled by that coolant channel, then the maximum safe value of current density J can be found.

The results of some calculations of maximum safe currents are shown in Fig. 3.37.

Fig. 3.37 Maximum safe current versus length for various sizes of square, hollow copper conductors, assuming $\Delta T = 60$ K, average conductor T = 313 K, $\Delta p = 4.4 \times 10^5$ Pa (60 psi) (It is possible for coils to fail at lower currents, due to clogged coolant channels, etc.)
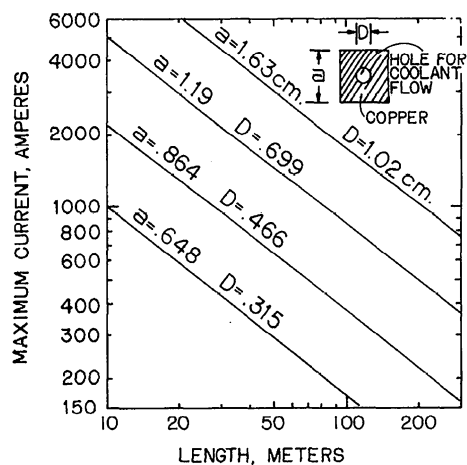
The resistance of one segment of a hollow-conductor coil is given by

$$R_s = \eta L_c / A_c \quad \text{(Ohm)} \tag{3.73}$$

where A_c = cross sectional area of copper (m^2).

Example Problem 3.7: Coil resistance If the coil of Example Problem 3.6 is wound from the conductor with a = 8.64 mm and D = 4.66 mm (Fig. 3.37), and the 16 segments are connected in series, estimate the coil resistance at T = 320 K.

From Eq. (3.65) we find $\eta = 2.0 \times 10^{-8}$ Ohm m. The coil conductor cross sectional area $A_c = a^2 - \pi D^2/4 = 5.76 \times 10^{-5}$ m^2. From Eq. (3.73) we find $R_s = 0.0104$ Ohm, so the total resistance $R = 16 R_s = 0.167$ Ohm.

Contact resistance in conductor joints can substantially increase R, unless the joints are carefully made. The conductor size can be chosen so that the coil resistance = (maximum power supply voltage)/(maximum power supply current), in order to fully utilize the supply capability. Various series-parallel connections of coil segments can be made to aid in impedance matching.

During coil winding fiberglass and epoxy (and sometimes stainless steel) are laid between layers of copper to provide electrical insulation and mechanical rigidity. Special brazing techniques have been developed to ensure good electrical conductivity and mechanical strength wherever two copper conductors must be joined together. These techniques are so good that poloidal field windings can be wound around a form, cut apart, slid under the toroidal field coils, and brazed back together (as was done on the Princeton Large Torus). It is more difficult to make good joints in aluminum than in copper.

3.11 Problems

3.11.1 Problems on Pulsed Magnets

3.1. A small theta pinch experiment has the following parameters: (Fig. 3.38)

one-turn aluminum coil
inside diameter = 3.0 cm
outside diameter = 5.0 cm
length = 20.2 cm
parallel plate transmission line (aluminum, $\eta = 2.8 \times 10^{-8}$ Ohm m)
width = 35.5 cm
length = 45.7 cm
thickness = 1.3 cm
insulation gap = 0.15 cm
capacitor
capacitance = 15.0 μF

Fig. 3.38 A theta pinch
experiment

side view
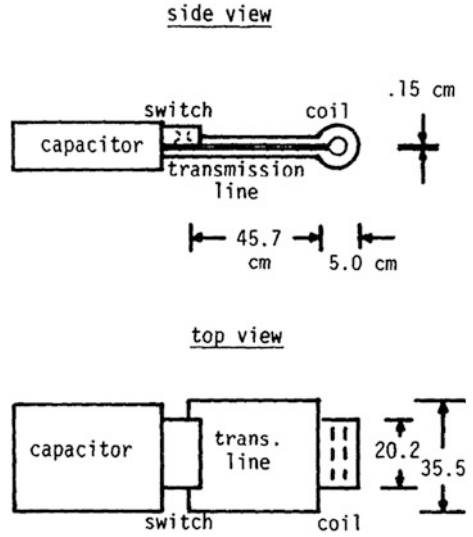
inductance = 5 nH
resistance = negligible
charging voltage = 20 kV
switch (rail type spark gap)
inductance = 5 nH
assume resistance = 1 Ohm m

(a) calculate the total circuit resistance and inductance.
(b) Find the maximum current in the coil, and the corresponding energy stored in the coil $\left(\frac{1}{2}LI^2\right)$ What fraction of the original energy stored in the capacitor is this?
(c) Estimate the peak magnetic induction produced by the coil.
(d) Estimate the skin depth of the transmission line, and the magnetic field between the plates. Hint: Use the line integral of Ampere's Law Eq. (3.5) with the contour shown in Fig. 3.39.
(e) Estimate the magnetic pressure between the plates and the instantaneous force tending to separate them. (Because the force is large, heavy insulated bolts and used to fasten the layers together. Although the instantaneous force may appear to create a dangerously high stress in the bolts, the total energy available is not enough to rupture them, if they are properly designed.

3.2. Verify the equations for I(t) and I_{max} in a simple RLC circuit.
3.3. A cylinder 10 cm in diameter is initially filled with a uniform magnetic induction of 0.7 T. Then a thin metallic liner is imploded by chemical explosives and compressed to an inside diameter of 0.6 cm. What is the peak magnetic induction produced by this flux compression, ignoring flux leakage?

Fig. 3.39 Cross sectional view of a parallel plate transmission line. The current density J is concentrated within a few skin depths of the inner surfaces. The magnetic field between the plates may be found by evaluating the contour integral in the limit of small x. In that case $\int_d^a d\vec{1} \cdot \vec{B} + \int_b^c d\vec{1} \cdot \vec{B} = 0$ Since B is the same and the $d\ell$ have opposite directions
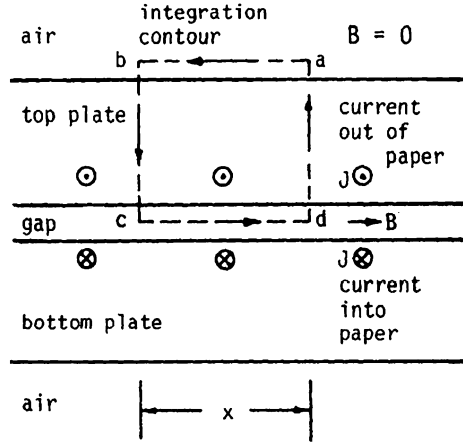
If the liner is aluminum 1 mm thick, about how fast must the compression be to prevent the magnetic field from penetrating through the liner ? (For non-ferrous metals, $\mu = \mu_o$.) What DT fusion power density could be achieved at this pressure if $\beta = 1$?

3.4. A large capacitor bank system has 470 capacitors with failure rates of 2.E-6 per shot, 470 switches with failure rates of 3.E-6 per shot, and 2,820 cables with failure rates of 4.E-6 per shot. Assuming that the components are used enough to get rid of defective items, but not yet near the end of life, estimate the approximate number of shots between failures.

3.5. If a second capacitor and switch, identical to the first ones, were added in parallel to the circuit of Problem 3.1, what would be the new maximum current and peak magnetic induction be? Assume that the transmission line and coil inductance and resistances remain the same.

3.11.2 Problems on Water-Cooled Magnets

3.6. How much power is required to generate a field of 6 T in a short solenoid with 10 cm bore diameter?

3.7. A solenoid has inner and outer radii of 1.00 and 1.20 m, and it generates a magnetic induction of 4 T. Estimate the hoop stress in the conductor.

3.8. A solenoid has length = 3 m, inner radius = 1 m, and outer radius = 2 m, and $\lambda = 0.9$. If 1 MW is available to power the coil, what is the maximum field that can be generated?

3.9. A coil with inner radius = 0.1 m and optimum shape is to be wound with one of the conductors of Fig. 3.37 and connected to a welding power supply that provides up to 1,000 A at 50 V. The coil segments will be pancake shaped and connected electrically in series. Which of the conductors

Fig. 3.40 Circular magnet coils wound from ¼ inch square copper tubing. Inner radius $r_1 = 1.7$ cm, outer radius $r_2 = 7.5$ cm. Each coil has 64 turns of conductor, $I = 300$ A
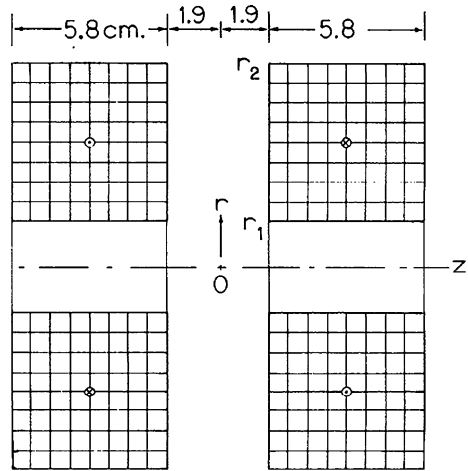
provides the highest magnet field, and what is the maximum field? [Hint: $a^2 L_c$ (total) $= \pi(r_2^2 - r_1^2)L$. Try large size conductors first and match the power supply impedance.]

3.10. For the coil of the previous problem assume that the cooling water flows into 20 parallel segments of the coil. Estimate the length of each segment, the required flow rate, and the pumping power, assuming that the coolant temperature rise is 60 K and the pump efficiency is 80 %.

3.11. Assume that the two coils shown in Fig. 3.40 have their currents in opposite directions, producing a spindle cusp magnetic field (Fig. 1.6). Approximating each coil as a single loop, find the magnetic field at $r = 5$ cm, $z = 0$.

3.12. Assume that the two coils shown in Fig. 3.40 have their currents in opposite directions, producing a spindle cusp magnetic field (Fig. 1.6). Find the magnetic field at $r = 0$ and $z = -5$ cm, approximating each coil as a single loop.

3.13. For the coils of Fig. 3.40 find the field at $r = 0$, $z = -5$ cm using Eq. 3.20, and compare it with the single loop approximation (previous problem).

3.14. Estimate the force between the coils of Fig. 3.40 using the single-loop approximation.

3.15. A solenoid is to be constructed of pancake coils each two turns wide, with $r_1 = 0.15$ m and $r_2 = 0.45$ m, using the conductor with $a = 1.19$ cm and $D = 0.699$ cm (Fig. 3.37). Estimate

   (a) the number of turns and conductor length for each pancake coil.
   (b) the maximum safe current, coil resistance, and power required by each pancake coil at maximum current
   (c) the require water flow rate and coolant pumping power for each pancake
   (d) the number of pancakes required for an optimum length solenoid, assuming a 2 mm gap between pancakes

Fig. 3.41 Tape wound coil
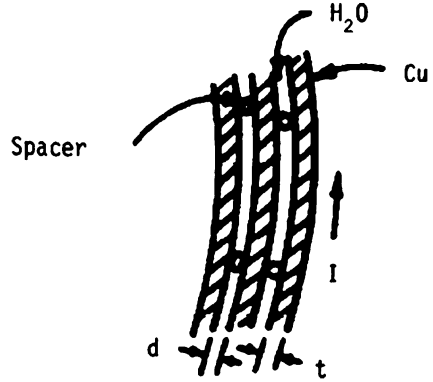
(e) the total power required and the maximum B_z produced by the optimum length solenoid.

3.16. Assume $\Delta T = 60$ K and coolant pressure drop $= 0.414$ MPa. Estimate the maximum safe current for a 50 m long conductor with a $= 0.864$ cm, $D = 0.466$ cm by calculating the coolant flow rate and coil resistance, and compare with the value of Fig. 3.37.

3.17. A tape-would coil uses copper conductor with width w and thickness t (Fig. 3.41) The layers of copper are separated by nylon monofilament spacers with diameter d, which are spaced azimuthally about 10d apart. If the average coil radius is r, estimate the resistance per turn of conductor, the power dissipated per turn at current I, and the required water flow rate to keep the water temperature rise at a given ΔT in terms of these symbols.

3.12 Review Questions

3.12.1 Water-Cooled Magnets

1. Explain the following equation. What is it called? What does ρ represent?

$$\overrightarrow{B}(r) = \int d\overrightarrow{B} = \frac{\mu_0}{4\pi} \int \frac{dV \overrightarrow{J} \times \overrightarrow{\rho}}{\rho^3} \quad (T)$$

In the above equation what does J dV become for a thin wire? Explain the "right hand rule".

2. What is the following equation called? What does it become for the case of a long, straight wire? For a toroidal solenoid (toroidal field coils)?

$$\oint d\ell \cdot \overrightarrow{J} = \mu_0 \iint d\overrightarrow{S} \cdot \overrightarrow{J} = \mu_0 I \text{ (enclosed)}$$

3. For what case is the following equation useful, and what do the parameters r, a, and z represent?

$$k = \left[\frac{4ra}{z^2 + (r+a)^2} \right]^{\frac{1}{2}}$$

4. For what case is the following equation useful, and what do the variables represent?

$$F_z = \int dF_z = I_2 B_{r1} \int dl_2 = 2\pi a I_2 B_{r1} \quad (N)$$

5. For what case is the following equation useful, and what do the variables represent?

$$\sigma = (B^2/2\mu_0)\left(\frac{r_1}{\Delta r} + \frac{1}{3}\right) \quad (Pa)$$

6. Explain the concept of force-reduced torsatron coils.

7. Explain the parameters in the following equation:

$$B_z = \lambda^{3/2}\mu_0 g(\alpha, \beta)(P/\eta r_1)^{\frac{1}{2}}$$

8. Explain the parameters in the following equation:

$$P = C\rho_m \Delta T(dV/dt)$$

9. In the following equation what is f and how is it determined?

$$\Delta p = fL_c \rho_m v^2/2D$$

10. Sketch and explain the three types of coil winding, including coolant flow directions.
11. Why are toroidal field coils often "D-shaped"?
12. What two quantities are equated to estimate the maximum safe current in a coil?
13. For efficient use of a power supply what quantities must be matched during coil design?

3.12.2 Pulsed Magnets

1. Write Kirchoff's Law for the sum of voltages around an RLC circuit in terms of the charge on the capacitor.
2. Sketch the circuit for a "crowbar switch", explain its operation, and sketch the resulting current waveform.

3. What case is described by the following equation? How can the characteristic diffusion time be estimated, and what is the result?

$$\frac{\partial \overrightarrow{B}}{\partial t} = \nabla^2 \overrightarrow{B}/\sigma\mu.$$

4. What does the following equation represent, and what is an approximate value of B_y for Cu and steel?

$$B \; < \; B_y[(r_2 - r_1)/2r_1]^{1/2}.$$

5. Sketch the circuit diagram for inductive energy storage and explain its operation. What transfer efficiency can be attained?
6. Sketch a spark gap switch and explain how it works.
7. Sketch a Marx bank and explain how it works.
8. Sketch a magnetic flux compression device and explain its operation.
9. Sketch and explain a "bathtub curve".

References

Abramowitz M, Stegun IA (1964) Handbook of mathematical functions, Applied mathematics series 55. National Bureau of Standards, Washington, DC

Bird MD (2004) Resistive magnet technology for hybrid inserts. Superconducting Sci Technol 17:R19–R33

Bird MD (2011) private communication

Boicourt GP (1973) The prediction of failures in C.T.R. systems. In: 5th symposium on engineering problems of fusion research, IEEE, New York, pp 308–313

Chen HS, Cong TC, Yang W, Tan CQ, Li YL, Ding YL (2009) Progress in electrical energy storage system: a critical review. Prog Nat Sci 19:291–312

Connolly D (2010) A review of energy storage technologies for the integration of fluctuating renewable energy, University of Limerick Report 11 Oct, Version 4

Dolan TJ (1982) Fusion research. Pergamon Press, Elmsford, New York (Chaps. 20 and 21)

Gralnick SL, Ojalvo IU, Zatt IJ, Balderes T (1979) Compatibility consideration for zero moment tokamak toroidal field coils, Nucl Technol 45:233–243

Henning CD (1966) FORCE—A Computer Program for Calculating Magnetic Forces Developed in Electromagnets, Proceedings of the symposium on engineering problems of controlled thermonuclear research, CONF-661016, p 53

Kalnavarns J, Jassby DL (1979) Steady-state resistive toroidal-field coils for tokamak reactors, Proceedings of the 8th symposium on the engineering problems of fusion research, San Francisco, 148–153

Kemp EL (1969) In: Proceedings of symposium on engineering problems of fusion research, Los Alamos Scientific Laboratory, April 8–11, Los Alamos Scientific Laboratory Report LA-4250, p F1-8

Knoepfel H (1970) Pulsed high magnetic fields. American Elsevier, New York

Knoepfel H (1972) Very high magnetic fields generated in single-turn solenoids. J Phys E: Sci Instrum 5:1133–1141

Kolm H, Lax B, Bitter G, Mills R (eds) (1962) High magnetic fields. Wiley, New York

Montgomery DB (1969) Solenoid magnet design. Wiley, New York

Parkinson DH, Mulhall BE (1967) The generation of high magnetic fields. Plenum, New York

Perkins WA, Brown JC (1966) MAFCO—a magnetic field code for handling general current elements in three dimensions, UCRL-7744-Rev II

Post RF, Post SF (1973) Flywheels. Sci Am 229(6):17

Schoenung S (2011) Energy storage systems cost update, a study for the DOE energy storage systems program, Sandia National Laboratories Report SAND2011-2730

Shadowitz A (1975) The electromagnetic field, McGraw-Hill, New York, Section 5.1

Turchi PJ (ed) (1980) Megagauss physics and technology. Plenum Press, New York

Chapter 4
Superconducting Magnets

Thomas J. Dolan and Denis P. Ivanov

Objectives

After studying this chapter one should understand

The conditions associated with superconductivity
Stabilization of superconductors
Protection of superconducting coils
Issues of conductor fabrication and heat removal
Designs of large coils for ITER, LHD, and W7-X.

4.1 Superconductivity

4.1.1 Domain of Superconductivity

When Onnes (1911) was measuring the resistivity of metals at low temperatures, he discovered that the resistance of a sample of mercury dropped abruptly from 0.125 Ω at 4.27 K down to less than 3×10^{-6} Ω (which was the limit of his instrument) at about 4.22 K, as illustrated in Fig. 4.1.

Onnes named this condition *superconductivity*. Many other metals and alloys have been found to exhibit similar behavior: their resistance drops to zero when the temperature is lowered below a *critical temperature* T_c, which is different for each material. Onnes also found that superconductivity can be destroyed by applying a sufficiently strong magnetic induction, called the *critical magnetic induction* B_c.

T. J. Dolan (✉)
NPRE Department, University of Illinois, Urbana, IL 61801, USA
e-mail: dolantj@illinois.edu

D. P. Ivanov
Kurchatov Institute, Moscow, Russian Federation
e-mail: denis.ivanov30@mail.ru

Fig. 4.1 Drop of resistance as temperature goes below T_c. Courtesy of Noe (2008), Karlsruhe Institute of Technology (KIT), Germany
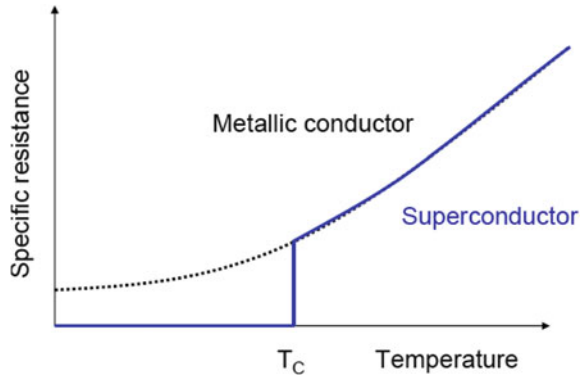
Fig. 4.2 Bounding surface of superconducting domain in T, B, J space. Courtesy of Noe (2008), Karlsruhe Institute of Technology (KIT), Germany
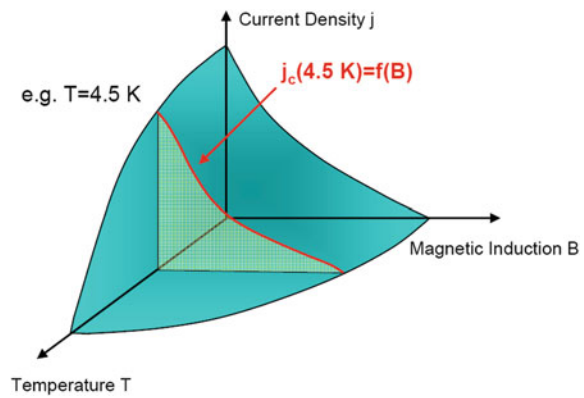
(As stated in Sect. 3.1, the magnetic field is denoted by **H** and the magnetic induction or magnetic flux density by **B**, where $\mathbf{B} = \mu\mathbf{H}$, and μ is the permeability of the medium. However, in fusion technology **B** is often called the "magnetic field", and this book follows that imprecise terminology.)

In addition to the temperature (T) and magnetic induction (B) limitations, there is also a limit on the current density J which may be flowing in the superconductor. The maximum value of J, called the *critical current density* J_c is a function of T and B. Thus, there is a domain in T, B, J space within which the material is in the superconducting state, as illustrated in Fig. 4.2 for a specific case. The central j_c curve shows the variation of critical current density with B at 4.5 K. Figure 4.3 shows the domains for three superconductors.

If either T, B, or J becomes too large, superconductivity ceases, and the material returns to normal resistivity.

The discoveries of various superconductors are illustrated in Fig. 4.4.

4.1.2 Electron Pairing

A metal can be pictured as a sea of mobile electrons flowing through a lattice of positive ions. The lattice ions vibrate back and forth, and the quantized lattice
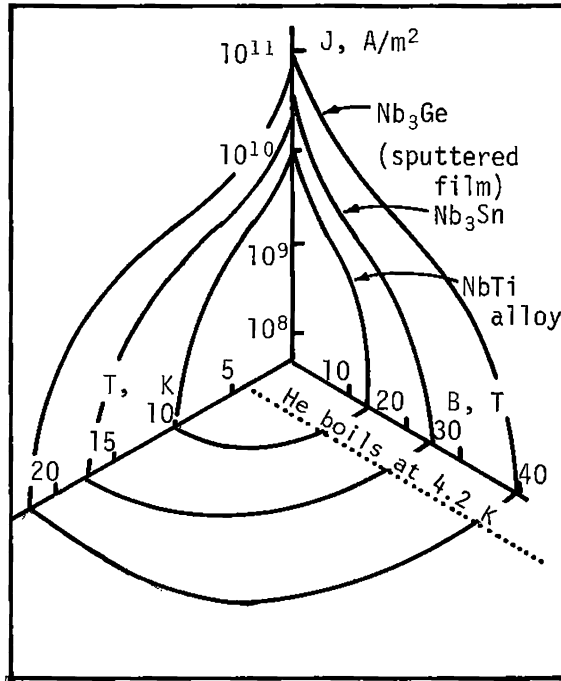
Fig. 4.3 Domains of superconductivity for several materials. These materials are superconducting inside the critical surfaces, and they have normal resistivity outside the surfaces. Reprinted with permission from Schwartz and Foner (1977), © 1977 American Institute of Physics
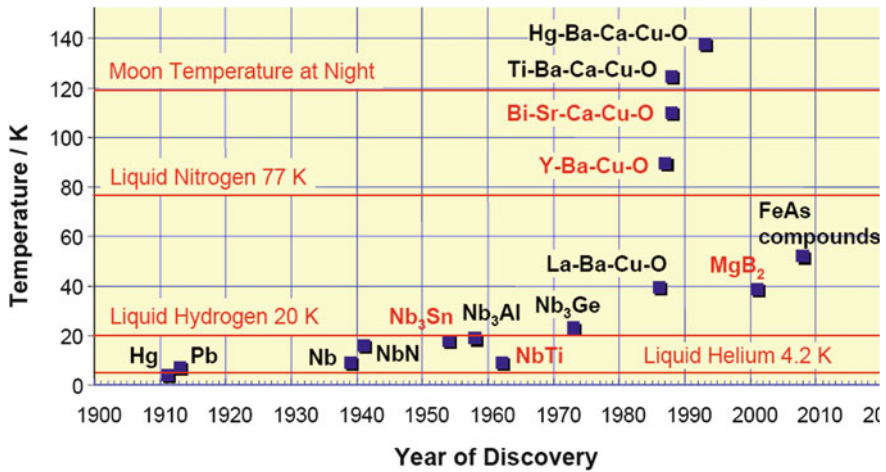
Fig. 4.4 Discoveries of various superconductors. Courtesy of Noe (2008), Karlsruhe Institute of Technology (KIT), Germany

vibrations (phonons) may interact with the wave functions representing electrons. When one electron produces a phonon that is absorbed by a second electron, a mutual attraction between the electrons results, according to the BCS theory (Bardeen et al. 1957). If this attraction is stronger than the mutual Coulomb repulsion, then the two electrons may become loosely bound together by repeated electron–phonon–electron interactions, even though they are separated by a large distance. Formation of such Cooper pairs is most probable for electrons having equal and opposite momenta and opposite spins. The separation between the paired electrons is much larger than the average distance between electrons. Many pairs of electrons overlap in the same spatial region, but the interactions between two paired electrons are much more important than their interactions with other electrons.

In an ordinary metal, electrons may be accelerated by an applied electric field and decelerated by collisions with the lattice. A balance between the acceleration and frictional forces determines the resistivity of the metal. In a superconductor, the paired electrons interactions with the lattice affect only each other, without dissipation by the lattice. Then the frictional force is zero, and so is the resistivity.

Metals that have high conductivity at room temperature, such as copper, have weak electron-lattice interactions. The attraction of electron-lattice-electron interactions is not great enough to overcome Coulomb repulsion, so pairing cannot occur, and those metals cannot become superconducting.

4.1.3 Energy Gap and Coherence Length

At zero Kelvin, with no applied magnetic induction or current density, all electrons are paired. If energy is supplied to the metal, some of the Cooper pairs will be broken apart. For each pair split, the electron system energy changes by an amount 2Δ, which is called the energy gap. Energy may be supplied by heat conduction, by applying an external magnetic induction, by forcing a large current density to flow through the metal, and by incident electromagnetic waves. If the added energy is large enough, all the Cooper pairs will be broken, and the metal will return to normal resistivity. At $T = 0$ K, the

$$\text{Energy gap} = 2\Delta(0) = 3.5 \, kT_c \tag{4.1}$$

where k = Boltzmann constant and T_c = critical temperature. (The average energy of a diatomic molecule is 3.5 kT.) This gradual transition from pair bonding at $T = 0$ to no bonding at $T = T_c$ is illustrated in Fig. 4.5.

As the temperature is raised, the presence of more unpaired electrons reduces the possible scattering states for the paired electrons, according to Pauli Exclusion Principle. The reduction of possible scattering states decreases the strength of the electron–phonon–electron interactions, reduces the attraction between electrons, and therefore reduces the energy gap. Thus, as T increases, $\Delta \rightarrow 0$. The temperature where $\Delta = 0$ (and all electrons become unpaired) is, by definition, the critical temperature T_c.

Fig. 4.5 Pair bonding at T = 0, followed by pair bonds breaking at T > 0
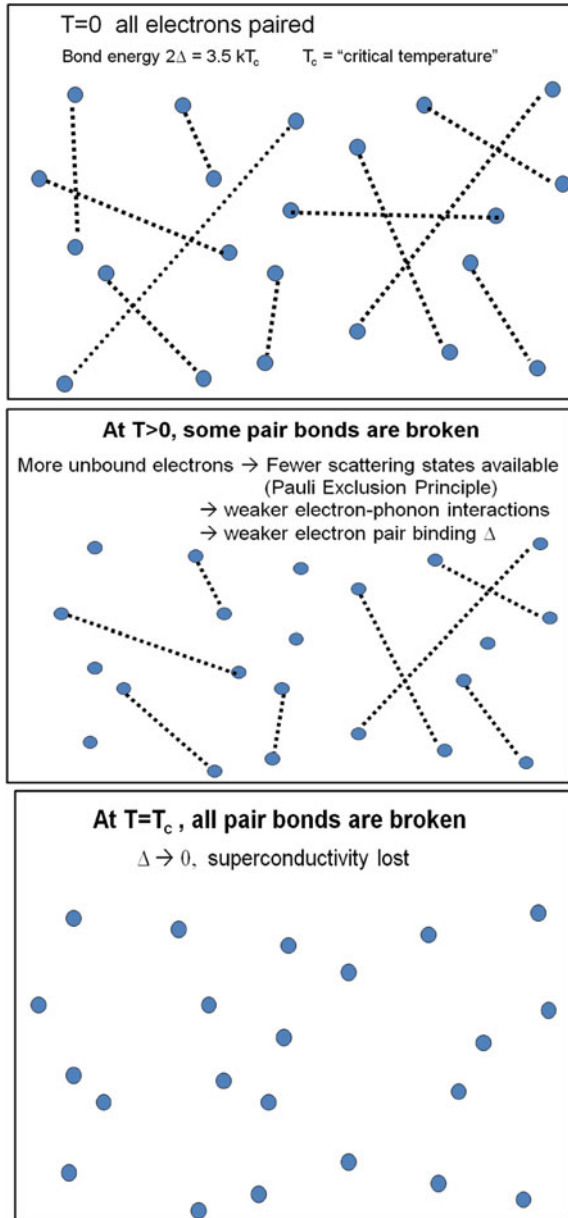
The *coherence length* ξ is the spatial scale length over which the transition between a superconducting region and a normal region occurs. Thus, it is the approximate distance over which the density n_s of electrons in the superconducting state (the density of paired electrons) varies, as illustrated in Fig. 4.6.

The coherence length is also roughly equal to the average separation between any two paired electrons. In pure metals $\xi \sim 1$ μm, but in impure metals, alloys,

Fig. 4.6 Definition of
coherence length ξ, relative
to the spatial distance over
which the fraction of paired
electrons changes
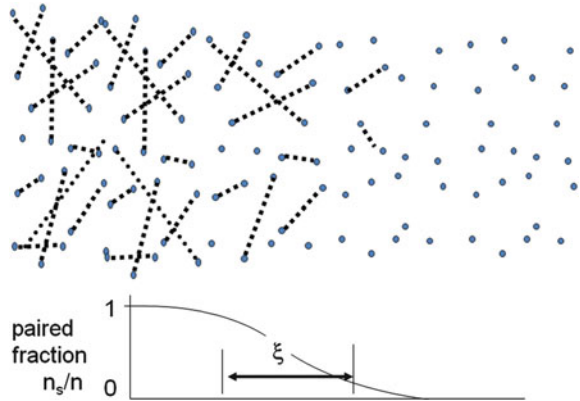
compounds, and metals with lattice defects ξ can be much shorter, on the order of
the electron mean free path.

4.1.4 Diamagnetism and Penetration Depth

A superconductor tends to exclude an applied magnetic field from its interior, as
was discovered by Meissner and Ochsenfeld (1933). This self-shielding effect was
explained by London and London (1935). The current density J due to n_s super-
conducting electrons per m^3 moving with average velocity v is

$$\mathbf{J} = -n_s e \mathbf{v} \tag{4.2}$$

Moving particles have waves associated with them, with the DeBroglie
wavelength λ and wavenumber k given by

$$\lambda = h/p, \quad k = 2\pi/\lambda = 2\pi p/h \tag{4.3}$$

where h is Planck's constant and p is the particle momentum. In a magnetic field,
the momentum of a particle with mass m, velocity c, and charge q is

$$\mathbf{p} = m\mathbf{v} + q\mathbf{A} \tag{4.4}$$

where $\mathbf{A}$ = magnetic vector potential. Consider the case of a wave representing a
Cooper pair, for which $m = 2m_e$, $q = -2e$. The phase difference between any two
points along the wave is

$$\phi_b - \phi_a = -\int_a^b d\ell \cdot \mathbf{k} = -(2\pi/h)\int_a^b d\ell \cdot (2m_e\mathbf{v} - 2e\mathbf{A}) \tag{4.5}$$

where $d\ell$ is a differential along the path from point a to point b. If we take the limit
as $b \rightarrow a$, the result is

$$\nabla\phi = -(4\pi/h)(m_e\mathbf{v} - e\mathbf{A})$$

or

$$\mathbf{v} = -\,h\nabla\phi/4\pi m_e + eA/m_e \tag{4.6}$$

Eliminating **v** between Eqs. (4.2) and (4.6), we get

$$\mathbf{J} = n_s eh\nabla\phi/4\pi m_e - n_s e^2 A/m_e \tag{4.7}$$

Taking the curl of this equation, we find

$$\nabla \times \mathbf{J} = -\,n_s e^2 \mathbf{B}/m_e \tag{4.8}$$

since $\nabla \times (\nabla\phi) = 0$ and $\nabla \times \mathbf{A} = \mathbf{B}$, we can eliminate J using Ampere's Law $\mathbf{J} = \nabla \times \mathbf{B}/\mu_o$. (Please see Appendix D for vector identities.) Then, since $\nabla \times (\nabla \times \mathbf{B}) = (\nabla \bullet \mathbf{B}) - \nabla^2 \mathbf{B}$ and $\nabla \bullet \mathbf{B} = 0$, we find

$$\nabla \times (\nabla \times \mathbf{B}/\mu_o) = -\nabla^2 \mathbf{B}/\mu_o = -\,n_s e^2 \mathbf{B}/m_e \tag{4.9}$$

If we let x be the direction perpendicular to the surface of a metal, then

$$d^2 B/dx^2 = B/\lambda_L^2; \tag{4.10}$$

where

$$\lambda_L = \left(m_e/n_s e^2 \mu_o\right)^{1/2} = \left(m_e c^2 \varepsilon_o/n_s e^2\right)^{1/2} = 5.3 \times 10^6 \, n_s^{-1/2} \tag{4.11}$$

If λ_L is constant, the solution of this equation for a thick metal is

$$B = B_o \exp(-x/\lambda_L) \tag{4.12}$$

where B_o is the value of B at the surface $x = 0$. Thus, the magnetic field is attenuated exponentially in the metal over a distance λ_L, called the *London penetration depth*.

The exclusion of a magnetic field by a superconductor is illustrated in Figs. 4.7 and 4.8.

(This penetration depth λ_L for magnetic induction is comparable to the Debye length of electrostatics with kT replaced by $m_e c^2$.)

Fig. 4.7 The Meissner-Ochsenfeld effect. A superconductor (*circle*) expels the magnetic field lines (*dashed*)
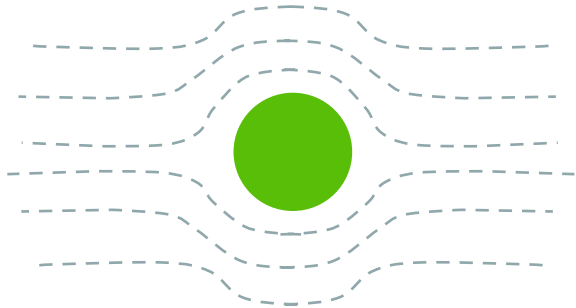
Fig. 4.8 Exponential
attenuation of magnetic
induction in a superconductor
over the London penetration
depth
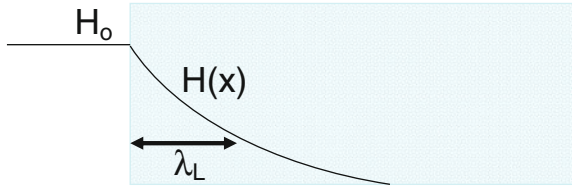
For a typical case with $n_s \sim 10^{28}$ m^{-3} (less than one electron per atom in the superconducting state), $\lambda_L \sim 5 \times 10^{-8}$ m $= 50$ nm. Thus, the magnetic induction is attenuated very close to the metal surface. (Some error is introduced into these equations when the separation of the Cooper pairs is greater than λ_L.)

4.1.5 Flux Quantization

Consider the case of a superconducting region surrounding a normal region (Fig. 4.9).

We can apply Eq. (4.5) to the integration path indicated by the dashed line. If we close the loop so that b coincides with a, then the phase difference must be an integer multiple of 2π

$$2\pi n = (2\pi/h) \int d\ell \cdot (-2m_e \mathbf{J}/n_s e - 2e\mathbf{A}) \tag{4.13}$$

where n is an integer (not to be confused with electron density) and the integral is a closed loop (Fig. 4.9). Using Stoke's Theorem (Appendix D)

$$\int d\ell \cdot \mathbf{A} = \int d\mathbf{S} \cdot (\nabla \times \mathbf{A}) = \int d\mathbf{S} \cdot \mathbf{B} = \phi \tag{4.14}$$

Fig. 4.9 Integration path
around a normal region
surrounded by a
superconducting region
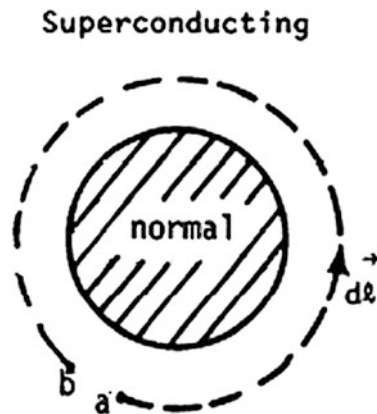
where ϕ is the magnetic flux enclosed by the integration path. The current density is concentrated right at the boundary between the normal and superconducting regions. If the contour is drawn sufficiently far outside the boundary, the J term of Eq. (4.13) may be negligible.

Then Eq. (4.13) reduces to

$$2\pi n = (2\pi/h)\ 2e\phi \tag{4.15}$$

or

$$\phi = n\phi_o \tag{4.16}$$

where

$$\phi_o = h/2e = 2.07 \times 10^{-15}\ \text{Wb} \tag{4.17}$$

is called a *fluxon*. Thus, the flux is *quantized*: the enclosed flux must be an integer number of fluxons. If the normal region is small, only one fluxon may be enclosed. Magnetic flux lines penetrating a superconductor tend to space themselves uniformly in a close packed triangular lattice, as can be seen in Fig. 4.10.
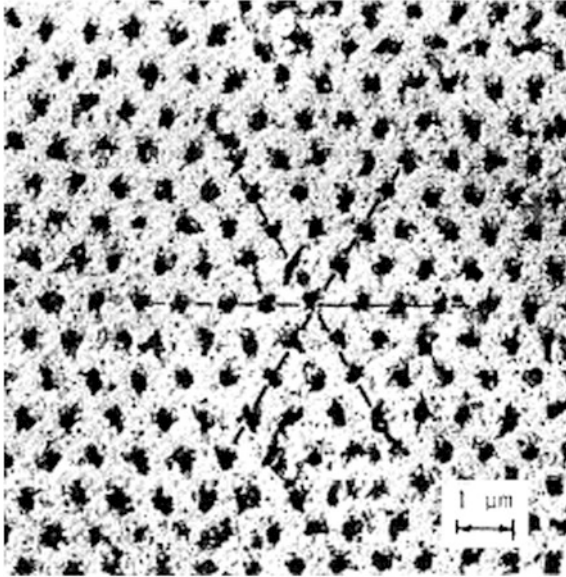
Fig. 4.10 Pattern of individual fluxons in a Type II superconductor. The pattern is revealed by allowing tiny (50 nm) ferromagnetic particles to settle on the surface of a magnetized Pb-In alloy specimen. The particles settle where the magnetic flux intersects the surface. The photograph was obtained by electron microscopy of the deposited particles. Lines are drawn along the lattice directions. Reprinted with permission from Trauble and Essmann (1968), © 1968 The American Institute of Physics

4.1.6 Type I and Type II Superconductors

Superconductors may be classified into two categories, depending on the size of the coherence length ξ (average spacing between electron pairs) relative to the magnetic field penetration depth λ_L:

$$\begin{array}{ll} \xi > 2^{1/2}\lambda_L & \text{Type I} \\ \xi < 2^{1/2}\lambda_L & \text{Type II} \end{array} \tag{4.18}$$

Most pure metal superconductors are Type I. (Not all metals are superconductors.) The critical magnetic field above which Type I superconductors lose their superconductivity is given by

$$H = H_{co}\left[1 - (T/T_c)^2\right] \tag{4.19}$$

where T = temperature, T_c = critical temperature (in the absence of a magnetic induction), and H_{co} is a constant. All Type I superconductors have low values of H_{co}, as illustrated in Table 4.1 for a few metals, so they are unsuitable for winding magnet coils. [In what follows we use the symbol B instead of H, as explained in Sect. 3.1].

Niobium and vanadium are the only pure metals which are Type II superconductors. The discovery that Nb_3Sn wire can carry a high current density at $B > 8$ T (Kunzler et al. 1961) stimulated development of high-field magnets for fusion research and other applications.

In Type II materials at low applied magnetic inductions the magnetic induction is excluded from the conductor, as in Type I materials. At the lower critical magnetic induction B_{c1} the magnetic flux lines begin to penetrate into the metal. The flux lines (fluxons) carry a small normal core into the superconductor, similar to the normal region of Fig. 4.9. Currents flow around each flux line, as shown in Fig. 4.11.

The existence of such Type II superconductors and their current vortices was predicted by Abrikosov (1957). A one-dimensional plot of the superconducting electron density n_s versus position in such a case is shown in Fig. 4.12.

Table 4.1 Transition temperatures and magnetic flux density constants for some typical Type I metals. Minervini and Iwasa (2003)	Material (Type)	T_c (K)	$\mu_0 H_{c_0}$ [a] (T)
	Ti (metal)	0.40	0.0056
	Zn	0.85	0.0054
	Al	1.18	0.0105
	In	3.41	0.0281
	Sn	3.72	0.0305
	Hg	4.15	0.0411
	V	5.40	0.1403
	Pb	7.19	0.0803

[a] 0 K
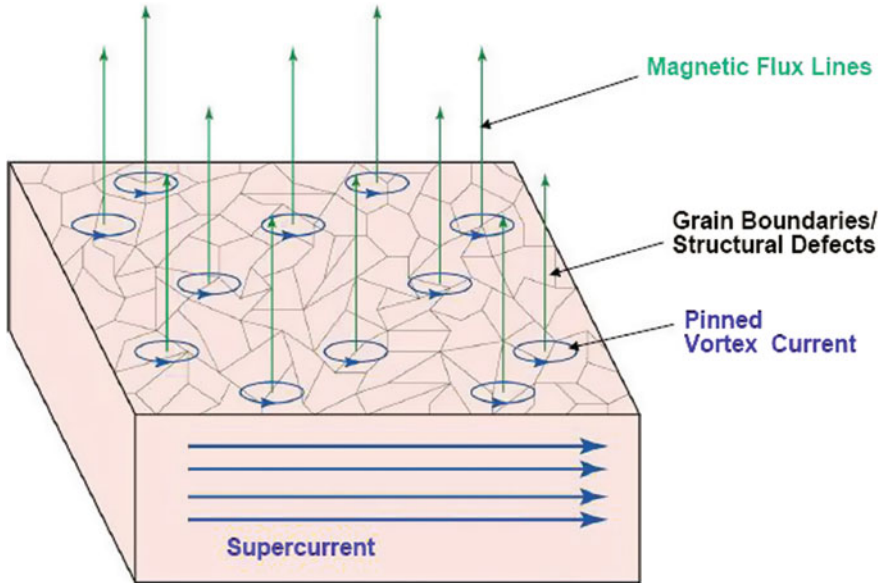
Fig. 4.11 Schematic drawing of "pinned" vortices. Flow of vortex currents around fluxons in a Type II superconductor. Each flux quantum is in a local normal region, where the superconducting electron density n_s is very small, surrounded by vortex currents. Courtesy of Minervini and Iwasa (2003)

Fig. 4.12 One-dimensional variation of the density ns of electrons in the superconducting state as a function of position x. **a** Low flux density. **b** High flux density (near B_{c2})
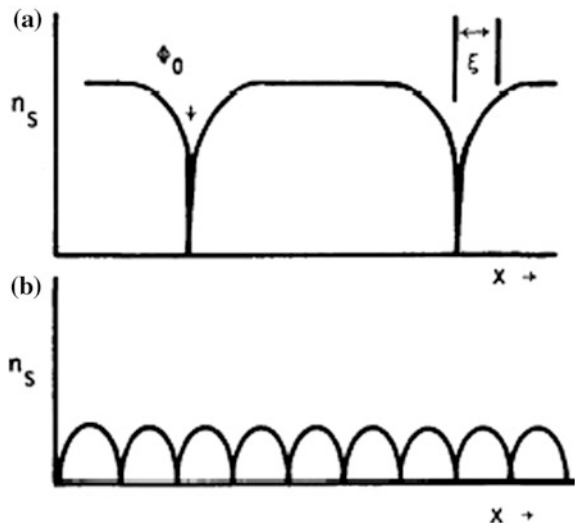
As the magnetic induction is increased, the flux lines move closer together. Finally, at the upper critical magnetic induction B_{c2} the overlapping of the effects of the flux lines reduces n_s to very small values, and superconductivity is lost. Thus, the condition for the flux density at the upper critical induction may be written

$$B_{c2} \sim \phi_o/(2\xi)^2 \quad \text{(Tesla)} \tag{4.20}$$

4.1.7 Critical Current Density in Type II Materials

At very high magnetic inductions, the critical current density is limited by the density n_s of electrons in the superconducting state. As n_s is decreased by overlapping of flux line effects, fewer electrons are available to carry the current.

At lower magnetic inductions, where overlapping has a negligible effect on n_s, the Lorentz force limits the current that the material can carry. The fluxons tend to locate themselves along defects in the lattice, where their potential energy is lowest. The potential energy as a function of distance is illustrated in Fig. 4.13.

The flux lines are said to be *pinned* to the defect locations. The Lorentz force $(\mathbf{J} \times \mathbf{B})$ pushes on the flux lines. When the transverse current density (dashed arrow in Fig. 4.11) is high enough, the Lorentz force exceeds the pinning force of the potential barrier, and a fluxon can move from one location to the next. Such flux creep dissipates energy in the lattice (Anderson 1962; Kim et al. 1963). The motion of many flux lines, called *flux jump*, may raise the local temperature above the critical temperature T_c, causing the material to become normal locally. To attain high critical current densities, it is desirable to minimize flux jumps, by having strong pinning forces in the material. One means for achieving this is by extensive cold working, which increases the number of lattice defects. It has been said that the "worst lattice microstructures" produce the "best Type II superconductor properties".

4.1.8 Magnet Coils

A superconducting material should have the following properties in order to be satisfactory for winding magnets:
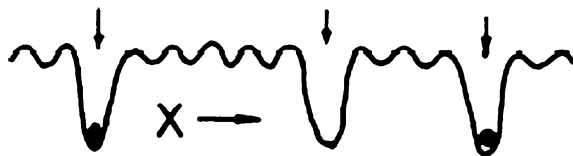
Fig. 4.13 One-dimensional variation of the potential energy of magnetic flux lines versus position in the metallic lattice. *Arrows* denote lattice defects, and *dots* denote pinned flux lines

Table 4.2 Some applications of superconductivity (Minervini and Iwasa 2003)

Energy

- Electricity generation and storage, superconducting magnetic energy storage
- Transmission and distribution cables; transformers
- Motors

Transportation

- Magnetic levitation

Medicine

- Magnetic resonance imaging (MRI); superconducting quantum interference device (SQUID) (biomagnetism); magnetic steering; biological separations

Space and Ocean

- Sensors; undersea cables; magnifiers

High tech

- Magnetic bearings; magnetic separations

Information/communication

- Electronics; filters

Research

- MRI; accelerators; high-field magnets, proton radiography

- High critical temperature T_c
- High critical magnetic induction B_{c2}
- High critical current density J_c
- Commercial availability at affordable cost
- Good mechanical properties, such as ductility (Brittle conductors may be used if special fabrication techniques are employed.)

Type II superconductors, such as Nb_3Sn and NbZr, were used to build small magnets in the early 1960s, but the coils would often *quench* (transfer from the superconducting state to the normal state) unexpectedly, which can be caused by epoxy cracking, by conductor motion, or by exceeding the critical current density. Nowadays, superconducting magnet technology has progressed to the point where large, high-field magnets can be built with much better reliability.

There are now many applications of superconductivity, Table 4.2.

4.2 Superconductors

Conductors available commercially include NbTi and Nb_3Sn. Some properties of these materials are listed in Table 4.3.

Because of its good ductility, NbTi can be drawn into multiple thin filaments in a matrix of copper in order to help avoid quenching. The critical magnetic induction data for NbTi and Nb_3Sn are shown in Fig. 4.14.

The critical current densities of these materials are shown in Fig. 4.15.

Nb_3Sn is very brittle, and its critical current density J_c decreases with strain as indicated in Fig. 4.16.

Table 4.4 compares Nb_3Sn with NbTi.

Table 4.3 Properties of some Type II superconductors

Material (Type)	T_c (K)	$\mu_0 H_{c_0}$ (T)
Nb (metal)	9.5	0.2[a]
Nb–Ti (alloy)	9.8	10.5[b]
NbN (metalloid)	16.8	15.3[b]
Nb_3Sn (intermetalic compound: A15)	18.3	24.5[b]
Nb_3Al	18.7	31.0[b]
Nb_3Ge	23.2	35.0[b]
MgB_2(compound)	39	~ 15[a]
$YBa_2Cu_{3-x}O_x$(oxide:Perovskite) <YBCO>	93	150[a]
$Bi2Sr_2Ca_{x-1}Cu_xO_{2x+4}$ <BSCCO2223 or 2212>	110	108[a]

(High temperature superconductors like YBCO will be discussed in Sect. 4.9). Courtesy of Minervini and Iwasa (2003), MIT Plasma Science and Fusion Center
[a] 0 K
[b] 4.2 K

Fig. 4.14 Upper critical magnetic induction versus temperature for Nb_3Sn and NbTi. Courtesy of Noe (2008), Karlsruhe Institute of Technology (KIT), Germany

$$B_{c2}(T) = B_{c2,0}\left(1 - \left(\frac{T}{T_c}\right)^2\right)$$

Nb_3Sn
T_c=18,3 K
$B_{c2,0}$=27,9 T

NbTi
T_c=9,3 K
$B_{c2,0}$=14,5 T
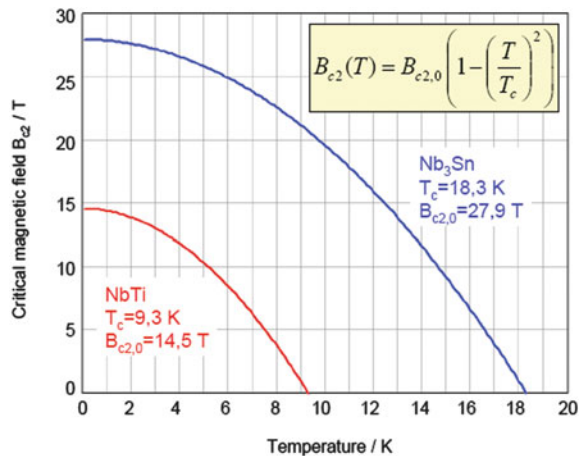
NbTi is not suitable for inductions B > 8.5 T, unless the temperature is reduced below 4.2 K. Thus, NbTi is usually used for B < 8 T, Nb_3Sn for 8 < B < 13 T, and other materials for higher inductions. Nb_3Sn is brittle, expensive, and very difficult to fabricate. Some high-temperature superconductors are discussed in Sect. 4.9.

Magnesium diboride (MgB_2) is a low-temperature superconductor, but it is cheaper than NbTi and may replace NbTi for some applications. At T = 4.2 K. It has critical current densities of $0.64 - 1.7 \times 10^5$ A/cm^2 at 4 T and $0.42 - 1.3 \times 10^4$ A/cm^2 at 8 T (Schlachter 2010).
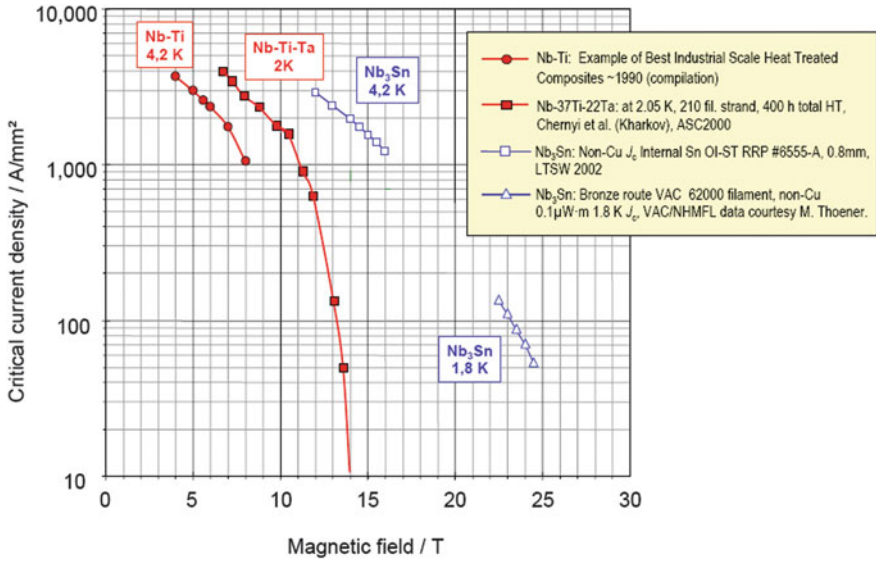
Fig. 4.15 Critical current density versus magnetic induction for Nb₃Sn and NbTi. From Courtesy of Noe (2008), Karlsruhe Institute of Technology (KIT), Germany, based on data from University of Wisconsin-Madison

Fig. 4.16 Effect of strain on critical current density of Nb₃Sn. Minervini and Iwasa (2003)
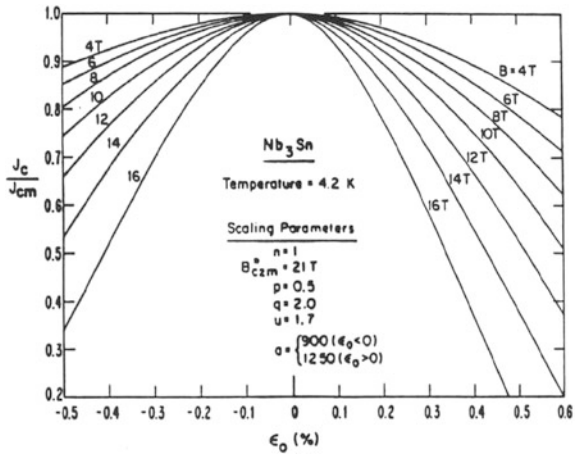
Table 4.4 Comparison of Nb_3Sn with NbTi. Courtesy of Noe (2008), Karlsruhe Institute of Technology (KIT), Germany

Nb_3Sn has higher stability
+Larger temperature margin ($T_c = 18$ K, NbTi 10 K)
+Less Cu reruired
+Higher B_{c2}
Disadvantage of Nb_3Sn
−Brittle compound
−Strain dependance of j_c
−Higher cost

The ideal current densities are not always attainable, however. In order to avoid quenches, superconducting coils must be stabilized.

4.3 Stabilization

4.3.1 Need for Stabilization

Various processes, such as flux jumps and conductor movement, can generate heat and make $T > T_c$ in a small region of the superconductor, causing that region to go normal. When this occurs, the local resistance of the conductor goes from zero up to a finite value instantaneously. One might expect the finite resistance to lower the current, but any change in current develops a large voltage equal to L(dI/dt), where L is the coil inductance, and this voltage maintains the current nearly constant if the inductance is large. (The current will gradually decay with a time constant of L/R). Since a high current is flowing through a finite resistance, it dissipates heat at a rate $P = I^2 R$ (W), heating up the surrounding conductor, too. This heating may drive the surrounding conductor normal, and the region of normalcy may spread rapidly throughout the entire coil. This rapid spread of the superconducting-to-normal transition is called a *quench*.

Many types of disturbance can affect superconducting magnets, as illustrated in Table 4.5.

In small magnets quenching can cause much of the liquid helium coolant to vaporize suddenly. If provisions for pressure-relief were not made, the resulting overpressure could rupture the cryostat. (A *cryostat*, or *dewar*, is an insulated container for low temperature devices, such as magnets.) If the magnet's stored energy is large, quenching could dissipate enough energy to melt part of the coil. Therefore, coils must be stabilized against quenching in order to attain their design fields, and they must be protected against the consequences of a quench, in case it occurs.

There are three main methods of stabilization: cryogenic, adiabatic, and dynamic.

Table 4.5 Sources of disturbance in superconducting magnets (Minervini and Iwasa 2003)

Mechanical—*Lorentz force; thermal contraction*
- Wire motion/"micro-slip"
- Structure deformation
- Cracking epoxy; debonding

Electrical/Magnetic—*Time-varying current/field*
- Current transients, includes AC current
- Field transients, includes AC field
- Flux motion, flux jump

Thermal
- Conduction, through leads
- Cooling blockage (poor ventilation)

Nuclear radiation
- Neutron flux in fusion machines
- Particle showers in accelerators

4.3.2 Cryogenic Stabilization

When normalcy occurs in the superconductor, its resistance suddenly becomes higher than that of the surrounding copper, so most of the current is shunted into the copper substrate. Thus, the overall resistance is lower than it would be if only the superconductor were present, and less heat is generated. If the substrate has good thermal contact with the helium coolant, then the heat generated may be quickly transferred to the coolant without overheating surrounding areas, and a quench is avoided. This type of stabilization can occur when

$$\alpha_s = (\text{power dissipated})/(\text{power removed}) = I^2 \eta \ell / Aq\,S \ \leq 1 \qquad (4.21)$$

where α_s is called the *Stekly number*, η = resistivity of the conductor (Ohm-m): I = current (A), A = cross-sectional area of the conductor (m^2), ℓ = length under consideration, S = conductor surface area in contact with the helium coolant (m^2), and q = maximum heat flux that the coolant can remove. For nucleate boiling in liquid helium q $\sim$ 4,000 W/m^2 = 0.4 W/cm^2. Cryogenic stabilization relies on two phenomena: *current sharing* by the substrate and rapid *heat removal* by the coolant.

4.3.3 Adiabatic Stabilization

This method involves the use of thin superconductor filaments so thin that the heat dissipated by a flux jump is too small to raise the temperature above T_c. The stability criterion for circular filaments is

$$dJ_s < \pi \left(\rho_m C_p T_o / \mu_o \right)^{1/2} \qquad (4.22)$$

where d = filament diameter (m), J_s = current density in the filament (A/m^2), ρ_m = mass density (kg/m^3), C_p = specific heat (J/kg K) of the filament, μ_o = permeability of free space, and

$$T_o = - J_s(\partial J_s/\partial T)^{-1}_{B=constant}. \tag{4.23}$$

Values of T_o for NbTi and Nb$_3$Sn are shown in Fig. 4.17 as functions of B and T. Typically ρ_m $C_p \sim 1{,}000$ J/m^3 K. If d ~ 10 μm and $T_o \sim 10$ K, then J_s: $< 3 \times 10^{10}$ A/m^2.

To prevent current loops from being induced between adjacent filaments as the field is increased, the filaments in a given substrate must be *transposed* (braided or twisted) with at least 4 transpositions occurring in a "critical length".

$$\ell_c = [2J_s d\eta/(dB/dt)]^{1/2} \tag{4.24}$$

where η = substrate resistivity (Ω m) and (dB/dt) = time rate of change of the magnetic induction (T/s). Thus, a pulsed coil must have a short transposition length.

Adiabatic stabilization allows higher current densities than cryogenic stabilization, and it permits the induction to be changed rapidly, provided that transposition of filaments is adequate. Devices with pulsed coils use adiabatic stabilization. Epoxy may be used to prevent conductor motion.
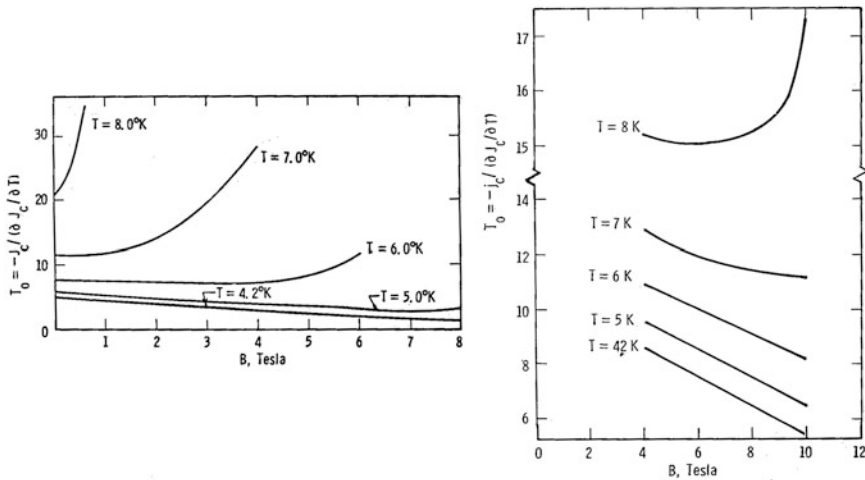
Fig. 4.17 Adiabatic stability parameters T_o for NbTi (*left*) and Nb$_3$Sn (*right*) as functions of magnetic field and temperature. Buncher et al. (1976)

4.3.4 Dynamic Stabilization

Dynamic stabilization, used mainly with Nb_3Sn tapes, relies on magnetic damping of flux jumps by the substrate material to reduce the heat generated, combined with heat removal by conduction. Two conditions must be met:

$$H_\perp < \pi(K_{cu}T_o/4\eta)^{1/2} \tag{4.25}$$

and

$$J_s < (\pi T_o d_n K_s/\eta d_s^3)^{1/2} \quad (A/m^2) \tag{4.26}$$

where $H\perp$ = magnetic field (A/m) perpendicular to the ribbon (in the radial direction), K_{Cu}, and K_S = thermal conductivities of the copper and superconductor (W/mK), η = resistivity of the substrate ($\sim 3 \times 10^{-10}$ Ω m for copper), J_s = current density in the superconductor (A/m^2), and d_n and d_s = thicknesses of the normal conductor and superconductor ribbons (m). Since the Stekly number is greater than one, higher current densities might be achieved, but dynamic stabilization alone is not reliable, and tape wound coils are rarely used.

Devred (2004) gives a thorough discussion of stabilization methods.

4.4 Coil Protection

The main areas of failure in superconducting magnets, in the order of decreasing reported incidents, are:

- Insulation
- Mechanical
- System performance
- Conductor
- External system
- Coolant.

(Minervini and Iwasa 2003).

Fusion reactor coils will have stored energies on the order of GJ per coil. The coils must be protected against several specific fault conditions, including quench, broken circuit, short circuit to ground, and coolant channel blockage.

4.4.1 Quench

If a 1.5 GJ coil containing 70 t of copper quenched and the entire energy were dissipated uniformly in the copper, then the coil temperature would rise to about 140 K, with little damage. If the energy were dissipated in a small region of the

coil, however, the insulation or epoxy could overheat, and the copper could melt. Thus, it is desirable to ensure that the energy is either dumped uniformly in the coil or (preferably) transferred to an external heat sink. The helium will be boiled and expelled from the dewar, which should be protected against rupture from over-pressure. Large rubber or plastic bags may be used to temporarily contain the expelled helium.

4.4.2 Broken Circuit

One or more arcs would occur between the broken ends of the conductor and the coil case, with an arc voltage on the order of 100 V. The arc could puncture a thin steel coil case, destroying the vacuum insulation and causing associated problems. The resistance of surrounding room temperature structures is too high for much energy to be dumped into them.

4.4.3 Short Circuit to Ground

If the coil is grounded, a current-limiting resistor is usually inserted in the ground connection. This can limit the current to about 10 A, which will not cause too much damage.

4.4.4 Coolant Channel Blockage

If a normalcy occurred, inadequate heat removal could prevent recovery of superconductivity. In the early days of superconducting magnets many failures occurred, such as hot spots and arcing, power lead failure, or conductor movement (Hsieh et al. 1978). Reliability is much better now.

4.4.5 Protection Circuitry

Protection circuitry can be passive (in place constantly) or active (actuated by switching devices). An example of a coil protection circuit is shown in Fig. 4.18.

During superconducting operation the winding resistance R_w is zero, and current from the power supply flows through R_w and L. If a quench occurs, R_w suddenly increases and the current flows through the external resistances R_e, which can be massive (~ 10 t) bars of iron, or water-cooled stainless-steel, and the switch can be opened. If the coil current is 10 kA and $R_e = 1~\Omega$, then 10,000 V are

Fig. 4.18 Simplified illustration of coil protection. When the coil is superconducting practically all the current flows through it. When it quenches, a large voltage develops, and current is forced through external resistors, such as iron bars in water
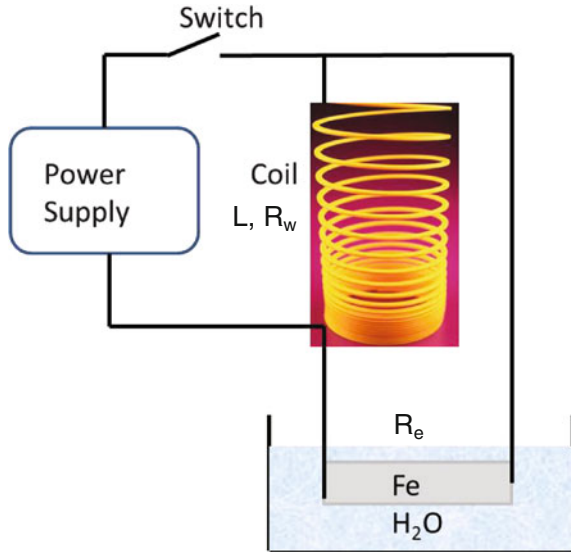
developed across the insulation. If the inductance $L = 30$ H, then the current decays exponentially with decay time $L/R = 30$ s. The initial power dissipation rate $I^2 R_e = 100$ MW.

4.4.6 Fault Detection

Good instrumentation is required to detect fault conditions. Some parameter changes that can be monitored to identify various problems are listed in Table 4.6.

In a Cable in Conduit Conductor (Sect. 4.5) it is essentially impossible to dump energy internally as the CICC is too stable: quenches do not propagate. Hence, good internal insulation and an external high-voltage dump are required.

4.4.7 Normal Phase Detection

The transition from superconductivity into normal conductivity starts at a point where, for some reason, superconductivity is lost. The reasons could be current increasing too quickly, a shift of conductor inside the coil, insulation cracking, coolant supply loss, heat inflow, AC losses from varying magnetic field, etc. If cooling is insufficient (not cryogenically stabilized), the temperature rises, and this hot spot can spread inside along the conductor at about 1–10 m/s. This spread of normal conductivity is called a quench. A single turn quench in a middle size coil would produce a voltage drop ~ 30 mV, which is much higher than the voltage

Table 4.6 Coil fault detection methods. Buncher et al. (1976)

Problem	Parameter changes
Quench	Increased coil local resistance and voltage
	Increased local temperature in winding
	Increased helium heat load and pressure drop
Coil insulation failure and turn to turn short circuit	Lower resistance and capacitance to ground;
	Strong He evaporation during charging and current damping; Inability to get rated current
Break of coil lead	Big powerful arc which shunts the protection resistor and dissipates considerable part of magnet energy
Coil movement	Coil position change
Coolant tube rupture or pump failure	Decreasing helium pressure and flow rate
	Cryostat vacuum fault
	Loss of coolant
	Magnet quench
Dewar or vacuum pump failure	Rise of dewar pressure
	Increase heat load on helium system
	Magnet quench
Refrigeration system failure	Increased helium temperature
	Magnet quench

noise. The inductive voltage drop during slow charging should be compensated by a balanced bridge. For normal phase detection the voltage from two halves of magnet or from number of its parts (having same inductance) are carried by insulated wires called "voltage taps" to a balanced bridge, and their imbalance is compared with some DC preset voltage. Usually the preset voltage 100–200 mV used for full winding halves or for two adjacent coils, and just 30 mV on busbars or links. A separate detector with small preset on the links was not provided on the Large Hadron Collider (LHC), and this was a contributing cause of the magnet failure in 2008.

4.5 Coil Design and Conductor Fabrication

Some coil design considerations are listed in Table 4.7. Several of these may require iteration, in order to satisfy overlapping criteria.

4.5.1 Conductor Design

The required coil energy $\frac{1}{2} LI^2$ is comparable to $VB^2/2\mu_o$, where $B^2/2\mu_o$ is the average magnetic energy density (or pressure) in the coil bore volume V. It is desired to have low inductance and high current, large conductors, not too many

Table 4.7 Coil design considerations

Magnet	Field distribution, ampere-turns, inductances
Conductor	Current, size, stabilization, cooling method, strain, AC losses, winding scheme, joints, availability, cost
Coil protection	Fault conditions, damage minimization
Heat removal	Method, coolant flow rate and channel design, pressure drop and pumping power, stresses (Chap. 3)
Structure	Forces and stresses under normal and fault conditions, thermal stresses, coil shape to reduce bending moments, coil support structure, coil winding and clamping
Cryogenics	Heat loads, refrigeration, cryostat design (Chap. 10)
Radiation damage	Neutron and gamma doses to coil and structure, effects on properties, such as resistivity of substrate (Chap. 8)

turns to wind, and the ability to discharge the coil energy into the protective system in a reasonable length of time L/R. However, as the conductor size is increased, cryogenic stabilization becomes increasingly difficult, because the heat transfer area grows linearly with conductor size, while the current is proportional to the square of the conductor size.

The conductor current in large coils for ITER is up to 70 kA. Large coils use multifilamentary conductors and enough copper to provide cryogenic stabilization. This limits the attainable current density to $J < 5$ kA/cm^2 (50 MA/m^2). The conductor cross sectional area is increased by 30–40 % to provide coolant channels (total area >20 cm^2).

The conductor strain, which can be estimated from bending radius and stress under ponderomotive force, is typically limited to values $\varepsilon \leq 0.3$ % (Nb_3Sn) to avoid degradation of performance. In order to plan cryogenic refrigeration requirements and ensure stability, AC losses induced by pulsed ohmic heating fields must be calculated. Very large coils may be wound at the reactor site, instead of at a factory, due to shipping difficulty. Joints between superconductors have been made by soldering, clamping, or cold-welding. Cold-welding was used with the Mirror Fusion Test Facility magnet conductor cores. Because the tiny superconducting filaments do not mate at joints, the current must flow through a thin layer of copper, resulting in a slight voltage drop and resistive heating.

4.5.2 Heat Removal

Three methods are available for heat removal: bath cooling (pool boiling), forced two-phase flow, and forced flow supercritical cooling.

4.5.3 Bath Cooled (or Pool Boiling or Ventilated Winding)

The coil may be immersed in a bath (or pool) of freely boiling liquid helium. Small magnets could be solid, filled with epoxy between windings and cooled by heat conduction. For large magnets helium coolant channels are necessary.

Bath cooling provides very effective cooling and good conductor stability. Bubbles rising in the hotter channels increase circulation where it is needed. Worldwide, bath cooling is used for over 20.000 magnetic resonance imaging (MRI) magnets, and for thousands of accelerator magnets. It was also used for the Mirror Fusion Test Facility-B magnets at Lawrence Livermore National Laboratory, California. The 300 M$ experiment, which had a cryostat 64 m long and 12 m in diameter, was constructed and had tested successfully in the 1980s, but never used for plasma experiments, due to cancellation of government support.

4.5.4 Forced Two-Phase Flow Cooling

A pump is used to increase the flow rate of the helium, which can remove higher heat fluxes than natural convection. It was used on T-7, HT-7 and T-15. On T-7 some regulation of flow through 48 parallel coils with 384 parallel channels within ± 12 % was foreseen, but proved to be unnecessary. Two-phase flow provided lower and more uniform temperature along the coils than supercritical flow.

Two-phase flow was successfully used during the SST-1 tokamak coil tests. When KSTAR got a helium leak, the pressure in the leaking bus bar was reduced from 5 to 1.5 bar, changing from supercritical flow to two-phase flow. Then the desired vacuum was recovered, and the magnet tests and first plasma were successful, with lower temperature and more uniform temperature distribution along the leaking bus bar.

4.5.5 Forced Flow Supercritical Cooling

For supercritical flow the coolant is pressurized enough that boiling does not occur. So only the heat capacity of liquid helium, which is four times less than latent heat of evaporation (used in two phase flow cooling), is available for heat removal. Therefore, the coolant temperature rises along the cooling channel, in contrast to two phase flow, where it is stays close to the boiling temperature. Supercritical flow provides predictable flow distribution, but it requires higher pumping power, which also adds extra heat to the helium that must be removed by the refrigeration system.

4.5.6 Structural Design

Large coil design is dominated by stress considerations. Almost half the magnet cost and technical difficulty is associated with the coil *structure*. For toroidal field coils a D shape is chosen to minimize bending moments on the coil. The design criteria include many considerations, including the allowable stress, the number of stress cycles (fatigue life), the change of dimensions with temperature, and thermal stress. Development of reliable welding techniques for coil structures is of particular concern. Structural materials problems are discussed by Henning and Dalder (1979).

4.5.7 Conductor Fabrication

Fabrication of NbTi wires is relatively easy, because of its good ductility. NbTi rods in a copper matrix may be extruded many times until they become tiny filaments, combined into a cable, and wound into a coil.

Fabrication of Nb_3Sn cables, on the other hand, is difficult, because Nb_3Sn is very brittle. To produce Nb_3Sn the coil must be heated to a high temperature (~ 700 °C) for many hours until some of the Sn diffuses into the Nb, forming Nb_3Sn (Walter 2010).

If the Nb_3Sn is formed before the coil is wound ("wind after reactions"), then degradation may occur during winding. Usually Nb and some form of Sn are extruded in a copper matrix, combined into a cable, and wound into a coil, then heated to produce Nb_3Sn. (This is called "wind, then react" or "react after winding").

The T-15 tokamak Nb_3Sn magnet was wound after reaction. Its degradation due to winding after reaction was close to that obtained on cables for ITER reacted after winding, but "react after winding" is used for most coils.

There are four general methods: bronze, internal tin, jelly roll (and modified jelly roll), and powder in tube (Devred 2004).

1. The **bronze method** starts with Nb rods in a bronze matrix, Fig. 4.19.

   The starting components are ductile and can be stretched and drawn through smaller orifices (extruded) to a small diameter wire. Then multiple wires can be joined and extruded further. After the magnet coil is wound, it is heated in vacuum or in an inert gas for many hours (such as 700 °C for 100 h). Some tin diffuses out of the bronze and into the Nb, forming Nb_3Sn filaments. The pure copper region is for stabilization. (In some designs the Cu is placed around the bronze wire.) The tantalum barrier prevents tin from diffusing into the pure copper and spoiling its high electrical conductivity T.

Fig. 4.19 The bronze method for production of Nb_3Sn conductors
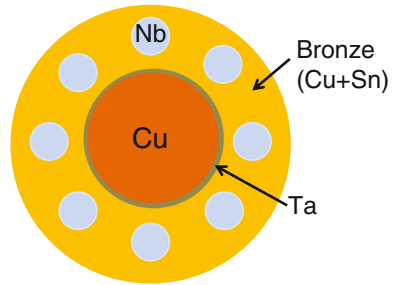
Fig. 4.20 Rods of niobium surrounding a core of tin in a copper matrix for the internal tin process
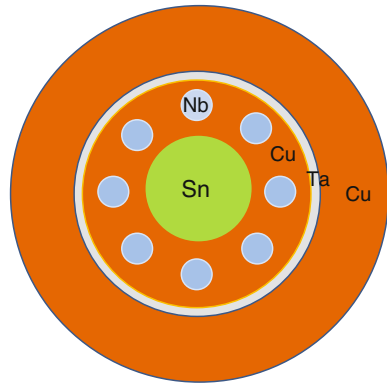
2. The **internal tin method** begins with pure tin in a copper matrix containing Nb rods, Fig. 4.20.

   After extrusion and winding, prolonged heating (such as 660 °C for 240 h) causes some of the tin to diffuse into the Nb, forming Nb_3Sn. The tantalum barrier protects the external pure copper from tin diffusion.
   (These figures are for illustrative purposes and do not represent actual conductor designs.)

3. The **jelly roll method** begins with sheets of Nb and bronze wrapped around a copper core, Fig. 4.21.

   After extrusion and coil winding, heat treatment forms rings of Nb_3Sn filaments.

4. The **powder in tube** method begins with $NbSn_2$ powder (<3 μm) mixed with Sn (and possibly Cu) powder in Nb tubes, surrounded by a Cu tube. The tube is extruded to a small diameter rod with hexagonal shape. Multiple hexagonal rods are assembled and further extruded. The wires are combined into cables and the coil is wound. Heat treatment causes Nb diffusion into the $NbSn_2$ powder, forming many tiny Nb_3Sn filaments.

Fig. 4.21 Sheets of Nb and bronze wrapped around a Cu core for extrusion in the jelly roll method. Minervini and Iwasa (2003)
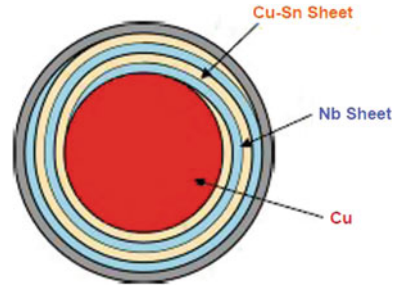
All four methods can produce coils with current density in the non-copper area on the order of 1,000–3,000 A/mm^2.

Conductors capable of carrying >70 KA have been built by combining many conductors in parallel in a copper substrate. Coils for B > 8 T are sometimes wound with NbTi on the outside and Nb$_3$Sn in the high-field region on the inside of the coil. Water-cooled copper coil inserts may be used to attain higher fields in a "hybrid" coil. The record steady state magnetic induction is 45 T using a "Florida-Bitter" inner coil set surrounded by a CICC (cable in conduit conductor) outer coil set at the National High Magnetic Field Laboratory in Tallahassee, Florida, USA.

Large superconducting coils have been built or designed for several fusion experiments, including T-7 (Russia), TRIAM-1 M (Japan), TORE–SUPRA (France), T-15 (Russia), LHD (Japan), EAST (China), KSTAR (Korea), W7-X (Germany), SST-1 (India), and ITER.

4.6 ITER Coils

4.6.1 Coil Set

The ITER Magnet System comprises 18 superconducting Toroidal Field (TF) and 6 Poloidal Field (PF) coils, a Central Solenoid (CS), and a set of Correction coils (CC), that magnetically confine, shape and control the plasma inside the Vacuum Vessel. The coils systems are shown in Figs. 4.22 and 4.23 (Foussat 2010).

The TF and PF coils lie between the Vacuum Vessel and the Cryostat, where they are cooled and shielded from the heat generating neutrons of the fusion reaction. The CS and TF coils both use Nb$_3$Sn. The PF coils and the Correction coils use NbTi, because it is less expensive for coils that do not require inductions >8 T. All coils are cooled with supercritical Helium at T $\sim$ 4 K. Table 4.8 shows the main ITER coil parameters.

Table 4.9 shows some considerations related to the choice of a conductor for ITER.

Fig. 4.22 The ITER coil
system, showing TF coils
(*brown*), circular PF coils
(*thick grey* and *green*), and
CS coils (*blue*). The thin
green segments represent part
of the Correction coils.
Courtesy of ITER
Organization
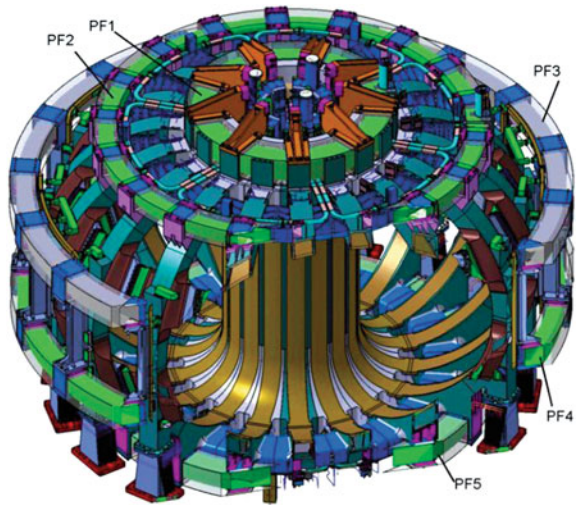
Fig. 4.23 The TF coils (*red*),
PF coils (*brown*), and their
high-current leads, which
accommodate the transition
from room temperature to
temperatures ∼4 K.
Courtesy of ITER
Organization
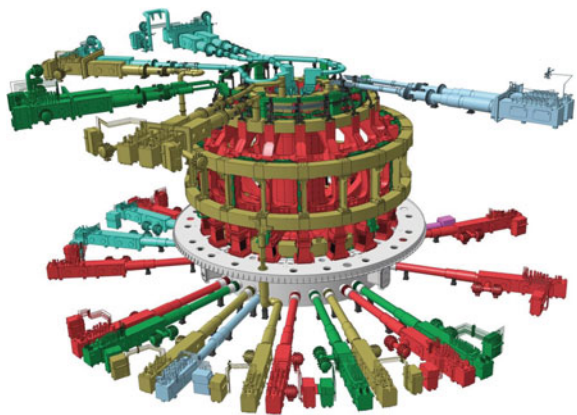
Table 4.8 ITER coil sets

System	Energy (GJ)	Peak field (T)	Cond. length (km)	Total weight (t)
Toroidal field (TE)	41	11.8	82.2	6,540
Central solenoid (CS)	6.4	13.0	35.6	974
Poloidal field (PF)	4	6.0	61.4	2,163
Correction coils(CC)	–	4.2	8.2	85

A cable in conduit conductor (CICC) was chosen for ITER. One potential disadvantage of the CICC is possible motion of strands inside the conduit.

The CICC concept requires a complex network of leak-tight helium tubes with many welds and a cryogenic helium pumping system that monitors and controls the pressurized liquid helium flow (Chap. 10).

Table 4.9 Choice of conductor for ITER. (Based on Noe 2008)

High conductor current → many parallel strands
Large heat removal capacity → 1/3 void fraction for coolant flow
High stability → cryogenic stabilization
High mechanical strength → strong outer jacket
Quench protection → external dump circuit

Fig. 4.24 The ITER cable in conduit concept. Fietz et al. (2012)

Figure 4.24 shows the CICC chosen for ITER.

The TF, PF, and CS strands are assembled in multistage, rope-type cables around a hollow spiral that carries helium coolant. The cables are inserted into a conduit made up of seamless stainless steel tubes that are butt-welded together. The requires a jacketing line that is about 1 km long (Devred et al. 2012).

4.6.2 Toroidal Field System

The strands in the ITER TF coils have a total length of 150,000 km, and the CICC will carry I = 68 kA. (The circumference of the earth at the equator is about 40,075 km.)
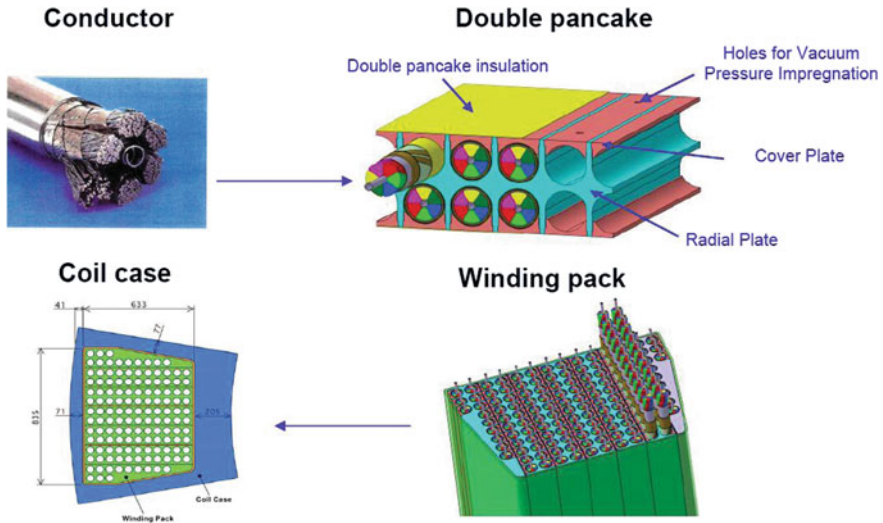
Fig. 4.25 The ITER TF conductor is laid intro the grooves, insulated, assembled into a winding pack, then welded into the coil case. Dimensions are mm. Courtesy of ITER Organization

Each TF coil is 9 m high, 6 m wide, and weighs 360 t. They will be shipped by boat to a Mediterranean port, and then transported to Cadarache along the 106 km "ITER Itinerary" (a specially modified road) on radio-controlled transporters.

TF coil winding techniques are under development to ensure accurate dimensions and reliable welds. The coil insulation must be able to sustain reliable operation after neutron irradiation to a fluence of 10^{22} n/m^2 (Koizumi 2008). Figure 4.25 shows how the conductor, radial plate, and winding pack fit together.

The steps of the TF coil radial plate machining, coil winding, and baking are shown in Fig. 4.26.

After baking the windings are insulated and impregnated with epoxy to prevent motion. Then the "pancake coils" are stacked together and welded into stainless steel cases.

The failure of a single element could require months for repair. At each step tests are needed to ensure reliable performance: quality of CICC, joints, welds, insulation, leads, strength, etc. (Devred et al. 2012).

Figure 4.27 illustrates toroidal field ripple. Experiments on JET indicate that ITER may need to have TF ripple <0.5 % in order to sustain good confinement during "ELMy H-Mode" operation and attain Q = 10 (Romanelli and JET-EFDA Contributors 2009). Since the normal ripple with 18 TF coils exceeds this value, iron inserts may be used between coils to reduce the ripple.

Each TF coil pair will be aligned relative to its best fit nominal position with radial and vertical tolerances of ± 3 and ± 2 mm, respectively. Since the coil temperature goes from 293 K down to about 4 K and back, thermal contraction and expansion must be taken into account.

The steps of machining grooves in the TF coil radial plate; TF coil winding machine where cable is wound into the grooves. At the La Spezia (Italy) winding line, 750 m lengths of toroidal field conductor will be bent into a *D-shaped* double spiral trajectory. The large inert atmosphere oven (48 × 20 × 5 m) in La Speziay will be used to react the Nb_3Sn TF coils. Courtesy of ITER Organization

Radial plate

TF coil winding machine
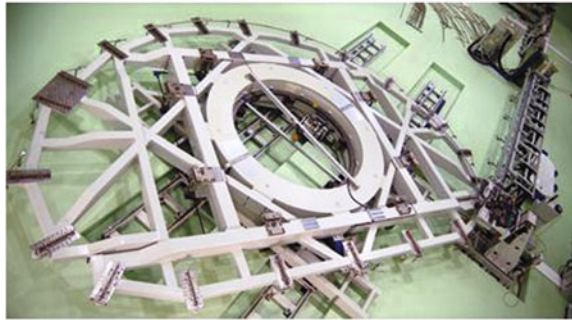
Oven to react Nb_3Sn

Six parties will participate in the TF coil manufacture. This is an inefficient and expensive duplication, but it will give each country experience in this manufacturing technology.

Figure 4.28 shows the forging of part of the inner leg of a TF coil.

Fig. 4.27 Exaggerated view
of TF coil ripple
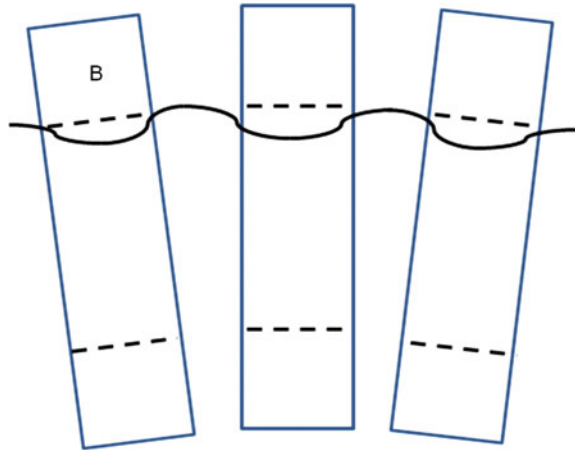
Fig. 4.28 Forging part of the
inner leg curved section of a
TF coil case as a hollow tube.
Courtesy of ITER
Organization

4.6.3 Poloidal Field System

The poloidal magnetic field, induced by both the PF coils and the toroidal plasma current, controls the plasma shape and position. Figure 4.22 showed the PF coils along with the TF and CS coils. The PF coil system consists of six independent coils placed outside the TF coil structure. Due to their large size, five of the six PF coils will be wound in a dedicated, 250-m long coil winding building on the ITER site in Cadarache. The smallest of the PF coils will be manufactured offsite. The ITER PF also coils use CICC. Two different types of strands are used, differing in high-current and high-temperature behavior. Some extra coils made to compensate for possible coil failures.

Figure 4.29 shows the PF coil winding machine, and Fig. 4.30 shows the coil windings, joints, and helium inlets.
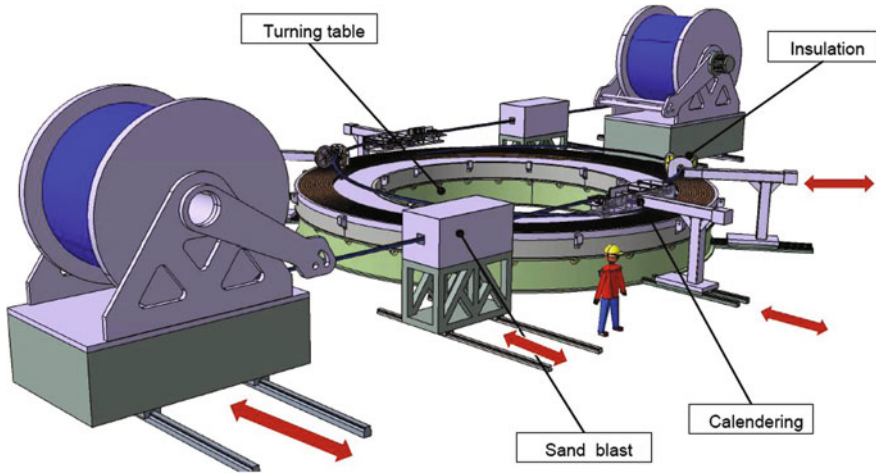
Fig. 4.29 The ITER PF coil winding machine. Courtesy of ITER Organization
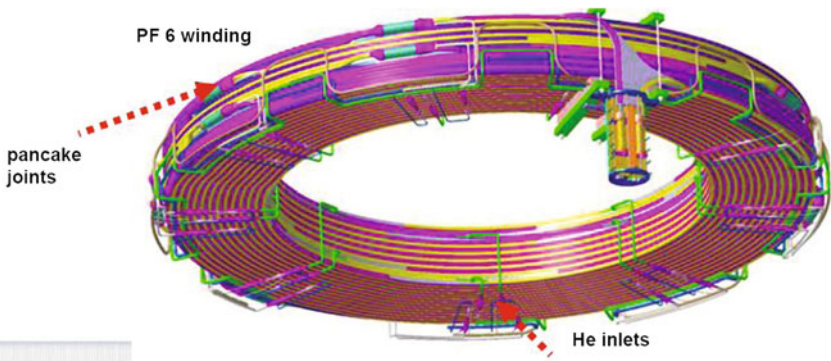
Fig. 4.30 ITER PF coil windings. Courtesy of ITER Organization

4.6.4 Central Solenoid

The CS serves as a transformer to induce a toroidal plasma current of up to 17 MA. The CS also helps to shape the B field lines in the Divertor region, and to promote vertical stability control. The CS is made of six independent coils using Nb_3Sn CICC superconductor, held together by a vertical pre-compression structure. This design enables ITER to access a wide operating window of plasma parameters, covering both inductive and non-inductive operation. Figure 4.31 shows one CS coil module, and Fig. 4.32 shows the assembled coil and support frame.

Each coil contains a stack of multiple pancake windings that minimizes joints. A glass-polyimide electrical insulation, impregnated with epoxy resin, gives a high
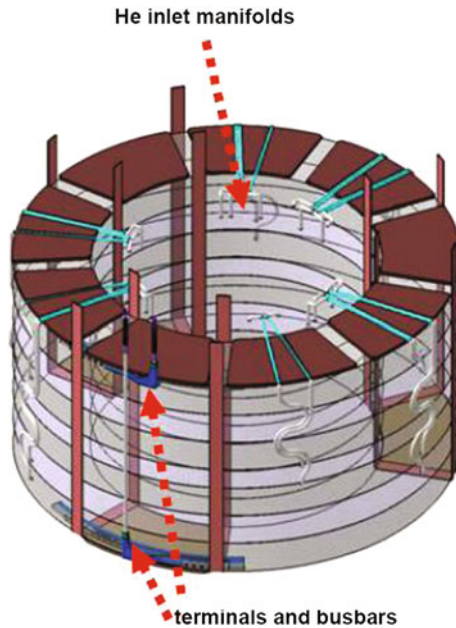
Fig. 4.31 One of the 6 CS coils. Courtesy of Neil Mitchell, ITER Organization

voltage operating capability, tested up to 29 kV. The conductor jacket material has to resist the large electromagnetic forces arising during operation and be able to demonstrate good fatigue behavior. The conductor is being produced in unit lengths up to 910 m. Some extra pancake coils will be manufactured for use in case of a coil failure. A CS model test coil at Naka, Japan, is shown in Fig. 4.33

This coil was tested successfully under pulsed operation in Japan to ensure that the design specifications could be met, but further testing of the Nb_3Sn conductor is needed to ensure that the CS coil can operate reliably for 30,000 cycles without significant degradation.

4.6.5 Correction Coils

The Edge Localized Modes (ELMs) occurring in tokamaks could spoil confinement in ITER, making it difficult to attain Q = 10. One means of combating ELMs is by the use of "resonant magnetic perturbations" to maintain edge pressure gradient levels just below the level where ELMS are deleterious (Wade 2008). The ITER Correction Coils, illustrated in Figs. 4.34 and 4.35, will attempt to provide feedback-control of ELMs.

To test this method, a set of 24 correction coils is being installed in the AS-DEX-Upgrade experiment (Gruber and Team 2008).
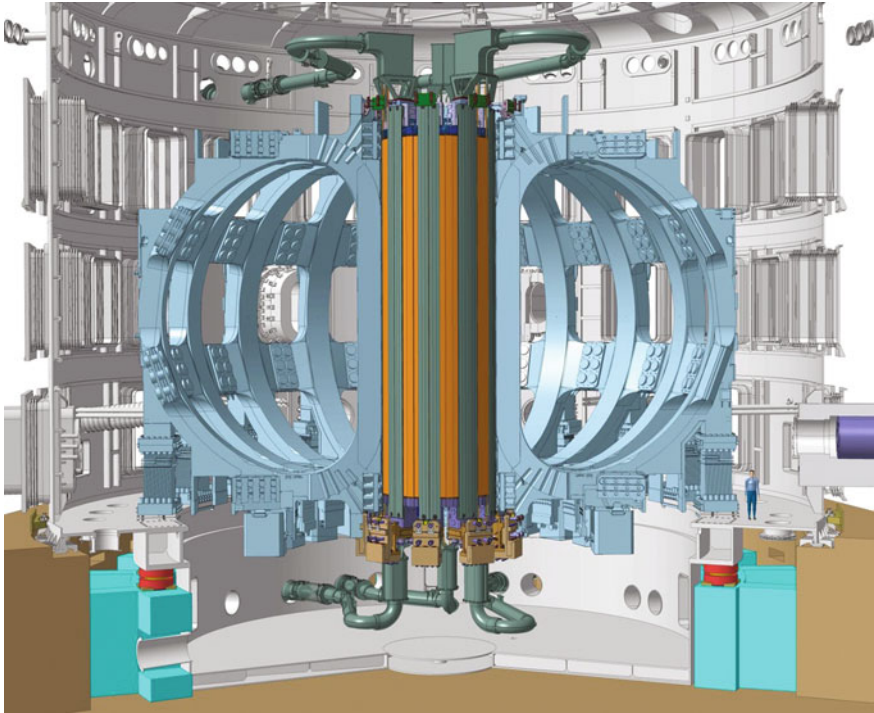
Fig. 4.32 The Central Solenoid coil (*orange*) with precompression supports (*green*), which compress the coils axially, and TF coils (*light blue*). Courtesy of ITER Organization

Fig. 4.33 A CS test coil outer module. Courtesy of ITER Organization

Fig. 4.34 The ITER correction coils. From Neil Mitchell, SOFT (2008)
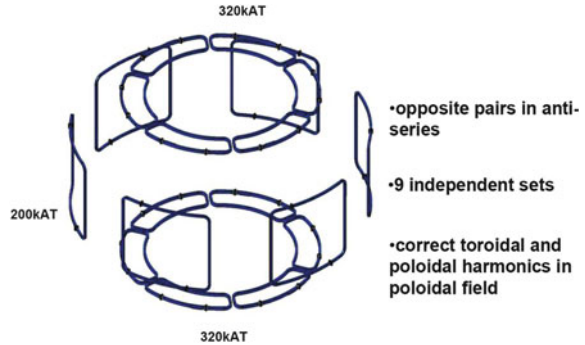
Fig. 4.35 ITER correction coils (*thin green coils*). Mounted in the torus. Courtesy of ITER Organization
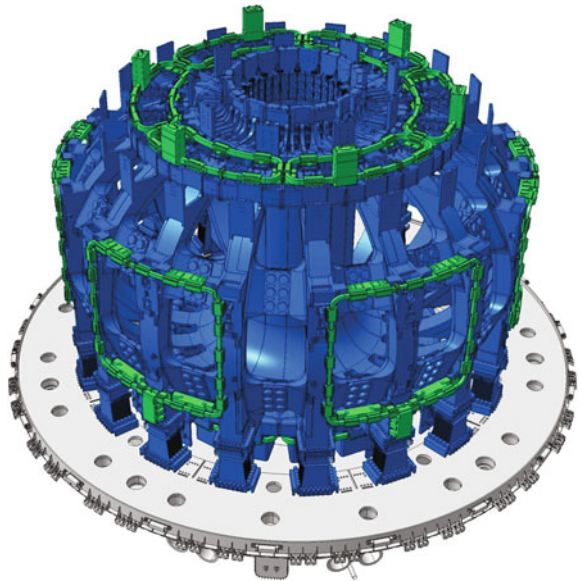
4.6.6 HTS Current Leads

If ordinary copper cables connected the power supplies to the superconducting coils the heat leak along the copper from room temperature to the coils at 4.5 K would be very large, causing much of the liquid helium to boil. Two technologies reduce this heat leak:

1. Cold helium vapor flowing along the conductor removes much of the heat before it reaches the coil.
2. The use of high temperature superconductor (HTS) for the lower half of the cables (between 65 and 4 K) reduces the heat generated in the lead conductor.

   An HTS current lead is compared with a conventional current lead in Fig. 4.36.

Fig. 4.36 Comparison of a conventional current lead with an HTS current lead. Courtesy of M. Noe, Karlsruhe Institute of Technology, Germany
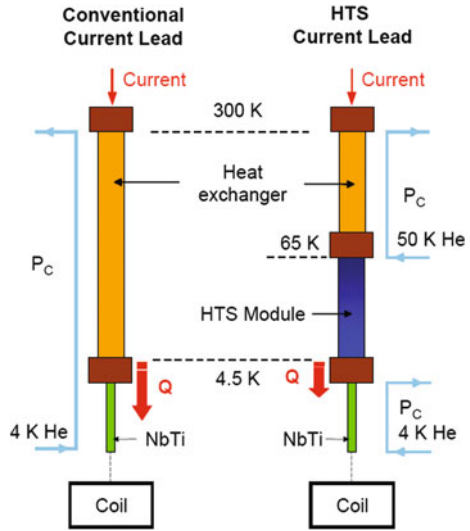
The conventional leads would require 2.2 MW of refrigeration power, while the HTS leads would need only 0.63 MW.

Figure 4.37 shows an HTS current lead developed in Germany.

Similar leads have been developed in China and installed on the Experimental Advanced Superconducting Tokamak (EAST) in Hefei.

HTS Part
- Bi 2223 HTS tapes manufactured by AMSC
- Conduction cooling from 4.5 K end
- Maximum operating temperature of HTS = 65 K

Heat Exchanger
- Perforated plates around a central Cu conductor
- Active cooling with 50 K He
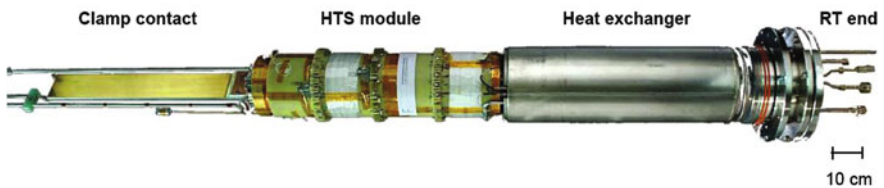
Fig. 4.37 An HTS lead developed in Germany. Courtesy of Noe (2008), Karlsruhe Institute of Technology (KIT), Germany

4.7 Large Helical Device Coils

The Large Helical Device (LHD) is the world's largest operating stellarator. It has two superconducting helical coils and six superconducting poloidal coils. The plasma has an adjustable major radius $R_o \sim 3.5$ to 3.8 m, and an approximate minor radius $a \sim 0.6$ m. The $\ell = 2$ helical coils can produce $B \approx 3$ T. LHD has three pairs of poloidal field coils to control the plasma shape and major radius, Fig. 4.38.

Figure 4.39 shows how the helical coils fit inside the vacuum vessel.
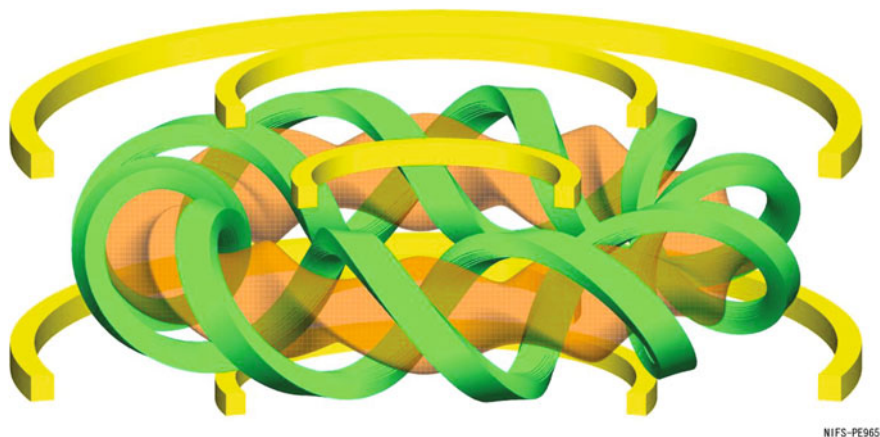
Fig. 4.38 The $\ell = 2$ helical coils (*green*) and the three pairs of poloidal field coils (*yellow*) and plasma shape (*orange*). © National Institute for Fusion Science, Toki, Japan

Fig. 4.39 The LHD helical coils (*violet color*) inside the vacuum vessel (*grey*) and cryostat (*blue*). © National Institute for Fusion Science, Toki, Japan
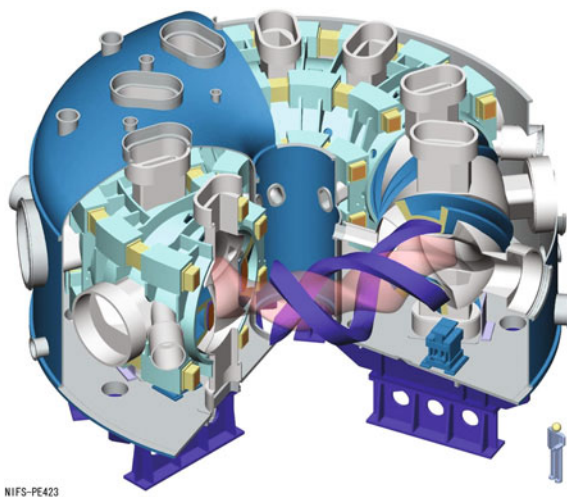
The parameters of the poloidal and helical coils are shown in Table 4.10.

The helical coil-winding machine that had to wind the cable precisely into a helical slot by rotating around the torus in both the poloidal and toroidal directions. It is shown in Fig. 4.40.

This winding machine is a great engineering achievement, without which the LHD could not have been built successfully. Figure 4.41 shows a photograph of the inside of the helical coil system.

Table 4.10 Some parameters of the LHD coils

Poloidal coils	Inner	Middle	Outer	Helical	Coils
Inner diameter, m	3.2	5.4	10.4	Major radius	3.9 m
Outer diameter, m	4.2	6.2	11.6	Minor radius	0.975 m
Weight, ton	16	25	45	Weight, ton	65
B_{max} T	6.5	5.4	5.0	B_{max}, T	6.9
Current, kA	20.8	21.6	31.3	Current, kA	13
# turns	240	208	144	# turns	450

Fig. 4.40 The LHD helical coil winding machine. © National Institute for Fusion Science, Toki, Japan
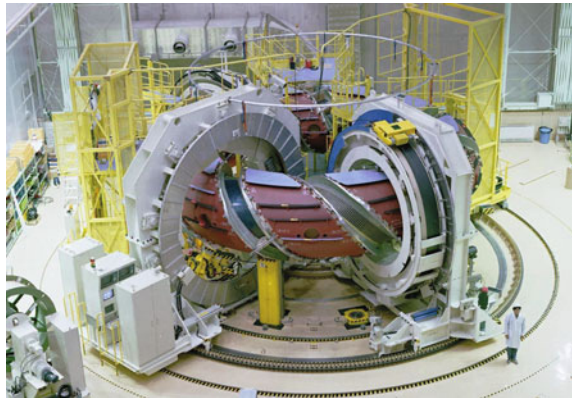
Fig. 4.41 The inside of the LHD helical coils. © National Institute for Fusion Science, Toki, Japan
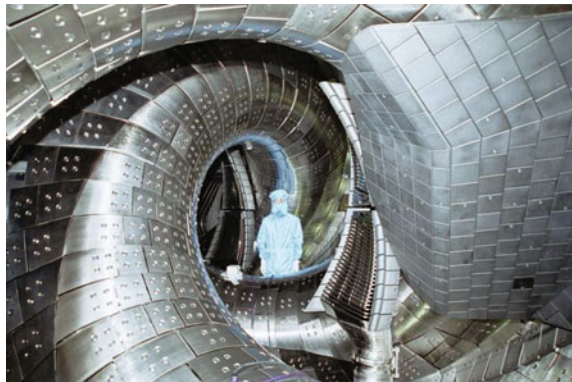
The helical coils have operated reliably since 1998. In the future the helical coil current may be increased to 17 kA by subcooling the coil below 4 K, which could increase the magnetic induction to about 4 T.

4.8 Wendelstein 7-X Modular Coils

4.8.1 Modular Coil Design

When construction is completed in about 2015, the Wendelstein 7-X in Greifswald, Germany, will be the world's largest stellarator. With discharges lasting up to 30 min it is intended to demonstrate the suitability of stellarators for fusion power plants. The W 7-X has 50 modular coils and five field periods, as illustrated in Fig. 4.42.

In order to vary the magnetic field, a second set of 20 flat, superconducting coils is superposed on the stellarator coils. The coils are held rigidly in position by a massive ring-shaped support structure. The coil ring is enclosed by a cryostat 16 m in diameter, as shown in Fig. 4.43 and the total mass of the coils and support ring is 1,425 t.

Fig. 4.42 The modular coils of Wendelstein 7-X (*blue*) and the plasma shape (*orange*). There are 50 coils, each about 3.5 m high. (Courtesy of Lutz Wegener, Max-Planck Institut für Plasmaforschung, Greifswald, Germany)
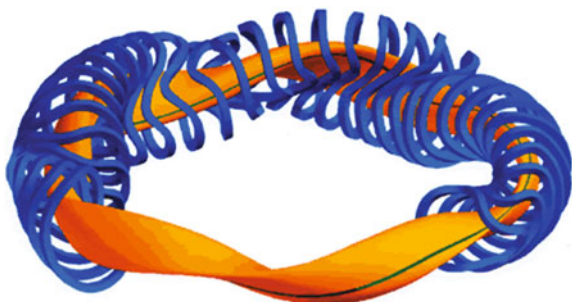
Fig. 4.43 Sketch of Wendelstein 7-X, showing coils (*blue*), vacuum chamber (*green*), cryostat (*grey*), gravity supports (*below*). (Courtesy of Lutz Wegener, Max-Planck Institut für Plasmaforschung, Greifswald, Germany)
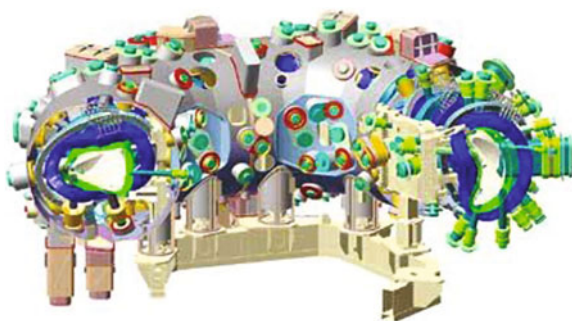
Fig. 4.44 Final production of the magnet coils at Babcock Noell Magnettechnik GmbH in Zeitz. Courtesy of Lutz Wegener, Max-Planck Institut für Plasmaforschung, Greifswald, Germany. (*Photo* IPP, André Künzelmann)

The cryogenic system can remove 5 kW of heat to maintain the coils near liquid helium temperature (4 K). The vacuum chamber conforms to the plasma shape and contains 245 ports for plasma heating and diagnostics. The ports are connected with the outer wall of the cryostat by tubes passing between the coils with good thermal insulation. Each of the five field periods is preassembled, and then the five sections are joined into a ring in the experimentation hall. Figure 4.44 shows the production of the individual coils.

4.8.2 Assembly

Each field-period module contains 10 modular coils. The assembly procedure is as follows:

First assembly rig

- A 6 t coil is carefully hoisted and moved onto a vacuum vessel segment, Fig. 4.45.
- The second vessel segment is added and brazed onto the first segment.
- Thermal insulation is installed.

Fig. 4.45 A modular coil is strung onto a segment of the plasma vessel. (Courtesy of Lutz Wegener, Max-Planck Institut für Plasmaforschung, Greifswald, Germany)

- Then more coils and vessel segments are added, one at a time, onto the front and back, until a half-module (five modular coils plus two auxiliary coils) is assembled, brazed, and insulated.
- A segment of the support ring is bolted onto the coils.
- The alignments are checked and adjusted as necessary. Figure 4.46 shows a completed half-module.

Second assembly harness

- The 50 t half-module is hoisted into the second assembly rig in a special harness, where it is joined hydraulically to the other half-module. The support ring segments are bolted together, and the plasma vessel halves are brazed. This assembled module weighs 100 t.
- Then 24 coil leads, each up to 14 m long, are brazed onto the coils, insulated, and leak-tested. They will carry high currents from the external bus bars at room temperature down to the superconducting coils at 4 K with minimal heat inflow.
- Helium coolant tubes are connected to each coil and leak-checked.

Fig. 4.46 A completed first half-module on the way to the second pre-assembly rig. (Courtesy of Lutz Wegener, Max-Planck Institut für Plasmaforschung, Greifswald, Germany)
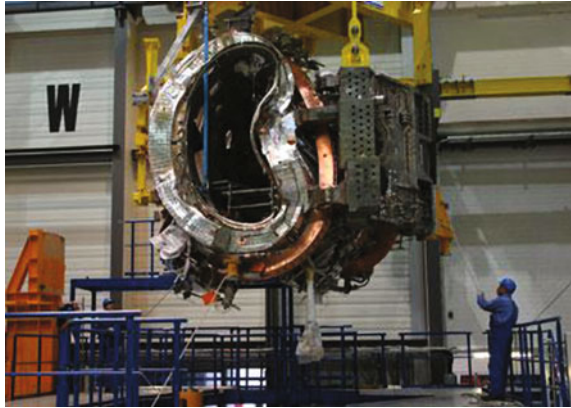
- Magnet coil instruments and connecting cables are installed.
- The completed module can leave the assembly jig after 28 weeks of assembly. (The first module assembly was completed in 2008.)

Third assembly in experiment hall

- The module is transported into the experiment hall and hoisted into the bottom shell of the outer vessel; connections and supports are attached.
- The 120 t component is now lifted onto the actual machine foundation and attached to auxiliary supports.
- The top shell of the outer vessel (Fig. 4.47) is put on and brazed.
- Sixty ports connecting the plasma and outer vessels through the cold coil region are connected and insulated.
- The in-vessel components, including divertor plates, heat shields, and cryo-pumps, are installed.
- These steps are done for the other four modules.

Fig. 4.47 One of the five sections of the outer vessel of Wendelstein 7-X (Courtesy of Lutz Wegener, Max-Planck Institut für Plasmaforschung, Greifswald, Germany.) (*Photo* IPP, Wolfgang Filser)
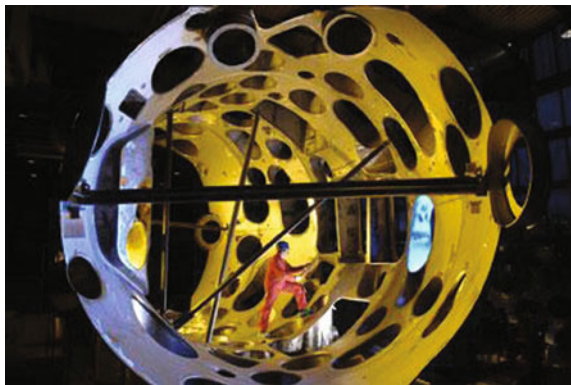
- The five modules are joined: The brazing seams of the plasma and outer vessels are closed.
- The magnets are connected to the power supplies, helium supplies, and cooling pipes, followed by repeated control measurements and leak tests. This completes the main assembly process.

Assembly of the basic machine is accompanied by installation of the microwave heating, electric power supply, cryogenic, machine control, and plasma diagnostic systems. Assembly is expected to be completed in about 2014. The first stage of operation will have short-pulsed operation at full power using an uncooled divertor. Then a water-cooled, steady-state divertor will be installed, facilitating steady-state operation for up to 30 min (limited by the external heat-rejection system).

4.8.3 Superconducting Magnetic Energy Storage

Superconducting magnetic energy storage (SMES), could be used for several purposes:

- Input power for fusion reactor coils and heating systems.
- Energy storage for load leveling by electric utility companies, including output power from fusion power plants.
- Energy storage for solar and wind power plants, to provide continuous power when the sun or wind are not sufficient.
- Stabilization of long-distance power transmission systems.

A huge magnet coil held together by subsurface rock, could store up to 5000 MW-hours of electricity (Dolan 1982).

4.9 High Temperature Superconductors

High temperature superconductivity achievements began in 1986: (Minervini and Iwasa 2003)

1986
J.G. Bednorz and K.A. Muller of IBM (Zurich) discovered La–Ba–Cu–O, a layered copper oxide perovskite, a superconductor with $T_c = 35$ K.
1987
P.W. Chu and others at U. of Houston and U. of Alabama discovered YBaCuO (Y-123 or YBCO), $T_c = 93$ K, also a copper oxide perovskite.

1988

H. Maeda, of the National Institute for Metals ("Kinzai-Ken"), Tsukuba, discovered BiSrCaCuO (BSCCO); now in two forms: Bi-2212 (Tc = 85 K); and Bi-2223 (T_c = 110 K).

Z. Z. Sheng and A. M. Hermann at U. of Arkansas discovered TlBaCaCuO (Tl-2223), $T_c \sim$ 125 K.

1993

P. W. Chu discovered HgBaCaCuO (Hg-1223), $T_c \sim$ 135 K (164 K under a pressure of 300 atm).

Table 4.11 lists some superconductors of interest.

There are thousands of materials with superconductivity, but only a few with T_c > 10 K, B_c > 10 T, J_c > 1 MA/cm^2 at 5 T, and metallurgical properties (such as ductility) suitable for winding into magnet coils. At low temperatures the critical fields of some HTS are even higher than those of low-temperature superconductors (Nb_3Sn, NbTi, MgB_2), as can be seen in Fig. 4.48. Their high critical current densities at high fields permit the HTS cables to be smaller, so that the HTS coil cost can be comparable to that of Nb_3Sn, even though the HTS conductor is more expensive. An HTS magnet operating in liquid He (T $\sim$ 4 K) can achieve 35 T without the conventional water-cooled Cu insert that is usually used for very high magnetic fields (45–50 T in a 40 mm bore).

Table 4.11 Some high temperature superconductors. Here RE means "rare earth" elements. Schlachter (2010)

Superconductor	Name	Tc, K	Uses
$YBa_2Cu_3O_7$	YBCO	92	Bulk material, tapes, thin films
$REBa_2Cu3O_7$	REBCO (RE = Y, Yb, Dy, …)	$\sim$88–96	Bulk material, tapes, thin films
$Bi_2Sr_2CaCu_2O_8$	BiSCCO(2212)	85	Bulk material, wires
$Bi_2Sr_2Ca_2Cu_3O_{10}$	BiSCCO(2223) Bi-2223	110	Tapes

Fig. 4.48 Parameters of some high-temperature superconductors (Minervini and Iwasa 2003)
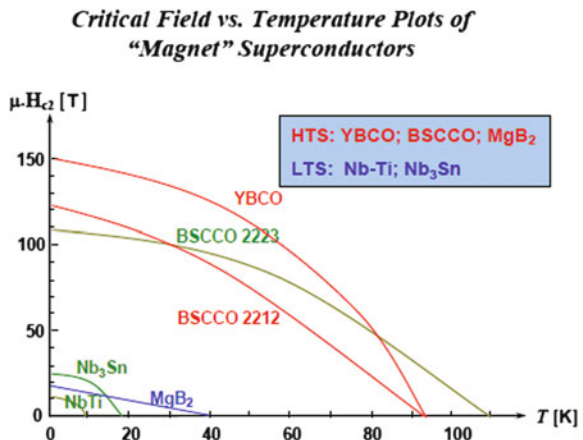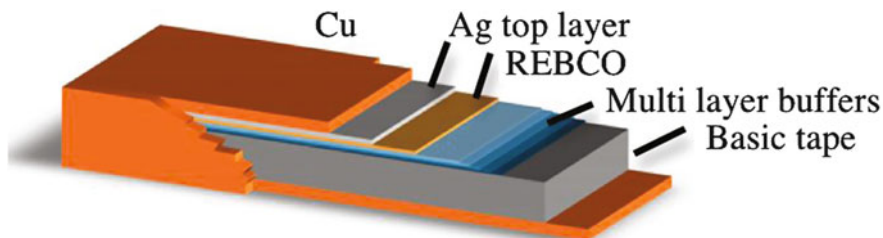
Fig. 4.49 Principle of a REBCO tape. Fietz et al. (2012)

REBCO and BiSCCO are highly anisotropic, with good superconductivity in one grain direction, so grains must be aligned with the tape or wire to minimize resistivity. First generation tapes (circa 2004) used BiSCCO, but an efficient use of this material is limited to lower magnetic fields when temperatures well above 4 K are used. In addition the large amount of Ag required does not allow an attractive price to be reached for this conductor. Second generation tapes use REBCO with a fabrication by Ion Beam Assisted Deposition or by first texturing a substrate by the RABiTS technique with subsequent REBCO deposition e.g. by Pulsed Laser Deposition to achieve good alignment of the grains. The principle of such a tape is illustrated in Fig. 4.49.

Doping REBCO with Zr increases the critical current density by pinning flux lines, so tapes can sustain currents over 300 A per centimeter width. The critical current of REBCO tapes does not degrade at strains of 0.1–1 % like Nb_3Sn does (Fig. 4.16) (Fietz et al. 2012).

A thin REBCO tape can be cut into many narrower meandering ribbons, which can then be linked together without straining the ribbons much, Fig. 4.50.
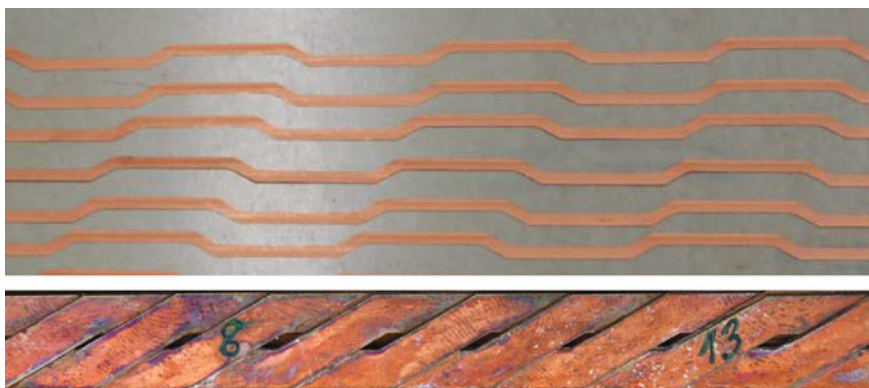
Fig. 4.50 Thin ribbons cut from a REBCO tape (*top*), and a "Roebel cable" made from linking them together (*bottom*). Fietz et al. (2012)

Many flexible Roebel cables can then be assembled into high-current conductors without the large strain and degradation that might occur if the original tapes were twisted together. Other solutions like CORC cable or twisted stacked-tape cables show the possibility to come to a high current REBCO cable.

Some advantages of REBCO cable are: (Fietz et al. 2012)

- A high-current REBCO cable could potentially have a smaller cross-sectional area than a comparable Nb_3Sn conductor, so more superconductor could be packed into a given case, increasing the magnetic field; or there could be more space for structural support, or the coil could be smaller.
- Good solder joints have been demonstrated, but the joint formation is still an issue, such as with respect to the necessary space.
- Cyclic loading of 750 MPa for 10^6 cycles does not degrade performance.
- Neutron irradiation slightly improves the tape performance by introducing additional pinning center and smearing out the anisotropy of critical current versus magnetic field angle.
- Going to higher operating temperature, the cryostat, insulation, and refrigeration system could be much simpler; the input power could be lower; and the total system cost could be much lower than for low-temperature superconductors.

For example, a typical fusion reactor magnet system might require 19 MW at 4.5 K (liquid He) and 14 MW at 80 K (liquid nitrogen), total 33 MW. If HTS coils could be used at 65 K, then the refrigeration power could be reduced to 12 MW at 4.5 K (for cryo pumps), 3 MW at 65 K, plus 5 MW at 80 K, total 20 MW. This reduction form 33 to 20 MW would provide a substantial cost savings, a complex radiation shield could be avoided, and the reactor size could be slightly reduced (Schlachter 2010). Further savings could occur if cryo pumping requirements could be reduced, such as by not using NBI.

The cost of REBCO cables was about 150–200 \$/kA-m in 2012, but expected to fall rapidly, due to improved performance and large-scale manufacturing, with a goal price of 30 \$/kA-m at operating conditions (Fietz et al. 2012).

Figure 4.51 shows a 32 T hybrid coil design with high temperature superconductor in the inner coil.

If large HTS magnets could achieve 11 T in the plasma (requiring a field $\sim$ 25 T at the coil), and beta = 5 %, then a fusion power density of 1 MW/m^3 could be achieved with a catalyzed DD fuel cycle, obviating the need for tritium breeding in the blanket and greatly reducing the tritium hazard (Problem 1–7).

In addition to fusion research applications, HTS magnets are also being used for motors and generators, transformers, ship propulsion motors, fault current limiters, and magnetic energy storage (Fietz et al. 2012).

Fig. 4.51 The outer low-temperature superconductor coil develops 15 T, and the YBCO inner coil adds 17 T around a cold inner bore of 3.2 cm. The coil current, inductance, and stored energy are 172 A, 619 H, and 9.15 MJ. (Courtesy of Tim Cross, National High Magnetic Field Laboratory, Tallahassee, Florida)
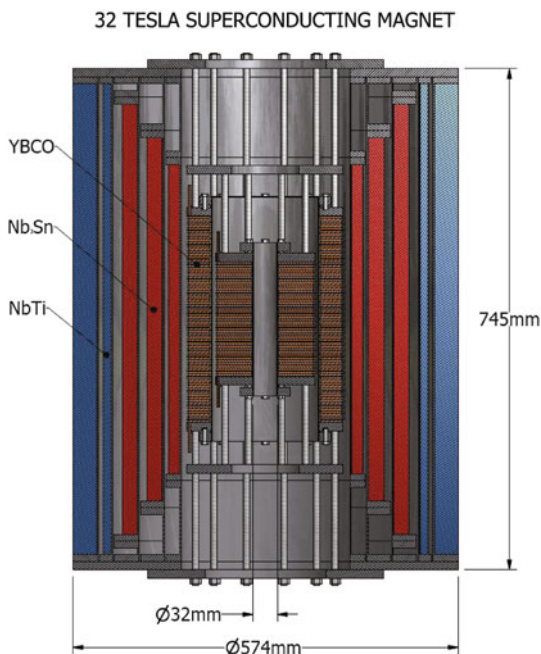
4.10 Lessons Learned in Coil Manufacture

Denis P. Ivanov
Kurchatov Institute, Moscow

The most widely used method of superconducting (SC) magnet cooling is the bath cooling (also called "pool boiling" or "ventilated winding"). It was used in all early small magnets, which were simply immersed in liquid He and cooled by heat conduction through the windings. Gaps for He passage are needed in large magnets.

The TORE-SUPRA tokamak in Cadarache, France (R = 2.3 m; a = 0.72 m; started in 1988) used NbTi wire operating at 1.8 K to achieve 4 T on the axis and ∼7 T at the inner side of coils. It operates stably with simple, reliable automatic magnet control. The plasma experiment time losses due to problems with of magnet and cryogenic systems was less than 4 %, while on T-7 it was about 15 %.

Reliable operation was also demonstrated on the TRIAM-1M tokamak (Fukuoka, Japan). In this magnet Nb_3Sn monolithic cable with Al stabilization in bath cooled windings produce $B_o \sim 8$ T with R = 0.8 m, a = 0.2 m. This cryostable magnet has never quenched.

The disadvantage of pool boiling magnets is their loose winding structure with many coolant flow paths and weak insulation between turns. For example one

TORE-SUPRA tokamak coil had an internal short circuit, which limited the coil to a lower magnetic field for the first 1.5 years with a slow charging rate until the replacement of the bad coil. Since then the magnet has performed reliably. Similar problems have occurred in the 1970s in the small magnetic mirror machine Ogra-5 (Kurchatov Institute, Moscow) and in some other SC magnets for MHD energy conversion and for Energy Storage.

The magnets for the T-7 Tokamak (coil radii $R_c = 1.25$ m; $a_c = 0.42$ m; $B_o = 2.5$ T) were force cooled with two-phase flow. So were the magnets for the T-15 Tokamak, which was the biggest Nb_3Sn magnet at that time (R = 2.5 m, a = 1.12 m; $B_o = 3.5$ T), which was wound using already-reacted monolithic electroplated conductor.

A disadvantage of the force cooled concept was encountered during T-15 coil tests. Effective cooling requires many parallel cooling channels with He inlets and outlets (plus many current sensors), which develop different high voltages during rapid changes of the B field. The He leads must be separated from the He manifolds by insulators. At first designers relied on the cryostat vacuum for electrical insulation, and the T-15 He leads were bare and not insulated. But the vacuum can be weakened by mechanical disturbances that accompany fast current variations, so the possibility of vacuum loss during high voltage generation must be taken into account. Six breakdowns happened during the T-15 coil tests, before insulation able to withstand 8 kV at any vacuum was installed. Nevertheless, three more breakdowns occurred even with the new insulation, and so the dumping voltage was reduced from ±1 kV down to ±250 V.

Unfortunately, some magnet designers still considered such incidents as improbable and continued using simplified insulation on the leads and feeders. Another 7 similar incidents occurred on HT-7, EAST, KSTAR and SST-1. Therefore, the reliability of such force flow magnets for ITER is questionable, due to lack of attention to insulation of leads and feeders. The leads are the most complicated and delicate part of magnet design.

There was limited prior experience with cable in conduit conductor (CICC) and forced flow cooling before the ITER design:

- the IAEA Large Coil Test Project. The Westinghouse N_3Sn coil had strands inside a conduit, but that coil generated 200 W heat (an excessive amount) at its rated current;
- the DPC Project where the problem of current distribution restricted the current ramp rate.

The loose fixation of strands can permit strand movement and SC degradation.

Forced flow supercritical cooling can have good coil insulation, adequate cooling, and reliability, but the **current leads** are often unreliable, and these coils require complex sensors, isolators, and wiring to monitor coil conditions during operation and quenches. The cyclic stress of each plasma pulse can diminish the reliability of force-cooled magnets. Loose strands and cables degrade more than fixed ones, so each must be rigidly held in place. The CICC must compromise

between tight strand twisting to suppress motion and looser twisting to allow higher void fraction for helium coolant flow.

To reduce pumping power coils may have many parallel coolant channels, although the electrical cables are connected in series. This requires good insulation, because the helium coolant tube leads are all at different voltages. A vacuum is a good insulation at first, but if the pressure rises during operation, breakdown can occur. The gas absorbed on cold surfaces and the magnetic field can facilitate breakdown.

Large coils have hundreds of cooling channels with insulators, flow meters, other sensors, feedthroughs, and instrumentation lines. They are subjected to mechanical stresses, from multiple cooling cycles, coil dumps, vibrations, vertical displacement events, and disruptions. During cryogenic operation new leaks may appear that were not found previously at room temperature. The tightly sealed casing needed for vacuum pressure impregnation (VPI) of insulation can complicate the coil insulation problem.

We should **not rely on vacuum** to be a good insulator. A sudden vacuum leak could lead to a quench, high voltage generation, electrical breakdown, and coil damage. Having the same vacuum everywhere in the cryostat is bad. A leak in one place affects performance everywhere. A separate vacuum shell for magnet connections is desirable.

The weakest point is the *leads* coming out of the coils, which are subjected to high voltages during normal operation, also during dumps. The leads were often insulated by simply wrapping with Kapton and epoxy-filled FG tape, but this is unsatisfactory. People relied on the cryostat vacuum to provide insulation, which caused many breakdowns in T-15 leads, even when wrapped with various kinds of tape. The dumping voltage in magnets was sometimes chosen without consideration of the breakdown danger.

There have been at least 17 cases of lead breakdowns in various coils, such as:

- Electrical breakers cracking
- Coolant channel damage
- Coolant supply loss
- Detachment of frozen gas causes pressure rise
- Overvoltage damage to V-taps and PFC feeds
- Mechanical damage of cryostat valves, pressure gages, etc.
- Missed quench detection
- Cooling tube detachment.

The breakdowns occurred in the *outer parts* of the coils—leads, feeders, terminals, sensor feedthroughs, and not inside the coils, because the coils were well insulated internally with VPI technology.

Some coil systems, such as W7-X, use Paschen tests (high voltage tests) of each coil in a big tank before their assembly into the cryostat. The Paschen tests are inadequate for acceptance tests to give confidence in coil performance, however, unless they include magnetic field effects and gas desorption effects on the end connections. These tests are time-consuming and complicated, especially for the insulation over hundreds of joints after device assembly.

ITER coils, which must withstand operating voltages up to 12 kV, are to be tested at 29 kV, but previous magnets have had reliability problems at only 0.3–3.0 kV. If the ITER coils do not use a vacuum tight casing over the insulation, then they should be tested under poor vacuum conditions to see whether break-down occurs.

Leads for large coils like ITER should be placed into vacuum tight stainless steel cases filled by epoxy with vacuum pressure impregnation (VPI) technology. The cooling method for the ITER coils cannot be changed, but the insulation could be improved, which could improve reliability and save time by reducing the need for many single coil voltage tests.

Ideally, a grounded vacuum-tight stainless steel shell could be used, to separate the coil leads from the interior region, and the leads could have solid insulation, such as Al_2O_3, MgO powder, frozen nitrogen, or fiberglass/epoxy insulation using VPI. This arrangement should avoid the problem of breakdowns caused by low-pressure gas. The POLO Coil (Karlsruhe, Germany), which has a Guarding shell filled with epoxy (instead of vacuum), demonstrated successful voltage holding.

The main goals of single coil tests were:

1. to ensure that insulation will not crack during cooling (but the loads on insulation during operation are much stronger than during cool-down)
2. to avoid cold leaks (the casing practically excludes them)
3. to check current carrying ability, but this is inadequate in a single coil's self field. The fields of other coils are needed for adequate testing.
4. joint tests. These should be done by standard quality assurance methods before the coils are encased.

Instead of such unnecessary single coil tests, all coils should be tested together in the main cryostat before installation of other systems around the cryostat. The time saved by avoiding single coil tests could be better spent installing vacuum tight casing over the leads insulation.

Some problems occurred during manufacture of ITER coils (Mitchell 2013):

- Conductor damage during compaction
- Broken strands in cabling
- Cable stuck during insertion into jacket
- Water in the shipping crates
- Strand filament breakage during cycling reduces cable performance.

4.11 Summary

The superconducting domain is bounded by a critical surface of T_c, B_c, and J_c. When the (J, B, T) values move outside the bounding surface the superconductor quenches (loses its superconductivity).

Quantized fluxons ϕ_o are surrounded tubular normal regions in Type II superconductors. The J × B (Lorentz) force pushes the fluxons sideways, which generates heat. The heat can raise T above T_c, causing that region to go normal. Lattice defects pin fluxons and inhibit their motion, helping to preserve superconductivity.

Coil conductorss can be stabilized by current sharing with Cu, Al, or Ag, with rapid heat removal via the helium coolant. Coils should be protected against overheating by fast magnetic damping. Heat can be removed

- by forced liquid or gas flow
- by pool boiling (normal He or superfluid HeII), used for 20,000 MRI magnets and many accelerators
- by forced two-phase flow, or
- by forced supercritical flow, which was chosen for ITER.

Normal copper coils inside superconducting coils ("Hybrid coils") can generate ultrahigh magnetic fields, limited by heat removal and stress.

Conductors must be stabilized to prevent quenches. Coil protection is required to safely convert magnetic energy released during a quench into heat in a controlled manner. Two approaches are possible: internal and external dumping.

Large Nb_3Sn coils with $B_{max} \sim 13$ T at the conductor are designed to operate safely and reliably for long periods, as demonstrated in the ITER central solenoid model coil (Naka, Japan).

Further development of HTS may yield magnets that achieve higher magnetic fields than present Nb_3Sn coils. For example, HTS operating at low temperatures (~ 4 K) can achieve fields of 35 T without a water-cooled copper coil insert. High fields might facilitate fusion power plants that could use the catalyzed DD fuel cycle, with reduced tritium hazard. HTS might also facilitate the use of simpler cryogenic systems that require less refrigeration power.

4.12 Problems

4.1. Estimate the magnetic flux density B for the case of Fig. 4.3.
4.2. Estimate the order of magnitude of the coherence length of NbTi from its B_{c2}.
4.3. A superconducting magnet is to be wound from square conductors with side = a. The windings are to be grouped in square bunches (n turns) × (n turns), as shown in Fig. 4.52. The outside perimeter of the bunches is cooled by liquid helium. Show that the Stekly number for this case may be written

Fig. 4.52 A bunch of square conductors
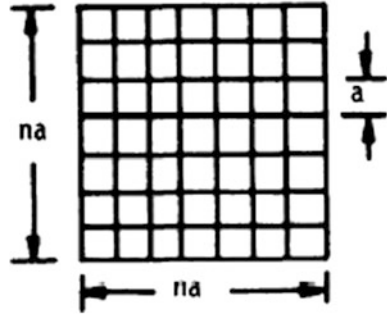
$$\alpha_s = nI^2\eta/4a^3q,$$

where q is the maximum heat flux for nuclear boiling. (Hint: Consider the bundle as one conductor).

If $q = 0.4$ W/cm^2, $I = 50$ A, $a = 1$ mm, and $\eta = 3 \times 10^{-8}$ Ω cm, what is the maximum number of turns that can be grouped together and still have cryogenic stabilization?

4.4. Estimate the maximum allowable dB/dt for adiabatically-stabilized NbTi at 4.2 K and 3 T, assuming that the filament diameter is 7×10^{-5} m and that the transposition length is 1 cm.

4.5. For circular superconducting coils with rectangular cross section, it is sometimes desirable to find the coil dimensions that minimize the coil volume and conductor cost, while producing a given B in a given bore radius r_1. Defining $\alpha = r_2/r_1$ and $\beta = L/2r_1$, write Eq. (3.62) in the form $B_z = \mu_o\lambda Jr_1 f(\alpha, \beta)$, and express the coil volume in the form $V = r_1^3 v(\alpha, \beta)$. Find f($\alpha$, β) and v α, β For any given required r_1 and B_z and attainable λJ, the first equation determines the required value of f. Eliminating α algebraically in terms of f, show that $v = 2\pi\beta[(g^2 - \beta^2)^2/4g^2 - 1]$, where $g = e^{f/\beta}[1 + (1 + \beta^2)^{1/2}]$.

For any given required value of f, the minimum value of v can be found either by setting $dv/d\beta = 0$ and solving for β or by simply calculating v for several values of β. The required number of Ampere-meters of conductor can be found from $IL_t = \lambda JV$, where L_t is the total conductor length. Find the minimum conductor volume and required number of Ampere-turns to produce a central induction $B = 7$ T in a bore diameter of 2 m with cryogenic stabilization and $\lambda J = 20$ MA/m^2. What are the coil length and outer radius?

4.6. A large superconducting coil with inductance of 85 H carries a current of 9,000 A. If the protective circuit has a resistance of 0.7 Ω, how long does it take to reduce the current to 100 A?

4.7. A tape conductor which is 1 cm wide and 0.15 mm thick carries a current of 300 A. If the average normal resistivity of the ribbon is three times that of pure copper, and the conductor is cooled only on the thin edges by liquid helium, calculate the Stekly number.

4.8. A coil with inductance of 1 H is charged up to full current, then its input leads are connected together by a superconducting switch (a "persistent switch"). If the current decreases by 0.2 % per month, what is the total resistance of the coil joints?

4.13 Review Questions

1. Explain the domain of superconductivity. Under what conditions can a material be superconducting?
2. Why can metals with high conductivity at room temperature not be superconductors?
3. Define "coherence length", "London penetration depth", "fluxon", and "quench".
4. What is the difference between Type I and Type II superconductors. Which type are most pure metal superconductors? Which Type is unsuitable for fusion reactor magnets, and why?
5. Explain the following diagram.
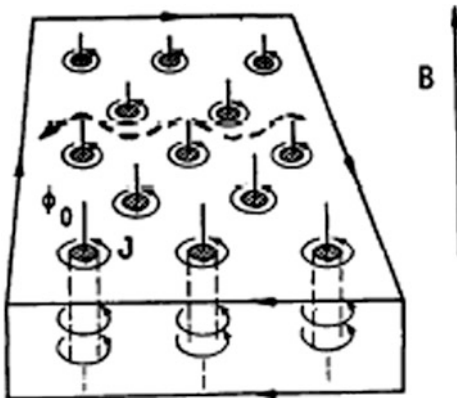
- What do the black tubes represent?
- The circular arrow?
- The dashed arrow?
- What force is acting, and what does it cause?

6. Explain the following diagram, and how it is related to B_{c2}.
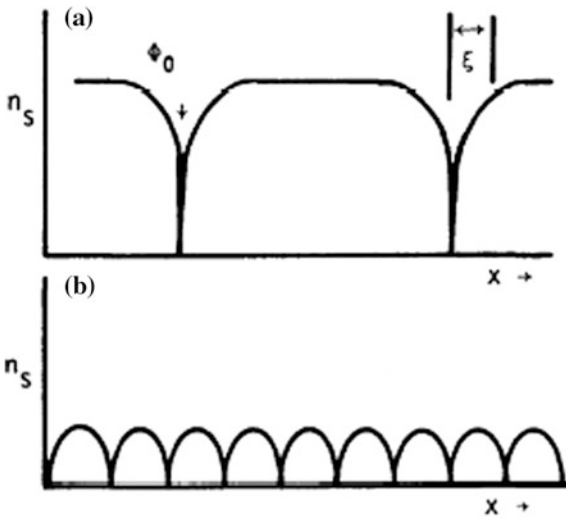
Explain fluxon motion, flux pinning, and flux jump.
7. What are two disadvantages of Nb_3Sn in comparison with NbTi?
8. What is the advantage of a "hybrid" coil?
9. Why is stabilization needed, and how can it be achieved?
10. How do cryogenic stabilization and adiabatic stabilization work?
11. Sketch a coil protection circuit and explain its operation.
12. Which type of cooling is preferred nowadays (pool boiling, two-phase flow, forced flow supercritical), and why?
13. What type of cable is used for ITER?
14. How can Nb_3Sn be manufactured and wound, even though it is very brittle?
15. How can the TF ripple be reduced in ITER?
16. What two technologies are used to reduce the heat leak along the current leads to a superconducting magnet coil?
17. How do the Wendelstein 7-X coils differ from the LHD coils?
18. What advantage would occur if HTS wires could be used for fusion magnets?

References

Abrikosov AA (1957) Soviet Physics JETP 5:1174
Anderson PW (1962) Theory of flux creep in hard superconductors. Phys Rev Lett 9:309
Bardeen J, Cooper LN, Schrieffer JR (1957) Theory of superconductivity, Phys Rev B 108(1175):162–164
Buncher BR, Chi JWH, Fernandez R (1976) Conceptual studies of toroidal field magnets for the tokamak experimental power reactor. Final report, ORO-5153-1, Westinghouse Electric Corporation, Pittsburgh, (USA). 6)

Devred A (2004) Practical low-temperature superconductors for electromagnets. Report CERN–2004–2006, Organisation Européenne pour la Recherche Nucléaire, Geneva

Devred A, Backbier I, Bessette D, Bevillard G, Gardner M, Jewell M, Mitchell N, Pong I, Vostner A (2012) Status of ITER conductor development and production. IEEE Trans Appl Supercond 22(3):4804909

Dolan TJ (1982) Fusion research. Pergamon Press, NY

Fietz WH, Barth C, Drotziger S, Goldacker W, Heller R, Schlachter SI, Weiss DP (2012) Prospects of high temperature superconductors for fusion magnets and power applications. In: 27th symposium on fusion technology, Liege, Belgium, 24–28 Sept 2012

Foussat A (2010) ITER overview, international school on fusion technologies. Karlsruhe Institute of Technology (KIT), Germany, 6–17 Sept 2010

Gruber O, ASDEX Upgrade Team (2008) ASDEX Upgrade enhancements in view of ITER application. 25th SOFT, Rostock, Germany, 15–19 Sept 2008

Hsieh SY, Reich M, Powell JR (1978) Safety issues for superconducting magnets. Report CONF-780508, p 901

Henning CD, Dalder ENC (1979) Structural materials for fusion magnets. 5th international conference on structural mechanics in reactor technology, West Berlin, UCRL-81591

Kim YB, Hempstead CF, Strnad AR (1963) Flux creep in hard superconductors. Phys Rev 131:2486–2495

Koizumi N et al (2008) Study of ITER-TF coil winding pack manufacturing procedure. 25th symposium on fusion technology, Rostock, Germany, 15–19 Sept 2008

Kunzler JE, Buehler E, Hsu FSL, Wenick JH (1961) Superconductivity in Nb_3Sn at high current density in a magnetic field of 88 KGauss. Phys Rev Lett 6:89

London F, London H (1935) The electromagnetic equations of the supraconductor. Proceedings of the Royal Society A149(866):71

Minervini J, Iwasa Y (2003) Superconducting magnets. Lecture Notes 22.68 J/2.64 J, MIT OpenCourseWare, Viewed in 2010. See http://ocw.mit.edu/courses/nuclear-engineering/22-68j-superconducting-magnets-spring-2003/

Meissner W, Ochsenfeld R (1933) Ein neuer effekt bei eintritt der supraleitfähigkeit. Naturwissenschaften 21(44):787

Mitchell N (2008) Status of the ITER magnets. 25th symposium on fusion technology, Rostock, Germany, 15–19 Sept 2008

Mitchell N (2013) Challenges of the ITER magnet construction. Presentation at ITER France, 12 Feb 2013

Noe M (2008) Superconducting magnets. Summer School on Fusion Technology, Karlsruhe Institute of Technology (KIT), Germany

Onnes HK (1911) Communications of the physics laboratory of Leiden. Numbers 119, 120, 122 (1911)

Romanelli F, Contributors JET-EFDA (2009) Recent contribution of JET to the ITER physics. Fusion Eng Des 84(2-6):150–160

Schlachter S (2010) High temperature superconductivity. International School on Fusion Technologies, Karlsruhe Institute of Technology (KIT), Germany, 6–17 Sept 2010

Schwartz BB, Foner S (1977) Large-scale applications of superconductivity, Phys Today, July

Trauble H, Essmann U (1968) Flux-line arrangement in superconductors as revealed by direct observation. J Appl Phys 39(9):4052–4059

Van Delft D, Kes P (2010) The discovery of superconductivity, Phys Today, 38–41 Sept

Wade MR (2008) Physics and engineering issues associated with edge localized mode control. In ITER 25th symposium on fusion technology, Rostock, Germany, 15–19 Sept 2008

Walter W (2010) Manufacturing of Superconducting Magnets. International School on Fusion Technologies, Karlsruhe Institute of Technology (KIT), Germany, 6–17 Sept 2010

Chapter 5
Plasma Heating and Current Drive

Thomas J. Dolan

Objectives

After reading this chapter one should understand

Ohmic heating
Heating by beam injection and by alpha particles
Heating by waves using various plasma resonances
Equipment used in heating systems for large experiments.

5.1 Introduction

An electric stove utilizes the I^2R ohmic heating power generated by flow of an electric current I through a heating element with resistance R. A diesel engine heats its fuel-air mixture to ignition temperature by compression. A microwave oven heats food by absorption of electromagnetic waves. Electron beam welders heat the metal to be welded by the impact of energetic electron beams. The principle methods of plasma heating are these four plus alpha particle heating:

- Ohmic heating—current flow through plasma.
- Compression—by magnetic field, shock wave, or beam pressure.
- Wave heating—radio waves, microwaves, laser beams.
- Particle beam injection—electron beams, ion beams, or neutral beams.
- Heating by 3.5 MeV alpha particles slowing down in the plasma.

For example, to heat a fusion plasma to ignition conditions, if $n = 10^{20}$ m^{-3}, T = 10 keV, V = 200 m^3, then the plasma thermal energy $W = 1.5n(T_e + T_i) V \approx 100$ MJ. (Note that the temperatures must be converted from keV to J in this equation). If the energy confinement time were 2 s, then the plasma would

T. J. Dolan (✉)
NPRE Department, University of Illinois, Urbana, IL 61801, USA
e-mail: dolantj@illinois.edu

Fig. 5.1 The general heating methods used in ITER. Although the neutral beam is injected against the plasma current in this drawing (counter-injection), injection parallel to the current (co-injection) is used more often. The NBI momentum influences plasma toroidal rotation. Used by permission of United Kingdom Atomic Energy Authority
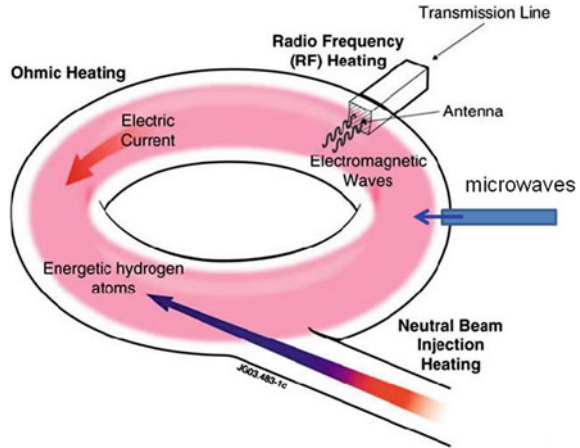
lose about 50 MJ/s of energy, so a heating power >50 MW would be needed to raise the temperature to ignition temperatures. This heating power estimate could be reduced on account of fusion product alpha particles heating the plasma, but increased somewhat by radiation losses, which are not accounted for in the usual definition of energy confinement time.

Tokamaks require non-inductive current drive for steady-state operation, and the required current drive power limits the attainable energy gain ratio Q. Current drive methods also heat the plasma, but not all heating methods generate substantial plasma current density.

The ITER experiment will use three external heating methods: ohmic heating, neutral beam injection (NBI), and electromagnetic waves, Fig. 5.1.

A plasma heating method for a reactor should have the following characteristics:

- High power flux, so small ports may be used in the chamber walls.
- High efficiency of generation and transmission.
- Large fraction of energy absorbed in plasma.
- Steady state operation (or *very long* pulses).
- Reliable operation.
- Long-lived, low-activation materials in the waveguides and launchers.
- Control of gas flow between heating source and plasma chamber (such as a cryopump in a neutral beam injection system or a waveguide window).
- Low neutron streaming through the blanket.
- Easy maintenance.
- Low capital cost per Watt of injected power.

5.2 Alpha Particle Heating

Alpha particles produced by fusion reactions will heat plasma electrons and ions collisionally as they slow down. Some alphas may have bad orbits and leave the plasma quickly, but, if the magnetic field configuration is good, most of them will

stay in the plasma until they have lost most of their energy. For example, some 3D computer codes for magnetic field design in stellarators compute the orbits of many alphas to optimize their retention.

Let n_*, m_*, q_*, and T_* be the density, mass, charge, and temperature of the Maxwellian "field particles" (plasma ions and electrons). The alpha energy loss rate dW/dt to electrons and ions can be computed from Coulomb collision theory. The result may be written

$$dW/dt = -\Sigma n_* q^2 q_*^2 b_* L\ H(x, m_*/m)/(4\pi\varepsilon_0^2 m_*) \qquad (5.1)$$

where the summation is over field particle species, $L \sim 18$ is the Coulomb logarithm, ε_o is the permittivity of free space, m = alpha mass, $x = (m_* W/mT_*)^{1/2}$, $b_* = (m^*/2kT^*)^{1/2}$, and

$$H(x, m_*/m) = erf(x)/x - (2/\pi^{1/2})(1 + m_*/m)exp(-x^2) \qquad (5.2)$$

and erf(x) is the error function (Appendix C) (Dolan 1982). If $x > 2$, then $H = 1/x$, except for impurities heavier than alpha particles. Figure 5.2 shows H as a function of x and m_*/m.

At first most of the alpha energy loss is to electrons, but when their energy W is <15 T_e the loss rate to plasma ions becomes dominant (Goldston and Rutherford 1995). The fraction of total alpha energy that goes to electrons and ions are shown in Fig. 5.3, assuming losses to impurities are negligible.

Fig. 5.2 The H function versus x, for various mass ratios (Dolan 1982)

The time that it takes for an alpha particle to slow down in a plasma is approximately

$$\tau_\alpha = C/n_{20}$$

where n_{20} = plasma density in units of 10^{20} m^{-3}, C = 0.45 s at T_e = 10 keV, and C = 0.9 s at T_e = 20 keV (Sheffield 1994).

Fast alpha particles also contribute significantly to the plasma pressure and beta value, which can lead to instability if beta becomes too high. If the alpha density becomes more than a few percent, the fusion power drops significantly, due to dilution of the DT fuel, so very long alpha confinement can be deleterious. For example, in one estimate a 10 % alpha density fraction reduced the fusion power density by a factor of about 2 (Sheffield 1994).

If f_α is the fraction of alpha particle energy retained in the plasma, then the alpha heating power in a DT plasma with fuel ion density n is

$$P_\alpha = (1/4)f_\alpha n^2 \langle \sigma v \rangle_{DT} W_\alpha \tag{5.3}$$

where $\langle \sigma v \rangle_{DT}$ is the reaction rate parameter (Chap. 1) and W_α = 3.5 MeV = 5.61 × 10^{-13} J.

For example, if f_α = 0.9, n = 10^{20} m^{-3} and T = 15 keV, then $\langle \sigma v \rangle_{DT}$ = 2.65× 10^{-22} m^3/s, and P_α = 0.33 MW/m^3. For this case approximately 70 % of the alpha heating goes to electrons and 30 % to ions (Fig. 5.3).

The fusion power density varies with radial position and the alpha particles diffuse radically as they slow down, so this equation gives only an average for the whole plasma.

The Fokker–Planck equation provides a more accurate description of energetic ions slowing down in a plasma (Goldston and Rutherford 1995).

5.3 Ohmic Heating

Plasma currents and $\mathbf{E} \times \mathbf{B}$ drifts may be driven by magnetic induction or by metallic electrodes in contact with the plasma. The power dissipated per unit volume is

$$P = E_{\parallel}J_{\parallel} + E_{\perp}J_{\perp} = \eta_{\parallel}J_{\parallel}^2 + \eta_{\perp}J_{\perp}^2 \ \left(W/m^3\right) \tag{5.4}$$

where the components are parallel or perpendicular to the magnetic field. By definition

$$\eta_{\parallel} = E_{\parallel}/J_{\parallel} = E_z/neu_{ez}, \tag{5.5}$$

Taking the z direction parallel to B and equating the accelerating force of the electric field to the frictional force of electron–ion collisions, we find

$$- eE_z = -m_e u_{ez} \nu_{ei} \rightarrow u_{ez} = eE_z/m_e \nu_{ei} \tag{5.6}$$

Then

$$\eta_{\parallel} = m_e \nu_{ei}/ne^2 = 2.38 \times 10^{-9} Z_{eff} \ L \ T_{ek}^{-3/2} \ (\Omega m) \tag{5.7}$$

An alternative value of the numerical coefficient is 1.65×10^{-9} (Wesson 2011). where L is the "Coulomb logarithm", Z_{eff} is an effective atomic number of the plasma ions, and T_{ek} is the electron temperature in keV. If $Z \approx 1$ and $L \sim 18$, then

$$\eta_{\parallel} \approx 4 \times 10^{-8} T_{ek}^{-3/2} \ (\Omega m) \tag{5.8}$$

For comparison, the resistivity of copper at room temperature is about $2 \times 10^{-8} \ \Omega m$. At temperatures of a few keV, a hydrogen plasma becomes a better conductor than copper. Ohmic heating becomes less effective at high temperatures.

5.3.1 Increased Resistivity

The resistivities given in Eq. (5.8) represent minimum values due to Coulomb collisions, if neutral atoms are present, the resistivity is increased by the ratio $(\nu_{en} + \nu_{ei})/\nu_{ei}$, where ν_{en} and ν_{ei} are the electron-neutral and electron–ion momentum-transfer collision frequencies. Impurity ions increase the effective value of Z, thus enhancing the resistivity. Effects of toroidal geometry and trapped particles result in "neoclassical" values of $\eta_{\parallel}$. Plasma turbulence can greatly increase the effective resistivity. Turbulence refers to a condition in which many random collective oscillations are excited by microinstabilities. The collective oscillations may be Langmuir plasma oscillations, ion acoustic waves, Alfven waves, etc. Turbulence may increase the resistivity to a value

$$\eta_{\parallel} = m_e \nu_{eff}/ne^2 \tag{5.9}$$

where n, m_e, e, and ν_{eff} are the density, mass, charge, and effective collision frequency of the electrons, and ν_{eff} can be much larger than the collisional ν_{ei}.

Although plasma turbulence increases resistivity and makes ohmic heating more effective, turbulence also increases plasma energy loss rates, and the high electric fields needed to drive plasma turbulence can lead to electron runaway.

5.3.2 Electron Runaway

The retarding force of electron–ion Coulomb collisions decreases at high relative velocities u. For electrons with high velocities, this frictional force may be less than the force of the applied electric field, and they will be accelerated to even higher velocities, until they are lost or some other energy loss mechanism balances the applied electric field force. Such *runaway electrons* may carry a substantial fraction of the plasma current. The energy they absorb from the electric field does not heat the plasma directly, and they may be poorly confined, resulting in high-energy x-rays when they hit the wall. Thus, the plasma control system of a large tokamak will try to avoid creating runaways.

Ignition could in principle be attained solely by ohmic heating at very high magnetic fields (Wagner 1981), but it would be difficult, so auxiliary heating methods are usually employed.

5.4 Compression

If plasma is compressed slowly, energy losses during compression will prevent effective heating, and the compression is said to be *nonadiabatic*. If plasma is compressed on a time scale much less than the energy confinement time, then the compression can be *adiabatic*, meaning that energy flow across the boundary is negligible. Adiabatic heating is reversible: if the plasma were allowed to expand, it would return to its original temperature. Typical time scales for adiabatic compression are $\tau \sim 0.1$–1 ms. If compression occurs on a much shorter time scale $\tau \sim 1$ μs, then shock waves may form and produce intense irreversible heating.

5.4.1 Shock Heating

In an ordinary gas, a perturbation in density may propagate as a sound wave. The perturbation may be caused by rupturing a diaphragm between gases at different pressures, by detonation of an explosive, or by motion of a "piston", such as an airplane wing, through the gas. The speed of sound is larger at higher densities, as shown in Fig. 5.4a, which makes the velocity at point A larger than that at point B (Fig. 5.4c).

The result is that the higher-density gas portion of the wave at point A catches up with points B and C, producing a very steep wave front, called a shock front
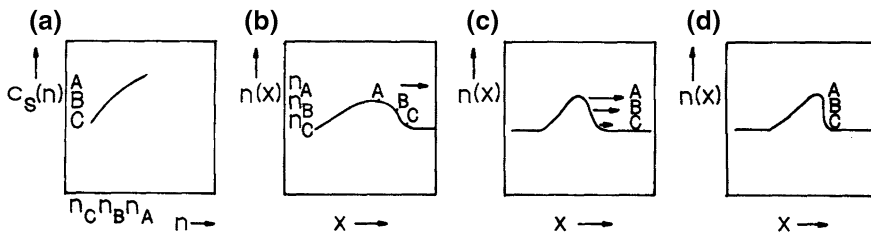
Fig. 5.4 Development of a shock wave. **a** Variation of the sound speed with density. **b** A density perturbation moving to the *right*. **c** Because the density at point *A* is higher, so is its velocity, and it tends to overtake points *B* and *C* resulting in a steep wave front (**d**)

(Fig. 5.4d). The discontinuity of density propagates through the gas, raising the density from n_c to n_A very rapidly, and heating the gas irreversibly. Further "overturning" of the wave is limited by heat conduction and viscosity, so that the shock front develops a certain thickness on the order of a few collisional mean free paths. Such a hydrodynamic shock wave, which propagates via molecular collisions, is probably not of interest for heating fusion reactor plasmas.

Shock waves in plasmas are also caused by the increase of wave speed with density. The wave may be a large-amplitude MHD wave, instead of an ordinary sound wave; and wave propagation is facilitated by changing electromagnetic fields, leaving the plasma in its wake irreversibly heated. In some cases a large current density flows in the wave front. This current-carrying "sheath" acts as a magnetic piston, driving the plasma ahead of it like snow in front of a snowplow. The current may be driven by electrodes in contact with the plasma, or by the electric field induced by pulsed magnet coils. At high temperatures the mean free path for collisions may be very large compared to the shock front thickness, which may be on the order of ρ_i (the ion Larmor radius). Such collisionless shock waves can result in ion temperatures $T_i \sim 10$ keV.

Shock heating is used in some plasma pinch devices (Dolan 1982, Chap. 12). In order to work on microsecond time scales, shock heating coils must have low inductance and operate at high voltage, which leads to a number of technological problems. Since large coils have high inductances, shock heating coils must be small and placed near the plasma, where they will be bombarded by an intense flux of fast neutrons, making them highly radioactive and difficult to replace. The fatigue problems associated with cyclic stresses limit the coil stress and magnetic field to values lower than those attainable in steady-state coils. For these reasons it is unlikely that fusion reactors will use repetitive shock wave heating to ignition.

5.4.2 Adiabatic Compression

The adiabatic equation of state is

$$p_i/n_i^{\gamma} = \text{constant} \tag{5.10}$$

where $p_i = n_i\, T_i = (2/3)n_i\langle W_i\rangle$, n_i = ion density, and $\langle W_i\rangle$ = average ion energy. Using $n_i = N_i/V$, where N_i = total number of ions (assumed constant) in plasma volume V, we can rearrange (5.10) to read

$$\langle W_i\rangle V^{\gamma-1} = \text{constant}$$
$$\gamma = (N + 2)/N \tag{5.11}$$

where N is the number of degrees of freedom during compression. For example, in a one-dimensional compression $\gamma = 3$. Halving the volume would quadruple the ion energy in the direction of compression. A similar relation applies to electrons. Often the average energies will be different in the parallel and perpendicular directions relative to the magnetic field. Then

$$\langle W\rangle = \langle W_\parallel\rangle + \langle W_\perp\rangle$$
$$\langle W_\parallel\rangle = 1/2\ kT_\parallel \tag{5.12}$$
$$\langle W_\perp\rangle = kT_\perp$$

Only the energy component in the direction of compression is affected by a compression. If the collision frequency is high enough to equalize $T_\parallel$ and $T_\perp$, then the system behaves three-dimensionally during any compression, and $\gamma = 5/3$. Toroidal plasma compression is illustrated in Fig. 5.5. Relations between dimensions and energies are summarized in Table 5.1.

Fig. 5.5 Top view of compression of a toroidal plasma **a** initial state, **b** after compression along minor radius a, and **c** after compression along major radius R
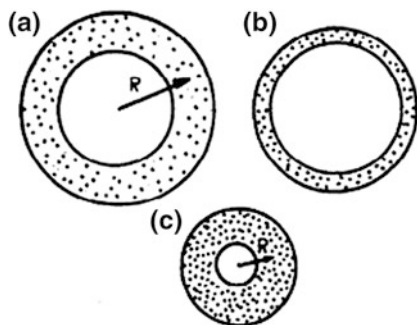
Table 5.1 Relation of energies to dimensions during adiabatic compression

Case	N	γ	Equation
Axial compression	1	3	$\langle W_\parallel\rangle L^2 = \text{constant}$
Compression along major radius	1	3	$\langle W_\parallel\rangle R^2 = \text{constant}$
Compression along minor radius	2	2	$\langle W_\perp\rangle a^2 = \text{constant}$
3-dimensional compression, or any compression in which a high collision rate makes the energy distribution isotropic	3	5/3	$\langle W\rangle V^{2/3} = \text{constant}$

In a *low-beta* plasma, the particles are tied to field lines, and

$$VB = \text{constant (radial compression)}$$
$$V/L = \text{constant (axial compression)} \tag{5.13}$$

where L = plasma length and B = magnetic field. (For a toroidal plasma L = $2\pi R_o$). For a *high-beta* plasma, the plasma pressure balances the magnetic field pressure:

$$2nT = \beta B^2/2\mu_o \tag{5.14}$$

$$TB^{-2}V^{-1} = \text{constant} \tag{5.15}$$

For a given change in B (or L) the change of volume may be computed from Eqs. (5.13) or (5.15), and then the corresponding energy change in the direction of compression may be computed from Eq. (5.11) or Table 5.1.

In tokamaks, conservation of toroidal flux requires that $B_t\, a^2 = $ constant. The toroidal field varies as $B_t = B_o R_o/R$. If B_o is not changed while the plasma is moved to smaller R, then

$$a^2/R = \text{constant} \tag{5.16}$$

Thus, a decrease of major radius with constant B_o also decreases the minor radius.

Example Problem 5.1: Adiabatic compression of a tokamak plasma A uniform tokamak plasma is compressed adiabatically (no heat loss) by using the vertical field to move the plasma from $R_o = 1.5$ m to R = 1.0 m without changing B_o. If the initial temperatures = 1 keV and density n = 10^{19} m^{-3}, what are the final density and temperatures?

The compression of the major radius heats $T_\parallel$ according to the equation (Table 5.1)

$$\langle W_\parallel \rangle R^2 = \text{constant} \rightarrow T_\parallel/T_{\parallel_o} = \langle W_\parallel \rangle/\langle W_{\parallel_o} \rangle = R_o^2/R^2 = 2.25$$

So **T = 2.25 keV**.

The compression of the minor radius heats $T_\perp$ according to the equation (Table 5.1)

$$\langle W_\perp \rangle a^2 = \text{constant} \rightarrow T_\perp/T_{\perp o} = \langle W_\perp \rangle/\langle W_{\perp o} \rangle = a_o^2/a^2 = R_o/R = 1.5,$$

where Eq. (5.16) has been used. Thus, **$T_\perp$ = 1.5 keV**.

The density change is

$$n/n_o = V_o/V = a_o^2 R_o/aR = R_o^2/R^2 = 2.25.$$

The final density is **n = 2.25 $\times$ 10^{19} m^{-3}**, assuming particle loss is negligible during compression.

If particles and energy are lost during compression, then the compression (no longer adiabatic) may be described using the transport equations.

Experiments with the Adiabatic Toroidal Compressor (ATC) tokamak demonstrated the effectiveness of this heating method. A tokamak could be compressed to ignition, and then allowed to expand with its temperature maintained by alpha heating. However, control of plasma size and shape is not easy, and pulsed coils present technological problems, such as fatigue.

Compression will not be used in tokamaks or stellarators, but it is the key feature of "magnetized target fusion" (MTF), where an imploding metallic liner compresses a "field reversed configuration" plasma up to high density and temperature.

5.5 Charged Particle Injection

5.5.1 Charged Particle Beams

It is difficult to inject charged particles across magnetic field lines, because the $q\mathbf{v} \times \mathbf{B}$ force reflects them. It is easy to inject them into a magnetic cusp or mirror along magnetic field lines, but they tend to follow field lines out the other end. The mean free path for Coulomb collisions is usually orders of magnitude larger than the size of the magnetic bottle, so Coulomb collisions are not effective in trapping the beam energy. However, microinstabilities, such as the beam-plasma instability, can extract beam energy over short distances and heat the plasma via wave-particle interactions.

Plasmas in magnetic mirrors have been heated to keV temperatures by axial injection of electron beams (Seidel 1979). Electron beams have also been injected into toruses, by varying the magnetic field during injection. Powerful electron and ion beams may also be used to compress solid fuel pellets in inertial confinement fusion experiments to very high temperatures and densities, resulting in small thermonuclear explosions.

5.5.2 Plasma Guns

A coaxial plasma gun is illustrated in Fig. 5.6.
When a high voltage is applied to the electrodes, breakdown occurs along the insulator. The $\mathbf{J} \times \mathbf{B}$ force accelerates the plasma outwards, then axially along the tube. Finally, the plasma momentum carries it off the end of the electrode as a blob of plasma moving along the chamber axis. Such plasma blobs, having keV temperatures, may be injected into plasma confinement systems. During injection

Fig. 5.6 Operation of a coaxial plasma gun a breakdown along the insulator, b acceleration of the plasma sheath, c continued acceleration past the end of the inner electrode, and d plasma blob leaving the end of the gun. The directions of plasma current density, self-magnetic field, and resultant $\mathbf{J} \times \mathbf{B}$ force are indicated at the *right*
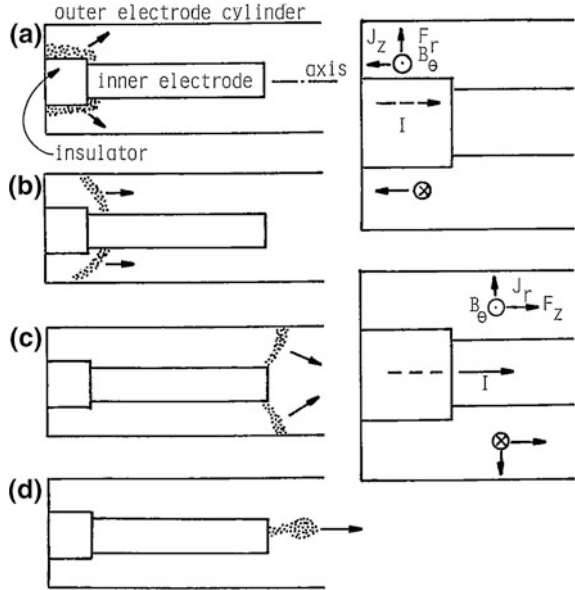
across B, the $q\mathbf{v} \times \mathbf{B}$ force produces a charge-separation electric field. This polarization field aids plasma penetration via the $\mathbf{E} \times \mathbf{B}/B^2$ drift.

A variation of the above method involves adding a solenoid inside the inner electrode. The solenoid field which connects the inner and outer electrodes gets stretched by the flowing plasma resulting in the generation of a spheromak in a formation chamber. A second electrical discharge with this spheromak accelerates it to high velocities through $J \times B$ forces.

Figure 5.7 shows a successful experiment that injected such plasma spheromaks from a magnetized coaxial plasma gun at $v = 2 \times 10^5$ m/s into the Tokamak de Varennes (TdeV) in Canada. For successful penetration, to first order, the kinetic energy density of the plasmoid must exceed the magnetic field energy density of the tokamak (Perkins et al. 1988).

The Mark III CT injector at 25 kV can inject compact toroids with density $\sim 7 \times 10^{21}$ m^{-3} at speeds ~ 200 km/s into the JFT-2 M Tokamak at the Japan Atomic Energy Research Institute (JAERI). These plasmas can also be injected into a spheromak flux conserver (Fukumoto et al. 2004).

Compact toroid injection may also be useful to inject fuel into the plasma core, which is desirable for plasma profile control and bootstrap current control (Sect. 7.4 and Raman 2006).

In some experiments the plasma blob leaving the end of a coaxial plasma gun collapses down to a very small diameter, *dense plasma focus*, which can be a source of intense neutron and x-ray emission. Such plasma focus devices have been constructed at many universities. Detailed photographs of the plasma sheath sometimes reveal tiny plasma vortex filaments (Bostick et al. 1966).
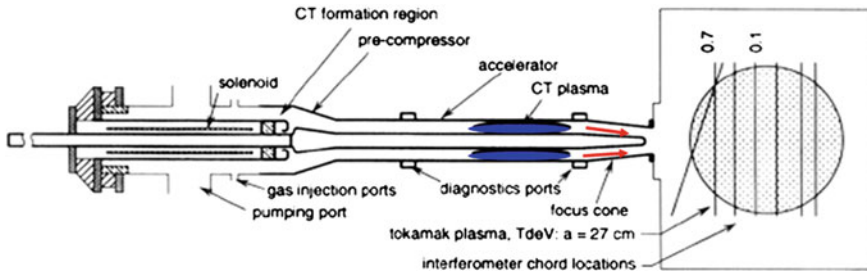
Fig. 5.7 The coaxial plasma gun used to inject plasma spheromaks into the TdeV experiment in Canada (Raman et al. 1994)

Another type of plasma gun uses a stack of titanium washers impregnated with deuterium. When a high current is pulsed through the stack, the deuterium is emitted, ionized, and accelerated.

Plasmas from guns also make good target plasmas for trapping injected neutral atom beams.

5.6 Neutral Beam Injection

5.6.1 Penetration into the Plasma

High velocity neutral atom beams can be injected across magnetic field lines and trapped in the plasma by ionization. If the plasma is not dense enough, most of the fast neutrals will pass through the plasma without being ionized. Conversely, if the plasma is too dense, or the beam energy is too low, most of the beam will be stopped at the plasma edge, without penetrating to the center where it is needed, Fig. 5.8.

The resultant density peak at the plasma edge may lead to instability. Thus, beam penetration and trapping requirements are relative to plasma density and beam energy. The unattenuated beam density $n_b(x)$ is trapped at a rate

$$dn_b/dx \ = -n_b/\lambda_a \qquad (5.17)$$

where x is the distance of penetration measured from the plasma edge, and λ_a is the attenuation length. In a uniform plasma

$$n_b = n_{bo}exp(-x/\lambda_a). \qquad (5.18)$$

Values of the product $n_e\lambda_a$ for deuterium and tritium beams in a DT plasma are shown in Fig. 5.9 as functions of beam energy.

The ions trapped in distance dr at radius r will quickly spread out to fill the volume $(2\pi R_o)2\pi rdr$, for the case of circular flux surfaces in a torus with major radius R (Fig. 5.10).

Fig. 5.8 Beam penetration versus energy. The penetration distance also depends on plasma density
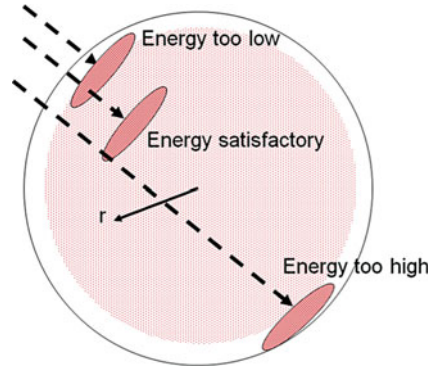
Fig. 5.9 Product of attenuation length λ_a and plasma density n_e versus neutral beam energy, for deuterium and tritium injection. *Smooth curves* $T_e = 10$ keV, *dashed curves* $T_e = 1$ keV (Dolan 1982)
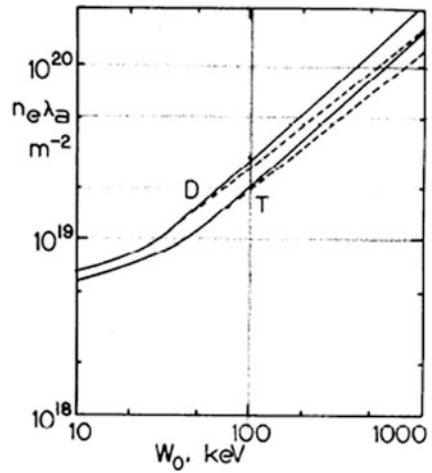
Fig. 5.10 Volume filled by trapped ions at radius r
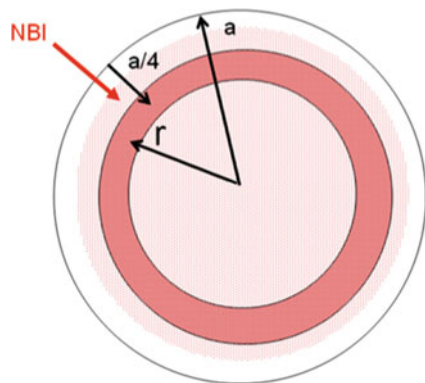
This means that a few ions deposited at small r will provide a source density equal to that of many ions deposited at large r. If we let λ_{av} be the value of λ_a at the average values of n_e and T_e, then requiring that

Fig. 5.11 Variation of ion temperature with radius and time for an expanding radius tokamak reactor case. Neutral beam heating is turned on from t = 2–6 s, with radius a = 1.4 m. Then the plasma becomes ignited and is allowed to expand to a = 2.5 m, with T_i sustained by alpha heating (Houlberg et al. 1980)
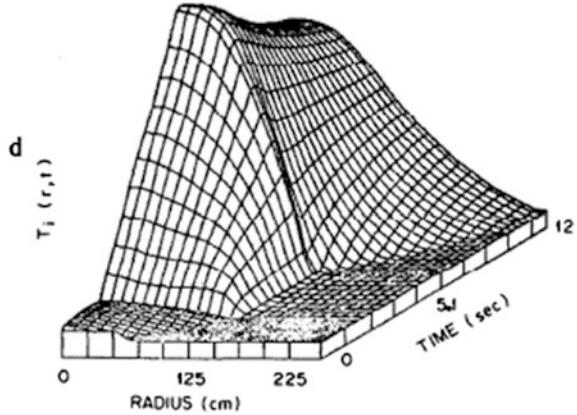
$$\lambda_{av} > a/4 \tag{5.19}$$

may give adequate penetration. For example, consider a case in which the average electron density $n_e = 8 \times 10^{19}$ m^{-3}, a = 1.25 m. For this case $n_e a = 10^{20}$ m^{-2}. To attain $n_e \lambda_{av} > 2.5 \times 10^{19}$ m^{-2}, the desired deuterium atom beam energy is about 100 keV.

It is possible to ignite large reactor plasmas without using much higher beam energies by keeping the plasma radius small until neutral beam heating has ignited the plasma, then allowing the plasma to expand to full size. For example, a tokamak reactor case with the following parameters was studied:

R_o = 10 m, B_t = 4.2 T, plasma elongation (height/width) = 1.6, initial minor radius a = 1.4 m, $n_e = 10^{20}$ m^{-3}, neutral beam energy = 150 keV, beam power = 130 MW, heating pulse length = 4 s, initial plasma current = 3 MA; final expanded radius a = 2.5 m, final current I = 8 MA. The time variation of the ion temperature profiles for this case is shown in Fig. 5.11.

These data illustrate the type of calculations needed for neutral beam energy deposition studies. They are not conclusive, because the results depend strongly on

- Transport model assumed
- Alpha particle confinement
- Alpha energy transfer to electrons and ions.

Small ripples in the toroidal field ($\delta B_t/B_t \sim 1$ %) may help transport trapped ions inwards, permitting somewhat lower injection energies to be used, if instabilities do not interfere.

5.6.2 Neutral Beam Generation

Neutral atoms cannot be accelerated, since they are not much affected by electromagnetic fields. However, ion beams can be accelerated and then partially

Fig. 5.12 The steps of neutral beam generation and injection
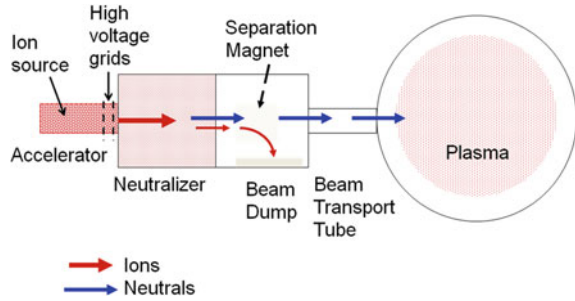
neutralized by charge transfer in a gas cell. Figure 5.12 illustrates the steps of neutral beam generation.

Hydrogen ions from an ion source are accelerated by high voltage grids. The ion beam passes through a neutralizer cell, which may contain a gas like deuterium or nitrogen. Part of the ions grab electrons and become neutral atoms that are not affected by the magnetic field of the separation magnet. The part of the beam that is not neutralized is deflected by a separation magnet into a beam dump, so that it does not hit the walls of the beam transport tube.

Figure 5.13 shows more details, including Doppler shift spectroscopy to measure neutral atom velocities.

5.6.2.1 Need for Negative Ions

The D_2 gas pressure in the neutralizer region is on the order of 0.1 Pa (10^{-3} Torr). The fraction of the ion beam neutralized by charge exchange is
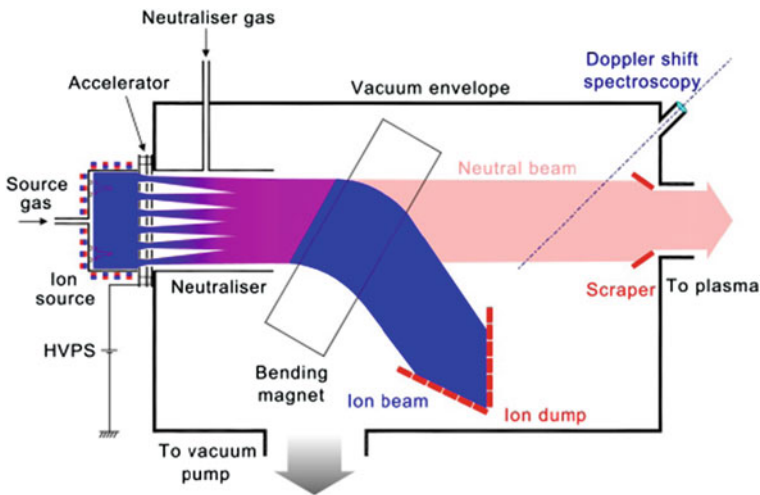
Fig. 5.13 The main components of a neutral beam injector (Day et al. 2010). Used by permission of United Kingdom Atomic Energy Authority

Fig. 5.14 Neutralization efficiency η versus beam energy for deuteron beams in deuterium gas (Dolan 1982)
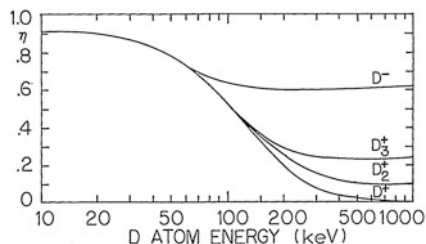
$$\eta = \frac{\sigma_{10}}{\sigma_{10} + \sigma_{01}} \left\{ 1 - \exp\left[-(\sigma_{10} + \sigma_{01}) \int_0^x dx\, n_n \right] \right\} \qquad (5.20)$$

where x is the path length in the gas, n_n is the gas density, σ_{10} is the cross section for neutralization by charge exchange, and σ_{01} is the cross section for reionization of the neutrals. For values of

$$\int_0^x dx\, n_n \geq 2 \times 10^{20}\,\mathrm{m}^{-2}, \qquad (5.21)$$

the exponential function is very small, and

$$\eta \cong \sigma_{10}/(\sigma_{10} + \sigma_{01}). \qquad (5.22)$$

Since σ_{10} drops off at high energies, the neutralization of positive ions becomes inefficient there, as shown in Fig. 5.14.

The rapid drop of the D+ curve means that efficiency will be poor for neutralization of D+ beams above 200 keV. Negative ion (D$^-$) beam sources are being developed for production of high-energy neutral beams, because such beams have much higher neutralization efficiencies than D+ beams. 1 MeV negative ion sources have been developed for ITER. Direct recovery of unneutralized ion energy in the beam dump can improve the power efficiency of neutral beam production.

Negative ions can be generated by contact with a low-work-function surface (such as Cesium) and by dissociative recombination of a vibrationally excited molecule, such as D_2^* (energy levels $\sim$ 5–10)

$$D_2^* + e^- \rightarrow D_2^{-*} \rightarrow D^- + D^o$$
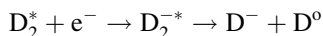
5.6.3 Ion Sources

The ion source needs to provide a large uniform plasma. One way to do this is with permanent magnet multipole cusp arrangement, as illustrated in Fig. 5.15.
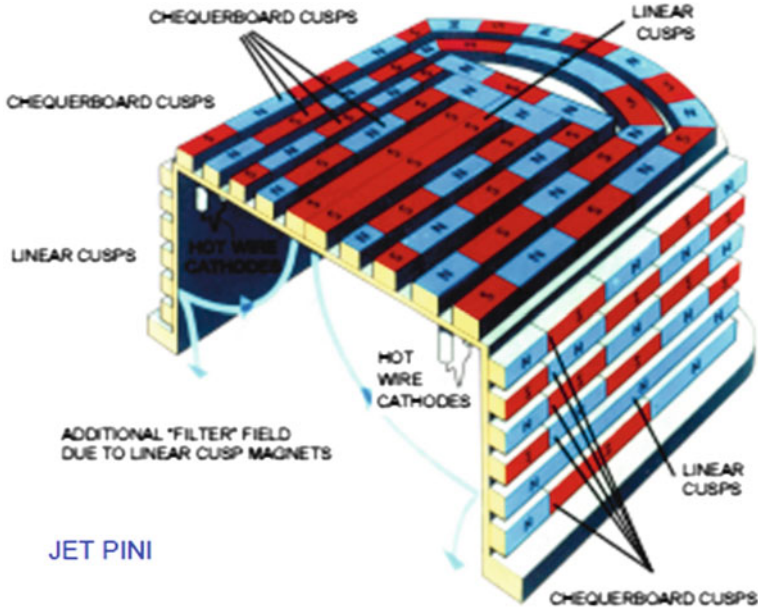
Fig. 5.15 The JET PINI multipole cusp ion source (Day et al. 2010). Used by permission of United Kingdom Atomic Energy Authority

The magnetic field provides thermal insulation at the wall, and the weak field in most of the volume allows the plasma to be uniform. Figure 5.16 shows an expansion region between the ion source and the accelerating grids.

Fig. 5.16 Plasma expansion up to the accelerating grids. The magnetic field filters out electrons (Day et al. 2010). Used by permission of United Kingdom Atomic Energy Authority
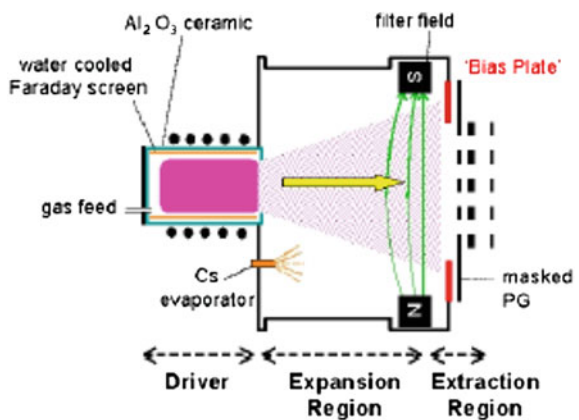
Fig. 5.17 Accelerating electrodes (*black*), magnetic fields (*red*), and beam (*blue*) (Day et al. 2010). Used by permission of United Kingdom Atomic Energy Authority

-130kV   -110kV   0

Plasma   Electron   Ground
grid   trap   grid
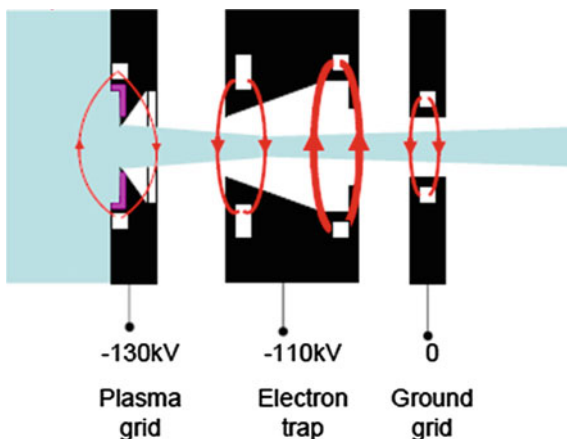
5.6.4 Accelerator

Beam divergence is typically about half a degree in the plane parallel to the electrode slits and 1.3° in the plane perpendicular to the electrodes (at 37 % of peak intensity). Grid rails are fastened at one end only, to allow for thermal expansion, and the grids (usually copper) are water-cooled. Current densities attainable by ion beam sources are typically around 3 kA/m^2 (0.3 A/cm^2). A grid misalignment of just 0.1 mm can cause a beam deviation of 3.6 cm after 8 m travel to the torus.

Figure 5.17 shows a set of accelerating electrodes for negative ion acceleration.

The magnetic fields help trap co-injected electrons, so that energy is not wasted accelerating them. The electron current can also be reduced by positively biasing the area around the aperture (Day et al. 2010).

Multiple aperture electrodes will accelerate many beamlets, over 1,000 each in JT-60U and ITER.

In the event of sparking, the high voltage must be rapidly disconnected to prevent arc damage to the electrodes.

5.6.5 Beam Duct and Pumping

Figure 5.18 shows how several neutralized beams merge as they pass through the JET beam duct into the torus.

The cryogenic vacuum pumping system must remove most of the neutral gas, to prevent it from flowing into the plasma region. A fast shutter valve can be closed after the end of the beam pulse to prevent further gas flow, if needed, and to facilitate glow discharge cleaning between plasma discharges. The entire injector may be pivoted around flexible bellows to vary the injection angle. Buildup of neutral gas in the beam duct during injection may cause reionization of the beam and prevent its penetration across the magnetic field.
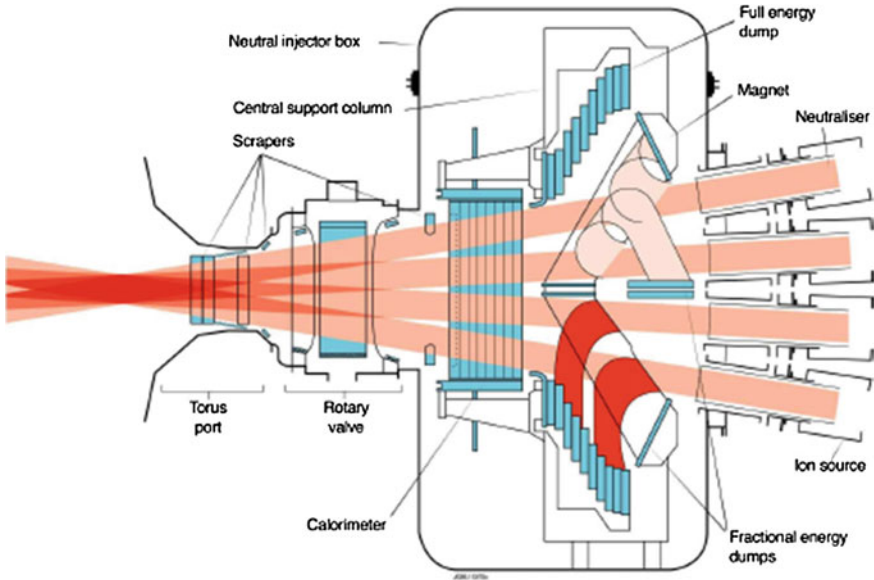
Fig. 5.18 Convergence of several neutral beams as they pass through the beam duct into JET (Day et al. 2010). Used by permission of United Kingdom Atomic Energy Authority

In order to prevent reionization from spoiling beam heating, the parameter $P_o t \ell/C$ should be minimized, where P_o is the desired beam power of primary D^o, t is the pulse length, R is the duct length, and C is the conductance of the vacuum system for deuterium leaving the beam duct. Large cryogenic pumps with surfaces at $T \sim 5$ K must provide very high vacuum pumping speeds for many minutes in ITER. Vacuum pumps will be discussed in Sect. 9.3.

Some design considerations for neutral beam injectors are listed in Table 5.2 (There are also many other considerations related to mechanical design, vacuum system, cryogenics system, magnet system, and electrical systems).

Table 5.3 lists the ITER NBI systems.

Experimental injectors have achieved the desired values of current density (200 A/m^2), (electron/ion) ratio (<1), and operating pressure (0.3 Pa). Full power capability for 3,600 s is under development.

Figure 5.19 shows the ITER neutral beam injector system.

This system has a source of D^- negative ions that are accelerated up to 1 MeV and then neutralized. The vertical bushing provides high voltage insulation. The injected beam power is 1 MW, and the beam must perform reliably for many seconds. The fast shutter closes when the beam is not being injected to keep unwanted gas from streaming into the tokamak. The calorimeter is used to measure beam power.

Two heating Neutral Beam Injectors (HNB) are currently foreseen for ITER with a possible third, plus a Neutral Beam for diagnostic purposes (DNB). A preliminary idea of their locations around the torus are shown in Fig. 5.20.

Table 5.2 Some neutral beam injection design considerations

- Long pulse duration
- Negative ion beams at high energies
- Current density—need narrow electrode gaps and high voltage
- High voltage breakdown—desire large gaps and smooth surfaces
- Beam divergence angle—computerized electrode design
- Beam blowup—narrow beamlets, electrode thermal expansion allowance
- Overheating—flowing water or helium
- Arc damage—fast-cutoff circuitry
- Electrode sputtering—low neutral gas pressure
- Radiation damage—electrodes shielded from neutron flow paths
- Gas flow—powerful cryogenic vacuum pumps
- Efficiency—recover un-neutralized ion beam energy at beam dump

Table 5.3 ITER NBI system plans

	Energy	Power
Heating and current drive	1 MeV	2×16.5 MW, 3,600 s
Diagnostics	100 keV	6 MW
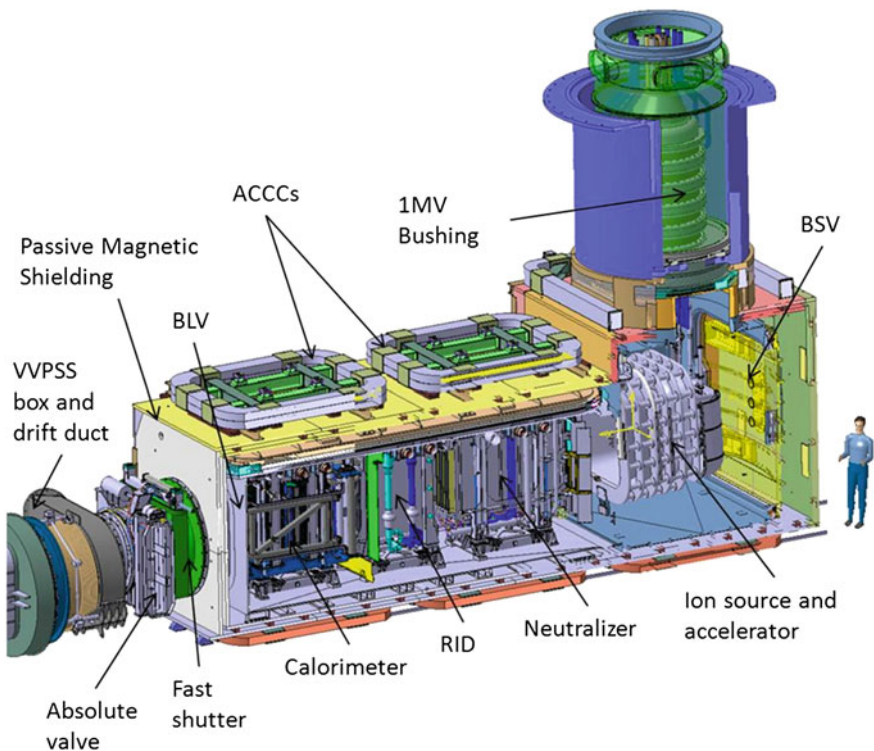
Fig. 5.19 The ITER neutral beam injector. Courtesy of ITER Organization
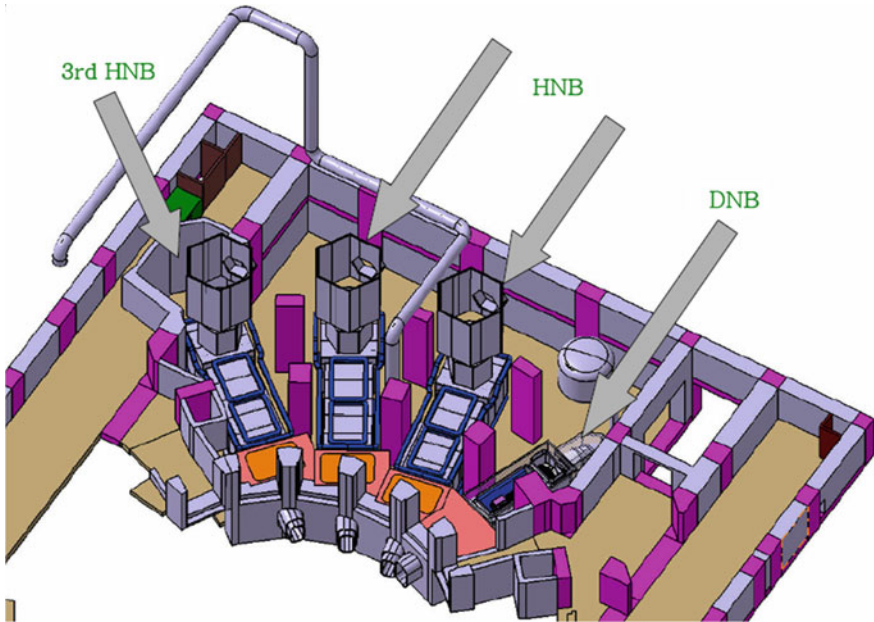
Fig. 5.20 A preliminary concept for arrangement of neutral beam injectors (Design is evolving). Courtesy of ITER Organization

5.7 Wave Heating Fundamentals

5.7.1 Electromagnetic Waves

Plasma may be heated with various forms of electromagnetic waves, including radio waves, microwaves, and laser beams. Laser beams may be used to heat high density plasma ($n > 10^{23}$ m^{-3}) and to compress solid fuel pellets, but absorption of laser light is ineffective at lower plasma densities, as in tokamaks ($n \sim 10^{20}$ m^{-3}).

Electromagnetic waves are represented in terms of their angular frequency ω (radians/s) and wave vector **k**, which has a magnitude $= 2\pi/\lambda$ ($\lambda =$ wavelength) and direction equal to the direction of wave propagation. The frequency f in Hz (cycles/s) $= \omega/2\pi$. The wave frequency is fixed by the generator, and the wavelength depends on the response of the plasma. In a vacuum

$$\lambda = c/f \tag{5.23}$$

where c = speed of light. The wave vector **k** has components $k_\parallel$ parallel and $k_\perp$ perpendicular to the magnetic field direction. The electric field of each wave varies sinusoidally with space and time according to:

$$E = E_o \exp(i\mathbf{k} \cdot \mathbf{x} - i\omega) \tag{5.24}$$

(which can also be written in terms of sines and cosines). There will be many such waves in the plasma simultaneously with various $\mathbf{k}$ and ω, so the total electric field is the sum of all the individual wave electric fields. The phase velocity and "group velocity" v_g of the wave are

$$v_{ph} = \omega/k$$
$$v_g = \partial\omega/\partial k \tag{5.25}$$

The wave fields travel at v_{ph}, which can exceed the speed of light c, but energy and information travel at v_g, which is always <c. These can be seen from the ratio of ω/k and from the slope of a graph of ω versus k. To study plasma waves we assume that the plasma density has a large constant part n_o and a small part n_1 that varies exponentially at the wave frequency

$$n = n_o + n_1 \exp(i\mathbf{k} \cdot \mathbf{x} - i\omega t) \tag{5.26}$$

We make similar assumptions about other plasma quantities and insert these approximations into the conservation equations and Maxwell equations. The goal is to derive a "dispersion relation" (an equation that relates $\mathbf{k}$ to ω). Then we can analyze that equation to study the wave propagation.

Figure 5.21 shows graphs of the dispersion relations for waves propagating parallel to B and perpendicular to B in a "cold plasma" (meaning that plasma temperature and pressure effects are ignored).

The slopes of these curves are the group velocities, always less steep than the dashed line c. We can identify resonances that may be useful for plasma heating or current drive: electron cyclotron resonance (ECR), ion cyclotron resonance (ICR), upper hybrid resonance (UHR), and lower hybrid resonance (LHR). We can also heat the plasma at twice the ECR and ICR frequencies (the "second harmonic") or even higher harmonics, though perhaps less effectively. In general the wave propagates at an intermediate angle relative to B, so these are special, simplified cases.

The Index of Refraction

$$N = c/v_{ph} = kc/\omega \tag{5.27}$$

can vary between 0 and infinity. (When $N < 1$, $v_{ph} > c$.) The variation of the wavelength in a plasma approaching a cutoff and a resonance is shown in Fig. 5.22.

5.7.2 Stages of Wave Heating

The stages of electromagnetic wave heating are illustrated in Fig. 5.23.
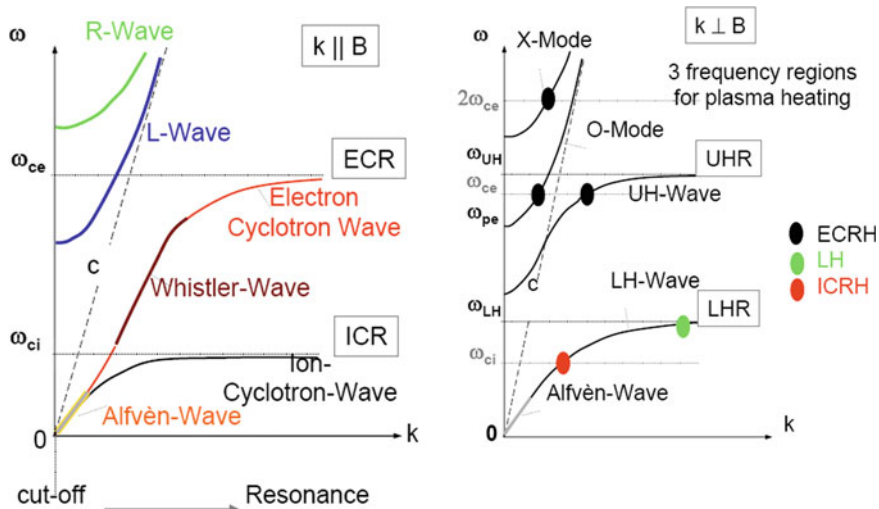
Fig. 5.21 Dispersion relations for electromagnetic waves propagating parallel to B and perpendicular to B in a "cold plasma". The places where k → ∞ (v_{ph} → 0) are "resonances" where the plasma absorbs the wave energy, and the places where k → 0 (v_{ph} → ∞) are "cutoffs", where the wave cannot propagate (it may be reflected or modified into a different wave) (Laqua 2008)
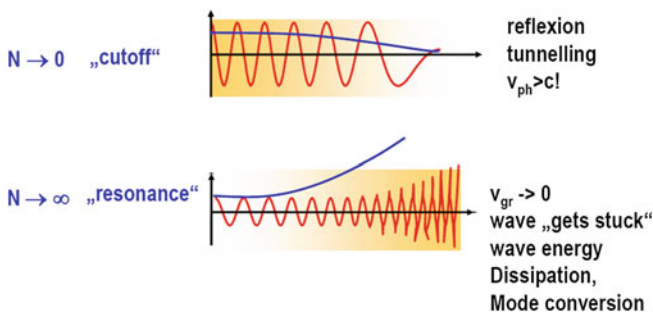
Fig. 5.22 Variation of wavelength as the wave approaches a cutoff and a resonance. The *blue curve* shows how N varies near the cutoff and resonance. Near the cutoff λ → ∞ (k → 0), and near the resonance λ → 0 (k → ∞) (Laqua 2008)

The problems of generation and transmission are fairly well resolved, except for high power generation of waves at frequencies >100 GHz. Coupling is most effective near resonances of the plasma or near resonant frequencies of the plasma-filled chamber.

A vacuum window is usually needed between a microwave generator and the plasma. It should have low absorption of the waves, high thermal conductivity, and resistance against cracking at high power densities of waves passing through. Diamond and sapphire are excellent materials, because of their high thermal

Fig. 5.23 Stages of wave heating (Stix 1972)
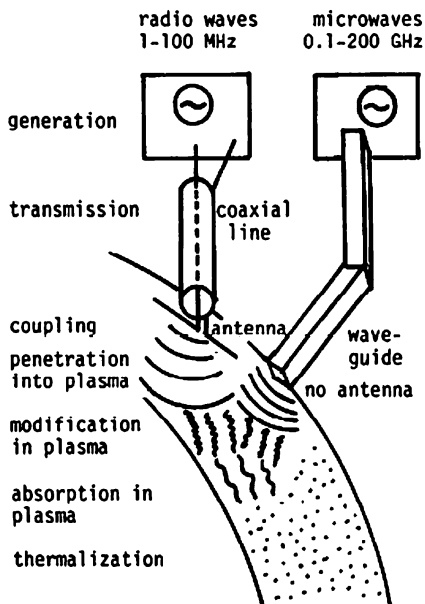
conductivities, but expensive. The waveguide should have several bends in it to prevent neutrons from streaming to the outside and causing high radiation levels outside the reactor.

Radio waves are transmitted through coaxial lines, and microwaves usually travel through rectangular waveguides. Special dielectric-filled or convoluted waveguides may be used where the wavelength is large.

A waveguide grill couples microwaves to the plasma, and an antenna is used for radiofrequency waves. Antennas must couple efficiently, without arcing or introducing impurities into the plasma. For all types of heating, the antenna structure or waveguide array should be arranged so as to excite desired modes in the plasma. Otherwise, coupling may be inefficient, and required antenna voltages may become excessive, or waves may merely heat the surface plasma without penetrating to the core.

The physics of wave-plasma interactions are described in plasma physics textbooks (Chen 1984; Kikuchi et al. 2012; Stix 1972). Penetration into the plasma depends upon the relation of the wave frequency and wave number k $= 2\pi/\lambda$ to the local plasma properties. The wave may be reflected by the plasma, which prevents effective heating or current drive. It may pass through the plasma with little interaction. It may change into other wave forms inside the plasma, and part of the wave energy may be absorbed by the plasma. Computer programs model the wave propagation and interaction in the plasma to predict the effectiveness of heating and current drive.

Absorption is strongest at natural resonances of the plasma, which include the electron cyclotron, ion cyclotron, lower hybrid, and upper hybrid resonances. Absorption could also be enhanced by resonances of the "cavity" (chamber).

Fig. 5.24 Multiple
reflections of wave in a cavity
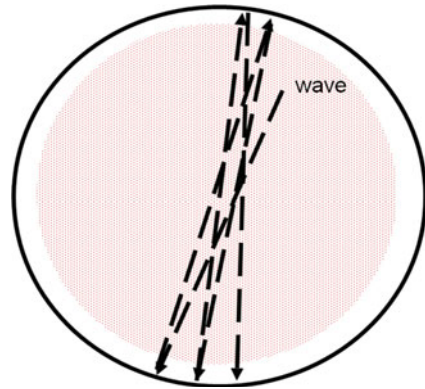
5.7.3 Cavity Resonances

Cavity resonances of electromagnetic waves, similar to those of sound waves in a musical instrument, can occur when the size of the cavity (in this case, the vacuum vessel) is an integral number of half-wavelengths. An electromagnetic wave that is weakly absorbed by plasma can pass through the plasma many times, reflecting from the vacuum chamber walls, Fig. 5.24.

If the wave frequency is tuned to one of the natural resonant frequencies of the plasma-filled cavity, then the wave amplitude in the plasma can become very large (limited by the reflectivity of the walls and by wave absorption in the plasma), resulting in effective plasma heating in spite of the weak absorption.

Changes of the plasma density profile alter the resonant frequencies of a cavity. For effective plasma heating, the radio wave generator frequency must follow the resonant frequency of the cavity and plasma. This frequency variation is called mode tracking. Usually the impedance of the plasma and chamber is low compared to that of the radio wave transmission system and antenna. The impedance mismatch may result in ineffective coupling of the wave energy to the plasma. Near a resonance, the plasma impedance increases, and coupling becomes more efficient. In the 1960s resonant cavities were studied as a possible means of *confining* a fusion plasma, but the input power requirements were too high (Dolan 1982, Chap. 17).

5.7.4 Propagation and Resonances

Electromagnetic waves propagating perpendicular to the magnetic field have two basic modes: the "ordinary mode" (E parallel to B) and the "extraordinary mode" (E perpendicular to B). Usually E will have components both parallel and perpendicular to B. These modes have different propagation characteristics. The direction of E can be controlled by the orientation of E in the waveguide or

antenna leading to the plasma. The ordinary mode wave will be reflected at the plasma layer where the wave frequency ω = the electron plasma frequency

$$\omega = \omega_{pe} = (ne^2/m_e\varepsilon_o)^{1/2} = 56.4 \ n^{1/2} \ \text{rad/s} \tag{5.28}$$

where n = electron density (m^{-3}). For example, if n = 10^{20} m^{-3}, then ω_{pe} = 56.4×10^{10}, and $f_{pe} = \omega_{pe}/2\pi$ = 90 GHz, so only very high microwave frequencies could penetrate.

The extraordinary mode can penetrate further, but propagation of the waves is complicated, because they can interact with various other waves and resonances in the plasma (Bellan 2006; Chen 1984; Goldston and Rutherford 1995; Kikuchi et al. 2012; Stix 1992) Here we will look at some of the hardware used to generate, transmit, and couple the waves to the plasma.

The plasma has several resonant frequencies at which the wave energy may be readily absorbed:

Electron cyclotron resonance heating (ECRH or ECH or EC)

$$\omega_{ce} = eB/m_e\gamma \qquad \text{rad/s} \tag{5.29}$$

where e = electron charge, B = magnetic field, m_e = electron mass, $\gamma = (1 - v^2/c^2)^{1/2}$ (same as Eq. 2.12. We assume $\gamma = 1$ unless otherwise specified.). The frequency in Hertz is

$$f_{ce} = \omega_{ce}/2\pi = 28.0 \, B \ \text{(GHz)} \tag{5.30}$$

Ion cyclotron resonance heating (ICRH or ICH or IC)

$$\omega_{ci} = qB/m_i \ \text{rad/s} \tag{5.31}$$

where q = ionic charge, B = magnetic field, m_i = ion mass. The frequency in Hertz is

$$f_{ci} = \omega_{ci}/2\pi \ \text{Hz} \tag{5.32}$$

For deuterons this becomes

$$f_{ci} = 7.63 B \ \text{MHz} \tag{5.33}$$

At B = 5 T this becomes 38 MHz, which corresponds to a vacuum wavelength of 7.9 m. The ITER ion cyclotron heating system uses radio waves at frequencies of 30–50 MHz.

Lower hybrid resonance (LH)

The lower hybrid resonance frequency is

$$\omega_{LH} \simeq \omega_{pi}(1 + \omega_{pe}^2/\omega_{ce}^2)^{-\frac{1}{2}} \ \text{rad/s} \tag{5.34}$$

where $\omega_{pi} = (ne^2/m_i\varepsilon_o)^{1/2}$ and $\omega_{pe} = (ne^2/m_e\varepsilon_o)^{1/2}$ are the ion plasma frequency and electron plasma frequency, and m_i and m_e are the ion and electron masses. The frequency $f_{LH} = \omega_{LH}/2\pi$ is typically a few GHz.

Table 5.4 Some wave heating methods and ITER plans (partly from Jacquinot et al. 2008)

	IC	LH	EC
Frequency in ITER	35–65 MHz	3.7–5 GHz	170 GHz
Objectives in ITER	Central ion heating; sawtooth control; wall cleaning	Off-axis current drive	Heating; current drive; NTM[a] control; plasma startup
CW power to ITER plasma (MW)	20	20	20
Transmission means	Coaxial line	Waveguide	Waveguide
Coupling means	Loop antenna or cavity-backed aperture antenna	Waveguide array with specified phases	Waveguide array
Generation efficiency (%)	70	60	55
Performance achieved in 2008	22 MW/3 s	3 MW/360 s	1 MW/800 s

[a] *NTM* neoclassical tearing modes

Upper hybrid resonance

The upper hybrid resonance frequency is

$$\omega_U \equiv (\omega_{pe}^2 + \omega_{ce}^2)^{\frac{1}{2}} \tag{5.35}$$

This frequency is used less than other resonances, because it is very high.

For example, in a deuterium plasma with $n = 10^{20}$ m^{-3} and $B = 5$ T, these frequencies are $f_{ce} = 140$ GHz, $f_{ci} = 38$ MHz, $f_{LH} = 1.25$ GHz, and $f_U = 166$ GHz.

Electromagnetic waves may undergo mode conversion (transformation to another type of plasma wave) in the plasma. The wave energy may be absorbed by Landau damping (in which particles gain energy from the wave, like a surfer on an ocean wave) or other processes. Then collisions between particles thermalize the energy, raising the plasma temperature.

Examples of wave heating systems applicable to ITER are listed in Table 5.4.

Wave heating methods are discussed by Wesson (2011) and by Kikuchi et al. (2012).

5.8 Ion Cyclotron Resonance Heating

The Ion Cyclotron Resonance Heating (ICRH) method is also called "Ion cyclotron range of frequencies" (ICRF), since the frequencies used may vary from the exact cyclotron frequency.
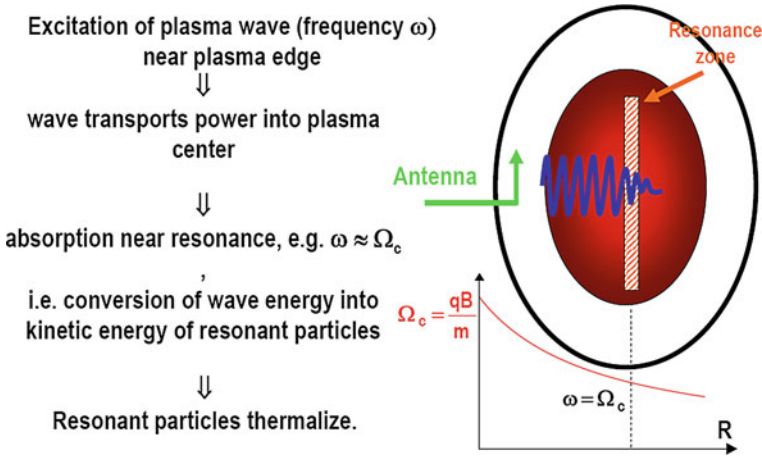
Fig. 5.25 Location of resonance zone at a specific magnetic field and radius R (Laqua 2008)

Based on Eq. (2.8) the toroidal magnetic field in a tokamak varies as

$$B(R) = B_o R_o / R \tag{5.36}$$

where B_o is the magnetic field at the plasma axis R_o. Each value of radius has a value of B corresponding to a specific cyclotron resonance frequency. By choosing the generator frequency we can choose the radius where the ion cyclotron resonance occurs, hence the radius where the ICR heating occurs. Other resonances, like ECR, can also be aligned to specific plasma locations. This is illustrated in Fig. 5.25.

5.8.1 Propagation and Coupling

There are two modes of propagation: the "slow wave" and the "fast wave". The slow wave requires a complex antenna to facilitate launching and penetration. The fast wave decays as $\exp(-2 k_\parallel x)$, where x is the distance from the antenna to the cutoff layer and $k_\parallel$ is the parallel wave number component parallel to the magnetic field. If the antenna size is $>4\pi x$, then most of the wave energy penetrates through the cutoff layer (Sheffield 1994).

If several percent of protons are present in a deuterium plasma, these protons can absorb the heating at their cyclotron frequency and transfer it collisionally to the deuterons and electrons. ^{3}He ions are also used for this "minority heating" process. At higher minority concentrations part of the wave energy may be coupled to Bernstein electrostatic waves and absorbed by collisionless Landau damping (Wesson 2011).

Wave energy can also be absorbed at harmonics of ω_{ci} (ω_{ci}, $2\omega_{ci}$, $3\omega_{ci}$, …). Second harmonic heating can yield temperatures >10 keV in large tokamaks.
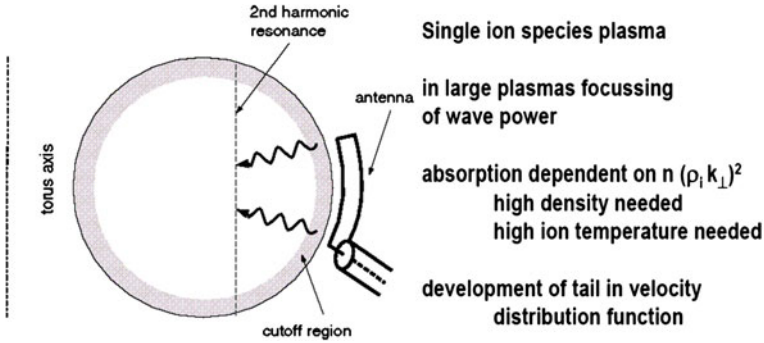
Fig. 5.26 Second harmonic ICRH in ITER. Here ρ_i represents the ion cyclotron radius (Laqua 2008)

High voltage breakdown must be avoided in the transmission line, vacuum window, and antenna. The radiofrequency voltages expected at high power are on the order of 30 kV. Cool plasma near the antenna may short out the antenna voltage, and arcs may develop at joints, windows, in waveguides, etc. The generators must be rapidly switched off if an arc persists for more than one cycle, to avoid damage to equipment. In a reactor environment, radiation damage to rf antennas may be severe.

One heating method in ITER can be at the ion cyclotron resonance second harmonic, as shown in Fig. 5.26.

5.8.2 ICRF Generators and Transmission Lines

A 2 MW radiofrequency generator is shown in Fig. 5.27.

Figure 5.28 shows the ASDEX Upgrade power transport system with large coaxial transmission lines. The matching network needs to adjust the wave phase in order to minimize reflection and losses along the transmission line and to try to match the impedance to the load.

The Tore Supra tokamak (R = 2.4 m, a = 0.8 m, B = 4.5 T) has sustained 1 MA plasma current for 30 s using 6 MW ICRH plus 3.4 MW LHCD (Bucalossi 2010).

5.8.3 Antennas

A widely used antenna design is a strap antenna behind a Faraday cage screen, Fig. 5.29. Radiofrequency current oscillates back and forth in the strap antenna, inducing an electromagnetic wave that propagates towards the plasma. The Faraday screen helps separate the high electric field of the antenna from the plasma, reducing
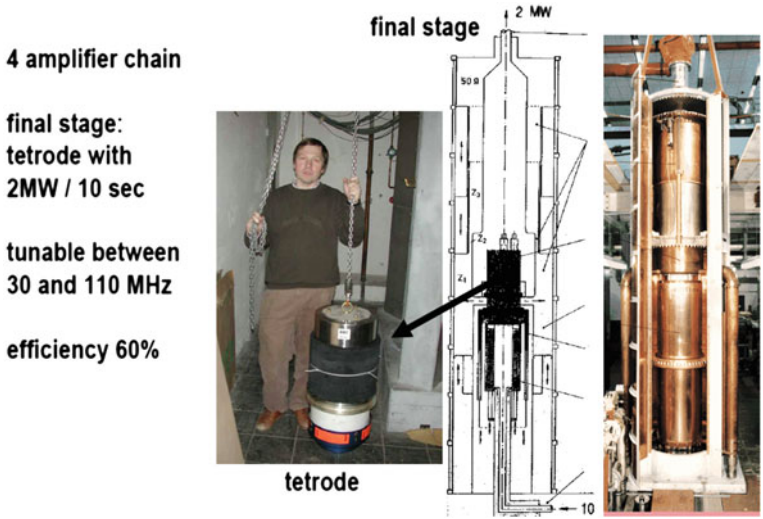
Fig. 5.27 A 2 MW tetrode generator for ICRH (Laqua 2008)
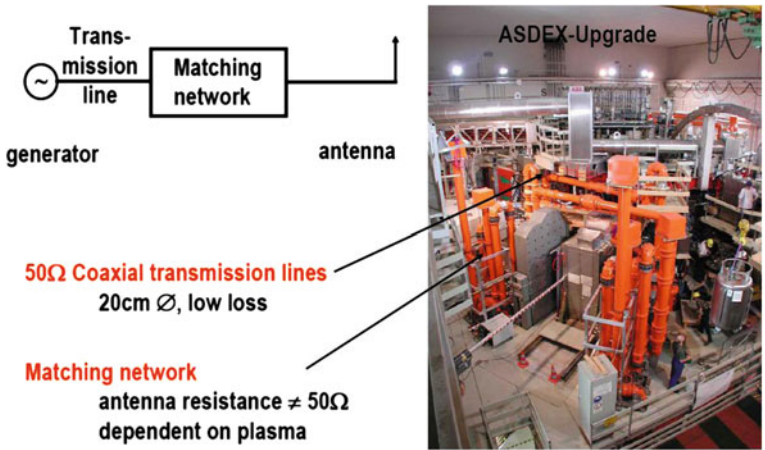
Fig. 5.28 The ITER ICRH power transport system (Laqua 2008)

arcing and sputtering. The antenna must be close to the plasma, because there is usually a thin "cutoff" region near the wall through which wave penetration is difficult. Close to the antenna the fields are stronger and penetration is more probable, but sputtered impurities from the antenna can cause problems, such as arcing.

The ITER ICRH antenna system is shown in Fig. 5.30.

This is similar to the antenna of the Joint European Torus (JET), Fig. 5.31.

The impedances of the coaxial lines and antennas are carefully designed to minimize power losses and to maximize the efficiency of energy transfer to the plasma.
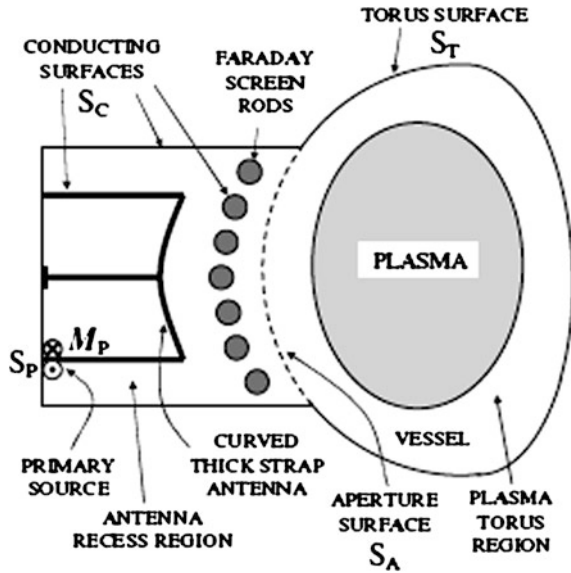
Fig. 5.29 Schematic sectional view of a typical ICRF antenna (Lancellotti et al. 2006, Fig. 1)
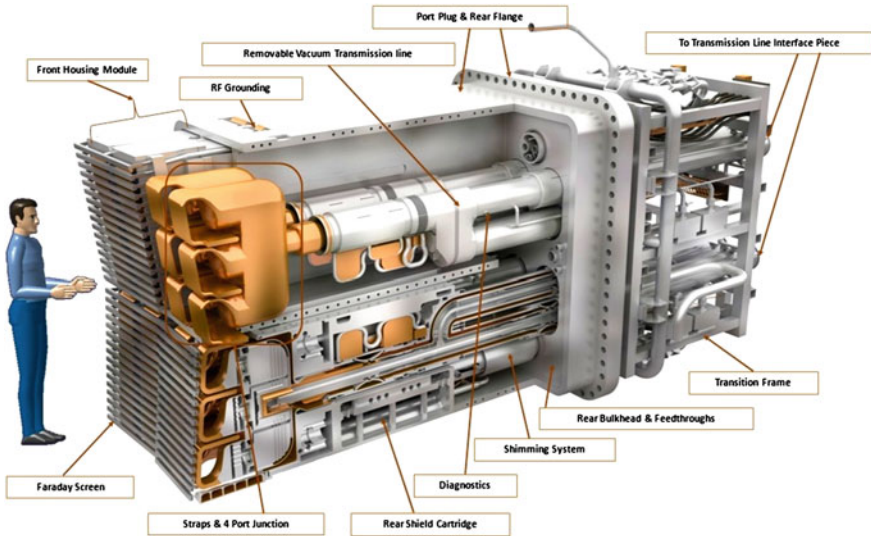
Fig. 5.30 The ITER ion cyclotron resonance heating and current drive antenna. Courtesy of ITER Organization
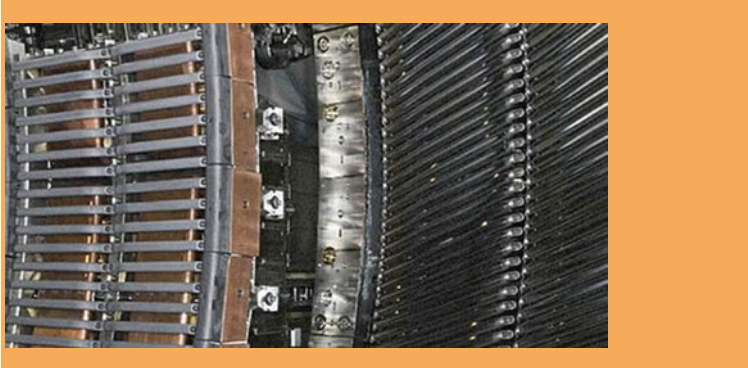
Fig. 5.31 Ion cyclotron antennae at JET. *Vertical* copper straps are visible behind the *horizontal* Faraday screen bars. Image supplied courtesy of Culham Publication Services, copyright EURATOM

A study of tungsten sputtering from ICRF antennas in ASDEX-Upgrade finds that the sputtering can be reduced by

- Increasing plasma–antenna clearance;
- Strong gas puffing;
- Decreasing the intrinsic light impurity content (mainly oxygen and carbon);
- Extending the antenna box and structures parallel to the magnetic field;
- Increasing the number of toroidally distributed straps;
- Better balance of (0π)-phased contributions to RF image currents (Bobkov et al. 2010).

Studies of ICRF antenna designs aim to reduce the rf sheath potential and sputtering of the antenna surface, which shortens its lifetime and adds impurities to the plasma (Mendes et al. 2010). The ITER ICRH antenna designs are being studied with complex computer models (Messiaen et al. 2010; Milanesio et al. 2010).

Heating and current drive with the "high harmonic fast wave" in the National Spherical Torus Experiment (NSTX) were improved when the plasma density was reduced near the antenna, such as by coating nearby vessel surfaces with lithium to reduce plasma density near the antenna (Phillips et al. 2009; Taylor et al. 2010).

ICRH waves can provide strong central heating with high efficiency and low cost, but their use for current drive is less promising.

5.9 Electron Cyclotron Heating

5.9.1 Wave Propagation

By adjusting the wave frequency to a specific magnetic field value, the Electron Cyclotron Heating (ECH) system can deposit energy at a specified radius R. This

Reflection at cut-off region

electron cyclotron resonance

wave guide

Dispersion

$$\omega^2 = k^2 c^2 + \omega_p^2$$

Density gradient leads to diffraction away from plasma center.

torus axis

mirror

cutoff region

ne
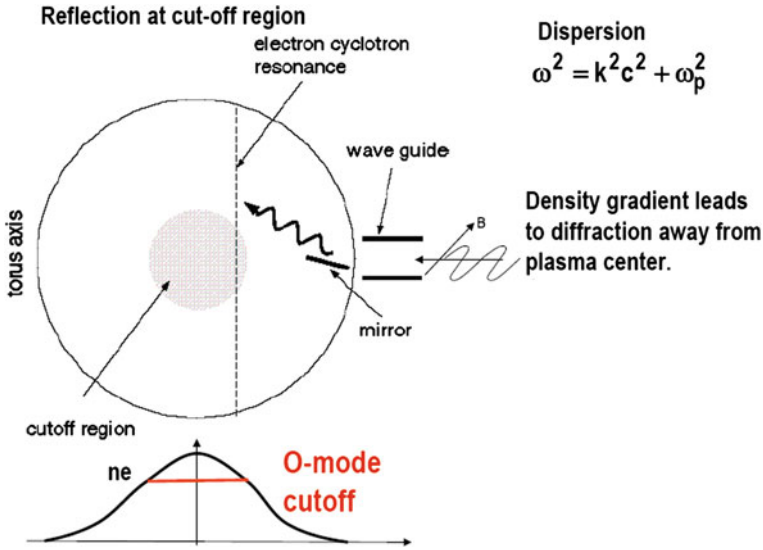
O-mode cutoff

Fig. 5.32 Cutoff of the O-mode in the high density region (Laqua 2008)

spatial selectivity helps control the plasma profiles and current drive, which can help maintain good plasma stability and energy confinement. ECH can also be effective at the second harmonic.

The ECH microwave beam can be transmitted through air, which allows the source to be far from the plasma, simplifying maintenance. The ITER design includes the development of a 1 MW gyrotron operating at 170 GHz with a pulse duration of more than 500 s.

Vacuum windows will be placed outside of the neutron shielding. Alloys retaining high electrical conductivity after neutron bombardment will be used for components requiring good electrical conductivity, such as waveguides. Waveguides will have several bends to reduce neutron streaming.

The "ordinary mode" (O mode) wave has a cutoff (k → 0) where $\omega = \omega_{pe}$, so the wave will be reflected where the plasma density is high enough for this match to occur, as illustrated in Fig. 5.32.

In this example case the O mode cannot penetrate into the high density plasma near the axis, and the density gradient tends to diffract the wave away from the high density region. The extraordinary mode (X-mode) has different propagation, as shown in Fig. 5.33.

Figure 5.34 shows a more complex phenomenon. The O-mode (red curve) propagates to a cutoff, where it is converted into an X-mode (green curve), which then converts into a Bernstein wave, which is finally absorbed at the cyclotron resonance.
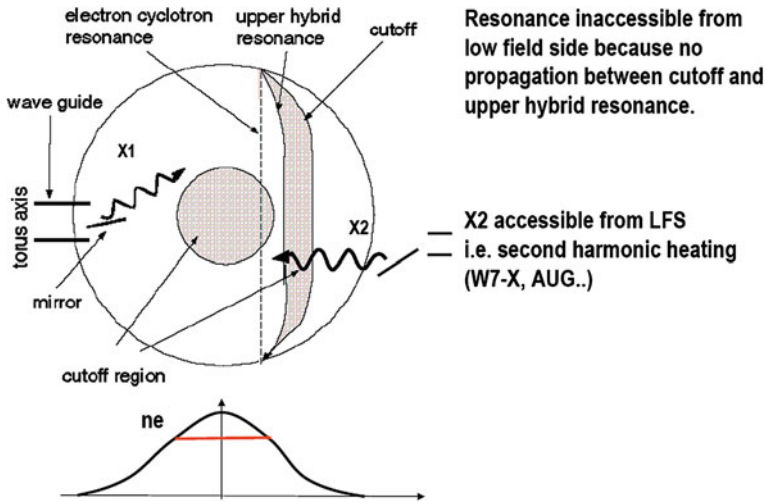
Fig. 5.33 Propagation of the X-mode from the high field side (*left side*) and from the low field side. The cutoff prevents propagation from the low field side to the resonance. The resonance can be reached from the high field side or by use of the second harmonic (Laqua 2008)
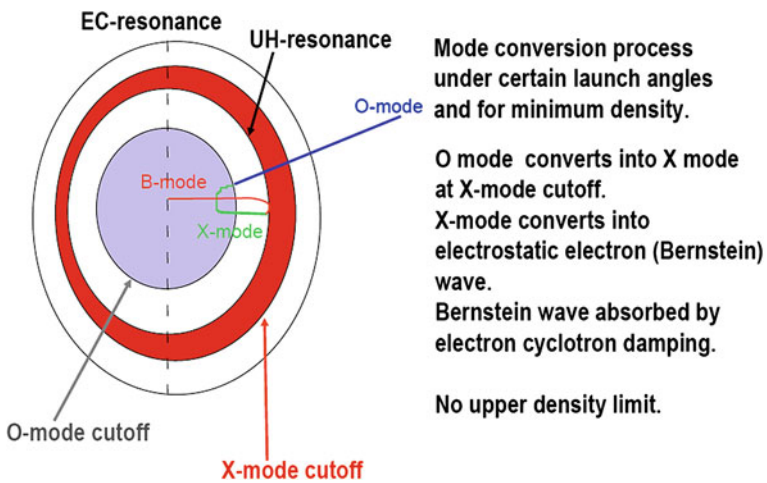
Fig. 5.34 Mode conversion of O-mode to X-mode to Bernstein wave, followed by absorption at the cyclotron resonance (Laqua 2008)

5.9.2 Heating and NTM Suppression

Figure 5.35 shows how choice of the resonance layer affects the electron temperature profile Te(r) in a stellarator.

Fig. 5.35 Effect of ECRH resonance position on $T_e(r)$ in a stellarator. When the resonance is at the plasma center the profile is peaked. When the resonance is at $r/a = 0.37$ the profile is flat, almost hollow (Laqua 2008)
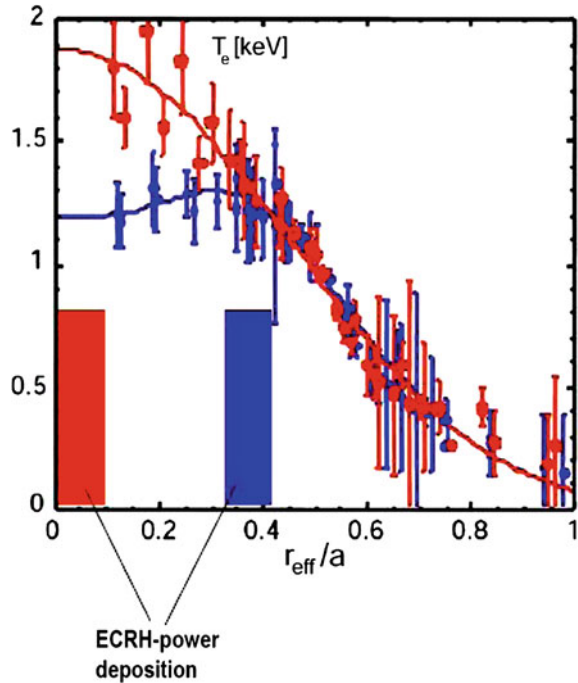
Neoclassical tearing modes (NTMs) involve the growth of "magnetic islands", which deteriorate confinement. Application of ECCD and heating at the island location can help alleviate this instability. This is illustrated in Fig. 5.36.
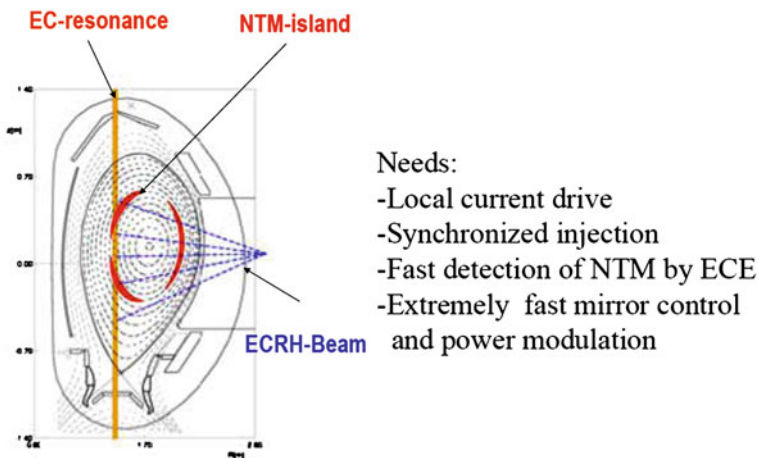
Fig. 5.36 Application of ECRH near the neoclassical tearing mode (*NTM*) island radius to suppress the instability. Here *ECE* means an electron cyclotron emission diagnostic, which measures the $T_e(r)$ (Laqua 2008)

ECCD has been used to suppress the NTM instability in JT-60U, and it is more effective when the microwaves are modulated (Isayama et al. 2009).

5.9.3 Wave Generation

Figures 5.37 and 5.38 show a 1 MW gyrotron developed for ECRH in the W7-X stellarator at Greifswald, Germany.

Similar gyrotrons at a higher frequency (170 GHz) are under development for ITER.

Fig. 5.37 A 1 MW 140 GHz gyrotron for the W7-X stellarator. An electron gun at the *bottom shoots* an annular (cylindrical) electron beam *upwards* through the resonator, where the magnetic field causes it to oscillate, giving up some kinetic energy to the wave before being stopped at the collector. The microwave beam is reflected by mirrors and then exits through the diamond window (Laqua 2008)
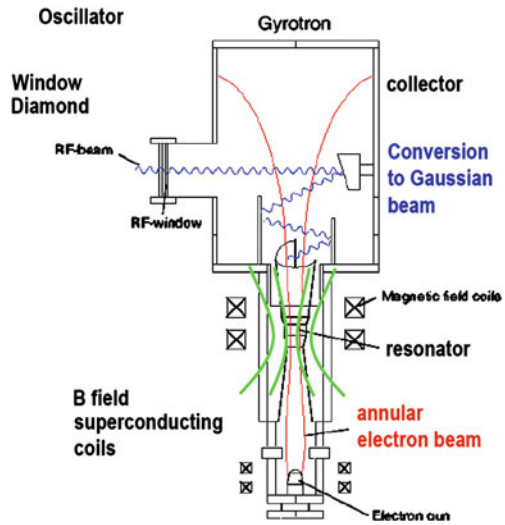
Fig. 5.38 Photograph of the W7-X gyrotron (Laqua 2008)
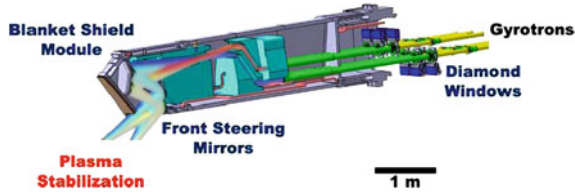
Fig. 5.39 ECH launchers for ITER (Strauss 2010)
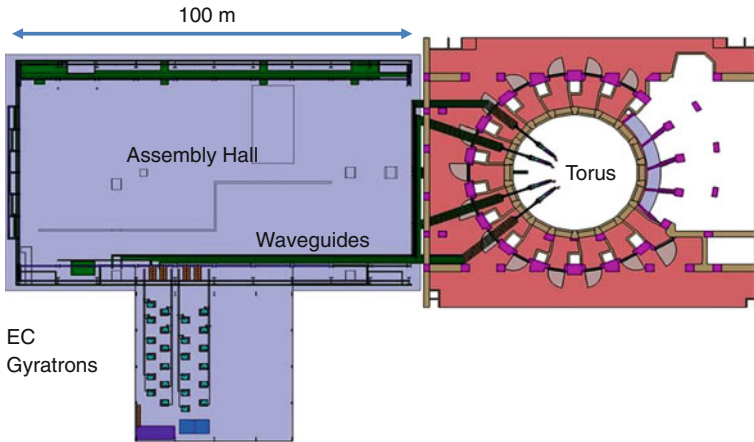
Fig. 5.40 Conceptual layout of the ITER tokamak hall, assembly hall, and ECH power supply building. Courtesy of ITER Organization

5.9.4 Transmission and Launching

ECH launchers with steerable mirrors are shown in Fig. 5.39.

Diamond windows are used because of their low power absorption and high thermal conductivity. The zigzag path reduces neutron streaming.

Figure 5.40 shows the ITER EC building next to the assembly hall and tokamak.

A series of international workshops have been conducted on ECH (Prater 2011).

5.10 Lower Hybrid Waves

The JET lower hybrid current drive (LHCD) system is shown in Fig. 5.41.

The klystrons generate the waves, and the circulators permit them to pass in the forward direction only, preventing reflected waves from damaging the klystrons.
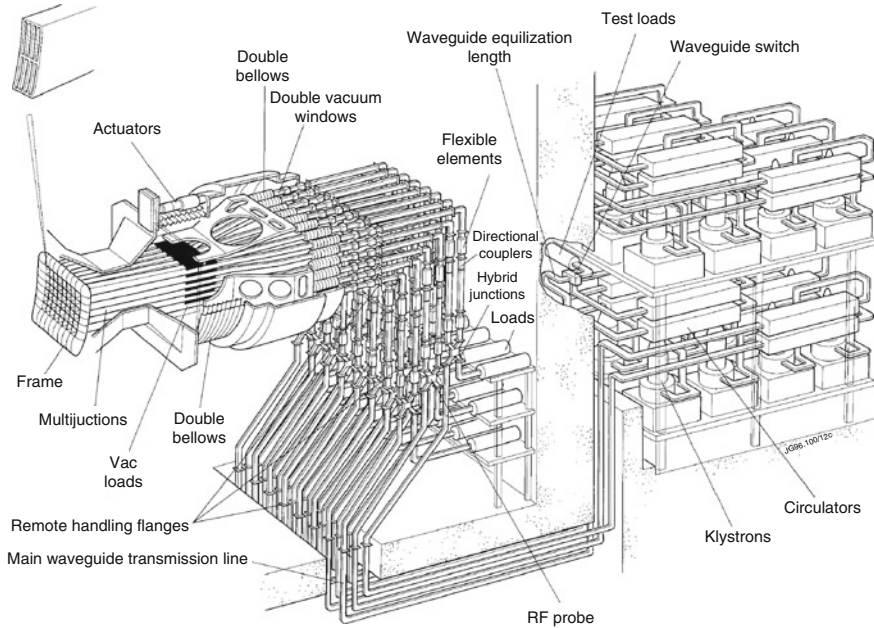
Fig. 5.41 Major components of the JET LHCD system (Jacquinot et al. 2008, Fig. 19)

Waveguides transmit the waves through couplers that adjust the wave parameters for maximum efficiency of coupling to the desired plasma modes. Windows isolate the klystrons from the plasma. Actuators adjust the position of the waveguide frame, which is mounted on double bellows for flexibility. The vacuum loads facilitate testing the system when no plasma is present.

The waveguide grill launches the waves to travel along the magnetic field as shown in Fig. 5.42.

The lower hybrid waveguide grill used in the ASDEX tokamak is shown in Fig. 5.43.

Some problems associated with electromagnetic wave heating are:

- Radiofrequency voltages can be as high as 30 kV, need to avoid breakdown.
- Plasma contact with antennas can lead to arcing.
- In case of a breakdown rapid shutoff of generators is required.
- Radiation damage to antennas can be severe.
- Vacuum windows should withstand high power fluxes without cracking.
- Waveguide bends are needed to reduce neutron streaming.

Electromagnetic wave heating offers some advantages in comparison with neutral beam heating:

- The problems of unwanted neutral gas inflow and the requirement for huge cryopumps are eliminated.
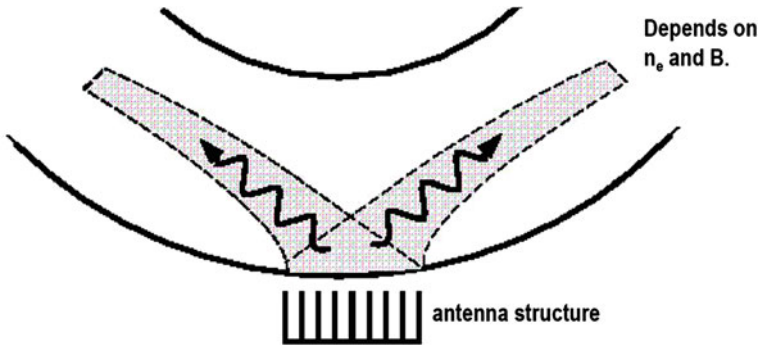
Fig. 5.42 Lower hybrid waves launched along the magnetic field (Laqua 2008)

Fig. 5.43 The ASDEX lower hybrid waveguide grill (Laqua 2008)
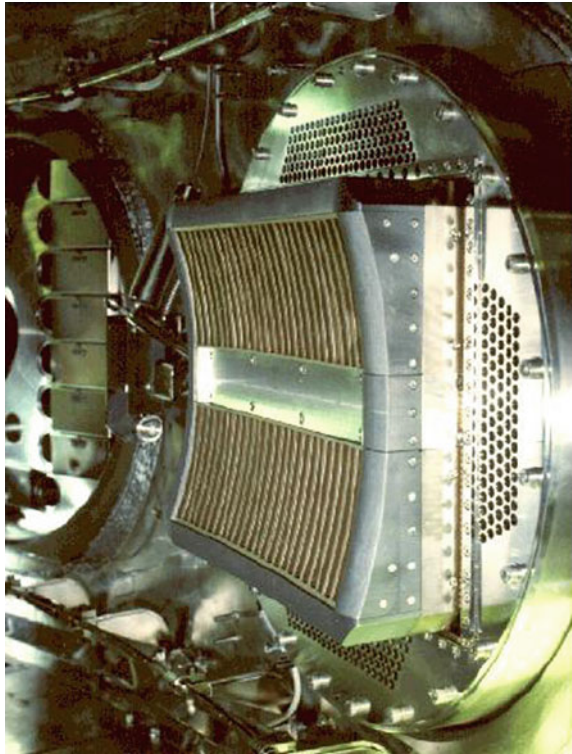
- The large neutral beam lines are replaced by smaller rf coaxial lines or wave-guides, permitting easier access to the torus for maintenance.
- Capital costs of rf heating are lower.

Table 5.5 Approximate efficiencies of some wave generating systems for large tokamaks and stellarators (B $\sim$ 3–6 T, n $\sim$ 10^{20} m^{-3})

System	Electrical efficiency (%)	Remarks
1 MeV NBI	30	Reliability and cost issues
ICRF	70	Relatively inexpensive, reliable
ECRH	40	Effective, but expensive
Lower hybrid	70	Relatively inexpensive

By "efficiencies" of wave generating systems we mean (wave power generated) / (input electrical power). Table 5.5 compares the efficiencies of some wave generating systems for plasma heating.

Portions of the generated wave power are lost in transmission, penetration, coupling, and absorption (Fig. 5.23), so the actual heating power is less than the generated power, and the net heating efficiency is lower than the generation efficiency.

5.11 Current Drive and Profile Control

5.11.1 Steady State Operation

Steady state operation of a fusion reactor is very desirable, in order to avoid:

- Downtime that reduces plant availability and profits
- Fluctuations in electrical power available to the grid that must be compensated by other sources or by energy storage systems
- Temperature changes of coolant and structure that cause thermal stresses and fatigue
- Pulsing the ohmic heating coils, causing structural fatigue
- Eddy current losses that require additional refrigeration
- The need to restart the plasma and ramp up its current periodically, with possible influx of impurities or plasma disruptions.

Some methods of plasma current drive in toroidal systems are

- Magnetic Induction.
- Neutral beam injection.
- Lower hybrid resonance.
- Electron cyclotron resonance.
- Ion cyclotron resonance.
- Alpha particle "channeling".
- Helicity injection by electrodes or by sinusoidal induction.

The current density of electrons with velocity distribution function f(v) is

$$J = e \int dv \, f(v) v \tag{5.37}$$

where e = electronic charge. If the distribution function is symmetric about v = 0, then J = 0. Thus, the problem of electron current drive is to create an **asymmetric** distribution function. If the electrons were monoenergetic, then the electron current density would be

$$J = -nev \tag{5.38}$$

where n = electron density, e = electronic charge.

5.11.2 Bootstrap Current

The name "bootstrap current" refers to an English saying about "lifting oneself up by one's bootstraps" (which would normally be impossible). This current is induced by outward diffusion of plasma in the "banana regime" (high T_e, low collision frequency). The magnitude of the toroidal bootstrap current is approximately

$$J_b = (a/R_o)^{1/2} [2.44(T_e + T_i)(dn/dr) + 0.69n(dT_e/dr) - 0.42n(dT_i/dr)]/B_\theta \; (A/m^2) \tag{5.39}$$

where B_θ = poloidal magnetic field, a = minor radius, R_o = major radius, n = plasma density (m^{-3}), and T_e and T_i are the electron and ion temperatures (J) (Wesson 2011). Fueling by pellet injection can provide a good source of fuel ions in the core plasma to maintain the density gradient dn/dr. If fueling were only by cold neutral gas at the plasma edge, then the bootstrap effect would be reduced.

For low-aspect-ratio tokamaks ($R_o/a \sim 1.5$) most of the particles are trapped, and a simpler estimate may be used:

$$J_b = -(dp/dr)/ \, B_\theta \tag{5.40}$$

where p = plasma pressure. For example, if n = 10^{20} m^{-3} and $T_e = T_i = 10$ keV, then the pressure 2nT = 0.3 MPa. If this decreased linearly over a meter and $B_\theta = 0.3$ T, then $J_b \approx 1$ MA/m^2.

Using a large-volume plasma close to the wall for stability, JT-60U achieved a bootstrap current fraction of 92 % at an edge safety factor $q_{95} = 5.6$, with plasma density 87 % of the "Greenwald limit" (Sakamoto et al. 2009).

ITER operating scenarios to achieve high f_b are under study.

5.11.3 Lower Hybrid Current Drive

Lower Hybrid Current Drive (LHCD) is an effective non-inductive way of driving a strong toroidal current in a tokamak. The resonance condition is
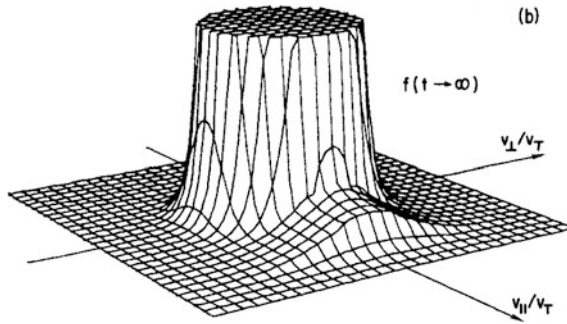
Fig. 5.44 Contours of steady-state electron velocity distribution f when lower-hybrid waves are injected with parallel-phase velocities between 3 and 5 times the thermal velocity v_T. In this picture the surface is truncated at low speeds. Reprinted with permission from Karney and Fisch (1979), © 1979 The American Institute of Physics

$$\omega - k_{ll}v_{ll} - n\omega_{ce} = 0 \qquad (5.41)$$

where ω = wave frequency (rad/s), k_{ll} = wave vector component along B, v_{ll} = component of electron velocity along B, ω_{ce} = electron cyclotron frequency, and n is the mode number (not the electron density). For lower hybrid waves n = 0, and the wave travels parallel to B.

Current lasts longer when it is carried by electrons with lower collision frequencies, meaning higher energy electrons, since the collision frequency is proportional to v^{-3}, where v is the relative velocity of colliding particles.

In a tokamak magnetically trapped electrons and ions do not carry toroidal current, so energy that they absorb does not contribute to current drive.

Figure 5.44 shows the velocity distribution function of electrons heated by LHCD, with parallel phase velocities 3–5 times the thermal speed v_T. The asymmetry of the distribution function produces current drive. By convention the direction of the current is opposite to the direction of electron flow, as can be seen from the minus sign in Eq. (5.38).

One measure of the efficiency of current drive is the ratio of current driven to the input power Pd. For LHCD it is given approximately by

$$I/P \approx \left(v_{ph}/v_T\right)^2[T_{10}/(30R_o n_{20})] \text{ A/W} \qquad (5.42)$$

where $v_{ph} = \omega/k$ = wave phase velocity,

$$v_T = (kT/m_e)^{1/2} \qquad (5.43)$$

is the electron thermal speed, T_{10} is the electron temperature in tens of keV, R_o is the plasma major radius (m), and n_{20} is the plasma density in units of 10^{20} m^{-3} (Fisch 1987).

For example, if ITER had $(v_{ph}/v_T)^2 \approx 20$, $T_{10} = 1$, $n_{20} = 1$, and $R_o = 6$ m, then $I/P \approx (1/9)$ A/W. If the entire 15MA current were to be provided by LHCD, the required microwave power would be 135 MW. The situation could be improved if much of the current were provided by the bootstrap effect, and if we operated at higher temperature and lower density.

For temperatures in the range $1 < T_{10} < 3$, the ratio of radiofrequency (rf) power to fusion thermal power is estimated to be approximately

$$P_{rf}/P_f \approx 15 / \left[(J/P_d)(n_{20}T_{10}aR_o)^{1/2}(3T_{10} - 2) \right] \qquad (5.44)$$

where $J/P_d \approx 30$ is a current drive efficiency parameter, and a = plasma minor radius = 2 m for ITER (Fisch 1987). For a reactor with typical ITER parameters ($T_{10} = 1$, $n_{20} = 1$, a = 2 m, and $R_o = 6$ m), this yields $P_{rf}/P_f \approx 0.14$. If ITER generated 400 MW thermal power and it were converted at 40 % efficiency to electricity, the gross electrical power would be 160 MWe. The required $P_{rf} = 0.14 \times 400 = 56$ MW. If this were generated at 60 % efficiency, the required electrical power would be 93 MW, so the recirculating power fraction would be $93/160 = 58$ %. Such a high recirculating power fraction would be unacceptable for an economical power plant. It is not proposed to build a power plant with ITER parameters, but this illustrates the problem of the recirculating power required for current drive, even at high efficiency (60 % assumed here).

Not all the rf power leaving the antenna or waveguide is absorbed usefully by the plasma.

- The incident waves may be scattered by edge plasma turbulence
- They may be reflected by a plasma cutoff
- Their direction may be bent by the plasma ("ray tracing" computer codes calculate the paths of the incident waves)
- They may be transformed into other types of waves ("mode conversion"). Mode conversion can be helpful by aiding penetration into the plasma or harmful by preventing the desired absorption mechanism
- They may be absorbed by a less desirable resonance.

Thus, the wave power finally absorbed for current drive will be less than the power provided by the generator.

When a tokamak plasma is started inductively and then LHCD is applied, the LHCD reduces the measured loop voltage. In some cases the plasma current may be wholly sustained by the LHCD, and the inductive current drive may be turned off (the ohmic heating coil current may be turned off or kept constant).

The "electron runaway velocity" v_R is the velocity above which the electric field force is greater than the retarding force of collisions, and the electrons continuously accelerate to higher velocities. Its magnitude is approximately

$$v_R \approx [m\Gamma/eE]^{1/2} \qquad (5.45)$$

where e = electron charge, E = electric field, and

$$\Gamma = ne^4 \ln\Lambda / 4\pi\varepsilon_o^2 m^2 \qquad (5.46)$$

represents a retarding force due to collisions, n = electron density, $\ln\Lambda$ = "Coulomb logarithm" ($\ln\Lambda \sim 18$, also called L elsewhere), and ε_o = permittivity of free space. When the electric field is strong or the collision rate is weak, then v_R is low and runaway occurs easily.

Electrons with $v/v_T < 1$ are in the bulk plasma and have high collision frequencies. Electrons with $v/v_T \gg 1$ have very low collision frequencies. If we induce a current in the bulk plasma, it is quickly dissipated by collisions, but if we induce current in high energy electrons, the current tends to persist longer, so it is advantageous for current drive to push the fast electrons. This can be done by adjusting the LHCD wave phase velocity:

$$v_{ph}/v_T \sim 3 \text{ to } 5$$

The efficiency of generating lower hybrid waves can be ~ 70 %, and they can be efficiently transmitted by waveguides to a grill in the torus wall where they are launched with specified phase. The fraction of the wall surface required for the waveguides can be reasonably small, and the waveguides can have bends to minimize neutron streaming. A window is needed between the wave generator and the transmission waveguide, which can carry power fluxes ~ 20 MW/m^2. In order for the waves to penetrate adequately to the plasma center their parallel phase velocity should satisfy

$$\omega/k_{\parallel}c < 1/[1 + 15\beta/T_{10}] \qquad (5.47)$$

where $\beta = 2\mu_o p/B^2$, and p = plasma pressure. If T = 10 keV and $\beta = 0.04$, then $\omega/k_{\parallel}c < 0.62$. For DT reactors with $T_{10} \sim 1$ to 2 the wave parallel phase velocity should be

$$\omega/k_{\parallel} \sim 4.5 \ v_T$$

which corresponds to resonant electrons with energies ~ 100 keV (Fisch 1987). The current drive efficiency is then

$$I/P \approx (0.6/n_{20}R_o) [1 + (T_{10} - 1)/3] \text{ A/W} \qquad (5.48)$$

For example, if $T_{10} = 1$, $n_{20} = 1$, and $R_o = 6$ m, then I/P = 0.1 A/W.

LHCD has sustained the plasma current in the TRIAM-1 M superconducting tokamak for 2 h, and driven up to 3 MA in the JT-60 tokamak (Fisch 2000).

LH waves are very good at generating off-axis current drive, which is beneficial for tailoring the current density profile J(r) and the safety factor profile q(r).

LHCD in Alcator C-Mod has demonstrated current drive efficiency I/P $\approx$ 0.25/ n_{20}R (A/W), consistent with expectations. During LHCD the core current (r/a < 0.44) drops and the edge current (r/a > 0.44) increases (Wilson et al. 2009).
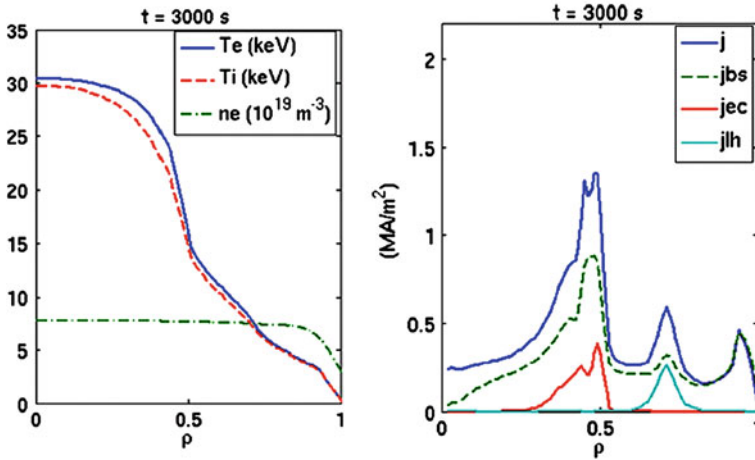
Fig. 5.45 Radial profiles of plasma temperatures and density and of current density components *jbs* (bootstrap current), *jec* (ECCD), *jlh* (LHCD) and *j* (total) in ITER for the conditions cited above (Hoang et al. 2009)

LHCD was applied to JET at 3.7 GHz with power typically modulated between 0.5 and 3 MW at 41.67 Hz. As the plasma density is increased the LHCD waves were absorbed at larger radii until a significant portion of the power was lost outside the plasma (Kirov et al. 2010).

A 20 MW, 5 GHz LHCD system for ITER is under design, but funding for its implementation is not yet allocated. The computer simulations predict fully RF steady-state $Q \sim 7$ plasmas lasting 3,000 s (non-inductive fraction ~ 97 %, resistive loop voltage ~ 2 mV) using 21 MW of ECCD power, 20 MW of ICRF power and 12 MW of LH power, as illustrated in Fig. 5.45. LHCD can provide the required off-axis current at $r/a \sim 0.7$, while ECCD helps to sustain an internal transport barrier position at $r/a \sim 0.5$ (Hoang et al. 2009).

Computer simulations indicate that loss of LH wave power to alpha particles would be negligible (Schneider et al. 2009).

Very high levels of LHCD can trigger plasma instabilities, such as the "fishbone mode" (Cesario et al. 2009). LHCD produces hot electrons at large radii, which can limit penetration of injected fuel pellets (Budny 2010).

Some current drive can also be accomplished by ECRH, ICRH, and NBI. A combination of several techniques can be used to achieve some control over the current density profile, which could help to sustain an "internal transport barrier" (Wesson 2011).

5.11.4 Electron Cyclotron Current Drive

LHCD drives parallel fluxes and Electron Cyclotron Current Drive (ECCD) drives perpendicular fluxes. Electron cyclotron heating increases $v_\perp$, leaving $v_{\parallel}$ relatively unchanged, and it can be done for electrons with high $v_{\parallel}$. As the microwaves enter the torus from the low-field side (large R) they pass through an increasing B and ω_{ce}. The electrons are resonant with the wave at the radius where

$$k_{\parallel} v_{\parallel} = \omega - \omega_{ce}(R) \tag{5.49}$$

If the microwaves are injected from the high-field side (small R), they pass through a decreasing B and ω_{ce}.

If the microwaves are tuned to heat electrons with positive $v_{\parallel}$, their increased perpendicular energies decreases their collision frequencies, which means that they slow down more gradually than electrons with the same magnitude of $v_{\parallel}$ but negative sign, which are not so heated. This makes the electron distribution function anisotropic in the parallel direction, creating an effective plasma current.

ECCD in JET at 170 GHz (2nd harmonic) has achieved efficiencies of 3–6 kA/MW at $n \approx 5 \times 10^{19}$ m^{-3} and confirmed that the current drive efficiency is inversely proportional to plasma density (Farina and Figini 2010).

5.11.5 Neutral Beam Current Drive

A neutral beam injected into a tokamak becomes ionized and trapped. The trapped ions moving in the toroidal direction provide a toroidal current density. However, electrons pulled along by the ions may neutralize this current. Then the whole plasma would rotate, but with very little current density.

One way to maintain the ion current density would be to retard the electron flow, or to use two different ion charge states. For example if a beam He^{++} (charge state $Z_b = 2$) ions were injected into a D$^+$ plasma ($Z_i = 1$), the pull on the electrons is proportional to Z^2, while the current is proportional to Z, so electrons would be pulled more strongly by the He^{++} ions, and a net current could be generated (Fisch 1987). Some of the background electrons are trapped in "banana orbits" and cannot go all the way around in the toroidal direction to neutralize the ion flow.

An approximate estimate of neutral beam current drive efficiency is

$$I/P \approx (0.6T_{10}/n_{20}R_o)[(1/Z_b) - (1/Z_i)] \text{ A/W} \tag{5.50}$$

where Z_b is the charge state of the ionized beam and Z_i is the charge state of the background plasma ions (Fisch 1987). This equation would imply no current drive if $Z_b = Z_i$. For the ITER example, If $T_{10} = 1$, $n_{20} = 1$, $R_o = 6$, $Z_b = 2$, and $Z_i = 1$, then $I/P \approx -0.05$ A/W. (The negative sign indicates net current flow opposite to the beam direction.) If we wanted to drive 15 MA entirely by neutral beams, then the

required beam power would be 15/0.05 = 300 MW. If the efficiency of the neutral beam generator were 50 %, then the required electrical power to drive the current would be 600 MW, an impractical amount. The situation could be somewhat ameliorated by using higher temperature, lower density, and higher Z_b.

NBI can be aimed radially inwards, toroidally parallel to current density (co-injection), toroidally opposite to the current density direction (counter injection), or at any toroidal direction in between. The poloidal angle can also be controlled during design. The beam energy can be chosen to match the desired penetration depth. The angles and energy afford some control over heat deposition profile, current drive profile, poloidal rotation, toroidal rotation, and particle flow. These functions cannot be controlled independently, however, so it is necessary to focus on one or two that are most important, without causing harmful effects, such as instabilities. For example, if current drive were most important, then co-injection would be chosen at optimum depth and angles.

Figures 5.46 and 5.47 show a case where off-axis NBI was used in JT-60U to establish an internal transport barrier. This case has B = 4.4 T, I = 2.6 MA, NBI power = 15 MW, $n_o T_{io} \tau_E = 8.6 \times 10^{20}$ m^{-3} keV s, which corresponds to $Q_{DT} = 1.25$, but the configuration disrupted, due to low-n, ideal kink-ballooning modes.

When the ITB is established the ion temperature rises in about 0.6 ms, and the negative toroidal rotation velocity also increases.

NBI often causes toroidal plasma rotation. A "critical energy" W_{crit} is defined to be the energy at which beam energy losses to electrons and ions are equal. If the beam energy in the rotating frame $W \gg W_{crit}$, then plasma rotation will have little effect on the driven current. If $W \sim W_{crit}$, however, plasma rotation can reduce the current drive significantly, especially if the rotation velocity $v_\phi \geq 0.05 \, (2W_{crit}/M)^{1/2}$, where M = beam ion mass (Cottrell and Kemp 2009).

The neutral beam injector height and direction have a strong effect on the resulting profiles of current density and safety factor q in ITER simulations (Budny 2010).

Some problems of neutral beam current drive are

- High power required.
- High voltage breakdown.
- Lifetime of electrodes.
- Neutral gas in injection ports.
- Very high vacuum pumping speeds, large cryopanels and refrigeration systems required.
- Limited tunabililty of beam parameters (energy, current, direction).
- Neutron streaming out beam ports and activating the whole beamline. (Bends to attenuate neutrons are not feasible).
- Reliability and maintenance of radioactive NBI systems.
- Cost.

In view of these issues it would be good if DEMO could work without requiring NBI.

Fig. 5.46 Profiles of density, temperatures, and safety factor in JT-60U with an ITB established by off-axis NBI (Ishida and JT-60 Team 1999)
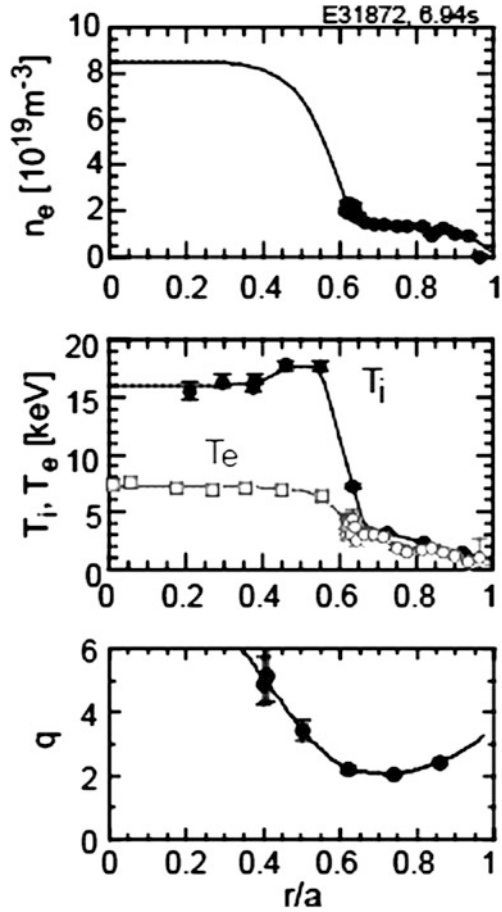
5.11.6 ICRF Current Drive

Some current might be driven by ICRF heating, but it is less promising for ITER than current drive by LHCD, ECCD, and NBI (Budny 2010). Current drive by ICRF waves is discussed in Chap. 6 of Kikuchi et al. (2012).

5.11.7 Alpha Particle Channeling

The goal is for the 3.5 MeV alpha particles to transfer their energy to drive plasma current. The alpha particle gyrofrequency is

$$\Omega = 2eB/M \ (rad/s) \tag{5.51}$$

Fig. 5.47 Variation of ion temperature profile and rotation velocity profile during establishment of the ITB of the previous figure (Koide et al. 1995)
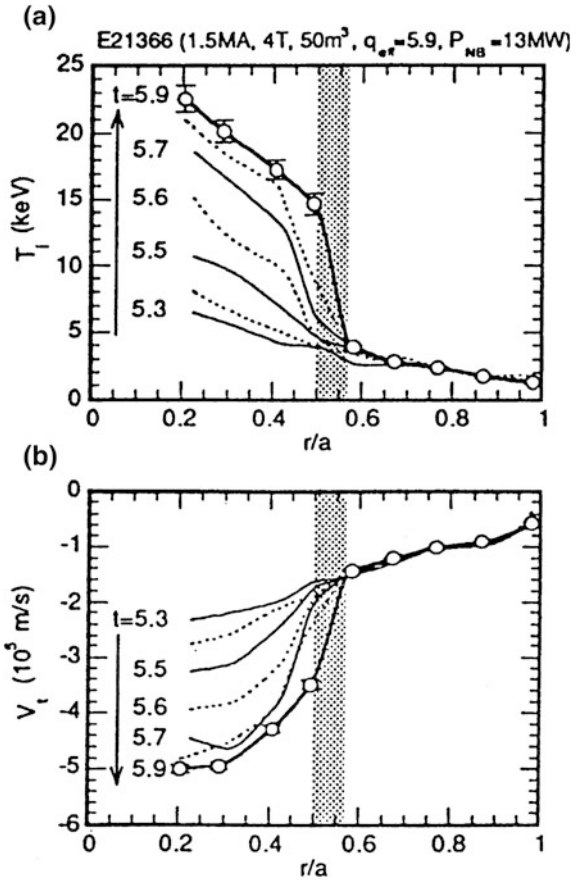
where M = alpha particle mass. For example, if B = 5 T, then $\Omega = 2.4 \times 10^5$ rad/s. The interactions are described in terms of three parameters that tend to remain constant in the absence of collisions or interactions with waves:

$$\mu = mv_\perp^2/2B \ = \text{"magnetic moment"} \tag{5.52}$$

$$\varepsilon = \mu B + mv_\parallel^2/2 = \text{kinetic energy} \tag{5.53}$$

$$P_\phi = R(mB_\phi v_\parallel/B - eA_\phi) = \text{canonical angular momentum} \tag{5.54}$$

For current drive to occur the invariance of the magnetic moment can be broken by interaction with an ion Bernstein wave (IBW) that is externally generated. The $k_\parallel$ of the launched IBW changes sign at the "mode conversion layer", which

facilitates extraction of energy from the alpha particles. Then the alpha particle can diffuse perpendicular to B by interaction with a second wave, such as a toroidal Alfven eigenmode (TAE) wave, while losing energy to that wave.

The induced waves and collisionless slowing down of alpha particles (called "alpha channeling") could induce an electronic current in the plasma. Experimental data from the TFTR experiment indicate that the perpendicular diffusion rate was much faster than predicted by simple quasi-linear theory (Fisch 2000).

5.11.8 Helicity Injection

By definition the helicity K in a volume bounded by a magnetic surface is

$$K = \int dV \mathbf{A} \cdot \mathbf{B} \tag{5.55}$$

where B is the magnetic field, A is the magnetic vector potential satisfying $\mathbf{B} = \nabla \times \mathbf{A}$, and dV is a volume element. Plasmas tend to conserve helicity while relaxing to a minimum energy state. Helicity injection induces current flow in the plasma. The rate of change of helicity is described by

$$\partial K / \partial t + \nabla \cdot \mathbf{Q} = -2\eta \mathbf{J} \cdot \mathbf{B} \tag{5.56}$$

where the helicity flux is

$$\mathbf{Q} = \mathbf{B}\Phi_{el} + \mathbf{E} \times \mathbf{A} \tag{5.57}$$

Φ_{el} = electric potential, $\mathbf{E}$ = electric field, $\mathbf{J}$ = inductive current density, and η = plasma resistivity. Helicity can be injected by passing an electric current along a magnetic flux surface, and it is dissipated (lost) by ohmic heating. If we apply a voltage V around a toroidal loop the helicity injection rate is

$$\partial K / \partial t = 2V\Phi_T \tag{5.58}$$

where Φ_T is the toroidal magnetic flux. A similar equation applies to a poloidal loop and poloidal flux. Bellan (2006) discusses the mathematical and topological aspects of magnetic helicity.

Helicity has been injected into small toroidal devices by applying a voltage to electrodes in the poloidal direction, resulting in poloidal current flow that evolved into toroidal current flow as the plasma adjusted towards a minimum energy state.

Coaxial helicity injection (CHI) has been used in the National Spherical Torus Experiment (NSTX). The method is shown in Fig. 5.48.

The divertor coils generate a magnetic flux Φ_T (blue circle). The capacitor bank voltage V drives current along this field in the counterclockwise direction (big orange arrow). This voltage and flux produce the $\partial K / \partial t = 2 V\Phi_T$ term that injects helicity. The $J_{pol} \times B_{tor}$ force pushes plasma upwards, and magnetic reconnection results in a toroidal plasma current.
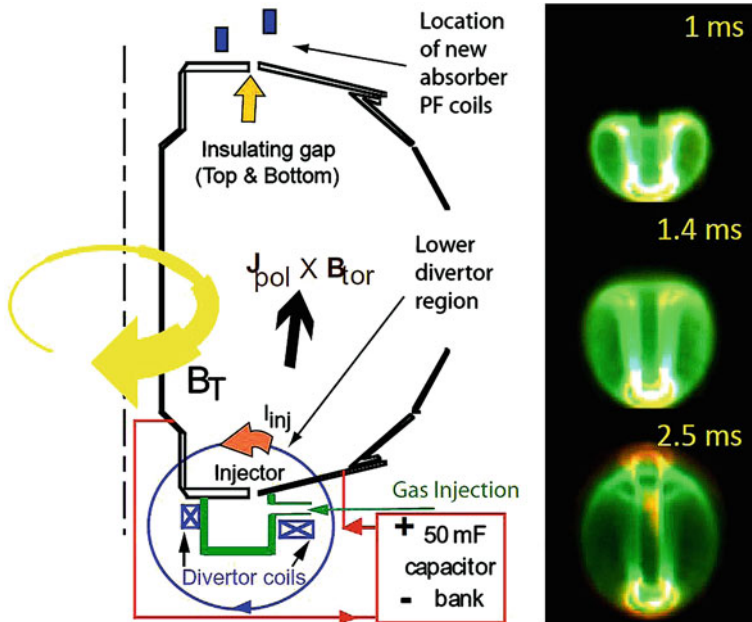
Fig. 5.48 a On the *left*, is a *line drawing* showing the main components in NSTX required for plasma startup using the CHI method. *Top-right* **b** fast camera fish-eye image of the plasma during the early phase of plasma growth at the *bottom* and **c** later in time after the CHI started discharge has filled the vessel. The *vertical black post* in the center contains both poloidal and toroidal field coils (Raman et al. 2009)

There are five requirements for success of this CHI method:

- Capacitor bank energy must be sufficient to generate a current that can "break the bubble" and inject plasma upwards.
- The voltage must be high enough that the plasma fills the chamber quickly.
- The capacitor bank energy must be sufficient to fully ionize and heat all the injected gas.
- The maximum plasma current I that can be generated is limited by $\frac{1}{2}LI^2 < \frac{1}{2}CV^2$ where L = plasma inductance, C = capacitance, V = capacitor voltage.
- The "footprints" of the divertor flux on the electrodes must be sufficiently narrow (controlled by coil and electrode design).

An injector current of below 10 kA has induced a plasma current up to 300 kA, with an amplification factor over 50. In some experiments CHI drove toroidal currents ∼300 kA, which were then ramped up to higher currents using the ohmic heating transformer. For success of the ramp-up the radiated power must be kept below the input power, or else an additional heating method is needed. Additional heating by ECRH can ionize low-Z impurities, reducing plasma resistivity and
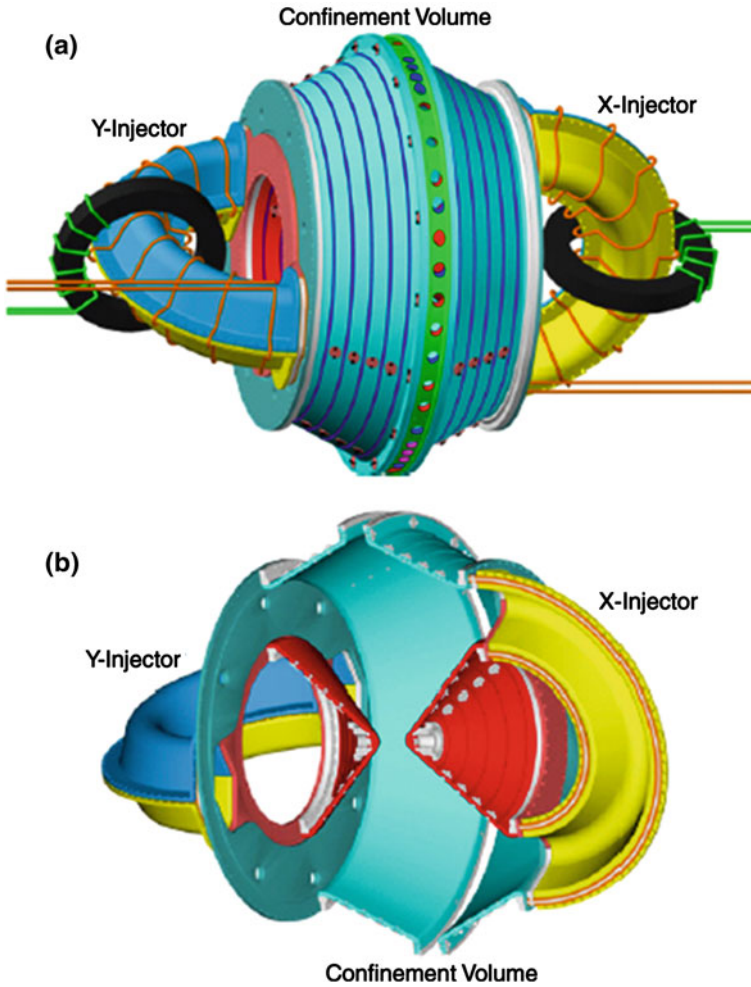
Fig. 5.49 The HIT-SI device consists of two semi-toroidal injectors attached to a central confinement volume. **a** Injector loop voltage coils are shown in *green* with the injector flux coils shown in *orange*. Solid transformer coils are only depicted for loop voltage circuit clarity, as in reality air-core transformers are used. Thin *lavender* rings identify several of the axial flux loops used to measure the total toroidal current. **b** A cutaway of the HIT-SI vacuum vessel from the X-injector to the Y-injector annulus, making evident the bow-tie cross section of the confinement volume (viewing angle slightly rotated) (Ennis 2010)

increasing plasma current. The NSTX-Upgrade experiment should achieve non-inductively driven currents over 0.5 MA (Raman et al. 2009, 2011).

The Helicity Injected Torus-Steady Inductive (HIT-SI) experiment, Fig. 5.49, consists of a toroidal confinement volume with two external loops, the X-injector and the Y-injector. Each injector has toroidal field coils producing flux Φ_T and a ring-shaped inductor that generates a sinusoidal voltage V. The voltage along the

toroidal flux causes sinusoidal helicity injection $\partial K/\partial t = 2\ V\Phi_T$. The X and Y injectors are 90° out of phase, so that the total helicity injection rate is proportional to $\sin^2\theta + \cos^2\theta = 1$, hence constant.

The width and outer radius of the flux-conserver chamber are each <0.6 m, and the minor radii of the injectors are ~ 0.1 m. Using injector voltages ~ 300–450 V modulated at 5.8 kHz with 6 MW power input they achieved formation of a spheromak plasma with toroidal plasma current >30 kA and poloidal flux 6 times larger than the injector flux. When the spheromak flux was lost into the metallic walls, the current direction flipped (Ennis et al. 2010). This experiment is very small, so plasma-wall interactions and impurities make it difficult to sustain the plasma. A much larger experiment is needed to adequately test this concept (Jarboe et al. 2012) (See also Sect. 1.3.4).

5.12 Summary

Compression is not used in tokamaks and stellarators, but is a key feature of magnetized target fusion.

Ohmic heating is inherent in tokamaks, which must have a strong toroidal current, but not in stellarators, which do not require a plasma current for equilibrium. Ohmic heating is usually insufficient to ignite a tokamak, so auxiliary heating methods are needed.

If non-inductive current drive can be successful, then the central solenoid should be avoided. The absence of a central solenoid would facilitate lower aspect ratio, higher beta, and higher power density at a given magnetic field. The ability to start up a tokamak non-inductively is under study in several experiments, such as NSTX, which has achieved 300 kA toroidal current.

Neutral beam injection current drive is valuable for heating and for profile control at modest density. The injector is complex and expensive, requiring very high vacuum pumping speed, and the large port permits neutron streaming, creating shielding problems. High voltage injectors (1 MeV) using negative ion beams are under development for ITER.

ICRH is relatively inexpensive, with well-developed components. It provides efficient heating, but not strong current drive. Plasma-antenna interactions can lead to plasma impurities.

ECRH is very effective and helps control profiles of electron temperature and current density. Long-pulse, high-power generators (1 MW) are under development for ITER.

LHCD is effective and can help with profile control. It works best at low density.

Coaxial helicity injection in NSTX has achieved toroidal currents over 50 times the injector current. The HIT-SI device uses sinusoidally-pulsed magnet coils to induce the required voltage and flux in external loops, without using electrodes, which could release impurities, but it needs to be tested in a larger experiment.

Table 5.6 Summary of heating/current drive methods. Based partly on (Laqua 2008)

Method	Heating	Current drive	Disadvantages
Alpha heating	Excellent	Maybe by channeling	Need to exhaust He ash
Ohmic	Simple, good for startup	Effective at T < 1 keV	Pulsed only, ineffective at high T, uses central solenoid coil
Compression	Effective heating	Not used for current drive	Uses too much plasma volume, pulsed, fatigue problems
NBI	Effective, controls rotation, can be somewhat localized for profile control	Effective at low n	Ineffective at high n, complex, requires 1 MeV negative ion beams, reliability problems, expensive
ICRH	Effective, central heating, inexpensive	Low effectiveness	Plasma-antenna interactions can damage antenna and yield impurities
ECRH	Effective, can be localized for profile control	Effective, can help control current density profile	Expensive, heats only electrons
LH	Effective, can be localized for profile control	Good at low n, most effective	Waveguide close to plasma can cause impurity injection, not good at high n
Helicity injection	Gives rise to some Ohmic heating	Useful for startup and sustainment	Plasma contact with electrodes injects impurities (avoided in HIT-SI experiment which uses sinusoidal inductive helicity injection)

Plasma heating methods are summarized in Table 5.6.

With any tokamak current drive system it will be important to attain a high **bootstrap current** fraction. We should use methods that couple effectively to the plasma, attain high efficiency of generation and transmission, and are affordable; supplemented by modest amounts of less efficient and more expensive systems as needed for profile control. If high input power is required for current drive, then the attainable Q value of the ignited tokamak could be uneconomically low.

5.13 Problems

5.1. Estimate the ohmic heating power per unit volume in a tokamak plasma where $J_\parallel = 10^6$ A/m^2, n = 5×10^{19} m^{-3}, and B = 4 T, (a) if $T_e = 0.2$ keV, (b) if $T_e = 2$ keV.

5.2. A cylindrical low-beta plasma is compressed radially by tripling B. Initially $T_\parallel = T_\perp = 1$ keV. What are the final temperatures (a) if the plasma is collisionless, (b) if collisions are dominant?

5.3. A collisional, cylindrical, high-beta plasma is compressed radially by tripling B. By what factor does the temperature increase?

5.4. A collisional, low-beta, toroidal plasma is compressed by decreasing the major radius to 80 % of its original value, with B_o constant. By what factor does the temperature increase?

5.5. Assume that a plasma gun uses electrical energy from a 20 kJ capacitor bank to inject a plasma blob of 10^{18} ions with $T_i = 0.8$ keV, $T_e = 0.1$ keV. What is the efficiency = (plasma energy output)/(electrical energy input) of this heating device?

5.6. Estimate the required deuterium atom beam energy for effective penetration into a DT plasma with $n = 2 \times 10^{20}$ m^{-3}, $T_e = 10$ keV, and a = 2 m. What are the neutralization efficiencies of D^+ and D^- beams at this energy?

5.7. Consider a laboratory plasma experiment with $B_{max} = 0.5$ T, $n = 3 \times 10^{18}$ m^{-3}. If you have generators at 1 MHz, 100 MHz, and 10 GHz available, what means might be used to couple the energy to the plasma?

5.8. Assume that ITER generates 400 MW steady state thermal power. Assume that I/P = 0.1 A/W for LHCD and 0.05 A/W for NBI. If the bootstrap current fraction is 64 %, and the remaining current is to be driven half by LH, and half by NBI, what is the maximum value of Q that could be attained, ignoring other input powers?

5.14 Review Questions

1. Why does ohmic heating fail at high temperatures?
2. What phenomena can increase plasma resistivity?
3. What causes electron runaway, and why is it undesirable?
4. Why will plasma compression not be used on large tokamaks?
5. Why is charged particle injection not used in tokamaks?
6. Can plasma guns be used to heat a tokamak plasma? If so, how does it work?
7. About how much penetration is desired for neutral beam injection to be effective?
8. Sketch a neutral beam injector and explain how it works.
9. Why are negative ion beams used for high energy neutral beam injectors?
10. What energy neutral beam injection will be used for heating in ITER?
11. What are the stages of wave heating, beginning with generation?
12. Why should a waveguide have several bends in it?
13. What is a "second harmonic resonance"?
14. How are radiofrequency waves transmitted and coupled to the plasma?
15. How are microwaves transmitted and coupled to the plasma?
16. How can sputtering from ICRF antennas be reduced?
17. How can the growth of magnetic islands be reduced?

18. Name two advantages of wave heating in comparison with neutral beam injection.
19. Under what conditions can a bootstrap current be generated? About what fraction of the total plasma current has been driven by this method in experiments?
20. What kind of fueling can help promote the bootstrap current?
21. Approximately what value to I/P (A/W) can be achieved for an ITER example case by LHCD? By NBI?
22. What phenomenon is described by the equation $\partial K/\partial t = 2\, V\Phi_T$?
23. How can helicity injection be done experimentally? What are the general requirements for capacitor bank voltage and energy?
24. What is the advantage of the HIT-SI experiment?

References

Alexeff I (1975) A theoretical predication of the observed plasma heating in the compression experiment at Ito's group at Osaka University, IEEE Trans Plasma Sci PS-3, 15–17

Badger B et al (1979) NUWMAK, A tokamak reactor design study. University of Wisconsin Report UWFDM-330

Bellan PM (2006) Fundamentals of plasma physics. Cambridge University Press

Bobkov V et al (2010) Assessment of compatibility of ICRF antenna operation with full W wall in ASDEX Upgrade. Nucl Fusion 50:035004, (11 pp)

Bostick WH, Prior W, Grunberger L, Emmert G (1966) Pair production of plasma vortices. Phys Fluids 9:2078

Bucalossi J (2010) Tore Supra, Towards steady-state tokamak operation, Karlsruhe International School on Fusion Technologies September 6–17

Budny RV (2010) Current control in ITER steady state plasmas with neutral beam steering. Phys Plasmas 17:042506

Cesario R et al (2009) Lower hybrid wave produced supra-thermal electrons and fishbone-like instability in FTU. Nucl Fusion 49:075034 (7 pp)

Chen FF (1984) Introduction to plasma physics and controlled fusion, vol 1. Plasma physics. Springer

Colas L et al (2006) Key results of long pulse ICRH operation in Tore Supra. Nucl Fusion 46:S500–S513

Cottrell GA, Kemp R (2009) Effect of plasma rotation on the beam-driven current. Nucl Fusion 49:042001 (5 pp)

Day I, Surrey E, Jones T, Ciric D, Stork D (2010) Introduction to neutral beam injection technology. Karlsruhe International School on Fusion Technologies, 7 Sept 2010

De Lazzari D, Westerhof E (2010) On the merits of heating and current drive for tearing mode stabilization. Nucl Fusion 49:075002 (8 pp), and Erratum (2010) Nucl Fusion 50:079801 (2 pp)

Dolan TJ (1982) Fusion research. Pergamon Press, Elmsford, NY

Ennis DA et al (2010) New understandings and achievements from independent-injector drive experiments on HIT-SI. Nucl Fusion 50:072001 (4 pp)

Farina D, Figini L (2010) Investigation of electron cyclotron wave absorption and current drive in JET. Nucl Fusion 50:095007

Fisch NJ (1987) Theory of current drive in plasmas. Rev Mod Phys 58:175–234

Fisch NJ (1993) Review of current drive theory: selected topics. Plasma Phys Controlled Fusion 35:A91–A104

Fisch NJ (2000) Physics of alpha channeling and related TFTR experiments. Nucl Fusion 40:1095–1100

Fukumoto N, Ogawa H, Nagata M, Uyama T, Shibata T, Kashiwa Y, Kusama Y (2004) Characteristics of modified CT injector for JFT-2 M. Fusion Eng Des 70:289–297

Goldston RJ, Rutherford PH (1995) Introduction to plasma physics. Taylor and Francis, London

Hoang GT et al (2009) A lower hybrid current drive system for ITER. Nucl Fusion 49:075001 (11 pp)

Houlberg WA, Mense AT, Attenberger SE (1980) Neutral beam energy and power requirements for expanding radius and full bore startup of tokamak reactors. Nucl Fusion 20:811–820

Isayama A et al (2009) Neoclassical tearing mode control using electron cyclotron current drive and magnetic island evolution in JT-60U. Nucl Fusion 49:055006 (9 pp)

Ishida S, JT-60 Team (1999) JT-60U high performance regimes. Nucl Fusion 39:1211 (Fig. 4)

Jacquinot J et al (2008) JET mission and highlights during 1978—1999. Fusion Sci Technol 53:887 (Figure 19. Copyright by the American Nuclear Society, LaGrange Park, Illinois, USA)

Jacquinot J et al (2009) Progress on the heating and current drive systems for ITER. In: Proceeding of the 25th symposium on fusion technology (SOFT-25). Fusion Engineering and Design, vol 84, pp 125–130

Jarboe TR, Victor BS, Nelson BA, Hansen CJ, Akcay C, Ennis DA, Hicks NK, Hossack AC, Marklin GJ, Smith RJ (2012) Imposed dynamo current drive. Nucl Fusion 52:083017 (9 pp)

Karney CFF, Fisch NJ (1979) Numerical studies of current generation by radio-frequency traveling waves, Phys Fluids 22:1817

Kikuchi M, Lackner K, Tran MQ (2012) Fusion Physics, International Atomic Energy Agency, Vienna, Austria

Kirov JK et al (2010) LH power deposition and CD efficiency studies by application of modulated power at JET. Nucl Fusion 50:075003 (17 pp) doi:10.1088/0029-5515/50/7/075003

Koide Y, Ishida S, Kikuchi M, Mori M, Tsuji S, Nishitani T, Kawano Y, Hatae T, Fujita T, Ozeki T, Shirai H, Kamada Y, Yoshino R, Ninomiya H, Azumi M, JT-60 Team (1995) Improved confinement and transport barrier in the JT-60U high β_p H mode. International atomic energy agency, plasma physics and controlled nuclear fusion research 1994. In: Proceedings of the fifteenth international conference on plasma physics and controlled nuclear fusion research held by the International Atomic Energy Agency in Seville, 26 Sept–1 Oct 1994, vol 1. IAEA, Vienna, 1995, paper IAEA-CN-60/A2-3 (Fig. 6)

Lancellotti V et al (2006) TOPICA: an accurate and efficient numerical tool for analysis and design of ICRF antennas. Nucl Fusion 46:S476–S499

Laqua H (2008) Plasma waves and RF-plasma heating. Summer School on Fusion Technology, Karlsruhe Institute of Technology, Germany

Litvak A, Sakamoto K, Thumm M (2011) Innovation on high-power long-pulse gyrotrons. Plasma Phys Controlled Fusion 53:124002 (14 pp)

Mendes A et al (2010) Reduction of RF-sheaths potentials by compensation or suppression of parallel RF currents on ICRF antennas. Nucl Fusion 50:025021 (17 pp)

Messiaen A et al (2010) Performance of the ITER ICRH system as expected from TOPICA and ANTITER II modeling. Nucl Fusion 50:025026 (21 pp)

Messiaen A, Vervier M, Dumortier P, Lamalle P, Louche F (2006) Study of the ITER ICRH system with external matching by means of a mock-up loaded by a variable water load. Nucl Fusion 46:S514–S539

Milanesio D et al (2010) ITER ICRF antenna analysis and optimization using the TOPICA code. Nucl Fusion 50:025007 (10 pp)

Perkins LJ, Ho SK, Hammer JH (1988) Deep penetration fueling of reactor grade tokamak plasmas with accelerated compact toroids. Nucl Fusion 28:1365

Phillips CK et al (2009) Spectral effects on fast wave core heating and current drive. Nucl Fusion 49:075015 (8 pp)

Portone A et al (2008) ITER TF coil ripple: Evaluation of ripple attenuation using Fe insert and of ripple enhancement produced by TBM. Fusion Eng Des 83:1619–1624

Prater R (2011) Electron cyclotron emission and electron cyclotron resonance heating (EC-16). In: Proceedings of th 16th joint workshop. World Scientific, Singapore

Raman R (2006) Advanced fueling system for use as a burn control tool in a burning plasma device. Fusion Sci Technol 50:84

Raman R (2008) Advanced fueling system for ITER. Fusion Eng Des 83:1368–1374

Raman R et al (1993) Design of the compact toroid fueler for center-fueling-Tokamak-de-Varennes. Fusion Technol 24:239–250

Raman R et al (1994) Experimental demonstration of non disruptive, central FUELING of a Tokamak by compact toroid injection. Phys Rev Lett 73:3101

Raman R, Martin F, Haddad E, St-Onge M, Abel G, Côté C, Richard N, Blanchard N, Mai HH, Quirion B, Lachambre J-L, Gauvreau J-L, Pacher GW, Décoste R, Gierszewski PJ, Hwang DQ, Hirose A, Savoie S, Leblanc B-J, Mclean H, Xiao C, Stansfield BL, Côté A, Michaud D, Chartre M (1997) Experimental demonstration of tokamak fuelling by compact toroid injection. Nucl Fusion 37:967–972

Raman R et al (2009) Solenoid-free plasma startup in NSTX using transient CHI. Nucl Fusion 49:065006 (6 pp)

Raman R, Mueller D, Jarboe TR, Nelson BA, Bel MG, Gerhardt S, LeBlanc B, Menard J, Ono M, Roquemore L, Soukhanovskii V (2011) Experimental demonstration of tokamak inductive flux saving by transient coaxial helicity injection on national spherical torus experiment. Phys Plasmas 18:092504

Sakamoto Y et al (2009) Development of reversed shear plasmas with high bootstrap current fraction towards reactor relevant regime in JT-60U. Nucl Fusion 49:095017 (8 pp)

Schneider M et al (2009) Self-consistent simulations of the interaction between fusion-born alpha particles and lower hybrid waves in ITER. Nucl Fusion 49:125005 (18 pp)

Seidl M (1979) A review of electron-beam heating of magnetic-mirror confined plasmas, with application to the tandem mirror experiment. Lawrence Livermore National Laboratory report UCRL-52759, 10 Apr 1979

Sheffield J (1994) The physics of magnetic fusion reactors. Rev Mod Phys 66:1015

Stix TH (1972) The physics of wave heating. Project Matterhorn report MATT-929

Stix TH (1992) Waves in Plasmas. American Institute of Physics, New York

Strauss ID (2010) ECRH upper port plugs and diamond window technology. In: 4th Karlsruhe international summer school on fusion technologies

Taylor JB (1974) Relaxation of toroidal plasma and generation of reverse magnetic fields. Phys Rev Lett 33:1139–1141

Taylor G et al (2010) Advances in high-harmonic fast wave physics in the national spherical torus experiment. Phys Plasmas 17:056114

Tokamak Fusion Test Reactor Final Design Report (1978) Princeton plasma. Physics Laboratory, report PPPL-1475, Aug 1978

Wagner CE (1981) Possibility of achieving ignition in a high-field ohmically heated tokamak, Phys Rev Lett 46:654–657

Wesson J (2011) Tokamaks, 4th edn. Oxford University Press, Oxford

Wilson JR et al (2009) Lower hybrid heating and current drive on the Alcator C-Mod tokamak. Nucl Fusion 49:115015 (8 pp)

Chapter 6
First Wall, Blanket, and Shield

Thomas J. Dolan, Lester M. Waganer and Mario Merola

Objectives

After reading this chapter one should understand

Materials for high heat fluxes
Materials for breeders, coolants, and structure
Heat transfer and pumping power
Fundamentals of neutronics
Blanket design issues
Energy conversion methods

6.1 Introduction

Figure 6.1 illustrates the main elements of the first wall, blanket, and shield.

The functions of the first wall, blanket, and shield are to absorb the energy generated by fusion reactions and blanket reactions, to transport the heat via a coolant to an energy conversion system, to breed tritium fuel, to control the tritium inventory, and to shield the external subsystems, including the vacuum vessel and magnet coils, from the intense neutron and gamma radiation generated in the

T. J. Dolan (✉)
NPRE Department, University of Illinois, Urbana, IL 61801, USA
e-mail: dolantj@illinois.edu

L. M. Waganer
Fusion Consultant, O Fallon, MO, USA
e-mail: lesw@centurytel.net

M. Merola
ITER Organization, 13115 St Paul Lez Durance, France
e-mail: Mario.Merola@iter.org

Fig. 6.1 The main elements of the first wall, blanket, and shield. The blanket contains lithium and usually neutron multipliers (Be or Pb)
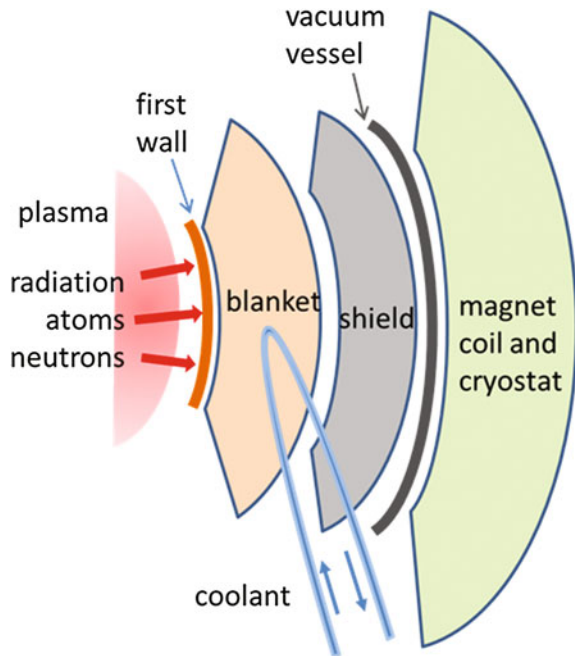
plasma and blanket. Smith et al. (1984) provide a thorough review of blankets, coolants, and shields.

In this chapter we will consider

- Components

  – High heat flux components (HHFC)
  – Breeding materials
  – Coolants
  – Structural materials
  – Shielding

- Calculations

  – Heat transfer
  – Stresses
  – Pumping power
  – Neutronics

- Blanket types

  – Molten salt
  – Ceramic
  – Liquid metal

- Lithium walls
- Energy conversion methods.

6.2 High Heat Flux Components

The ideal fusion reactor first wall and divertor surface materials should have the following capabilities

- Survival under high heat flux and prolonged high temperature operation
- Survival of plasma disruptions and edge localized modes (ELMs)
- Survival of electro-magnetic loads
- Chemical compatibility with coolant
- Reliable welds or joints
- Low sputtering yield
- Sustainment of gravity, atmospheric pressure, coolant pressure, and thermal and mechanical stresses
- Capability to withstand high fluencies of 14-MeV neutrons without failure
- Low tritium trapping
- Low inventories of long-lived radioisotopes
- Wide availability
- Low cost
- Adequate operational lifetime.

Since no known material is wholly suitable, many materials combinations have been studied in order to find a compromise solution.

6.2.1 Heat Fluxes

The ITER divertor may be subjected to steady state heat fluxes up to 20 MW/m^2 for several seconds, and higher values, for a fraction of a second, during vertical displacement events (VDEs), disruptions, and edge localized modes (ELMs). When unstable profiles of p(r) and J(r) develop the plasma may disrupt, dumping hundreds of MJ/m^2 onto the wall or divertor in ms or tens of ms, which can cause melting, splashing, and permanent damage to the surface, shortening its lifetime. For example, a tungsten monoblock was accidentally melted in the C-Mod tokamak (Pitts 2010). Fuel rods in fission reactor cores have lower maximum heat fluxes, around 1.5 MW/m^2. Figure 6.2 shows some anticipated heat loads onto the ITER divertor under various conditions.

Thus, the ITER divertor will be replaced a couple of times during the 20 years of the planned operational life of the machine. The DEMO reactor following ITER (upper right side of Fig. 6.2) must practically eliminate disruptions, VDEs, and large ELMs, to survive for long operational periods.

The heat flux on the ITER divertor is compared with other high heat fluxes in Fig. 6.3.

The design of high heat flux components (HHFC) requires careful selection of materials. HHFC are needed for limiters, wall armor, beam dumps, calorimeters, divertor targets, and direct convertors. Some desirable properties are:

Fig. 6.2 Divertor power flux
and duration of possible
ITER events. *ELMs* edge
localized modes. *VDEs*
vertical displacement events
(Norajitra 2010)
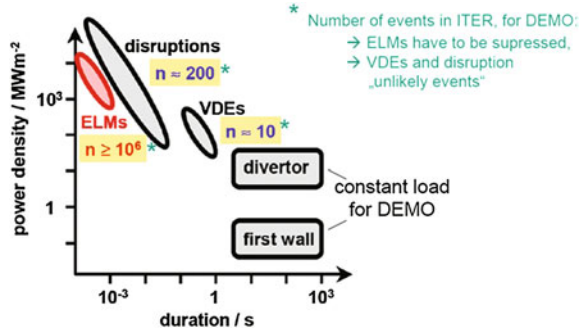
Fig. 6.3 Comparison of
ITER heat fluxes during
normal operation and during
disruptions with heat fluxes
of other devices (Norajitra
2010)
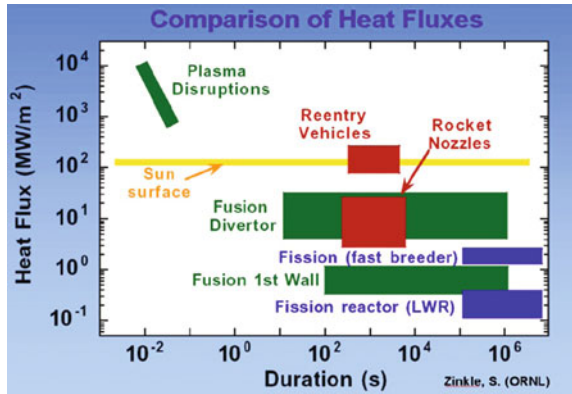
- High melting temperature
- High thermal conductivity
- Good radiation damage resistance
- High heat capacity
- High fracture toughness
- Good adhesion to substrates
- Low ablation rate.

The maximum heat fluxes which various materials can tolerate for a 0.5 s pulse
are shown in Table 6.1.

Thus, graphite has the best thermal shock resistance. Thermal fatigue limits for
multiple pulses are somewhat lower. Other materials under consideration include
Ta–10 % W, TiC, and TiB_2. Ta–10 % W was chosen for the limiter of the Doublet
III tokamak because of its good thermal shock resistance. Although Ta reacts with
hydrogen, it was estimated that these reactions would not be a serious problem for
the anticipated cyclic temperature and alternate vacuum-hydrogen atmospheres.

Tungsten powder can be melted onto a SiC surface using a 300 kW infrared plasma
arc lamp providing 23 MW/m^2 for about 3 s in an argon flow environment. Pre-
liminary heating and deposition enhance the quality of the coating. If the heating time
is too short the tungsten layer is porous, and if it is too long, cracks may form in the SiC

Table 6.1 Thermal shock limits (MW/m^2) of some materials for a 0.5 s pulse, assuming one-dimensional heat flow

Material	Surface melting	Surface cracking
OFHC copper	52	31
Tungsten	94	69
Molybdenum	70	48
Pyrolytic graphite	130	197
ATJ graphite	53	68
Boron carbide	19	3
Silicon carbide	28	3
Aluminum	22	9

From DOE/ET-0032/4 (1978), Table 3.F.2 (Based on work by G. Lewin, J. Schivell, and M. Ulrickson, PPPL)

(Hinoki et al. 2005). Nanoscale powders of SiC (<30 nm) and W can also be bonded by hot pressing at 1,700–1,900 °C and 20 MPa for 10–120 min (Son et al. 2004).

6.2.2 Materials Selection

Some criteria for selecting the ITER divertor target material are:

- Sputtering yield and sputter threshold for impact by D, T, He, Be, C, W, …
- Self-Sputtering
- Structural strength
- Neutron activation
- Tritium retention
- Thermal shock resistance
- Thermal stress figure of merit (high heat conductivity, low thermal expansion, …).

Tungsten is good because of its high melting temperature, low sputtering ratio, and low tritium retention. Carbon fiber composite (CFC) was a candidate for the highest heat flux areas of ITER because of its better thermal shock resistance, but was rejected because of its sputtering yield and tritium retention.

The ITER first wall will experience lower heat fluxes, typically 1–2 MW/m^2 (but up to 5 MW/m^2 in specific areas during start-up and shut-down) than the divertor, so W is not required there. ITER will use Be tiles, because Be is a low atomic number element (which means it produces low radiation losses from Be impurities in the plasma), and it performed satisfactorily in JET. The first wall Be dust is toxic, however, so this health hazard must be controlled.

6.2.3 Armor Tile Configurations

The divertor targets and blanket first wall will have armor tiles of refractory metal or ceramics bonded to a metallic substrate with high thermal conductivity, such as
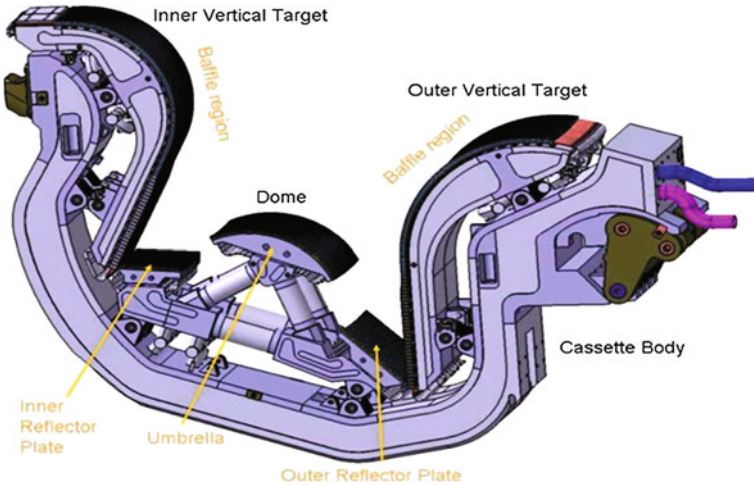
Fig. 6.4 The ITER divertor. Courtesy of ITER Organization

copper alloy. The ITER divertor will use W, Fig. 6.4. The ITER Organization has decided to start operation with a divertor having a full-W armor. The main advantages of this strategy are:

- Gaining operational experience with a W divertor early on and thus influence the design of the second divertor to be procured—a decade after the first one;
- Learn on how to operate with a W divertor already during the non-nuclear phase;
- Reduce manufacturing risks.

There is a small gap between armor tiles to allow for thermal expansion. Ordinarily the plasma streaming in would overheat the "leading edge" of the tiles, see Fig. 6.5. By slanting the tile face slightly, the leading edge can be shielded from bombardment by plasma.

The armor tiles may be bonded to a copper alloy substrate, Fig. 6.6, or formed as monoblocks that surround the coolant tube. The monoblock form has better thermal fatigue performance but more difficult manufacturing than separate tiles. As a consequence, it is used in those areas where the heat flux can exceed 10 MW/m^2, namely most of the divertor surface.

The thermal expansions of Cu alloy and Be are much higher than those of W and carbon fiber composites (CFC):

Cu alloy = 17×10^{-6} K^{-1}
Be = 16×10^{-6} K^{-1}
W = 4×10^{-6} K^{-1}

Fig. 6.5 Slanting the tile faces to shield the leading edges

Plasma hits leading edge with high heat flux

Plasma does not hit leading edge
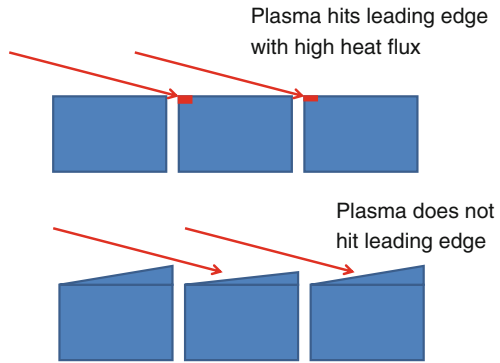
Fig. 6.6 Armor with separate tiles and with monoblocks

W

Cu alloy

water

Separate tile   monoblock
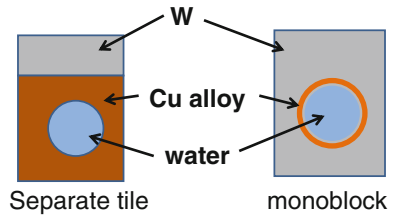
CFC = 1.0×10^{-6} K^{-1}
(Merola 2008).

This difference of thermal expansion can cause failure of joints between the tiles and the copper alloy substrate. A thin, soft layer of pure copper shall be bonded between the W or CFC and the copper alloy, to help compensate for differential thermal expansions.

The use of conventional SS-316 in the ITER divertor structure generates isotopes that make it unsuitable for clearance or recycling, but this limitation does not apply to other future reactors that avoid this alloy.

Since tungsten is very brittle, alloying elements have also been considered to increase its ductility. Of seven candidate tungsten alloys considered for future divertor use the W–La$_2$O$_3$, W–TiC, W–Ta, and W–K alloys have the best potential for *recycling*, close to that of tungsten with nominal impurities, and W–Re is the worst. The elements Fe, Ni, Mn, Nb, and Mo in the alloys tend to produce troublesome radioisotopes. The presence of water or Be behind the tungsten softens the neutron energy spectrum, resulting in more transmutations. Some materials that could be recycled or treated as low level waste in the USA might require disposal in a geological repository in France, due to differences in nuclear regulations (Desegures and El-Guebaly 2012).
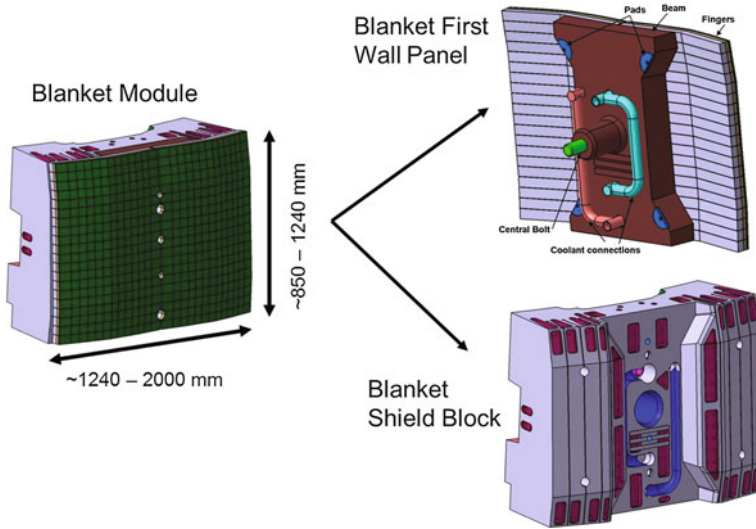
Fig. 6.7 One design of the ITER first wall. Courtesy of ITER Organization

6.2.4 ITER Blanket and Divertor First Wall

The Blanket System provides a physical boundary for the plasma transients and contributes to the thermal and nuclear shielding of the Vacuum Vessel and external ITER components. It covers $\sim 600 \ m^2$ and consists of 440 Blanket Modules comprising two major components: a plasma facing First Wall panel and a Shield Block. Each Blanket Module is about $1 \times 1.4 \times 0.5$ m and is attached to the vacuum vessel through a mechanical attachment system (Fig. 6.7).

Accommodating the high heat fluxes resulting in some areas (in particular in the inboard and outboard for start-up and shut-down and in the upper region near the secondary X-point) has necessitated the use of "enhanced heat flux" panels capable of accommodating an incident heat flux of up to 5 MW/m^2 in steady state. "Normal heat flux" panels, which had been developed and well tested for a heat flux of the order of 1–2 MW/m^2, are kept in the other locations.

Be is chosen as plasma-facing material because it has a low atomic number (which means that Be impurities in the plasma do not cause severe radiation losses), fair high-temperature performance, oxygen gettering capabilities, potentially low tritium retention.

The ITER divertor uses blocks of W mounted on copper alloy substrate, cooled by water in stainless steel coolant tubes. Figure 6.8 shows a medium-scale prototype, which was manufactured to qualify the high heat flux technologies.

Fig. 6.8 Armor tiles of W and CFC bonded to copper substrate containing copper alloy and stainless steel coolant tube (Merola 2008)
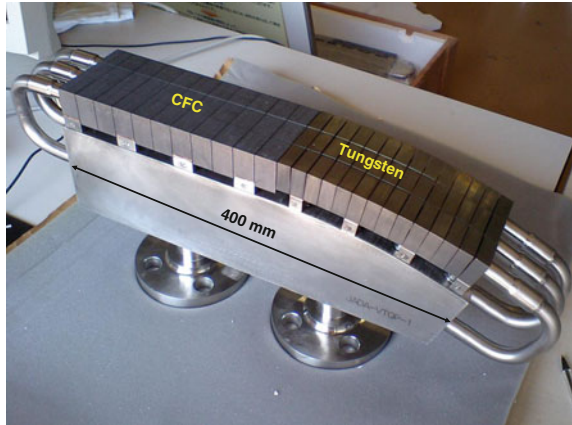
6.2.5 HHFC Research

Researchers have studied ways to enhance the critical heat flux limit inside the tubes in the high heat flux regions. The goal is to maximize the turbulence in the water thus minimizing the amount of vapor formed in contact to the cooled surfaces. One enhancement technique is the use of twisted tapes to swirl the water azimuthally, Fig. 6.9.

It is estimated that this and other cooling methods could facilitate heat fluxes up to about 20 MW/m^2. Divertor design and heat removal issues are discussed further in Chap. 7. Remote maintenance of the ITER first wall and divertor will be discussed in Chap. 13.

6.2.6 HHFC Testing

HHFCs have been tested by electron beam bombardment and by plasma bombardment in many facilities to study failure mechanisms and limiting heat fluxes. Tungsten monoblocks are being irradiated by neutrons and then tested for 1,000

Fig. 6.9 Swirl flow to enhance the critical heat flux limit (from Merola 2008)

JUDITH 1

Electron beam power:	60 kW
Acceleration voltage:	120 - 150 kV
Electron beam diameter:	~ 1 mm
Power density:	< 15 GW/m²
Pulse duration:	> 1 ms
Scanning frequency:	100 kHz
max. scanning area:	100 x 100 mm²
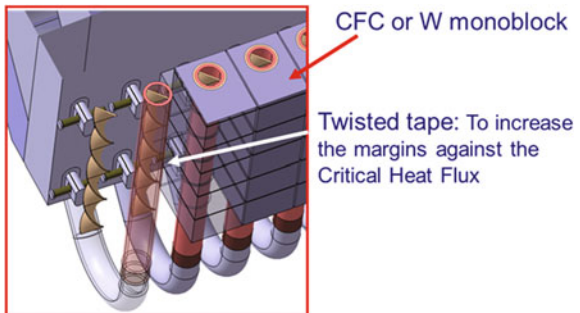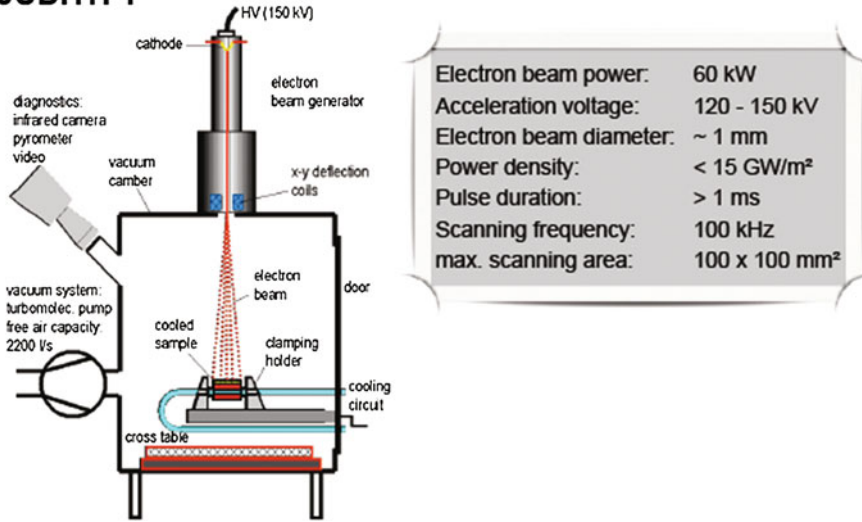
Fig. 6.10 The JUDITH high heat flux test facility in Jülich, Germany (Coenen et al. 2010)

cycles to see whether radiation damage leads to failure (Linke et al. 2007). Results with high fluencies of high-energy neutrons are not yet available, due to the lack of a high-flux 14 MeV neutron source.

Figure 6.10 shows a test facility in Jülich, Germany.

Be first wall qualification models have been successfully tested at the NRI (Czech Republic) and Sandia National Laboratory (USA) for thousands of cycles at heat fluxes of 0.5–0.9 MW/m^2 and various pulse lengths (0.7–5 min) (Merola 2008). After the successful completion of this preliminary qualification phase, a number of mock-ups and prototypes are now being manufactured with the aim of reaching the ITER required performances. Prototypical components, manufactured and tested by the Efremov Institute (St Petersburg, Russia) have demonstrated the capability to remove 4.7 MW/m^2 for 16,000 pulses.

Figure 6.8 showed a prototype divertor target with both W and CFC monoblocks. The design goal for the high heat flux regions is 300 cycles at 20 MW/m^2 for CFC/W divertor or 5,000 cycles at 10 MW/m^2 plus 300 cycles at 20 MW/m^2 in case of a full-W armored divertor. Outside those regions, the design target is 1,000 cycles at 5 MW/m^2. These goals have been exceeded by tests in European, Japanese, and Russian laboratories, but this does not mean that the reliability problem is solved. Even if most modules are successful, there could be failures in some of the hundreds of modules during ITER operations.

Bombardment by a hydrogen plasma increases the crack depth and growth rate produced by the thermal shock of electron beam impact in JUDITH, so under plasma operation tungsten may degrade faster than observed in vacuum tests (Wirtz et al. 2011).

Figure 6.11 shows how much DT ions are be trapped in various materials.

Tritium retention in W at high temperatures is very low. Very high heat fluxes can form "fuzz" on the surface of W, Fig. 6.12.

Upon further heating the fuzz may overheat and vaporize or it may break and disintegrate into dust. Both processes can reduce the armor thickness. The sputtering ratio of ions incident on tungsten fuzz is significantly lower than on an ordinary tungsten surface (Nishijima et al. 2011).

Tritium retention in the wall is a serious issue that will limit the number of full-power operating cycles in ITER. Tritium retention in C, Be, BeO, WC, and W decreases with temperature, Fig. 6.13.

Deuterium/Tritium retention increases with radiation damage, Fig. 6.14.
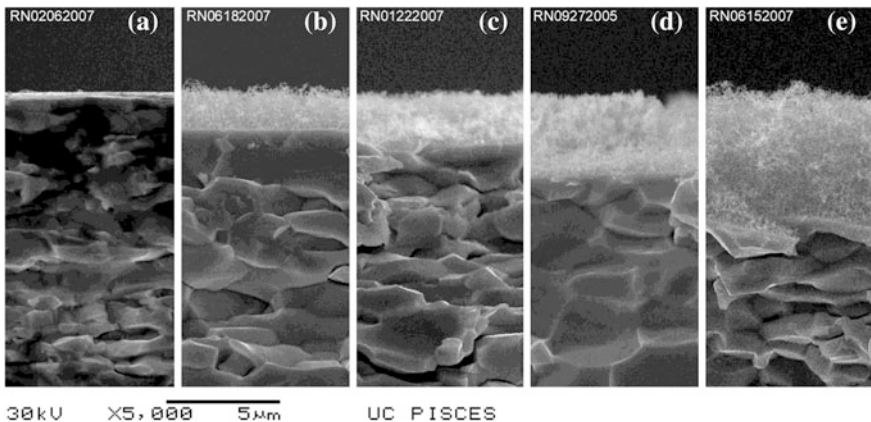
Fig. 6.12 Formation of tungsten fuzz during exposure to fluxes of 4–6 × 10^{22} m^{-2} s^{-1} of 60 eV helium ions at 1,120 K, at times of 300, 2,000, 4,300, 9,000, and 22,000 s, measured in PISCES. From Baldwin and Doerner (2008, Fig. 3)

Fig. 6.13 Tritium concentration (tritium atoms per wall atom) in various materials versus temperature, measured in PISCES-B (Roth et al. 2008)
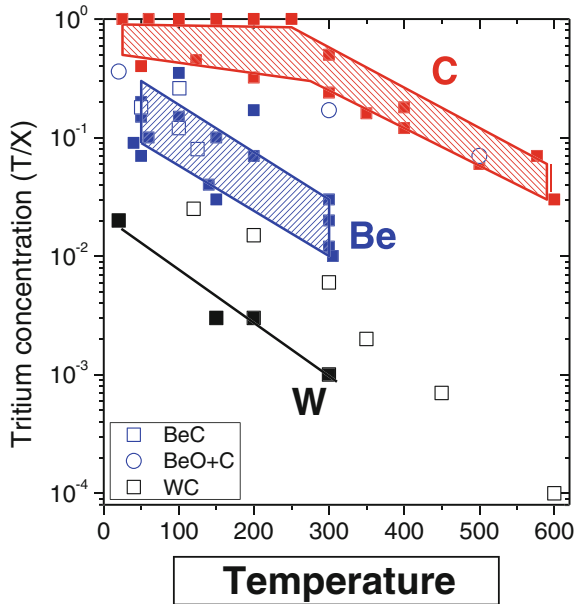
Fig. 6.14 Increase of tritium retention with radiation damage in W and Mo (Lipschultz et al. 2010, Fig. 4.1.1)
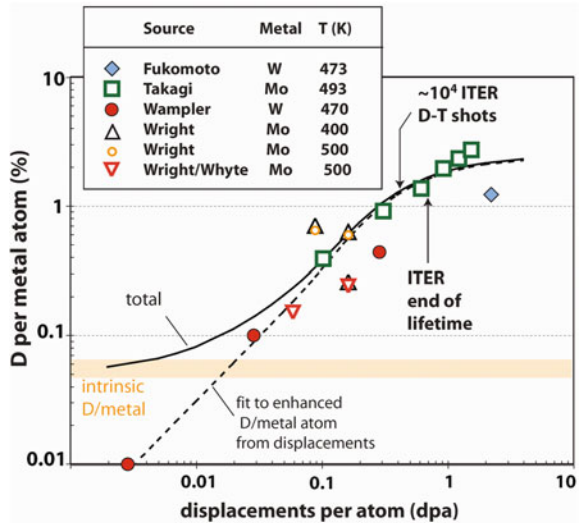
Thus, deuterium retention was about 2 % of the metal atom concentration at 1 dpa. Annealing at high temperature would reduce the radiation damage, and might reduce tritium retention. ITER will operate at lower wall temperatures than DEMO, so it will not produce the required data on high temperature operation. Almost all surface processes depend on temperature, including:

- Tritium retention
- Diffusion
- Surface recombination
- Sputtering
- Vaporization
- Chemical reactions
- Codeposition
- Damage annealing (Doerner 2008).

6.2.7 Plasma-Surface Interaction Studies

The PISCES-B experiment (San Diego, USA) bombards a target with high fluxes of ions at 20–300 eV to simulate divertor conditions. Table 6.2 compares the PISCES parameters with the ITER divertor parameters.

Figure 6.15 shows how the PISCES-B experiment represents the ITER scrape off layer (SOL) and divertor.

The PISCES group found that Be in the plasma helped mitigate physical and chemical erosion of graphite, and that Be reacts with W to form a low-melting-temperature alloy. With ion bombardment at 69–250 eV at 1,120 K for long times the equilibrium W fuzz thickness reaches about 1–2 μm. The ultimate effects of W fuzz in ITER could include arcing, dust generation, wall loss, or even improved resistance to erosion. Further study is needed, including radiation damage during high temperature operation (Doerner 2010).

ITER will **not** demonstrate the following:

- High temperature coolant operation ($\sim$600 °C)
- High neutron radiation dose and damage up to 100 dpa
- Steady state operation for many days
- Extensive use of refractory metals
- Electricity generation
- Tritium breeding ratio >1
- High availability.

Table 6.2 Comparison of PISCES-B and ITER edge parameters (Doerner 2010)

	PISCES	ITER edge
Ion flux (m^{-2} s^{-1})	10^{21}–10^{23}	$\sim 10^{23}$–10^{24}
Ion energy (eV)	20–300 (bias)	10–300 (thermal)
T_e (eV)	4–40	1–100
n_e m^{-3}	10^{18}–10^{19}	$\sim 10^{19}$
Be impurity fraction (%)	A few %	1–10
Pulse length (s)	Steady state	1,000
Materials	C, W, Be	C, W, Be
Plasma species	H, D, He	H, D, T, He
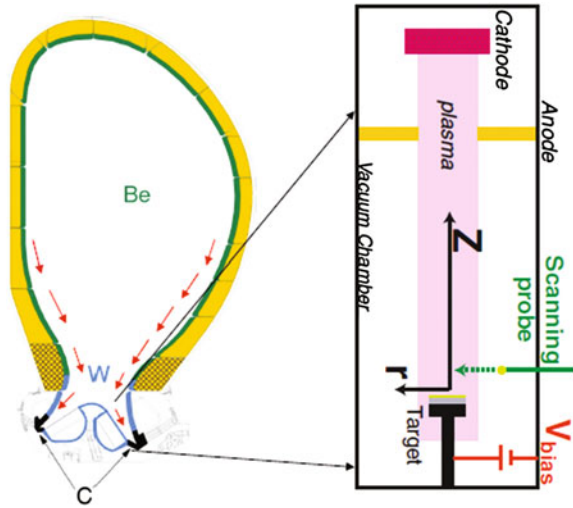
Therefore, a facility that tests high plasma power fluxes onto high-temperature walls is probably required to develop HHFC and other technologies, in order to prepare for DEMO (Nygren 2010).

6.3 Breeding Materials

One of the key criteria for the blanket is to breed adequate tritium so that the plant is tritium self-sufficient, meaning a net tritium breeding ratio (TBR) > 1.0. Certain plasma chamber wall areas will have to be non-breeding areas, such as divertors, CD ports and diagnostic ports, so the remaining wall areas must have TBR > 1.0. The blanket region behind the first wall of a high power fusion experimental facility or power plant will contain lithium or a lithium compound to multiply neutrons via the endothermic ^{7}Li(n,2n) reaction and to breed tritium by neutron capture in ^{7}Li and ^{6}Li. The current tritium breeding material candidates include metallic lithium, PbLi, Li_2BeF_4 (called "FLIBE"), solid ceramic lithium compounds, and molten salts. The solid breeding blankets employ solid pellets or pebbles of lithium ceramic compounds, typically Li_4SiO_4, Li_2TiO_3 or Li_2ZrO_3. Due to the low breeding capacity of solid breeders, this class of breeders usually requires neutron multiplying materials, such as Be and $Be_{12}Ti$. If the breeding ratio is too low, the TBR can be improved by increasing the ^{6}Li fraction above its natural value (7.42 %), but with additional cost.

6.3.1 Neutron Multipliers

Be (including $Be_{12}Ti$ and $Be_{12}V$) and Pb can serve as "neutron multipliers" when fast incident neutrons cause (n,2n) reactions, so their use helps achieve a viable tritium breeding ratio in the blanket. Be has resource limitations, high helium generation rates, and toxicity. Lead has toxicity and lower (n,2n) cross sections and is a very heavy material, but inexpensive and widely available. Figure 6.16 shows the cross sections for (n,2n) reactions in Be and Pb.
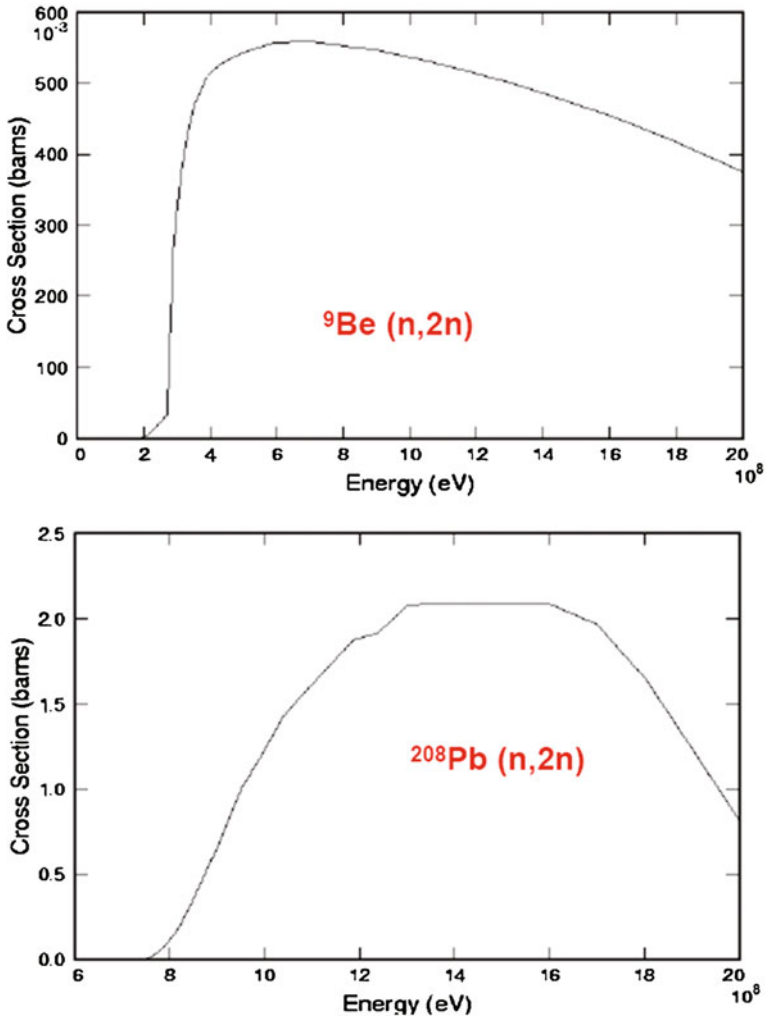
Fig. 6.16 Cross sections for (n,2n) reactions in Be and Pb versus neutron energy. 1 barn $= 10^{-28}$ m^2. Note that the Energy axis should be MeV and the Be cross sections are in millibarns. Courtesy of U. Fischer, Karlsruhe Institute of Technology

Some combinations of breeding materials, structural materials, and coolants are incompatible. For example, liquid lithium reacts violently with water, so use of water coolant with a liquid lithium blanket would be unacceptable. Slow moving liquid metals might be acceptable, but as the flow rate is increased, so is the MHD pumping power. This pumping power can be reduced by using an insulating liner inside the flow channels and orienting the channels along the local magnetic fields. High pressure helium flow through solid breeder blanket pebble beds may also have high pumping power requirements.

6.3.2 Lithium and PbLi

Natural lithium (7.42 % ^{6}Li, 92.6 % ^{7}Li) produces tritium by fast neutron inter-actions with ^{7}Li and by thermal neutron capture in ^{6}Li. Natural lithium will be assumed unless specified otherwise. Lithium has melting and boiling temperatures $T_m = 450$ K and $T_b = 1,600$ K. About 5 % expansion occurs during melting. Local tritium breeding ratios up to 1.6 (tritium atoms/incident neutron) can be attained, depending on the amount of structural material, the neutron multiplier, the ^{6}Li fraction, and the thickness of the blanket. Tritium would be continuously removed from a flowing lithium stream. Figure 6.17 shows the tritium breeding cross sections (reaction probabilities) of ^{6}Li and ^{7}Li versus neutron energy.

In order to avoid excessive corrosion and mass transfer problems with lithium, stainless steels will be limited to temperatures $T < 770$ K, and higher-strength Fe–Ni–Cr alloys will have lower temperature limits. Mo, V, Nb, Zr, and Ti might be able to operate with lithium at temperatures over 1,100 K, but concentrations of impurities, such as oxygen, must be kept very low. Aluminum alloys are incom-patible with lithium. The currently preferred structural material is ferritic steel, either EUROFER, F82H, or possibly a nano-strengthened or oxide dispersion strengthened (ODS) alloy.

A diagram of melting temperature versus atomic % lithium in Li–Pb mixtures is shown in Fig. 6.18. At $T > 770$ K, Pb attacks Fe–Cr–Ni alloys via solution corrosion.

Local tritium breeding ratios up to 1.6 can be obtained with PbLi.

Solid lithium compounds

Local tritium breeding ratios up to 1.4 can be attained with lithium oxide (Li_2O), a solid compound with molecular weight 0.02988 kg/mole, and mass density 2,013 kg/m^3. Table 6.3 shows the parameters of some potential ceramic breeder materials.

Li_2O has the highest Li density (good breeding potential), but it does not last well under irradiation. Li_2TiO_3 has lower Li density, but it has good mechanical properties. Furthermore, Li_2TiO_3 has potential for recycling and is being irradia-tion-tested. Li_4SiO_4 is also a good candidate material, but its melting temperature is
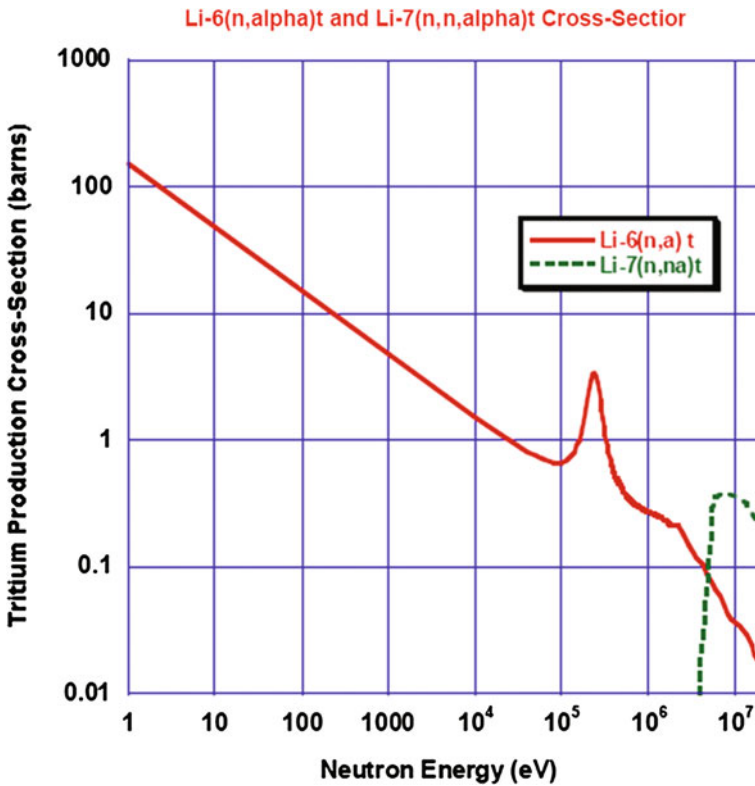
Fig. 6.17 Cross sections for tritium breeding in ^{6}Li and ^{7}Li versus neutron energy. Here (n,a) means that the lithium absorbs a neutron and the reaction releases an alpha particle, and (n,na) means that both an alpha and a neutron are released (1 barn = 10^{-28} m^2). Courtesy of U. Fischer, Karlsruhe Institute of Technology

lower. Operation at T > 0.6 T$_m$ (melting temperature) may cause sintering and close the pores, trapping more tritium.

Solid lithium compounds have low thermal conductivities, but they are much less corrosive than pure lithium, and may operate at temperatures of 700–950 K, depending on structural materials and coolant. Tritium may be removed by flowing helium gas, from which tritium removal is relatively easy.

6.3.3 Molten Salts

The molten salt "FLIBE" (LiF + BeF$_2$) has a high heat capacity (2.4 J/kg K at 810 K), but a comparatively low thermal conductivity (1.0 W/m K at 810 K). The eutectic mixture (slightly more than half BeF$_4$) has a melting temperature is over
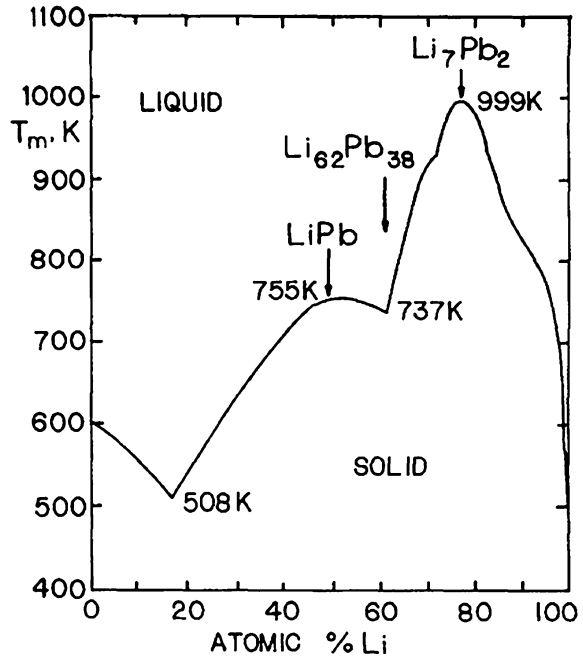
633 K, and a mixture with twice as much Li as Be melts at 732 K. This salt has good chemical stability and resistance to radiation damage in the liquid state. It is compatible with Mo, Nb, and Ni alloys at all temperatures where their strength is adequate (up to about 970 K). The concentration of tritium fluoride (TF) must be controlled, such as by adding Be.

However, the tritium breeding ratio of FLIBE with a PE-16 structure (an alloy of Ni–Fe–Cr) was estimated to be less than 1.07. Since many neutrons are lost out various ports and do not enter the blanket, this breeding ratio is only marginally satisfactory. The main problems associated with FLIBE are its high melting point, low thermal conductivity, and low breeding ratio.

The Molten Salt Reactor Experiment (fission reactor) at Oak Ridge National Laboratory, USA, had a core containing uranium or thorium fluorides in FLIBE. It operated successfully from 1965 to 1969, and demonstrated the advantages of this type of fission reactor core—low pressure, high temperature, good control, possible online reprocessing to remove fission products, and safety in accident conditions. After several years of operation the Hastelloy-N structure showed little sign of corrosion (Haubenreich and Engel 1970).

Several fusion reactor design studies have used FLIBE breeder, including the Princeton Reference Design, HYLIFE-II, OSIRIS, and the Japanese Force Free Helical Reactor (FFHR) series (Mills 1974; Meier 1994; Moir et al. 1994; Moir 1996; Sagara et al. 2005).

Table 6.3 Properties of some Li-ceramic breeder materials (Courtesy of Karlsruhe Institute of Technology)

Items	Materials				
	Li_2O	Li_2TiO_3	Li_2ZrO_3	Li_4SiO_4	γ-$LiAlO_2$
Li density (g/cm^3)	0.94	0.43	0.38	0.51	0.27
Thermal conductivity (500 °C) (W/m/ °C)	4.7	2.4	0.75	2.4	2.4
Thermal expansion (500 °C) ($\Delta L/L_0$ %)	1.25	0.8	0.50	1.15	0.54
Reaction of water	Very	Less	Less	Little	Little
Residence time (440 °C) (h)	0.03	(−)	0.01	3.0	50
Swelling ($\Delta V/V_0$ %)	7.0	(−)	<0.7	1.7	<0.5
Transmutation nuclides	$^{16}O(n,p)$: 7s	$^{46}Ti(n,p)$: 84d $^{47}Ti(n,p)$: 3.4d $^{48}Ti(n,p)$: 1.8d	$^{90}Zr(n,p)$: 64h $^{91}Zr(n,p)$: 57d $^{94}Zr(n,2n)$: 10^6y $^{96}Zr(n,2n)$: 64d	$^{28}Si(n,2n)$: 4s $^{29}Si(n,p)$: 6m $^{30}Si(n,\alpha)$: 9m	$^{27}Al(n,2n)$: 6s $^{27}Al(n,p)$: 9.5m $^{27}Al(n,\alpha)$: 15h
Melting point (°C)	1,430	1,550	1,615	1,250	1,610
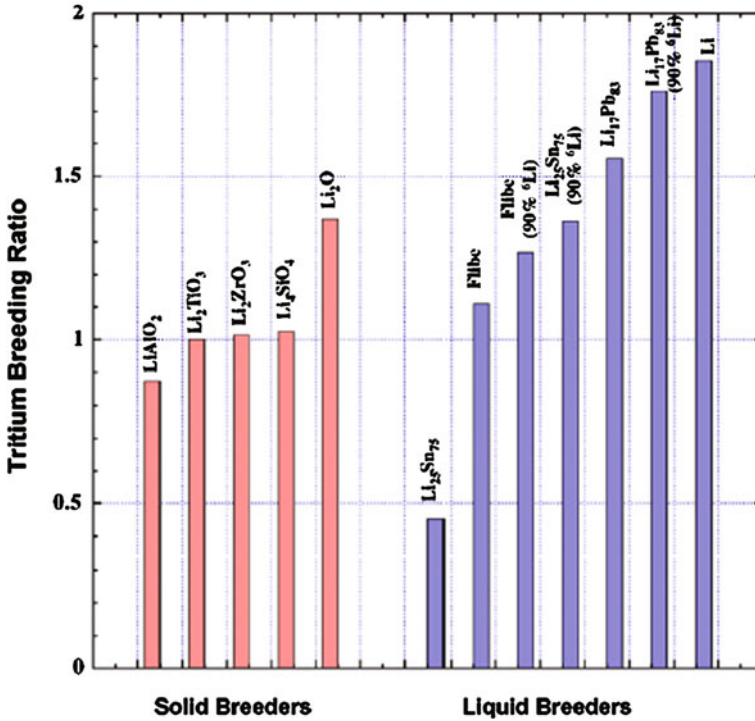
Fig. 6.19 Attainable breeding ratios in selected liquid and solid breeders (fairly thick cylindrical blanket, 2 m), with no structure, 100 % dense materials, room temperature, and natural lithium (except as noted), using FENDL-2.1 data (from El-Guebaly and Malang 2009, Fig. 6)

The local tritium breeding ratios attainable in various blankets with no structural material are shown in Fig. 6.19.

Thus, most of the solid breeders would require much Be or ^{6}Li enrichment.

6.3.4 Catalyzed DD Fuel Cycle

If the catalyzed DD fuel cycle is used, tritium breeding materials are unnecessary, and blanket design is considerably simplified, but the fusion power density is much lower at a given plasma pressure (Sect. 1.2). A higher plasma pressure would be required, so it is considered to be an "advanced" fuel cycle.

6.4 Coolants

6.4.1 Water

A blanket may be cooled by pressurized water or by boiling water, as in fission reactors. Water has excellent heat-transfer properties and low required pumping power. It is also a good neutron moderator. Water coolant at 100–200 °C was chosen for ITER, because it is simple, reliable, and inexpensive and thermal conversion to electricity was not a requirement. Both H_2O and D_2O could be adequate coolants, but they should not be used near liquid metals, unclad solid breeders, or near beryllium at high temperatures, due to the danger of an exothermal Be-steam reaction:

$$Be + H_2O \; \rightarrow \; BeO + \; H_2 + 370 \; kJ/mol, \qquad (6.1)$$
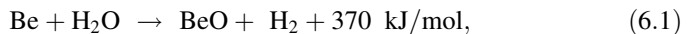
yielding hydrogen, which is also dangerous (Norajitra 2008). Water is used in ITER, but not in most other designs, for these reasons.

Tritium removal from water is difficult, because it is chemically indistinguishable from the ordinary hydrogen in the water. However, Canada has developed tritium separation technology for the Canadian Deuterium Uranium (CANDU) fission reactor program.

The efficiency of converting thermal energy to electricity is currently limited to about 40 %, due to temperature and pressure limitations of water. (Future "supercritical water" systems might be able to go higher temperatures and efficiencies.)

6.4.2 Liquid Metals

Liquid metals have high thermal conductivities and heat capacities. They can carry high heat fluxes at high temperatures and low pressures.

The use of lithium as both the breeding material and the coolant is attractive in its simplicity, but Li causes several problems:

1. Pure lithium is chemically very active, poses compatibility problems with water, and is a fire hazard.
2. High pumping powers may be needed to move lithium coolant across the magnetic field (which could be mitigated by insulating sleeves in the coolant passages).
3. The resultant high pressures create high stresses in the coolant ducts.

Many designs use PbLi, which is usually 15–17 % Li, with the remainder Pb. It is much less reactive and hazardous than pure lithium. Pure lead is not as good, because it does not breed tritium.

It may be possible to use boiling lithium at T $\sim$ 1,200–1,400 °C for removal of high heat fluxes with tungsten structure (Ihli 2008). Lithium may be pumped across the surface of plasma-facing materials by a thermoelectric effect (Ruzic et al. 2011).

6.4.3 Helium

Helium coolant is compatible with many alloys, nonradioactive, unaffected by the magnetic field, conducive to easy tritium extraction, and has a well-developed technology in the High-Temperature Gas-Cooled Reactor (HTGR) program. Pressures of about 5 MPa (50 atm) are needed to obtain good heat transfer properties, and about 5–10 MW/m^2 may be removed from the HHFC by helium.

Impurities in the helium may come from the breeding materials, seals, etc. Trace amounts of oxygen are especially active. Austenitic stainless steels and nickel alloys will probably be compatible with helium up to about 970 K, because of the protective oxide films formed on them. Refractory and reactive metals may be limited to T < 870 K by oxygen attack. Helium has low thermal conductivity and heat capacity at lower pressures. Therefore, high pressures, high flow rates in small tubes, and large coolant manifold ducts are necessary. Neutron streaming out the large ducts is a shielding problem. Pumping powers for helium can be quite large, from 1 to 10 % of the reactor thermal power, and the high gas pressures cause large hoop stresses in the tubes. Reliability of the welds is essential with thousands of high-pressure helium tubes. Gas cooling is discussed by Abdel-Khalik et al. (2008) and by Ihli and Ilic (2009).

There may be a shortage of helium in the future, due to its growing use in many technologies (Chap. 12).

6.4.4 Molten Salts

Because of their high boiling points and low vapor pressures, molten salt coolants can be used at low pressures. Turbulent flow is required for effective heat removal. Molten salts are affected little by magnetic fields, but the small voltages developed by their motion may cause chemical breakdown of some compounds and increased corrosion problems. FLIBE, which also serves as a tritium breeder, was described in Sect. 6.3.

Other molten salts, such as "Heat Transfer Salt" (HTS) composed of 53 % KNO_3, 40 % $NaNO_2$ and 7 % $NaNO_3$, might be suitable for an intermediate coolant loop.

6.4.5 Solid Lithium Oxide

Flowing Li_2O particles ($\sim$ mm size) were considered as both breeding material and coolant. Such a system would operate at low pressures, simplify structural design, and have easy tritium removal. Some disadvantages of this scheme are:

- Poor heat transfer
- Reactivity with water
- Uncertain radiation stability
- Danger of particles sintering together
- Electrostatic forces could clog pipes
- Possible voids and neutron leakage.

Therefore, it is unlikely that Li_2O particles will be used as a coolant, although they may be used as a breeding material.

6.4.6 Comparison

Properties of some coolants are compared in Table 6.4.

Table 6.4 Properties of some coolants

	Units	H$_2$O (1 atm)	Li	Pb(83 %)– Li(17 %) at 850 °C	FLIBE	He (60 atm)
Melting temperature	K	273	454	507–510	633–732	None
Operating temperature, T	K	373	$\sim$1,200	$\sim$1,200	$\sim$1,200	$\sim$1,200
Density, ρ_m	kg/m^3	960	450	8,560	1,840	2.5
Viscosity, μ	Pa s	2.84E−4	2.5E−4	6.51E−4	3.E−3	5.E−5
Kinematic viscosity, v	m^2/s	2.96E−7	5.5E−7	7.6E−8	1.6E−6	2.E−8
Specific heat, C$_p$	J/kg K	4,190	4,200	185	2,400	5,200
Thermal conductivity, k	W/m K	0.7	65.	24.1	1.0	0.4
Electrical conductivity, σ	A/V m	Low	2.E6	6.7E5	394	Low
Prandtl number Pr = μC_p/k	–	1.7	0.017	0.005	7.2	0.65

Allowable operating temperatures vary widely with materials, due to corrosion (Miley 1976; Raffray et al. 2007; Dolan 1982). Additional PbLi properties and their variations with temperature are available in Mas de les Valls et al. (2008)

6.5 Structural Materials

The requirements for structural materials within the power core (first wall, blanket, high temperature shield and low temperature shield) are quite difficult to achieve (Chap. 8).

- High temperature operation for long durations
- Adequate strength at elevated temperature
- Low activation for waste disposal
- Creep resistance
- Good ductility after irradiation
- Fatigue resistance
- Minimal tritium retention.

The current choice for most first wall, breeding blankets and shield structures is reduced activation ferritic/martensitic steels (called RAFM, RAF, or F/M) of the F82H or EUROFER class. The composition of these alloys are shown in Table 6.5.

Thus, F82H is similar to EUROFER, but with added traces of Si, Mn, V, and N. These steels are not yet qualified for their requirements of swelling, ductility, and fracture toughness at the nominal first wall (FW) fluence of 3 MW year/m^2.

Vanadium alloy has good compatibility with lithium at high temperatures and has been used in some design studies.

SiC$_f$/SiC composite (SiC fibers in SiC matrix) will be simply called "SiC" here, since pure SiC without the fibers is not considered as an option. It is a potentially useful material, which may have much higher operating temperatures, strength, and fracture toughness, but it has not yet been developed to the level of F/M steel. Some properties of F/M, V alloy, and SiC are compared in Table 6.6. SiC issues are discussed by Raffray et al. (2001).

Bonds of tungsten on SiC have been tested up to 23.5 MW/m^2. The most successful bond (least cracking) was achieved with vapor deposition and pre-heating of the W powder before coating. Tungsten carbide grains formed near interface within W the coating (Hinoki et al. 2005).

	F82H (Jitsukawa et al. 2002)	EUROFER (Rieth 2010b)
Cr	7.46	9.2
C	0.09	0.1
Si	0.10	0.043
Mn	0.21	0.5
V	0.15	0.2
W	1.96	1.15
Ta	0.023	0.14
N	0.006	0.023

Table 6.5 Compositions of F82H and EUROFER F/M steels, weight %. The rest is Fe

Table 6.6 Some properties of F/M, SiC, and V4Cr4Ti (Raffray et al. 2007; Jitsukawa et al. 2002; Zinkle and Ghoniem 2000; Chen et al. 2008; Tavassoli et al. 2002; Billone)

	Units	F/M steel (~500 °C)	V4Cr4Ti (~600 °C)	SiC
Melting temperature	K	~1,800	2,170	
Density	kg/m^3	~7,900	6,050	2,500–3,200
Young's modulus	GPa	190 (Tavassoli)	120	200–300
Poisson's ratio	–	0.29–0.31	0.37	0.16–0.18
Thermal expansion coefficient	10^{-6} K^{-1}	11.5	10	3–4
Specific heat	J/kg K	630 (Tavassoli)	550	600
Thermal conductivity	W/(m K)	32.5 at 400 °C 33.0 @ 500 (Tavassoli)	36	5–20
Thermal stress figure of merit (Zinkle and Ghoniem 2000)	kW/m	~5.4 Fe–8–9Cr martensitic at 400 °C	~6.4 at 450–700 °C	2.0 at 800 °C
Maximum allowable combined stress	MPa	≈160	≈180	≈190
Maximum allowable burnup	%			≈3 %
Maximum temperature for compatibility with Li	°C	550–600	650–700	550
Maximum temperature for compatibility with PbLi	°C	450	650	800
Electrical resistivity	Ω m	0.07E−6	0.71E−6	0.002–0.05

In bonds of beryllium on SiC the presence of beryllium oxide has indirect influence on creep strength, but at T > 600 °C the creep strength is reduced, with further reduction at higher levels.

Alpha-induced swelling of Be decreases with increasing BeO (Scaffidi-Argentina). The maximum operating temperature is limited by compatibility with coolant, thermal creep, helium embrittlement, and void swelling. After irradiation many materials also have minimum operating temperatures, below which they do not perform well, due to radiation hardening or ductile-to-brittle transition temperature shift (these phenomena are discussed in Chap. 8). Figure 6.20 shows the upper and lower temperature limits for various materials.

Some advantages and disadvantages of reduced activation ferritic/martensitic steels are listed in Table 6.7.

The Japanese JK2LB steel has a low Ni content so that it decays to safe radioactivity levels in about 3 years after shutdown (Fig. 6.21).

Researchers at Kyoto University are studying the use of SiC structure with PbLi breeder and He coolant at high temperatures. A 200-h test at temperatures up to 900 °C revealed no corrosion. They will also irradiate a W-SiC structure with a proton beam at 10 MW/m^2 to simulate ELMs and test its performance as an HHFC (Konishi et al. 2008).
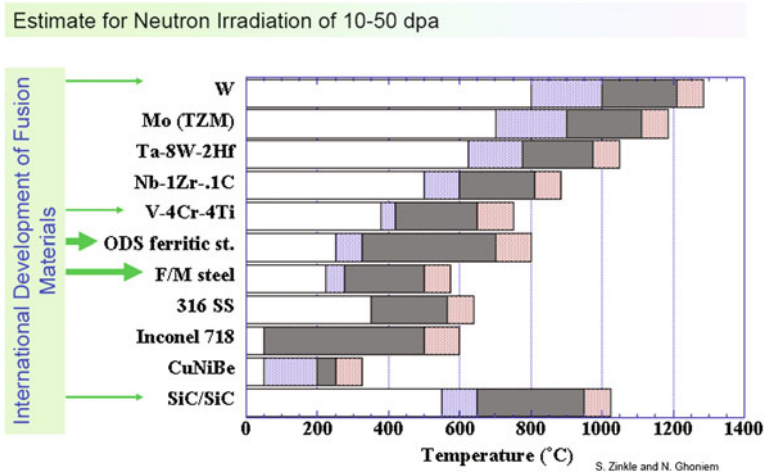
Fig. 6.20 Upper and lower temperature limits of various structural materials. The *light pink and lavender bands* represent uncertainties. *TZM* name of alloy; *ODS* oxide dispersion strengthened (Zinkle and Ghoniem 2000)

Table 6.7 Advantages and disadvantages of reduced activation 8–10 % CrWVTa F/M steels (Rieth 2010)

Advantages

- Long–term industrial experience with 10–12 % CrMoNbV steels up to 140 dpa
- Better thermal conductivity than austenitic steels (such as stainless steel 316LN)
- High aging resistance (almost no alloy decomposition at least up to 5×10^4 h)
- Mechanical properties tuneable by heat treatment
- Sufficient corrosion resistivity in Pb–Li-blankets
- Irradiation properties—at high dpa-doses just small changes in strength, hardness, and ductility; almost negligible He und void swelling

Known disadvantages

- DBTT decrease after irradiation at $T_{irr} < 400$ °C; but RAFM steels show clearly better behavior compared to commercial steels
- 4–5 welding techniques available, but the welds need heat treatments
- Upper operation temperature limited by creep strength: $T_{max} \cong 550$ °C
- Deterioration of mechanical properties at >40 dpa from helium generated by (n,α) reactions
- Possible solution: achieve T_{max} in the range of 650–750 °C by powder metallurgy (ODS)

Fig. 6.21 Decay of JK2LB and Inconel-908 radioactivity versus time after shutdown, compared with the IAEA clearance limit, below which the metal is safe to handle (Merrill et al. 2008, Fig. 32) © 2008 by the American Nuclear Society, LaGrange Park, Illinois
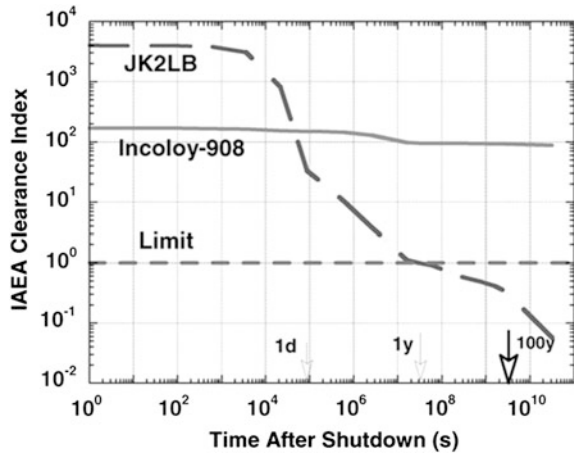
6.6 Shielding Materials

The purpose of the shield is to attenuate the neutron and gamma fluxes passing through the first wall, blanket and divertor enough that the magnet coils will last the lifetime of the plant and to reduce external dose rates and activation of materials.

The optimum blanket/shield thickness is a compromise between blanket/shield performance and fusion power density. A very thick blanket could capture practically all the fusion energy, but its larger size would reduce the magnetic field inside the plasma, the attainable plasma pressure, and the fusion power density. A thin blanket/shield facilitates a higher fusion power density, but might not have an adequate tritium breeding ratio, and the fluxes of neutrons and gammas to the magnet coils might be too high.

The shield will moderate (slow down) and absorb neutrons and attenuate gammas. Low-Z materials like graphite and lithium are good neutron moderators, while high-Z materials like Fe, Pb, and W good at attenuating gammas. A shield must perform both functions, so both types of materials are desirable. If the flow rate is adjusted well, the temperature of the shield coolant can be high enough for efficient energy conversion. A hot shield can serve as a high temperature structural element tying all the blankets and divertor modules together, so they can be removed as a unit in horizontal or vertical maintenance schemes.

In principle there could also be a low temperature shield outside the hot shield, but most designs have the hot shield structure directly supported by a cool vacuum vessel. Cool shielding must be provided around all penetrations, including the large maintenance ports in some toroidal machines for horizontal sector or vertical segment replacement.

The shielding requirements for the ARIES Compact Stellarator design are listed in Table 6.8 (ARIES stands for Advanced Research, Innovation, and Evaluation Study).

Table 6.8 Shielding requirements for the ARIES-CS (compact stellarator) design (El-Guebaly et al. 2008)

	Radiation limits, 40 full-power years
Fast neutron fluence to coils	10^{19} cm^{-2}
Nuclear heating in Nb$_3$Sn coils	2 mW/cm^3
Dose to coil insulator	10^{11} rad
Copper stabilizer displacements per atom	6×10^{-3} dpa
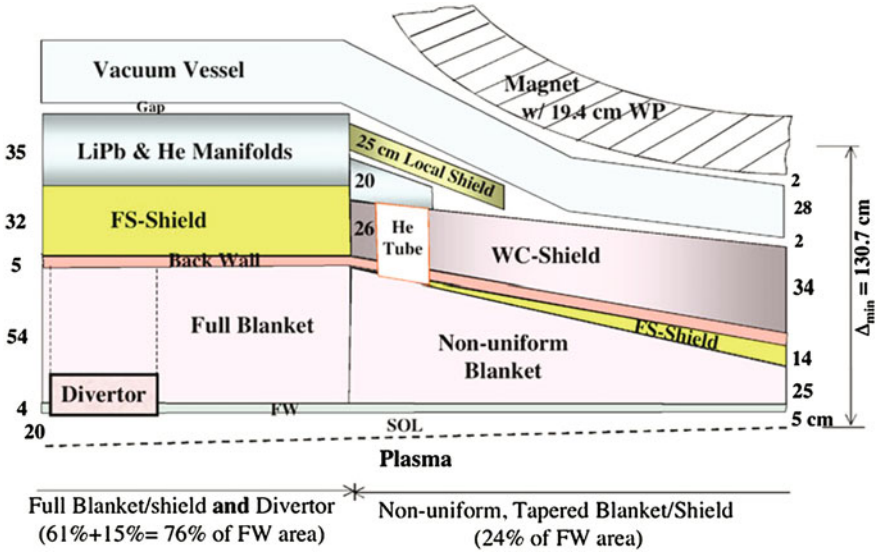
Fig. 6.22 Toroidal cross section through uniform and nonuniform blankets, showing the He feeding tube for the latter (El-Guebaly et al. 2008) © 2008 by the American Nuclear Society, LaGrange Park, Illinois

The design meets all these limits, of which the dominant ones are those on neutron fluence and nuclear heating.

In some designs, such as stellarators, the cost of electricity (COE) depends strongly on the distance between the plasma and the magnet coil in some toroidal locations. The blanket/shield can be full thickness in most places, to achieve a good tritium breeding ratio, and tapered to a minimum thickness at the critical points, to keep the coil close to the plasma, with the local reduction of tritium breeding. Figure 6.22 shows the tapered blanket/shield of the ARIES-CS design.

The tapering of the blanket/shield in this design enabled the major radius to be decreased from 10.1 to 7.75 m, which reduced the estimated cost of electricity from 8.7 to 7.8 cents/kWh (in 2004 $). Tungsten carbide (WC) is effective at attenuating both neutrons and gammas. The double-walled vacuum vessel,

optimized to reduce the radiation levels at the magnet coil, is 28 % F/M structure filled with 23 % borated steel filler and 49 % water (El-Guebaly et al. 2008).

Detailed studies are needed to calculate the effects of neutrons streaming out through ports and ducts, which may require additional shielding. Shielding issues for ITER are reviewed by Vayakis et al. (2008).

6.7 Heat Transfer

6.7.1 Radiation

The first wall material may be tiles of high-temperature materials, such as graphite, beryllium, tungsten, or molybdenum. If they were not actively cooled by good thermal contact with a cooling system they would be heated to very high temperatures and cooled by radiation to the next surface. Let us estimate how high that temperature might be.

The tiles will reach a temperature at which their cooling rate by infrared radiation to the supporting wall equals its heating rate from the plasma. If the wall and armor tile are nearly flat and parallel, the net heat flow per m^2 from the armor to the wall is

$$\frac{q}{A} = \frac{\sigma(T_a^4 - T_W^4)}{\frac{1}{e_a} + \frac{1}{e_w} - 1} \; (W/m^2) \tag{6.2}$$

where T_a and T_w are the armor and wall temperatures (K), e_a and e_w are their emissivities, and $\sigma = 5.670 \times 10^{-8}$ W/m^2 K^4 is the Stephan–Boltzmann constant. Spectral emissivities of various materials are given in Table 6.9.

A similar equation applies to the case of other high temperature surfaces. However, Eq. 6.2 must be modified to include shape factors for surfaces that are not planar and parallel (Chapman 1960).

Example Problem 6.1: Radiative Heat Transfer A heat flux q = 0.63 MW/m^2 is deposited on graphite armor and radiated to a plain steel wall at 770 K (Fig. 6.23). What is the equilibrium temperature of the side of the graphite facing the wall?

From Table 6.9 the emissivities are both about 0.8. Solving Eq. (6.2) for T_1, we find $T_1 = 2,030$ K. Thermal expansion could make armor support difficult.

Table 6.9 Approximate emissivities of smooth materials in the temperature range 300–1,000 K

Aluminum	Unoxidized	0.1 ± 0.05
	Oxidized	0.3 ± 0.2
Stainless steel, nickel alloys, refractory alloys		0.4 ± 0.3
Graphite, ceramics, plain steel, heavily oxidized metals		0.8 ± 0.1

Emissivities increase with temperature and with surface roughness

graphite   steel
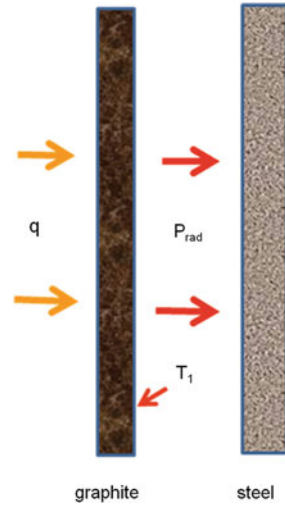
The conclusion from this example problem is that radiative cooling would limit
the heat flux of the first wall or divertor to **unacceptably low values**, so active
cooling by good contact with actively cooled substrate is needed.

6.7.2 Heat Conduction

Steady state heat flow by conduction through a region of several materials may be
written in the form

$$q/A = \Delta T/(R_1 + R_2 + R_3 + \ldots) \left(W/m^2\right) \tag{6.3}$$

where ΔT is the overall temperature difference and R_1, R_2, $\ldots$ are thermal resis-
tances of the various layers. This equation is analogous to the electrical circuit
equation $I = \phi/R$, where I is the current, ϕ is the voltage, and R is the sum of the
electrical resistances. For heat conduction, the thermal resistances may be calcu-
lated from the equations

$$\text{Cylindrical layer:} R = r_q \ln(r_o/r_i)/k \tag{6.4}$$

$$\text{Planar layer:} R = \Delta x/k \tag{6.5}$$

where r_q is the radius where q/A is to be found, r_o and r_i are the outer and inner
radii of the cylindrical layer, k is the thermal conductivity of the layer, and Δx is
the thickness of a planar layer. The electrical circuit analogy may be extended to
include the thermal resistances of convection boundary films, which are given by
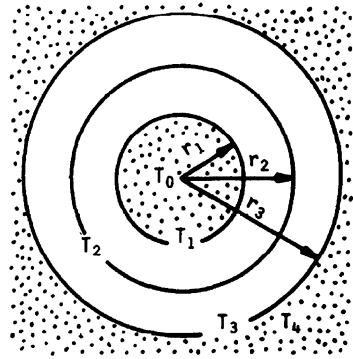
$$\text{Cylindrical surface with convection at radius } r: R = r_q/hr \quad\quad (6.6)$$

$$\text{Planar surface}: R = 1/h \quad\quad (6.7)$$

Example Problem 6.2: Conductive heat transfer Consider the case shown in
Fig. 6.24, consisting of a double-layer tube with a hot fluid at temperature T_o on
the inside and a cool fluid at temperature T_4 on the outside. Find the heat flow q/A_3
(at radius r_3), and find T_2.

Here $r_q = r_3$. If L is a given length along the tube, then $A_3 = 2\pi r_3 L$. Call the
convective heat transfer coefficients h_{o1} at r_1 and h_{34} at r_3, and call the thermal
conductivities k_{12} between r_1 and r_2, and k_{23} between r_2 and r_3. Using the thermal
resistances are given by the above equations,

$$\frac{q}{A_3} = \frac{T_0 - T_4}{\left(\frac{r_3}{h_{01}r_1}\right) + \frac{r_3 \ln\left(\frac{r_2}{r_1}\right)}{k_{12}} + \frac{r_3 \ln\left(\frac{r_3}{r_2}\right)}{k_{23}} + \frac{1}{h_{34}}} \quad\quad (6.8)$$

The temperature at an intermediate point such as r_2 can now be found by Eq.
(6.3) for heat transfer between T_o and T_2 with $r_q = r_2$:

$$\frac{q}{A_2} = \frac{T_0 - T_2}{\left(\frac{r_2}{h_{01}r_1}\right) + \frac{r_2 \ln\left(\frac{r_2}{r_1}\right)}{k_{12}}} \qu\quad (6.9)$$

where $A_2 = 2\pi r_2 L$. The value of q from Eq. (6.8) is used in this equation, which is
then solved for T_2:

$$T_2 = T_0 - \frac{r_3(T_0 - T_4)\left[\frac{r_2}{h_{01}r_1} + \frac{r_2 \ln\left(\frac{r_2}{r_1}\right)}{k_{12}}\right]}{r_2\left[\frac{r_3}{h_{01}r_1} + \frac{r_3 \ln\left(\frac{r_2}{r_1}\right)}{k_{12}} + \frac{r_3 \ln\left(\frac{r_3}{r_2}\right)}{k_{23}} + \frac{1}{h_{34}}\right]}$$ (6.10)

(In a real case there may also be a contact thermal resistance between the two tubes.)

The thermal conductivities of F/M steel and SiC were given in Sect. 6.6. Next we need to calculate the convective heat transfer coefficients h.

6.7.3 Heat Convection

Convective heat transfer from a hot surface at temperature T_s to a fluid at temperature T_f is described by "Newton's Law of Cooling",

$$q/A = h\ (T_s - T_f)\ (W/m^2)$$ (6.11)

where h is called the *convective heat transfer coefficient*, or *film coefficient*, and has units of W/m^2 K. This equation does not accurately represent what is happening on a microscopic scale at the surface, but it permits evaluation of the net heat flow, provided that the correct value of h is used. Usually h is expressed in terms of the following dimensionless quantities:

$$\text{Reynolds Number}\ Re = Dv\rho_m/\mu$$ (6.12)

$$\text{Prandtl Number}\ Pr = c_p\mu/k$$ (6.13)

$$\text{Nusselt Number}\ Nu = hD/k$$ (6.14)

where D = a characteristic dimension, such as the diameter of a tube, v = average fluid velocity, ρ_m and μ are the density and viscosity of the fluid, and c_p and k are its heat capacity and thermal conductivity. If Nu is known, h can be calculated from Eq. (6.14). Usually Nu is expressed as a function of Re and Pr by means of empirical equations or graphs, which are called *correlations*. The usual procedure for obtaining h is to calculate Re and Pr for the given fluid conditions (which depend on temperature), to use the appropriate correlation for Nu, and then to calculate h from Eq. (6.14). Some correlations of interest for fusion reactor blanket design are given in Table 6.10 and by Kays (1966).

Table 6.10 Various convective heat transfer correlations for turbulent flow (Re $\gtrsim$ 3,000)

Nonmetallic coolants (He, H_2O, molten salts, …)

Nu = 0.023 $(Re)^{0.8}$ $(Pr)^{0.4}$

where Re and Pr are evaluated at the fluid bulk temperature T_f.

For high velocity gas coolants with Mach number M $\gtrsim$ 1, Re and Pr should be evaluated at the "adiabatic wall temperature" T_{fa}, defined by

T_{fa} = $T_f[1 + 0.45(\gamma - 1)M^2]$

where $\gamma \sim 1.4$ is the ratio of specific heats.

Liquid metal coolants (PbLi, Li, …)

Constant heat flux along channel: Nu = 7 + 0.025 $(RePr)^{0.8}$

Uniform wall temperature along channel: Nu = 5 + 0.025 $(RePr)^{0.8}$

For noncircular channels, replace D by D_e = 4(flow area)/(wetter perimeter) (From M.M. El Wakil, Nuclear Heat Transport, © American Nuclear Society, La Grange Park, Illinois, 1978)

6.8 Stresses

Coolant tubes will have stresses induced by gravity, by coolant pressure, by thermal gradients, and perhaps by swelling and electromagnetic forces. Assuming that the tube thickness is much less than its radius (t/r $\ll$ 1), the temperature drop across a tube wall with thickness t is

$$\Delta T = (q''t + q'''t^2/2)/k \, (K), \qquad (6.15)$$

where $q'' = q/A$ is the heat flux through the surface of the tube (W/m^2), q''' is the heat deposited internally by nuclear radiation (W/m^3), and k is the thermal conductivity of the tube (W/m-k). Stress is actually a tensor quantity with nine components. Here we will use a scalar stress approximation for simplicity. The approximate thermal stress is given by

$$\sigma_{th} \approx \frac{\alpha E}{2k(1 - v)} \left[q''t + q''' \frac{t^2}{2} \right] = \frac{\sigma_y}{M} \left[q''t + q''' \frac{t^2}{2} \right] (Pa) \qquad (6.16)$$

where E = modulus of elasticity (Pa), v = Poisson ratio, σ_y = yield strength, and M = thermal stress parameter (to be used in Chap. 8). The hoop stress due to internal pressure may be estimated from the equation

$$\sigma_h = (pr/t)(1 + t/2r) \, (Pa) \qquad (6.17)$$

where p = pressure difference across the tube wall (Pa), and r = tube radius (m). (This is similar to the equation for the hoop stress in solenoid magnet coils.) If the pressure stress and thermal stress are dominant, then the total stress is

$$\sigma \approx \sigma_h + \sigma_{th} \, (Pa). \qquad (6.18)$$

The hoop stress becomes very large at small t, and the thermal stress is great at large t. There is a value of t for which the total stress is a minimum (These equations are for simple estimates only. Accurate calculations involve tensor quantities.).

Example Problem 6.3: Minimum Stress A stainless steel 316 tube with r = 3 cm, q″ = 0.5 MW/m², T = 770 K, E = 1.9 × 10¹¹ Pa, v = 0.3, contains helium at 6 MPa (60 atm). Internal heat generation is negligible. How large is the minimum total stress?

From Table 6.6, α = 18.4 × 10⁻⁶/K, k = 23 W/m K, by interpolation. From Eqs. (6.16), and (6.17) we find

$$\sigma_{th} = 5.4 \times 10^{10} t \,(Pa) \tag{6.19}$$

$$\sigma_h = 1.2 \times 10^5 / t \,(Pa). \tag{6.20}$$

These stresses and the total stress are plotted as functions of t in Fig. 6.25.

The minimum total stress is about 160 MPa (24 ksi) at t = 1.5 mm. For SS 316 at 770 K, the stress should be kept below 100 MPa, so a redesign would be necessary. For example, a different structural material, having a better thermal stress parameter could be used instead of SS 316, or q″ could be reduced.

Some coolant tube configurations giving rise to severe thermal stresses are shown in Fig. 6.26.

Round tubes welded to a flat plate cause low-temperature regions in the plate, as shown in the sketch. The steep temperature gradients are accompanied by high thermal stresses. Thermal expansion and contraction during startup and shutdown cause severe bending stresses in the short straight sections of a "hockey stick" heat exchanger. The temperature difference on the hot and cold sides of a U tube shell-and-tube heat exchanger induce shear stresses in both the shell and the end plates (headers).

Rectangular coolant channels are not as strong as circular tubes, because rectangular channels have bending stresses, while circular tubes have mainly tensile stress, if the pressure is higher on the inside. If the pressure is higher on the outside of the tube, then there is a danger of creep buckling (Fraas 1975; Fraas and Thompson 1978).

Fig. 6.25 Thermal stress, hoop stress, and total stress versus tube thickness for the case of Example Problem 6.3

T(X)

X

plate

ΔT

COOLANT

HOCKEY STICK HEAT EXCHANGE

COLD FLUID IN

HOT FLUID OUT

HOT FLUID IN

COLD FLUID OUT

U-TUBE SHELL-AND-TUBE HEAT EXCHANGER
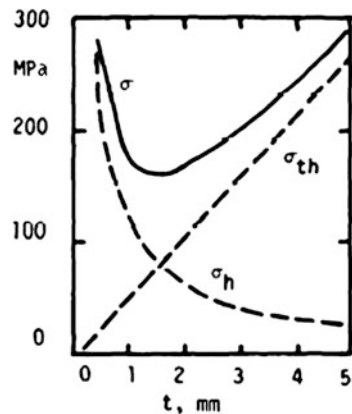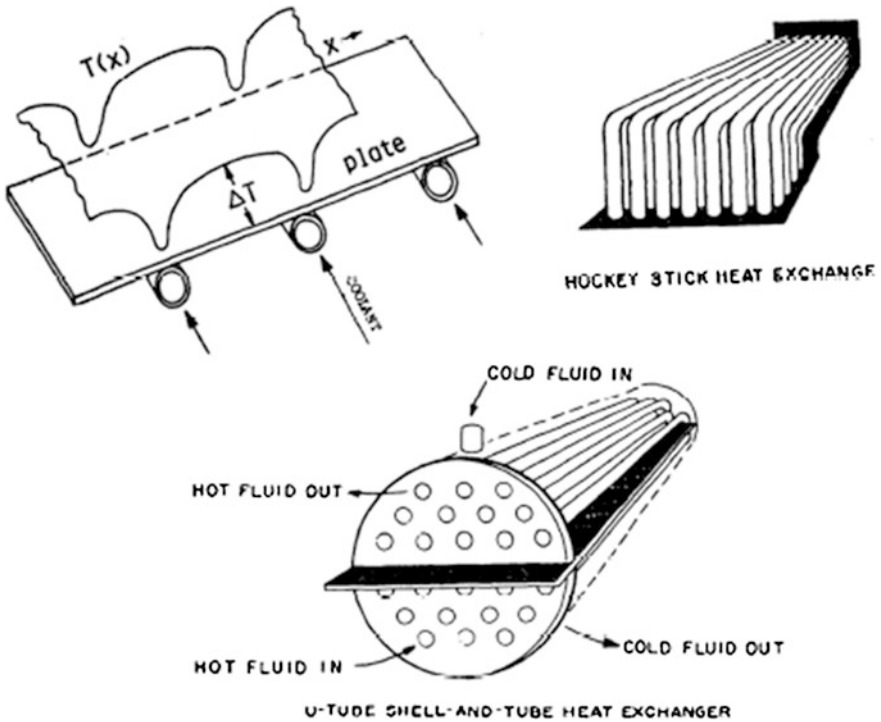
Fig. 6.26 Examples of situations that give rise to thermal stress problems (Fraas 1975)

6.9 Flow Rate and Pumping Power

6.9.1 Flow Rates

If boiling does not occur, the required coolant mass flow rate (dm/dt) (kg/s) may be found from the equation

$$P = (dm/dt)c_p\Delta T \ (W) \tag{6.21}$$

where P = heat to be removed (W), c_p = coolant specific heat (J/kg K), and ΔT is the coolant temperature rise as it flows through the given blanket region. (These equations were also discussed in Sect. 3.9.) The average coolant flow velocity v_c is related to (dm/dt) by the equation

$$(dm/dt) = \rho_m A_c v_c \ (kg/s) \tag{6.22}$$

where ρ_m = coolant mass density (kg/m³) and A_c = coolant channel cross sectional area (m²). The volumetric flow rate is

$$A_c v_c = (dm/dt)/\rho_m \ (m^3/s) \tag{6.23}$$

Table 6.11 Required flow rates for various coolants in a 1 GW-thermal reactor with $\Delta T = 100$ K

Coolant	ρ_m kg/m^3	c_p J/kg K	dm/dt kg/s	$A_c v_c$ m^3/s
Li	450	4,100	2,440	5.4
PbLi	8,560	185	54,100	6.29
FLIBE	183	2,400	4,170	23
He, 6 MPa, 800 K	3.6	5,200	1,920	530
H$_2$O	900	4,100	2,440	2.7

Example Problem 6.4: Helium Coolant For helium at p = 6 MPa (60 atm) and T = 800 K, $\rho_m = 3.6$ kg/m^3 and $c_p = 5{,}200$ J/kg-K. If $\Delta T = 100$ K, estimate the required mass flow rate, volumetric flow rate, and helium velocity for a reactor with P = 1 GW and 20 m^2 total duct area.

From Eq. (6.21), we find (dm/dt) = 1,920 kg/s. From Eq. (6.23), the volumetric flow rate is $A_c v_c = 533$ m^3/s, and $v_c = 27$ m/s.

Typical flow rates for various coolants to remove 1 GW with $\Delta T = 100$ K are compared in Table 6.11.

Water has good heat capacity and a low required mass flow rate. The low heat capacity of PbLi requires high mass flow rate, but the volumetric flow rate is modest. The value for helium is similar to that computed in Example Problem 6.4. The volumetric flow rate of helium is very high, requiring high flow speeds. Attempting to lower the flow rates by raising ΔT can exacerbate thermal stress problems, but $\Delta T \sim 300$ K is used in some designs.

6.9.2 Pressure Drop and Pumping Power

For electrically *non-conducting* coolants, the pressure drop in a coolant tube with length L_c and inner diameter D is given by the equation

$$\Delta p = f L_c \rho_m v_c^2 / 2D \ (\text{Pa}), \tag{6.24}$$

where f = friction factor (Fig. 3.35). For *conducting* coolants, the pressure drop is much larger, because flow across the magnetic field does work in generating electrical voltage and current. The MHD pressure drop is given approximately by the equation

$$\Delta p = \oint_0^{Lc} \frac{dx v_c B_\perp^2 \sigma C}{(1+C)} = \frac{L_C v_C B_\perp^2 \sigma C}{(1+C)} \ (Pa) \tag{6.25}$$

where σ = electrical conductivity of the fluid (A/V m),

$$C = 2\sigma_w t / \sigma D \text{ is the conductivity ratio}, \tag{6.26}$$

σ_w is the tube wall electrical conductivity (A/V-m), t = tube wall thickness (m), and $B_\perp$ is the component of the magnetic induction (T) perpendicular to the coolant flow direction. This equation is valid for large values of the

$$\text{Hartmann number Ha} = B_\perp D(\sigma/\mu)^{1/2} \qquad (6.27)$$

where μ = viscosity of the fluid (Pa s). The pumping power required to force a fluid through a channel with pressure drop Δp is

$$P = \Delta p \ (dm/dt)/\rho_m \eta_p = \Delta p \ A_c v_c/\eta_p \qquad (W) \qquad (6.28)$$

where η_p = pump efficiency.

MHD effects can have the following deleterious effects

- Making flow uneven in adjacent channels, causing hot spots
- Distorted velocity profile with jets and possible reversed flow
- Turbulence/stability modification and Joule dissipation
- Chemical reactions, such as dissociation of compounds.

These phenomena can affect heat transfer, corrosion rate, and tritium permeation (Ricapito 2010).

It is useful to compare the pumping power with the blanket thermal power. If the ratio of pumping power to heat removed were 10 % and the energy conversion efficiency were 50 %, then about 20 % of the gross electrical power would be required just to pump the coolant (unsatisfactory).

Example Problem 6.5: Lithium Coolant A 2.5 GWth reactor uses lithium coolant at T ∼ 1,100 K with ΔT = 100 K, flowing at 3 m/s for distances of 3 m in and out across an average magnetic field of 4 T in Nb–1Zr tubes with diameter 30 cm, thickness 0.2 cm. The pump efficiency is 90 %. Estimate the MHD pressure drop, number of coolant tubes, and the pumping power.

From Table 6.4 for lithium $\sigma = 2 \times 10^6$ A/V m, and for Nb–1Zr $\sigma_w = 2.3 \times 10^6$ A/V m (reciprocal of resistivity). Then C = 0.0153. From Table 6.4 $\mu = 2.5 \times 10^{-4}$ Pa s, so Ha = 1.1×10^4, and Eq. (6.25) may be used. Using L_c = 3 m in this equation the pressure drop flowing inwards is Δp = 4.3 MPa. An equal pressure drop occurs for the outward flow, so the total MHD pressure drop is Δp = 8.6 MPa. From Table 6.11, $A_c v_c$ = 13.5 m³/s. The area of one tube $\pi D^2/4$ = 0.0707 m², so 64 tubes are needed. From Eq. (6.28), the required pumping power is P = 129 MW, or about 5 % of the reactor thermal power.

However, pumping power per unit length means almost nothing in an insulated system. Nearly all of the pressure drop comes from 3D effects in the tubing, such as manifolds, bends, and flow area changes. Simple estimates like this are highly uncertain and dependent on design details.

If a non-conducting layer were used on the coolant ducts for liquid metals, the MHD pumping power could be greatly reduced. Then the friction factor in Eq. (6.24) would become a function of Ha (Miley 1976, Fig. 5.14). However, it is

difficult to prevent the insulating layer from flaking off at high temperatures. To avoid this difficulty one could use a solid freestanding insulating sleeve, such as SiC, inside the coolant tube. Alternatively a compound could be added to the fluid that would constantly coat the walls and repair any damaged areas.

A fully self-cooled concept with insulating SiC piping (similar to ARIES-AT) is estimated to have about 1 MPa total pressure drop (including an allowance of 0.25 MPa for the non-MHD portion outside the power core, including the heat exchanger). If the pressure drop exceeds about 2 MPa, then the stresses in the blanket become difficult to manage. With a flow rate of 0.15 m^3/s per blanket module, the pumping power would be about 1 % of the thermal power. The range of 1–2 MPa is reasonable. If the pressure drop is higher, then the self-cooled concept is unattractive. In a DCLL blanket, the PbLi flow rate would be lower than in fully self-cooled blanket, and its MHD pressure drop could be a lot lower, perhaps ∼0.5 MPa, but additional pumping power would be required for the helium. A typical He-cooled divertor at 10 MW/m^2 would require a pumping closer to 10 % of the thermal power it receives (Tillack 2012).

6.9.3 Power Flux Limitations

The allowable power flux on the first wall may be limited by several different problems:

- Convective heat transfer capability of coolant and coolant channel (including jet cooling)
- Pumping power
- Stresses
- Radiation damage
- Materials compatibility at high temperatures.

At high flow rates across a magnetic field, the voltage induced in molten salts may be high enough (∼1 V) to cause chemical breakdown and enhanced corrosion.

A high neutron wall load could accept more power in a given reactor size, thus lowering the cost of electricity. Wall loads of 3–4 MW/m^2 would be good, if the wall could have an adequate lifetime, but many materials issues must be accommodated (Chap. 8).

6.10 Neutronics

The main goals of neutronics calculations are listed in Table 6.12.

If many neutrons are lost through ports in the chamber walls (such as neutral beam injection ports), then the effective tritium breeding ratio R_B (also called TBR) will be reduced by approximately the ratio of blanket area to total surface

Table 6.12 Predictions of neutronics calculations

Breeding ratio R_B = number of tritium atoms produced per DT fusion neutron (also called TBR)

Blanket energy gain M = total energy deposited in blanket by neutrons (including neutron capture reactions) divided by neutron kinetic energy

Nuclear heating = power deposited per unit volume at each point in the first wall, blanket, shield, and coils

Radiation attenuation (neutrons and gammas)

Radiation streaming through ducts and cracks

Structure activation by neutron absorption

Radiation damage to materials: number of displacements per atom per year (dpa/year), and hydrogen and helium gas production rates via (n,p), and (n,α) reactions

Corrosive element production by nuclear transmutations

area of the chamber. If $R_B > 1$, then more tritium fuel is produced than is consumed, and the amount of tritium on hand increases with time. Fusion-fission hybrids may also breed U-233 or Pu-239 (Chap. 14).

The blanket energy gain is used in calculating reactor power balance. Typical values of M are 1.1–1.2 without beryllium, 1.5–1.7 with beryllium, and M $\sim$ 10 with fast fission of U-238. The value of M has a strong influence on net electrical power output and on reactor economics.

In calculating nuclear heating, it is usually assumed that the energy lost by a neutron from a collision is deposited at the point of the collision. If gamma rays are emitted, their paths are calculated to determine where their energy is deposited. The power deposition per unit volume at each point is used as the starting point for thermal-hydraulics calculations.

The radiation reaching the magnet coils must be attenuated by a factor of about 10^{-7}, in order to keep nuclear heating of the coils and radiation damage to the coil copper, superconductor, and insulation satisfactorily low. Materials that are good neutron moderators and absorbers, such as B, C and borated water, are needed to stop the neutrons. Dense, high-Z materials, such as iron and lead, are effective at stopping the gammas. The required thickness of the blanket plus shield is roughly 1–1.5 m.

Predictions of the residual radioactivity induced in the structure are needed for estimating dose-rates to workers, for remote maintenance planning, and for planning the final decommissioning of the reactor and subsequent disposal of radioactive wastes. Use of high-purity materials with short half-lives can significantly reduce the maintenance and waste disposal problems. Calculations of radiation damage and transmutations are needed to predict structural lifetimes.

Two main neutronics methods are used in blanket and shield design: transport theory and the Monte Carlo method.

6.10.1 Transport Theory: Boltzmann Transport Equation

The usual Boltzmann transport equation says that the total derivative of the distribution function $f(x,v,t)$ with respect to time is equal to the change of f due to collisions. Using the chain rule for derivatives of a function of several variables, this may be written

$$
\begin{aligned}
df(\mathbf{x},\mathbf{v},t)/dt \quad &= \quad \partial f/\partial t + (\partial f/\partial \mathbf{x})\cdot(\partial \mathbf{x}/\partial t) + (\partial f/\partial \mathbf{v})\cdot(\partial \mathbf{v}/\partial t) \\
&= \quad \partial f/\partial t + \mathbf{v}\cdot(\partial f/\partial \mathbf{x}) + (\mathbf{F}/M)\cdot(\partial f/\partial \mathbf{v}) \quad = \quad (\partial f/\partial t)_{col}
\end{aligned}
\tag{6.29}
$$

Since the neutrons and gamma rays have no charge, the Lorentz force on them is zero, and the $\mathbf{F}/m$ term vanishes. For steady state equilibrium the $\partial f/\partial t$ term also vanishes.

For the purpose of illustrating the transport theory method, a simple slab geometry will be considered here. The independent variables are the spatial coordinate x, the neutron energy E, and μ, the cosine of the angle between the neutron velocity vector and the x direction. It is customary to replace the distribution function $f(x, \mu, E)$ with a "flux distribution function" $\phi(x, \mu, E) = vf(x, \mu, E)$, where v is the neutron speed. The transport equation is a conservation equation for the number of neutrons in the differential volume element $dx\, d\mu\, dE$ at (x, μ, E). It may be expressed in words as

(Change due to neutron flow) = (Scattering in from other angles and energies)

$$+ \text{(Source of neutrons)}$$

$$- \text{(Removal of neutrons)}. \tag{6.29}$$

All terms in this equation have units of neutrons/m^3 s. The removal term is equal to the total rate for neutron interactions,

$$
(\textit{Removal rate of neutrons}) = \Sigma_t(x,E)\phi(x,\mu,E)
$$

$$
\Sigma_t(x,E) \equiv \sum_j n_j(x)\sigma_{tj}(x,E) \equiv \textit{macroscopic total cross section}
$$

$$\tag{6.30}$$

where n_j is the atomic density of species j and σ_{tj} is the total neutron cross section of species j (Here "species" means the different isotopes present in the first wall, blanket, or shield.). Since $v_x = \mu v$, the "change due to neutron flow" term $v_x(\partial f/\partial x)$ may be written $\mu(\partial \phi/\partial x)$.

The rate at which neutrons from volume element $dx\, d\mu'\, dE'$ scatter into volume element $dx\, d\mu\, dE$ is written in the form

$$
\phi(x, \mu', E')\Sigma(x, E' \to E, \mu' \to \mu)dE'd\mu'
$$

The in-scattering term in Eq. (6.29) is the integral of this rate over all E' and solid angles $d\Omega'$. Since $d\Omega = d\mu'd\phi'$, where ϕ' is the azimuthal angle (not the neutron flux), Eq. (6.29) may be written in the form

$$\mu\left(\frac{\partial\phi}{\partial x}\right) = \int_0^{2\pi} d\phi' \int_0^{\infty} dE' \int_{-1}^1 d\mu' \phi(x,\mu',E')\Sigma(x,E'\to E,\mu'\to\mu) + S(x,\mu,E)$$

$$- \Sigma_t(x,E)\phi(x,\mu,E) \tag{6.31}$$

where S(x, μ, E) represents an arbitrary neutron source term. This Boltzmann equation has a similar form in cylindrical geometry, but with added complexity from the effects of curvature.

6.10.2 Legendre Expansion

Let μ_o be the cosine of the angle between v and v′, the velocities of a neutron before and after scattering. Then the macroscopic in-scattering cross section may be written as $\Sigma(x, \mu_o, E' \to E)$, since its angular dependence is solely a function of μ_o. It is convenient to represent the scattering cross section in terms of a series of Legendre polynomials:

$$\Sigma(x,\mu_0,E'\to E) = \sum_{\ell=0}^L \Sigma_\ell(x,E'\to E)P_\ell(\mu_0) \tag{6.32}$$

where Σ_ℓ are the expansion coefficients. Some properties of Legendre polynomials are listed in Table 6.13.

Table 6.13 Properties of Legendre polynomials $P_L(\mu)$

Differential equation:

$(1-\mu^2)(\partial^2 P_\ell/\partial\mu^2) - 2\mu(\partial P_\ell/\partial\mu) + \ell(\ell+1)P_\ell = 0$

Values of P_ℓ:

$P_0(\mu) = 1$, $P_1(\mu) = \mu$, $P_2(\mu) = (3\mu^2 - 1)/2$, $P_3(\mu) = (5\mu^3 - 3\mu)/2$, etc.

Recurrence relation:

$P_{\ell+1}(\mu) = [(2\ell+1)\mu P_\ell(\mu) - \ell P_{\ell-1}(\mu)]/(\ell+1)$

Orthogonality condition:

$\int_{-1}^1 \partial\mu P_\ell(\mu)P_m(\mu) = \begin{cases} 0, & l \neq m \\ 2/(2\ell+1), & l = m \end{cases}$

Expansion theorem: Any continuous function F(μ) in the domain (−1,1) may be represented as a series of Legendre polynomials

$F(\mu) = \sum_{\ell=0}^\infty a_\ell P_\ell(\mu)$, where the coefficients a_ℓ are given by

$a_\ell = \frac{2\ell+1}{2} \int_{-1}^1 \partial\mu F(\mu)P_\ell(\mu)$

Addition Theorem: If μ_0 is the cosine of an angle between two vectors having polar angles θ and θ' and azimuthal angles ϕ and ϕ' relative to a given coordinate system, then

$P_\ell(\mu_0) = P_\ell(\mu)P_\ell(\mu') + 2\sum_{m=1}^\ell \frac{(\ell-m)!}{(\ell+m)!} P_\ell^m(\mu)P_\ell^m(\mu')\cos m(\phi-\phi')$,

where $\mu = \cos\theta$, $\mu' = \cos\theta'$ and the functions $P_\ell^m(\mu)$ are "Associated Legendre Polynomials"

In the Expansion Theorem the upper limit $L = \infty$, but accuracy is usually satisfactory with $L = 3$ or 5. The transport Eq. (6.31) becomes

$$\mu\left(\frac{\partial\phi}{\partial x}\right) = \int_0^{2\pi} d\phi' \int_0^\infty dE' \int_{-1}^1 d\mu'\, \phi(x, \mu', E') \sum_{\ell=0}^L \Sigma_\ell(x, E' \to E)P_\ell(\mu_0) + S(x, \mu, E)$$
$$- \Sigma_t(x, E)\phi(x, \mu, E) \tag{6.33}$$

The integration over ϕ' may be carried out after using the Addition Theorem for $P_\ell(\mu_o)$. Thus,

$$\int_0^{2\pi} d\phi' P_\ell(\mu_0) = 2\pi P_\ell(\mu)P_\ell(\mu') \tag{6.34}$$

since

$$\int_0^{2\pi} d\phi' \cos m(\phi - \phi') = 0 \tag{6.35}$$

Then Eq. (6.33) becomes

$$\mu\left(\frac{\partial\phi}{\partial x}\right) = 2\pi \int_0^\infty dE' \int_{-1}^1 d\mu'\, \phi(x, \mu', E') \sum_{\ell=0}^L \Sigma_\ell(x, E' \to E)P_\ell(\mu)P_\ell(\mu') + S(x, \mu, E)$$
$$- \Sigma_t(x, E)\phi(x, \mu, E) \tag{6.36}$$

6.10.3 Discrete Ordinates Method

The discrete ordinates method involves dividing up the spatial, angular and energy regions into discrete locations (x_i, μ_j, E_k) separated by intervals Δx, $\Delta\mu$, ΔE, as illustrated in Fig. 6.27.

The discrete ordinates equation is formally derived by integrating the Boltzmann equation (6.29) over the volume of one of the little cubes. For simplicity, we will use a less rigorous approach here. Since the Boltzmann equation is a neutron conservation equation, it must hold for each little cube, denoted by (x_i, μ_j, E_k) or simply by (i,j,k). The summation sign may be moved to the left of the integral signs. Then the integrals over dE' and $d\mu'$ may be replaced by summations over k' and j'. For example

$$\int_{-1}^1 d\mu'\, \phi(x, \mu', E')P_\ell(\mu') \approx \sum_{j'=1}^N \phi(i, j', k')P_\ell(j')\Delta\mu(j')w(j') \tag{6.37}$$

Fig. 6.27 Division of the space into discrete values of x, μ and E. For the case shown I = 10 spatial intervals, N = 4 angular intervals, and K = 10 energy intervals. The flux is to be found at the center of each of the 400 little cubes
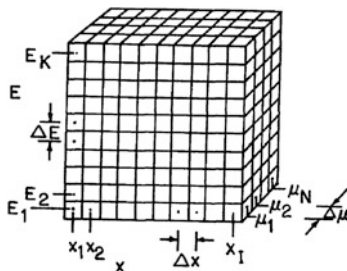
where w(j′) are weighting factors appropriate to the numerical approximation of the integral. The simplest value of w(j′) is 1, which approximates the curve by a series of rectangles. Greater accuracy can be obtained by approximating the curve with a series of straight line segments (the trapezoidal approximation) with a series of parabolic segments (Simpson's Rule), or with a Gaussian quadrature formula (With Gaussian quadrature, the $\Delta\mu(j')$ vary). The derivative of ϕ appearing in Eq. (6.36) may be replaced by the finite difference approximation.

$$\frac{\partial\phi(i,j,k)}{\partial x} \approx \frac{[\phi(i+l,j,k)-\phi(i,j,k)]}{\Delta x} \tag{6.38}$$

or a similar alternative. The discrete ordinates version of Eq. (6.36) for one little cube may now be written

$$\left(\frac{\mu_j}{\Delta x}\right)[\phi(i+l,j,k)-\phi(i,j,k)] = S(i,j,k) - \Sigma_t(i,k)\phi(i,j,k)$$
$$+ 2\pi\sum_{j'=1}^{N}\sum_{k'=1}^{K}\sum_{\ell=0}^{L}\Delta\mu(j')\Delta E(k')w(j')w(k')$$
$$\phi(i,j',k')\Sigma_\ell(i,k'\to k)P_\ell(j)P_\ell(j') \tag{6.39}$$

Except for the fluxes, the parameters of this equation are all known. The flux, or its derivative, will be known along a boundary (such as x_1). In the original S_N method, the weighting factors w_j were derived assuming that the flux varies linearly between neighboring locations. In more recent versions other weights have been used to improve accuracy and convergence, and some quantities may be evaluated at the edges of the little cubes of Fig. 6.27, as well as at their centers.

Equations of the form (6.39) are written at every point where the flux is to be found, and the resulting set of linear, algebraic equations must be solved simultaneously. In principle, the equations could be written in matrix form and the matrix inverted to determine the fluxes. In practice, however, the inversion of an enormous matrix is too time-consuming, so the equations are solved iteratively. Initial values of ϕ are assumed at all locations. Then each equation of the form (6.39) is solved for a new value of $\phi(i, j, k)$ in terms of the present values at the adjacent points. The order of calculations should correspond to the direction of

neutron motion. For example, if the neutrons start off at x_1 with high energy in the forward direction, then the calculations would start off at x_1, high energy, large μ. Solving for the new fluxes at every point in the volume of Fig. 6.27 constitutes one iteration. After many iterations, the values of the fluxes will usually converge to the desired solution.

The term "S_N approximation" means that N angular intervals are used. For instance, a P_3S_8 approximation uses N = 8 angular intervals and has L = 3 in the Legendre expansion of the scattering cross section. A typical blanket calculation might use on the order of 100 spatial points (I = 100) and 100 energy groups (K = 100). The discrete ordinates method is also used to calculate gamma fluxes, using about 30 gamma energy groups. It may also be adapted to two or three spatial dimensions, with a great increase in computer time and memory.

If the angular dependence is dropped from the Boltzmann equation (by taking L = 0, N = 1), then the "multigroup diffusion equations" are obtained. This loss of angular resolution reduces the accuracy of the results, so the multigroup diffusion equations are obsolete. Once the neutron flux is known, the reaction rates r_q for neutron absorption, tritium breeding, energy deposition, etc., may be calculated using equations of the form

$$
r_q(x) = 2\pi \int_{-1}^{1} d\mu \int_{0}^{E_{max}} dE \phi(x, \mu, E) \Sigma_q(x, E)
$$

$$
\approx 2\pi \sum_{j=1}^{N} \sum_{k=1}^{K} \Delta\mu(j)\Delta E(k)w(j)w(k)\phi(i,j,k)\Sigma_q(i,k) \left(\text{reactions/m}^3 \text{ s}\right)
$$

(6.40)

where

$$
\Sigma_q \equiv \sum_{j} n_j \sigma_{qj}
$$

(6.41)

is the macroscopic cross section for reaction type q, and the w's are again weighing factors for numerical integrations. Some sources of error in neutron transport calculations are listed in Table 6.14.

Table 6.14 Sources of error in neutron transport calculations

Convergence error can be made very small by using a large number of iterations
Roundoff error is usually negligible on modern computers with many significant digits
Human error can be minimized by thorough checking of programs, and by having the same set of calculations done independently by two or more groups of researchers, using different codes
Truncation error arises from using a finite number of increments I, N, K, L to approximate continuous variables. Methods of estimating this error are well developed
Model error arises from representing the blanket by an idealized model. For example, helium coolant tubes might be represented by a uniform void fraction and a uniform structure fraction
Data error arises from uncertainty in nuclear cross sections, typically a few percent

Convergence, round-off, and human error can be made negligible. The overall probable error of the results can be estimated by combining the probable errors due to truncation, model, and data. The spatial details of a blanket are poorly represented by a one-dimensional transport model, but they can be taken into account with the Monte Carlo technique.

6.10.4 The Monte Carlo Method

The Monte Carlo method simulates a large number of individual particle trajectories, and then averages the results to determine the desired quantities, such as breeding ratio and energy deposition. We will again consider neutrons, keeping in mind that the technique applies also to gamma rays. To simulate a given neutron's history, a series of questions are posed, and the answer to each question is decided statistically. For example, if only two choices were available, and if they had equal probability, we could flip a coin to decide. In practice many choices are available, and they have probabilities determined by factors such as nuclear scattering cross sections. Instead of flipping a coin, a "random number generator" is used. The random number generator is a computer algorithm (procedure) to generate decimal fractions randomly and uniformly between 0 and 1.

The random number is compared with the probability of an event to decide whether or not it occurs. For example, if the probability of an event were 0.300, we could decide that the event will occur if the random number is less than 0.300, and that it will not occur if the random number is greater than 0.300. A flow chart for Monte Carlo neutron simulations is shown in Fig. 6.28.

To illustrate the method we will consider the case of a monoenergetic beam of neutrons entering a slab of thickness L at angle θ_o, as illustrated in Fig. 6.29.

6.10.5 Location of Next Interaction

The probability that a neutron travels a distance ℓ *without* having an interaction is equal to $\exp(-\ell/\lambda)$, where $\lambda = 1/\Sigma_t$ is the neutron mean free path and Σ_t is the total macroscopic neutron cross section (reaction probability per unit distance). Therefore, the probability that a neutron *does* have an interaction within distance ℓ is

$$P_{int}(\ell) = 1 - \exp\left(\frac{-\ell}{\lambda}\right) \tag{6.42}$$

which is plotted in Fig. 6.30.

In order to decide how far the neutron goes before it has an interaction, we can equate $P_{int}(\ell)$, which ranges between 0 and 1, to a random number N_r between 0 and 1. Then, solving for ℓ/λ, we find that
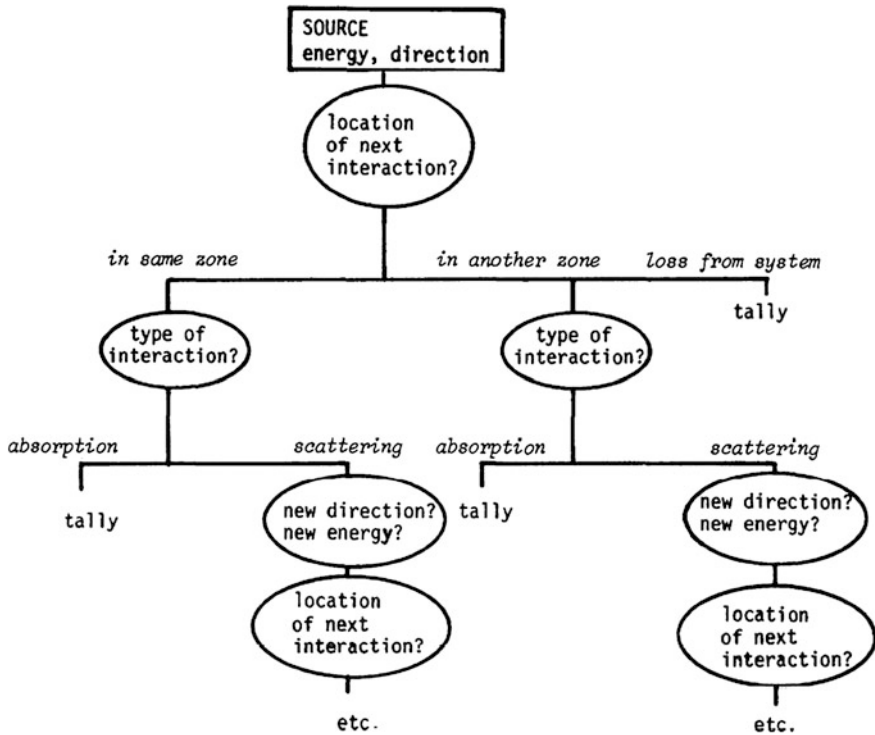
Fig. 6.28 Flow chart for decision-making in the Monte Carlo method

Fig. 6.29 A beam of neutrons incident on a single-zone slab. It is desired to know the numbers of neutrons absorbed at each point in the slab, the number transmitted through the slab, and the number backscattered out of the slab. The axes have been chosen so that the initial velocity of the neutrons lies in the y–z plane
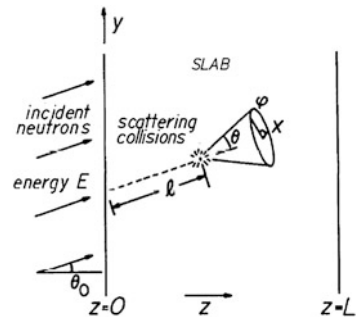
$$\ell/\lambda = -\ln(1 - N_r) = -\ln(N_r') \tag{6.43}$$

where $N_r' = (1 - N_r)$ is also a random number. For example, if $N_r' = 0.386$, this equation decides that the neutron travels a distance of 0.952 mean free paths before its first collision. The z distance of travel is equal to $\ell\cos\theta$. If the z distance travelled is greater than the slab thickness L (not the L of Eq. 6.33), then the neutron has escaped from the slab. If not; it has a collision within the slab.

Fig. 6.30 Graph of the
equation $P_{int}(\ell) =$
$1 - \exp(-\ell/\lambda)$
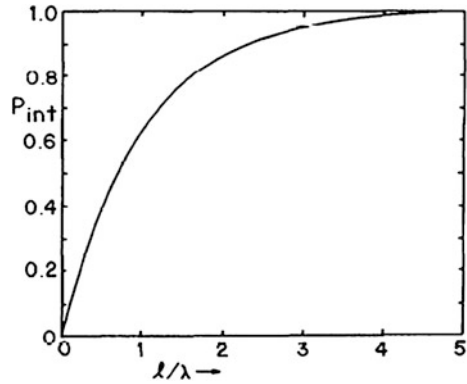
6.10.6 Type of Interaction

Consider a case in which four types of neutron interactions can occur:

- Σ_{el} elastic scattering
- Σ_{in} inelastic scattering (inelastic means that the target nucleus absorbs energy internally during the collision and is raised to an excited nuclear energy level, usually followed by gamma emission)
- Σ_{2n} (n,2n) reactions
- $\Sigma\gamma$ radiative capture (Radiative capture refers to neutron absorption by a nucleus, followed by gamma decay of the new nucleus.)

The following algorithm could be used to decide which type of interaction occurs:

$$
\begin{array}{lll}
if & 0 \leqq N_r \leqq \frac{\Sigma_{el}}{\Sigma_t} & elastic\ scattering \\
if & \frac{\Sigma_{el}}{\Sigma_t} < N_r \leqq \frac{(\Sigma_{el}+\Sigma_{in})}{\Sigma_t} & inelastic\ scattering \\
if & \frac{(\Sigma_{el}+\Sigma_{in})}{\Sigma_t} < N_r \leqq \frac{(\Sigma_{el}+\Sigma_{in}+\Sigma_{2n})}{\Sigma_t} & (n,2n)\ reaction \\
if & \frac{(\Sigma_{el}+\Sigma_{in}+\Sigma_{2n})}{\Sigma_t} < N_r \leqq 1 & radiative\ capture
\end{array}
\tag{6.44}
$$

where the total cross section $\Sigma_t = \Sigma_{el} + \Sigma_{in} + \Sigma_{2n} + \Sigma_\gamma$.

If scattering occurs, the scattering angle and new energy are chosen using random numbers (described below). If an (n,2n) reaction occurs, the second neutron trajectory must be traced later on. If radiative capture occurs, then the gamma energy deposition must be calculated.

6.10.7 New Direction and Energy

Nuclear collision scattering angles are usually calculated in the center of mass (COM) coordinate system. The position $\mathbf{r}_c$ of the center of mass is defined to be
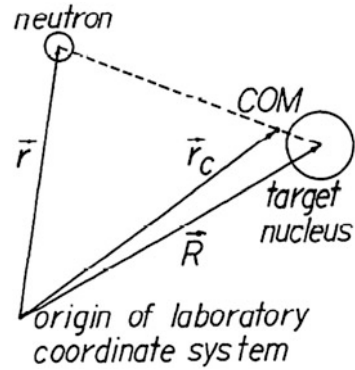
$$(m + M)\mathbf{r_c} = m\mathbf{r} + M\mathbf{R} \tag{6.45}$$

where m and M are the neutron and target nucleus masses, and **r** and **R** are their position vectors, as illustrated in Fig. 6.31.

The velocity of the center of mass is found by differentiating Eq. (6.45) with respect to time:

$$\mathbf{v_c} = (m\mathbf{v} + M\mathbf{V})/(m + M) = (v + Av)/(1 + A), \tag{6.46}$$

where **v** and **V** are the velocities of the neutron and target nucleus, and A = M/m.

The COM coordinate system has its origin at the COM, so it moves relative to the fixed ("laboratory") coordinate system with a velocity $\mathbf{v_c}$.

Let $\sigma(\psi, E)d\psi$ be the cross section for a neutron with energy E to scatter into a differential angle $d\psi$, at ψ, where ψ is measured relative to the COM coordinate system. The total scattering cross section is $\sigma(E) = \int d\Omega' \sigma(\psi', E)$ where $d\Omega'$ is a differential solid angle. The probability of scattering through an angle less than ψ is equal to

$$P(\psi, E) = \frac{\int_{\psi=0}^{\psi} d\Omega' \sigma(\psi', E)}{\int_{\psi=0}^{\pi} d\Omega' \sigma(\psi', E)} = \frac{\int_{0}^{\psi} 2\pi \sin \psi' d\psi' \sigma(\psi', E)}{\int_{0}^{\pi} 2\pi \sin \psi \prime d\psi' \sigma(\psi', E)} \tag{6.47}$$

The scattering angle is found by equating $P(\psi, E)$ to a random number and solving Eq. (6.47) for ψ. This can be accomplished on a computer by tabulating $P(\psi, E)$ versus ψ and E, then inverting the table and interpolating to get the value of ψ corresponding to any given E and $P(\psi) = N_r$. For the simple case in which scattering is equally probable in all directions (*isotropic scattering*) in the COM system, the equation for ψ simplifies to

$$\psi = \cos^{-1}(1 - 2N_r). \tag{6.48}$$

For example, if $N_r = 0.215$, then the COM scattering angle $\psi = 55.2°$.

Consider the case of inelastic scattering, in which the target nucleus receives an excitation energy ε. If E was the initial neutron energy, the final neutron energy E' is given by

$$\frac{E'}{E} = \frac{1}{(A+1)^2}\left[1 + A^2\left(1 - \frac{\varepsilon}{E}\right) + 2A\cos\psi\left(1 - \frac{\varepsilon}{E}\right)^{\frac{1}{2}}\right] \qquad (6.49)$$

and the neutron scattering angle θ measured in the laboratory system is found from

$$\cos\theta = \frac{1 + A\cos\psi(1 - \frac{\varepsilon}{E})^{\frac{1}{2}}}{[1 + A^2\left(1 - \frac{\varepsilon}{E}\right) + 2A\cos\psi\left(1 - \frac{\varepsilon}{E}\right)^{\frac{1}{2}}]^{\frac{1}{2}}} \qquad (6.50)$$

(Schaeffer 1973). The kinetic energy imparted to the target nucleus is equal to $(E-E'-\varepsilon)$. For elastic scattering we can set $\varepsilon = 0$ in these equations. All values of the azimuthal scattering angle ϕ (Fig. 6.29) are equally probable, so ϕ is distributed uniformly between 0 and 2π:

$$\phi = 2\pi N_r. \qquad (6.51)$$

If (α, β, γ) are the original direction cosines of the neutron velocity relative to the x, y, and z axes, the new direction cosines are given by

$$\alpha' = \alpha\cos\theta + \gamma\alpha\frac{\sin\theta\cos\phi}{(1 - \gamma^2)^{\frac{1}{2}}} - \beta\frac{\sin\theta\sin\phi}{(1 - \gamma^2)^{\frac{1}{2}}}$$

$$\beta' = \beta\cos\theta + \gamma\beta\frac{\sin\theta\cos\phi}{(1 - \gamma^2)^{\frac{1}{2}}} - \alpha\frac{\sin\theta\sin\phi}{(1 - \gamma^2)^{\frac{1}{2}}} \qquad (6.52)$$

$$\gamma' = \gamma\cos\theta - \left(1 - \gamma^2\right)^{\frac{1}{2}}\sin\theta\cos\phi$$

$$\textit{except for the case } \left(1 - \gamma^2\right) \ll 1, \textit{ where} \qquad (6.53)$$
$$\alpha' = \sin\theta\cos\phi, \ \beta' = \sin\theta\sin\phi, \ \gamma' = \gamma\cos\theta$$

may be used for better accuracy (Schaeffer 1973).

Having calculated the new neutron energy E' and direction $(\alpha', \beta', \gamma')$, we are ready to return to the starting point of the flow chart, Fig. 6.28, and ask whether the neutron escapes from the slab or has another collision. The new path length R is calculated from Eq. (6.43), and so on until the particle escapes from the slab or is absorbed. (Gamma rays are also "killed" if their energy falls below some chosen value, to save computer time by not tracking low-energy gammas.)

6.10.8 Tallying

For the case in which several isotopes are present, the algorithm Eq. (6.44) is further divided up according to the macroscopic cross sections for each isotope.

Thus, it determines both the type of interaction and the species of the target nucleus. The slab (or cylinder, in the case of a fusion reactor blanket) is divided up into small spatial regions, and each region is assigned several "bins" in the computer program. The computer then counts the number of times a neutron has various types of interactions in that region (such as tritium breeding) and the amount of energy deposited in that region. For example, if a neutron loses 1.2 MeV in an interaction in the spatial region between $x = 55$ cm and $x = 60$ cm, then 1.2 MeV is added to the energy deposition bin for that region. If part of this energy is then emitted as a gamma ray, however, the gamma ray should be tracked to see where its energy is deposited, and some of the 1.2 MeV may go into other bins. After tallying case histories of thousands of neutrons, the numbers in the bins are analyzed to determine the desired quantities, such as energy deposition versus radius and tritium breeding ratio per incident neutron. The required number of neutron histories that must be run is determined from the desired accuracy by a statistical error analysis.

6.10.9 Error Estimates

Some parameters used in statistical error analysis are defined in Table 6.15.

Consider the problem of determining the fraction of neutrons that are transmitted through a given slab of blanket material. In ordinary Monte Carlo calculations without "splitting" (discussed below), each neutron penetrating through the slab adds one count to the tally, and those which don't penetrate add zero, so the data points X_j are all either 0 or 1.

Example Problem 6.6: Monte Carlo Error Estimate In a given Monte Carlo simulation with $N = 80$ neutron histories, 4 neutrons penetrated through the slab. Find the fractional penetration, and estimate the standard error of this value.

Here we have 4 data points with $x_j = 1$ and 76 data points with $x_j = 0$. The mean value is $\bar{x} = 4/80 = 0.05$, which is the simulation estimate of the true fractional penetration μ. The standard deviation of the sample is found from the equation of Table 6.15 to be $s = \left[\frac{80(4)-16}{80(79)}\right]^{\frac{1}{2}} = 0.2193$.

We make the customary approximation that $\sigma \simeq s$, and find that $\sigma_{\bar{x}} \simeq 0.2193/(80)^{\frac{1}{2}} = 0.0245$. Then we can use the consequence of the Central Limit Theorem to estimate the probable error of $\bar{x}$. It is 68 % probable that the experimental value $\bar{x}$ is within ± 0.0245 of the true value μ. This may be called the "standard error" of $\bar{x}$. Thus, we estimate that $\mu = 0.050 \pm 0.0245$, which is a relative error of about 49 %.

Such a large relative error would make the results practically worthless. To avoid such difficulties, we need to plan ahead to make N large enough to ensure the desired level of accuracy. For example, if we increased N to 800 in the above

Table 6.15 Parameters used in statistical error analysis

Individual data points $x_1, x_2, x_3, \ldots x_j, \ldots x_N$			
Number of data points in sample	N		
Mean value of data	$\bar{x}$	$=$	$\frac{\sum x_j}{N}$ where summation is from 1 to N
True value sought, to which $\bar{x}$ is an approximation	μ		(The value of μ is a secret known only to Mother Nature)
Sample variance (variance of data about $\bar{x}$)	s^2	$\equiv$	$\frac{\sum (x_j - \bar{x})^2}{N-1} = \frac{N\sum(x_j)^2 - (\sum x_j)^2}{N(N-1)}$
Standard deviation of sample	s		(x_j relative to $\bar{x}$)
Standard deviation (of data about μ)	σ		(x_j relative to μ)
Standard deviation of the mean	$\sigma_{\bar{x}}$	$=$	$\sigma/N^{\frac{1}{2}}$ ($\bar{x}$ relative to μ)
Error	ε	$=$	$\lvert \bar{x} - \mu \rvert$
Probability that error is less than z	$P(\varepsilon < z)$		

ESTIMATION OF PROBABLE ERROR

Central Limit Theorem: If N is large ($N \gtrsim 30$), the distribution of $\bar{x}$ about μ is closely approximated by a normal (Gaussian) distribution with standard deviation $\sigma_{\bar{x}}$

Consequence: $\quad\quad\quad\quad P(\varepsilon < z) = \mathrm{erf}\left(z/2^{\frac{1}{2}}\sigma_{\bar{x}}\right)$ (Error function: Appendix C)

Example: $\quad\quad\quad\quad$ It is 68.3 % probable $\quad$ (the standard error)

that $\varepsilon < \sigma_{\bar{x}}$

It is 95.4 % probable

that $\varepsilon < 2\sigma_{\bar{x}}$

It is 99.7 % probable

that $\varepsilon < 3\sigma_{\bar{x}}$

RELATION BETWEEN s AND σ (Burlington and May 1970)

If $N = 5$, it is 90 % probable that $0.73 < (s/\sigma) < 2.65$

If $N = 10$, it is 90 % probable that $0.77 < (s/\sigma) < 1.73$

If $N = 20$, it is 90 % probable that $0.81 < (s/\sigma) < 1.41$

If $N = 30$, it is 90 % probable that $0.84 < (s/\sigma) < 1.30$

example, and if 39 neutrons penetrated the slab, then the revised estimate would be $\mu = 0.0488 \pm 0.0076$, or a relative error of 16 %. If we further increased N to 8,000 and observed 394 neutrons penetrated, the estimate would become $\mu = 0.04925 \pm 0.00242$, a relative error of 4.9 %.

6.10.10 Number of Case Histories Needed

For the simple situation in which the data are either 0 or 1, $\Sigma(x_j)2 = \Sigma \, x_j$, and the expression for s may be simplified to the form

$$s = \left[\frac{N\bar{x}(1 - \bar{x})}{N - 1}\right]^{\frac{1}{2}} \quad\quad\quad (6.54)$$

so the standard error estimate yields

$$\frac{\sigma_{\bar{x}}}{\mu} \approx \frac{s}{N^{\frac{1}{2}}\bar{x}} = \left[\frac{1-\bar{x}}{\bar{x}(N-1)}\right]^{\frac{1}{2}} \tag{6.55}$$

This gives the same error estimates obtained above, namely 49, 16, and 4.9 %, respectively. For large N and small $\bar{x}$, the relative error reduces to

$$\frac{\sigma_{\bar{x}}}{\mu} \approx \left[\frac{1}{N\bar{x}}\right]^{\frac{1}{2}} \quad or \quad N = \left(\frac{\mu}{\sigma_{\bar{x}}}\right)^2 \frac{1}{\bar{x}} \tag{6.56}$$

We can use this formula to estimate the number of histories required for a given degree of accuracy $\frac{\sigma_{\bar{x}}}{\mu}$, if we have an estimate of $\bar{x}$ (or of μ). For example, if we expect $\bar{x} = 0.003$ and want a relative error of less than 5 %, then the required value is $N = 1/(0.05)^2\bar{x} = 1.3 \times 10^5$ neutron histories. This large value illustrates the main limitation of ordinary Monte Carlo methods: study of improbable phenomena requires excessively large numbers of case histories. To get around this difficulty, a number of "variance reduction" techniques have been devised to decrease the probable error without increasing N.

6.10.11 Variance Reduction Techniques

The main types of variance reduction techniques are:

- **Statistical tallying**. Instead of counting each particle as 0 or 1, the particle is given a variable weight W_j, which may be split up and deposited in many bins during the particle history. For example, if the probability of absorption during a given collision is 0.12, then $0.12W_j$ is deposited in the absorption bin at that point, and $0.88W_j$ continues the history. In the slab penetration problem, each neutron flight path could be extended to the exit boundary to estimate the penetration probability at that step, and the corresponding fractional penetration weight tallied and subtracted from the particle weight.
- **Importance functions**. An "importance function" is a means for increasing the number of particles in a spatial, angular, or energy region of interest. The region of interest in the slab penetration problem is the spatial region near the exit boundary. To conserve particles, $N_g W_g = $ constant, where N_g is the number of particles in a group g, and W_g is their weight. For example, if the number of particles in a given region is doubled, then their weights must be halved. (This is called splitting.)
- **Avoidance of gaming**. Every time a random number N_r is used to make a decision, the variance of the data is increased, and so is $\sigma_{\bar{x}}$. It is thus desirable to get a maximum amount of information from a Monte Carlo program with a minimum of random-number decisions. Reducing the use of random-number

Table 6.16 Variance reduction techniques used with Monte Carlo simulation of radiation transport

Avoidance of gaming

Statistical tallying of fractional weights

Statistical estimation of fractional penetration, backscatter, etc.

Systematic sampling = using an ordered cycle to replace N_r at one point in the program

For example, if there are N = 100 cases, the values replacing N_r could be 0.005, 0.015, 0.025,…, 0.995

Importance functions

Source biasing = artificially increasing the number of incident particles going in the desired direction or having the desired energy (with a corresponding reduction of their weights)

Path-length biasing = artificially decreasing the flight path lengths (to increase the number of interactions in a given region) or increasing the flight path lengths (to increase the number penetrating through the region), with a corresponding adjustment of particle weights

Splitting = artificially doubling the number of particles entering a given region, while halving their weights

Russian Roulette = "killing" some of the particles in regions of little interest, and increasing the weights of the remaining particles (opposite of splitting)

decisions is called "avoidance of gaming." Some techniques for variance reduction are listed in Table 6.16.

In shielding problems with thick slabs, many splitting planes may be placed in the slab, to keep the number of particles roughly constant through the slab, while greatly decreasing their individual weights. Thus, for the case in which N = 1,000 and $\mu = 0.002$, instead of 2 particles emerging from the slab, one might have over 1,000 particles emerging with an overall average weight of about 0.002. For this case, the probable error is greatly reduced in comparison to the case of 2 neutrons emerging. In spite of the advantages of variance reduction techniques, their use complicates the program and should be avoided if ordinary Monte Carlo can do an adequate job (when $\bar{x}$ is not small).

A sample ordinary Monte Carlo program for estimating neutron penetration, absorption, and reflection in a slab is listed by Schaeffer (1973). For one-dimensional problems and two-dimensional problems with simple geometry, transport theory is probably faster and more accurate than Monte Carlo. However, for complex two- and three-dimensional problems, transport theory is too cumbersome, and Monte Carlo must be used. For example, estimation of the radiation streaming out a neutral beam injection port is best done with the Monte Carlo method.

6.10.12 Neutronics Results

Neutronics studies for fusion power plant studies produce information on

- Neutron energy spectra versus position
- Tritium breeding ratio
- Nuclear heating and blanket energy gain

Fig. 6.32 Variation of
Tritium breeding ratio (*TBR*)
with ^{6}Li enrichment for
ARIES-CS. M_n is the energy
gain in the blanket due to
neutron reactions there
(El-Guebaly et al. 2008).
© 2008 by the American
Nuclear Society, LaGrange
Park, Illinois
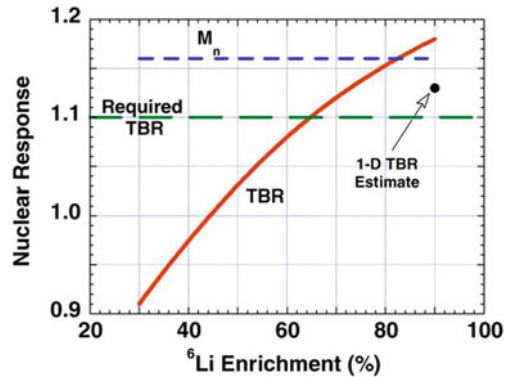
- Attenuation by shield
- Neutron streaming through ducts
- Radioisotope generation
- Decay heat after shutdown
- Radioactivity of components and dose rates versus time after shutdown
- Possibility of recycling or clearance of radioactive materials.

For example, Fig. 6.32 shows how the TBR of the ARIES Compact Stellarator (ARIES-CS) varies with ^{6}Li enrichment.

The one-dimensional calculation yields an estimate that is too low. Uncertainties in the TBR come from:

- Deficiencies in nuclear data (6–10 %)
- Inaccuracies of modeling (3–7 %) Even 3-D models cannot include all the details accurately
- Uncertainties in design elements (0–3 %), such as changes to structure or armor
- Margin that accounts for breeding in excess of consumption (1–2 %). The tritium inventory in each location (storage, coolant, wall, blanket, processing system, etc.) varies with time.

The start-up tritium inventory could be several kg. High TBR yield short inventory doubling times, which would be helpful for starting up new fusion power plants. If a short doubling time were not needed, then safe storage of the excess tritium could become a concern, and the ^{6}Li enrichment in the blanket might be adjusted to limit the breeding ratio (El-Guebaly and Malang 2009).

A high plasma edge recycling mode could increase the tritium burnup fraction, which would reduce the required start-up inventory (El-Guebaly and Malang 2009). On the other hand a lithium wall coating has been proposed to minimize wall recycling, in order to keep edge temperatures high and minimize plasma instabilities. The capture of tritium by flowing lithium followed by its prompt re-injection into the core plasma might help reduce the required startup inventory.

Fig. 6.33 Variation of nuclear heating with radius in the ARIES-AT tokamak (El-Guebaly et al. 2006)
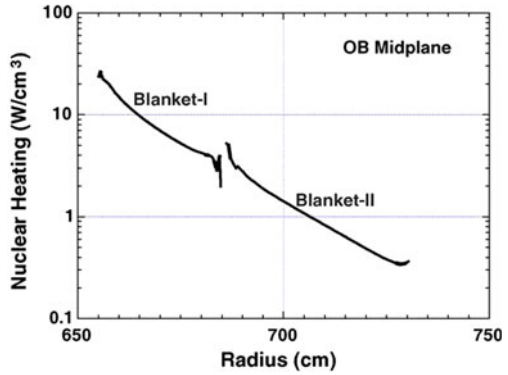
Fig. 6.34 Decrease of radioactivity in ARIES-CS with time after shutdown (El-Guebaly et al. 2005). © 2005 by the American Nuclear Society, LaGrange Park, Illinois
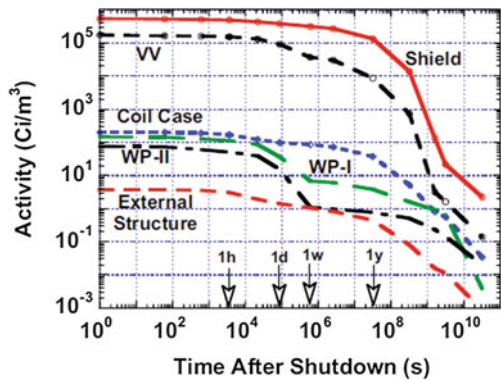
Figure 6.33 shows how the nuclear heating during operation varies with radius in the blanket and shield of the ARIES-AT tokamak.

Figure 6.34 shows how the radioactivity of ARIES-CS decreases in time after shutdown.

The tungsten carbide filler in the shield is the slowest to decay. It was chosen to minimize the distance between the coil and the plasma, which minimizes the cost of electricity (COE). Materials that decay more rapidly could be chosen, at the expense of thicker shield and a higher COE. However, all materials decay well within 100 years.

Figure 6.35 shows how the radiation is attenuated in the concrete biological shield outside the coils.

(1 mrem/h = 10^{-5} Sievert/h). A thickness of at least 1.9 m is required to meet the design specifications.

The University of Wisconsin group developed the Direct Accelerated Geometry Monte Carlo (DAGMC) code, which couples a Computer Aided Design (CAD) code to a 3-D Monte Carlo neutronics code. With this code they analyzed the ARIES "Aggressive Conservative Tokamak" (ACT) DCLL blanket, starting with the basic configuration. Step by step they added the various blanket components
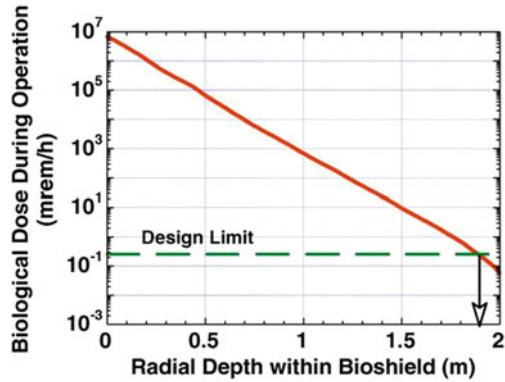
(including walls, cooling channels, flow channel inserts, stabilizing shells, and assembly gaps) and evaluated their impacts on the TBR. With 90 % enrichment of ^{6}Li, the basic configuration in a straight cylinder with infinitely thick blanket yields a TBR = 1.79, Fig. 6.36.

Changing to toroidal geometry drops the TBR to 1.64. Making the inboard and outboard blanket thicknesses 45 and 80 cm lowers the TBR to 1.27. Adding walls, cooling channels, 2 cm assembly gaps, flow channel inserts (insulators to reduce MHD pressure drop), and a tungsten stabilizing shell reduce the TBR to 1.015. At this point the designers increased the inboard/outboard blankets to 65 and 97 cm to increase the TBR. They also reduced the enrichment to 70 % (to provide the possibility of increasing the TBR during operation, if needed), yielding TBR = 1.05.
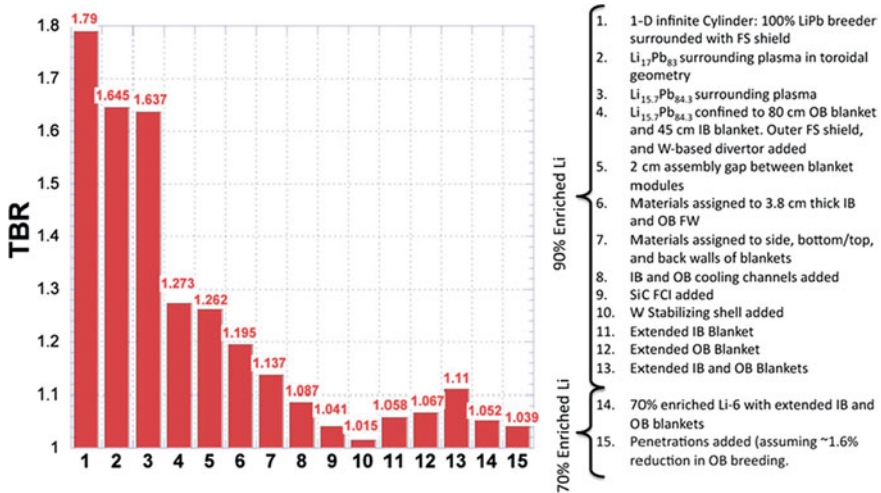
Fig. 6.36 Bar chart showing how the TBR is changed by the addition of various features (El-Guebaly et al. 2012). © 2012 by the American Nuclear Society, LaGrange Park, Illinois

Addition of penetrations for heating and fueling would reduce it slightly, to about 1.04. Their findings show how the individual design elements degrade or enhance the TBR, which is important for all blanket designs (El-Guebaly and Malang 2009).

Calculations of neutron energy spectra, TBR, blanket energy gain, decay heat, attenuation by shield, neutron streaming, radioisotope generation, dose rates, and recycling or clearance of radioactive materials are required to guide reactor designers in materials selection and blanket design.

6.11 Blanket Configurations

6.11.1 Coolant Flow Configurations

Some coolant channel design considerations are listed in Table 6.17.

Various compromises are made in choosing coolant temperature, pressure, and tube size.

- High outlet temperatures are needed for good thermal conversion efficiency, but they are detrimental to strength and compatibility.
- Large coolant ΔT through the blanket permits lower flow rates and pumping powers, but creates thermal stress problems.
- High helium coolant pressures decrease the required velocities, but increase duct stresses.

Table 6.17 Coolant channel design considerations

Temperature distribution
Maximum coolant outlet temperature
Cool first wall
Hot breeder for tritium removal
Avoidance of hot spots
Temperatures within compatibility limits
Pumping power
Stress
Stresses from gravity, pressure, temperature gradients
Thermal expansion allowance
Avoidance of creep, thermal strain fatigue, stress corrosion fatigue
Neutronics
Low void fraction
Small structure fraction
Avoidance of long-lived radioisotope generation
Tritium removal and inventory
High reliability
Easy maintenance—vital, yet very difficult to achieve
Materials that are abundant, inexpensive, noncorrosive, and easily fabricated and joined

- Thin tubes have high hoop stresses, and thick tubes have high thermal stresses.
- Large He tube diameters decrease the number of tubes and welds needed, but they increase hoop stress and neutron streaming.

Coolant flow may be of three general types:

6.11.2 Flowing Liquid Metal or Molten Salt

These systems can operate at low pressure and high temperature. They need to keep the liquid fuel from solidifying, so mixtures with high melting points may be difficult to use. Volumetric changes of LiPb during freezing and melting can cause stress. In some cases double-walled tubes might be needed to isolate tritium or to prevent contact of incompatible metals. These blankets may be self-cooled by the flowing breeder; separately cooled by helium; or dual-cooled by both flowing liquid breeder and helium coolant.

6.11.3 Pressure Tube Designs

In general, coolant channels will be spaced close together near the first wall, where heat deposition is greatest. This configuration may be used with any type of breeding material.

Helium is the most popular coolant for pressure tube designs. Trace amounts of oxygen in helium make it incompatible with many structural materials at high temperatures.

Design of tube manifolds and headers is a major problem. Tube joints are vulnerable to thermal stress and radiation damage problems. Coolant tubes leaving a module should be few in number and simple to disconnect for remote maintenance. With helium coolant, there is danger of neutron streaming out through the helium ducts.

6.11.4 Pressurized Modules

Some early designs used pressurized modules with solid breeders, such as Li_2O spheres clad by SiC. The helium coolant flows first to the first wall, to keep it cooler, then radially outwards. The pressurized module concept offers higher helium outlet temperature, and lower pumping power, but the high void fraction requires a thicker blanket.

Here we will consider ceramic breeders, liquid metal breeders, and molten salt breeders.

Fig. 6.37 Helium-cooled pebble bed (*HCPB*) blanket study in Europe. Courtesy of Karlsruhe Institute of Technology
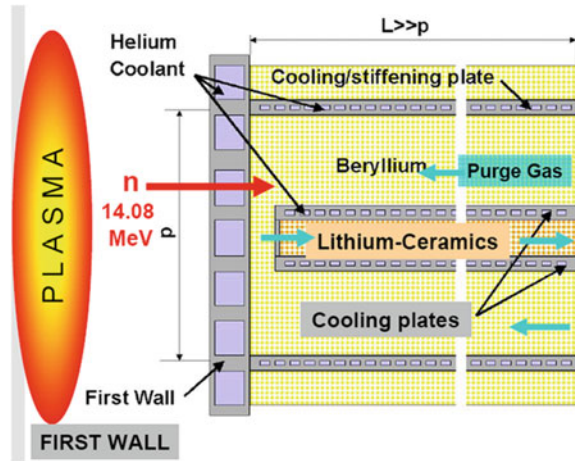
6.12 Ceramic Breeder Blankets

The ceramic blanket would use a solid lithium compound breeder material, such as Li_2O, Li_4SiO_4, or Li_2TiO_3. Small porous "pebbles" (<1 mm diameter) undergoing nuclear heating should have lower temperature gradients than larger "pellets" (~ 1 cm diameter), hence lower stress and better durability (Ihli 2008). With 30 % porosity they could also release the tritium within hours to avoid accumulation of high inventories.

A European design uses Eurofer (reduced activation ferritic steel) with helium coolant, Fig. 6.37.

Beryllium occupies much of the blanket volume, and Li_4SO_4 pellets (~ 0.2 mm diameter) are contained in tubes. A helium purge gas stream would collect the tritium from the Be and Li_4SO_4. The surface heat flux q $\sim$ 0.4 MW/m^2, and the neutron wall load is 4 MW/m^2. The first wall would be cooled by helium at 8 MPa, T = 300–500 °C, flowing at v = 84 m/s with heat transfer coefficient h = 6,500 W/m^2 K. High velocity gas flow might cause oscillations, such as whistling. In the DEMO blanket design the pressure drop Δp = 117 kPa. Cooling manifolds would be behind the breeding zone.

A Japanese water-cooled blanket also uses reduced activation ferritic steel. The first wall has a heat flux q = 1 MW/m^2 and neutron wall load = 5 MW/m^2. The first wall is cooled by supercritical water at 25 MPa, T = 280–510 °C.

If SiC could be successfully developed as a structural material, it might be able to withstand very high temperatures, promoting high energy conversion efficiency. A hypothetical SiC blanket design is shown in Fig. 6.38.

Ceramic breeder blankets require large heat transfer surfaces, such as pressure tubes, which complicate the design, require more expensive structure, and have more reliability issues. Their high void fraction requires thicker blankets than with liquid breeders. If coupled to a Rankine cycle there is a potential for a water leak to
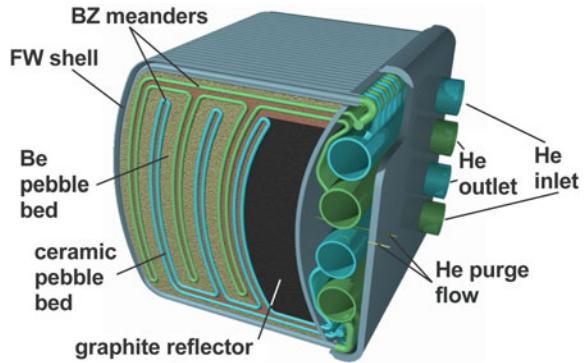
interact with beryllium, releasing substantial quantities of tritium. With a Brayton
cycle the efficiency is lower than that attainable with a liquid breeder blanket
(Raffray et al. 2004).

6.13 Molten Salt Blankets

A self-cooled Flibe blanket can have a simple configuration with exit temperatures
$\sim 700\ °C$. Its low electrical conductivity obviates the need for insulating liners,
reduces MHD pumping power, and it can be thinner (~ 0.4 m) than other breeding
blankets. It has lower chemical reactivity than liquid metals. Its low pressure
operation (<0.5 MPa) allows lighter structure and easier module replacement.

On the other hand, Flibe has very low thermal conductivity (~ 1 W/m-K at
500 °C) and high viscosity (100 times that of water in a pressurized water reactor)
(Ihli 2008). Flibe requires additional Be for fluorine control and neutron multi-
plication, and the Be has swelling and tritium trapping issues. Flibe is limited to a
temperature range of about 459–700 °C by melting temperature and corrosion
issues (Raffray et al. 2004).

The Japanese FFHR2m Heliotron Reactor design uses Flibe in the blanket. It
will be described in Sect. 13.6 (Sagara et al. 2005). Molten salt blankets have also
been used in inertial fusion power plant designs, including Osiris and HYLIFE-II
(Meier 1994; Moir et al. 1994).

6.14 Liquid Metal Blankets

A liquid metal blanket may be self-cooled (flowing out to an external heat
exchanger), cooled by a separate coolant (such as helium, molten salt, or water), or
cooled by a mixture of the two processes. The main candidate liquid metals are
lithium and lithium–lead.

Liquid metal blankets afford the following advantages (Ricapito 2010):

- No breeder damage or swelling
- Breeder composition adjustment outside the blanket to maintain tritium breeding
- Tritium extraction outside blanket modules during operation.

Their main disadvantages are materials compatibility problems (reactivity, corrosion, lower tritium permeation) and electromagnetic field effects (pressure and pumping power).

6.14.1 Self-Cooled Liquid Metal Blanket

This blanket could have a lithium coolant outlet temperature of 600 °C, providing good energy conversion efficiency. It would need a durable insulating film, such as Er_2O_3 (proposed, but not yet qualified), on the inside of the vanadium ducts to minimize pressure and pumping power, or an insulating liner, such as SiC. If very pure V–4Ti–4Cr alloy were used, its induced radioactivity would decay enough in 60 years for it to be recycled (Dolan and Butterworth 1994).

The ARIES-AT (Advanced Tokamak) uses PbLi15.7 breeder/coolant at 1 MPa in SiC structure flowing out at 1,100 °C to a heat exchanger where He gas is heated to 1,050 °C. An optimized Brayton cycle produces a thermal efficiency of 58.5 % (Sect. 13.8.2).

6.14.2 Helium Cooled Lithium Lead

In the HCLL blanket helium flows radially in and then back out through the Eurofer tubes at p = 8 MPa, T = 300–500 °C. The PbLi flows outside the tubes very slowly (several round trips per day) to a tritium removal system outside the blanket.

6.14.3 Water Cooled Lithium Lead

In the WCLL blanket PbLi flows slowly in the radial direction to the tritium removal system and back. Water flows through the coolant channels at 25 MPa, 265–325 °C. This is a simple, reliable design. The TBR = 1.1, which is marginal, and the comparatively low outlet temperature results in lower thermal efficiency. There are also concerns about possible water interactions with the liquid metal.
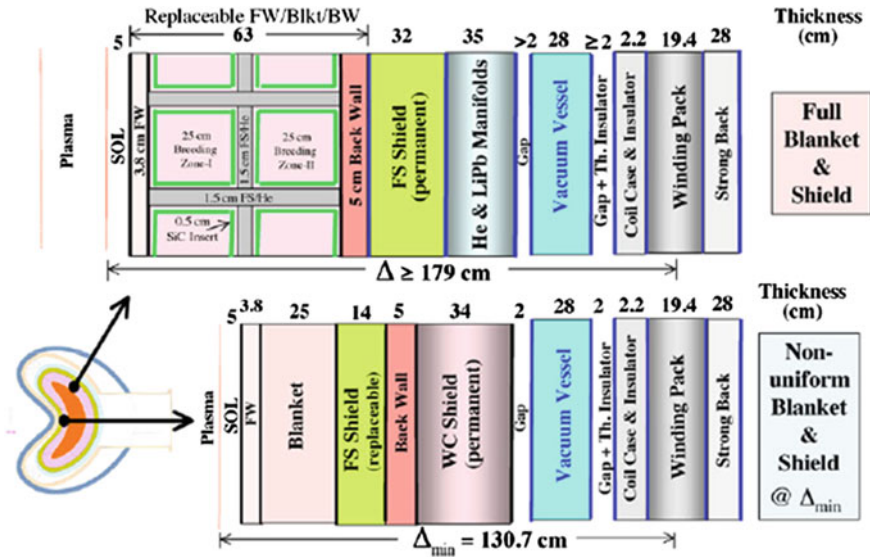
Fig. 6.39 The ARIES-CS blanket and shield radial build (El-Guebaly et al. 2008, Fig. 10). © 2008 by the American Nuclear Society, LaGrange Park, Illinois

6.14.4 Dual-Cooled Lithium Lead

One European DCLL design has ferritic/martensitic steel walls cooled by fast-flowing He. The SiC flow channel inserts provide thermal decoupling (insulation) between the steel and the PbLi and electrical insulation that reduces the MHD pressure drop and pumping power. The PbLi temperature can exceed 700 °C, which facilitates high efficiency of electrical power generation. The PbLi15.7 breeder circulates to an external heat exchanger (Ricapito 2010).

If the blanket materials can attain a high breeding ratio, it is not necessary to surround the plasma completely with a breeding blanket. The thickness of the blanket can also be varied in the poloidal direction, to allow the coils to be closer to the plasma on the inboard side of a stellarator. Figure 6.39 shows the ARIES-CS (Compact Stellarator) blanket and shield at two poloidal locations.

The variation of this blanket with poloidal angle was shown in Fig. 6.22. The thicker part of the blanket (top) supports a high TBR. The thinner blanket (bottom) breeds less tritium, but must still provide adequate shielding, which is achieved by using a permanent tungsten carbide shield to attenuate the gammas generated in the blanket and replaceable inner shield. This allows the plasma to be closer to the magnet coils, which elevates the magnetic field in the plasma, increasing the fusion power density and facilitating a smaller major radius and decreased cost.

Instead of using Be to enhance the breeding ratio, ARIES-CS uses 70 % enriched ^{6}Li with F/M (or 90 % with SiC) in the PbLi to attain TBR $\approx$ 1.1 (El-Guebaly et al. 2008). The reliability of the MHD pressure drop reduction and

the chemical compatibility of flowing PbLi with SiC at high temperatures under neutron irradiation need to be tested.

The ARIES-CS power plant has two versions: a conventional version with F/M structure attaining 42 % thermal efficiency, and an optimistic high-temperature SiC structure version that could attain 56 %. The resulting COE estimates in 2004 US$ are 7.8 cents/kWh with F/M and 6.1 cents/kWh with SiC structure, in spite of the high cost of SiC (El-Guebaly et al. 2008; Najmabadi et al. 2008).

6.15 Corrosion and Tritium Issues

6.15.1 Corrosion

Typical operating temperature windows for structural materials were shown in Fig. 6.20.

Compatibility issues (corrosion) limit the operating temperatures of all blanket concepts. Figure 6.40 shows the corrosion rates (μm/a, where a = annum = year) of PbLi$_{15.7}$ with structure versus temperature, with circles showing the relevant areas for some blanket concepts.

Some conclusions from the corrosion studies are Ricapito (2010):
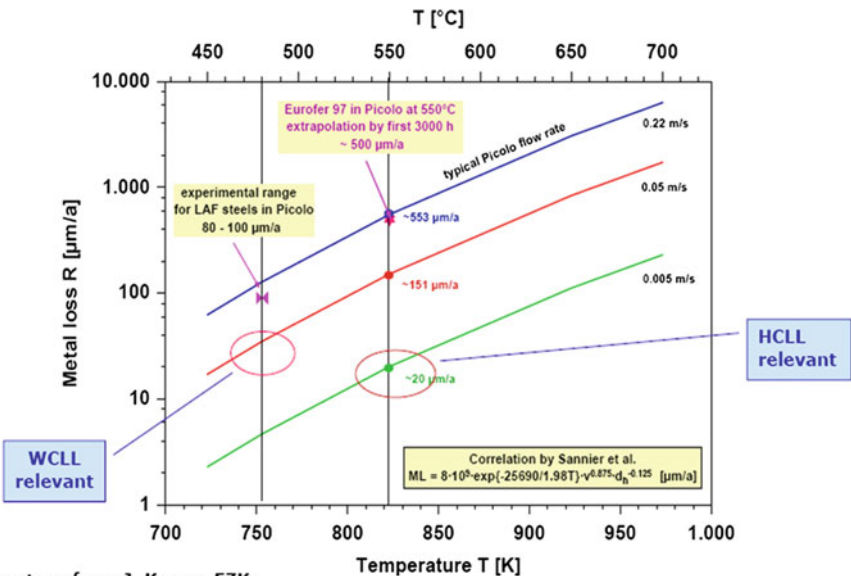
Courtesy from J. Konys, FZK

Fig. 6.40 Corrosion rates versus temperature for various PbLi flow rates. Courtesy of Jürgen Konys, Karlsruhe Institute of Technology

- Austenitic steels have high corrosion rates due to dissolution of Ni.
- Corrosion of FM steels depends strongly on temperature and flow rate, as in Fig. 6.40.
- Eurofer (9Cr–W–V–Ta) has lower corrosion than other FM steels, probably because of its fine grain size.
- SiC has good corrosion resistance in PbLi up to 1,100 °C.

6.15.2 Tritium and Radioactivity Issues

Tritium's low solubility in PbLi gives it a high partial pressure, so that it permeates easily into nearby materials, such as heat exchangers. It is desirable to extract tritium quickly from the PbLi, to keep its partial pressure low, minimizing its leakage into the heat removal system.

Possible tritium extraction concepts include:

- Vanadium getters
- Vacuum permeator (Nb, SiC)
- Liquid–gas contactors

  - Spray columns
  - Plate columns
  - Bubble columns
  - Packed columns.

Some conclusions about liquid metal blankets (due to Ricapito 2010) are:

- PbLi15.7 is better than Li, because of Li reactivity and fire hazard.
- Many data are now available about PbLi15.7 corrosion, reactivity with water, MHD effects, hydrogen isotope interaction, tritium extraction technology.
- ITER blanket modules will test the most advanced concepts to

  - Determine which concepts are best
  - Evaluate reactor development issues
  - Benchmark models and codes relating to blanket design.

- Many liquid metal test loops and experimental facilities are now operating.

Tritium issues will be discussed further in Sect. 12.1.

6.16 Energy Conversion Methods

6.16.1 Electrical Power Generation

Since the revenues generated by a power plant are directly proportional to its efficiency, it is important to attain high efficiency. Plants with high efficiency also discharge less "waste heat" to the environment than those with lower efficiencies.

Fig. 6.41 A conventional Rankine steam cycle coupled to a fusion reactor blanket
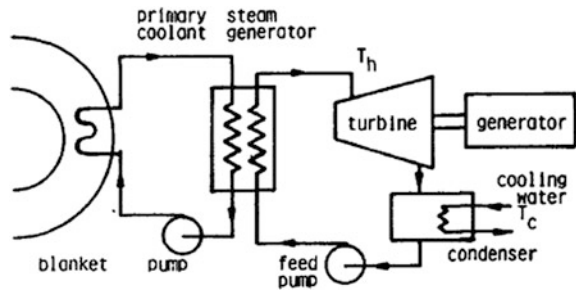
Heat engines are the most likely means for conversion of fusion power into electricity. A fraction of the charged particle energy could be directly converted into electricity, but the majority of the fusion power will be extracted as thermal energy. Magnetohydrodynamic (MHD) generators, thermoelectric convertors, and thermionic convertors are not economically competitive with heat engines. A simplified diagram of a conventional Rankine steam cycle coupled to a fusion reactor blanket is shown in Fig. 6.41.

The primary coolant may be liquid metal, helium gas, pressurized water, or molten salt.

Alternatively, a closed cycle gas turbine (Brayton cycle) may be used, as illustrated in Fig. 6.42.
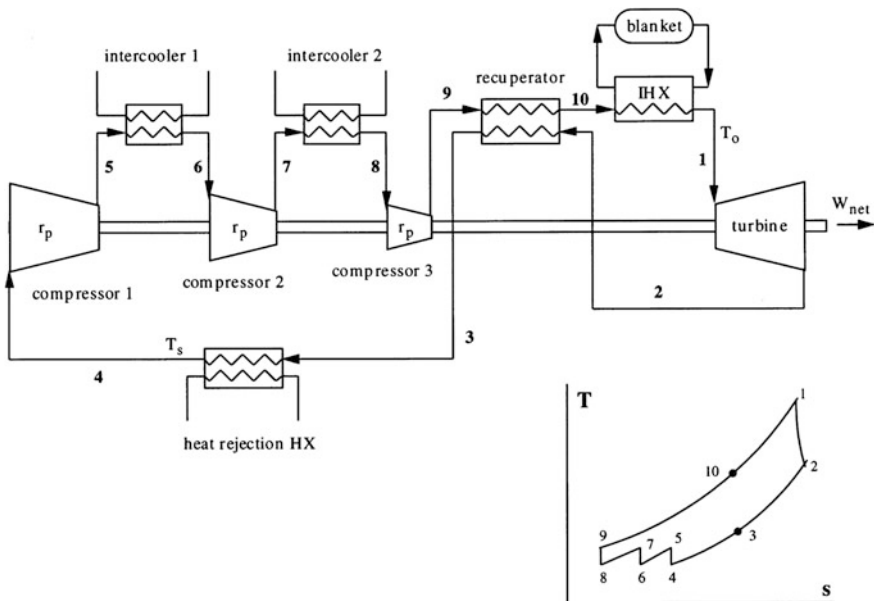
Fig. 6.42 A high-pressure Brayton cycle with intercoolers and recuperator (Malang et al. 1998, Fig. 3)

The hot, high-pressure helium at p = 18 MPa and temperature $T_o \sim 650$ °C spins the turbine and draft shaft, which turns the three compressors and the electrical power generator (not shown). After expansion through the turbine part of the heat remaining in the gas is removed in the recuperator (points 2–3 on the T–S diagram) to preheat the gas entering the intermediate heat exchanger (IHX), which may be located inside a PbLi blanket. The gas is further cooled in the heat rejection heat exchanger (HX) (points 3–4). This is the minimum temperature and pressure point of the cycle. It is compressed in three stages, with cooling between each stage to facilitate further compression (points 4–9). The preheating of the gas by the recuperator (points 9–10) greatly boosts the starting temperature of the coolant going through the IHX, but the temperature T_{10} must be kept low enough to prevent the divertor and first wall from overheating. This system could be coupled to a self-cooled PbLi blanket with outlet temperature $T_o \sim 650$ °C and pressure = 18 MPa. If the recuperator efficiency

$$\eta_x = (T_{10} - T_9)/(T_2 - T_9) \tag{6.57}$$

can be ~ 96 %, then the conversion efficiency of thermal energy into electricity can be ~ 46 %, which is comparable to that of a corresponding Rankine cycle (Malang et al. 1998).

The ARIES-AT tokamak power plant would use PbLi breeder/coolant at 1,100 °C with SiC structure to attain high outlet temperature (1,100 °C) and 58 % thermal efficiency, again with a high-pressure Brayton cycle (Raffray et al. 2007, 2008). It will be described further in Chap. 13. The cycle diagrams in these papers show the current trend to use intercoolers and recuperators.

An intermediate heat exchanger and secondary coolant loop will likely be required to limit tritium migration to the turbine and ultimately to the environment.

The thermal efficiency is the product of heat engine efficiency η_{he} and generator efficiency η_g

$$\eta_t = \eta_{he}\eta_g \tag{6.58}$$

Generators convert mechanical energy into electricity with efficiencies $\eta_g \approx 98$ %. Heat engines (like turbines) convert thermal energy into mechanical energy with efficiencies less than the Carnot efficiency

$$\eta_{he} < \eta_c = 1 - T_c/T_h, \tag{6.59}$$

where T_h is the "hot" temperature of the cycle (the turbine inlet temperature) and T_c is the "cold" temperature (the cooling water temperature). Conventional steam cycles attain $\eta_t \approx 0.64\eta_c$, Gas turbines can operate at much higher T_h. and have been preferred in several recent power plant studies.

Gas turbine systems require use of high-temperature materials in order to attain high efficiencies. At T > 900 K minute quantities of oxygen in the helium rapidly attack metals like vanadium and niobium. High heat rejection temperatures T_c in some gas turbine cycles would reduce cooling tower costs, and the absence of a steam cycle would remove a major pathway of tritium leakage.

The "gas turbine-steam binary cycle" means that the heat rejection HX of Fig. 6.42 is replaced by a steam generator driving a steam turbine. Higher efficiency could also be attained by a supercritical (very high pressure) CO_2 cycle or by large potassium vapor turbines (not yet developed), coupled with steam cycles.

Calculation of heat engine efficiencies is described by El-Wakil (1978), and fusion energy conversion systems are described by Miley (1976). Efficiencies of energy conversion systems using He, He $+$ N, and CO_2 gases are discussed by Oh et al. (2006).

6.16.2 Fuel Production

Heat and electricity from fusion reactors can be used to produce hydrogen from water. High temperature steam produced in a fusion reactor blanket may be split into hydrogen and oxygen via high-temperature electrolysis (HTE), as illustrated in Fig. 6.43.

The process heat module shown in Fig. 6.44 has high-temperature ceramic balls surrounded by a cooler wall.

Either the pressurized module or the pressurized tube configuration may be used, with ceramic rods or balls cooled by steam or CO_2 at T $\sim$ 1,500–2,000 K. A water-cooled outer shell at about 650 K is insulated from the interior by MgO fibers. The attainable temperature will depend upon materials problems, such as thermal strain fatigue. Most high temperature materials have poor ductility. For a DT reactor most of the blanket modules must also breed tritium, not shown in Fig. 6.45.

Fig. 6.43 Use of a high-temperature fusion reactor blanket for production of electricity, high-temperature steam, and hydrogen by high temperature electrolysis (Fillo et al. 1978a, b)
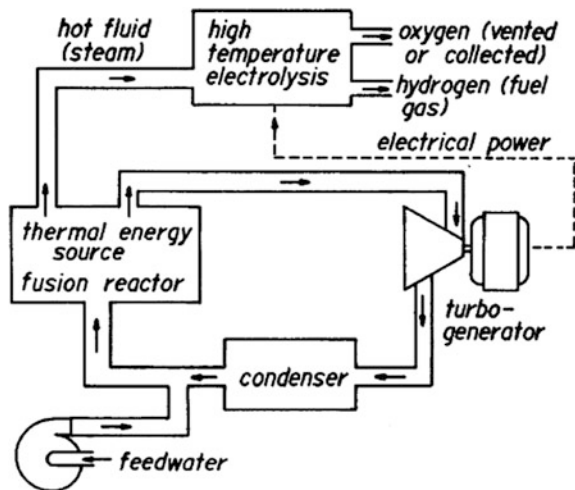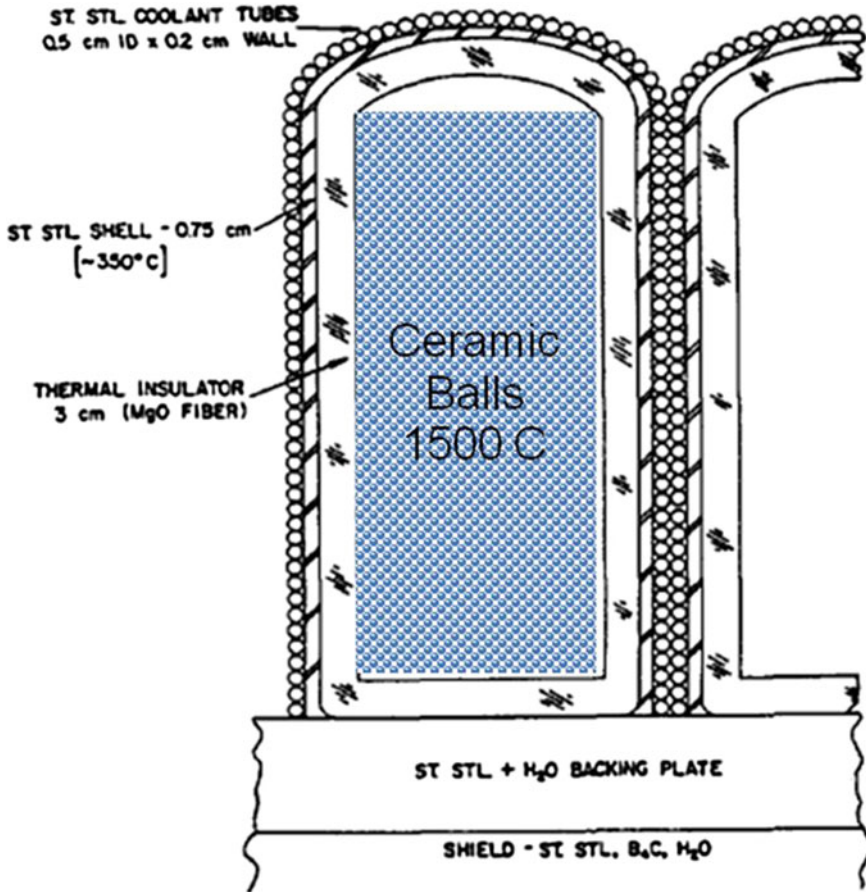
Fig. 6.44 Cross section of a blanket module for production of high-temperature steam to be used in high-temperature electrolysis (Fillo et al. 1978a, Fig. 3)

The hydrogen produced by HTE may be burned directly as fuel or used in production of other synthetic fuels.

One study, characterized in Fig. 6.45, used a SiC blanket structure and LiPb coolant at 1,150 °C (1,423 K) with He coolant to generate electricity and hydrogen (Sheffield 2001). This system uses process heat and electricity in a high-temperature electrolyzer to produce hydrogen. At temperatures over 1,600 K, over 50 % of the fusion energy could potentially be converted into H_2 fuel energy, assuming 40 % efficiency for production of electricity in the steam cycle. One of the advantages of generating hydrogen and electricity in a single plant is that the plant can produce and sell electricity at peak electricity demand periods and during off-peak periods
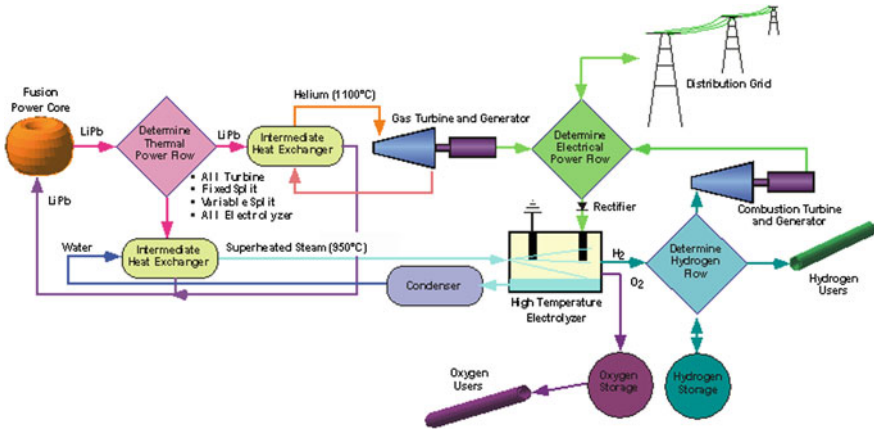
Fig. 6.45 Large fusion power plant with hydrogen production (Sheffield et al. 2001, Fig. 6). © 2001 by the American Nuclear Society, LaGrange Park, Illinois

the plant can generate hydrogen, which can be stored for use upon a future demand. This more efficiently utilizes the base load capabilities of a large fusion plant.

6.16.3 Other Applications of Fusion Energy

The Fusion and Materials Evaluation "FAME" study (Bourque et al. 1988) concluded that the most promising applications of fusion are

- Electricity production
- Fissile fuel and tritium breeding
- Radioisotope production for irradiation sterilization, especially ^{60}Co
- Other radioisotope production
- Synthetic fuel production
- District and process heat generation
- Rare metals production
- Space propulsion and power.

A later study listed 30 potential applications grouped according to which fusion reaction products were used (neutrons, charged particles, or radiation), as shown in Table 6.18.

This study applied a decision analysis technique with several high level criteria to rank the attractiveness of the products. Hydrogen production, transmutation of nuclear waste, disassociation of chemical compounds, and generation of electricity were the most highly ranked. As international priorities evolve, other potential uses may become more attractive (Waganer 1998).

Table 6.18 Potential fusion products (Waganer 1998)

Neutrons	Charged particles	Radiation
Hydrogen	Hydrogen	Hydrogen
Process heat	Waste processing	Waste sterilization
Rocket propulsion	Rocket propulsion	Rocket propulsion
Electricity + space power	Electricity + space power	Electricity + space power
Potable water	Potable water	
Fissile fuel	Ore reduction	
Transmuted waste	Transmuted waste	
Tritium	Destruction of chemical warfare agents	
Radioisotopes	Radioisotopes	
Detection and remote sensing	Detection and remote sensing	Detection and remote sensing
Neutron radiography + tomography	Radiography + tomography	
Radiotherapy	Radiotherapy	Radiotherapy
Neutron activation analyses/testing	Proton activation analyses/testing	Radiation testing
Altered material properties	Altered material properties	
	Lithography	Lithography

6.16.4 Direct Energy Conversion Principles

Fusion product charged particles slow down in the plasma, heating electrons and ions. Some of this energy is lost by radiation, and the rest eventually leaves the core and goes to the walls or divertor in a toroidal device. In a magnetic mirror much of the charged particle energy flows out along magnetic field lines. For that case the power of charged particles leaving a mirror reactor core is

$$P_{ch} = P_f(1/Q + \psi_R)\,(W) \tag{6.60}$$

where P_f = thermal fusion power (W), Q = power gain ratio, and ψ_R = the radiation power parameter (Figure 4C2 of Dolan 1982). For a DT reactor, $\psi_R \sim 0.2$, and for a catalyzed DD reactor, $\psi_R < 0.62$. Thus, if $Q \sim 10$, the charged particle power may be up to 30 % of the fusion power in a DT reactor and up to 70 % in a catalyzed DD reactor. This charged particle power flows out the ends of a mirror machine, where it can be converted directly into electricity. Direct conversion might be used with charged particles flowing into the divertor of a toroidal reactor. However, space would be limited, the average particle energies would be much lower, and particle fluxes much higher than in mirrors, so direct convertors would be very difficult to use with toroidal reactors.

The simplest direct conversion scheme would be a metal plate intercepting a stream of energetic positive ions. If the plate were biased at a high positive voltage (slightly less than the ion energy) and electrons were removed from the beam, then the ions impinging on the plate would produce an electrical current at that high

Fig. 6.46 Expansion and separation of plasma streaming out of a fusion reactor into a direct convertor (Moir et al. 1974)
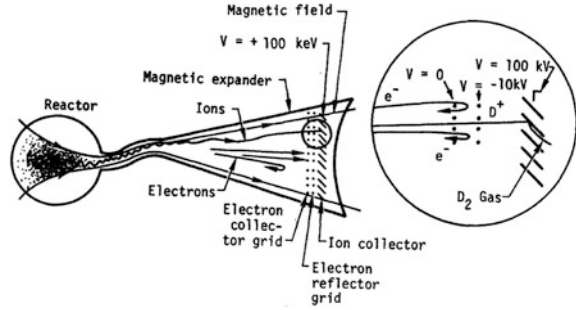
voltage. Hence, their kinetic energy would be converted directly into electrical energy. There are four main steps in direct conversion systems:

- **Expansion**. The plasma is expanded by flowing along a diverging magnetic field to reduce its power flux to <1 MW/m^2 and increase its Debye length to >1 cm, so that the self-shielding effect will not prevent proper grid operation.
- **Separation**. The electrons must be removed from the plasma, so that only ions are incident on the positive high voltage collectors. This is the most difficult stage.
- **Collection**. The ions strike the high-voltage collectors, and are neutralized.
- **Conversion**. If more than one collector voltage is used, the output powers at various voltages are converted to the desired common voltage. This stage can be accomplished by solid state devices with very high efficiency.

The expansion and separation stages are illustrated in Fig. 6.46.

Electrons are repelled back into the plasma by the negative electron-reflector grid and collected by the grounded electron collector. Most of the ions pass on through these grids to the ion collector, where they deposit their energy and are neutralized. The newly-formed neutral atoms constitute a substantial gas throughput, which must be removed with a very high pumping speed to keep the residual gas pressure in the direct convertor $p < 2$ mPa (1.5×10^{-5} Torr). Otherwise, losses of fast ions by charge exchange would be excessive. Cryopanels will probably be needed, since other vacuum pumps do not have high enough pumping speeds.

6.16.5 Plasma Direct Convertors

An experimental two-stage "Venetian blind" collector is illustrated in Fig. 6.47.

High-energy ions pass directly through to the second collector (at high positive voltage V_2) while intermediate-energy ions are caught by the first collector (at intermediate voltage V_1) as they curve around during reflection. Low energy ions may be reflected by the first collector and returned to the plasma.

Fig. 6.47 A two-stage "venetian blind" direct convertor. A grounded grid is followed by an electron repulsion grid ($-V_e$) and two ion collector grids (V_1, V_2) (Moir et al. 1974)
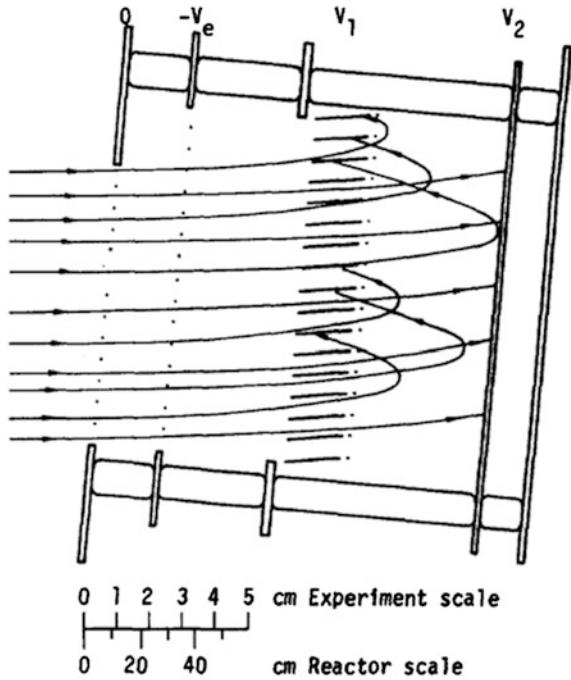
For a reactor with high power fluxes, high voltages, and a spread of ion energies, the efficiency of a two-stage collector would be about 59 %. With additional thermal conversion of collector heat into electricity at about 40 % efficiency, about 74 % of the ions' energy could be converted into electricity. (Neutron energy and radiation would still have conversion efficiencies ~ 40 %.) Additional collection stages would provide slightly higher direct conversion efficiencies, but would add complexity and cost. The maximum power flux that can be handled by Venetian blind direct convertors is about 1 MW/m^2. A single-stage convertor has been run continuously at 0.7 MW/m^2 for many hours, attaining about 77 % efficiency with a 100 keV monoenergetic ion beam.

6.16.6 Beam Direct Convertors

Direct conversion is also needed in the process of generating neutral atom beams for plasma heating. In order to keep the total area of neutral beam ports low, high beam power densities must be achieved. There will not be much room for expansion of the un-neutralized beam ions, so beam direct convertors will have to handle higher power densities than plasma direct convertors, and separation of electrons is difficult. The beams can be kept narrow enough that the electrons can be repelled by biasing a close-fitting electrode to a high negative potential.
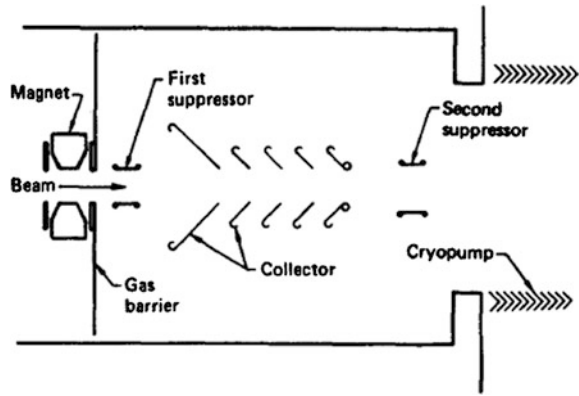
The Debye length is very short where $n_e = n_i$, but near the repeller $n_e \ll n_i$, and the shielding effect is slight.

A beam direct convertor is shown in Fig. 6.48.

Ions incident from the left will spread radially (space-charge blowup) and strike the conical collectors. The resultant neutral gas flow is pumped by cryopanels (Sect. 9.3). The suppressors act to repel electrons, like the electron reflecting grid V_e of the plasma direct convertor. A water-cooled tube is used because grid wires would melt. Alternatively, the magnet at the left may be used to reflect incident electrons. Successful development of magnetic suppression would permit larger beam diameters to be handled than with electrostatic suppression.

Such a beam direct convertor has operated at 0.7 MW/m^2 with a hydrogen beam for 0.5 s. The beam consisted of 100 keV H$^+$ (1.4 A), 67 keV H$_2^+$ (0.04 A), 50 keV H$^+$ (0.24 A), and 33 keV H$^+$ (0.11 A). The peak power efficiency of the beam direct convertor was about 61 % with electrostatic suppression, 39 % with magnetic suppression. Increasing neutral gas pressure caused a drop of efficiency during the pulses, in spite of cryopumping.

Plasma energy may also be converted directly into electricity by magnetic induction: plasma expansion against a magnetic field induces currents in the magnet coils. Various energy conversion concepts are discussed by Miley (1976).

6.17 Problems

6.17.1 Blankets

6.1 Estimate the waste heat released by a 3 GW$_{th}$ fusion power plant operating with a conventional steam cycle (no direct conversion) at a peak cycle temperature of 700 K, assuming Q = 10, η_{in} = 0.7, M = 1.2. (Hint: Find η using equations from Chap. 4 of Dolan 1982.)

6.2 The ratio of first wall heat power (charged particles and radiation) to neutron wall loading is $(P_{ch} + P_{rad})/P_n = (0.25 + 1.25/Q)$. A given reactor has $Q = 10$, $P_n/A = 1.5$ MW/m^2, steel walls with $T_w = 700$ K, $e_w = 0.7$, and radioactively-cooled SiC armor tiles with $e_a = 0.85$. Estimate the temperature of the SiC on the wall side.

6.3 Helium at 6 MPa, 1,200 K flows with $v_c = 10$ m/s through a tube with $D = 0.05$ m, and receives a power flux of 0.1 MW/m^2 through the tube walls. What is the tube inner wall temperature? (For this case the Mach number $M \ll 1$.)

6.4 A TZM (Molybdenum alloy) tube outer wall temperature is not to exceed 1,100 K. The inner wall temperature is maintained at 1,000 K by a coolant at 6 MPa. The tube inner diameter is 0.04 m and the thickness is 2 mm. What is the maximum allowable heat flux through the outside of the tube? What are the thermal and hoop stresses in the tube, assuming internal heat generation is negligible? (Use data from Sects. 8.2 and 8.3.)

6.5 If a reactor is cooled entirely by tubes of the kind in problem 3, and other pressure drops are negligible, what would the ratio of pumping power to thermal power be?

6.6 A SS 316 coolant tube with $t = 3$ mm, $D = 10$ cm carrying liquid Li at 800 K is to remove 2 MW from the blanket with a temperature rise of 140 K. Pump efficiency is 80 %. The average value of B^2 perpendicular to the 15-m long channel is 20 T^2. What are the Li velocity and pumping power?

6.17.2 Neutronics

6.7 Legendre polynomials: (a) Show that $P_3(\mu)$ satisfies the basic differential equation. (b) Derive $P_4(\mu)$ using the recurrence relation.

6.8 Derive the equation for the Legendre expansion coefficients a_ℓ (Hint: multiply the expansion theorem by $P_M(\mu)d\mu$ and integrate, using the orthogonality condition.).

6.9 Given $\Sigma(x, \mu_o, E' \to E) = S(x, E' \to E)(1 + a\mu_o + b\mu_o^2)$, calculate the expansion coefficients $\Sigma(x, E' \to E)$ of the expansion Eq. (6.32).

6.10 A 1 MeV neutron is incident at $x = 0$, $y = 0$, $z = 0$ on a slab with the following parameters: $\Sigma_{n,2n} = 0.001$ cm^{-1}, $\Sigma_{in} = 0.02$ cm^{-1}, $\Sigma_{el} = 0.410$ cm^{-1}, $\Sigma_a = 0.030$ cm^{-1}, $L = 10$ cm, isotropic scattering, $A = 30$, and angle of incidence $\theta_o = 30°$ (in the y–z plane, Fig. 6.29). Track the neutron history with the Monte Carlo technique, and determine the location (x, y, z) where it has its second collision, using the following random numbers in order of appearance: 0.5149, 0.7830, 0.2365, 0.4482, 0.3389, 0.7124, … (In the equation for path length, use $N_r' = 0.5149$).

6.11 Estimate the number of ordinary Monte Carlo neutron histories needed for calculation of magnet coil heating with 10 % accuracy, if the attenuation factor is to be 10^{-6}.

6.12 Given the masses of ten apples chosen randomly from an orchard: (190, 205, 187, 212, 220, 171, 203, 194, 213, 192 g), estimate the mean apple mass for the orchard, and the probability that your estimate is close to the true mean value within certain limits. If you weighed 30 apples from the same orchard altogether, and the mean and standard deviation were 196 and 8.2, what could you say about the true mean value?

6.13 The benchmark case study result for breeding in ^{7}Li was found to be 0.523 $\pm$ 0.003. If only ordinary Monte Carlo were used with no variance reduction, how many neutron histories would be required to achieve this accuracy?

6.18 Review Questions

1. What is "Carnot efficiency" and how does it limit energy conversion?
2. What is the difference between a Rankine cycle and a Brayton cycle?
3. What material is used for the first wall surface of ITER (not the divertor)?
4. What material is used for the ITER divertor surfaces?
5. What two materials are good neutron multipliers?
6. What materials are considered for liquid breeders, and for solid breeders?
7. What is Flibe?
8. Name two problems of liquid lithium coolant.
9. Name two problems of helium coolant.
10. What material is most popular for the blanket structure, and why?
11. What are the advantages and disadvantages of SiC structure?
12. How can the convective heat transfer coefficient be calculated?
13. How is the optimum tube wall thickness estimated?
14. How can the MHD pressure drop of liquid metal coolants be reduced?
15. What three general blanket material types are being studied?
16. What are the advantages and disadvantages of a ceramic breeder blanket?
17. What are the advantages and disadvantages of a flowing liquid metal blanket?
18. What are the potential advantages of a lithium wall?
19. What are the stages of direct energy conversion of charged particles?
20. What are the two general methods for calculating neutronics information?
21. Explain the discrete ordinates method.
22. Explain the variables and terms in the equation

$$\mu\left(\frac{\partial\phi}{\partial x}\right) = \int\limits_0^{2\pi} d\phi' \int\limits_0^\infty dE' \int\limits_{-1}^1 du' \, \phi(x, \mu', E') \sum_{\ell=0}^L \Sigma_\ell(x, E' \to E) P_\ell(\mu_0) + S(x, \mu, E)$$
$$- \Sigma_t(x, E)\phi(x, \mu, E)$$

23. Explain the Monte Carlo method.

24. Explain the terms in the following equation.

$$\frac{\sigma_{\bar{x}}}{\mu} \approx \left[\frac{1}{N\bar{x}}\right]^{\frac{1}{2}} \quad or \quad N = \left(\frac{\mu}{\sigma_{\bar{x}}}\right)^2 \frac{1}{\bar{x}}$$

25. Explain "avoidance of gaming".
26. Explain "importance functions".

References

Abdel-Khalik S et al (2008) Experimental validation of thermal performance of gas-cooled divertors. International high heat flux components workshop, La Jolla, CA, Dec 10–12

Badger B et al (1979) NUWMAK, a tokamak reactor design study. University of Wisconsin Report UWFDM-330

Baldwin MJ, Doerner RP (2008) Helium induced nanoscopic morphology on tungsten under fusion relevant plasma conditions. Nucl Fusion 48:035001 (5 pp)

Baldwin MJ, Schmid K, Doerner RP, Wiltner A, Seraydarian R, Linsmeier Ch (2005) Composition and hydrogen isotope retention analysis of co-deposited C/Be layers. J Nucl Mater 337–339(2005):590–594

Baluc N et al (2007) Status of R&D activities on materials for fusion power reactors. Nucl Fusion 47:S696–S717

Barr WL, Moir RW, Hamilton GW (1979) Tests of high-power direct conversions on beams and plasma. In: Proceedings of the 18th symposium on engineering problems of fusion research, IEEE

Billone M (undated) Properties of V-4Cr-4Ti. At http://aries.ucsd.edu/LIB/PROPS/vprop.html

Bourque RF, Schultz KR, Project Staff (1988) Fusion applications and market evaluation (FAME) study. Technical Report GA-A18658, UCRL 21073, UC-420, UC-424, UC-712, February

Burlington RS, May, Jr. CD (1970) Handbook of probability and statistics with tables, 2nd edn., McGraw-Hill, New York.

Chapman AJ (1960) Heat Transfer, Macmillan, New York.

Chen H et al (2008) A high temperature blanket concept for hydrogen production. Fusion Eng Des 83:903–911

Coenen J et al (2010) Material and power-handling properties of tungsten PFCs after steady state melting and additional transients, Monaco ITER International Fusion Energy Days - Part II, 25 Nov

Desecures M, El-Guebaly L (2012) Environmental aspects of W-based components employed in ITER, ARIES, and PPCS fusion designs. University of Wisconsin Fusion Technology Institute Report UWFDM 1411

Doerner R (2008) PMI issues beyond ITER. International high heat flux components workshop, La Jolla, CA, Dec 10–12

Doerner R (2010) Multi-component plasma interactions with elemental and mixed-material surfaces. ITER-IAEA technical meeting: ITER materials and technologies, Monaco, 25 Nov

Dolan TJ (1982) Fusion research. Pergamon Press, New York

Dolan TJ, Butterworth GJ (1994) Vanadium recycling. Fusion Technol 26:1014–1020 (EGG-FSP-10378)

El-Guebaly L, Malang S (2009) Toward the ultimate goal of tritium self-sufficiency: technical issues and requirements imposed on ARIES advanced power plants. Fusion Eng Des 84:2072–2083

El-Guebaly L et al (2004) Initial activation assessment for the ARIES-CS power plant. In: 16th ANS topical meeting on the technology of fusion energy (TOFE), University of Wisconsin, Sept 14–16

El-Guebaly L, Wilson P, Paige D (2005) Initial activation assessment of ARIES compact stellarator power plant. Fusion Sci Technol 47:440–444 (Fig. 6)

El-Guebaly L et al (2006) Nuclear performance assessment of ARIES-AT. Fusion Eng Des 80:99–110 (© Elsevier, 2006)

El-Guebaly L et al (2008) Designing Aries-CS compact radial build and nuclear system: neutronics, shielding, and activation. Fusion Sci Technol 54:747–770 (Fig. 10. Copyright by the American Nuclear Society, LaGrange Park, Illinois, USA, 2008)

El-Guebaly L, Jaber A, Malang S (2012) State-of-the-Art 3-D assessment of elements degrading the TBR of the ARIES DCLL blanket. Fusion Sci Technol 61:321–331

El-Wakil MM (1978) Nuclear energy conversion. American Nuclear Society, Illinois

Federici G, Andrew P, Barabaschi P, Brooks J, Doerner R, Geier A, Herrmann A, Janeschitz G, Krieger K, Kukushkin, Loarte A, Neu R, Saibene G, Shimada M, Strohmayer G, Sugihara M (2003) Key ITER plasma edge and plasma–material interaction issues. J Nucl Mater 313–316:11–22

Fillo JA et al (1978a) Hydrogen production from fusion reactors coupled with high temperature electrolysis. Brookhaven National Laboratory Report BNL-24625

Fillo JA et al (1978b) Fusion energy for hydrogen production. In: 10th Symposium on fusion technology, Padua, Italy; and Brookhaven National Laboratory Report BNL-24906

Fraas AP (1975) Comparative study of the more promising combinations of blanket materials, power conversion systems, and tritium recovery and containment systems for fusion reactors. Oak Ridge National Laboratory Report ORNL-TM-4999

Fraas AP, Thompson AS (1978) ORNL fusion power demonstration study: fluid flow, heat transfer, and stress analysis considerations in the design of blankets for full-scale fusion reactors. ORNL/TM-5960

Garber DI, Kinsey RR (1976) Neutron cross sections, Volume II, Curves. Brookhaven National Laboratory Report BNL 325, 3rd edn

Giancardi L (2004) The PPPS in-vessel components concepts. ERICE Summer School

Haubenreich PN, Engel JR (1970) Experience with the Molten-Salt reactor experiment. Nucl Appl Technol 8:118–136

Hinoki T, Snead LL, Blue CA (2005) Development of refractory armored silicon carbide by infrared transient liquid phase processing. J Nucl Mater 347:207–216

Ihli T (2008) Presentations on blankets, solid breeder, and divertors. Karlsruhe Institute of Technology Summer School on Fusion Technology, Germany

Ihli T, Ilic M (2009) Efficient helium cooling methods for nuclear fusion devices: status and prospects. Fusion Eng Des 84(2–6):964–968

Ihli T, Basu TK, Giancarli LM, Konishi S, Malang S, Najmabadi F, Nishio S, Raffray AR, Rao CVS, Sagara A, Wu Y (2008) Review of blanket designs for advanced fusion reactors. Fusion Eng Des 83:912–919

Jitsukawa S et al (2002) Development of an extensive database of mechanical and physical properties for reduced-activation martensitic steel F82H. J Nucl Mater 307–311:179–186

Jung JC (1979) The neutronic performance of candidate tritium breeding materials. Special purpose materials, Annual progress report, U.S. Department of Energy Report DOE/ET-0095

Kays WM (1966) Convective Heat and Mass Transfer, McGraw-Hill

Konishi S et al (2008) Japan PFC/Divertor concepts for power plants. International high heat flux components workshop, La Jolla, CA, Dec 10–12

Linke J, Escourbiac F, Mazul IV, Nygren R, Rödig M, Schlosser J, Suzuki S (2007) High heat flux testing of plasma facing materials and components—status and perspectives for ITER related activities. J Nucl Mater 367–370:1422–1431

Lipschultz B, Roth J, Davis JW, Doerner RP, Haasz AA et al (2010) An assessment of the current data affecting tritium retention and its use to project towards T retention in ITER. Report SFC/RR-10-4, Plasma Science and Fusion Center, Massachusetts Institute of Technology

Lorenzetto P (2008) EU considerations on design and qualification of plasma facing components for ITER. International high heat flux components workshop, La Jolla, CA, Dec 10–12

Maisonnier D, Campbell D, Cook I (2007) Power plant conceptual studies in Europe. Nucl Fusion 47:1524–1532

Malang S, Schnauder H, Tillack MS (1998) Combination of a self-cooled liquid metal breeder blanket with a gas turbine power conversion system. Fusion Eng Des 41:561–567

Mas de les Valls E et al (2008) Lead-lithium eutectic material database for nuclear fusion technology. J Nucl Mater 376:353–357

Meier WR (1994) Osiris and SOMBRERO inertial fusion power plant design–summary, conclusions, and recommendations. Fusion Eng Des 25:145–157

Merola M (2008) Overview of the ITER plasma facing components. International high heat flux components workshop, La Jolla, CA, Dec 10–12

Merrill BJ, El-Guebaly LA, Martin C, Moore RL, Raffray AR, Petti DA, Aries-CS Team (2008) Safety assessment of the Aries compact stellarator design. Fusion Sci Technol 54:838–863

Miley GH (1976) Fusion energy conversion. American Nuclear Society, IL

Mills RG (ed) (1974) A fusion power plant. Princeton Plasma Physics Laboratory Report MATT-1050

Moir RW (1996) Liquid wall inertial fusion energy power plants. Fusion Eng Des 32–33:93–104

Moir RW, Barr WL (1973) 'Venetian blind' direct energy converter for fusion reactors. Nucl Fusion 23:35–45

Moir RW, Barr WL, Carlson GA (1974) Lawrence Livermore National Laboratory Report UCRL-76051

Moir RW, Bieri RL, Chen XM, Dolan TJ, Hoffman MA et al (1994) HYLIFE-II: a Molten Salt inertial fusion energy power plant design-final report. Fusion Technol 25:5–25

Najmabadi F, Raffray AR, Abdel-Khalik SI, Bromberg L, Crosatti L et al (2008) The Aries-CS compact stellarator fusion power plant. Fusion Sci Technol 54:655–672

Nuclear Regulatory Commission (2003) Radiological assessments for clearance of materials from nuclear facilities, NUREG-1640. See http://www.nrc.gov/reading-rm/doc-collections/nuregs/staff/sr1640/

Nishijima D, Baldwin MJ, Doerner RP, Yu JH (2011) Sputtering properties of tungsten 'fuzzy' surfaces. J Nucl Mater 415:S96–S99

Norajitra P (2008) EU divertor concepts for fusion power plants. International high heat flux components workshop, La Jolla, CA, Dec 10–12

Norajitra P (2010) Divertors. Karlsruhe Institute of Technology Summer School on Fusion Technologies, Germany

Nygren R (2010) HHFC designs and constraints in a reactor environment. ARIES Town Hall meeting on plasma edge, San Diego, May 20–21

Oh CH, Barner RB, Davis CB, Hawkes BD, Morton JD (2006) Energy conversion advanced heat transport loop and power cycle, INL/EXT-06-11681, August

Pitts RA (2010) Key physics and materials aspects of plasma–wall interactions in ITER. ITER-IAEA technical meeting: ITER materials and technologies, Monaco, 25 Nov

Raffray AR, Jones R, Aiello G, Billone M, Giancarli L, Golfier H, Hasegawa A, Katoh Y, Kohyama A, Nishio S, Riccardi B, Tillack MS (2001) Design and material issues for high performance SiC_f/SiC based fusion power cores. Fusion Eng Des 55:55–95

Raffray AR, El-Guebaly L, Malang S, Wang X (2004) Attractive design approaches for a compact stellarator power plant. University of Wisconsin Report UWFDM-1243, September

Raffray AR, El-Guebaly L, Malang S, Sviatoslavsky I, Tillack MS, Wang X (2007) Advanced power core system for the ARIES–AT power plant. Fusion Eng Des 82:217–236

Raffray R et al (2008) Example of US PFC/Divertor concepts for power plants. International high heat flux components workshop, La Jolla, CA, Dec 10–12

Raffray AR, Nygren R, White D (2009) Summary. International HHFC workshop on readiness to proceed from near term fusion systems to power plants, fusion energy sciences advisory committee meeting, Gaithersburg, Maryland Jan 13

Ricapito I (2010) Liquid metal blankets for fusion reactors. Summer School on Fusion Technology, Karlsruhe Institute of Technology, Germany

Rieth M (2010) High temperature materials. Summer School on Fusion Technology, Karlsruhe Institute of Technology, Germany

Rieth M (2010a) Materials development for reactors Part A: Structure and texture of metallic solids, karlsruhe international summer school, Karlsruhe Institute of Technology, Germany, Sept

Rieth M (2010b) Materials development for reactors Part B: High temperature materials, karlsruhe international summer school, Karlsruhe Institute of Technology, Germany, Sept

Rieth M (2010c) Materials development for reactors Part C: Interaction of neutron radiation and fusion materials, karlsruhe international summer school, Karlsruhe Institute of Technology, Germany, Sept

Roth J, Tsitrone E, Loarer T, Philipps V, Brezinsek S et al (2008) Tritium inventory in ITER plasma-facing materials and tritium removal procedures. Plasma Phys Controlled Fusion 50:103001

Ruzic DN, Xu W, Andruczyk D, Jaworski MA (2011) Lithium–metal infused trenches (LiMIT) for heat removal in fusion devices. Nucl Fusion 51:102002 (4 pp)

Sagara A, Imagawa S, Mitarai O, Dolan T, Tanaka T et al (2005) Improved structure and long-life blanket concepts for heliotron reactors. Nucl Fusion 45:258–263

Schaeffer NM (1973) Reactor shielding for nuclear engineers, TID-25951. AEC Technical Information Center, Oak Ridge, 1973

Sheffield J, Brown W, Garrett G, Hilley J, McCloud D, Ogden J, Shields T, Waganer LM (2001) A study of options for the deployment of large fusion power plants. Fusion Sci Technol 40:1–36 (Fig. 6)

Smith DL, Morgan GD et al (1984) Blanket comparison and selection study—final report. Argonne National Laboratory Report ANL/FPP-84-1, vols 1, 2, 3

Son SJ, Park KH, Katoh Y, Kohyama A (2004) Interfacial reactions and mechanical properties of W–SiC in situ joints for plasma facing components. J Nucl Mater 329–333:1549–1552

Takatsu H (2011) The ITER project and fusion technology. Nucl Fusion 51:094002

Tavassoli A-AF, Rensman J-W, Schirra M, Shiba K (2002) Materials design data for reduced activation martensitic steel type F82H. Fusion Eng Des 61–62:617–628

Tillack M (2012) Personal communication, May 10

Vayakis G, Hodgson ER, Voitsenya V, Walker CI (2008) Generic diagnostic issues for a burning plasma experiment. Fusion Sci Technol 53:699 (Chap. 12)

Waganer LM (1998) Can fusion do better than boil water? In: 13th Topical meeting on the technology of fusion, American Nuclear Society, Nashville, TN, 7–11 June. See: http://aries.ucsd.edu/LIB/REPORT/CONF/ANS98/waganer/

Wirtz M, Linke J, Pintsuk G, Rapp J, Wright GM (2011) Influence of high flux hydrogen-plasma exposure on the thermal shock induced crack formation in tungsten. J Nucl Mater 420:218–221

Zakharov LE (2008) Physics/ECE/NE 922 seminar. The University of Wisconsin, Madison, WI, Mar 24

Zakharov LE (2011) LiWall fusion—the new concept of magnetic fusion, problems of atomic science and engineering. http://vant.iterru.ru/vant_2011_1.ht, #1, p 29

Zakharov LE, Gorelenkov NN, White RB, Krasheninnikov SI, Pereverzev GV (2004) Ignited spherical tokamaks and plasma regimes with LiWalls. Fusion Eng Des 72:149

Zakharov LE, Li J, Wu Y (2011) Fusion-fission research facility (FFRF) as a practical step toward hybrids, problems of atomic science and engineering, http://vant.iterru.ru/vant_2011_3.htm, #3, p 27

Zinkle SJ, Ghoniem NM (2000) Operating temperature windows for fusion reactor structural materials. Fusion Eng Des 51–52:55–71

Chapter 7
Control Systems

Thomas J. Dolan

Objectives

After reading this chapter one should understand

Effects of impurities
How to control plasma power flow
How to control particles
Issues of divertor design and construction
Other impurity control methods.

7.1 Impurity Causes and Effects

7.1.1 Effects of Impurities

Impurities can enter the plasma from interaction with the wall or divertor, in-leakage through the core hardware or from generated plasma "ash". Impurities are generally deleterious to the plasma. They affect practically every aspect of plasma behavior, including:

- Coulomb collision processes
- Runaway electrons
- Neutral beam trapping
- Radiation losses
- Plasma resistivity and ohmic heating
- Current density and magnetic field distributions

T. J. Dolan (✉)
NPRE Department, University of Illinois, Urbana, IL 61801, USA
e-mail: dolantj@illinois.edu

- Onset of disruptive instability (tokamaks)
- Transport coefficients and confinement times
- Fuel ion density
- Fusion power density.

Impurities inhibit neutral beam penetration. Impurity enhancements of radiative and ionization power losses tend to lower T_e, while impurity enhancement of plasma resistivity and ohmic heating tends to increase T_e. The variation of T_e and conductivity affect the current density distribution, magnetic field topology, and plasma stability. Heavy impurities, such as tungsten, emit intense line radiation even in a hot plasma core, so only small density fractions ($\sim 10^{-4}$) are tolerable. Light atomic weight impurities, such as carbon and oxygen, will be completely stripped in a hot plasma core, so their main contribution to core radiation losses is enhancement of bremsstrahlung radiation. Reduction of edge plasma temperature by line radiation from impurities can be beneficial, because a cooler edge plasma may produce less wall erosion and impurity influx. The effect of impurities on reactor energy gain ratio Q is indicated in Fig. 7.1.
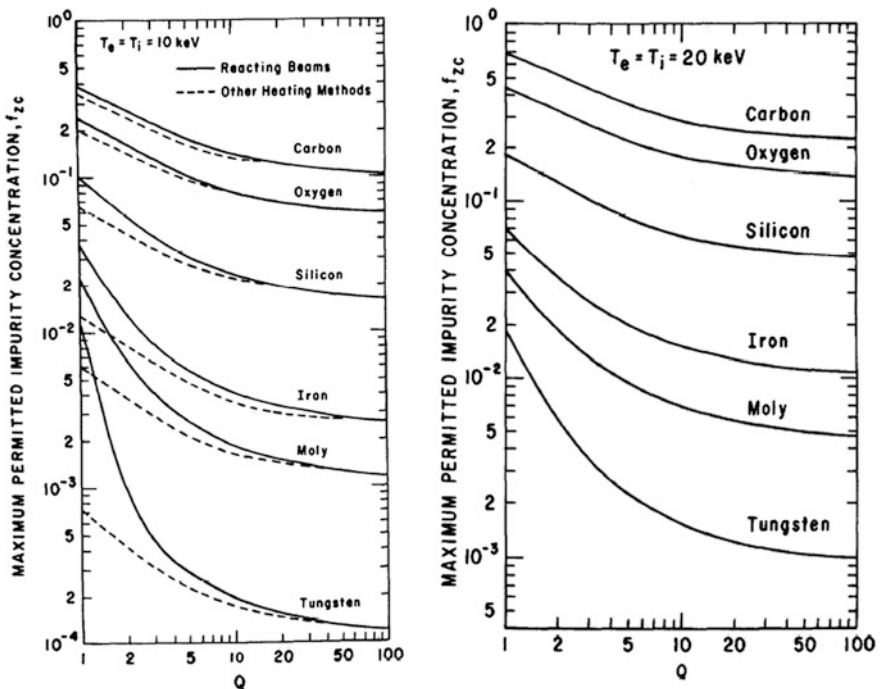
Fig. 7.1 Maximum allowed impurity concentrations of various species for attaining given Q values in a DT plasma using 200 keV deuteron beam heating. The *dashed curves* are for other heating methods, such as rf heating (Jensen et al. 1978). Copyright 1978 by the American Nuclear Society, LaGrange Park, Illinois
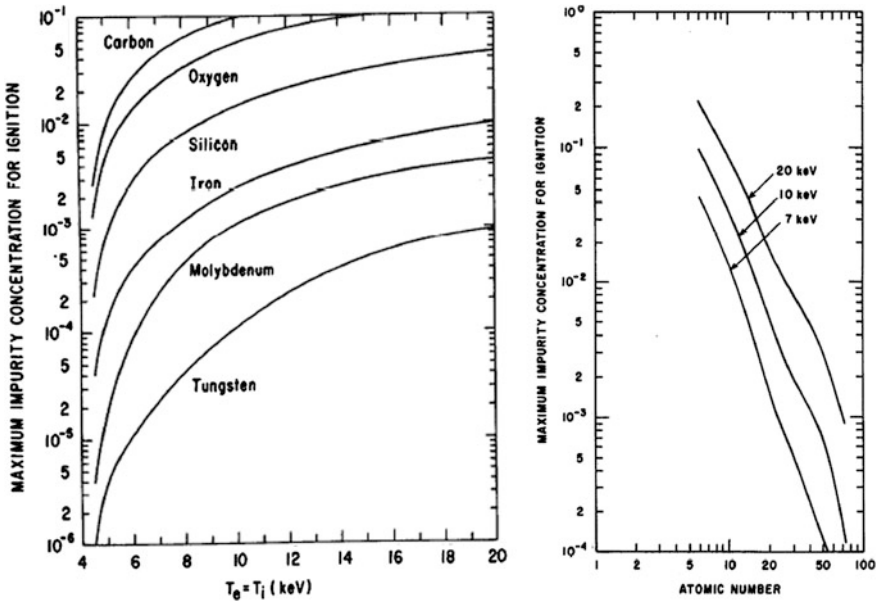
Fig. 7.2 Maximum allowed concentration of various impurities for ignition of a DT plasma versus temperature, assuming zero non-radiative energy losses (Jensen et al. 1978). Copyright 1978 by the American Nuclear Society, LaGrange Park, Illinois

These curves show the maximum allowable impurity concentrations for a given Q, or conversely, they indicate the maximum possible Q for a given impurity concentration, even if confinement is perfect (zero conduction and convective heat losses).

Ignition requirements for an ideal plasma are summarized in Fig. 7.2. For a real plasma with transport losses, the allowable impurity fractions for ignition are lower. Thus, the plasma impurity control system should have the goal of keeping impurity fractions for low-Z elements (0, C, N) $< 10^{-2}$, for intermediate-Z elements (V, Fe) $< 10^{-3}$, and for high-Z elements (Mo, W) $< 10^{-4}$. (If only one or two impurity species were present, slightly higher values might be tolerable).

7.1.2 Impurity Concentrations

We will make a rough estimate of the equilibrium concentration of a single species of impurity sputtered from the walls in a steady-state reactor. The particle conservation equation for an impurity with density n_z, confinement time τ_z, and reflection coefficient R_z is

$$V(dn_z/dt) = \text{(production rate by sputtering)} - \text{(net flow rate to walls)}$$
$$= n_i VS_i/\tau_i + n_\alpha VS_\alpha/\tau_\alpha + n_z VS_z/\tau_z - n_z V(1 - R_z)/\tau_z \quad (7.1)$$

where V = plasma volume (m^3), n and τ are volume averaged densities and confinement times, S are sputtering yields, and the subscripts i and α represent fuel ions and alpha particles. At equilibrium,

$$\frac{n_z}{n_i} = \frac{\tau_z(S_i/\tau_i + n_\alpha S_\alpha/n_i\tau_\alpha)}{1 - S_z - R_z} \tag{7.2}$$

Consider the case of a plasma with pressure $p = \beta B^2/2\mu_o \sim$ limited by the attainable value of β. For simplicity we will assume $p = $ constant and $T_e = T_i = T_\alpha = T_z = T$. Then,

$$(n_e + n_i + n_\alpha + n_z)kT = p = \text{constant} \equiv 2n_0kT \tag{7.3}$$

where $n_i = n_e$ when $n_\alpha = n_z = 0$. By quasineutrality

$$n_i + 2n_\alpha + Zn_z = n_e \tag{7.4}$$

where Z is the impurity charge number.

Example Problem 7.1: **Beryllium fraction** Estimate the steady-state Be impurity fraction and the reduction of DT fusion power density for the case of walls coated with Be, if the edge plasma temperature $T = 200$ eV, $R_z = 0.05$, and $n_\alpha/n_i = 0.1$, $S_{DT} = 0.028$, $S_\alpha = 0.086$, $S_{Be} = 0.314$. Assume all species have equal confinement times.

$$\frac{n_z}{n_i} = \frac{\tau_z(S_i/\tau_i + n_\alpha S_\alpha/n_i\tau_\alpha)}{1 - S_z - R_z}$$
$$\frac{n_z}{n_i} = 0.058.$$

$$n_e = n_i + 2n_\alpha + 4n_z = n_i[1 + 2(0.1) + 4(0.058)] = 1.432\, n_i.$$

From Eq. (7.3), $(n_i + n_e + n_z + n_\alpha)kT = p_o = 2n_okT,$

$$n_i(1 + 1.432 + 0.058 + 0.1) = 2n_o,$$

$$n_i/n_o = 0.772. \quad P_f/P_{fo} = (n_i/n_o)^2 = 0.60.$$

Thus the fusion power density would be 60 % of its value without impurities.

7.1.3 Helium Accumulation

Helium "ash" produced by DT fusion reactions displaces fuel ions in a pressure-limited plasma. If a fraction R_α of the alpha particles incident on the walls is reflected back into the plasma, then the alpha particle conservation equation becomes

$$dn_\alpha/dt = \frac{1}{4}n_i^2\langle\sigma v\rangle_{DT} - n_\alpha(1 - R_\alpha)/\tau_\alpha \tag{7.5}$$

We will use this equation to estimate how fast the ash accumulates when none is removed (when $R_\alpha = 1$) and to estimate the equilibrium concentration of helium attainable for various ash removal efficiencies $(1 - R_\alpha)$. For simplicity, assume $n_z = 0$.

$$\text{Let } f_\alpha \equiv n_\alpha/n_0$$

From Eqs. (7.3) and (7.4) we find

$$n_i = n_0 - 3n_\alpha/2 = n_0(1 - 3f_\alpha/2) \tag{7.6}$$

With $R_\alpha = 1$, Eq. (7.5) becomes

$$df_\alpha/dt = A_1(1 - 3f_\alpha/2)^2 \tag{7.7}$$

where

$$A_1 \equiv n_0\langle\sigma v\rangle_{DT}/4$$

If $f_\alpha(0) = 0$, the solution is

$$f_\alpha(t) = A_1 t/(1 + 3A_1 t/2)$$

The reduction of fusion power density due to alpha particle accumulation is

$$P_f(t)/P_{f_0} = (n_i/n_0)^2 = (1 - 3f_\alpha/2)^2 = (1 + 3A_1 t/2)^{-2}. \tag{7.8}$$

If R_α is less than one, then the general equation may be written in the form

$$df_\alpha/d\theta = A(1 - 3f_\alpha/2)^2 - f_\alpha$$

where dimensionless time $\theta \equiv (1 - R_\alpha)t + \tau_\alpha$

$$A \equiv n_0\langle\sigma v\rangle_{DT}\tau_\alpha/4(1 - R_\alpha).$$

Assuming $f_z(0) = 0$, the solution is

$$f_\alpha(\theta) = \frac{3A + 1}{4.5A} - \frac{(6A + 1)^{\frac{1}{2}}}{4.5A}\tanh\left[\tanh^1 - \frac{3A + 1}{(6A + 1)^{\frac{1}{2}}} + \frac{(6A + 1)^{\frac{1}{2}}\theta}{2}\right] \tag{7.9}$$

Example Problem 7.2: **Helium accumulation without removal** Assume $R_\alpha = 1$. If helium ash is not removed from a pressure-limited plasma with $n_0 = 10^{20}\,\text{m}^{-3}$ and $T = 20$ keV, how long does it take for the helium accumulation to reduce the fusion power density by a factor of two?

$$t = \left[(P_{f_0}/P_f)^{\frac{1}{2}} - 1\right]/(3A_1/2) \tag{7.10}$$

For this case $A_1 = 0.0106\,\text{s}^{-1}$ and $P_{f_0}/P_f = 2$, so $t = 26\,\text{s}$.

Thus, if helium ash is not removed, fusion burn will be quenched in tens of seconds, even if no other impurities are present.

7.1.4 Equilibrium Helium Concentration

For simplicity, we will again assume $n_z = 0$. For small values of burnup fraction,

$$f_b \simeq n_i \tau_i \langle \sigma v \rangle_{DT}/2, \quad (f_b \ll 1). \tag{7.11}$$

The equilibrium solution of Eq. (7.5) may be written

$$n_\alpha/n_i = a \equiv n_i \langle \sigma v \rangle_{DT} \tau_\alpha/4(1 - R_\alpha) = f_b \tau_\alpha/2\tau_i(1 - R_\alpha). \tag{7.12}$$

The helium concentration may also be expressed in terms of n_0, with the result

$$f_\alpha \equiv n_\alpha/n_0 = a/(1 + 3a/2). \tag{7.13}$$

The reduction in fusion power density caused by the helium alone (ignoring effects of other impurities) is

$$P_f/P_{f_0} = (n_i/n_0)^2 = (1 - 3f_\alpha/2)^2 = (1 + 3a/2)^{-2} \tag{7.14}$$

(same as Eq. 7.9).

In order to keep $P_f/P_{f_0} \geq \frac{1}{2}$, we must have $a \leq 2(2^{1/2} - 1)/3 = 0.28$. The case $P_f/P_{f_0} = \frac{1}{2}$ corresponds to $n_\alpha/n_0 = 20\%$. For example, if $(\tau_\alpha/\tau_i) = 1$ and we desire $f_b = 0.1$, then we need $R_\alpha < 0.82$. Usually, several species of impurities will be present at once.

7.1.5 Modes of Operation

With regard to impurity control and fueling, three modes of reactor operation may be distinguished (Table 7.1). Even in the short-pulse mode, low impurity fractions are needed initially to obtain ignition. Impurities from the walls will be ionized near the edge of the plasma. From there they may diffuse inwards and accumulate near the plasma center, according to simple diffusion theory. However, several phenomena tend to inhibit such accumulation, and various techniques have been suggested to exploit these phenomena for impurity control (Table 7.2).

Table 7.1 Modes of fusion reactor operation

Short-pulse	(t ≤ 30 s)	Fusion burn occurs until impurity buildup quenches it. Impurity control and refueling are minimal or non-existent. Recirculating power fraction is high, and rapid pulsing creates problems like fatigue (pinches, ICF, early tokamaks)
Long-pulse	(t ≥ 30 s)	Impurity control and refueling prolong plasma burn (tokamaks)
Steady-state	Continuous	Very effective impurity control and refueling. (tokamaks, stellarators, mirrors, …) Plasma current sustained non-inductively (tokamaks)

Table 7.2 Phenomena and techniques for impurity control

Phenomena	
Density gradient force	A positive dn_i/dr makes impurities tend to diffuse outwards.
Temperature gradient force	A negative dT_i/dr makes impurities tend to diffuse outwards.
Ion-impurity frictional force	When the parallel ion flow velocity is in the right direction, the ion-impurity frictional force makes impurities tend to diffuse outwards.
Electric field force	An outward electric field inhibits inward flow of impurities, as in magnetic mirrors.
Centrifugal force	In a rotating plasma, the centrifugal force tends to make impurities move outwards.
Radiative cooling	Cooling of edge plasma by line radiation lowers wall sputtering rates. Low-Z elements are preferable for radiative cooling, because high-Z impurities also cause line radiation from the hot plasma core.
Techniques	
Wall modification	Honeycomb surfaces, bakeout, discharge cleaning, gettering, low-Z coatings, such as lithium (Sect. 7.9).
Discharge dynamics	The plasma current may be controlled to avoid plasma contact with walls, especially during the initial breakdown phase, when divertors may not be effective.
Divertors	Outer layers of plasma are channeled to another chamber, cooled, neutralized, and pumped away.
Neutral gas blanket	Neutral fuel gas between the plasma and wall enhances density- and temperature-gradient forces, reduces sputtering rates, blocks flight of wall atoms into the plasma, and provides a source of new fuel. However, the high density at the plasma edge may lead to instability.
Impurity injection	Impurity gases may be deliberately injected to enhance radiative cooling of the plasma edge.
Gas flow	Azimuthal gas flow may lead to outward flow of impurities via the ion-impurity frictional force.
Neutral beam injection	Neutral beam injection may induce desirable ion-impurity frictional forces. Low-energy neutral beam injection may produce a "cool plasma mantle", with a positive fuel ion density gradient (similar to gas blanket, but lower density)
Limiter-reflectors	Limiters around the plasma periphery may scrape off edge plasma and neutralize it. High-speed vacuum pumps would then remove some of the neutralized gas
Selective rf plugging	If impurities have substantially different charge-to-mass ratios than fuel ions have, then rf waves may be selectively absorbed by one species. (a) Fuel ions can be selectively confined in open magnetic systems or in divertor throats. (b) Heating impurities might enhance their diffusion rates

7.2 Plasma Power Flow

7.2.1 Normal Target Heat Flux

The heat flux profile width parameter λ_q typically has a width of about 4–5 mm for large tokamaks. The outer divertor target power load is

$$q_{div} = P_{SOL}f_{div}/2\pi R_t\lambda_q f_{amp}, \tag{7.15}$$
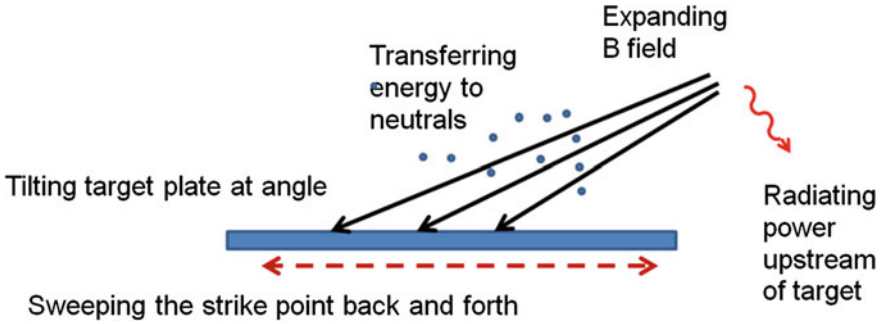
Fig. 7.3 Five methods for reducing divertor target heat flux. The target plate would be stationary, and the magnet field lines could be swept back and forth to spread the heat load (*dashed red arrow*)

where

P_{SOL}	Power flowing into the scrape-off layer (SOL),
f_{div}	Fraction of P_{SOL} going to the outer target,
R_t	Major radius of the outer target,
λ_q	Width of power flux distribution in SOL at the midplane,
f_{amp}	Ratio of target to midplane heat flux width (Loarte et al. 2007, p. S208).

The ITER design values are $R_t = 5.5$ m, $P_{SOL} \sim 80$ MW. If there were no flux spreading ($f_{amp} = 1$), $f_{div} = 0.5$, and $\lambda_q = 0.005$ m, then $q_{div} = 230$ MW/m^2. Since the acceptable heat load is only 10 MW/m^2, this would clearly be unacceptable. A heat flux of 200 MW/m^2 arriving at an angle of 3° to the surface is spread out over a large areas, making the effective heat flux $= 200 \sin(3°) = 10.5$ MW/m^2, which might be tolerable. Federici et al. (2003) discuss plasma-material interactions in ITER.

Five methods for reducing divertor heat flux are shown in Fig. 7.3.

ITER will gain a factor of 4 from flux expansion and factor of 2.5 from target inclination angle, making $f_{amp} \sim 10$, and reducing q_{div} to 23 MW/m^2. Further reduction to 10 MW/m^2 could be achieved by making $f_{div} = 0.22$. One way to accomplish this is with enhanced impurity radiation.

7.2.2 Radiation

Radiation from injected impurities like argon has been used successfully to spread out the power flux, reduce divertor target heat load, and reduce plasma temperature near the target, thus reducing sputtering yields. For example, JET and JT-60U have demonstrated high radiated power fractions $f_R \geq 0.7$ with good confinement factors $H_{H98(y.2)} \geq 0.9$ (a ratio of the energy confinement time to a standard model scaling law) and densities $n/n_G \geq 0.9$, where n_G is the Greenwald density limit.

(Loarte 2007, p. 213) Argon accumulation in the core plasma was within acceptable levels.

Even if the normal target load can be reduced to an acceptable level, ITER must still cope with off-normal events. Off-normal events include highly energetic vertical displacement events (VDEs), disruptions, and large edge localized modes (ELMs).

7.2.3 Vertical Displacement Events

VDEs occur when the forces maintaining the plasma vertical position become unbalanced. This can occur when the poloidal field coils are not effective in maintaining vertical stability. VDEs can be avoided by using a conducting shell near the plasma surface, by keeping the vertical elongation within safe limits (typically b/a $\leq$ 2), and by careful design, programming, and control of the PF coils.

7.2.4 Disruptions

The causes of disruptions are (Wesson 2011)

- Unstable current density profile J(r)
- Low edge safety factor $q_a \leq 2$
- Density $n > n_G = 10^{20}$ I(MA)/πa^2, the Greenwald limit (Impurities increase radiation power to 100 %, plasma shrinks, q_a becomes too low)
- dJ/dt too high $\rightarrow$ skin current
- B field errors
- Impurities
- Falling fragments
- Vertical instability.

Some data indicating the stability boundaries of JET against disruptions are shown in Fig. 7.4.

If the current rises too fast, then ℓ_i is low, and the current rise disruption occurs. The other cases relate to the plasma density becoming too high.

In order to **predict** the onset of a disruption we need to

- Have a large database of disruption events in present experiments
- Understand the safe operating limits, such as J(r), density limit, q profile
- Know the present plasma conditions, such as n(r), $T_e(r)$, $T_i(r)$, J(r), q(r)
- Identify precursor signals that indicate a disruption is coming (Hazeltine et al. 2009).
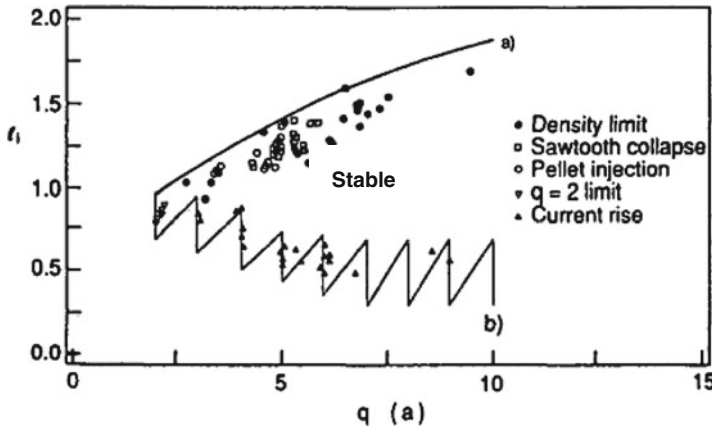
Fig. 7.4 Disruption boundaries in JET. Here the internal inductance $\ell_i = \langle B_q^2 \rangle / B_{qa}^2$ (Snipes et al. 1988)

Some methods for disruption avoidance or mitigation include (Wesson 2011):

- Use a conducting shell (with associated radiation damage and radioactivity)
- Minimize impurities by use of a divertor
- Keep $n < n_G$ (requires control of hydrogen recycling)
- Keep J(r) safe with current drive, $q_a > 2$
- Keep dI/dt below safe limit
- Feedback controlled saddle coils to limit 2/1 mode and suppress runaway electrons
- Gas injection
- Electron heating
- Neon pellets cause radiation to reduce divertor heat flux
- Optimal vertical position control can avoid vertical instability
- Low $p_0/\langle p \rangle \rightarrow$ ELMS limit edge pressure
- High $p_0/\langle p \rangle \rightarrow$ internal β_p collapses
- High triangularity δ and electron cyclotron current drive $\rightarrow$ higher stable β.

7.2.5 Edge Localized Modes

Edge localized modes (ELMs) with high poloidal mode numbers m $\sim$ 10 have been associated with H mode operation, caused by high ∇p or ∇J at the plasma edge. Three types of ELMs have been identified:

Type I Giant ELMs with big peaks of Hα light and high power flux to the divertor
Type II Intermediate
Type III "Grassy" ELMs that make confinement worse, but are not catastrophic.
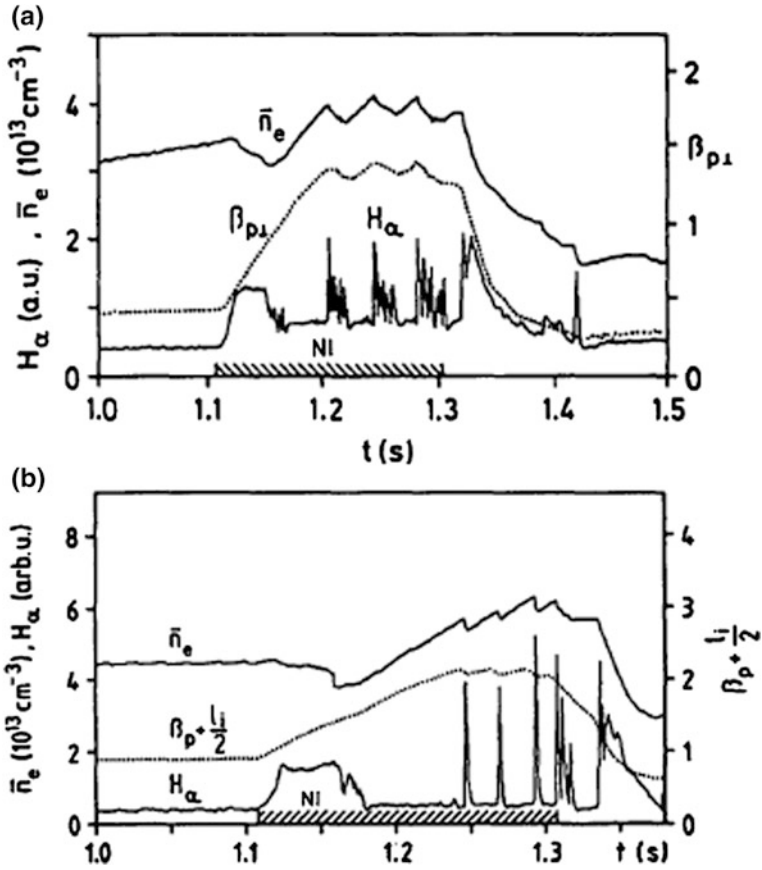
Fig. 7.5 **a** Variation of n_e, $\beta_{p\perp}$ from the diamagnetic signal and H_α at a sudden termination of Type-III "Grassy" ELMs. **b** Variation of n_e, $\beta_p + \ell_i/2$ from equilibrium and H_α with singular large ("giant") ELMs. *NI* neutral beam injection (ASDEX Team 1989)

When no ELMs are active (the "ELM-free H-mode"), impurity accumulation increases, so some ELM activity may be desirable. Hydrogen Hα light intensities versus time from two types of ELMs are illustrated in Fig. 7.5.

ASDEX-Ugrade is able to use feedback from divertor neutral particle flux and electron temperature to control HFS pellet injection. This enables it to trigger ELMs and avoid the impurity accumulation caused by ELM-free operation. The "effective divertor temperature" is obtained from thermoelectric currents between the inner and outer divertors (Loarte 2007, p. 214).

ASDEX-Upgrade is installing 24 in-vessel saddle coils for MHD control experiments. They can produce static and changing error fields to control ELMs, locked mode rotation, and resistive wall modes via feedback stabilization. These are key issues for ITER control (Suttrop 2008).

Off-normal heat loads in ITER are estimated by the RACLETTE code to be (Raffray 2008a):

- Disruptions—28–45 MJ/m^2 near X-point, lasting 1–3 ms.
- VDSs—60 MJ/m^2 over 0.2 s
- ELMs—0.77–3.8 MJ/m^2 over 0.4 s at up to 4 Hz unless controlled.

7.2.6 Erosion

ITER is expected to have several hundred ELMs per discharge, so the surface temperature rise from each discharge must be kept below the limit for melting. Disruptions may occur in 1–10 % of ITER discharges, and the heat deposition is about an order of magnitude higher that from ELMs.

From a semi-infinite slab model of target surface temperature rise during an ELM or disruption caused by energy ΔE (J/m^2) deposited in time t, it is found that the maximum acceptable values of energy and time are

$$\Delta E/t^{1/2} \leq 35 \, \text{MJ/m}^2\text{s}^{1/2} \text{ for sublimation of C and}$$
$$\Delta E/t^{1/2} \leq 40 \, \text{MJ/m}^2\text{s}^{1/2} \text{ for melting of W.} \tag{7.16}$$

Figure 7.6 shows the erosion lifetime of a CFC target estimated as a function of ELM energy density and power deposition time.
Thus, short ELM pulse widths are dangerous. Data from JET show that the temperature rise of the outboard target from a Type-I ELM goes from $0.1\Delta T$ to the full ΔT in a time $\tau_{IR} \sim 0.4$ ms. About 15–40 % of the total ELM energy flux is
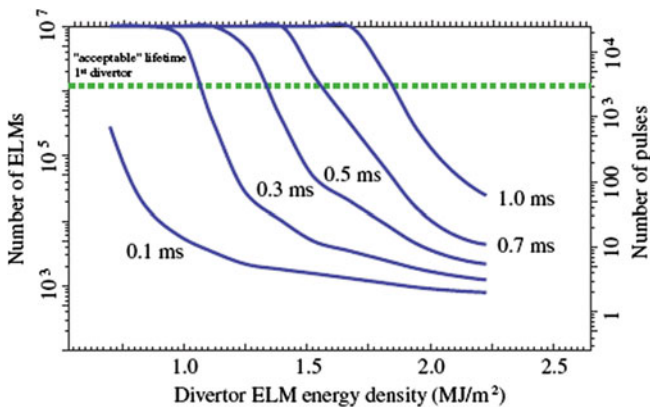
Fig. 7.6 Erosion lifetime, in number of ELMs (*left side scale*) or number of ITER full power pulses (*right side scale*), of a 2 cm thick CFC ITER target versus deposited energy density for various deposition times. The *dotted curve* indicates the ITER goal of 3,000 pulses (Loarte et al. 2007)

deposited during this short time. The time τ_{IR} correlates with the ion parallel flow time (convection time)

$$\tau_{\parallel} = 2\pi R q_{95}/c_s, \tag{7.17}$$

where c_s is the ion sound speed calculated using the pedestal parameters and q_{95} is the safety factor at the 95 % flux surface. The target plasma sheath has a strong influence on limiting the energy flux from the pedestal plasma to the target. The deposition width λ_q of the power flux onto the target during an ELM broadens less than 50 % or stays about the same (Loarte 2007, p. S216).

In single-null divertor plasmas, it is common for ELMs to deposit more energy on the inner divertor than on the outer divertor. About 50–80 % of the ELM energy goes to the divertor, with the rest probably going to the main chamber wall.

Reflectometry measurements appear to be consistent with a model in which ELMs have a poloidally/toroidally asymmetric, peeling–ballooning character with approximate toroidal mode number 10–15 (Loarte 2007, p. S217). There is rapid energy transport to plasma facing materials (PFMs), both in the divertor target and in the first wall limiter. At high pedestal densities, conductive losses decrease strongly, but convective losses remain high.

During a Type I ELM, the pedestal plasma just inside the separatrix becomes "connected" to the divertor target. There is a sudden burst of electron energy approximately equal to the pedestal T_e conducted to the target and formation of a high-energy sheath. This is followed later by convective ion fluxes at lower velocities. As the pedestal density is increased from 0.2 to $0.8n_G$, the dominant energy flow changes from fast conduction to slower convection (Loarte 2007, p. S219).

At the low values of pedestal collisionality required for ITER, data from JET indicate that about 15–20 % of the pedestal energy goes to the divertor target during an ELM. Such a large amount of power would be excessive for ITER plasma facing components (PFCs), which emphasizes "the need for ELM control" in ITER, but there are also some data indicating lower energies to the target. The heat fluxes may be limited by plasma parameters, such as collisionality, or by atomic physics processes, such as collisions with neutral atoms.

"Radiation buffering" caused by impurity injection with radiated power fraction $f_R \sim 0.8$ limits the target energy flux in small Type III ELMs, but its efficacy is less for large Type I ELMs. Erosion by sputtering, vaporization, etc., will be discussed in Sect. 8.6.

7.3 Particle Control

The main sources of plasma impurities are:

- Sputtering of the main-chamber walls by neutral particle bombardment, especially near gas and NBI ports
- Sputtering of the main-chamber by ion bombardment, including from ELMs

- Sputtering of RF antennas and limiters by energetic ions due to acceleration in RF sheaths
- Divertor target erosion by sputtering, melt layer losses, evaporation, and sublimation (and chemical sputtering of carbon)
- Impurity-induced sputtering, especially by heavy elements
- Unipolar arcing
- Helium produced by fusion reactions.

7.3.1 Hydrogen and Helium

Hydrogen recycling from walls is a major issue requiring careful wall conditioning. Recombination of deuterium reduces the plasma flux to the target plates and the sputtering rate. At low temperatures and high densities ($>10^{20}$ m^{-3}), the three-body recombination rate, which is proportional to n_e^3, dominates over radiative recombination. Molecular assisted recombination, in which a molecule is excited by some of the recombination energy, may be significant under some conditions, but its importance is not yet clear.

The divertor should help to prevent buildup of helium ash in the core plasma, which may be characterized by the ratio of helium residence time τ_{He}^* to energy confinement time τ_E, and by the ratio $\eta_{He,exh}$ of helium fraction in the exhaust plasma to helium fraction in the core plasma. Helium's high ionization potential (28 eV compared with 13.6 eV for hydrogen) gives it a longer mean free path for ionization. This makes it more difficult to prevent helium backstreaming from the divertor, but a large divertor like in ITER with longer flow paths may have a greater probability of re-ionization trapping. It appears that the helium exhaust efficiency can be improved by a factor of 3–5 in ITER, compared with present tokamaks (Loarte 2007, p. S223).

7.3.2 Redeposition

The main chamber and outer divertor usually suffer net erosion, while the inner divertor, which is generally cooler, often has net redeposition of atoms. The rates of ion impact from plasma blobs and ELMs are very difficult to predict, so there is significant uncertainty in predictions of wall erosion rates for future machines like ITER and DEMO.

Atoms sputtered from targets, limiters, and walls can be redeposited elsewhere, and in new forms, such as carbohydrate films, which can trap tritium. Redeposition of combinations of elements, such as H, Be, C, and W in ITER, is another uncertainty that can change the wall composition and performance. Tracer radioisotopes

like ^{13}C may be used to correlate redeposition sites with sources of impurities. ITER will replace plasma facing components (PFCs) in the wall and target robotically, since the torus will become highly radioactive.

7.3.3 Graphite and Beryllium

Metals are better for most areas because of lower tritium retention. In low heat flux areas, like the ITER main chamber wall, Be is chosen for its low Z, which minimizes impurity radiation. In high heat flux areas, like divertor targets, W is chosen. Graphite and CFCs are better under sudden high power fluxes, as from ELMs, but redeposited CHx films are bad due to tritium retention. Therefore, tungsten will be used in ITER divertor areas previously planned for graphite.

ITER will inject about 50 g of tritium per discharge during high-power ($Q_{DT} = 10$) discharges. A goal for surface conditioning between discharges is to remove trapped tritium so that only 10^{-3} of the injected tritium remains. If this could be accomplished, then ITER could have about 7,000 such discharges before shutdown would be required for tritium removal.

Beryllium has low atomic number, which means that it would probably not cause serious radiation losses, and it can trap oxygen impurities at its surface, forming BeO. Hydrogen retention in Be and BeO is much lower than in graphite. Its low melting temperature (1,550 K) makes it vulnerable to damage by energy impact from VDEs, ELMs and disruptions.

In JET a single large ELM depositing ~ 1 MJ in less than 1 ms, led to substantial melting of the Be JET divertor target and terminated the high performance ELM-free phase of the discharge. However, the effects of Be melting on subsequent plasma operations were not catastrophic, due to the plasma's high tolerance to the low-Z Be.

7.3.4 Tungsten and Molybdenum

For ignition the tolerable fractions are 10^{-4} of W and 10^{-3} of M_0. Accumulation of such high-Z materials in the core can cause high radiation losses and hollow electron temperature profiles, which can lead to instability. Tungsten transport can be controlled by applying central heating, so a serious concentration of W is not expected in the ITER high-Q operating regime, but an internal transport barrier could permit tungsten accumulation (Loarte 2007, p. 230). ELM-free operation may also facilitate high-Z impurity accumulation. Boronization of the walls helps to reduce high-Z accumulation in the plasma.

Sputtering of W by deuterium is slight because of the high sputtering threshold energy (290 eV). Sputtering of M_0 and W by heavier, multiply charged ions, such

as carbon, may be high, but those atoms are generally redeposited nearby because of their short ionization mean free path.

Hydrogen retention in tungsten is low in pure tungsten, but it is much higher when other impurities are deposited on the surface.

Tokamak inner surfaces may be cleaned with the toroidal field on using continuous wave ECRH or ICRH at $n_e < 10^{17}$ m^{-3} and $T_e < 40$ eV.

Graphite, beryllium, and tungsten will be discussed further in Sect. 8.8.

7.3.5 Tritium Retention

TFTR used 5.2 g (T) in experiments, and 1.7 g was trapped in the walls, but half of that was later removed by cleaning. JET used 35 g (T), of which 11.5 g were retained in the walls, and again half was removed by cleaning.

ITER will inject about 50 g per pulse. The ITER goal is to have less than 350 g of tritium inventory in the chamber walls. Compounds of W, Be, C, O, and other impurities on the surface of W can greatly increase its tritium retention, so predictions for ITER are not yet reliable.

Usually there are more hydrogenic atoms adsorbed onto the walls than there are hydrogen ions in the plasma, so control of recycling is important.

Tritium accumulation is caused by:

- Direct **implantation** of ions and neutrals in a shallow surface layer and possible diffusion into the bulk, which tends to saturate with time.
- **Co-deposition** of hydrogen with other elements, such as C, which continues to increase, instead of saturating. This is generally the dominant mechanism.
- Production of tritium by **transmutation** reactions, such as in Be.

Data from 6 tokamaks indicate hydrogen fuel retention fractions ranging from 3 % (JET closed divertor) to 50 % (Tore Supra long pulse discharges), with most in the range 10–20 % (Loarte 2007, p. S235). Retention in JT-60U was reduced by operating the divertor at 600 K.

Most carbon deposition forms initially on surfaces within line-of-sight of the sputtered carbon surface. But the atoms can then be sputtered and redeposited elsewhere again and again, so they can gradually migrate elsewhere, stopping in places where there is little ion impact. The computer model results depend strongly on the assumed "sticking coefficients" for atoms or ions hitting a wall. Nitrogen injection in the divertor region may greatly reduce hydrocarbon redeposition (Loarte 2007, p. S237). Codeposited atoms may accumulate in gaps between armor tiles, which are necessary for thermal expansion.

Possible tritium removal methods for ITER are:

1. **Plasma cleaning**, such as by pure deuterium discharges. This is not effective in regions where plasma bombardment of the surface is slight.

2. **Surface heating** by a laser or flashlamp, or by a high-radiation discharge seeded by impurities, but dust production should be avoided.
3. **Oxidation** of surface films, such as hydrocarbons, by oxygen gas at high temperatures (>550 K), which may be too high for use in ITER, or by ozone.
4. **Conditioning** methods, such as radiofrequency discharges, which affect mainly plasma-facing components.

Density control methods are discussed in Sect. 7.4.

7.3.6 Theory and Modeling

Many theories are being studied to model power and particle flow in the scrape off layer (SOL), with codes such as COMPASS, ASCOT, UEDGE, EDGE2D, COCONUT, DIVIMP/NIMBUS, and B2-Eirene. Variations of magnetic field strength along B can cause mirror reflection of some particles. Atomic and molecular collisions, including dissociation, ionization, charge exchange, excitation, radiation, and recombination need to be taken into account. In the divertor there are $E_\theta x B_t$ and $E_r x B_t$ drift velocities across the toroidal magnetic field B_t, with $E_r \sim 3T_e/\lambda_q \sim 5\text{--}20$ kV/m, and the corresponding cross-field fluxes can be as high as the parallel transport fluxes (Loarte 2007, p. S213).

The diffusion coefficient and thermal diffusivity in the SOL are not predicted with confidence by any theory, so values are assumed based on experimental data. For ITER modeling values of D ~ 0.3 and $\chi_e \sim 1.0$ m^2/s are generally assumed.

The major parameters for ITER edge plasma control modeling are:

- Fusion power
- Power entering the SOL, P_{SOL}
- Fuelling methods—gas puffing and core fuelling
- D/T neutral pressure in the divertor p_{DT}—affects target power flux
- Helium and carbon concentrations at the separatrix, c_{He} and c_C
- Pumping speed
- The connection length, represented by the edge safety factor q_{95} value.

Models show that satisfactory power fluxes (<10 MW/m^2) can be tolerated at the divertor targets up to P_{SOL} 1.5 times the nominal value of 86 MW. Values of $p_{DT} \sim 10$ Pa can help prevent helium backflow towards the separatrix. Pellet fueling is required to maintain the desired core density.

A model for the peak divertor target power flux as a function of P_{SOL}, p_{DT}, q_{95}, f_f (fueling scheme), and f_w (surface properties) gives a good fit to a wide range of data for ITER with PSOL from 80 to 30 MW (Loarte 2007, p. S245).

Transport in the SOL is an intermittent process characterized by high density fluctuations, instead of a diffusive process, so the use of a diffusion coefficient is not strictly correct.

> While most of the energy flows to the divertor during steady state this is not the case with particle fluxes; significant particle fluxes are inferred to reach main-chamber PFCs in present experiments. These are associated with turbulence whereby filaments (along the field) of high density plasma travel radially at high velocity (~ 0.5 km/s), reaching the first wall before the particles can be lost parallel to the field…. Initial empirical extrapolations of these fluxes to ITER, based on inter-machine experiments, indicate that such fluxes should not pose a problem for the lifetime of first wall components…. it has been found that a significant fraction of the ELM energy (up to ~ 50 % for very large ELMs) can be deposited on main-chamber PFCs and not in the divertor. ELMs lead to a fast radial expulsion of ions and electrons from the core—in essence carrying plasma energy from the pedestal directly to main-chamber PFCs. The radial transit time of the ELM is similar to the ion energy parallel loss time, such that ELM main-chamber fluxes are of similar magnitude to those reaching the divertor (Loarte 2007, p. 255).

Beryllium atoms may deposit on tungsten, making its surface properties (melting temperature and tritium retention) worse.

The main issues are target surface melting during plasma energy dumps and tungsten accumulation in the core plasma when an internal transport barrier (ITB) is active. The ITER goal for tritium retention is to have <0.1 % of injected tritium trapped in the vessel, but current experiments have experienced much higher retention fractions for hydrogen isotopes.

7.4 Fueling

Possible fueling methods include gas injection, molecular beam injection, cluster injection, plasma guns, compact toroid injection, neutral beam injection, and pellet injection.

7.4.1 Gas injection

Gas injection (also called gas "puffing") can create a density peak at the outside edge of the plasma. The inverted density profile and steep temperature gradient associated with a cold plasma edge promote outward diffusion of helium ash and inward diffusion of fuel ions. When hydrogen gas was admitted to the Alcator tokamak plasma, the new ions quickly flowed into the plasma core, instead of slowly diffusing inwards, as predicted by neoclassical theory.

A very high edge neutral pressure has been called a "gas blanket". The Ringboog experiment operated at higher densities than conventional tokamaks. Gas pressures of l–10 Pa and central plasma densities of 0.8–2.5×10^{21} m^{-3} were observed at plasma currents of 5–20 kA, with electron temperatures of a few eV. The configuration appeared stable at low currents, but became unstable at high currents. Hydrogen line radiation played a dominant role in the energy balance of

high-density regions. The observed particle fluxes agreed with highly collisional transport theory. Theoretical predictions indicated certain parameter ranges in which gas-blanket fueling of reactors might be feasible, but this method is unlikely to be used (Gas blankets are discussed further in Sect. 7.7.2).

In tokamaks with high recycling of hydrogen from the walls, the plasma density tends to rise to high levels, exceeding the "Greenwald limit". If the edge neutral density and plasma density are too high, the edge plasma will be cold with a high resistivity, which makes the current density profile shrink to smaller radii. This shrinkage distorts the safety factor profile q(r), and the plasma becomes unstable.

For most tokamaks high edge neutral pressures are unacceptable, so elaborate wall conditioning techniques are used to limit recycling. Modern tokamaks use short bursts of gas (gas "puffing") at various locations to control the edge fueling. It is desirable to deposit the fuel further inside the plasma to avoid this high edge density problem.

7.4.2 Supersonic Molecular Beam Injection

Supersonic molecular beam injection (SMBI) shoots hydrogen through a nozzle at v $\sim$ 1 km/s, which is substantially higher than the 300 m/s from gas puffing.

Injection from the high field side (inside of the torus), Fig. 7.7, gives better penetration than from the low field side.

This jet penetrates significantly farther than gas puffing. Experiments on the HL-2A indicated that there were two groups of molecules: a slow group, which penetrated about 4 cm, and a fast group, which penetrated about 8.5 cm. Ionization of the slow group creates a local high plasma density, which blocks further penetration of the following molecules (a self-blocking effect). Gas puffing achieves a fueling efficiency $\sim$10–15 %, SMBI $\sim$30–60 %, and pellet injection up to 80 % (Yu et al. 2010).

7.4.3 Cluster Injection

The term *cluster* refers to a tiny droplet of solid hydrogen (H_2, D_2 or T_2) containing fewer than a million molecules. A cluster injection system involves the following components:

- **Source** Typical clusters of 10^3–10^6 molecules are formed by expanding H_2 in a nozzle cooled at 20–40 K. Beams with 100 A-equivalent current have been produced.
- **Ionizer** The clusters are ionized and their size is adjusted to contain on the order of 100 molecules.
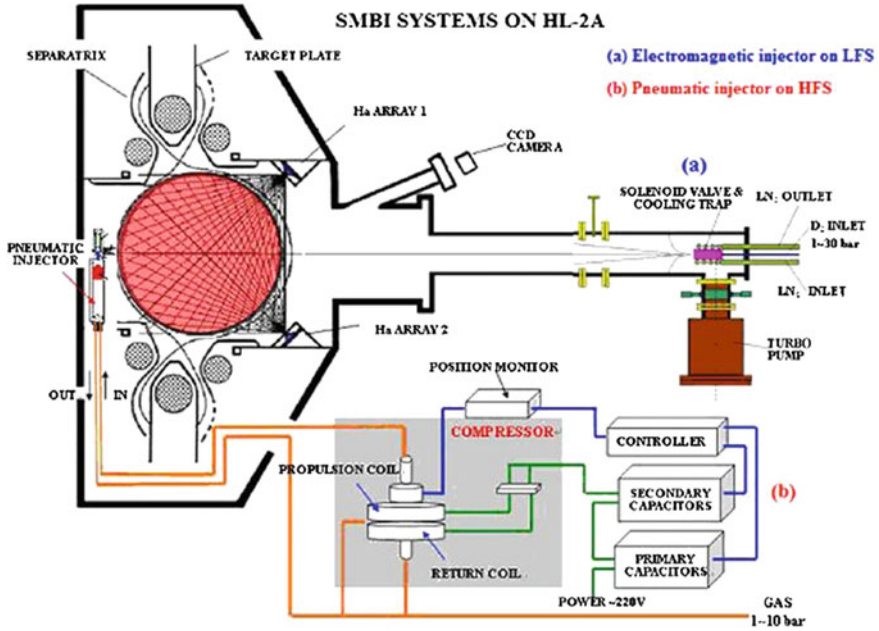
Fig. 7.7 Supersonic molecular beam injection in the HL-2A tokamak. The pneumatic injector is at the high field side (*left side*) of the tokamak (Yu et al. 2010, Fig. 1)

- **Accelerator** The clusters are accelerated up to MeV energies (1–100 keV/atom) by a high voltage electrode gap.
- **Drift tube** The accelerated clusters flow through a drift tube to the plasma confinement region.

The solid H_2 crystals have densities of 2.2×10^{28} molecules/m^3, mass densities of 73.6 kg/m^3, and intermolecular binding energies of about 10^{-2} eV (Van der Waals forces). The small ratio of charge to mass permits cluster injection across the magnetic field. Clusters may also be neutralized by passing them through a gas cell, as with neutral beam production. When the clusters impinge on the plasma, electron impact ionization increases their charge, and they split apart, because the Coulomb repulsion is greater than the intermolecular binding energy. Non-ionizing collisions with ions transfer kinetic energy to the crystal lattice, which is responsible for about 10–20 % of the total fragmentation. Surface evaporation also removes molecules, but it does so at a slower rate than fragmentation.

The particle deposition per unit length in a uniform plasma is represented approximately by the expression

$$dN/dx = C\beta^2 x \exp[-(\beta x)^{1.9}/1.9] \qquad (7.18)$$

$$\text{with} \quad \beta = 5.8 \times 10^{-8}(Bn/E_o)^{1/2} \ (m^{-1}), \qquad (7.19)$$

where x = distance into the plasma (m), B = magnetic field (T), n = plasma density (m^{-3}), and E_o = energy per unit mass of injected particles (eV/u), and u represents atomic mass units (for deuterium M = 2u). Equation (7.18) is valid for $E_o < 50$ keV/u. The maximum deposition occurs at a depth $L_o = 1/\beta$. For example, if B = 4 T, and n = 10^{20} m^{-3}, then L_o = 0.09 m. If E_o is small, then L_o will be small and penetration will be poor. If E_o is too large, then the injection power will be large and the reactor Q will be low, as with neutral beam injection.

7.4.4 Plasma Guns and Compact Toroid Injection

Plasma guns can produce plasmas containing many particles ($>10^{21}$ per shot) with MJ of energy at efficiencies over 50 %. Gun plasmas can sometimes penetrate across magnetic field lines into toroidal confinement systems. Some gun plasmas have very low impurity content. Let S_i be the volume-average fuel ion source (ions/m^3s) and V be the plasma volume (m^3). Since each fuel ion undergoing fusion produces $W_{DT}/2$ of energy, the fusion power may be written

$$P_f = f_b S_i V W_{DT}/2 \quad (W), \qquad (7.20)$$

where f_b = fuel burnup fraction. The required fuel ion source is

$$S_i V = 2P_f/f_b W_{DT} \text{ (ions/s)}. \qquad (7.21)$$

For example, if a reactor produces P_f = 3.3 GW (thermal) and has a burnup fraction f_b = 0.05, then the required fueling rate is $S_i V = 5 \times 10^{22}$ ions/s. If plasma guns produced 10^{21} particles per blob, and half of those particles had adequate penetration into the confinement system, then about 100 plasma blobs per second would be needed to sustain the reactor fuel.

A tokamak based system must operate at high values of the bootstrap current, which requires density and pressure profile control. A compact toroid (CT) injector for ITER could have a pulse repetition rate of about 20 Hz. Each CT would provide less than 1 % of the plasma ion population, and the penetration depth could be controlled by the CT velocity (200–500 km/s). The injector electrodes would be stainless steel with thin copper (flux conserver) and tungsten coatings. A CT injection system could potentially provide real-time density profile control, momentum injection, and increased fuel burnup fraction, hence reduced tritium flow rates (Raman 2008).

7.4.5 Neutral Beam Injection

Neutral beam injection was discussed in Sect. 5.4. The required beam current for fueling a reactor is

$$I = eS_iV = 2eP_f/[f_bW_{DT}] \quad (A). \tag{7.22}$$

For the example with $P_f = 2$ GW and $f_b = 0.05$, the required current is $I = 4.5$ kA. If the beam energy were 200 kV, the beam power would be 0.9 GW. This enormous power requirement illustrates the inefficiency of trying to fuel a reactor with high-energy neutral beam injection. It could be difficult to achieve high $Q =$ (fusion power)/(input power) if high-energy neutral beams were used for fueling.

Higher Q could be attained with a reactor using low-energy (~ 10 keV) neutral beam fueling, if the burnup fraction and shallow penetration were adequate. Neutral beam fueling is technologically feasible, but neutral beam injectors are complex and expensive.

7.4.6 Pellet Injection

7.4.6.1 Production

Small pellets of solid deuterium or tritium may be suitable for fueling reactors if they can be accelerated to a velocity adequate for penetration. Solid hydrogen pellets may be produced by two methods. A jet of liquid hydrogen forced through a nozzle may be broken up into droplets, which freeze if they are injected into a vacuum. Alternately, solid hydrogen may be extruded through an orifice and then cut with a laser beam or arc into tiny cylinders.

7.4.6.2 Acceleration

A variety of means have been considered for acceleration of the pellets, including electrostatic accelerators, electromagnetic accelerators, ablation, centrifugal acceleration, and light gas guns. It is difficult to get the pellets to hold a large electrostatic charge without breaking apart, because of the very low strength of solid hydrogen. Very high voltages (>10 MV) and long accelerators would be required to accelerate 1 mm pellets up to the required velocities (several km/s), so electrostatic accelerators appear to be impractical.

Electromagnetic accelerators have been proposed to accelerate a sabot (carrier) holding a pellet. At the end of the accelerator the carrier would be separated from the pellet. The pellet would go into the plasma and the carrier would be caught. Accelerators like rail guns could operate with acceptable lengths (<l00 m), but they have not been developed for pellet fueling. [There were once proposals for inertial confinement fusion reactors based on DT explosions triggered by one-gram pellet impact at 100 km/s onto a solid target (Dolan 1982, p. 543).]

A laser or electron beam incident on one side of a pellet could ablate away part of the pellet surface, accelerating the pellet away from the beam. The ablation

must be done gradually, to avoid shock waves which would fracture the pellet. However, in laser fusion experiments it has been observed that when a pellet is illuminated by a single laser, a spherical cloud quickly surrounds the pellet, ablating it on all sides so that acceleration away from the beam is impeded.

Light gas guns can inject pellets at speeds of 1–4 km/s, and a pellet launcher with 10 Hz repetition rate has been developed at Tore Supra. Losses in the guide tube may limit pellet velocities to about 500 m/s.

A pellet may be accelerated by placing it in a rotating arm, like throwing a baseball. The pellet velocity attainable is ultimately limited by the strengths of the arm and pellet to less than 5 km/s. ITER will use a centrifugal arm that launches 6.5 mm diameter pellets at 500 m/s from the high field side, which will be deposited outside r/a = 0.65, in order to trigger high-frequency Type I ELMs, which have lower energy per pulse and do less damage (Loarte 2007, pp. S241–S242).

7.4.6.3 Interaction with Plasma

When a pellet is injected into a plasma, the outer surface of the pellet is ablated away, forming a large cloud of neutral gas around the pellet. The radius of the cloud may be up to 100 times as large as the radius of the pellet. The outer edge of the cloud is ionized and heated by the plasma, and heat transported to the pellet continues to ablate its surface as it penetrates into the plasma. This neutral gas shielding permits the pellet to penetrate much farther into the plasma than it would if the plasma interacted directly with the pellet surface. The plasma at the outer edge of the gas cloud may also distort the local magnetic field, providing further shielding.

Let f be the ratio of the number of atoms in the pellet to the number of ions in the plasma. Then for a spherical pellet,

$$f = (4/3)\pi r_p{}^3 n_s / \langle n \rangle V, \tag{7.23}$$

where r_p = pellet radius (m), n_s atomic density of the pellet (m^{-3}), $\langle n \rangle$ is the volume-average plasma density (m^{-3}), and V is the plasma volume (m^3). For solid hydrogen, $n_s = 4.4 \times 10^{28}$ m^{-3}. Values of f > 1 may disrupt plasma confinement, so values of f ~ 0.1–0.3 are likely to be used. Smaller values of f would correspond to small r_p, which would not penetrate as well into the plasma.

Assuming $n/n_0 = [1 - (r/a)^2]$ and $T/T_o = [1 - (r/a)^2]^2$, a neutral gas shielding model of pellet lifetime gives the following estimate of the velocity required to penetrate a distance ℓ (measured from the plasma edge) into a plasma with radius a (m):

$$u = aM^{-1/3}(fV)^{-5/9}\langle n \rangle^{-2/9}\langle T_e \rangle^{1/6}G[\langle T_e \rangle, (\ell/a)] \ (m/s), \tag{7.24}$$

where M = molecular weight of fuel (u) (for D_2, M = 4), $\langle T \rangle$ = volume-averaged electron temperature (keV), and the function G is available elsewhere (Milora 1978; Dolan 1982). Some approximate values of G are:

$$\begin{aligned}
\text{For } (\ell/a) = 0.3 \qquad & G \approx 4 \times 10^6 \, \langle T_e \rangle^{1.29} \\
\text{For } (\ell/a) = 0.5 \qquad & G \approx 2.5 \times 10^7 \, \langle T_e \rangle^{1.29}
\end{aligned} \tag{7.25}$$

Example Problem 7.3: **Pellet velocity** Deuterium pellets are injected into a plasma with a = 1.3 m, R/a = 3, $\langle n \rangle = 10^{20}$ m^{-3}, V = 300 m^3, $\langle T_e \rangle$ = 10 keV. If f = 0.3 and penetration to (r/a) = 0.7 is desired, what is the required pellet velocity, according to the neutral gas shielding model?

For this case $(\ell/a) = 0.3$ and $G \approx 8 \times 10^7$. Then from Eq. (7.24) we find u $\approx$ 280 m/s.

During pellet injection experiments in some tokamaks, pellet lifetimes, typically hundreds of microseconds, were in fair agreement with predictions of this neutral gas shielding model.

Cryogenic hydrogen pellet injection has the following disadvantages:

- Requires cryogenic systems
- Pellets difficult to handle and store
- Acceleration limited by pellet strength
- Pellet losses in the transit tube
- Deep penetration difficult to achieve in large reactors.

It may also be feasible to inject pellets of LiD or LiT, which do not require cryogenic systems. They could provide partial fueling and coat the walls with lithium (Sect. 7.9).

7.4.7 ITER Fueling System

Figure 7.8 shows the ITER fueling system.

ITER uses gas injection, pellet injection, and neutral beam injection. The exhaust gas processing system separates out the deuterium and tritium for recycle as fuel. One of the pellet injection systems under study for ITER is shown in Fig. 7.9.

The rotating twin screws force liquid deuterium through a cryogenic nozzle, where a frozen deuterium rod emerges. This rod is then cut into pellets and injected into the tokamak. Figure 7.10 shows the ITER pellet injection system.

The ITER pellet injection system will be able to inject 5 mm diameter pellets at 10 Hz with speed $\sim$300 m/s (Maruyama 2010).

Let N_{pel} = number of fuel atoms in the pellet and N_{pl} = number of fuel ions in the plasma. If N_{pel}/N_{pl} is too small, the pellet will not penetrate well; and if this
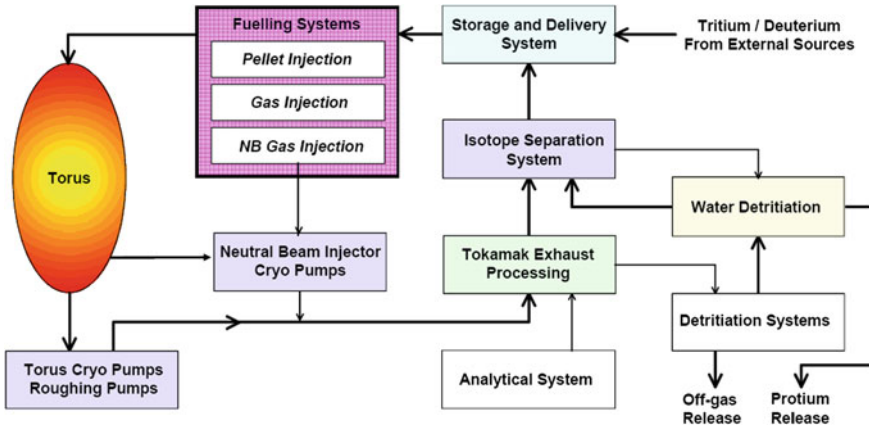
Fig. 7.8 The ITER fueling system. From S. Murayama, KIT Summer School 2008

Fig. 7.9 A twin screw extrusion system for producing solid D_2 pellets. From S. Murayama, KIT Summer School 2008
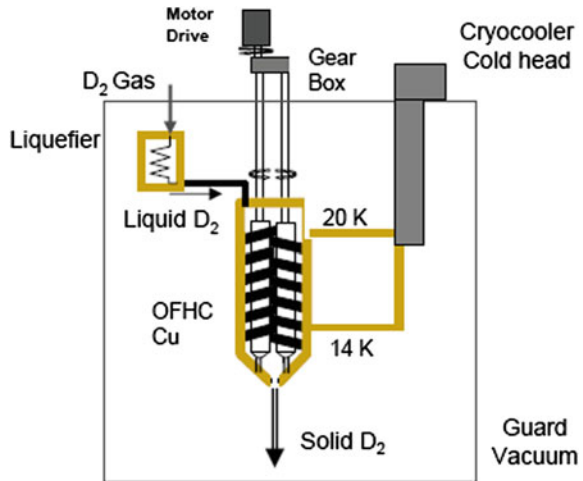
ratio is too large, the plasma may become unstable. Values of $N_{pel}/N_{pl} \sim 0.1–0.5$ may be suitable.

After acceleration the pellets travel through a flight tube to reach the inside of the torus, Fig. 7.11.

Pellets are injected from the high field side, from where they can penetrate better. This requires a long flight tube to transport the pellets from the gas gun.

Pellet fueling experiments were reviewed by Milora et al. (1995) and by Pégourié (2007).
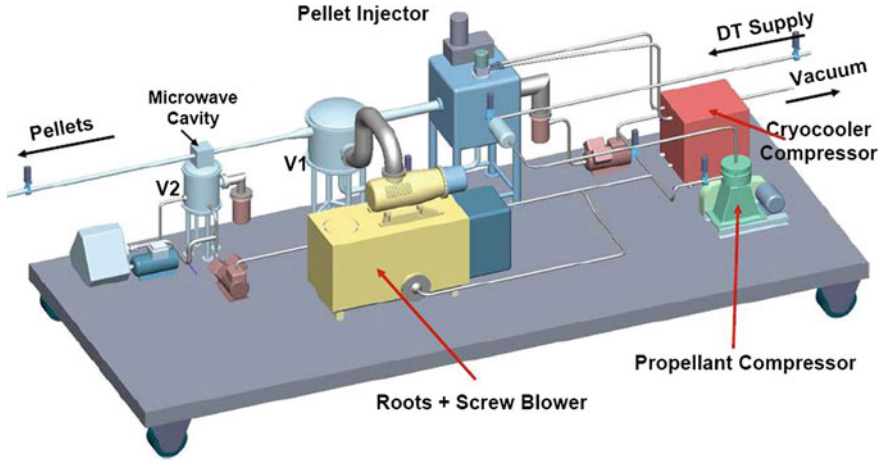
Fig. 7.10 The ITER pellet injection system. From S. Maruyama, KIT Summer School, 2008

Fig. 7.11 The ITER pellet
flight tube. From
S. Maruyama, KIT Summer
School 2008
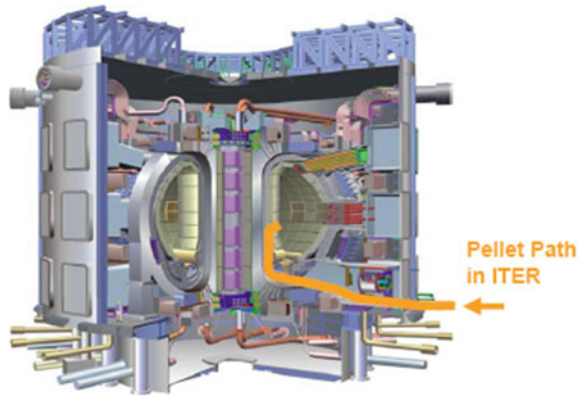
7.4.8 Summary of Fueling

- **Gas puffing** Easy, but makes density peak at edge
- **Molecular beam injection** High speed provides some penetration
- **Cluster injection** Penetration, but complex technology
- **Plasma guns** Needs high repetition rate; probable radiation damage and fatigue problems
- **Neutral beam injection** Requires too much power for fueling application
- **Pellet injection** Best, but requires cryogenic pellets and acceleration, unless normally solid pellets, such LiD, are used.

7.5 Divertor Functions

7.5.1 Types of Divertors

A divertor is a device that bends the outer magnetic field lines away from the plasma and leads them to a separate external chamber. The outer layers of plasma flow along these diverted field lines to the outer chamber, where the plasma deposits its energy via several processes. These include radiation, collisons with neutral gas, and impact on a "target plate". The cooled plasma recombines into neutral gas, which can be pumped away by vacuum pumps. Thus, the outer layers of plasma are continuously removed, cooled, neutralized, and pumped away by the divertor.

The separatrix, is the boundary of the last closed flux surface (LCFS) and the scrape-off layer (SOL), where open magnetic field lines intercept the limiter or wall. Plasma inside the separatrix is confined, and magnetic field lines in the SOL lead to the divertor. Plasma in the SOL flows towards the divertor while gradually diffusing across the magnetic field and undergoing atomic collisions that may cause charge exchange or radiation. Divertors may divert the toroidal magnetic flux, the poloidal flux, or a small bundle of flux. Tokamak divertors are usually poloidal divertors.

The purposes of the divertor are to:

- Reduce the **heat flux** on the first wall of the main chamber by moving much of the heat load to the divertor.
- Reduce **sputtering** by having cooler temperatures near the wall.
- Remove helium **ash** from the outer layers of the plasma, so that it does not build up to high levels and dilute the fuel ion density.
- Prevent **impurity** atoms sputtered from the wall from entering the plasma core.

These are illustrated in Fig. 7.12.

Figure 7.13 shows single null and double null divertors for a tokamak.

The *poloidal* magnetic field component is zero at the X point, hence the term "null", but the equilibrium *toroidal* field is normally not zero anywhere inside the tokamak. (The toroidal field can be zero at one radius in a reversed field pinch). A double null divertor has more target area and facilitates more plasma triangularity, but has lower plasma volume and more complexity.

A single null divertor is simpler, with a longer connection length and more plasma volume. An enclosed divertor chamber reduces neutral backflow towards that main plasma, and causes higher neutral pressure in the divertor region, lowering the temperature there, and reducing target sputtering.

In general the outer target receives a higher heat flux because the Shafranov shift moves flux surfaces outwards, making a shorter connection length to outer target, and less time for the flowing plasma to cool before reaching target. This can be somewhat reduced by change of current direction, which changes the ion ∇B drift direction.

Fig. 7.12 Divertor
functions: reduction of heat
flux and sputtering of first
wall; channeling of helium
and sputtered impurities to
divertor chamber target
below
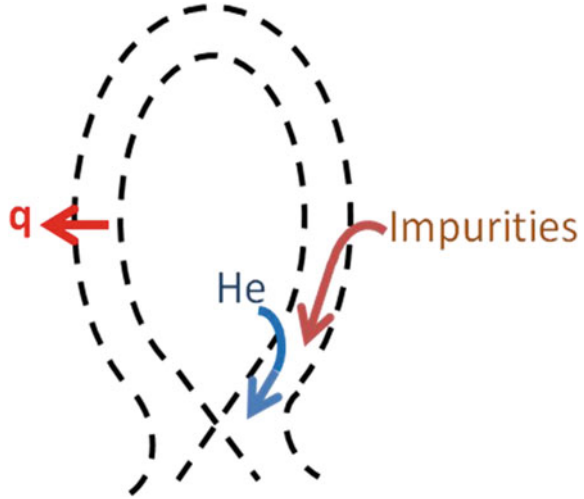
Fig. 7.13 Tokamak poloidal
divertors
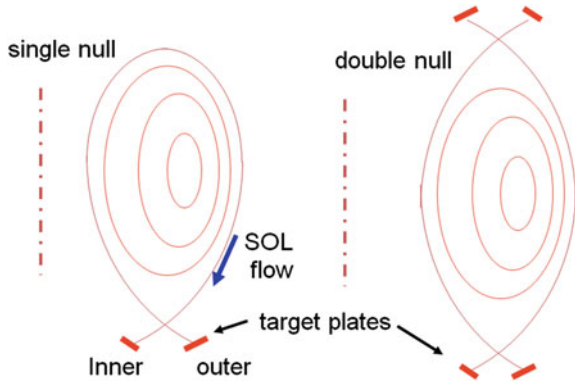
7.5.2 Plasma Flow

Plasma flow in a double-null tokamak poloidal divertor is illustrated in Fig. 7.14.

The exact location of the separatrix depends upon plasma current distribution, and a poloidal divertor may not be effective during start-up, when plasma current is low. The plasma could become contaminated with impurities by contact with the walls during startup. Plasma crossing the separatrix may flow along the magnetic field to the target, or it may diffuse across the field to the walls. Since the toroidal field $B_t \gg B_p$ the ions travel a long way in the toroidal direction (out of the plane of the drawing), while going a short poloidal distance towards the target. At the null point, the poloidal field $B_p = 0$, but $B_t \neq 0$.

Fig. 7.14 The *upper half* of a double-null tokamak poloidal divertor (coils not shown). Plasma crossing the separatrix may flow along the B field to the target, or may diffuse across the B field to the walls
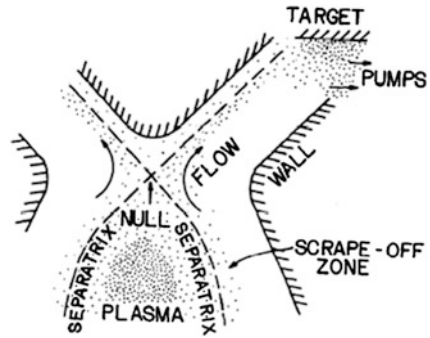
The approximate variations of plasma density, temperature, and neutral density along the magnetic field from the separatrix to the divertor target are illustrated in Fig. 7.15.

The plasma cools by radiation as it flows from the x-point (separatrix) to the divertor target, especially if impurities like argon are injected into the SOL.

For a simplified analysis of plasma flow in the SOL, we use the following definitions:

$$\tau_\parallel \approx \text{sum of time delays for flow to target or limiter}$$
$$\approx (\text{ambipolar flow along B}) + (\text{mirror detrapping})$$
$$+ (\text{electrostatic potential detrapping})$$

$$\tau_\parallel \approx L/c_s + F(\tau_i, R_m, \phi(x)),$$

where $c_s \approx [(T_e + 1.7\, T_i)/m_i]^{1/2}$ is the ion sound speed,

L   Flow path length
τ_i Ion collision time
ϕ Electrostatic potential
R_m Magnetic mirror ratio along B

Fig. 7.15 Variations of plasma density, electron temperature, and neutral density along the magnetic field in the divertor channel, showing where ionization and recombination are dominant (Based on drawing of Asakura et al. 2010)
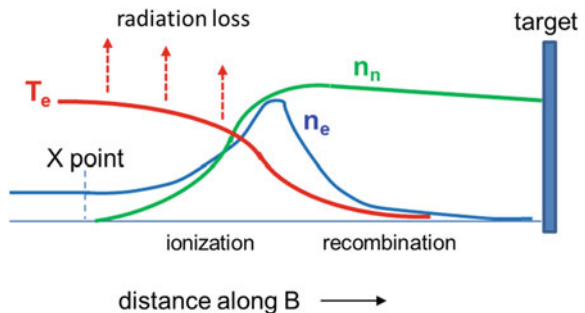
The plasma continuity equation may be written in the form

$$\partial n/\partial t \ + \nabla \bullet \Gamma = \Sigma nn_k \langle \sigma v \rangle_k - n^2 \langle \sigma_r v \rangle, \ \text{or}$$
$$\text{outflow} \ = \ \text{ionization} \ - \ \text{recombination.}$$

(7.26)

where k denotes neutral atom species.

Assuming a constant diffusion coefficient D_∞, we consider the separate flows parallel and perpendicular to B

$$\nabla \bullet \Gamma \approx n/\tau_\parallel - D_\infty \partial^2 n/\partial x^2$$

(7.27)

At equilibrium, ignoring recombination,

$$n/\tau_\parallel - D_\infty \partial^2 n/\partial x^2 \approx \Sigma nn_k \langle \sigma v \rangle_k$$
$$\partial^2 n/\partial x^2 \approx n/D_\infty \tau_\parallel - n \Sigma n_k \langle \sigma v \rangle_k /D_\infty = n/\lambda^2$$
$$\text{parallel flow} \quad \text{ionization}$$

(7.28)

where

$$\lambda^2 = D_\infty \tau_\parallel / \left(1 - \Sigma n_k < \sigma v > \tau_\parallel \right).$$

(7.29)

The sign of λ^2 determines the curvature of the density profile perpendicular to B. The situation is illustrated in Fig. 7.16.
If ionization dominant, then

$$d^2 n/dx^2 < 0.$$

The curvature is concave downwards and dn/dx is not steep at the separatrix.
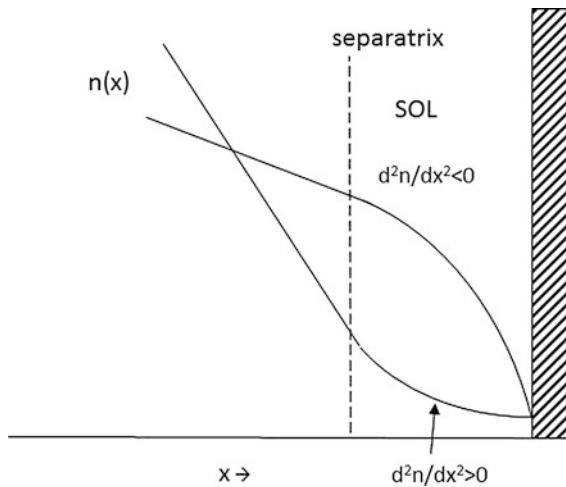
Fig. 7.16 Density profile in the SOL

If ionization negligible, then the curvature is upwards, and the density decays roughly exponentially away from the separatrix,

$$n = n_s \exp(-(x - x_s)/\lambda). \qquad (7.30)$$

Example Problem 7.4: **Scrape off layer processes** Estimate λ in a hydrogen plasma SOL with $n = 10^{19}$ m^{-3}, $n_k = 3 \times 10^{16}$ m^{-3}, $T_e = T_i = 0.3$ keV, $L = 100$ m, $B = 4$ T, Bohm diffusion, and negligible magnetic mirror effect.

$c_s \approx ((T_e + 1.7T_i)/m_i)^{1/2} = (0.81 \times 1.60 \times 10^{-16}/1.67 \times 10^{-27})^{1/2}$
$= 2.79 \times 10^5$ m/s
$\tau_{11} \approx L/c_s = 3.59 \times 10^{-4}$ s
$D_\infty \approx kT_e/16eB = 300/16(4) = 4.69$ m^2/s
$<\sigma v>_k \approx 3 \times 10^{-14}$ m^3/s (Dolan 1982, Chap. 3)
$\lambda^2 = D_\infty \tau_{11}/(1 - \Sigma n_k <\sigma v> \tau_{11}) = 3.0 \times 10^{-3}$ m^2
$\lambda \approx 5.4$ cm.
(If the neutral density n_k were 10^{17} m^{-3}, then ionization would be dominant, and $\lambda^2 < 0$).

This example merely illustrates the fact that the balance between parallel flow loss, cross field diffusion, and ionization determines the local density profile curvature. In a real case, the parameters assumed to be constant (n_k, $D_\perp$, T, $\langle \sigma v \rangle_k$) would not be constant, and a simple solution would not be easy to obtain. In some cases ionization may dominate near the wall, but not near the separatrix, as shown in Fig. 7.17.

Recombination may also be significant in places where n is very high, such as near the target.

Most of the impurities coming from the first wall are also ionized in the SOL and channeled to the divertor so that they do not reach the core plasma.
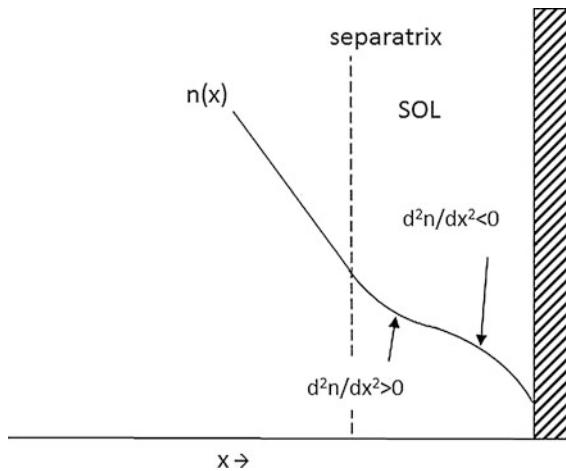
Fig. 7.17 A case where ionization is dominant near the wall, but transport is dominant near the separatrix (Dolan 2011)
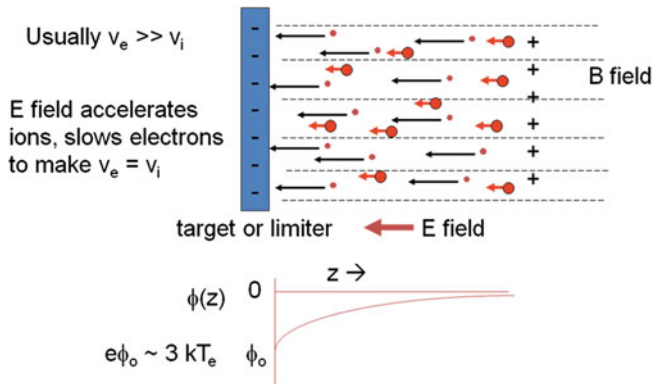
Fig. 7.18 The plasma sheath region near a divertor target or limiter

7.5.3 Plasma Sheath

The plasma flow onto the divertor target or limiter generates a plasma sheath, as illustrated in Fig. 7.18.

Electrons flowing rapidly along B leave slower ions behind, creating a charge separation electric field that tends to accelerate ions and decelerate electrons. This allows them to travel at the same rate near the target. The sheath potential is typically about 3 times T_e. Therefore, we want T_e to be low near the target so that the potential accelerating the ions does not give them enough energy to cause much sputtering. A high neutral gas density in the divertor chamber can facilitate this electron cooling. The dome and baffles of "closed" divertor designs serve to increase the neutral gas density, while inhibiting neutral gas backflow to the separatrix. When a high neutral gas pressure separates the divertor target from the plasma flowing from the separatrix, the divertor is said to be "detached".

Ionization and secondary electron emission from the target tend to broaden the sheath and reduce the sheath potential fall, thus reducing the sputtering yield. At very high B and T_e intense cyclotron radiation from the plasma will tend to ionize sputtered impurities in the scrape-off region, reducing their chance of penetrating across the separatrix, and consequently enhancing the screening efficiency of the divertor.

Divertors are being simulated in detail by two-dimensional computer codes, taking into account plasma flow, neutral density, diffusion, ionization, charge exchange, recombination, frictional forces, viscosity, radiative cooling, reflection, adsorption–desorption, secondary emission, and sputtering. Many species, ionization states, and their interactions must be taken into account. Values of diffusion coefficients and thermal conductivities for various species are assumed, which introduces uncertainty to the results.

7.5.4 Divertor Target and Pumping

The divertor target for a reactor will probably have heat loads of several MW/m^2, so overheating is a potential problem. Unless the plasma has cooled substantially, sputtering will also be a serious problem. Sputtered target metal atoms may become ionized in the sheath and accelerated back into the target, causing self-sputtering with high yield. Honeycomb shape surfaces have been proposed to catch many of the sputtered atoms. If the temperatures are reduced to very low values (<30 eV), then the sheath potential accelerating the ions may be below the sputtering threshold, and sputtering rates will be low. A low sheath potential is also desirable to prevent unipolar arcing in the target and chamber walls (Sect. 8.7).

High vacuum pumping speeds may be needed to handle the gas load from a fusion reactor divertor exhaust. The heat flow is typically hundreds of MW. If this is carried by low-energy particles striking the target (to reduce sputtering), then the particle flow rate is very large.

To alleviate the vacuum pumping problem, we can

- Reduce the heat load to the divertor, and increase heat flow to the first wall. This would increase first wall sputtering rates.
- Allow higher energy per particle hitting the divertor target. This would increase divertor target sputtering rates.
- Allow higher pressure near the target. This would increase neutral gas flow across the separatrix, tending towards the gas blanket concept, which could cause the pedestal density to increase too much for stability.
- Increase the pressure near the target without increasing the pressure along the separatrix by making the divertor more "closed".

7.5.5 Closed Divertors

"Closure" of the divertor chamber, illustrated in Fig. 7.19, greatly increases the neutral pressure near the target, which helps to dissipate energy upstream from the target by atomic and molecular collision processes.

At a given pedestal density the divertor pressure increased by a factor of about 5 as the closure was increased from Mark I to Mark IIGB. It is desirable

- To keep the divertor pressure relatively high
- To keep the main chamber pressure low
- To avoid excessive charge exchange and sputtering of the wall
- To avoid excessive neutral influx across the separatrix, which could cause a pedestal density spike, cooling the edge plasma and narrowing the current density profile, with possible destabilizing effect.
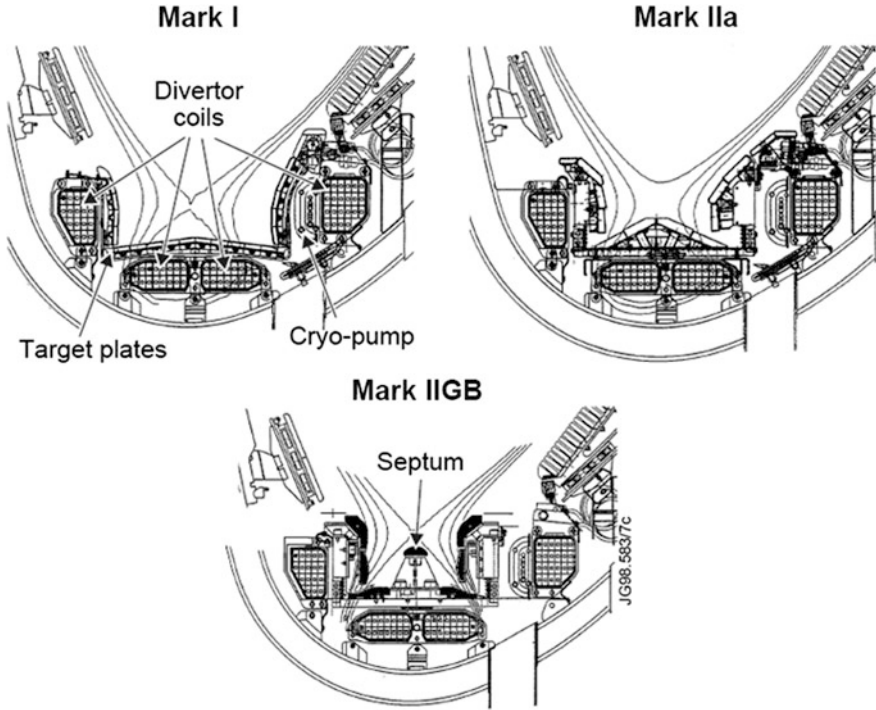
Fig. 7.19 Greater closure of the JETdivertor as it was changed from the Mark I → Mark IIA/P → Mark IIGB (JET Team 1999, Fig. 1). Copyright 1999, International Atomic Energy Agency

7.6 Divertor Examples

The ITER divertor is shown again in Fig. 7.20 (same as Figs. 2.10 and 6.4).

7.6.1 Power Load

The dome and baffles help to prevent neutralized atoms from flowing backwards towards the core plasma, so more of the gas goes to the vacuum pumps. The backflow is thereby reduced by about two orders of magnitude. Figure 7.21 shows the ITER divertor power load.

The heat flux at the divertor is reduced by expansion of the magnetic flux surfaces and by tilting the target relative to the field lines (Fig. 7.3).
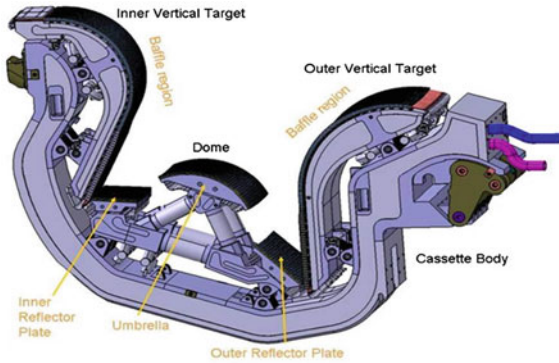
Fig. 7.20 The ITER divertor. Courtesy of ITER Organization
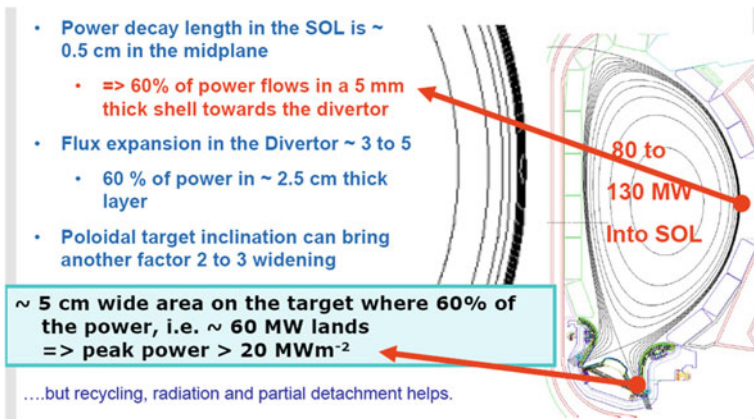
Fig. 7.21 ITER divertor power load. Courtesy of ITER Organization

7.6.2 Thermal Stress

Thermal stress was discussed in Sect. 6.8. Table 7.3 shows the pertinent parameters for iron and tungsten.

If the heat flux is 10 MW/m^2 and the tube wall thickness is 1 mm, the resulting thermal stress in iron is 1,160 MPa (unacceptable), but in tungsten it is 130 MPa (acceptable).

Table 7.3 Parameters of iron and tungsten

	Units	Fe	W
α	K^{-1}	1.8×10^{-5}	4.5×10^{-6}
E	Pa	1.8×10^{11}	4.0×10^{11}
ν		0.3	0.3
λ	W/m-K	20	100

7.6.3 Divertor Cooling

There are 58 divertor assemblies, each 8.8 tons, containing 4,320 actively cooled heat flux elements, which can be baked to 350 °C to remove impurities like water vapor. In the new design the graphite is replaced by tungsten.

Impurities such as Ne or Ar will be added to the plasma to radiate about 70 % of the thermal energy upstream onto the first wall and divertor channel, so that the heat load on the target plates is reduced from 40 MW/m^2 to about 10 MW/m^2.

Data from DIII-D and NSTX indicate that the "power width" where power is concentrated at the divertor decreases with increasing plasma current, so the value for ITER at 15 MA could be very small (a few mm), making the heat flux very high (Pitts 2010).

Disruptions can cause high J × B forces, local melting and splashing, and thermal shock stresses, which can reduce the wall thickness and shorten its lifetime. In order to mitigate the effects of disruptions in ITER various ideas are considered, such as injection of impurity pellets to help dissipate the plasma thermal energy.

7.6.4 Developmental Divertors

The ARIES-AT design uses a divertor cooled by flowing PbLi, Fig. 7.22.

This design uses high velocity PbLi flow close to the plasma facing surface, and slower return flow elsewhere. The individual channels have PbLi flowing 2 cm in the toroidal direction while cooling the surface coated with a 2.5 mm tungsten sacrificial layer. The peak stress and heat load limit are 190 MPa and 6 MW/m^2 (Raffray 2008a).

For safety reasons water will probably not be used in fusion power plant divertors. It is difficult to accommodate very high heat fluxes (>10 MW/m^2) with liquid metal or molten salt coolants, so most of the developmental divertor designs use helium coolant:

- Plate type—ARIES TNS
- Open-cell foam tube

Fig. 7.22 One section of the ARIES-AT SiC divertor cooled by PbLi (Raffray et al. 2007, Fig. 19)
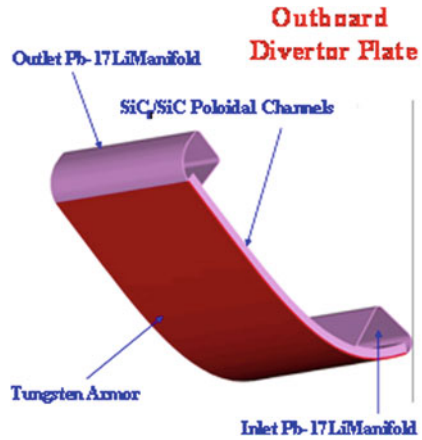
- T-Tube design—ARIES-CS
- Helium-cooled multi-jet (HEMJ).

We will consider these ideas and their possible application to the DEMO divertor.

7.6.5 Plate Type Divertor

Figures 7.23 and 7.24 show a plate type divertor.

The helium would operate at 10 MPa in the range 700–800 °C to avoid neutron radiation embrittlement and to keep the tungsten temperature below its

Fig. 7.23 A large plate type divertor (Tillack et al. 2011)
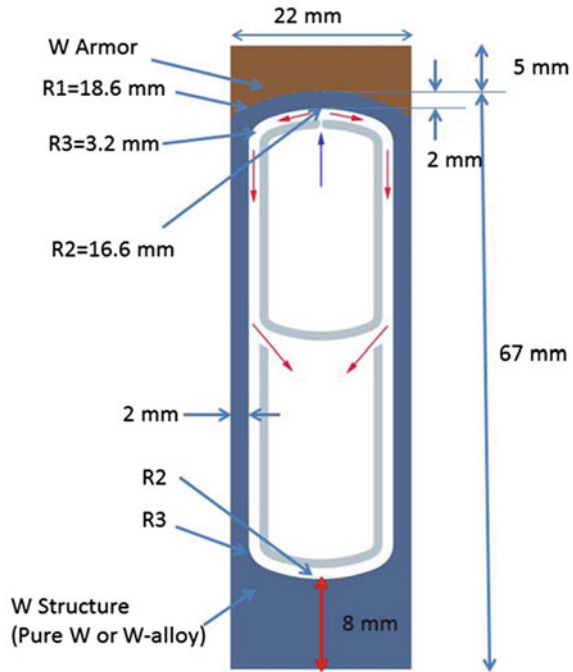
recrystallization limit ~1,300 °C. 3D thermal-fluid and 3D finite element stress analyses find that the $3S_m$ stress criterion of the ASME code would limit the plate-type design to heat fluxes of about 9 MW/m^2. It would have a pumping power of about 10 % of the divertor thermal power load. It could accommodate the ARIES-AT heat fluxes, which have a maximum heat flux of 11 MW/m^2 and average heat flux of 3.5 MW/m^2 (Wang 2012).

7.6.6 Open-Cell Foam in Tube

Figure 7.25 shows the SOFIT concept.

Helium enters along the axis, flows radially outward at high speed, then exits axially in the annulus between the inner and outer tubes. The open-cell metallic foam promotes turbulent mixing and increases the cooling area. The foam is selectively located in the region of high heat flux to minimize the pressure drop through the foam. Such a device has achieved a maximum heat flux of 22 MW/m^2 (Sharafat 2007).

The Reynolds numbers of the flow are high enough for turbulent mixing and high heat transfer coefficients. Tests in air can simulate helium flow well, because the Nusselt number depends only weakly on the Prandtl number.
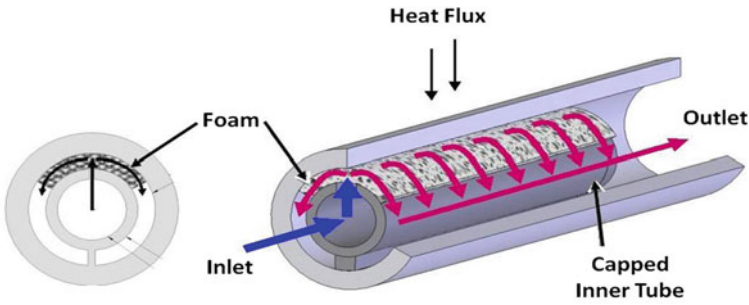
Fig. 7.25 The "Short-Flow-Path-Foam-in-Tube" (*SOFIT*) concept (Sharafat et al. 2007, Fig. 6)

7.6.7 T-Tube divertor

Figure 7.26 shows a T-Tube of the ARIES-CS divertor.

Helium flows up in the center of the ODS F/M support tube, axially along the tube, and radially up against the tungsten tube and castellated tungsten armor surface. Many T-tubes can be connected to a common inlet/outlet manifold. The 10 MPa helium temperature would rise from 575 to 700 °C as it cools the surface. At 10 MW/m^2 the peak stress and temperature are predicted to be about 370 MPa and below 1,300 °C, which are probably satisfactory. The outer tube thickness is only 1 mm, though, which does not leave much room for erosion or for design improvement. Many such T-Tubes can be joined together to form a divertor plate (Raffray 2008a).
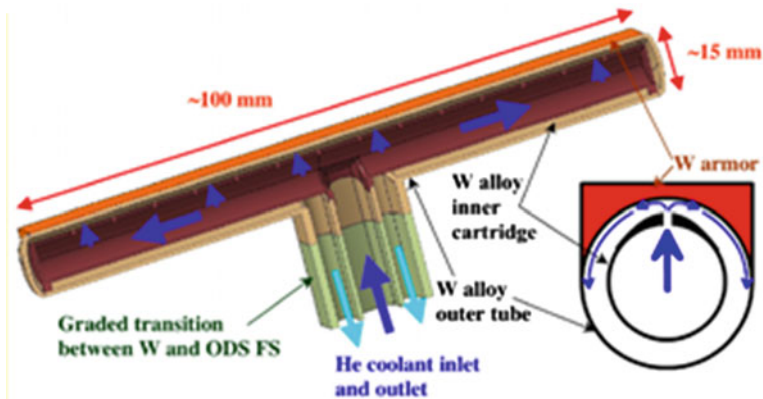
Fig. 7.26 A T-Tube divertor element (Raffray 2008b, Fig. 18). Copyright 2008 by the American Nuclear Society, LaGrange Park, Illinois
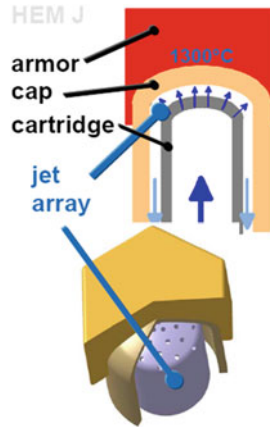
Fig. 7.27 Helium jets from a steel C tube hitting a tungsten alloy cap under the hexagonal tungsten armor tile to enhance convective heat transfer. Courtesy of P. Norajitra, Karlsruhe Institute of Technology

7.6.8 Finger Tube Divertors

Figure 7.27 shows a single finger tube of a divertor.

A computer model shows helium jet flow lines, Fig. 7.28.

The resulting temperature distributions are shown in Fig. 7.29.

The individual jet-cooled "fingers" may be grouped in 9-finger modules, Fig. 7.30.

This concept and others are being actively tested in high power flux facilities. The Efremov Institute electron beam facility in Russia tests specimens with a 27 keV electron beam at powers up to 67 kW and heat fluxes up to 12 MW/m^2. Figure 7.31 shows a 9-finger module being tested at 600 °C helium temperature.

A typical reactor divertor would need about

535,000 finger units, or
110,000 T tubes, or
750 plate type units.

This shows one advantage of plate type units. Large numbers of units might result in higher net failure rates. The plates might be used in 6–8 MW/m^2 areas, and the T-tubes in 10–12 MW/m^2 areas, and fingers used in >12 MW/m^2 areas (Raffray 2008a).

The DEMO divertor material should have thermal conductivity >100 W/m-K at 1,200 °C, creep strength >55 MPa, 20 kh at 1,200 °C, unirradiated ductile-to-brittle transition temperature <300 °C, and recrystallization temperature >1,300 °C for 20 kh. Much work will be required to develop a material with these qualities (Rieth 2008).
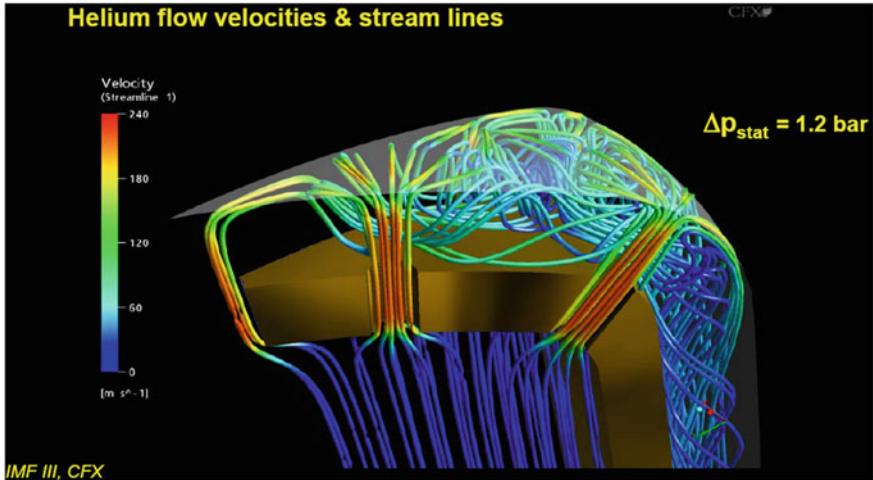
Fig. 7.28 Helium jet flow lines and their velocities, indicated by *colors*. Courtesy of P. Norajitra, Karlsruhe Institute of Technology

Fig. 7.29 Temperature distributions of armor resulting from simulation of helium jet cooling. Courtesy of P. Norajitra, Karlsruhe Institute of Technology
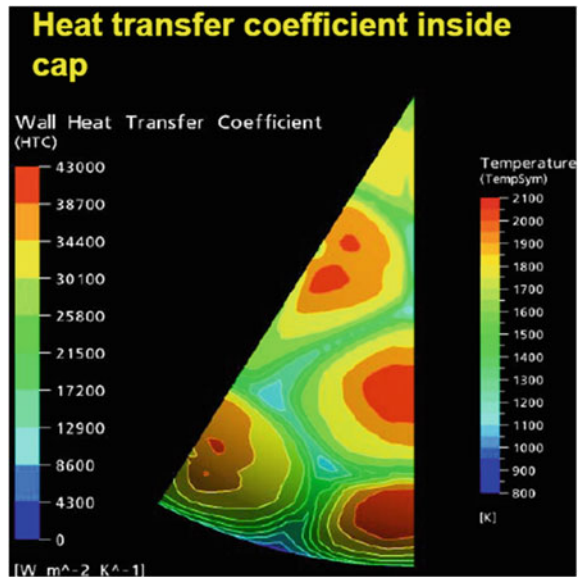
7.6.9 Stellarator Divertors

The torsatron magnetic field configuration provides a natural helical poloidal divertor, as shown in Fig. 7.32.
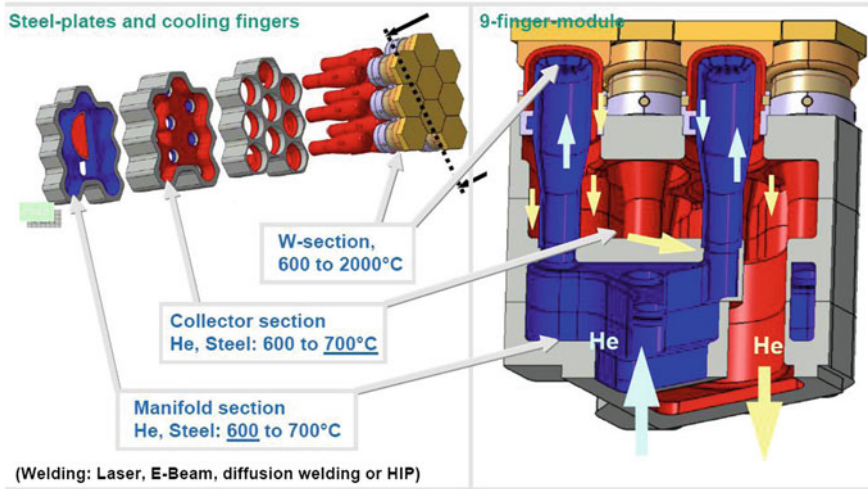
Fig. 7.30 A nine-finger module of jet-cooled hexagonal tiles. Courtesy of P. Norajitra, Karlsruhe Institute of Technology

Fig. 7.31 A 9-finger module under test at 600 °C helium temperature. Courtesy of P. Norajitra, Karlsruhe Institute of Technology
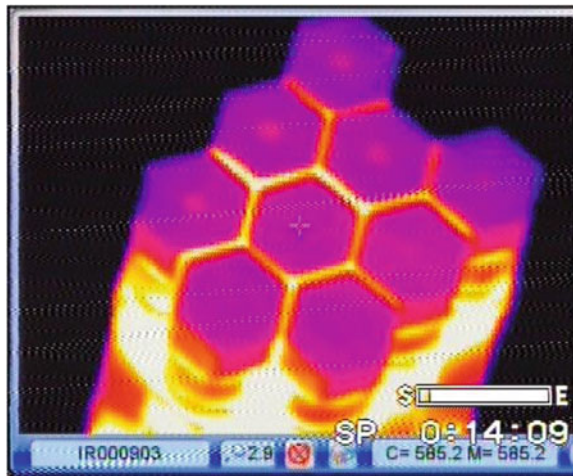
Sometimes *island divertors* may be used, in segments that do not extend toroidally all the way around the torus.

Figure 7.33 shows a cross section of the divertor in the W7-X modular stellarator, which is under construction in Greifswald, Germany.

The helical shape and non-uniform cross section make this divertor design very complex. The divertor target plates are designed to withstand up to 10 MW/m², and the baffles, 0.5 MW/m². The high heat flux areas will be covered with graphite

Fig. 7.32 Cross section of an
$\ell = 3$ torsatron. *c* magnet
coils, *b* blanket and shield,
p plasma, *dashed lines*
poloidal magnetic surfaces,
s separatrix, *d* divertor target
plates
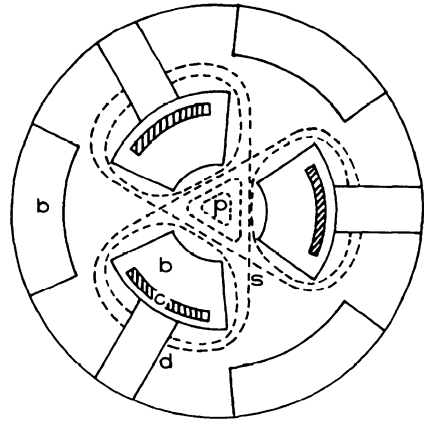
Fig. 7.33 The W7-X island
divertor, showing magnetic
flux surfaces and target
plates. *top* cross section;
bottom 3D drawing of
magnetic surfaces and baffle
plates (Lore et al. 2011)
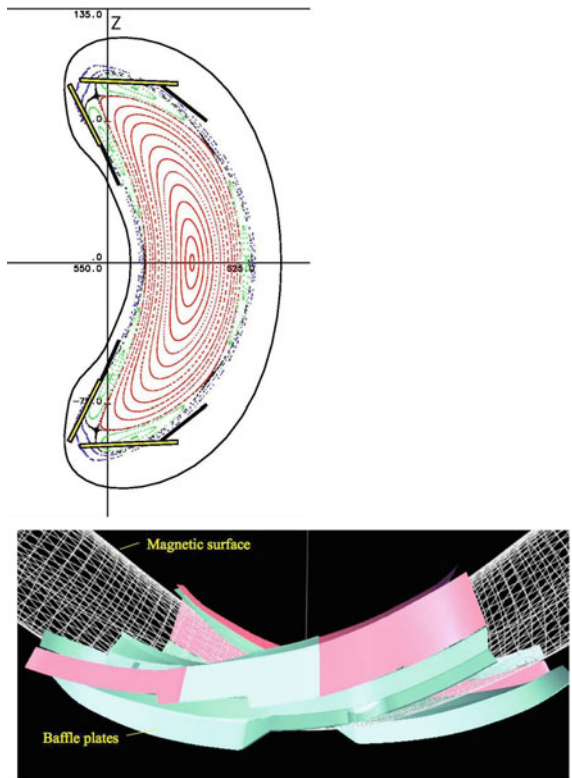
tiles clamped to water-cooled CuCrZr substrate. These have been designed using
3D analyses of temperatures and stresses, which have been checked with experi-
mental tests (Gruener 2003).

7.6.10 Super-X and Snowflake Divertors

Advanced divertor designs spread out the heat flux over a wide area. A Snowflake divertor generates a hexagonal separatrix, which widens the SOL and reduces the heat flux (Fig. 7.34).

Using slightly higher divertor coil currents can stabilize a potential topological instability, which could spoil the configuration. The SOL is much larger with the snowflake than with the standard X-point divertor, Fig. 7.35.

The flux expansion is 2–3 times greater in the snowflake configuration, reducing the heat flux at the targets. It increases the magnetic shear in the pedestal region, which can help suppress ELMs. The poloidal field coils could be placed outside the toroidal field coils. The snowflake can increase radiation cooling of the SOL plasma. The snowflake requires higher divertor coil currents, and the broader SOL may permit more impurity backflow into the main SOL bounding the plasma core (Ryutov 2007; Umansky et al. 2010).

A Super-X divertor extends the SOL radially outwards (Fig. 7.36).

The Super-X configuration results in a long connection length, lower SOL temperature near the divertor target, and higher power handling capability. It places the target (slanted plate in drawing) in a region of lower neutron radiation damage, and it could isolate liquid metals from the main chamber (Valanju 2010).

Fig. 7.34 A Snowflake divertor (Ryutov 2007)
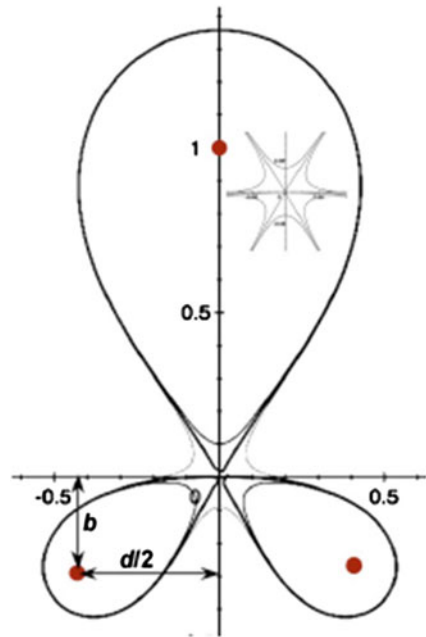
Fig. 7.35 Comparison of the SOL in a snowflake divertor (*lines 1, 2*) with the SOL in an X-point divertor (*lines 3, 4*) (Ryutov 2007)
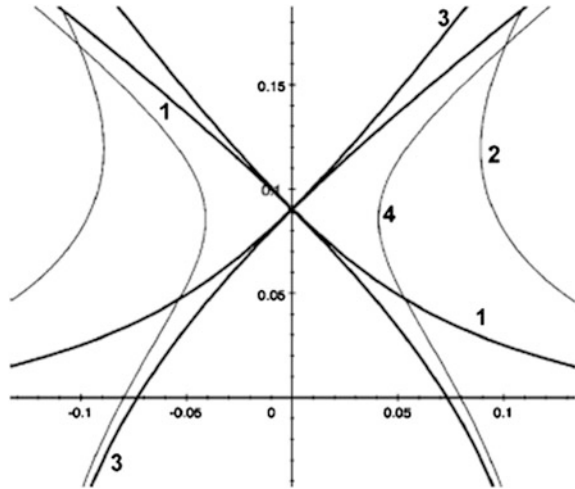
Fig. 7.36 A Super-X Divertor for a "SLIM-CS" reactor. The poloidal field is extended radially outwards to increase the wetted area and reduce the heat flux (Valanju et al. 2010, Fig. 1)
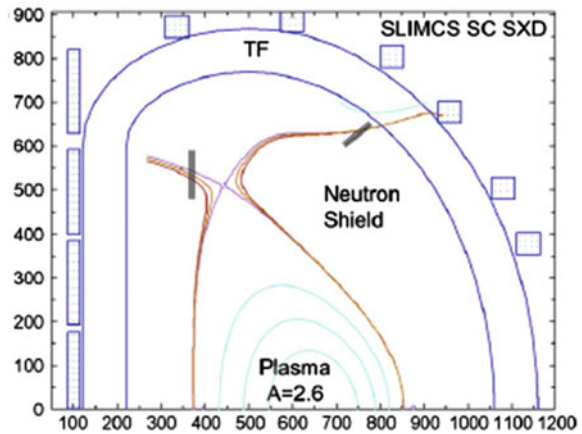
7.6.11 Divertor Conclusions

The ITER divertor is not relevant to DEMO, because it uses low-temperature materials and cold water. DEMO will need to accommodate 10 MW/m^2 using 10 MPa He at up to 700 °C and tungsten armor at 1,500–1,800 °C. Much new R&D and testing will be needed to meet these requirements reliably. The major observations from the International High Heat Flux Components (IHHFC) Workshop are (Raffray 2009):

- DEMO will require much higher temperatures than ITER (700 °C He, vs. 100 °C water) and will avoid graphite.
- A large R&D effort is underway for ITER, but DEMO is at an early stage.

- ITER is designed to accommodate off-normal conditions (disruptions, VDE, ELMs), but power plants must avoid VDEs and disruptions.
- ITER plasma facing components are almost ready, but power plant PFCs are not yet developed.

Many types of divertors are being studied in ITER member countries. It is desirable to use the same coolant for both the divertor and the blanket. A high coolant exit temperature is important to achieve high thermal efficiency. Helium appears to be the best divertor coolant, capable of handling 10 MW/m^2. The dominant design in Europe is the finger-type divertor (HEMJ), which has been successfully tested. The main uncertainty is performance during neutron irradiation (Norajitra 2008).

7.7 Other Impurity Control Concepts

7.7.1 Pumped Limiters

Figure 7.37 shows a pumped limiter. Plasma in the scrape-off layer (SOL) may be neutralized behind the limiter and pumped away by the vacuum pumps.

The STARFIRE tokamak reactor design employs two limiter-reflectors extending toroidally around the torus and occupying less than 5 % of the wall area. If a particle just missed a limiter, it would make half a revolution poloidally and q/2 revolutions toroidally before encountering the other limiter, where q is the safety factor. Thus, the distance travelled is

$$L = 2\pi R(q/2). \tag{7.31}$$

Fig. 7.37 A pumped limiter for impurity control in a tokamak. The "leading edge" is set back to a lower power flux ~ 4 MW/m^2 in this case. The vacuum duct would have several bends (not shown) to reduce neutron streaming
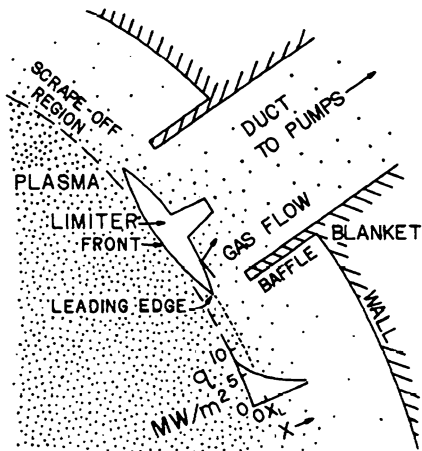
The STARFIRE design, for example, has R = 7 m, q = 3.6, and L = 80 m. The limiters define a scrape-off region similar to that defined by the separatrix of divertors. The plasma thickness in the scrape-off layer is estimated to be $\lambda = 7$ cm, assuming Bohm diffusion and free flight along the magnetic field.

The peak power incident on the limiters is

$$P_{lim} = (P_{ext} + P_\alpha) - (P_{rad} + P_{cx} + P_{ioniz}) \tag{7.32}$$

where P_{ext} is the external heating power, P_α is the fusion alpha power, P_{rad} is the power radiated from the plasma core and edge regions, P_{cx} is the power flowing to the walls by charge exchange, and P_{ioniz} is the power expended in ionizing neutrals and ions. To reduce P_{lim} to acceptable values, P_{rad} is increased by admitting controlled amounts of impurity gas (such as 0.1 % Xe) to the plasma. The peak heat flux flowing poloidally onto the limiters is estimated to be $q_o = 7$ MW/m^2.

However, this heat is at grazing incidence on the front of the limiter, affording larger areas and greatly reducing the heat flux encountered by the metal. The maximum heat flux encountered by the limiter is at the "leading edge," where q has dropped off to about 4 MW/m^2.

Let R_L, R_V, and R_w be the reflection coefficients of the limiter, vacuum duct, and wall for alpha particles. Alpha particles reflected from the limiter have a probability a_p of returning directly to the plasma, probability a_v of entering the vacuum duct, and probability a_w of hitting the walls ($a_p + a_v + a_w = 1$). Thus, the total reflection probability for alpha particles is

$$R_\alpha = R_L(a_p + a_w R_w + a_v R_v) \tag{7.33}$$

Initially, the reflection coefficients from clean surfaces might be low, but at steady state, the surfaces become saturated with gas, and helium atoms will leave the surface almost as fast as they arrive, due to thermal and stimulated desorption processes. Therefore, it is likely that $0.95 \leq R_L \leq 1$, and $0.95 \leq R_w \leq 1$. Since atoms are pumped away in the duct, its effective reflection coefficient may be lower. Possible values might be

$$a_p \sim 0.4, \ a_v \sim 0.4, \ a_w \sim 0.2, \ R_v \sim 0.5, \ R_L \sim R_w \sim 0.97.$$

For these values, the net alpha particle reflection probability is $R_\alpha \sim 0.77$, which would be marginally acceptable. (In Sect. 7.1 the estimated requirement was $R_\alpha < 0.82$). This means that about 23 % of the alpha particles leaving the plasma would be pumped away. An optimum design would maximize a_v and minimize R_α.

The problems of the limiter-reflector concept are the high limiter heat loads and impurity sputtering rates. Low-Z coatings (Be or Li) are envisioned to avoid high-Z contamination. Enhanced radiation could be used to cool the plasma radiatively, reducing the heat carried by particles to the limiter. A high toroidal field could be employed to sustain higher plasma pressures, so that acceptable fusion power densities might be attained, even in the presence of substantial impurity fractions (He, Be, and Xe). The magnetic field and coils are simpler than for a divertor system, permitting easier maintenance and lower cost. Limiters have been used on

many past tokamaks, but are unlikely to be the main power control method on very high power devices.

7.7.2 Neutral Gas Blankets

Neutral gas incident on a dense plasma will be ionized in a thin layer at the plasma edge. A plasma layer of thickness L and density n will be impermeable to neutral atoms from the walls if

$$nL \gg 3\text{-}10^{18} \text{ m}^{-2} \tag{7.34}$$

(Lehnert 1973). Admitting cold neutral gas around the outside of the plasma will form a cool, high-density plasma layer, called a gas blanket or cool plasma blanket. For example, if the layer thickness $L \sim 0.1$ m, then a neutral gas density $n_n > 3\text{-}10^{20}$ m^{-3} is needed to make the plasma layer impermeable. At a wall temperature of 500 K, this density would correspond to a gas pressure $P > 2$ Pa (16 mTorr). Figure 7.38 shows hypothetical profiles of the gas blanket concept.

Near the walls the high-resistivity cold plasma will conduct only a small current density J, so the pressure gradient

$$\nabla p = \vec{J} \times \vec{B} \tag{7.35}$$

is small, and the pressure profile is nearly flat. Multigroup transport codes and Monte Carlo codes have been developed to calculate neutral atom density profiles. The neutral gas density n_n drops off rapidly away from the walls, but reaches a low equilibrium value, limited by recombination, in the plasma core. Near the walls the neutral gas contributes significantly to the total pressure.

Fig. 7.38 Gas blanket concept. Hypothetical radial variations of plasma density, helium density, pressure, temperature, and neutral gas density, relative to the central values of plasma density, temperature, and pressure. The thickness of the edge impermeable layer is indicated by L
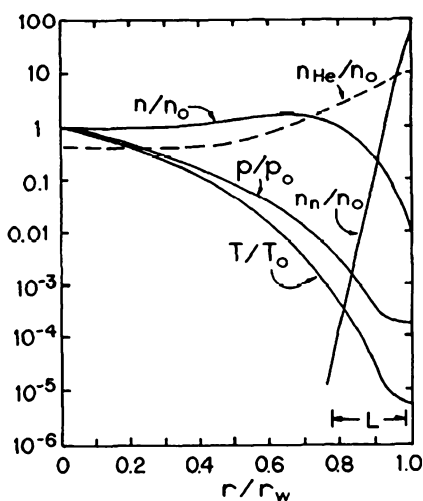
For a reactor, the parameters might be $T_o \sim 15$ keV, $n_0 \sim 2 \times 10^{20}$ m^{-3}, $p = 2n_0kT_o \sim 1$ MPa $= 10$ atm, plasma density peak $n_{max} \sim 3 \times 10^{21}$ m^{-3}, with values at the wall $T_w \sim 700$ K, neutral density $n_n \sim 10^{22}$ m^{-3}, neutral gas pressure $p_w \sim 100$ Pa. The temperature gradient force causes the helium ion density to increase with radius.

When the plasma is impermeable to neutral penetration, the driving forces for ballooning and flute instabilities inside the plasma are reduced. Impermeability, however, makes penetration of neutral atom beams for plasma heating difficult, so injected neutral atom beams would be trapped near the outside of the plasma, not at the center. The resulting density spike (not shown in Fig. 7.42) might cause instability. The impermeability condition also requires high plasma density and pressure, which might not be attainable in small low-beta systems. Magnetically stabilized arcs have operated with central densities around 3×10^{21} m^{-3} and temperatures around 10 eV, with the temperature dropping off to about 0.05 eV at the wall. The surrounding gas pressure was about 10 Pa. Such arc experiments are similar to the gas blanket scheme, although the central temperature is much lower than needed for in a reactor. The high plasma densities and low impurity levels attained in the Alcator tokamaks indicate that gas blanket effects may be active there. However, the concept has not been tested in a large device. Some advantages and problems of the neutral gas blanket concept are summarized in Table 7.4.

High density plasmas induced by intense microwaves and stabilized by high neutral gas pressure were studied by Kapitza. Cord-shaped plasma discharges with lengths ~ 0.1 m and radii $a \ll L$ were produced in high-pressure gases ($p \sim 25$ atm) by intense rf power ($\lambda \sim 0.2$ m, $P \sim 100$ kW). Hot electrons may have been confined by a thin (~ 1 mm) *double layer* containing a strong outward electric field. Electron temperatures up to 5 keV were observed in such cord discharges, but ion temperatures were much lower. If convective heat losses were not too large and effective ion heating could be developed, then this scheme might have had promise as a fusion reactor, but the experiments were terminated (Kapitza 1979).

Table 7.4 Advantages and problems of the neutral gas blanket concept

Advantages
Reduced sputtering and arcing
Reduced impurity penetration
Refueling by inward diffusion
Helium density minimum in plasma core
Absence of divertor simplifies chamber and coils
Problems
High pressures
Possible plasma instability
Incompatible with NBI
High equilibrium alpha particle density
Ion cooling by gas

7.7.3 Impurity Injection

Controlled amounts of low-Z impurity gases, like neon, may be added to the plasma to enhance line radiation cooling of the edge regions. Because the ions are fully stripped in the plasma core, the core radiation losses would not be increased as much as the edge losses. The increased radiation loss also helps to limit the equilibrium plasma temperature, if transport scaling does not provide a sufficiently low value.

7.7.4 Gas Flow

Each ion species has a flow pattern where the vertical gradient and curvature drift is followed by return flow along a magnetic field line. Species with different charges will have different flow velocities, and the collisional friction forces between species will alter their drift motion. Normally, the outward motion of hydrogen and inward motion of impurities would be enhanced by friction between them. If the relative velocity of hydrogen and impurities can be reversed, however, then the inward impurity flow and outward hydrogen flow may be reversed. One means of changing the relative velocity is to inject hydrogen gas azimuthally at one poloidal position and remove it with vacuum pumping at the diametrically opposite position. Such *impurity flow reversal* was demonstrated with the ISX-A tokamak.

7.7.5 Neutral Beam Injection

Neutral beam injection in the direction of the plasma current (co-injection) results in better confinement and heating than injection in the opposite direction (counter-injection). Impurity flow reversal can be induced by co-injection under certain circumstances (Stacey and Sigmar 1979). The required neutral beam currents are near those planned for large tokamaks.

7.8 Computer Control and Remote Operations

The Plasma Control System (PCS) at DIII-D provides software for viewing plasma data in real-time during plasma discharges, with calculations of frequency, amplitude, and mode numbers from the smoothed cross power spectrum of Mirnov probe data. It is also used by other fusion research experiments in Princeton, Wisconsin, UK, China, and Korea (Penaflor 2008, 2009).

DIII-D researchers have implemented a system to control the plasma current density profile, in order to establish a reversed magnetic shear configuration. They have demonstrated active feedback control of the evolution of q(0) and q_{min} during the initial phase of the through electron heating. The q profile is calculated in real time from a complete equilibrium reconstruction using data from the motional Stark effect (MSE) diagnostic and the CORSICA code to predict the current profile evolution. The controller solves a finite-time optimal control problem for a non-linear partial differential equation (PDE) system, and then it requests a power level to the ECH or NBI actuator to affect the desired change (Oh 2008).

TEXTOR uses LabVIEW Real-Time (RT) modules, divided into three parts: Host, target, and I/O periphery. The "Host" is a desktop machine running MS-Windows where the less time-critical tasks are handled, such as user interface and data display. The "target" delivers deterministic, real-time performance for control. The I/O peripherals transmit digital data over optical links to the target and from the target to the actuator, over a complete digital way from the sensor to the actuator. The system is used to calculate in RT the plasma density profile (10 μs), the Shafranov shift (10 μs), and the plasma vertical and horizontal positions (20 μs). The control system is also used to control coils that stabilize the plasma shape (Mitri et al. 2009).

The TEXTOR control system analyzes real-time data to determine where magnetic islands are forming. Then it directs a high-power electron cyclotron beam to heat that layer and suppress magnetic island growth, using fast sensors and actuators (Hennen et al. 2009).

A physics analysis shows that ITER must be robustly stabilized against vertical displacement when operating at full current (15 MA). The stabilization system will also use the in-vessel correction coils proposed for generation of resonance magnetic perturbations to control the vertical stability (Cavinato et al. 2008).

JET has implemented a control system using an open-source operating system, Linux. The Real Time Application Interface (RTAI) and i386 multicore processors enable the system to stabilize the JET plasma vertical position with a computation time of a few μs, which includes running functions from the standard C library (Neto et al. 2009).

In some cases researchers in one laboratory can take data on an experiment in another laboratory, or even control some of its operations. A series of conferences have been held on remote participation in fusion research experiments. For example, the International Atomic Energy Agency (IAEA) sponsored the 8th Technical Meeting on Control, Data Acquisition and Remote Participation for Fusion Research in San Francisco, CA, USA, June 24–28, 2011, and some papers from this meeting were published in Fusion Engineering and Design.

In addition to controlling the plasma position, shape, and MHD activity, fusion power plant control systems and operators must control:

- Diagnostics systems
- Divertor parameters

- Fueling systems
- Tritium processing systems
- Magnet coil operation and safety
- Vacuum systems
- Cryogenics systems
- Wall-blanket-shield heat removal systems
- Heat exchangers
- Steam turbines (or helium turbines)
- Electric power generators
- Remote handling systems
- Radioactivity
- Accident response
- Environmental monitoring and response systems.

7.9 Lithium Wall Concepts

7.9.1 Swirling Liquid Walls

Liquid metal or molten salt wall coatings could be injected from nozzles in magnetic confinement systems and extracted at the bottom. Centrifugal force and surface tension could help keep the liquid flowing along the wall. The flowing lithium could transport the heat deposited out to a heat exchanger, while protecting the solid walls from erosion by sputtering or overheating (Moir 1997, 2000). A molten salt layer would have less interaction with the magnetic field than liquid metal, but a liquid lithium surface would have the advantage of reducing hydrogen recycling at the wall.

7.9.2 Recycling Effects

The hydrogen recycling coefficient R_h is the ratio of hydrogen atoms (including all three isotopes) leaving the wall to hydrogen ions and atoms striking the wall. For example, if $R_h = 0.7$, then 30 % of the flux to the wall is absorbed and 70 % is promptly re-emitted.

Coating the divertor, limiter, or walls with lithium can absorb much of the hydrogen leaving the plasma, reducing the recycling coefficient and lowering the edge plasma density. The lower edge density cools the edge plasma less and allows higher edge temperature, Fig. 7.39.

Tokamaks usually have high recycling coefficients, causing steep temperature gradients and associated instabilities, such as the Electron Temperature Gradient Mode and Edge Localized Modes, which degrade plasma confinement and can
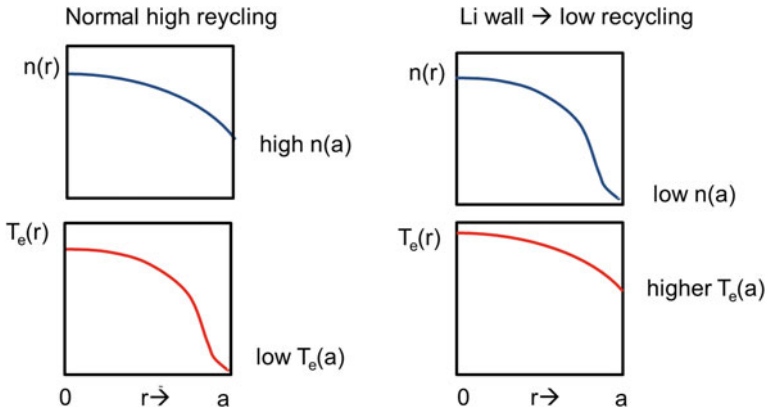
Fig. 7.39 Effect of recycling on density and temperature profiles. High recycling lowers edge temperature and requires more heating (These profiles are simplified for clarity. There will usually be other features, such as an edge pedestal)

damage the wall or divertor. The low recycling regime can reduce or eliminate such instabilities, increasing the energy confinement time τ_E. The broader temperature profile also increases the volume where the fusion power density is high, making more heat and electricity. For ITER parameters this could triple the fusion power (Zakharov 2004).

7.9.3 Fueling

In order to keep the edge density low the DT fuel must be injected into the main plasma (inside the separatrix) and not introduced by gas puffing. Molecular beam injection and cluster injection are not likely to penetrate well in large high-power reactors. Plasma guns are possible, but would be difficult to implement in large, high-field reactors. Neutral beam injection requires very high power, unless the burnup fraction is very high and low-energy beams can be used. The best fuelling method is probably injection of cryogenic DT pellets or of solid LiD/LiT pellets.

7.9.4 Confinement

The ratio of plasma edge density to average core density may be written approximately as

$$n_{edge}/\langle n \rangle \approx (1 + \Gamma_{gas}/\Gamma_{beam})(\delta/a)/(1 - R_r) \tag{7.36}$$

where Γ_{gas} = gas influx, Γ_{beam} = fuel influx by NBI or pellets inside the separatrix, δ = a characteristic width (such as a banana width) determining the ion outflow rate, a = plasma minor radius, and R_r = the larger of the electron and ion recycling coefficients. Thus, if R > 0.5 the edge density can be very high (Zakharov 2011a).

With lithium wall fusion the electron heat losses may be low enough that confinement is dominated by ion diffusion losses at the neoclassical diffusion rate D. One simple model assumes that the thermal diffusivities are

$$\chi_i = D, \quad \chi_e = fD \tag{7.37}$$

where $f \geq 1$. This model has been applied to a hypothetical ST1 tokamak experiment with the following parameters:

$R_o = 1.05$ m

a = 0.63 cm

B = 1.5 T

$\beta = 0.2$

I = 4 MA

Fueled by $1 - 3$ MW of 80 keV NBI

$Q = 5 - 8$(Higher Q might be obtained by pellet fueling).

The estimated energy confinement time at $R_r = 0.5$ varies from 3.5 s at f = 1 to 2.9 s at f = 1,000, so the dependence on electron thermal conductivity is weak (Zakharov 2011a).

7.9.5 Lithium Replenishment

A thin lithium wall coating could be applied by flow through a porous substrate (such as tungsten cloth), by evaporation of lithium in the chamber, by lithium use in limiters and divertors, by injection of lithium streams from nozzles onto the wall, by inserting lithium pellets or droplets into the plasma, or by injection of LiD/LiT pellets. LiD/LiT pellets might help coat the walls with lithium and reduce the cryogenic pellet fueling requirements, with the following potential advantages:

- Easier pellet manufacture and storage than cryogenic pellets
- Stronger pellets, easier acceleration, higher speeds, less pellet loss in guide tube, better penetration into plasma
- Lithium would deposit where sputtering is the worst, where it is needed the most (Dolan 2012).

Since the lithium will saturate with hydrogen absorption, it must be replenished at a rate sufficient to keep the recycling coefficient $R_h < 0.5$. The rate of hydrogen leaving the plasma is approximately

$$dN_i/dt \approx \langle n \rangle V / \tau_i \tag{7.38}$$

where τ_i is the ion confinement time, V = plasma volume. The lithium mass flow rate dM_{Li}/dt must exceed this number.

$$dM_{Li}/dt \geq m_{Li}(dN_i/dt) \tag{7.39}$$

where m_{Li} = lithium atom mass = 1.165×10^{-26} kg. For example, if $\langle n \rangle = 2 \times 10^{20}$ m^{-3}, $V = 300$ m^3, and $\tau_i = 1$ s, then $dN_i/dt = 6 \times 10^{22}$ atoms/s and $dM_{Li}/dt \geq 0.7$ g/s.

The lithium-coated plates should be actively cooled to keep the surface film temperature <400 °C, minimizing evaporation. The lithium-coated plates could sustain heat loads ~ 5 MW/m^2.

7.9.6 Experimental Results

In the Tokamak Fusion Test Reactor (TFTR) the use of lithium enhanced energy confinement times and fusion reaction rates (Mansfield et al. 1995).

The National Spherical Tokamak Experiment (NSTX) has operated successfully with lithium wall coatings, which suppressed ELMs and reduced the H-Mode power threshold. Although 1.3 kg of lithium was evaporated onto the walls, it did not accumulate in the plasma core, where its concentration, deduced from spectroscopic measurements, remained below 0.1 % in a broad range of experimental parameters, although carbon impurity levels were several percent (Podesta et al. 2012).

Lithium walls reduce the recycling and plasma pedestal density, raising the temperature profiles, Fig. 7.40.

With lithium coating the EAST tokamak (China) achieved an H-Mode discharge lasting 6.4 s (limited only by OH flux). In the T-10 and T-11M tokamaks (Russia) lithium use has reduced the radiated power and Z_{eff} from ~ 2 to about 1.2 The lithium-infused tungsten felt surface has withstood 1,000 shots at heat fluxes up to 10 MW/m^2 for 0.2 s. One limiter acts as source and the other as sink for the lithium (Ono et al. 2012).

The FTU tokamak (Italy) has stainless steel mesh and tungsten mesh limiters through which lithium flows to the surface. The heat flux is ~ 1.5 MW/m^2 when the limiter is 1.5 cm from the separatrix, resulting in T ~ 450 °C after a 1 s pulse. The heat flux reaches 5 MW/m^2 when the limiter is at the separatrix, and the temperature self-limits to ~ 600 °C by evaporation, with no damage to the mesh. Lithium use increases energy confinement time by 40 % and halves the electron thermal diffusivity (Ono et al. 2012).

Fig. 7.40 Profiles of density, temperatures, and pressure in NSTX without Li walls (*black triangles*) and with Li walls (*red squares*) (Canik 2011)
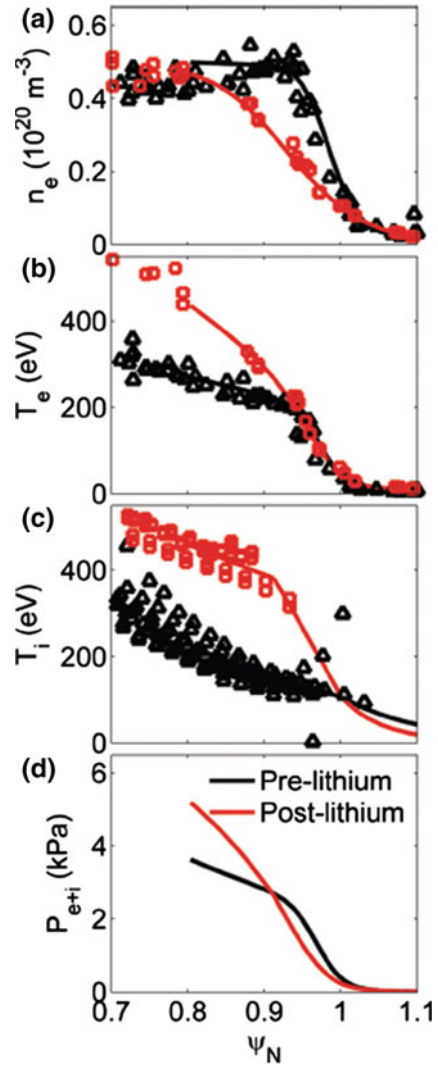
The TJ-II stellarator (Spain) lithium use (with boronization) has reduced hydrogen recycling to 10 % of previous values (Ono et al. 2012).

The International Fusion Materials Irradiation Facility (IFMIF) will generate neutrons by bombarding a 25 mm thick lithium target flowing at 15 m/s with a 125 MA, 40 MeV deuteron beam (Sect. 8.10). Thus, lithium is receiving a lot of attention for fusion applications.

The main technical issues associated with lithium use are:

- Divertor heat flux handling and removal
- Lithium flow in strong B fields

- D/T removal from lithium
- Deposition on reactor components (mirrors, antennas, …) and in situ cleanup
- Lithium corrosion of materials (wall, divertor, pipes, valves, pumps) and deposition of impurities
- Safety of flowing liquid lithium.

The biennial International Symposia on Lithium Applications for Fusion Devices (ISLA) are held in odd-numbered years (Ono et al. 2012).

7.9.7 Heat Transfer

Lithium flow is affected by gravity, by a pressure gradient ∇P, by the $J \times B$ force, by the thermoelectric force associated with a temperature gradient ∇T, and by viscous drag.

Figure 7.41 shows an experiment to study lithium flows on a surface under high heat load.

The vertical temperature gradient generates a radial thermoelectric current, and the $J \times B$ force causes azimuthal swirling flow. The measured particle flow velocities are consistent with theoretical estimates (Jaworski et al. 2010).

The thermoelectric magnetohydrodynamic flow (TEMHD) can be used to pump lithium in thin trenches along a fusion reactor plasma facing surface, such as a divertor. The divertor trenches could run in the poloidal direction, as illustrated in Fig. 7.42.

The vertical temperature gradient and transverse magnetic field drive rapid lithium flow along the trenches, which can transport very high heat fluxes. The tendency of the $J \times B$ force to eject lithium from the trenches is counteracted by the capillary force due to surface tension if the trench is not too wide. The experimental flow rate is consistent with theoretical predictions. The self-flowing lithium in stainless steel trenches can remove 3 MW/m^2, and higher fluxes should be available in molybdenum trenches with optimized widths (Ruzic et al. 2011).
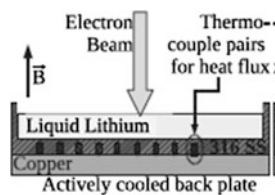
Fig. 7.41 The solid/liquid divertor experiment (*SLIDE*). An *electron beam* flows downward with a heat flux up to 0.7 MW/m^2 onto the lithium pool (depth 5–15 mm) in the presence of a vertical magnetic field (3–78 mT). Thermocouples measure the temperature distribution. Reprinted with permission from Jaworski et al. (2010), Fig. 1, copyright 2010 The American Institute of Physics

Fig. 7.42 Quasi-poloidal lithium trenches and quasi-toroidal heat flux strip. Trench widths ~ 2 mm in current experiments (Ruzic et al. 2011)
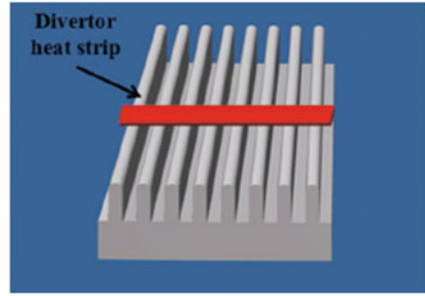
If the lithium wall confinement worked well, a proposed "Reactor Demonstration Facility" (RDF) could produce ~ 300 MW fusion power in a small plasma volume (~ 30 m^3) and be self-sufficient in tritium production (Zakharov 2011a).

7.10 Problems

These problems are for illustrative purposes only and do not represent accurate solutions of real technology problems, which are more complex.

7.1. A steady state reactor with aluminum walls has $n_z/n_i = 0.12$, edge temperature $= 60$ eV, and $R_z = 0.2$ for aluminum. Assume equal confinement times for all species. Estimate the equilibrium fraction of aluminum in the plasma, the reduction of fusion power density by the helium and aluminum, and whether ignition would be prevented by the aluminum.

7.2. Estimate f_α at t $= 30$ s for a reactor with $R_\alpha = 0.9$, $n_0 = 10^{20}$ m^{-3}, T $= 15$ keV $\tau_\alpha = 5$ s. Take the limit as $\theta \to \infty$ to find the equilibrium concentration f_∞, and evaluate f_∞ for the above case.

7.3. Estimate λ in the scrape-off layer when L $= 120$ m, n $= 10^{19}$ m^{-3}, $T_i = 2$ keV, $T_e = 1$ keV, B $= 5$ T, $x_w = 0.6$ m, and neutral hydrogen atom (not molecular) density $= 1.3 \times 10^{17}$ m^{-3}. The ionization rate by electrons at that temperature is $\langle \sigma v \rangle = 2.3 \times 10^{-14}$ m^3/s.

7.4. A divertor target region is to be kept at p $= 0.2$ Pa, and its walls are at 700 K. Two-thirds of the transported energy is carried by ions, and the average energy per ion is 60 eV. The divertor target area is 130 m^2, and 300 MW of heat flow into the divertor. Using methods of Chap. 9 estimate the required vacuum pumping speed and cryopanel area.

7.5. Assume that the electron density in the SOL is represented by

$$n(x) = n_o \exp(-x/\lambda)$$

where $x = 0$ at the separatrix and x_w at the wall. Then the impurities coming from the wall are attenuated according to

$$dn_z/dx = -n(x)\langle\sigma v\rangle_{tot}/u$$

where $\langle\sigma v\rangle_{tot}$ represents attenuation by ionization and charge exchange and u is the average velocity of the impurities away from the wall (u is negative). Show that the fraction of impurities penetrating to the separatrix is given by

$$\frac{n_z(0)}{n_{zw}} = \exp\{\lambda b_0[1 - \exp(-x_w/\lambda)]\}$$

where n_{zW} is the impurity concentration at the wall. Evaluate $n_z(0)/n_{zW}$ for the case of 5 eV Be atoms with $x_w = 0.15$ m, $\lambda = 0.07$ m, $n_0 = 5 \times 10^{18}$ m^{-3}, and $\langle\sigma v\rangle_{tot} = 10^{-13}$ m^3 s^{-1}.

7.6. Assume that the average energy per particle in the scrape-off layer of the limiter in Fig. 7.37 is constant, so that the particle flux is proportional to the energy flux. If x_L is the position of the leading edge of the limiter, show that the approximate fraction of particles hitting the limiter on the plasma side is $a_p = 1 - \exp(-x_L/\lambda)$. If $q_0 = 7$ MW/m^2 at the limiter boundary and $q = 4$ MW/m^2 at the leading edge, how large is a_p? How large is $(a_v + a_w)$? Assuming $a_v = a_w$, $R_L = R_w = 0.95$, and $R_v = 0.5$, estimate R_α for this case. If $\tau_\alpha = \tau_i$ and $f_b = 0.05$, estimate the equilibrium value of f_α.

7.7. Estimate the maximum value of Q attainable with fueling by 80 keV neutral beams with burnup fraction of 4 %.

7.8. If the pellet of Example Problem 7.3 had $u = 10^4$ m/s, how far could it penetrate? What is its radius?

7.11 Review Questions

1. What types of impurities have the most impact on Q?
2. How are impurities produced and how are they lost?
3. What is bad about helium in the plasma? What is good?
4. Explain the following equation and its parameters:

$$q_{div} = P_{SOL}f_{div}/2\pi R_t\lambda_q f_{amp}$$

5. Name four methods for reducing divertor target heat flux.
6. How can VDEs be avoided?
7. What are some causes of disruptions?
8. What happens during ELMs, and how can they be controlled?
9. Define "separatrix" and "SOL".
10. What are the functions of a divertor?

11. What are two advantages of a single-null divertor?
12. If parallel flow loss dominates in the SOL, what is the shape of n(x)?
13. Sketch and explain a plasma sheath.
14 How does "closure" of a divertor channel improve the plasma?
15. What material is used for the first wall in ITER, and why?
16. What are the advantages of a tungsten wall?
17. How are pellets accelerated for injection into ITER?
18. Explain the equation $P_f = f_b S_i V W_{DT}/2$.
19. What is the best fueling method?
20. Explain how a pumped limiter works.
21. What materials are used in the ITER divertor?
22. How can convective heat transfer be enhanced in divertor components?
23. What are the benefits of lithium walls?
24. What problems are associated with lithium walls?

References

Abdel-Khalik S et al (2008) Experimental validation of thermal performance of gas-cooled divertors. International high heat flux components workshop, La Jolla, CA, 10–12 Dec 2008

Asakura N et al (2010) Power exhaust simulation for the Slim CS divertor with the SONIC code. ARIES Town meeting on edge plasma physics and plasma material interactions in the fusion power plant regime, University of California, San Diego, May 2010

ASDEX Team (1989) The H Mode of ASDEX, Nuclear Fusion 29, 1959, Fig. 20

Canik JM, Maingi R, Kubota S, Ren Y, Bell RE, Callen JD, Guttenfelder W, Kugel HW, LeBlanc BP, Osborne TH, Soukhanovskii VA (2013) Edge transport and turbulence reduction with lithium coated plasma facing components in the National Spherical Torus Experiment. Phys Plasmas 18:056118, Fig. 2. Reprinted with permission from American Institute of Physics, Copyright 2011

Cavinato M et al (2008) ITER vertical stabilization system, Symposium on Fusion Technology 2008, P3.20

Dolan TJ (1982) Fusion research, Chap. 25. Pergamon Press, Elmsford, New York

Dolan TJ (2011) Influence of scrape-off layer on plasma confinement. Phys Plasmas 18:032509

Dolan TJ (2012) Lithium deuteride/lithium tritide pellet injection. Fusion Sci Technol 61:240–247

Federici G, Andrew P, Barabaschi P, Brooks J, Doerner R, Geier A, Herrmann A, Janeschitz G, Krieger K, Kukushkin AS, Loarte A, Neu R, Saibene G, Shimada M, Strohmayer G, Sugihara M (2003) Key ITER plasma edge and plasma–material interaction issues. J Nucl Mater 313–316:11–22

Greuner H, Boswirth B, Boscary J, Hofmann G, Mendelevitch B, Renner H, Rieck R (2003) Final design of W7-X divertor plasma facing components—tests and thermo-mechanical analysis of baffle prototypes. Fusion Eng Des 66–68:447–452

Hazeltine R, Hill D, Neilson H et al (2009) Research needs for magnetic fusion energy devices. In: Report of the research needs workshop (ReNeW), Office of Fusion Energy Sciences, US Department of Energy, Bethesda, Maryland, 9–12 June 2009

Hennen BA et al (2009) A closed-loop control system for stabilization of MHD events on TEXTOR. Fusion Eng Des 84:928–934

Ihli T (2008) Divertors. KIT Summer School on Fusion Technology, Karlsruhe, Germany, 1–12 Sept 2008

International Atomic Energy Agency (2011) 8th technical meeting on control, data acquisition and remote participation for fusion research, San Francisco, CA, USA, 20–24 June 2011

Jaworski M, Gray TK, Antonelli M, Kim JJ, Lau CY, Lee MB, Neumann MJ, Xu W, Ruzic DN (2010) Thermoelectric magnetohydrodynamic stirring of liquid metals. Phys Rev Lett 104:094503

Jensen RV, Post RE, Jassby DL (1978) Critical impurity concentrations for power multiplication in beam-heated toroidal fusion reactors. Nucl Sci Eng 65:282–289. Copyright by the American Nuclear Society, LaGrange Park, Illinois, USA, 1979

JET Team (Prepared by Monk RD) (1999) Recent results from divertor and scrape-off layer studies at JET. Nucl Fusion 39:1751

Kapitza PL (1979) Plasma and the controlled thermonuclear reaction. Science 205:959–964

Kotschenreuther M, Mahajan S, Valanju SP, Covelle B (2010) Divertor issues and magnetic geometry on FNSF. FNST/PFC/MASCO meeting, 2–6 Aug 2010. http://www.fusion.ucla.edu/FNST/

Krasheninnikov SI, Zakharov LE, Pereverzev GV (2003) On lithium walls and the performance of magnetic fusion devices. Phys Plasmas 10:1678–1682

Loarte A, Lipschultz B, Kukushkin AS et al (2007) Chapter 4: Power and particle control. Nucl Fusion 47:S2003–S263, Fig. 18a

Lehnert B (1973) Stability of plasmas penetrated by neutral gas, Nucl Fusion 13:781–791

Lore JD, Canik JM, Harris JH, Tipton J, Lumsdaine A (2011) Physics design calculations for the W7-X divertor scraper element, Oak Ridge National Laboratory, Presentation, U.S. Department of Energy, 17 Aug 2011

Mansfield DK, Strachan JD, Bell MG, Scott SD, Budny R et al (1995) Enhanced performance of deuterium-tritium-fueled supershots using extensive lithium conditioning in the Tokamak Fusion Test Reactor. Phys Plasmas 2:4252

Maruyama S (2010) ITER fueling system, Karlsruhe Summer School on Fusion Technology, 13 Sept 2010

Milora SL, Foster CA (1978) IEEE Trans Plasma Sci PS-6:578–582

Milora SL, Houlberg WA, Lengyel LL, Mertens V (1995) Review paper—pellet fueling. Nucl Fusion 35:657–754

Mitri M, Nicolai D, Neubauer O, Lambertz HT, Schmidt I, Khilchenko A, Schweer B, Maier U, Samm U (2009) Optimized plasma stabilization at TEXTOR with an advanced, real-time digital control scheme. Fusion Eng Des 84:1329–1332

Moir RW (1997) Liquid first walls for magnetic fusion energy configurations, Lawrence Livermore Laboratory, Livermore, CA, UCRL-JC-125098. Nucl Fusion 37:557–566

Moir RW (2000) Liquid walls for fusion reaction chambers. Comments Plasma Phy Control Fusion, Comments Mod Phys 2:99–111

Neto A, Sartori F, Piccolo F, Barbalace A, Vitelli R, Fernandes H (2009) Linux real-time framework for fusion devices. Fusion Eng Des 84:1408–1411 JET-EFDA

Norajitra P (2008) EU divertor concepts for fusion power plants, KIT Summer School on Fusion Technology, Karlsruhe, Germany, 1–12 Sept 2008

Oh YS et al (2008) Corsica-based optimal current profile control in DIII-D. In: Proceedings of the Symposium on Fusion Technology (SOFT), P3.27

Ono M, Bell MG, Hirooka Y, Kaita R, Kugel HW, Mazzitelli G, Menard JE, Mirnov SV, Shimada M, Skinner CH, Tabares FL (2012) Conference report on the 2nd international symposium on lithium applications for fusion devices. Nucl Fusion 52:037001, 7 pp

Pégourié B (2007) Review: pellet injection experiments and modeling. Plasma Phys Control Fusion 49:R87

Penaflor BG, Ferron JR, Walker ML, Humphreys DA, Leuer JA, Piglowski DA, Johnson RD, Xiao BJ, Hahn SH, Gates DA (2008) Worldwide collaborative efforts in plasma control software development. Fusion Eng Des 83:176–180

Penaflor BG, Ferron JR, Walker ML, Humphreys DL, Leuer JA, Piglowski DA, Johnson RD, Xiao BJ, Hahn SH, Gates DA (2009) Extending the capabilities of the DIII-D Plasma Control System for worldwide fusion research collaborations. Fusion Eng Des 84:1484–1487

Pitts RA (2010) Key physics and materials aspects of plasma-wall interactions in ITER. ITER-IAEA technical meeting: ITER materials and technologies, Monaco, 25 November

Podesta M, Bell RE, Diallo A, LeBlanc BP, Scotti F, NSTX Team (2012) Measurements of core lithium concentration in a Li-conditioned tokamak with carbon walls. Nucl Fusion 52:033008, 7 pp

Raffray AR, El-Guebaly L, Malang S, Sviatoslavsky I, Tillack MS, Wang X, ARIES Team (2007) Advanced power core system for the ARIES-AT power plant. Fusion Eng Des 82:217–236, Fig. 19

Raffray AR, Abdel-Khalik S, Ihli T, Malang S, Wang X (2008a) Example of US PFC/Divertor concepts for power plants. International high heat flux components workshop on readiness to proceed from near term fusion systems to power plants, University of California San Diego, La Jolla, CA, 10–12 Dec 2008

Raffray AR, El-Guebaly L, Malang S, Wang XR, Bromberg L, Ihli T, Merrill B, Waganer L, ARIES-CS Team (2008b) Engineering design and analysis of the ARIES-CS power plant. Fusion Sci Technol 54(3):725–746, Fig. 18

Raffray AR (2009) Fusion energy sciences advisory committee meeting, Gaithersburg, Maryland, USA, 13 Jan 2009

Raman R (2006) Advanced fueling system for use as a burn control tool in a burning plasma device. Fusion Sci Technol 50:84

Raman R (2008) Advanced fueling system for ITER. Fusion Eng Des 83:1368–1374

Rieth M, Hoffmann A (2008) Tungsten as structural material for power plant high heat flux components. In: International high heat flux components workshop, La Jolla, CA, 10–12 Dec 2008

Rognlien TD (2008) Empirical and modeling scalings of SOL/divertor profiles. In: International high heat-flux component workshop, UCSD, San Diego, CA, 10–12 Dec 2008

Ruzic DN, Xu W, Andruczyk D, Jaworski MA (2011) Lithium-metal infused trenches (LiMIT) for heat removal in fusion devices. Nucl Fusion 51:102002, 4 pp

Ryutov DD (2007) Geometrical properties of a 'snowflake' divertor. Phys Plasmas 14:064502

Ryutov DD (2010) Snowflake divertors for power plants. In: ARIES Workshop, San Diego, CA, 20–21 May 2010

Sharafat S, Mills S, Youchison D, Nygren R, Williams B, Ghoniem B (2007) Ultra Low Pressure-Drop Helium-Cooled Porous-Tungsten PFC. Fusion Sci Technol 52(3):559–565, Fig. 6. Copyright by the American Nuclear Society, LaGrange Park, Illinois, USA, 1979

Snipes JA, Campbell DJ, Haynes PS, Hender TC, Hugon M, Lomas PJ, Lopes Cardozo NJ, Nave MFF, Schuller FC (1988) Large amplitude quasi-stationary MHD modes in jet. Nucl Fusion 28:1085, Fig. 2, p 1087

Tillack MS, Raffray AR, Wang XR, Malang S, Abdel-Khalik S, Yoda M, Youchison D (2011) Recent US activities on advanced He-cooled W-alloy divertor concepts for fusion power plants. Fusion Eng Des 86:71–98, Fig. 1

Umansky MV, Rognlien TD, Ryutov DD, Snyder PB (2010) Edge plasma in snowflake divertor. Contrib Plasma Phys 50:350

Valanju PM, Kotschenreuther M, Mahajan SM (2010) Super X divertors for solving heat and neutron flux problems of fusion devices. Fusion Eng Des 85:46–52

Suttrop W et al (2008) In-vessel saddle coils for MHD control in ASDEX Upgrade, SOFT, O5.2

Wang XR, Malang S, Raffray AR, Team ARIES (2009) Design optimization of high-performance helium-cooled divertor plate concept. Fusion Sci Technol 56:1023

Wang XR, Malang S, Tillack MS, Team Aries (2011) High performance divertor target plate for a power plant: a combination of plate and finger concepts. Fusion Sci Technol 60:218

Wang XR, Malang S, Tillack MS, Burke J, ARIES Team (2012) Recent improvements of the helium-cooled W-based divertor for fusion power plants. Fusion Eng Des 87:732–736, Fig. 1

Wesson J (2011) Tokamaks, 4th edn. Oxford University Press, Clarendon

Yu DL, Chen CY, Yao LH, Feng BB, Han XY (2010) Penetration characteristics of supersonic molecular beam injection on HL-2A tokamak. Nucl Fusion 50:035009, 9 pp, Fig. 1

Zakharov LE, Gorelenkov NN, White RB, Krasheninnikov SI, Pereverzev GV (2004) Ignited spherical tokamaks and plasma regimes with Li walls. Fusion Eng Des 72:149–168

Zakharov LE, Li J, Wu Y (2010) Fusion-fission research facility (FFRF) as a practical step toward hybrids. In: Proceedings of the 18th conference on nuclear engineering ICONE18-30269, 17–21 May 2010, Xi'an, China, © American Society of Mechanical Engineers

Zakharov LE (2011a) Li wall fusion—the new concept of magnetic fusion. Problems of Atomic Science and Technology, Series Thermonuclear Fusion, Vol 1, pp 29–38

Zakharov LE (2011b) Basics of fusion-fission research facility (FFRF) as a fusion neutron source. Princeton Plasma Physics Laboratory Report 4629

Zakharov LE, Li J, Wu Y (2011c) Fusion–fission research facility (FFRF) as a practical step toward hybrids. Problems of Atomic Science and Technology, Series Thermonuclear Fusion, vol 3, pp 27–37

Chapter 8
Materials Issues

Thomas J. Dolan

Objectives

After reading this chapter one should understand the fundamentals of

Radiation damage mechanisms and effects
Structural life predictions and testing
Mechanical behavior of materials
Hydrogen recycling
Wall erosion mechanisms and composition changes
Special materials used for fusion experiments
Dust generation
Planned irradiation facilities.

8.1 Introduction

Materials issues limit the achievements of almost all modern technologies, and they are crucial for fusion reactors, which operate in temperature ranges from 10^8 K down to 4 K. This chapter will describe the many materials issues that must be accommodated simultaneously, beginning with radiation damage. The International Atomic Energy Agency provides a series of books with useful materials data for fusion research (IAEA 2012). Baluc (2007) discusses materials issues for fusion reactors, and Was (2007) explains radiation damage.

T. J. Dolan (✉)
NPRE Department, University of Illinois, Urbana, IL 61801, USA
e-mail: dolantj@illinois.edu

8.1.1 Damage Production

At a neutron wall loading of 1 MW/m^2, the 14.1 MeV neutron current is $4.43 \times 10^{17} \text{ m}^{-2} \text{ s}^{-1}$, and the total neutron flux (including neutrons of all energies going both directions) is typically about $3.6 \times 10^{18} \text{ m}^{-2} \text{ s}^{-1}$. The neutron wall loading and flux may vary by more than a factor of two with poloidal angle in a tokamak.

Neutrons can penetrate deeply into materials and interact by three mechanisms:

- Elastic scattering (n, n)—some kinetic energy lost to lattice atom
- Inelastic scattering—energy lost by both collision and nuclear excitation
- Neutron capture—various possible reaction products, such as

  - (n, γ)
  - (n, 2n)
  - (n, p)
  - (n, α).

The (n, α) and (n, p) reactions produce He and H gas atoms within the material, which can alter its properties. Thus, the atomic parts per million (appm) of He and H produced are measures of radiation damage via transmutations. Another measure of radiation damage is the displacements of lattice atoms caused by scattering of a fast neutron N, Fig. 8.1.

The primary knock-on atoms (PKA) displace secondary knock-on atoms S, and so on. The knock-on atoms become interstitials I and leave vacancies V behind where they had been. The first stage of damage begins when a primary knock-on atom is produced. This stage ends when the primary and other knock-on atoms have all slowed to energies below the displacement threshold energy (20–60 eV), so that no more knock-on atoms can be produced by the cascade from that neutron. Fast neutrons produce more PKAs, higher energy PKAs and more secondary lattice damage than slow neutrons.

Fig. 8.1 Production of primary (*P*) and secondary (*S*) knock-on atoms by an incident fast neutron *N*, resulting in interstitials (*I*) and vacancies (*V*)
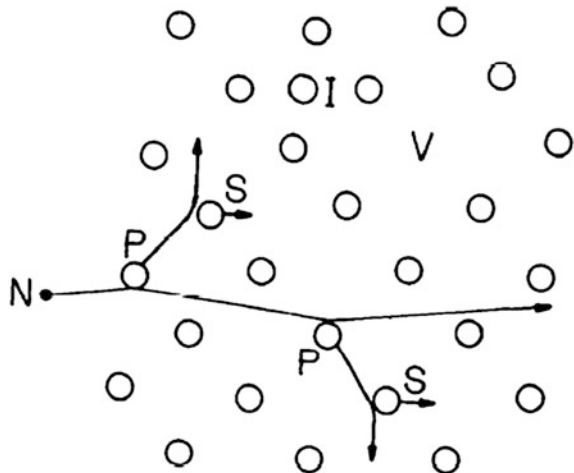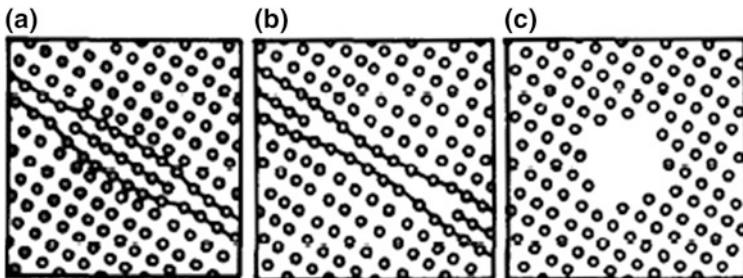
Fig. 8.2 The major types of defect: **a** interstitial loop, **b** vacancy loop, **c** cavity

In the second phase, the motions are transformed into heat, and individual defects (vacancies and interstitials) are clearly defined. During the third stage, short-term annealing occurs: defect migration results in defects clustering together, annihilating each other (interstitial plus vacancy) or escaping from the region of interest. The configuration at the end of the third stage is called the primary damage state. Three types of defect clusters are illustrated in Fig. 8.2.

Cavities may be either empty voids, which shrink during annealing, or gas-filled bubbles, which swell during annealing.

The *molecular dynamics* method describes displacement cascades theoretically by integrating the equations of motion of the atoms in a small region after an atom has been displaced. This method, most useful for low energies of the primary knock-on atoms (<1 keV), can describe focusing and channeling of energy along various crystal planes. The *binary collision approximation* method describes the trajectory of a knock-on atom as a series of isolated binary collisions in a discrete lattice. It can describe cascade development, sputtering, and backscattering, but it loses accuracy at low energies. Continuum methods based on transport theory can also be applied to radiation damage studies.

The energy acquired by a lattice atom as a result of a projectile impact (Fig. 8.3) is found from conservation of energy and momentum to be

$$T = 4E \sin^2(\theta/2) \, M_1 M_2 / (M_1 + M_2)^2 = T_{max} \sin^2(\theta/2) \tag{8.1}$$

Then the primary knock-on atom (PKA) displaces other atoms from their lattice sites and excites electrons, generating heat. This is called secondary damage. The number of displaced atoms is approximately

$$N = kT_{dam}/2E_d \tag{8.2}$$

Fig. 8.3 Energy T imparted to lattice atom by projectile impact (Rieth 2008)
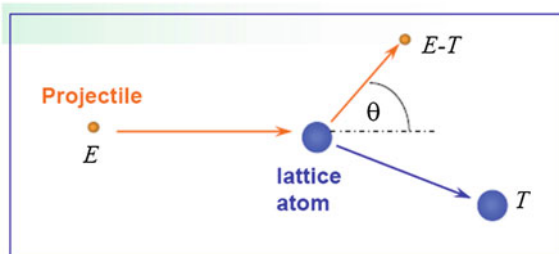
where $T_{dam} = T - T_{el}$, T_{el} = energy given to electrons, E_d = displacement energy (≈ 40 eV in steel), and $k \approx 0.8$ is a constant. For example, if $T_{dam} = 10$ keV in steel, then $N \approx 100$ displacements could be expected. Figure 8.4 shows a simulation of a displacement damage cascade.

Most interstitials recombine quickly with vacancies to restore the lattice in picoseconds, and few defects survive. Movies of radiation damage simulation can probably be seen at the Oak Ridge National Laboratory website (ORNL 2012).

Table 8.1 shows some types of irradiation experiments and the average energies of PKAs.

The primary knock-on atom (PKA) energy spectra of a monoenergetic 14 MeV neutron source, a fusion reactor first wall, and a fission reactor are compared in Fig. 8.5.

The PKA spectra of fusion neutrons have higher energies, so they produce more displacements per incident neutron. The cross sections of (n, α) and (n, p) reactions grow rapidly at neutron energies of a few MeV, where there are few fission neutrons. So, the gas generation rates produced by fusion neutrons are also much higher, in general, than those produced by fission neutrons. An exception is in alloys containing nickel, where the reactions can occur at thermal neutron energies.

$$^{58}\text{Ni} + \text{n} \rightarrow {}^{59}\text{Ni} + \gamma \quad (\sigma = 4.6\text{b})$$
$$^{59}\text{Ni} + \text{n} \rightarrow {}^{56}\text{Fe} + \alpha \quad (\sigma = 12.5\text{b})$$
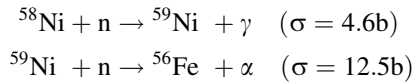
If there are 1,000 atomic displacements in a region containing a million atoms, then there are 10^{-3} displacements per atom (dpa). Using the neutron spectrum estimated for a typical fusion reactor, the number of dpa produced per year have been calculated for a variety of materials.

Vanadium, stainless steels, Mo, and Nb have effective displacement threshold energies of 40–60 eV and displacement damage rates of 7–12 dpa/year at 1 MW/m^2 neutron wall load. Stainless steels produce ~ 200 appm(He)/year and ~ 530 appm(H)/year, while V and Mo produce ~ 7–12 appm(He)/year and ~ 100 appm(H)/year.

Under these conditions each wall atom would be displaced many times a year. The type of damage occurring depends partly on the ratio of appm(He) to dpa, which is much higher for fusion reactors (~ 3–20) than for fission power reactors (~ 0.03–0.1).

Solid transmutation products are also produced by incident fast neutrons, as indicated for a few cases in Table 8.2.

8.1.2 Damage Microstructure Evolution

During bombardment self-interstitials and vacancies are produced in equal numbers. Later, as the interstitials and vacancies gradually diffuse through the lattice, the interstitials are preferentially attracted to and trapped in dislocations, leaving

Fig. 8.4 Cross sectional views of atom locations at various instants of time during the evolution of 10 keV cascades in Ni. The empty space represents where the melt used to be, while the squares represent the location of the vacancies (Averback and Ghaly 1997, Fig. 2)
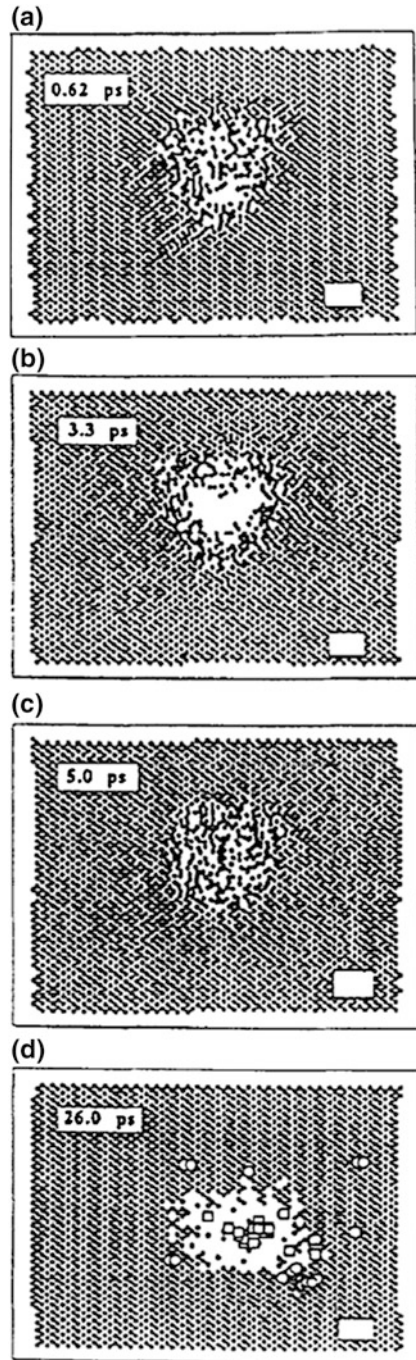
Table 8.1 Typical PKA energies from various types of irradiation (Rieth 2008)
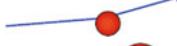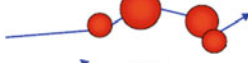
Particle type ($E_{kin} = 1$ MeV)	Typical recoil (or PKA) feature	Typical recoil (PKA) energy T (eV)	Dominant defect type
Electron		25	Frenkel pairs (Vacancy and Insterstitial)
Proton		500	
Fe-ion		24,000	Cascades and sub-cascades
Neutron		45,000	

Fig. 8.5 PKA spectra for various neutron spectra incident on copper (Kulcinski 1976)
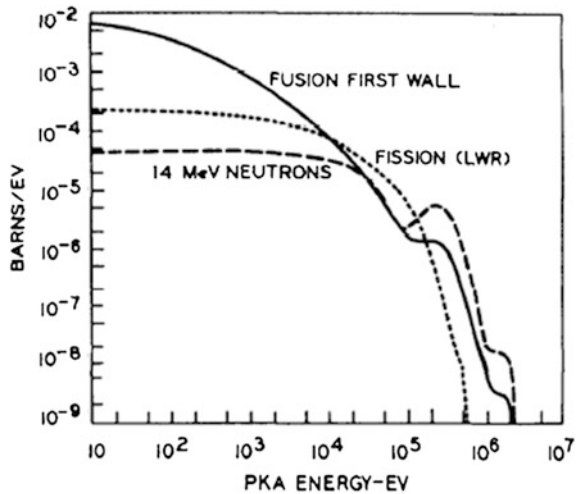
Table 8.2 Solid transmutation rates in fusion reactor materials for a neutron wall loading of 1 MW/m^2 (Kulcinski 1976)

Original metal	Transmutation product	Transmutation rate, appm/year
Al	Mg	400
	Si	40
SS 316	Mn	1,200
	V	200
	Ti	50
V	Cr	130
	Ti	80
Nb	Zr	700
Mo	Tc	400
	Ru	30

an excess of free vacancies. The vacancies gradually form voids, and the net lattice distortion results in macroscopic swelling. At the same time, helium gas may accumulate in the cavities, increasing the amount of swelling. Helium bubbles sometimes accumulate at grain boundaries, leading to intergranular fracture at low strain (helium embrittlement).

As vacancies and self-interstitials recombine, lattice damage anneals out, especially at high temperatures. Additionally, more damage may be produced by incident neutrons. Thus, the lattice condition may depend on the *damage rate*, and not just on the total number of dpa produced. Significant annealing may occur between reactor pulses. The combination of both lattice damage (dpa) and gas production (appm of He) can produce swelling greater than expected for either phenomenon alone. Such synergistic effects, in which two or more processes combine nonlinearly, have been observed in other materials phenomena as well. Because synergistic effects involve several simultaneous phenomena with many parameters, they are difficult to model and predict. Small changes in composition can make large changes in resistance to swelling and embrittlement, so there is hope that optimized alloys with favorable properties can be developed.

Past research involved producing many "heats" of alloys with various compositions and then testing them to determine their ductility, fracture toughness, etc. This is time-consuming and expensive. Nowadays materials researchers can use *computational thermodynamics* to do preliminary evaluations of phase stability for hundreds of thousands of possible steel compositions and solutes. Then they can focus on the best combinations and eliminate the rest. In this way the allowable stress and operating temperatures have been greatly improved (Zinkle 2011).

The key radiation damage failure modes are:

Temperature limitations

- Radiation hardening and embrittlement at $T \sim 0.4 \, T_m$ (melting temperature) and 0.001–0.1 dpa
- Helium embrittlement of grain boundaries at $>0.5 \, T_m$ and > 10 appm(He) (roughly >1 dpa).

Lifetime limitations

- Potential matrix or grain boundary embrittlement at 0.3–0.6 T_m and 1–10 dpa
- Irradiation creep at $< 0.45 \, T_m$ and > 10 dpa
- Swelling due to void formation at 0.3–0.6 T_m and > 10 dpa.

The materials development challenges are to expand the allowable temperature window and to prolong the component lifetimes (Zinkle 2011).

8.2 Analysis

8.2.1 Structural Life Predictions

Some material properties to be considered in the design of a fusion reactor first wall (nearest the plasma) are listed in Table 8.3.

The mechanical failure modes are (Zinkle 2011):

- Monotonic stress-induced failure

  - Plastic collapse
  - Plastic instability
  - Brittle fracture
  - Thermal creep

- Cyclic stress induced failure

  - Ratcheting
  - Fatigue
  - Fatigue-creep

- Irradiation-accelerated failure

  - Plastic instability
  - Hardening and embrittlement

Table 8.3 Desired properties of first wall

Physical	Mechanical
Low mass density	High yield strength and ultimate strength
Low vapor pressure	Good ductility
Electrical	Resistant to crack growth
Resistance to unipolar arcing	High creep rupture strength
Low conductivity (Ohmic-heated Tokamaks)	Good thermal stress parameter
Non-magnetic (not necessary)	*Radiation environment*
Chemical	Resistant to sputtering and blistering
Compatible with blanket and coolant	Resistant to swelling
Low affinity for O, C, H, N	Resistant to embrittlement
Permeable to tritium	Many data available
Neutronic	*Fabrication*
Low neutron cross sections, except (n, 2n)	Easy to form, machine, and weld
Low transmutation rates	Welds durable under operating conditions
Short half-lives of transmutation products	*Supply*
Thermal	Abundant domestic supply
High thermal conductivity	Established industrial production
High melting point	Cost not prohibitive
Low vapor pressure	
Low thermal expansion	
High heat capacity	

Table 8.4 Sources of stress and failure mechanisms

Sources of stress	Gravity
	Atmospheric pressure
	Coolant pressure
	Magnetic forces
	Thermal gradients
	Swelling
Failure mechanisms	Embrittlement → brittle fracture
	Fatigue failure
	Thermal creep
	Irradiation creep
	Swelling
	Creep-fatigue interaction
	Corrosion
	Erosion
	Overheating (such as from loss of coolant)

- Irradiation-accelerated creep
- Dimensional instabilities due to creep and swelling.

Corrosion can also exacerbate these problems, limit operating temperatures, and shorten component lifetimes. Welds need special attention to guard against failure, because they may become brittle, corroded, fatigued, etc. before the bulk material.

Failure of a structural component could be collapse, buckling, or fracture; or it could be simply a leak of coolant, tritium, or atmospheric pressure. Failure can be caused by stresses, radiation damage, surface bombardment, chemical reactions, and various combinations. Some sources of stress and failure mechanisms are listed in Table 8.4.

Stresses due to atmospheric pressure, magnetic forces, and coolant pressure are discussed elsewhere.

8.2.2 Thermal Stress

Thermal stress is also discussed in Sect. 6.8.

If a metal rod is constrained at the ends (so that it cannot expand) and then heated up, a compressive thermal stress will be produced in the rod. The stress will be the same as if the rod were allowed to expand freely during heating, then compressed back to its original length. Similarly, since an objects tends to expand different amounts in neighboring regions, thermal stresses can be created in other shapes, materials, and any containing a temperature gradient. For a long tube with inner radius r, thickness Δr, and a temperature difference ΔT between the inner and outer walls, thermal stresses will be generated within the tube. If the tube is

restrained at the ends, the azimuthal and axial stress components at the inner and outer radii are given by

$$\sigma_\theta(r) = \sigma_Z(r) = \frac{-\alpha E \Delta T}{2(1-v)}(1 + \Delta r/3r)$$

$$\sigma_\theta(r + \Delta r) = \sigma_Z(r + \Delta r) = \frac{\alpha E \Delta T}{2(1-v)}(1 - \Delta r/3r) \tag{8.3}$$

where α is the thermal expansion coefficient (K^{-1}), E is the modulus of elasticity (Pa), v is the Poisson ratio, which is 0.25–0.35 for most metals, and it is assumed that $\Delta r < 0.2$ r. If the cylinder is not restrained at the ends, the maximum thermal stress near the free ends is about 1.25 times the stresses given by Eq. (8.3) with $\Delta r = 0$. These equations relate to cases in which boundary temperatures are fixed and there is no internal heat generation. Thermal stresses in fusion reactor components are discussed by Fraas and Thompson (1978).

The heat flux q/A through a wall with radius r, thermal conductivity k (W/m K), temperature difference ΔT, and thickness Δr is given by

$$q/A = k\Delta T/\Delta r \quad (W/m^2), \tag{8.4}$$

if $\Delta r \ll r$. If most of the heat goes to the first wall (and not to the divertor) the average heat flux through a fusion reactor first wall may be written as

$$q/A = (\text{heating power} + \text{fusion power} - \text{neutron power})/(\text{wall area}), \tag{8.5}$$

since little of the neutron power P_n appears as heat in the first wall. By definition, $Q = P_f/P_{in}$, where P_f and P_{in} are the fusion and input powers. For DT reactions, $P_n = (4/5)P_f$, and Eq. (8.5) may be expressed in terms of P_n:

$$q/A \cong (P_{in} + P_f - 0.8P_f)/A = (1/Q + 1/5)P_f/A$$

$$= \left(\frac{1}{4} + \frac{5}{4Q}\right)\frac{P_n}{A} \quad (W/m^2) \tag{8.6}$$

Example Problem 8.1: Thermal Stress A fusion reactor with neutron wall loading $P_n/A = 2$ MW/m^2 and Q = 10 has a first wall 0.5 cm thick made of stainless steel with k = 20 W/m K. If E = 1.8×10^{11} Pa, $\alpha = 1.8 \times 10^{-5}$ K^{-1}, and $v = 0.3$, estimate the magnitude of the thermal stress in the wall.

From Eq. (8.6) q/A = 0.75 MW/m^2, and from Eq. (8.4) $\Delta T = 188$ K. If we approximate the toroidal reactor by a long cylinder with free ends, then the maximum thermal stress is approximately $1.25\alpha E\Delta T/2(1-v) = 544$ MPa (79,000 psi). For comparison the yield strength of annealed SS 316 is about 240 MPa.

The thermal stress can be reduced by decreasing Δr (hence decreasing ΔT), reducing the wall power flux, or using materials with higher k$(1-v)/\alpha E$. If we

Fig. 8.6 Thermal stress parameter. *TZM* is an alloy of *Mo* (Data from Badger et al. 1976)
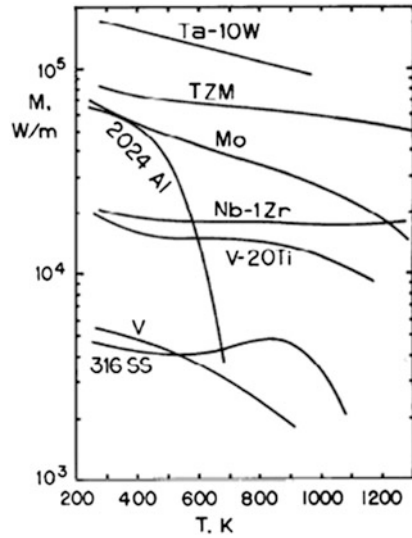
eliminate ΔT between Eqs. (8.3) and (8.4) for the case $\Delta r/r \ll 1$, we can express the ratio of the yield stress to the thermal stress as

$$\frac{\sigma_y}{\sigma_z} = \frac{\sigma_y}{\sigma_\theta} = \frac{M}{\Delta r(q/A)} \tag{8.7}$$

where

$$M \equiv \frac{2(1-\nu)\sigma_y k}{\alpha E} \quad (W/m) \tag{8.8}$$

is called the thermal stress parameter. Large values of M are desirable to permit large heat fluxes while keeping the thermal stresses below the yield stress. Values of M versus temperature for various materials are shown in Fig. 8.6.

Mo and Ta are good and V alloy is fair, but SS is poor. The other stresses must be added to the thermal stresses to find the total stresses in the structure. (The stress is really a tensor with 9 components. Here, for simplicity, we discuss stress as if it were a scalar quantity.) Then the effects of the stresses on the various failure mechanisms can be estimated by comparison with experimental test data. Materials such as SS 316 might attain lifetimes of 5–10 MW a/m^2 neutron fluence, but a lifetime of 40 MW a/m^2 is needed. (Here "a" means "annum" or years.)

After decades of studying various metals and alloys, the choice of structural and first wall materials has narrowed to

- Reduced activation ferritic/martensitic steels (abbreviated RAFM, RAF, or F/M) including oxide-dispersion-strengthened (ODS) steels
- Vanadium alloys, such as V4Cr4Ti
- Tungsten and its alloys

- Silicon carbide composite (SiC fibers in SiC matrix, denoted here simply as SiC).

These will be discussed in Sect. 8.8. The reduced activation materials have eliminated Mo, Nb, Ni, Co, Cu, and N because of their activation, and used W, V, and Ta, which have less long-lived activation. (Zinkle 2011) Liquid lithium wall coatings may also help improve plasma performance and first wall lifetime (Sect. 7.10).

8.2.3 Irradiation Testing

Some desirable radiation source features are:

- High flux $>10^{18}$ neutrons/m^2 s
- Energy spectrum similar to that expected for fusion reactor, to simulate reactor conditions: $\sim$ 10 dpa/year; >100 appm(He)/year; appm(He)/dpa $\sim$ 10
- Large test volume, to accommodate many specimens
- Surface bombardment by charged particles and x-rays
- Capability for either continuous or pulsed operation.

Fast fission reactors, mixed spectrum fission reactors, accelerator neutron generators, ion bombardment, and theoretical modeling are all being used to simulate the fusion reactor environment, but none of these is entirely satisfactory. Fission reactors lack high-energy neutrons. Ion bombardment has different effects from neutron bombardment, and ions do not penetrate deeply beneath the surface. Accelerator neutron generators do not produce high fluxes over large test volumes. Irradiation facilities will be discussed in Sect. 8.10.

8.2.4 Compatibility

Combinations of materials that are prone to adverse chemical reactions are said to be "incompatible." Some combinations may be compatible at low temperatures but incompatible at high temperatures. A few examples of compatibility problems are listed below:

- Plain steels rust when exposed to air and moisture.
- Liquid lithium reacts with air or water, posing a combustion hazard.
- Stainless steel is corroded by lithium at high temperatures (>800 K). Aluminum additives help to suppress this corrosion. (The penetration rate of corrosion cracks caused by lithium in iron is greatly increased by applied stress. Creep strain may break protective corrosion product coatings at the grain boundary interface.)

- Minute quantities of oxygen in He coolant at high temperatures (>800 K) can cause problems with V structures.
- Some metals, such as Ta, are embrittled by hydrogen.
- Graphite is attacked by hydrogen to form methane and other molecules at $500 < T < 1{,}200$ K.

Virtually every structural material has some compatibility problems, which limit allowable coolant-structure combinations and temperature ranges. Lithium can dissolve metal atoms from the structure and then deposit them somewhere else. Such mass transfer processes can cause clogging of coolant passages, over-heating, and tube failure.

8.2.5 Fabrication

Welding is the primary fabrication technique for structural components. Welds must be durable under operating conditions, whether at very high temperatures (first wall) or cryogenic temperatures. Welds may be more vulnerable to failure mechanisms (such as embrittlement) than the metals that are welded. The process of welding may introduce impurities, residual stresses, and variations in the microstructure. With some metals (Group V), welding must be done in vacuum or in very pure inert gases to avoid the detrimental effect of interstitial (0, C, N) pickup during welding. Brittleness of welds makes pure tungsten unsuitable for use as a welded structural material.

After the reactor is in operation, the structure will become radioactive from neutron bombardment. Damaged first-wall, blanket, and shield modules may be removed from the reactor and taken to a hot cell for repair or disposal.

8.3 Mechanical Behavior

Several aspects of mechanical behavior need to be considered for many combinations of alloy compositions, microstructures, temperatures, and neutron fluences. A few common terms are defined in Fig. 8.7.

8.3.1 Strength

Figure 8.8 shows the Young's modulus for various metals.

Figure 8.9 shows the stress–strain curves for EUROFER, a reduced activation ferritic steel.
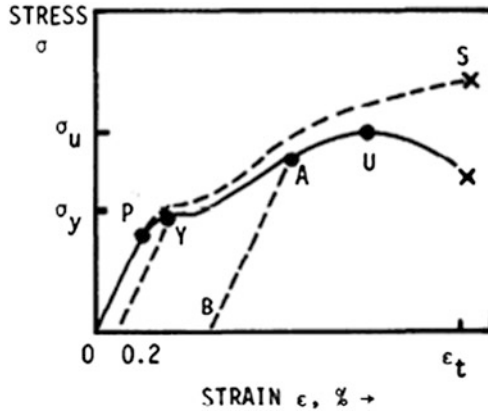
Fig. 8.7 Nominal (conventional) stress σ versus strain for a tensile test of steel. Nominal stress = force divided by original cross sectional area, and strain ε = change in length divided by original length. Strain is linearly proportional to stress up to the proportional limit P. The modulus of elasticity (Young's modulus) $E = d\sigma/d\varepsilon$ along the linear portion of the curve. At the yield stress σ_y, plastic deformation begins, and the specimen no longer returns to its original length when the load is removed. For example, if the load were removed at point A, the strain would follow curve A-B. Ultimate stress σ_u is the peak conventional stress. The specimen cross sectional area decreases, so the "true stress" (force divided by actual area) continues to increase up to the point of failure (*dashed curve* O–P–S)

Fig. 8.8 Young's modulus versus temperature for W, Al, and steel (Rieth 2008)
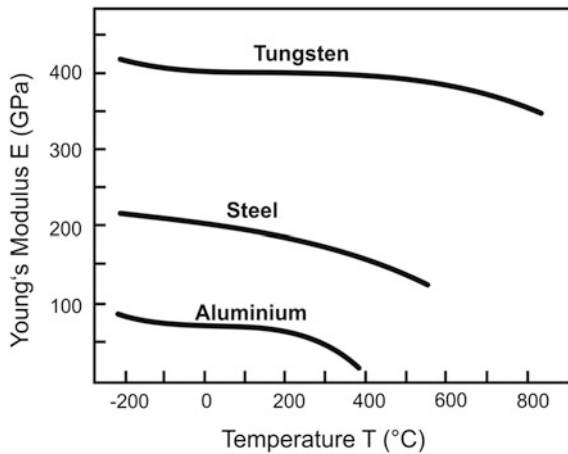
Effects of irradiation-induced defect loops, voids, and precipitate particles tend to increase the yield strength. On the other hand, precipitation reactions, which remove strengthening elements from solution, tend to weaken alloys. At low temperatures (T < 670 K in stainless steels), the defect strengthening effect is dominant, and yield strengths increase with irradiation, but at high temperatures,
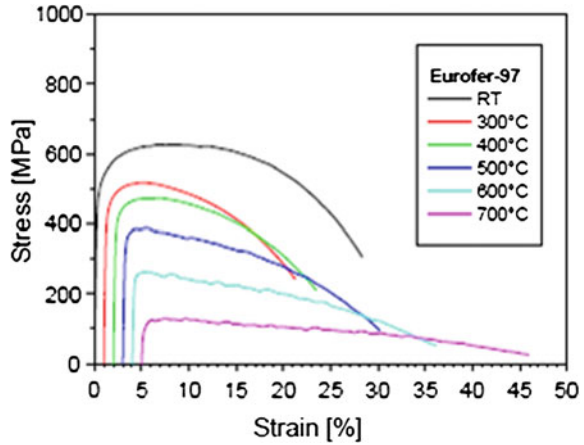
the yield strengths may decrease with irradiation. In both cases ductility is reduced
by irradiation.

8.3.2 Ductility

"Ductility" is the ability of a material to deform under tensile stress, and
"malleability" is the ability to deform under compressive stress. Gold has good
malleability. Both are types of "plasticity", the ability to deform plastically
without fracture.

A rubber band has good ductility. If the rubber band is immersed in liquid
nitrogen, however, it loses its ductility and becomes very brittle; it will break
without stretching. The rubber band may also be embrittled if it is immersed in
certain chemicals or left out in the sun's rays. Thus, embrittlement may be caused
by temperature changes, chemical changes, and radiation damage.

It is essential that a fusion reactor structure have adequate ductility, to bear high
strain rates and high stresses without cracking. Local cracking could result in loss
of vacuum chamber integrity, coolant leakage, or tritium leakage. Ductility is
measured in terms of the fractional elongation (strain) which a material can
undergo up to its maximum stress (uniform elongation), or up to the point where it
ruptures (total elongation). Engineering Test Facility components and fission
reactor components would need to have at least 0.4 % uniform elongation. Duc-
tilities of various annealed, unirradiated alloys are shown as functions of tem-
perature in Fig. 8.10.

The materials to be chosen must maintain ductility at all temperatures to which
they will be exposed. For example, some materials (like irradiated Mo) may be
ductile at operating temperatures, but become brittle when cooled down to room
temperature. Temperature changes and inclusion pickup during welding tend to

Fig. 8.10 Tensile ductilities
of various annealed,
unirradiated alloys versus
temperature (Badger et al.
1976)
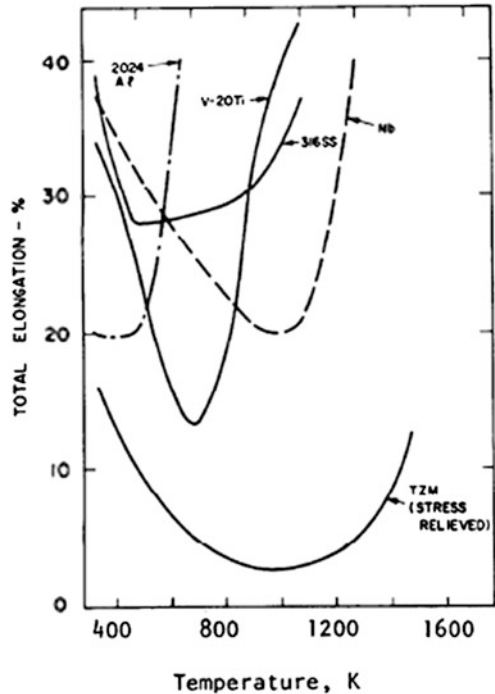
make welds brittle. Chemical attack can cause surface embrittlement and cracking. Embrittlement caused by radiation damage from 0.1 to 5 MeV fission neutrons has been a severe problem of the LMFBR program. Extensive studies have been done in fast fission reactors to define effects of neutron dose, irradiation temperature, helium production, etc. on the ductility of reactor materials, and to develop alloys that are resistant to embrittlement.

8.3.3 Fatigue

If you pull on a tin can lid, you probably can't pull it apart, because your muscles cannot provide enough force. If you bend it back and forth a many times, however, it will gradually crack and break apart, even though the applied force is much lower than that required to pull it directly apart. Such crack growth and fracture during cyclic loading is called "fatigue." Fatigue has been the most difficult materials problem to overcome in aircraft wing design, bridge design, automobile engines, steam turbines, jet engines, pressure vessels, railroad wheels, and many other mechanical devices with cyclic stresses. According to one estimate, about a billion dollars were spent annually on fatigue-related research (Fong 1979).

Chemical attack can cause stress corrosion fatigue. Changing temperatures can cause thermal stress fatigue, and so on. Fusion reactors will have stress changes at various times, including when:

- The magnet coils are turned on or off
- The walls heat up or cool off during plasma burn or quench
- The vacuum chamber is evacuated or let up to air pressure
- The magnet coils are cooled down or warmed up
- The coolant flow rate is changed.

In general, fatigue can cause failure at stresses less than expected for static loading, so it must be taken into account in any design involving cyclic stresses. The surface of a metal normally has microscopic flaws in it, such as machining grooves, corrosion pits, weld defects, and, in the case of fusion reactor walls, damage from sputtering. When stress is applied, the local stress at cracks is much higher than the average stress on the whole piece of metal, and this local stress concentration may cause the cracks to grow. With each stress cycle, the crack may propagate a little further, until the material fractures.

Fatigue crack growth rates depend on many conditions, including

- Alloy composition
- Microstructure (grain size distribution, defects from cold-work, etc.)
- Irradiation and dpa
- appm(He)
- Gases present in the crack, such as water vapor
- Temperature
- Stress amplitude, wave shape, and frequency.

(Fong 1979).

If the applied stress is high, the crack propagates rapidly, and only a few stress cycles are needed to cause failure, as in the case of the tin can lid. If the applied stress is low, on the other hand, the crack propagates very slowly, and it may take millions of stress cycles to cause complete failure. This relation between applied stress and the number of cycles required to cause failure is illustrated in Fig. 8.11 for an unirradiated aluminum alloy. Sometimes such graphs are drawn with cyclic strain (instead of stress) versus N.

The cyclic strain $\Delta\varepsilon$ required to cause failure at N_f cycles of fatigue may be represented approximately by an equation of the form

$$\Delta\varepsilon = 3.5\varepsilon_f N_f^{-0.12} \tag{8.9}$$

where the fatigue strain parameter ε_f varies with material and temperature. For example, values of ε_f are approximately 0.37 for stainless steel and 0.57 for vanadium alloy.

The stress or strain below which the failure probability is very low has been called the "fatigue life" or "endurance limit" of the material. However, such
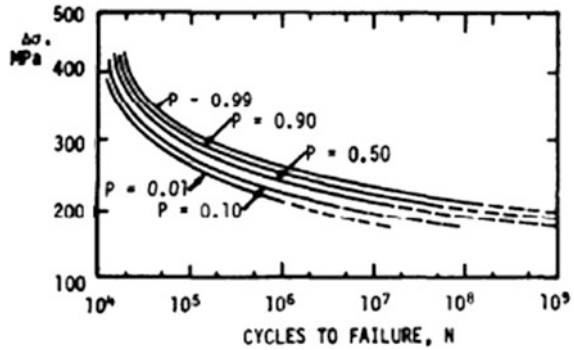
terminology could mislead design engineers into believing that the material is safe
from failure at lower stresses. Radiation damage and chemicals affect all failure
modes, including fatigue. Testing at high fluences of 14 MeV neutrons is needed
before service lives of cyclic fusion reactor components under irradiation can be
reliably predicted.

8.3.4 Thermal Creep

If we hang a weight on a rubber band it will gradually elongate. This is called
"creep". At temperatures $T > 0.5\ T_m$, metals subject to constant stresses over long
periods of time ($\sim 10^4$ h) will gradually creep, and the metal may ultimately
rupture. The time to creep rupture is a function of stress, as shown in Fig. 8.12, and
also a strong function of temperature.

At low temperatures the creep rate is negligible, and creep rupture usually does
not occur in unirradiated metals.

Fig. 8.12 Creep rate versus
stress for stainless steel 316-
LN at various temperatures
(Rieth 2008)
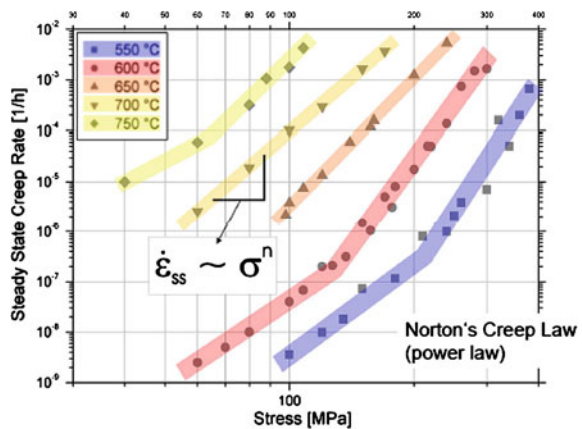
ITER uses several types of austentic stainless steel, including 316-LN, which has a face-centered cubic (fcc) lattice. It is corrosion-resistance, non-magnetic, and relatively inexpensive, and it can operate up to about 600 °C.

Fusion reactor components should be designed to function at least 10^4 h (14 months) before creep rupture occurs. This means keeping stresses below about 160 MPa in 316 SS at 870 K. Creep can also be induced by irradiation, and the required stresses for 316 SS may be a factor of two lower (about 80 MPa, or 40 MPa with a safety factor of two). Making the design stresses this low is problematic.

8.4 Irradiation Effects

Various changes in microstructure occur during irradiation:

- Enhanced diffusion. During irradiation diffusional processes are accelerated, due to creation of many point defects and addition of vibrational energy to the lattice.
- Phase changes. The presence of irradiation-produced defects can change the free energy of one phase relative to another, enabling phases to appear which would not appear in the absence of irradiation.
- Solute segregation. One constituent element may be readily bound to point defects, like vacancies. As the defects flow to sinks, such as cavities, the element is carried along. Many atoms of that element may concentrate at the sink.
- Dissolution of precipitates. Small precipitate particles may be broken up or disordered when interacting with collision cascades or moving dislocations.

These changes in microstructure cause changes in dimensions (swelling and creep) and in mechanical behavior (hardening, embrittlement, toughness).

8.4.1 Embrittlement

There are four principal types of radiation-induced embrittlement

- Radiation hardening
- Ductile to Brittle Transition Temperature (DBTT) shift
- Plastic instability
- Helium embrittlement.

8.4.2 Radiation Hardening

An increase of ultimate tensile stress produced by irradiation, called radiation hardening, is accompanied by a reduction of uniform and total elongation. Figure 8.13 shows interstitial loops, which inhibit shear flow and "harden" the steel.

Fig. 8.13 Interstitial loops formed in steel that cause radiation hardening (Rieth 2008. From work by Materna-Morris et al. 2003)
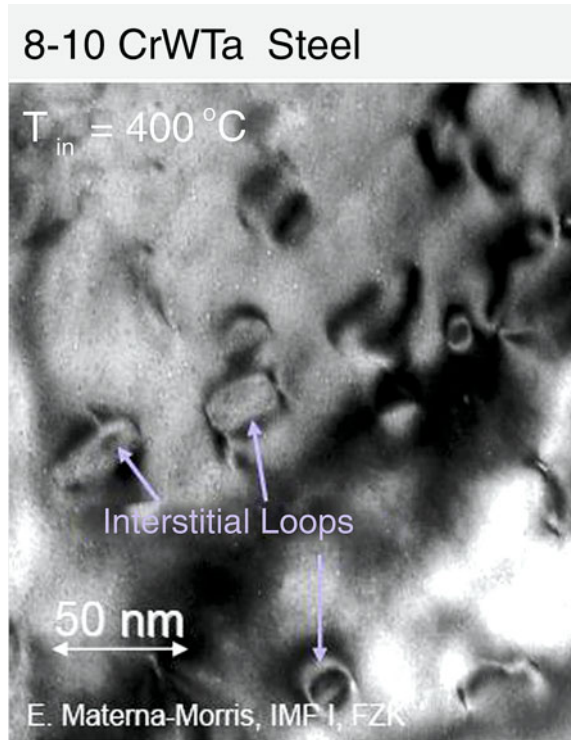
Figure 8.14a shows the stress–strain curves for Nb before and after irradiation at 733 K by fission neutrons.

With radiation hardening the ultimate stress increases from 180 MPa before irradiation to 450 MPa after irradiation. The uniform elongation decreases from about 25 % before irradiation to about 5 % after irradiation; and the total elongation decreases from 39 to 12 %.

8.4.3 DBTT Shift

During World War II some cargo ships suddenly broke apart and sank in the North Atlantic. An investigation revealed that the welds became brittle at low temperatures and failed. There was a "ductile-to-brittle transition temperature" (DBTT), below which ductile steels became brittle. After they improved the metals and welds, the non-combat sinkings stopped. The DBTT (also called "null ductility temperature" or NDT) is a function of alloy composition, microstructure, strain rate, and irradiation dose. During irradiation the DBTT shifts upwards, making the brittle regime more prevalent. Stress–strain diagrams for Mo illustrate this phenomenon in Fig. 8.14b. As with radiation hardening, the ultimate stress increases,
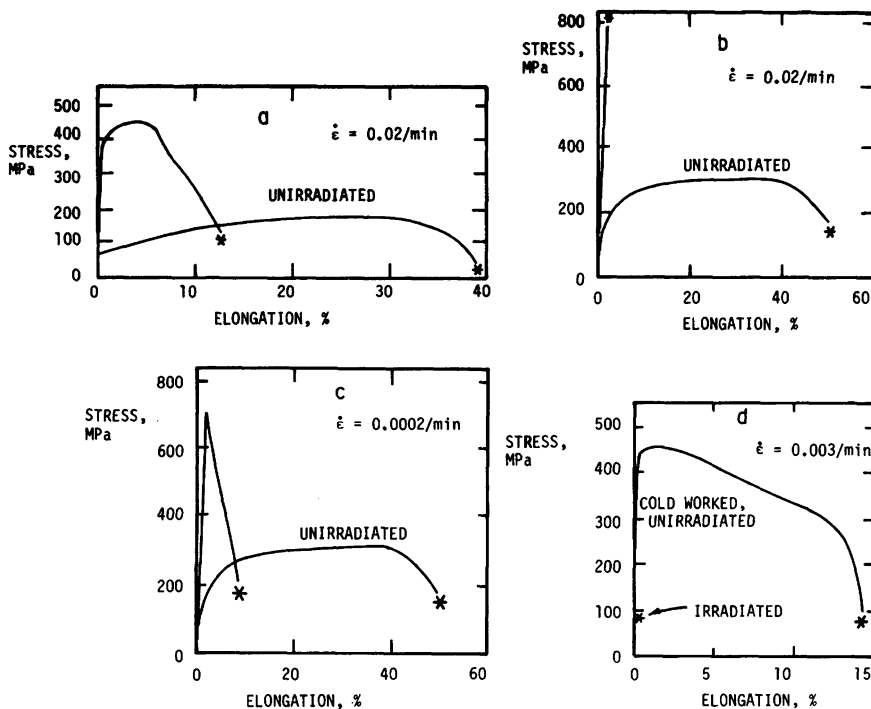
Fig. 8.14 Stress–strain curves illustrating the four types of radiation-induced embrittlement. **a** radiation hardening of Nb, **b** DBTT shift of Mo-0.5 % Ti, **c** plastic instability of Mo-0.5 % Ti, **d** helium embrittlement of Inconel 600. Cases (**a**), (**b**), and (**c**) were irradiated in EBR-II to 3×10^{26} neutrons/m^2 at 733, 698, and 698 K, respectively. Case (**d**) was irradiated in HFIR to 0.88×10^{26} neutrons/m^2 at 973 K after cold work, and acquired 1,260 appm(He). Tensile tests were done at 673 K, except case (**d**) at 973 K (Wiffen 1976)

but now there is very little ductility left; total elongation decreases from about 50 % to about 2 % in this example.

The *strain-rate* (rate at which the specimen is stretched) has a significant effect on ductility and DBTT. For example, the Mo specimen of Fig. 8.14 would retain about 8 % ductility if the strain rate were reduced to 0.0002 min^{-1} (meaning that it takes 100 min to stretch the sample to 2 % elongation). In effect, the DBTT increases with strain rate. The DBTT is also a function of irradiation temperature. If Mo is irradiated above 1,070 K, no significant change in DBTT occurs. Photographs of the microstructure for the two cases indicate dimples and high local deformation for the ductile case at low strain rate (above the DBTT) and a cleavage fracture, with no secondary cracking and little deformation for the brittle case at high strain rate (below the DBTT).

8.4.4 Plastic Instability

The irradiated curve of Fig. 8.14c illustrates the "plastic instability". After reaching maximum stress, the stress drops abruptly, ending in fracture with small total elongation. For the case of metals with body-centered cubic (bcc) lattices irradiated at relatively low temperatures, a *diamond-shaped pattern* of light channels may be observed accompanying the plastic instability. (Mo, V, Nb, Fe, and Cr have bcc structure.) Once *shear flow* occurs along these channels, further flow may occur at a lower stress. Microstructures dominated by dislocation loops are susceptible to the plastic instability, while those with high concentrations of cavities (voids and bubbles) are not susceptible. Dislocation loops formed at low temperatures may join to form cavities at higher temperatures, inhibiting the plastic instability, so raising the temperature increases the ductility.

8.4.5 Helium Embrittlement

Helium produced during neutron irradiation migrates to grain boundaries, forming bubbles along the grain boundaries. This consequently weakens cohesion between the grains, as shown in Fig. 8.15.

Thus, helium buildup promotes intergranular fracture, leading to rupture at low elongations. This problem is especially severe at high irradiation temperatures, where enhanced helium mobility permits rapid accumulation along grain boundaries. Helium embrittlement, Fig. 8.16, is the most serious problem for stainless steels, nickel alloys, and aluminum alloys.

To maintain a total elongation of 1 % in this material at temperatures around 670 K, it would be necessary to limit fission neutron fluence to less than 8×10^{25} neutrons/m^2 (approximately 0.7 MW a/m^2 or 7 dpa).

The roles of the four main ductility-reduction mechanisms with various alloys are shown in Table 8.5.

Fig. 8.15 Helium bubbles accumulating along grain boundaries. Courtesy of M. Rieth and E. Materna-Morris, Karlsruhe Institute of Technology

0.1 µm
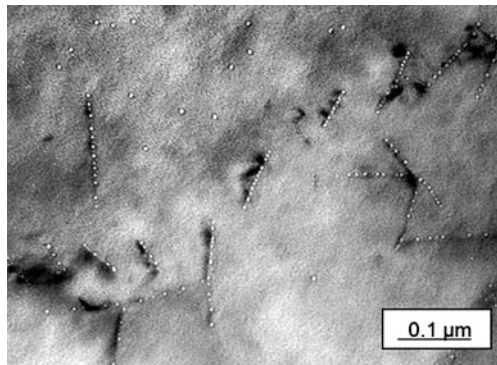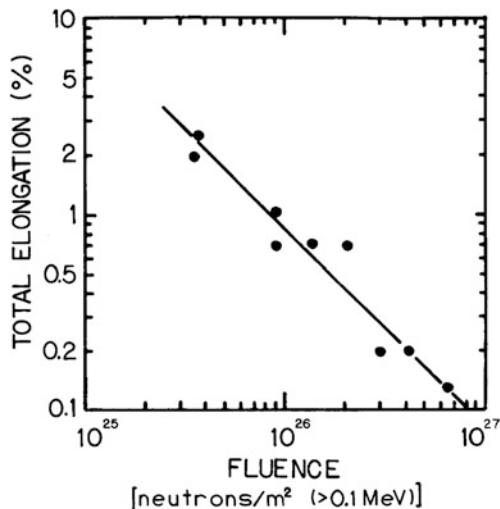
Fig. 8.16 Helium embrittlement of SS-304 creep tested to failure at 873 K. Irradiation was done in EBR-II at an initial stress of 190 MPa at 640 K < T < 740 K. Ductility before irradiation was about 20 %. (Bloom and Stiegler 1971) Reprinted with permission from ASTM STP 484—Irradiation effects on structural alloys for nuclear reactor applications, copyright ASTM International, 100 Barr Harbor Drive, West Conshohocken, PA 19428

Table 8.5 Mechanisms limiting the ductility of irradiated fusion reactor materials

Alloy system	Most severe restraint	Secondary restraint
Stainless steels and nickel-based alloys	He embrittlement	Hardening
Aluminum based alloys	He embrittlement	Hardening
Mo and W based alloys	DBTT shift	Plastic instability
Nb or Ta based alloys	Plastic instability	Hardening
V based alloys	Hardening	He embrittlement

This summary was developed from a very limited data base, so it is subject to revision (Wiffen 1976)

8.4.6 Irradiation Creep

Change of elongation with time during static loading and irradiation, called irradiation creep, varies strongly with applied stress, but only weakly with temperature.

According to one theory of irradiation creep, strain rate (rate of change of elongation) is given by

$$\dot{\varepsilon} \equiv \frac{d\varepsilon}{dt} = \frac{A\sigma^2 L}{\mu^2 bd}\ v_{\text{climb}} \tag{8.10}$$

where A = a constant, σ = applied stress, L = average spacing between "obstacles" (barriers to motion of dislocations through the metal lattice), μ = shear modulus, d = average height of the obstacles, b = Burgers vector, and v_{climb} is the dislocation climb velocity. The dislocation climb velocity is roughly proportional to the damage rate (dpa/s), so strain rate should vary almost linearly with damage rate and irradiation flux.

8.4.7 Swelling

When vacancies precipitate as cavities, the corresponding interstitials create new lattice sites by precipitation at dislocations, and the macroscopic dimensions increase, resulting in swelling. Vacancy migration rates are high enough to promote void growth when the temperature $T > \frac{1}{4}T_m$ (T_m = melting temperature). As temperature increases voids combine to form larger voids, spaced farther apart. The amount of swelling depends upon several conditions:

- Alloy composition. Slight changes in the nickel content of SS 316, for example, can change the amount of swelling by an order of magnitude.
- Metallurgical state. Distributions of grain size, precipitates, phase, and degree of cold work may all affect the amount of swelling. For example, cold worked SS 316 has less swelling than solution annealed SS 316.
- Temperature. The amount of swelling generally increases with temperature.
- Displacements. Swelling usually increases with the number of dpa.
- Helium. Swelling increases with the concentration of He. Helium appears to promote void nucleation and growth.
- Other conditions. Swelling may also depend on damage rates (dpa/s), applied stresses, ratio of dpa/appm(He), and reactor duty cycle.

Experimentally, the amount of swelling may be studied by measuring macroscopic dimension changes, differences between irradiated and unirradiated portions of a sample, change in mass density (by immersion in fluid), and with transmission electron microscopy (TEM) of microstructure. If the length of a specimen increased by $\Delta\ell/\ell = 1$ % in every direction, then the volume would increase by ΔV such that $(V + \Delta V)/V = (1.01)^3 = 1.0303$, and $\Delta V/V = 3.0$ %. Thus, for small isotropic swelling the linear growth (percent) is roughly 1/3 the volumetric swelling (percent).

Figure 8.17 shows pores in pure Fe after irradiation to 6.2 dpa, which results in swelling.

Figure 8.18 shows the swelling observed in 20 % cold worked (CW) and solution annealed (SA) SS 316 in fission reactors.

For this case helium increases swelling and cold working decreases swelling at low temperatures. In this experiment the average cavity diameters varied from about 15 nm (CW) and 30 nm (SA) at 700 K up to 100 nm (both cases) at 950 K

Fig. 8.17 Pores in pure iron after 6.2 dpa irradiation by neutrons (Garner et al. 2000, Fig. 23)
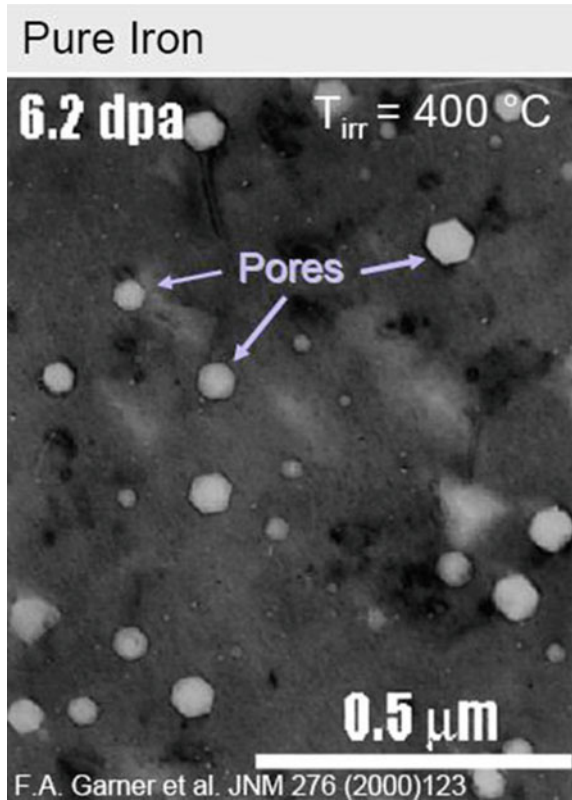
Fig. 8.18 Variation of volumetric swelling with irradiation temperature for annealed (circles) and 20 % cold worked (squares) SS 316 samples irradiated in fission reactors. Open squares and circles: irradiated to 31–37 dpa and about 15 appm(He) in EBR-II. Solid squares and circles: irradiated to 42–60 dpa and 3,000–4,000 appm(He) in HFIR (Maziasz et al. 1976)
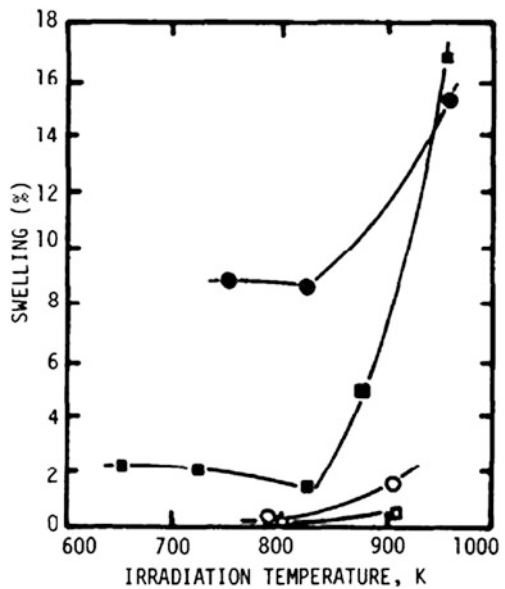
Table 8.6 Processes limiting the allowable operating temperatures (based on Zinkle and Ghoniem 2011)

	dpa	T/T_{melt}
Radiation hardening and embrittlement	<0.1	<0.4
Grain boundary/matrix embrittlement	>1	0.3–0.6
Creep (thermal + irradiation)	>10	<0.45
Swelling	>10	0.3–0.6
Helium embrittlement at He > 10–100 appm	>1	>0.5

for the samples irradiated in HFIR to 3,000–4,300 appm(He). Gradients of swelling magnitude produce internal stresses, just as gradients of temperature and thermal expansion produce thermal stresses. Solid transmutations can also lead to swelling, but the magnitude of the effect is usually much less. For example, transmutation of 1 % of a Nb wall to Zr would produce a 0.2 % volume swelling, and transmutation of 1 % of a V wall to Cr would produce a 0.2 % shrinkage.

Five phenomena limiting the allowable operating temperatures are listed in Table 8.6.

In most structural materials, radiation hardening and helium embrittlement are dominant. The other three determine the material lifetime.

Development of oxide dispersion strengthened (ODS) steels containing 8–14 % Cr may facilitate operation at higher temperatures by providing superior thermal creep strength, improved fracture toughness, and better resistance against embrittlement and swelling (Zinkle 2011).

8.5 Hydrogen Recycling

Here "hydrogen" includes all three isotopes H, D, and T. "Recycling" refers to the processes by which hydrogen gas atoms leave the walls and return to the plasma.

- Reflection (also called backscattering). During its interaction with wall atoms, an incident atom or ion may re-emerge from the wall.
- Spontaneous desorption (also called thermal desorption). Hydrogen atoms adsorbed on the wall surface may leave the surface as they recombine into H_2 molecules.
- Stimulated desorption (also called gas sputtering). Atoms adsorbed on the surface or absorbed near the surface may be ejected by incident ions, atoms, electrons, or photons.

Recycling is important because it helps determine the rate at which hydrogen atoms are incident on the plasma. This rate affects the ionization and charge exchange rates, and thus influences the plasma density and temperature profiles. High recycling rates tend to increase plasma density and decrease ion temperature.

During a long plasma pulse, each hydrogen atom recycles from the wall many times. Recycling was also discussed in Sects. 7.3 and 7.9.

8.5.1 Reflection

Reflection coefficients have been calculated using the Monte Carlo technique and measured experimentally. The results may be expressed in terms of the Linhard reduced energy

$$\varepsilon = \frac{32.5 m_2 W_1}{(m_1 + m_2) Z_1 Z_2 \left(Z_1^{\frac{1}{2}} + Z_2^{\frac{1}{2}}\right)^{2/3}} \text{ (dimensionless)}, \qquad (8.11)$$

where W_1 is the incident particle energy (monoenergetic) or temperature (Maxwellian) expressed in keV, m_1 and Z_1 are the incident particle mass and nuclear charge number, and m_2, Z_2 are the target atom mass and nuclear charge number.

Let θ be the angle between the incident particle velocity and a normal to the surface. Cases with normal incidence ($\theta = 0$), with a $\cos\theta$ distribution of incident particles, and with an isotropic distribution of incident particles have been studied. Experimental measurements for the case of monoenergetic ions at normal incidence are in fair agreement with theoretical predictions. Light ions scattering from solids have been measured also for sliding incidence of ions from rough and smooth surfaces with $r_n \sim 1$ for 30 eV D impinging W with $\theta \sim 80°$, and r_n decreases at lower energies due to attraction of the scattered ion by the surface (Kurnaev 2012).

For the *cosine distribution*, which probably best represents a fusion plasma, the theoretical values of particle reflection coefficient (number of reflected particles per incident particle) are fit approximately by the equation

$$r_n = 0.35 - 0.2 \log_{10}\varepsilon \quad (0 < \varepsilon < 10). \qquad (8.12)$$

For the cosine case, values outside this range are not available. The theoretical results for most target materials studied agree fairly well with Eq. (8.12), but r_n for Be is about a factor of 2 lower than the equation. Values for the normal incidence case are lower than Eq. (8.12), and values for the isotropic distribution case are slightly higher (Haggmark and Biersack 1979). Values of the "energy reflection coefficient" (energy reflected divided by incident energy) have also been calculated for the three angular distribution cases.

Example Problem 8.2: Deuteron Trapping Assume that deuterons with temperature 1 keV are incident on an aluminum surface with cosine angular distribution. Estimate the fraction of the deuterons that are trapped in the surface.

For this case, $m_1 = 2$, $m_2 = 27$, $Z_1 = 1$, $Z_2 = 13$, and $W_1 = 1$. From Eq. (8.11) we find $\varepsilon = 0.841$, and from (8.12), $r_n = 0.36$. The fraction trapped is $(1 - r_n) = 0.64$.

8.5.2 Spontaneous Desorption

Incident energetic particles not reflected will be implanted inside the wall. From there they may gradually diffuse back to the surface and be desorbed. The time it takes for them to re-emerge from the surface is the sum of the times for diffusion and desorption. Spontaneous desorption of hydrogen occurs via molecular recombination on the surface, so the recombination rate determines the time delay before desorption. Thus, the spontaneous desorption flux may be limited either by diffusion or by recombination, whichever process is slower. Let $c(x,t)$ be the hydrogen atom concentration (atoms/m^3), where x is the distance from the surface and t is the time. The spontaneous desorption flux may be written

$$(\text{spontaneous desorption flux}) = Kc^2(0,t)\,(\text{atoms/m}^2\text{s}), \qquad (8.13)$$

where K is a recombination rate parameter (m^4/s). The values of K are shown as functions of 1,000/T in Fig. 8.19, where T is the surface temperature (K). Energy must be supplied for hydrogen to enter endothermic metals like Al and Fe, but energy is released when hydrogen enters exothermic (reactive) metals like Ti and Zr. This energy of solution makes K very low for exothermic metals.

The untrapped concentration $c(x,t)$ at depth x can be determined by solving a diffusion equation of the form

Fig. 8.19 Surface recombination coefficient K versus inverse temperature for various metals (Baskes 1980, Fig. 3
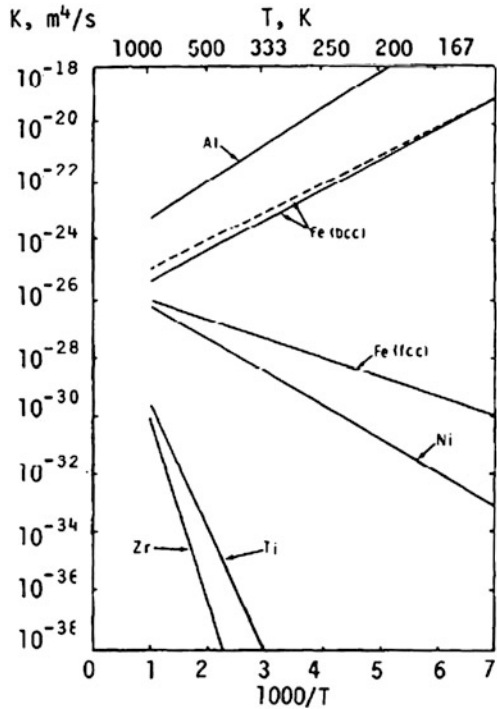
$$\partial c/\partial t = (\partial/\partial x)[D(\partial c/\partial x)] + S(x,t) - dC_T/dt \qquad (8.14)$$

$$dC_T/dt = D(C_t^m - C_T)/\lambda^2 - \nu C_T \exp(-E_T/kT)$$

where D is the diffusion coefficient, S(x,t) is the volumetric source of hydrogen atoms from implantation, C_T = trapped atom concentration, C_t^m = maximum concentration of traps, E_T = energy of atom release from a trap, λ = lattice parameter, ν = lattice vibration frequency (Kurnaev 2012).

(If a strong temperature gradient is present, then a term proportional to $\partial T/\partial x$ is also needed.) Thus, a slow diffusion rate can keep the surface concentration c(0, t) low, and limit the spontaneous desorption rate. The diffusion coefficient varies with temperature T as

$$D = D_o \exp(-E_d/T), \qquad (8.15)$$

where D_o is a constant for any given metal, E_d is the "activation energy for diffusion," and T is expressed in energy units. (Some values of D_o and E_d for hydrogen are given in Sect. 12.2.)

8.5.3 Stimulated Desorption

The gas flux emitted from the surface by stimulated desorption is proportional to the incident fluxes causing the desorption, including energetic ions, neutrals, electrons, and photons. If the bombarding particles mainly knock atoms out of the surface, then the stimulated desorption flux is also proportional to c(0, t). If the bombarding particles act mainly to accelerate the rate of diffusion to the surface, then the stimulated desorption flux is proportional to $(\partial c/\partial x)_{x=0}$. Thus, according to these two models, the flux emitted by energetic incident ions is

$$\text{(stimulated desorption flux)} = \begin{cases} A r_i c(0, t) & \text{(gas sputtering)} \\ A_1 r_i (\partial c/\partial x)_{x=0} & (\textit{accelerated diffusion}) \end{cases}$$
$$(8.16)$$

Γ_i is the incident ion flux, and A, A_1 are constants. The constant A may be expressed in terms of an effective desorption cross section σ_d (m^2) and incident ion mean range λ as

$$A \sim \sigma_d \lambda/4, \qquad (8.17)$$

where $\lambda/4$ is taken as the maximum depth from which stimulated desorption is effective. Rough experimental measurements indicate values of $\sigma_d \sim 10^{-19}$–10^{-20} m^2, but accurate data are lacking. Accelerated diffusion is discussed by Hotston (1980).

The above estimates of spontaneous and stimulated desorption ignore the possible buildup of monolayers of adsorbed gas on the wall surface. If several

monolayers are present, then atoms could be more easily knocked off, and stimulated desorption rates would be much higher (much larger values of σ_d would be measured). At equilibrium gas atoms would leave the surface as fast as others arrived, and the number of adsorbed monolayers could be calculated from their binding energies and the surface temperature. Under transient conditions, however, no equations or data are available for calculating the number of monolayers present as a function of temperature, species, incident fluxes, etc. The recycling situation is further complicated by chemical reactions of hydrogen with oxygen, carbon, and metals; by other surface films; and by trapping of hydrogen in lattice defects with binding energies of eV.

Wall models incorporating recycling processes are used to describe:

- Boundary conditions for transport codes describing various plasma confinement experiments (tokamaks, etc.).
- Variation of plasma density with time in gettered (sublimation pumped) and ungettered tokamak discharges.
- Operation of tokamaks for many discharges with hydrogen, then switching to deuterium. For the first few discharges, hydrogen coming out of the walls dominates the discharge.
- Absorption of atoms by the wall ("wall pumping").
- Pressure rise with time after the end of a plasma discharge, due to hydrogen coming out of the walls (Dolan 1980).
- Neutral gas—wall interactions in divertors, limiters, and beam dumps.
- Effect of neutral beam injection on plasma density.
- Time variation of gas trapping efficiency as a metal saturates with gas.

8.6 Impurity Introduction

8.6.1 Physical Sputtering

Incident ions (or atoms) may eject atoms from wall surfaces, by either primary or secondary collisions, Fig. 8.20.

The average number of wall atoms ejected per incident ion, called the sputtering yield S, varies with wall material, incident ion type, energy, angle of incidence, and

Fig. 8.20 Physical sputtering of surface atoms by incident ions. Wall atoms may be ejected by primary collisions (*left*) or by secondary collisions (*right*)
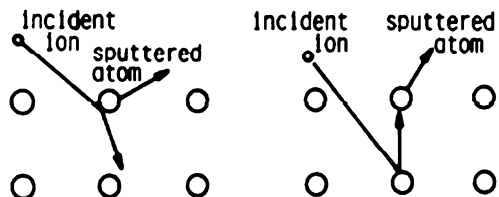
surface conditions. For the case of light ions at normal (perpendicular) incidence, the sputtering yield may be represented in terms of a universal formula:

$$S = 0.0064\, m_2 \gamma^{5/3} E^{\frac{1}{4}} \left(1 - \frac{1}{E}\right)^{7/2} \quad (1 < E \le 30),\, (m_1/m_2 \le 0.4) \qquad (8.18)$$

$$\gamma \equiv \frac{4 m_1 m_2}{(m_1 + m_2)^2}, \qquad (8.19)$$

where m_1 and m_2 are the incident ion and wall atom mass numbers ($m_2 = 27$ for aluminum),

$$E = W/W_{th}, \qquad (8.20)$$

W is the incident ion energy, W_{th} is the "threshold energy" given by

$$W_{th} = \frac{W_B}{\gamma(1 - \gamma)}, \qquad (8.21)$$

and W_B is the surface binding energy of the wall atoms (Valid if $m_1 < 0.3\, m_2$).

The variation of sputtering yield with normalized energy E given by Eq. (8.18) is compared with data points for a wide variety of wall atoms and incident ions in Fig. 8.21. Agreement is satisfactory for $E < 30$. Values of threshold energy W_{th} for various cases are listed in Table 8.7.

If Eq. (8.18) is integrated over a Maxwellian distribution of incident particle energies, the resulting sputtering yield has the form shown in Fig. 8.22 as a function of incident ion temperature.

Some Maxwellian-ion sputtering yields are listed in Table 8.8 for various species and temperatures.

For cases in which the ions are not normally incident, the sputtering yield increases with angle of incidence (measured from the normal), as illustrated in Fig. 8.23 for nickel.

Thus, the sputtering yield for ions incident with a distribution of angles (such as a cosine distribution) would be larger than for the case of normal incidence.

Sputtering yields have been measured for a variety of alloys and compounds, including stainless steel, Al_2O_3, BeO, SiC, and WC. Sputtering may preferentially deplete one element of a compound or alloy. Sputtering by heavy atoms, such as Ni^+ striking a Ni wall, produces very large yields, exceeding 1 at high energies (keV). Sputtering yields for 14 MeV neutrons are on the order of $1\text{--}4 \times 10^{-5}$ atoms/neutron for Nb, Au, and Cu. Neutrons can sputter atoms from both sides of a wall, in contrast to ions, which usually do not penetrate so far.

The wall surface erosion rate by sputtering from various fluxes ϕ_j (particles/m^2s) with sputtering yields S_j is given by

$$\frac{dx}{dt} = \frac{1}{n_W} \sum_j \phi_j S_j \quad (m/s), \qquad (8.22)$$

Fig. 8.21 Sputtering yield versus normalized energy E, for various wall materials and incident ions. Smooth curve is from Eq. (8.18) (Roth et al. 1979)
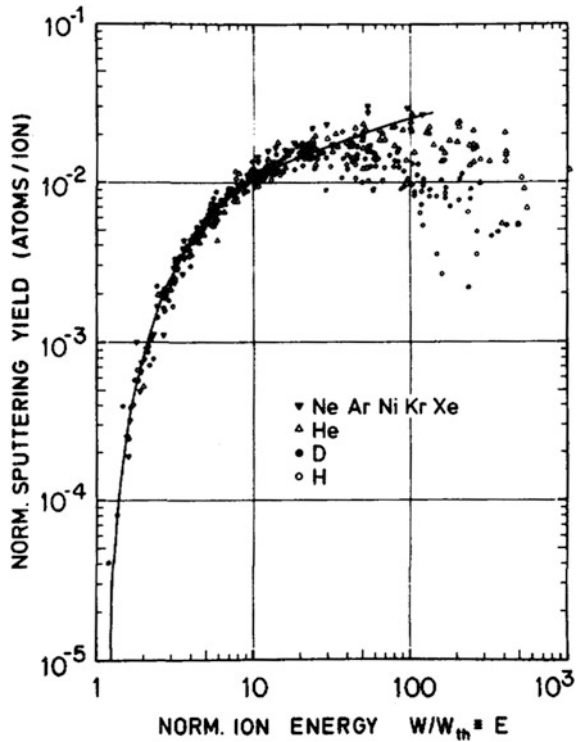
Table 8.7 Values of the threshold energy W_{th} (eV) for various ions and wall atoms (Roth et al. 1979)

Ion	H	D	He^3	He^4
Target				
Al	53	34		20.5
Au	184	94	60	44
Be	27.5	24		33
C	9.9	11		16
Fe	64	40		35
Mo	164	86	45	39
Ni	47	32.5		20
Si	24.5	17.5		14
Ta	460	235		100
Ti	43.5			22
V	76			27
W	400	175		100
Zr				60

where the summation is over the various bombarding ion species j.

Example Problem 8.3: Steel Wall Sputtering A plasma has the following ion fluxes to its steel walls: DT $= 4 \times 10^{19}$, alpha particles $= 3 \times 10^{19}$,

Fig. 8.22 Sputtering yields from Maxwellian ions (*upper curve*) and S_N from monoenergetic ions (*lower curve*) versus normalized temperature or energy (Roth et al. 1979)
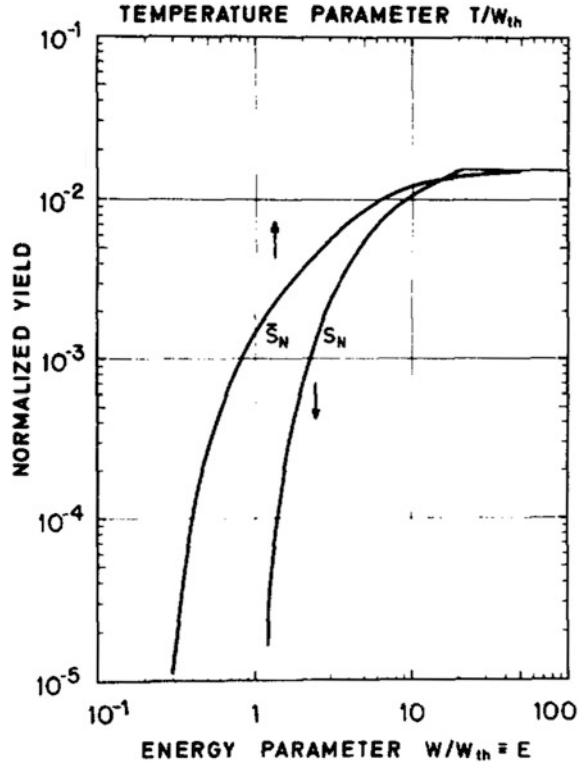
iron $= 10^{18}$ (m^{-2} s^{-1}). The ion temperatures are 200 eV. Estimate the wall erosion rate and the wall atom flux into the plasma. Assume that the steel behaves like iron.

From Table 8.8 the average sputtering yields are S(DT) = 0.014, S(alphas) = 0.029, S(Fe) = 0.548. Then the wall atom flux is

$$\sum_j (\phi_j S_j) = 2.0 \times 10^{18} \text{ atoms/m}^2\text{s}.$$

The mass density of iron is 7,870 kg/m^3, and its atomic weight is 0.05585 kg/mole, so

$$n_w = 8.49 \times 10^{28} \text{atoms/m}^3.$$

The wall erosion rate is dx/dt $= 2.36 \times 10^{-11}$ m/s $= 0.74$ mm/a ("a" = annum = year).

In most fusion reactor designs, wall erosion is not as serious a problem as impurity influx. However, local "hot spots" of high particle fluxes may occur, where sputtering damage can be severe.

Table 8.8 Predicted sputtering yields for Maxwellian ions on various materials

	T_i (eV)	S_D	S_T	S_{He}	S_{z1}	S_{z2}
Be	60	0.0187	0.0280	0.0546	0.1571	
	200	0.0224	0.0337	0.0858	0.3142	
	1000	0.0140	0.0210	0.0742	0.3899	
B	60	0.0105	0.0160	0.0297	0.1040	
	200	0.0140	0.0210	0.0508	0.2365	
	1000	0.0096	0.0145	0.0492	0.3716	
C	60	0.0081	0.0121	0.0220	0.0851	
	200	0.0115	0.0173	0.0401	0.2113	
	1000	0.0086	0.0130	0.0427	0.3999	
Al	60	0.0108	0.0164	0.0260	0.2088	
	200	0.0204	0.0307	0.0598	0.6383	
	1000	0.0227	0.0341	0.0959	2.221	
Si	60	0.0077	0.0116	0.0182	0.1518	
	200	0.0149	0.0223	0.0429	0.4685	
	1000	0.0172	0.0259	0.0715	1.695	
Ti	60	0.0046	0.0072	0.0109	0.1482	
	200	0.0107	0.0162	0.0285	0.4753	
	1000	0.0159	0.0238	0.0595	2.036	
V	60	0.0041	0.0063	0.0096	0.1372	
	200	0.0096	0.0144	0.0251	0.4409	
	1000	0.0145	0.0217	0.0536	1.910	
Fe	60	0.0047	0.0072	0.0109	0.1695	
	200	0.0114	0.0171	0.0292	0.5478	
	1000	0.0183	0.0275	0.0660	2.438	
Nb	60	0.0012	0.0022	0.0035	0.0964	
	200	0.0044	0.0068	0.0110	0.3153	
	1000	0.0093	0.0140	0.0303	1.494	
Mo	60	0.0014	0.0025	0.0038	0.1078	
	200	0.0049	0.0075	0.0120	0.3526	
	1000	0.0103	0.0155	0.0333	1.674	
W	60	0.0001	0.0004	0.0009	0.0829	
	200	0.0016	0.0030	0.0049	0.2743	
	1000	0.0060	0.0092	0.0176	1.342	
BeO	60	0.0094	0.0143	0.0257	0.0694	0.1371
	200	0.0134	0.0201	0.0467	0.1561	0.3603
	1000	0.0101	0.0151	0.0497	0.2402	0.7834
B_4C	60	0.0095	0.0145	0.0268	0.0932	0.1067
	200	0.0129	0.0194	0.0464	0.2140	0.2565
	1000	0.0091	0.0136	0.0459	0.3433	0.4518
BN	60	0.0095	0.0144	0.0259	0.0875	0.1190
	200	0.0135	0.0203	0.0470	0.2082	0.3050
	1000	0.0102	0.0152	0.0501	0.3595	0.6225
MgO	60	0.0088	0.0132	0.0219	0.1631	0.1062
	200	0.0152	0.0227	0.0469	0.4849	0.3020
	1000	0.0147	0.0220	0.0656	1.522	0.8186

(continued)

Table 8.8 (continued)

	T_i (eV)	S_D	S_T	S_{He}	S_{z1}	S_{z2}
Al_2O_3	60	0.0072	0.0107	0.0177	0.1500	0.0865
	200	0.0123	0.0185	0.0382	0.4492	0.2460
	1000	0.0120	0.0180	0.0534	1.447	0.6668
SiC	60	0.0071	0.0106	0.0175	0.1547	0.0626
	200	0.0122	0.0183	0.0377	0.4662	0.1710
	1000	0.0118	0.0177	0.0528	1.5369	0.4112
SiO_2	60	0.0071	0.0106	0.0175	0.1547	0.0855
	200	0.0122	0.0183	0.0377	0.4662	0.2430
	1000	0.0118	0.0177	0.0528	1.5369	0.6589
TiO_2	60	0.0057	0.0087	0.0138	0.2025	0.0652
	200	0.0108	0.0163	0.0319	0.6370	0.1908
	1000	0.0119	0.0179	0.0505	2.494	0.5657
ZrO_2	60	0.0032	0.0052	0.0079	0.2130	0.0362
	200	0.0074	0.0112	0.0202	0.6897	0.1097
	1000	0.0101	0.0151	0.0391	3.099	0.3688
Nb_2O_5	60	0.0032	0.0051	0.0079	0.2132	0.0357
	200	0.0077	0.0117	0.0207	0.6920	0.1092
	1000	0.0113	0.0169	0.0426	3.150	0.3803

S_z represents self-sputtering. Subscripts 1 and 2 represent the two elements of a compound, in order. For BeO, S_{z1} represents sputtering by Be, and S_{z2} represents sputtering by O (Smith 1978, Table 4)

Fig. 8.23 Sputtering yield of nickel versus angle of incidence of H^+, D^+, and $^4He^+$ ions (Bay and Bohdansky 1979), Fig. 3
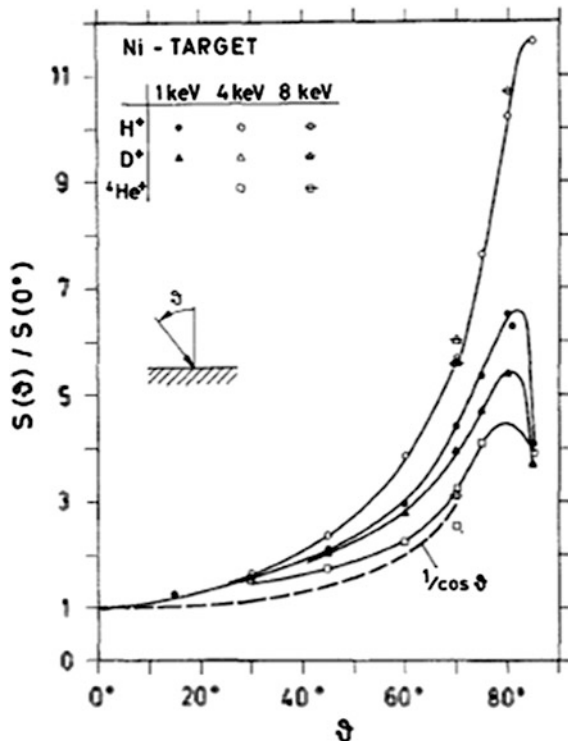
8.6.2 *Physichemical Sputtering*

When oxygen ions strike a metal surface, chemical reactions may occur, which alter the effective sputtering yields. Similar effects may occur for carbon, nitrogen, and hydrogen ions with formation of carbides, nitrides, and hydrides at the wall surface. (Some industries deliberately implant ions to improve surfaces of metals.) Various chemical films may be formed, which have different sputtering rates from the original wall material The term physichemical sputtering refers to sputtering where both kinetic energy and chemical binding energy affect the sputtering yield.

8.6.3 *Chemical Erosion*

In some cases chemical effects alone may cause wall erosion, even at low incident kinetic energies. For example, hydrogen isotopes incident on graphite can produce hydrocarbons like methane and acetylene, and consequently erode the wall. Chemical erosion (also called chemical sputtering) of graphite reaches a maximum at $T \sim 870$ K, with a peak yield of about 0.08 atoms lost per incident hydrogen ion, Fig. 8.24.

The chemical erosion rate of graphite is typically less than its physical sputtering rate for $T < 570$ K or $T > 1{,}170$ K.

Fig. 8.24 Temperature dependence of sputter yields for 1–10 keV protons incident on carbon. Courtesy of W. M. Stacey, Jr
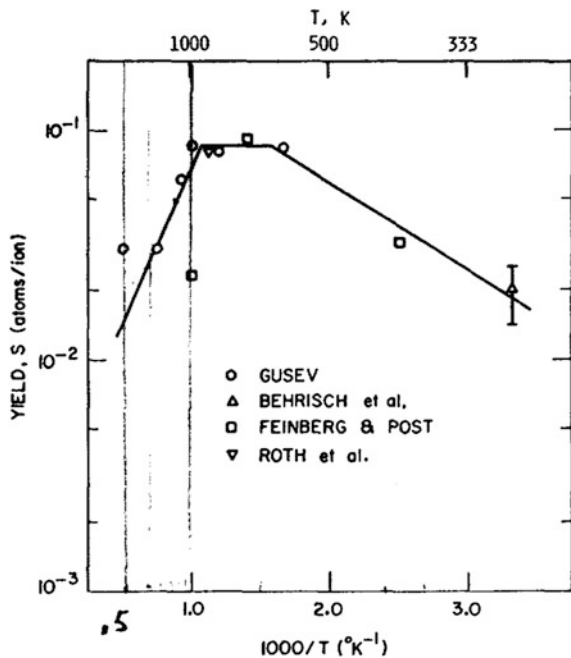
8.6.4 Impurity Desorption

Light impurities like C, N, H_2O, and O are frequently adsorbed on chamber walls. Surface impurities come from:

- Residual gases present in the chamber
- Redeposition of sputtered atoms
- Segregation to the surface of impurities present in the wall material.

Baking out the vacuum chamber helps to clean most of the adsorbed monolayers of light impurities. Plasma discharges are often repeated for days on large experiments to clean the chamber walls. Plasma particles and photons striking the walls may stimulate desorption to remove impurities. Loosely-bound molecules have the highest yield for any kind of desorption. Since loosely-bound molecules are removed by bakeout, the apparent stimulated desorption yields decrease with increasing bakeout temperature.

Cross sections for stimulated desorption on the order of 10^{-19}–10^{-20} m^2 and higher have been measured for impact of H^+ and Ar^+ ions on various adsorbed residual gases. For the case of one monolayer coverage, this corresponds to gas sputtering yields around 0.5–10 atoms per ion.

Electron-impact desorption typically has yields on the order of 0.01–0.1 molecules per incident electron for electron energies of 0.1–5 keV. Stimulated desorption by photons typically has yields of 10^{-3} molecules per photon or less, so it is not likely to be significant in comparison with ion-impact desorption, except at very high photon fluxes. Cooling a tokamak wall to 77 K greatly reduces the desorption and influx of oxygen (Marmar et al. 1979).

Although plasma discharges for cleaning chamber walls generally do not raise the wall temperature much, the transient wall temperature in high-density pulsed fusion reactors can become high enough that vaporization is significant, such as during giant ELMs in tokamaks.

8.6.5 Vaporization

The energy required to remove an atom from the surface of a metal, called the heat of sublimation ΔH, is typically 5–10 eV. The equilibrium vapor pressure of a metal is given approximately by the equation

$$p = p_o \exp(-\Delta H/T), \tag{8.23}$$

where p_o is a constant and T is the temperature (in energy units). This relation is shown in Fig. 8.25 for some elements.

Table 8.9 shows some data of vapor pressures versus temperature.

The surface evaporation flux is given approximately by the equation

Fig. 8.25 Equilibrium vapor pressure for various wall materials versus temperature. For dashed curves read the top temperature scale (Based on data of Honig and Kramer 1969)
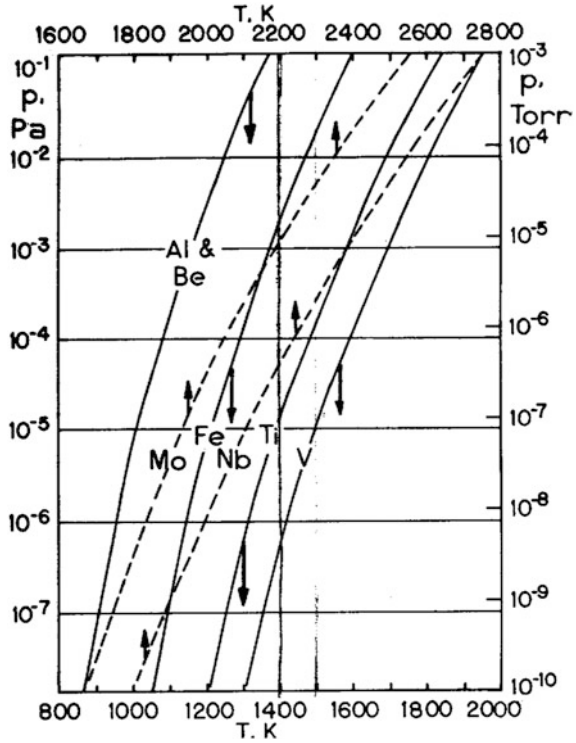
Table 8.9 Temperatures (Celsius) corresponding to various vapor pressures

	1 Pa	10 Pa	100 Pa	1 kPa	10 kPa	100 kPa
Carbon	–	2,566	2,775	3,016	3,299	3,635
Lithium	524.3	612.3	722.1	871.2	1064.3	1337.1
Copper	1,236	1,388	1,577	1,816	2,131	2,563
Iron	1,455	1,617	1,818	2,073	2,406	2,859
Nickel	1,510	1,677	1,881	2,137	2,468	2,911
Tungsten	3,204	3,500	3,864	4,306	4,854	5,550
Vanadium	1,828	2,016	2,250	2,541	2,914	3,406

Data from Handbook of Chemistry and Physics Web Edition, Vapor Pressure. (http://www.hbcpnetbase.com/tables/default.asp Accessed March 2012)

$$\phi_n = 2.6 \times 10^{24} \alpha p / (AT)^{1/2} \quad (\text{atoms/m}^2\text{s}), \tag{8.24}$$

where $\alpha \approx 1$ is the sticking coefficient, p is the vapor pressure (Pa), A is the atomic weight (g/mole), and T is the temperature (K). The wall erosion rate is

$$dx/dt = \phi_n/n_w \quad (\text{m/s}). \tag{8.25}$$

Example Problem 8.4: Vanadium Wall Erosion If one tried to operate a vanadium wall at 1,600 K, what would the wall erosion rate be?

For vanadium the mass density is 6,110 kg/m^3 and the atomic weight is 0.05094 kg/atom, so $n_w = 7.21 \times 10^{28}$ atoms/m^3.

From Fig. 8.25, $p = 1.3 \times 10^{-4}$ Pa.
From Eq. 8.24 $\phi_n = 1.2 \times 10^{18}$ atoms/m^2 s.
From Eq. 8.25 dx/dt $= 1.7 \times 10^{-11}$ m/s = 0.54 mm/a.

This would be unacceptably high, so a lower operating temperature would be required.

The above estimate is for a constant wall temperature. For a pulsed reactor, there will be a peak temperature at the end of each pulse when the plasma energy dumps onto the wall. If a total energy W(J) is dumped onto a surface area S(m^2) during a brief time interval τ, then the surface temperature rise is

$$\Delta T = 2W/S(\pi c_p k \rho_m \tau)^{\frac{1}{2}} \quad (K), \tag{8.26}$$

where ρ_m = mass density (kg/m^3), c_p = specific heat (J/kg K) and k = thermal conductivity (W/m K) of the wall material. The consequent number of wall atoms evaporated by the pulse is approximately

$$\Delta n/S \cong 0.1\tau\phi_n(T_{max}) \quad (atoms/m^2), \tag{8.27}$$

where $\phi_n(T_{max})$ is the evaporation rate at the peak temperature. Some pertinent thermal properties of various materials are listed in Table 8.10.

Table 8.10 Thermal properties of various materials. Data are from Behrisch (1972), Table 1

		V	Nb	Mo	C	SS 304
Z, atomic number		23	41	42	6	18 % Ci
A, atomic mass (gm/mole)		50.94	92.9	95.94	12	8 % Ni
ρ_m, mass density (kg/m^3)		5,870	8,570	9,010	2,250	7,900
n_w, atomic density (10^{28} atoms/m^3)		6.93	5.56	5.65	11.3	8.6
T_m, melting temperature (K)		2,192	2,688	2,883	(vap.) 3,925	1,400
ΔH, heat of sublimation (eV/atom)	300 K	5.33	7.5	6.83	8.2–10.4	
	500 K	5.27	7.43	6.78		
	1,000 K	5.16	7.28	6.63		
	1,500 K	4.96	7.14	6.48		
	2,000 K	4.75	6.97	6.3		
k, thermal conductivity (W/m K)	500 K	33.1	56.7	130	80–100	19
	1,000 K	38.6	64.4	112	49–64	
	1,500 K	44.7	72.1	97	40–50	
	2,000 K	50.9	79.1	88	30–40	
c_P, specific heat (J/kg K)	500 K	500	280	254	1,200	500
	1,000 K	640	300	290	1,670	
	1,500 K	700	330	330	1,800	
	2,000 K	850	370	380	2,000	

For plasma energy dumps with $\tau > 0.1$ s in tokamak reactors, evaporation will not be a serious problem, unless the energy is concentrated on a small area. The above equations may underestimate the evaporation, however, if the thermal conductivity is reduced by oxide films, cracks, etc.

8.6.6 Blistering and Flaking

When energetic helium ions strike the first wall, they penetrate to a given depth and come to rest. Irradiation by monoenergetic ions thus produces a buildup of helium atoms at a depth corresponding to the range of the incident particles.

If the irradiation dose is high enough, these atoms coalesce to form bubbles. The gas pressure in the bubbles and shear stresses in the metal may cause plastic deformation of the surface skin to form visible blisters. Once the blister is formed, the skin tends to overheat, and increased gas pressure from additional helium bombardment may cause the blister to rupture. The ruptured blisters cause wall erosion and plasma contamination. Blistering can also be caused by hydrogen ion bombardment (including deuterons and tritons), but hydrogen ions have a much higher solubility and diffusivity in metals, so they can usually diffuse back out of the metal before the pressure builds up in the blisters. On active metals like Ti and Zr, hydrogen can form hydride layers which may flake off. The effect of wall temperature on blister formation is illustrated in Fig. 8.26.

Exfoliation of blisters and wall erosion are most severe in the temperature range $0.3 < T/T_m < 0.5$. Above 0.5 the increased diffusivity of helium allows the gas to escape, forming a porous surface structure in the metal. The blister skin thickness t is roughly equal to the theoretical range of the helium ions. The bubble height h and radius r are related to the gas pressure p and metal yield strength σ_y approximately by the equation

$$\frac{(r^2 + h^2)}{h} = \frac{4\sigma_y t}{p} \tag{8.28}$$

The yield strength and gas pressure are practically independent of bombardment energy. As the energy is increased, the skin thickness t increases and the bubble size (r and h) also increase. The critical pressure for blister formation is given by

$$P_{cr} = \frac{4\sigma_y t^2}{3r^2} \tag{8.29}$$

For a given incident ion energy, t and r vary little with wall temperature, but σ_y decreases with increasing temperature. Therefore, less pressure is required for
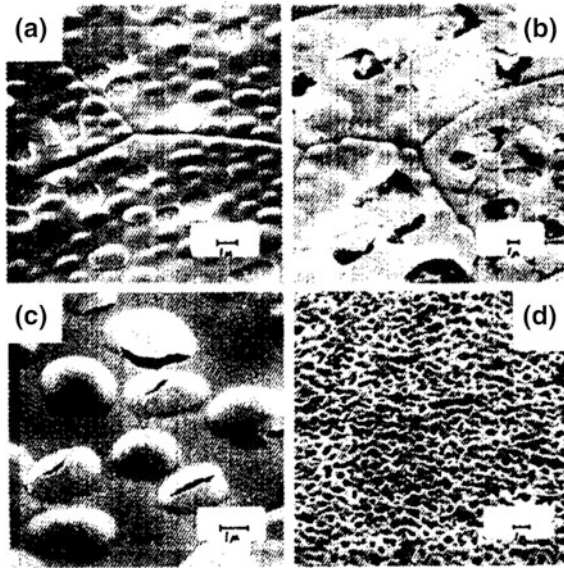
Fig. 8.26 Blistering of molybdenum surfaces after bombardment with 36 keV He$^+$ ions. **a** T/T$_m$ = 0.1, **b** T/T$_m$ = 0.3, **c** T/T$_m$ = 0.4, **d** T/T$_m$ = 0.6, where T$_m$ is the wall melting temperature (Erents and McCracken 1973), Fig. 8, copyright 1973 Taylor and Francis, http://tandfonline.com

blister formation at high temperatures. The critical gas concentration (He atoms/wall atom) for blistering decreases almost linearly from about 0.5 at T/T$_m$ = 0.1 to 0.1 at T/T$_m$ = 0.6, where T is the wall temperature and T$_m$ is the wall melting temperature.

As the total dose is increased at constant energy, the blister density (number of blisters per m^2) increases, but the average blister size changes little. When the blisters are fully grown, or when they overlap, exfoliation begins. In some cases several layers of blisters may be eroded away. The data are often for monoenergetic ion bombardment at normal incidence, where the helium gas tends to accumulate at a depth equal to the ion range. In a fusion reactor, three factors tend to broaden the helium distribution:

- The angular distribution of the incident alphas tends to produce varied ranges.
- Not all alphas will hit the wall with 3.5 MeV energy. Most will slow down to lower energies first.
- The surface will also be eroded away by sputtering, so that the old helium will become closer to the receding surface, and the new helium will be implanted
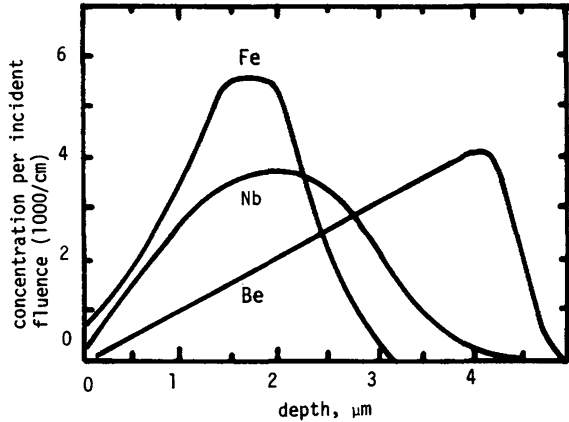
further into the wall. The angular distribution of 3.5 MeV alpha particles striking a typical tokamak wall has been calculated. The implantation profiles corresponding to that angular distribution are shown in Fig. 8.27 for various wall materials.

Blistering can be a source of plasma contamination when the heat flux is high, shortening the lifetime of plasma facing components. Blistering can occur when the critical helium concentration occurs inside the metal before it occurs at the surface. Blistering and flaking may be a problem in cases where sputtering rates are low, most of the alphas are at 3.5 MeV, and the alpha flux is high. If the alpha flux is low, if the alphas are more uniformly distributed in energy, or if sputtering rates are high, then blistering is not likely to be a serious problem.

8.6.7 Unipolar Arcs

Small arcs between the plasma and walls or limiter can constitute a significant source of impurities. The arcs can occur when the plasma potential near the wall $\phi > 15$ V positive with respect to the wall. Such a positive potential could arise as a sheath potential, resulting from rapid electron flow along magnetic field lines to the walls in an adjacent region, or as the result of electric fields parallel to the walls generated within the plasma. In a unipolar arc, the plasma is the anode. A cathode spot with a diameter of a few μm forms on the chamber wall or limiter, as illustrated in Fig. 8.28.

A current flow I > 10 A is required to maintain the arc, and the current density $J \sim 10^9$–10^{12} A/m^2. In vacuum arcs about 8 % of the current is carried by the ions, but such measurements have not been made in unipolar arcs in strong

magnetic fields. An electron return current flows to the walls in an adjacent region over an area on the order of 1 cm^2. The cathode spot moves along the wall in a direction opposite to the $J \times B$ force (retrograde motion) with a velocity on the order of 100 m/s. The cathode spot temperature may exceed 3,000 K, and metal atoms are rapidly lost by vaporization and sputtering, forming a crater in the wall surface. In metals with low melting points, droplets of metal may be sprayed out the sides of the crater by the arc plasma pressure. On the order of 0.02–0.1 wall atoms are lost per unit charge flowing in the arc. If this value were 0.05 and the arc current were 30 A, then about 10^{19} atoms/s would be lost from the wall. In a plasma with $n = 3 \times 10^{19} m^{-3}$ and volume $V = 1$ m^3, a single arc of this size could produce an impurity fraction of 1 % in 30 ms. Some of the metal ions acquire kinetic energies of tens of eV.

The small scratches and fern-like projections attributed to arcing have been observed in many tokamaks and other plasma experiments. It appears that arcing in tokamaks occurs mainly during the buildup of plasma current and during plasma disruptions.

Arcing could be combated by segregating the wall into insulated cells, with areas too small for collection of the return current, but this appears to be impractical. Materials selection involves determining which materials are resistant to arcing and have low atom loss rates per unit of charge flow. A strong preference is given to low-Z elements, since larger impurity fractions of low-Z elements are tolerable in the plasma. Arcing may also be inhibited by use of gas blankets or divertors to reduce the plasma density and temperature near the wall, thus reducing the potential for arcing (The electric field at the wall is proportional to $(n_e T_e)^{1/2}$).

8.6.8 Synergistic Effects

When two or more phenomena act simultaneously on the wall surface, interactions between the phenomena may produce synergistic effects, meaning that the net impurity release rate is not simply a linear sum of the individual process rates. For example:

- The physichemical sputtering process is a combination of both physical and chemical effects.
- Gas desorption rates are influenced by diffusion rates (affected by radiation damage) and by surface conditions (affected by sputtering, etc.)
- Photon and ion irradiation may cause the skin of blisters to overheat and rupture.
- Impurity release from blistering may be reduced if the sputtering rate is high. Almost all the phenomena occurring at the wall are influenced in some way by other phenomena.

Experimental data points usually describe one bombarding species at one energy and angle. The combined effects of many species, energies, and angles may be significantly different.

Total wall erosion rates in ITER are estimated to be about one tonne per year. The wall thinning rates for low-Z materials are about 3.5 mm/y, while for W the rate is about 0.22 mm/y. In contrast to graphite, tungsten does not trap much tritium. Alpha particle heating of the core plasma may tend to inhibit tungsten accumulation there (Behrisch et al. 2003).

8.7 Wall Modifications

The wall is modified by exposure to the plasma (sputtering, etc.). It may also be deliberately modified by controlled processes to minimize damage during plasma bombardment. In addition to impurity introduction and wall surface erosion, bombardment may also weaken the wall's structural integrity by processes like erosion of grain boundaries and crack growth. The near-surface wall modifications may be grouped into five main categories:

1. Phase changes
2. Alloy composition changes
3. Microstructure changes
4. Macrostructure changes
5. Property changes.

8.7.1 Phase Changes

Phase changes may result in surface films, such as oxides, carbides, and hydrides. The changes of thermal conductivity can result in flaking. A phase change can also occur internally, such as a strain-induced austenitic-martensitic transformation in stainless steels. This transition changes the steel's mechanical properties and makes it vulnerable to hydrogen cracking.

8.7.2 Alloy Composition Changes

The composition of an alloy may be modified near the surface by three processes:

- Nuclear transmutations. Both gaseous and solid transmutants are produced.
- Preferential sputtering. Elements with high sputtering yields will be preferentially removed from the surface of an alloy. This also depends upon relative diffusion rates of the alloy constituents towards the surface.
- Diffusion and surface segregation. Various impurities, like carbon, gradually diffuse to the surface, where they are desorbed or sputtered away. In stainless steel, the chromium normally segregates to the surface as an oxide. In a reducing environment (hydrogen), the chromium may be depleted by reduction and solution. The resulting loss of chromium could make the near-surface properties of the wall more like those of an iron-nickel alloy.

8.7.3 Microstructural Changes

Ion bombardment produces many vacancies, interstitials, and dislocation loops in the first 10 nm of the surface, in addition to the neutron-induced radiation damage. These defects can lead to internal stresses, swelling, creep, recrystallization and grain growth, and tritium trapping in the near-surface region.

8.7.4 Macrostructural Changes

Macrostructural changes include nonuniform erosion, cracking, and changes in surface shape.

- Nonuniform erosion and redeposition. The particle fluxes in toroidal devices vary with poloidal angle, and so does the wall erosion rate. The metallic impurities may be redeposited at other locations on the walls, building up flakes.

Cracking. Cracks may be initiated by phase changes, hydrogen implantation, helium production, and neutron damage. Cracks grow under cyclic stresses (fatigue), especially in the presence of chemically active elements. Crack growth may lead to leaks and reduced heat transfer, which increases the surface temperature.

- Topological changes. Blistering and exfoliation leave the surface scarred. Sputtering can leave the surface pitted like a honeycomb. These changes in the surface and near-surface regions reduce sputtering reflux and heat transfer.
- Tungsten fuzz. Under high heat fluxes tungsten may develop a fuzzy surface (Sect. 6.2) The fuzz may have a lower sputtering rate than the original metal.

8.7.5 Property Changes

Many properties near the surface will be affected by the wall modifications, including:

- Physical properties: electrical and thermal conductivity, emissivity, density, optical reflectivity, radioactivity, work function, and magnetic permeability.
- Mechanical properties: ductility, creep rate, crack growth rates.

Plasma-surface interactions and experimental methods for surface studies are reviewed by McCracken and Stott (1979).

8.8 Specific Materials

Most materials under consideration for fusion reactors have already been discussed in previous chapters. In this section we continue the discussion of some materials that are considered for use in ITER and beyond—Be, RAFM, ODS, W, V, SiC, CFC, Cu, superconducting magnets, and liquid metals.

8.8.1 Beryllium

Beryllium is used for the first wall in ITER because it has low atomic number and reasonable mechanical and thermal properties. There is good experience from its use in JET, and it can be bonded well to a water-cooled copper alloy substrate. Its retention of tritium, low allowable temperature, and toxicity, however, would probably prevent its use for the first wall in DEMO.

Type-I (Giant) ELMs would deposit enough energy to melt some of the Be wall, so their occurrence must be minimized by stimulating more frequent Type-III ELMs. A computer code model of the Be wall response finds that much of the sputtered Be would be promptly redeposited in nearby cooler (~ 200 C) "shadow"

regions, trapping some codeposited tritium. The code results are compared with data from Pisces and JET, but there are large uncertainties in the edge plasma parameters and resulting Be wall lifetime estimates. The tritium trapping by Be in ITER could be on the order of several g(T)/hr (Carpentier et al. 2011).

8.8.2 RAFM Steels

After decades of materials research the best candidates for fusion reactor structure are:

- Reduced activation ferritic-martensitic (RAFM, RAF, or FM)
- Oxide dispersion strengthened (ODS) type of RAFM steels with nano-size dispersoids, such as Y_2O_3
- Vanadium alloys, such as V-4Cr-4Ti
- Fiber reinforced Silicon-Carbides SiCf/SiC
- Tungsten alloys.

RAFM steels are designed to have few atoms that will transmute into radioactive isotopes with long half-lives. They have a high initial dislocation density and many lath/grain boundaries, which act as recombination centers for diffusion Frenkel (vacancy/interstitial) pairs. Therefore swelling is very low, and He bubble agglomeration is suppressed down to the nanometer range (Rieth 2008).

RAFM 8–10 % CrWVTa Steels have the following advantages (Reith, 2008):

- Long-term industrial experience with 10–12 % CrMoNbV steels up to 140 dpa
- Better thermal conductivity than austenitic steels (e.g. 316LN)
- High aging resistance (almost no alloy decomposition up to 5×10^4 h)
- Mechanical properties tunable by heat treatment
- Sufficient corrosion resistivity in Pb–Li-Blankets
- Good irradiation Properties.

  - "Low-activation" capable
  - Above irradiation temperature of 400 °C also at high dpa-doses, just small changes
  - Strength, hardness, and ductility
  - Almost negligible He and void swelling.

They also have the following disadvantages

- DBTT decrease after irradiation at $T_{irr} < 400$ °C (but RAFM steels are better than commercial steels)
- 4–5 welding techniques available, but the welds need heat treatments
- Upper operation temperature limited by creep strength: $T_{max} \sim 550$ °C.

Fig. 8.29 Offset yield stress versus dose for EUROFER97 and F82H steels irradiated at 300–355 C and tested at 300–350 C. Full symbols represent BOR60 (fission reactor) experimental data, and open symbols are from previous studies. The solid line is a least square fit to the EUROFER97 data, and the dashed line is just a guide to the eye (Gaganidze et al. 2011, Fig. 1)
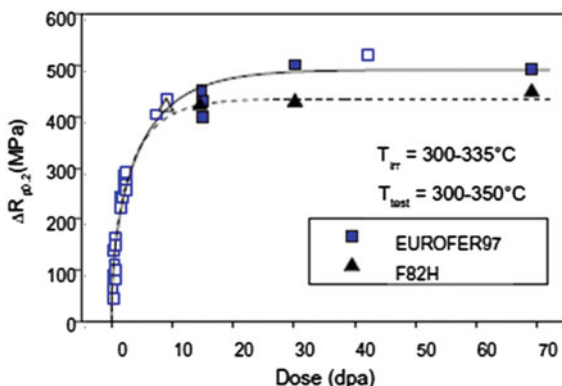
The Japanese RAFM steel F82H (Fe–8Cr–2 W–0.2 V–0.04Ta) has been produced in large heats (∼5 tons) for over 20 years, using techniques such as vacuum induction melting (VIM) and electroslag refining. It has been forged and hot rolled into various thicknesses of plates (15–90 mm) without any cracking or chemical inhomogeneity. Variations of its composition are being studied to improve its qualities (Tanigawa et al. 2011).

EUROFER97 (Fe–9Cr–1W–0.2V– 0.12Ta) is a reduced-activation martensitic steel with a body-centered cubic (bcc) lattice, which has been produced in quantities of many tons using VIM and vacuum arc remelting and formed into plates (up to 48 mm) and tubes. Its microstructure and hardness can be controlled by heat treatment (annealing, quenching), and it can operate up to 550 °C.

Figures 8.29 shows the effects of irradiation in the BOR60 fission reactor on offset yield stress in F82H and EUROFER.

Offset yield stress here means the stress that corresponds to 0.2 % strain. If this stress increases it means that the stress–strain curve is steeper (radiation hardening embrittlement).

Figure 8.30 shows the ΔDBTT (increase of DBTT) caused by irradiation of FH2H and EUROFER.

Radiation hardening and embrittlement appear to saturate at doses over 20 dpa, but the ΔDBTT does not saturate until over 40 dpa. The DBTT limits the lower operating temperature of these steels. The fatigue data, on the other hand, are similar before and after irradiation (Gaganidze et al. 2011). A separate study found that hardening of EUROFER97 did not saturate at doses up to 78 dpa (Henry et al. 2011).

Figure 8.31 shows the creep rupture time versus applied stress for EURO-FER97 and F82H. The creep rupture strength and failure time become too short at T > 550 C.

It is important to remove impurities, which affect mechanical and irradiation properties, and to ensure good homogeneity, because inhomogeneity can reduce strength. Irradiation doses over 10 dpa can cause significant irradiation hardening
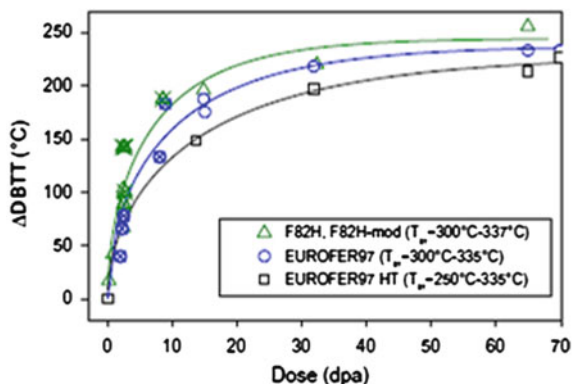
Fig. 8.30 Irradiation shifts of the DBTT versus irradiation dose for EUROFER97, EURO-FER97, HT, and F82H steels. The open symbols represent BOR60 experiment results and the crossed symbols are from previous studies. The solid lines are a model description of the data (Gaganidze et al. 2011, Fig. 4)
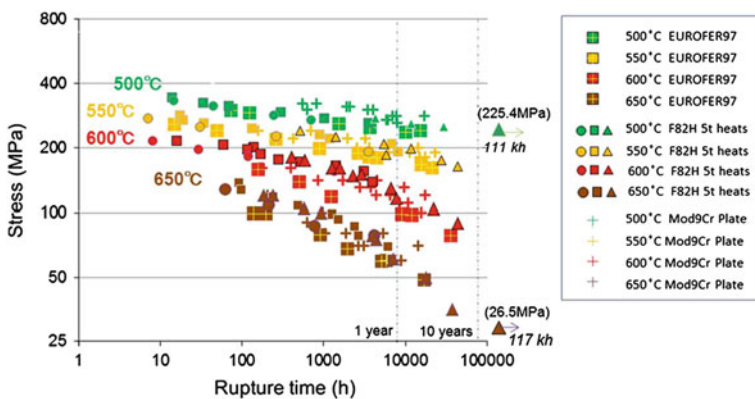
Fig. 8.31 Creep rupture time of F82H and EUROFER at various temperatures. Mod9Cr plate data is plotted for comparison (Tanigawa et al. 2011 Fig. 4)

and DBTT shift in RAFM steels. Welded joints may require post-weld heat treatment to restore ductility (Tanigawa et al. 2011).

8.8.3 ODS Steels

The high temperature creep limit may be improved by using oxide dispersion strengthened (ODS) RAFM produced by powder metallurgy, which might raise T_{max} to the range of 650–750 °C. In an optimum procedure the constituent powders (such as Fe–14Cr–2 W–0.3Ti–0.3Y_2O_3) are rolled in a ball mill to mix sub-

Table 8.11 Comparison of two developmental ODS steels (Rieth 2008)

	Advantages	Disadvantages
12–16 % ODS ferritic steel	Higher temperature	Anisotropic mechanical properties
	Better oxidation resistance	Lower fracture toughness
9 % ODS martensitic steel	Nearly isotropic properties after heat treatment	Limited to T < 700 °C
	Better fracture toughness Scalable fabrication	Marginal oxidation resistance at high temperature

micrometer particles for 45 h. Then they are degassed in a vacuum at 650–850 C for 2 h. Finally they are joined by hot isostatic pressing (HIP) at 1,150 C and 200 MPa for 4 h. So far only small quantities (~10 kg) of RAFM steels have been produced, but European labs and industry are planning to develop larger production capabilities (Baluc et al. 2011).

Table 8.11 compares two developmental ODS steels.

Both ODS alloys promise much better radiation resistance against ductility reduction than RAFM steels without nano-dispersoids.

8.8.4 Tungsten

A fully tungsten wall is being tested in JET, and the ITER divertor will be fully tungsten, in order to minimize tritium trapping.

Table 8.12 lists some properties of tungsten.

Pure tungsten is very brittle and cannot be welded at all, just brazed. The brittleness of tungsten cannot be improved by alloying Ta or Y (nor by Mo, V, Zr, Nb).

Figure 8.32 illustrates how increasing power density affects the surface of tungsten armor.

Melting redistributes the tungsten on the surface. Spraying of tiny droplets (~4 μm diameter) may be tolerable, but splashing larger droplets (>30 μm) may cause a disruption. Resolidified metal has different crystal structure, worse properties, cannot tolerate such high heat flux as originally (Coenen et al. 2010).

Table 8.12 Some properties of tungsten

Melting temperature	3,696 K
Density	18,950 kg/m^3
Thermal conductivity	113 W/(m K)
Poisson's ratio	0.2
Young's modulus	370 GPa
Thermal expansion coefficient	4.5×10^{-6} K^{-1}

Fig. 8.32 Effects of increasing power flux (*top* to *bottom*) on tungsten surface (based on Coenen et al. 2010)
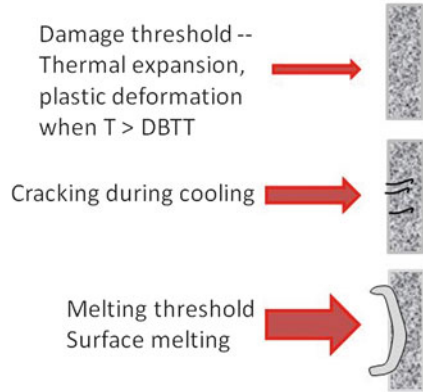
Cracking and melting under high heat loads may damage the tungsten surface and shorten its lifetime. Reliable control of ELMs and disruptions is essential (Philipps 2011).

Tungsten retains much less tritium than Be or C, as shown in Fig. 8.33.

At high temperatures the implanted tritium diffuses out more rapidly, reducing the trapped inventory.

The tungsten impurity fraction in the plasma may be reduced under the following conditions (Philipps 2011):

Fig. 8.33 Retention fraction of T in co-deposited C, Be and W versus Temperature (Roth et al. 2008, Fig. 4)
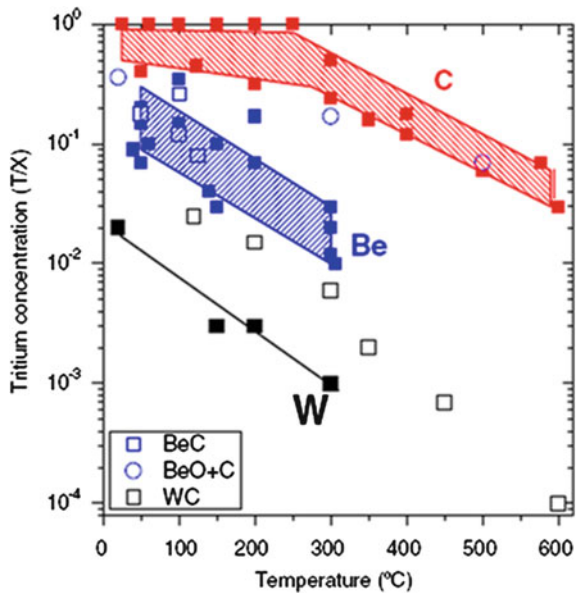
- Low density peaking
- High edge plasma density
- Low plasma temperature at the first wall and divertor target
- Sufficient sawtooth and ELM activity
- Particle transport control by ERCH
- Low densities of medium and high Z elements in the SOL (heavy atoms have high sputtering yields).

Tungsten alone is a poor structural material, so W alloys will probably be used as a surface layer on RAFM to protect it from high heat fluxes. The alloy W-2Ti-$0.47Y_2O_3$ has improved properties, such DBTT below 300–400 °C. Tungsten can be sprayed onto high-heat-flux surfaces or brazed onto RAFM using 55Ni–45Ti brazing material heated by a high-power diode laser beam (infrared wavelength 810 or 940 nm) in vacuum, being careful to exclude oxygen. The problem of thermal stress due to different thermal expansion coefficients may be mitigated by using intermediate soft layers. Gases trapped in the melt layer can cause porosity of the joint (Munez et al. 2011).

8.8.5 Vanadium

Vanadium alloys like V–4Cr–4Ti are compatible with lithium coolant up to about 700 C, with a low-temperature limit ∼400 °C (Zinkle 2000). Impurities have a significant influence on irradiation hardening of vanadium alloy in liquid lithium during tests at 425–509 C up to 3.7 dpa (Fukumoto et al. 2011). In order to avoid embrittlement the annealing temperature should be below 1,000 °C, because at 1,100 °C TiNOC blocks dissolve, increasing the number of free impurities and resultant radiation hardening (Muroga et al. 2011).

Advanced fine-grain alloys may use plastic deformation, heat treatments, and additives like W, TiC, and Y to expand the operating temperature window by improving strength and ductility. Processes are being developed to minimize impurities like C, N, and O, which can degrade performance. Titanium can bind with these elements to inhibit their bad effects. High annealing temperatures (∼1,100 C) tend to cause significant radiation hardening and DBTT shift, while lower annealing temperatures (800–1,000 °C) are better (Chen et al. 2011).

The radioactivity of V–4Cr–4Ti might cool enough to permit recycling after about 60 years, if impurity concentrations were low enough, but Al, Nb, Ag, Mo, and Co impurities could make this unfeasible. Impurities like O and H also affect the ductility of V alloy welds. At oxygen levels > 300 wppm concentrations of Cr + Ti greater than about 10 % cause an increase of the DBTT, but lower oxygen concentrations could permit more Cr + Ti, which are good for high temperature creep strength (Muroga et al. 2002; Dolan and Butterworth 1994).

A tungsten layer can be bonded to vanadium by vacuum plasma spraying or by brazing, but embrittlement may occur (Nagasaka et al. 2011).

8.8.6 Ceramics

Ceramics are used for high heat flux materials in divertors, limiters, and first walls; for insulators; for windows; for thermal insulation, and for neutron moderation and shielding. Ceramics are subject to thermal stress, creep, and fatigue problems, compounded by the fact that most of them are brittle even before irradiation. Neutron irradiation can cause a significant swelling, loss of thermal conductivity, and degradation of the *loss tangent*, which increases power loss in rf windows by radio waves and microwaves. Most of the ceramics applications have fabrication difficulties related to their large size, configuration, unusual materials, or need for very high quality (Clinard 1979).

8.8.7 Graphite

Graphite has good thermal shock resistance, neutron reflection and moderation capability, high-temperature stability, and low atomic number. During neutron irradiation graphite first shrinks, then swells, as shown in Fig. 8.34.

Arjakov et al. (2011) present equations to describe graphite swelling in the parallel and perpendicular directions.

Graphite suffers from chemical sputtering, absorbs much tritium, and co-deposits with tritium in hydrocarbon compound films, creating a high tritium inventory. However, if the graphite is operated at very high temperatures ($\sim$1,000 °C), the tritium retention is greatly reduced (Stangeby 2010).

The useful life of graphite at 1,000–1,400 °C is limited to about 1–20 dpa. Graphite cloths and fibers have withstood fast fission neutron fluences of 10^{26} neutrons/m^2 and remained intact.

Fig. 8.34 Length changes of type 9,640 graphite parallel and perpendicular to the direction of molding as functions of the number of dpa (Kulcinski 1976)
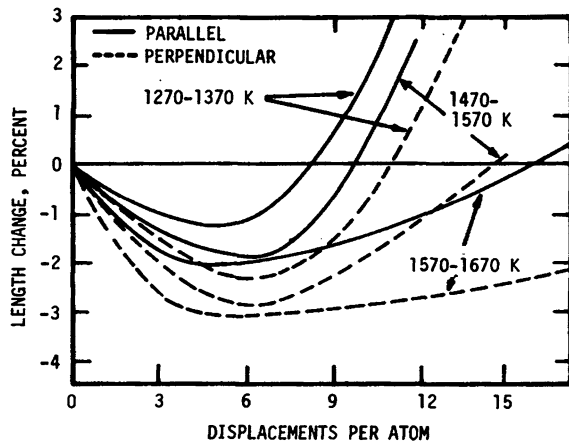
The various forms of graphite may have markedly different properties. For example, the stress limit of bulk graphite is about 15–25 MPa, while that of pyrolitic graphite is about 250 MPa.

8.8.8 Silicon Carbide

Silicon carbide is not quite as good as graphite for thermal shock, but it has better stability under neutron irradiation up to its maximum use temperature.

Table 8.13 shows some properties of Silicon carbide composite. Fiber thicknesses are typically around 7–12 μm.

A silicon carbide composite (SiC) first wall with PbLi coolant with a neutron wall load of 6 MW/m^2 would typically suffer up to 100 dpa/FPY (FPY = full power year) and generate up to 10^4 appm(He)/FPY.

Figure 8.35 shows how the thermal conductivity and swelling of SiC vary with neutron fluence (represented in dpa) and temperature.

It is apparent that high temperature operation increases thermal conductivity and reduces swelling.

Inclusion of carbon nanofibers in SiC composite reduces its strength and elastic modulus, but increases its thermal conductivity (Taguchi et al. 2011).

Irradiation to 6 dpa at 800–1,300 °C caused insignificant change of tensile strength of the SiC composites tested. An interphase PyC thickness (between fiber and matrix) of 20 nm allowed slippage and failure, but thicknesses of 50–150 nm yielded good results (Katoh et al. 2011).

Table 8.14 shows some solid transmutation products that would be produced in SiC.

Most of the Al produced is stable ^{27}Al, but a fraction would be further changed into ^{26}Al, which emits a 1.8 MeV gamma ray with a half-life of 726,000 years, so the SiC could require safe disposal if the dose rate were significant.

SiC is also useful for flow channel inserts to provide electrical and thermal insulation in ducts containing Li or PbLi coolant, to reduce the MHD pressure drop and to protect the steel walls from the hotter coolant temperatures.

Table 8.13 Properties of silicon carbide composite (Chen et al. 2008; Snead et al. 2011)

Density ρ_m	kg/m^3	2,500
Porosity	%	10
Specific heat c_p	J/kg K	600
Poisson ratio		0.18
Thermal expansion coefficient α	K^{-1}	3E−6
Thermal conductivity k	W/m K	5–15
Young's modulus E	GPa	200
Electrical conductivity σ	$(\Omega\ m)^{-1}$	20

Fig. 8.35 Fluence-dependent evolutions of swelling and thermal conductivity of carbon vapor deposited (CVD) SiC (Katoh et al. 2010)

	appm
Li	0.6
Be	851
B	0.6
Mg	22.3
Al	762
P	16.4
Total	3,862
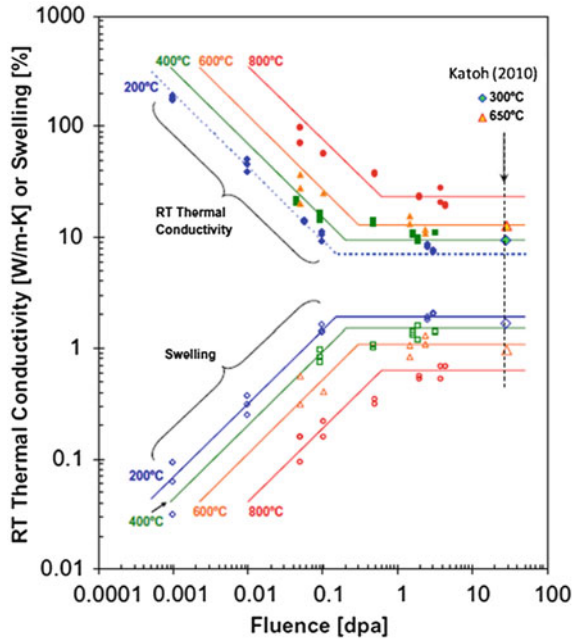
Table 8.14 Solid transmutation products produced in SiC at a fast neutron (>0.1 MeV) fluence of 10^{23} cm^{-2} (Snead et al. 2011)

Researchers are developing improved methods of manufacturing SiC fibers for use in composites, such as varieties of the Nano-Infiltration and Transient Eutectic-phase (NITE) form. By controlling fiber structure, matrix density, and homogeneity they have achieved fiber strengths over 2 GPa (Kohyama et al. 2011).

Several methods, including diffusion bonding, are under development for joining SiC components. For example, the NITE form of SiC may be joined using powders of $SiO_2 + Al_2O_3 + Y_2O_3$ at 10–20 MPa pressure and temperatures of 1,700–1,900 °C. This joint did not degrade after 6 dpa irradiation at 800 °C (Snead et al. 2011).

A tungsten layer can be bonded onto SiC by diffusion bonding or sintering (Kishimoto et al. 2011). Direct bonds between F82H RAFM steel and SiC at 1,000 °C

Table 8.15 Advantages and disadvantages of SiC

Advantages
Low decay heat
Low tritium trapping
Low radioactivity of pure SiC
Low chemical reactivity
Good electrical insulator
Disadvantages
Low thermal conductivity
Irradiation damage at high neutron fluences not quantified
Compatibility with PbLi uncertain at high temperatures

and 10 MPa under vacuum fail, due to differences of thermal expansion coefficients, but intermediate layers of W/Cu or W/Ni/Cu/Ni yield durable bonds (Zhong et al. 2011). Table 8.15 compares some features of SiC.

8.8.9 Copper

Copper or copper alloy is used to stabilize superconducting magnets (Chap. 4) and as substrate for actively-cooled plasma facing components, such as beryllium and tungsten. Copper is also widely used in electrical and cooling water systems, but those uses are not unique to fusion reactors and will not be discussed here.

For radiation damage levels of 10^{-5} to 0.01 dpa, resistivities of Cu and Al increase to unacceptably high values, as shown in Fig. 8.36. Most of the resistivity increase accumulated at 4 K may be annealed out by warming the coils to room temperature, however.

In pulsed coils, the cyclic strain increases the resistivity of the stabilizer, as shown in Fig. 8.37.

This problem can be avoided by keeping the strain low, which requires stiff structural materials.

8.8.10 Superconducting Magnets and Cryostats

In addition to copper, the other components of superconducting magnets may also be affected by radiation.

Radiation damage effects on NbTi are slight, but the critical current and critical temperature of Nb_3Sn and similar compounds drop off at fluences around 10^{-3} dpa (3×10^{22} neutrons/m^2). Adequate shielding can avoid this problem.

Pulsed magnetic fields induce eddy current dissipation in metallic structures, adding to the heat load on the refrigeration system. A non-conducting composite

Fig. 8.36 Radiation-induced resistivities of aluminum and copper (Kulcinski 1976)
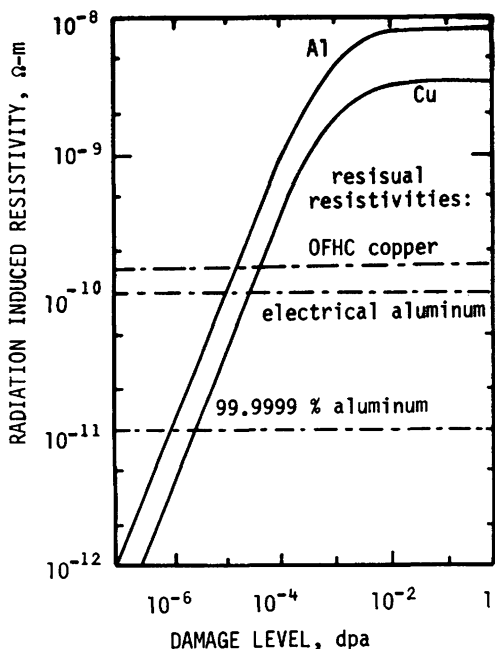
Fig. 8.37 Degradation of residual resistivity ratio, R(295 K)/R(9 K), of the copper stabilizer in a commercial NbTi conductor with number of cycles of cyclic strain, for various values of strain range (Fickett et al. 1979, Fig. 7)
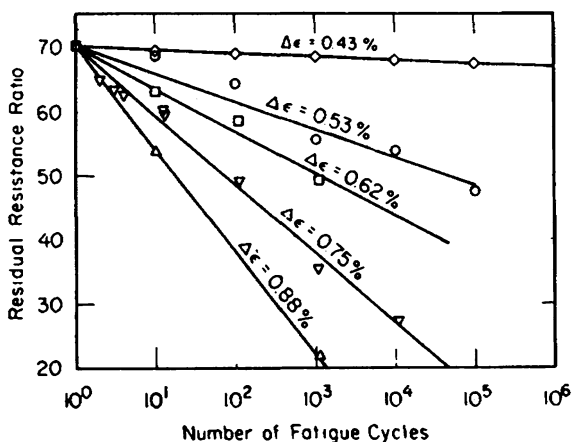
structure, such as epoxy-fiberglass, would eliminate this problem. However, the low modulus of elasticity of the epoxy-fiberglass composite would permit high conductor strains, causing degradation of the stabilizer conductivity. Use of strong, stiff fibers such as graphite, boron, and Kevlar-49 (Du Pont Co.) is under study.

Electrical insulation in coils and thermal insulation in cryostats may be seriously degraded by neutron and gamma irradiation. Their properties during low temperature irradiation are not well known. Eddy-current heating in aluminized

plastic superinsulation may produce unacceptable heat loads for pulsed coils. Inorganic insulators are being considered, but they are brittle and may not be durable under stress.

Many structural materials are brittle at 4 K, including carbon steels, alloy steels, titanium alloys, ferritic and martensitic stainless steels, and magnesium alloys. Nickel alloys and superalloys are ferromagnetic at 4 K and expensive. Austenitic stainless steels have been used for most cryogenic structural applications, but weld strength and ductility are major problems. Because the neutron fluence through superconducting coils is kept very low, radiation damage to the structure is not a problem. Properties of some materials at low temperatures are discussed in Chap. 10.

8.8.11 Liquid Metals

Liquid metals, such as gallium, tin, and lithium, are considered for use in high heat flux areas, because they can carry high heat loads, are not affected by radiation damage, and can repair themselves after a disruption. Some properties of Ga, Sn, and Li are listed in Table 8.16. Lithium-lead eutectic data are provided by Mas de les Valls et al. (2008).

Gallium and tin have little chemical reactivity with hydrogen isotopes, so they are not effective at reducing hydrogen recycling from the walls, but lithium absorbs hydrogen, forming LiH, which decomposes at 688 °C. Hydride formation can saturate the lithium ability to absorb hydrogen unless the lithium flows quickly

Table 8.16 Properties of Ga, Sn, and Li (Majeski 2010)

Gallium

> Z = 31, atomic weight = 69.7
> Melting point = 29.8 °C, boiling point = 2,204 °C
> Liquid density = 6. g cm^{-3}, sp. heat capacity = 0.37 J/g °C
> Thermal conductivity: 40.6 W/m °C, electrical res. = 140 nΩ m
> Vapor pressure = 10−7 Torr at 900 °C

Tin

> Z = 50, atomic weight = 118.7
> Melting point = 232 °C, boiling point = 2,602 °C
> Liquid density = 7.0 g cm^{-3}, sp. heat capacity = 0.23 J/g °C
> Thermal conductivity: 66.8 W/m °C, electrical res. = 115 nΩ m
> Vapor pressure = 10−7 Torr at 1,000 °C

Lithium

> Z = 3, atomic weight = 6.9
> Melting point = 180.5 °C, boiling point = 1,342 °C
> Liquid density = 0.5 g cm^{-3}, sp. heat capacity = 3.58 J/g °C
> Thermal conductivity: 84.8 W/m °C, electrical res. = 93 nΩ m
> Vapor pressure = 10−7 Torr at 400 °C
> Hydrogen diffusivity $\sim 10^{-4}$ cm^2/s

Fig. 8.38 Evaporation rates of Li, FLIBE, SnLi, Sn, and Ga versus temperature (Majeski 2010)
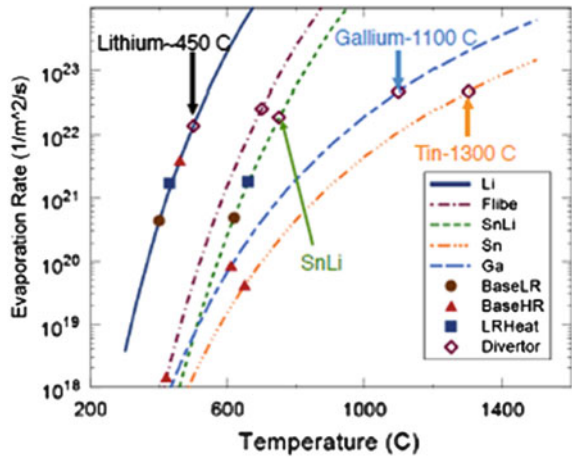
out of the reactor and is regenerated externally by decomposition. This saturation problem does not occur in Sn and Ga.

For high power reactors where recycling is not a problem Ga and Sn may be better than Li, because they can operate at higher temperatures, so that the wall and its coolant could be hotter, reducing the amount of tritium trapped in the wall. The wall would not need to tolerate such a high heat flux as the liquid metal film, so it could be of simpler, more reliable materials. Lithium, on the other hand, could improve plasma confinement (Sect. 7.10), facilitating smaller fusion reactors, so it might play a different role than Ga and Sn (Majeski 2010).

Lithium is the most chemically active of the three, and gallium, the least. Lithium is compatible with refractory metals, vanadium, niobium, and steels even above 400 °C, but it attacks most ceramics, except for Y_2O_3 and Er_2O_3. PbLi is preferred over Li as a breeder and coolant (Chap. 6).

Figure 8.38 shows the evaporation rates of candidate liquid metals.

In spite of its high evaporation rate, little accumulation of lithium was observed in the core plasmas of many tokamaks, such as NSTX. The required flow rates of lithium in a heat flux of 2–5 MW/m^2 are 5–10 m/s. Lower flow rates ($\sim$cm/s) are satisfactory for removal of tritium from the lithium to avoid saturation. To replenish the lithium film two processes are being tested:

- Lithium could gradually seep out of porous tungsten mesh or cloth by capillary action to provide a source of fresh lithium on the wall, but on a time scale of many seconds. For example, in the Red Star laboratory (Russia) lithium film has handled power fluxes up to 50 MW/m^2 for short periods.
- A thermo-electrical effect can propel lithium rapidly along the surface (Jaworski et al. 2010).

8.9 Dust in Fusion Devices

Dust is produced by ejection of matter from plasma facing components (by sputtering, melting, splashing, blistering, vaporization, arcs) followed by solidification and deposition on surfaces. The dust particles may contain many elements, including wall materials, divertor materials, H, C, N, O, and other impurities, with many possible compounds, especially if graphite is present in the device. Dust may contain toxic and radioactive material, so it should be considered a potentially hazardous source term in safety analyses.

The dust particles may interfere with plasma confinement, increase radiation losses, or even trigger a disruption, if they fall into the plasma. Therefore, researchers are measuring dust particle locations, composition, and size distribution, in order to predict what will happen in future experiments like ITER. Dust accumulation in ITER is likely to occur in hidden areas, such as between armor tiles. ITER has in-vessel inventory limits for C, Be and W dust of 200, 100, and 100 kg. The amount of dust on hot surfaces is limited to 6 kg for each species (Rudakov et al. 2008).

8.9.1 Dust Measurement on Surfaces

A novel electrostatic dust detector for monitoring dust in these regions has been developed and tested at PPPL. In DIII-D tokamak dust diagnostics include Mie scattering from Nd:YAG lasers, visible imaging, and spectroscopy. Laser scattering resolves size of particles between 0.16 and 1.6 μm in diameter; the total dust content in the edge plasmas and trends in the dust production rates within this size range have been established. Individual dust particles are observed by visible imaging using fast-framing cameras, detecting dust particles of a few microns in diameter and larger. Dust velocities and trajectories can be determined in 2D with a single camera or 3D using multiple cameras, but determination of particle size is problematic. In order to calibrate diagnostics and benchmark dust dynamics modeling, pre-characterized carbon dust has been injected into the lower divertor of DIII-D. Injected dust is seen by cameras, and spectroscopic diagnostics observe an increase of carbon atomic, C2 dimer, and thermal continuum emissions from the injected dust. The latter observation can be used in the design of novel dust survey diagnostics (Rudakov et al. 2008).

Samples collected during entry vents allow to determine dust size distribution, chemical composition, and estimate the in-vessel dust inventory. However, this technique typically provides information averaged over months of operations and thousands of plasma discharges, so correlating dust production and accumulation rates with the discharge parameters is hardly possible (Rudakov et al. 2008).

Electrostatic dust collectors use fine interlocking grids that can discharge when a dust particle lands, providing an electrical signal and removing the dust, Fig. 8.39.

These are not sensitive to very small amounts of dust, but will function better in large devices like ITER. Other measurement techniques include capacitive diaphragm microbalance, infrared thermography, and laser breakdown spectroscopy (Rudakov et al. 2008).
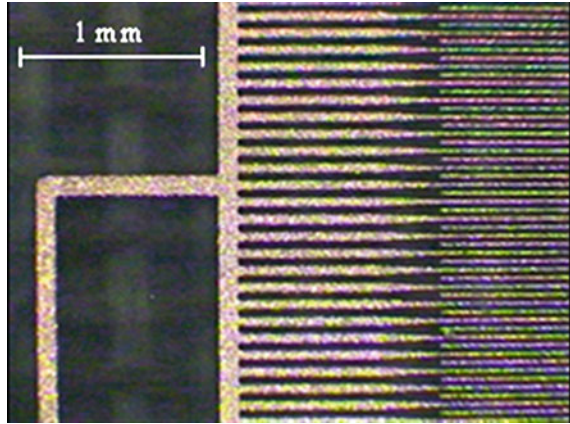
8.9.2 Dust Measurement in Plasma

Many plasma diagnostic techniques can also be used to detect dust particles and their motion. Multiple cameras can detect motion in 3D. Laser scattering can distinguish sizes of very small particles. Spectroscopic measurements provide information about average constituents of dust particles.

In DIII-D, dust particles have been injected into the scrape-off layer (SOL). Multiple short-pulse ND:YAG lasers can illuminate dust particles in a small volume (<1 cm^3) for viewing by multiple polychromators. Thomson scattering measurements can provide information about particle size distribution and spatial profiles in the SOL.

A fast framing CMOS camera ($<26,000$ frames/s at 256×256 pixel resolution) can detect particle speeds and breakup into smaller particles. Thousands of dust particles are seen during disruptions and in subsequent discharges.

8.9.3 Dust Effects and Removal

Dust particles are a drag force on ion flows and their motion is similar to plasma residual rotations in tokamaks. They may be electrostatically charged to high values ($\sim 10^4$ e). They affect the radial electric field, which affects the internal transport barriers in tokamaks (Tsypin et al. 2004). In Z pinches and tokamaks dust particles may form nanoscale tubular filaments that persist for long times (Kolbasov et al. 2001).

Dust tends to adhere to surfaces, so energy is needed to remove it. Laser beam impact can blast dust off the surface ("dry surface cleaning"). For heavy atoms like W, the beam ejects photoelectrons from the dust, giving it a positive charge that can push it off the surface. A short-pulse uv laser is best for this purpose, which would be difficult to implement in ITER. Alternatively a laser-induced shock wave

could blast particles out of cracks ("laser-induced shockwave cleaning"). Collection of the ablated dust is difficult in vacuum, but can be done with a suction device in air. The laser source and suction device could both be mounted on a remote handling arm inside the tokamak. Cleaning rates of about 1 m^2/hr are anticipated for both techniques (Vatrya et al. 2011). A special dust transporter as adjacent thin planar electrodes designed for KSTAR demonstrated 10 mg/h dust removal rate (Kurnaev 2012).

8.10 Irradiation Facilities

8.10.1 Need for Fusion Neutron Source

Figure 8.40 shows why a strong 14 MeV neutron source is needed to study fusion reactor materials. The production of gases (H, D, He) occurs mainly at high energies, and the fission reactor neutrons mainly have lower energies.

Figure 8.41 shows how the ratio of helium atoms generated by (n, α) reactions to dpa varies from fission reactors (He/dpa ∼ 0.5–2) to fusion reactors (He/dpa ∼ 10) to spallation neutron sources (He/dpa ∼ 30).

The European Spallation Source (ESS) in Lund, Sweden, will produce an intense source of neutrons by impact of a 5 MW, 2.5 GeV proton beam onto a target of tungsten or Pb–Bi eutectic, but the neutron energy spectrum will not match that of a fusion reactor (Banks 2011).

In the Rotating Target Neutron Source—II (RTNS-II), a 400 keV, 0.15 A deuteron beam struck a rotating tritiated target to generate up to 4×10^{12} 14 MeV neutrons/s, which resulted in a neutron flux $\sim 10^{17}$ m^{-2} s^{-1}.

Fig. 8.40 Neutron energy spectra from fission reactors (BOR60, HFR, HFIR) and the predicted fusion neutron spectrum for the DEMO fusion power plant. The fission reactors lack high energy neutrons. The curves at the right show the cross sections for production of He, H, and D in steel by neutron impact, which are greatest at high neutron energies (Rieth 2008, From work by A. Möslang, KIT)
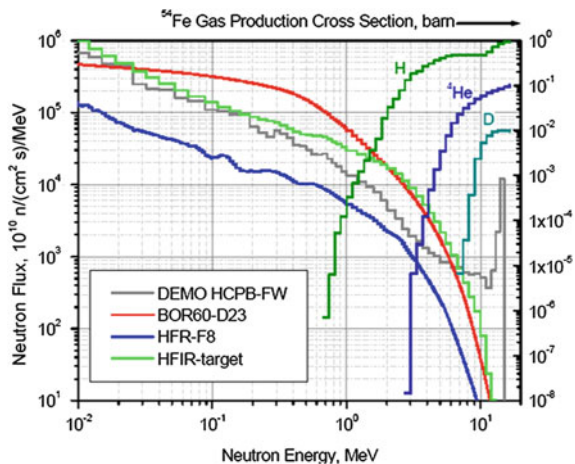
Fig. 8.41 Ratio of He/dpa from various neutron sources (Rieth 2008)
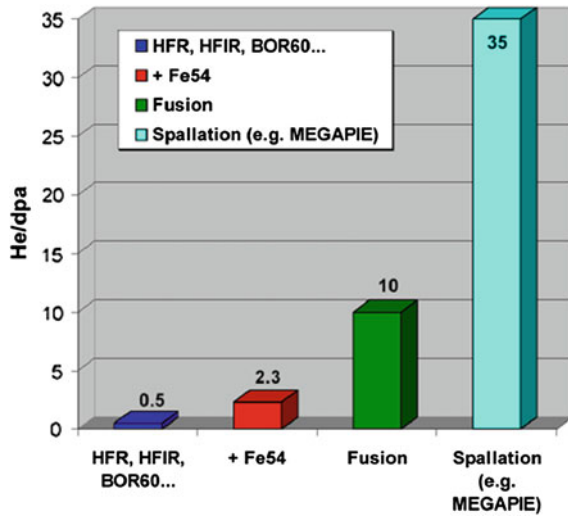
8.10.2 IFMIF Parameters

Japan and Europe are collaborating on the International Fusion Materials Irradiation Facility (IFMIF), which will be built at Rokkasho, Japan. This will use deuteron beams striking a flowing lithium target.

The predicted neutron energy spectra from IFMIF and DEMO are compared in Fig. 8.42.

The following information is based on the "International Fusion Materials Irradiation Facility (IFMIF) Comprehensive Design Report", IFMIF International Team (2004).

The capabilities of IFMIF will be:

- High flux region (V = 0.5 L) $\geq$ 20 dpa/a
- Medium-flux region (V = 6 L) $\geq$1 dpa/fpy
- Temperature control
- Miniaturized specimens
- Post-irradiation examination (PIE)
- Availability $\geq$70 %.

  First phase: 3 years, half-intensity

- Screening candidate structural materials
- Calibrating data from fission reactors and ion beams.

  Second phase: 20 years, full power test facility
  Figure 8.43 shows a cutaway drawing of IFMIF.
  The main IFMIF parameters are:
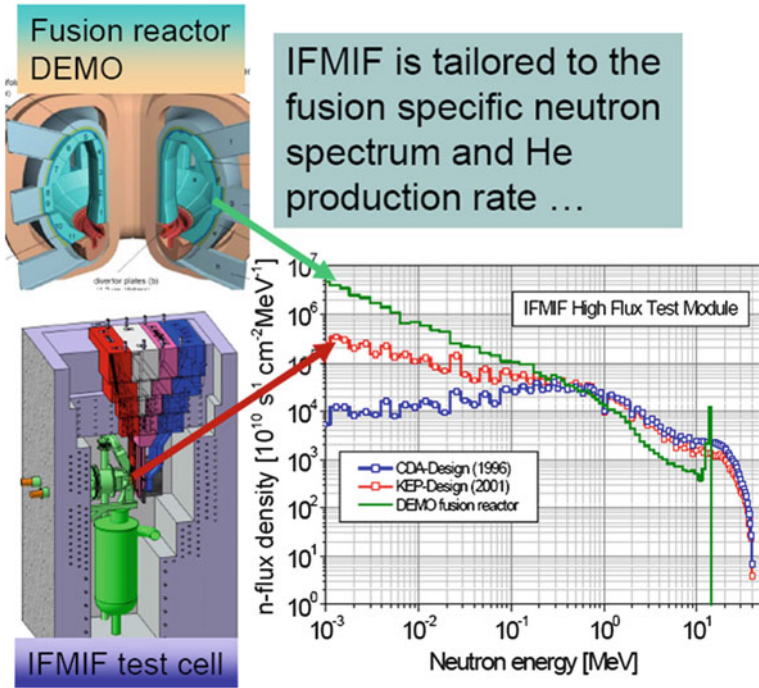
Fig. 8.42 Comparison of predicted IFMIF and DEMO neutron energy spectra (Rieth 2008, From work by A. Möslang, KIT)

2 D$^+$ beams each	40 MeV, 125 mA
Beam deposition area on target	0.2 m × 0.05 m
Jet velocity	15 m/s
Average target heat flux	1 GW/m^2
Li flow rate	130 l/s
Pressure at Li surface	10^{-3} Pa
Hydrogen isotopes content in Li	<10 wppm
Impurity content (each C, N, O)	<10 wppm
Structure	SS-316
Back wall replacement period	11 months
Other components lifetime	30 years
Availability	>95 %

The IFMIF Accelerators will have the following parameters:

- Two Electron Cyclotron Resonance (ECR) ion sources will provide 95 keV 140-mA deuteron beams.
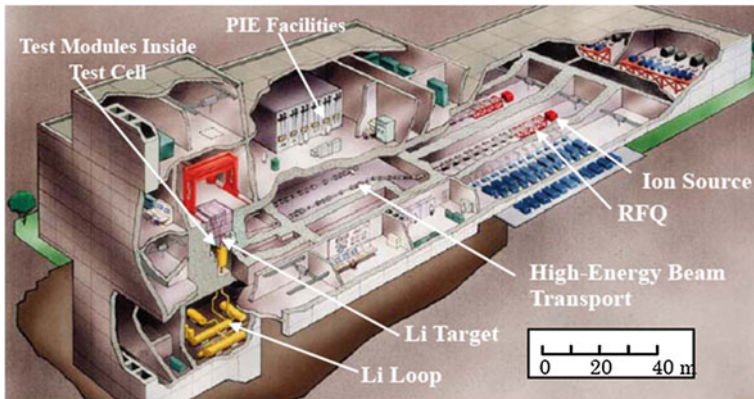
Fig. 8.43 The International Fusion Materials Irradiation Facility (IFMIF 2004)

- Two Radio-Frequency-Quadrupoles (RFQ) will accelerate 125 mA each from 95 keV up to 5 MeV.
- Two Alvarez Drift Tube Linacs, each 124 mA, will boost the beam energies up to 40 MeV.
- Each accelerator uses 13×1 MW, 175-MHz amplifiers.

The accelerator design lifetime is 30 years. Figure 8.44 shows the IFMIF test cell.

A thermal analysis shows that the flowing lithium target will stay well below its boiling temperature.

The main impurities in the lithium will be H, D, T, C, N, O, activated corrosion products, and ^{7}Be (53 day half-life). A cold trap can remove most of the ^{7}Be, but some will stick to tube walls. If it is not removed, the ^{7}Be saturation activity would be 4.5×10^{15} Bq = 140 kCi.

The specimens will be in helium-cooled modules, as in Fig. 8.45.

The two-dimensional distribution of the dpa rate is shown in Fig. 8.46.

High flux zone specimens will be irradiated to 80–150 dpa at the temperatures shown:

Ferritic-martensitic (ODS) steels	250–650 °C, 150 dpa
Vanadium alloys	350–650 °C, 150 dpa
SiC/SiC- composites:	600–1,100 °C, 150 dpa
Refractory metals (e.g. W-alloys)	650–1,100 °C, 80 dpa
Brazing materials and joints	650–1,100 °C, 80 dpa

Fig. 8.44 The IFMIF Test Cell (IFMIF 2004)
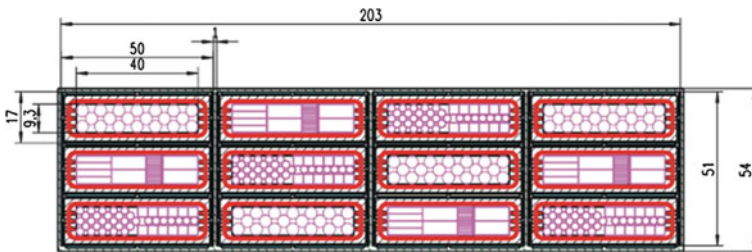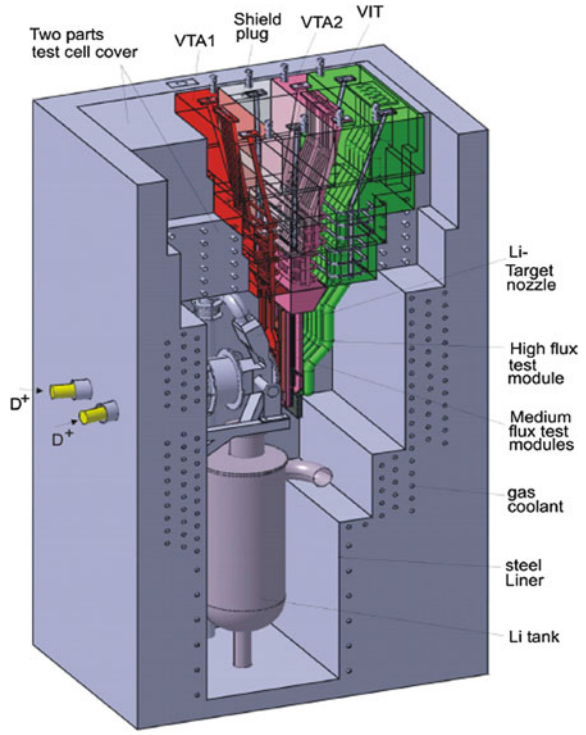
Fig. 8.45 A helium-cooled high flux module. Dimensions are in mm (IFMIF 2004)

Table 8.17 shows the tests planned.

The design will provide good safety and environmental characteristics. Remote handling will be able to deal with dose rates $>10^5$ Sv/h, including recovery of failed equipment. The design is fail-safe, fault-tolerant, and redundant. It is able to cope with foreseeable hazards, including a lithium fire, radioactivity release, and high voltage breakdowns.
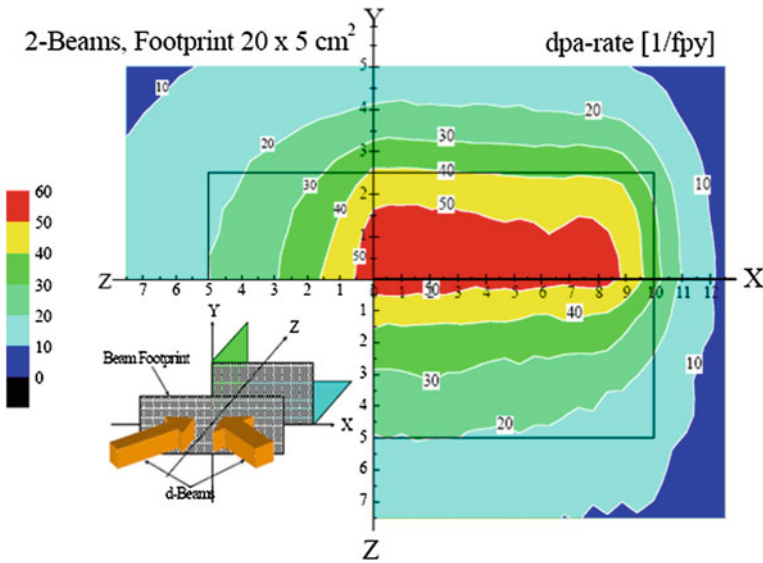
Fig. 8.46 The dpa rate in high flux module is on the order of 30–60 dpa/a (IFMIF 2004)

Decommissioning and Waste Disposal are planned to ensure compliance with pertinent standards. The dose rate is expected to decrease to the "hands-on level" of 10 μSv/h after a cooling period of 100–300 years.

The 2003 cost estimate had the following items:

	M\$ (2003)
Engineering design	88
Construction	540
Installation and testing	117
Operations 23 years	1,827
Decommissioning	50
Total	2,622

The host country (Japan) will manage the waste products.

Fusion researchers in the USA are considering a "Fusion Nuclear Science Facility" (FNSF) to cover the knowledge gaps that ITER does not resolve. It might have the following features: (Abdou 2012)

- Q ∼ 2–3
- Normal TF coils
- Thermal power ∼ 100–200 MW
- First wall neutron power flux ∼ 1–2 MW/m^2
- Test long-term burn control
- Test materials
- Demonstrate tritium breeding and inventory control

Table 8.17 Tests planned in the IFMIF facility

Specimen type	High flux zone		
	Multiplicity	Volume per specimen (cm^3)	Total in HFTM*
Microstructure/swelling	≥ 5	0.0014	≥ 120
Tensile	6	0.075	144
Fatigue	9–10	0.249	216–240
Fracture toughness	3	0.560	72
Crack growth	2	0.280	48
Dynamic fracture toughness	12	0.291	288
Creep	8	0.133	192
Specimen type	Low flux zone		
	Multiplicity	Volume per specimen (cm^3)	Total in HFTM
Microstructure/swelling	≥ 5	0.0014	≥ 120
Tensile	6	0.075	144
Fatigue	9–10	0.249	216–240
Fracture toughness	3	0.560	72
Crack growth	2	0.280	48
Dynamic fracture toughness	12	0.291	288
Creep	8	0.133	192

*HFTM means high flux test module

- Test Reliability, Availability, and Maintenance (RAM) issues
- Provide data for the DEMO reactor design
- Maybe generate some electricity.

8.11 Materials Selection Considerations

Figure 8.47 shows the approximate operating temperatures of some structural materials (same as Fig. 6.20).

These estimates are for materials irradiated to 10–50 dpa, which somewhat narrows the operating range, due to radiation damage. The lavender bars on the left and pink bars on the right represent uncertainties in those temperature limits. The low temperature limits are due to embrittlement, and the high temperature limits are due to many processes, such as creep, sputtering, corrosion, melting, and vaporization.

Usually the design stress is kept below the yield stress (elastic regime), but it is also possible to use "Design by Analyses", including the effects of plastic flow to accommodate higher heat fluxes. Tungsten components should be operated above 800 °C to avoid embrittlement and below 1,300 °C to avoid recrystallization. The maximum plastic strains accumulated over the operating life should be less than 50 % of the uniform elongation. For the pure tungsten, the allowable plastic strain is ~0.8 % at 270 °C and 1 % at about 1,200 °C. The finger-tube concept could
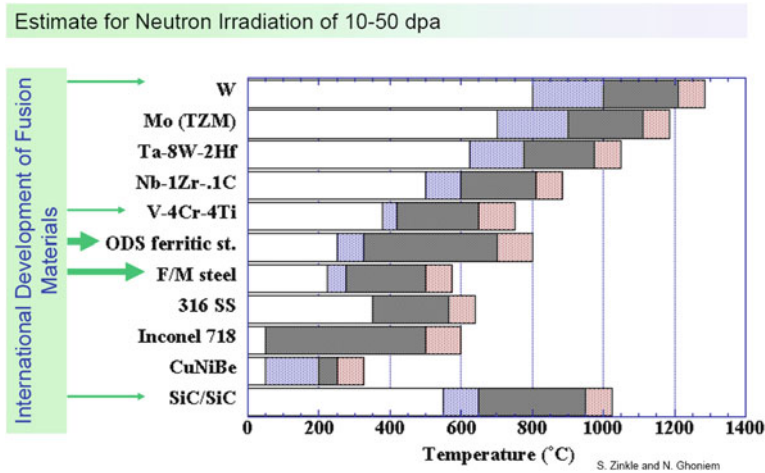
Fig. 8.47 Operating temperatures of some structural materials. Arrows indicate favored materials (Zinkle and Ghoniem 2000)

handle up to 13 MW/m^2 in the elastic regime, and about 20 % higher heat fluxes in the plastic regime, while keeping the pumping power below 10 % of the divertor power flow (Wang et al. 2011, 2012).

8.12 Summary

Materials limit the allowable coolant temperature, which affects the energy conversion efficiency. Wall materials sputtering causes plasma contamination, which can limit the plasma temperature and duration. Radiation damage limits component lifetimes, which affect the power plant availability. Mechanical failure might result in release of tritium, a safety hazard.

Radioactivity affects the recycle and clearance of structural materials when the plant is decommissioned.

Some ideas for dealing with these issues should be demonstrated in ITER, including test blanket modules, but its water-cooled stainless steel structure is not suitable for an economical power plant. Additional research and development of advanced materials, such as RAF and SiC composites, will be needed for DEMO and beyond. The lack of an intense 14-MeV neutron source, which has delayed materials research for several decades, should be alleviated by IFMIF. A volumetric neutron source is also needed for materials development.

8.13 Problems

8.1. Assume that a stainless steel wall may be represented as iron for a sputtering estimate, and that the plasma edge temperature is 1,000 eV. Calculate the wall erosion rate (mm/year) due to a total ion flux of 10^{20} ions/m^2 s, of which 95 % are D-T ions, 5 % are alpha particles, and 0.07 % are wall atoms.

8.2. If the reactor of problem 1 is a torus with R = 10 m, a = 3 m, and the plasma density is 2×10^{20} fuel ions/m^3 (constant), estimate the rate at which Fe impurities build up as a result of sputtering, assuming that the impurities are perfectly confined. How long does it take to build up an impurity fraction of 10^{-3}?

8.3. Estimate the evaporation rate (mm/year) for a Ti wall at 1,400 K. $\rho_m = 4,540$ kg/m^3.

8.4. If 0.1 MJ of plasma energy is dumped on 1 m^2 of a 1,000 K vanadium reactor wall in 0.1 ms, estimate the peak temperature, number of atoms evaporated by the thermal spike per m^2, and the wall thickness loss.

8.5. Vanadium has a linear expansion coefficient of 7.9×10^{-6}/K, a modulus of elasticity of 1.3×10^{11} Pa. Assume Poisson's ratio is 0.3. If the reactor has Q = 12, $P_n = 2.2$ MW/m^2 (maximum), and the wall temperature is approximately 1,000 K, estimate the peak thermal stress in a 5 mm wall.

8.6. A SS 316 wall (annealed) undergoes a wall loading $P_n = 1.9$ MW/m^2 (total flux $= 6.9 \times 10^{18}$ neutrons/m^2 s) for 2 years. Estimate the displacement damage (dpa), total helium production (appm) and total Mn production (appm). Estimate the volumetric swelling, assuming swelling is linearly proportional to appm(He). What would the corresponding linear expansion be? Assume wall temperature = 773 K.

8.7. A wall with $P_n = 1.9$ MW/m^2 has a graphite armor plate in front of it. What would be the dimensional change of the graphite at 1,700 K parallel and perpendicular to the molding direction after 1 year?

8.8. If the first wall neutron flux is 7×10^{18} neutrons/m^2 s, what attenuation factor must the blanket and shield provide to avoid significant damage to Nb$_3$Sn coils over a 20 year lifetime?

8.14 Review Questions

1. What is a secondary knock-on atom?
2. Sketch an interstitial dislocation loop.
3. What are the consequences of (n,α) and (n,p) reactions?
4. In what metal do thermal neutron (n,α) reactions lead to He production?
5. Explain dpa/year, and how large the values are for typical fusion reactor materials.

6. Name four sources of stress in fusion reactor materials.
7. Explain radiation hardening and DBTT shift.
8. What is indicated by a diamond-shaped pattern of light channels in a metal?
9. What is the mechanism of He embrittlement?
10. What occurrences in fusion reactors lead to cyclic stresses?
11. Explain thermal creep.
12. What conditions affect the swelling rate?
13. What is the difference between spontaneous and stimulated desorption?
14. How can the rate of spontaneous desorption be estimated?
15. Explain the meaning of the following equation and its parameters:

$$S = 0.0064 \, m_2 \gamma^{5/3} E^{1/4} \left(1 - \frac{1}{E}\right)^{7/2}, \quad \gamma \equiv \frac{4 m_1 m_2}{(m_1 + m_2)^2}$$

$$(1 < E) < 30), \quad (m_1/m_2 \leq 0.4)$$

16. What is "physichemical sputtering"?
17. Explain the following equation and its parameters:
    $\phi_n = 2.6 \times 10^{24} \, \alpha p/(AT)^{1/2}$
18. Under what conditions might blistering be significant?
19. Describe a unipolar arc, and when it may occur.
20. Name two disadvantages of graphite as a plasma facing material.
21. What problems are associated with ceramics in fusion reactors?
22. What problems are associated with pulsed Nb_3Sn coils in a fusion reactor?
23. For IFMIF what will be the ion beam species, energy, current, and target?
24. What are the disadvantages of RAFM steels?
25. What are the advantages of ODS over other FM steels?

References

Abdou M (2012) Revitalizing fusion power. Technology of fusion energy conference, Nashville, TN, USA, 23–29 Oct

Arjakov MV, Subbotin AV, Panyukov SV, Ivanov OV, Pokrovskii AS, Kharkov DV (2011) Irradiation induced dimensional changes in graphite: the influence of sample size. J Nucl Mater 420:241–251

Averback RS, Ghaly M (1997) Fundamental aspects of defect production in solids. Nucl Instrum Methods Phys Res B I27(128):1–11

Badger B, et al (1976) UWMAK III, a noncircular tokamak power reactor design, Electrical Power Research Institute report ER-368

Baluc N et al (2007) Status of R&D activities on materials for fusion power reactors. Nucl Fusion 47:S696–S717

Baluc N, Boutard JL, Dudarev SL, Rieth M, Brito Correia J, Fournier B, Henry J, Legendre F, Leguey T, Lewandowska M, Lindau R, Marquis E, Munoz A, Radiguet B, Oksiuta Z (2011) Review on the EFDA work programme on nano-structured ODS RAF steels. J Nucl Mater 417:149–153

Banks M (2011), Neutron target station takes the heat, Physics world, September 29. http://physicsworld.com/cws/article/indepth/47369. Accessed 11 Apr 2011

Baskes MI (1980) A Calculation of the Surface Recombination Rate Constant for Hydrogen Isotopes on Metals. J Nucl Mater 92:318–324

Bauer W, Wilson KL, Bisson CL, Haggmark LG, Goldston RJ (1979) Alpha transport and blistering in tokamaks. Nucl Fusion 19(93):102 Figures 5, 6, 7

Bay HL, Bohdansky J (1979) Sputtering yields for light Ions as a function of angle of incidence. Appl Phys 19:421–426, Figure 3 (Institut fuer Plasmaphysik der Kernforschungsanlage Juelich GmbH, D-5170 Juelich, Fed. Rep. Germany)

Behrisch R (1972) First-wall erosion in fusion reactors. Nucl Fusion 12:695–713

Behrisch R, Federici G, Kukushkin A, Reiter D (2003) First-Wall erosion in fusion reactors, J Nucl Mater 313–316:388

Bloom EE, Stiegler JO (1971) Irradiation effects on structural alloys for nuclear reactor applications. ASTM-STP-484, American Society for Testing Materials, 1916 Race St., Philadelphia, PA, 19103

Carpentier S, Pitts RA, Stangeby PC, Elder JD, Kukushkin AS, Lisgo S, Fundamenski W, Moulton D (2011) Modeling of beryllium erosion–redeposition on ITER first wall panels. J Nucl Mater 417:S165–S169

Chen H, Wu Y, Konishi S, Hayward J (2008) A high temperature blanket concept for hydrogen production. Fusion Eng Des 83:903–911

Chen JM, Chernov VM, Kurz RJ, Muroga T (2011) Overview of the vanadium alloy researches for fusion reactors. J Nucl Mater 417:289–294

Clinard FW Jr. (1979) Ceramics for applications in fusion systems. J Nucl Mater 85 & 86:393–404

Coenen J, et al (2010) Material and power-handling properties of tungsten PFCs after steady state melting and additional transients, MIIFED

De Temmerman G, Baldwin MJ, Doerner RP, Nishijima D, Seraydarian R, Schmid K (2009) Insight into the co-deposition of deuterium with beryllium: influence of the deposition conditions on the deuterium retention and release. J Nucl Mater 390–391:564

Dolan T, Lazan, Horger (1954) Basic concepts of fatigue damage in metals, Fatigue. American Society for Metals, Materials Park, Ohio, USA

Dolan TJ (1980) Gas emission from chamber walls. J Nucl Mater 92:112–120

Dolan TJ, Butterworth GJ (1994) Vanadium recycling. Fusion Technol 26:1014–1020

Erents SK, McCracken GM (1973) Blistering of molybdenum under helium ion bombardment. Radiation effects 18:191 Figure 8

Fickett FR, Reed RP, Dalder ENC (1979) Structures, insulators and conductors for large superconducting magnets. J Nucl Mater 85 & 86:353–360, (Figure 7)

Fong JT (ed) (1979) Fatigue mechanisms, special technical publication 675. American Society for Testing and Materials, Philadelphia

Fraas AP, Thompson AS (1978) ORNL fusion power demonstration study: fluid flow, heat transfer, and stress analysis considerations in the design of blankets for full-scale fusion reactors, ORNL/TM-5960

Fukumoto K, Kuroyanagi Y, Kuroiwa H, Narui M, Matsui H (2011) Effect of impurities on mechanical properties of vanadium alloys under liquid-lithium environment during neutron irradiation at HFIR. J Nucl Mater 417:295–298

Gaganidze E, Petersen C, Materna-Morris E, Dethloff C, Weiß OJ, Aktaa J, Povstyanko A, Fedoseev A, Makarov O, Prokhorov V (2011) Mechanical properties and TEM examination of RAFM steels irradiated up to 70 dpa in BOR-60. J Nucl Mater 417:93–98

Garner FA, Toloczko MB, Spencer BH (2000) Comparison of swelling and irradiation creep behavior of fcc-austenitic and bcc-ferritic/martensitic alloys at high neutron exposure. J Nucl Mater 276:123, (Figure 23)

Haggmark LG, Biersack JP (1979) Monte Carlo studies of light ion reflection from metal surfaces", Joumal of Nuclear Materials 85 & 86: 1031–1036

Henry J, Averty X, Alamo A (2011) Tensile and impact properties of 9Cr tempered martensitic steels and ODS-FeCr alloys irradiated in a fast reactor at 325 C up to 78 dpa. J Nucl Mater 417:99–103

Honig RE, Kramer DC (1969) Vapor pressure data for the solid and liquid elements, RCA Review 30:285

Hotston ES (1980) A current induced diffusion model of gas sputtering. J Nucl Mater 88:279–288

IAEA (2012) Atomic and Plasma–Material Interaction Data for Fusion, vol 15. International Atomic Energy Agency, Vienna, Austria, and previous volumes in this series

IFMIF Design Team (2004) International fusion materials irradiation facility comprehensive design report. International Energy Agency, Paris

Jaworski MA, Gray TK, Antonelli M, Kim JJ, Lau CY, Lee MB, Neumann MJ, Xu W, Ruzic DN (2010) Thermoelectric magnetohydrodynamic stirring of liquid metals. Phys Rev Lett 104:094503

Katoh Y, Snead LL, Nozawa T, Kondo S, Busby JT (2010) Thermophysical and mechanical properties of near-stoichiometric fiber CVI SiC/SiC composites after neutron irradiation at elevated temperatures. J Nucl Mater 403:48

Katoh Y, Ozawa K, Hinoki T, Choi Y, Snead LL, Hasegawa A (2011) Mechanical properties of advanced SiC fiber composites irradiated at very high temperatures. J Nucl Mater 417:416–420

Kishimoto H, Shibayama T, Shimoda K, Kobayashi T, Kohyama A (2011) Microstructural and mechanical characterization of W/SiC bonding for structural material in fusion. J Nucl Mater 417:387–390

Kohyama A, Park JS, Jung HC (2011) Advanced SiC fibers and SiC/SiC composites toward industrialization. J Nucl Mater 417:340–343

Kolbasov BN, Kukushkin AB, Rantsev Kartinov VA, Romanov PV (2001) Tubular structures in various dust deposits in tokamak t-10. Plasma Devices Oper 8(4):257–268

Kulcinski GL (1976) Radiation damage: the second most serious obstacle to commercialization of fusion power, vol 1, Radiation effects and tritium technology for fusion reactors, CONF-750989, pp 1–61

Kurnaev V (2012) Personal communication

Majeski R (2010) Liquid metal PFC development for power plants. ARIES town meeting on edge plasma physics and plasma material interactions in the fusion power plant regime, University of California, San Diego, 20–21 May

Marmar ES, Overskei D, Helava H, Chen KI, Terry JL, Moos HW (1979) The effects of wall temperature on light impurities in Alcator (1979). Nucl Fusion 10:485–488

Mas de les Valls E et al (2008) Lead-lithium eutectic material database for nuclear fusion technology. J Nucl Mater 376:353–357

Materna-Morris E, Schneider H-C, Dafferner B, Rolli R, Romer O, Möslang A (2003) Mechanical properties and structural analysis of martensitic low-activation alloys after neutron irradiation. In: Proceedings of 20th IEEE/NPSS symposium on fusion engineering, 14–17 Oct 2003, San Diego, CA USA, Figure 6. (Author address: Forschungszentrum Karlsruhe GmbH, Institut for Materials Research, P.O. Box 3640, 76021 Karlsruhe, Germany.)

Maziasz PJ, Wiffen FW, Bloom EE (1976) Radiation effects and tritium technology for fusion reactors. CONF- 750989, US Energy Research and Development Administration, March

McCracken GM, Stott PE (1979) Plasma-Surface interactions in tokamaks. Nucl Fusion 19:889–981

Munez J, Garrido MA, Rams J, Urena A (2011) Experimental study of W-EUROFER laser brazing for divertor application. J Nucl Mater 418:239–248

Muroga T, Nagasaka T, Abe K, Chernov VM, Matsui H, Smith DL, Xu Z-Y, Zinkle SJ (2002) Vanadium alloys—overview and recent results. J Nucl Mater 307–311:547–554

Muroga T, Nagasaka T, Watanabe H, Yamazaki M (2011) The effect of final heat treatment temperature on radiation response of V–4Cr–4Ti. J Nucl Mater 417:310–313

Nagasaka T, Muroga T, Watanabe H, Kasada R, Iwata N, Kimura A (2011) Mechanical properties of V–4Cr–4Ti alloy after first-wall coating with tungsten. J Nucl Mater 417:306–309

ORNL (2012) The following site was active in 2012. http://www.ornl.gov/sci/MATextreme/particle.shtml

Philipps V (2011) Tungsten as material for plasma-facing components in fusion devices. J Nucl Mater 415:52–80

Rieth M (2008) High temperature materials, 2nd International Summer School on Fusion Technology, Karlsruhe Institute of Technology (KIT), Germany, 1–12 Sept

Roth J, Bohdansky J, Ottenberger W (1979) Data on low energy light ion sputtering. Max-Planck-Institut fuer Plasmaphysik Report IPP 9/26

Roth J, Tsitrone E, Loarer T, Philipps V, Brezinsek S, Loarte A, Counsell GF, Doerner RP, Schmid K, Ogorodnikova OV, Causey RA (2008) Tritium inventory in ITER plasma-facing materials and tritium removal procedures. Plasma Phys Control Fusion 50:103001, 20 pp, (Figure 4)

Rudakov DL, Yu JH, Boedo JA, Hollmann EM, Krasheninnikov SI, Moyer RA, Muller SH, Pigarov A Yu, Rosenberg M, Smirnov RD, West WP, Boivin RL, Bray BD, Brooks NH, Hyatt AW, Wong PC, Roquemore AL, Skinner CH, Solomon WM, Ratynskaia S, Fenstermacher ME, Groth M, Lasnier CJ, McLean AG, Stangeby PC (2008) Dust Measurements in Tokamaks. Rev Sci Instrum 79:10F303

Smith DL (1978) Physical sputtering model for fusion reactor first-wall materials. J Nucl Mater 75:20–31, Table 4

Snead LL, Nozawa T, Ferraris M, Katoh Y, Shinseki R, Aswan M (2011) Silicon carbide composites as fusion power reactor structural materials. J Nucl Mater 417:330–339

Stangeby P (2010) Carbon as a flow-through, consumable PFC material, ARIES Town Meeting on edge plasma physics and plasma material interactions in the fusion power plant regime. University of California, San Diego, May

Taguchi T, Hasegawa Y, Shampoo S (2011) Effect of carbon nanofibers dispersion on the properties of PIP-SiC/SiC composites. J Nucl Mater 417:348–352

Tanigawa H, Shiba K, Moslang A, Stoller RE, Lindau R, Sokolov MA, Odette GR, Kurtz RJ, Jitsukawa S (2011) Status and key issues of reduced activation ferritic/martensitic steels as the structural material for a DEMO blanket. J Nucl Mater 417:9–15

Tsypin VS, Vladimir SV, Galvão RMO, Nascimento IC, Tendler M, Kuznetsov YK (2004) Particle flows in dusty plasmas of the tokamak edge. Phys Plasmas 11:4138–4141

Vatrya A, Grisolia C, Delaporte P, Sentis M (2011) Removal of in vessel Tokamak dust by laser techniques. Fusion Eng Des 86:2717–2721

Wang XR, Malang S, Tillack MS, ARIES Team (2011) High performance divertor target plate for a power plant: a combination of plate and finger concepts. Fusion Sci Technol 60:219

Wang XR, Malang S, Tillack MS, Burke J, ARIES Team (2012) Recent improvements of the helium-cooled W-based divertor for fusion power plants. Fusion Eng Des 87:732-736

Was GS (2007) Fundamentals of radiation materials science, metals and alloys. Springer, Berlin

Wiffen FW (1976) Oak Ridge National Laboratory report ORNL/TM-5624

Zhong ZH, Hinoki T, Kohyama A (2011) Microstructure and mechanical strength of diffusion bonded joints between silicon carbide and F82H steel. J Nucl Mater 417:395–399

Zinkle SJ, Ghoniem NM (2000) Operating temperature windows for fusion reactor structural materials. Fusion Eng Des 51–52:55–71

Zinkle SJ, Ghoniem NM (2011) Prospects for accelerated development of high performance structural materials. J Nucl Mater 417:2–8

Chapter 9
Vacuum Systems

Thomas J. Dolan and Martin J. Neumann

Objectives

After studying this chapter one should understand

Gas flow and pumping rate calculations
Vacuum pumps and gages
Vacuum chambers, components and techniques
ITER vacuum systems.

9.1 Background

9.1.1 Historical Development

The notion that "Nature abhors a vacuum" can be traced back as far as Aristotle (384–322 BC). It was known in the Middle Ages that one must make a hole in the top of a wine barrel in order to let wine out a small hole in the bottom of the barrel. The first artificial vacuum was produced by Galileo (1564–1642) using a piston and cylinder. He stated that the maximum height to which water may be raised by suction is about 10 m (1638). Torricelli inverted a mercury-filled tube, and related the height of the column of mercury to the pressure of the atmosphere around 1644. Pascal discussed the variation of pressure with altitude (1647), and Perier verified these predictions by carrying a mercury barometer up a mountain (1648) (Middleton 1964).

T. J. Dolan (✉)
NPRE Department, University of Illinois, Urbana, IL 61801, USA
e-mail: dolantj@illinois.edu

M. J. Neumann
Department of Nuclear, Plasma and Radiological Engineering University of Illinois
at Urbana-Champaign, Champaign, IL, USA
e-mail: mneumann@illinois.edu; martin@mjneumann.com

The first successful vacuum pump was built in 1650 by Otto von Guericke. He demonstrated the force of the atmosphere in 1654 by putting two copper hemispheres together and pumping out air. Two teams of eight horses were unable to separate the hemispheres until air was readmitted.

Boyle (1627–1691) combined the vacuum pump and barometer, and he obtained pressures less than 0.01 atm. He observed that the volume of a gas at constant temperature is inversely proportional to its pressure. Charles (1787) stated that at constant pressure, the volume of a gas increases linearly with its temperature. In 1801 Dalton observed that the total pressure of a mixture of gases is equal to the sum of the partial pressures of the constituents.

In 1874 H. McLeod invented a mercury gage which could measure pressures down to about 10^{-3} Pa. In 1892 Fleuss used an oil seal with a piston-cylinder pump, of the type invented by von Guericke, to obtain low pressures. In 1905 W. Kaufman and W. Gaede invented a rotary pump that could produce pressures of 10^{-3} Pa. In 1906 pressure gages were devised by Volge and by Pirani, based on the principle that the thermal conductivity of a gas is proportional to its pressure. These gages were effective in the range from 0.1 to 200 Pa.

During the period from 1910 to 1920 many advances were made. Gaede invented a rotary turbine molecular pump and also the mercury diffusion pump. D. E. Buckley invented the ionization gage, which could measure pressures down to 10^{-6} Pa. In 1928 C. R. Burch introduced oil as a pumping fluid in diffusion pumps.

For many years it appeared that pressures below 10^{-6} Pa could not be obtained. Then in 1947 Nottingham discussed the limitation of ionization pressure gages by photoelectron emission from X-rays. Based on this theory in 1950 Bayard and Alpert devised a new ionization gage, which could measure down to 10^{-8} Pa. Since then the development of cryogenic technology has further improved vacuum technology.

The standard unit of pressure in the Systeme Internationale (SI) units is the Pascal (Pa), but the units of Torr (named after Torricelli) have been standard in vacuum technology for many years (760 Torr = 1 atm). Some units of pressure are summarized in Table 9.1.

Various regimes of vacuum have been defined, Table 9.2.

Table 9.1 Units of pressure

Unit	Pa
atmosphere (760 torr)	1.01325×10^5
bar	10^5
dyne/cm^2	0.10000
kg-force/mm^2	9.80665×10^6
mm (Hg)	133.322
torr	133.322
pound-force/in^2, psi	6894.76
ksi	6.89476×10^6

Table 9.2 Vacuum regimes versus pressure (Pa)	High	10^{-4} to 0.1
	Ultrahigh	$<10^{-4}$
	Extreme high	$<10^{-10}$

9.1.2 Need for Ultra-High Vacuum

An ultra-high vacuum (P < 1 mPa) is needed in fusion devices in order to keep the fuel mixture of deuterium and tritium very pure. In a typical experiment, the air is first pumped out of the chamber until a pressure $\sim 10^{-5}$ Pa or lower is attained. Then the gas to be used for the experiment is admitted to the desired pressure, typically around 0.1–10 Pa. Finally, the gas is ionized and the resulting plasma is heated up to high temperatures, which increases its pressure by many orders of magnitude. If the initial vacuum pressure were 10^{-3} Pa and the filling pressure of experimental gas were 0.1 Pa, then gas would already have an impurity content of about 1 %, which could cause large radiative power losses (Chap. 3). Plasma discharges gradually remove adsorbed impurities from the walls. In some experiments many days of operation elapse before the chamber becomes sufficiently clean.

The following sections describe the equations for gas flow in vacuum, pumps, gages, chambers, and ultrahigh vacuum techniques.

9.2 Viscous Flow and Molecular Flow

The mean free path of gas molecules between collisions is

$$\lambda = k_1/p \quad \text{(m)} \tag{9.1}$$

where p is the pressure (Pa) and the constant k_1 has the following values:
air = 0.0068 (Pa-m)
H_2 = 0.0141
He = 0.0195
N_2 = 0.00813
O_2 = 0.00916
Ar = 0.00933
Ne = 0.0149
H_2O = 0.0127

There is a decrease in λ at low temperatures, due to intermolecular forces. The Knudsen number is defined as

$$\text{Knudsen number} = Kn = \lambda/D$$

Viscous flow Kn = λ/D < 0.01

Molecular flow Kn = λ/D > 1
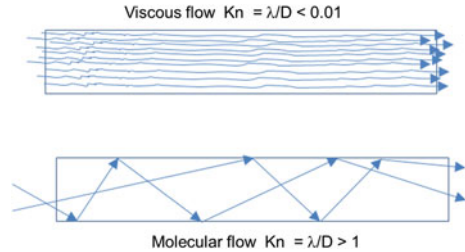
where D is the tube diameter. At low values of Kn. the gas molecules collide with each other much more frequency than with the wall (viscous flow).

$$\text{If Kn} = \lambda/D < 0.01, \text{ the flow is \textbf{viscous}.}$$
$$\text{If Kn} = \lambda/D > 1, \text{ the flow is \textbf{molecular}.}$$

(9.2)

The "transition region" $0.01 < \lambda/D < 1$ has characteristics of both types of flow.

At high values of Kn. the molecules collide with the walls more than with each other (molecular flow), Fig. 9.1.

At high flow velocities, viscous flow becomes turbulent flow. In terms of the gas viscosity η, mass density ρ, and flow velocity v, turbulent flow can be expected when the dimensionless Reynold's Number

$$\text{Re} = Dv\rho/\eta \geq 2200.$$

(9.3)

The average velocity of the fluid, v, should not be confused with the random velocities of the thermal motion of individual molecules, which are much larger. For simplicity, we will consider only viscous and molecular flow.

9.2.1 Throughput

Consider the case of two chambers at pressure P_1 and P_2 with volume V_1 and V_2 connected by a tube with length L and diameter D, as illustrated in Fig. 9.2.

The gas flow rate past any plane perpendicular to the tube axis from the high-pressure chamber P_2 to the low-pressure chamber P_1 is called the "throughput" Q, and has units of Pa m^3/s (1 Pa m^3/s = 1 W). The throughput may be calculated from the equation:

$$Q = C(P_2 - P_1) = (P_2 - P_1)/Z \quad (\text{Pa m}^3/\text{s})$$

(9.4)

Fig. 9.2 Gas flow from a chamber at pressure P_2 to a chamber at a lower pressure P_1. The connecting tube has conductance C and impedance Z = 1/C. The throughput or energy flow rate is Q
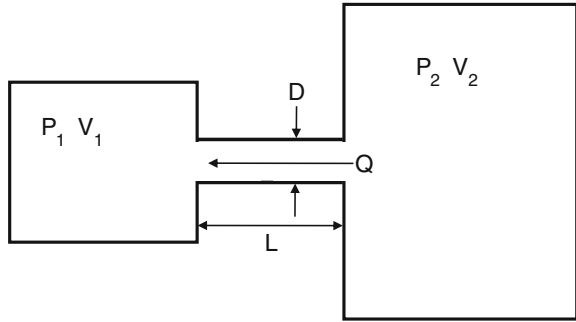
where C is called the "**conductance**" of the tube (m³/s), and Z = 1/C is called the "**impedance**" of the tube (s/m³). This flow circuit is analogous to an electrical circuit: Q corresponds to current, Z to resistance, and $(P_1 - P_2)$ to the voltage difference across the resistance.

The throughput Q represents an energy flow rate, which may be expressed in terms of the number of molecules flowing past a given point per second:

$$Q = d(PV)/dt = kT \, d(nV)/dt = kT \, dN/dt \qquad (9.5)$$

where k is the Boltzmann constant, T is the gas temperature, dN/dt is the number of molecules flowing past per second. Therefore,

$$dN/dt = Q/kT. \qquad (9.6)$$

The average flow velocity v of a gas with local pressure P flowing through a tube with area A is given by:

$$v = Q/PA. \qquad (9.7)$$

The average speed of molecular thermal motion is:

$$v_{th} = (8kT/\pi m)^{1/2}. \qquad (9.8)$$

Where m is the mass of one gas molecule (kg). Usually $v \ll v_{th}$.

Example Problem 9.1 Flow Rate: N_2 gas at 293 K is flowing through a 0.1 m diameter tube at 1 Pa with throughput of 0.1 Pa-m³/s. Find the average flow velocity, the average speed of thermal motion, the molecular flow rate, and the flow regime.

The area $A = \pi D^2/4 = 0.00785$ m²,

From Eq. (9.7) we find v = 12.7 m/s.

From Eq. (9.8) with m = 4.68×10^{-26} kg for N_2, we find that $v_{th} = 469$ m/s.

From Eq. (9.6) dN/dt = 2.47×10^{19} molecules/s.

From Eq. (9.1) $\lambda = 8.1$ mm, so $\lambda/D = 0.08$, and the flow is in the transition region.
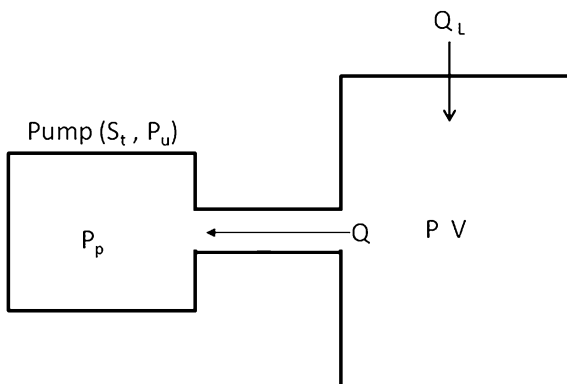
9.2.2 Flow Equations

The throughput of a pump is given approximately by the equation:

$$Q = S_t(P_p - P_u) \qquad (9.9)$$

where S_t is the theoretical pumping speed (commonly called the *pumping speed*), P_p is the pressure at the pump, and P_u is the *ultimate pressure* attainable by the pump, limited by gases backstreaming from the pump. Pumping speeds have units of m^3/s, as do conductances. If the pump is connected to a chamber at pressure P by a tube with conductance C, as shown in Fig. 9.3, then

$$Q = C(P - P_p) \qquad (9.10)$$

If P_p is eliminated between Eqs. (9.9) and (9.10), the throughput may be written:

$$Q = (P - P_u)S_tC/(S_t + C). \qquad (9.11)$$

The rate of change of pressure in the chamber can be calculated from the equation

$$V(dP/dt) = \text{inflow} - \text{outflow} = Q_L - Q \qquad (9.12)$$

where Q_L is the leak rate. The leak rate has contributions from leakage through cracks, virtual leaks (gas trapped in internal cracks), desorption of adsorbed monolayers of molecules on vacuum chamber surfaces, outgassing of materials in the vacuum system, vapor pressures of materials in the vacuum system, and permeation of gases through the system walls and windows.

The above Eqs. (9.4–9.12) apply to both viscous and molecular flow. If the conductance is known, the time variation of pressure can be estimated from these equations, but the leak rate is usually difficult to quantify, and it may vary in time.

Pumping speed S_t and conductance C both have units of m^3/s, but different meanings. Conductance gives the flow rate relative to pressure difference between two locations, while pumping speed tells the flow rate relative to the pressure at the pump inlet minus its ultimate pressure.

9.2.3 Conductance

In the **viscous flow** regime, Re < 1200 and the conductance of a circular tube with diameter D and length L is found from the Poiseuille equation:

$$C = 1430(D^4 P_{av}/L) \, (\eta_{air}/\eta) \quad (m^3/s) \tag{9.13}$$

where P_{av} is the average pressure in the tube, η is the viscosity of the flowing gas, and η_{air} is the viscosity of air at 1 atm, 273 K. Viscosities of some gases are listed in Table 9.3.

For rectangular ducts with length L and cross sectional dimensions a and b, the viscous regime conductance is

$$C = 2070(Y \, P_{av} a^2 b^2/L) \, (\eta_{air}/\eta) \quad (m^3/s) \tag{9.14}$$

where Y is a function of the ratio a/b with values as follows (Roth 1976, p. 76):

a/b	Y
1.0	1.00
0.9	0.99
0.8	0.98
0.7	0.95
0.6	0.90
0.5	0.82
0.4	0.71
0.3	0.58
0.2	0.42
0.1	0.23

For the **molecular flow** regime, consider the situation of Fig. 9.4.

According to the kinetic theory of gases the rate at which molecules pass through the hole from left to right is $n_1 \, v_{th1} \, A/4$, where n_1 and v_{th1} are the density and average molecular speed of gas 1 (flowing left to right). A similar relation holds for gas 2 (flowing right to left), so the net molecular flow rate from right to left is

$$dN/dt = (A \, n_2 v_{th2}/4) - (A \, n_1 v_{th1}/4). \tag{9.15}$$

Table 9.3 Viscosities of selected gases at 100 kPa (http://en.wikipedia.org/wiki/Viscosity#Gases)

Gas	At 0 °C (273 K)	At 27 °C (300 K)
Air	17.4 μPa·s	18.6 μPa·s
Hydrogen	8.4	9.0
Helium		20.0
Argon		22.9
Xenon	21.2	23.2
Carbon dioxide		15.0
Methane		11.2
Ethane		9.5
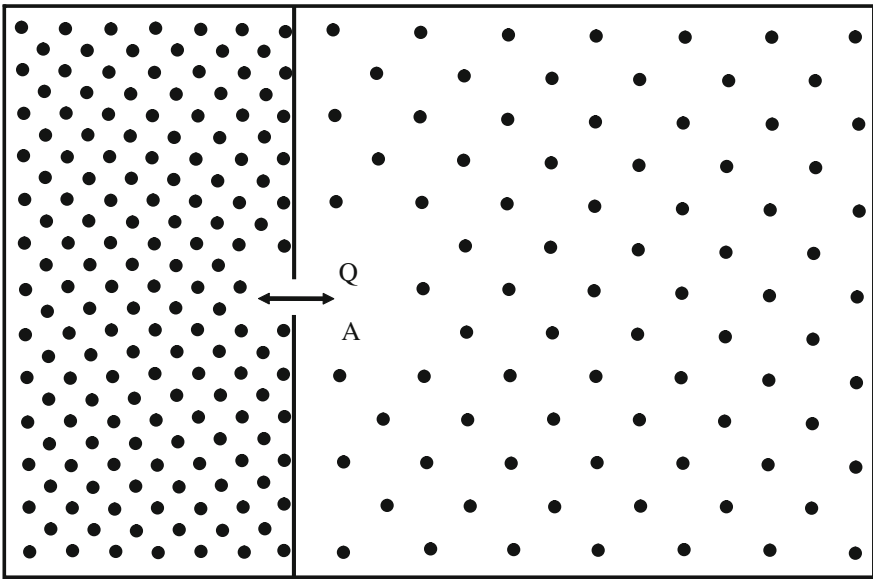
Fig. 9.4 Two gases separated by a wall containing a small orifice with area A

According to the ideal gas law,

$$P_1 = n_1 k T_1 \text{ and } P_2 = n_2 k T_2. \tag{9.16}$$

Combining Eqs. (9.8), (9.15), and (9.16), the net flow rate is found to be

$$dN/dt = \left[P_2 . T_2^{-1/2} - P_1 . T_1^{-1/2} \right] A/(2\pi \, mk)^{1/2}. \tag{9.17}$$

assuming $m_1 = m_2 = m$. After a long time, equilibrium is reached, dN/dt goes to zero, and

$$P_1/P_2 = (T_1/T_2)^{1/2} \tag{9.18}$$

so that the colder chamber will be at a lower pressure. On the other hand, if the temperatures are nearly equal, the conductance can be found from Eqs. (9.4), (9.5), and (9.17) to be

$$C = Q/(P_2 - P_1) = kT(dN/dt)/(P_2 - P_1) = A(kT/2\pi m)^{1/2} \tag{9.19}$$

which is independent of pressure. For air at 293 K passing through an orifice with area A (m^2), this reduces to

$$C = 116\ A \quad (m^3/s). \tag{9.20}$$

The conductance of a circular tube with diameter D and length L for air at 293 K is

$$C = 122\ D^3/L(1 + 4D/3L) \quad (m^3/s). \tag{9.21}$$

In the limit as L → 0, C = 3 (122) D^2/4 = π (116) D^2/4 = 116 A, the equation for an orifice. For a rectangular duct with sides a and b,

$$C = 309K\ a^2 b^2 /L(a + b) \quad (m^3/s), \tag{9.22}$$

where K is a function of a/b (Roth 1976, p. 82):

a/b	K
1	1.108
0.667	1.126
0.5	1.151
0.33	1.198
0.2	1.297
0.125	1.400
0.1	1.444

Precise formulas have been derived for flow in the **intermediate (transition) regime** between viscous and molecular flow. However, for rough calculations the approximation

$$C = C_{viscous} + C_{molecular} \tag{9.23}$$

may suffice, where the terms on the right are the conductivities for the viscous and molecular flow regimes. For circular tubes the error of this approximation does not exceed 13 %.

Figures 9.5 and 9.6 show combinations of conductances in series and in parallel.

If several conductances are in series, they add reciprocally, Fig. 9.5. If several conductances are connected in parallel, they add linearly, Fig. 9.6. Thus, the flow

Fig. 9.5 Combinations of conductances in series

SERIES

$$1 / C = 1 / C_1 + 1 / C_2 + 1 / C_3$$
$$Z = Z_1 + Z_2 + Z_3$$
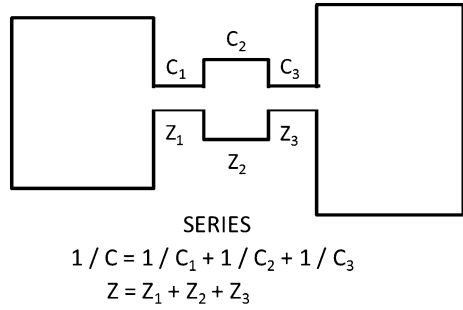
Fig. 9.6 Conductances in parallel

PARALLEL

$$C = C_1 + C_2 + C_3$$
$$1 / Z = 1 / Z_1 + 1 / Z_2 + 1 / Z_3$$
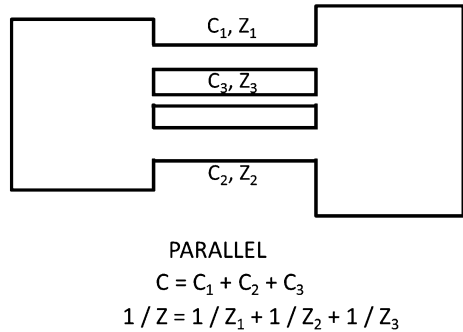
impedances Z combine like electrical resistances. Conductances for complex shapes are available in the references. Conductances of various gases relative to air are listed in Table 9.4. In viscous flow they vary according to the reciprocal of viscosity, while for molecular flow they vary roughly according to molecular speed.

9.2.4 Pumpdown Time

Equations (9.12) and (9.11) may be combined to give

$$dP/dt + \alpha P = Q_L(t)/V + \alpha P_U, \text{ where } \alpha \equiv S_t C/V(S_t + C). \tag{9.24}$$

If both sides are multiplied by $e^{\alpha t} \, dt$, the left side becomes equal to $d(Pe^{\alpha t}) = d \, Pe^{\alpha t} + \alpha \, Pe^{\alpha t} \, dt$, so the equation may be integrated:

$$\int_0^t d(Pe^{\alpha t}) = \int_0^t dt' e^{\alpha t'} (Q_L/V + \alpha P_U) \tag{9.25}$$

to obtain

Table 9.4 Some conductances for various gases relative to the conductance for air (Roth 1976; Dennis and Heppell 1968; Berman 1992)

Gas	C_{gas}/C_{air}	
	Molecular flow	Viscous flow
Air	1.0	1.0
Hydrogen	3.8	2.1
Helium	2.7	0.93
Neon		0.56
Argon	0.85	0.83
Xenon		0.80
Nitrogen	1.03	1.03
Oxygen	0.95	0.90
CO	1.03	1.03
CO_2	0.81	1.2–1.3
Water vapor	1.26	1.9
Mercury vapor	0.38	
Methane		1.66
Ethane		1.96

$$Pe^{\alpha t} - P_0 = \int_0^t dt' e^{\alpha t'} Q_L(t')/V + P_U(e^{\alpha t} - 1), \qquad (9.26)$$

where P_o = initial pressure. We cannot proceed further unless the time variation of the leak rate is known. If it is assumed to be a constant Q_o, then the solution is

$$P(t) = P_0 e^{-\alpha t} + (P_L + P_u)(1 - e^{-\alpha t}) \quad \text{(Pa)} \qquad (9.27)$$

where

$$P_L \equiv Q_0/\alpha V = Q_0(S_t + C)/S_t C. \qquad (9.28)$$

Thus, the pressure tends to vary exponentially with a time constant

$$\tau = 1/\alpha = [(S_t + C)/(S_t C)]V \quad \text{(s)} \qquad (9.29)$$

If we take the limit as $t \to \infty$ in Eq. (9.27) we find that the pressure approaches $P = (P_L + P_u)$, which are the pressure limitations due to leakage and due to backstreaming from the pump.

Example Problem 9.2 Pressure in Chamber: A vacuum chamber with $V = 0.1 \text{ m}^3$, $T = 293$ K and $p = 0.01$ Pa is connected to a pump with $S_t = 0.2 \text{ m}^3/\text{s}$ by a tube with $D = 0.1$ m and $L = 0.9$ m. If there is a constant leakage of 10^{-7} Pa-m^3/s and the ultimate pressure of the pump is 10^{-6} Pa, find τ and the ultimate pressure.

From Eq. (9.1) $\lambda = 0.68$ m, so the flow is molecular. From Eq. (9.21), $C = 0.118$ m^3/s. Then $\alpha = S_t C/V (S_t + C) = 0.742$/s, $\tau = 1.3$ s, $p_L = Q_o/\alpha V = 1.35 \times 10^{-6}$ Pa, and $(P_L + P_u) = 2.4 \times 10^{-6}$ Pa.

In practice, however, such fast pumpdown times are rarely attained because of higher leak rates, old oil, and bad conductance. These will gradually decrease in time, so that the pressure is in transient equilibrium, $P(t) \approx P_L(t) + P_u$. The gradually decreasing leak rate is caused by gradual desorption of gas from surfaces, materials, and cracks. Water vapor is particularly tenacious, and does not desorb readily unless the chamber is heated.

Since the leakage term

$$P_L(t) = Q_L(t)(1/S_t + 1/C), \tag{9.30}$$

either a small pumping speed or a small conductance can result in a high system pressure.

9.3 Pumps

The main categories of vacuum pumps are

- mechanical pumps,
- jet pumps (diffusion pumps),
- ionization pumps,
- sublimation pumps (getters),
- crysorption pumps and cryogenic pumps.

There is no single ideal pump for all vacuum regimes. Rather, by combining pumps and their effective pumping ranges, the desired vacuum pressure can be achieved. Figure 9.7 illustrates the operating ranges for several of the most common types of vacuum pumps in operation. Pumps are discussed by Tompkins and Gessert (2001).

9.3.1 Mechanical Pumps

Early mechanical pumps used reciprocating pistons in cylinders, but such pumps have problems with vibrations, noise, and wear. Most mechanical pumps now are rotary pumps. A rotary vane pump is illustrated in Fig. 9.8.

As the piston rotates, the vanes sweep the gas azimuthally around the outside from the inlet port to the exit port. Oil is used to attain a good seal between the vanes and the cylinder wall. Such mechanical pumps can typically evacuate a chamber down to about 0.1 Pa (0.0008 Torr).

Fig. 9.7 Operating ranges for several of the most common types of vacuum pumps in operation (Pressure, Pa)

sputterion

cryogenic

diffusion

turbomolecular

cryosorption

roots blower

rotary vane

1.E-10 1.E-08 1.E-06 1.E-04 1.E-02 1.E+00 1.E+02 1.E+04
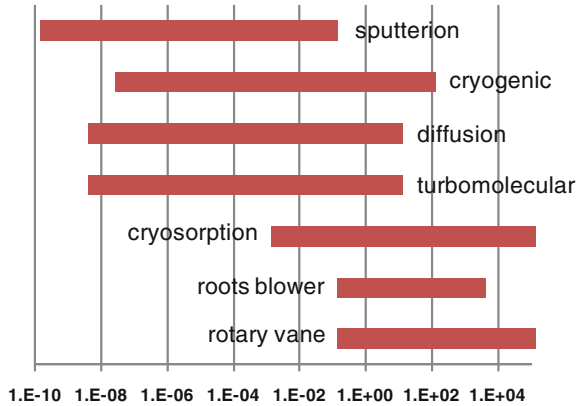
Fig. 9.8 A rotary vane mechanical Pump. As the rotor turns, the spring-loaded vanes sweep the gas from the inlet port around to the outlet port, where it is squeezed out. From J. M. Lafferty, "Techniques of High Vacuum", General Electric Company Report 66–3791 (1964), Fig. 7
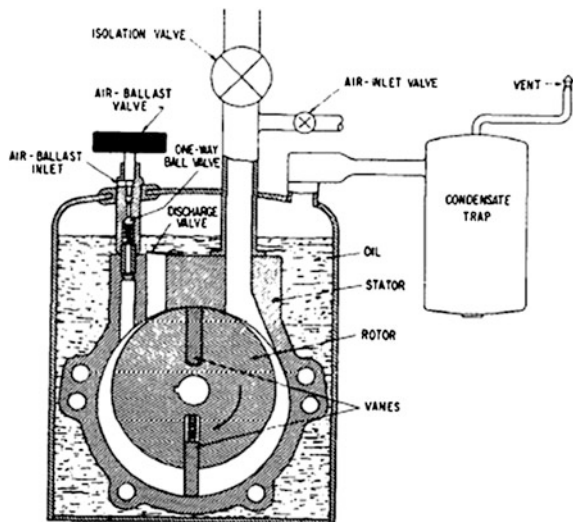
Mechanical booster pumps of the Roots type (Fig. 9.9) can be used to augment other mechanical pumps.

They are a type of gear pump, in which meshing gear teeth (two teeth per rotor) squeeze fluid out the exit. Because of their high throughput per unit cost, Roots blowers were selected for use in the Reversed Field Pinch Reactor design.

A **turbomolecular pump**, Fig. 9.10, is like the turbine of a jet engine. Rotor disks turning at high speed impart momentum to the gas molecules, pumping them away from the vacuum chamber.

A turbomolecular pump consists of various stages, which include rotating and stationary blades. These blades are set at opposing angles such that gas molecules caught in the space in between the blades are projected with forward momentum, as shown in Fig. 9.11.
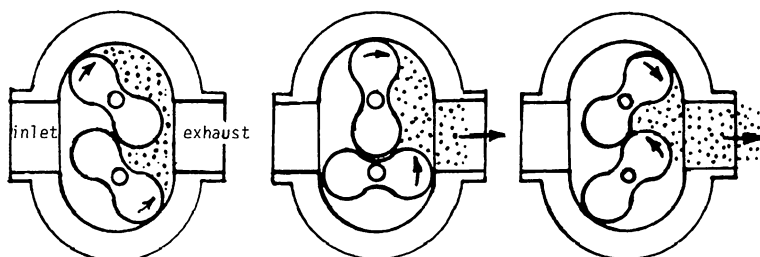
Fig. 9.9 Operation of a Roots mechanical booster vacuum pump. The rotating two-teethed gears sweep the gas around the outside of the chamber from inlet to outlet. Based on A. Guthrie, *Vacuum Technology*, Wiley, New York, 1963, Fig. 5.3b, p. 114
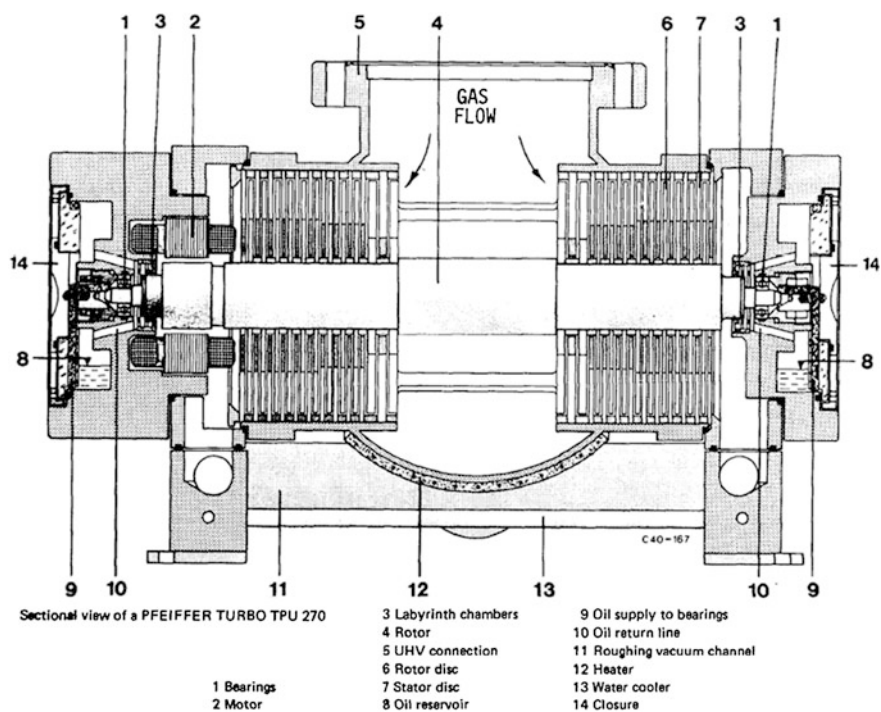
Fig. 9.10 Cutaway view of a turbomolecular pump. The rotor turns at a speed of 60,000 rpm (1000 Hz). Courtesy of Balzers Corporation, Hudson, NH. *1* Bearings. *2* Motor. *3* Labyrinth chambers. *4* Rotor. *5* UHV connection. *6* Rotor disc. *7* Stator disc. *8* Oil reservoir. *9* Oil supply to bearings. *10* Oil return line. *11* Roughing vacuum channel. *12* Heater. *13* Water cooler. *14* Closure
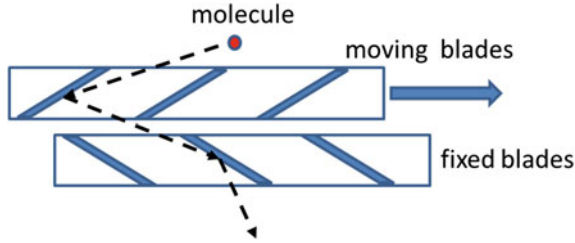
Fig. 9.11 Illustration of gas molecule bouncing through rotating and stationary blades in a turbomolecular pump. The arrows indicate molecules reflecting or desorbing from the moving blades and the stationary blades. Based on Tompkins and Gessert (2001)

This system of moving and stationary blades limits back diffusion of molecules to the vacuum chamber.

Various types of turbomolecular pumps are available, with pumping speeds up to 4 m^3/s and ultimate pressures $P_u < 10^{-7}$ Pa. The low P_u is a significant advantage in comparison with other mechanical pumps. Because the flow is molecular and the temperatures are much lower, the turbine blade design is simpler than those for steam turbines and jet engines.

A turbomolecular pump that operates at 20 K, called a "cryomechanical pump", can attain pumping speeds about 9 times higher than conventional turbomolecular pumps. It might alleviate the need for large, expensive cryogenic pumps that are required in fusion reactors like ITER (Sect. 9.7). An 80 K CMP is also under development (André et al. 2012).

9.3.2 Jet Pumps

The basic principle of a jet pump is illustrated in Fig. 9.12. A high-velocity spray of fluid from a nozzle imparts momentum to surrounding fluid, moving that fluid through a tube.

This principle is used for pumping water in a variety of applications (a pump must be provided for the primary stream), to create a vacuum in the condensers of

Fig. 9.12 A jet pump
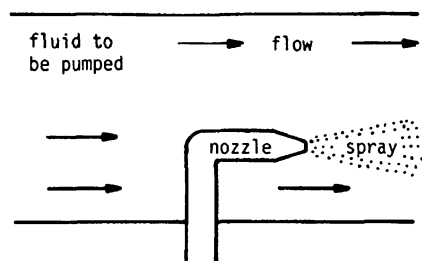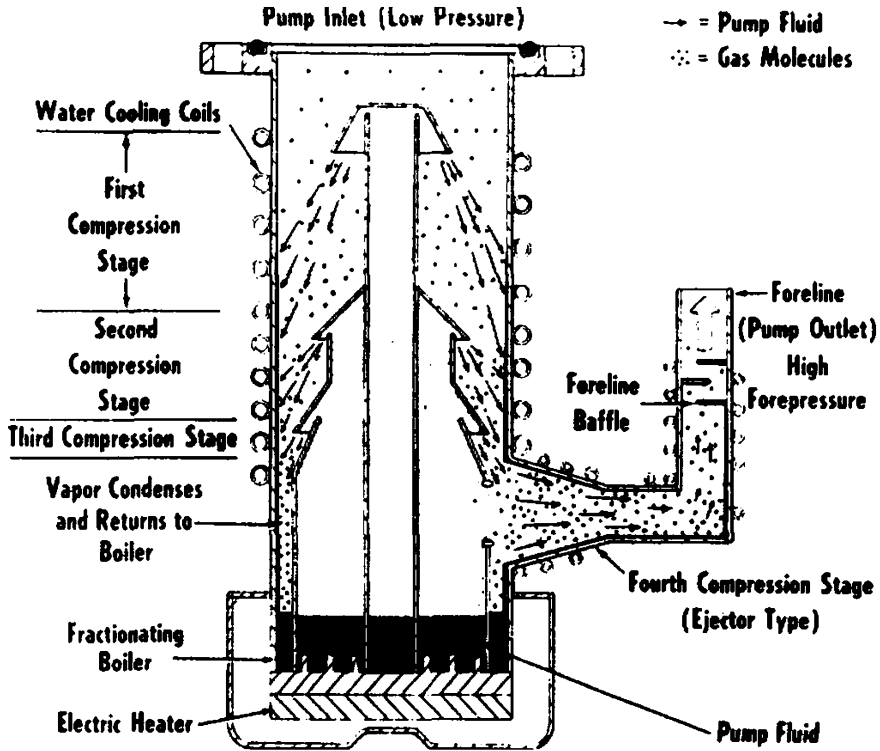
Fig. 9.13 A multistage oil diffusion pump, NRC Corporation. From J. M. Lafferty, "Techniques of High Vacuum", General electric Company Report GG-RL-3791 (1964), Fig. 10

steam turbines using a jet of steam to drive out air and water vapor, and in high vacuum systems to remove gases using a jet of hot oil vapor or mercury vapor. In high vacuum systems, these jet pumps are called diffusion pumps.

A typical multistage diffusion pump is illustrated in Fig. 9.13.

Oil (or mercury) is boiled in a tank at the bottom. The hot vapor rises through the central column and then sprays downward around the outside, pumping gases downward from the chamber above. Since diffusion pumps are only effective at pressures below about 1 Pa (0.008 Torr), a mechanical pump is used in series with the diffusion pump to take the exhaust gases and pump them up to atmospheric pressure. Diffusion pumps have the advantages of no moving parts, high pumping speeds, and low ultimate pressures. On the other hand, the pumping fluid can diffuse up into the chamber and contaminate its walls, so flow baffles and cold traps must be placed between the main chamber and the diffusion pump to prevent contamination. Cold traps not only prevent contamination due to the diffusion pump fluid, but also permit pressures many orders of magnitude below the room-temperature vapor pressure of the pump fluid to be attained. A typical cold trap is cooled with water, Freon®, or liquid nitrogen, with lower temperatures being more
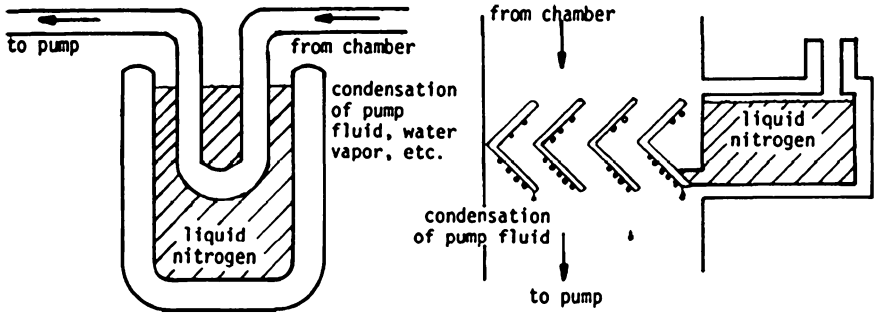
Fig. 9.14 A U-tube cold trap and a chevron baffle for prevention of pump fluid streaming into the vacuum chamber

effective. Pump fluid condenses out in the trap, so it does not reach the chamber. A U-bend cold trap and a chevron baffle are illustrated in Fig. 9.14.

9.3.2.1 Ionization Pumps

An ionization pump is illustrated in Fig. 9.15.

Permanent magnets mounted outside the chamber create a strong magnetic field. A strong electric field parallel to the magnetic field is created by applying +3 kV to the anode. When an electron–ion pair is created (by a cosmic ray, for example), the electron will oscillate back and forth through the hole in the anode, until it diffuses across the magnetic field and is lost to the anode. This Penning discharge is similar to that in a Duopigatron ion source. The oscillating electron has enough energy to ionize neutral gas atoms it collides with, creating more oscillating electrons. The newly formed ions are then accelerated into the cathode
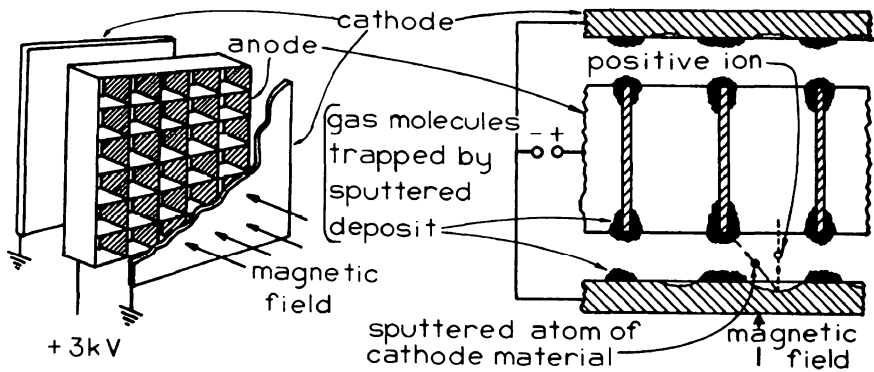
Fig. 9.15 Cutaway view of an ionization pump (*left*), and symbolic diagram of the effects of sputtering titanium from the cathode (*right*). The magnetic field of 0.15 T is produced by permanent magnets, which are not shown here

and buried. In addition, an active metal such as titanium may be sputtered off the cathodes. The titanium atoms combine chemically with the gases being pumped and fasten them to the walls. Thus, there are two pumping mechanisms at work simultaneously: ionization of the neutral gases by the cloud of oscillating electrons, and chemical pumping by the sputtered titanium. Noble gases (helium, neon, argon, krypton, and xenon) are not affected by the chemical action of titanium. They can still be ionized and buried in the walls, but the pumping speed for noble gases is usually much lower than the pumping speed for chemically active gases. More complex electrode shapes have been devised (triode pumps) to enhance the pumping speed of noble gases.

The ionization or sputter-ion pump can attain pressures below 10^{-7} Pa (8×10^{-10} Torr), has no moving parts, and has no volatile fluid, so cold traps are not required. However, these pumps cannot operate until the chamber has been evacuated to pressures of about 1 Pa (0.008 Torr), so roughing pumps are needed initially to pump the chamber down to a pressure where the ionization pump can be started. When the ion pump is started, the roughing pump can be turned off.

9.3.3 Sublimation Pumps

Sublimation pumps, or *getters*, use chemically active metals such as titanium and barium to adsorb gases chemically. Filaments of titanium may be heated in a vacuum chamber to boil off titanium vapor and deposit a thin film inside the chamber walls. This thin film of fresh metal has a high pumping speed for active gases, so it can produce a very low pressure in the chamber in a short time. However, after a period of hours, sometimes just minutes, the titanium film becomes saturated, and more titanium must be deposited to renew the pumping effect. The saturation time is inversely proportional to the incident gas flux $nv_{av}/4$, very short at high pressures. Thus, sublimation pumps are limited by the amount of titanium contained in the filaments or porous metal balls. Typical commercial elements are rated at tens to hundreds of hours of operation at low heater current, or minutes at high current. Commercial electronic vacuum tubes often use sublimation pumps in the form of active metal filaments which are "flashed", after the tube is sealed. This removes impurity gases and improves the vacuum, thereby prolonging the life of the thermoelectric filament. When you look at a vacuum tube you may see a silvery metallic deposit from the getter on the inside of the glass at the base of the tube.

9.3.4 Cryosorption Pumps

Figure 9.16 shows a typical cryosorption pump.

Zeolite pellets contained in a metal can are cooled by liquid nitrogen to 77 K or by liquid helium to 4 K. They strongly adsorb gases coming out of the chamber,

Fig. 9.16 Cutaway view of a cryosorption pump

GAS FLOW

HIGH PRESSURE
RELIEF VALVE
  RUBBER SLEEVE
  EXHAUST HOLE
RETAINER SCREEN
ZEOLITE PELLETS
STAINLESS STEEL
OR ALUMINUM CAN
LIQUID NITROGEN
STYROFOAM DEWAR

INTERNAL COOLING
FINS NOT SHOWN
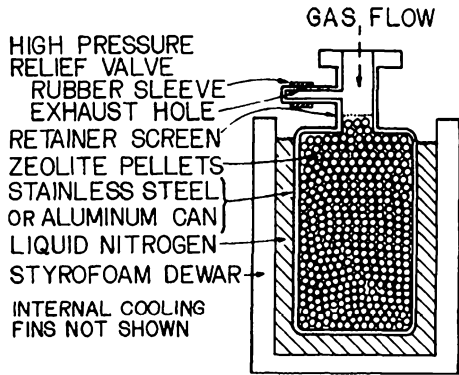
and can pump a chamber down to pressures less than 1 Pa in a few minutes. When the desired pressure is attained, the cryosorption pump may be valved off and allowed to warm up. The adsorbed gases are then desorbed, building up a high pressure inside the can, which is vented by a relief valve to prevent explosion. When the gases are desorbed, the pump can be cooled again and recycled. In addition to zeolite, other adsorbent materials may be used, including charcoal and porous ceramics.

Cryosorption pumps are simple and relatively inexpensive, but they do require a cryogenic (low-temperature) fluid for their operation. They may be used to pump a chamber down to pressures where ionization pumps can be started.

Fig. 9.17 A cryogenic pump. N_2 = liquid nitrogen-cooled surfaces. He = liquid helium-cooled surfaces. Without the radiation barriers radiative heating would boil the liquid helium away too rapidly

GAS FLOW

N_2

He

ADSORPTION
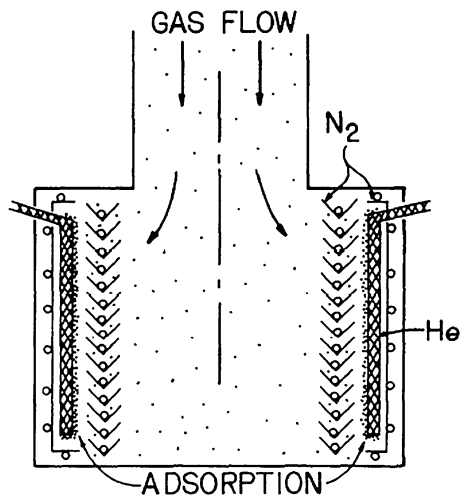
9.3.5 Cryogenic Pumps

A cryogenic pump consists simply of a metal plate cooled to a very low temperature. At low temperatures the probability that a molecule striking the plate will stick to it is high, so gases are readily adsorbed onto the plate, lowering the chamber pressure. The plate is usually cooled by liquid nitrogen (77 K) or by liquid helium (4 K). Lower pressures are attainable at the lower temperatures.

A cryopump at 4.2 K, Fig. 9.17, can pump all gases well except He. To be effective the cryogenic pump must be thermally insulated from the surroundings and from the plasma discharge, so that the liquid coolant is not boiled away too rapidly.

The pumping speed of a cryopump is roughly one-fifth the conductance of an orifice, Eq. (9.20). For deuterium at temperature T (K) with pump area A (m^2),

$$S_t = 89 \, A(T/300)^{1/2} \quad (m/s). \tag{9.31}$$

The advantages of cryopumps are listed in Table 9.5.
Various kinds of vacuum pumps are compared in Table 9.6.

Table 9.5 Advantages of cryopumps for nuclear fusion devices (based on Day 2010)

- Produce the biggest pumping speeds of all vacuum pumps:
- Can be installed in situ
- absolutely oil-free and generate a clean vacuum, completely free of oil or hydrocarbons
- No movable parts
- No bearing and shaft seal problems (maintenance aspects, lubrication)
- High reliability and no known problems with dust and particles
- Compatible with strongest safety requirements, cryogen-based
- Good for areas with difficult maintenance access
- Lowest pressures of all vacuum pumps
- Pumping speed of cryopumps high for light gases
- Operable over a wide pressure range

Table 9.6 Typical operating ranges of various vacuum pumps. All except the first two require roughing pumps

Rotary Vane Mechanical	10^5–0.1 Pa	(760–0.0008 Torr)
Crysorption	10^5–0.1	(760–0.0008)
Roots Blower	100–0.01	(0.8–8 × 10^{-5})
Diffusion Pump	1–10^{-6}	(0.008–8 × 10^{-9})
Turbomolecular	1–10^{-6}	(0.008–8 × 10^{-9})
Ionization	1–10^{-7}	(0.008–8 × 10^{-10})
Sublimation	0.01–10^{-7}	(8 × 10^{-5} to 8 × 10^{-10})
Cryogenic	0.001–10^{-8}	(8 × 10^{-6} to 8 × 10^{-11})

Fig. 9.18 A Bourdon tube
vacuum gauge. T = elliptical
cross section tube. L = levers
and gears (not shown) to
amplify motion
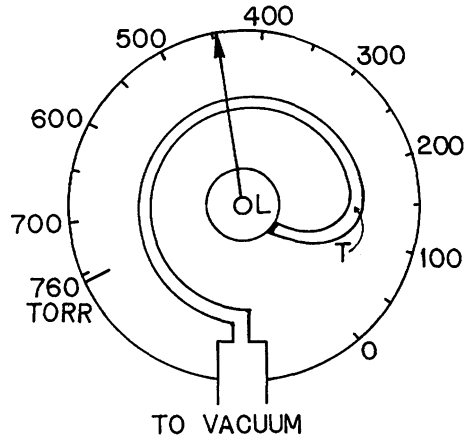
9.4 Pressure Gages

Vacuum gages use many different phenomena to measure pressure: mechanical
expansion, gravity, momentum transfer, viscosity, thermal conductivity, and ion-
ization rates. A Bourdon tube gage consists of a spiral tube of elliptical cross
section connected to the vacuum to be measured and exposed to atmospheric
pressure on the outside (Fig. 9.18).

As the pressure in the tube is reduced, the tube curls up tighter, and the needle
attached to the end of the tube indicates the pressure. Such gages are accurate
down to about 1,000 Pa (8 Torr).

Another type of mechanical vacuum gage uses a *diaphragm* with a reference
vacuum on one side and the vacuum to be measured on the other side. Deflection
of the diaphragm is amplified by mechanical linkage and displayed by a needle.

The use of gravity to measure pressure is familiar in mercury barometers and
manometers. A more sophisticated version, called a *McLeod gage*, can measure
pressures accurately down to 10^{-3} Pa (8×10^{-5} Torr) by compressing part of the
trapped gas and then comparing the pressure of the trapped gas with atmospheric
pressure. The gas is trapped and compressed by a rising column of mercury, as
illustrated in Fig. 9.19.

By Boyles' Law,

$$PV = P_1 A\ell. \tag{9.32}$$

Furthermore,

$$P_1 - P = \rho gL, \tag{9.33}$$

where L = height of the column of mercury supported by the pressure difference,
ρ = density of mercury, g = acceleration of gravity. Therefore,

Fig. 9.19 A McLeod gage. Initially the volume V is at the same pressure p as the vacuum to be measured. When air is admitted through the valve, air pressure forces the mercury up the center tube into volume V. The trapped gas is compressed to a new pressure P_1 and volume $A\ell$, where A is the cross sectional area of the small tube (Dolan 1982)
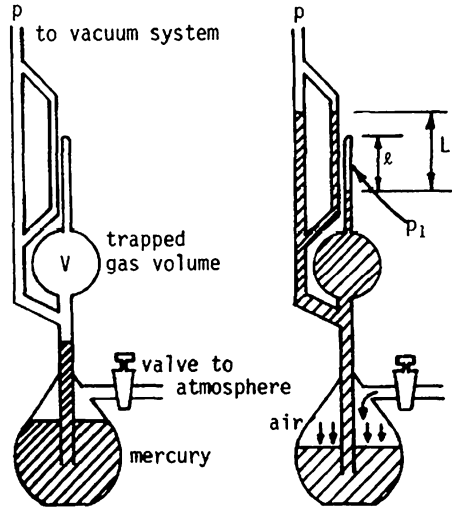
$$p = \rho g L A\ell/(V - A\ell). \tag{9.34}$$

These gages are useful for calibration of other gages at 0.001–10 Pa, but they are slow and cumbersome, so other gages are employed for routine measurements.

A thermocouple gage is illustrated in Fig. 9.20.

In the molecular flow regime, the thermal conductivity of a gas is proportional to its pressure. A heated filament can be cooled by conduction along its supports, by conduction through the gas, and by radiation. The support loss can be made

Fig. 9.20 Schematic diagram of a thermocouple gage tube and associated circuitry. The micro ammeter scale is calibrated in terms of pressure, with readings typically from 0.1 to 1,000 millitorr (0.013–133 Pa)
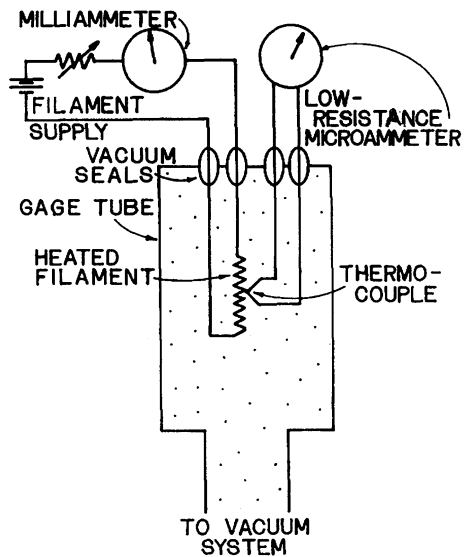
Fig. 9.21 Circuit diagram of a Pirani gage. Initially the current through the galvanometer G is balanced to zero by adjusting variable resistance R. When the pressure is changed in the gage tube, the temperature and resistance of the filament F change, causing a current to flow through the galvanometer, which can be calibrated in terms of system pressure
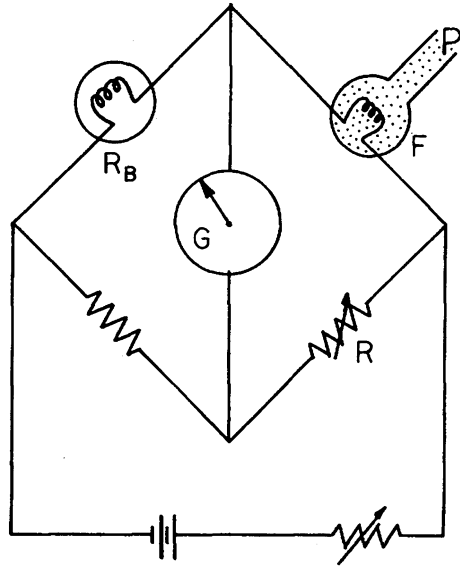
negligibly small. If the filament is not too hot, the radiation loss will be much smaller than the heat transfer by conduction through the gas (down to a pressure of about 0.1 Pa). Then the temperature of the filament is controlled by the thermal conductivity of the gas, which is proportional to its pressure. A thermocouple mounted on the filament can be used to measure its temperature, which can be calibrated to give pressure readings of the gas. In some gages, two or three thermocouples are used in order to compensate for ambient temperature drift (the Hastings gage).

Alternatively, the filament resistance itself may be measured, since it increases with temperature. The resistance is measured with a "Wheatstone bridge", which compares the variable filament resistance with a reference, Fig. 9.21.

Thermal conductivity gages are most useful between 0.1 and 200 Pa (0.0008 and 1.5 Torr).

At pressures below 0.1 Pa, ionization gages are used. An ionization gage uses electrons from a hot filament to ionize some of the low-pressure gas atoms entering the gage. The ions are then collected by a negative electrode, and the ion current is linearly proportional to the gas pressure below about 0.1 Pa. A typical Bayard-Alpert gage tube is shown in Fig. 9.22.

Electrons from the filament spiral in and out of the grid until they hit the grid wires. Some of these electrons produce ionization, and the ions are collected by the thin "ion collector" wire at the center. The ion collector has been made very small to minimize the effect of X-ray-produced photoelectrons from the ion collector, which would give a false current reading. At very low pressure (10^{-7} Pa), the ion currents are so low that very large electron currents from the filaments are needed. The filament requirements can be eased by the addition of a magnetic field to prolong the electron flight time. With a magnetic field of 250 Gauss (0.025 T), the

Fig. 9.22 Bayard-Alpert
ionization gage. Typical
voltages:
filament = grounded,
grid = +150 V, ion
collector = −45 V. From
J. M. Lafferty, "Techniques
of High Vacuum", General
Electric Company Report
66-RL-3791 (1964), Fig. 24
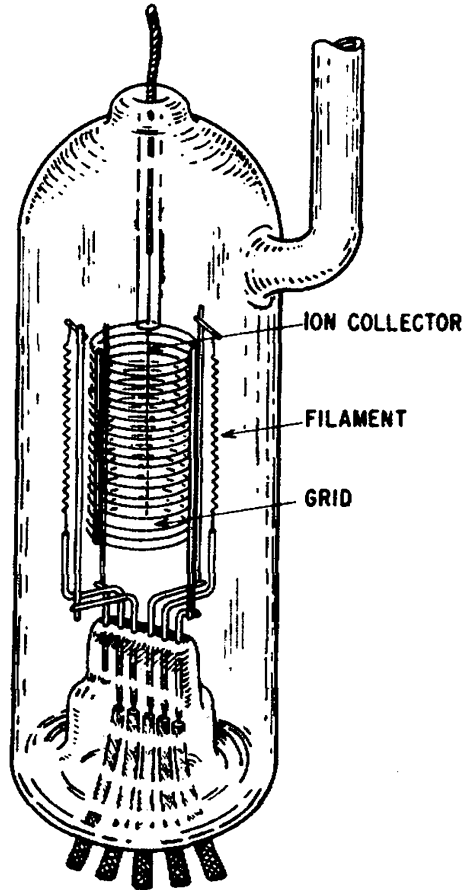
ion currents are more than 10^4 times as large as without the magnetic field, and the pressure measurements can be extended down to about 10^{-11} Pa. Such a magnetron vacuum gage is illustrated in Fig. 9.23.

In this case the filament is mounted at the center, and a positive anode surrounds it. The electrons spiral around the filament in the axial magnetic field, producing ionization, and the resulting positive ions are collected by the negative collector at the end. The ion collector and shield are negative relative to the cathode, to prevent axial electron losses. Because thermal conductivity and ionization rates are different for different gases, gages relying on these phenomena must be calibrated for each gas to be used. Usually the gage is calibrated for air, and correction factors are calculated for other gases. For example, the calibration curves for a Pirani gage are shown in Fig. 9.24.

Typical operating ranges of various pressure gages are listed in Table 9.7.

ASDEX researchers developed an ionization gage for use in high magnetic fields. The filament, control grid, acceleration grid, and collector lie along an axis

Fig. 9.23 A hot-cathode magnetron gage. The vertical magnetic field inhibits radial electron motion. From J. M. Lafferty, "Techniques of High Vacuum", General Electric Company report 66-RL-3791 (1964), Fig. 25

CERAMIC INSULATOR

STAINLESS STEEL ENVELOPE

ION COLLECTOR

MAGNET

ANODE

LANTHANUM BORIDE COATED FILAMENT

SHIELD

CERAMIC INSULATORS

TUBULATION
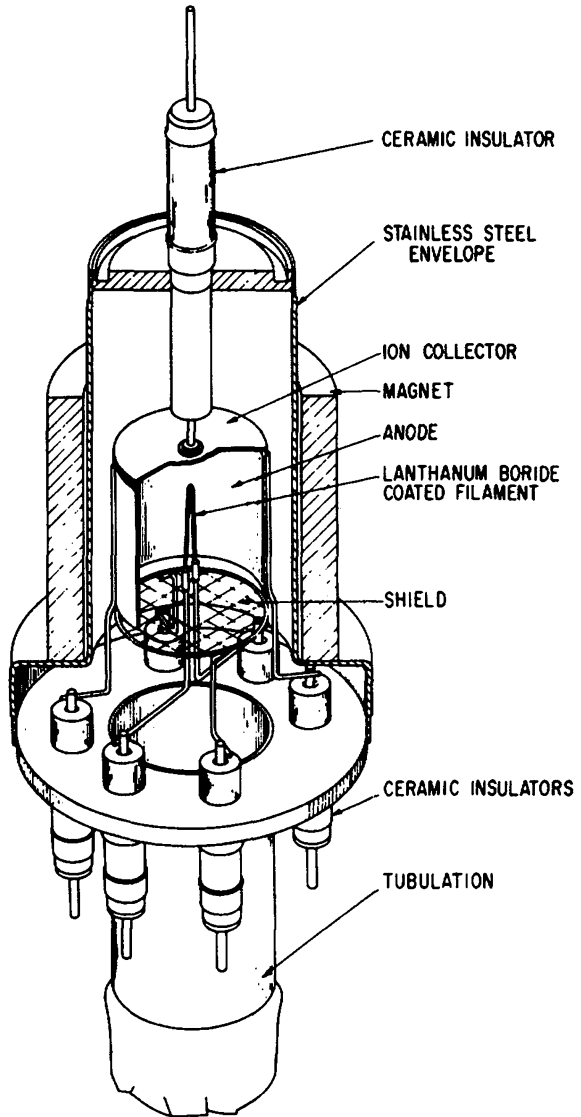
parallel to B, so that ions confinement by the magnetic field increases collector current and makes the gage more sensitive. The gage can operate from about 10^{-4} to 1 Pa with time resolution of 1–10 ms.

A quadrupole mass spectrometer can be used to measure small fractions of gases, but it ordinarily cannot distinguish ^{4}He from D_2. A penning gage (axial magnetic field with negative end plates to repel electrons) can be used to ionize gases for measurement of their spectral line emissions. Elements such as H, He, Ne, and Ar can be detected with filtered photomultipliers and their relative concentrations estimated.

Fig. 9.24 Calibration curves for a Pirani gage. Adapted from A. Guthrie, Vacuum Technology, Wiley, New York, 1963, Fig. 6.7, p. 166
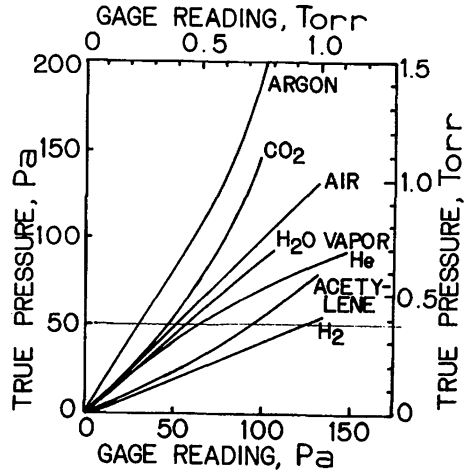
Table 9.7 Typical operating pressure ranges of common pressure gages

Bourdon	$10^5–10^3$ Pa	(760–8 Torr)
Diagram	$10^5–100$	(760–0.8)
Manometer (Barometer)	$10^5–100$	(760–0.8)
McCleod	$10–10^{-3}$	($8–8 \times 10^{-6}$)
Thermocouple, pirani	$200–0.1$	($1.6–8 \times 10^{-4}$)
Bayard-Albert ionization	$0.1–10^{-9}$	(8×10^{-4} to 8×10^{-12})
Magnetron	$0.1–10^{-11}$	(8×10^{-4} to 8×10^{-14})

9.5 Vacuum Chambers and Components

You are probably familiar with the experiment of boiling water in a metal can which has a screw-on lid. When the water is boiling you take it off the stove and screw on the lid. Then as the steam condenses inside, a vacuum is produced, and air pressure collapses the can. Vacuum chambers must be made strong enough so that they don't collapse from atmospheric pressure. There is a minimum thickness required to prevent buckling of vacuum vessels. For thin-walled cylindrical chambers, the ratio of the required thickness t to the chamber diameter D is a function of the chamber length L, as illustrated in Fig. 9.25.

Design of vacuum vessels is discussed by Steinherz and Redhead (1963). Stiffening rings can be added to permit the use of thinner walls.

Metal-to-metal joints can be made by soldering, brazing or welding. Soft solder is usually avoided, because of its higher vapor pressure. Silver brazing works well on small chambers of copper, brass, stainless steel, etc., but the brazing rod is expensive. Tungsten-inert-gas (TIG) welding is the best technique for stainless steel, which is the most common vacuum chamber material. A jet of argon or helium around the weld zone prevents oxidation of the weld.

Fig. 9.25 Illustrative curves of the required ratio of vessel thickness to diameter for thin cylindrical vacuum chambers, as a function of the ratio of the length to diameter. These curves are for illustrative purposes only. For actual design work, consult the ASME pressure vessel code
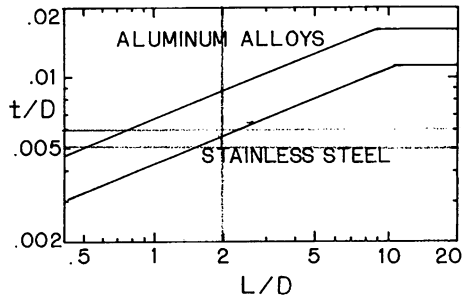
In designing welded joints, one should avoid virtual leaks and cracking from thermal stress. Virtual leaks are thin cracks on the inside of the chamber, which can trap gases. When the chamber is pumped down to very low pressures, the gas molecules diffusing out of the crack can substantially raise the pressure. To prevent virtual leaks, it is best to run the weld around the inside of the chamber, instead around the outside, as illustrated in Fig. 9.26.

Thermal stresses are caused by cooling of the heated weld zone. To avoid cracking or warping, the metal layer next to the weld should be thin, so that it reaches nearly the same temperature as the weld and cools with it. Some good techniques are illustrated in Fig. 9.27.

Only a few aspects of vacuum chambers and seals are discussed here. A book has been written on vacuum sealing techniques (Roth 1966).
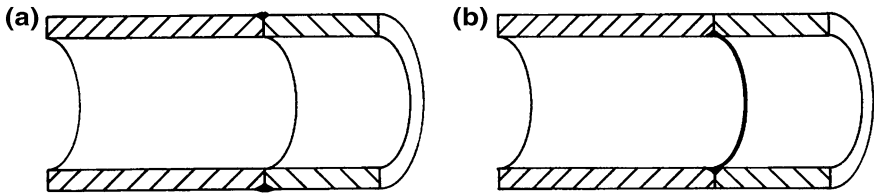
Fig. 9.26 Cutaway views of welds between two tubes. **a** Weld on outside, crack on inside may cause virtual leak. **b** Weld on inside, no virtual leak
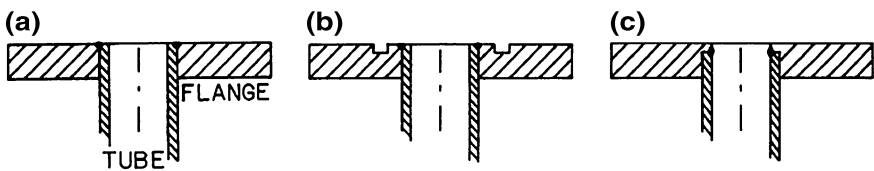
Fig. 9.27 Methods of welding a circular flange to a tube. **a** Poor-warpage or cracking likely. **b** Good-stress relief groove machined into flange. **c** Good-thin ridge on inside of flange abuts tube
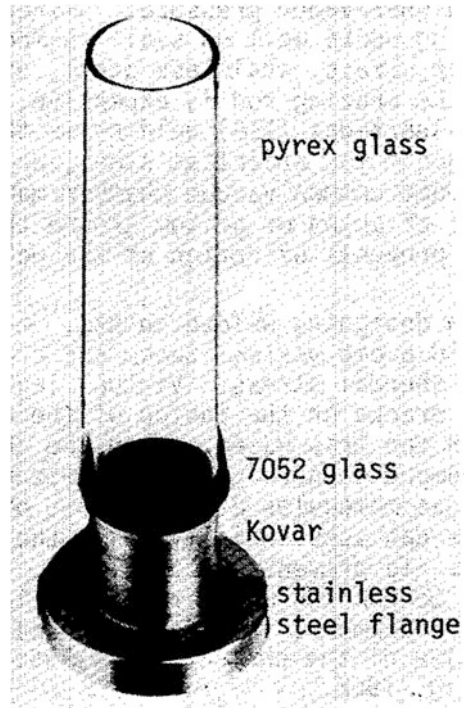
In joining glass to metal, the thermal expansion of the two materials must be matched to prevent cracking of the glass as it cools. An alloy called Kovar® has a thermal expansion coefficient nearly equal to those of some types of glass, so Kovar®-to-glass seals are widely used, Fig. 9.28.

The Kovar® may be welded or brazed into the metallic chamber, but it is ferromagnetic. Other seals have been developed for applications where nonmagnetic materials are required.

Flange joints are usually sealed with elastomer O-rings (such as Viton) or with metallic gaskets, as illustrated in Fig. 9.29.

O-ring flanges are simpler and cheaper, but metallic gaskets are needed for ultrahigh vacuum systems ($p < 10^{-5}$ Pa), which require bakeout at high temperatures, because the O-rings have too high a vapor pressure at high temperatures (T > 600 K). Metallic gaskets are also needed for very low temperature (cryogenic) applications.
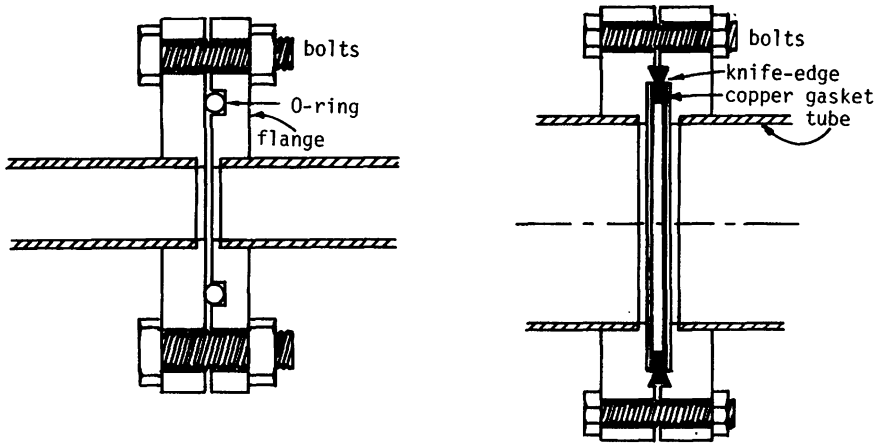
Fig. 9.29 Flange sealing techniques. An O-ring seal (*left*), and a bake able metal seal (*right*)

9.6 Vacuum Techniques

9.6.1 Monolayers

Even the best vacuum equipment is useless if the proper techniques are not followed to ensure cleanliness of everything inside the vacuum system. For example, outgassing from the miniscule amount of grease deposited by a human fingerprint can be very significant in the ultrahigh vacuum range ($p < 10^{-5}$ Pa). This is true because the molecular density at 10^{-6} Pa is small about 2.4×10^{14} m^{-3}. So, a fingerprint containing about 10^{16} molecules can flood a 0.01 m^3 chamber, when compared to the number of gas molecules already present.

Ordinarily, the walls of a vacuum chamber are covered with several layers of adsorbed gas molecules. Adsorption refers to molecules sticking to the surface, while absorption refers to molecules penetrating into the wall. Each layer one molecule thick is called a monolayer. The outer monolayers are weakly bound, and at equilibrium they are knocked off by thermal agitation as fast as they are adsorbed, Fig. 9.30.

At a pressure of 10^{-4} Pa, the first monolayer would form on a perfectly clean surface in about 3 s. At 100 Pa, it would form in about 3 μs. Each monolayer contains about **8×10^{18} molecules/m^2**. Molecules will absorb onto a surface according to

$$t = 3.2 \times 10^{-4}/P \quad (s) \tag{9.35}$$

where P is in Pa. Figure 9.31 is a graph of molecule absorption time from 1×10^{-5} to 1,000 Pa.
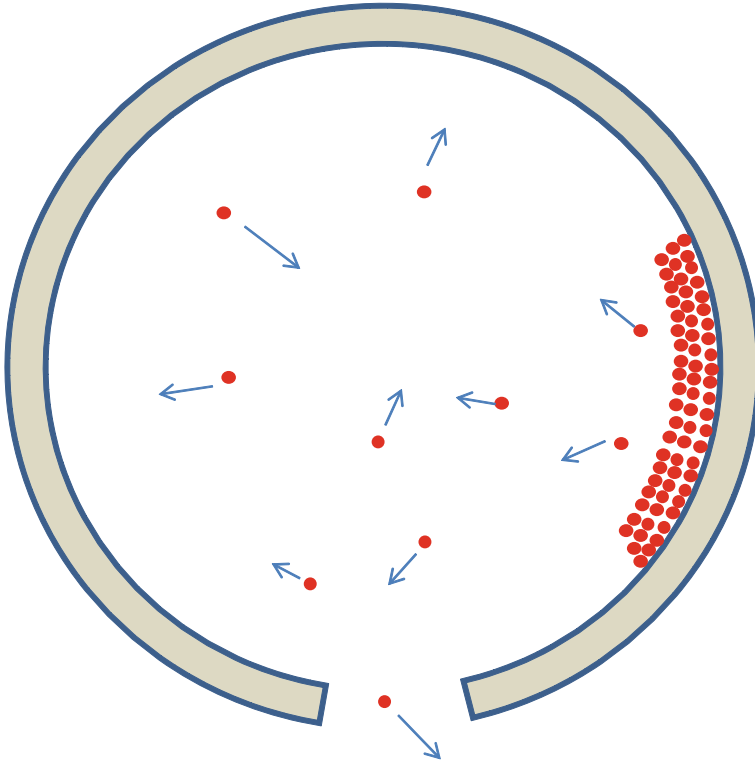
Fig. 9.30 Part of a chamber wall covered with three monolayers, and desorbed molecules flying around in the chamber. Some may flow out the hole at the *bottom* leading to the vacuum pump

If one monolayer is knocked off the wall of a fusion experiment by heat from the plasma, the influx of neutral atoms is substantial. At equilibrium during an experiment, each charge-exchange neutral leaving the plasma is replaced by an incident neutral refluxing off the walls. It is important that these neutrals be mostly hydrogen, so that impurity buildup does not cool the plasma too rapidly. One means of reducing the impurity influx is by thorough cleaning of the chamber walls. This cleaning can remove the oil, grease, oxides, etc. normally present on metallic surfaces.

9.6.2 Vacuum Chamber Cleaning

The following steps are often used to clean vacuum chambers.

The surface should be mechanically polished before cleaning is begun.
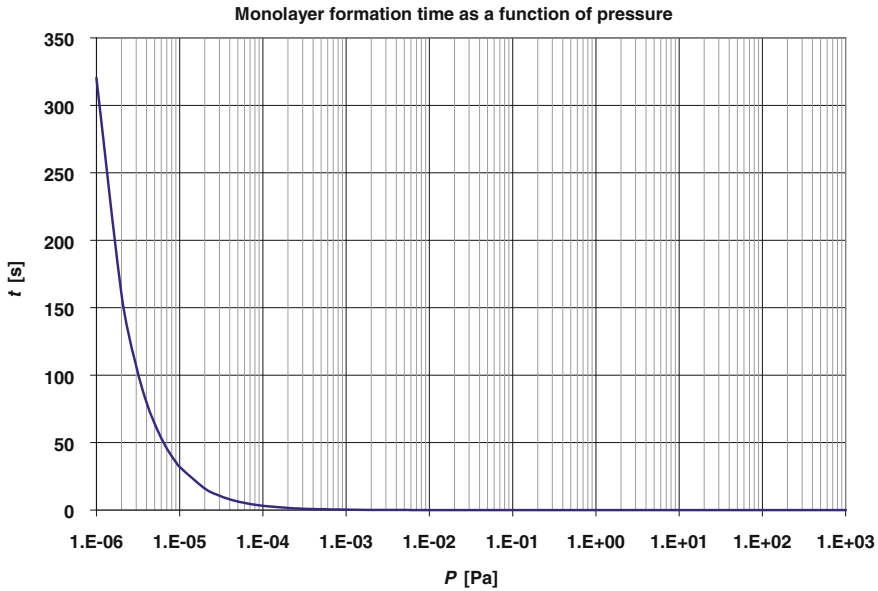
Fig. 9.31 Time of monolayer absorption on a surface as a function of pressure

1. **Degreasing.** This is done by washing with detergent, followed by multiple rinses with hot water, cold water, and deionized water. Alternatively, a vapor degreaser may be used for small items. It consists of a heated bath of solvent, such as carbon tetrachloride, above which the parts to be cleaned are placed on a rack. The CCl_4 vapor condenses on the parts, dissolves the oils, and drips back down into the bath. Some cleaning compounds, like CCl_4, are toxic, so contact with skin, eyes, mouth, and lungs should be avoided.
2. **Rinsing.** Then the part is washed and rinsed.
3. **Oxide removal and surface smoothing.** Acid etching or electropolishing removes oxides and some of the rough bumps normally present on a metallic surface. The decrease in surface roughness can lead to a reduction in the number of adsorbed gas molecules. For example, anodized aluminum can adsorb 100 times as many gas molecules as a smooth polished aluminum surface can.
4. **Rinsing.** To remove the acids, the surface may be repeatedly rinsed using deionized water, then pure alcohol.
5. **Bakeout.** After the chamber is assembled and pumped down, it is heated up to 400–700 K for many hours. The heat desorbs many of the molecules, such as water vapor, which would otherwise cling tenaciously to the surface.
6. **Discharge cleaning.** Repeated plasma discharges or illumination with high intensity electromagnetic waves are used to reduce the quantity of adsorbed gases in some fusion devices, like tokamaks.

Proper cleaning and bakeout are essential for the attainment of ultrahigh vacuum. Without such procedures the pressure will usually remain around 10^{-4} Pa for many days.

9.6.3 Leak Detection

Leaks can be detected by a variety of means. During initial pumpdown at high pressures, one can sometimes hear a hiss of air around the leak. The search can be aided by a stethoscope. Alternatively, one can pressurize the inside of the chamber and look for bubbles with a soap solution, or look for the deflection of smoke. Usually, however, leaks are much smaller than the gross leaks for which these procedures apply.

Leaks in glass systems can often be spotted by exciting the gas with a Tesla coil. The high voltage from the coil tip makes the gas glow, and the glow will be especially bright where air is leaking in through a crack. In metal systems with a glass section, the gas can be excited in the glass section, and acetone can be sprayed around the other sections. When the acetone hits the leak, the intensity, or color, of the glow will change. Spraying acetone or helium can also be used in conjunction with a vacuum pressure gage, such as a thermocouple gage or an ionization gage. When the fluid sprayed hits the crack, the gage needle will deflect one way or the other due to the low vapor pressure of acetone which results in a rapid expansion of the acetone in the chamber. However, acetone fumes can be hazardous.

Helium mass spectrometers can be used in conjunction with spraying helium gas to look for leaks. This method is much more sensitive, as the detector responds only to helium. Such leak detectors are very convenient.

Another technique for leak detection is to spray a small amount of a radioactive tracer gas around possible leaks, and to detect this radioactive gas inside the chamber with an appropriate radiation detector.

Once the leak is located, if it is in a seal, the bolts may be tightened a little, to compress the gasket further. If this does not help, or if the leak is in a weld or joint, the system must be opened up, rewelded, recleaned, pumped down, and baked out again. This is a slow process, which is ample incentive to do it right the first time. An exception is the case of a chamber where pressures below about 10^{-5} Pa are not required. In this case one can try to seal the leak with liquid sealant or with epoxy. Special epoxies have been developed with low vapor pressures, and they can be used temporarily to seal cracks in glass.

Table 9.8 Constituents of air (exclusive of water vapor). Based on data from CRC Handbook of Chemistry and Physics, 79th edition, 1998–1999, p. 14–3. Copyright 1998, The Chemical Rubber Co., CRC Press Inc

Atmosphere composition	
N_2	78.08 %
O_2	20.95 %
CO	0.03 %
Ar	0.93 %
Ne	0.0018 %
CO	0.0001 %

9.6.3.1 Diffusion

In addition to leakage and desorption effects, the ultimate pressure is limited by permeation of gases through the chamber walls. The constituents of air are listed in Table 9.8.

Only the light gases, hydrogen and helium, have significantly high diffusion rates through most metals and glasses. Since helium is inert, it is not as likely to become chemically bound as hydrogen, and helium is about ten times as abundant as hydrogen in the air. Thus, in the ultrahigh vacuum region, the pressure may be limited by helium diffusion to around 10^{-10} Pa, with a wide variation from this number is possible. We will not be concerned with this limitation, however, because vacuums of about 10^{-6} Pa are probably adequate for fusion reactors.

9.7 ITER Vacuum Systems

ITER will have the largest vacuum system yet built for a fusion experiment, and it will have stringent requirements, such as very high required pumping speed for helium.

The ITER vacuum vessel is water cooled with many large ports. It has a volume of about 1,400 m^3. In fusion reactor systems, the pumping problem is not the volume but all the surfaces inside the vacuum vessel, which are affected by many phenomena, such as adsorbed gases, heat, radiation, sputtering, chemical reactions, co-deposited films, hydrogen embrittlement, and cracking.

Fuel gases are provided to the gas injection system, the NBI systems, and the pellet injection system. Exhaust gases pumped from the tokamak by cryopumps and turbomolecular pumps go to an exhaust gas processing system. Ordinary hydrogen is separated from deuterium/tritium and emitted from the stack whereas the deuterium and tritium are recycled. Other gases may be recycled or sent to radioactive waste disposal. The fusion vacuum pumping system requires very high pumping speeds and throughputs, tritium compatibility, operation in high magnetic fields, and reliability.

Figure 9.32 shows the pumping speeds of the main ITER vacuum systems.

Fig. 9.32 Pumping speeds of
the main ITER vacuum
systems. (Day 2010).
Courtesy of ITER
organization and Karlsruhe
Institute of Technology
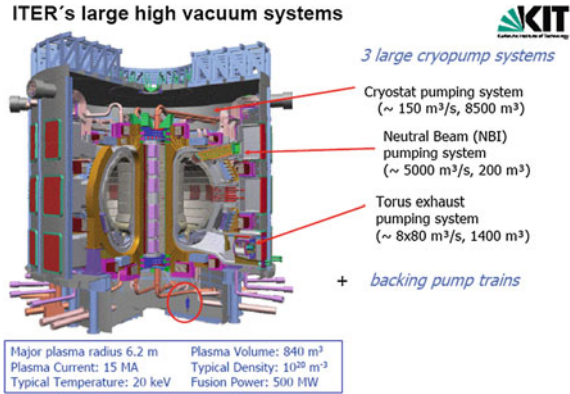
Fig. 9.33 Arrangement of
ITER torus cryopumps.
Courtesy of ITER
organization
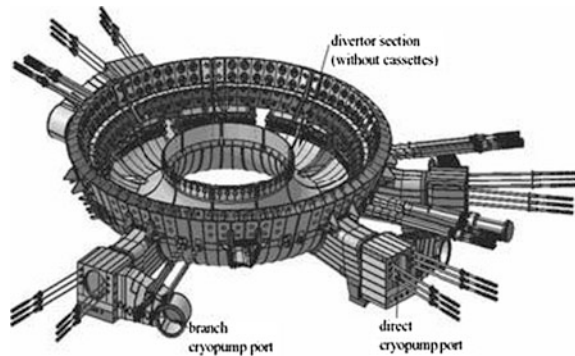
Figure 9.33 shows the locations of cryopumps near the ITER divertor.

The required throughput is 150 Pa-m^3/s at a divertor pressure of 1–10 Pa. The pumping speed of each cryopump will be 80 m^3/s. Each pump needs a charcoal coated surface area of 12 m^2. The regeneration temperature will be 90 K. The cryopump operations are staggered so that some pumps are operating while others are regenerating.

The prototype cryopump design is shown in Fig. 9.34.

Bellows compensate for torus displacement due to vibrations and thermal expansion. The surfaces in the yellow zone are at cryogenic temperatures to adsorb gases. The cryogenic surfaces become saturated with adsorbed gases. Then they are allowed to warm up with the valve closed to desorb the gases and pump them out ("regeneration").

The ITER cryostat will have two torus cryopumps in lower ports, and additional cryopumps in each NBI system, Fig. 9.35.

There are also vacuum pumps for service systems and for diagnostics systems. Each of the cryopumps must be backed up by a pump that removes its gases during regeneration. All pumps must be tritium-compatible, having only metal gaskets.
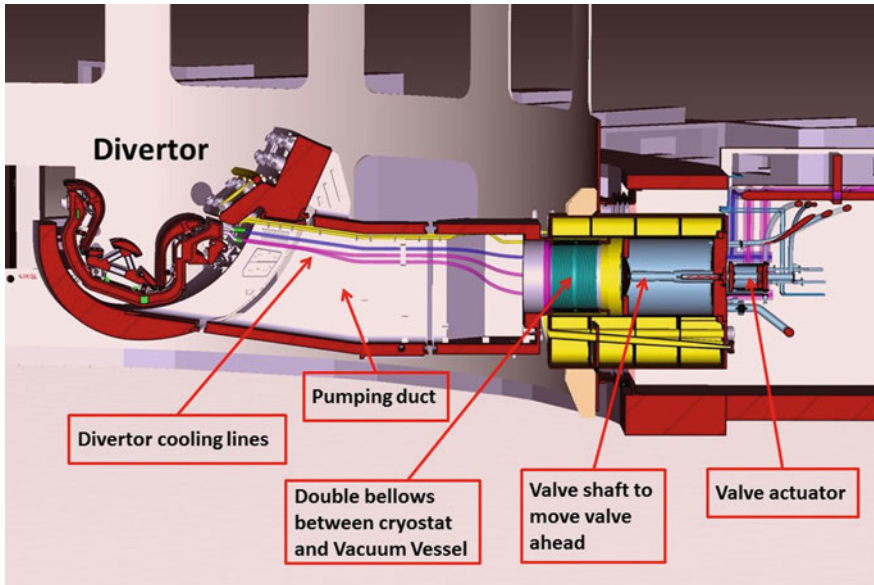
Fig. 9.34 The ITER torus cryopump design. Courtesy of ITER organization
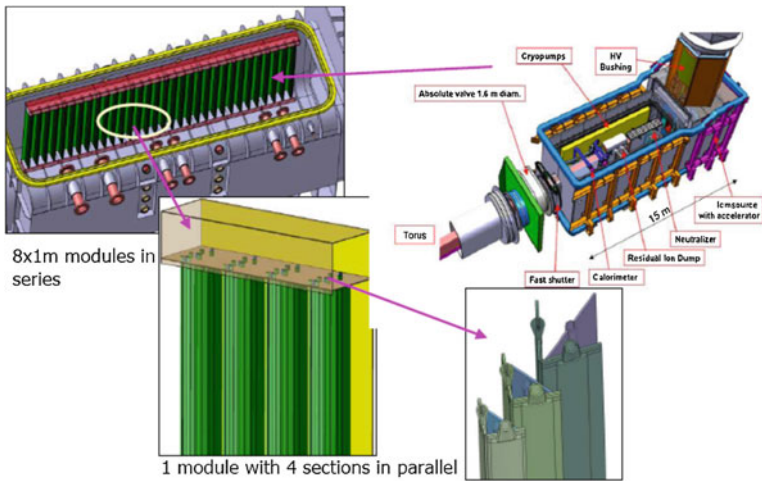
Fig. 9.35 An ITER neutral beam injector and cryopumps (Day 2010). Courtesy of ITER organization

The available tritium compatible pumps include diaphragm pumps, piston pumps, scroll pumps, and turbomolecular pumps, but these pumps have pumping speeds that are not high enough. Roots pumps, perhaps together with screw pumps,

may be used, since they have higher pumping speeds. A project is underway to develop a new pump that can meet ITER needs. The cryopump regeneration will pump down to 10 Pa in <200 s. The torus roughing system will pump from 1 atm to 10 Pa in 40 h.

9.8 Conclusions

Some conclusions by Day (2010) about the ITER vacuum system are:

- Vacuum pumping systems of ITER are typical for any DT fusion experiment (using the lessons learned at JET).
- The large ITER high vacuum cryopumping systems (torus, cryostat, NBI) share a common modular approach of charcoal coated cryosorption panels, developed by the Karlsruhe Institute of Technology.
- The torus and cryostat vacuum pumping system is testing a prototype and starting pump manufacture.
- The NBI vacuum system is in detailed design phase, and the test bed for the prototype is under preparation.
- The fore-vacuum pumping systems are still in a conceptual phase.
- The ITER vacuum systems will become the most complex vacuum system on the world.

9.9 Problems

9.1. If Otto von Guericke's copper hemispheres had a diameter of 1 m, how large was the force holding them together? Express the number in N, lbs, and tons.

9.2. Two astronauts in a satellite orbiting station observe the pressure in their chamber ($V = 90$ m^3) drops from 1.0×10^5 to 0.987×10^5 Pa in 17 min, due to outflow through a small crack. Gas is not being added to the chamber from storage bottles. What is the effective conductance of the crack? At what time will the pressure be 0.90×10^5 Pa if the leak is not fixed? Assume constant conductance.

9.3. Air is flowing in a 5 cm diameter tube at $P = 100$ Pa, $T = 300$ K, with flow velocity $v = 0.3$ m/s. Find (a) the throughput, (b) the average molecular speed, (c) the molecular flow rate (d) the flow regime, (e) the tube conductance and pressure drop in a distance of 0.1 m.

9.4. A chamber of 0.05 m^3 volume at 77 K is connected through a 2 cm orifice to another chamber with 0.07 m^3 volume at 298 K and 10^{-4} Pa air. What is the equilibrium pressure in the first chamber?

9.5. Two chambers, in Fig. 9.2, are connected by a tube with 3 cm diameter and length 28 cm. The air pressure in one chamber is 0.1 Pa, and in the other chamber it is 0.002 Pa. (a) What kind of flow is occurring? (b) What is the throughput? (c) How many molecules are flowing through the tube per second? (d) What is the pumping speed at the entrance to the lower-pressure chamber (taking $P_u = 0$)?

9.6. A pump with speed 0.08 m^3/s and ultimate pressure 10^{-7} Pa is connected to a 1.7 m^3 chamber with a tube 0.8 m long, 1 cm diameter. When the pressure at the pump is 10^{-5} Pa (air), find the throughput and chamber pressure for tube diameters of (a) 1 cm (b) 10 cm.

9.7. A vacuum chamber with volume V at pressure p and temperature T is connected to two pumps with speeds S_1 and S_2 through tubes with conductances C_1 and C_2. Both pumps have the same ultimate pressure P_u. Find the equilibrium pressure corresponding to a constant leak rate Q in terms of these parameters.

9.8. A pump with speed 0.1 m^3/s is connected to a 0.4 m^3 chamber by two 0.6 m long tubes in parallel. Tube diameters are 0.04 and 0.07 m. The ultimate pump pressure is 10^{-6} Pa, and the leak rate is 10^{-5} Pam^3/s. (a) Find the equilibrium chamber pressure. (b) Find the equilibrium chamber pressure for the case in which the tubes are connected in series, instead of in parallel.

9.9. An accelerator is to be pumped every 3 m with a pump connected through a conductance of 0.1 m^3/s. The ultimate pressure of the pumps is 10^{-8} Pa, and the pumping speed is 0.2 m^3/s. If a pressure of 3×10^{-8} Pa is desired, what is the maximum leak rate (including desorption) which can be tolerated in a 3 m section?

9.10. A spherical chamber with R = 0.5 m initially has 10 monolayers of adsorbed gases on its interior. During the first 1,000 s of bakeout, five of the monolayers are removed, and the gas temperature is about 500 K. What is the average throughput of desorbed gases to the pump during this period?

9.11. A stainless steel soup kettle 0.5 m in diameter and 0.7 m long is to be made into a vacuum chamber for a plasma experiment. The walls are 3 mm thick. Is the kettle safe, or does it need to have reinforcement? If the kettle were made of aluminum, how thick would the walls need to be?

9.12. A space colony is constructed in a large cylinder 3 km in diameter and 5 km long, which rotates to produce artificial "gravity". It contains air at 1 atm pressure. A meteor blasts a hole about 10 m in diameter in one wall, and the air begins to rush out the hole. How long does it take before the pressure has dropped to 0.95 atm? (Because $P_2 \gg P_1$, the flow is "critical" or "choked", and the effective conductance C = 200 A.)

9.13. A McLeod gage is used to calibrate a Pirani gage in air. The trapped gas volume V = 121 cm^3, the trapped gas tube area is 0.14 cm^2, the measured heights are L = 8.3 cm and ℓ = 6.1 cm. The density of mercury is 13.546 g/cm^3, the acceleration of gravity is about 9.806 m/s^2 (varies with altitude). The Pirani gage reads 0.17 Torr. Is it accurate? At the same true pressure, what would the Pirani gage read if the gas were argon?

9.10 Review Questions

1. Explain "viscous flow", "molecular flow", and "transitional flow".
2. Define "throughput" and "conductance".
3. Explain the equation $Q = kT \, (dN/dt)$.
4. Explain the equation $v = Q/PA$. How does v differ from v_{th}?
5. Explain the equation $Q = S_t \, (P_p - P_u)$.
6. How can we calculate the conductance of three tubes in series?
7. At what frequency does a turbomolecular pump rotor turn?
8. Explain how a jet pump works.
9. How does a cryosorption pump work?
10. How does a cryogenic pump work, and what feature is used to prevent rapid boiling?
11. What are the advantages of cryogenic pumps?
12. Sketch a thermocouple gage and explain its operation.
13. Explain how an ionization gage works. At very low pressure how can its sensitivity be increased?
14. How can virtual leaks be avoided when welding a flange to a tube?
15. What kind of gaskets are needed for very low pressures, very high operating temperatures, and very low temperatures?
16. What contains about 8×10^{18} molecules/m^2?
17. What processes are used to clean vacuum chambers?
18. How can leaks be detected and cured?
19. What process limits the attainable pressure in the ultrahigh vacuum region?
20. What types of vacuum pumps are used in ITER?
21. What ITER system requires the highest cryopump speed?
22. Why are the ITER torus cryopumps "staggered"?

References

André J, Millet F, Perin JP, Saint-Bonnet P (2012) An alternative vacuum pumping system for fusion reactors. 27th Symposium on Fusion Technology. Liege, Belgium, 24–28 Sep 2012

Berman A (1992) Vacuum engineering calculations, formulas, and solved exercises. Academic Press, San Diego

Carpenter LG (1970) Vacuum technology. American Elsevier, New York

Day C (2010) Vacuum pumping systems (in DT fusion devices) summer school on fusion technology. Karlsruhe Institute of Technology, Germany

Dennis NTM, Heppell TA (1968) Vacuum system design. Willmer Bros. Limited, Birkenhead, England, and Chapman and Hall Limited, London

Dolan TJ (1982) Fusion Research. Pergamon Press, Elmsford

Middleton WEK (1964) The history of the barometer. Johns Hopkins Press, Baltimore

Roth A (1966) Vacuum sealing techniques. Pergamon Press, Elmsford
Roth A (1976) Vacuum technology. North Holland, New York
Steinherz HA (1963) Handbook of high vacuum engineering. Reinhold, New York
Steinherz HA, Redhead PA (1962) Ultrahigh vacuum. Scientific American, March
Tompkins HG, Gessert TA (2001) Pumps used in vacuum technology, American vacuum society
    monograph series, 2nd edn. Education Committee, American Vacuum Society, New York

Chapter 10
Cryogenic Systems

Thomas J. Dolan

Objectives

After reading this chapter one should understand

Materials properties at low temperatures
Cryogenic refrigeration
Insulation and cryostats
ITER cryogenic systems.

10.1 Introduction

The term "cryogen" was originated by H. K. Onnes from the Greek stems "cryo", which means "cold," and "genes," meaning "that which generates." Today, the term cryogenics refers to the physical, chemical, engineering, and industrial applications of phenomena at low temperatures, below about 123 K (-150 °C). The four common temperature scales are related by the equations

$$\begin{aligned}
T(F) &= 1.8\,T(°C) + 32 \\
T(R) &= T(F) + 459.67 \\
T(K) &= T(°C) + 273.15
\end{aligned} \tag{10.1}$$

Study of cryogenic phenomena is roughly one hundred years old. Early developments in production of liquid oxygen and nitrogen occurred in Europe in 1877–1890. James Dewar invented vacuum insulated flasks in 1892, and he liquefied hydrogen in 1898. Carl Von Linde and Georges Claude developed practical systems for the liquefaction of air in 1895 and 1902. H. K. Onnes liquefied helium

T. J. Dolan (✉)
NPRE Department, University of Illinois, Urbana, IL 61801, USA
e-mail: dolantj@illinois.edu

(the last gas to be liquefied) in 1908 and discovered superconductivity in 1911. After the end of the First World War, production of industrial gases (such as oxygen and nitrogen) by cryogenic processes grew rapidly.

The first expansion engine for liquefying helium was built by P. Kapitza in 1934. A comparatively economical process for producing liquid helium was developed by S. C. Collins in 1947, which facilitated expansion of research on low-temperature phenomena.

Large V-2 rockets fueled by liquid oxygen and alcohol were developed during the Second World War. Development of rocket technology continued in the USSR and in the USA, leading to the launching of satellites and space flights. Cryogenics has now become an important industrial field with many practical applications, Table 10.1.

Cryogenic systems are essential to the success of neutral beam injection systems and superconducting magnets. Cryopumps, having the highest attainable pumping speed, prevent excessive influx of cold neutral gas from neutralizing cells into the confinement region.

Table 10.1 Applications of cryogenic technology

Industrial gas production and uses
Gases O_2, N_2, CO_2, He, Ar, Ne, etc
Steel refining (oxygen)
Prestressing of pressure vessels (liquid nitrogen)
Ammonia production (cryogenic systems)
Welding (argon or helium)
Food preservation
Dry ice production
Rapid-freezing with liquid nitrogen
Freeze drying processes
Biomedical applications
Preservation of tissue, blood, semen
Cryosurgery
Mechanical devices
Frictionless bearings and gyroscopes
Refrigeration processes
Electrical devices
Low-noise electronics and masers
Computers
Superconducting motors, generators, energy storage, transmission
Physics studies
Radiation damage
Neutron moderation
Bubble chambers
Low-temperature phenomena, such as superfluidity and superconductivity
Space technology
Rocket propulsion
Space simulation systems and vacuum chambers
Fusion research
Superconducting magnet coils
Cryopanel vacuum pumping systems

The cryogenic systems for magnets involve the following considerations:

- **Materials.** Materials must have suitable low-temperature mechanical, thermal, and electrical properties.
- **Refrigeration.** For a reactor heat loads of tens of kW must be removed at $T \sim 4$ K.
- **Insulation.** Effective insulation must minimize conductive, convective, and radiative heat transfer.
- **Structure.** The cryostat must sustain magnetic and gravity forces with a minimum of heat leakage.

10.2 Properties of Materials at Low Temperatures

The properties of some materials change markedly at low temperatures. For example, some organic materials (flowers, banana peels) immersed in liquid nitrogen (at 77 K) become brittle and will shatter like glass when struck with a hammer.

10.2.1 Mechanical Properties

Some properties of interest are yield stress, ultimate stress, percent elongation, impact energy, and modulus of elasticity. In general, the percent elongation and impact energy decrease at low temperatures as shown in Fig. 10.1.

Fig. 10.1 Percent elongation of various metals as a function of temperature. Data from Cryogenic Systems, by R. Barron, Figs. 2–5, p. 21. Copyright 1966 used by permission
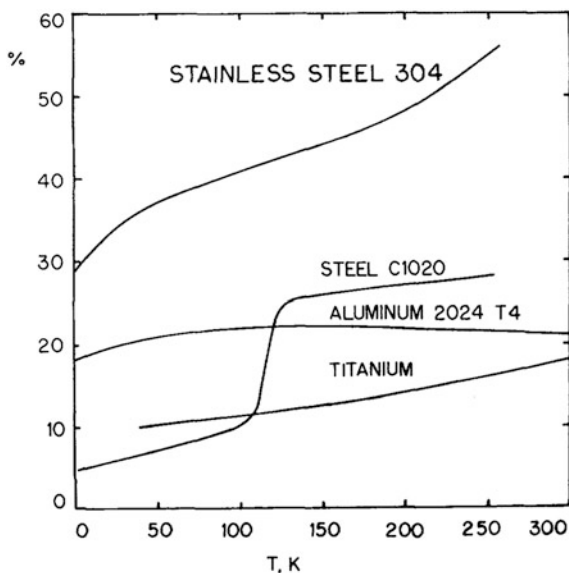
Fig. 10.2 Ultimate stress of various materials as a function of temperature
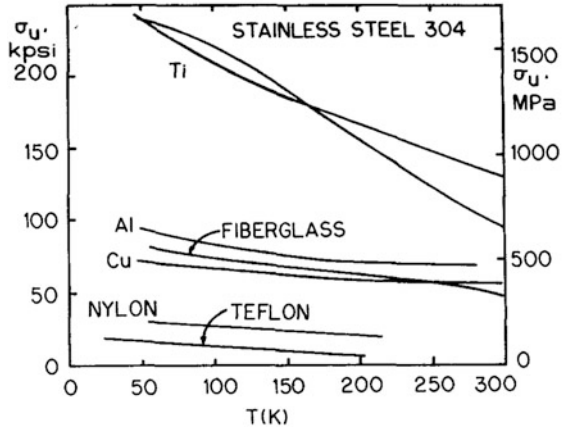
In the early 1940s, several cargo ships unexpectedly broke apart and sank in the North Atlantic before it was discovered that their welds became brittle at low temperatures. Brittle materials usually perform better in compression than in tension. Because plastics are very brittle at low temperatures, thermal shock must be avoided. For most materials the yield stress and ultimate stress increase slightly at low temperatures, as illustrated in Fig. 10.2 for ultimate stress.

Modulus of elasticity usually remains about constant or increases slightly with decreasing temperature (except for some plastics, where a large increase occurs). If the magnets are to be repetitively turned on and off, the possibility of low-cycle fatigue failure should be considered.

10.2.2 Thermal Properties

Pertinent thermal properties include specific heat, thermal conductivity, emissivity, and thermal expansion coefficient. The specific heats of most inorganic solids at low temperatures follow the Debye equation

$$C = 9R \left(\frac{T}{\theta_D}\right)^3 \int_0^{\theta_D/T} \frac{dx \, x^4 e^x}{(e^x - 1)^2} \tag{10.2}$$

where C = specific heat at constant volume (J/mol K), R = 8.314 (J/mol K) is the universal gas constant, T = material's temperature (K), and θ_D is the "Debye temperature," which is a constant for a given material. If this equation is divided by the molecular weight, C will be expressed in J/kg-K. The values of θ_D for various materials are shown in Table 10.2.

The ratio of C/R from Eq. (10.2) is plotted as a function of temperature is shown in Fig. 10.3.

Table 10.2 Debye temperatures for various materials

Al	390 K
Cu	310 K
Alpha-Fe	430 K
Gamma-Fe	320 K
Pb	86 K
Li	430 K
Ni	375 K
Ti	350 K

Fig. 10.3 Ratio of specific heat to universal gas constant R as a function of the ratio of temperature T to Debye temperature θ_D. From Cryogenic Systems, by R. Barron, Figs. 2–8, p. 28. Copyright 1966, McGraw-Hill, New York. Used by permission of McGraw-Hill Book Company
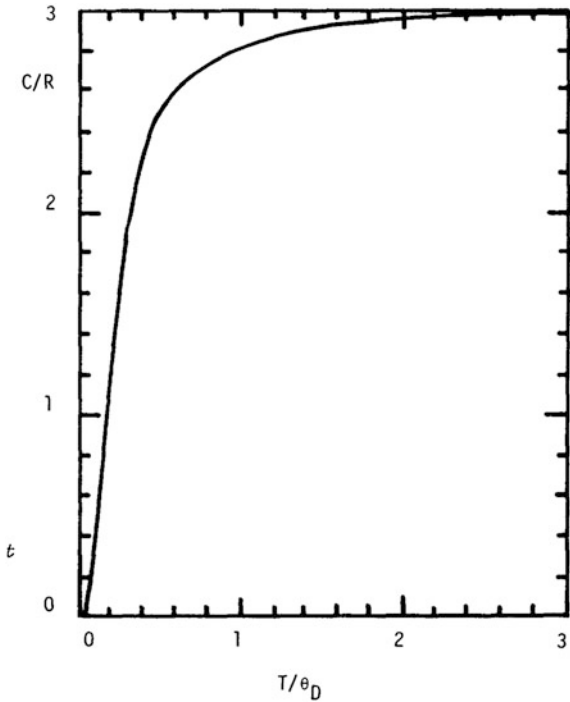
At temperatures $T < \theta_D/12$, this equation reduces to

$$C/R = 233.8 \, (T/\theta_D)^3 \tag{10.3}$$

The specific heat for stainless steel (18 % Cr, 8 % Ni) falls from 476 J/kg-K at room temperature to 159 J/kg-K at 77 K and 4.6 J/kg-K at 20 K.

The enthalpy of a material is defined by

$$h \equiv \int_0^T dT \, C + h_0 \; (\text{J/kg}) \tag{10.4}$$

where h_0 is the enthalpy at $T = 0$. The heat added per kg to raise the temperature from T_1 to T_2 is

Table 10.3 Enthalpies of various materials at low temperatures, J/g

T,K	Cu	Al	Nb	Sn	Fe	Ni	C	Teflon
300	79.6	170.4	59.2	53.6	81.1	82.4	88.7	167.8
280	72.0	152.5	53.9	49.1	72.3	73.6	75.0	144.6
260	64.4	135.0	48.6	44.7	63.6	65.0	62.5	125.5
240	56.9	117.8	43.4	40.3	55.2	56.7	51.2	107.8
220	49.6	101.0	38.2	36.0	47.0	48.6	41.1	91.3
200	42.4	84.8	33.1	31.7	39.2	40.8	32.2	75.9
180	35.3	69.2	28.0	27.4	31.8	33.4	24.5	61.7
160	28.5	54.4	23.1	23.2	24.6	26.3	18.0	49.0
140	22.1	40.7	18.3	19.1	18.2	19.7	12.7	37.7
120	16.1	28.4	13.8	15.1	12.4	13.8	8.4	27.9
100	10.6	17.8	9.6	11.1	7.6	8.6	5.1	19.5
80	6.0	9.4	5.8	7.6	3.8	4.6	2.7	12.5
60	2.6	3.6	2.8	4.3	1.4	1.8	1.2	7.0
40	0.6	0.8	0.8	1.8	0.3	0.4	0.4	3.0
20	0.03	0.05	0.07	0.3	0.03	0.04	0.04	0.5
10	0.0024	0.005	0.007	0.02	0.005	0.007	0.003	0.05

$$W/M = \int_{T_1}^{T_2} dT\, C = h_2 - h_1 \qquad (10.5)$$

where W = heat added (J), M = mass of the material (kg), and h_2 and h_1 are the enthalpies at T_1 and T_2. Enthalpies of several materials are given in Table 10.3.

Example Problem 10.1: Temperature after quench A 1 GJ coil stabilized by aluminum at 10 K is not to exceed 100 K after a quench in which all the energy is distributed uniformly in the aluminum, ignoring heat absorption in superconductor and insulators. What is the required mass of aluminum?

For aluminum, the enthalpy difference $h_2 - h_1 = 17{,}800$ J/kg = W/M.

Since $W = 10^9$ J, we find that $M = 56{,}000$ kg of aluminum.

Thermal conductivities vs. temperature for various materials are shown in Fig. 10.4.

Structural materials extending between the coil and the cryostat (container) should have low thermal conductivity and high strength, so the ratio of yield stress to thermal conductivity is often used as a figure of merit. The mean value of these ratios between room temperature and 90 K, relative to the ratio for stainless steel 304, is given in Table 10.4 for various materials.

The linear thermal expansion is used to calculate thermal stresses, which arise from temperature gradients. Thermal expansion values for various materials are listed in Table 10.5, relative to the length of the material at 0 K.

The thermal emissivity is the ratio of the amount of heat radiated by a surface to that which would be radiated by a pure "black body." Values of thermal emissivity will be used in estimating radiative heat transfer between walls separated by a vacuum. The thermal emissivities of some common materials are given in Table 10.6.

Fig. 10.4 Thermal conductivities of various materials versus temperature
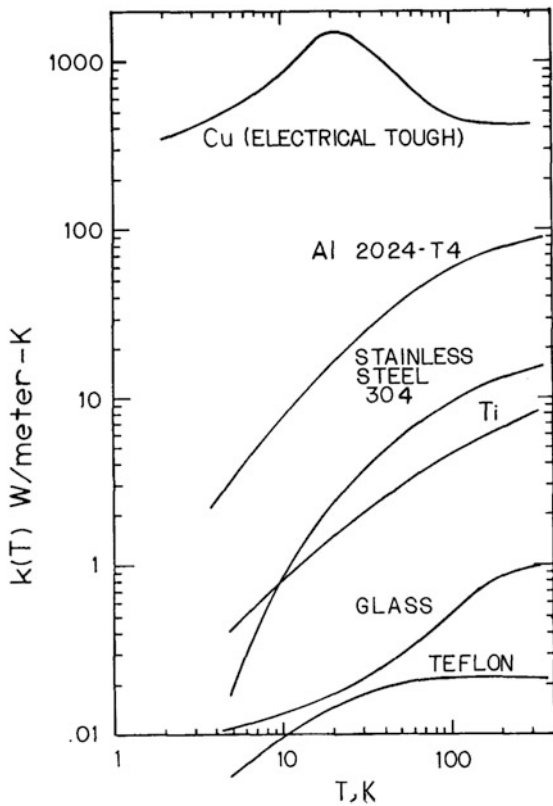
Table 10.4 Ratio of strength to thermal conductivity between room temperature and 90 K, relative to the ratio for 304 stainless steel

Stainless steel 304	1.00
Aluminum 2024-0	0.017
Teflon	0.269
K Monel	0.68
Hastelloy C	0.606
Nylon	0.957
Glass fibers	3.63
Mylar	5.67
Kel F oriented fibers	10.8
Dacron fibers	12.5

From Cryogenic Systems, by R. Barron, Tables 7–5, p. 466. Copyright 1966, McGraw-Hill, New York. Used by permission of McGraw-Hill Book Company

Table 10.5 Thermal expansion of various materials

Material	20 K	60 K	100 K	150 K	200 K	250 K	300 K
Copper	0	10	44	105	178	256	339
Aluminum	0	10	46	121	214	319	431
Nickel	0	4	23	64	117	172	239
Titanium	0	1	14	41	74	113	155
Stainless 304	−1.1	2.8	30	85	151	225	304
Yellow brass	0	15	57	130	214	303	397
Polyester and fiberglass	3	21	49	99	159	223	291
Nylon	10	81	217	443	716	1,050	1,450
Teflon	45	200	410	717	1,130	1,747	2,695

Data from Scott (1959), Tables 10.5 and 10.6, p. 331 and 333. Some interpolations are given here. $[L(T) - L(0)]/L(0)$ in units of 10^{-5}

Table 10.6 Thermal emissivities of some common materials

Material	T = 77 K	T = 293 K
Bright aluminum foil	0.018	0.03
Polished copper	0.019	0.03
Glass		0.94
Stainless steel 304	0.061	0.150
Titanium		0.11
Silver	0.01	0.022
Nickel	0.022	0.04

10.2.3 Electrical Resistivity

Resistivities of Cu and Al, relative to the values at room temperature, are shown in Fig. 10.5.

These values vary strongly with the impurity content, and the purity is sometimes spoken of in terms of the ratio of the resistivity at 293 K to that at 4.2 K, called the *residual resistivity ratio* (*RRR*), which is about 30 for the aluminum of Fig. 10.5. Values of RRR of several thousand can be obtained by careful refining, though at increased cost. The resistivities increase with applied magnetic field and with neutron irradiation fluence.

10.2.4 Cryogenic Liquids

At cryogenic temperatures ordinary gases become liquids or solids. Properties of some cryogenic fluids are listed in Table 10.7.

The gases cannot be liquefied above the "critical temperature," no matter how high a pressure is applied. Only about 1.3 ppm of ordinary helium is helium-3, the majority being helium-4. Helium-4 cannot be solidified at atmospheric pressure,

Fig. 10.5 Ratio of the electrical resistivities of Cu and Al to their resistivities at 293 K. Very pure samples would have lower resistivities. From Cryogenic Systems, by R. Barron, Figs. 2–12, p. 42. Copyright 1966, McGraw-Hill, New York. Used by permission of McGraw-Hill Book Company
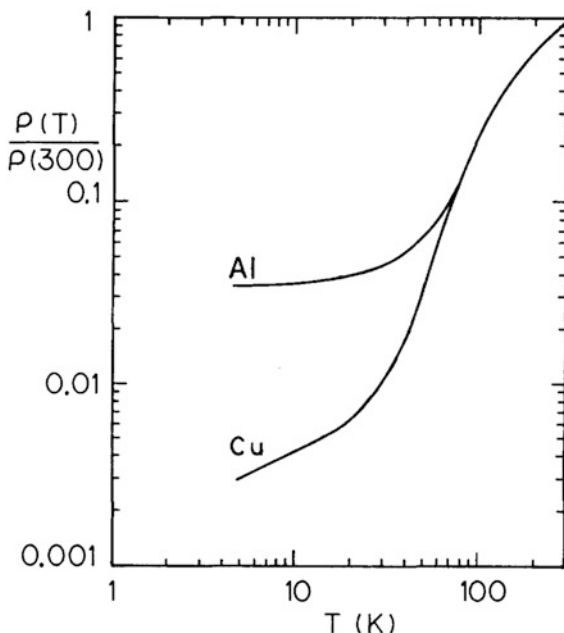
Table 10.7 Properties of cryogenic liquids and water at 1 atm

	Helium-4	Hydrogen	Nitrogen	Oxygen	Water
Boiling point (K)	4.2	20.3	77.4	90.2	373.2
Melting point (K)	None	13.8	63.2	54.4	273.2
Critical temperature (K)	5.2	33.2	126	155	645
Properties at boiling temperature					
Density (kg/m^3)	125	71	800	1,140	1,000
Heat of vaporization (MJ/m^3)	2.72	31.6	161.3	243	2,257
Specific heat c_p (kJ/kg-K)	4.56	9.76	2.04	1.70	4.22
Thermal conductivity (W/m-K)	0.0269	0.118	0.139	0.148	0.023

Data from Laquer (1973), Table I, and Cryogenics Systems by R. Barron, Tables 2–3, p. 38. Copyright 1966 McGraw-Hill, New York. Used by permission of McGraw-Hill Book Company

but it can be solidified at about 25 atm. Liquid helium has many unusual properties, such as superfluidity, which are described in the references.

Figure 10.6 shows vapor pressures of common fluids at low temperatures.

These curves are taken into account when designing cryogenic pumping systems. At T = 85 K oxygen liquefies, but nitrogen does not, so hazardous amounts of liquid oxygen could accumulate.
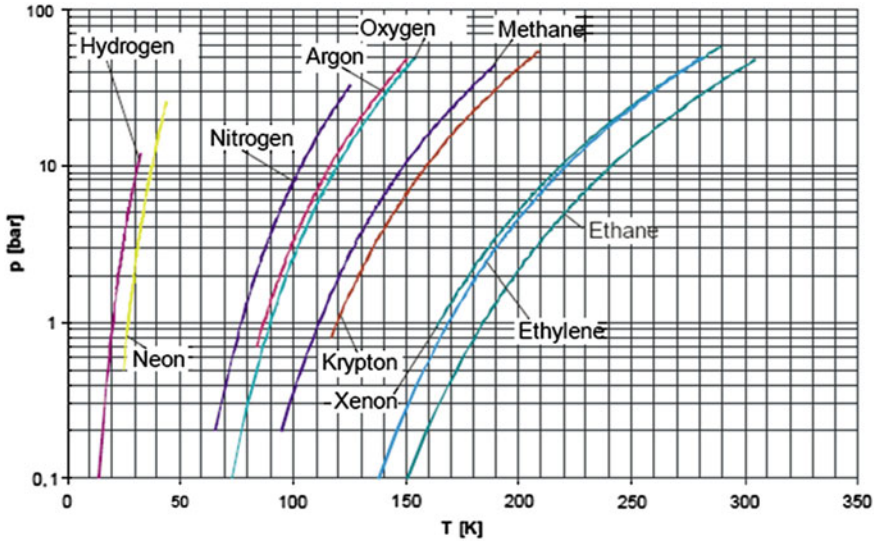
Fig. 10.6 Vapor pressure versus temperature for some common fluids. From H. Neumann, KIT Summer School, 2010, slide 9

10.3 Refrigeration and Liquefaction

Liquefaction refers to the process of condensing gases into liquids, while refrigeration refers to the process of heat removal from a substance. If superconducting magnets are cooled by liquid helium, then helium liquefaction will be necessary; if they are cooled by chilled helium vapor, then only refrigeration may be needed. Both processes are similar, however, in that they require cycles involving compression (with a temperature rise), cooling by a heat sink, and then expansion cooling (with or without condensation to the liquid phase), as illustrated in the simple diagram of Fig. 10.7.

According to the Joule-Thomson effect, expansion of a gas lowers its temperature, provided that its initial temperature is below the inversion temperature. Gases like nitrogen and oxygen, which have inversion temperatures greater than room temperature, can be cooled by expansion at room temperature. Household refrigerators use this cycle with a fluid like Freon®. (Nowadays, industries cannot use chlorinated fluorocarbons.) On the other hand, hydrogen and helium have inversion temperatures of about 204 and 40 K, so they require precooling below these temperatures if they are to be cooled by expansion. Such gases have been called "permanent gases" because of the difficulties encountered in attempting to liquefy them.

In liquefiers, the gas to be liquefied is usually the working fluid. It is precooled below the inversion temperature, and during expansion part of it condenses into the liquid state, forming a pool at the bottom of the expansion chamber. To cool

Fig. 10.7 A simple refrigeration cycle. Cryogenic refrigerators use similar steps, but with additional measures to improve efficiency
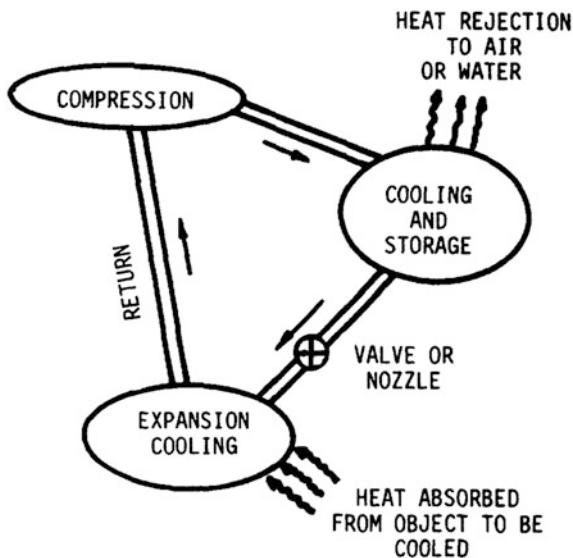
and liquefy 1 mol of helium starting at 298.15 K, about 27.2 kJ of thermal energy must be removed. However, a much greater amount of energy must be expended by the machine to accomplish this amount of heat removal. For liquefaction of helium, the precooling below the inversion temperature can be done either by evaporation of liquid hydrogen (which boils at 20.3 K) or by using heat exchangers with returning chilled helium vapor as the coolant. The latter method has the advantage of not requiring liquid hydrogen and a separate liquefier for it. Approximately **280 W** of electricity are required per Watt of heat removed at 4 K.

Ordinary expansion through a valve or nozzle is thermodynamically irreversible: heat energy is wasted in increasing the entropy, and cooling is inefficient. (Entropy is the ratio of energy to temperature, and it measures the amount of energy which is bound up in matter and unavailable for use). The expansion can be made more efficient by letting the gas expand gradually in an expansion engine, such as a cylinder-and-piston or a gas turbine. In such an engine, the expansion becomes more nearly reversible or isentropic (constant entropy), and less thermal energy is trapped in entropy. Consequently, the amount of cooling produced by the expansion of a given quantity of gas is greatly increased. For this reason expansion engines are often employed in cryogenic refrigeration and in liquefaction of permanent gases.

The Collins helium-liquefaction system is illustrated in Fig. 10.8.

In this system, helium gas at room temperature and atmospheric pressure is compressed to about 14 atm, and then it is cooled in a series of heat exchangers with counterflowing chilled helium vapor. Any number of expansion engines may be used. For simplicity only two are shown in the figure. For this case about 25 % of the mass flow rate would be channeled through the first expansion engine and

Fig. 10.8 The collins system
for helium liquefaction.
Based on Cryogenic Systems
by R. Barron, Figs. 3–30,
p. 122. Copyright 1966,
McGraw-Hill, New York.
Used by permission of
McGraw-Hill Book Company
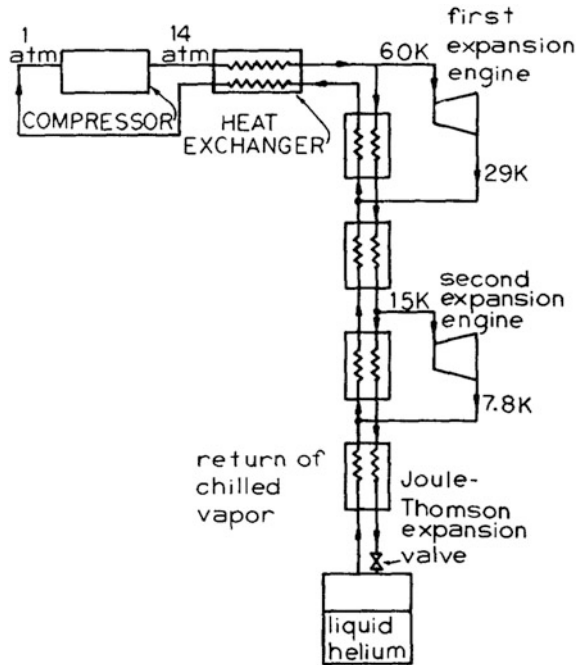
about 50 % through the second engine, leaving about 25 % to pass through the
Joule-Thomson expansion valve. About 12 % of the mass flow condenses in the
expansion chamber, and the remaining 13 % vapor returns up through the heat
exchangers, where it is joined by returning chilled vapor from the expansion
engines.

In some refrigeration systems regenerators are used in place of heat exchangers.
A regenerator is a heat storage device with a large internal surface area from which
heat may be rapidly transferred to the working fluid. For example, a tube packed
full of steel wool could be used as a regenerator. A regenerator first receives heat
from the hot fluid and then gives up this heat to the cold fluid. The two fluids flow
through it alternately. Regenerators have the advantage of a low pressure drop,
ease of construction, and a very large internal surface area per unit volume. They
are limited by their low heat capacity (which may require rapid interchanging) and
by the mixing of fluids from the two streams as they are interchanged. In practice,
two regenerators may be used simultaneously, one for the hot fluid and one for the
cold, and they may be rapidly interchanged to permit almost continuous flow of the
two fluids.

For simplicity, only the Collins system has been illustrated here. Detailed
analyses of the efficiencies of various types of heat exchangers, regenerators,
expansion engines, and systems for refrigeration and liquefaction are given by
Barron (1966). If high temperature superconducting coils could be used at 65 K,

then the cryostat could be much simpler, and the refrigeration power could be substantially reduced (from 33 to 20 MW in the example of Sect. 4.9).

10.4 Insulation

Effective insulation must combat all three heat transfer mechanisms: conduction, convection, and radiation. The thermal power flow by conduction along a body with cross sectional area A and length L is

$$P_{cond} = \frac{A}{L} \int_{T_1}^{T_2} dT \, k(T) \, (W), \tag{10.6}$$

where k(T) is the thermal conductivity (W/m-K), and T_1 and T_2 are the temperatures at the endpoints of the body. To minimize the heat flow, one can use materials with low thermal conductivity, small cross sectional area A, or a long heat-flow path length L. Some values of the integral are given in Table 10.8.

Example Problem 10.2: Heat leak through support A coil at 10 K is partially supported by a stainless steel tube with D = 7 mm, thickness 1 mm, and length 20 cm to an intermediate surface at 80 K. What is the heat flow into the coil along this tube?

From Table 10.8 the difference in conductivity integrals is 3.46 W/cm. The cross sectional area of the tube $A = p(r_2^2 - r_1^2) = 0.251$ cm^2. Then from Eq. (10.6) $P_{cond} = 0.043$ W.

Convection is reduced by dividing the gas into small cells (as in foam insulation) or by removing the gas (as in vacuum insulation). When both conduction and convection have been minimized, radiation may become the dominant heat transfer process.

The thermal power transferred radiatively from a spherical or cylindrical surface with area A_2, temperature T_2, and emissivity e_2 to another concentric surface with area A_1, temperature T_1, and emissivity e_1 is

$$P_{rad} = \frac{\sigma(T_1^4 - T_2^4)}{\frac{1}{A_1 e_1} + \frac{1}{A_2 e_2}(1 - e_2)} \tag{10.7}$$

where $\sigma = 5.67 \times 10^{-8}$ W/m-K^4 is the Stefan-Boltzmann constant. To minimize radiant heat transfer, surfaces with low emissivity are used, and multilayer radiation barriers may be employed. For example, if $e_1 = e_2 = 0.90$, and if ten radiation shields with emissivity $e_s = 0.05$ are placed in between A_1 and A_2, then the radiant heat transfer rate P_{rad} drops to only 0.3 % of what it would be without the shields.

Table 10.8 Thermal conductivity integrals (Stewart 1961) $\int_4^T dT\, k(T)$ (W/m)

T, K	Electrical tough pitch copper	(Pb) Brass	Aluminum 6063-T5	Stainless steels	Glass
6	8.00	0.053	0.850	0.0063	0.00211
8	19.1	0.129	2.05	0.0159	0.00443
10	33.2	0.229	3.60	0.0293	0.00681
15	80.2	0.564	9.00	0.0816	0.0131
20	140	1.12	16.5	0.163	0.0200
25	208	1.81	25.8	0.277	0.0279
30	278	2.65	36.5	0.424	0.0368
35	345	3.36	48.8	0.607	0.0471
40	406	4.76	62.0	0.824	0.0586
50	508	7.36	89.5	1.35	0.0846
60	587	10.4	117	1.98	0.115
70	651	13.9	143	2.70	0.151
76	686	16.2	158	3.17	0.175
80	707	17.7	167	3.49	0.194
90	756	22.0	190	4.36	0.240
100	802	26.5	211	5.28	0.292
120	891	36.5	253	7.26	0.408
140	976	47.8	293	9.39	0.542
160	1,060	60.3	333	11.7	0.694
180	1,140	73.8	373	14.1	0.858
200	1,220	88.3	413	16.6	1.03
250	1,420	128	513	23.4	1.50
300	1,620	172	613	30.6	1.99

Although Eq. (10.6) is only valid for simple cases of conductive heat transfer, it is convenient to define an "apparent mean thermal conductivity" k_{app} such that

$$P = k_{app}\, A\, (T_2 - T_1)/L \tag{10.8}$$

where P is the total heat flow from *all three processes*. This definition, although it is not rigorously accurate, facilitates comparison of k_{app} for various types of insulation, as illustrated in Table 10.9.

Table 10.9 Apparent mean thermal conductivities for various types of insulation, between 300 and 77 K. From Glaser et al. (1967) and Vance and Duke (1962)

Material	(μW/cm-K)	mW/m-K
Foams, 1 atm	300–400	30–40
Evacuated foams	100–200	10–20
Unevacuated powders	200–1,000	20–100
Evacuated powders ($p \leq 0.01$ Pa)	2–20	0.2–2
Evacuated multilayer re-reflective barriers ($p \leq 0.01$ Pa)	0.1–2	0.01–0.2

The multiple-barrier insulation, which consists of alternate layers of reflective aluminum or copper foil and insulating substances, such as thin mesh or plastic or fiberglass, is clearly the best. Very thin sheets of aluminized Mylar® incorporate both the plastic and the reflector into one sheet. It has been found that k_{app} rises rapidly as the pressure is raised above 0.03 Pa. Holes about 5 mm diameter occupying about 5 % of the sheet surface facilitate vacuum pumping without spoiling the insulation. As the number of layers of this "superinsulation" is increased, radiant heat transfer is drastically reduced, but when they are packed too tightly, conduction becomes significant. The optimum layer density is about 25 layers per cm.

Compaction of the layers must be avoided, as it can increase k_{app} by an order of magnitude. One advantage of evacuated powders over superinsulation is ease of installation, especially around complex shapes but the lower value of k_{app} provided by super insulation is probably worth the extra cost of installation. Various types of multilayer insulation are reviewed by Glaser et al. (1967).

Figure 10.9 shows some ways of installing superinsulation.

The heat leak into liquid helium dewars can also be reduced by using *vapor shielding*. The vaporized helium from the inner vessel passes through a tube to cool an intermediate vessel as it escapes. In this way the temperature difference seen by the inner vessel is reduced, and boiloff may be reduced by about a factor of
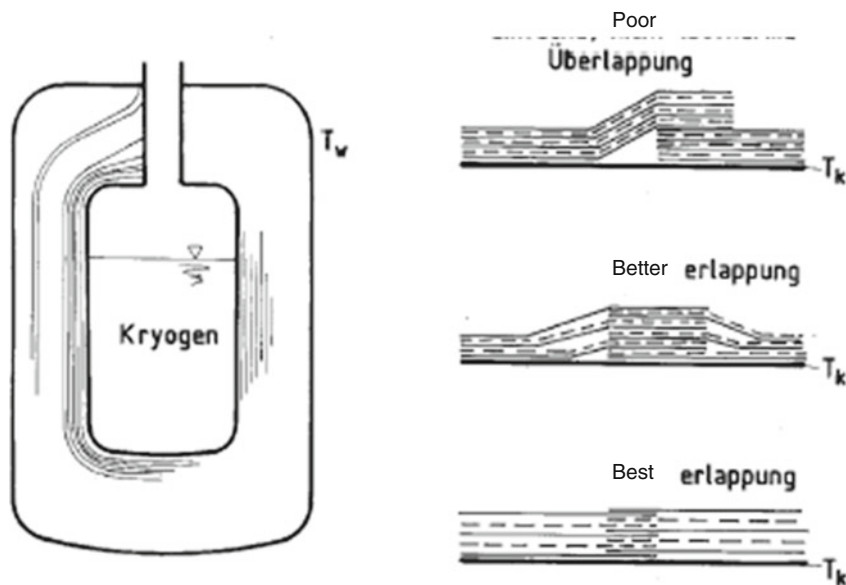
Fig. 10.9 Methods of installing superinsulation. The overlapping method (*top right*) is the poorest, and the individual sheet overlapping (*bottom right*) is the best, but the most time-consuming (Neumann 2010)

4. High-current leads for superconducting magnets are usually vapor-shielded tubes, and high-temperature superconductors may be used for part of the lead where T < 65 K.

10.5 Cryostats

The vessels used to contain and insulate superconducting magnets are called *cryostats* or *dewars*. The main problem is to sustain the magnetic and gravity forces without introducing large heat leaks through the structure. Part of the structure may be at coil temperature (cold reinforcement) and some parts may make the transition up to 77 and 293 K (warm reinforcement). Cold reinforcement does not add to heat inflow during normal operation, but steels with good low-temperature properties must be used, and more metal must be cooled down initially. If much structural steel is involved, then using plain steel at room temperature may result in cost savings (Powell and Bezler 1974).

A cryostat may have multiple heat shields to reduce heat leaks into the cryogenic liquid. Figure 10.10 shows a cryostat for long-term storage of liquid nitrogen.
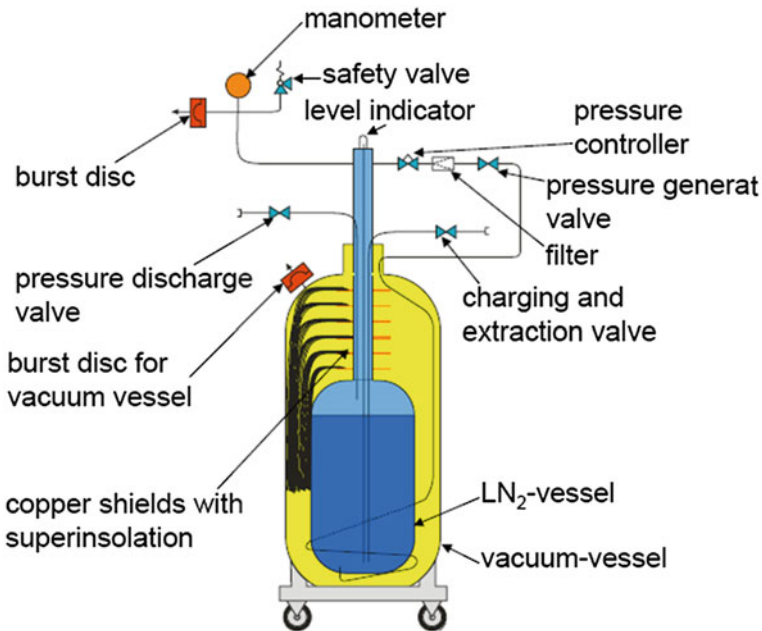
Fig. 10.10 A liquid nitrogen vessel with built-in pressure generation (Neumann 2010, slide 14)
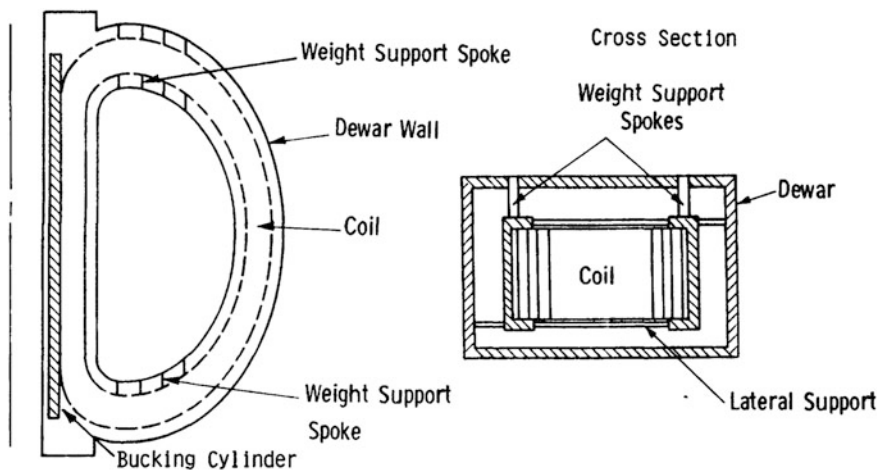
Fig. 10.11 Supports for a large toroidal field coil. The coil bore is about 7 m wide and 11 m high (Buncher et al. 1976)

Heat leaks boil some of the LN2, generating pressure, which is measured by the manometer. Multiple heat shields minimize the heat leak.

The support for a large TF coil is shown in Fig. 10.11.

The bucking cylinder at coil temperature sustains the centering forces, and thin Kromarc spokes transmit gravity and lateral fault forces out to the dewar (at 77 K). The dewar is insulated from room temperature by foam plastic. The heat loads estimated for a torus consisting of 16 such TF coils, producing B = 12 T at the coils, are listed in Table 10.10.

The losses in the pump are due to heat added in compressing the liquid helium coolant and overcoming frictional pressure drops.

Cryostats need to have instrumentation to measure temperature, pressure, mass flow rate, cryogenic fluid level, and stress.

10.6 ITER Cryogenic System

The ITER cryogenic system will provide an average cooling power of 65 kW at 4.5 K and a peak power of 1.3 MW at 80 K. The liquid helium system must be able to accommodate the large pulsed heat loads from the magnets. It must be able to support plasma pulses lasting up to 50 min at hundreds of MW, including the pulsed loads of the central solenoid and regeneration of the NBI cryopumps (Sect. 9.7).

Figure 10.12 shows the ITER cryogenic system.

The magnetic coils and cryopumps are cooled by forced supercritical flow of liquid helium (SHe) from distribution boxes at 3.7–4.2 K using cold circulators

Table 10.10 Helium
refrigeration requirements for
an array of 16 TF coils
producing a peak field of 12 T
at the coils (Buncher et al.
1976)

Structural conduction	kW
Vertical spokes	0.075
Horizontal spokes	2.941
Residual gas conduction	
Dewar	0.472
Vertical spokes	0.036
Horizontal spokes	0.732
Thermal radiation	
Dewar	0.321
Vertical spokes	0.017
Horizontal spokes	0.355
Nuclear radiation	
Conductor	0.156
Structure	0.260
AC losses	
Conductor	12.9
Structure	3.2
Joint losses	17.3
Losses in pump	
($\sim$50 % efficiency pump)	29.2
Total thermal load Pth	68.0
Electrical load $P_e \approx 280\ P_{th}$	19000

Fig. 10.12 A simplified
diagram of a supercritical
helium system. The helium
bath removes heat from the
SHe loop, and the LHe bath is
replenished by the cryoplant
(Courtesy of ITER
Organization)
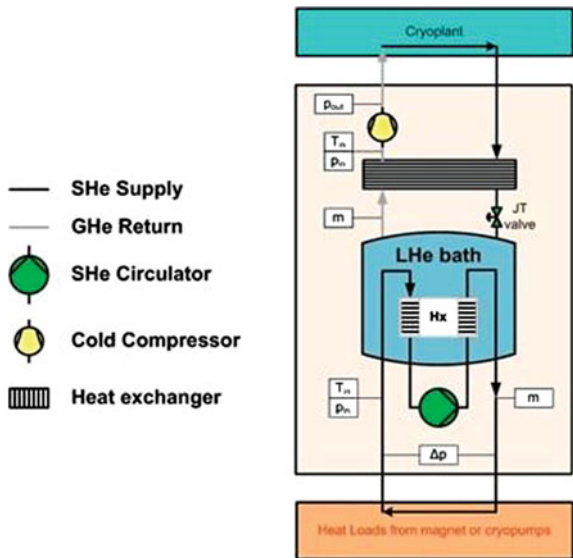
and long length transfer lines within the Tokamak building. Heat exchangers at the inlet and outlet of the cold circulators are employed to transfer the heat loads to the helium bath while maintaining stable operating conditions. Liquid helium will be stored in a 120 m^3 dewar. Three liquid helium refrigerators operate in parallel to supply and recover helium from the main users and provide the required cooling power at 4 and 50 K. An air separation unit will produce liquid nitrogen (LN2) on-site for the liquid helium refrigerators, the 80 K gaseous helium loop and the auxiliary systems. The 80 K helium loop provides cooling for the machine and components thermal shields (Serio 2012).

Liquid helium (LHe) is stored in 3 large tanks (baths), which remove heat via a heat exchanger (Hx) from the supercritical helium (SHe) that flows through the magnet coils and cryopumps, Fig. 10.12.

The cryodistribution system carries liquid helium and nitrogen from the cryoplant building to the tokamak building via the plant bridge. The cryogenic distribution lines have a total length of 3.7 km. The Tokamak building and equipment (including cryogenic components) must be protected against earthquakes by isolation pads. The system includes 7 large cryogenic distribution boxes, a cold compressor box, a large interconnecting box, 31 magnet feeders housing the valves, instrumentation, and flow control devices to maintain safe, reliable operation during cool-down, warm-up and plasma operations.

During a 16 months experimental campaign, the cryogenic system will operate 24 h per day for 11 consecutive days, followed by 2–3 days maintenance. More than 200 possible cryogenic system failure modes and 500 safety hazard failure modes have been studied, and mitigation actions have been implemented. The overall cryogenic system availability is expected to be above 97 %, and no major critical safety failure mode remains (Serio 2012).

In conclusion, cryogenic engineering is a mature discipline, and the large, complex ITER cryogenic systems should be able to operate safely and reliably.

10.7 Problems

10.1. Assume that the fiberglass support tubes of Fig. 10.13 have outer radius 28 cm, inner radius 27 cm and length 28 cm, and that the superinsulation is 1 cm thick with $k_{app} = 10^{-4}$ W/m-K. The copper leads have a total cross sectional area of 0.1 cm^2 and lengths of 0.9 m. Assume that the thermal conductivity integral of the fiberglass is about twice that of glass, and that the coils may be considered to be all copper in estimating their mass and enthalpy. Estimate (a) the coil mass (read dimensions from sketch), (b) heat flow rate along the fiberglass support tubes, (c) heat flow rate along the coil leads, (d) heat leak rate through the superinsulation.

10.2. Estimate the heat which must be removed and the number of liters of liquid nitrogen that are boiled off in cooling 1 kg of copper from 300 to 80 K, and
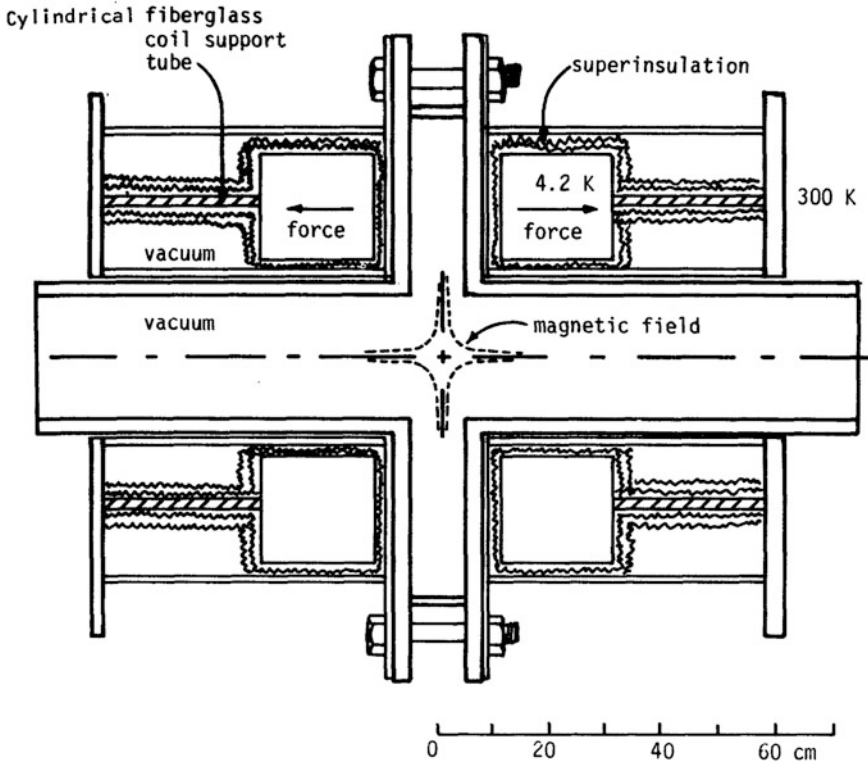
Fig. 10.13 The cryostat for a pair of spindle cusp magnet coils. The helium fill lines and coil current leads enter vertically from above (not shown)

the how many liters of liquid helium are boiled off in cooling it from 80 to 4.2 K. How many liters of nitrogen and helium will be consumed in cooling down the coils of problem 1, ignoring other losses?

10.3. How many liters of liquid helium will be boiled off per hour by a heat input of 1 kW? By the total heat input to the coils of Problem 1?

10.8 Review Questions

1. What invention by Collins greatly facilitated development of low-temperature research?
2. What are some applications of cryogenic technology?
3. Explain the equation $W/M = \int_{T_1}^{T_2} dT\, C = h_2 - h_1$
4. For what materials is the ratio of strength/(thermal conductivity) important?

5. Define "critical temperature" and "inversion temperature".
6. Sketch a simple refrigeration cycle and explain its operation.
7. What is the advantage of using an expansion engine instead of a simple nozzle for cooling of a gas?
8. Explain how a Collins liquefier works.
9. Explain the equation $P = (A/L) \int_{T_1}^{T_2} dT \, k(T)$
10. Explain the meaning of the equation $P = k_{app} \, A \, (T_2 - T_1)/L$
11. What is vapor shielding, and where is it useful?
12. What instrumentation is needed for a cryostat?

References

Barron R (1966) Cryogenic systems. McGraw-Hill, New York

Buncher BR, Chi JWH, Fernandez R (1976) Conceptual studies of toroidal field magnets for the tokamak experimental power reactor. Final report, ORO-5153-1. Westinghouse Electric Corporation, Pittsburgh

Glaser PE, Black IA, Lindstrom RS, Ruccia FE, Wechsler AE (1967) Thermal insulation systems, National Aeronautics and Space Administration report NASA SP-5027. Washington, DC

Laquer HL (1973) Cryogenics, the uncommon cold. USAEC Technical Information Center, Oak Ridge

Neumann H (2010) Cryogenics. Summer School on Fusion Technology, Karlsruhe Institute of Technology, Germany

Powell JR, Bezler P (1974) Warm reinforcement and cold reinforcement magnet systems for tokamak fusion power reactors: a comparison, technology of controlled thermonuclear fusion experiments and the engineering aspects of fusion reactors, CONF-721111, USAEC, pp 358.

Scott RB (1959) Cryogenic engineering. Van Nostrand, Princeton

Serio L (2012) Challenges for cryogenics in the nuclear fusion quest: the ITER cryogenic system. In: 24th international cryogenic engineering conference, Fukuoka, 14–18 May 2012

Stewart RB, Johnson VJ (1961) A compendium of properties of materials at low temperatures, WADD technical report 60-56, part IV

Vance RW, Duke WM (eds) (1962) Applied cryogenic engineering. Wiley, New York

Chapter 11
Plasma Diagnostics

Thomas J. Dolan, Alan E. Costley and Jana Brotankova

Objectives

After reading this chapter one should understand

    Electric and magnetic probes
    Passive and active particle diagnostics
    Passive and active wave diagnostics
    ITER diagnostic systems.

11.1 Requirements

Machine protection requires knowledge of many components, such as

magnets
wall temperatures and damage
divertor performance
vacuum, cooling, and cryogenic systems
tritium retention and tokamak dust monitoring.

A. E. Costley (Retired), Former Head of Diagnostics in ITER

T. J. Dolan (✉)
NPRE Department, University of Illinois, Urbana, IL 61801, USA
e-mail: dolantj@illinois.edu

A. E. Costley
Diagnostics in ITER, Henley on Thames, UK
e-mail: alan.costley@physics.org

J. Brotankova
James Cook University, Townsville, Queensland 4811, Australia
e-mail: brotance@matfyz.cz; j.brotankova@seznam.cz; brotance@gmail.com

Plasma control requires diagnostics for plasma current, loop voltage, plasma shape, plasma position and motion, MHD modes, current drive, and fueling rate.

Evaluation of plasma behavior involves many topics, such as

MHD instabilities
Impurities
Plasma-wall interactions
Fluctuations and transport
Energy and particle confinement times
Fusion products.

Some features desired in plasma diagnostics systems are listed in Table 11.1.

The possible measurements cover a wide spectrum of frequencies, wavelengths, and energies, as illustrated in Fig. 11.1.

Several techniques are available for measuring main parameters like n_e, T_e and T_i. Some techniques that are incapable of giving the desired resolution are still useful to provide redundancy of the measurements. Plasma diagnostic techniques may be grouped in the following categories:

- **Electrical probes**. The simplest example is a wire, with a variable voltage applied, inserted into the plasma. From the data on current drawn by the wire versus applied voltage, the plasma density, temperature, and potential can be estimated.
- **Magnetic flux measurements**. Wire loops placed around the outside of the plasma (or immersed in the plasma) measure magnetic flux changes, from which magnetic field variations, plasma current, and plasma pressure can be deduced.

Table 11.1 Desirable features of plasma diagnostics systems

Parameters. Measure all important plasma parameters, including n, T_i or
f (v_i), T_e or f (v_e), $\vec{B}$, $\vec{J}$, $\vec{E}$ or ϕ, n_n, impurity concentrations, drift velocity, MHD instabilities, plasma waves, and microinstabilities. For ITER about 45 different parameters need to be measured (Donné et al. 2007)

Redundancy. Measure each parameter with more than one technique, if possible

Accuracy. Attain accuracy of measurements $\lesssim 10\ \%$ where feasible

Spatial resolution. Attain spatial resolutions from a few mm in edge plasma to about 10 cm in core

Time resolution. Attain time resolutions of about 10 ms for main confinement and <1 μs for instabilities and turbulence

Completeness. Get a radial scan of important parameters at many times during the plasma pulse, so that a complete space–time mapping will be available

Computer analysis. Use a computer system to record, store, and analyze data

- Inversion techniques to convert data taken along chords through the plasma into variations of the parameter with radius
- Analytical techniques like Fourier analysis to improve accuracy
- Statistical techniques to estimate magnitudes of errors
- Computer graphics to provide multidimensional displays of parameter space–time mappings

Experimental techniques. Use experimental techniques which improve signal-to-noise ratios. For example, optical filters or gratings may be used to screen out photons at undesired wavelengths; and an incident wave may be modulated at a given frequency, with the detector electronics tuned to amplify only signals at that frequency

Fig. 11.1 Possible diagnostic measurements versus frequency, wavelength, and energy. Courtesy of A. J. H. Donné

- **Passive particle diagnostics**. Detectors measure fluxes and energies of particles emitted by the plasma, from which plasma composition and ion energy distributions may be deduced.
- **Passive wave diagnostics**. Analysis of electromagnetic waves emitted by the plasma (x-rays, ultraviolet photons, visible light, infrared, microwaves, and radio waves) yields estimates of plasma density, impurity content, temperatures, magnetic field, etc.
- **Active particle diagnostics**. Beams of ions, electrons, or neutral atoms are shot through the plasma. From their interactions with the plasma, parameters such as plasma density, potential, and internal magnetic field can be estimated.
- **Active wave diagnostics**. Electromagnetic waves, such as microwaves or laser beams, are sent into the plasma. From their transmission, reflection, scattering, refraction, change of polarization, and phase shift in the plasma, many plasma parameters can be deduced.

The major techniques in these categories will be discussed briefly. The diagnostics used with a particular experiment will be described, and then the techniques used for measuring particular plasma parameters will be summarized. The book by Hutchinson (2002), Chap. 4 in Kikuchi et al. (2012), and Chap. 10 in Wesson (2011) provide valuable descriptions. A special issue of *Fusion Science and Technology* (2008) on plasma diagnostics edited by A. E. Costley and D.W. Johnson gives the details of

modern diagnostics techniques and includes a forward look to the conditions that will be experienced in diagnosing burning plasmas and the preparations being made for ITER diagnostics. It has the following chapters:

1. Plasma Measurements: An Overview of Requirements and Status (Young 2008)
2. Magnetic Diagnostics (Strait et al. 2008)
3. Microwave Diagnostics (Luhmann et al. 2008)
4. Laser-Aided Plasma Diagnostics (Donné et al. 2008)
5. Passive Spectroscopic Diagnostics for Magnetically Confined Fusion Plasmas (Stratton et al. 2008)
6. Active Spectroscopy (Thomas et al. 2008)
7. Tomography Diagnostics: Bolometry and Soft-X-Ray Detection (Ingesson et al. 2008)
8. Particle Diagnostics (Kislyakov et al. 2008)
9. Fusion Product Diagnostics (Sasao et al. 2008)
10. First Wall and Operational Diagnostics (Lasnier et al. 2008)
11. Data Validation, Analysis, and Applications for Fusion Plasmas (Arshad et al. 2008)
12. Generic Diagnostic Issues for a Burning Plasma Experiment (Vayakis et al. 2008)
13. Challenges in Fusion Diagnostic Development: a Virtual Tour of ITER (Johnson and Costley 2008).
    See also Costley et al. (2001 and 2006).

11.2 Electrical Probes

Jana Brotankova

Electrostatic probes are valuable for local measurements of the electron distribution function or temperature, plasma potential, electron density, and their fluctuations. They are relatively simple and cheap, but they perturb the plasma and cannot survive in hot, dense plasmas.

11.2.1 Single Langmuir Probe

The simplest type of electrical probe is a wire inserted into the plasma. The wire, called a *Langmuir probe*, is insulated, except at its tip, as shown in Fig. 11.2.

An electrostatic charge layer called the "sheath" surrounds the probe (Fig. 7.18). The sheath potential is on the order of $2T_e$, and is usually few Debye lengths thick (Hutchinson 2002).

If we vary the probe voltage we obtain a current–voltage characteristic as shown in Fig. 11.3. At the point V_{pl}, the potential of the probe is equal to the plasma potential (also called the space potential). Due to higher mobility of electrons, the probe collects predominantly electron current. If we apply voltage higher than V_{pl}, electrons will be attracted and ions repulsed. The sheath will build up with a

Fig. 11.2 A Langmuir probe
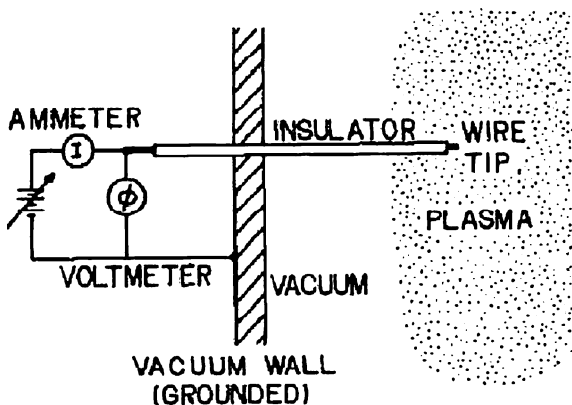
non-zero electric field around the probe. Outside of the sheath, the plasma will be undisturbed. Electrons at the sheath boundary are accelerated to the probe, and the "electron saturation current" depends on how fast electrons migrate into the sheath.

If we apply a voltage below the plasma potential V_{pl}, the probe will repel the electrons and attract the ions. The current driven by the probe drops until the number of collected electrons and ions equalize. This point is known as the floating potential V_{fl}. An insulated probe inserted into plasma will assume this potential. In part of the region between V_{fl} and V_{pl}, the current increases exponentially with voltage ("exponential region" in Fig. 11.3). The electron temperature can be obtained from relations

$$\ln(I_2/I_1) = e(V_2 - V_1)/T_e \qquad (11.1)$$

where 1 and 2 denote any two points along the exponential curve.

The relation between the floating potential and plasma potential is given by the ratio of electron and ion saturation currents:
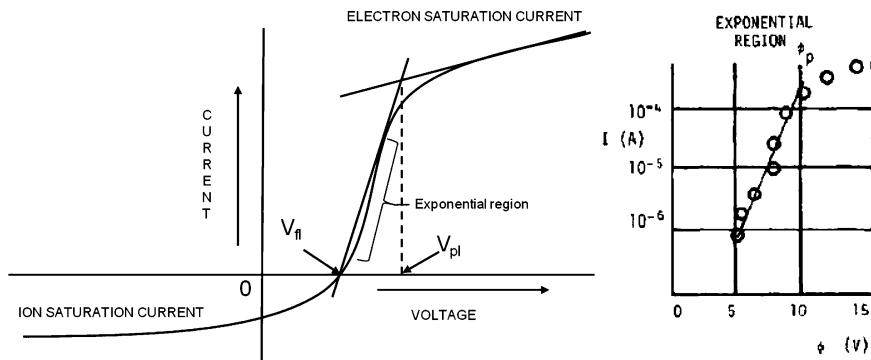
Fig. 11.3 Current-voltage characteristic for a single Langmuir probe (*left*). The "exponential region" above the "floating potential" V_{fl} becomes a straight line on a semi-logarithmic plot (*right*). The "plasma potential" V_{pl} is approximately the voltage where the curvature changes

$$V_{fl} = V_{pl} - T_e ln \left| \frac{I^-_{sat}}{I^+_{sat}} \right|. \tag{11.2}$$

When a large negative voltage is applied to the probe, the electrons are repulsed and all the nearby ions will be drawn in towards the probe. The rate at which other ions wander into the sphere and replenish lost ions is called the *ion saturation current* I^+_{sat}. The electron density may be estimated from I^+_{sat} using the relation

$$I^+_{sat} = A_i j^+_{sat} = A_i en \sqrt{\frac{k_B(T_e + T_i)}{m_i}} = A_i enc_s, \tag{11.3}$$

where n is the plasma densitiy (m^{-3}), A_i is the active probe area (m^2), j^+_{sat} is the ion saturation current density (Am^{-2}), m_i ion mass (kg), T_e and T_i the electron and ion temperatures and c_s is the ion sound speed.

The accuracy of probe results may be distorted, however, if the probe size is larger than either the electron mean free path for collisions or the electron cyclotron radius in a magnetic field.

11.2.2 Double Probe

A double probe system consists of two probes with a voltage applied between them as shown in Fig. 11.4. The whole system is floating. The I–V characteristic will reduce to two ion saturation current branches of the respective probes as shown in Fig. 11.4 right.

The electron temperature can be obtained from

$$\frac{I + i_{1+}}{i_{2+} - I} = \frac{A_1}{A_2} e^{\frac{eV}{kT_e}}, \tag{11.4}$$

where A_1 and A_2 are the surfaces of the probes, which for the equal surfaces $A_1 = A_2$ converts into

$$I_1 = j_1 A_1 \tanh\left(\frac{V_s}{2T_e}\right), \tag{11.5}$$

Fig. 11.4 Scheme of a double probe set-up (*left*). Voltage-current characteristic for a double probe with unequal probes (*right*)
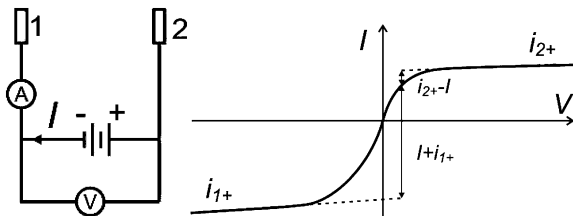
or simply from the slope of the characteristic at the origin:

$$\frac{dI}{dV}\bigg]_0 = \frac{e}{kT_e}\frac{i_{1+} \times i_{2+}}{i_{1+} + i_{2+}}. \tag{11.6}$$

The maximum current flowing through the system is the ion saturation current, which minimizes the disturbance of the plasma. If one probe is significantly larger, then the characteristic becomes like that of the smaller probe.

Reciprocating probes can be pulsed about 1 cm into a plasma and withdrawn in about 100 ms (Lasnier et al. 2008). A *triple probe,* which facilitates fast measurement of T_e, has three tips in the plasma: the middle one is floating, and the other two function like a double probe (Wesson 2011).

11.2.3 Effect of Magnetic Field

Electrons and ions spiral around magnetic field lines with the Larmor radius $r = mv_\perp/qB$, where m is the mass, $v_\perp$ is its velocity component perpendicular to the field line, q is its electron charge and B is the magnetic field. At the same temperature the ratio of ion to electron Larmor radius is $(m_i/m_e)^{1/2}$, which is about 60 for deuterons. Both ion and electron currents will be affected by a strong magnetic field. The probe current is mainly from electrons and ions flowing along magnetic field lines intersecting the probe, so the effective probe area is changed.

11.2.4 Other Designs of Electrostatic Probes

Other designs of electrostatic probes attempt to compensate disadvantages of Langmuir probes, or they change the concept of the probe so that it measures other plasma parameters.

11.2.4.1 Emissive Probe

An emissive probe is usually a loop of tungsten wire heated so that it emits electrons, and it is supposed to float near the plasma potential. The emitted electrons change the sheath around the probes, creating a potential minimum that reflects some of the emitted electrons back to the probe, so the probe does not float at exactly the plasma potential, but it is still a valuable tool for measurements of plasma potential in various plasmas, including edge plasmas with high temperature fluctuations (Sheehan and Hershkowitz 2011; Schrittwieser et al. 2002 and 2006).
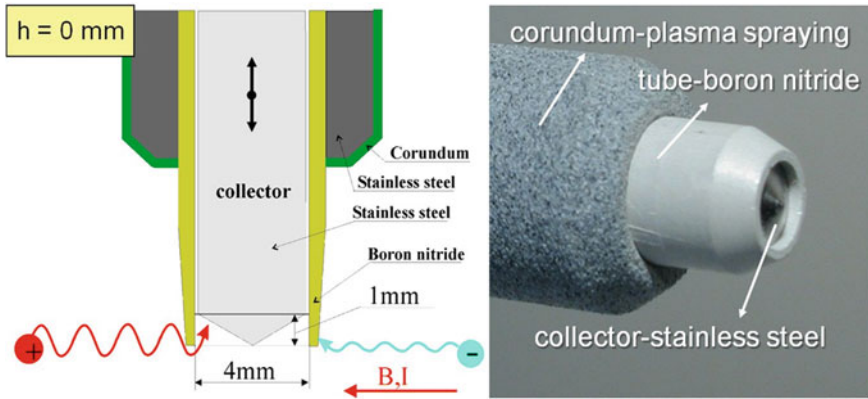
Fig. 11.5 Scheme of a ball-pen probe (*left*) and a picture of a ball-pen probe head (*right*) installed in the CASTOR tokamak, in Prague (Adamek et al. 2004)

11.2.4.2 Ball-Pen Probe

A geometrical restriction can limit the inflow of electrons to the probe. A Ball-Pen probe (Adamek et al. 2005) takes the advantage of large difference in between electron and ion Larmor radii. The probe consists of a metal collector with a conical tip housed inside an insulating shield, oriented perpendicular to the magnetic field lines as depicted in Fig. 11.5.

The collector height h is adjusted to collect equal fluxes of ions and electrons. Then the collector is floating, and the collector potential will be equal to the plasma potential. If the Ball-Pen probe also has another Langmuir tip near the orifice of the shaft (not shown in the Figure), the electron temperature can be estimated from the difference of the floating potential it measures and the plasma potential measured by the conical collector. The advantages of the Ball-Pen probe are its robust design (the collector is shielded by the shaft, so it is less likely to melt) and it doesn't need voltage sweeping, so the values can be obtained with high time resolution.

A *Katsumata probe* (Katsumata and Okazaki 1967; Schrittwieser et al. 2006; Adamek et al. 2008) is based on the same principle as the Ball-Pen probe: the inflow of the electrons inside is restricted by a tunnel. The tunnel is metallic (insulated from the plasma), and the collector is flat. It can measure the ion temperature from the I–V characteristics of the swept collector.

11.2.4.3 Tunnel Probe

The tunnel probe (Gunn et al. 2005; Dejarnac et al. 2007) was developed for measurements of the electron temperature and parallel ion saturation current in fusion devices. It consists of two hollow tunnels with axis parallel to the magnetic
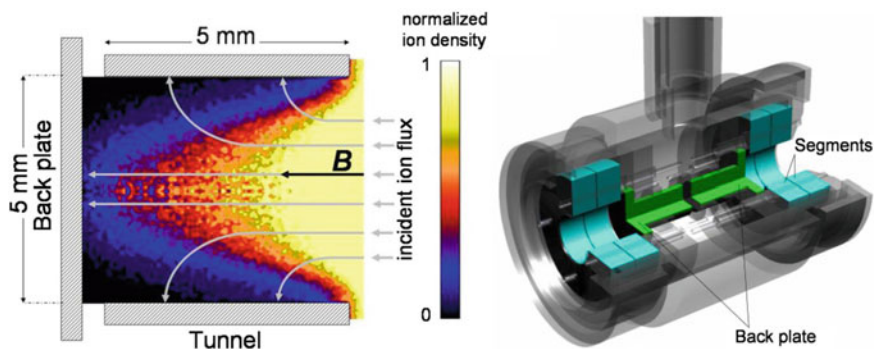
Fig. 11.6 Scheme of a tunnel probe (*left*) showing ion trajectories, and a segmented tunnel probe (*right*), installed in the CASTOR tokamak (Stockel et al. 2007)

field: one is upstream (facing the ion current) and the second one is downstream oriented (facing the opposite side). Each tunnel has the diameter and depth of about 5 mm, ending with a metal back plate. The inner sides are made of hollow-conducting tunnels as depicted in Fig. 11.6 left.

Each of these parts is negatively charged to measure the ion saturation current. The ions flowing into the probe are demagnetized by a strong electric field and redistributed among the back plate and the tunnel. The ratio of the currents flowing to the tunnel and the back plate is a function of electron temperature. The probe was calibrated by the code XOOPIC.

A *Segmented Tunnel probe* has two internal rings: the ratio of the current flowing to the first and to the second inner ring is proportional to the parallel ion temperature (Adamek et al. 2008).

11.2.4.4 Mach Probe

The plasma flow can be measured by placing two Langmuir probes on one field line, insulated from each other. This arrangement is called Mach probe. The ratio of the upstream and downstream currents is called Mach number and determines the ratio of the plasma flow to the ion sound speed.

11.2.4.5 Rotating Mach Probe, Gundestrup Probe

In order to estimate the relation between parallel and perpendicular Mach numbers (ratios of plasma flow speeds to ion sound speed), two varieties of Mach probe were developed. A Rotating Mach probe is a pair of planar probes that rotates in time as shown in Fig. 11.7 left side. A Gundestrup probe consists of pairs of planar probes mounted on one support, which provides Mach numbers in different angles, see Fig. 11.7 right side (Gunn et al. 2001).
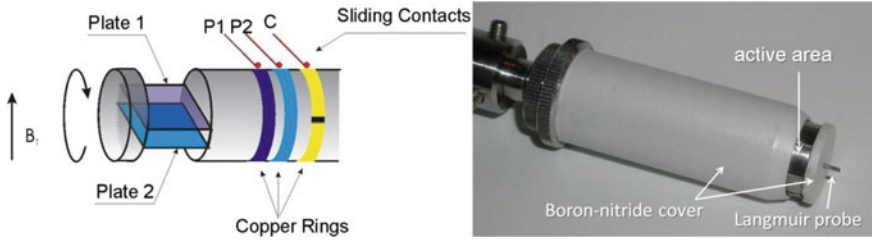
Fig. 11.7 Scheme of rotating Mach probe (Dyabilin et al. 2002) (*left*) and a head of a Gundestrup probe (*right*)

Probe triplets in the ITER divertor will be cooled by conduction to the water-cooled target support. Such Langmuir probes will give the most direct indication of plasma detachment from the divertor, because T_e drops below about 1 eV and the ion saturation current also drops (Donné et al. 2007).

11.3 Magnetic Flux Measurements

11.3.1 Flux Coils

A changing magnetic flux will induce a voltage in a loop of wire in accordance with Faraday's Law.

$$\oint d\vec{\ell} \times \overrightarrow{E} = -\oint d\overrightarrow{S} \times (\partial \overrightarrow{B}/\partial t) \tag{11.7}$$

For a small wire loop with area A_c and magnetic field B_n normal to the plane of the loop, the voltage induced in the loop is $\phi = A_c(\partial B_n/\partial t)$. For a coil with N turns, the induced voltage is N times as great:

$$\phi = NA_c(\partial B_n/\partial t). \tag{11.8}$$

Such coils can be mounted around the outside of a plasma with various orientations to measure changes in various components of **B**. Some magnetic loop arrangements are illustrated in Fig. 11.8.

Since the coils measure $(\partial B_n/\partial t)$, time integration is needed to obtain B, and circuits have been developed to do this accurately. The plasma equilibrium magnetic flux configuration can be modeled by a computer solution of the Grad-Shafranov equation, and the variable parameters can be adjusted to match external magnetic probe measurements. Thus, external measurements can provide good knowledge of the plasma shape and some information on the internal current density distribution (Strait et al. 2008; Vayakis and Walker 2002).
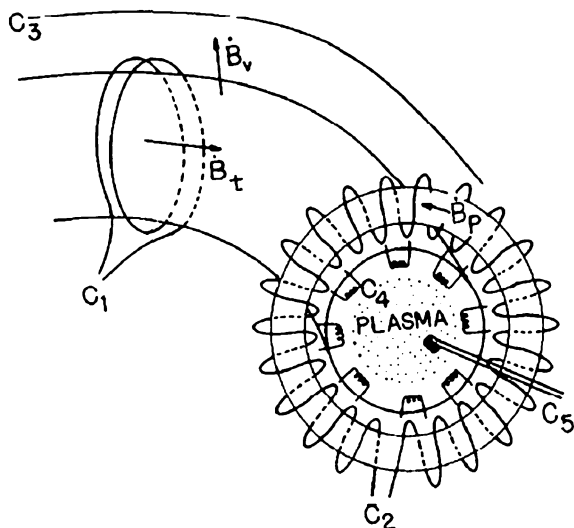
Fig. 11.8 Arrangement of coils for magnetic flux measurements on a toroidal plasma. Coil C_1 measures the rate of change of toroidal magnetic field $(\partial B_t/\partial t)$, which is related to plasma pressure. Coil C_2 (called a Rogowski loop) measures the rate of change of poloidal magnetic field $(\partial B_p/\partial t)$, which is proportional to dI/dt (where I = toroidal plasma current). Coil C_3 measures changes of the vertical field B_v. Coils C_4 measure azimuthal variations of $(\partial B_p/\partial t)$ related to MHD instabilities. Coil C_5 measures variations of B inside the plasma region (useful only in vacuum, in low-pressure plasmas, or for very short pulses)

The magnetic induction can be measured with or without plasma present. The change due to plasma diamagnetism can be related to plasma pressure. Plasma rotation and high-energy electrons complicate the interpretation of diamagnetic data.

Coils C_4 (also called "Mirnov coils") can measure the perturbations of the plasma boundary. They are very useful for determination of the plasma shape and position. For example, MHD instabilities are usually characterized by their toroidal mode number n and poloidal mode number m, where the edge magnetic field is approximately

$$B_a(\phi, \theta) \propto \cos(m\phi)\cos(n\theta) \tag{11.9}$$

where ϕ is the toroidal angle and θ is the poloidal angle (Sect. 1.2). The shape of the plasma boundary is related to B_a. When MHD instabilities occur, the signals at different coils will vary according to the mode numbers (n,m) of the instability. The mode numbers can be determined from analysis of the probe signals, even if two modes are occurring at the same time. For example, if m = 3, then the boundary has three lobes (trefoil). The probe coils C_4 just measure the edge values. The mode numbers inside the plasma may be different (Wesson 2011).

In the case of a low-pressure plasma or a short-pulsed plasma, small magnetic probe coils C_5 may be inserted into the plasma volume to measure radial variations

of ($\partial\mathbf{B}/\partial$t). However, such coils tend to be destroyed by high-pressure plasma, they tend to perturb the plasma configuration, and they are a source of impurities. The plasma current density can be estimated from Ampere's Law

$$J = \nabla x B/\mu_o \qquad (11.10)$$

when $\mathbf{B}$(r) is known.

A **rotating-coil magnetometer** rotates at a constant frequency ω about an axis perpendicular to B and to the coil axis. This induces a coil voltage

$$V = \omega NAB \sin \omega t,$$

where A is the coil area and N is the number of turns, from which the magnetic field can be calculated. Rotating coil probes are well-developed, but could become unreliable in the neutron environment of a burning plasma (Strait et al. 2008).

11.3.2 Hall Probes

When current flows across a magnetic field, the positive and negative charge carriers are separated by the Lorentz force until the force goes to zero

$$F = q(E + v \times B) = 0. \qquad (11.11)$$

This effect can be used to measure the magnetic field, as illustrated in Fig. 11.9. The current density

$$J = I/wt = nqv = -nqE/B \qquad (11.12)$$

where n is the density of charge carriers, q is their charge, and v is their velocity. The voltage developed is

$$V = Ew = -IB/nqt. \qquad (11.13)$$

Fig. 11.9 A current *I* flowing perpendicular to *B*
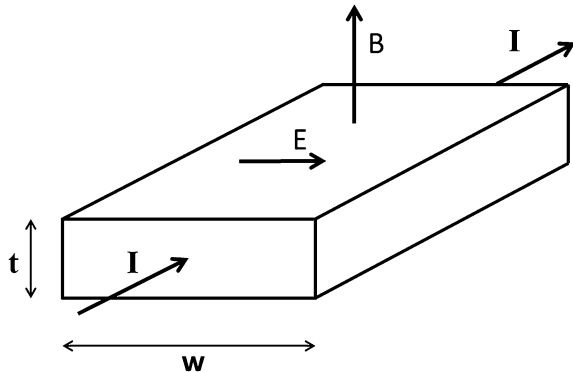
The Hall coefficient $(nq)^{-1}$ is a property of the material. From measurement of V and I the magnetic field can be calculated (Strait et al. 2008). A material with a large Hall coefficient $(nq)^{-1}$ would give a large signal.

Integrated **Hall sensors** contain a sensing element together with electronic circuitry on a few-mm semiconductor chip. The integrated circuits stabilize the voltage, amplify the output, suppress high frequency noise, improve frequency response and signal-to-noise ratio, and minimize output temperature dependence. Widespread use has lowered the cost. Hall probes are used to measure the absolute value of B and its fluctuations in tokamak edge plasmas, but they are vulnerable to radiation damage (Van Oost 2008).

11.4 Ions and Neutral Atoms

Electrons and ions spiral around the magnetic field lines, but ions can become neutralized by charge exchange, and the resulting energetic neutral atoms can cross the magnetic field until they are re-ionized or hit a surface. Many types of particles, including electrons, ions, charge-exchange neutral atoms, impurity atoms, alpha particles, and neutrons, will be emitted by a high temperature plasma. Measurement of the particle fluxes can provide information about their concentrations and velocity distributions.

11.4.1 Electrons and Ions

Measurements of electron and ion fluxes across the magnetic field are difficult, due to their small Larmor radii and diffusive flows. However, flow along magnetic field lines, as from the ends of a magnetic mirror, can be measured with gridded analyzers. Figure 11.10 illustrates a gridded electrostatic energy analyzer for measuring the ion velocity distribution.

The repeller grid is negatively biased to repel incident electrons. The bias grid repels incident ions, except for those with energies larger than $e\phi_b$, which can pass through to the collector. The screen grid and grounded case help avoid spurious currents from secondary electrons and inductive pickup. The current of ions reaching the collector is

$$I = eA\varepsilon_g^4 \int\limits_{v_{min}}^{\infty} dv_{||} f(v_{||}) v_{||} \tag{11.14}$$

where e is the electronic charge, A is the beam area entering the detector, ε_g is the grid transparency of each grid (assumed equal), $v_{||}$ is the ion velocity component along the magnetic field, $f(v_{||})$ is the ion distribution function at the collector, and
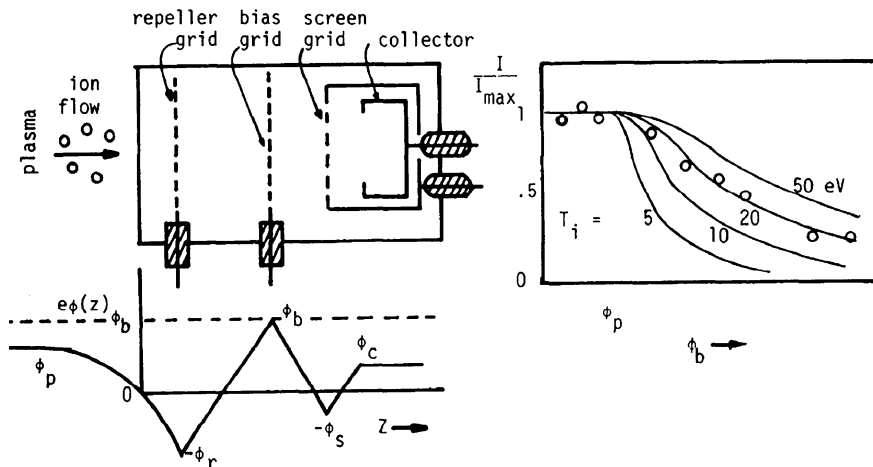
Fig. 11.10 A gridded electrostatic energy analyzer (*top left*) for measuring ion velocity distribution; the potential distribution produced by the grids (*bottom left*); and a graph of the theoretical collector current versus bias grid voltages for various ion temperatures (*right*). Circles represent hypothetical data (to illustrate what real data might look like), and ϕ_p is the plasma potential

$$v_{min} = [2e(\phi_b - \phi_c)/m_i]^{\frac{1}{2}} \tag{11.15}$$

is the velocity at the collector of ions that barely pass over the potential barrier. The current I can be measured as a function of ϕ_b. The distribution function at the collector $f(v_{\parallel})$ can be found in terms of $dI/d\phi_b$ by differentiating Eq. (11.14) with respect to ϕ_b. Then the ion distribution function in the plasma can be deduced from $f(v_{\parallel})$ at the collector, taking into account the difference in potentials $e(\phi_p - \phi_b)$. A similar technique may be used with electrons.

11.4.2 Charge-Exchange Neutral Atoms

Neutral hydrogen atoms (meaning all three isotopes) are produced in the plasma by three processes:

- Charge exchange (CX) with background neutrals
- Recombination of hydrogen ions with electrons
- Electron capture from hydrogen-like impurity ions (significant at energies $\gtrsim 100$ keV).

Part of the energetic neutral atoms from the plasma are ionized in a gas stripping cell (or in a 5–40 nm carbon foil), and the resulting ions are analyzed
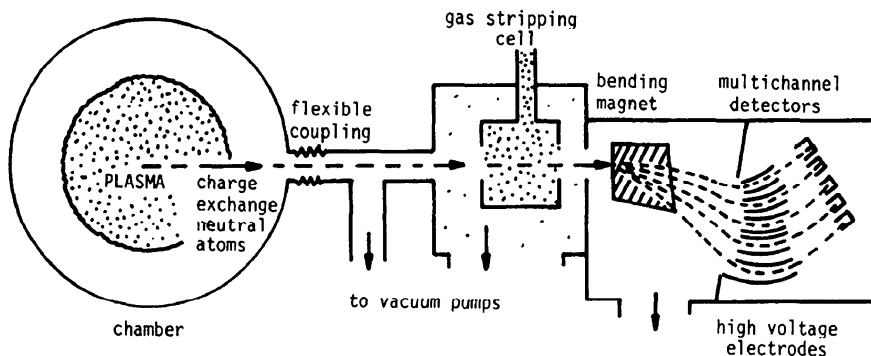
Fig. 11.11 An energy analyzer for charge-exchange neutral atoms

using a combination of magnetic and electric fields to determine their energy and mass. One such neutral particle analyzer (NPA) is shown in Fig. 11.11.

The assembly may be pivoted about the flexible coupling to observe other chords through the plasma.

Another type of NPA has the applied electric field E parallel to B, Fig. 11.12. The ions are displaced in the Y direction by

$$Y_j = (p^2/2)(E/B^2)(m/e)_j \qquad (11.16)$$

And in the Z direction by

$$Z_{jk} = (2/B)(m/e)_j v_k \qquad (11.17)$$

Fig. 11.12 NPA with E ∥ B (Medley and Roquemore 1998, Fig. 1)
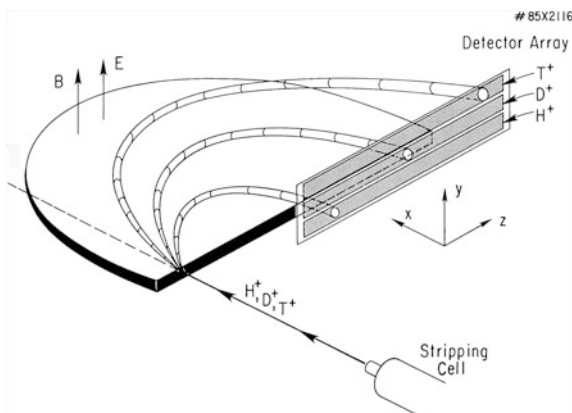
where m and e are the ion mass and charge, v_k = ion velocity. From these sets of data both the (m/e) ratio and the ion velocity can be calculated. The energy resolution is

$$\Delta W/W \ = \Delta Z_j/Z_j \tag{11.18}$$

where $W \ = \ mv_k^2/2$ and ΔZ_j is the width of the detector segments in the Z direction (Kislyakov et al. 2008).

The Tokamak Fusion Test Reactor (TFTR) NPA used a stripping cell with 1–4 Pa (1–3 mTorr) helium. The operational energy range was $0.5 \le AW \le 600$ keV-u, where A is mass of atoms in atomic units (u) and E is the energy in keV. The energy resolution was 7 % at low E and 3 % at high E.

E ∥ B type NPAs have been used on many tokamaks and stellarators. To discriminate against neutrons and gammas large experiments use shielding (such as borated paraffin and lead). They may mask some detectors to make them insensitive to the ions, then subtract that noise signal from the working channels. Another technique is to chop the ion beam electrically or mechanically and subtract the beam-off noise data from the beam-on signal-plus-noise data (Kislyakov et al. 2008).

A sensitive type of ion detector is illustrated in Fig. 11.13.

Ions striking the cathode eject secondary electrons, which produce photons in the scintillation crystal. The photons eject photoelectrons e from the cathode c of the **photomultiplier tube**. The electrons are accelerated successively to dynodes at higher voltages, and the secondary electrons they eject greatly multiply the electronic current. Alternatively, the ions could impinge directly on the scintillator (simpler but less sensitive).

Hydrogen neutral beam injection at known energy and flow rate is used to calibrate the neutral particle analyzer (NPA) energy, resolution, and efficiency (Kislyakov et al. 2008).

Fig. 11.13 The Daly system for detection of positive ions
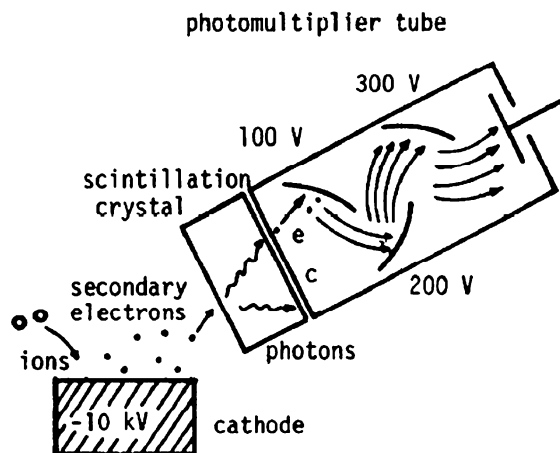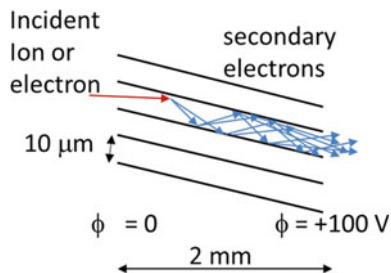
Fig. 11.14 Segment of a microchannel plate

Instead of the photomultiplier tube a **microchannel plate** (MCP) may be used to amplify the electron signal. A microchannel plate has thousands of tiny tubes with a positive electric field accelerating the electrons, Fig. 11.14.

As the electrons bounce off the inside of the tube walls, which have a high secondary emission coefficient, they generate many secondary electrons, which greatly amplify the current pulse.

Several NPAs may be used simultaneously along different chords. Then the chord data can be inverted mathematically to obtain $T_i(r,t)$. (Abel inversion will be discussed later in this chapter). Due to banana drifts in tokamaks, the radial distribution may appear to be asymmetric.

In analyzing the data, the distribution of neutral gas density $n_n(r)$ in the plasma must be known or assumed, since it appears in the charge exchange reaction rate $n_i n_n \langle \sigma v_i \rangle$. Cold neutral gas atoms may be ionized near the surface, but Franck–Condon neutrals, with energies near 2 eV, may penetrate further into the plasma. The neutral atoms resulting from charge exchange may gradually "diffuse" inwards, via successive charge exchange reactions, with the result that the central density $n_n(0)$ may be on the order of 10^{13} to 10^{15} m^{-3}.

In large tokamaks the charge-exchange neutral atoms leaving the hot core are attenuated before they get to the surface of the plasma. Then particles reaching the analyzer come mainly from near the plasma surface, and it becomes unfeasible to measure $T_i(r)$ near the plasma center with this technique. At high values of line density $n_e a > 3 \times 10^{19}$ m^{-2}, where a is the plasma minor radius, the central ion temperature may be underestimated. A diagnostic neutral beam may be used to induce charge exchange recombination spectroscopy (CXRS, Sect. 11.7) to get better accuracy (Kislyakov et al. 2008).

11.4.3 Suprathermal Ions

Measurements of suprathermal ions, such as fusion product **alphas** and ICRF heated ions, can yield information about alpha particle confinement, MHD activity, "fishbone" modes, high-harmonic fastwave heating, and density ratios of hydrogen isotopes. Confined alphas can be detected by charge exchange

recombination spectroscopy (CXRS, discussed in Sect. 11.7) and by collective Thomson scattering (Sect. 11.8). ITER will use a low-energy NPA for atoms at 10–200 keV and a high-energy NPA for atoms with 0.1–4 MeV (Kislyakov et al. 2008).

Assuming plasma parameter profiles are known, the effects of alpha particles on plasma stability can be assessed by Mirnov coils, correlation reflectometry, beam emission spectroscopy, and ion cyclotron emission (Young 2002).

Escaping alphas can be measured by Faraday cups, scintillation detectors, and infrared cameras, but they might not function well in high radiation environments, so new instruments are needed.

11.4.4 Particle Deposition Diagnostics

Particles in the plasma bombard the walls, causing erosion; compounds, such as oxides, may form; and films, such as polymers of carbon and hydrogen, may be deposited. Tritium implantation and deposition are especially important, because the tritium might be released during an accident, posing a radioactivity hazard. Agglomeration of particles produces "tokamak dust", which may also be radioactive and hazardous. Therefore, it is important to monitor and ameliorate particle deposition. Particle deposition diagnostics examine particles from the plasma, such as C, Si, O, Fe, Ni, Be, and W, that are deposited on surfaces. They measure particle size distribution, composition, and quantity. They may also need to measure the radioactivity and toxicity of depositions and dust.

The Divertor Materials Evaluation System (DiMES) program in DIII-D measured erosion and redeposition of carbon, W, and Be, including postmortem analyses by removal of coupons or tiles. A silicon depth marker layer was implanted 300 nm below the surface of graphite disks to measure erosion depth. Disks of different materials were inserted for one plasma discharge, then analyzed by techniques such as Rutherford backscattering, which measured the depth of the silicon layer after erosion. Retention of D (deuterium) was quantified by injection of a 700 keV ^{3}He beam and measurement of the (D + ^{3}He) fusion reaction rate. DiMES has been used for the following studies:

- Effect of divertor detachment on carbon erosion rate
- Chemical sputtering
- Effects of lithium in the tokamak scrape-off layer (SOL)
- Benchmarking of modeling codes
- Effect of sample temperature
- Carbon deposition in gaps
- Transport of tokamak dust (Lasnier et al. 2008).
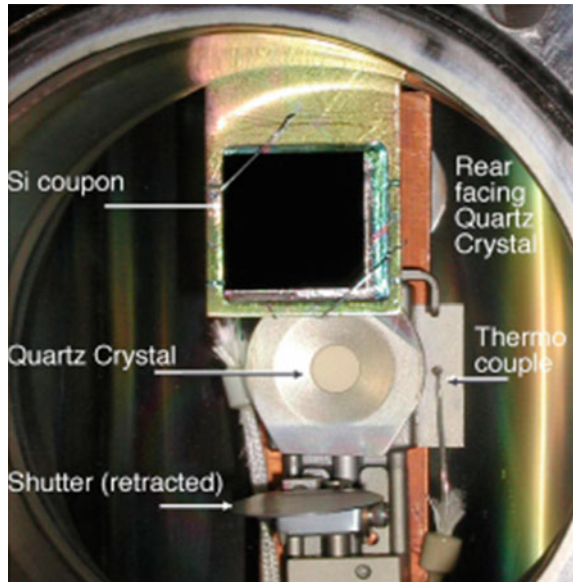
Quartz crystal microbalances can monitor the growth of thin films. When mass is added to the face of a resonating quartz crystal, the frequency of the resonance is reduced. For example, 0.1 nm layer of aluminum reduces the resonant frequency of 6.0 MHz crystal by 2.27 Hz. Heating by the plasma changes the resonant frequency, but when the crystal cools its normal resonant frequency is recovered (except for the shift due to mass loading). Such studies provide information on divertor performance, erosion and redeposition of plasma facing materials (such as Be, C, W), polymer film formation, and hydrogen retention (Lasnier et al. 2008).

Figure 11.15 shows a silicon coupon on which a hydrocarbon film has deposited. The layer thickness is measured with a 6 MHz quartz crystal microbalance.

The lifetime of windows and mirrors in a tokamak is limited by surface damage and by formation of surface films. Measurement of dust generated in tokamaks was discussed in Sect. 8.9 (Voitsenya et al. 2001).

Thermocouples embedded in surfaces such as divertor targets can measure temperature gradients, from which high heat fluxes (50–500 MW/m^2) can be estimated (Lasnier et al. 2008).

11.5 Neutron Measurements

Neutron measurements can provide information on

- Fusion power (The emission of one neutron per second corresponds to a DT fusion power of 2.82 pW)

- Neutron fluence on the first wall
- Two-dimensional neutron emission profile
- Neutron energy spectrum
- Ion temperature
- Fuel isotope ratio n_T/n_D.

and other parameters.

The sources of neutrons in fusion experiments are:

- Thermonuclear fusion of DT and of DD
- Beam-plasma reactions
- Beam-beam reactions
- Neutron bursts due to plasma instabilities (mistaken for thermonuclear fusion in some early experiments)
- Energetic ions bombarding surfaces containing absorbed deuterium or tritium, such as walls and limiters
- Secondary DT reactions of tritons emitted by DD reactions (about 10^{-3} of primary DD reactions)
- Neutron emission caused by impact of high-energy runaway electrons or gammas onto nuclei (photoneutrons)
- Reactions caused by energetic alpha particles colliding with other nuclei ("alpha knock-on reactions").

Secondary reactions may occur among high energy plasma ions and by ion impact on the wall. For example, deuterons accelerated by ICRF (Sect. 5.6) may reach MeV energies and cause reactions such as

$$Be^9 + D \rightarrow B^{10} + n \qquad (11.19)$$
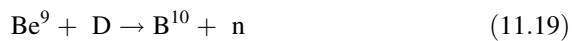
producing more neutrons.

Neutrons may be detected by several methods, including:

- Gas-filled proportional counters (BF_3, ^3He)
- Fission chambers (^{235}U, ^{238}U).
- Scintillation detectors
- Foil activation.

11.5.1 Gas-Filled Proportional Counters and Fission Chambers

A gas-filled proportional counter is usually a cylindrical tube with an axial wire maintained at a positive voltage of about 500 V, Fig. 11.16. The tube contains BF_3 or ^3He gas.

Neutron absorption in the gas produces energetic alpha particles or protons via the reactions
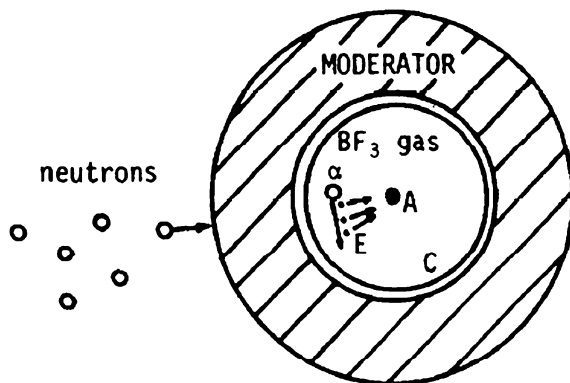
Fig. 11.16 A proportional counter for neutron detection (*end view*). Incident fast neutrons are slowed down in the moderator. Some of them interact with ^{10}B in BF$_3$ gas, producing energetic alpha particles α, which ionize some gas atoms. The resulting free electrons are accelerated to the anode *A*, producing a current pulse. The ions are collected at the cathode *C*

$$^{10}\text{B} + \text{n} \rightarrow {}^4\text{He} + {}^7\text{Li} + 2.78\,\text{MeV} \tag{11.20}$$

$$^3\text{He} + \text{n} \rightarrow \text{H} + \text{T} + 0.77\,\text{MeV}. \tag{11.21}$$
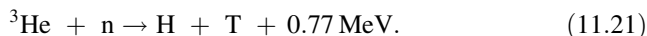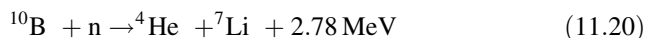
These charged particles ionize the gas, and the resulting electrons produce a current pulse. (At higher voltages, field intensified ionization would produce very large current pulses, and the device would be a Geiger-Mueller tube). The neutron reaction rates are proportional to neutron energy $E^{-1/2}$, so these detectors are more sensitive to low-energy neutrons, and moderators of low-Z materials (such as paraffin and plastic) are usually used to slow down fast neutrons.

Fission chambers containing ^{235}U are similar, but with higher energy yield (E $\sim$ 200 MeV). The fission fragments ionize the gas and cause a current pulse. These chambers are useful over wide ranges of neutron fluxes and are often used to measure the total neutron yield from plasma. A ^{238}U fission chamber detects only high energy neutrons ($\gtrsim$1 MeV). BF$_3$ and ^{3}He chambers are 100 times more sensitive than ^{235}U fission chambers. Pulse height discrimination can be used to screen out pulses due to x-rays and gamma rays. A pulse counting mode is used for low rates, and a *Campbell mode* (measuring the mean-square voltage) can be used for high count rates, where pulses overlap.

A high-Z shield (such as Pb) may be needed to reduce detector noise, and pulse height discrimination can also be used to discriminate against x-rays and gamma rays. Graphite and beryllium moderators with a ratio of BeO/C = 0.25 can be used to flatten energy response of the detectors (Sasao et al. 2008).

The measurements of neutron emission rate can be calibrated with a neutron source, moved around inside the tokamak reactor vessel to determine the detector efficiency versus source position. The source could be ^{252}Cf for DD neutron simulation or a compact neutron generator tube for DT neutron emission. Then the

average efficiency can be computed for any assumed neutron emission profile. If multiple detectors are used, each must be calibrated separately, because the detectors themselves differ and because neutron attenuation and scattering vary from one detector position to another. In ITER, it will be necessary to cover seven orders of magnitude in neutron flux intensity. None of the available detectors have such a wide range, so multiple detectors with overlapping sensitivities will be used. The most sensitive will be calibrated using the in-vessel calibration sources and the others will be cross calibrated using the plasma (Sasao et al. 2008).

A prototype microfission chamber with 12 mg UO_2 is being developed, to check its reliability under ITER conditions, such as high vacuum, neutron and gamma radiation, high temperature, and mechanical vibration (Sasao et al. 2008).

11.5.2 Scintillation Detectors

Energetic neutrons incident on organic liquids and plastics produce energetic recoil protons by elastic collisions. The protons cause the scintillator to emit photons, which in turn eject photoelectrons from the cathode of a photomultiplier tube, which amplifies the current pulse, as shown in Fig. 11.17.

The detectors need to be shielded from background neutron radiation, which can be done using paraffin wax moderator containing lithium, which absorb neutrons without emitting gamma rays. To attenuate both neutrons and gammas boron-loaded concrete may be better (Sasao et al. 2008).
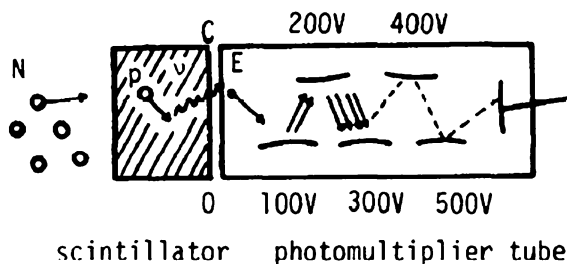
Fig. 11.17 A scintillation detector and photomultiplier tube. Incident fast neutrons N produce knock-on protons P, which cause the scintillator to emit photons ν. The photons eject photoelectrons E from the cathode C of the photomultiplier tube. The electrons are accelerated successively to dynodes at higher voltages, knocking off more secondary electrons at each stage. Thus, the electron current pulse is greatly amplified after many stages. Since the proton energy and light output increase with incident neutron energy, the pulse amplitudes may be analyzed to deduce the neutron energy spectrum

	Threshold energy (MeV)	Half life
For D–D neutrons		
58Ni(n, p) 58Co	1.0	70.82 day
64Zn(n, p) 64Cu	1.8	12.70 h
115In(n, n') 115mIn	0.5	4.486 h
232Th(n, f) F.P.	1.2	1 min
238U(n, f) F.P.	1.0	1 min
For D-T neutrons		
27Al(n, p) 27Mg	2.6	9.458 min
28Si(n, p) 28Al	5.0	2.25 min
56Fe(n, p) 56Mn	4.5	2.577 h
63Cu(n, $2n$) 62Cu	10.9	9.74 min
93Nb(n, $2n$) 92mNb	9.0	10.25 day

Table 11.2 Activation reactions. F.P. means fission products. From Jarvis (1994) Neutron measurement techniques for tokamak plasmas, Plasma Physics and Controlled Fusion, 36, 209, Table 4

11.5.3 Foil Activation

Foils of ^{109}Ag or other metals may be activated by neutron absorption via the reaction

$$^{109}\text{Ag} \; + \; \text{n} \rightarrow ^{110}\text{Ag}^* \rightarrow ^{110}\text{Cd} \; + \beta^-. \tag{11.22}$$
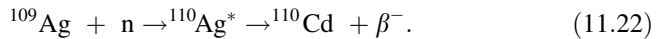
The resultant ^{110}Ag nucleus is radioactive, emitting beta rays (energetic electrons) with a half-life of 24 s. From the number of beta rays emitted by the foil after activation, the number of neutrons emitted by the plasma during the time the foil was exposed to the plasma can be calculated. Although this method lacks spatial and time resolution, it is insensitive to x-rays, and it can yield an absolute neutron intensity for calibration of other neutron detectors. Some other activation reactions of interest are listed in Table 11.2.

The activated foils can be transported from inside the fusion device to the counting station outside the device by a pneumatic tube. An unfolding code, such as SANDII, can calculate the neutron energy spectrum at the foils, which can be compared with neutronics code predictions (Sect. 6.10), but the energy resolution is not sufficient to consider this technique as a neutron spectrometer. Activation of water flowing near the plasma by the reaction ^{16}O(n, p)^{16}N can also be used for detection of high-energy neutrons (threshold energy 10.24 MeV). The resulting half-life of ^{16}O is 7.13 s, so the water must flow rapidly out to a shielded detector (Sasao et al. 2008; Wesson 2011).

11.5.4 Neutron Spectroscopy

From the ratio of D-D and D-T neutron fluxes, one could estimate the triton burnup ratio in D-D plasmas and the deuterium/tritium fuel ratio (n_d/n_t), which is important for burn control in D-T plasmas.
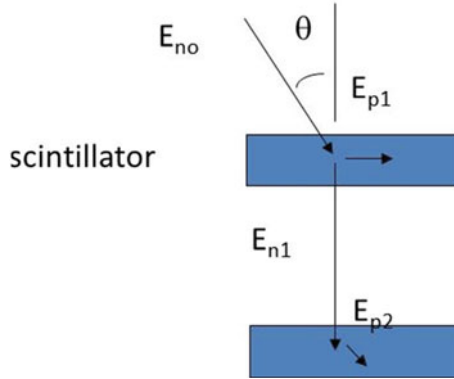
Fig. 11.18 A neutron time-of-flight spectroscopy system with two scintillator plates. Photo-multiplier tubes are not shown

There are several methods of measuring the neutron energy spectrum:

- Time of Flight
- Proton Recoil
- Natural and Synthetic Diamond Detectors
- Scintillator Plates and Fibers.

11.5.5 Time-of-Flight Spectrometry

A system with two scintillator plates can be used to measure the neutron energy spectrum, as shown in Fig. 11.18.

A neutron with energy E_{n0} strikes a proton in the first scintillator, producing a proton with recoil energy E_{p1}, which generates light in that scintillator with intensity proportional to E_{p1} (assuming that E_{p1} is totally absorbed in that scintillator). The scattered neutron then interacts with a proton in the second scintillator, generating a proton with energy E_{p2}. The time between the two scintillator pulses gives the time of flight of the scattered neutron, from which its energy E_{n1} can be calculated. Then the energy of the incident neutron is known from

$$E_{n0} = E_{n1} + E_{p1}. \qquad (11.23)$$

Figure 11.19 shows data from such a neutron spectrometer. With a 1 m separation between the scintillators this system had an energy resolution of 7 % at 2.45 MeV and 3 % at 14.1 MeV.

11.5.6 Proton Recoil

When a neutron strikes a proton nearly head-on the proton receives almost all the neutron energy, and the recoil proton energy can then be measured in a variety of ways, such as by its radius of curvature in a magnetic field, illustrated in Fig. 11.20.
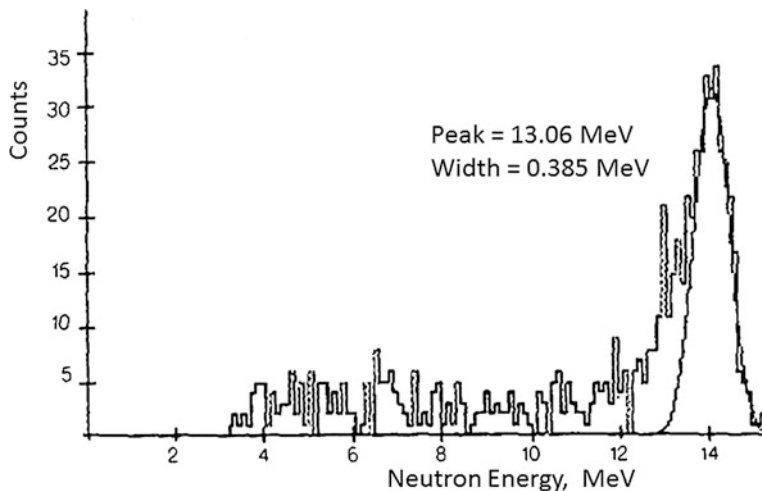
Fig. 11.19 Data from neutron time-of-flight spectrometer. The peak is at 14.06 ± 0.39 MeV. Reprinted with permission from Walker et al. (1986), double scatter neutron time of flight spectrometer as a plasma diagnostic, Review of Scientific Instruments 57, 1740–1742, Fig. 4, copyright 1986, American Institute of Physics

Fig. 11.20 A magnetic proton recoil (MPR) neutron spectrometer. An applied magnetic field curves the proton trajectories as shown, and the proton energy is calculated from its arrival point on the segmented scintillator detectors. The device is surrounded by neutron and gamma shielding (not shown)
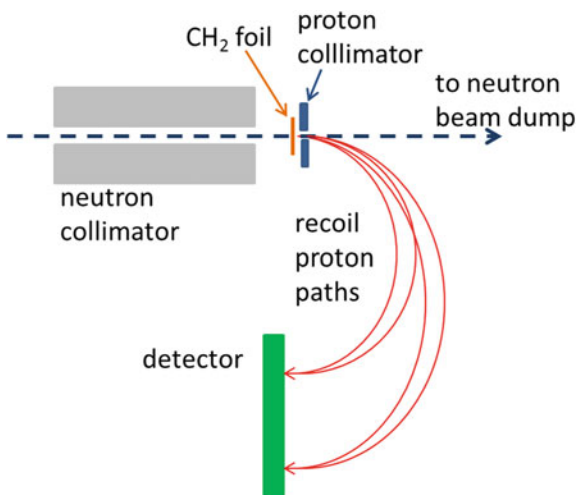
Magnetic proton recoil (MPR) measurements of total neutron yield were consistent with fission chamber values for neutron emission rate in JET over two orders of magnitude. Monitoring of the triton to deuteron density ratio n_t/n_d in the core plasma is required for burn control in ITER. This can be estimated from D-T and D-D neutron yields, which in principle can be obtained by the separation of D-T and D-D components from a neutron energy spectrum. In practice, the

measurement can be complicated by the intense neutron and gamma background fluxes caused by interactions of the fusion neutrons with the vacuum vessel and other internal structures. TOF is well suited to measurements of DD neutrons ($\leq$2.5 MeV), while the MPR may be better suited for high energy neutrons ($\geq$2.5 MeV). Both methods can give energy resolutions $\sim$2 %, but MPR requires a large access area (Sasao et al. 2008).
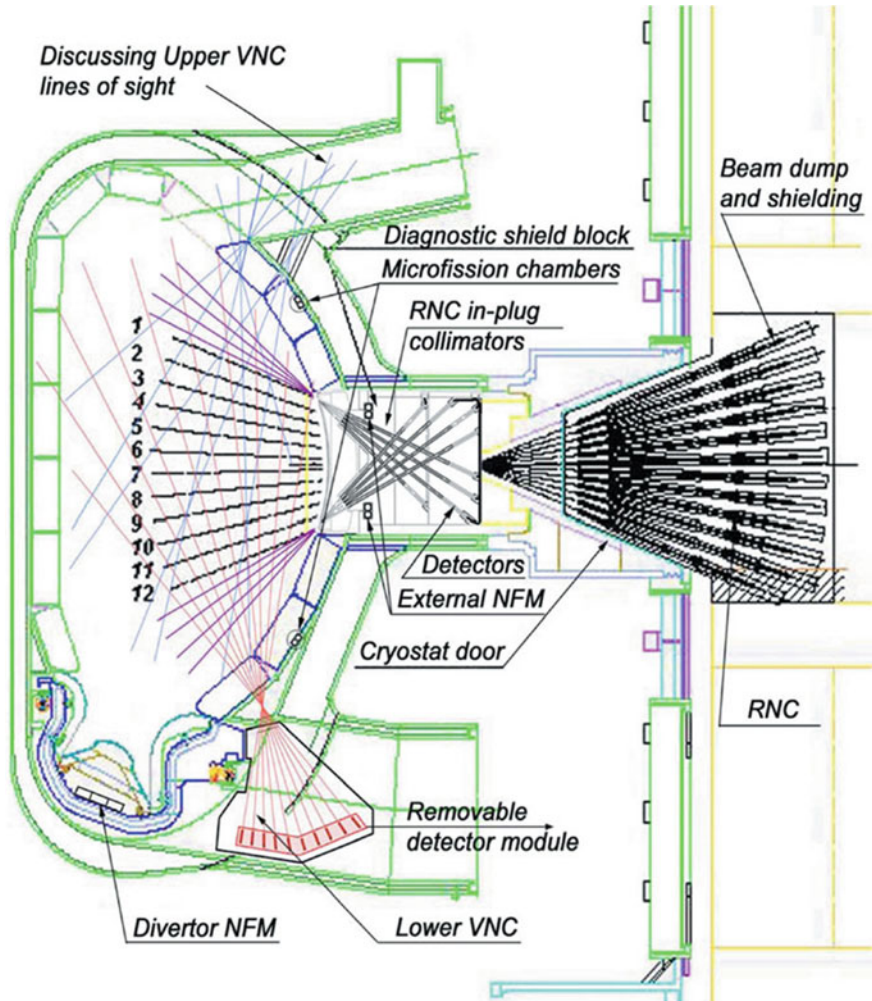
Fig. 11.21 Arrangement of ITER neutron diagnostic systems integrated from several toroidal planes. The 2-D neutron source strength and energy distribution measurements in ITER can have temporal resolutions of 1 ms for source strength and 0.1 s for energy distribution, and spatial resolution $\sim$0.1 a, where a is the plasma minor radius. Courtesy of ITER Organization

Compact neutron spectrometers use a scintillation detector as both the source of the recoil proton and as its detector. The recoil proton energy can be calculated from the scintillation pulse height. However, a 1 MeV monoenergetic neutron beam would generate recoil protons with a spread of energies up to 1 MeV, so there is not a unique relation between the recoil proton energy and the incident neutron energy. A computer program is used to unfold the neutron energy spectrum from the measured spectrum of proton energies.

11.5.7 Neutron Emission Imaging

ITER will have vertical neutron cameras (VNC) and radial neutron cameras (RNC), as illustrated in Fig. 11.21.

Figure 11.22 shows some neutron images from JET.

Fusion product diagnostics are discussed in Stott et al. (1998), pp. 409–528, by Krasilnikov et al. (2008), and by Sasao et al. (2008).

Fig. 11.22 Images of 14 MeV neutrons from JET during triton beam injection at $q_a = 8.5$ (*left column*) and $q_a = 3.3$ (*right column*), compared with simulations (*bottom images*) from tracking fast triton orbits. From Jet Bulletin 060314
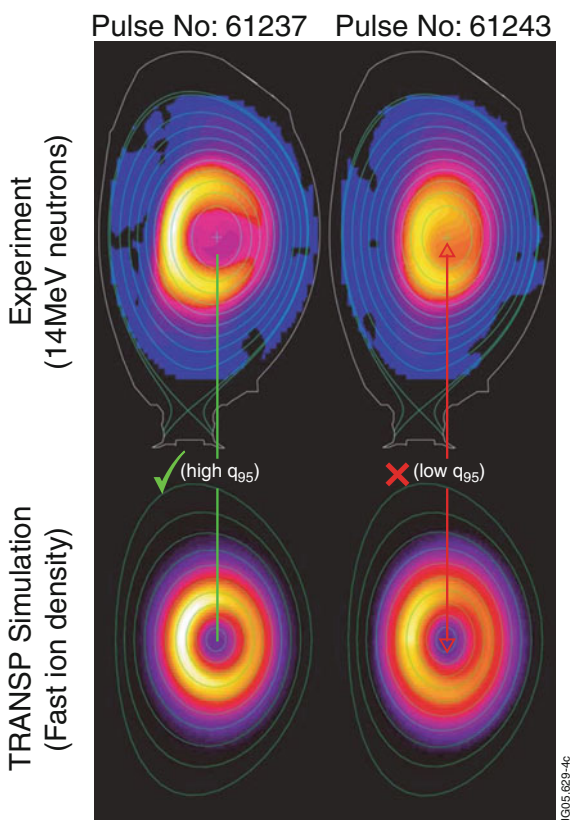
Table 11.3 Some spectral regions relevant to spectroscopy of magnetically confined plasmas (Stratton et al. 2008)

Spectral region		Wavelength (nm)	Energy region (eV)
Far infrared	FIR	>1,200	<1
Near infrared	IR	700–1,200	1–2
Visible		400–700	2–3
Ultraviolet	UV	200–400	3–6
Vacuum ultraviolet	VUV	30–200	6–40
Extreme ultraviolet	EUV	10–30	40–120
Soft X-ray	SXR	0.1–10	120–12,000

11.6 Passive Wave Diagnostics

Some spectral regions of interest are listed in Table 11.3.

Because UV radiation at wavelengths <185 nm is strongly attenuated in air, spectroscopic equipment for short wavelengths must operate in a vacuum (or in a more transparent gas, like He), hence the name **vacuum ultraviolet (VUV)** spectroscopy.

Most radiation from a hot plasma core is from impurity emissions in the vacuum ultraviolet to soft x-ray region. Ignition of D-T plasmas can be prevented by the presence of only 3 % of low-Z elements, such as oxygen, 1 % of intermediate-Z elements, such as iron, or 0.1 % of high-Z elements, such as tungsten (Isler 1984).

11.6.1 Ionization States and Atomic Energy Levels

11.6.1.1 Degree of Ionization

The rate of change of the density of ions with charge state z is given by

dn_z/dt = (net inflow of n_z) + (ionization of state n_{z-1}) − (ionization of n_z) + (recombination of n_{z+1}) − (recombination of n_z)

$$\frac{\partial n_z}{\partial t} = -\nabla \cdot \Gamma_z + n_e[n_{z-1}S_{z-1} - n_zS_z + n_{z+1}\alpha_{z+1} - n_z\alpha_z] \tag{11.24}$$

where Γ_z is the flux of particles with ionization state z; S is the ionization rate, and α is the recombination rate, which are functions of electron and ion temperatures (De Michelis and Mattioli 1984; Isler 1984).

Recombination can be significant in high density, cool plasmas ($n \sim 10^{21} \mathrm{m}^{-3}$, $T_e \lesssim 3$ eV). For example, this beneficial process reduces the heat load of ions striking a divertor target by neutralizing the ions and radiating energy upstream of the target, producing a "detached" plasma. At $T_e \lesssim 3$ eV three-body

recombination and molecular-activated recombination are dominant, while radiative recombination could be significant at $T_e \gtrsim 4$ eV (Terry et al. 1998).

11.6.1.2 Atomic Energy Levels

The rate of change of density of excited atoms in energy level j may be represented as

dn_j/dt = (gain by collisional excitation of level k to j) − (loss by collisional de-excitation of j to level k) + (gain by radiative decay from level k higher than j) − (loss by radiative decay to level k below j)

$$\frac{dn_j}{dt} = n_e \sum_k n_k C_{kj} - n_e \sum_k n_j C_{jk} + \sum_{k>j} n_k A_{kj} - \sum_{k<j} n_j A_{jk}, \qquad (11.25)$$

where the C are collision rates (mainly with electrons, dependent on T_e), A are radiative decay rates (line radiation), and the summations are over all other related states.

These equations for ionization state and excitation states can be modeled by computer programs, using large atomic data tables. Since particle flow along the magnetic field is rapid, the plasma core may be modeled as a one-dimensional function of magnetic flux surface (or dimensionless radius $\rho = r/a$, if the plasma cross section is nearly circular). At the plasma edge additional terms may be needed to account for wall interactions (Stratton et al. 2008).

If plasma confinement times are long enough compared to collision times, then some sort of equilibrium may occur. In hot, **low-density** plasmas, like the solar corona, the populations of excited levels are determined by balancing the rates of collisional excitation and ionization with the rates of **radiative** de-excitation and recombination, called **coronal equilibrium**, and

$$n_e n_g C_{g1} - n_j A_{jg} \approx 0 \qquad (11.26)$$

where g denotes the ground state (Stratton et al. 2008).

In **high-density** plasmas, on the other hand, **collisional** processes may dominate de-excitation and recombination, and the relative populations may be in **local thermodynamic equilibrium** (**LTE**), governed by the Boltzmann and Saha equations, depending only on the temperature. Sometimes the upper energy levels are dominated by collisional processes (LTE), while the lower levels are dominated by radiative de-excitation (coronal equilibrium). Equilibrium conditions are discussed by Griem (1997). Many processes, including electron impact ionization, ion impact ionization, charge exchange, and several types of recombination, must be considered, and the plasma may be out of an equilibrium condition.

As a plasma heats up, higher charge states of impurity ions become dominant. For example, an estimate of the distribution of iron charge states is shown in Fig. 11.23.
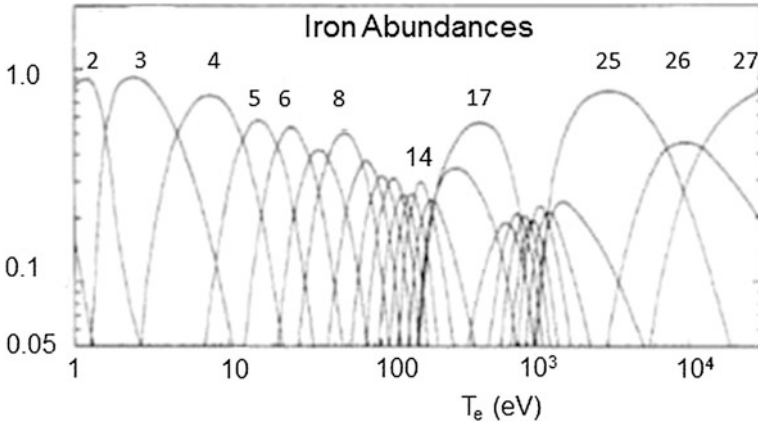
Fig. 11.23 Equilibrium abundances of different ionization states of iron versus electron temperature. State 27 means 26^+ (fully ionized), state 26 means 25^+,..., state 1 means a neutral atom (Carolan and Piotrowicz, IAEA, 1983)

At 10 keV there is a mix of states 25, 26, and 27. At 1 eV the iron is mostly singly ionized. Thus, iron can emit line radiation over a wide temperature range.

11.6.2 Radiation Power Density

Radiation power loss processes include line radiation P_L; bremsstrahlung P_b (German for "braking radiation", from interactions of free electrons and ions); $P_r + P_d$, (radiative plus dielectronic recombination), and cyclotron radiation P_c (also called "synchrotron radiation"; from electrons spiraling around magnetic field lines). The total radiative power loss per unit volume is

$$P_{rad} = P_L + P_b + P_r + P_d + K_c P_c \quad (W/m^3) \tag{11.27}$$

where K_c is the fraction of cyclotron radiation escaping and not reabsorbed in the plasma (to be discussed later). The terms may be grouped into the following form:

$$P_{rad} = n_e \sum_z n_z Q_z + K_c P_c \quad (W/m^3) \tag{11.28}$$

where the "radiation power parameter" Q_z is a function of T_e for each species z, shown in Fig. 11.24.

The left and middle portions are due to line radiation, and the rising straight lines at the right are due to bremsstrahlung. At high T_e low-Z species become fully ionized, line radiation ceases, and only bremsstrahlung is significant for them. However, high-Z species may still emit intense line radiation.
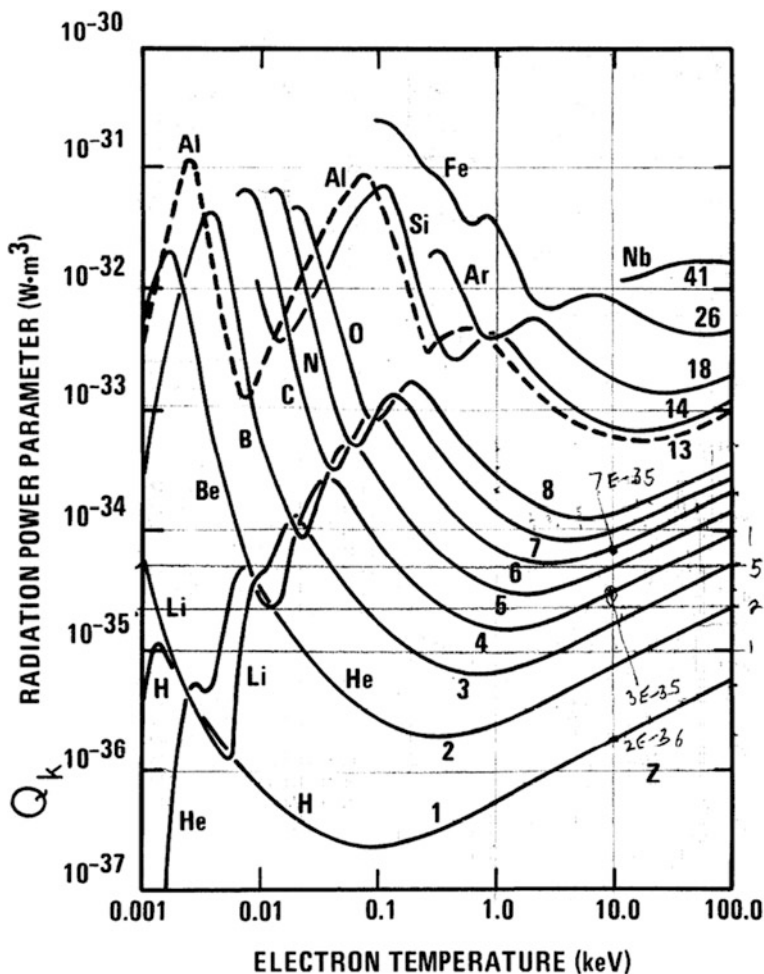
Fig. 11.24 The radiation power parameter versus electron temperature for various elements Z (Z = 6 means carbon). Cyclotron radiation loss must be computed separately. (Hopkins 1979) © 1979 by the American Nuclear Society, LaGrange Park, Illinois

The average values of $\langle Z \rangle$ and $\langle Z^2 \rangle$ for partially ionized atoms are shown in Fig. 11.25.

These values are useful to compute the fuel ion density and Z_{eff}. (The graphs illustrate the trends of increasing ionization levels, but should not be relied on for accurate calculations.) At $T_e = 1$ keV the average charge state of Fe (Z = 26) is ~ 22 on the graph. At $T_e \sim 3$ keV the low-Z elements (Z < 14) are already fully stripped.

Regardless of the degree of ionization the plasma tends to remain **quasineutral**, with equal densities of negative and positive charges:
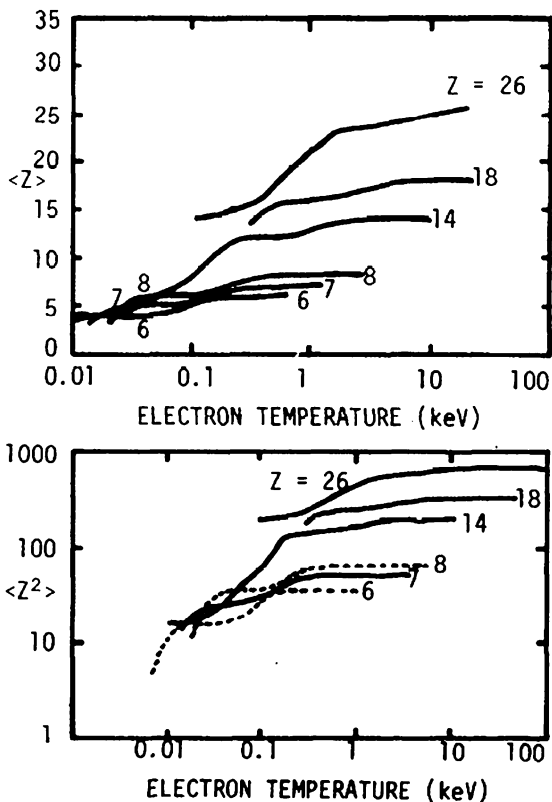
$$n_e = n_i + \sum_z n_z \langle Z \rangle \quad (m^{-3}) \tag{11.29}$$

(This was also discussed in Sect. 1.2.)

Example Problem 11.1: Radiation Power Loss Estimate the hydrogen ion density and radiation power loss from a hydrogen plasma at $T_e = 1$ keV, $n_e = 5 \times 10^{19}$ m^{-3}, and iron impurity fraction 1 % of n_e, assuming that cyclotron radiation loss is negligible.

For this case $\langle Z \rangle \sim 22$.

From the quasineutrality condition $n_i = n_e - 0.01\, n_e\, 22 = 0.78\, n_e$.

The radiation power parameters of H and Fe at 1 keV are 6×10^{-37} and 3×10^{-32} Wm^3.

The radiation power loss is

$$
\begin{aligned}
P_{rad} &= \left(10^{19}\,m^{-3}\right)^2 \left[0.78\left(6 \times 10^{-37}\,Wm^3\right) + 0.01\left(3 \times 10^{-32}\,Wm^3\right) \right] \\
&= 3.0 \times 10^4\,W/m^3.
\end{aligned}
$$

This problem also shows how a small impurity fraction can dilute the fuel ion density (to 78 % of n_e in this case). Since the DT fusion power density is proportional to n_i^2, it would be reduced to 61 % of the value from a pure DT plasma.

11.6.3 Bremsstrahlung

If the nuclear charge is completely screened, the total bremsstrahlung power density per unit energy interval is

$$\frac{dP_{ff}^{Total}}{dE} = 1.54 \times 10^{-38} n_e^2 Z_{eff} \bar{g}_{ff} \frac{e^{-E/T_e}}{\sqrt{T_e}} \text{ W m}^{-3} \text{ eV}^{-1} \tag{11.30}$$

where T_e is in eV, g_{ff} is the Gaunt factor (for soft x-rays $g_{ff} \sim 1$, and for visible light $g_{ff} \sim 2$–5) and Z_{eff} is the effective ionic charge

$$Z_{eff} = \sum_k n_k \langle Z^2 \rangle_k / n_e \tag{11.31}$$

where Z and n_z are the charge and density of each ion species. (For a pure hydrogen plasma $Z_{eff} = 1$). For a plasma with multiple impurity species this may be combined with the quasineutrality condition to yield

$$Z_{eff} = 1 + f_1 Z_1 (Z_1 - 1) + f_2 Z_2 (Z_2 - 1) + f_3 Z_3 (Z_3 - 1) + \cdots \tag{11.32}$$

where $f_k = n_k/n_e$.

Even though the spectrum is integrated along a central plasma chord, along which T_e varies significantly, the continuum spectrum is still approximately linear on a semi logarithmic plot, meaning that the central temperature can be determined. T_e chord-integrated X-ray spectrum is strongly dominated by emission near the core due to the n_e^2 factor and the exponential factor in Eq. (11.29) (Stratton et al. 2008).

An approximate equation for the total bremsstrahlung power loss is

$$P_b \approx 5 \times 10^{-37} Z_{eff} n_e^2 T_e^{1/2} \left(\text{W/m}^3 \right) \tag{11.33}$$

where T_e is in keV (Dolan 1982).

Example Problem 11.2: Z_{eff} Estimate Z_{eff} for a hydrogen plasma with 1 % fully stripped oxygen impurity (Z = 8) plus 0.1 % fully stripped iron (Z = 26).

$$Z_{eff} = 1 + 0.01(8)7 + 0.001(26)25 = 2.21$$

Thus, small amounts of medium Z materials like Fe have a strong effect on radiation losses.

The power densities per unit energy due to line radiation, bremsstrahlung, and radiative recombination due to iron in a hydrogen plasma are shown in Fig. 11.26.

Fig. 11.26 Calculated soft x-ray (SXR) spectrum of iron in a hydrogen plasma, showing the contributions of line, bremsstrahlung, and radiative recombination radiation, assuming $T_e = 2$ keV, $n_e = 10^{20}$ m^{-3}, and an iron fraction $= 1$ %. (Stratton et al. 2008 Fig. 5, courtesy of A. Weller. Copyright 2008 by the American Nuclear Society, LaGrange Park, Illinois)
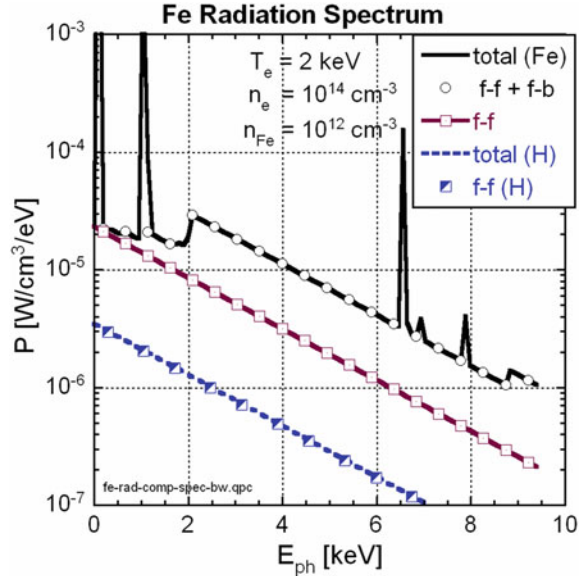
The continuum radiation power of pure hydrogen (bottom curve) is very low. The middle straight line adds the contribution of iron bremsstrahlung, and the top curve adds radiative recombination (straight line) and line radiation (spikes).

The total power emitted due to recombination radiation scales as Z^4, so even a small amount of a medium-Z element, such as iron, can dominate the total emission. Since the SXR continuum radiation depends strongly on T_e, the slope of the continuum line can be used to calculate T_e (Stratton et al. 2008).

11.6.4 Spectral Line Shapes

If we plot the intensity of light emitted by an atom versus wavelength, the spectral lines will appear as spikes with finite width. In the absence of broadening phenomena, the natural line widths are very narrow (10^{-14} m). However, there are several processes that cause the measured peaks to appear broader.

11.6.4.1 Instrumental Broadening

The spectroscopic instrument will make the line appear broader than it really is, due to the finite width of the collimating slits, imperfections of alignment, and so on. Wider slits produce greater instrumental broadening. Instruments with large distances between the slits and the diffraction grating and narrow slits can achieve the best (narrowest) instrumental broadening. Thus, a one- meter monochromator can have much better spectral resolution than a quarter-meter monochromator.

11.6.4.2 Doppler Broadening

If an atom is moving away from an observer with velocity v_x, the wavelength of the light it emits appears to be longer:

$$\lambda = \lambda_o(1 + v_x/c), \tag{11.34}$$

where λ_o is the wavelength from an atom at rest and c is the speed of light. Similarly, if the atom is moving towards the observer, $v_x < 0$, and λ is shorter. A plasma has many atoms with various v_x, so the light intensity I seen at wavelength λ is proportional to the number of atoms having the corresponding v_x,

$$I(\lambda)d\lambda = Cf(v_x)dv_x \tag{11.35}$$

$$I(\lambda_0)d\lambda = Cf(0)dv_x, \tag{11.36}$$

where $f(v_x)$ is the velocity distribution function and C is a proportionality constant. If we divide Eqs. (11.35) by (11.36), use a Maxwellian distribution function

$$f(v_x)dv_x \approx n(\beta/\pi)^{\frac{1}{2}}\exp(-\beta v_x^2), \tag{11.37}$$

$$\beta \equiv (m_i/2kT_i) \tag{11.38}$$

and use Eq. (11.34) to eliminate v_x, then the result is

$$\frac{I(\lambda)}{I(\lambda_0)} = \exp\left[-\frac{m_ic^2(\lambda - \lambda_0)^2}{2kT_i\lambda_0^2}\right] \tag{11.39}$$

This is a Gaussian distribution centered at λ_o, as illustrated in Fig. 11.27 curve b.

At the wavelengths where $I(\lambda)/I(\lambda_o) = 1/2$, the "full width at half maximum intensity" (FWHM) is found from Eq. (11.39) to be

$$\delta\lambda/\lambda_0 = (2/c)(2kT_i\ln2/m_i)^{\frac{1}{2}} \tag{11.40}$$

which may be solved for T_i,

$$T_i = \frac{m_ic^2(\delta\lambda)^2}{8k \ln2\lambda_0^2}. \tag{11.41}$$

Thus, if Doppler broadening is dominant, the ion temperature can be calculated from the measured $\delta\lambda$. For carbon impurity ions at $T_i = 1$ keV, it is found from Eq. (11.40) that $\delta\lambda/\lambda = 7 \times 10^{-4}$. For wavelengths $\lambda_o \sim 200$ nm, $\delta\lambda \sim 0.14$ nm. To observe this effect, the instrumental broadening should be significantly less than $\delta\lambda$. Some other spectral line shapes are also illustrated in Fig. 11.27.

Figure 11.28 shows an early measurement of the ion temperature profile Ti(r) estimated from Doppler broadening of several different spectral lines, which are dominant at different radii.
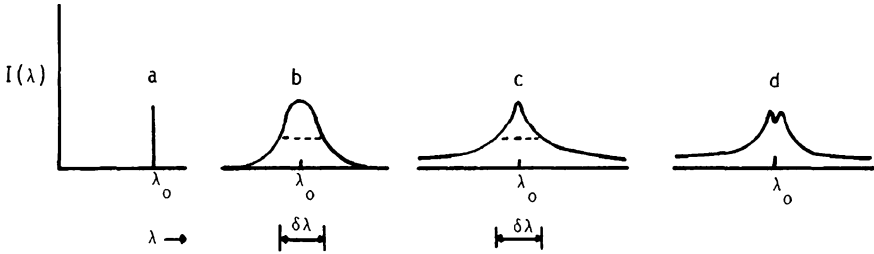
Fig. 11.27 Graphs of intensity versus wavelength for an isolated spectral line. **a** Unbroadened, **b** A Gaussian shape due to Doppler broadening, **c** and **d** Holtzmark profiles due to Stark broadening

Fig. 11.28 Radial profile of ion temperature before and during heating by neutral beam injection in the PLT tokamak from Doppler broadening of Fe XX 266.5, OVII 162.3, CV 227.1, and CIII 223.7 nm lines (Eubank et al. 1979)
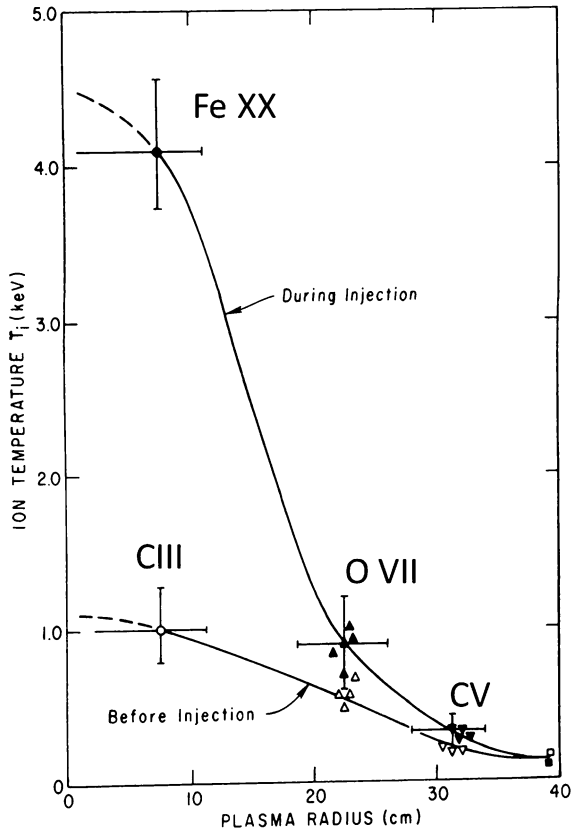
11.6.4.3 Pressure and Stark Broadening

Pressure broadening includes effects of collisions with neutral particles (van der Waals forces), resonance interactions between identical atoms, and collisions with charged particles (Stark broadening). The first two processes are not significant in

highly ionized plasmas, but Stark broadening can be significant in high density plasmas.

Strong electric fields produce splitting of atomic energy levels, so that the spectral lines resulting from transitions between the levels are also split (the Stark effect). Collisions with charged particles produce locally strong electric fields in high-density plasmas. Since the electric fields have random direction and magnitude, the observed spectral lines appear broadened (Fig. 11.27c and d), rather than split into several thin lines. The line width due to Stark broadening is given approximately by

$$\delta\lambda \simeq A_s n^{2/3}, \tag{11.42}$$

where n is the electron density (m^{-3}), and A_s is a constant for a given spectral line. For the visible hydrogen lines, the values of A_s are:

line	λ, nm	A_s (10^{-24} m^3)
Hα	656.3	1.4
Hβ	486.1	2.0
Hγ	410.2	2.9
Hδ	397.0	3.1

(For deuterium the values may be slightly different.) For example, at $n = 10^{20}$ and 10^{23} m^{-3}, the lines widths are approximately $\delta\lambda = 0.043$ and 4.3 nm. If Stark broadening is dominant, measurement of $\delta\lambda$ gives an estimate of the plasma density. However, several regions of different density may be viewed by the spectroscopic instrument simultaneously, complicating the interpretation. In cases where both Stark and Doppler broadening are significant, the combination of the two processes produces a complicated expression for the line shape. If the Stark broadening is approximated by a Lorentzian shape

$$\left[1 + (\lambda - \lambda_0)^2/(0.5\delta\lambda)^2\right]^{-1}, \tag{11.43}$$

the convolution of the Gaussian (Doppler) and Lorentzian profiles leads to *Voigt profiles* (Griem 1997).

11.6.4.4 Zeeman Effect

Interaction of the magnetic moment of an atom with an applied magnetic field produces splitting of the atomic energy levels, and consequent splitting of the spectral lines. The magnitude of the Zeeman splitting is

$$\delta\lambda_Z \sim 1000\,\lambda_0^2 B^2, \tag{11.44}$$

where the wavelengths are in meters and B is in Tesla. For example, a line at 500 nm in B = 1 T would have $\delta\lambda_z \sim 0.25$ nm. There is some problem in distinguishing the Zeeman effect from other effects, such as Doppler and Stark broadening, and in obtaining good spatial resolution. One solution is to study the Zeeman splitting of an injected neutral beam of atoms, such as lithium or barium. Spatial resolution is determined by the small volume where the viewing optics intersect the beam, and the line of sight may be rapidly scanned along the beam with a rotating mirror (discussed below). By viewing at 90° relative to the beam direction, Doppler effects are minimized, and the Zeeman effect can be distinguished to determine the magnetic field inside the plasma.

11.6.5 Spectral Line Intensities

Particle densities may be estimated from the absolute intensities of spectral lines or of the continuum of radiation emitted by free electron collisions (bremsstrahlung), but calibration of absolute intensities is difficult. From various spectral line **intensity ratios** the electron temperature may sometimes be estimated, provided that the theoretical distribution of atomic states can be calculated, such as for the cases of local thermodynamic equilibrium or coronal equilibrium.

11.6.6 Visible Spectroscopy

A fully ionized pure hydrogen plasma does not emit line radiation, and the bremsstrahlung photons from a hot plasma are not in the visible region, so a fully ionized hydrogen plasma would appear invisible to the human eye. However, there is often visible light from the edge plasma, where **neutral hydrogen** comes from the walls or divertor. The concentration of neutral hydrogen atoms can be determined from the absolute intensities of H_α or H_β radiation at wavelengths of 656.28 and 486.13 nm, using a detector with a monochromator or an interference filter to screen out other wavelengths. The absolute intensity measurements can be calibrated with a tungsten lamp of known intensity. Spatial resolution may be obtained by the use of fiber optics to view many chords.

   Impurities come from fusion reaction products (He), wall sputtering (Fe, Ni, Be, C, O, Mo, W,…) impurities injected for diagnostics or plasma control (Ar, Ne,…), and wall coatings (Li, B). Studies of the divertor and scrape off layer (SOL) are especially important for control of particle and thermal power flows (Chap. 7).

   Often lenses or mirrors focus the light into high-purity fused silica optical fibers, which carry the 220–2000 nm light signal out to a lower-noise, shielded location for analysis by spectrometers or filtered detectors.

   Recent advances, such as volume phase holographic (VPH) gratings are described by Stratton et al. (2008).

The steep electron temperature gradient in the SOL can form thin shells of charge states, such as C^+, C^{2+}, C^{3+}, which can viewed along chords through the SOL. The results can be analyzed spectroscopically and inverted to estimate the ion spectral line emissivity, velocity, and temperature. Assuming toroidal symmetry, tomographic reconstruction techniques can yield two-dimensional poloidal profiles of C^{2+} line emission during ELMs, revealing whether the divertor is "detached" from the hot plasma.

The shape of the deuterium line emission from the divertor region contains information on the velocity distribution of the deuterium atoms and their recycling processes. The velocity distribution of the atoms determines their penetration depth into the plasma. Understanding of the emission processes of the deuterium lines is necessary for diagnosis of divertor plasmas.

Here are some examples of how spectroscopic analysis helps elucidate processes occurring in the edge plasma (Stratton et al. 2008):

- The spectra from electron collisional excitation, collisional-radiative (three-body) recombination, and molecular-assisted recombination have distinctive signatures, which permit the dominant process producing hydrogen emission to be identified.
- On JT-60U the D_α profile had both a narrow component attributed to dissociative excitation ($D_2 \rightarrow D + D^*$) and electron collisional excitation of the dissociated atoms, and a broad component is attributed to electron collisional excitation of the atoms from the wall and from charge exchange.
- In Tore Supra two groups of deuterium atom temperatures were observed, ~ 2 and 22 eV.
- Using a scanning Fabry-Perot interferometer (wavelength resolution ~ 0.023 nm) the tritium/deuterium ratio in TFTR was measured to increase to 11 % after 8 tritium-only neutral beam injections.
- In JET Stark broadening analysis yielded radial distributions of the electron density across the outer divertor target plate, up to 5×10^{20} m^{-3}.
- Predications of neutral gas Monte Carlo codes, such as DEGAS, can be verified.

11.6.7 Photography

Modern digital cameras make photography a simple and relatively inexpensive means of plasma diagnostics, which provides insight into the plasma shape, plasma-wall interactions, and plasma instabilities, such as edge localized modes (ELMs).

For infrared use windows can be sapphire ($\lambda \leq 5$ μm) or zinc selenide ($\lambda \sim 8$–12 μm), and lenses can be germanium. At $\lambda < 3$ μm molecular emission lines from plasma can interfere. IR cameras can operate at framing rates up to 10 kHz. Rough surface mirrors may still work, due to the long wavelengths of IR light. Quartz fiber image guides can be used for visible and UV light, but neutron irradiation degrades performance (Lasnier et al. 2008).
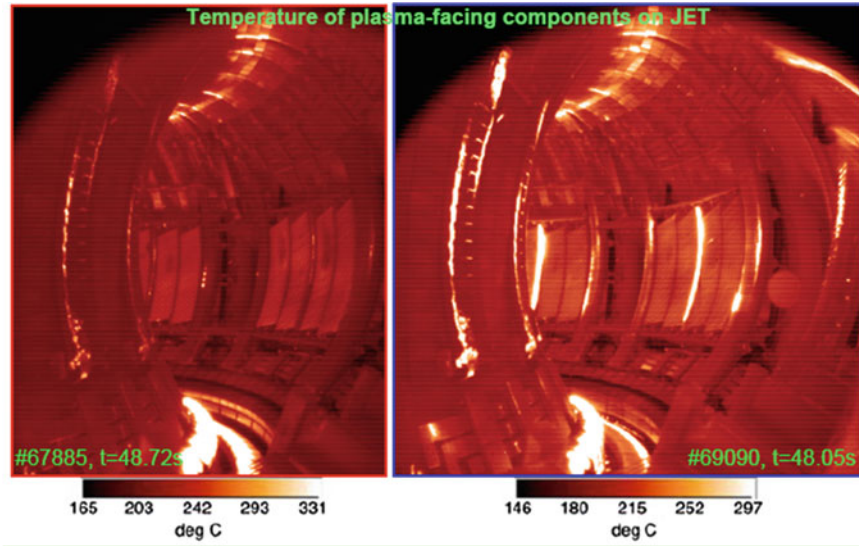
Fig. 11.29 Infrared camera photos of the walls of JET showing local hot spots (Hacquin 2008). Image supplied courtesy of JET-EFDA, copyright EURATOM

Figure 11.29 shows photos of hot spots in JET.

The synchrotron radiation spectrum from relativistic runaway electrons provides information about their energy, pitch angle, runaway current, and beam radius. Infrared cameras can image this radiation, which is emitted at $\lambda \sim 1$ to 15 μm in a narrow cone in the forward direction of the electron motion, so the camera should point tangentially towards the oncoming beam. The graph of intensity versus wavelength has a steep slope below its peak, and measurement of this slope provides information about the maximum electron energy. The optimum spectral region for observation of runaway electrons with energies up to 50 MeV in ITER is 1–5 μm. A tangential infrared camera has provided 2D images of synchrotron radiation (1–5 μm) from runaway electrons in TEXTOR (Stratton et al. 2008).

Most cameras need to be shielded against magnetic fields, radio waves, microwaves, x-rays, gamma rays, and neutrons. Multiple cameras operating for many seconds generate large amounts of data to be stored and partially analyzed. Two wavelengths can be used to distinguish light emitted by a tile (indicative of its temperature) from light generated elsewhere and reflected by the tile. Thin films on a surface may heat and cool faster than the surface. IR TV cameras can be used to compare upper and lower divertor heat loads as a function of separatrix position (Lasnier et al. 2008).

Cameras with interference filters can make 2D images of visible spectral line emission from H, He, C, Ne, Ar, and other species. Such data are of interest for studies of

- Recombination and divertor detachment
- Density limit physics
- Hydrogen recycling
- Impurity sources and transport
- Carbon temperatures near divertor target
- Particle flows in SOL
- Spatial structure of microsecond events, such as ELMs and disruptions (Lasnier 2008).

11.6.8 Bolometers

The power emitted by a plasma in particles and waves can be measured by bolometers. A bolometer contains an absorbing surface (such as a thin film of Au, Pt, or graphite), coupled to a thermometer, which may be a temperature-sensitive resistor or an infrared detector. The bolometer temperature rise is related to power flux by calibration with a lamp of known intensity. In some applications a pair of bolometers may be compared, with one of the screened from the radiation, in order to subtract the background noise of the screened detector. A Wheatstone Bridge may be used to measure tiny changes of resistivity (Ingesson et al. 2008).

The main job of bolometers is to calculate the total radiated power and to study local hot spots using tomographic imaging. Some collimated bolometer arrays on JET and resulting radiation power distributions are shown in Figs. 11.30 and 11.31.

Edge Localized Modes (ELMs) occur when the edge pressure gradient becomes too high. The plasma suddenly bursts across the last closed flux surface (LCFS) of a tokamak into the scrape-off layer (SOL), depositing a high power onto the wall, limiter, and divertor (Wesson 2011). Triggering frequent small ELMs to replace large ELMs reduces the plasma power loss. ELM control may be done by:

- Correction coils that produce resonant magnetic perturbations of the boundary
- Vertical plasma kicking by frequent voltage pulses to vertical field coils (de la Luna 2012; Duval 2012)
- ECRH
- Frequent pellet injection (Pégourié et al. 2009).

Techniques for 2D imaging tomography are similar to those used for soft x-ray tomography (discussed below). A thorough review of bolometry is given by Ingesson et al. (2008). Bolometery, neutral particle analysis, and spectroscopy are discussed in Stott et al. (1998), pp. 297–408.
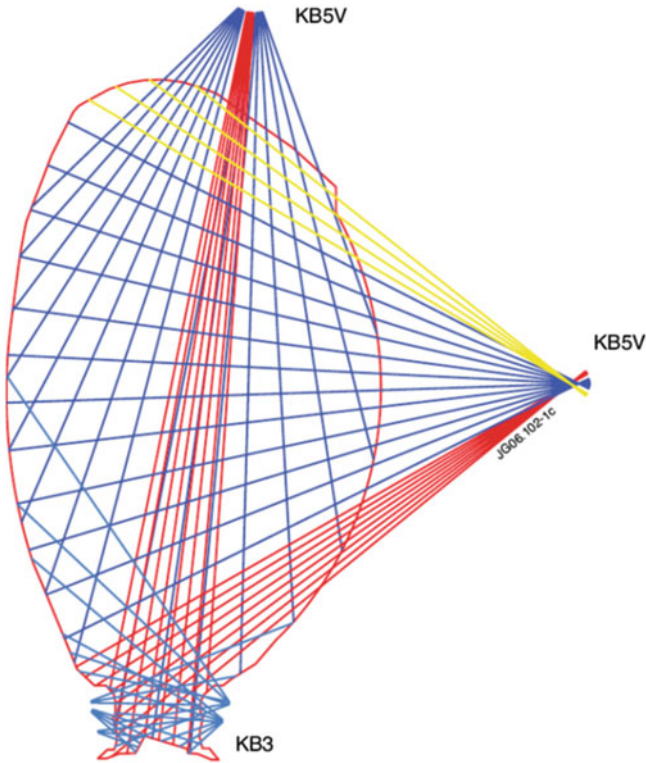
Fig. 11.30 Bolometer arrays on JET. A vertical camera (*top*), horizontal camera (*right side*), and divertor cameras (*bottom*) take pictures along several lines of sight. Then a computer does a tomographic reconstruction of the emission intensity (Huber et al. 2007, Fig. 1)

11.6.9 Ultraviolet Measurements

Multiply-ionized impurity atoms in plasmas with keV temperatures emit radiation in the vacuum ultraviolet (VUV), extreme ultraviolet (EUV) and soft x-ray regions of the spectrum.

Plasma spectroscopy in the ultraviolet, VUV, and EUV regions is usually done using a **diffraction grating** with plane, spherical-concave, or toroidal-concave substrate ruled with a large number of grooves, which diffract the light into spectral orders according to the grating equation:

$$m\lambda = d \ (\sin\alpha + \sin\beta) \tag{11.45}$$

λ = wavelength of the light
d = groove spacing
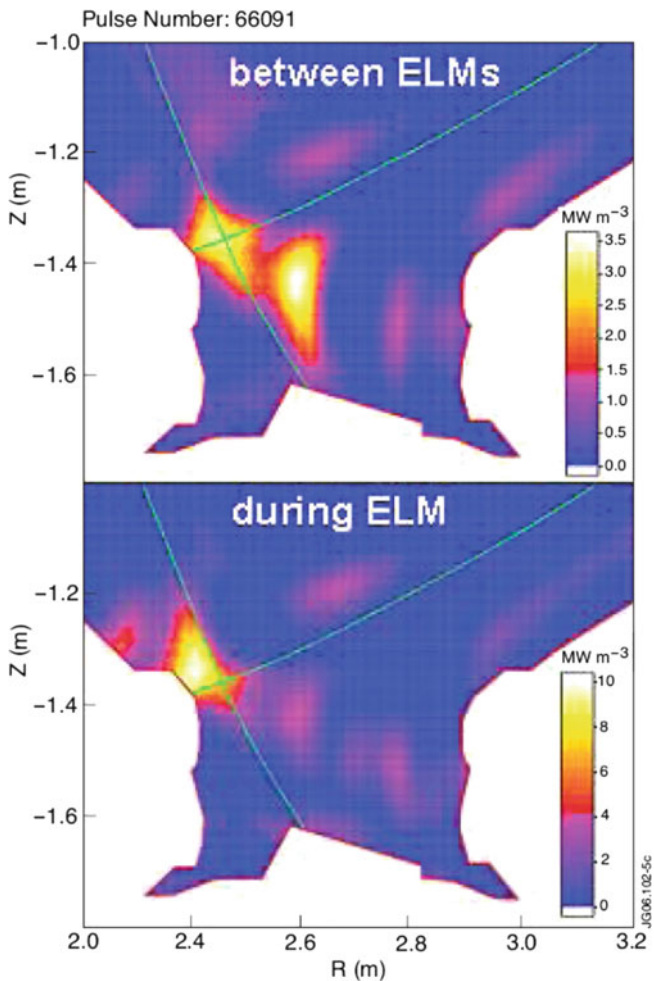
Fig. 11.31 Bolometer data from JET, showing hot spots near the divertor (Huber et al. 2007, Fig. 6)

m	=	spectral order number
α, β	=	angles of incidence and diffraction measured with respect to normal to the grating surface.

At wavelengths >200 nm mirror and grating coatings with reflectivity >90 % at near-normal incidence provide high efficiency. At wavelengths <200 nm (the VUV and EUV spectral regions), the reflectivity of most coatings falls significantly below 90 %, so spectrometers use concave gratings because a single reflection is required. In the VUV region (30–200 nm) concave grating spectrometers can operate at nearly **normal incidence** because coating reflectivities are typically ∼50 %. At wavelengths <30 nm, normal-incidence reflectivities are low, and instruments use

grazing incidence. The short-wavelength cutoff of available window materials requires vacuum instruments below 105 nm (Stratton et al. 2008).

Photodiode arrays and charge-coupled devices (CCDs) are used as detectors with time resolution $\lesssim 10$ ms at wavelengths >200 nm. At wavelengths <200 nm a microchannel plate coupled to a phosphor screen converts the VUV radiation to visible light, which is then coupled to the photodiode array or CCD. The input surface of the microchannel plate is usually coated with a photocathode for improved quantum efficiency. Where high time resolution of a single spectral line is required, single channel detectors such as photomultiplier tubes (PMTs) and photodiodes are used. Stratton et al. (2008) explain the designs and uses of many types of spectrometers.

Filtered detectors may be used instead of gratings to measure the time evolution of individual spectral line intensities, if the spectrum consists of a few well-separated, intense lines. The spectral resolution is poorer, but the filtered detector approach is simpler and has higher optical throughput and better time resolution with good signal-to-noise ratio. For example, filtered detectors can be used to monitor concentrations of low-Z impurities (such as C and O) at 1–100 nm (Stratton et al. 2008).

Grazing incidence grating spectrometers have high spectral resolution, but low optical throughput because the effective grating area is small, which limits the time resolution, and they have few spatial channels. An alternative is **multilayer mirrors** (MLMs) with alternating high-Z reflecting layers and low-Z spacer layers, which can be used at near-normal incidence in the EUV region. For example, at $\lambda = 9$–18 nm a Mo/B_4C mirror with 75 layers spaced 19 nm apart (per 2 layers) achieved reflectivities at Bragg angles of 30–70° of 20–27 % with a bandpass of 0.7 nm (Stratton et al. 2008).

To determine VUV impurity concentrations, the **absolute intensities** of the spectral lines must be calibrated. Two methods are used: branching ratio and synchrotron radiation.

The **branching ratio** method views the same plasma volume simultaneously with a calibrated visible-light spectrometer (or monochromator), and compares the apparent intensities of two spectral lines, one visible and one VUV, originating from the same upper energy level of an atom, such as the hydrogen lines at 410.2 and 93.7 nm (caused by transitions from the n = 6 level to the n = 2 and n = 1 levels, respectively). When the two instruments are properly calibrated, the intensity ratio of these two lines should equal the ratio of their transition probabilities, which is 0.606 for the above example. This is called the branching ratio method of calibration. Uncertainty in the absolute intensities of VUV lines is often at least ±50 %. This technique has the advantage that it can be performed in situ, but it has the disadvantage that the number of usable line pairs is limited by the available impurity elements, blending of lines with those emitted by other species, and the low intensity of the visible line in many cases (Stratton et al. 2008).

The spectral distribution and absolute intensity of the **synchrotron radiation** emitted by relativistic electrons in a storage ring can be accurately calculated, and several facilities are available around the world. The emission is a continuum, so a detailed calibration curve can be obtained. With high electron energies strong signals can be obtained down to wavelengths below 5 nm. The existence of more
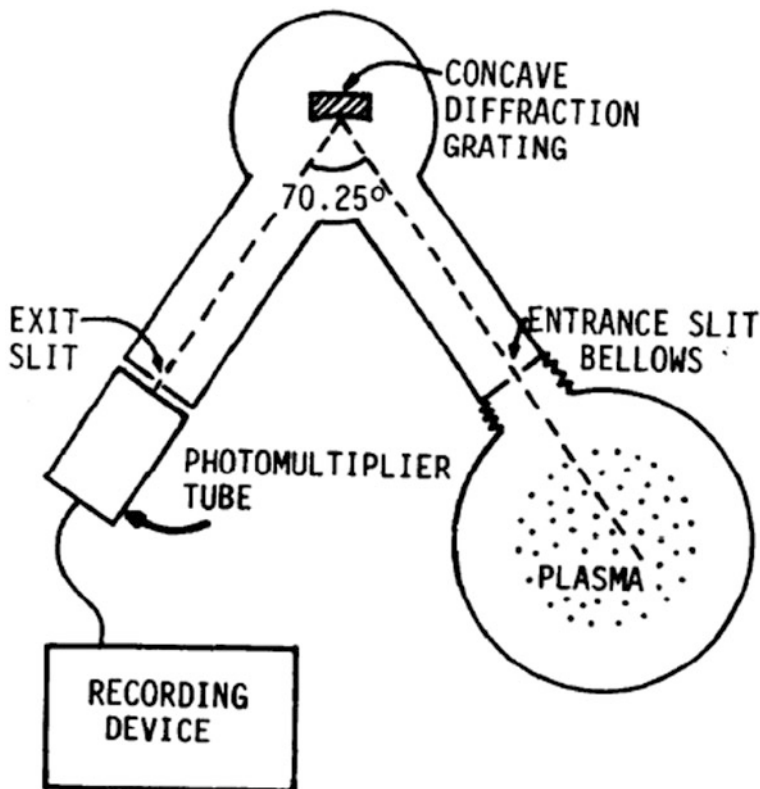
Fig. 11.32 Top view of a Seya-Namioka mount VUV monochromator. Rotation of the diffractions grating about a vertical axis scans the wavelengths seen by the phototube. The instrument may be pivoted around the bellows to view different chords through the plasma

than one spectral order can be corrected by using filters and by varying the electron energy (Stratton et al. 2008).

One type of VUV monochromator is illustrated in Fig. 11.32.

As the grating is rotated, the recording device stores a record of intensity versus wavelength. At wavelengths below 50 nm, the reflection coefficients of materials for normal incidence are very small, and a grazing incidence spectrograph must be used. Some spectrometers can record many wavelength channels simultaneously.

The **bremsstrahlung continuum** intensity can be measured in a visible wavelength region where line radiation is insignificant (such as visible light in a fully ionized core plasma), and the value of Z_{eff} can be estimated if n_e and T_e are known from other measurements. The bremsstrahlung emission is weak compared to line and edge molecular band radiation in the visible, so care must be taken to choose a spectral region free of such radiation and to avoid contamination of the signal with visible light from other sources, such as reflections inside the vacuum vessel. An accurate radiometric calibration is done with standard calibrated light sources.

Interference filters may be used instead of a spectroscope to facilitate multiple spatial channels with fast time response. Such a system can also be adapted to view transport of injected impurities (Stratton et al. 2008).

In DIII-D MgF_2 lenses focused 2D images of VUV radiation from C^{3+} (~ 150 nm) through an interference filter onto a phosphor plate in a secondary vacuum chamber (which isolated the system from the tokamak chamber), from where its light emission was recorded with a CID-based camera. This line is dominant in some divertor plasmas. Comparison with a visible line of C^{2+} (465 nm) indicated a steep temperature gradient (25–5 eV) near the divertor target. Such 2D images of VUV radiation can be done at other wavelengths, and may be valuable for burning plasma experiments (Lasnier et al. 2008).

11.6.10 Soft X-ray Measurements

Three types of Soft X-ray (SXR) diagnostics have been developed:

- Pulse-height-analysis (PHA) 1–100 keV spectrum $\rightarrow T_e$, impurity concentrations
- X-ray crystal spectroscopy (XCS) high resolution impurity K-shell spectra $\rightarrow T_i$ and rotation velocity (Doppler broadening and shift), T_e (line ratios), impurity ionization states
- X-ray imaging systems (XIS) one-dimensional cameras observing many intersecting lines of sight through a poloidal cross section $\rightarrow$ 2D tomographic images. With interference foils such systems can also provide some energy resolution.

These three methods will be discussed in the following paragraphs.

11.6.11 Pulse Height Analysis Systems

Each x-ray photon absorbed in the semiconductor detector creates electron–ion pairs, collected on a capacitor. The voltage pulse from the capacitor is amplified and counted, and the photon energy can be estimated from the data. The result of analysis is a histogram showing the number of pulses versus photon energy. The curve is usually a smooth bremsstrahlung curve plus line radiation peaks.

The detectors are usually lithium-drifted silicon Si(Li) below 30 keV and pure germanium from 30 to 100 keV (requiring cryogenic cooling to reduce noise). Na(I) scintillator-photomultipliers are used at higher energies. Peltier-cooled Si-PIN diodes and avalanche photodiodes have easier cooling requirements, but less precise energy resolution. Improved detectors and digital signal processing techniques are under development (Stratton et al. 2008).

Another technique is to use absorber foils in front of the detectors. For example, two or three detectors may be covered with foils of different thicknesses, as illustrated in Fig. 11.33 for just two detectors.

T_e can be computed from comparison of the two or three signals. This method can give good time resolution. The width of the line of sight is determined by lead collimators placed between the plasma and detectors.

If the foils have different low-energy cutoffs at 4.5 and 5 keV, as in Fig. 11.34, then the difference of the two signals yields the intensity of x-rays between these energies.
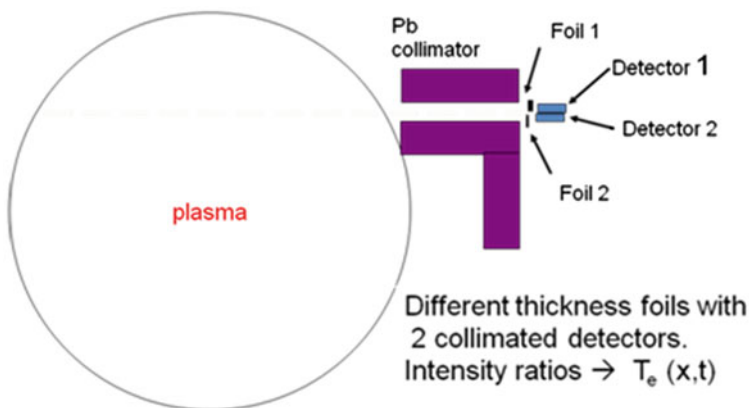
Fig. 11.33 Measurement of x-rays emitted by the plasma, using collimated detectors with foils of different thicknesses

Fig. 11.34 Soft x-ray detector sensitivity with two types of foils, Be/Sc and Be/Ti. The difference of the two detector signals (taking into account detector efficiencies) would measure radiation emitted between 4.5 and 5.0 keV. (Stratton et al. 2008) © 2008 by the American Nuclear Society, LaGrange Park, Illinois
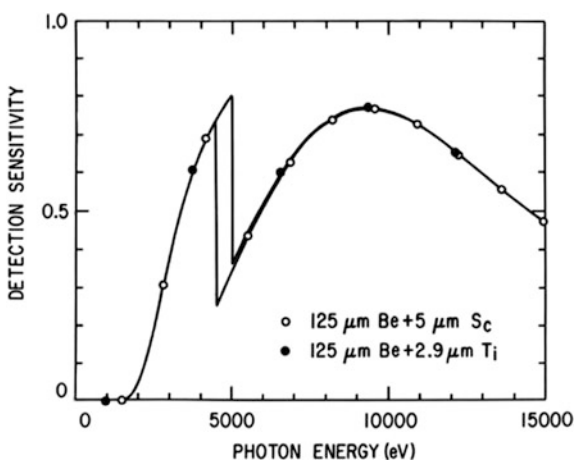
Silicon photodiode arrays with pinhole cameras can view many lines of sight from several different positions for absolute power measurements in the extreme ultraviolet (EUV). For example, tomographic reconstruction showed the events during a disruption mitigation by massive neon gas injection in ASDEX (Reiter et al. 2009).

11.6.12 X-ray Crystal Spectroscopy

X-ray crystal spectroscopy (XCS) can measure the ion temperature and flow velocity (Doppler width and shift) in the plasma core, especially with helium-like ionization states of medium-Z impurities (such as Ar^{16+}, Fe^{24+}, Ni^{26+}, Kr^{34+}), because they are stable at many temperatures, due to their closed electron shells. Argon is good in present tokamaks (1–6 keV), but krypton may be needed in ITER $T_i \gtrsim 10$ keV) (Stratton et al. 2008).

A spherical grating combines focusing and diffraction. Radiation from one point on the *Rowland circle* will be diffracted according to its wavelength and focused onto another point on the circle, Fig. 11.35.
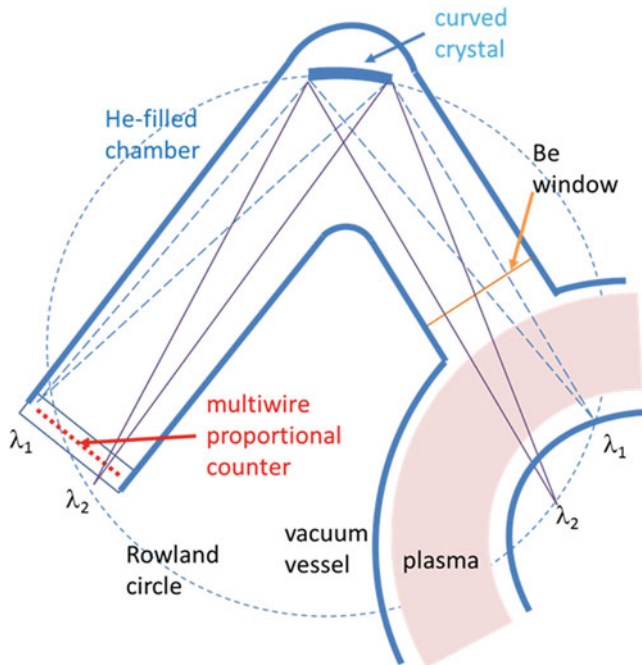
Fig. 11.35 A curved crystal spectrometer, like the one used on PLT. The tube width is exaggerated for clarity. Based on drawing of Hillis et al. (2004)

The wavelength resolution is limited by the detector wire spacing, which is usually about 0.3 mm. The crystal grating radii are typically 2–5 m, but one with 25 m radius is used on JET, to reduce the neutron and gamma flux at the grating. XCS instruments can typically attain resolving power $\lambda/\Delta\lambda \sim 10,000$ at wavelengths 0.1–0.5 nm (Stratton et al. 2008).

The LHD spectrometer uses a CCD detector with small pixels (~ 23 µm) to achieve good wavelength resolution and a square, rotatable crystal holder with four concave quartz crystals (R $\sim$ 3 m), so that the instrument can cover four wavelength regions.

A two-dimensional CCD can measure wavelength in one direction and line-of-sight through the plasma in the other direction with high counting rate. For example, the PILATUS II system on Alcator C-Mod can study the Ar^{16+} spectra at 3.1 keV with 10 ms resolution (Stratton et al. 2008).

11.6.13 Soft X-ray Tomography

Soft x-ray (SXR) tomography can provide 2D images of x-ray emissivity from the plasma, which provide valuable information on plasma shape and MHD activity.

Computed axial tomography (CAT) scans are widely used in medicine, but there the x-rays come *from outside* the body and pass through to the detector, partially attenuated by the body, with no need for sub-second time resolution. In plasmas the x-rays are emitted *from inside* the plasma, with little attenuation in the plasma, and fast time resolution is needed, so the mathematical inversion problem is somewhat different.

The data can be interpreted by solving a set of integral equations. Some methods used for plasmas include the Radon Transform, Fourier Transform, maximum entropy method, and series expansions in terms of natural basis functions. For example, the Cormack method represents the data with a series of Zernicke polynomials as natural basis functions, for which the solution is obtained analytically as a series of Chebyshev polynomials. Bessel functions may also be used as the natural basis functions. The solution often involves solution of large matrix equations by methods like "truncated singular value decomposition". Many sophisticated procedures have been developed to improve the accuracy of the 2D emissivity calculations. If the plasma has circular symmetry, then a simpler Abel inversion technique may be used. It is also possible to develop tomography of vector quantities (such as flow velocity) and 3D imaging, but those require much more data and analysis. Tomographic inversion techniques are reviewed by Ingesson et al. (2008).

In plasma diagnostics systems collimated detectors look at many angles from several different poloidal locations around the plasma, such as shown in Fig. 11.36.

Fig. 11.36 Lines of sight of
five detector arrays for soft
x-ray tomography. Each
detector array has 12 lines of
sight (Eshelman et al. 1991)
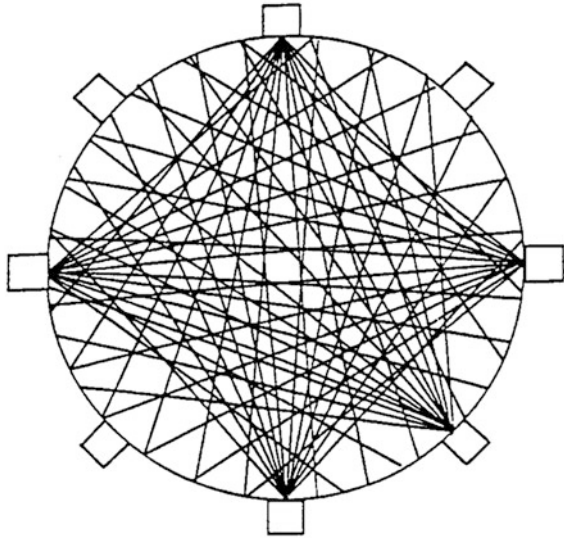
In this case one detector array consists of a housing, an entrance slit, twelve
photo-sensitive diodes, a preamplifier for each channel, and a thin (~ 20 µm Be)
foil to screen out visible light while transmitting soft x-rays, as shown in
Fig. 11.37.

Each channel is carefully calibrated, so that the computer can compensate for
different sensitivities. A computer program unfolds the data to derive a twodi-
mensional plot of x-ray emission intensity, such as the one in Fig. 11.38.

In this Figure a ring of high emissivity with a slight asymmetry can be seen.
This may be indicative of a hot electron layer.

SXR tomography has been used in tokamaks, stellarators, magnetic mirrors,
reversed field pinches, and other devices to study

- T_e profiles
- Hot electron layers and hollow profiles
- MHD instabilities, such as

  - Global Alfvén eigenmodes
  - Sawteeth
  - Snakes
  - ELMs

- Magnetic islands
- Pellet injection effects
- Disruptions
- Impurity densities and Z_{eff}
- Particle transport using the injection of trace heavy impurities
- Transport modeling $\rightarrow$ diffusion coefficient and convection velocity
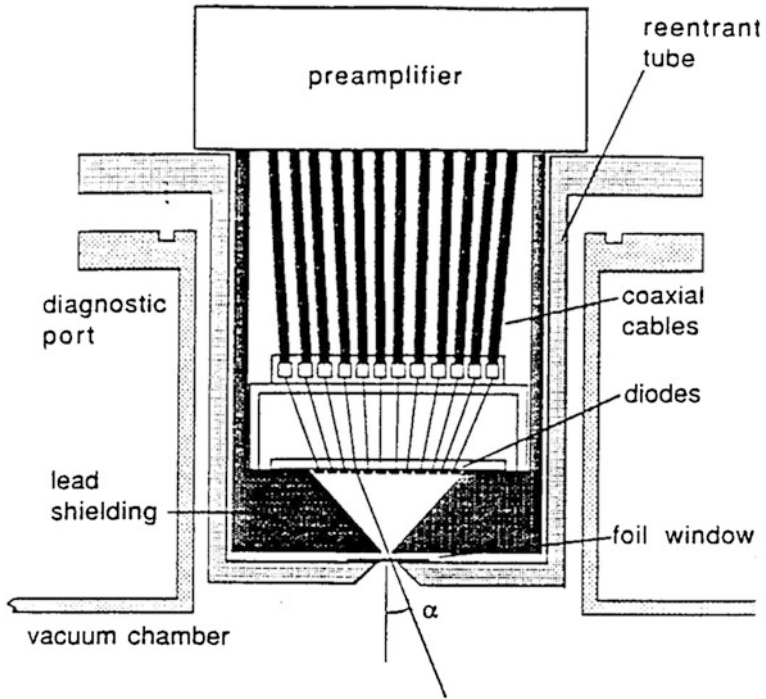
Fig. 11.37 A 12-channel diode array for soft x-ray tomography. From Eshelman et al. (1991)
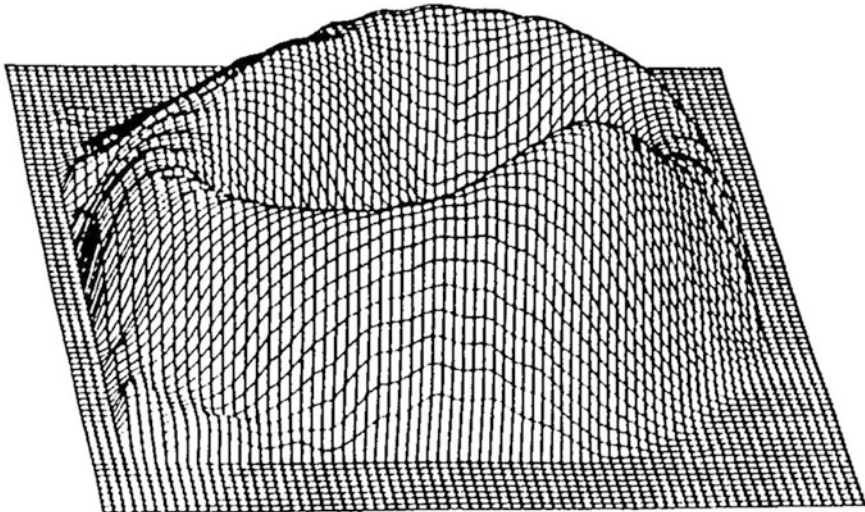
Fig. 11.38 Contour plot of soft x-ray emissivity from plasma in the Missouri magnetic mirror with 1 kW ECH heating power. (Eshelman et al. 1991)

- Heat transport, such as cold pulses and power modulation
- Poloidal asymmetry due centrifugal force of toroidal rotation on heavy impurities
- Asymmetry during radio-frequency heating
- Plasma position control (Peacock 1996; Ingesson et al. 2008).

The present detectors, such as semiconductor photodiodes, may not function well in a burning plasma experiment like ITER, especially inside the vacuum vessel, so development of radiation-hardened detectors is needed. Vacuum photodiodes may become useful for this application, if they prove to have good sensitivity, spectral response, and lifetimes in a severe radiation environment. (Ingesson et al. 2008).

11.6.14 Hard X-ray Measurements

Hard x-rays (hundreds of keV and above) are produced by runaway electrons in toroidal devices and by very hot electrons produced by electron cyclotron resonance heating. The energy distribution and number of runaway electrons can be estimated from the hard x-ray spectrum, which can be measured with NaI(Tl) scintillation detectors, and from their synchrotron radiation emission. (Synchrotron emission from runaway electrons was discussed under "Photography" above.)

Data from hard x-ray emission measurements are shown in Fig. 11.39.

From the slope of the line, the effective electron temperature can be determined. In this case there are two slopes, corresponding to two electron populations with different T_e.

Groups of electrons with several MeV energies have been observed in tokamaks.

Fig. 11.39 An x-ray spectrum with a high-energy tail caused by radio frequency current drive (Texter et al. (1986), Fig. 4)
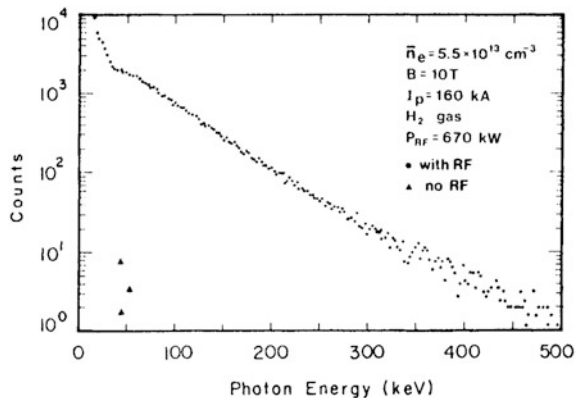
11.6.15 Electron Cyclotron Emission

Cyclotron radiation is emitted by electrons at integer multiples of the cyclotron frequency

$$
\begin{aligned}
\omega_{ce} &= eB/\gamma m_e (radians/s) \\
f_{ce} &= \omega_{ce/2\pi(Hz)} \\
f_{ce} &= 28.0 \ B/\gamma (GHz)
\end{aligned}
\tag{11.46}
$$

where

e   =   electronic charge,
B   =   magnetic induction,
m_e =   electron mass

Lorentz factor $\gamma = (1 - v^2/c^2)^{-1/2}$. For modern fusion devices B is in the range 2–7 T and so the ECE radiation frequency $f_{ce} \approx 50$ to 200 GHz, but higher harmonics are also important. Figure 11.40 shows the frequency ranges for use of ECE and microwave reflectometry in a tokamak.

Since

$$
B(R) = B_o R_o/R,
\tag{11.47}
$$

where B_o is the value of B at R_o, each value of $2f_{ce}$ corresponds to a unique value of R.

When the plasma density and temperature are sufficiently high, the plasma becomes **optically thick** to some harmonics of the ECE, usually the first harmonic *ordinary mode* (electric filed polarization parallel to B) and the second-harmonic *extraordinary mode* (electric field perpendicular to B). (See also Sect. 5.7) Emission from plasmas of magnetic fusion interest is in the Rayleigh-Jeans limit ($\hbar\omega \ll kT_e$) so that the radiation intensity of optically thick ECE harmonics reaches that of blackbody radiation:

$$
I(\omega) = \omega^2 kT_e/8\pi^3 c^2.
\tag{11.48}
$$

Therefore, the plasma electron temperature and its fluctuations can be determined by measuring the intensity of ECE in the optically thick regime. Under some conditions, ECE measurements can also determine electron density and its fluctuations (Luhmann et al. 2008).

The emission is separated into many frequency bands, each corresponding to a particular value of R, so the result is a one-dimensional profile of emission versus R. From these data $T_e(R)$ can be calculated. By using multiple spatial channels a 2D image $T_e(R, z)$ can be computed.
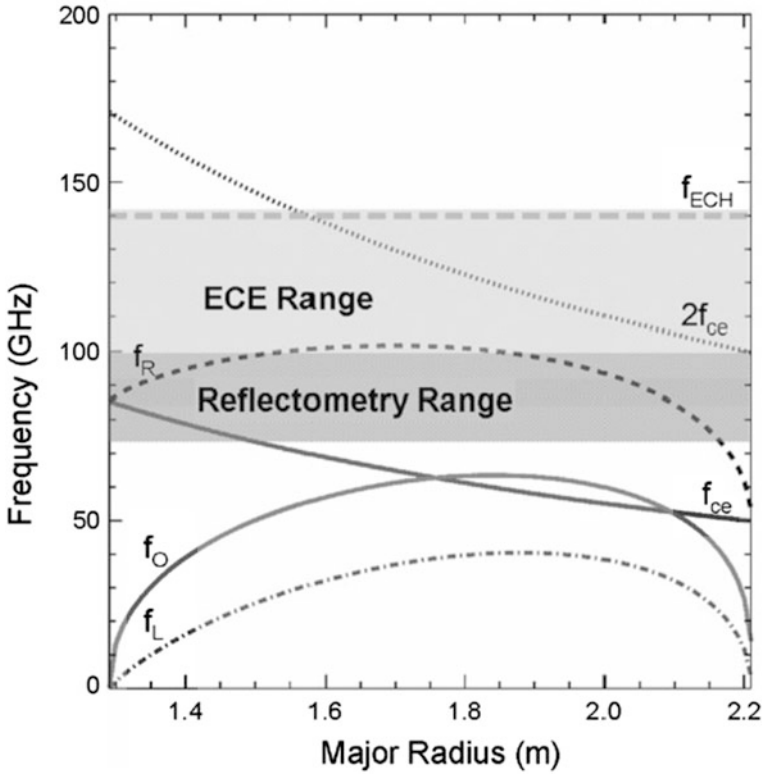
Fig. 11.40 Characteristic frequencies for the TEXTOR tokamak (Luhmann et al. 2008). © 2008 by the American Nuclear Society, LaGrange Park, Illinois

For propagation with wave vector $\mathbf{k} \perp \mathbf{B}$ the emission occurs in both the O-mode and X-mode. The radiation transport for a single-ray trajectory is determined by the balance between emission and absorption.

$$\frac{d}{ds}\left[\frac{I(\omega)}{N_r^2}\right] = \frac{1}{N_r^2}[-\alpha(\omega)I(\omega) + j(\omega)], \qquad (11.49)$$

where

$\alpha(\omega)$ = absorption coefficient
$j(\omega)$ = emission coefficient
N_r = plasma refractive index
$I(\omega)$ = emission intensity.

Integrating over ds from the emission radius to the detector radius

$$I_{(s)}(\omega) = I_{(s_0)}(\omega)\exp(-\tau_s) + \frac{j(\omega)}{\alpha(\omega)}[1 - \exp(-\tau_s)], \qquad (11.50)$$

where the "optical depth" is

$$\tau_s = \int_0^s \alpha(\omega)ds. \qquad (11.51)$$

If $\tau_s \gg 1$, this becomes

$$I(\omega, s) = \frac{j(\omega)}{\alpha(\omega)}. \qquad (11.52)$$

In the case of optically thin or "grey" emission, the wall reflections (with reflection coefficient ρ_{refl}) must be taken into account, leading to the following expression

$$\begin{aligned} I(\omega, T_e) &= I_{BB}\frac{(1 - e^{-\tau})}{(1 - \rho_{\text{refl}}e^{-\tau})} \\ &= \frac{\omega^2}{8\pi^3 c^2}k_B T_e\frac{(1 - e^{-\tau})}{(1 - \rho_{\text{refl}}e^{-\tau})} \end{aligned} \qquad (11.53)$$

For the case of X-mode normal emission in the equatorial plane with $n \geq 2$, the optical depth in a circular plasma is given by

$$\tau_n^x = 9.5 \times 10^{12}\frac{(R_0 + r)^2 n_e\left[n^{2n-2}(9.78 \times 10^{-4}T_e)^{n-1}\right]}{10 R_0 B_\phi(R)(n-1)!} \qquad (11.54)$$

where

R_0 = major radius
r = radial position $(-a \leq r \leq a)$ (cm)
T_e = electron temperature (keV)
n_e = electron density (cm^{-3})
B = magnetic field (T)
n = harmonic number.

For the fundamental O-mode emission, the optical depth is given by

$$\tau_{n=1}^O = 9.8596\left[\frac{1.16 \times 10^4 k_B T_e}{m_e c^2}\right]\left[\frac{R_0 \omega_{ce}}{2\pi c}\right] \times \frac{\omega_{pe}^2}{\omega_{ce}^2}\sqrt{1 - \frac{\omega_{pe}^2}{\omega_{ce}^2}}, \qquad (11.55)$$

where ω_{pe} is the electron plasma frequency. [See Sect. 5.7 or Eq. (11.69)].

Oblique viewing at 70 or 80° to the magnetic field can be used in addition to perpendicular viewing to measure second harmonic X-mode ECE at high energies,

and thereby study distortions in the electron velocity distribution, which may be non-Maxwellian (de la Luna et al. 2008).

The coarse temperature resolution limit is determined by the **intrinsic radiation noise**, which is given by

$$\Delta T_{rms} = (T_e + T_n)/\sqrt{\Delta\omega\tau}, \tag{11.56}$$

where

T_e	=	electron temperature to be measured
$T_n \ (\ll T_e)$	=	overall noise temperature including the antenna contribution
$\Delta\omega$	=	bandwidth of the radiation to be collected
τ	=	integration time (not to be confused with optical depth).

Typical values are bandwidth ≈ 0.5 GHz and frequency response of 250 kHz ($\tau \approx 4$ μs), yielding relative temperature resolution $\Delta T_{rms}/T_e \approx 1$ to 3 %. *Cross-coherence* techniques between two detector signals from the same plasma volume can be used to distinguish T_e fluctuations among the intrinsic noise (Luhmann et al. 2008).

Electron cyclotron *absorption* (ECA) measurements could in principle determine the optical depth τ_s of the plasma from the incident and transmitted powers (Luhmann et al. 2008):

$$P_{trans} = P_{inc}\exp(-\tau_s). \tag{11.57}$$

but this method is difficult and rarely used.

ECE measurements have been made by Fourier transform spectrometers, grating polychromators, and heterodyne receivers. Only the heterodyne system will be discussed here.

Usually the radiometer is placed at the outboard side of the torus. Figure 11.41 shows some elements of a heterodyne receiver system.

The heterodyne method combines the ECE signal with a local oscillator signal at a similar frequency. For example, if the magnetic field at one place in the plasma were 3.2 T, then the second harmonic frequency would be 179.2 GHz.
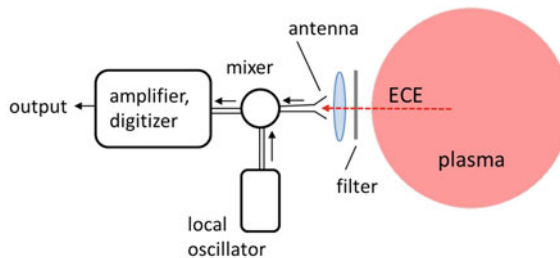
Fig. 11.41 Elements of a heterodyne ECE receiver system

This signal could be detected and combined with a local oscillator signal at 182 GHz to produce an intermediate beat frequency at 2.8 GHz, which is easier to process accurately than the original 179.2 GHz signal. If the ECE signal varies over a wide range, then multiple receivers and oscillator frequencies can be used. The radiometer must be accurately calibrated, which is carried out using large aperture blackbody radiation sources.

Most modern tokamaks have ECE systems. For example, the 12-channel, 176–188 GHz heterodyne system on the JT-60 tokamak uses a 182 GHz oscillator and achieves frequency resolution of 0.5 GHz, spatial resolution of 1.2 cm, and time resolution of 2–20 μs.

In ITER ECE measurements with accuracy of 10 % and 10 ms time resolution are desired from 0.05–10 keV (edge plasma) and from 0.5–40 keV (core plasma). The ECE radiation will be transmitted with a long oversized waveguide system to reach the detectors and electronics, which must be well shielded from the neutrons and gammas (Luhmann et al. 2008).

Figure 11.42 shows electron temperature profiles calculated from ECE data.

When the electron density is so high that the plasma frequency $\omega_{pe} > 1.6\omega_{ce}$ the electron cyclotron waves do not propagate well in the first harmonic. (The second harmonic could still be used.) Electrostatic **electron Bernstein waves (EBWs)** can propagate across the magnetic field and be converted at the upper hybrid resonance to X-mode electromagnetic waves (Sect. 5.7), which may sometimes be further converted to the O-mode (B-X-O conversion) and reach the detectors. This is in the opposite direction from the process shown in Fig. 5.34. The signals can be analyzed to estimate T_e profiles in overdense plasmas. Experimental results are comparable to Thomson scattering data. EBW radiometry can measure the T_e profile relatively inexpensively with good temporal and spatial resolution in cool, dense plasmas; but a computer must do EBW ray tracing and model the EBW mode conversion process, which requires accurate n_e profile data. Similar EBW measurements have been made on several other experiments, but will probably not be needed for ITER, since its plasma will not be overdense (Luhmann et al. 2008).

Fig. 11.42 Evolution of the temperature profile in Alcator C tokamak as determined from optically thick second harmonic cyclotron emission (Hutchinson 2002, Fig. 5.8). Used by permission of Cambridge University Press
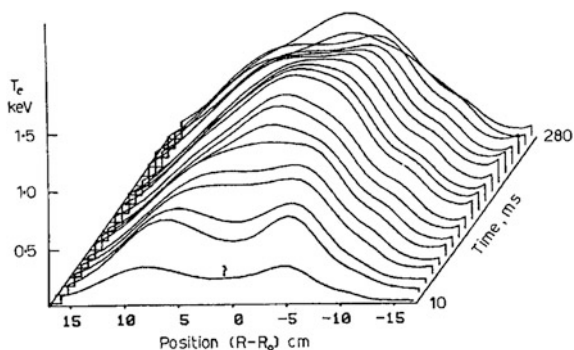
11.7 Active Particle Diagnostics

Electron beams have been used to probe plasmas in weak magnetic fields, in order to map out spatial variations of the electrostatic potential. Energy loss of electron beams passing through magnetic mirrors along the axis indicates the amount of heating produced by the beam, which may be correlated with plasma parameters. However, electron beams cannot be injected across strong magnetic fields, due to their small Larmor radii. Ion beams can be used if they are heavy and high-energy, so that their Larmor radius is large enough to penetrate into the plasma.

Neutral beams may be used for plasma diagnostics, provided that they can penetrate adequately, are narrow enough for good spatial resolution, and do not perturb the plasma too much. Neutral beam injection has several potential advantages over passive spectroscopy:

- Better spatial resolution (intersection of the beam with the spectrometer line of sight)
- Rejection of background noise by modulation of the beam and detector
- Ability to populate weak emitter states.

This section will describe the following uses of diagnostic beams

- Beam emission spectroscopy (BES)—light from *beam* atoms
- Charge exchange recombination spectroscopy (CXRS—light from neutralized *plasma* ions
- Motional Stark effect (MSE)—electric field and magnetic field
- Zeeman splitting—magnetic field
- Rutherford scattering—T_i
- Lithium beam probe
- Heavy ion beam probe (HIBP).

11.7.1 Beam Emission Spectroscopy

During neutral beam injection the beam atoms, excited by collisions with electrons and ions, emit light, which is analyzed by a spectrometer. The spatial resolution is determined by the volume of the beam viewed by the spectrometer.

The main goal of beam emission spectroscopy (BES) is to help understand fluctuations of plasma parameters, such as n_e, v_{et}, T_e, T_i, B, electrostatic potential ϕ, and velocities. These are related to phenomena such as

- Magneto hydrodynamics (MHD) activity
- Edge-localized modes (ELMs)
- Turbulence
- Energetic-particle-driven modes, such as the toroidal Alfvén eigenmodes.

The radial particle flux caused by turbulence is

$$\Gamma_j = \langle \tilde{E}_\perp \tilde{n}_j \rangle / B \; + n_j \langle \tilde{v}_{j\parallel} \tilde{B} \rangle / B \tag{11.58}$$

where $\tilde{B}$, $\tilde{E}_\perp$, $\tilde{n}_j$ and $\tilde{v}_{j\parallel}$ = fluctuating components of magnetic field, electric field component perpendicular both to B and to the radial direction, density, and parallel velocity. The angular brackets denote averages of the ensemble of particles in a particular flux surface. This average is usually replaced by a time average at a particular spatial point, since flux surface averages are generally impractical. The first term is electrostatic transport that depends on the correlation of $\tilde{E}_\perp$ and $\tilde{n}_j$, and the second term depends on the correlation of $\tilde{B}$ and $\tilde{v}_{j\parallel}$. The *convective* radial heat flux is $2.5T\Gamma_j$, and the *conductive* radial heat flux is $1.5n_j \langle \tilde{E}\tilde{T}_{\perp j} \rangle$, where $\tilde{T}_j$ = temperature fluctuation of species j. An additional transport term is proportional to $g\nabla T_i$, where g is a function of $(\tilde{B}/B)$. Thus, measurements of these fluctuating parameters and their correlations are essential for understanding turbulence and the associated anomalous transport, which limits the energy confinement time. On the other hand, a gradient of the radial electric field causes shear of the $\mathbf{E} \times \mathbf{B}$ drift velocity, which stabilizes some fluctuations and provides an *internal transport barrier* (Wesson 2011).

BES can measure local fluctuations of density at long wavelengths λ:

$$k\rho_i < 1 \quad (\text{or } \lambda > 2\pi\rho_i) \tag{11.59}$$

where $k = 2\pi/\lambda$ is the wave number perpendicular to B and ρ_i is the ion Larmor radius.

With deuterium atom beam injection BES observes the Doppler-shifted Balmer D_α emission (n = 3 to n = 2 transition) near $\lambda_o = 656.1$ nm. Since the accelerated ions include D^+, D_2^+, and D_3^+, the neutral beam has components at full beam energy, half energy, and third energy. (When a D_3 molecule is accelerated to 90 keV, each atom carries 30 keV). The resulting beam emission manifold is Doppler shifted to shorter wavelengths (higher energies), as illustrated in Fig. 11.43.

The intensity I of the beam emission is proportional to the local plasma density according to

$$I = An_a n_b / 4\pi \tag{11.60}$$

where

n_b	=	beam density
n_e	=	local plasma density
A	=	excitation rate constant

The Doppler shift separates the beam emission from the brighter edge light, which is also attenuated by a filter. The beam energy levels and ionization can be
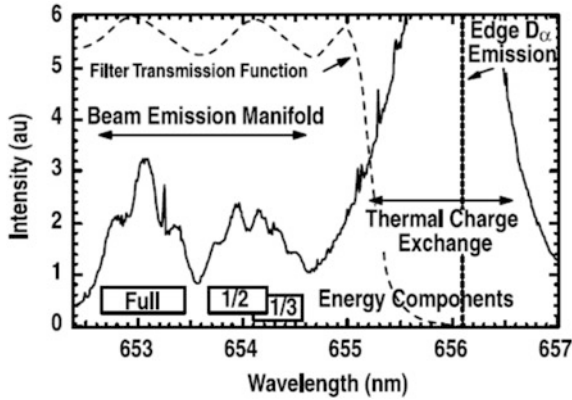
Fig. 11.43 Spectrum of beam emission manifold, blue shifted at nearly 3 nm for full-energy beam component. Stark splitting evident with second and third energy components overlapping. Thermal deuterium charge exchange (edge plasma) is also blue shifted because of significant toroidal rotation. Edge recycling D_α emission is orders of magnitude more intense than beam emission. The transmission function of the filter, which largely rejects the edge plasma light, is the dashed curve (Thomas et al. 2008). © 2008 by the American Nuclear Society, LaGrange Park, Illinois

calculated from rate equations, such as (11.24)–(11.25), using excitation, ionization, and charge-exchange cross sections for hydrogen and common impurity ions from the Atomic Data and Analysis Structure (ADAS) database (Thomas et al. 2008).

For the $n = 3$ to $n = 2$ transition the intensity fluctuation is related to the density fluctuation by

$$\tilde{I}/I = C(\tilde{n}/n) \tag{11.61}$$

where the coefficient C depends on n, Z_{eff}, and beam energy, and only weakly T_e. For typical plasma parameters, 0.5–1 % of the beam atoms are in the $n = 3$ state, with ions and electrons contributing roughly equally to the excitation processes, and $C \sim 2$ to 3 (Thomas et al. 2008).

Figure 11.44 shows the DIII-D tokamak BES system.

A shutter (not shown) can be closed to protect the optics during discharge cleaning. The viewing direction is chosen to avoid red-shifted beam light, which would overlap with emissions from carbon near 658 nm. The spatial resolution around the line of sight is about 1 cm. Incoming light is focused onto small diameter PIN diodes, which minimizes capacitance and voltage noise. The diodes and preamplifiers are cryogenically cooled to $-140\,^\circ$C, which reduces current noise (Thomas et al. 2008).

Calculations based on cross correlations of several adjacent channels (lines of sight) can yield the plasma radial and poloidal advection velocities. BES can provide information on the following properties of density turbulence:
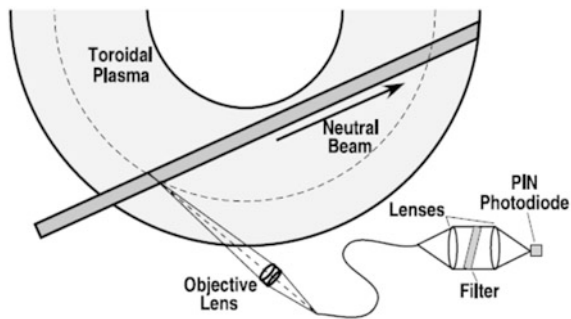
Fig. 11.44 Typical viewing geometry for BES measurement in DIII-D: high radial resolution is obtained at intersection of beam volume and sightline. The sightline is angled approximately at pitch angle in "vertical" dimension out of page for optimal poloidal resolution (Thomas et al. 2008). © 2008 by the American Nuclear Society, LaGrange Park, Illinois

- Normalized density fluctuation amplitude ñ/n
- Radial and poloidal correlation lengths
- Decorrelation time
- 1-D and 2-D wave number spectra [$S(k_r)$, $S(k_\theta)$, $S(k_r, k_\theta)$]
- Poloidal velocity, velocity fluctuations
- Movies of turbulent flow
- Zonal flows and geodesic acoustic modes
- Relation to internal transport barriers.

BES can also be used to study the beam itself, such as its density n_b (Thomas et al. 2008).

11.7.2 Charge Exchange Recombination Spectroscopy

Charge exchange recombination spectroscopy (CXRS) uses a fast diagnostic hydrogen (or He, Li,…) neutral beam, which undergoes charge exchange with a plasma ion Z^z, which could be either hydrogen or an impurity, resulting in a lower charge state ion or neutral $Z^{(z-1)}$. The reaction may be written

$$H^o + Z^z \rightarrow H^+ + Z^{(z-1)*} \tag{11.62}$$

where the asterisk denotes excitation. For example, if the original ion were fully stripped C^{6+}, then the reaction product would be C^{+5*}.

The resulting charge-exchange neutral or ion $Z^{(z-1)*}$ (still having the original plasma ion velocity) radiates a photon. Analysis of such photons provides information on

- Plasma ion toroidal and poloidal rotation velocities v_ϕ, v_θ (Doppler shift)
- T_i (Doppler broadening)
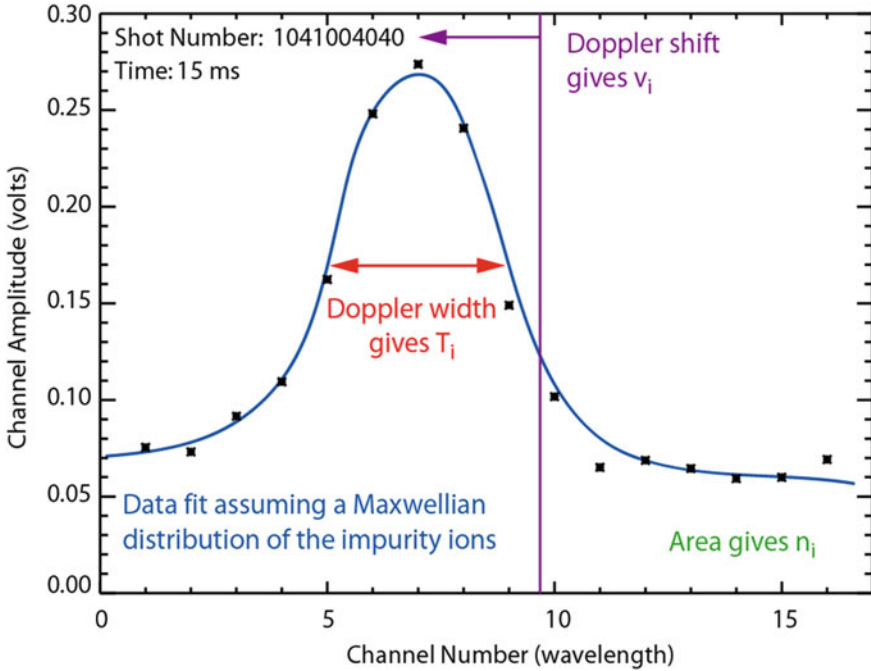
Fig. 11.45 CXRS data showing the Doppler width. The Doppler shift is exaggerated for clarity. Courtesy of Sanjay Gangadhara and David Ennis, University of Wisconsin

- Impurity density n_z
- Estimation of E_r from
  $E_r = (Zen_z)^{-1}dp_z/dr - v_\theta B_\phi + v_\phi B_\theta$ (Wesson 2011, pp. 207)
- Local B field from Stark splitting of the D_α or D_β lines of the beam neutrals (Thomas 2008).

Some CXRS data are shown in Fig. 11.45.

We can estimate the ion density from the area under the curve.

Figure 11.46 shows how CXRS is used to measure the helium ash in JET.

Relative to passive emission spectroscopy, active charge-exchange spectroscopy has several advantages.

- Study of fully stripped, low Z ions, which are dominant in most present machines. (Without charge-exchange excitation, no line emission would occur from fully stripped ions.)
- Spatially localized measurement at intersection of beam and spectrometer line of sight.
- Line emission in the near ultraviolet and visible wavelength ranges, allowing visible spectrometers with lenses and fiber optics. (Passive emission spectroscopy usually requires VUV instruments with a direct line of sight to the plasma.)
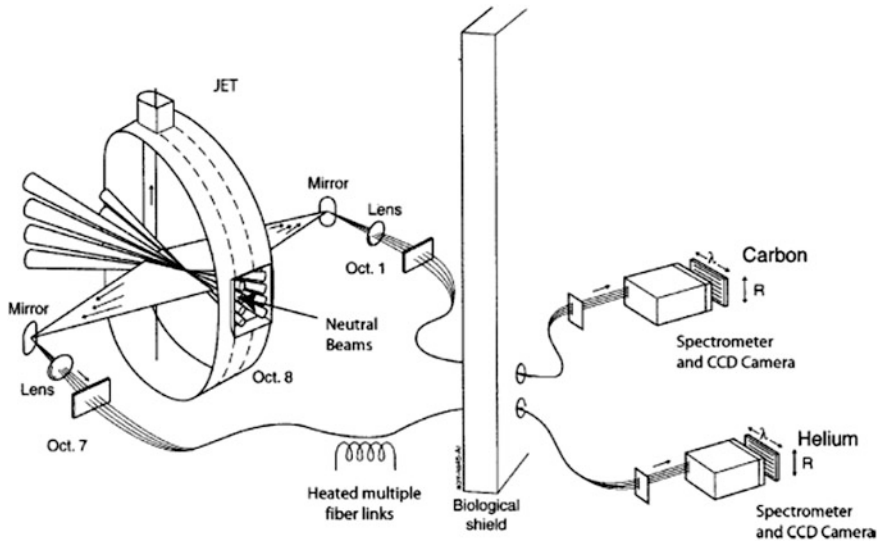
Fig. 11.46 Measurement of helium in JET. The neutral beams neutralize some helium ions in the plasma, and the spectrometer measures the resulting spectral emissions, from which the helium ions' velocities and density may be estimated. The quartz fibers are heated to prevent browning during DT operation. Reprinted with permission from Hillis et al. (2004), A high throughput spectrometer system for helium ash detection on JET, Review of Scientific Instruments 75, 3449, Fig. 1, Copyright 2004 American Institute of Physics

- Radiative recombination is slow enough that the fully-stripped ions exist from the center of the plasma out to the scrape-off layer, so measurements at one wavelength can be extended to all radii.

Fine structure and Zeeman splitting affect the spectral line shape, but these effects are usually small, except in the scrape-off layer. A spectral line shape viewed along a chord may contain multiple components, which can sometimes be distinguished by computer modeling: a broad CXRS peak from the hot plasma core; a narrower peak from the cooler plasma edge; and nearby peaks from a different ion species (Thomas et al. 2008).

Figure 11.47 shows measurements of T_i and rotation velocity from DIII-D.

CXRS measurements of Ti showed that ion thermal conductivity was not consistent with neoclassical theory. Calculations of E_r from CXRS data explained ExB velocity shear stabilization of turbulence and the L Mode to H Mode transition in tokamaks. CXRS data have also illuminated phenomena such as localized modes (ELMs) and plasma rotation. An intense short-pulse neutral beam (100 keV, 50 kA, 1 μs) could be used to achieve enhanced signal/noise ratio for CXRS measurements in ITER (Thomas et al. 2008).

Fig. 11.47 Radial profiles of
C^{+5} ion temperature and line-
of- sight velocity for the
toroidally viewing (x) and
vertically viewing (•) chords.
From a quiescent H-mode
discharge in DIII-D at
1.3 MA plasma current, 2.0 T
toroidal field,
2.3×10^{19} m^{-3} line-
averaged density and
8.8 MW injected neutral
beam power. The neutral
beam injection direction is
opposite to the plasma current
in this shot. The toroidal
rotation speed plotted
includes the correction for the
energy dependence of the
charge exchange cross
section (Thomas et al. 2008).
© 2008 by the American
Nuclear Society, LaGrange
Park, Illinois
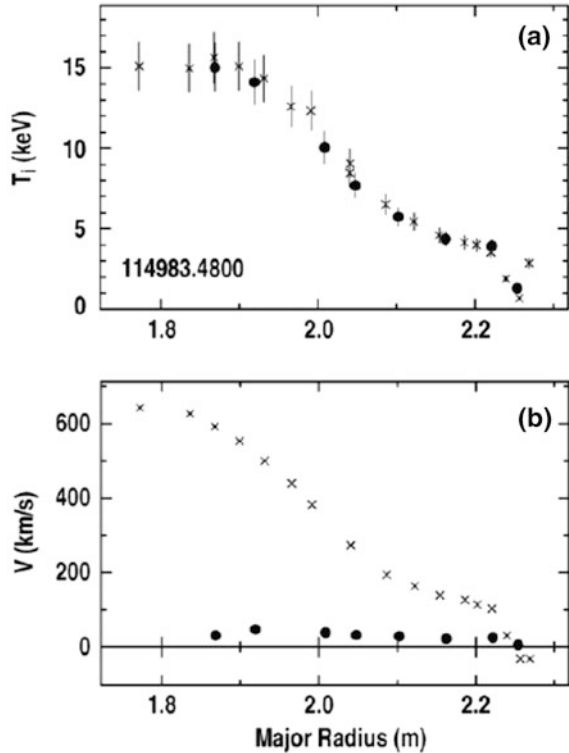
11.7.3 Lithium Beam Spectroscopy

Use of lithium beams for spectroscopy has the following advantages:

- Spectrum is well understood, including hyperfine splitting and Zeeman splitting
- Strong $n = 2$ to $n = 1$ transition (670.8 nm) that can be isolated from other transitions
- Large charge exchange cross sections facilitate CXRS
- Low atomic number, so reduced impurity effects
- Higher velocity at given accelerating voltage than with heavier ions
- Low-power, thin beams can be used for mm spatial resolution
- Acceleration at 3–100 keV is relatively simple with good neutralization efficiency in Na vapor ($\sim$90 % at 25 keV) (Thomas et al. 2008).

However, the large lithium beam attenuation rate in the plasma restricts its use to the edge region. The high emission cross sections facilitate measurement of absolute impurity ion concentrations and profiles in the plasma edge.

The resonance transition is split by the magnetic field into three Zeeman components: π (magnetic quantum number change $\Delta m = 0$), σ ($\Delta m = 1$), and

$-\sigma$ ($\Delta m = -1$). For magnetic fields above ~ 1 T, the σ components are shifted symmetrically from the (unshifted) π component by an amount

$$\Delta\lambda_B = \Delta m(\mu/hc)\lambda_0^2 B \qquad (11.63)$$

where μ = Bohr magneton, h = Planck constant, and c = speed of light in vacuum. For the lithium resonance wavelength, the shift is ~ 0.021 nm/T, roughly an order of magnitude smaller than that typically encountered in MSE systems using hydrogen beams. The direction of the magnetic field can be estimated from the measured polarizations of the spectral components (Thomas et al. 2008).

Interference filters may be used to select the wavelength for density measurements, and spectrometers are better for Doppler measurements requiring narrower bandwidth.

Lithium beam spectroscopy has illuminated the relation between scrape-off layer plasma profiles and central plasma during phenomena like edge localized modes (ELMs), and has shown the different effects of NBI and ECH on the profiles. It is also valuable for studies of fluctuations and turbulence and for measurement of current density profiles (Thomas et al. 2008).

11.7.4 Motional Stark Effect

The Motional Stark Effect is the best method of measuring the magnetic field components and the q profile in plasmas with good spatial and temporal resolution. Neutral beam flow at velocity v across the magnetic field induces an electric field $\mathbf{E} = -\mathbf{v} \times \mathbf{B}$ on the atoms, which via the Stark effect causes linear polarization and spectral line splitting of radiation emitted by beam atoms (collisionally excited by plasma electrons and ions).

Stark splitting of spectral lines from injected beams provides data containing information about local plasma density and magnetic field. The process is illustrated in Fig. 11.48.

The Stark splitting in hydrogen is linear with $\mathbf{E}$ and much stronger than the Zeeman effect at beam energies above a few kilovolts. The π component ($\Delta m = 0$ transition) is linearly polarized parallel to $\mathbf{E}$, and the σ components ($\Delta m = \pm 1$ transitions) are linearly polarized perpendicular to $\mathbf{E}$.

A *polarimeter* is an instrument that can measure the directions and intensities of the linearly polarized π and σ components. From such data the magnetic field components can be calculated. A polarimeter can be calibrated by injecting the beam into a background gas with the magnetic field turned on.

An example of MSE data is shown in Fig. 11.49.

Assuming a statistical population of excited states, one can estimate the local magnetic field with good precision (~ 2 %). In the case of Fig. 11.49, it was found that B = 0.37 T.

- H atom beam is excited and radiates

$$H^0 + e^- \rightarrow H^{0*} \rightarrow H^0 + h\nu$$

- H^0 electron energy levels are split by motional $\mathbf{E} = v_{beam} \times \mathbf{B}$

- Measure spectral lines → v_{beam}, $\mathbf{B}$ field
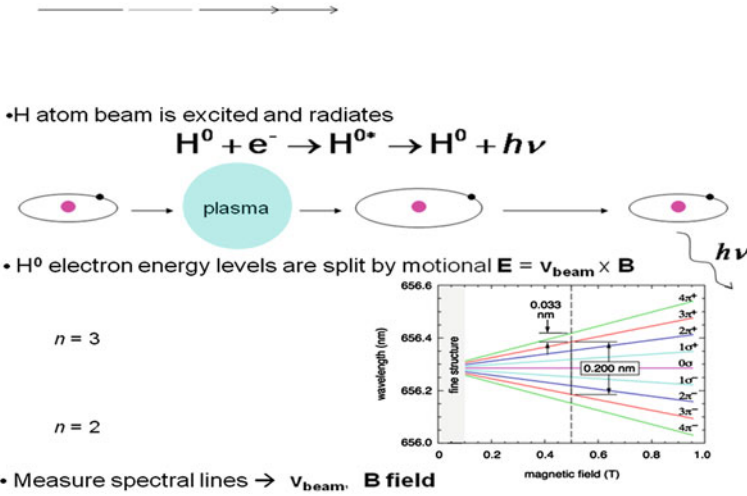
Fig. 11.48 The motional stark effect. The neutral hydrogen atom beam is excited by collision with an electron (or ion) and radiates. The beam motion across the magnetic field creates an electric field that splits the spectral line. The amount of spectral line shift is proportional to B, as shown in the graph. Since the beam speed is known, a measurement of the spectral line shift enables one to calculate B. (The energy level diagram is for illustration only, not a precise energy level diagram.) Courtesy of Darren Craig, University of Wisconsin

Fig. 11.49 Data from Motional Stark Effect. The green components are added to get the total black curve, which is fitted to the red curve. Courtesy of Daniel J. Den Hartog, University of Wisconsin
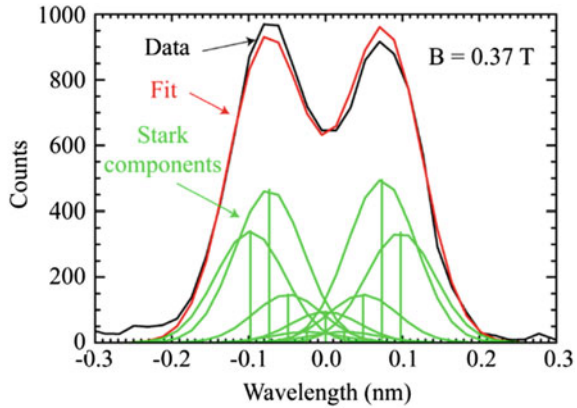
Then the pitch angle γ_m of the magnetic field can be found from

$$\tan \gamma_m = \frac{v_b B_\theta \cos(\alpha + \Omega) + E_r \cos \Omega}{v_b B_\phi \sin \alpha} \tag{11.64}$$

where B_θ poloidal field, B_ϕ toroidal field, $\mathbf{v}_b$ beam velocity, $\mathbf{E}_r$ radial electric field in plasma, α = angle between $\mathbf{v}_b$ and B_ϕ, Ω = angle between the viewing sightline and B_ϕ. If E_r is negligible, then this reduces to $\tan \gamma_m = (B_\theta/B_\phi)$. For a clear

signal the Stark shift should be greater than the spectral line width, which can be reduced by use of a narrow lens. A correction term is needed if the plasma radial electric field is strong (Thomas et al. 2008).

MSE measurements have provided valuable information on evolution of q profiles, radial electric fields, shear stabilization of turbulence, and MHD modes, such as sawteeth. For burning plasma experiments a zigzag path to the detector may be needed to shield against neutrons, and multiple reflections may adversely affect the polarization of the light (Wesson 2011).

11.7.5 Rutherford Scattering

A collision between a neutral beam atom and a plasma ion is called *Rutherford scattering* if the impact parameter (distance from the incident beam line to the nucleus) is very small, so that electron screening can be neglected. The scattered beam energy depends on the plasma ion temperature. The full width at half maximum of the graph of intensity versus scattered beam energy is

$$\Delta E_{FWHM} = 4\theta \left(E_b T_i \ln 2 \; m_p / m_b \right)^{1/2} \tag{11.65}$$

where θ = scattering angle, E_b = beam energy, m_p = plasma ion mass, m_b = beam ion mass (Kislyakov et al. 2008). Most applications use small scattering angles ~ 3–$5°$ to obtain a strong signal and good time resolution. Rutherford scattering measures the temperature of the *hydrogenic* ions, while CXRS usually measures the *carbon* ion temperature.

Figure 11.50 shows some Rutherford scattering data from the University of Wisconsin.

In this case the ion temperature was determined to be 153 ± 17 eV.

Charge exchange recombination spectroscopy (CXRS) yielded better results than Rutherford scattering on TEXTOR. Although Rutherford scattering can be made to work well, it would be difficult to implement on ITER, because the required vertical access would not be feasible, and the beam attenuation would be too strong (Kislyakov et al. 2008).

11.7.6 Heavy Ion Beam Probes

A beam of singly-ionized heavy ions, such as Tl^+, Cs^+, I^+, Rb^+, or K^+ with an energy of 10–100 keV and a current of a few μA may be injected across the magnetic field. Some of the beam ions will be further ionized by collisions in the plasma. The doubly charged ions will have half the Larmor radius of the primary beam ions, hence divergent trajectories. In Fig. 11.51 the Tl^{++} ions produced at point 1 will travel to the electrostatic analyzer and detector.
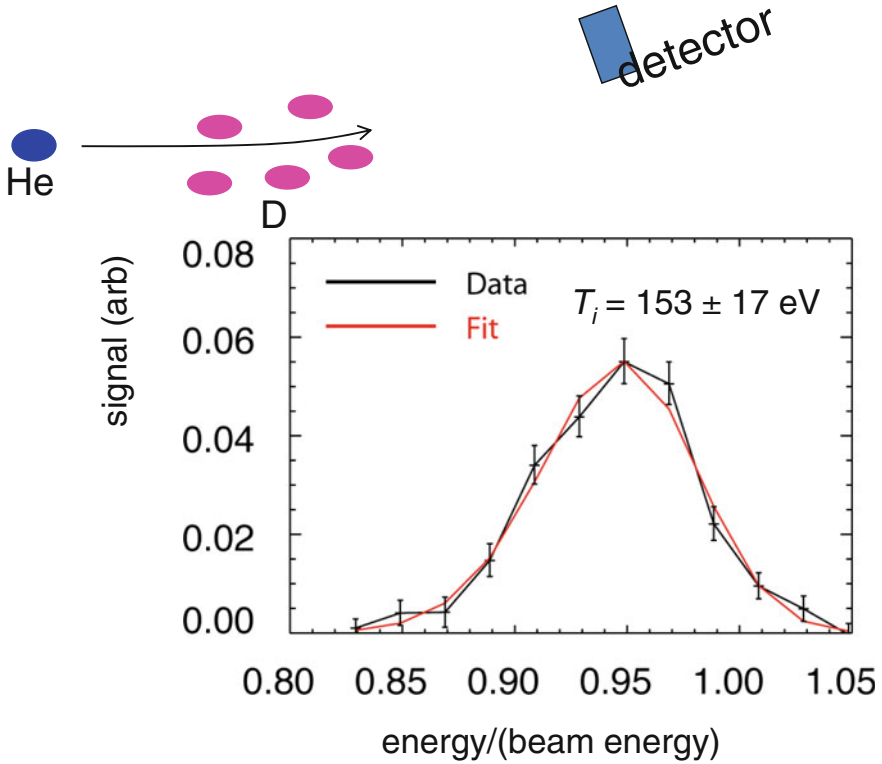
Fig. 11.50 Data from Rutherford scattering of a helium beam at 10° by plasma ions. Courtesy of Gennady Fiksel, University of Wisconsin

The current of such Tl^{++} ions is typically 10–100 nA, The electrostatic analyzer measures the energy of the Tl^{++} ions, from which the plasma potential at point 1 may be calculated.

The primary singly-charged beam ions have energy $W_o = e\phi_o$, where ϕ_o is the accelerating voltage. As they enter the plasma, their kinetic energy is reduced to $e(\phi_o - \phi)$, where ϕ is the plasma potential. (If the plasma potential is negative, the ions gain kinetic energy.) After ionization the doubly-charged ions leaving the plasma gain $2e\phi$ of kinetic energy, so their final kinetic energy at the electrostatic analyzer is

$$W_f = e(\phi_o - \phi) + 2e\phi = e(\phi_o + \phi) \rightarrow \phi = (W_f - W_o)/e \quad (11.66)$$

For example, if the primary beam energy is $W_o = 120$ keV and energy measured by the analyzer is $W_f = 118$ keV, then the plasma potential at the ionization point is $\phi = -2$ kV. The electrostatic analyzer voltage ϕ_A may be feedback-controlled using signals from detectors D_1 and D_2. If the beam only hits D_1, ϕ_A is increased, and if it only strikes D_2, ϕ_A is decreased, until the two detector signals are equal. Then the beam energy is a known function of ϕ_A.
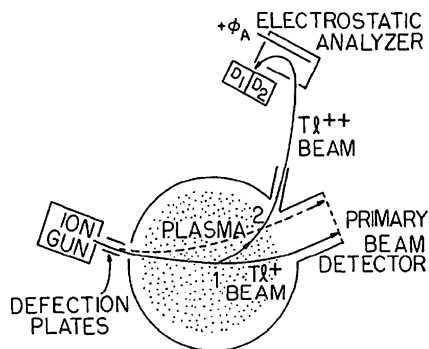
Fig. 11.51 A heavy ion beam probe (HIBP) system. By deflecting the primary beam (*dashed curve*), the interaction region viewed by the analyzer is moved from point 1 to point 2

If the ion gun is tilted (dashed curve in Fig. 11.15) then the Tl^{++} ions produced at point 2 will be the ones entering the analyzer. In this way the variation of plasma potential with known radius can be determined. Plasma potential measurements on TJ-II showed a strong impact of the heating method (ECRH or NBI) on the radial electric fields, which influence the formation of internal transport barriers (Kislyakov et al. 2008).

The poloidal magnetic field will cause the beam trajectories to bend out of the plane of the drawing. From the amount of deflection, the poloidal field can be estimated. The current of the doubly-ionized beam can be related to the electron density and temperature. By using two beams with different masses, the electron density and temperature profiles can both be determined. The HIBP system can also measure fluctuations of density and potential (Kislyakov et al. 2008).

An HIBP system for ITER could probe the outer plasma with beams of several MeV energy, but it would be difficult to find space for the accelerator and ports.

11.7.7 Impurity Injection

Impurities may be introduced by gas puff injection (such as helium), as neutral beams, by pellet injection, by hypervelocity dust beam injection, or by laser ablation of a surface (*laser-blowoff*). These can be used to study

- Impurity transport
- 2D imaging of edge turbulence, including frequency, correlation lengths, and wave number spectra
- Pellet ablation and penetration
- Magnetic field direction (from pellet trajectory) and q profile
- Zeeman splitting of pellet ablation cloud.

11.8 Active Wave Diagnostics

11.8.1 Wave Propagation

An electromagnetic wave, such as a microwave or laser beam, injected into a plasma may result in:

Reflection
Scattering, with possible change of polarization
Transmission
Emission of fluorescence radiation
Modification to a different type of wave

as illustrated in Fig. 11.52

Reflectometry measures reflected waves that are reflected from "cutoff" layers in the plasma, to study the density profile and fluctuations

Interferometry measures the plasma refractive index to determine the plasma density.

Polarimetry measures the polarization of the waves, which is affected by the **Faraday effect** (rotation of the polarization plane) and the **Cotton-Mouton effect** (change in ellipticity of the wave). The Faraday effect can be used to calculate the magnetic field component in the direction of the wave vector k, and the Cotton-Mouton effect can be used to measure the plasma density.

The type of scattering is determined by the Salpeter parameter α:

$$\alpha = (k\lambda_D)^{-1} = \frac{\lambda_0}{4\pi\lambda_D \sin\frac{\theta}{2}} \tag{11.67}$$

$\lambda_D = $ Debye length $= 7400 \, (T_e/n_e)^{1/2} \, (T_e \text{ in eV})$
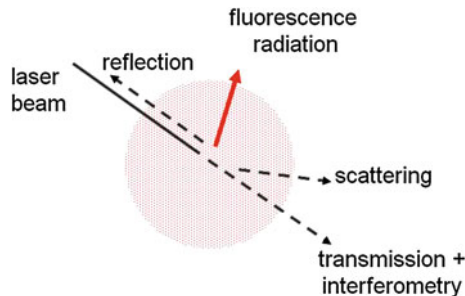
Fig. 11.52 Wave processes in a plasma. Modification to a different type of wave is not shown here, but was described in Sect. 5.7

where k = differential scattering vector, λ_o = incident wavelength, and θ = angle between incident and scattered wave vectors. Four types of interactions are of interest:

If $\alpha \ll 1$, then incoherent scattering of the wave by individual free electrons, called **Thomson scattering** (TS), occurs. The wavelength is so short (and the frequency so fast) that the ions are not able to respond. The scattered wavelengths depend on the Doppler shifts from individual electron velocities, so the scattered wave spectrum is Doppler broadened, from which T_e is determined. If precise calibration is done, n_e can be estimated from the scattered wave intensity.

If $\alpha \geq 1$ then the wavelength is long enough (and the frequency low enough) that ions can respond. Electrons effectively cling to the moving ions, screening them from the incident electric field, and the electron response to the wave is synchronized with the ion velocities. The scattered wave Doppler shift then provides information about the ion velocity distribution, including T_i. This is called coherent scattering (or ion collective Thomson scattering).

If $\alpha \gg 1$, the scattered power is proportional to the square of the electron density fluctuation level, so it can be used to measure the electron density fluctuation spectrum. This situation is called **collective scattering** (Donné et al. 2008).

Fluorescence is the emission of light by a substance that has absorbed electromagnetic radiation. If the emitted radiation has the same wavelength as the absorbed radiation, it is called *resonance* fluorescence. In plasma diagnostics a tunable laser can excite a chosen atomic energy level, and a spectrometer or filtered detector can then measure the **laser induced fluorescence** (**LIF**) radiation.

These phenomena will be discussed further after an introduction to the equations that are used for microwave and infrared wave propagation.

11.8.2 Wave Propagation Equations

A plasma wave can be represented in terms of its frequency ω (radian/s) and its wave propagation vector **k**, which points in the direction of wave propagation and has a magnitude k = $2\pi/\lambda$. By definition the refractive index N $\equiv$ kc/ω, where c = speed of light in vacuum. A **dispersion relation** between ω and k is found by solving Maxwell's equations for **E** and **B** together with the plasma particle and momentum conservation equations. Assuming that the plasma ions are cold, the resulting Appleton-Hartree equation is

$$N^2 = 1 - \frac{X[1-X]}{1 - X - \frac{1}{2}Y^2\sin^2\theta \pm \sqrt{(\frac{1}{2}(Y)^2\sin^2\theta)^2 + [1-X]^2 Y^2\cos^2\theta}} \tag{11.68}$$

where
$$X = (\omega_P/\omega)^2$$
$$Y = \omega_{ce}/\omega$$

ω =   frequency of the propagating wave

θ =   angle between the wave vector **k** and the magnetic field **B**.

$$\omega_{pe} = (ne^2/m\varepsilon_o)^{1/2} = \text{electron plasma frequency(radian/s)} \qquad (11.69)$$

$$\omega_{ce} = eB/\gamma m = \text{electron cyclotron frequency(radian/s)} \qquad (11.70)$$

n   =   electron density,

e   =   electronic charge,

m   =   electron mass,

ε_o =   permittivity of free space

v   =   electron velocity, and

$\gamma\ (1 - v^2/c^2)^{-1/2}$

Donné et al. (2008).

For propagation along the magnetic field $\theta = 0$, and this equation reduces to

$$N^2 = 1 - X/(1 \pm Y). \qquad (11.71)$$

where the plus sign is a left hand circularly polarized wave (L wave, rotating counterclockwise) and the minus sign is a right hand circularly polarized wave (R wave, rotating clockwise). At high frequencies (small X and Y) the denominator may be expanded in a Taylor series and the higher order terms in $Y \left(Y^2, Y^3, \ldots\right)$ may be dropped. The result is

$$N = kc/\omega \approx 1 - \tfrac{1}{2}(X \pm XY) \qquad (11.72)$$

the R wave has a lower kc/ω than the L wave, so its propagation velocity (phase velocity) ω/k is higher.

The phase angle of the wave ϕ changes by an amount $\Delta\phi$ going a distance L through a plasma:

$$\Delta\phi = 2\pi \int_0^L dx/\lambda = \int_0^L kdx \qquad (11.73)$$

The sum of the R and L waves is a plane polarized wave whose phase angle is the average of the R and L phase angles.

$$
\begin{aligned}
\Delta\phi &= 1/2[\Delta\phi_R + \Delta\phi_L] = 1/2 \int dx\ (k_R + k_L) \\
&= (\omega/c) \int dx\{\,[1 - 1/2(X - XY)] - [1 - 1/2(X + XY)]\,\} \\
&\quad \omega/c \int dx\ XY \quad (X \text{ and } Y \ll 1) \\
&= (e^3/\varepsilon_o m^2 c\omega^2) \int dx\ nB_k
\end{aligned}
\qquad (11.74)
$$

where the limits of integration are from 0 to L, and B_k is the component of the magnetic field in the direction of propagation.. Thus, the phase angle of the plane polarized wave rotates by an amount proportional to nB_k, called **Faraday rotation**, which can be measured by polarimetry.

The following subsections will discuss polarimetry, reflectometry, interferometry, Thomson scattering, coherent scattering, collective scattering, and laser induced fluorescence.

11.8.3 Polarimetry

The goal is to measure $\Delta\phi$ at along multiple chords using polarimetry and n by another means (or with second polarimeter at a different wavelength), then to use these data to calculate B_k. Polarimetry is usually done at far infrared (FIR) wavelengths 100–500 μm (Donné et al. 2008).

Figure 11.53 shows a simplified sketch of one type of polarimeter.

The laser beam passes through a polarizing filter P1, then a ferrite modulator, actuated by a magnet coil driven by $\omega_m \sim 10$ kHz. The modulator rotates the plane of polarization $\theta_m(t)$ back and forth. After the beam passes through the plasma, the angle of rotation is $\theta_m + \theta_p$. The beam passes through another polarizing filter P2 into the detector. The detector signal is amplified by a lock-in amplifier tuned to ω_m, and the amplifier output signal voltage is

$$\phi = \phi_0\sin(2\theta_p) \simeq 2\phi_0\theta_p \text{ (for small } \theta_p), \qquad (11.75)$$

where ϕ_o is a constant determined by calibration, and θ_p is produced by the plasma. Thus, the amplifier signal voltage is dependent on the rotation angle θ_p.

If the plasma is poloidally symmetric, then measurements along several chords can be inverted by a computer to estimate $B_k(r)$.

The *Verdet constant* is an optical property of materials (with units of radians/T-m) that describes the strength of the Faraday effect in a particular material. Materials with a low Verdet constant, such as diamond, are preferred for windows, because they cause less Faraday rotation in the window.
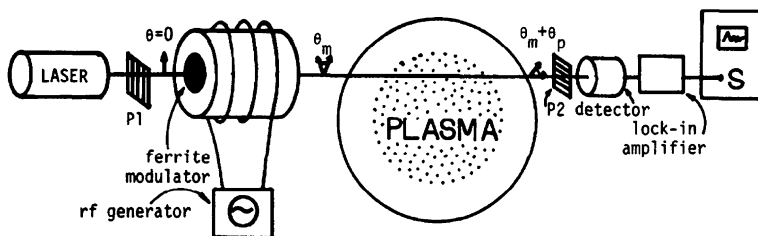
Fig. 11.53 Measurement of Faraday rotation with an FIR laser (Instead of using an oscilloscope, the data is digitized and stored in a computer)

11.8.4 Reflectometry

A police radar shoots radio waves at cars, and the Doppler frequency shift of the reflected signal tells how fast the car is going. In plasmas the wave "cutoff" layers reflect incoming wave pulses. The time delay of the reflected wave pulse tells the location of the cutoff; and plasma motion, such as MHD instabilities or turbulence, shifts the wave frequency.

For propagation across the magnetic field $\theta = \pi/2$, and Eq. (11.68) has two solutions:

$$N^2 = 1 - X \quad \text{"ordinary mode (O − Mode)"} \tag{11.76}$$

$$N^2 = 1 - X(1 - X)/(1 - X - Y^2) \quad \text{"extraordinary mode (X − Mode)"} \tag{11.77}$$

Waves are absorbed at **resonances** (where $N \rightarrow \infty$) and reflected at **cutoffs** (where $N \rightarrow 0$). Resonances are used for plasma heating (Sect. 5.7). Solving these equations for ω, the O-mode and X-mode **cutoff** frequencies are found to be

$$O - Mode \quad \omega_o = \omega_{pe} \quad \text{rad/s} \tag{11.78}$$

$$X - Mode \quad \omega_x = (\omega_{ce}^2 + 4\omega_{pe}^2)^{1/2}/2 \pm \omega_{ce}/2 \quad \text{rad/s} \tag{11.79}$$

At temperatures above 1 keV thermal and relativistic effects may alter these equations. These cutoffs were illustrated in Figs. 5.32 and 5.33. For example, if B = 1 T and $n_e = 10^{19}$ m^{-3}, then $f_{ce} = 28.0$ GHz, $f_{pe} = 28.4$ GHz, $f_o = 28.4$ GHz, and $f_x = 45.7$ GHz.

O-Mode reflection occurs where $n \geq n_c$ (the **cutoff density**)

$$n_c = m_e \varepsilon_o \omega^2/e^2 = 0.0124 \, f^2 = 1.11 \times 10^{-15}/\lambda_o^2 \quad (m^{-3}), \tag{11.80}$$

where f is the wave frequency (Hz) and λ_o is the vacuum wavelength (m). For example, if f = 10 GHz, then $n_c = 1.24 \times 10^{18}$ m^{-3}. Such cutoffs also affect plasma heating (Sect. 5.7). A 10-GHz O-mode wave could not penetrate inside the plasma layer where $n = 1.24 \times 10^{18}$ m^{-3}.

Reflectometry is usually carried out using probing beams with frequencies between 5 GHz ($\lambda = 6$ cm) and 150 GHz ($\lambda = 2$ mm) (Luhmann et al. 2008).

The incident waves may also be *absorbed* at the cyclotron resonances (integer multiples of ω_{ce}) and at the upper and lower hybrid resonances (Eqs. 5.34 and 5.35).

The phase shift of the reflected wave can be measured using a microwave interferometer (as described later). From the time variation of the phase shift, density fluctuations near the critical layer (where $n = n_c$) can be determined. Such information is useful for study of microinstabilities. As an example, a 94 GHz microwave backscatter (180°) has been used to probe short-wavelength (large k) turbulence at wave numbers k = 30–40 cm^{-1} with k resolution about ± 1 cm^{-1} (Rhodes et al. 2004).

If the plasma column is moving, the reflected microwaves will be Doppler shifted in frequency with $\Delta v/v = v_c/c$, where v_c is the velocity of the critical layer towards the microwave receiver/source antenna, and c is the speed of light. Using several such reflection probes, the motions of the plasma can be detected, facilitating feedback control of the plasma position.

The "thickness of the reflecting layer" for the O-Mode

$$\Delta r = 1.5 \times 10^5 \left[\left(\frac{dn_e}{dr} \right)_{r_c} \right]^{-1/3} \text{m} \tag{11.81}$$

is a conservative limit to the spatial resolution of O-mode reflectometry. For example, if n_e drops linearly by 10^{19} m^{-3} over a distance 0.3 m, then $\Delta r \leq 0.05$ m.

The phase differences or round-trip times of the reflected pulses at many frequencies can be used to map the radial density profile. The measurement can be made using frequency modulation, amplitude modulation, pulse radar, or ultrashort pulses at a spread of frequencies. Measurements of the edge density are difficult, due to the low frequency and long wavelength, but the estimated profiles are usually consistent with those from other diagnostics. Instruments with multiple spatial channels can provide 2D images of the plasma. Reflectometry is also widely used to study MHD modes, internal transport barriers, plasma fluctuations, and plasma rotation (Park et al. 2004).

Figure 11.54 shows reflectometer data of the density profile measured in ASDEX-U.

This reflectometer uses several frequency bands with a scanning time of 20 μs to cover a wide range of densities, up to 8×10^{19} m^{-3}. These data show how the density profile near the separatrix changes from before an ELM (150 μs) to after the ELM (later curves).

Fig. 11.54 ASDEX-U reflectometer data (Nunes et al. (2005), Fig. 1)
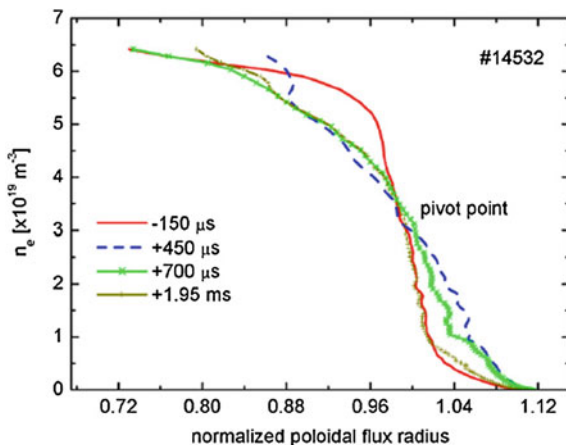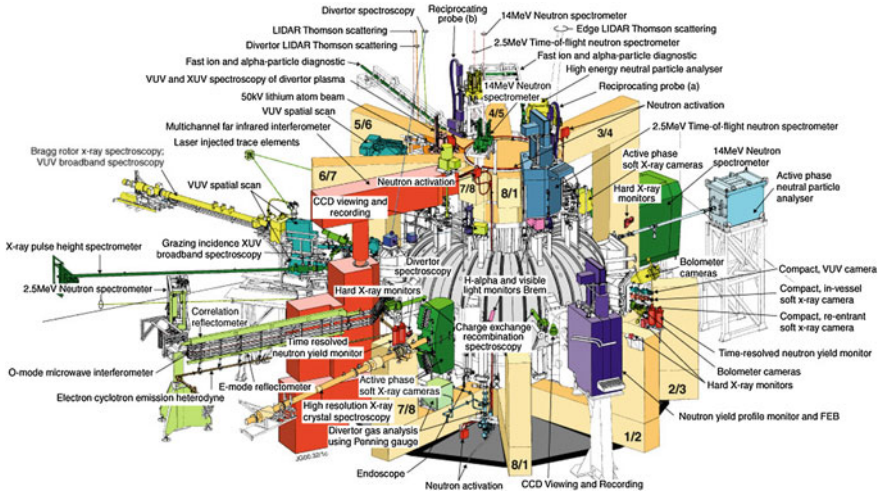
Fig. 11.55 Locations of some JET diagnostic systems (Hacquin 2008)

With its metallic antennas and remotely located windows reflectometry could function well in a burning plasma experiment like ITER, but wave access to the plasma core may be difficult, because of its high T_e and relatively flat density profiles. A reflectometer on the low field side (outside of the torus) will use the O-mode cutoff (15–155 GHz) to measure the densities between 0.03×10^{20} m^{-2} and 3×10^{20} m^{-3}, and the X-mode cutoff (76–220 GHz) to study plasma in the SOL. A reflectometer on the high-field side (inside of the torus) will use the X-mode and O-mode to study the core plasma profile and inner density gradient, respectively (Luhmann et al. 2008).

Large machines like JET, JT60-U, and LHD have many complex diagnostic systems, such as the JET diagnostics illustrated in Fig. 11.55.

These large machines, together with many smaller experiments, are developing the diagnostics that will be needed for ITER. FIR polarimeters can also use the Cotton-Mouton effect to measure plasma density (Donné et al. 2008).

11.8.5 Interferometers

For propagation across the magnetic field ($\mathbf{k} \perp \mathbf{B}$) the refractive index of the X mode varies with the magnetic field, so it is preferable to use the O-mode, for which:

$$k = (\omega/c)(1 - \omega_p^2/\omega^2)^{1/2} = (\omega/c)(1 - n/n_c)^{1/2} \tag{11.82}$$

The change in phase when the plasma is turned on is

$$\Delta\phi = \Delta\phi(\text{plasma}) - \Delta\phi(\text{vacuum})$$
$$= (\omega/c) \int dx \left[(1 - n/n_c)^{1/2} - 1 \right] \quad (11.83)$$
$$\approx - (\omega/2cn_c) \int dx\, n \quad \text{if } (n/n_c) \ll 1.$$

From measurements of $\Delta\phi$ viewing along many chords through the plasma, a computer can invert the data to calculate $n(r)$. If the plasma is poloidally symmetric, the result is

$$n(r) = -(2cn_c/\pi\omega) \int_r^a dh \left(h^2 - r^2\right)^{-\frac{1}{2}} (d\Delta\phi/dh), \quad (11.84)$$

where h = distance from the plasma center to each chord. This method is called **Abel inversion**. If the plasma density is *uniform*, then

$$n = 2cn_c\, \Delta\phi/\omega\ell = 1.18 \times 10^6 f\, \Delta\phi/\ell = 3.55 \times 10^{14}\, \Delta\phi/\lambda_o\ell \,\,(\text{m}^{-3}) \quad (11.85)$$

where $f = \omega/2\pi$ (Hz) and λ_o is the vacuum wavelength. The microwave or laser beam frequency should be chosen high enough that $(n/n_c) < 1$, yet low enough that (n/n_c) is large enough to make $\Delta\phi$ easily measureable. An interferometer can measure $\Delta\phi$.

Figure 11.56 shows the components of a **heterodyne Mach–Zehnder** interferometer system.

The primary signal at ω is combined with the auxiliary signal at $(\omega + \Delta\omega)$ in the detector, so the detector signal is at the much lower beat frequency $\Delta\omega$, with a phase shift $\Delta\phi$ caused by the plasma. With a two-laser system, such as a CO_2-pumped far-infrared laser system with two slightly detuned cavities, beat frequencies in the MHz range can be generated (Donné et al. 2008).

If $\Delta\phi$ is small (a fraction of a radian), then the variation of the detector signal strength I/I_{max} will be small. On the other hand, if $\Delta\phi$ is several cycles (multiples of 2π), then I/I_{max} will pass through several maxima and minima (called fringes), as illustrated in Fig. 11.57.

Fig. 11.56 A single-channel heterodyne Mach-Zehnder interferometer. *Beamsplitters* (partially silvered mirrors) transmit part of the beam and reflect part of it
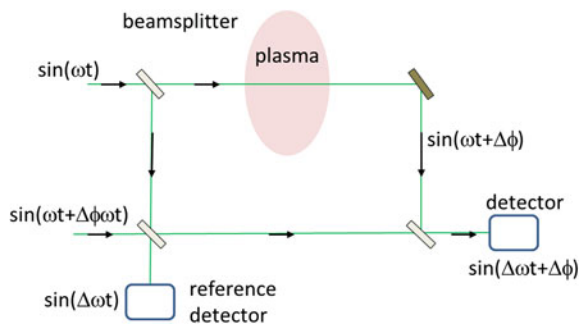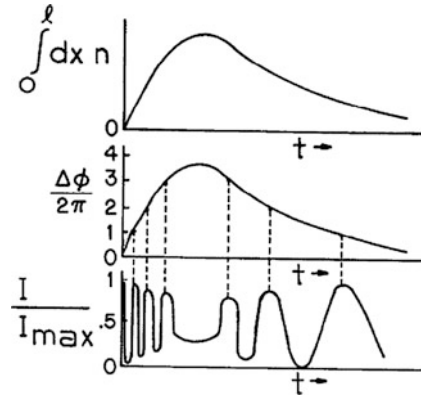
Fig. 11.57 Time variation of plasma density line integral, microwave phase shift, and interferometer signal. Each "fringe" represents a phase change of 2π
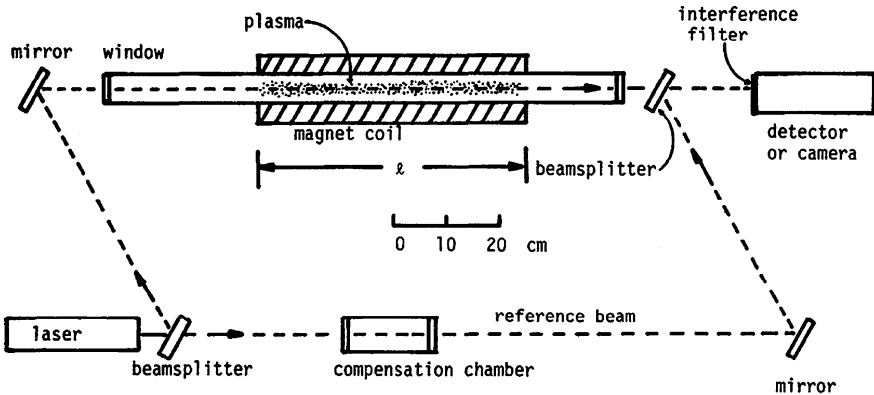
Fig. 11.58 Schematic diagram of a laser Mach-Zehnder interferometer for plasma diagnostics

Microwave interferometers are relatively sensitive to low plasma densities and provide good time resolution.

A laser Mach–Zehnder interferometer is illustrated in Fig. 11.58.

The laser beam is divided into two paths by a partially-silvered mirror (*beamsplitter*). One path goes through the plasma, and the reference path goes through a compensation chamber, to make the optical path lengths nearly equal. The beams are recombined by another beamsplitter and then impinge on the detector or camera. An interference filter may be used to screen out unwanted light. The optics are aligned so that the initial pattern at the camera is straight, parallel fringes (black and white stripes, representing places where $I/I_{max} = 0$ or 1). When the plasma is produced, the phase shifts created by the plasma density produce circular fringes, as shown in Fig. 11.59.

Fig. 11.59 Fringe pattern of a theta pinch plasma, taken with a Mach-Zehnder interferometer (courtesy of Los Alamos National Laboratory)

Counting inwards from the outside, each fringe represents a phase difference of 2π radians, with a corresponding density increase. For high density and relatively small plasmas such as theta pinches, Z pinches, and magnetized target fusion, the most suitable probing radiation has wavelengths in the visible and near infrared ranges. Mach–Zehnder interferometers are used to study these plasmas.

For lower density tokamak and stellarator plasmas, interferometers using **far-infrared lasers** of high-frequency microwaves ($10~\mu m \leq \lambda_o \leq 2000~\mu m$) are used. They are sensitive to electron density changes and their wavelengths are still short enough to give excellent spatial resolution. Electrical detectors provide a signal that can be digitized and used in computer systems. Some common types are (Wesson 2011):

InSb detectors	~ 4 K (liquid He)	High sensitivity
Schottky diodes	Room temperature	High frequency response
Pyroelectric crystals	Room temperature	Simple, inexpensive

Some FIR data from the National Institute for Fusion Science (NIFS) in Japan are shown in Fig. 11.60.

This interferometer, mounted on a large vibration-proof frame, has 13 channels, a 50 mm beam width, 1 μs time resolution, and 1/100 fringe phase resolution.

Fig. 11.60 Electron density profile versus time from the Large Helical Device FIR interferometer showing the density jump following cryogenic hydrogen pellet injection. Courtesy of Prof. K. K. Kawahata, NIFS
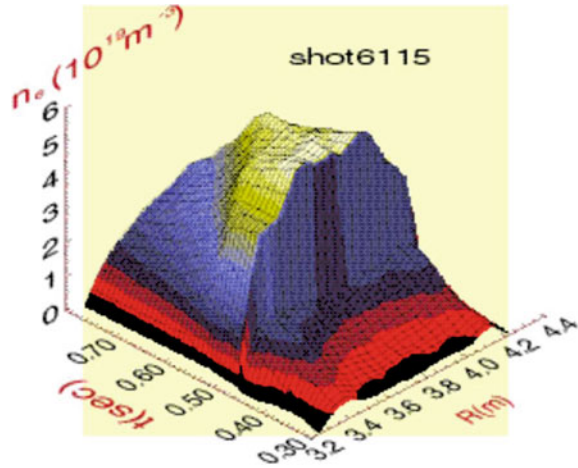
11.8.6 Thomson Scattering

When a charged particle is accelerated, it radiates electromagnetic waves. If the acceleration is caused by an incident electromagnetic wave, the radiation process is called Compton scattering at high energies (x-rays and gamma rays) and Thomson scattering at low energies (visible and infrared). The theory and practice of Thomson scattering are explained by Sheffield et al. (2011).

For **incoherent** Thomson scattering the spectrum will generally have a Gaussian shape with a $1/e$ half-width

$$\Delta\lambda_e = (2\lambda_o/c)(2k_B T_e/m_e)^{1/2}\sin(\theta/2) \tag{11.86}$$

where k_B Boltzmann constant, m_e electron mass, and θ scattering angle.

For a ruby laser at $\lambda_o = 694.3$ nm and perpendicular scattering this becomes

$$\Delta\lambda_e(\text{nm}) = 1.94\, T_e^{1/2} \tag{11.87}$$

where T_e is in eV (Donné et al. 2008). At $T_e = 1$ keV, this yields $\Delta\lambda_e = 61$ nm.

The scattered power spectra are shown in Fig. 11.61 as functions of scattering wavelength, for various T_e.

At high temperatures relativistic corrections are necessary, and the peak shifts towards shorter wavelengths. The plasma density can be calculated from the ratio of scattered power P_s (proportional to the areas under the curves of the Figure) to incident power P_o. Sometimes the scattered spectra differ from the anticipated shapes, which may be due to anisotropy in the electron velocity distribution function.

The required beam power and pulse duration are determined by the need for a satisfactory signal-to-noise ratio (SNR). There will be spurious signals (noise) from the detectors and electronic circuits; from plasma radiation; and from laser
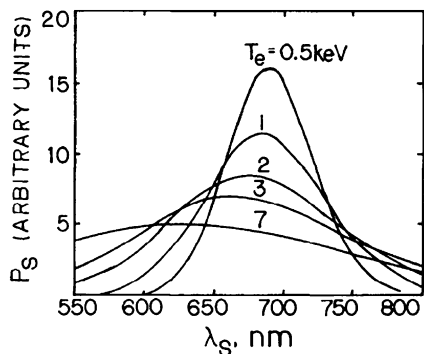
Fig. 11.61 Spectra of Thomson scattered ruby laser light ($\lambda_o = 694.3$ nm) at $\theta_o = 90^o$ for various electron temperatures (based on Equipe TFR 1978, Fig. 41)

beam photons multiply-scattered by the walls, baffles, etc. (parasitic radiation). Stray light can be minimized by

- Tilting the windows under the Brewster angle
- Locating windows far from the plasma
- Using baffles in entrance and exit ducts
- Mounting a non-reflecting viewing dump on the vessel wall opposite to the collection optics, such as carbon tiles.

If the scattered light must be transmitted over long distances ($\gtrsim 10$ m), then fiber optics are preferred over conventional mirrors and lenses.

Since P_s/P_o is typically $< 10^{-14}$, and there is much stray light (noise), laser beam powers $\gtrsim 100$ MW are usually needed, except for continuous wave (cw) lasers, which can be modulated and synchronously detected. A typical ruby laser used in Thomson scattering has a beam energy ~ 10 J, pulse length ~ 20 ns, $P_o \sim 2$ GW, wavelength spread $\Delta\lambda_o \sim 10^{-3}$ nm, and beam divergence ~ 1 mrad. A small divergence is desired to be able to focus the beam to a small diameter in the plasma region. If the incident beam is not monochromatic (if $\Delta\lambda_o$ is not $\ll \Delta\lambda_s$), then interpretation of the scattered spectra is more difficult. Pulsed lasers can be used to observe the time variation of plasma profiles. For example, Nd:YAG lasers (1,064 nm) can provide 1 Joule, 15 ns pulses at 20–50 Hz.

Wavelength discrimination can be done by interference filters or by grating spectrometers, which have better wavelength resolution.

The magnitude of n_e requires a calibration, which can be done by cross calibration using the plasma and another diagnostic, such as an interferometer. The relative spectral response is calibrated using a tungsten filament lamp with quantified emission versus wavelength, and the absolute sensitivity of the system can be calibrated by Rayleigh or Raman scattering with the vessel containing nitrogen or hydrogen at 0.1–10 kPa (Donné et al. 2008).

Three main TS systems are in use nowadays:

- Periodic photodiode systems using fast pulsed lasers (usually Nd:YAG) with a separate filter spectrometer for each spatial point
- Single or multipulse TVTS systems with high spatial resolution, high-power ruby lasers, and intensified CCD or CMOS cameras. (The TEXTOR system has 120 spatial points and can attain density and temperature precisions ~ 3 and 6 %, respectively.)
- **LI**ght **D**etection **A**nd **R**anging (LIDAR) systems view backscattered light pulses (0.3 ns, 90 mm long) and measure their time-of-flight to obtain spatial resolution along the laser chord (T_e accuracy is 8 % at n = 5×10^{19} m^{-3}). LIDAR will be used on ITER, because it requires only one port, and the laser beam is automatically aligned with the detector. The first optical mirror is deeply recessed into the port plug to minimize degradation from erosion and deposition. A possibility under consideration is to use two different lasers to give high spatial/low temporal resolution measurements and high temporal/low spatial resolution measurements. For example, one laser (t = 3 ps) could provide ~ 7 cm resolution (a/30) at a moderate time rate (10 Hz), while the second laser (t = 1 ns) would provide faster measurement rate (100 Hz) with a more coarse spatial resolution (20 cm).

The Tore–Supra Thomson Nd:YAG scattering equipment is illustrated in Fig. 11.62.

Figure 11.63 shows temperature profiles measured with this system.
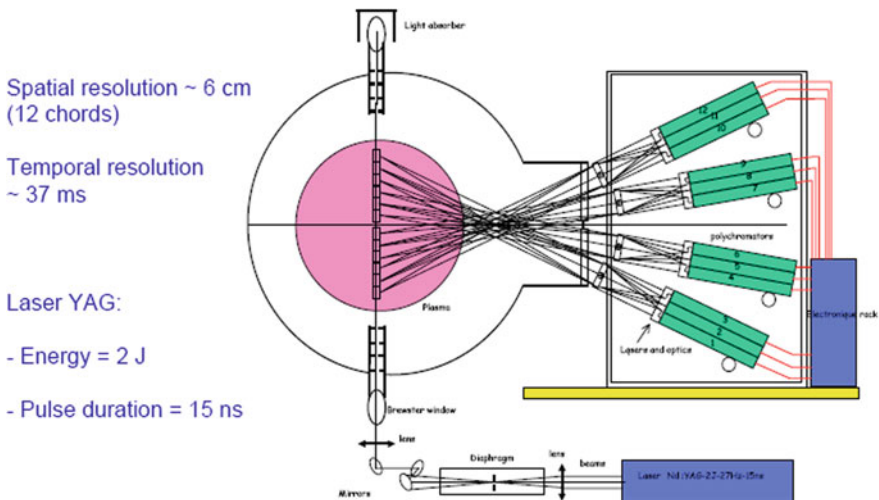
Fig. 11.62 The Tore Supra Thomson scattering system. From S. Hacquin, FZK Summer School, (2008)

Fig. 11.63 Electron temperature profiles in Tore Supra measured by Thomson scattering in an ohmically heated plasma (*bottom curve*) and with wave heating (*top curve*) (Hacquin 2008)
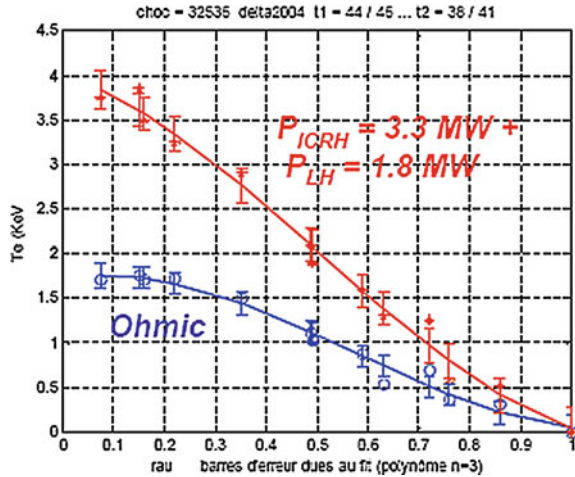
By use of multiple-pulse or high-power continuous-wave lasers, a Thomson scattering system can provide density and temperature profiles at several times during the discharge. The theory and practice of Thomson scattering are described by Sheffield et al. (2011).

The signal-to-noise ratio of Thomson scattering can be improved by having the laser beam pass through the plasma twice or multiple times, reflecting back along its original path by a mirror on the other side of the plasma. This is especially effective when a "phase conjugate mirror" is used, because it refocuses the beam returning through the plasma and minimizes the stray light that would otherwise occur from the beam spreading (Hatae et al. 2004).

Coherent scattering measurements can be made at small scattering angles using powerful FIR lasers, and they yield estimates of T_i and n_e. The spectrum has a wide electron peak with width kv_{Te} and a narrow ion peak with width kv_{Ti} where the thermal velocities are $v_{Te} \approx (2k_BT_e/m)^{1/2}$, $v_{Ti} \approx (2k_BT_i/M)^{1/2}$ M is the ion mass, and the temperatures k_BT_e and k_BT_i are in Joules.

The emphasis of these diagnostics is put on the measurement of the velocity distribution of confined alpha particles and fast ions. Two types of systems are in use:

- High-power pulsed (~ 20 Hz) CO_2 lasers ($\lambda \sim 10$ μm). The wavelength is far from background light and the laser technology is well developed, but the scattering angle must be very small ($\sim 0.5°$).
- High-power gyrotrons ($\lambda \sim$ mm) which allow measurements to be made a much larger scattering angles.

Forward scattering of **far infrared (FIR) waves** at f $\sim$ 288 GHz and small scattering angles ($\pm 1°$) can study long-wavelength turbulence at wave numbers k = 0–2 cm^{-1}. Forward scattering at 8–15° probes medium-wavelength turbulence at k = 8–15 cm^{-1} (Rhodes et al. 2004). Figure 11.64 shows some turbulence data from FIR scattering and microwave reflectometry.
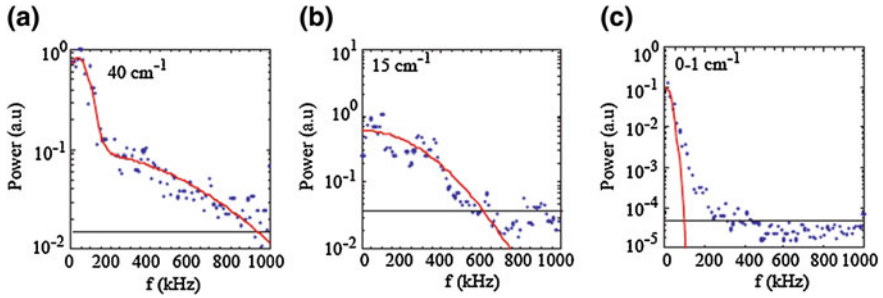
Fig. 11.64 Turbulence data from microwave reflectometry (**a**) and from FIR scattering (**b** and **c**) on the DIII-D tokamak. From Rhodes et al. (2004) Comparison of Broad Spectrum Turbulence Measurements and Gyrokinetic Code Predictions on the DIII-D Tokamak, Fig. 3, International Atomic Energy Agency, 20th IAEA Proceedings of an International Conference Held in Vilamoura, Portugal, 1–6 Nov 2004, IAEA-CN-116/P6-23. Copyright IAEA, Vienna, 2005

Such data can be compared with predications of various turbulence theories, which are important for calculating heat transport by electrons, a major topic in plasma physics. Many articles on reflectometry, ECE, interferometry, polarimetry, and Thomson scattering are found in the book by Stott et al. (1998), pp. 97–260.

11.8.7 Laser Induced Fluorescence

A tunable laser can excite a chosen atomic energy level, and a spectrometer or filtered detector can then measure the fluorescence radiation. LIF has good spatial resolution, it does not perturb the plasma, and it is based on well-known phenomena. However, it requires bound electrons, which are scarce in hot, dense plasmas, so it is most useful in edge plasmas or with a neutral beam. A collisional-radiative computer model can calculate the level populations, including effects of collisional excitation and de-excitation, and photon emission and absorption, such as by laser excitation. If the collision frequencies are high enough to populate the energy levels of interest, LIF cannot be used, because it is not possible to achieve a significant population change by laser excitation. Tunable lasers are available in the visible range, but not in the vacuum ultraviolet (Thomas et al. 2008).

The scanning single-frequency tunable dye laser allowed selection of the wavelength corresponding to a particular atom velocity, so a spectrometer could be avoided. High-power diode lasers are available now at some wavelengths. LIF measurements from the hydrogen ground state, such as Lyman-α line at 121.6 nm (VUV), are difficult, but can be done by two-photon absorption (low cross sections) or by a frequency-tripled dye laser. (A 4 MW laser pulse at 365 nm is needed to produce a 200 W pulse at 121.6 nm) (Thomas et al. 2008).

Fig. 11.65 Schematic diagram of the lithium beam Zeeman effect measurement of magnetic field direction. A dye laser excites the desired lithium energy level, causing fluorescence, which is measured by the collection optics at several positions. From the amount of Zeeman splitting, the local magnetic field can be determined (Hutchinson 2002, Fig. 8.8)
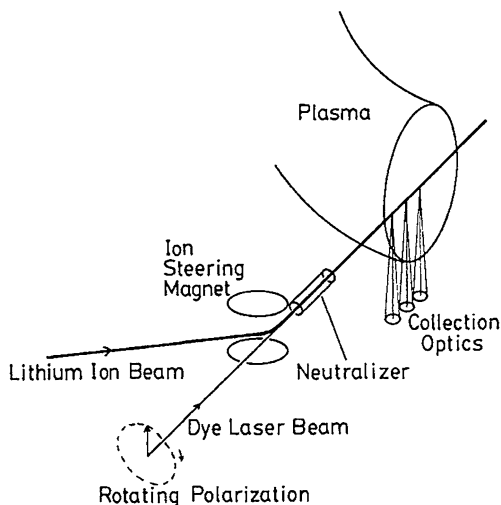
In spite of the difficulties, LIF can be used to study:

- Neutral hydrogen density in edge plasmas
- Edge plasma fluctuations and turbulence
- Magnetic field from Zeeman splitting of an injected neutral atom beam, such as Li or Ba, Fig. 11.65 (but such beams cannot penetrate into the core of hot plasmas) (See also Sect. 11.7.3)
- Ion velocity distribution function
- Electric field from excitation of "forbidden" transitions, which occur only in strong electric fields
- E x B ion flow and velocity-space transport coefficients
- n_e and T_e (indirectly, using two different LIF diagnostics)
- Plasma sheath potential and velocity profiles (Thomas 2008).

11.9 ITER Diagnostics

ITER diagnostics serve to protect the machine, to control the plasma, and to evaluate plasma behavior.

Some measurements for **machine protection** include

- Gap between plasma edge and first wall
- Wall temperature
- Line-averaged plasma density
- Disruption precursors (such as "locked modes")
- Divertor surface temperature
- Fusion power
- Halo currents (Current flowing in the scrape-off layer, which can cause local wall overheating)

- Edge localized modes (ELMs)

  Additional measurements for **plasma control** include

- Plasma shape and position
- Plasma current and loop voltage
- Vertical speed
- MHD modes

  Additional measurements for **plasma evaluation** include

- $n_e(r)$, $n_{He}(r)$
- $T_e(r)$, $T_i(0)$
- P_{rad}
- P_{fus}
- n_T/n_D
- neoclassical tearing modes (NTMs)
- toroidal and poloidal rotation velocities
- divertor ionization front location
- $q(r)$ for control of MHD modes and internal transport barrier.

Over 45 plasma parameters will be measured, Table 11.4. The main ITER plasma diagnostics systems are listed in Table 11.5.

Table 11.4 Some plasma parameters to be measured in ITER (Donné et al. 2007) (This list is not comprehensive. For example, some additional parameters include erosion, dust, and edge turbulence)

Plasma current	First wall image and temperature	Fuel radio in edge plasma
Plasma shape and position	Chamber gas pressure and composition	Neutron fluence
Loop voltage	Duct gas pressure and composition	Impurity and DT influx in the divertor
Plasma energy	In-vessel inspection	Divertor plasma parameters
Radiated power	Halo currents	Radiation profile
Line-averaged electron density	Toroidal magnetic field	Divertor heat load profile
Neutron flux and emissivity	Electron temperature profile	Divertor helium density
Locked modes	Electron density profile	Divertor fuel ratio
Low (m, n) MHD modes, sawteeth, disruption precursors	Current profile	Divertor electron parameters
Plasma rotation	Zeff profile	Divertor ion temperature
Fuel ratio in plasma	High-frequency microinstabilities	Divertor plasma flow
Impurity species	Ion temperature profile	n_H/n_D ratio in plasma core
Line averaged Zeff	Core He density	Neutral density between plasma and first wall
L to H mode transitions and ELMs	Confined alphas	
Runaway electrons	Escaping alphas	
Divertor parameters	Impurity density profile	

Table 11.5 ITER diagnostics systems

Magnetic diagnostics
Vessel wall sensors, Divertor magnetics
Continuous rogowski coils, Diamagnetic loop

Neutron diagnostics
Radial neutron camera, Vertical neutron camera
Micro-fission chambers (In-Vessel)
Neutron flux monitors
Neutron spectrometer
Gamma-ray spectrometer
Activation system (In-Vessel)
Lost alpha detectors

Bolometric systems
Arrays for main plasma, Arrays for divertor

Spectroscopic and neutral particle analyzer systems
H Alpha spectroscopy, Visible continuum array
Main plasma and divertor impurity monitors
X-ray crystal spectrometers
Charge eXchange recombination spectroscopy (CXRS)
Based on diagnostic neutral beam
Motional stark effect (MSE) based on heating beam
Soft X-ray array (SXR)
Neutral particle analyzers (NPA)
Laser induced fluorescence (LIF)

Optical/IR (infra-red) systems
Thomson scattering
 Core
 Edge
 X-Point
 Divertor
Toroidal interferometer/polarimeter
Polarimeter (poloidal field measurement)
Collective scattering system

Diagnostic neutral beam
Microwave Diagnostics
Electron cyclotron emission (ECE)
Plasma reflectometers, low and high field sides X-mode and O-mode
Plasma position reflectometer
Divertor reflectometer

Plasma-facing components and operational diagnostics
IR/Visible cameras, thermocouples, pressure gauges residual gas analyzers, IR thermography
 (Divertor), Langmuir probes, Dust and retained tritium monitors

---

Figure 11.66 shows how these diagnostics are arranged around the torus on the upper level, middle level, and lower level (divertor).

Figure 11.67 shows schematically how some of these will look when mounted on the torus.
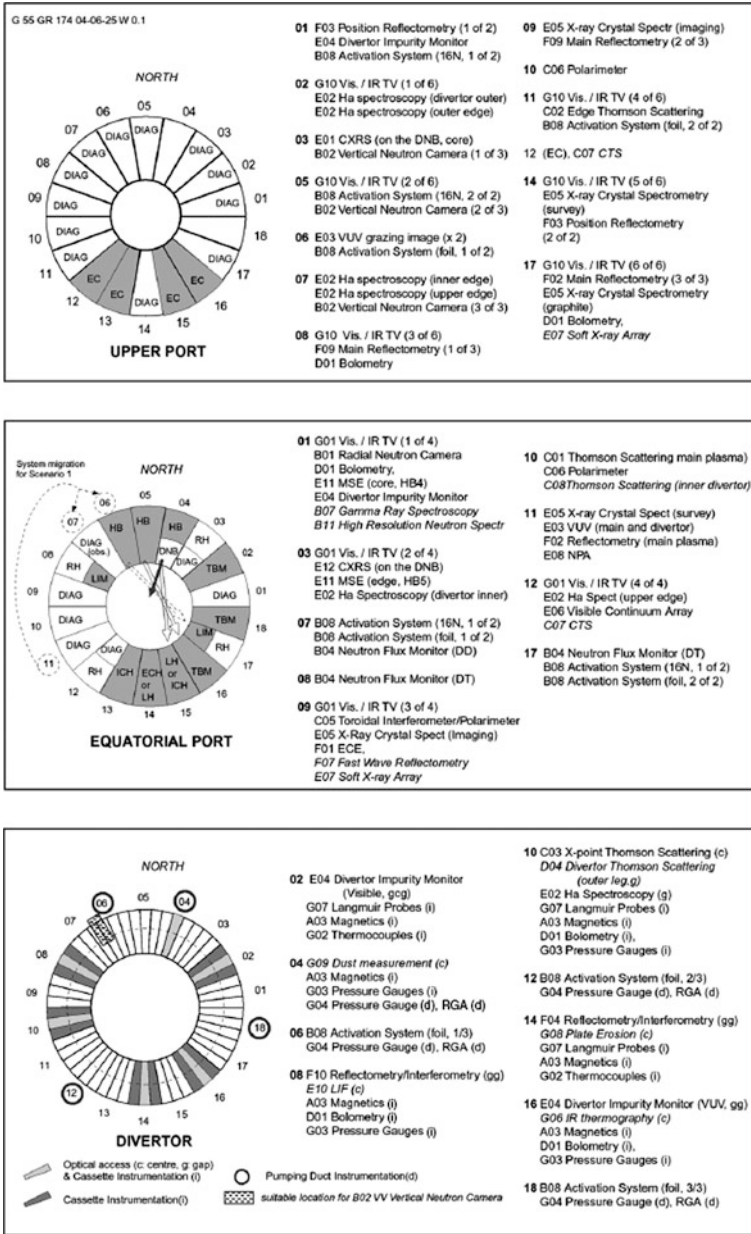
Fig. 11.66 Plan for arrangement of ITER diagnostics on the upper, middle, and lower levels (Donné et al. 2007, Figs. 18, 20, 22)
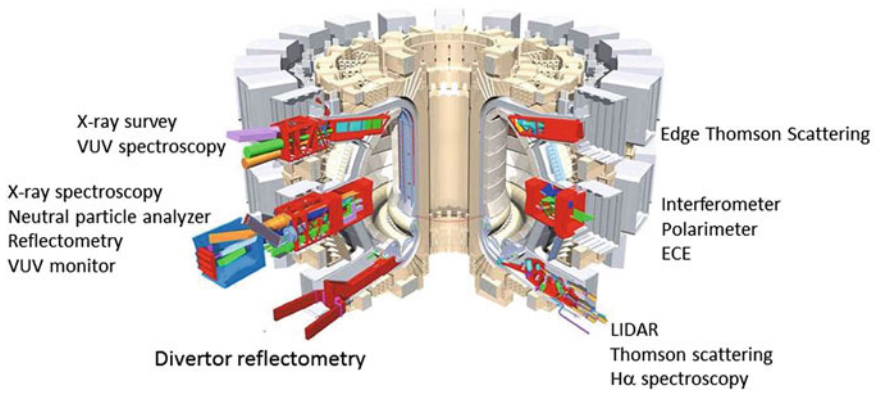
Fig. 11.67 Cutaway view of ITER showing where some diagnostics instruments will be mounted. For simplicity, only a few are labelled. Courtesy of ITER Organization. (Donné et al. 2007, Fig. 15)
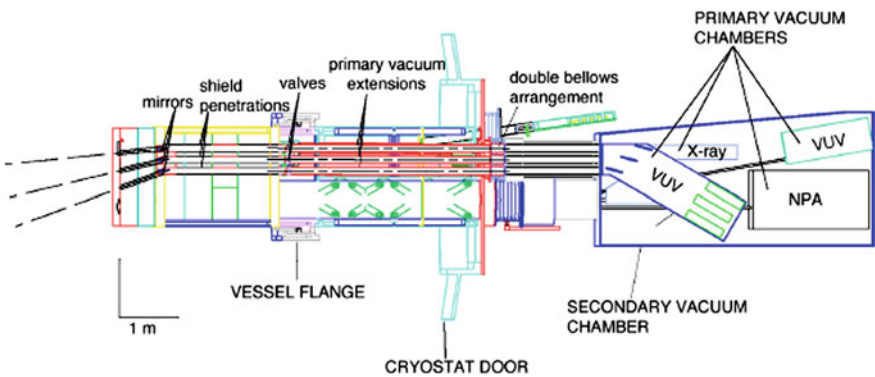
Fig. 11.68 The port plug for equatorial port 11 containing several different diagnostics. Courtesy of ITER Organization

The design of a diagnostic port plug to accommodate diagnostic instruments can be complex, as can be seen in Fig. 11.68.

On the inside there are mirrors to steer the lines of sight, protected by shutters during vessel discharge cleaning. The mirrors are followed by shield penetrations and vacuum valves, which can isolate the diagnostic systems from the vacuum vessel. There are vacuum pumps to evacuate the diagnostics instruments before the valves are opened to the torus, and a cryostat door to protect the cryostat from heat inflow. Each of the four instruments shown here has its own independent vacuum chamber. There must be power supply lines to each system, sensors to detect system faults and radiation levels, a computer control system, and all will be designed for easy maintenance.
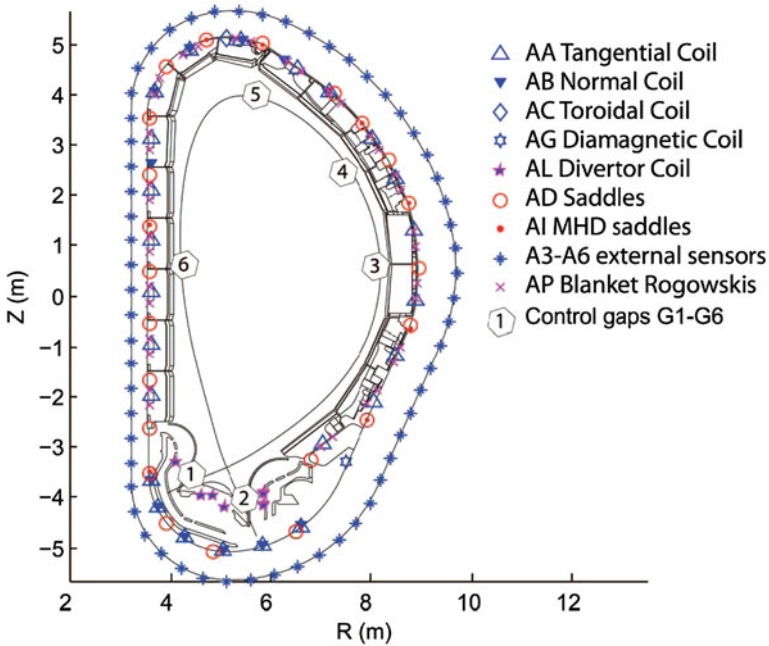
Fig. 11.69 Some ITER magnetic diagnostics (Vayakis et al. 2012). Development of the ITER magnetic diagnostic set and specification, Review Of Scientific Instruments 83, 10D712 (2012), Fig. 1. Reprinted with permission Review of Scientific Instruments, Copyright 2012, American Institute of Physics

Magnetic probes will be located all around the torus, Fig. 11.69, to monitor plasma shape and to detect instabilities (sawtooth mode, kink mode, Mirnov oscillations, tearing modes, resistive wall modes, ELMs, etc.).

Signals from these diagnostics and others will be used by the control system when an instability becomes dangerous, so that bad consequences, like vertical displacement events and disruptions, can be avoided by feedback to the poloidal field coils and correction coils and other protection measures.

The internal magnetic field will be measured by an infrared polarimeter in the poloidal plane, with additional data from the toroidal interferometer (Fig. 11.70). Independent measurements will be made by the motional Stark effect system (MSE).

This interferometer will operate at two CO_2 laser wavelengths: 9.27 and 10.6 μm, with opto-acoustic modulators at a frequency of 10 MHz. The 20 mm diameter laser beams will pass through the plasma and then be reflected back along the same path to the detector. This double pass gives added sensitivity and avoids the need for more diagnostic ports at inconvenient places. Operation at two wavelengths allows the Faraday rotation equations to be solved simultaneously for both density and magnetic field along the beam path. This is the primary density
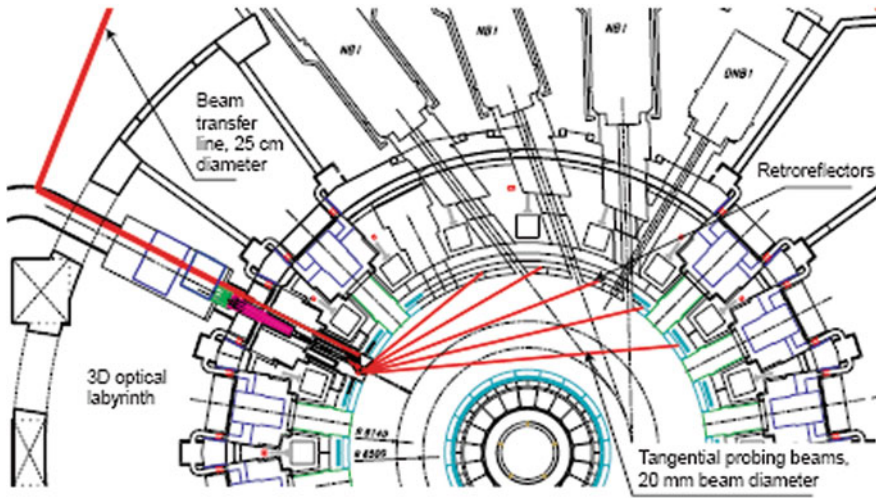
Fig. 11.70 The ITER toroidal infrared interferometer. Courtesy of ITER organization
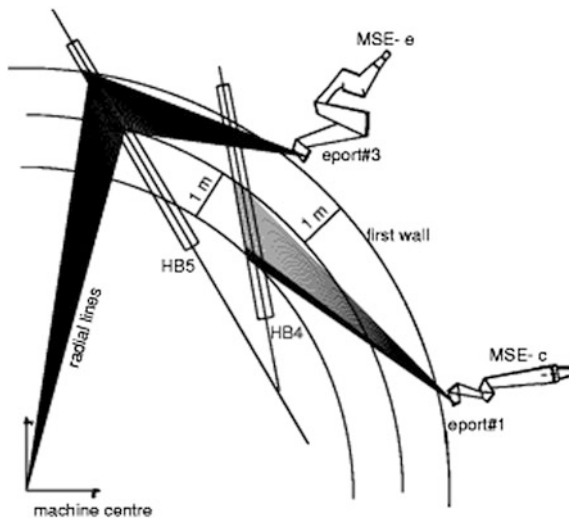
Fig. 11.71 Lines of sight for MSE measurements using neutral beams HB4 and HB5 in ITER. Reprinted with permission from Malaquias et al. (2004) Active beam spectroscopy diagnostics for ITER: Review of Scientific Instruments 75, 3393, Fig. 1, Copyright 2004 American Institute of Physics

diagnostic against which the others will be checked. The windows will probably be BaF$_2$ or CVD diamond, due to their low Verdet constants. The synthetic diamond is preferred, due to its better durability, but it is expensive.

The MSE system will also provide data on the internal magnetic field, Fig. 11.71.
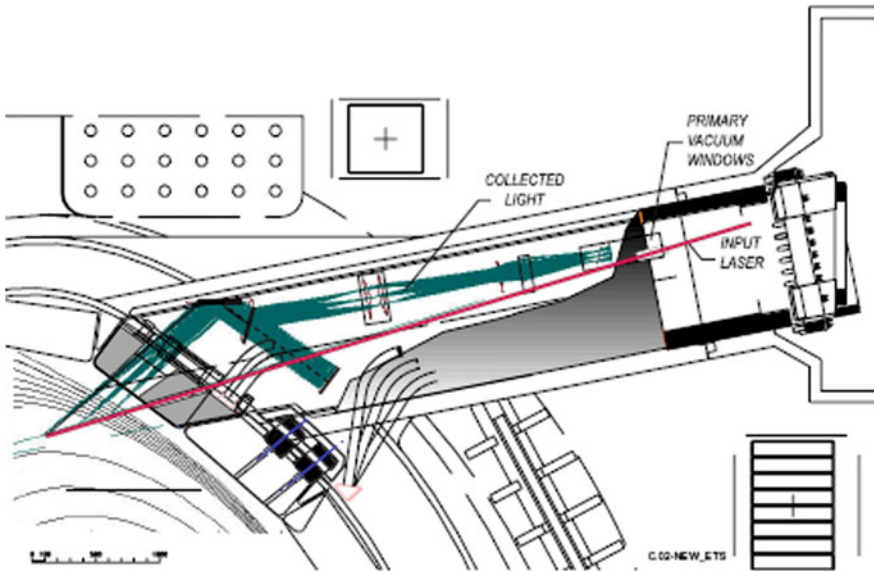
Fig. 11.72 The ITER port in which the edge Thomson scattering system is located. Courtesy of ITER Organization

Figure 11.72 shows a port in which Thomson scattering is used for edge measurements. The input laser beam (red) goes straight in through a primary vacuum window. The scattered light (turquoise) returns via several mirrors, with separate channels corresponding to each spatial position in the plasma.

The plasma facing mirror is a critical element, because it is subjected to bombardment by charge exchange atoms and deposition of contaminants, which reduce its reflectivity (Voitsenya 2001). It may be made of single-crystal metals, such as Mo or W, or a Rh coating on a Cu substrate. Polycrystalline metals degrade too quickly, as seen in Fig. 11.73.

Fig. 11.73 Decrease of normal incidence mirror reflectivity at 600 nm due to surface sputtering. (Vayakis et al. 2008, Fig. 18) © 2008 by the American Nuclear Society, LaGrange Park, Illinois
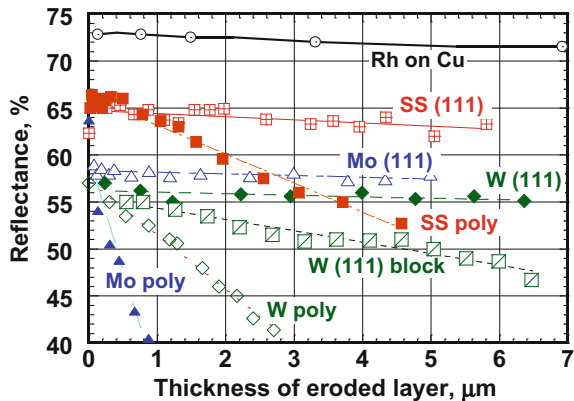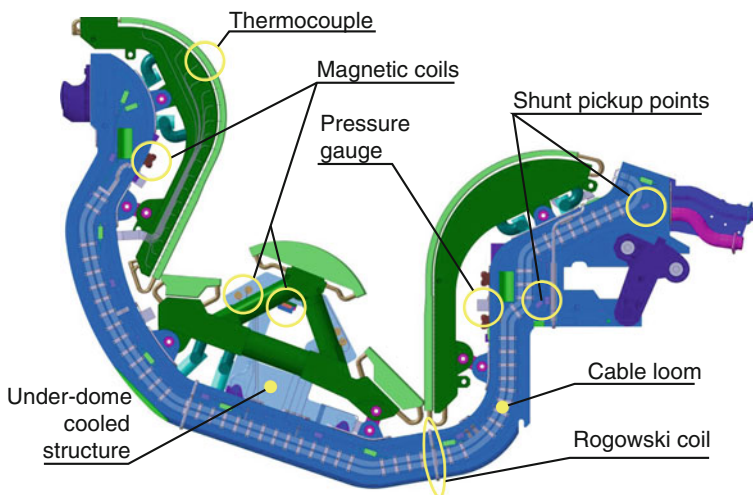
Fig. 11.74 Some of the diagnostics in the ITER divertor region. Courtesy of ITER organization

Single crystal mirrors of Mo or W tested in TEXTOR had much less degradation from plasma exposure than polycrystalline mirrors. Plasma exposure tests in DIII-D found that room temperature mirrors became coated with up to 100 nm of carbon, while mirrors heated to 80–140 °C had no carbon deposition (Donné et al. 2007).

Diagnostics are needed in the ITER divertor chamber to measure plasma density and temperature, neutral gas species and densities, flow rates, and wall temperatures. Some of these are shown in Fig. 11.74.

Neutron measurements will be required during operation with deuterium fuel and later with DT fuel. Neutron cameras are shown in Fig. 11.75.

From these arrays of many collimated neutron detectors, it will be possible to calculate the two-dimensional neutron emission profile, as for soft x-ray tomography. The arrays are at different toroidal locations, so some assumption about toroidal symmetry will be needed to interpret the data.

Table 11.6 lists some ITER diagnostics for spectroscopy and neutral particle analysis.

11.9.1 Burning Plasma Issues

ITER components must contend with many serious issues caused by the severe environment:

(Costley et al. 2001, 2005; Donné and Costley 2004; Vayakis et al. 2008).
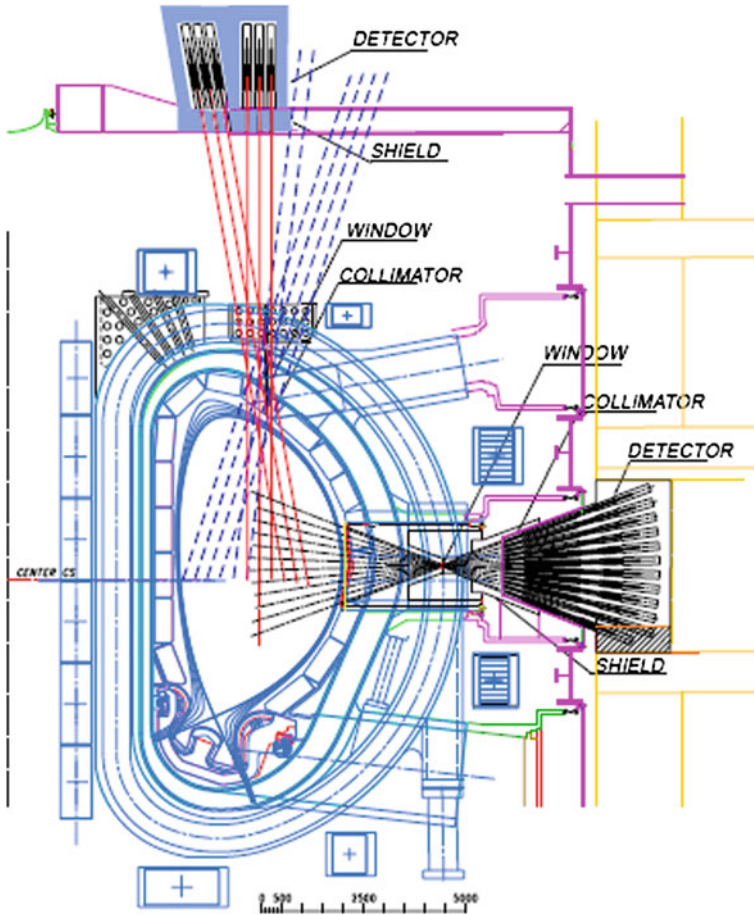
Fig. 11.75 ITER Neutron cameras. Courtesy of ITER organization

- Nuclear heating up to 1 W/cm^3 will require active cooling of components near the first wall,
- Thermal cycling and expansion during operation and bakeout
- Electromagnetic loads
- Vibrations during disruptions
- Radiation induced electromotive force (RIEMF) in cables, causing spurious voltages in mineral-insulated coaxial cables between the inner conductor and outer sheath, and even a smaller voltage along the cable, which interfere especially with magnetic diagnostics. (Plastic insulators are not used, because radiation damage degrades them too quickly).
- Temperature induced electro-motive force (TIEMF). Temperature differences (~ 10–100 K) along a cable can produce voltages in the microvolt range.
- Radiation induced conductivity (RIC) in insulators.

Table 11.6 Summary of ITER spectroscopy and NPA diagnostics. Courtesy of ITER organization (from the ITER 2009 baseline document, plant description, chap. 8: Diagnostics)

Instrument	Wavelength/ Energy range	Regions probed/ Viewing directions	Function
CXRS BES	Visible region	Core and edge	T_i (r), He ash density, impurity density profile, plasma rotation, alphas
Hα system	Visible region	Main plasma: inner, outer and upper regions; Divertor: inboard and outboard regions	ELMs, L/H mode indicator, n_T/n_D and n_H/n_D at edge and in divertor
VUV (main plasma)	2.3–160 nm	Upper and equatorial regions; divertor region	Impurity species identification
Divertor impurity monitor	200–1,000 nm	Divertor and X-point regions	Impurity species and influx, divertor He density, ionisation front position, T_i
X-ray spectroscopy-(high resolution)	0.1–0.5 nm	Core and edge	Impurity species identification, plasma rotation, T_i
Radial X-ray camera	1–200 keV	Full poloidal profile	MHD, impurity influxes, Te
NPA	N/A (10–200 keV, 0.1–4 MeV)	Core and edge	n_T/n_D and n_H/n_D at edge and core. Fast alphas
Laser induced fluorescence	Visible-near-UV	Divertor outer leg	Divertor neutrals
MSE	Visible region	Core and edge	q (r), internal magnetic structure
X-Ray spectrometry(Survey)	0.1–10 nm	Central chord	Impurity species identification
Hard X-ray monitor (H-PHASE)	100 keV–20 MeV	One or more locations on equatorial plane	Runaway electron detection
Divertor spectroscopy (VUV)	15–40 nm	Divertor outer leg	Divertor impurity influxes, particularly Tungsten

LOS line of sight, *VUV* vacuum ultraviolet, *CXRS* charge exchange recombination spectroscopy, *MSE* motional stark effect, *NPA* neutral particle analyzer

- Radiation induced electrical degradation (RIED), swelling and cracking of insulators. This occurs at E > 200 kV/m, T > 200 °C, radiation level >100 Gy/s, and exposure time >1000 s.
- Radiation induced thermo-electric sensitivity (RITES) in a high radiation field.
- Radiation-induced noise in microchannel plate, image intensifiers, photodiodes, CCD detectors.
- Neutron-induced transmutation of elements, leading to changes of properties.
- Lifetime of in-vessel magnetic and electrostatic probes.

- Damage to optical components

  – Erosion of mirrors by sputtering (single crystal Mo or W may be best)
  – Coating of mirrors and windows by impurities and polymer films
  – Radiation-induced darkening of windows and optical fibers
  – Radiation induced luminescence in optical materials.

- Neutron streaming

  – Large distance needed from plasma to detectors to reduce neutron flux
  – Multiple-bend labyrinths to reduce streaming

- Tritium retention in spectrometers and other components
- Rapid replacement of damaged items by remote handling

  Donné et al. (2007); Johnson and Costley (2008).

  Several techniques could help spectroscopic systems to function in burning-plasma devices: (Stratton 2008)

- **Grazing-incidence** X-ray mirrors or mosaic Bragg crystals to reduce neutron streaming.
- Bundles of **glass capillaries** to increase the effective solid angle of the X-ray source while partially shielding the nuclear radiation
- Detectors with **lower response** to neutrons and gamma rays and with higher radiation-damage thresholds
- Optimization of neutron and gamma-ray **collimation and shielding** of the detectors
- Active **rejection** or background subtraction of detector events resulting from neutrons or gamma rays.

  – If a detector is triggered by a neutron or gamma ray, the electronic circuits can close the gate of the x-ray detector (**anticoincidence** system), so that noise from the neutron/gamma is avoided in the XCS.
  – X-rays generate pulses with faster risetimes than those from energetic recoil electrons in gamma detectors, so the gamma pulses can be rejected (**risetime discrimination**).
  – Using a second detector near each diode that is blind to the X-rays and **subtracting** the (nuclear radiation signal) from the (X-ray plus nuclear radiation signal).

  The intense radiation environment problems will be worse for DEMO, so much R&D will be needed. Additional development and testing are needed for diagnostics relating to dust, retained tritium, surface erosion, and lost alpha particles. (Stott et al. 1998; Donné et al. 2007; Orsitto et al. 2008; Stratton et al. 2008; Vayakis et al. 2008; Costley 2010; Donné and Costley 2004).

11.9.2 ITER Schedule

ITER is expected to begin preliminary technical commissioning in 2019–2020, then gradually begin the **H Phase** plasma operations in about 2021, using light hydrogen. Plasma heating systems will be installed and the plasma current, density, and temperature will be gradually increased. Next, the **D Phase** will begin burning deuterium fuel to test power and particle flows and fusion power diagnostics. After all these systems are working properly, in about 2026–2027, it is planned that the **T Phase** will begin burning DT fuel and gradually increase to full power. During this phase fusion product alpha and high energy neutron diagnostics will be used. Finally, tritium breeding modules will be installed to test their performance and to verify neutronics predictions.

Part of ITER's mission will be to determine, for DEMO, the set of optimized stable scenarios and the reduced set of diagnostics and data analysis tools needed to monitor them. A promising area for significant impact is integrated numerical simulation of the ITER plasma performance. Given the sophistication of present-day simulations, one might expect the state of the art to progress such that each ITER shot is simulated beforehand, complete with diagnostic responses to compare with real experiments. Going further, one might even imagine these simulators making use of constraints provided by real-time data to predict the evolution of the plasma and to provide controls to keep within safe operating limits. There will be some measurements assessed in the ITER control room that will have a profound impact on ITER operations because they may be involved in decisions affecting personnel safety. These include measurements of tritium and dust accumulated inside the machine. Limits on these accumulations exist to keep releases to acceptable levels if containment boundaries are breached (Johnson and Costley 2008).

11.10 Summary

ITER will have ubiquitous instruments to monitor machine protection, plasma control, and plasma performance. They will measure plasma parameters, magnetic fields, fusion power, radiation levels, temperatures, flow rates, voltages, currents, pressures, surface erosion and redeposition, and other parameters (Costley et al. 2006; Donné et al. 2007).

Magnetic fusion experiments gather huge quantities of data during each discharge. After the data from each diagnostic system are checked, different diagnostic systems results are compared, such as different measurements of electron density. Model predictions are compared with the experimental results. Discrepancies may be caused by faulty diagnostics or by inadequate models. Some key parameters to be assessed are plasma kinetic energy, fast particle energy, Z_{eff} (from bremsstrahlung and charge exchange), neutron yield, and energy confinement time. A large database of tokamak data has been assembled and used for

analysis of parameter scaling in various regimes and for validation of models (Arshad et al. 2008).

Table 11.7 summarizes some diagnostic techniques that have been developed for each of the major plasma parameters. For brevity some of these techniques have not been described in this Chapter.

11.11 Problems

11.1 If Fig. 11.2 represents a hydrogen plasma with random ion current of 50 μA and probe area of 1 mm², estimate the plasma density and electron temperature.

11.2 A 100-turn magnetic probe coil 3 mm in diameter records a voltage of 2 V with no integrating circuit during the pulsing of a magnet coil. What is the rate of change of the magnetic field?

11.3 Assume that the poloidal field in an axisymmetric torus with large aspect ratio is found to be

$$B_p(r) = B_{po}r/(a + r)$$

Find the variation of toroidal current density $J_t(r)$, approximating the torus as a long cylinder.

11.4 Assume that a ten-turn coil C_1 (Fig. 11.8) is very close to the plasma, so that its radius $\approx$ a (the plasma surface radius) = 0.6 m. If the average plasma pressure increases linearly from 0 to 10^4 Pa in 5 ms and B = 3 T, estimate the voltage induced in C_1. (Relate dB/dt to dp/dt.)

11.5 A uniform deuterium plasma with density 10^{21} m^{-3} and volume 0.01 m³ is constant for 2 μs, during which time a detector counts 10^5 neutrons. If the detector measures 10^{-4} of the neutrons emitted by the plasma, what is the approximate ion temperature?

11.6 A 10 keV K$^+$ beam probes a plasma. The energy of the K^{++} ions arriving at the detector from one point in the plasma is 9.3 keV. What is the plasma potential at that point?

11.7 If the Doppler width of the helium spectral line at 468.6 nm is 0.17 nm, what is the approximate ion temperature?

11.8 If the measured line width of H$_\beta$ is 2.0 nm, and the Doppler width is estimated to be $\ll$ 2 nm, what is the approximate plasma density? (Assume instrumental broadening and the Zeeman effect are negligible.)

11.9 From soft x-ray measurements it is determined that the power radiated at W_v = 2, 4, and 6 keV is dP/dW$_v$ = 10^{-3}, 10^{-4}, and 10^{-5} (relative units). What is the electron temperature?

11.10 A sensitive microwave interferometer operating at a wavelength of 1.5 cm measures a phase shift of 3.6° across a plasma path length of 7 cm when the plasma is pulsed on. What is the average plasma density?

Table 11.7 Some techniques for measuring various plasma parameters

Electrostatic potential and electric field

Electrical probes

Plasma conductivity from voltage-current measurements

Heavy-ion beam probe

Electron beam probe (weak magnetic field)

Stark effect

Plasma impedance from applied oscillating electric field

Magnetic field components

Magnetic flux measurements

Hall probes

Generation of microwave harmonics

Zeeman effect

Heavy-ion beam probe

Neutral beam emission spectroscopy

Faraday rotation

Motional Stark effect

Electron density or ion density

Langmuir probe

Microwave, FIR, and optical

Microwave cavity resonance

Reflectometry

Heavy-ion beam probe

Neutral beam emission spectroscopy

Stark broadening

Holographic interferometry

Thomson scattering

RF conductivity probes

Interferometers

Alfven wave and sound wave propagation

Charged particle collectors

Photography

Cotton-Mouton effect

Electron velocity distribution or temperature

Gridded analyzers

Thomson scattering

Visible & UV spectroscopy

X-ray intensity with filters

Electron cyclotron emission

Spectral line intensity ratios

Langmuir probes

Ion velocity distribution or temperature

Neutral atom energy analyzer

Doppler broadening

Neutron emission

Table 11.7 (continued)

Coherent Thomson scattering
Neutral beam scattering
Gridded analyzers
Diamagnetism
Calorimetry
CXRS

Plasma flow velocity
Time-of-flight from probes or photography
Doppler frequency shift of waves emitted
Doppler shift of reflected microwaves
Magnetic flux measurements
Runaway electrons from hard x-ray measurements

Neutral atoms and impurities
Optical, UV, VUV spectroscopy, and CXRS
Low-energy and high-energy NPAs
Mass spectrometer
Resonance absorption & scattering (light, infrared)
Ion cyclotron resonance absorption
Vacuum pressure gage
Refractivity measurements (high density)
Neutral beam emission spectroscopy
Laser induced fluorescence

Instabilities and Turbulence
Magnetic flux measurements
Electrical probes
X-ray fluctuations
Microwave reflectometry
Electromagnetic wave scattering (microwaves and FIR)
Heavy-ion beam probe
Electron cyclotron emission
Photography of plasma shape
Plasma resistivity (external V–I measurements)
Neutron energy spectrum and isotropy
Charge exchange recombination spectroscopy

Plasma-facing components
Infrared camera
Bolometry
Particle collection diagnostics

11.11 If $L = 1$ m and a ruby laser (694.3 nm) was used to make the Mach–Zehnder circular fringe pattern shown in Fig. 11.59, compute the central plasma density.

11.12 How much rotation would be produced in an HCN laser beam (337 µm) propagating through a plasma with $n = 3 \times 10^{19}$ m^{-3} and $B_k = 0.4$ T over a path length of 0.7 m, assuming n and B_k are uniform along the path?

11.13 Derive Eq. (11.32) for Z_{eff}.

11.14 Assuming a uniform plasma, if $\ell = 0.8$ m and $f = 100$ GHz for the data of Fig. 11.57, what is the peak plasma density?

11.12 Review Questions

1. What plasma parameters should be measured?
2. About what time and spatial resolutions are needed for magnetically confined plasmas?
3. What are the 6 main categories of plasma diagnostics methods?
4. Sketch a Langmuir probe and explain how it works. What plasma parameters can be estimated with this method?
5. How can the rate of change of the poloidal magnetic field be measured?
6. Sketch a gridded electrostatic energy analyzer and explain the functions of the grids.
7. How can the energies of charge-exchange neutral atoms be measured?
8. Why does a charge-exchange neutral energy analyzer not measure the temperature near the center of a large, hot plasma?
9. How does a photomultiplier tube work?
10. How can neutron energies be measured?
11. How can the spatial distribution of neutron emission be measured?
12. For what is a quartz crystal microbalance useful?
13. How can the electrostatic potential inside a plasma be measured?
14. How does a Zeeman splitting system work, and what can it measure?
15. How does CRXS work, and what can it measure?
16. How does MSE work, and what can it measure?
17. How does BES work, and what can it measure?
18. Why would a high temperature hydrogen plasma emit no light?
19. How is a Voight profile useful?
20. What is a bolometer, and what information does it yield?
21. Sketch an xray spectral power density versus wavelength, including bremsstrahlung and line radiation.
22. How are foils used to estimate electron temperature?
23. How does an ECE diagnostic work, and what does it yield?
24. How does a soft xray interferometer work?
25. Identify the variables in the equation

$$I/I_{max} = \frac{1}{2}[1 + \cos(\phi_{1V} + \Delta\phi - \phi_2)]$$

26. How does microwave reflectometry work, and what can it measure?
27. Sketch a microwave interferometer and explain how it works.
28. What is the advantage of FIR interferometers in comparison with visible and infrared interferometers?
29. Sketch a Thomson scattering system and explain how it works. Why are high power lasers required?
30. What is the advantage of a phase conjugate mirror?
31. Why does each ultraviolet instrument have its own vacuum system?
32. How can one Faraday rotation instrument measure both density and magnetic field simultaneously?
33. What are the problems of the plasma facing mirror?

References

Adamek J, Stockel J, Hron M, Ryszawy J, Tichy M, Schrittwieser R, Ionita C, Balan P, Martines E, Van Oost G (2004), A novel approach to direct measurement of the plasma potential, Czechoslovak Journal of Physics, 3, vol. 54

Adamek J, Stockel J, Duran I, Hron M, Panek R, Tichy M, Schrittwieser R, Ionita C, Balan P, Martines E, Van Oost G (2005) Comparative measurements of the plasma potential with the ball-pen and emissive probes on the CASTOR tokamak. Czechoslovak J Phys 55

Adamek J, Kocan M, Panek R, Gunn JP, Martines E, Stockel J, Ionita C, Popa G, Costin C, Brotankova J, Schrittwieser R, Van Oost G (2008) Simultaneous measurements of ion temperature by segmented tunnel and Katsumata probe. Contrib Plasma Phys 48(5–7): 395–399

Arshad SA, Cordey JG, McDonald DC, Farthing J, Joffrin E, Von Hellermann M, Roach CM, Svenssone J (2008) Chapter 11—Data Validation, Analysis, and Applications for Fusion Plasmas. Fusion Sci Technol 53:667

Carolan PG, Piotrowicz VA (1983) The behaviour of impurities out of coronal equilibrium. Plasma Phys 25:1065–1086 (Figure 5(b))

Costley AE et al (2001) ITER R&D: Auxiliary systems: plasma diagnostics. Fusion Eng Des 55:331

Costley AE et al (2005) Technological challenges of ITER diagnostics. Fusion Eng Des 74:109

Costley AE et al (2006) The design and implementation of diagnostics systems on ITER. 21st IAEA fusion energy conference, Chengdu, 16–21 Oct

Costley AE (2010) Towards diagnostics for a fusion reactor. IEEE Trans Plasma Sci 38:2934–2943

Costley AE, Johnson DW (eds) (2008) Plasma diagnostics for magnetic fusion research. Special edition of fusion science and technology 53(2):281–760

De Michelis C, Mattioli M (1984) Spectroscopy and impurity behavior in fusion plasmas. Rep Prog Phys 47:1233

de la Luna E et al (2008) Recent results on the discrepancy between T_e measurements in high-T_e plasmas in JET. In: Proceedings of 15th joint workshop electron cyclotron emission and electron cyclotron resonance heating (EC-15), World Scientific Press, Yosemite, California, March 2008

de la Luna E et al (2012) The effect of ELM pacing by vertical kicks on the access to stationary H-mode with $H_{98} \sim 1$ on JET. 24th IAEA Fusion energy conference, IAEA CN-197, San Diego, CA, 8–13 Oct 20112 (paper EX/6-1)

Dejarnac R, Gunn JP, Stockel J, Adamek J, Brotankova J, Ionita C (2007) Study of ion sheath expansion and anisotropy of the electron parallel energy distribution in the CASTOR tokamak. Plasma Phys Controlled Fusion 49(2007):1791–1808

Dolan TJ (1982) Fusion research. Pergamon Press, Elmsford, NY, USA

Donné AJH, Costley AE (2004) Key issues in diagnostics for burning plasma experiments. IEEE Trans Plasma Sci 32:177

Donné AJH et al (2007) Chapter 7: Diagnostics. Nucl Fusion 47:S337

Donné AJH, Barth CJ, Weisen H (2008) Chapter 4: Laser-Aided Plasma Diagnostics. Fusion Sci Technol 53:397

Duval B (2012) Real time ELM, NTM and Sawtooth Control on TCV. 24th IAEA fusion energy conference, IAEA CN-197, San Diego, CA, 8–13 Oct 2012 (paper EX/1-2)

Dyabilin K, Hron M, Stockel J, Zacek F (2002) Rotating mach probe for ion flow measurements on the CASTOR tokamak. Contrib Plasma Phys 1:99–108

Equipe TFR (1978) Tokamak plasma diagnostics. Nuclear Fusion 18:647–730 (Figure 41)

Eshelman CD, Tseng HK, Dolan TJ, Prelas MA (1991) Plasma diagnostic x-ray tomography system. Rev Sci Instrum 62:751–754

Eubank H, Goldston R J, Arunasalam V, et al (1979) "PLT neutral beam heating results", International Atomic Energy Agency, Plasma Physics and Controlled Nuclear Fusion Research 1978. In: Proceedings of the seventh international conference on plasma physics and controlled nuclear fusion research, held by the International Atomic Energy Agency in Innsbruck, 23–30 Aug 1978, vol I, IAEA, Vienna (Paper IAEA-CN-37/C-3, pp 167–198, Fig. 9)

Griem HR (1997) Principles of plasma spectroscopy. Cambridge University Press, England

Gunn JP, Boucher C, Devynck P, Duran I, Dyabilin K, Horacek J, Hron M, Stockel J, Van Oost G, Van Goubergen H, Zacek F (2001) Edge flow measurements with Gundestrup probes. Phys Plasmas 8(5):1995–2001 (Part 2)

Gunn JP, Panek R, Stockel J, Van Oost G, Van Rompuy T (2005) Simultaneous measurements of ion current, electron temperature and floating potential fluctuations with a tunnel probe. Czech J Phys 55(3):255–263

Hacquin S (2008) "Plasma diagnostics in fusion devices", International Summer School on Fusion Technology. Karlsruhe Institute of Technology, Germany, 2–13 Sept 2008

Hatae T, Nakatsuka M, Yoshida H (2004) Improvement of Thomson scattering diagnostics using stimulated-brillouin-scattering-based phase conjugate mirrors. J Plasma Fusion Res 80:870–882

Hillis DL, Fehling FT, Bell RE, Johnson DW, Zastrow K-D et al (2004) A high throughput spectrometer system for helium ash detection on JET. Rev Sci Ins 75:3449 (Fig. 1)

Hopkins GR, Rawls JM (1979) Nuclear technology 43, 382, Fig. 1. Copyright by the American Nuclear Society, LaGrange Park, Illinois, USA

Huber A, McCormick K, Andrew P, Beaumont P, Dalley S, Fink J, Fuchs JC, Fullard K, Fundamenski W, Ingesson LC, Mast F, Jachmich S, Matthews GF, Mertens Ph, Philipps V, Pitts RA, Sanders S, Zeidner W (2007) Upgraded bolometer system on JET for improved radiation measurements. Fusion Eng Des 82:1327–1334

Hutchinson IH (2002) Principles of plasma diagnostics, 2nd edn. Cambridge University Press, UK

Ingesson LC, Alper B, Peterson BJ, Vallet J-C (2008) Chapter 7: Tomography diagnostics: bolometry and soft-x-ray detection. Fusion Sci Technol 53:528

Isler RC (1984) Impurities in Tokamaks. Nucl Fusion 24:1599

Jarvis ON (1994) Neutron measurement techniques for tokamak plasmas. Plasma Phys Controlled Fusion 36:209 (Table 4)

Johnson DW, Costley AE (2008) Chapter 13: Challenges in fusion diagnostic development: a virtual tour of ITER. Fusion Sci Technol 53:751

Katsumata I, Okazaki M (1967) Ion sensitive probe—a new diagnostic method for plasma in magnetic fields. Jpn J Appl Phys 6:123–124

Kikuchi M, Lackner K, Tran MQ (2012) Fusion physics. International atomic energy agency, Vienna, Austria

Kislyakov AI, Donné AJH, Krupnik LI, Medley SS, Petrov MP (2008) Chapter 8: Particle diagnostics, fusion science and technology 53, 577–603, Fig. 3a. Copyright by the American Nuclear Society, LaGrange Park, Illinois, USA

Krasilnikov AV, Sasao M, Kaschuck, Nishitani T, Batistoni P, Zaveryaev VS, Popovichev S, Iguchi T, Jarvis ON, Källne J, Fiore CL, Roquemore AL, Heidbrink WW, Fisher R, Gorini RG, Prosvirin DV, Tsutskikh AY, Donné AJH, Costley AE, Walker CI (2008) Status of ITER neutron diagnostic development. Nuclear Fusion 45:1503–1509 (Fig. 1)

Lasnier CJ, Allen SL, Boedo JA, Groth M, Brooks NH, Mclean A, Labombard B, Skinner CH, Rudakov DL, West WP, Wong CPC (2008) Chapter 10: First wall and operational diagnostics. Fusion Science and Technology 53, 640. Copyright by the American Nuclear Society, LaGrange Park, Illinois, USA

Luhmann, Jr, NC, Bindslev H, Park H, Sánchez J, Taylor G, Yu CX (2008) Chapter 3: Microwave diagnostics. Fusion Science and Technology 5, 335–396. Copyright by the American Nuclear Society, LaGrange Park, Illinois, USA

Malaquias A, von Hellermann M, Tugarinov S, Lotte P, Hawkes N et al (2004) Active beam spectroscopy diagnostics for ITER: Present status (invited). Rev Sci Ins 75:3393 (Fig. 1)

Medley SS, Roquemore AL (1998) Construction and operation of parallel electric and magnetic field spectrometers for mass energy resolved multi-ion charge exchange diagnostics on the tokamak fusion test reactor. Rev Sci Instrum 69:2651

Nunes I, Manso M, Serra F, Horton LD, Conway GD, Loarte A, ASDEX Upgrade and CFN Reflectometry Teams (2005) Density profile analysis during an ELM event in ASDEX Upgrade H-modes. Nuclear Fusion 45:1550 (Fig. 1)

Orsitto FP, Gorini G, Sindoni E, Tardocci M (eds) (2008) Burning plasma diagnostics, American Institute of Physics Conference Proceedings 988, Melville, New York

Park H, Mazzucato E, Munsat T, Domier CW, Johnson M et al (2004) Simultaneous microwave imaging system for density and temperature fluctuation measurements on TEXTOR (invited). Rev Sci Instrum 75:3787 (Fig. 3a)

Peacock NJ (1996) Fusion Spectroscopy. Astrophys Space Sci 237:341–349

Pégourié B, Köchl F, Nehme H, Polevoi AR (2009) Recent results on the fuelling and control of plasmas by pellet injection, application to ITER. Plasma Phys Controlled Fusion 51:1

Reiter B, Pautasso G, Eich T, Fuchs JC, Giannone L, Dux R. Neuhauser J, Maraschek M, Igochine V, Herrmann A, Lunt T, the ASDEX Upgrade Team (2009) Application of AXUV diodes for broad-band plasma radiation studies in ASDEX Upgrade. 36th EPS Conference on Plasma Phys, Sofia, 29 June–3 July 2009 (ECA vol 33E, P-1.161)

Rhodes TL, Peebles WA, Van Zeeland M, Mikkelsen D, Gilmore MA et al (2004) Comparison of broad spectrum turbulence measurements and gyrokinetic code predictions on the DIII-D Tokamak. In: Proceedings of the 20th IAEA fusion energy conference. Vilamoura, Portugal, 1–6 Nov 2004 (IAEA-CN-116/P6-23, Fig. 3)

Sasao M, Nishitani T, Krasilnilov A, Popovichev S, Kiptily V, Kallne J (2008) Chapter 9: Fusion product diagnostics, fusion science and technology 53, 604 Copyright by the American Nuclear Society, LaGrange Park, Illinois, USA

Schrittwieser R, Adamek J, Balan P, Hron M, Ionita C, Jakubka K, Kryska L, Martines E, Stockel J, Tichy M, Van Oost G (2002) Measurements with an emissive probe in the CASTOR tokamak. Plasma Phys Contr Fusion 44(5):567–578

Schrittwieser R, Ionitá C, Adámek J, Stöckel J, Brotánková J, Martines E, Popa G, Costin C, van de Peppel L, van Oost G (2006) Direct measurements of the plasma potential by katsumata-type probes. Czechoslovak J Phys 56(2):B145–B150 (Fig. 1)

Sheehan JP, Hershkowitz N (2011) Emissive probes. Plasma Sources Sci Technol 20:063001 (pp 22)

Sheffield J, Froula D, Glenzer SH, Luhmann NC (2011) Plasma scattering of electromagnetic radiation, second edition: theory and measurement techniques. Elsevier, Amsterdam

Skinner CH, Roquemore AL, Bader A, Wampler WR et al (2004) Deposition diagnostics for next-step devices, Review of Scientific Instruments 75, 4213, Copyright 2004, American Institute of Physics

Stockel J, Adamek J, Balan P, Bilyk O, Brotankova J, Dejarnac R, Devynck P, Duran I, Gunn JP, Hron M, Horacek J, Ionita C, Kocan M, Martines E, Panek R, Peleman P, Schrittwieser R, Van Oost G, Zacek F (2007) Advanced probes for edge plasma diagnostics on the CASTOR tokamak. J Phys Conf Ser 63:012001

Stott PE, Gorini G, Prandoni P, Sindoni E (eds) (1998) Diagnostics for experimental thermonuclear fusion reactors 2. Plenum Press, New York, ISBN 0-306-45835-7

Strait EJ, Fredrickson ED, Moret J-M, Takechi M (2008) Chapter 2: Magnetic diagnostics. Fusion Sci Technol 53:304

Stratton BC, Bitter M, Hill KW, Hillis DL, Hogan JT (2008) Chapter 5: Passive spectroscopic diagnostics for magnetically confined fusion plasmas, Fusion Sci Technol 53, 431, Figs. 5 and 26, and Table 1. Copyright by the American Nuclear Society, LaGrange Park, Illinois, USA

Terry JL, Lipschultz B, Pigarov AYu, Krasheninnikov SI, LaBombard B, Lumma D, Ohkawa H, Pappas D, Umansky M (1998) Volume recombination and opacity in Alcator C-mod plasmas. Phys Plasmas 5:1759

Texter S, Knowlton S, Porkolab M, Takase Y (1986) high energy x-ray measurements during lower hybrid current drive on the Alcator C Tokamak. Nucl Fusion 24:1279

Thomas DM, McKee GR, Burrell KH, Levinton F, Foley EL, Fishera R K(2008) Chapter 6: Active spectroscopy. Fusion Science and Technology 53, 487, Figs. 1, 2, and 9. Copyright by the American Nuclear Society, LaGrange Park, Illinois, USA

Van Oost G (2008) Advanced probe edge diagnostics for fusion devices. Trans Fusion Sci Technol 53:387

Vayakis G, Walker C (2002) Magnetic diagnostics for ITER/BPX plasmas, presented at the HTPD, Madison, Wisconsin, July, Fig. 18. Copyright by the American Nuclear Society, LaGrange Park, Illinois, USA

Vayakis G, Hodgson ER, Voitsenya V, Walker CI (2008) Chapter 12: Generic diagnostic issues for a burning plasma experiment. Fusion Science and Technology 53, 699. Copyright by the American Nuclear Society, LaGrange Park, Illinois, USA

Vayakis G, Arshad S, Delhom D, Encheva A, Giacomin T, Jones L, Pate KM, Pérez-Lasala M, Portales M, Prieto D, Sartori F, Simrock S, Snipes KA, Udintsev VS, Watts C, Winter A, Zabeo L (2012) Development of the ITER magnetic diagnostic set and specification, Rev Sci Instrum 83, 10D712 (2012), Fig. 1. Reprinted with permission Review of Scientific Instruments, Copyright 2012, American Institute of Physics

Voitsenya V et al (2001) Diagnostic first mirrors for burning plasma experiments. Rev Sci Instrum 72:475

Walker SE, Preszler AM, Millard WA (1986) Double scatter neutron time of flight spectrometer as a plasma diagnostic. Rev Sci Instrum 57:1740–1742 (Fig. 4)

Wesson J (2011) Tokamaks, 4th edn. Oxford University Press, Oxford (Chap. 10)

Young KM (2002) Alpha particle measurements needed for burning plasma experiments, in Stott PE et al (eds) Advanced diagnostics for magnetic and Inertial Fusion, Kluwer Academic/Plenum, New York

Young KM (2008) Chapter 1: Plasma measurements: an overview of requirements and status. Fusion Sci Technol 53:281

Chapter 12
Safety and Environment

Thomas J. Dolan and Lee C. Cadwallader

Objectives

After reading this chapter one should understand

Tritium issues
Other radioactive materials in fusion reactors
Hazards associated with fusion power plants
Safety analysis techniques.

12.1 Introduction

A power plant interacts with the environment in many ways, as illustrated in Fig. 12.1.

Most of these apply to all types of power plants using heat engines (solar, fission, fusion, and fossil fuel). Tritium and other radioactive materials are the main environmental concerns of fusion reactors, but other issues must also be considered (Table 12.1).

Environmental and cost requirements will be the main basis for comparison between solar, wind, fission, fossil, and fusion power sources.

12.2 Tritium

Tritium is the isotope of hydrogen containing two neutrons in the nucleus. It decays by beta emission with a 12.3 year half-life into ^{3}He.

T. J. Dolan (✉)
NPRE Department, University of Illinois, Urbana, IL 61801, USA
e-mail: dolantj@illinois.edu

L. C. Cadwallader
Idaho National Laboratory Battelle Energy Alliance, LLC, Idaho Falls, ID, USA
e-mail: lee.cadwallader@inl.gov
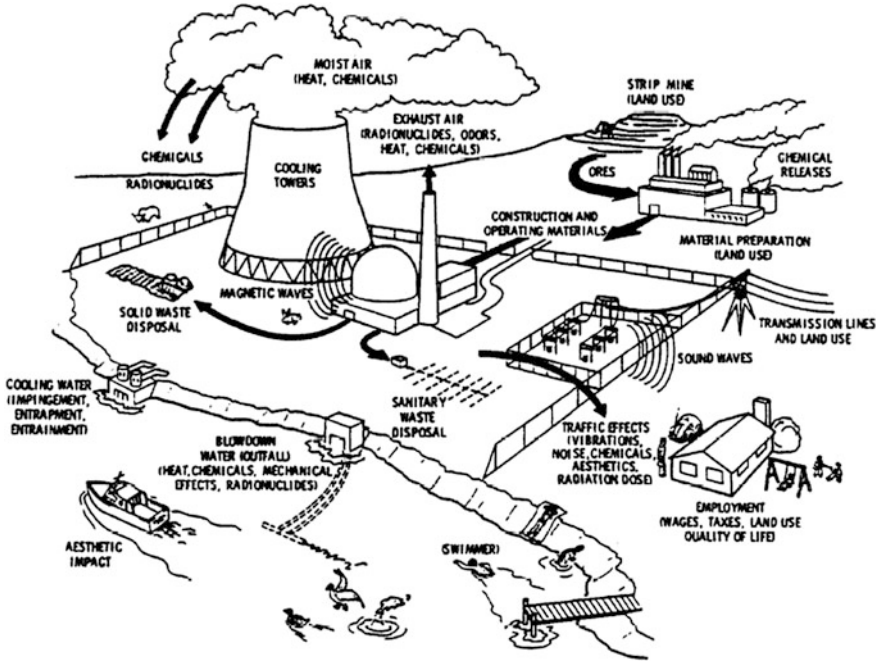
Fig. 12.1 Interactions of a power plant with the environment (Young 1976)

Table 12.1 Environmental and other hazards of fusion power plants

Routine tritium releases	Effects of stray magnetic fields
Disposal of activated structure	Plant decommissioning
Accidental releases	Proximity to
Tritium	Industry
Activated materials	Cities
Chemical discharges	Transportation facilities
Thermal discharge to water or air	Earthquakes, floods, storms
Stored energy release	Effects on local economic and
Liquid metal fire	Social conditions
Magnet coils	Aesthetic impact
Radioactive afterheat	
Atmospheric pressure on chamber	

$$T \rightarrow {}^3He + \beta + v^*(v^* = \text{ antineutrino}) \qquad (12.1)$$
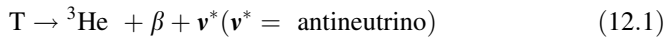
Its radioactivity makes it hazardous to humans. Since hydrogen isotopes can diffuse through materials, containment of the tritium is a major safety concern.

12.2.1 Tritium Inventory

There are three incentives for keeping the power plant tritium inventory low:

- Initial cost.
- Radioactivity hazard of tritium release to environment.
- Hydrogen embrittlement of structure.

Some early fusion reactor designs had inventories on the order of 10–20 kg. Modern designs try to keep the in-vessel inventory around 1–2 kg. Example Problem 12.1 is a simple estimate of blanket tritium inventory. There will be additional inventory in storage, tubing, pumps, valves, and processing systems.

Example Problem 12.1: A 2.5 GW_{th} DT fusion reactor has a wall surface area of 2,500 m^2 and the blanket contains a layer of Li 0.8 m thick. If the blanket contains 3 appm(T), what is the blanket tritium inventory (kg)?

The density of lithium is about 450 kg/m^3, and the atomic weight of lithium is 6.839×10^{-3} kg/mole, so its atomic density is found to be n = 3.906×10^{28} atoms/m^3. The lithium volume is 2,000 m^3, so the total number of lithium atoms is 7.8×10^{31}. The number of tritium atoms is then 2.34×10^{26}, and the tritium inventory in the blanket is 1.17 kg.

Some radiological properties of tritium are listed in Table 12.2.

The biological half-life refers to the time during which half of the tritium is eliminated from the body by urination, perspiration, and exhalation. The Derived Air Concentration (DAC) is the level which, if breathed by a worker for a working year of 2,000 h, leads to 20 mSv dose. This is the level at which evacuation from the contaminated room is triggered.

A person typically receives an annual dose of about 1 mSv from natural background radiation (cosmic rays, etc.), plus about 1 mSv due to inhalation of natural gaseous decay products of U and Th (such as Rn-222 and Rn-220). Tritium

Table 12.2 Radiological aspects of tritium

Abundance in upper atmosphere	kg	~10
Atomic mass	u	3.01605
Atomic mass	kg	5.00835×10^{-27}
Beta decay half-life	yr	12.3
Maximum beta energy	keV	18.5
Average beta energy	keV	5.7
Decay constant λ	s^{-1}	1.787×10^{-9} Bq
Biological half-life in humans	day	~10
Activity of 1 kg tritium	Bq	3.57×10^{17}
Activity of 1 kg tritium (1 Ci = 3.7×10^{10} Bq)	MCi	9.64
Dose from ingestion of 1 mg tritium	Sv	15
(1 Bq → dose of 4.2×10^{-11} Sv)		
Derived air concentration (DAC, see below)	Bq/m^3	3.0×10^5

is one of the least hazardous radionuclides. Its aqueous forms (T_2O, THO, TDO) are more hazardous than its gaseous forms (T_2, TH, TD). Aqueous forms do not disperse as readily as gaseous forms, and they can enter tissue more easily. If only gaseous TH, TD, or T came in contact only with skin, it would pose little hazard, because its maximum energy beta particles cannot even penetrate the exterior dead skin layer (an energy of 70 keV is required for penetration). However, if the TH, TD, or T_2 is inhaled, it may become THO, TDO, or T_2O and stay in the body in aqueous form, with danger to the body. Thus, it is usual to assume conservatively that all of the tritium released is in aqueous form.

12.2.2 Biological Hazard

If N_0 atoms of a radioactive element are present at time $t = 0$, the number N present at any later time is

$$N = N_o e^{-\lambda t}, \tag{12.2}$$

where

$$\lambda = \ln 2 / t_{1/2} (Bq) \tag{12.3}$$

is the decay constant, and $t_{1/2}$ is the half-life (s). When $t = t_{1/2}$, $N = 0.5 N_o$, hence the name "half-life." The activity of a radioisotope is

$$\text{Activity} = N\lambda \quad (Bq) \tag{12.4}$$

where the unit Becquerel (Bq) represents disintegrations per second. Units of radioactivity are defined in the Appendix.

12.2.3 Tritium Production Rate

The tritium consumption rate $= P/W'_{DT}$ (atoms/s), where P is the reactor thermal power (including blanket reactions), and the energy released per fusion

$$W'_{DT} = 1.6 \times 10^{-13}(3.5 + 14.1\,M)\,(J) \tag{12.5}$$

and M is the blanket energy gain. Typically $M \approx 1.2$, and $W'_{DT} \approx 3.2 \times 10^{-12}$ J. For example, if $P = 2.5\,GW_{th}$, then the tritium consumption rate $\approx 7.8 \times 10^{20}$ atoms/s, which corresponds to a mass consumption rate of 0.34 kg(T)/day. By definition, the tritium breeding ratio

$$R_B = (\text{production rate})/(\text{consumption rate}). \tag{12.6}$$

If $R_B = 1.2$ in the above example, then tritium would be produced at the rate of 9.4×10^{20} atoms/s $= 0.41$ kg/day. At the same time, the tritium is decaying radioactively with a time constant $\lambda = 1.79 \times 10^{-9}$ Bq. If N is the total number of tritium atoms in the system, its rate of change is given by the equation

$$dN/dt = R_B P/W'_{DT} - P/W'_{DT} - \lambda N. \tag{12.7}$$

Taking $N = N_o$ at $t = 0$, the solution is

$$N/N_0 = (1/x)\left(1 - e^{-\lambda t}\right) + e^{-\lambda t}, \tag{12.8}$$

where

$$x \equiv \frac{W'_{DT}\lambda N_0}{P(R_B - 1)}. \tag{12.9}$$

This equation may be solved for t:

$$t = \frac{1}{\lambda}\ln\left[\frac{1 - x}{1 - xN/N_0}\right]. \tag{12.10}$$

If $R_B > 1$ the quantity of tritium will increase with time. Let t_2 be the time at which $N = 2N_o$, the "doubling time". If $x \ll 1$ the logarithm terms can be expanded in a Taylor series to obtain

$$t_2 = (x/\lambda)(1 + 3x/2 + \cdots) \quad (s). \tag{12.11}$$

We will show that tritium fuel for fusion reactors has a much shorter doubling time than fissile fuel. In fission breeder reactors the decay rates of ^{239}Pu and ^{233}U are negligibly small, so we may set $\lambda = 0$ in Eq. (12.8) and find

$$N/N_0 = 1 + Pt(R_B - 1)/N_0 W,$$
$$t_2 = N_0 W/P(R_B - 1) \tag{12.12}$$

where $W = 200$ MeV $= 3.2 \times 10^{-11}$ J. Example Problem 12.2 compares fission and fusion fuel doubling times.

Example Problem 12.2: Fuel Doubling times Estimate the fuel doubling times of (a) a 2.5 GWth fusion reactor with 10 kg of T, (b) a 2.5 GWth fission breeder with 10^4 kg of fuel, assuming both have $R_B = 1.2$.

(a) For the fusion reactor $N_0 = 10$ kg/$(5.008 \times 10^{-27}$ kg/atom$) = 2.00 \times 10^{27}$ atoms (T). Then $x = 2.29 \times 10^{-2}$, and $t_2 = 1.32 \times 10^7$ s $= 5.1$ months.
(b) For the fission reactor, $N_0 = 10^4$ kg/$(238$ u$)(1.66 \times 10^{-27}$ kg/u$) = 2.53 \times 10^{28}$ atoms. Then $t_2 = 1.62 \times 10^9$ s $= 51$ years.

In general the doubling times for fission breeders are much longer than for tritium in fusion reactors of the same power.

Table 12.3 ARIES-AT in-vessel tritium inventory (Petti 2006, Table 1)

Component	Inventory, g
First wall	540
Divertor	55
PbLi coolant	<1
Co-deposited layers	150
Total	745

The mass flow rate $\dot{m}$ of tritium through a fusion reactor plasma is

$$\dot{m} = (\text{consumption rate})m_t/f_b = Pm_t/W'_{DT}f_b \quad (\text{kg/s}) \qquad (12.13)$$

where m_t is the mass of one tritium atom (kg), and f_b is the burnup fraction. For a 2.5 GW_{th} reactor with $f_b = 0.05$,

$$\dot{m} \cong 7.8 \times 10^{-5} \text{kg/s} = 6.8 \text{kg/day} \qquad (12.14)$$

The site tritium inventory limit of the JET tokamak is 20 g, and that of ITER is about 4 kg, with an in-vessel limit of 1 kg. The tritium codeposited in films on the ITER walls is estimated to increase by about 10–20 g per 1,000 s pulse, so removal of this tritium is important (Federici 1999).

The ARIES-AT tritium inventory is shown in Table 12.3.

(These values are for T trapped in in-vessel components and vulnerable for release in an accident. They do not include the T in the breeder, in the fuel cycle, and in storage, which would total several kg.) In contrast, an earlier tokamak design had about 20 kg of tritium. This great reduction illustrates an improvement of safety in later designs.

12.2.4 Routine Emissions

Tritium may flow out of the reactor through the following pathways:

- Vacuum pumping system
- Coolant system
- Blanket tritium removal system (if separate from coolant)
- Permeation through chamber walls
- Outgassing from removed components in storage awaiting disposal.

Secondary containment will be provided around the vacuum system and chamber walls.

The limits on tritium release to the air will probably require a dose at the site boundary of less than 50 μSv/a. For typical atmospheric conditions (dilution factor $\chi/Q = 10^{-5}$), this means that the releases to the air must be kept to about 1.5 TBq/day

(40 Ci/day). On a global scale, if each fusion reactor emitted 1.5 TBq/day into the air, then 1,000 such plants would emit about 5.5×10^{17} Bq/a (Here a = annum = year). Cosmic rays also produce about 2.0×10^{17} Bq/a of tritium in the stratosphere. ITER is limited to about 0.6 g/a, an average of 0.59 TBq/day (16 Ci/day).

The effects of long-term low-level exposure to radiation are under debate. The "linear no-threshold" model, which has been used for decades, leads to very strict regulations, which are expensive to implement and may result in unnecessary hazardous evacuations (Tubiana et al. 2009).

12.2.5 Tritium Permeation Rates

Consider the case of tritium permeation through a wall of thickness x_1 with tritium pressures p_1 on one side and p_2 on the other, with $p_2 < p_1$. Let $c(x)$ denote the tritium atom concentration within the wall. Usually, molecular recombination must occur before the tritium can leave the wall. At low driving pressures p_1, surface molecular recombination may be the tritium flow rate-limiting process. At high pressure p_1, or with fluids (such as liquid metals) capable of carrying atomic tritium on the p_2 side, diffusion through the wall is the rate-limiting process. These two cases are illustrated in Fig. 12.2.

The concentration at $x = 0$ may be estimated from *Sievert's Law*

$$c(0) = S p_1^{1/2} \quad (\text{atoms/m}^3), \tag{12.15}$$

where S is the "solubility" of tritium in the given metal (atoms/m^3 Pa$^{1/2}$).

For the case of *recombination-limited flow*, the maximum flow rate may be estimated from

$$J_{\text{rec}} = K c^2(x_1) \leq K c^2(0) = K S^2 p_1 \, (\text{atoms/m}^2 \text{s}), \tag{12.16}$$

where the surface recombination coefficient K (m^4/s) was given in Fig. 8.19 for a few metals.

Fig. 12.2 Distribution of tritium atom concentration c(x) in a tube wall. **a** permeation rate limited by diffusion in the wall. **b** permeation rate limited by surface recombination
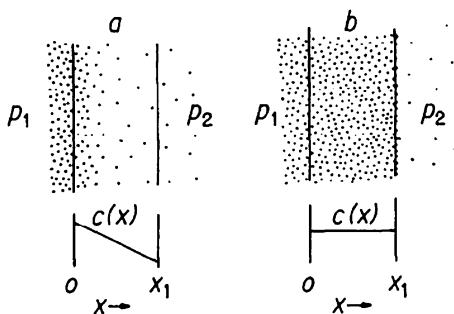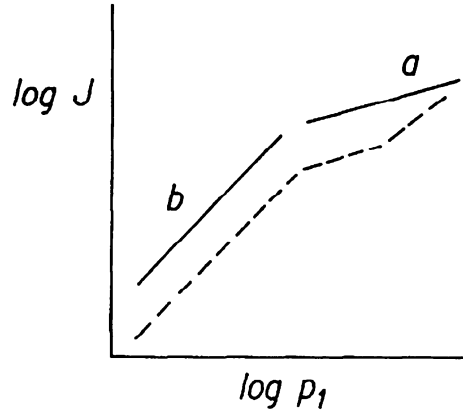
For the case of *diffusion-limited* flow, the concentration at $x = x_1$ may also be estimated from Sievert's Law

$$c(x_1) = Sp_2^{1/2} \; (atoms/m^3). \qquad (12.17)$$

Using Fick's Law for the diffusion flow rate, we obtain *Richardson's Equation*:

$$\begin{aligned} J_{dif} &= -D(dc/dx) = -D[c(x_1) - c(0)]/x_1 \\ &= DS\left(p_1^{1/2} - p_2^{1/2}\right)/x_1 \; (atoms/m^2s), \end{aligned} \qquad (12.18)$$

where D is the diffusion coefficient (m^2/s). The product DS is called the "permeation coefficient" or "permeability." The variation of J with p$_1$ is illustrated in Fig. 12.3.

The diffusion and solubility coefficients may be expressed in terms of the wall temperature T(K)

$$D \cong D_0 exp(-E_d/kT) \; (m^2/s) \qquad (12.19)$$

$$S \cong S_0 exp(-E_S/kT) \quad (atoms/m^3 Pa^{\frac{1}{2}}) \qquad (12.20)$$

where E$_d$ and E$_s$ are activation energies for diffusion and solution, k is the Boltzmann constant, and D$_o$ and S$_o$ are constants. Some values of these constants for ordinary hydrogen in various metals are given in Table 12.4.

Diffusion rates are inversely proportional to the square root of the isotopic mass, so

$$D_o(T) = 0.58D_o(H) \qquad (12.21)$$

Values of the permeability DS of hydrogen in various metals are shown in Fig. 12.4.

An approximate expression for the surface recombination coefficient is

$$K \cong (8/MT)^{\frac{1}{2}}(c_1\alpha/S_0^2)exp[(2E_s - E_x)/kT] \; (m^4/s), \qquad (12.22)$$

Table 12.4 Diffusion and solubility coefficients for hydrogen in various metals. Some values of S_o and D_o have large errors ($\sim 50\ \%$) (Baskes 1980; Cecchi 1979; Perkins 1973)

Metal	S_0 10^{23} atoms/ m^{3}Pa$^{\frac{1}{2}}$	E_s eV	D_0 10^{-7} m^2/s	E_d eV
Ni	9.7	0.16	4.0	0.41
Fe(bcc)	6.3	0.28	0.78	0.08
Fe(fcc)	14.0	0.32	6.7	0.47
Al	5.6	0.66	110.0	0.43
Ti	4.7	−0.50	18.0	0.54
Zr	20.0	−0.63	4.2	0.41
Mo	4.2	0.22	4.8	0.39
304 SS	1.1	0.061	4.7	0.56
Inconel 625	2.2	0.13	7.6	0.50
Cu	4.8	0.40	11.0	0.40

where M = atomic weight (u) of the metal, $\alpha \cong 0.5$ is the sticking coefficient,

$$c_1 = 2.60 \times 10^{24}\ \text{K}^{\frac{1}{2}}\text{u}^{\frac{1}{2}}/\text{Pa} - \text{s} - \text{m}^2 \tag{12.23}$$

and

$$E_X = \begin{cases} E_s + E_d, & \text{if } E_s + E_d > 0 \\ 0 & \text{otherwise.} \end{cases} \tag{12.24}$$

(Baskes 1980).

Fig. 12.4 Permeation coefficient versus reciprocal temperature, for hydrogen in various metals. T is in Kelvin (Fraas 1975)
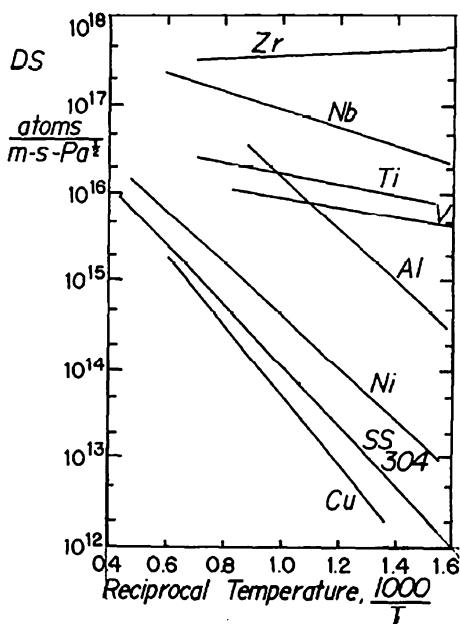
Example Problem 12.3: A steam generator with total tube surface area 2,000 m^2 has Ni tubes 2 mm thick at 800 K, with a partial pressure of 10^{-5} Pa tritium on the primary coolant side and a negligible tritium pressure on the steam side. Estimate the leakage of tritium (Ci/day) into the steam system.

We calculate both diffusion-limited flow and recombination-limited flow, to see which is lower. For diffusion-limited flow, from Eqs. (12.19) and (12.20) we find $DS = 9.5 \times 10^{13}$ atoms/m^{3}s$-$Pa$^{1/2}$ for hydrogen, or 5.5×10^{13} for tritium. (The value from Fig. 12.4 is $DS = 7 \times 10^{13}$ atoms/m^{3}s$-$Pa$^{1/2}$, but the graph is less accurate.) From Richardson's Equation with $p_1 \ll p_2$, we find $J_{dif} = 8.7 \times 10^{13}$ atoms/m^{2}s.

For recombination-limited flow, from Eq. (12.22) we find $K \approx 4.8 \times 10^{-28}$ m^4/s. From Eq. (12.16) $J_{rec} \le 4.4 \times 10^{13}$ atoms/m^{2}s, so the flow is recombination limited. The total atom flow rate $J_{rec}A \le 8.7 \times 10^{16}$ atoms/s, which represents an activity of $\lambda J_{rec}A \le 1.6 \times 10^8$ Bq/s = 360 Ci/day.

Since the two rate-limiting processes are in series, we could estimate the net effect using a reciprocal sum:

$$1/J \approx 1/J_{dif} + 1/J_{rec}$$

Here this yields $J \approx 2.9 \times 10^{13}$ atoms/m^{2}s, which might be more accurate, but for a conservative estimate it may be safer to use the smaller of J_{dif} and J_{rec}.

Due to parameter uncertainties, such estimates are highly uncertain. Cracks in materials could facilitate higher permeation rates, and oxide films could reduce permeation rates by orders of magnitude (dashed curve, Fig. 12.3). Low-permeation tube coatings are under development. If necessary an intermediate "barrier" coolant loop may be used to reduce tritium leakage into the steam generator, as shown in Fig. 12.5. Tritium can be trapped in co-deposited films on plasma-facing surfaces (Baldwin 2005).

The intermediate coolant could be a fluid with good compatibility and a low fire hazard, such as molten nitrate-nitrite salt. Use of an intermediate loop, however, would increase capital costs and lower steam temperature and thermal efficiency.

12.2.6 Tritium Recovery Systems

Tritium can be removed from the vacuum system by cryogenic distillation or by diffusion through permeable membranes. Tritium removal from the blanket and coolant, however, is more difficult, because of the need to keep the partial pressure of tritium very low. (In Example Problem 12.3, a pressure $p_1 = 10^{-5}$ Pa led to an excessive release rate.)

There must be a tritium removal system for the coolant. There may also be a direct tritium removal system for the blanket (such as a "purge stream" of He). Some techniques for recovery of tritium from the blanket and coolant are shown in Table 12.5.
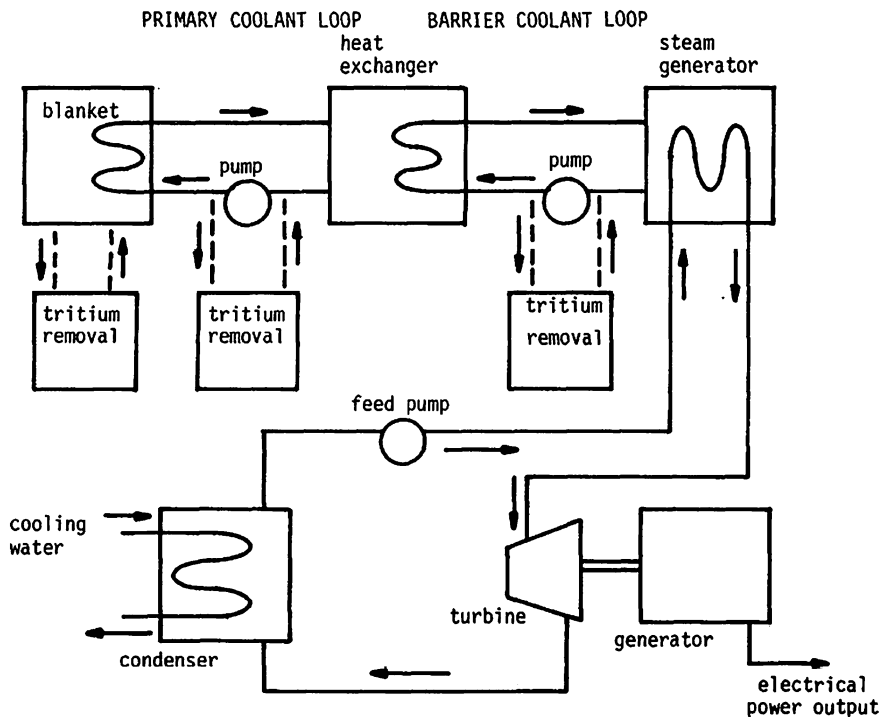
Fig. 12.5 Flow diagram for a system using an intermediate "barrier" coolant loop to reduce tritium leakage into the steam system

Water **distillation** uses the boiling point difference (1.5 °C) between tritiated water and ordinary water. However, due to the low relative volatility (p(H20)/p(HTO) = 1.056) and the high throughput (0.38 m³/min), water distillation requires several hundred boiling plates, a high reflux ratio (>25), and multiple

Table 12.5 Some tritium removal methods

Fluid	Removal method
Water	Boiling temperature difference
Water (ITER)	Electrolysis and catalysis
PbLi	Diffusion into He gas and extraction from He
PbLi	Permeation through window (such as Nb) into tritium removal tubes
He	Oxidation by O_2, then condensation in cold trap
He	Diffusion through Nb or Pd window into vacuum (only if high tritium pressures are allowable)
He	Solid sorbents, if high tritium pressures are allowable
Molten salt	Spray droplets into vacuum
Molten salt	Bubble He through molten salt

large diameter distillation columns (~ 8 m) for large facilities, like the Hanford Laboratory (Washington, USA). This process is large, energy intensive, and expensive (DOE 2009).

Combined electrolysis catalytic exchange (CECE) uses the hydrogen/water exchange equilibrium reaction that favors formation of liquid HTO when liquid H_2O is contacted with tritiated hydrogen (HT) gas

$$HT(g) + H_2O(1) \rightarrow HTO(1) + H_2(g).$$
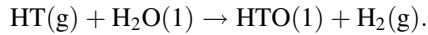
Then the mixture of HTO and H_2O is electrolyzed in the presence of a catalyst (such as Pd), separating some of the water into H_2, HT, and O_2 gases. Since H_2O is electrolyzed faster than HTO, the HTO concentration remaining in the liquid gradually increases.

The **ITER** project is developing CECE based water detritiation using solid polymer electrolyte cells and gas/liquid phase catalytic exchange columns to process 60 kg/h of wastewater (3 systems, each 20 kg/h). A cryogenic isotope separation system will be used for recovery of concentrated tritium from the partially concentrated product of the CECE system. Atomic Energy of Canada, Limited (AECL) built a pilot plant with a 7.5 kA electrolysis cell and a 5 cm diameter column with a total water flow of approximately 1.5 L per hour, which achieved a detritiation factor over 30,000 (DOE 2009).

Tritium may be extracted from **PbLi** flowing through a permeable tube (such as Nb) by diffusion through the tube wall into a vacuum. The performance depends strongly on the mass transfer coefficient, which depends on temperature, flow velocity, surface conditions, etc. The permeator might have parameters like the following:

- PbLi flow rate for Demo: 26,270 kg/s
- With 1 cm dia. tubes and 5 m/s flow velocity: 7,592 tubes
- Total Nb required for 5 m tubes: 2.6 t
- Diameter of vessel to contain tube cross sections + twice that area for space between tubes: 1.7 m.

The following permeator system issues need to be resolved:

- Mass transfer coefficients for the PbLi-T system
- Compatibility of PbLi with Nb at 700 C
- Surface resistance to tritium permeation
- Effective partial pressure of tritium at the PbLi-membrane interface
- Nb tube degradation (such as by oxidation) (Willms 2007).

Recovery from **Flibe molten salt** may be done with a spray of hot droplets into a vacuum chamber ("vacuum disengager"), as illustrated in Fig. 12.6.

Figure 12.7 shows the vacuum disengager for tritium removal from Flibe molten salt.
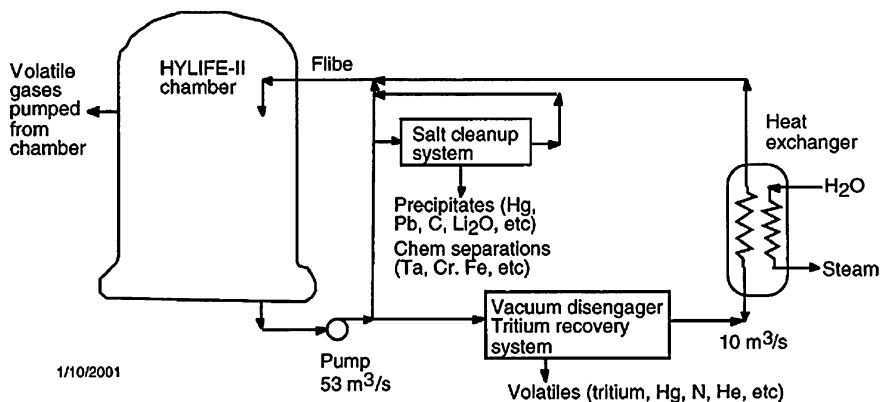
Fig. 12.6 The HYLIFE-II inertial confinement fusion reactor blast chamber, Flibe coolant loop, steam generator, and vacuum disengager tritium recovery system
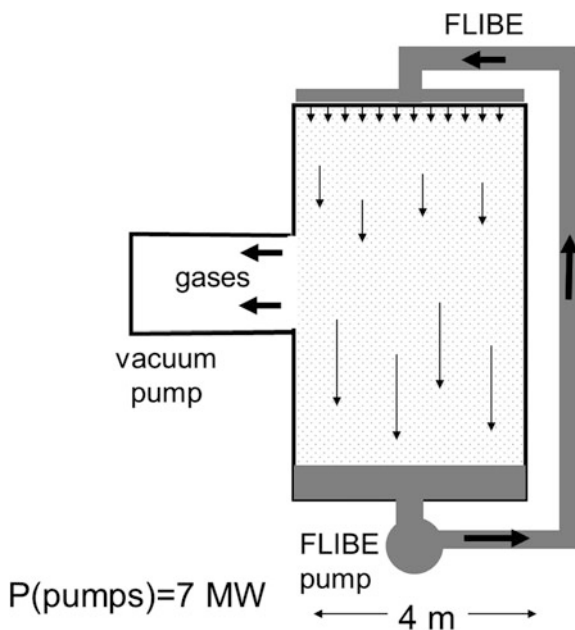
Fig. 12.7 The HYLIFE-II vacuum disengager. Molten salt droplets fall down through a vacuum (Dolan et al. 1992)

Tritium diffuses out of the hot 0.4 mm diameter droplets of LiF-BeF$_2$ (Flibe) as they fall downward in the large vacuum chamber. The exhaust gas containing tritium is removed by the vacuum pumps. This system removes most of the

8.6 MCi/day of tritium that is bred in the FLIBE. About 10^{-5} of the source remains in the Flibe, causing ~ 11 Ci/day tritium leaks into steam system. The estimated system cost in 1994 was 92 M\$, of which

Vacuum disengagers 56 %

Blast chamber vacuum system 15 %

Cryogenic plant 9 %

And the rest is air cleanup systems, waste treatment, protium removal system, storage system, inert gas system, and other components.

12.2.7 Accidental Tritium Release

During an accident the tritium released into the air would probably be in gaseous form, rather than HTO, so it would tend to diffuse and disperse more rapidly than HTO. Tritium gas, being much lighter than air, tends to rise and spread out. These potentially beneficial effects are ignored in conservative estimates, which assume that tritium releases are in aqueous form (HTO, DTO, or T_2O). The aqueous form is much more dangerous to humans: for instance, the Annual Limit of Intake (ALI) for HTO is 20,000 times lower than that for HT, so HTO is much more radiotoxic than HT.

If 1 kg of tritium (3.57×10^{17} Bq, approximately 10 MCi) were released as HTO from a fusion reactor under the worst atmospheric conditions [no thermal plume rise; very stable atmosphere (Pasquill condition F); mean wind $= 1$ m/s, dry deposition velocity $= 1$ cm/s], there would be no area receiving a prompt lethal dose of about 3 Sv (300 rem), as can be seen from the 10 MCi curve in Fig. 12.8.

It is desired to keep the tritium release low enough that site evacuation plans would not be necessary (Sect. 12.5). Tritium loss could also be expensive, since its replacement cost is high.

12.2.8 Tritium Supply and Cost

A 1,000 MW fusion power reactor would require about 56 kg/year of tritium, but ITER would use much less, due to its lower power and duty cycle. About 3 kg would be required for ITER startup. After that some tritium would be produced in the tritium breeding blanket modules.

Tritium is produced in the Canadian CANDU reactors by neutron absorption in deuterium, and in nuclear weapons programs of several countries by neutron absorption in lithium. About 19 kg of tritium were available in 2003, and 1.5 kg/year are recovered from the CANDU reactors. The cost of tritium in Canada (2004) was about 30 M\$/kg. The estimated future cost of tritium production in the USA was about 100 M\$/kg (Willms 2004).
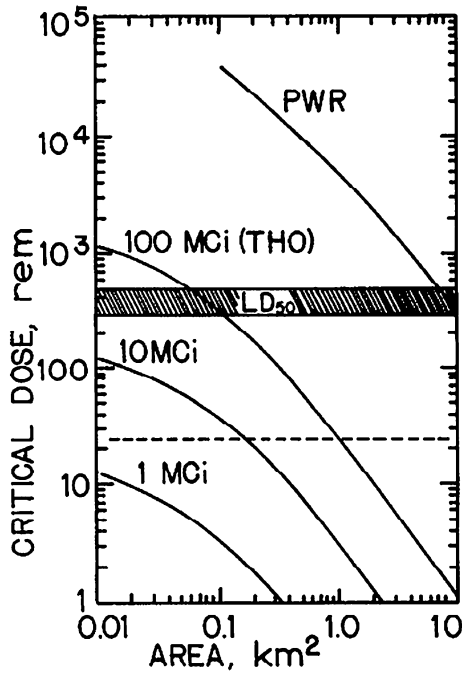
Fig. 12.8 Critical dose to bone marrow versus area receiving that dose for "worst possible case" accidents of a fission reactor (PWR) and of fusion reactors with various THO releases. A dose of 0.25 Sv (25 rem) is considered an emergency (*dashed line*). "Critical dose" means 100 % of the dose delivered in the first several days plus half the dose delivered in from days 8 to 30. The LD50 is the dose fatal within 60 days to half those exposed, in the absence of heroic medical measure. Redrawn from J. P. Holdren, Science 200 (1980) 168–180, Figure 4, © 1978 by the American Association for the Advancement of Science. Reprinted with permission from AAAS

After fusion reactor shutdown many materials must be decontaminated. Tritium decontamination techniques include (Zucchetti 2012)

- Plasma and glow discharges
- Vacuuming and purging
- Cleaning and washing
- Chemical and electrochemical etching
- Thermal desorption of tritium from 650 to 700 °C in hydrogen atmosphere (isotopic exchange of protium and tritium facilitates the removal of tritium from near surface regions).

12.3 Other Radioisotopes

In addition to tritium, other radioisotopes can be generated wherever the neutron flux is significant, such as in the first wall, divertor, blanket, coolant, shield, and ports for heating and diagnostics. Fusion reactor designs should

- Calculate radioisotope production rates
- Calculate decay heat and dose rates
- Minimize long-lived radioactivity by selection of materials
- Plan for decommissioning and disposal.

12.3.1 Production

Let n represent the densities of various isotopes (atoms/m^3), λ represent their decay constants (Bq), σ represent their neutron absorption cross sections (m^2), and ϕ represent the neutron flux (neutrons/m^{2}s). Consider the case in which isotope B is produced by neutron absorption in isotope A and by radioactive decay of isotope C. Then the rate of change of the density of B is given by

dn_B/dt = (production from A) + (production from C)—(loss by radioactive decay)—(destruction by neutron absorption)

$$dn_B/dt = n_A \sigma_A \phi + \lambda_c n_c - \lambda_B n_B - n_B \sigma_B \phi \qquad (12.25)$$

Here $\sigma_A \phi$ and $\sigma_B \phi$ represent values integrated over the neutron energy spectrum. Let the initial density of isotope B be n_{Bo}. The solution of this equation is

$$n_B(t) = n_{B_0} e^{-\alpha t} + \sigma_A \phi e^{-\alpha t} \int_0^t dt' n_A(t') e^{\alpha t'} + \lambda_C e^{-\alpha t} \int_0^t dt' n_C(t') e^{\alpha t'} \qquad (12.26)$$

where

$$\alpha \equiv \lambda_B + \sigma_B \phi$$

In general A may be considered constant over a time span of a few days, because only a tiny fraction of it is destroyed by transmutations, and $n_c \lambda_c$ will be very small if isotope C is stable or has a very long half-life. For simplicity we will consider the special case where $n_c \lambda_c$ is negligible and n_A is a constant. If neutron irradiation ends at time t_1, then the concentration of B at later times is

$$n_B(t > t_1) = [n_{B_0} e^{-\alpha t_1} + (n_A \sigma_A \phi/\alpha)(1 - e^{-\alpha t_1})]\exp[-\lambda_B(t - t_1)] \qquad (12.27)$$

The activity of B is $\lambda_B n_B$.

Fig. 12.9 Neutron activation chains of vanadium (Steiner 1972)
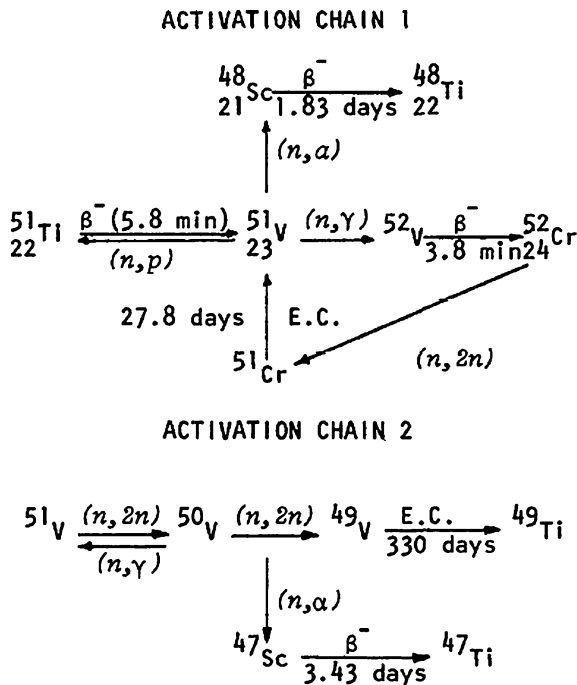
To illustrate the calculation of radioisotope production, we will consider the decay chains of vanadium, Fig. 12.9.

Natural vanadium consists of 0.25 % ^{50}V and 99.75 % ^{51}V.

The isotope $^{48}_{21}$Sc is produced by the reaction chain

$$^{51}_{23}V + n \rightarrow {}^{52}_{23}V \rightarrow {}^{48}_{21}Sc + {}^{4}_{2}He \qquad (12.28)$$
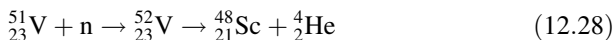
and it decays by beta emission to $^{48}_{21}$Ti with a half-life of 1.83 days (the compound nucleus ^{52}V also has several other modes of decay, the most probable being emission of two neutrons).

Example Problem 12.4: Scandium activity The density of natural vanadium is 7.212×10^{28} atoms/m^3, and the cross section for reaction (12.28) is about 0.2 barn. (One barn $= 10^{-28}$ m^2). Assume that the average neutron flux is 10^{18} m^{-2}s^{-1} in a blanket region containing 10 m^3 of V. The reactor operates continuously for 30 days, and then shuts down. Find the activity of ^{48}Sc 1 week after shutdown, assuming that its initial density is zero, its neutron absorption cross section is negligible, and the density of ^{51}V is roughly constant.

For this case $n_A = 0.9975(7.212 \times 10^{28}) = 7.194 \times 10^{28}$ m^{-3} and $\sigma_B = 0$.

The decay constant of ^{48}Sc is $\lambda_B = \ln 2/t_{1/2} = 0.379$/day, so $\alpha = 0.379$/day $= 4.38 \times 10^{-6}$ s^{-1}.

From Eq. (12.27), with $t_1 = 30$ days, $(t-t_1) = 7$ days, $n_{Bo} = 0$, $\sigma_A = 2 \times 10^{-29}$ m^2, we find $n_B = 2.31 \times 10^{22}$ m^{-3}.

The activity of ^{48}Sc at that time is $\lambda_B n_B V = 1.01 \times 10^{18}$ Bq $= 27$ MCi, where V is the volume of that blanket region.

Three safety concerns are associated with a molten salt blanket:

- Stored Heat
- Chemical toxins—Be and LiF
- Radioisotopes—such as ^{18}F and ^{3}H (tritium)

Workers could be protected from these hazards during an accident by standard precautions, such as protective clothing, ventilation control, or evacuation (Cadwallader and Longhurst 1999).

The materials used in a fusion power plant should be chosen to minimize long-lived radioactivity. It would be best to choose materials that can be cleared (released from regulatory control) for public use following a reasonable decay time (<100 years). Materials that cannot be cleared should be recycled, if feasible. For example, some radioactive metals might be recycled in the nuclear industry using remote handling. The goal is to minimize materials than cannot be either cleared or recycled, which would become long-lived radioactive waste.

For example, reduced activation ferritic and martensitic (RAFM) steels are favored structural materials, and plasma facing components like tungsten alloys should avoid elements that generate long-lived radioisotopes (Sects. 6.2, 6.5).

12.3.2 Radioactive Materials

If the structural radioactivity decays sufficiently in less than 100 years, it may be feasible to store the materials on site and then reprocess them.

One study estimated the dose to a machinist working 8 h/day, 260 days/year at distances of 2–10 m from a 1 m sphere of recycled metal. With SS-316 structure 50 years decay reduced the annual dose below 5 mSv. (Botts and Powell 1978). SS-316 is used in ITER, but will not be used in future devices, because RAFM steels have much lower activation.

The International Atomic Energy Agency (IAEA) has developed clearance standards for 1,650 radioisotopes, which would keep doses below 10 μSv (1 mrem) per year. The "Clearance Index" (CI) is the ratio of the actual dose rate to the clearance limit. When a material's CI decays below one it could be released from regulatory control. Fusion power plant designers try to achieve low CI values for their components, so that much of the plant could be released as non-radioactive

material, or recycled within the nuclear industry, minimizing the amount that must be controlled as radwaste.

Nonvolatile solids like SiC and steel may be stored at the plant site. Those that decay to clearance levels may be released. Some that do not may be recycled. Blanket fertile materials can be recycled into other fusion reactors, after processing to remove impurities. For example, a purification system that removed bismuth from PbLi would facilitate its re-use. Materials that are not are not suitable for clearance or recycle would be stored as radioactive waste.

The alloys W–TiC, W-1 %Ta, W–K and W-La$_2$O$_3$ are attractive for ARIES-ACT and PPCS divertors, because their activities would be close to the activity of pure tungsten with nominal impurities. The activity of W–Re alloy would be too high. Tungsten transmutes more in a soft neutron spectrum caused by water or beryllium. Less than 1 % transmutation occurs in a hard spectrum like that in ARIES-AT, and that level would probably not impair the structural properties of the W alloy (Zucchetti 2012).

Afterheat after reactor shutdown can be tens of MW initially, decaying to a few MW after 1 month. Adequate cooling must be provided to prevent overheating and possible escape of radioactive materials or contamination of hot cells by tritium and tungsten dust (Zucchetti 2012).

12.3.3 Disposition of Radioactive Materials

After a reactor is shut down, it may be dismantled using some of the following processes:

- Mechanical disassembling (bolted assemblies)
- Cutting
- Differential melting (to recover metals with different melting temperatures)
- Chemical processes for separation of elements
- Crushing for powder metallurgy needs.

These processes may need to be done remotely for highly radioactive materials, taking into account decay heat removal and thermal expansion, so experience with reprocessing of spent fission reactor fuel is helpful.

Decommissioning can consist of either entombment on site or complete removal and cleanup. Entombment on site is much cheaper, but it may leave the site unsatisfactory for other use.

The ARIES-AT reactor would generate about 1,270 m^3 of low-level radioactive waste and no high-level waste during 40 years of operation (Petti 2006; Najmabadi et al. 2006).

Table 12.6 Approximate values of stored energies in a 1 GWe fusion power plant (National Academy of Sciences 1973; Holdren 1980)

Energy source	GJ
Chemical energy, lithium blanket	50,000
Chemical energy, PbLi blanket	4,000
Thermal energy, lithium coolant	1,000
Thermal energy, helium coolant	100
Thermal energy, water coolant	20
Magnetic field energy	200
Radioactive afterheat, first hour (depends on materials)	50
Nuclear energy of fusion plasma (complete burnup is impossible)	50
Mechanical energy of atmospheric pressure on vacuum chamber	10
Thermal energy of plasma	1

12.4 Hazards and Materials Shortages

12.4.1 Hazards

In addition to hazards from radioactivity, there are various forms of stored energy present in fusion reactors, which may cause fire or structural failure, as indicated in Table 12.6.

The greatest potential hazard is with pure lithium. PbLi is much better, because the lead partially shields the lithium from contact with air and water. Ceramic lithium compounds, such as Li_4SiO_4, are used in some blanket design concepts (Sect. 6.3), but they may require beryllium as a neutron multiplier, which adds chemical toxicity to the radioactivity hazard.

The large magnetic field energy could cause structural failure or local coil melting, but these dangers can be avoided by proper coil system design. (Chap. 4).

Studies have shown that with low-activation structural material, such as RAFM steel, even with no forced cooling the peak temperatures are insufficient to challenge the structural integrity.

The stray magnetic field outside the reactor might conceivably affect the health of humans and animals. Magnetic resonance imaging (a routine medical procedure) exposes people to very high magnetic fields (~ 2 T) with no apparent harm, but pulsed magnetic fields, such as from a tokamak central solenoid, could be more hazardous than constant fields.

12.4.2 Materials Shortages

The materials requirements for construction of many 1 GWe fusion power plants have been estimated. Elements that may be in short supply include He, Li, Cu, Cr, Mo, Ni, Nb, Pb, W, and some rare earths. (Kulcinski 1974; Badger et al. 1976, 1979)

Nb should be avoided in structural materials exposed to neutrons, because of its induced radioactivity, but it will be used in magnet coils.

Helium is a vital, nonrenewable resource. Future developments of the following sophisticated technologies rely on helium:

- Superconducting motors
- Superconducting generators
- Superconducting transmission lines
- Superconducting energy storage systems
- Fusion reactors
- High temperature gas-cooled fission reactors
- New transport systems, such as levitated trains
- Magnetic resonance imaging
- MHD generators.

The cumulative demand up to 2050 for superconducting transmission lines was estimated to be about 12 Gcm (billion cubic meters). Demand for transmission lines and other applications could limit the helium resources available for fusion power plants. Some of the helium present in natural gas is vented to the atmosphere, instead of being conserved.

About 3,000 t/year of helium is generated inside the earth by alpha emission from uranium and thorium decay chains, and it is emitted at the same rate into the atmosphere (Bradshaw 2012).

The world production of helium in 2011 was 0.180 Gcm (billion m^3), of which 0.14 were in the USA. The estimated world helium resources and reserves are shown in Table 12.7.

A helium-cooled pebble bed fusion power plant would produce about 0.56 t He per year by DT fusion reactions, which is much less than the helium inventory of the power plant (about 57 t) (Bradshaw 2012).

Lithium is used in glass and ceramics 29 %, in batteries 27 %, in lubricating greases 12 %, in continuous casting 5 %, and other uses 27 %. Lithium is found in ores (spodumene, petalite, lepidolite) and in brines. Lithium production in 2011

Table 12.7 World helium resources and reserves

	Resources Mt	Gcm	Reserves Mt	Gcm
US	3.5	16.2	0.7	4.0
Qatar	1.7	10.1	na	na
Algeria	1.4	8.2	0.3	1.8
Russia	1.2	6.8	0.3	1.7
Canada	0.3	2.0	na	na
China	0.2	1.1	na	na
Others	0.5	3.5	na	na
Total	8.8	47.9	>1.3	>7.5

na not available. There are slight discrepancies between the columns for Mt and Gcm, which may be due to round-off of digits. (Mt from Bradshaw 2012, Gcm from USGS 2012)

Table 12.8 Estimated lithium resources of the world (USGS 2012)

Bolivia	9 Mt
Chile	7.5
China	5.4
USA	4.0
Argentina	2.6
Australia	1.8
Other	3.7
Total	34

was 34,000 t (metric tons), of which the leading producers were Chile, Australia, China, and Argentina. Lithium *reserves* (which can be extracted economically now) are mostly in Chile and China. (USGS 2012) Lithium *resources* (additional deposits that are more expensive to extract) on land in the world are shown in Table 12.8.

If the world's automobiles were converted to Lithium batteries, about 10 Mt would be required, and other industries are also increasing their use of lithium, so the cost of lithium may increase as reserves are used up. If the world power consumption doubled, the fraction consumed by electricity generation doubled, and 30 % were produced by fusion power plants, then about 2760 1-GWe fusion plants would be needed, requiring 10,000 t of natural lithium. This would be much less than the reserves, but the price could become high if lithium were widely used for large batteries (Bradshaw 2011).

Beryllium is a rare metal. Only bertrandite and beryl occur in mineable concentrations. Annual world production was 240 t in 2011, of which 210 t was in the USA and 22 t in China. (USGS 2012) Figures for the total reserves are not available, but the resources amount to only about 80,000 t, of which most are in the USA. The initial beryllium mass loading for the helium cooled pebble bed DEMO is 120 t, and the annual burn-up would be ~ 0.2 t/a. One hundred such reactors could require 12,000 t, about 15 % of the estimated resources (Bradshaw 2011).

Niobium is used mostly in steel 75 % and other alloys 25 %, and small amounts in superconducting wires. In 2011 Brazil produced 58,000 t, Canada 4,400 t, and other countries 600 t, totaling 63,000 t. World reserves were 3 Mt, of which 2.8 were in Brazil. World resource estimates, though not available, were deemed adequate to meet world needs (USGS 2012).

Lead production (from mines) in 2011 was 4.5 Mt, with more from recycling. Lead reserves amount to 85 Mt, mainly in Australia and China. Lead resources are estimated to be 1.5 Gt. (USGS 2012) The helium cooled lithium lead DEMO would require 4,000 t of lead, with annual burn-up of lead ~ 3 t/a (Bradshaw 2011).

Tungsten is mainly used in tungsten carbide parts for cutting and wear resistant materials, and also in tungsten alloys for high-temperature or high-density applications, such as welding electrodes and light bulb filaments. Tungsten production in 2011 was 72,000 t, of which 60,000 t were in China. Tungsten reserves were 3.1 Mt, of which 1.9 Mt were in China. Tungsten resource estimates are not available, but China, Russia, Kazakhstan, and the USA have significant deposits (USGS 2012).

Table 12.9 Summary of environmental effects of fusion reactors, in comparison with fission power plants. (Adapted from Young 1976)

Adverse	Increased use-of some scarce materials
Neutral	Biological effects of long-term exposure to low magnetic fields. Not an issue outside the plant. (Oscillating fields from power lines are more of an issue)
Unchanged	Assured fuel supply, waste heat released, radioactive structure
Better than fission	Safety against accidental criticality, prompt criticality, and loss-of-coolant accidents
	Reduction of safeguard concerns (regarding nuclear weapons production)
	Lower routine chemical releases, since fusion does not involve as extensive mining, milling, enrichment, fabrication, and reprocessing systems
	No fission product high-level radioactive wastes, lower biological hazard potential

Thus, significant shortages of helium and beryllium could occur. The price of lithium may escalate if large quantities are used for batteries and other applications. After enrichment of ^{6}Li for fusion blankets the remaining lithium (mainly ^{7}Li) could be used for other applications, and used lithium should be recycled. (Bradshaw 2011) The reserves of lead, niobium, and tungsten appear to be adequate.

12.4.3 Summary of Environmental Effects

Some potentially good and bad environmental effects of fusion reactors are summarized in Table 12.9.

12.5 Safety Analysis

Safety analysis is required to identify the risks of fusion power plants. The analysis guides the design to minimize the probabilities of bad consequences and to mitigate them if they occur. The resulting design should provide reasonable protection to the workers, to the public and to the environment. For example, a careful design could make public evacuation plans unnecessary. (IAEA guidelines recommend evacuation at 50 mSv avertable dose, but lower levels are specified in some national regulations.)

The general safety objectives of ITER are (Taylor 2009)

- To protect workers, the public and the environment,
- To minimize exposure to hazards and release of hazardous material, staying below prescribed limits
- To prevent accidents with high confidence,
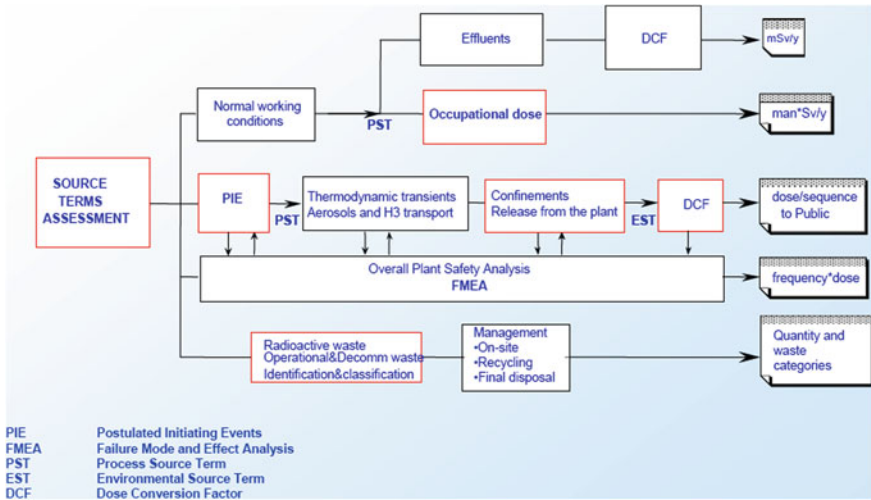
Fig. 12.10 The ITER safety methodology (From Pinna 2008)

- To ensure that the consequences of more frequent incidents, if any, are minor,
- To ensure that the consequences of accidents and incidents are bounded and that their likelihood is small,
- To demonstrate that there is no need for public evacuation,
- To minimize radioactive waste hazards.

  The elements of safety analysis are:

- **Energy Sources**. Liquid metals, other chemicals, magnetic fields, high pressure fluids, …
- **Hazardous Materials**. Toxic chemicals, radioisotopes
- **Potential Initiating Events**. Tube failure, fire, earthquake, …
- **Prevention**. barriers, pressure relief valves
- **Mitigation**. Containment, Air Cleanup,… (based on Pinna 2008).

  Figure 12.10 shows the ITER safety methodology.

  The process begins with an assessment of source terms, which includes potential hazardous materials and conditions, such as radioactivity, chemical reactivity, high pressure gas, magnetic energy, and high voltage. The two most important are tritium and activated dust.

12.5.1 Normal Operations

For normal operations safety analysts derive the Process Source Term and use it to estimate routine exposure of workers to radioactivity and emissions of chemicals

and radioactivity from the plant. Then they use dose conversion factors to estimate doses to the workers from these exposures and to the public from these emissions.

12.5.2 Accidents

Fission power plant safety analysts have developed powerful methods that can also benefit fusion power development.

The safety analysis team makes a comprehensive list of various possible Postulated Initiating Events (PIE) that could lead to an accident. They calculate the physical and chemical events that could follow each PIE, and the likelihood of those subsequent event scenarios. These events could be release of pressure, failure of magnets, high voltage breakdown, fire, explosion, etc. For each sequence they estimate the amount of hazardous chemicals or radioactivity that could be released from the reactor, and the resultant effects on the plant workers, public offsite, and environment.

Fission reactor safety analyses estimate the probable frequency of each accident sequence (such as 10^{-6} events per year) and make a chart of estimated offsite dose versus frequency. For fusion reactors such a probabilistic risk analysis is less feasible, because the failure rate data of many fusion reactor components are not available. Instead researchers use a "deterministic" approach and estimate the maximum consequences of postulated events without quantitatively considering their frequency.

They also calculate the quantities of chemical waste and radioactive waste that would be generated, and then consider possible disposal paths (on-site disposal, recycling, reprocessing, repository). Table 12.10 shows analytical methods suggested for various cases.

Out of thousands of possible sequences, the safety team tries to choose the sequences that could have significant **impact** on the workers or public. Also, the principal **release mechanisms** of radioactivity and hazardous chemicals are taken into account. Then they consider possible events involving:

- **Plant accidents**. Weld failure, high voltage arc, fire, …
- **Natural phenomena**. Earthquakes, high winds, floods,…

Table 12.10 Suggested Methods of Analysis. (From Pinna 2008)

Type of process	Commonly suggested method
Low-complexity operations	Only hazards analysis
Single-failure electro-mechanical systems	Failure Modes and Effects Analysis (FMEA)
Systems with redundant barriers or requiring multiple failures	Event Tree Analysis (ET)
Large, moderately complex processes	Fault Tree Analysis (FT)
Complex fluid processes	Hazard and Operability Studies (HAZOP)
High complexity facilities	Integrated ETs and FTs

Table 12.11 ITER quantitative safety objectives (Taylor 2009)

	For personnel	For the public and environment
Normal situations	As low as reasonably achievable and in any case less than	Releases less than the limits authorized for the installation. Impact as low as reasonably achievable and in any case less than
	Maximum individual dose **10 mSv/yr** *Average individual dose* **2.5 mSv/yr**	**0.1 mSv/yr**
Incidental situations	As low as reasonably achievable and in any case less than	Release per incident less than the annual limits authorized for the installation
	10 mSv per incident	(i.e. **0.1 mSv** per incident)
Accidental situations	Take into account the constraints related to the management of the accident and post-accident situation	No immediate or deferred counter-measures (sheltering, evacuation) **<10 mSv** No restriction of consumption of animal or vegetable products
Situations beyond design basis		
Hypothetical accidents	No cliff-edge effect; possible counter-measures limited in time and space	

- **External events**. Airplane crashes, terrorist attacks, …
- The Safety Analysis Report (SAR) includes "design basis accidents" and "beyond design basis events."

The **source term analysis** should give a conservative, quantitative analysis of the radioactivity (such as tritium) or toxic chemical (such as BeO) release from the building.

The **dose assessment** should give a conservative analysis of the dose to workers and to the public at the site boundary, using conservative assumptions about release conditions, weather, etc. It may also estimate the resulting health effects.

Table 12.11 shows the ITER safety goals for various situations.

The local nuclear regulator stipulates the regulations that the design must follow. ITER is being built in France, so French regulations are used. The USA also has a strong regulatory system, but with slightly different provisions. The regulations for fusion reactors are gradually evolving, based partly on regulatory experience with fission reactors. (See also "US Safety Standards" later in this Section.)

12.5.3 Failure Mode and Effect Analysis

The safety team studies all possible initiating events and failure modes and frequencies, causes, prevention, consequences, and corrective actions. Then the team

analyzes hundreds of possible failures. For example, some possible failure modes could include:

- Catalyst deactivation
- Heater failure
- Valve external leak
- Valve failure to remain open
- Boundary break
- Bellow failure
- Pump stop
- etc.

For each of these failures, an event tree can be made, considering possible events that follow the failure. For example, if a process line containing tritium failed inside a glovebox, we would ask, "Is the process line isolated?" The "yes" and "no" answers to this question would make two branches. The next question could be, "Does the glovebox confinement maintain its integrity?" The "yes" and "no" answers would split the two branches into four branches. Then the question, "Does the glovebox detritiation system operate correctly?" would make 8 branches, etc. Some branches may terminate at various questions, but with a sequence of 8 questions, there could be as many as $2^8 = 256$ branches.

12.5.4 Occupational Radiation Exposure (ORE)

Workers who operate, inspect, repair, and replace components may be exposed to radiation from tritium, activated structure, and other sources. Safety analysts identify tasks involving radiation exposure. For each task they consider task frequency, worker activities and locations, and time required to complete the task. Then they can estimate the worker radiation dose associated with that task.

The ITER Radiological Protection Guidelines include the following:

Maximum individual dose in normal operation	<10 mSv/a
Average individual dose	<2.5 mSv/a
Collective dose	<500 person-mSv/a
Maximum individual dose per incident	<10 mSv

The overall goal is to keep the doses to workers "As Low as Reasonably Achievable" (ALARA).

Figure 12.11 shows the estimated dose fractions (out of a total collective dose of 500 mSv) corresponding to various activities in ITER.
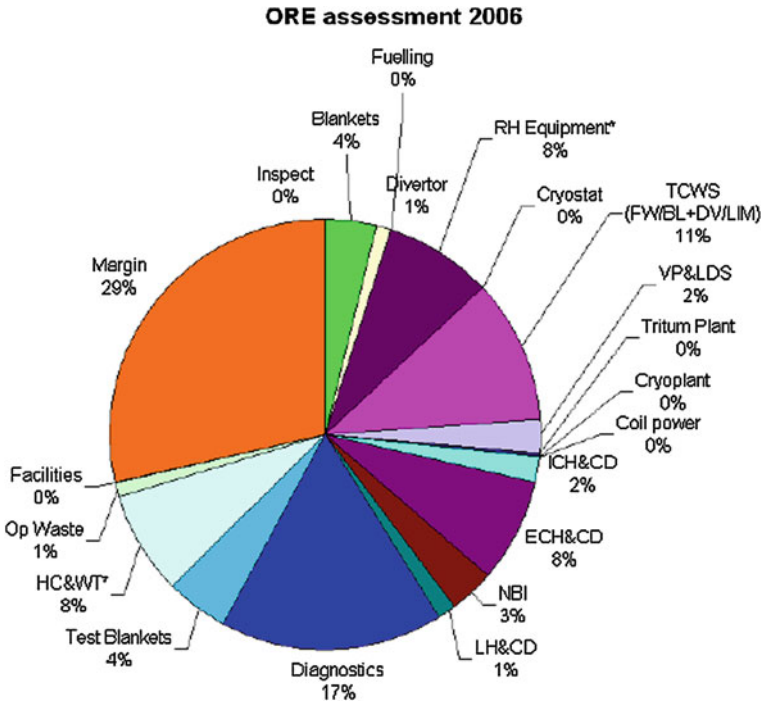
Fig. 12.11 Estimates of dose fractions from activities associated with various ITER components out of a total of 500 mSv (From Pinna 2008)

12.5.5 ARIES-AT Safety Analysis

The ARIES-AT (to be described in Chap. 13) is an advanced tokamak with SiC structure and PbLi coolant. It will operate for 10 months followed by two months maintenance to achieve 80 % availability. Its parts are to last 40 years, except for the plasma facing components, which must be replaced every 4 years. The safety goals are: (1) no evacuation plan needed for public near the plant (2) minimum amount of low-level radioactive waste and no high-level waste.

The safety team analyzed many possible off-normal events, such as:

- Loss of coolant accident (LOCA)
- Loss of flow accident (LOFA)
- Mobilization of tritium and tokamak dust with loss of confinement boundaries.

Figure 12.12 shows the radioactivity (Ci/m^3) and the decay heat (W/m^3) of ARIES-AT versus time after shutdown.

The decay heat of the SiC first wall falls rapidly during the first hour to that of the steel vacuum vessel and PbLi coolant.

Fig. 12.12 Radioactivity and decay heat of ARIES-AT versus time after shutdown, for two blanket cases, B-I and B-II. (Najmabadi et al. 2006, Fig. 10)
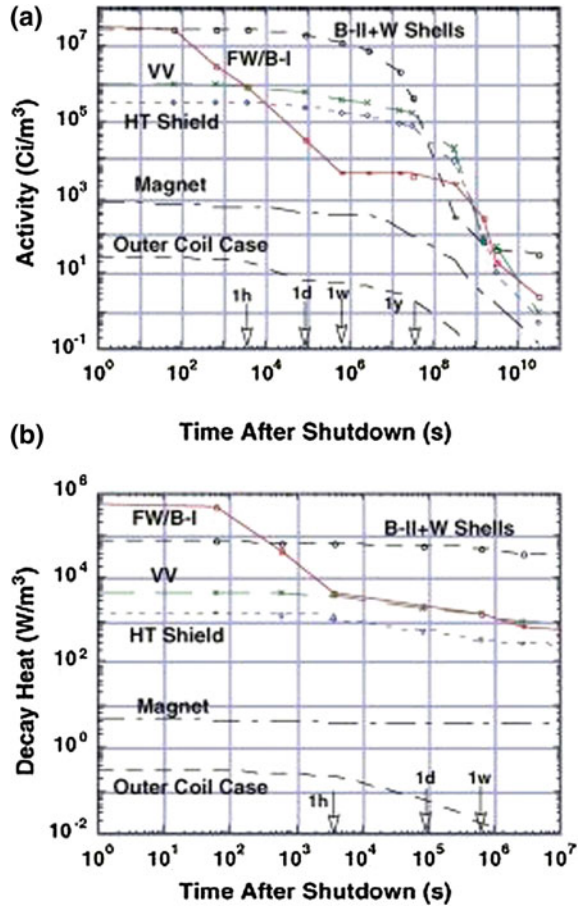
Tritium, W dust, and ^{203}Hg and ^{210}Po isotopes in the Pb–17Li could be mobilized during an accident. The offsite dose limit for no evacuation plan is 10 mSv (1 rem). Table 12.12 shows the release limits to avoid an evacuation plan.

ARIES-AT would have about 745 g of tritium in the vessel (plus more in the fuel cycle), including 680 g in the first wall, of which about 180 could be mobilized. Table 12.13 shows the estimated mobilizable inventories of hazardous materials.

Online removal of Bi (precursor of Po-210) to 1 ppm would meet the no-evacuation limit for Po-210.

The ARIES team analyzed three types of accidents:

- Breach of confinement boundary (vacuum system, coolant tube, …)
- Decay heat removal (LOCA, LOFA)
- Chemical reactivity (PbLi spill)

Table 12.12 No-evacuation release limits for a 1 km site boundary, assuming wind speed 4 m/s, atmospheric stability class D, and 10 mSv dose limit (Petti 2006, Table 6)

Release level	Ground	100 m stack
Tritium as HTO	150 g	1.3 kg
Activated W dust	6 kg	69 kg
Hg-203	925 TBq	9250 TBq
Po-210	0.92 TBq	9.215 TBq

Table 12.13 Mobilizable inventories compared with release limits (Petti 2006, Table 7)

Material	Mobilizable inventory	Release limit
Tritium	180 g	150 g
W dust	10–100 kg	6 kg
Hg-203	44 EBq*	0.93 EBq
Po-210	92.5 TBq*	0.92 TBq

*E = Exa = 10^{15} T = Tera = 10^{12}

They performed detailed calculations of heating, flow rates, pressures, and temperatures during various accidents to estimate possible releases of radioactivity. For example, a severe LOCA with containment bypass releases only 7.6 g of tritium, 207 g dust, 3.3 TBq of Hg-203, and 0.8 GBq Po-210, all far below the limits. Maximum temperatures due to radioactive decay are below 700 °C (Najmabadi et al. 2006; Petti 2006).

12.5.6 US Safety Standard

Lee C. Cadwallader

In the mid-1990s the US Department of Energy (DOE) convened a committee composed of fusion designers, experiment operators, and safety personnel to develop a safety standard for magnetic fusion energy, resulting in three documents. (DOE 1996a, b; 1999) The requirements document gives a succinct and comprehensible set of safety-based design and operations requirements along with high-level safety principles to achieve public and personnel safety at magnetic fusion facilities. The overall idea was to fashion criteria that are congruent with the basic safety requirements for nuclear fission power plants. The DOE fusion safety standard serves to promote safety in fusion engineering development as fusion develops toward electricity production. The fusion safety standard has two high-level requirements, to confine radioactive and hazardous material for public safety and to control operating hazards for worker safety. Presently, the fusion safety standard is unique among the countries exploring fusion research. Most countries license and operate fusion facilities as low hazard facilities more akin to radiological laboratories than large process facilities. One notable exception is that the

ITER International Project is being licensed in France as a basic nuclear installation similar to any other nuclear facility in France, but the regulator is giving attention to tritium inventory and safety concerns unique to fusion. The other two DOE documents are design guidance to support designers when they implement the requirements given in the standard. Longhurst (1996) gives a description of the process used to create the fusion safety standard and the results gained from the development effort.

12.6 Nonproliferation

Fusion reactors will normally contain no uranium, thorium, or plutonium, so they will not be sources of fissile materials that are essential for nuclear weapons. Tritium is useful in hydrogen bombs, but it would be useless without a fissile core, such as ^{239}Pu or ^{235}U, and the tritium extracted from a fusion reactor blanket can be measured and monitored. Nonproliferation of fusion-fission hybrids is discussed in Chap. 14.

12.7 Summary

The main hazards of fusion power are tritium and radioactive structure, including dust. Tritium gas is much less hazardous than HTO. Fusion reactors after ITER will need to have adequate tritium breeding ratios, because the world supply is limited. Shortages of He and Nb may develop, and widespread use of lithium for batteries could increase its cost, but the resources of most fusion reactor materials are adequate. Fusion reactors should be chosen to maximize clearance and recycling, and to minimize wastes that must be disposed of. Safety analysis aims to protect workers, the public, and the environment from routine releases and from accidents. Safety analysis studies hundreds of event trees that could follow postulated initiating events, and influences reactor design to minimize accident probabilities and to facilitate their mitigation. Fusion power plants will be designed so that public living nearby will not need an emergency evacuation plan.

12.8 Problems

12.1. A sealed bottle containing initially pure tritium is stored for 1 year. If permeation through the bottle is negligible, what fraction of the gas will be helium at the end of the year?

12.2. A fusion reactor has a breeding ratio of 1.07, a burnup fraction of 4.3 %, a tritium inventory of 21 kg, and fusion power 4.7 GWth. How long will it take to double the tritium inventory? What is the tritium mass flow rate through the reactor? How many kg(T) are consumed daily?

12.3. A reactor has a blanket of Li_2O spheres with total volume 520 m^3 and void fraction of 47 %. In order to keep the tritium in the blanket below 100 MCi, what average fraction of tritium (appm) is tolerable in the Li_2O sphere? (Ignore tritium in the helium coolant and cladding.)

12.4. Repeat Example Problem 12.3 for a case with Cu tubes instead of Ni tubes.

12.5. Derive Eqs. (12.26) and (12.27) by solving the appropriate differential equations.

12.6. The cross section of the ^{51}V(n,p) reaction is 0.2 barn. For the case of Example Problem 12.4 estimate the ^{51}Ti activity 10 min after shutdown. (Half-life is given in Fig. 12.8) Ignore neutron capture in ^{51}Ti.

12.9 Review Questions

1. What are the half-life of tritium and its approximate biological half-life in humans?
2. What is the maximum beta energy from tritium decay?
3. In what ways can tritium harm the body, and in what way is it harmless?
4. Explain the following equation and its parameters. $dN/dt = R_B P/W'_{DT} - P/W'_{DT} - \lambda N$
5. How does the doubling time for fusion fuel compare with the doubling time for fission fuel obtained in a fast breeder reactor?
6. Through what pathways could tritium leak into the atmosphere?
7. What two processes limit the flow rate of tritium through a wall of thickness x_1? Which may be dominant at very low driving pressures?
8. What are the advantage and disadvantages of a barrier coolant loop?
9. How can tritium be removed from Flibe?
10. From PbLi?
11. Define "LD50".
12. Explain the equation and define the parameters. $dn_B/dt = n_A \sigma_A \phi + \lambda_c n_c - \lambda_B n_B - n_B \sigma_B \phi$
13. What types of stored energy must be considered in fusion reactor safety analysis?
14. What material shortages might affect deployment of large numbers of fusion power plants?
15. What are the five elements of safety analysis?
16. The safety analysts consider various PIEs and the possible consequences, then derive a graph of probability of radiation dose to the public versus what?
17. What name is given to events with frequencies between 10^{-4}/a and 10^{-6}/a?

18. Name some possible "failure modes".
19. Define "event tree analysis" and "fault tree analysis".
20. To what does "ALARA" apply?
21. Will afterheat be a significant problem for fusion power plants?
22. How would BHP from a fusion power plant compare that BHP from fission reactors?

References

Badger B et al (1976) UWMAK-III, a noncircular tokamak power plant design. Electric Power Research Institute Report ER-368

Badger B et al (1979) NUWMAK, a tokamak reactor design study. University of Wisconsin Report UWFDM-330

Baldwin MJ, Schmid K, Doerner RP, Wiltner A, Seraydarian R, Linsmeier Ch (2005) Composition and hydrogen isotope retention analysis of co-deposited C/Be layers. J Nucl Mater 337–339:590–594

Baskes MI (1980) A calculation of the surface recombination rate constant for hydrogen isotopes on metals. J Nucl Mater 92:318–324

Botts TE, Powell JR (1978) Waste management considerations for fusion power reactors. Nucl Technol 37:129–137

Bradshaw AM, Hamacher T, Fischer U (2011) Is nuclear fusion a sustainable energy form? Fusion Eng Des 86:2770–2773

Bradshaw AM, Hamacher T (2012) Nuclear fusion and the helium supply problem. In: 27th symposium on fusion technology, Liege, Belgium, 24–28 Sept 2012

Cadwallader LC, Longhurst GR (1999) FLIBE Use in fusion reactors: an initial safety assessment. INEEL/EXT-99-00331. Idaho National Laboratory, Mar 1999

Cecchi JL (1979) Tritium permeation and wall loading in the TFTR vacuum vessel. J Vac Sci Technol 16:58–70

Desecures M, El-Guebaly L (2012) Environmental aspects of W-based components employed in ITER, ARIES, and PPCS fusion designs. University of Wisconsin Report UWFDM 1411

DOE (2009) Evaluation of Tritium removal and Mitigation technologies for wastewater treatment. US Department of Energy Report DOE/RL-2009-18, Revision 0

Dolan TJ, Longhurst GR, Garcia-Otero E (1992) A vacuum disengager for tritium removal from HYLIFE-II reactor Flibe. Fusion Technol 21:1949–1954

Federici G, Anderl RA, Andrew P, Brooks JN, Causey RA, Coad JP, Cowgill D, Doerner RP, Haasz AA, Janeschitz G, Jacob W, Longhurst GR, Nygren R, Peacock A, Pick MA, Philipps V, Roth J, Skinner CH, Wampler WR (1999) In-vessel tritium retention and removal in ITER. J Nucl Mater 266–269:14–29

Fraas AP (1975) Oak Ridge National Laboratory Report ORNL-TM-4999

Holdren JP (1980) Fusion energy in context: its fitness for the long term. Science 200:168–200

Kulcinski GL (1974) Fusion power—an assessment of its potential impact in the USA. Energy Policy 2:104

Longhurst GR et al (1996) Development of fusion safety standards. Fusion Technol 29:627–631

Najmabadi F, Abdou A, Bromberg L, Brown T, Chan V C, Chu MC, Dahlgren F, El-Guebaly L, Heitzenroeder P, Henderson D, St. John HE, Kessel CE, Lao LL, Longhurst R, Malang S, Mau TK, Merrill BJ, Miller RL, Mogahed E, Moore RL, Petrie T, Petti DA, Politzer P, Raffray AR, Steiner D, Sviatoslavsky I, Synder P, Syaebler GM, Turnbull AD, Tillack MS,

Waganer LM, Wang X, West P, Wilson P (2006) The ARIES-AT advanced tokamak, advanced technology fusion power plant. Fusion Eng Des 80:3–23

National Academy of Sciences (1973) Fusion power: an assessment of ultimate potential. Report WASH-1239

Perkins WG (1973) Permeation and outgassing of vacuum materials. J Vac Sci Technol 10:543–556

Petti DA, Merrill BJ, Moore RL, Longhurst GR, El-Guebaly L, Mogaheb E, Henderson D, Wilson P, Abdou A (2006) ARIES-AT safety design and analysis. Fusion Eng Des 80:111–137

Pinna T (2008) General safety analysis approach and techniques. 2nd International Summer School on Fusion Technologies, Karlsruhe Institute of Technology, Germany, Sept 5 2008

Ribeiro I, Damiani C, Tesini A, Kakudate S, Siuko M, Neri C (2011) The remote handling systems for ITER. Fusion Eng Des 86:471–477

Safety of Magnetic Fusion Facilities: Requirements (1996a) DOE-STD-6002-96. US Department of Energy, Washington, DC, May 1996

Safety of Magnetic Fusion Facilities: Guidance (1996) DOE-STD-6003-96. US Department of Energy, Washington, DC, May

Steiner D, Fraas AP (1972) Preliminary observations on the radiological implications of fusion power. Nucl Saf 13(5):353–362

Supplementary Guidance and Design Experience for the Fusion Safety Standards DOE-STD-6002-96 and DOE-STD-6003-96, DOE-HDBK-6004-99 (1999) US Department of Energy, Washington, DC, Jan 1999

Taylor N, Baker D, Barabash V, Ciattaglia S, Elbez-Uzan J, Girard J-P, Gordon C, Iseli M, Maubert H, Reyes S, Topilski L (2009) Preliminary safety analysis of ITER. Fusion Sci Technol 56:573

Tubiana M, Feinendegen LE, Yang CC, Kaminski JM (2009) The linear No-threshold relationship is inconsistent with radiation biologic and experimental data. Radiology 251:13–22

USGS (2012) Mineral Commodity Summaries 2012, United States Geological Survey, accessed at http://minerals.usgs.gov/minerals/pubs/mcs/2012/mcs2012.pdf

Watson JS (1972) A summary of tritium handling problems in fusion reactors. Oak Ridge National Laboratory Report ORNL-TM-4022

Willms S (2004) Tritium supply considerations. ITER Test Blanket Module Meeting, UCLA, Feb 23–25

Willms S, Merrill B, Malang S, Wong C, Sze DK (2007) Tritium extraction from a DCLL blanket. Los Alamos National Laboratory Report LA-UR-05-1711

Young JR (1976) Environmental analysis of fusion power to determine related R and D needs. Battelle Pacific Northwest Laboratories Report BNWL-2010, Figure 5

Zarchy AS, Axtmann RC (1978) Limitations on tritium transport through fusion reactors. Nucl Technol 39:258–265

Zucchetti M, Di Pace L, El-Guebaly L, Han JH, Kolbasov BN, Massaut V, Someya Y, Tobita K, Desecures M (2012) Recent advances in fusion radioactive material studies. In: 27th symposium on fusion technology, Liege, Belgium, 24–30 Sept 2012

Chapter 13
Power Plant Designs

Thomas J. Dolan, Lester M. Waganer and Lee C. Cadwallader

Objectives

After reading this chapter one should understand

Desirable features of power plants
Reliability, availability, and maintenance
Economics of fusion power plants
Some fusion reactor design studies in Europe, Japan, China, and the USA.

13.1 Introduction: Attractive Power Plants

Sheffield (1994) provides a thorough review of the physics issues of magnetic confinement concepts, a few of which were briefly described in Chap. 1. He discusses the physics constraints of many types of fusion reactors and the engineering features of several reactor designs (tokamak, stellarator, RFP, FRC).

Over 50 fusion power plant design studies have been conducted since the 1960s, including tokamaks, stellarators, reversed field pinches, spheromaks, field reversed configurations, magnetic mirrors, magnetized target fusion, inertial confinement fusion, and others. A power plant needs to operate continuously with high availability. El-Guebaly, who has extensively reviewed power plant design

T. J. Dolan (✉)
NPRE Department, University of Illinois, Urbana, IL 61801, USA
e-mail: dolantj@illinois.edu

L. M. Waganer
Fusion Consultant, O Fallon, MO, USA
e-mail: lesw@centurytel.net

L. C. Cadwallader
Idaho National Laboratory Battelle Energy Alliance, LLC, Idaho Falls, ID, USA
e-mail: lee.cadwallader@inl.gov

studies, states "Clearly, pulsed tokamaks cannot compete with steady-state systems due to the added complexity of energy storage, fatigue of critical power systems, and poor economics" (El-Guebaly 2009).

The inherent safety, environmental advantages, and abundant, cheap fuel of fusion power plants may compensate for their higher cost of electricity. The leading candidate is the tokamak, which is a Russian acronym meaning "Toroidal chamber with magnet coils" Over 100 tokamaks have been built around the world, and about 35 are still operating.

Electric power utility companies will need to consider many criteria when deciding whether to build commercial fusion power plants. Following Kaslow et al. (1994)[1] these criteria are grouped under "economics," "public acceptance," and "regulatory issues," but there is some overlap among the categories.

13.1.1 Economics

Simplicity. Is the reactor design simple or complex?

Capital cost of plant. Will it be competitive with contemporary power plants?

Construction time. How long will it take to build the plant and start it up? What things could cause delays? Can the design be more modular and factory built, rather that on-site construction?

Lifetime. Will the plant be operable for 60 years or more?

Fuel-cycle. Are the total fuel cycle costs low relative to those of other electrical power plants? Will adequate supplies of deuterium, tritium, and lithium be available at low cost without interruption?

Reliability, For example, will a tokamak be able to sustain H-Mode, high-Q operation for many days?

Availability. How many days per year will a fusion power plant be available to generate electricity? Availability >90 % may be needed.

Load following. Can it operate well at partial load?

Maintainability. When something fails, such as first wall armor, how long will it take to fix it?

Risk. Will the investors and owners of the utility agree to take the financial risk of building a fusion power plant, in spite of the fact that it has no track record of availability?

---

[1] This article lists two EPRI reports with additional information:

1. Report of the 1992 Fusion Panel, TR-101649, November 1992. (Expert panel's key criteria for comparing alternative fusion technologies).
2. Utility Requirements for Fusion, AP-2254, February 1982. (Broad-based industry derivation of fusion power plant characteristics judged most important to electric utilities).

Finance. Will financial institutions be willing to loan the money for construction at a reasonable rate of interest?

Staff. Can the plant be operated with a modest size work force of operators, technicians, radiation safety staff, security force, and support staff? Are their required qualifications similar to those of other energy technologies?

Market. Is it near a load center, such as a big city or industry that will buy the power?

Transmission. Is it near an electric power grid with adequate capacity, or will a new transmission line be required?

Grid stability. Will its outage cause an unacceptable perturbation of the grid?

Resources. Will there be adequate supplies of all the resources needed for the lifetime of the plant? For example, shortage of niobium, helium, or cooling water?

Natural hazards. What are the dangers from seismic activity, forest fires, site floods, wind storms, and lightning strikes?

Waste. Will disposal of radioactive waste be an economic and political problem, as it is with fission reactor spent fuel?

Decommissioning. Will the costs of decommissioning, decontamination, and disposal be reasonable?

International. Will we be able to sell fusion plants or components abroad?

Other economic advantages of fusion could include the absence of some technologies required for competing energy sources, such as fission reactor spent fuel reprocessing.

13.1.2 Regulatory Simplicity

Because fusion is different from existing fossil and nuclear power generation technologies, existing regulatory requirements will not all be relevant to fusion. The following issues may influence utility decisions:

Regulations. Will government regulations hinder fusion power deployment or promote it? Will the regulations be made stricter after the plant is in operation? (This happened to fission power plants.)

Law suits. Will interveners file law suits to prevent completion and operation of the plant? (This has been a serious problem for fission reactors.)

Safety. Can the fusion power plant avoid the need for engineered safety systems and the possibility of human error making situations worse (as happened at Three Mile Island)?

Emergency planning. Can the power plant avoid the need for off-site emergency planning, such as an evacuation plan? In the USA The DOE fusion safety standard DOE-STD-6002-96 requires all foreseeable fusion accidents to result

in public doses of less than 1 rem (10 mSv) per event, and 1 rem is the
Environmental Protection Agency threshold for requiring emergency evacuation. A similar requirement applies to ITER.

Emissions. Will the fusion power plant waste heat and emissions of radioactivity and toxic materials be lower than or similar to those of competing technologies? Can waste streams be handled easily under existing regulations?

Worker exposure. Will the radiation doses to workers be low?

Licensing. Will the regulatory process allow a lifetime power plant license to be granted before major capital commitment is made? (The USA now has a combined Construction and Operating License (COL) for fission power plants, Nuclear Regulatory Guide 1.206, 2007.)

An electric power utility company will consider these issues when deciding what kind of power plant to build. It will be a challenge for fusion technology to provide encouraging answers to all of them.

13.1.3 Public Acceptance

Public understanding. Will the public living nearby understand nuclear fusion? Will they welcome the plant or protest against it? Public education should be a high priority.

Environment. What environmental regulations might interfere with construction and operation? What are the limits on temperature rise of cooling water from a river or lake? Are there endangered species or archaeological sites to be protected?

Waste heat. How much waste heat will be generated, and how will it compare with that from competing technologies?

Emissions. Can we avoid emissions of toxic metals and chemicals?

Radwastes. Can we minimize radwaste and develop benign disposal solutions?

Public concerns. What are the possible public concerns, such as health impacts, that we should consider?

Perception. Can we assure an accurate public perception of fusion plant safety and environmental impact? Can we promote public involvement in setting safety standards and policies? Can we avoid negative terminology from fission power plants, such as "emergency cooling"?

Nonproliferation. Is the power plant in danger of leading to weapons of mass destruction, such as nuclear weapons or radiological dispersion devices? We need to ensure that the neutrons will not be used to breed weapons-usable fissile materials or radiological dispersion devices ("dirty bombs"). If there were any proliferation threat, then the IAEA should be invited to monitor the operations.

13.2 Reliability, Availability, and Maintainability

Lee C. Cadwallader, Idaho National Laboratory

As magnetic fusion experiments operate at higher energy and plasma power and become more robust in the path toward a power plant, the issues of reliability, availability, and maintainability of components, systems, and the entire plant become more important. To inspire confidence in both investors and the public, fusion demonstration plants must exhibit high safety levels, high reliability, competitive economics, and low environmental impact. In addition, the U.S. Department of Energy requires that fusion safety system unavailabilities are specified and that safety systems are designed for reliability (U.S. Department of Energy 1996). Each of these three attributes will be discussed in this section.

13.2.1 Reliability

Reliability is defined as "the ability of a component or system to perform its required design functions under the design conditions for a specified period of time" (Institute of Electrical and Electronics Engineers (IEEE) 1999, Hecht 2004). A simpler definition of reliability is the probability that a component will not fail during a selected time period.

   A reliable plant, where all the essential systems operate properly, is necessary for economic operation, and safer than a non-reliable plant (Cox and Tait 1998). Consider a few examples from fission power plants to illustrate these points. If no circuit breakers spuriously open, no coolant pumps trip off line, no valves spuriously transfer position, and no faulty commands are issued by the control computers, then the plant operates with few or no transient events and generates profitable electricity until its next planned shutdown. If plant equipment operates well—fuel elements do not leak fission products, steam generator tubes do not leak primary coolant to secondary coolant, and no equipment faults occur that cause unplanned plant outages—then the plant can operate without harm to the public, plant personnel, or the environment. If there is a transient event, such as a loss of off-site power (LOSP) coming into the plant, then plant safety equipment is demanded to operate, and reliability is again an issue. If the safety systems and equipment are reliable, that is, the equipment starts or operates on demand, then the plant is easily brought under control from the transient and safety is preserved. The plant undergoes an orderly shut down and can be restarted when conditions have stabilized.

   Overall, the fundamental measure of quantitative reliability is the failure rate of components. Calculating failure rates from operating experience data is a

statistical process. For engineering purposes, a simple, fundamental definition is adequate to describe the component failure rate and reliability:

$$\lambda = \frac{number\ of\ component\ failures}{Nt}, \tag{13.1}$$

where
λ = component failure rate
N = total number of components operating in the time interval
t = time interval of interest, such as a test period, usually measured in hours

The reliability over time interval T is

$$Rel = \exp(-\lambda T). \tag{13.2}$$

Example Problem 13.1: A laser fusion experiment has 192 flash lamps used to augment a laser pulse.

Over 20,000 pulses, two lamps fail to operate. (Here one "pulse" is used instead of a unit of time.) What is the failure rate of the flash lamps? What is the reliability over 50,000 pulses?
λ = (2 lamp failures)/(192 lamps × 20,000 pulses)
$\lambda = 5.2 \times 10^{-7}$ failures/pulse

The reliability over 50,000 pulses $Rel = \exp(-5.2 \times 10^{-7} \times 50,000) = 0.974 = 97.4\ \%$.

As you can see by Eq. (13.1), the larger the sample of components and the longer the time interval, the more accurate the failure rate will be for that type of component operating in the specified environment.

As in all engineering endeavors, a failure rate value should not be given without its associated error. The error bounds are calculated based on selection of a statistical distribution of the reported failures of the component. The analyst plots the failures on a time line and fits a distribution curve to the data. For this introduction to the subject, we will not discuss error bounds further.

In Eq. (13.2), if the product λT is small, much less than 0.01, then the right side of the equation can be rewritten as $1 - \lambda T$. In a similar fashion, for components that start and stop operating frequently rather than run for long times, the time interval is replaced with the number of starts. This is referred to as a *demand failure rate* because we are using the number of demands on the component to start or change state.

Collecting component failure rate information is a tedious and time-consuming task. Plant design records are needed to obtain component counts. Plant logs are needed to obtain system start demands and system run times. Plant failure records or maintenance records are needed to obtain the number of failed components and the manner in which the components failed. For this reason, analysts seek compilations of reliability data that they can apply to new analysis tasks. A few

examples of data handbooks are Moss (2005) and Center for Chemical Process Safety (1989). Analysts will infer known data values to apply those to new components (Cadwallader and Marshall 1996).

Information on the manner of component failure is needed because it is important for safety significance and maintainability. Some failures are easily repaired or the component merely requires a reset (such as mechanical component realignment or a personal computer restart). Other failures might require much downtime for replacing subcomponents, testing to return the component to service, etc. Therefore, failure rates are given according to the mode of failure. For example, consider a small-diameter coolant pipe. A failure rate for a pipe will specify the probability of failure per operating hour and per meter of pipe length. Separate failure rate values will be calculated for leakage, rupture, and plugging.

Analysis work is under way to evaluate component failure rates in magnetic fusion systems (Pinna et al. 2005, 2007; Cambi et al. 2008, Cadwallader 2001, 2007 and Cadwallader et al. 2007). These data have several uses, including in availability and maintainability calculations and in reliability allocation during system design. A system has an overall failure rate goal value. Reliability allocation distributes separate reliability goals to components and subsystems to meet the larger system goal.

There are many books that discuss the mathematical theory of reliability; two notable texts of that type are Tobias and Trindale (1995) and Elsayed (1996).

13.2.2 Availability

The availability of a power plant is simply a measure of its operating hours per year divided by the calendar hours per year (Jones 2007). A simple definition of availability is

$$A = \frac{uptime}{uptime + downtime}, \tag{13.3}$$

Availability can also be expressed as Jones (2007):

$$A = \frac{MTBF}{MTBF + MTTR}, \tag{13.4}$$

where
$MTBF$ = Mean time between failures
$MTTR$ = Mean time to repair.

Availability is a dimensionless number, usually expressed as a percentage. Because availability is an important aspect of power plant economics, the uptime is usually taken to be the actual on-line operating time. Uptime may also include the time that the plant is not operating but is ready to operate, however. Downtime

may include procurement delays to obtain spare parts, administrative delays, regulatory delays, or the time it takes to restart the plant. In what's referred to as the inherent availability, the MTTR is the active time to repair the component and does not include any delays in repair or in plant restart. Therefore, it is important to know how availability was calculated before comparing availability values.

A similar measurement to availability, the capacity factor is the plant availability multiplied by the fraction of the plant's design electrical rating that the plant is producing. For example, if a plant has an availability of 80 % and is running at 90 % power, its capacity factor is

$$CF = 0.80 \times 0.90 = 0.72 \text{ or } 72\%$$

Because most power plants are running at, or very close to, rated nameplate output to generate maximum income, the capacity factor is a direct indicator of plant availability.

Availability in fission plants is greatly influenced by plant trips. When a fission plant trips because of a loss of off-site power or other cause, the procedure is to stabilize and safely shut down the plant, investigate the cause of the scram, cool down the plant, inspect any equipment or components suspected of overstress, and make any necessary repairs. (That time might also be used to perform some maintenance or inspections.) Then, when the regulator has granted restart permission, the plant can be warmed up to operating temperature and restarted (about 12 h are required for a restart and power ascension to full power). In general, an unplanned outage requires roughly 2–3 days of downtime. Most existing fission power plants have reduced their trip frequency to less than one trip per year.

The new fission power plant designs are expected to have even better performance than current plants. An example is the advanced light water reactor fission power plant, which has a simplified design, uses fewer components than previous designs, and has gleaned improvements from the operating experience of the existing fleet of fission power plants. The designers of this advanced reactor believe they can achieve greater than 93 % availability (Schultz 2006). This performance improvement creates additional challenges to bring any new type of power plant into the power production industry; fusion power plants must compete with more matured technologies that already perform well. The current thinking is that the mature fusion plants (10th of a kind) should have an availability in the range of 90–95 %, the first of a kind plant achieving 70–75 % and the Demo performing in the range of 50 %.

It also must be noted that there is availability growth with new power plants (Cadwallader and Petti 1999). The first year or two of plant operations show poor on-line time, perhaps half of a year or less. This is usually caused by component "early-life" failures that require downtime for replacement or repair, retrofits so equipment will perform at rated conditions, and plant staff familiarizing themselves with the plant's unique characteristics as they formulate their strategy for optimum plant operations. After this initial period, availability begins to either ramp or stair-step up to higher values, sometimes gaining increases of an

additional 1,000–2,000 operating hours within a year (≈ 10–20 % additional availability). David et al. (1996) suggest that a plant has its most impressive availability growth in the first decade, with further increases gained only after great efforts by the plant personnel—designers, maintainers, and operations staff. In the 1970s, the plateau value was about 75 % availability; in more recent times it is above 85 %. By comparison, many fusion experiments reach the 80 % range of mission availability (Ciattaglia et al. 2005). Fusion experiments tend to be limited by financial constraints. For example, U.S. Department of Energy funding allows fusion experiments to operate for 8 h per day, and 12–25 weeks per year per facility. (To compensate, the experiments define a "mission availability", which is actual operating hours divided by the total paid operating hours per year.)

Experimental fusion analysts view operating days as counting toward their mission availability; they do not sum plasma pulse time. For example, the DIII-D experiment in San Diego, California operates with a 5-second plasma pulse once each 8–10 min. However, the 8–10 min is counted as the operating time because the machine is being prepared for another pulse. Cooling systems are removing heat primarily from the copper magnets, transformers, vacuum vessel, and plasma heating equipment. Diagnostic device data, hundreds of megabytes, from the previous plasma shot are being downloaded and archived in preparation for another shot. The vacuum system pumps are operating to reduce the vacuum vessel pressure so another plasma can easily be formed. Control computers are being given the shot profile data to operate the upcoming plasma pulse. Thus, most of the plant equipment is operating during preparation for the next plasma pulse. Some tokamak experiments are operated for one shift (e.g., 8–9 h per day) and some are operated for two shifts (i.e., 16 h per day). Fusion power plants are envisioned to operate with a steady state plasma; that is, operate a plasma continuously for months on end without pulsing, so that the fusion heat source will operate in the same manner as other thermal power plant heat sources.

Example Problem 13.2: An existing fusion tokamak experiment operates for 25 weeks/year, 5 days/week, in one shift operation. Assuming 80 % mission availability, what is the annual availability?

$$\text{Operating time } A = 0.80 \times 25 \text{ weeks/yr} \times 5 \text{ days/week} \times 8 \text{ hr/day}$$
$$= 800 \text{ operating hr/yr}$$

This gives a calendar availability of

$$A = \frac{800 \text{ hr}}{24 \text{ hr} \times 365 \text{ days/yr}} = \frac{800 \text{ hr}}{8,760 \text{ hr/yr}} = 0.09 \text{ or } 9\%.$$

The ITER experiment has a goal to perform 3,000 pulses per year, with 400-second pulses that require about 45 min of system operations per pulse (International Atomic Energy Agency 2002). So,

$$A = \frac{0.75 \text{ hr} \times 3{,}000 \text{ pulses/yr}}{8{,}760 \text{ hr/yr}} = 0.25.$$

Thus, ITER would operate for about 25 % of a calendar year. This is in line with estimates made by Buende (1988) who assigned representative reliability data to tokamak plant systems. For a major tokamak design, he estimated a plant availability of 33 %. (Taylor et al. 2000) discusses a modeling approach to calculate the expected availability for any new power plant design. See also (Waganer 2006, 2008).

13.2.3 Maintainability

Maintainability is the probability that a failed item or system in a plant can be repaired in a specified time using a specific set of resources (Jones 2007). Often the repair probability is assumed to be 100 % because, by common sense, there is no economic advantage for a power plant to operate with process systems not fully functional, and most power plants are not allowed by law to operate with any of their safety systems not fully functional. When the probability of repair is 100 %, maintainability is simply a measure of the time required to repair the item or system. The most well used measure of maintainability is the **mean time to repair** (MTTR) (Pecht 1995). This value is often estimated as just the active repair time for the work on the component to allow it to function again and does not include any logistical time or other factors that contribute to the plant overall outage. The formula for MTTR is

$$MTTR = \sum \frac{T_i}{n}, \tag{13.5}$$

where
T_i = Summation of repair times
n = The number of component malfunctions that were repaired in some time interval of interest, such as a year

Example Problem 13.3: At a fusion experiment, the instrument repair shop technicians repaired five different electronic modules removed from the plant instrumentation and control systems in a month. The shop times for module repair were 4, 0.5, 9, 2.25, and 1.75 h. What is the MTTR for plant instrumentation and control electronic modules?

$$MTTR = \frac{4 \text{ hr} + 0.5 \text{ hr} + 9 \text{ hr} + 2.25 \text{ hr} + 1.75 \text{ hr}}{5 \text{ repairs}} = 3.5 \text{ hr/repair}$$

Sometimes the MTTR is given in person-hours rather than in clock hours. Maintenance planning often uses compiled data to obtain the average man-hours value for component repair, and that average is used to estimate future manpower needs.

Another time value used for maintainability is called the **mean down time** (MDT). MDT includes the time to place the failed system or component in a safe state (e.g., cooldown), perform troubleshooting, procure spare parts, make repairs, do post-repair testing, and then return the system or component to service. MDT is sometimes called the mean time to restore (also denoted as MTTR), where restore means restoring the component to service. Care must be used to distinguish if the maintainability time is expressed as repair or restore, and in *clock hours* or *man-hours* of labor time.

There can be a number of variables affecting the MDT value. Plant staff is an important variable—whether the plant retains an adequately sized, trained maintenance staff with the traditional diverse set of skills, or the plant hires out to a maintenance subcontractor company. This decision makes a difference in the component idle time while awaiting repair. The spare parts inventory held on site versus parts being purchased as needed and shipped overnight to the plant is another factor affecting the MDT. In practical applications the facility-specific MDTs reflect the facility's time lags.

Actual MDT data are typically difficult to find in the literature because of the facility-specific nature of such. There have been a few publications that have presented traditional repair times for power plant large components (Derdiger et al. 1981, IEEE 2007) and industrial equipment (Hale et al. 1999, Procaccia et al. 1998). Typically, a new facility will build its own MDT data bank as part of its maintenance planning before plant operations commence. Initial estimates are often taken from a combination of manufacturer input and planner's judgment. Over the first few years of plant operations the judgments are refined with the plant's experience data.

MDT refers to corrective maintenance, meaning repair of a component. There are two other forms of maintenance: preventive maintenance and predictive maintenance (Leavitt 2003). Preventive maintenance and predictive maintenance are treated by a value called mean time to maintain (MTTM) (Pecht 1995). In general, preventive maintenance tasks are performed while the equipment is operating or when the equipment is already shut down for other reasons, so those efforts are not included in the MDT. Preventive maintenance entails periodic visits to the component and is sometimes referred to as tighten, lube, and clean (TLC). The equipment is visually inspected; cleaned of dirt, grime, debris, etc.; and minor adjustments are made (e.g., testing or replacing lubricating oil, inspecting seals, and monitoring shaft alignment).

Predictive maintenance is any inspection carried out on a component that uses advanced technology to detect when failures will occur. Some predictive maintenance techniques are vibration monitoring, tracking sensor data on bearing temperature in rotating machinery, and analyzing lube oil composition and contamination. Predictive maintenance is completed for trending purposes to predict

when equipment is operating outside of normal parameters and the changing parameter is accelerating toward failure. In this way, the equipment can be taken off-line and repaired before any major damage occurs. Predicting end of life and incipient failures will improve the maintenance of fusion power plants.

Magnetic fusion power plants have two maintenance methods: traditional and remote. **Traditional** maintenance is the work performed by computer technicians; instrumentation and controls technicians and craftspeople, such as electricians, welders, mechanics, and fitters. These personnel support the needs for the conventional part of the thermal power plant, the so-called "balance of plant." The balance of plant is the thermal power conversion system where electricity is produced, including the steam generators, piping, turbines, in-plant electrical power distribution equipment, instrumentation and controls, and computer control systems. Maintenance of this equipment is termed "hands-on" because the workers can, with a minimum of protective equipment, touch the components and work on the components with hand tools, visually inspect equipment at close range, perform surveillance tests in close proximity to the equipment, etc. MDTs from other types of power plants would apply to this part of the fusion power plant.

Remote maintenance is performed solely by robotic and remotely manipulated machines. These implements are used only where personnel cannot safely enter because of some adverse condition such as exposure to heat flux, chemicals, or ionizing radiation. For fusion remote maintenance is used in vacuum and high radiation fields. It may be required to move multi-ton masses with high spatial precision (Honda et al. 2002). Cambi et al. (2003) calculated the radiation dose fields for the ITER experiment. Cambi used a value of 10 μSv/hr as the dose limit for hands-on maintenance, which was found by taking the ITER radiological dose limit of 20 mSv/yr (2 rem/yr) per person divided by a typical 2,000 hr work year for an employee. Cambi found that all portions of the ITER vessel would be at least one order of magnitude greater than the hands-on dose limit at the end of life, and some small portions of the vessel would be more than five orders of magnitude greater than the hands-on dose limit. Therefore, it will be necessary for all maintenance within the fusion power core (inside the biological shield) to be fully remote. To assure that all systems can be fully maintained, the intention is to initially assemble the power core with remote systems as well as the deactivation of the power core. Remote handling equipment will also be required in the hot cell for processing all the power core equipment.

Remote handling equipment is most strongly needed inside the vacuum vessel. Periodically, the first wall, blanket segments and the divertor segments inside the shield must be replaced. The segments are neutron damaged, and segment reliability is a concern after high neutron fluence of a few MW-a/m^2. To save time remote tools will also be used in the vacuum cryostat that surrounds the magnet coils. Venting the cryostat to air, then warming up the magnets would require at least one month of time; restoring vacuum and cooling down would be at least another month of time. (A large mass takes a long time to cool down, and the changes must be gradual to avoid large thermal stresses.) Each magnet warm-up to room temperature and cool down to cryogenic temperature also poses a risk for

electrical insulation damage, so avoiding these evolutions is important. During the normal periodic replacement of the blankets and divertors, the coils will be de-energized but will remain in a cryogenic state to avoid the lengthy warm up and cool-down procedures.

In-vessel blanket segment replacement by remote handling tools will be time consuming, which is an impact to plant availability. The basic time issue with remote handling of segments is that access paths to the fusion vessel are few in number, so the remote equipment is forced to operate as though constructing a "ship in a bottle" (Burgess 2008). That is, the task is do-able but painstaking and time-consuming. In general, remote maintenance times are estimated by the **"time-and-motion" analysis** approach of dividing all the remote manipulator and other remote tool actions into small tasks and summing the results to obtain an estimate of the total maintenance outage time (Burgess et al. 1999). These results can be compared to actual machine performance of fusion experiments as an indication of validity. To improve the accessibility and preclude the "ship in a bottle" approach of replacing individual modules, larger sectors or segments may be removed between TF coil legs, either horizontally or vertically. This horizontal replacement has been proposed first by the Starlight study in 1980 and more recently by the ARIES design team (ARIES stands for Advanced Research, Innovation, and Evaluation Study). A vertical replacement scheme is being studied by the EU in their PPPS and DEMO studies. Waganer (2006 and 2008) has conducted maintainability and availability studies on several recent ARIES fusion power plant studies.

Recent advances in computers, automation, simulations, knowledge learning and autonomous operations in many fields would suggest that in a decade or two all fusion plant remote operations will be completely autonomous with only human supervisory oversight. This should result in higher precision, quality and repeatability of replacements and repairs. There will also be significant advances in the ability to predict wearout and incipient failures, thus increasing the systems availabilities.

A fusion power plant may either replace portions of the in-vessel modules, segments, or sectors during short annual or bi-annual outages or replace all components in one long outage each third or fourth year (depending on the component lifetimes). The Joint European Torus (JET) experiment in the United Kingdom is the leading tokamak experiment for testing and using remote equipment (Rolfe 2007). In 1998, JET had its first all-remote exchange of the entire set of divertor modules (Galbiati et al. 1998). The work was performed in two shifts per day with a 6 day work week over 15 weeks, plus 11 working Sundays (Cusak et al. 1998). (Thus, with a power plant working three shifts around the clock, the work could have been completed in less than 10 weeks.) By comparison, fission power plants refuel their cores on average in less than 38 days (Hansen 2008), and a few fission plants have refueled in less than 3 weeks. Such short MDTs mean higher plant availability. This uncovers another economic challenge to fusion: to decrease plant downtime by increasing the power core component (first walls, blankets, divertors and shields) reliability and lifetime by selecting materials so

that neutron activation remains low and component replacements are infrequent (long lived) (Perkins 1997). Fusion power cores require a certain duration of time to shut down and startup, which contributes to the downtime for any major maintenance action. These times have steadily decreased and there is incentive to significantly reduce those times.

Glossary

Availability a power plant's operating hours per year divided by the calendar hours per year	*Maintainability* the probability that a failed item or system in a plant can be repaired in a specified time using a specific set of resources
Capacity factor plant availability multiplied by the fraction of the plant's design electrical rating that the plant is producing	*Reliability* the ability of a component or system to perform its required design functions under the design conditions for a specified period of time (the probability that a component will not fail during a selected time period)

For economic power production a reliability of less than one failure per year is needed. If the structure fails and a 1 GW_e reactor is shut down for repairs, the value of the lost revenue at 0.1 $/kWh is 2.4 M$/day, so remote handling maintenance must be done quickly and efficiently.

The ARIES-AT study compared three maintenance strategies

- In situ replacement inside the power core
- Replacement of life-limited components immediately outside power core
- Replacement of life-limited components with a refurbished sector from remote hot cell.

  with merit ratings according to eight criteria:

- Replacement time
- Replacement sector reliability
- Building cost
- Maintenance equipment
- Spare equipment cost
- Waste volume
- Contamination control
- Applicability to scheduled and unscheduled maintenance.

They concluded, "The hot cell approach scored well because it is perceived to have high availability and reliability. Also, contamination control is good, as well as being applicable to both scheduled and unscheduled maintenance. As a result of these scores, the hot cell maintenance approach is the recommended maintenance scheme" (Waganer and Team 2006).

Maintenance issues for ITER are reviewed by Vayakis et al. (2008).

> Because of the difficulty involved in these remote handling operations, maintenance or replacement intervals will be long on ITER. For the majority of the diagnostic plugs, removal is not planned to be routine but is only possible in case of failure. For a given plug, typical average maintenance intervals are 2–4 year in present ITER operating scenarios used in planning remote handling capability and assessing other impacts. Thus, for practical purposes, diagnostic components housed in these plugs need to be designed to last for the life of ITER. (Johnson and Costley 2008).

13.2.4 Remote Handling

After the ITER walls have been irradiated by high fluxes of neutrons, remote handling will be required to inspect, repair, or change any of the Tokamak components in the areas with high dose rates. The remote handling (RH) equipment must be able to move components weighing many tons and place them with sub-millimeter accuracy. A manipulator will detach the component, such as a blanket module, remove it through a port, and place it into a transport cask. The RH equipment for ITER includes:

- Blanket RH system. An In-Vessel Transporter travels around inside the torus on a removable rail, Fig. 13.1, and can replace any of the 440 4.5 ton blanket modules. This system has positioning accuracy of about 0.5 mm and 0.1°. The rail and manipulator can deploy 90° around the torus in 30 min.
- Divertor RH system. Can replace each of the 54 10 ton divertor cassettes 3 times during 20 years operation.
- In-vessel viewing system. It must operate in ultrahigh vacuum, $T \leq 200$ °C, radiation dose ~ 5 MGy, neutron fluence $\sim 5 \times 10^{17}$ m^{-2}, $B \leq 8$ T.
- Multi-purpose deployer—a robotic system that can use tools to connect and disconnect components and can move components up to 2 tons.
- Transfer cask—carries blanket modules from the torus to the hot cells.
- Neutral beam RH system—has a 50 ton monorail crane to maintain all NBI system components.
- Hot cell RH system—can inspect, clean, refurbish many components safely (Ribeiro et al. 2011).

The vacuum vessel port is sealed by a temporary door and the cask is closed to prevent contamination. The cask is moved on air bearings along to the hot cell, where it will be repaired or replaced. Then the cask and manipulator return the repaired item to the tokamak and install it, making the necessary connections of coolant channels, cryogenics, electrical power, and instrumentation.

Models of these systems are being thoroughly tested, and paths for the transfer cask movement are being optimized by computer aided design. The design must
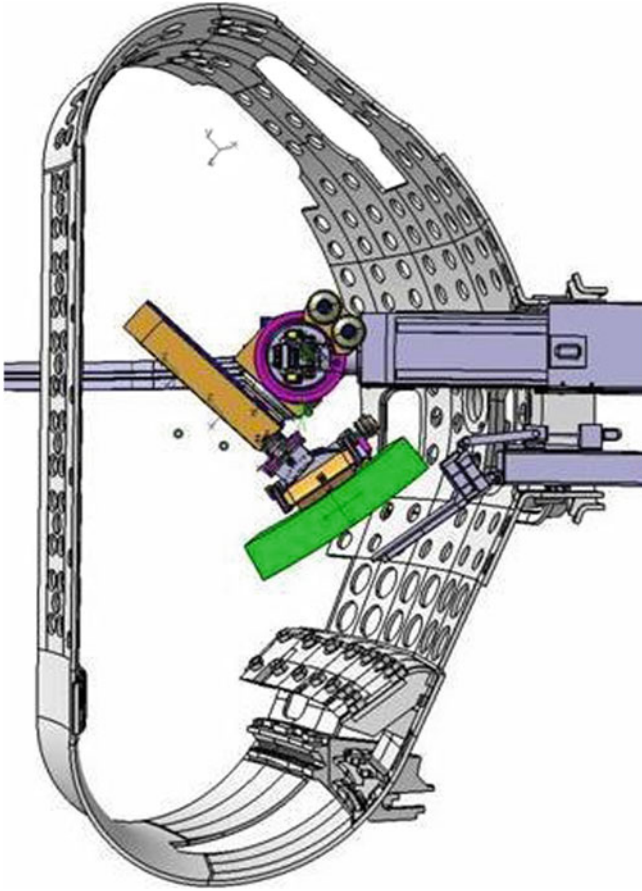
Fig. 13.1 A manipulator lifting one blanket module inside the vacuum chamber. The other blanket modules are not shown (Courtesy of ITER Organization)

ensure that the remote maintenance equipment will not be disabled by the high radiation environment, and that it, too, can be remotely replaced, if it fails.

The ability to replace damaged components quickly will be necessary if fusion power plants are to achieve high availability and low cost of electricity.

13.3 Economics

Here we follow the description of Sheffield et al. (1986).

Two general methods are used for estimating the cost of electricity (COE) from a power plant:

Current dollar mode: includes effects of price inflation The COE is quoted in dollars of a future year, but fuel and operations costs are quoted for the first year of operation.

Constant dollar mode: a simpler model that does not estimate effect of inflation directly.

The COE from a power plant in the first year of operation using the **current dollar mode** is estimated from

$$\text{COE} = [C_c * F_{CR} + (C_{o\&m} + C_f)(1 + i)^Y]/(P_e * h * f_{av})$$
$$\text{mills/kWh} = \text{US\$/MWh} \tag{13.6}$$

where

1 mill	=	10^{-3} US\$
C_c	=	Capital cost, including indirect costs (\$)
F_{CR}	=	Fixed charge ratio
$C_{o\&m}$	=	Annual cost of operations and maintenance, including component replacement and decommissioning (\$)
C_f	=	Annual fuel cost (\$)
i	=	Annual inflation rate
Y	=	Construction lead time (years)
P_e	=	Rated electrical capacity (MW)
h	=	8,760 h/year
f_{av}	=	Availability factor

Setting $i = 0$ in this equation yields the **constant dollar mode** equation.

The "fixed charge ratio" F_{CR} is set such that $C_c F_{CR}$ is the annual charge needed to pay for the capital cost of the plant, similar to a home mortgage payment. For the current dollar mode typically $F_{CR} \approx 0.165$, while for constant dollar mode $F_{CRo} \approx 0.10$.

The total capital cost

$$C_c = f_{ind} C_D \tag{13.7}$$

where C_D = direct capital cost and f_{ind} = indirect cost multiplier, which may be estimated from the construction lead time Y as

$$f_{ind} \approx (1 + 0.5Y/8) \quad \text{for } 6 \le Y < 12 \text{ years} \tag{13.8}$$

The factor 0.5 includes

Construction facilities, equipment and services 0.15.
Engineering management services 0.25.
Owner's costs 0.10.

This is a strong incentive to minimize the construction time.

The direct capital cost is

$$C_D = 1.15 \, (\text{reactor buildings} + \text{fusion island} + \text{balance of plant}) \quad (13.9)$$

where the 1.15 includes a 15 % contingency fund; "fusion island" includes the vacuum vessel, blanket, shield, magnet coils, cryostat, heating systems, control systems, diagnostics, etc.; and "balance of plant" includes all other components, such as the steam turbine, generator, switch gear, etc.

The constant dollar mode is often used, because it is simpler and yields lower COE estimates. When comparing COE values from various sources, such as fusion, fission and fossil fuels, the same mode should be used for all sources.

Some of the standard cost account numbers and items are illustrated in Table 13.1 for the ARIES-AT power plant design.

For simplicity many sub-categories, such as individual magnet coil systems, were omitted from this table.

The total capital cost of 2,844 M$ is about 1.9 times the direct capital cost of 1,521 M$.

The reactor plant equipment (item 22) is about half of the direct capital cost. This cost can be minimized by careful design, but the costs for the buildings and balance of plant are about the same as for other power plants.

Example Problem 13.4: Assume that the O&M, fuel, component replacement, and decommissioning costs of ARIES-AT remain as in Table 13.1 and that f_{ind} stays constant, $f_{av} = 0.88$ and $F_{cr} = 0.10$. Estimate the new constant dollar COE if the magnet system costs 30 M$ less.

Solution
From Eq. (13.7) $f_{ind} = C_C/C_D = 2844.0/1521.1 = 1.870$
The new $C_D = 1521.1 - 30 = 1491.1$ M$, so $C_C = 1.870*1491.1 = 2788$ M$
Now $C_C F_{cr}/(P_e*h*f_{av}) = 2788*0.10/(1{,}000*8{,}760*0.88) = 36.17$ mills/kWh, replacing the previous 36.87 mill/kWh, a decrease of 0.7 mills/kWh, so the new COE = 47.5 – 0.7 = 46.8 mills/kWh.

This illustrates the difficulty of reducing the COE, even if a major cost saving is achieved in one component.

Most current designs use reduced activation ferritic/martensitic steel (RAFS) structure. Some advanced designs use SiC composite structure (SiC/SiC), but large scale fabrication and testing of this material has not yet been done. Vanadium alloy (V-4Cr-4Ti) has low long-lived radioactivity, but is very expensive.

Compatibility limits of structural materials and coolants were described in Chap. 6.

There is a strong incentive to develop materials with high temperature capability and long service lifetimes, such as oxide dispersion strengthened ferritic steel (ODFS), nanograin-FS, RAFS, and SiC/SiC. RAFS blanket structures with SiC inserts enable temperatures up to about 700 °C, and SiC/SiC blanket structures may allow temperatures up to 1,100 °C. Most current fusion power plant designs

Table 13.1 ARIES-AT 1,000 MWe power-plant economic parameters (1992 $), assuming $f_{av} = 0.85$

Account number	Account title	M$
20.	Land and land rights	10.6
21.	Structures and site facilities	253.5
22.	Reactor plant equipment ("fusion island")	761.0
22.1.	Reactor equipment	482.0
22.1.1.	FW/blanket/reflector	64.3
22.1.2.	Shield	69.4
22.1.3.	Magnets	126.7
22.1.4.	Supplemental-heating/CD systems	37.1
22.1.5.	Primary structure and support	26.9
22.1.6.	Reactor vacuum systems (unless integral elsewhere)	98.8
22.1.7.	Power supply, switching and energy storage	50.7
22.1.8.	Impurity control	4.1
22.1.9.	Direct energy conversion system	0.0
22.1.10.	ECRH breakdown system	4.0
22.2.	Main heat transfer and transport systems	126.0
23.	Turbine plant equipment	243.0
24.	Electric plant equipment	98.5
25.	Miscellaneous plant equipment	47.4
26.	Heat rejection system	23.3
27.	Special materials	83.8
90.	Direct cost (not including contingency)	1,521.1
91.	Construction services and equipment	171.9
92.	Home office engineering and services	79.1
93.	Field office engineering and services	79.1
94.	Owner's cost	277.8
96.	Project contingency	311.8
97.	Interest during construction (IDC)	403.2
99.	Total capital cost	2,844.0
Unit costs		
	Unit direct cost ($/kWe)	1,521
	Unit overnight cost ($/kWe)	2,441
	Unit total cost ($/kWe)	2,844
Cost of electricity (*COE*)		
	Capital return (mill/kWh)	36.87
	O&M (2.10 %) (mill/kWh)	6.87
	Component replacement (mill/kWh)	3.51
	Decommissioning (mill/kWh)	0.25
	Fuel (D) cost (mill/kWh)	0.03
Total COE	(mill/kWh)	47.53

Note Item 22.1 = 22.1.1 + 22.1.2 + … + 22.1.10 (Najmabadi et al. 2006)

with higher blanket temperatures use Brayton cycles. There is little benefit from coolant temperatures >950 K with a steam system, because the turbine inlet temperature is limited to lower values in order to attain a long turbine lifetime.

13.3.1 Competitiveness of Fusion Energy

According to many fusion power plant studies, the COE is higher than from other sources, such as coal and nuclear fission. Nevertheless, there are several ways in which fusion reactors could become competitive:

- If there is a **carbon tax** (or "cap and trade and reduce") on fossil fuel use.
- If **fission** reactors are not widely accepted, due to public perceptions of safety or radioactive waste issues.
- If **compact** high power-density fusion reactors (such as spheromaks) are successfully developed.
- If fusion-fission **hybrid** reactors are built (discussed in Chap. 14).
- If fusion reactors are built in large sizes to achieve **economy of scale**. Large size (>1 GW$_e$) base-load fusion power plants might produce electricity and synthetic fuels competitively (Dolan 1993; Sheffield et al. 2000).

13.4 Economy of Scale

13.4.1 Economy of Scale Issues

There are several issues that could limit the deployment of high-power fusion reactors:

1. Too much **electricity** at one site. However, there are already about 10 power stations generating more than 4 GWe at one site.
2. Too much heat **rejection** at one site. The heat rejected per W generated is

$$P_{rej}/P_e \approx [1 - (1 - \varepsilon)\eta_e]/\eta_e(1 - \varepsilon), \qquad (13.10)$$

where η_e = thermal → electrical conversion efficiency and ε = recirculating power fraction. A coal plant or fission reactor with $\eta_e \approx 0.33$ and $\varepsilon \ll 1$ would have $P_{rej}/P_e \approx 2$.

A fusion reactor with a high-temperature blanket, such as ARIES-I, might achieve $\eta_e \approx 0.49$ and $\varepsilon \approx 0.1$ For this case $P_{rej}/P_e \approx 1.27$. Thus, a 1.5 GW$_e$ fission reactor would release 3 GW$_{th}$ ("th" means "thermal") to the environment. The high-temperature blanket fusion reactor could generate 2.36 GW$_e$ and still release the same amount of heat to the environment (3 GW$_{th}$) as the 1.5 GW$_e$ fission power plant. (A power plant site with four 1-GW$_e$ fission reactors may release 7–8 GW$_{th}$ to the

environment.) If this heat is available for alternate uses, such as space heating and hydroponic farming, some of the rejected heat could be beneficial.

3. **Public acceptance** depends upon whether the public understands the safety and environmental advantages of fusion.
4. **Investment risk**. Larger plants have greater investment risk. Utilities are reluctant to invest in large, expensive, risky ventures until the technology and availability are demonstrated.
5. **Market penetration**. Market penetration will be slower for large plants, since it is easier to site and purchase small plants, but increasing world demand may make large plants more popular.
6. **Load following**. Utilities may need to increase and decrease the power output to match the demand.

   - The fusion power output could be controlled by adjusting the plasma parameters, but for large steam turbines this is inefficient and wasteful of the capital equipment.
   - Large power plants (fission and fusion) would usually be run at full power to provide constant base-load power, and natural gas-fired generators would be adjusted to cover hourly fluctuations.
   - Large fusion reactors could use some of the output power to generate hydrogen fuel when the electricity demand is low.

7. **Grid perturbation**. Shutdown of a large fusion power plant could cause a severe power grid perturbation, and some outages cannot be prevented. Thermal, magnetic, or electrical energy storage could work for many minutes, but outages lasting many hours could exceed the affordable energy storage. One possible solution could be to have five 3-GW_e fusion power plants at one site, each plant selling 2.2 GW_e directly and using 0.8 GW_e-equivalent of its power to generate hydrogen, either by electrolysis or by a thermo-chemical cycle, such as the sulfur-iodine cycle. (Bourque 1998) The plant normal output would be 11 GW_e plus 4 GW_e worth of hydrogen. If one plant were shut down, then the other four could make less hydrogen, and still be able to sell the normal 11 GW_e off-site (see Sheffield et al. 2000).
8. "**Small is Beautiful**" philosophy. Small power plants have an important role to play in many locations. For example, solar and wind power plants can be attractive in small sizes, but energy storage may be needed for them, and the overall COE is generally high.

Present fusion confinement schemes do not lend themselves well to small scale power plants. Many have been proposed, but none to date have been cost-effective below 1 GWe. The 1 GWe size is, by default, the nominal design point for almost all fusion power plant designs. As the confidence that fusion power can be achieved and commercialized (Demo1 and perhaps Demo2 is fulfilled), it is likely that the nominal power plant size will be increased to the 1.5 or 2 GWe level.

13.4.2 Reasons for Economy of Scale

For fusion power we can ask, "At what power level would the COE become competitive?" To answer this question, we consider four effects that provide an economy of scale for fusion power:

Decreased **operating and maintenance** costs per Watt for high power plants. This has not been quantified for fusion power plants.

1. Decreased cost per Watt for large **equipmen**t items. The cost C at power P relative to cost C_o at a lower power P_o is

$$C = C_o(P/P_o)^{-n}. \tag{13.11}$$

The scaling exponents are:
n   0.45 for primary heat transport equipment,
n   0.20 for turbine plant equipment, and
n   0.51 for electrical plant equipment (Dolan 1993).

However, there is a size above which a single unit (such as a single turbine) cannot be made reliably, so a further increase in power would require two units, which would lose the economy of scale. Extrapolations to higher power units are not justified until the units have been built and tested.

A **geometric effect**. At a fixed neutron wall loading (MW/m^2) the reactor electrical power P_e per mass M of (blanket + shield + coils) with thickness Δ, increases at high powers according to the equation (Dolan 1993)

$$(P_e/M)_2/(P_e/M)_1 = (a_1/a_2)[(1 + \Delta/a_1)^2 - 1]/[(1 + \Delta/a_2)^2 - 1]. \tag{13.12}$$

For example, consider reactor with $\Delta = 3$ m. The increase in (P_e/M) caused by expanding the minor radius from 2 to 3 m would be a factor of 1.17. Since the reactor cost is roughly proportional to the mass, the cost per Watt would tend to decrease at high powers.

Lower **recirculating power fraction**. A tokamak requires high recirculating power for current drive, cryogenic refrigeration, etc. The cost of current drive scales roughly linearly with plasma current, and the fusion power would increase almost as the fourth power of the poloidal B field and plasma current, if stability could be maintained (It would probably require increasing the toroidal B field, too, to keep $q_a > 2$).

As a result of these four factors the COE from magnetically confined fusion power plants scales approximately as

$$COE/COE_o = (P/P_o)^{-n}. \tag{13.13}$$

Magnetic confinement and inertial confinement fusion power plant studies have found scaling exponent values n ranging from about 0.3 to 0.5. Using 0.4 as an approximate value, an increase of power from 1 to 3 GW$_e$ would decrease the

COE to 64 % of its original value. For example, the COE might drop from 8 to 5 cents/kWh. However, each plant must be studied in detail (taking into account limiting sizes of turbines, for example) before a firm conclusion can be drawn.

Another possible benefit of large sizes is that, at a constant neutron wall loading, the required magnetic field

$$B \propto a^{-0.25}. \tag{13.14}$$

At larger sizes the lower magnetic field could facilitate slight magnet coil cost savings (Dolan 1993).

> Siting and transmission line costs: The siting and transmission lines of a 2 GWe power plant would cost considerably less than twice the siting and transmission line cost of a 1 GWe power plant (Sheffield et al. 2000).

The incremental costs associated with increasing the size of fusion power plants are summarized in Table 13.2.

An effect in the opposite direction is the divertor target heat flux. If the heat flux width in the SOL stays constant at $\lambda_q \sim 5$ mm as the power P_{SOL} flowing into the SOL increases, then the heat flux q_{div} at the divertor target could become unmanageable. The divertor heat flux problem can be ameliorated by several means (Sect. 7.5), such as by sweeping the strike point back and forth across the target.

Thus, the fusion power economy of scale looks attractive, but it may be limited by grid perturbation issues and by divertor heat flux issues in tokamaks.

Table 13.2 Range of incremental and total costs for fusion power plants (Sheffield et al. 2000 Table 5)

Cost component	Unit size (MWe)			
	1,000	2,000	3,000	4,000
Extra spinning reserve ($M/y)	0	10.5	26.0	40.5
Incremental site cost ($M/y)	0	5.0	10.0	15.5
Inc. operational cost ($M/y)	0	15.0	30.0	60.0
Purchased electricity ($M/y)	0	22.0	33.0	44.0
Total extra annual cost <$M/y)	0	52.5	99.0	160.0
Incremental COE[a] (mills/kWh)	0	3.9	5.0	6.0
Incremental COE[b] (mills/kWh)	0	3.5	4.4	5.4
ARIES-RS COE[c] (mills/kWh)	87	68	60	56
ARIES-AT COE[c] (mills/kWh)	51	44	39	37

[a] An availability of 76 % was assumed for ARIES-RS
[b] An availability of 85 % was assumed for ARIES-AT
[c] Value derived by adding the incremental COE to the values in Table 13.1

13.5 European Power Plant Designs

El-Guebaly provides a comprehensive review of worldwide fusion power plant studies (El-Guebaly 2009).

European researchers have done many fusion power plant design studies, including the Power Plant Conceptual Study (PPCS). The guidelines for this study are

Safety/Environment

- No need for emergency evacuation
- No active systems for safe shut-down
- No structure melting following LOCA
- Minimum waste transport
- Minimum waste to repository.

Operation

- Steady state
- $\sim 1\ GW_e$
- Base load
- Availability 75–80 %, with only few unplanned shut-downs/year.

Economics

- Public acceptance could be even more important than economics
- Economic comparison among equally acceptable energy sources
- Licensing/regulation requirements strongly reduced versus fission
- Construction time ≤5 years (Maisonnier 2004).

Figure 13.2 shows the sizes of the four model designs (A, B, C, and D) that were considered in the PPCS.

The Models (A) & (B) anticipate only a modest improvement relative to ITER, with a monotonic q profile with $q_{95} = 3$, confinement enhancement factor $H_H < 1.2$, $n/n_{GR} < 1.2$, $\beta_N < 3.5$, and first stability region. Models (C) & (D) assume progressive improvements in performance, with high β and high confinement, MHD stabilization by strong plasma shaping, high bootstrap current fraction, and divertor protection. Table 13.3 shows the main parameters of these PPCS models.

All four models use tungsten alloy divertor armor. The materials used in the divertor and blanket structure are listed in Table 13.4.

The helium-cooled divertor can handle heat loads up to 10 MW/m^2. Figure 13.3 shows how the availability and COE depend on divertor lifetime.

This graph is just an illustrative calculation for one case, because the COE depends on many more factors than the divertor lifetime. Development of a durable divertor design is very important. It would be beneficial for the first wall and blanket to have the same lifetimes, so they could have a common maintenance procedure; or for the blanket to last the lifetime of the plant, requiring only replacement of first wall tiles.
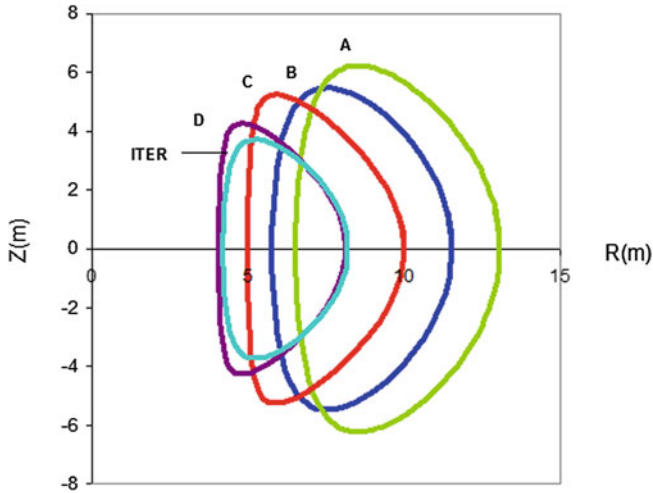
Fig. 13.2 Plasma shapes of the *four* PPCS tokamaks (Maisonnier 2004)

Table 13.3 Main parameters of the PPCS models (Maisonnier 2004)

Parameter	Model A	Model B	Model C	Model D
Unit Size (GW$_e$)	1.5	1.3	1.4	1.5
Fusion Power (GW)	5.0	3.6	3.4	2.5
Net efficiency	0.31/0.33	0.36	0.41	0.60
Major radius (m)	9.55	8.6	7.5	6.1
Plasma current (MA)	30.5	28.0	20.1	14.1
Bootstrap fraction	0.45	0.43	0.63	0.76
P$_{add}$ (MW)	246	270	112	71
Recirculating power fraction	0.28	0.27	0.13	0.11
Divertor peak load (MW/m^{-2})	15	10	10	5
Av. neutron wall load	2.2	2.0	2.2	2.4

Table 13.4 Materials used in the four models. W means tungsten alloy. RAFM means reduced activation ferritic/martensitic steel (Maisonnier 2004)

Model	Divertor structure	Blanket structure	Breeder/coolant
A	Cu/water or RAFM/water	RAFM	PbLi + water
B	W + RAFM/He	RAFM	Li$_4$SiO$_4$ + Be + He
C	W + RAFM/He	RAFM (ODS)	PbLi + SiC + He
D	SiC + PbLi	SiC	PbLi

Maintenance would be done by replacing large modules, segment, or sectors to minimize the required labor hours. Figure 13.4 shows the amount of radioactive waste and recyclable materials present 100 years after shutdown.
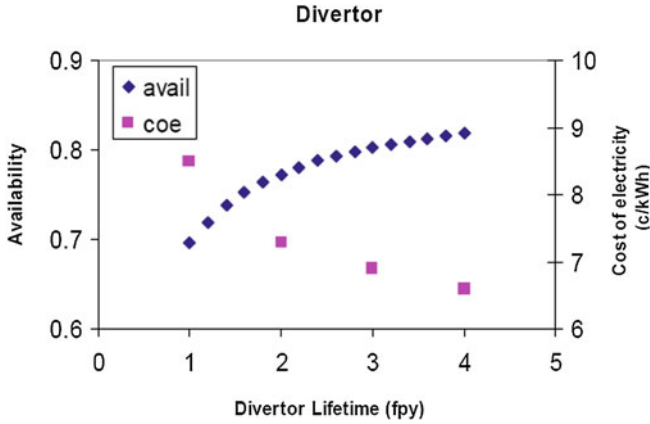
Fig. 13.3 Dependence of availability and COE on divertor lifetime (Ward 2004)

Fig. 13.4 Disposal of PPCS reactor materials (Maisonnier 2004)
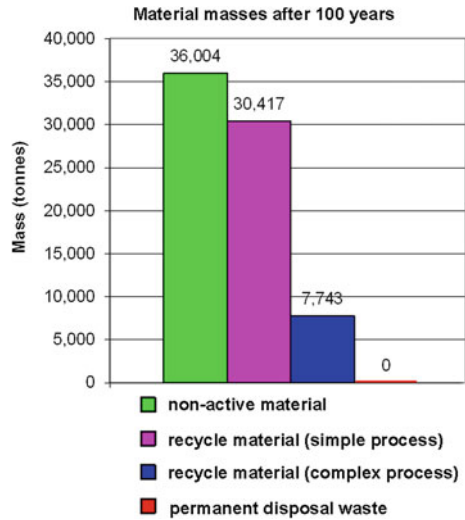
The achievements of the PPCS include:

- **Economic viability** of fusion power with plasma confinement only slightly better than the ITER physics basis.
- A **maintenance** concept that could facilitate 75 % availability
- A **divertor** concept capable of handling 10 MW/m^2
- Passively **safe**, so no offsite evacuation plan would be needed
- Possibility of **recycling** practically all the materials, with no wastes requiring permanent disposal.

More work is needed on development of divertors and maintenance procedures.

13.6 Japanese Power Plant Designs

13.6.1 Helical Reactor

The Japanese team has been designing several heliotron power plants, based on the successful LHD experiment. These designs generally have two helical windings and 10 field periods, like LHD. Figure 13.5 illustrates a toroidal cross section, showing the plasma, blanket, shield, and superconducting (SC) helical coils.

This is a simplified representation, because the actual plasma shape varies widely from one toroidal location to another, and the vertical field coils are not shown. Table 13.5 lists the main parameters of the FFHR2m2 design.

This design varies the pitch of the helical coil to reduce the hoop force on the helical coil support structure. Carbon armor tiles containing beryllium soften the neutron energy spectrum, facilitating a local breeding ratio of 1.2. Figure 13.6 shows the blanket design.

With a heat load of 0.1 MW/m^2 the carbon tile surface temperature is 1,600 K, high enough that tritium retention is small. The Be$_2$C pebble bed enhances heat transfer to the slowly flowing FLIBE coolant so that it can remove 1 MW/m^2.

The carbon tile lifetime is limited by swelling. A manipulator sliding on "screw coaster" helical tracks can replace armor tiles remotely during regular planned inspections. Although the *tile* lifetime is limited by radiation damage, the rest of the *blanket* can last much longer. This self-cooled FLIBE blanket with reduced activation ferritic steel structure is designed to last for 30 years, which reduces the COE, Fig. 13.7.
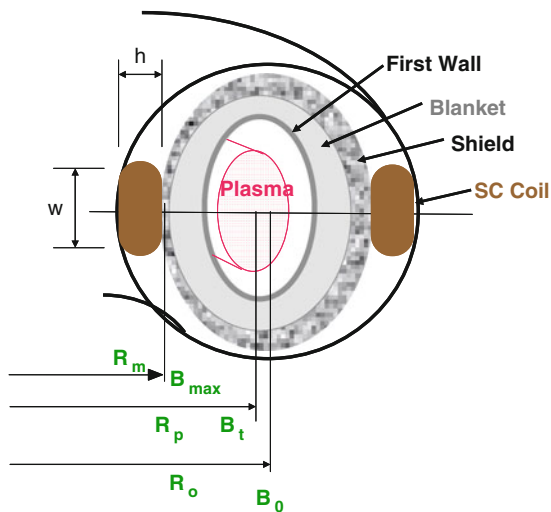
Fig. 13.5 Toroidal cross section of the FFHR2m2 reactor (Dolan et al. 2005)

Table 13.5 Parameters of the FFHR2m2 reactor, which has two helical windings and 10 field periods, like LHD (Sagara et al. 2005)

R	16.0 m	
A	2.80 m	
Blanket thickness	1.1 m	Ferritic steel and FLIBE
B_o in plasma	4.43 T	
B_{coil}	13.0 T	
P_{fus}	3.0 GW$_{th}$	
Neutron wall load	1.3 MW/m^2	
Heating power	100 MW	
n_e	1.9×10^{20} m^{-3}	
n/n_{sugo}	1.5	
Z_{eff}	1.35	
H_{ISS95}	1.76	
T_i	16.1 keV	
β	4.1 %	
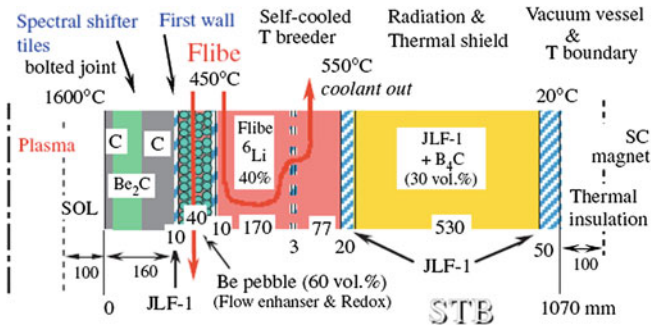
Fig. 13.6 The radial build of the FFHR2m2 reactor. JLF-1 is reduced activation ferritic steel (Sagara et al. 2005, Fig. 1)

Fig. 13.7 Variation of the COE (Yen/kWh) with blanket lifetime for the FFHR2m2 Heliotron power plant (Sagara et al. 2005, Fig. 17)
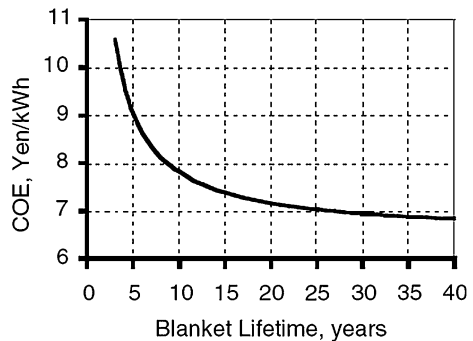
Table 13.6 Parameters of the VECTOR design (Nishio et al. 2003, Table 1, slightly modified) Copyright International Atomic Energy Agency, Vienna, 2003

Major radius	R	3.75 m
Minor radius	a	1.9 m
Ellipticity	κ	3.75
Plasma current	I_p	18.3 MA
Normalized beta	β_N	3.75
Fusion power	P_f	1.8 GW
Neutron wall load	P_n	3.5 MW/m^2
Maximum field at TF coil	B_{max}	19.6 T
Radius of center post		0.9 m

As the blanket lifetime is increased from 5 to 30 years by the carbon spectral-shifting tiles, the COE drops from 9 to 7 Yen/kWh.

13.6.2 Spherical Tokamak

The VECTOR spherical tokamak incorporates three unusual features:

No central solenoid coil in the center post. Plasma current is induced by rf waves or NBI.

1. No inboard breeding blanket, but an inboard shield protects the superconducting TF coil.
2. Use of Bi2212/Ag/AgMgSb high temperature superconductor to achieve both high field (20 T) and high current density at T = 20 K.

The main parameters are listed in Table 13.6.

Figure 13.8 shows a cutaway view of the VECTOR reactor, which uses SiC structure, be neutron multiplier, and Li breeder and coolant.

A compact, low-cost power plant might be based on this concept, if the magnet coil and materials requirements could be satisfied.

13.7 Chinese Power Plant Designs

China is developing LiPb blankets for conventional fusion reactors and also for fusion driven subcritical (FDS) reactors. There are several blanket concepts, most of which use reduced activation ferritic-martensitic (RAFM) steel structure and LiPb breeder (Wu et al. 2002).
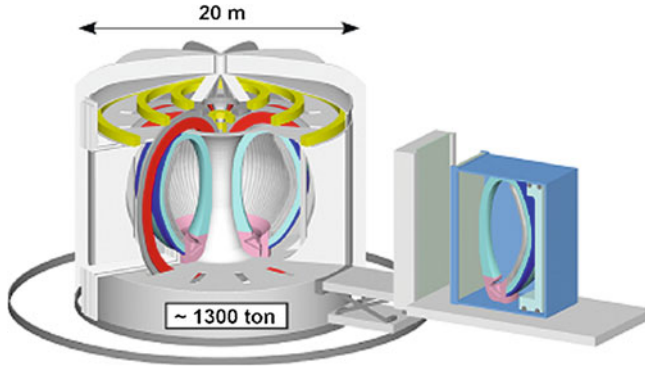
Fig. 13.8 The VECTOR spherical tokamak reactor. From Nishio et al. (2003), Fig. 6. CAD drawing by A. Meano. Copyright International Atomic Energy Agency, Vienna, 2003

13.7.1 Power Plant for Electricity Generation

The FDS-II power plant would have the following parameters: R = 6 m, a = 2 m, I_p = 15 MA, elongation = 1.9, β = 5.93 %, n = 2.2 × 10^{20} m^{-3}, T = 11 keV, P = 2,500 MW, Q = 31, neutron wall load = 2.6 MW/m^2 (average) to 3.5 MW/m^2 (peak), q = 0.54 MW/m^2, bootstrap current fraction = 0.69 (Wu and Team 2008). These parameters are similar to those of ITER.

The dual-cooled lithium lead (DLL) blankets would be used in reactors to produce electricity. SiC inserts in the LiPb flow channels reduce the MHD pressure drop and serve as thermal insulation so that the LiPb outlet temperature can be up to 700 °C. (Here SiC means a silicon carbide matrix strengthened by high-strength SiC fibers.) The quasistatic lithium–lead (SLL) blanket could be used if the MHD flow problems of the DLL were not successfully resolved, but the SLL outlet He temperature would be lower, about 450 °C (Wu and Team 2007a, b).

The outboard DLL blanket module dimensions are roughly 2 m toroidal, 2 m poloidal, and 1.2 m radial. The inner blanket to breed tritium would need to be replaced, but the shield would be designed to last the lifetime of the plant. Assuming ^{6}Li enrichment to 90 %, the tritium breeding ratio (TBR) would be 1.29. The maximum Von Mises stress is 333 MPa at the first wall helium channel, which is below the limit of 476 MPa.

Figure 13.9 shows the energy conversion system.

The helium gas turbine Brayton cycle with turbine input T = 680 °C can achieve 47 % efficiency. An intermediate heat exchanger isolates the turbine loop from the tritium in the primary He coolant loop (Wu and Team 2008).
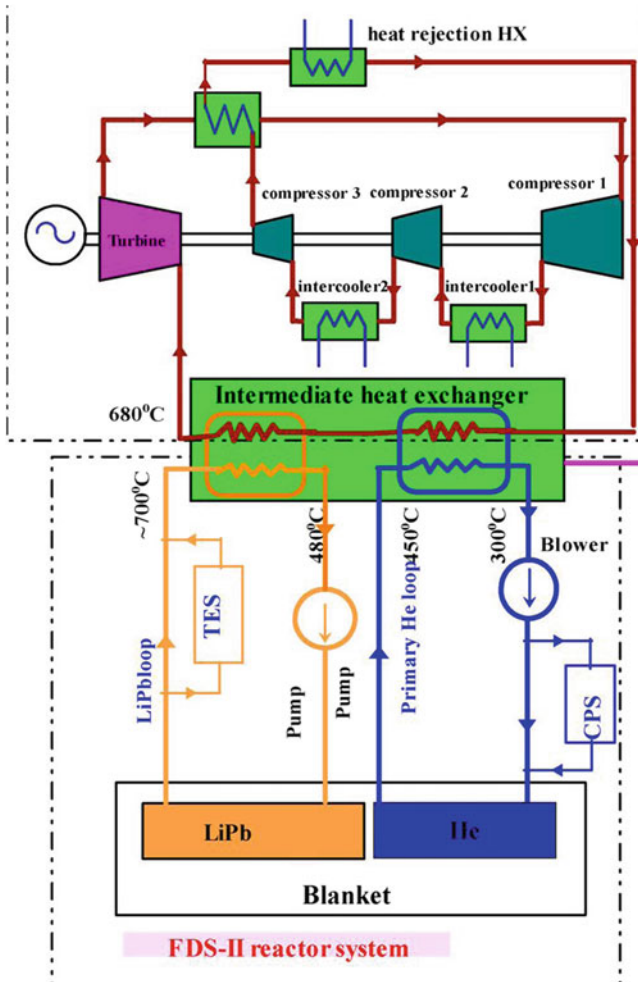
Fig. 13.9 Power conversion system of the FDS-II power plant (Wu and Team 2008)

13.7.2 Hydrogen Production Plant

A high temperature liquid LiPb blanket (HTL) is used in the FDS-III reactor optimized for hydrogen production. It has fusion power = 2,600 MW, R = 5.1 m, a = 1.7 m, I_p = 16 MA, B_t = 8 T, elongation = 1.9, toroidal β = 5.6 %, average n = 10^{20} m^{-3}, average T = 10 keV, bootstrap current fraction = 0.65. Helium coolant at 8 MPa will cool the first wall and structure. Using multilayer SiC flow channel inserts (FCI) the LiPb temperature can exceed the allowable RAFMs
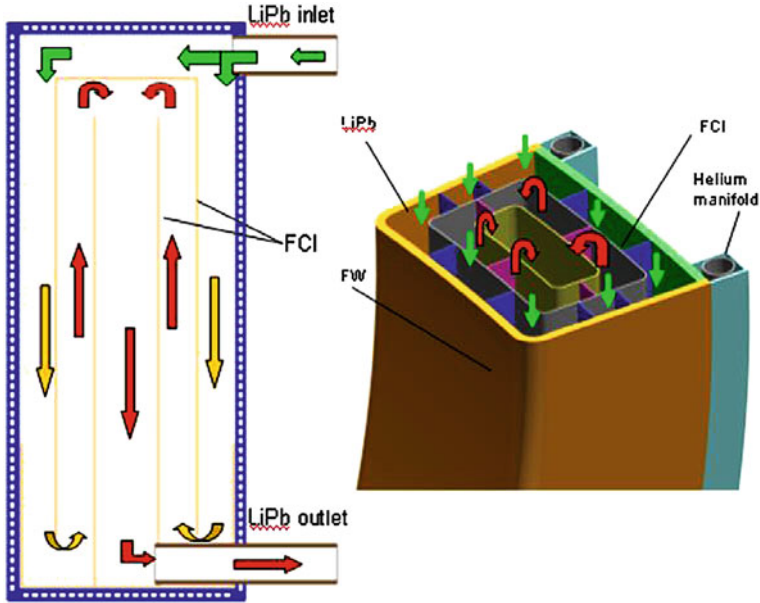
Fig. 13.10 The LiPb flow channels of the HTL blanket (Wu and Team 2007b)

upper operation temperature (550 °C), reaching up to 1,000 °C at a mass flow rate of ∼16 kg/s. Figure 13.10 shows the LiPb flow channels of a simplified design.

The temperature is highest in the inner FCI, away from the RAFMs. The LiPb pressure drop would be 0.28–0.56 MPa, with a pumping power 0.6–1.3 kW per module (Wu and Team 2007a, b, 2009; Chen et al. 2008).

The Iodine–Sulfur thermochemical cycle, using H_2SO_4, HI, and I_2, with a high temperature higher than 950 °C, would be used to produce hydrogen from water. Candidate high-temperature structural materials for this corrosive environment include SiC composite and Hastelloy. The toxic chemicals would be recycled, except for minor leakage. The inputs would be water and high-temperature heat, and the outputs would be H_2, O_2, and low-temperature heat with energy conversion efficiency ∼50 % (Chen et al. 2008).

13.7.3 Fusion-Fission Hybrid Power Plants

The dual-cooled waste transmutation (DWT) reactor is to transmute long-lived wastes from fission power plants and to produce fissile fuel. The DWT reactor would have a neutron wall loading ∼0.5 MW/m^2 and a fusion power ∼150 MW. The blanket would have an inner active core of fissile fuel that multiplies neutrons and generates fuel surrounded by a fission product zone that transmutes wastes.

The fuel would be pebbles of U or Pu carbide or oxide, surrounded by liquid metal LiPb. In some designs helium gas coolant is also used.

A fission–fusion research facility (FFRF) tokamak would use lithium-covered walls to reduce edge plasma density, to increase edge temperature, and to avoid electron turbulence and edge-localized modes. It would operate at a fusion power of 50–100 MW for hours (or steady state) with fertile blankets that greatly increase the thermal power and breed tritium and fissile fuel, while keeping the neutron multiplication factor k_{eff} less than 0.95 for safety (Zakharov et al. 2010).

13.7.4 Tritium Breeding Module (TBM) for ITER and DEMO

The Helium-cooled solid breeder module would use lithium orthosilicate (Li_4SiO_4) breeder pebbles (0.5–1 mm diameter) cooled by helium gas at 8 MPa flowing at 37 m/s in Eurofer97 steel tubes with inlet and outlet temperatures of 300 and 500 °C exposed to a neutron wall load of 0.78 MW/m^2 and surface heat flux of 0.5 MW/m^2 (Feng et al. 2006, 2008). A preliminary design is shown in Fig. 13.11.

The peak temperature of the Be first wall armor is 574 °C. A He purge gas at 0.1 MPa would flow through the pebbles to carry tritium to a tritium extraction system (Feng et al. 2006). A similar blanket considered for the DEMO reactor uses 80 % enriched ^{6}Li in Li_4SiO_4 in a 0.57 m thick breeding zone to achieve a TBR of 1.1 (Feng et al. 2009).
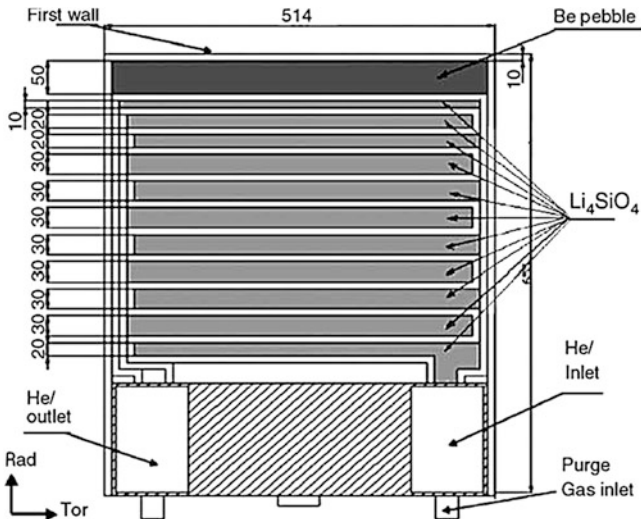
Fig. 13.11 Preliminary design of the helium-cooled solid breeder blanket module (Feng et al. 2006)

Fig. 13.12 Preliminary design of DFLL-TBM (Wu and Team 2007a, Fig. 1) (rpSP = radial poloidal stiffening plate, tpSP = toroidal poloidal stiffening plate)
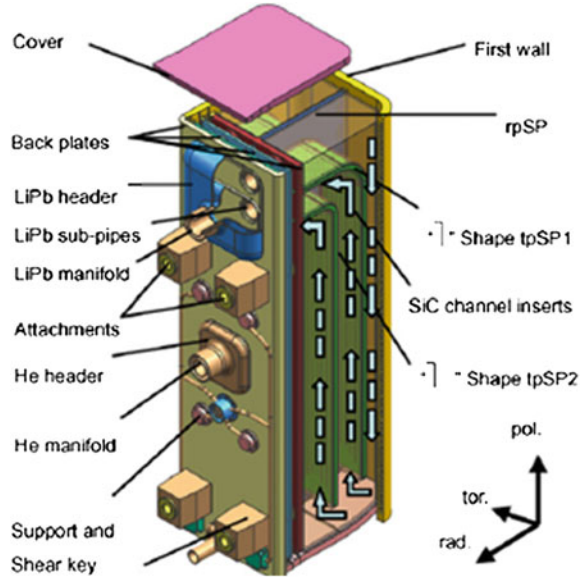
The dual-functional lithium–lead test blanket module (DFLL-TBM) was designed to demonstrate the technologies of SLL and DLL blankets by using similar structure and auxiliary systems. China Low Activation Martensitic steel (CLAM) was chosen as structure material, helium-gas/LiPb serve as coolant and/or breeder material. Without Flow Channel Insert (FCI), the DFLL-TBM will operate as an SLL blanket, which features a lower exit temperature of <450 °C and a lower velocity of <1 mm/s of LiPb flow. With FCI, the DFLL-TBM will operate as a DLL blanket, which features a higher exit temperature of <700 °C and a higher velocity of <10 mm/s. One preliminary design is shown in Fig. 13.12, (Wu and Team 2007a, b).

13.7.5 Materials Research

Chinese scientists are studying the corrosion resistance of CLAM in LiPb at high temperatures and the properties of RAFM under high-energy neutron irradiation. They are also studying the tritium permeation reduction factor of various coatings and flow inserts, such as Al_2O_3 and SiC. A MHD pressure-drop-reduction coating should have a product of thickness and electrical resistivity $>0.01 \ \Omega m^2$.

China is also designing a LiPb test blanket module (TBM) for ITER. A half-size TBM will be tested in the EAST tokamak at B $\sim$ 3.5 T, q $\sim$ 0.1–0.2 MW/m^2, with DD neutron rates up to 10^{17}/s, long before ITER reaches high power operation (2027) (Wu and Team 2007a, b).

13.8 United States Power Plant Designs

Early magnetically confined fusion conceptual fusion power plant design studies at Princeton and at the University of Wisconsin were discussed in the previous edition of this book. (Dolan 1982) The Starfire plant study (1980) employed the first steady-state, non-inductive plasma in a highly maintainable power core. Since then, many more designs have been conducted by several groups.

13.8.1 ARIES Designs

Starting around 1990, The "Advanced Research, Innovation, and Evaluation Study" (ARIES) Group has done a series of magnetic fusion power plant design studies to investigate attractive confinement schemes, potential plasma operating conditions and innovative technologies. The ARIES power plant designs are summarized in Table 13.7.

The nominal electrical power output of these designs was held at 1,000 MW$_e$. The COE values are in dollars pertinent to the date of the study and have been inflated to a common year of 2010 US dollars for comparison using the US Gross Domestic Product Price Level Deflator. Note that the COE is strongly influenced by the plant availability, which was held at 76 % for most ARIES studies, except for the most recent two at 85 %. With ARIES-RS, ARIES-AT and ARIES-CS, improvements of the power core maintainability and availability were key design drivers the plant design.

The confinement multipliers are the assumed energy confinement times divided by the times predicted by scaling laws (ITER89-P and ISS95). These enhancements are partially justified by the fact that some experimental data exceed those scalings. For example, LHD data have achieved multipliers up to 2.5 (Lyon et al. 2008). In some cases it is difficult to get ignition without either assuming confinement enhancement or using a larger minor radius, which would increase the capital cost per kW at constant P$_{out}$ = 1,000 MW$_e$. (Alternatively, one could use a larger minor radius to get ignition without confinement enhancement and allow the output power to increase).

13.8.2 ARIES-AT

The current best US example of an advanced tokamak is represented by ARIES-AT. It is intended to assess the potential of high-performance tokamak plasmas along with advanced technologies to highlight areas for productive R&D. These advanced plasmas and hardware technologies are not directly forthcoming from

Table 13.7 Magnetic fusion power plant designs of the ARIES group. COE is adjusted to 2010 dollars

Year	Name	Type	Parameters	COE[a] ¢/kWh	Remarks
1990	ARIES-I	First-stability regime tokamak	6.75 m/1.5 m, 10 MA, $\beta = 1.9$ %, $B_{coil} = 21$ T, SiC + Li_2ZrO_3 + He, 650 °C, $\eta = 49$ %, $\Gamma_n = 2.5$ MW/m²	10.8	Uses achieved physics. $P_{recirc} = 20$ %, A = 76 %
1991	ARIES-III	D-^{3}He fueled tokamak	7.5 m/2.5 m, 29.9 MA, $\beta = 24$ %, $B_{coil} = 14$ T, $\Gamma_n = 0.08$ MW/m²	12.4	2nd stability regime. $T_i = 55$ keV $P_{recirc} = 24$ %, A = 76 %
1992	ARIES-II, ARIES-IV	Second-stability regime tokamaks	II: R = 5.6, a = 1.4, $\beta = 3.4$ %, $B_{coil} = 15.9$ T, $\Gamma_n = 2.9$ MW/m² IV: R = 6.04, a = 1.51, $\beta = 3.4$ %, $B_{coil} = 15.9$ T, $\Gamma_n = 2.9$ MW/m²	10.7 9.8	II: $P_{recirc} = 15$ %, A = 76 % IV: $P_{recirc} = 19$ %, A = 76 %
1993	PULSAR	Pulsed tokamak		NA	
1994	SPPS	Stellarator	13.95 m/1.16 m, $\beta = 5$ %, $B_{coil} = 14.55$ T, 4 field periods, 32 modular coils, V + Li, $\eta = 46$ %	10.7	$P_{recirc} = 5$ %, A = 76 %
1996	ARIES-RS	Reversed-shear tokamak	5.52 m/1.38 m, 11.3 MA, $\beta = 5$ % $B_{coil} = 16$ T, V + Li, 610 °C, $\Gamma_n = 3.96$ MW/m²	11.0	$P_{recirc} = 17$ %, A = 76 %
1999	ARIES-ST	Spherical torus	3.2 m/2.0 m, 28 MA, $\beta = 54$ %, P(Cu coil) = 329 MW, $B_{coil} = 7.6$ T, ferritic + PbLi, 700 °C, $\eta = 45$ %	11.4	$P_{recirc} = 34$ %, A = 76 %, much radioactive material generated
2000	ARIES-AT	Advanced technology tokamak	5.2 m/1.3 m, 13 MA, $\beta = 9$ %, $B_{coil} = 11.5$ T, SiC + PbLi, 1,100 °C, $\eta = 59$ %	6.9	YBCO high-temperature superconductor, ITER89-Pconfinement multiplier = 2.0, $P_{recirc} = 14$ %, A = 85 %
2008	ARIES-CS	Compact stellarator	7.75 m/1.7 m, 4 MA, $\beta = 6.4$ %, T = 6.6 keV, $B_{coil} = 15$ T, $\Gamma_n = 2.6$ (max. 5.4) MW/m², ferritic +PbLi + He, Brayton 43 %, He pumping P = 183 MW	8.9	High-n, low-T, ISS95 confinement multiplier = 2.0, $P_{recirc} \sim 18$ %, A = 85 %

[a] The adjustment of these costs to 2010 dollars is not wholly accurate, because it is done using a coefficient based on commodity price inflation, while the energy sector inflation may be significantly larger
Source http://aries.ucsd.edu/ARIES/
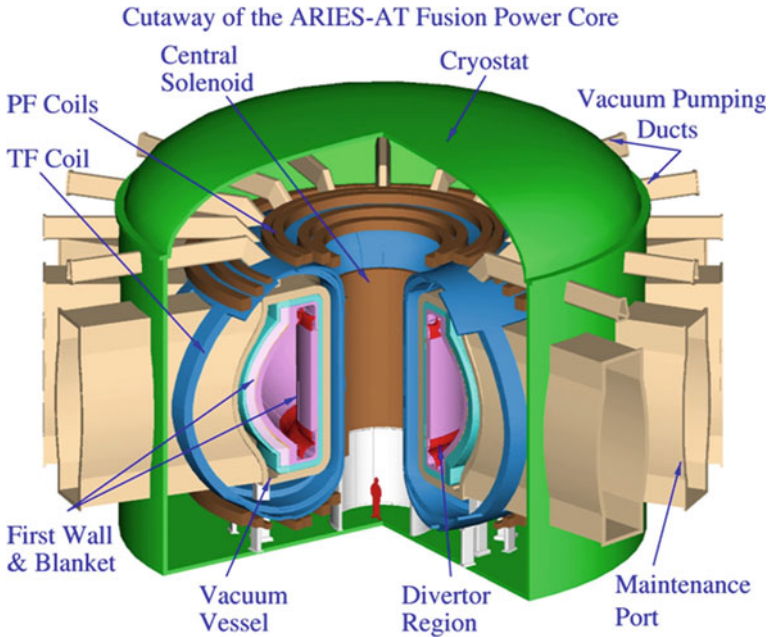
Fig. 13.13 The ARIES-AT reactor (Najmabadi et al. 2006, Fig. 1)

ITER, rather they will require some additional developmental work and testing to realize the potential promised by ARIES-AT. Figure 13.13 shows a drawing of the ARIES-AT reactor with its large ports for efficient horizontal maintenance.

It is designed so that a whole blanket sector can be removed between the TF coils and replaced, as shown in Fig. 13.14.

By assuming the use of advanced future technologies, like YBCO high-temperature superconductor and SiC structure with a high-temperature PbLi blanket, this ARIES-AT design achieves very high thermal conversion efficiency (59 %) and low COE, which could be reasonably competitive with other energy sources. This shows that a break-out from the old high-COE designs may become feasible in the future, if magnetic fusion technology development is successful. The ARIES-AT design report lists 7 developments that are needed for this level of performance:

1. **Plasma profile control**

A reversed-shear plasma produces an internal transport barrier, which facilitates long energy confinement times, high beta, and high bootstrap current fraction. Sustainment of this operating mode would require careful control of plasma profiles, especially J(R) by current drive methods like LHCD, NBI, ICRH, and ECRH.
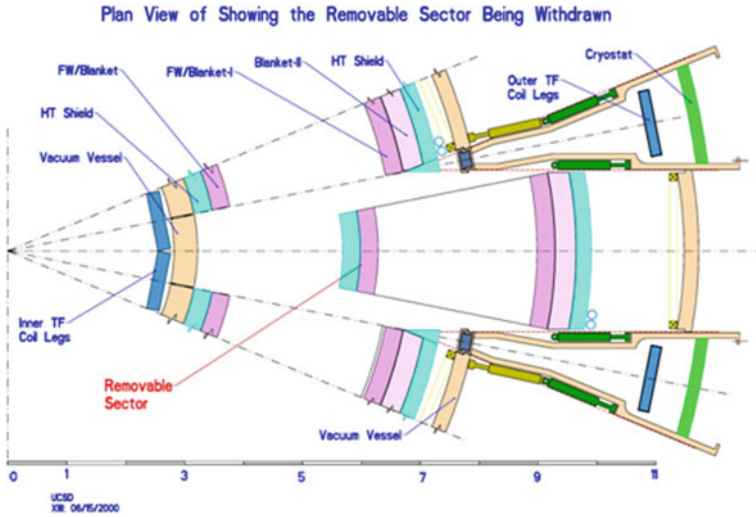
Fig. 13.14 Removal of a blanket module from the ARIES-AT reactor (Najmabadi et al. 2006, Fig. 8)

2. **Power flow control**

The heat loads to the first wall and divertor must be kept below what those plasma facing components can tolerate, including sudden, intense loads from vertical displacement events (VDEs), disruptions, and edge localized modes (ELMs).

3. **Disruption avoidance**

Plasma control systems must be able to actively control the plasma so that there is less than one large plasma disruption per year.

4. **Development of SiC composites**

The development of large-scale manufacturing of high-temperature SiC composite power core components with minimal radiation damage, high reliability, and reasonable production costs.

5. **Compatibility of SiC composites with flowing Pb-17Li at 1,000 °C**

Validation of the compatibility between flowing high-temperature Pb–Li must be established up to the temperature range of interest, 1,000–1,100 °C.

6. **Heat exchangers between Pb-17Li and He at 1,100 °C**

New heat exchangers must be designed and validated in the temperature range of 1,000–1,100 °C to allow the higher efficiencies possible with the advanced Brayton cycles.

7. **Development of materials for high heat flux, high-performance components**

Long-lived, very high heat flux plasma facing components are needed, especially in the divertor region. Tungsten alloy is a candidate material to be developed and validated.

13.8.3 Stellarators

Stellarators also show promise as attractive power plants. In 2008, the ARIES team designed a compact stellarator to improve performance and economics. In the end, the design point might have been too compact as many subsystems were up against hard constraints, such as maximum B field and neutron wall loading. Still, the intrinsic steady-state operation of the stellarator is a distinct advantage and the stellarator remains a viable candidate, under development in Japan and Germany. The USA began building the National Compact Stellarator Experiment (NCSX), but then discontinued funding in 2008.

The ARIES-CS is a low-aspect-ratio (R/a $\sim$ 4.5) stellarator, which used a detailed neutronics study to minimize the coil-to-plasma distance on the inboard side of the torus Fig. 6.22. The major radius of 7.75 m is much lower than previous stellarator designs. It uses LiPb and He coolants with RAF structure and a Brayton cycle with 43 % efficiency. However, the drive to low aspect ratio resulted in a peak heat flux at the divertor of 18 MW/m^2, which exceeds the usual 10 MW/m^2 engineering limit, so a larger aspect ratio $\sim$ 6 would probably be needed. [El-Guebaly 2009]

In addition to generating electricity, fusion reactors may be useful for some of the following applications: (El-Guebaly 2009)

- Hydrogen production
- Transmutation of radioactive wastes
- Breeding fissile fuels
- Production of medical radioisotopes
- Desalination of seawater
- Space propulsion.

13.9 Summary

Industrial companies have told us what criteria they have for choosing energy sources—economics, regulatory simplicity, and public acceptance. Fusion power plant design studies have shown the importance of reliability, availability, and maintenance. Remote handling will be required for fusion reactor internal components, and materials should be chosen to facilitate clearance and recycling. The

total capital cost of a power plant is almost twice the direct capital cost, due to the time value of money, so fast construction times are valuable. Fusion power economy of scale could lower the cost of electricity, if perturbations of the power grid could be tolerated. Europe, Japan, China, and the USA have produced power plant design studies that quantify the conditions for success. Fusion might become competitive with other energy sources if there were a carbon tax, if fission reactors were not widely accepted, if compact fusion reactors were developed, if fusion-fission hybrids were deployed, or if very large power plants were built.

13.10 Problems

13.10.1 Reliability

13.1. An older magnetic fusion experiment is purchased by a country wishing to initiate fusion research. This older experiment uses large capacitors to store electrical energy to operate the magnets for pulsed operation. There are 300 capacitors in the power building and all are used for each plasma pulse. The experiment operates for about 2,000 pulses per year. After 4 years, one capacitor suffers a catastrophic failure. In the post-accident investigation, the failure rate of capacitors is requested. Find the failure rate for these capacitors. Ignore the previous service life of the capacitors.

13.2. Consider a water storage tank that requires an annual pressure test to prove tank integrity. The tank's safety relief valves that protect the tank from overpressure will invalidate the test and therefore are gagged (i.e., locked shut) to perform the pressure test. Assume that the human error failure rate to remove the gag after testing is completed is 1E–03/demand. What is the safety valve gagging failure rate?

13.3. An alarm system is required to have a "failure to alarm on demand" failure rate of less than 1E–02/demand. That is, the system must properly respond to actual alarm conditions in more than 99 out of 100 challenges to the system. The electronics are very low failure rate items. Four candidate detector heads for this system have been tested in realistic conditions and one detector head has failed to alarm two times in the 75 tests. Is this type of detector head adequate?

13.10.2 Availability

13.4. In a calendar year, a car had 3 oil changes performed that each required 1.5 h at a lube, oil, and filter shop. The car was tuned up once in a mechanic garage and was left there for a business day (9 h). Tire rotation and steering alignment was performed once and required 2 h at a tire store. Otherwise,

the car ran well throughout the year. Calculate automobile availability using these data.

13.5. A fusion power plant completes 12 months of pre-operational testing and the following year it begins commercial operation. The plant on-line time values in its first 5 years are 1,150; 3,873; 4,725; 6,856; and 7,973 h. Find the annual availability and the 5 year average availability. Ignore leap years.

13.10.3 Maintainability

13.6. A water pump casing is found to be defective and leaking during a preventive maintenance visit. Plant management decides to replace the casing with the system on-line, just shutting down that one train of the system. The logistic time to obtain a new casing is 72 h; the repair time is 24 man-hours for each of three workers to remove the old casing and install the new casing. The train shutdown is 2 h, and post-installation testing and train restart to operational condition is 1 h. Find the time to restore the pump.

13.7. A wet-type expansion engine for a cryogenics plant has these repair times: O-ring blowby, 4 h; piston overhaul, 4 h; connecting rod repair, 4 h; wrist pin repair, 4 h; internal leak repair, 6 h. Each of these repairs is termed a major failure that requires a controlled engine warmup to room temperature for repair ($\approx$12 h). Find the inherent average MTTR and the MDT for this set of major repairs to the wet engine.

13.11 Review Questions

1. In the list of criteria for attractive power plants, what are the criteria for risk and finance?
2. What are the criteria for emergency planning and for licensing?
3. Define "reliability", "availability", and "capacity factor".
4. Explain the equation $R_{el} = \exp(-\lambda T)$. What is the definition of λ?
5. What is "demand failure rate"?
6. Explain how annual availability of a fusion experiment is calculated.
7. Explain how MTTR is calculated.
8. Distinguish "preventive maintenance" and "predictive maintenance"
9. How much time would be required to warm up fusion reactor magnets for maintenance? How long to cool them down again afterwards?

10. Identify the parameters in the following equation:

$$\text{COE} = 1,000[C_c(\text{fcr}) + (C_{o\&m} + C_{scr} + C_f)(1 + E)^P]/\text{PC}(\text{PAF}) \quad (\text{mills/kwh}),$$

11. How does the estimated COE vary with peak coolant temperature and with wall and blanket lifetime (MW-yr/m^2)?
12. Under what conditions could the COE from fusion power plants become competitive with COE from other power sources?
13. How could the grid perturbation issue be ameliorated for large (~ 3 GWe) fusion power plants?
14. Explain the meaning of the equation $\text{COE}/\text{COE}_o = (P/P_o)^{-n}$.
15. If the divertor heat flux width λ_q remained constant, how would the peak heat flux vary as the reactor power is increased?
16. In the European designs how do the assumptions and resulting parameters vary, going from A to B to C to D?
17. What blanket structural material is chosen for reactors A, B, C?
18. What breeders are considered?
19. How do availability and COE vary with divertor lifetime?
20. What heat flux could be handled by the divertor?
21. In the Japanese FFHR2m2 reactor what breeder and structural material are chosen?
22. How is the blanket lifetime extended from 5 to 30 years?
23. In the ARIES designs what was the usual electrical power level?
24. What assumptions were made in the ARIES-AT design about beta, structure, superconductor, and coolant outlet temperature?
25. In order to achieve AT performance, what additional developments would be needed with regard to profiles, power flux, and disruptions? With regard to structural material, coolant, and heat exchanger?

References

Blake EM (2008) U.S. capacity factors: another small gain, another new peak. Nucl News 51(May):28–34
Bourque RF (1998) The colliding compact torus: a steady state fusion reactor with pulsed heating, fueling, and current drives. J Fusion Energ 17:207–208
Buende R (1988) Reliability and availability assessments for the next European Torus. Fusion Technol 14:197–217
Burgess TW (2008) Nuclear science and technology division. Oak Ridge National Laboratory, Oak Ridge, TN. Private Communication. November 3 2008
Burgess T, Brown T, Chesser J, Dilling D, Heitzenroeder P, Nelson B (1999) Remote maintenance requirements and approach for the FIRE project. In: Proceedings of the 18th IEEE/NPSS symposium on fusion engineering, IEEE Albuquerque, NM. pp 484–487, 25–29 October 1999

Cadwallader LC (2001) Comparisons of facility-specific and generic failures rates for tritium-bearing components used in fusion applications. Fusion Eng Des 54:353–359

Cadwallader LC (2007) Failure rate data analysis for high technology components. In: Proceedings of the 8th international topical meeting on nuclear applications and utilization of accelerators (AccApp '07), American Nuclear Society, Pocatello, ID, pp 109–116, 29 July–2 August 2007

Cadwallader LC, Marshall TD (1996) Component reliability data estimation for fusion safety and risk assessment. In: Proceedings of the international topical meeting on probabilistic safety assessment (PSA '96), American Nuclear Society, Park City, UT, pp 637–648, 29 September–3 October 1996

Cadwallader LC, Petti DA (1999) A review of availability growth in energy production technologies. In: Proceedings of the 18th IEEE/NPSS symposium on fusion engineering, IEEE, Albuquerque, NM, pp 585–588, 25–29 October 1999

Cadwallader LC, Pinna T, Petersen PI (2007) Power supply reliability estimates for experimental fusion facilities. Fusion Sci Technol 52:979–984

Cambi G, Cepraga DG, Frisoni M, Carloni F, Chiasera A (2003) Vacuum vessel contact dose build-up from start to end of ITER operations. In: Proceedings of the 20th IEEE/NPSS symposium on fusion engineering, IEEE, San Diego, CA, pp 156–159, 14–17 October 2003

Cambi G, Pinna T, Angelone M (2008) Data collection on component malfunctions and failures of JET ICRH system. Fusion Eng Des 83(December):1874–1877

Center for Chemical Process Safety (1989) Guidelines for process equipment reliability data, with data tables. American Institute of Chemical Engineers, New York

Chen H, Wu Y, Konishi S, Hayward J (2008) A high temperature blanket for hydrogen production. Fusion Eng Des 83:903–911

Ciattaglia S, Angelini SBM, Cox M, Grüber O, Van Houtte D, Kurihara K, Petersen P, De Baar M, Sonato P (2005) Availability of present fusion devices. In: Proceedings of the 21st IEEE/NPSS symposium on fusion engineering, IEEE, Knoxville, TN. Paper 091, 26–29 September 2005

Cox S, Tait R (1998) Safety, reliability and risk management, an integrated approach, Chap. 1. 2nd edn. Butterworth-Heinemann, Oxford, UK

Cusak R, Brown P, Horn R, Loving A, Sanders S, Sanders SG, Stokes R (1998) Operational experience from the JET remote handling tile exchange, fusion technology 1998. In: Proceedings of the 20th symposium on fusion technology, EURATOM-CEA, Marseille, France, pp 1135–1138, 7–11 September 1998

David PA, Maude-Griffin R, Rothwell G (1996) Learning by accident? Reductions in the risk of unplanned outages in U.S. nuclear power plants after Three Mile Island. J Risk Uncertainty 13:175–198

Derdiger JA, Bhatt KH, Siegfriedt WE (1981) Component failure and repair data for coal-fired power plants, AP-2071. Electric Power Research Institute, Palo Alto, CA

Dolan TJ (1993) Fusion power economy of scale. Fusion Technol 24:97–111

Dolan TJ (1982) Fusion Research, Pergamon Press, Elmsford, New York

Dolan TJ, Yamazaki K, Sagara A (2005) Helical fusion power plant economics studies. Fusion Sci Technol 47:60–72

El-Guebaly LA (2009) History and evolution of fusion power plant studies: past, present, and future prospects. In: Aasen A, Olsson P (eds) Nuclear reactors, nuclear fusion, and fusion engineering. Nova Science Publishers, Hauppauge, pp 217–271

Elsayed EAA (1996) Reliability engineering. Addison-Wesley Publishers, New York

Feng KM, Pan CH, Zhang GS, Luo DL, Zhou ZW, Yang YW, Wang XY, Hu G, Yuan T, Chen Z, Wang HY, Chen CA, Li ZX, Zhao Z, Li ZQ (2006) Preliminary design for a China ITER test blanket module. Fusion Eng Des 81:1219–1224, Figure 2

Feng KM et al (2008) Overview of design and R&D of solid breeder TBM in China. Fusion Eng Des 83:149–1156

Feng KM, Zhang GS, Zheng GY, Zhao Z, Yuan T, Li ZQ, Sheng GZ, Pan CH (2009) Conceptual design study of fusion DEMO plant at SWIP. Fusion Eng Des 84:2109–2113

Galbiati L, Carter P, Gaberscik A, Haist B, Irving M, Locke D, Martin P, Mills S, Minchin R, Palmer J (1998) Experience from remote handling equipment support during the JET remote tile exchange, fusion technology. In: Proceedings of the 20th symposium on fusion technology, EURATOM-CEA, Marseille, France, pp 1131–1134, 7–11 September 1998

Hale PS Jr, Arno RG, Briggs SJ (1999) Operational maintenance data for power generation distribution and HVAC components. IEEE Trans Ind Appl 35:282–297

Hansen T (2008) How low can they go? Power Eng 112 (August)

Hecht H (2004) Systems reliability and failure prevention. Artech House, Inc., Norwood

Honda T, Hattori Y, Holloway C, Martin E, Matsumoto Y, Matsunobu Y, Suzuki T, Tesini A, Baulo V, Haange R, Palmer J, Shibanuma K (2002) Remote handling systems for ITER. Fusion Eng Des 63–64:507–518

IEEE (1999) IEEE guide for general principles of reliability analysis of nuclear power generating station safety systems, IEEE Std 352-1987. Institute of Electrical and Electronics Engineers, New York

IEEE (2007) IEEE recommended practice for the design of reliability industrial and commercial power systems, IEEE Std 493-2007. Institute of Electrical and Electronics Engineers, New York

International Atomic Energy Agency (2002) ITER technical basis, ITER EDA documentation series no. 24, plant description document, Chap. 5. International Atomic Energy Agency, Vienna, Austria

Johnson DW, Costley AE (2008) Chap. 13—challenges in fusion diagnostic development: a virtual tour of ITER. Fusion Sci Technol 53:751

Jones JV (2007) Supportability engineering handbook: implementation, measurement, and management, Chap. 5. McGraw Hill, New York

Kaslow J et al (1994) Criteria for practical fusion power systems: report from the EPRI fusion panel. J Fusion Energ 13(2/3):181–183

Kozaki Y, Imagawa S, Sagara A (2009) Design windows and cost analysis on a helical reactor. Nucl Fusion 49:115011 (p 8)

Leavitt J (2003) The complete guide to preventive and predictive maintenance, Chap. 2. Industrial Press, New York

Lyon J et al (2008) Systems studies and optimization of the ARIES-CS power plant. Fusion Sci Technol 54:694–724

Maisonnier D (2004) PPCS reactor models, 9th course on technology of fusion Tokamak reactors. International School of Fusion Reactor Technology, Erice

Maisonnier D, Campbell D, Cook I, Di Pace L, Giancarli L, Hayward J, Li Puma A, Medrano M, Norajitra P, Roccella M, Sardain P, Tran M Q, Ward D (2007) Power plant conceptual studies in Europe. Nucl Fusion 47:1524–1532

Moss TR (2005) The reliability data handbook. ASME Press, New York

Najmabadi F et al (1997) The starlite study: assessment of options for tokamak power plants—final report: UC San Diego Report UCSD-ENG-005.)

Najmabadi F, Abdou A, Bromberg L, Brown T, Chan VC, Chu MC, Dahlgren F, El-Guebaly L, Heitzenroeder P, Henderson D, John HE, Kessel CE, Lao LL, Longhurst R, Malang S, Mau TK, Merrill BJ, Miller RL, Mogahed E, Moore RL, Petrie T, Petti DA, Politzer P, Raffray AR, Steiner D, Sviatoslavsky I, Synder P, Syaebler GM, Turnbull AD, Tillack MS, Waganer LM, Wang X, West P, Wilson P (2006) The ARIES-AT advanced tokamak, advanced technology fusion power plant. Fusion Eng Des 80:3–23

Nishio S, Tobita K, Konishi S, Ando T, Hiroki S, Kuroda T, Yamauchi M, Nagata M, Azumi M (2003), Tight aspect ratio tokamak power reactor with superconducting TF coils. In: Proceedings of the 19th IAEA Fusion Energy Conference, Lyon, France, Paper FT/P/1-21, copyright International Atomic Energy Agency, Vienna, 14–19 October 2002

Oak Ridge National Laboratory (ORN) (1988) Nuclear energy cost data base: a reference data base for nuclear and coal-fired power plant power generation cost analysis (NECDB); DOE/NE–0095, Prepared by Oak Ridge National Laboratory, Oak Ridge, TN, USA, September 1988

Pecht M (ed) (1995) Product reliability, maintainability, and supportability handbook, Chap. 7. CRC Press, Boca Raton, FL

Perkins LJ (1997) Complexity and availability for fusion power plants: the potential advantages of inertial fusion energy. J Fusion Energ 16:307–316

Petti DA, Merrill BJ, Moore RL, Longhurst GR, El-Guebaly L, Mogahed E, Henderson D, Wilson P, Abdou M (2006) ARIES-AT safety design and analysis. Fusion Eng Des 80:111–137

Pinna T, Cambi G, Ciattaglia S, Lo Bue A, Knipe S, Orchard J, Pearce R, Besserer U (2005) Collection and analysis of data related to fusion machines (JET and TLF) operating experience on component failure. Fusion Eng Des 75–79:1199–1203

Pinna T, Cambi G, Gravanti F (2007) Collection and analysis of component failure data from JET systems: neutral beam injectors and power supply. Nucl Fusion 47:S453–S457

Procaccia H, Arsenis S P, Aufort P, (1998) EIReDA, European industry reliability data bank, 3rd edn. Crete University Press, Iraklion, Crete, Greece

Ribeiro I, Damiani C, Tesini A, Kakudate S, Siuko M, Neri C (2011) The remote handling systems for ITER. Fusion Eng Des 86:471–477

Rolfe AC (2007) A perspective on fusion relevant remote handling techniques. Fusion Eng Des 82:1917–1923

Sagara A, Imagawa S, Mitarai O, Dolan T, Tanaka T, Kubota Y, Yamazaki K, Watanabe KY, Mizuguchi N, Muroga T, Noda N, Kaneko O, Yamada H, Ohyabu N, Uda T, Komori A, Sudo S, Motojima O (2005) Improved structure and long-life blanket concepts for heliotron reactors. Nucl Fusion 45:258–263

Schultz TL (2006) Westinghouse AP1000 advanced passive plant. Nucl Eng Des 236:1547–1557

Sheffield J (1994) The physics of magnetic fusion reactors. Rev Mod Phys 66:1015

Sheffield J et al (1986) Cost assessment of a generic magnetic fusion reactor. Fusion Technol 9:2

Sheffield J, Brown W, Garrett G, Hilley J, McCloud D, Ogden J,. Shields T, Waganer LM (2000) A study of options for the deployment of large fusion power plants. Joint Institute for Energy Environment Report JIEE 2000–2006, June; http://web.utk.edu/~isse2006/pdf/jieepubs/2000-06.pdf. Also published in Fusion Science and Technology 40, Number 1. Table V, Copyright by the American Nuclear Society, LaGrange Park, Illinois, USA, pp 1–36, July 2001

Taylor NP, Knight PJ, Ward DJ (2000) A model of the availability of a fusion power plant. Fusion Eng Des 51–52:363–369

Tobias PA, Trindade DC (1995) Applied reliability, 2nd edn. Taylor & Francis, Inc, New York

U.S. Department of Energy (1996) Safety of magnetic fusion facilities: requirements, DOE-STD-6002-96

Vayakis G, Hodgson ER, Voitsenya V, Walker CI (2008) Generic diagnostic issues for a burning plasma experiment, Chap. 12. Fusion Sci Technol 53:699

Waganer LM et al (1992) Inertial fusion energy reactor design studies, Prometheus-L, Prometheus-HI, Final Report DOE/ER-54101, MDC 92E0008, March

Waganer LM, Najmabadi F, Tillack MS the ARIES team (1995) What must Demo do? 16th IEEE symposium on fusion engineering, Champaign IL, 30 September–5 October 1995

Waganer LM, ARIES Team (2006) ARIES-AT maintenance system definitions and analysis. Fusion Eng Des 80:161–180

Waganer LM, Peipert RJ, Jr, Wang XR, Malang S, ARIES Team (2008) ARIES-CS Maintenance system definition and analysis. Fusion Sci Technol 54(3):787–817

Ward D (2004) Impact of physics on power plant design and economics, 9th course on technology of fusion tokamak reactors. International School of Fusion Reactor Technology, Erice, Italy

Wu Y, FDS Team (2007a), Conceptual Design and Testing Strategy of a Dual Functional Lithium-lead Test Blanket Module in ITER and EAST, Nuclear Fusion, 47:1533-1539

Wu Y, FDS Team (2007b) Design status and development strategy of China liquid lithium-lead blankets and related material technology. J Nucl Mater 367:1410–1415

Wu Y, FDS Team (2008) Conceptual design study of the China fusion power plant FDS-II. Fusion Eng Des 83:1683–1689

Wu Y, FDS Team (2009) Conceptual design study of the China fusion power plant FDS-II, Fusion Engineering and Design 83:1683-1689

Wu YC, Qian JP, Yu JN (2002) The fusion-driven hybrid system and its material selection. J Nucl Mater 307:1629–1636. Also invited presentation at the international conference on fusion reactor materials (ICFRM-10), Baden-Basen, Germany, 14–19 October 2001

Yamamoto I, Nishitani T, Sagara A (2009) Overview of recent Japanese activities and plans in fusion technology. Fusion Sci Technol 52:347–356

Zakharov LE, Li J, Wu Y (2010) Fusion-fission research facility (FERF) as a practical step toward hybrids. In: Proceedings of the 18th conference on nuclear engineering ICONE18, Xi'an, China

Chapter 14
Fusion–Fission Hybrid Reactors

Ralph W. Moir and Wally Manheimer

Objectives

After reading this chapter one should understand

The need for hybrids.
What drivers would be suitable.
Neutronics issues.
Blanket design optimization for power, fuel production, or radwaste incineration.
Safety and nonproliferation issues.
The Energy Park concept.

14.1 Introduction: Why Fusion–Fission Hybrids?

A "Fusion-Fission Hybrid" is a fusion reactor that contains thorium, uranium or transuranic elements in its blanket, in order to increase power, to breed fissile fuel, or to incinerate (transmute) radioactive materials.

Hybrids may be useful to permit low-Q operation (Q = fusion power/input power). Some short-lived tokamak discharges have achieved energy gain ratios Q ∼ 1, but sustained tokamak discharges have achieved Q < 1 (Gibson et al. 1998; Loarte et al. 2004; Shirai et al. 1998; Kusama et al. 1999; Ide et al. 2000;

Wally Manheimer, Retired from the US Naval Research Laboratory

R. W. Moir (✉)
Vallecitos Molten Salt Research, Livermore, CA, USA
e-mail: rmoir@pacbell.net

W. Manheimer
US Naval Research Laboratory, Washington, DC, USA
e-mail: wallymanheimer@yahoo.com

Takenaga et al. 2001; Ishida et al. 2004; Isayamab et al. 2005; Hawryluk et al. 1998). The International Thermonuclear Experimental Reactor, ITER (Campbell 2001) project, being built now in France by an international consortium should achieve $Q \sim 5$–10 and a neutron power of about 400 MW in a 400 s pulse by the late 2020s. A pure fusion reactor needs $Q \gg 10$ to be economical, but a fusion-fission hybrid may be feasible with $Q \sim 5$. The lower Q permits operation with shorter confinement times, which relax the required values plasma size, magnetic field, neutral beam injection energy, or energy conversion efficiency.

Let

P_f = Fusion thermal power
η_e = Efficiency of converting this power into electricity
Q = Fusion energy gain ratio = (fusion power)/(input power)
η_d = Driver efficiency

Then

P_f/Q = Input power
$P_f/\eta_d Q$ = Input electrical power to driver, and the net electrical power output is

$$P_{net} = \eta_e(0.8M + 0.2 + 1/Q)P_f - P_f/(\eta_d Q) \tag{14.1}$$

where M = blanket energy gain (Sect. 6.10).

Typically $\eta_e \approx 0.33$ for current BWR and PWR power plants using the Rankine cycle. Advanced Brayton cycles with higher temperature blankets and coolants could achieve efficiencies approaching 60 %, however these cycles have not been implemented in large commercial power plants. Their utility will depend ultimately on their efficiency, reliability, durability and price. For now we will assume $\eta_e = 35\ \%$.

Tokamak heating and current drive were discussed in Chap. 5. Gyrotrons for ECRH with a single stage depressed collector have efficiency $\sim 45\ \%$. Another 5 % is lost in the 60 m transmission system, making the driver efficiency $\eta_d \sim 40\ \%$ (Thumm et al. 2008). High energy neutral beams, which accelerate negative ions, have a maximum efficiency of the neutralization efficiency of about 60 % (Koide et al. 1997). However there are other losses including neutralization in the acceleration chamber and propagation losses. A reasonable estimate for the efficiency of the neutral beams which will be used on ITER is also about 40 %. Thus we will consider $\eta_d \approx 40\ \%$. By developing direct conversion, similar to a depressed collector for the unneutralized ion beam, the efficiency of this particular driver could be increased (Barr et al. 1977; Moir 1994). Thus, assuming $M \approx 1.2$ and taking conservative existing values for the efficiencies, we find

$$P_{net} \approx P_f(0.406 - 2.15/Q). \tag{14.2}$$

For example ITER with $P_f = 500$ MW and $Q = 10$ could produce $P_{net} \approx 95$ MWe. If $Q = 5$, it could not produce net power. This indicates how far even such a large device as ITER has to go to produce economical power.

The National Ignition Facility (NIF) at the Lawrence Livermore National Laboratory (LLNL) uses 192 laser beams to compress and ignite target pellets. It is expected to achieve $Q \sim 10$, but reliable high-average-power lasers with

$\eta_d \sim 0.08$ are still under development. Furthermore, target gains ~ 100 would be needed to be viable as power producers, according to Eq. (14.1).

Even if ITER and NIF both succeed, additional decades may elapse before pure fusion power becomes economical. Fusion–fission hybrid reactors can perform any of three functions to varying degrees:

(1) increased power output
(2) fissile fuel breeding
(3) "incineration" of radioactive wastes (by neutron absorption).

A "fissile" material is a one that can sustain a fission chain reaction using low energy neutrons. The fissile isotopes ^{235}U and ^{239}Pu are fuels for today's nuclear reactors. The only fissile material found in nature is ^{235}U, which comprises only 0.72 % of natural uranium, the remainder being ^{238}U. Most of today's nuclear reactors, require a higher ^{235}U fraction, typically about 4 %, so the natural uranium must be "enriched" in ^{235}U. Nuclear weapons require an enrichment >20 % (preferably ~ 90 %), so conventional nuclear fuel is not a proliferation threat without further enrichment.

A "fertile" material is one that can absorb a neutron and be converted to a fissile material. The fertile materials found in nature are ^{238}U and ^{232}Th (this is the only long-lived thorium isotope). By absorbing a neutron, followed by two successive beta decays, ^{238}U becomes ^{239}Pu; and Thorium becomes ^{233}U.

Absorption of the DT fusion neutron in ^{238}U can result in formation of "fissile" ^{239}Pu via the reactions

$$n + {}^{238}\text{U} \rightarrow {}^{239}\text{U} \xrightarrow[24 \text{ min}]{\beta^-} {}^{239}\text{Np} \xrightarrow[2.4d]{\beta^-} {}^{239}\text{Pu} \quad \left[{}^{238}\text{U}(n, \gamma + 2\beta^-){}^{239}\text{Pu}\right] \qquad (14.3)$$
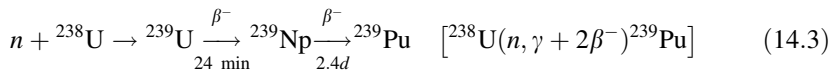
where the symbols (n, γ) mean that a neutron is absorbed and a gamma ray is emitted; β indicates beta decay (electron emission), and the 24 min and 2.4 days are the half-lives of the beta decays. The brackets show the condensed notation for this reaction.

Similarly, fertile ^{232}Th can breed fissile ^{233}U by the reactions

$$n + {}^{232}\text{Th} \rightarrow {}^{233}\text{Th} \xrightarrow[22 \text{ min}]{\beta^-} {}^{233}\text{Pa} \xrightarrow[27d]{\beta^-} {}^{233}\text{U} \quad \left[{}^{232}\text{Th}(n, \gamma + 2\beta^-){}^{233}\text{U}\right]$$
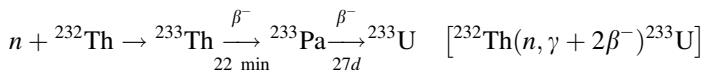
Although the amount of ^{235}U available is limited, the reserves of the fertile isotopes ^{238}U and ^{232}Th are vast (Table 1.1), including spent fuel from fission reactors. High energy neutron sources are needed to cause this breeding. If the Np and Pa are not removed from the reactor, neutron capture can prevent their decays to ^{239}Pu and ^{233}U, thus reducing fissile fuel production.

Example hybrid design

A hybrid reactor blanket would contain a "fertile" material like ^{238}U or ^{232}Th in addition to neutron multipliers and tritium breeding lithium or lithium compounds that would be found in pure fusion power plants.

We will describe a heterogeneous fusion blanket containing both structure and fertile material, run in the "fission suppressed mode" (Moir 1985). On average each 14 MeV neutron produces the following products:

- 1 tritium atom which is introduced back into the fusion reactor
- 0.6 ^{233}U atoms which are burned in conventional reactors located elsewhere
- 22 MeV thermal energy from DT fusion and tritium breeding
- Several MeV of energy from fission breeding reactions in the blanket
- 200 MeV per ^{233}U atom when it is burned in an external fission reactor, and of course more from fission of subsequently produced fissile atoms.

14.1.1 Advantages Over Fission Breeder Reactors

Fast fission breeders, such as Super Phoenix and the Integral Fast Reactor (IFR) are available now; hybrid fusion is decades in the future. Why consider hybrid fusion rather than fast fission breeders, which also convert fertile to fissile material?

(1) Hybrid fusion is a much more **prolific source** of nuclear fuel on a per unit of energy basis than fast breeders. It typically takes 2 IFR's to provide fuel for a light water reactor (LWR) of equal power (Chang 2002, 2009). But one fusion reactor can provide fuel for about 8 LWR's of equal nuclear power, or for about 6 of equal electrical power, a factor of 12 increase over fission breeders. The reason for the great increase is twofold. First of all, the fusion reaction, which produces a single neutron has an energy of only about 20 MeV instead of a fission reaction which has an energy of typically 200 MeV. Therefore in a fusion and fission plant of equal power, the fusion plant produces many more neutrons. It can be said that fusion is neutron rich and energy poor, fission is energy rich and neutron poor.

(2) The second reason why hybrids are superior is that some **neutron multiplication** is required and facilitated by the high energy of the neutron. For hybrid fusion, a 14 MeV fusion neutron must be multiplied to

 - Breed one tritium atom
 - Breed ^{233}U or ^{239}Pu
 - Account for losses by absorption in structure and coolant.

Potential neutron multipliers include beryllium, lead, and uranium. The 14-MeV fusion neutrons can produce much more neutron multiplication via (n, 2n) and fast fission reactions than the 2-MeV fission neutrons in a fission breeder reactor that are at or below the threshold for reactions.

(3) A hybrid breeder start up requires no **fissile material**, while 1 GWe IFR needs over 10 tons of fissile material to start up, and an LWR needs about 4 t (Garwin and Charpak 2001). The fusion breeder can produce enough tritium to start up other fusion breeders.

Table 14.1 Fissile fuel breeding capabilities of fusion and fission breeders

	Fissile atoms per reaction	Satellite LWR's of equal power	Tons of fissile material needed for startup
IFR[a]	0.5	0.5	10
Fusion	0.6	8.4[b]	0

[a] A 1 GW IFR plant in its normal breeding mode of operation
[b] LWR's of equal neutron power @0.333 kg/(MWe year)

Table 14.1 compares the breeding capabilities of the Integral Fast Reactor (IFR) fission breeder with a fusion hybrid system.

The potential benefits of hybrid reactors relative to liquid metal fast breeder reactors (LMFBRs) are summarized in Table 14.2.

Hybrids also have advantages relative to pure fusion. A fusion reactor needs $Q \gg 10$ to be economical, but a fusion–fission hybrid may be economical with $Q \sim 5$–10. The lower Q permits operation with shorter confinement times, which may relax the required values of some of the following parameters: plasma size, magnetic field, neutral beam injection energy, and energy conversion efficiency.

The idea of hybrid fusion is hardly new; Andrei Sakharov proposed it in 1950 (Sakharov 1990) and Hans Bethe advocated it in 1979 (Bethe 1979). In the 1970s and early 1980s the idea was taken very seriously, and many studies of it were published (Lidsky 1969, 1982; Lee and Moir 1981; Rose 1981; Moir 1982; Jassby 1981; Kelly and Rose 1981; Maniscalco et al. 1984).

A National Academy of Science panel review, "Outlook for Fusion Hybrid and Tritium Breeding Fusion Reactor" (Simpson 1987) recommended against a separate program for hybrids, assuming that pure fusion could advance quickly, and that there is sufficient fissile fuel available for the pace of world development. Although the US government discontinued its financial support of hybrid reactors,

Table 14.2 Comparison of fusion-fission hybrids with LMFBRs

Potential advantages relative to LMFBRs

No fissile fuel is needed for startup

Time required to breed enough fissile fuel to start up a new fission reactor is shorter than LMFBRs: (Example Problem 14.2)

One hybrid can provide fuel for many fission reactors

Hybrid blanket power density is lower than LMFBR, so fuel element design is easier

Hybrids have less afterheat, so a loss of coolant accident (LOCA) is less severe

Hybrids may have lower fission product inventories and lower fissile fuel inventories

Hybrids can also accelerate the development of pure fusion power

Potential disadvantage relative to LMFBRs

Hybrids are less developed; costs are uncertain

Hybrids, because they are fusion reactors, have large tritium-handing requirements

Fusion reactor design is more complex than LMFBR, and maintenance is more difficult

Power core has to accommodate 14 MeV neutrons for long duration operational periods

research continued (Manheimer 1999, 2003, 2005, 2006, 2009; Hoffert et al. 2002).

There are three general types of fusion-fission hybrid configurations (Lidsky 1975):

- "**fast fission**", which maximizes thermal power generated in the fusion reactor blanket. For example, ITER could be surrounded with fertile material, to increase its thermal power from 400 MW to 4 GW (Rebut 2006).
- "**fission suppressed**", which maximizes fissile fuel bred in the blanket. The blanket pellets or liquid would be processed to extract ^{239}Pu or ^{233}U, which would be fabricated into fuel elements for fission power plants. The ^{233}U would be diluted with ^{238}U to achieve the desired enrichment (typically ~ 5 %). The ^{239}Pu could be left in the hybrid blanket longer, to accumulate ^{240}Pu, which is not fissile, in order to make it less suitable for nuclear weapons.
- "**waste burner**", which maximizes destruction of radioactive isotopes (such as actinides) from spent fuel of fission reactors (Kotschenreuther et al. 2009; Stacey et al. 2008; Moses et al. 2009a, b; Freidberg and Kadak 2009).

A workshop was held to assess the prospects for hybrid fusion (U.S. Department of Energy, 2009).

The fission-suppressed hybrids have the following advantages over fast-fission hybrids:

- The fast-fission hybrid has a fusion reactor inside a **subcritical fission reactor**, which would be more complex and difficult to maintain
- The fast-fission hybrid would have a very high level of **afterheat** to remove during an accident or shutdown for maintenance.
- Thus, fission-suppressed blankets would be simpler and safer. The fissile material could be continuously removed, so its **inventory** in the blanket would be small.
- As fuel producers for existing nuclear reactors, fission-suppressed hybrids would fit better into current **infrastructure**
- A fast fission hybrid would have difficulty with load following, while the fission reactors supported by a fission-suppressed hybrid could do **load following** more flexibly.
- Shutdown of a fast fission hybrid would produce an enormous **grid** perturbation, but extra fuel could be stockpiled to compensate for shutdowns of a fission-suppressed hybrid.

The cost of electrical power from fusion–fission hybrid systems would probably be significantly less than from pure fusion reactors, but a recent thorough economic analysis is not available.

Spent fuel from light water reactors, containing plutonium and other actinides, were to be stored in Yucca Mountain, but that project is now cancelled, and the spent fuel will be kept in water pools or in above-ground dry storage casks. With reprocessing, these actinides could be recycled into an Integral Fast Reactor (IFR) or "incinerated" by 14-MeV neutrons in the blanket of a fusion–fission hybrid. This would alleviate long-term waste disposal problems.

14.2 Fusion Drivers

In principle, any fusion reactor could become a hybrid reactor "driver" if it could

- Operate steady state or with a high duty cycle (or rapid pulse rate for inertial confinement)
- Require reasonably low input power for plasma control and current drive (or for inertial confinement target compression)
- Have good availability, long wall lifetime, and reliable maintenance
- Be safe and "environmentally friendly".

Some confinement concepts were discussed in Sect. 1.3, of which the most developed are tokamaks, stellarators, and inertial confinement.

14.2.1 Tokamaks

The best tokamak results to date are the generation of 22 MJ of fusion energy in 4 s by JET, and triple product values 1.6×10^{21} m^{-3} s-keV by JT-60. The triple product values have grown steadily over time (Manheimer 1999 and Fig. 1.31).

Although tokamaks are far ahead of their nearest competitors as regards plasma confinement performance (Manheimer 1999, 2003, 2005, 2006, 2009; Hoffert et al. 2002) they have some serious problems:

- Tokamaks are vulnerable to wall damage from edge localized modes (ELMs) and from plasma disruptions, which could dump most of the poloidal field energy (~ 1 GJ in ITER) on part of the wall.
- They need current drive by NBI or by plasma waves, which requires complex hardware, instrumentation, and control systems.
- The current drive power lowers the attainable fusion energy gain ratio Q.
- JET discharges with $T_i \sim 10$ keV and modest emission rate could be sustained for many seconds, but discharges with intense NBI, $T_i \sim 40$ keV, and high neutron emission rates tended to disrupt (Fig. 14.1).

Fig. 14.1 DT fusion power
versus time in TFTR and JET
discharges. The power in two
1997 JET discharges
contrasts the hot ion transient
mode (16 MW briefly) with
that of a lower ion
temperature discharge that
lasts as long as the beam
injection (Gibson 1998)
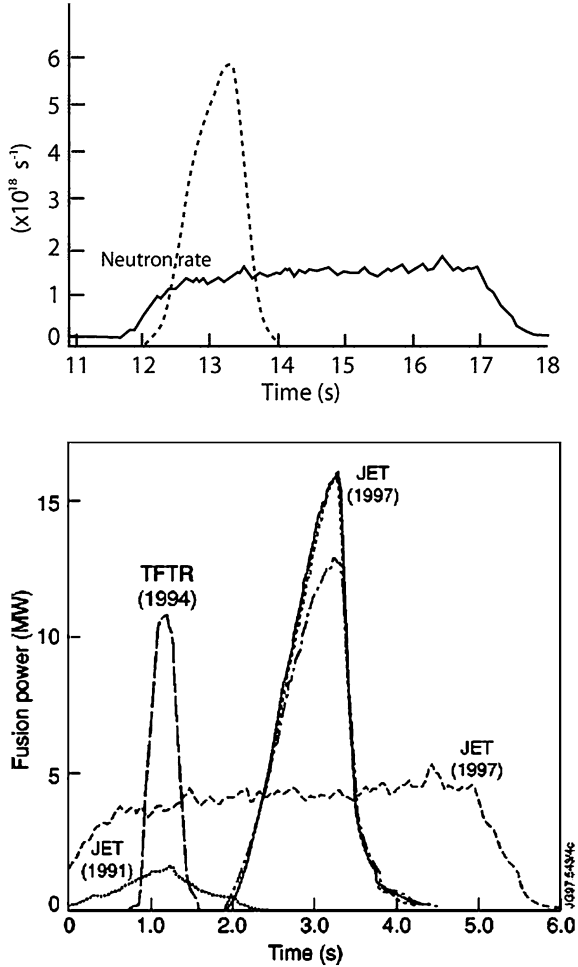
A "spherical tokamak" with low aspect ratio R/a can achieve high beta values, but radiation damage to the center post would severely limit its operational lifetime.

A proposed "scientific prototype" hybrid reactor could demonstrate the following:

- High average power operation with 20–50 MW of neutron power and Q $\sim$ 1.
- Tritium self-sufficiency.
- Fissile material breeding in appreciable quantity.

If a scientific prototype tokamak were operated successfully, it could provide some vital information towards a demonstration hybrid power plant system, but the plant would still need to develop long-lived components and high availability (Manheimer 2003, 2005, 2006, 2009).

Tokamak disruption control should be very reliable before large quantities of actinides are put in the blanket, to avoid accidental dispersal.

14.2.2 Other Magnetic Confinement Devices

Several other magnetic confinement devices are briefly described in Sect. 1.1. They have not achieved as high values of plasma pressure and energy confinement times as tokamaks have. They generally are smaller and have weaker magnetic fields, due to much lower budgets, but they could potentially achieve better performance, if fully developed. Stellarators could have the advantage of steady state operation without current drive. Research on magnetic mirrors, spheromaks, FRC, and RFP is either discontinued or funded at very low levels, so their potentials are not yet well quantified.

14.2.3 Inertial Fusion

Although this book focuses on *magnetic* fusion technology, we mention *inertial* confinement fusion here, since it is a candidate hybrid reactor driver.

The National Ignition Facility (NIF) at Lawrence Livermore National Laboratory (LLNL) approached ignition of a DT target pellet in 2013, but its repetition rate is only about two shots per day, and its 192 glass lasers have very low efficiency. The "Mercury" diode pumped solid state laser (DPSSL) program at LLNL and the "Electra" KrF laser program at the Naval Research Laboratory (NRL) intend to develop lasers with better efficiency (~ 8 %), high power, rapid pulsing capability (several Hz), long lifetimes, and affordable cost. For example, one Electra module can deliver 750 J pulses at 5 Hz.

The proposed "Laser Inertial Fusion Engine" (LIFE) would explode DT fusion targets, yielding about 50 MJ per target in a blast chamber (Fig. 14.2).

If the direct drive targets were injected at 10 Hz, the thermal power output would be about 500 MW. The inertial fusion blast chamber would be surrounded by a blanket containing about 40 t of subcritical fission fuel, which could be natural uranium, depleted uranium, spent fuel from light water reactors, thorium, or transuranic (TRU) waste. The inertial fusion reactor would provide a high flux of 14-MeV neutrons that would cause the blanket fuel to fission, releasing additional energy. A thin layer of beryllium pellets between the chamber wall and the fission fuel would generate about 1.8 neutrons for each neutron they absorb, to increase the neutron flux. The fission fuel pellets would be cooled by a flowing molten salt, such as $2LiF + BeF_2$ (called "Flibe"), which would carry about 3,000 MW of heat to a secondary coolant (water or helium) that would power a steam turbine or gas turbine to generate electricity.
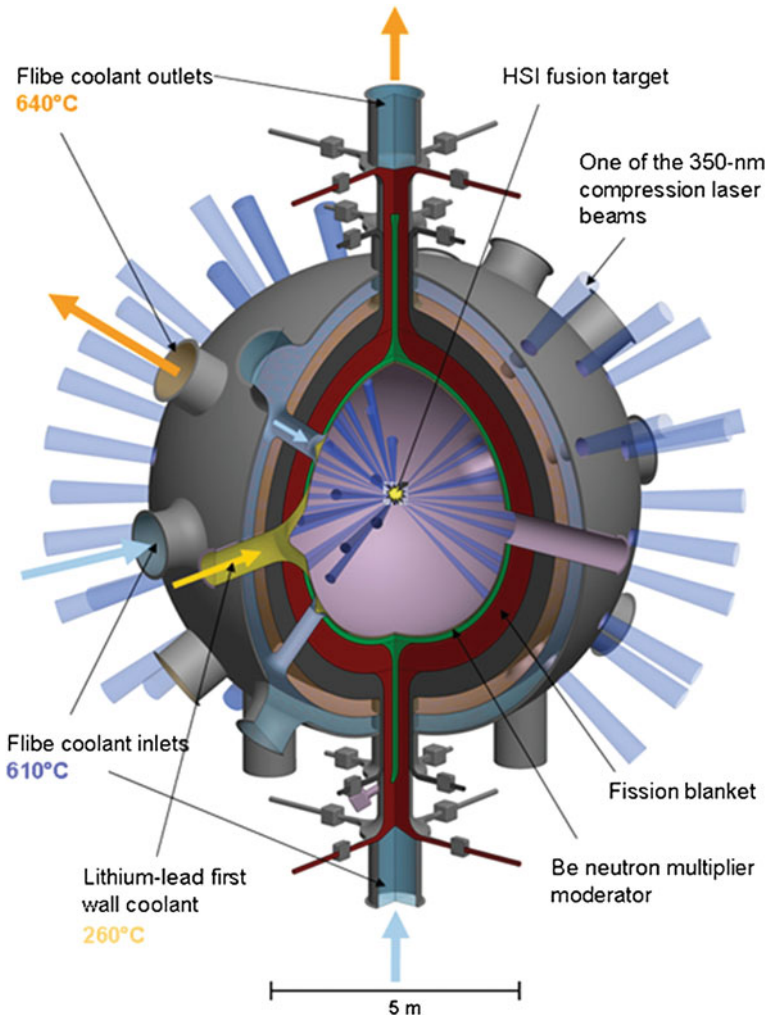
Fig. 14.2 A LIFE fusion–fission chamber for a 37-MJ hot-spot ignition target driven by a 1.4-MJ, 350-nm (ultraviolet) laser. Courtesy of LLNL

The LIFE power plant (Fig. 14.3) could fulfill the same functions as magnetic fusion–fission hybrids:

Some potential benefits of both magnetic hybrids and of the LIFE power plant are:

- Inherent safety—The plant shuts down when the lasers are turned off. No runaway fission reactions are possible.
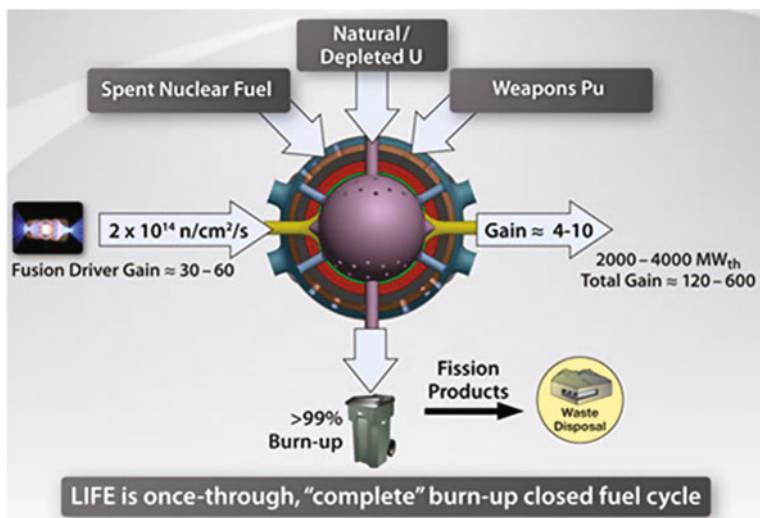
Fig. 14.3 Potential functions of a LIFE power plant system. Courtesy of LLNL

- Efficient use of nuclear fuel—The plant could extract over 99 % of the energy available in uranium, compared with less than 1 % that is extracted by current light water reactors (LWRs).
- Proliferation resistance—The plant does not require ^{235}U enrichment or fuel reprocessing, and the discharged fuel would not be suitable for use in weapons.
- Reduction of hazardous materials—The plant would incinerate most of the long-lived isotopes present in spent nuclear fuel and in depleted uranium.
- Reduction of the need for high-level waste repositories—Only about 5 % as much repository space would be needed, compared with current LWRs (Moses et al. 2009a, b).

The Naval Research Laboratory (NRL) has proposed a fusion test facility (FTF) (Obenschain et al. 2006). This would be a high average power (500 kJ per pulse of laser energy at 5 Hz) laser system that would implode fusion targets. Calculated energy gains would be about 50–100. The FTF would test many aspects of inertial fusion, which could be adapted to hybrid power plants, such as LIFE. The pulse repetition rate of an inertial fusion reactor would be limited by the rate at which the blast chamber could be evacuated after each shot and new targets could be injected and guided to the focus of the laser beams.

Heavy ion beams, such as uranium or cesium, could be used instead of laser beams to implode fusion targets. The accelerator could produce a 1 GeV, 10 kA, 100 ns beam and compress it by ballistic bunching to a 100 kA, 10 ns pulse that would deposit 1 MJ on the target. The advantages of an accelerator system over a laser system are:

- Effective coupling of beam energy to target
- Required beam parameters attainable with present technology
- More rugged beam steering system
- High repetition rates already attainable
- Higher efficiency (20–40 %) versus about 8 % for lasers.

With heavy ions it is difficult to symmetrically illuminate a target, so heavy ion beam fusion might need to use "indirect drive", in which the beams irradiate the inside of a cylinder containing the target pellet, producing X-rays that irradiate the target uniformly. In the USA the Lawrence Berkeley National Laboratory (LBNL) has been working on the accelerator technology development.

Light ion beams would require much higher beam currents, which would be more difficult to focus, due to space charge effects (mutual repulsion of the ions).

14.3 Blankets and Neutronics

14.3.1 Basic Processes

The nuclear fusion reactions and tritium breeding reactions of interest are listed in Table 14.3 and the fissile fuel breeding reactions are given in Eq. (14.3).

The DT fusion neutron energy in MeV is approximately

$$W(\text{MeV}) = 14.06 + 0.0026T \pm 0.11T^{1/2},$$

where T is the ion temperature in keV (Lessor 1975).

Table 14.3 Nuclear reactions of interest

Name	Abbreviation	Reaction (energy, MeV)	Total Energy	
			MeV	10^{-12} J
DT	$T(d,n)\,^4He$	$D + T \rightarrow {}^4He(3.54) + n(14.05)$	17.59	2.818
DDn	$D(d,n)\,^3He$	$D + D \rightarrow {}^3He(0.82) + n(2.45)$	3.27	0.524
DDp	$D(d,p)T$	$D + D \rightarrow T(1.01) + p(3.02)$	4.03	0.646
TT	$T(t,2n)\,^4He$	$T + T \rightarrow n + n + {}^4He$	11.3	1.81
D-^{3}He	$^3He(d,p)\,^4He$	$D + {}^3He \rightarrow {}^4He(3.66) + p(14.6)$	18.3	2.93
p-^{6}Li	$^6Li(p,\alpha)\,^3He$	$^6Li + p \rightarrow {}^4He + {}^3He$	4.02	0.644
p-^{11}B	$^{11}B(p,2\alpha)\,^4He$	$^{11}B + p \rightarrow 3({}^4He)$	8.68	1.39
Reactions for breeding tritium (Natural lithium = 7.42 % ^{6}Li and 92.58 % ^{7}Li)				
n-^{6}Li	$^6Li(n,\alpha)T$	$^6Li + n(\text{thermal}) \rightarrow {}^4He(2.05) + T(2.73)$	4.78	0.766
n-^{7}Li	$^7Li(n, n' + \alpha)T$	$^7Li + n(\text{fast}) \rightarrow T + {}^4He + n$	−2.47	−0.396
			(endothermic)	

Numbers in parentheses are approximate energies of reaction products, MeV. The exact energies vary with angle and incident particle energies. The symbols p, d, t, n, and α represent protons, deuterons, tritons, neutrons, and alpha particles (^{4}He), respectively (Same as Table 1.3)

The catalyzed DD reaction yields 7.21 MeV and 0.33 neutrons per D consumed, or 0.046 available neutrons for breeding per MeV. If we assume the resultant 14-MeV neutron can be multiplied to make two neutrons, then there are 0.069 available neutrons per MeV. The D–T reaction results in 17.58 MeV energy release and one neutron per D consumed, or, with multiplication, a second neutron available for breeding per 22.37 MeV, 0.045 available neutrons per MeV.

All the neutrons produced by catalyzed D–D reactions could be used to produce fissile fuel, without the need to breed tritium, which is a great advantage, but the DD reaction rate is about 100 times slower than for D–T (Greenspan 1977; Saltmarsh et al. 1979).

Combining the ^{6}Li tritium breeding reaction with the DT fusion reaction, the complete DT fuel cycle is:

$$D + {}^6\mathrm{Li} \rightarrow 2\,{}^4\mathrm{He} + 22.37 \text{ MeV} \tag{14.4}$$

However, any neutrons leaking out of the Li blanket or captured in structural materials will lead to a tritium deficit. An example of neutron loss in the structure would be parasitic capture by iron, which is common in structural materials.

$$n + {}^{56}\mathrm{Fe}_{26} \rightarrow {}^{57}\mathrm{Fe}_{26} + \gamma \tag{14.5}$$

The cross section is plotted in Fig. 14.4.

The fission of ^{238}U by fast neutrons is a good neutron multiplying reaction. The fission cross section and number of neutrons produced per fission are shown in Figs. 14.5 and 14.6. In thorium the fission probability of fission is much lower, and somewhat fewer neutrons are emitted by thorium fission than by uranium fission.

The cross section of other reactions in U and Th are given in Figs. 14.7 and 14.8. Some of these reactions are:

$$n + {}^{238}\mathrm{U} \rightarrow {}^{238}\mathrm{U} + \gamma + n(\textit{inelastic collison}) \quad \left[{}^{238}\mathrm{U}(n, n')\right] \tag{14.6}$$

$$n + {}^{238}\mathrm{U} \rightarrow 2n + {}^{237}\mathrm{U} \quad \left[{}^{238}\mathrm{U}(n, 2n)\right] \tag{14.7}$$
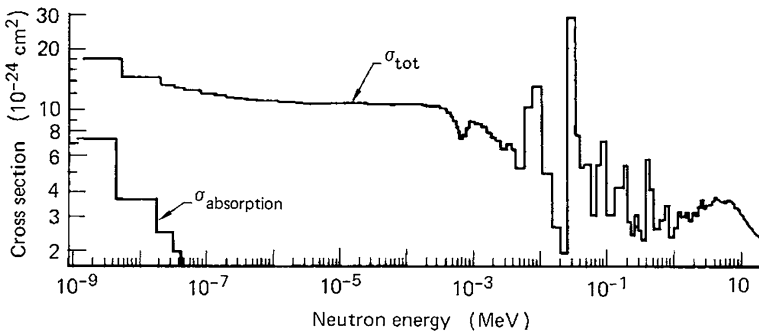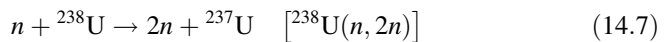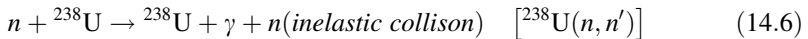
Fig. 14.4 Total and absorption cross section for a typical structural material, iron (^{56}Fe$_{26}$) (Plechaty et al. 1976; Moir 1981)
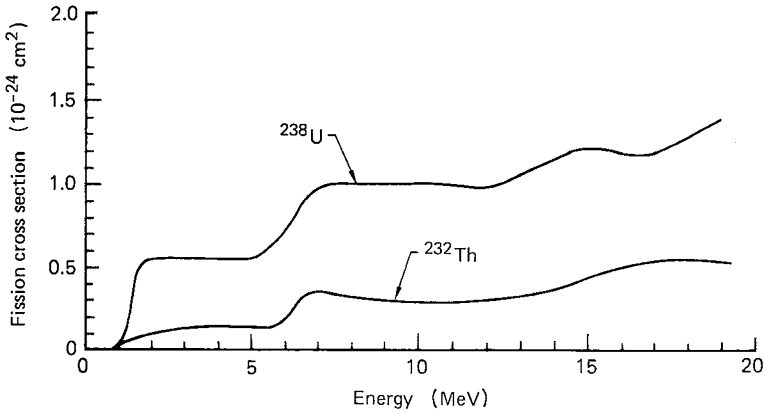
Fig. 14.5 Fission cross section versus neutron energy (Argonne National Laboratory 1963; Moir 1981)
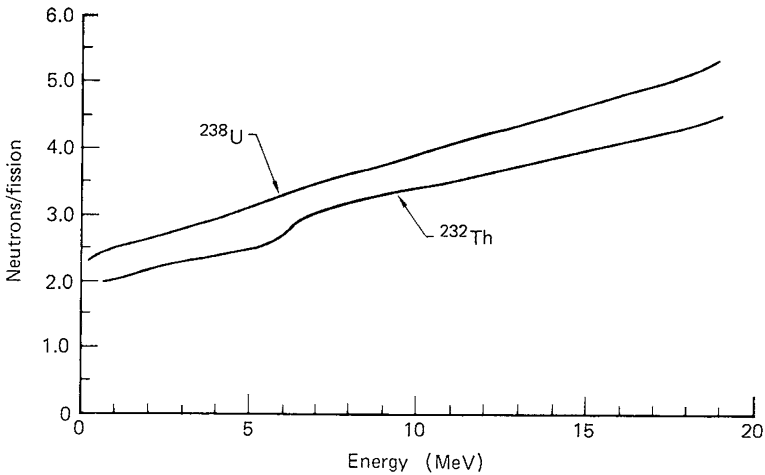
Fig. 14.6 Number of neutrons per fission event v versus incident neutron energy (Argonne National Laboratory 1963; Moir 1981)

$$n + {}^{238}U \rightarrow 3n + {}^{236}U \quad \left[{}^{238}U(n, 3n)\right] \tag{14.8}$$
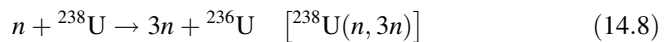
The energy of the bombarding neutron is all important. For instance, the fission (n, f) cross section of ^{238}U is very small below 1.3 MeV, whereas the $^{238}U(n, \gamma + 2\beta)$ ^{239}Pu reaction chain can occur at any energy. The (n, 2n) and (n, 3n) also have thresholds as shown. The largest cross section in the above 10-MeV range is the inelastic scattering reaction, where the neutron excites the nucleus, which emits a gamma ray.
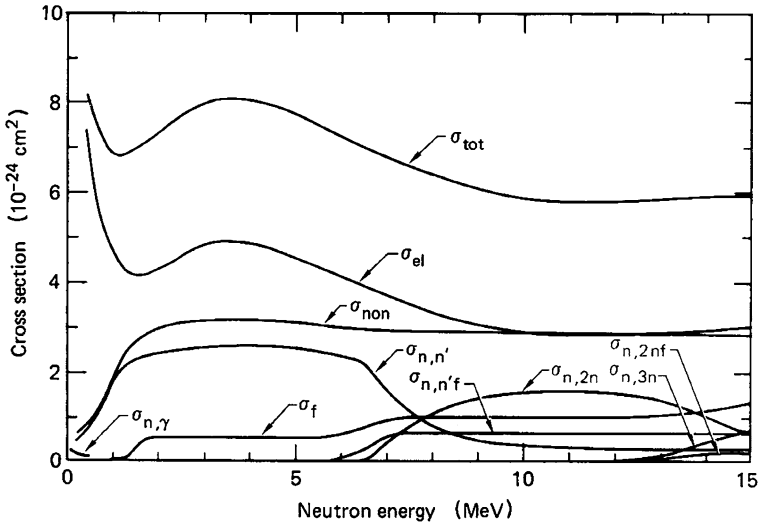
Fig. 14.7 Various cross sections for ^{238}U versus incident neutron energy (Brookhaven National Laboratory 1973; Moir 1981)

Fig. 14.8 Various cross sections for ^{232}Th versus incident neutron energy (Brookhaven National Laboratory, 1973 and Moir 1981)
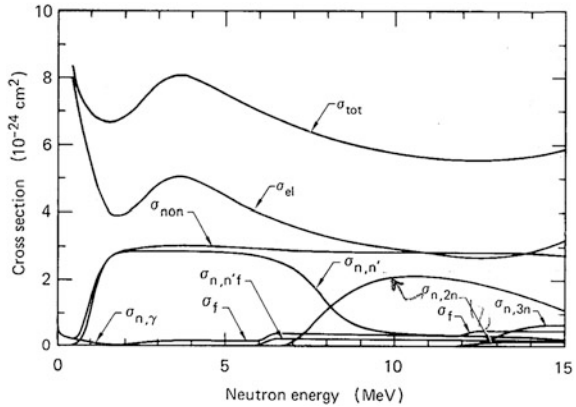
An important breeding parameter is η, the number of neutrons emitted per neutron absorbed in the fuel. Figure 14.9 shows η for the fissile isotopes ^{233}U, ^{235}U, and ^{239}Pu as a function of the incident neutron energy.

The "effective breeding threshold" refers to fast fission breeder reactors. The figure also shows the neutron spectra for fission neutrons, and for fast and thermal reactors. The condition for a chain reaction is $\eta > 1$, which is satisfied for all three isotopes. The condition for breeding as many fissile atoms as are consumed is $\eta > 2$ with a bit to spare (horizontal line at $\eta = 2.2$). The margin for extra neutron losses is very small for slow-neutron breeding.
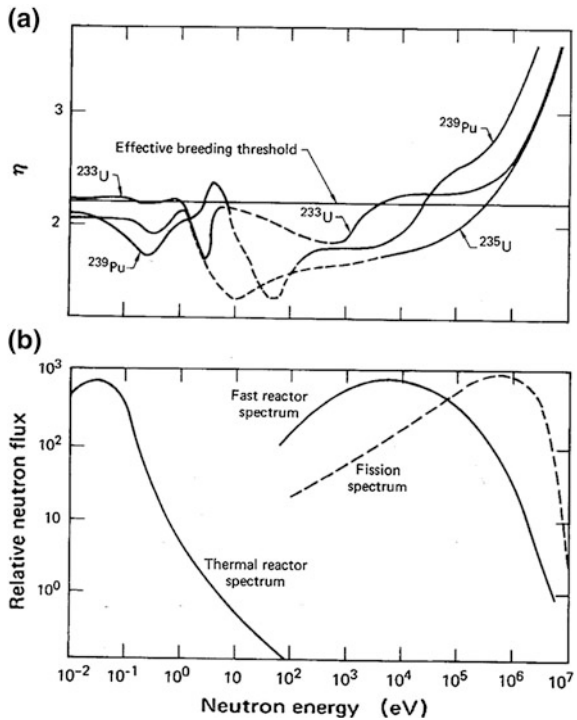
To convert fertile elements (^{232}Th or ^{238}U) to fissile elements (^{233}U or ^{239}Pu), one needs a supply of neutrons over and above those needed to breed tritium. To convert the D–T neutron into a greater number of lower-energy neutrons, several materials can give off more neutrons either by fission or by (n, 2n) and (n, 3n) reactions. Figure 14.10 shows the probability of neutron production vs. incident neutron energy.
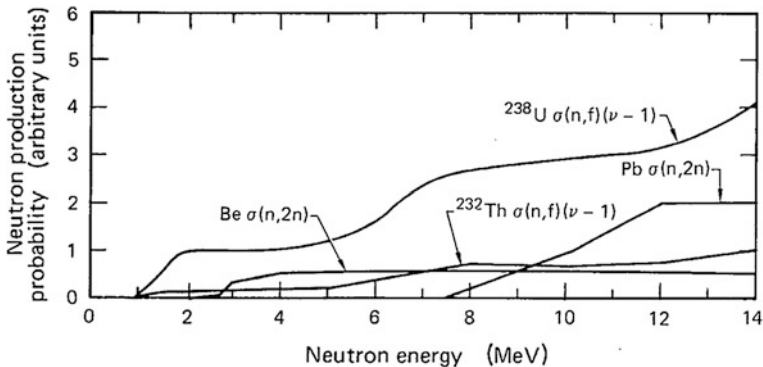
Fig. 14.10 The probability of producing neutrons is plotted versus incident neutron energy. The quantity plotted is the neutron production cross section times the number of neutrons produced per reaction (Moir 1981)

In this chart the fission cross sections have been multiplied by $v - 1$, where v is the number of neutrons emitted per fission (see Fig. 14.6), but no multiplier is needed for (n, 2n) reactions. ^{238}U produces considerably more excess neutrons than other multipliers, including ^{232}Th.

14.3.2 Infinite Homogeneous Medium

Neutronics calculations must consider material constituents, possible nuclear reactions, a wide range of neutron energies and directions, and many spatial positions in three dimensions. To include all these effects, sophisticated computer codes are essential. Neutron transport codes and Monte Carlo codes (Sect. 6.10) are used to calculate reaction rates. Plechaty et al. (1976) and Lee (1979) used the Monte Carlo code TART to study breeding ratios in infinite homogeneous media. For example, a 14-MeV neutron emitted into an infinite medium of ^{238}U, ^{232}Th, ^{6}Li, ^{7}Li, or natural Li results in the numbers given in Table 14.4.

The neutron production from ^{238}U is considerably larger than from ^{232}Th, resulting in more fissile-atom breeding. When the fertile isotopes ^{238}U and ^{232}Th are uniformly mixed (homogeneous lattice) with the proper amount of Li to breed tritium, then the fissile production drops, as shown in Table 14.5.

Table 14.4 Infinite-medium results per 14-MeV neutron

Medium	Product	Energy release (MeV)
^{238}U	4.18 ^{239}Pu	199
Nat. U	5.0 ^{239}Pu	300
^{232}Th	2.49 ^{233}U	50.5
^{6}Li	1.08 T	16.5
^{7}Li	0.89 T	12.3
Nat. Li (7.65 % ^{6}Li)	1.90 T	16.3

Table 14.5 Infinite homogeneous results per 14-MeV neutron

Case	Medium	Product atoms	Energy release (MeV)
1	^{238}U + 7.6 % ^{6}Li	3.1 ^{239}Pu + 1.1 T	193
2	^{232}Th + 16 % ^{6}Li	1.3 ^{233}U + 1.1 T	49
3	^{9}Be + 5 % ^{6}Li	2.7 T	22
4	^{9}Be + 5 % ^{232}Th	2.66 ^{233}U	30
5	^{9}Be + 1 % ^{238}U	2.4 ^{239}Pu	29
6	^{7}Li + 0.8 % ^{232}Th + 0.02 % ^{6}Li	0.8 ^{233}U + 1.1 T	17
7	Pb + 5 % ^{6}Li	1.74 T	18
8	Pb + 5 % ^{232}Th	1.58 ^{233}U	21
9	D	1.4	
10	47 m% LiF + 53 m% ^{9}BeF$_2$	1.27 T[a]	

[a] See UCRL84826 (1981)

Fig. 14.11 Performance of a fast-fission blanket with the fraction of heavy metal varied from all ^{238}U to all ^{232}Th (Moir 1981)
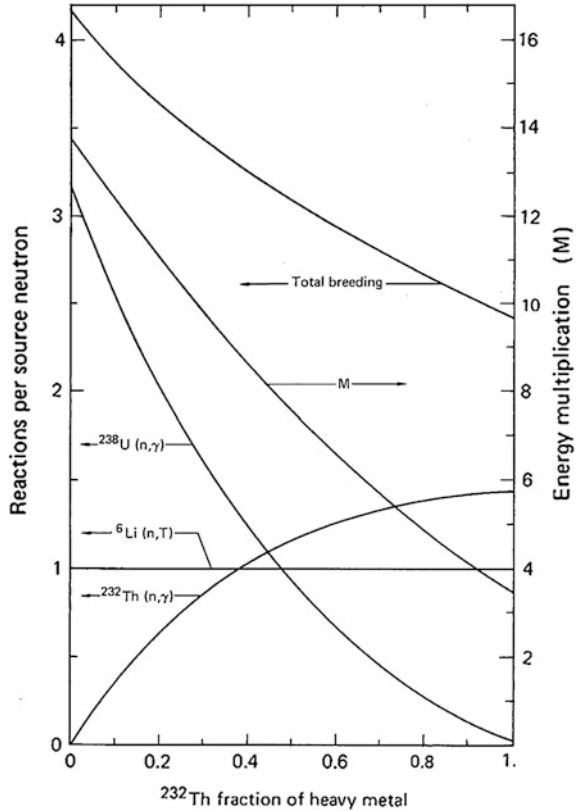
The highest fuel breeding (fissile plus tritium) is accomplished in ^{238}U, Case 1, with 4.2 atoms are bred. For ^{232}Th (Case 2) only 2.4 atoms are bred. For a blanket whose area is half Be/Li and half Be/Th, there are 2.7 atoms bred as can be seen by combining case 3 and 4.

For ^{7}Li (Case 6) there are 1.9 (T + U) atoms bred and for the Pb combination (Case 7), there are 1.7 atoms bred. Be is a better neutron multiplier than Li, which is in turn a little better than Pb.

One might predict that the substitution of ^{238}U for Be would result in more ^{233}U production, but this is not the case because the ^{238}U, in addition to being a good neutron multiplier, is also an absorber.

The performance for a mixture of ^{238}U, Th, and ^{6}Li is shown in Fig. 14.11, with the U/Th fraction varying to include at each extreme Case 1 and Case 2 of Table 14.5.

14.3.3 Two-Zone Heterogeneous Blanket

A heterogeneous lattice can use neutrons more efficiently than a homogeneous mixture of components. The first zone of a two-zone blanket would convert the incident 14-MeV neutrons into many lower-energy neutrons by fast fission of ^{238}U, and by (n, 2n) and (n, 3n) reactions. This is called a converter or a fission plate. ^{238}U is far superior to ^{232}Th, Be or Pb for neutron multiplication (Fig. 14.10). This zone should be thick enough to attenuate the neutrons above about 5 MeV, where ^{238}U has a significant neutron-multiplying effect, but not so thick that the resulting fission neutrons are absorbed in the ^{238}U zone. The second zone is loaded with ^{232}Th and Li, where ^{233}U and tritium are bred (or with more ^{238}U, if ^{239}Pu is to be bred). The lithium could be concentrated at the back of the second zone or mixed homogeneously in with the fertile material (^{232}Th or ^{238}U). The two-zone blanket can increase the breeding of ^{233}U, which has the highest values of η for slow-neutron reactors (Fig. 14.9).

Table 14.6 shows parameters of some two-zone blankets, based on the geometry of Fig. 14.12.

Table 14.6 Two-zone heterogeneous blanket results per 14-MeV neutron

Case	Zone 1 (g/cm^2)	Zone 2	^{233}U	^{239}Pu	T	Energy release (MeV)
1	^{9}Be 70	^{232}Th + 10 % ^{6}Li 468 g/cm^2	0.169		1.03	26
2	^{238}U 70	^{232}Th + 20 % ^{6}Li 468 g/cm^2	1.40	0.52	1.10	102
3	^{238}U 342	^{6}Li		2.75	1.10	185
4	^{232}Th 167	^{6}Li	0.84		1.10	41

Fig. 14.12 Arrangement of a two-zone blanket with paths of two neutrons shown (Moir 1981)
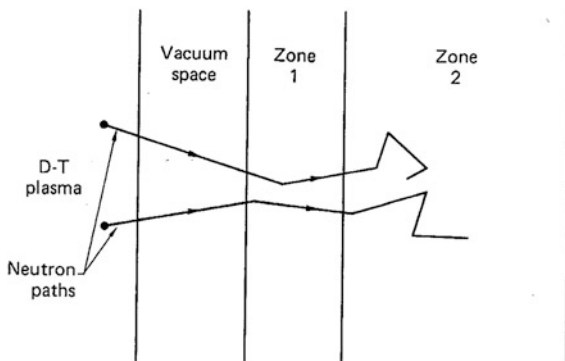
In some cases, two-zone lattices are less productive than one-zone lattices. For example, Case 1 of Table 14.6 shows a much lower ^{233}U production than Case 4. The reason is absorption in the thick beryllium-multiplier region. This could be remedied by mixing ^{6}Li in with the Be to usefully absorb neutrons. In Case 2 (with ^{238}U) the ^{233}U production is high.

Practical designs, including the fertile fuel in alloyed or chemical forms, will not perform as well as these ideal cases, because of neutron absorption in other materials, such as alloying elements, structure, and coolant. Table 14.7 gives more realistic results for an engineered blanket.

The ^{239}Pu and ^{233}U production are lower than the previous cases, due largely to parasitic absorption and extra neutron slowing down by the structural material. Uranium dioxide (UO_2, used in most LWRs) and uranium carbide (UC) could perform less well neutronically than pure uranium for neutron multiplication, because interactions with oxygen or carbon slow neutrons down without neutron multiplication reactions. Fuel operating temperature limits and radiation damage must also be considered.

The sources and sinks of neutrons for the U 7 %-by-weight molybdenum-alloy case of Table 14.7 are given in Table 14.8.

The examples up to this point assumed the fissile atoms were removed often enough so that the fissioning of the bred atoms was negligible. If the bred atoms are not removed they build up and themselves begin to fission or to transmute into

Table 14.7 Two-zone engineered-blanket results per 14-MeV neutrons[a]

Medium	Product atoms	Product atoms	Energy release (MeV)
UC	1.38 ^{239}Pu	1.05 T	113
U-MOLY	1.8 ^{239}Pu	1.1 T	141
Th	0.73 ^{233}U	1.08 T	35

[a] Blanket consists of a 0.5-cm stainless steel first wall followed by a uranium (or thorium) fuel zone containing 54 % fuel + 8.6 % stainless steel, followed in turn by a lithium zone consisting of 44 % graphite, 10 % ^{6} LiAlO$_2$ and 8.6 % stainless steel

Table 14.8 Neutron balance for U-moly blanket

Sources		Sinks	
D–T	1.0	^{238}U(n, γ) ^{239}Pu	1.8
^{238}U(n, f) fast fission[a]	2.4	^{6}Li(n, α)T	1.14
(n, 2n)	0.26	^{238}U(n, f)	0.68
(n, 3n)	0.24	Captures in structure	0.29
		Leakage	0.02
Total	3.9	Total	3.9

[a] $\eta = 3.6$

Fig. 14.13 Results versus burnup where fissile material builds up in a UC blanket (Lee 1976)
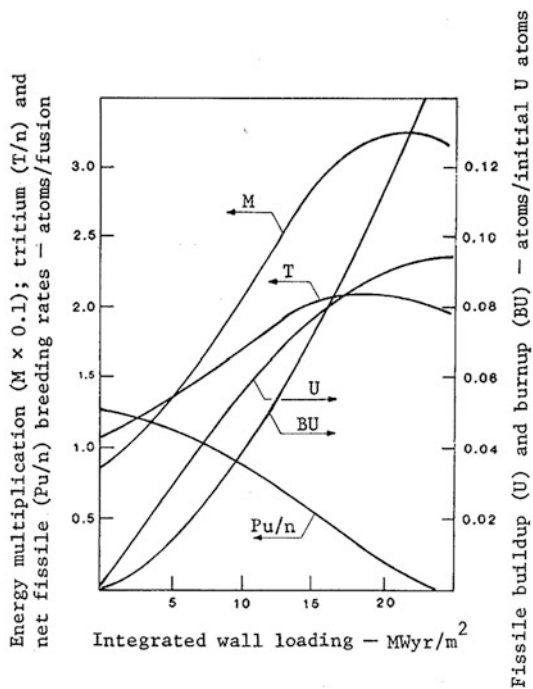
higher isotopes, such as ^{240}Pu. The results as a function of time measured by the wall load of 14 MeV neutrons in units of MW year/m^2 are given in Fig. 14.13.

Blanket energy multiplication (M) at the start of life is 8 and climbs to 32 after a first-wall exposure of $\sim$20 MW year/m^2. This increase in multiplication occurs because of the buildup of the plutonium, represented here by U. At start of life, Pu is at 0 % and after 25 MW year/m^2 it has peaked at almost 10 % of the initial U loading. At this point the net plutonium breeding rate has dropped to 0 (its conversion ratio has dropped to 1), since plutonium is being consumed as fast as it is being bred. This blanket is subcritical over its entire life; at time 0, the neutron multiplication factor k is approximately 0.3. After 20 MW year/m^2 when the peak occurs, k is increased to approximately 0.7. It is possible that the blanket could reconfigure into a critical assembly and therefore, such high integrated wall loading is not attractive. Thus, the blanket should be removed at an exposure well below 20 MW year/m^2 (Lee 1976).

Some problems to be considered in design of a hybrid blanket are listed in Table 14.9. Blanket placement around the first wall is the same as for fusion reactors. Low power densities are uneconomical, and high power densities create structural and cooling problems, especially during a loss-of-coolant accident (LOCA). In the following Sections we will consider hybrid reactor blankets that are optimized for fuel production, for high power output, or for waste incineration.

Table 14.9 Hybrid blanket design considerations

Thermomechanical
Conformance to plasma and coil shapes
Maximum surface coverage
Structural loads and lifetime
Heat removal, normal operation and loss-of-coolant accident (LOCA)
Low coolant pumping power
Minimum structural material
Low first-wall temperature
Easy remote handling and component replacement
Containment of fission fragments and tritium
Tritium removal and inventory
Materials compatibility
Hazards (fire, toxic material)
Cost
Neutronics
Average power density ~ 100 W/cm^3 (lower values are less economical; much higher values are difficult to cool)
Adequate tritium, breeding ratio (T $\sim$ 1.1)
Large fissile breeding ratio F
Large blanket energy gain M
Low-cross-section structural material
Blanket subcritical under all conditions
Neutron multiplier
Fuel management scheme (fissile inventory, residence time)
Radiation damage effects and blanket lifetime
Afterheat

14.4 Blanket Designs for Fuel production

14.4.1 Molten-Salt Blanket Designs-Fission-Suppressed Fusion Breeder

Molten salt blankets have several advantages (Lidsky 1969; Mills 1974; Blinkin and Novikov 1977). Lee (1978) suggests the use of beryllium to maximize fuel production. His idea is to flow a thorium and lithium-bearing molten salt over beryllium rods. The beryllium multiplies the fast (14 MeV) neutron, and the thorium and lithium capture the neutrons, producing ^{233}U and T. The total breeding is estimated by Lee to be 1 atom of T after all the losses and 0.6 of ^{233}U and the energy multiplication is 1.5 for engineered blankets. The salt is continuously processed to remove bred fuel and some fission products. The **radioactive inventory** of the blanket is consequently much less than in the other blanket designs, so the fission product afterheat is low, and a loss of cooling is much less of an issue than for the other designs. Fast fission is suppressed by using beryllium to

multiply and rapidly moderate energetic neutrons, and thermal fission is **suppressed** by processing to remove the fissile material before it has a chance to build up and fission. The performance is less, both in breeding (1.6 atoms versus 2.8 atoms) and in energy multiplication (1.5 compared to 10) compared to the fast-fission blankets. The goal is to provide fuel to a large number of fission reactors, where their energy release in effect multiplies the fusion energy. The fission-suppressed design with low energy release per reaction allows many more breeding reactions and hence far more fissile atoms produced than for a fast-fission reactor with the same power.

The molten-salt concept is a low-pressure system with a lower structural fraction than the liquid–metal case, but it has several problems. The thorium and uranium bearing molten salt react chemically with beryllium, so the beryllium had to be clad. Beryllium is the most prolific non-fissioning neutron multiplier, but it can swell up to 30 vol %. The use of Be pebbles up to ~ 10 mm diameter allows for this swelling and facilitates their removal for inspection, remanufacturing, and reuse.

In one design the molten salt was slowly circulated in steel tubes that prevented contact with beryllium and hence prevented chemical attack. Helium cooled both the beryllium pebbles and the tubes with molten salt inside.

Figure 14.14 shows a blanket designed for both a tandem mirror and a tokamak with pebbles and helium cooling.

The thorium is slowly circulated through the blanket in the form of molten salt and processed at a slow rate to remove the bred ^{233}U along with the spikant ^{232}U ("Spikant" refers to an isotope that can make the element unsuitable for nuclear weapons if enough of it is present). Helium cooling has the advantage of not slowing the neutrons before they are multiplied by beryllium.

Typical parameters are given in Table 14.10. The total cost includes the balance of plant but not the satellite LWRs.

14.4.2 Fission-Suppressed Blanket Based on Liquid Lithium Multiplier

Another blanket used ^{7}Li as a neutron multiplier to avoid feasibility issues associated with the use of beryllium (Lee et al. 1982). The configuration is shown in Fig. 14.15.

A 0.5 m thick first zone is flowing ^{7}Li followed by a molten salt zone. The breeding per unit of nuclear power was 20 % less than for the previous one-region beryllium design (Table 14.10), due partly to heterogeneous effects of the 2 zones and partly due to the poorer neutron multiplication characteristics of ^{7}Li. Steel was used as the structural material. Corrosion is greatly retarded by maintaining a frozen layer of salt on the steel, but calculations indicate that the steel could last many years even without this protective layer. Hastelloy might also be used with several years of service before radiation damage effects required its replacement. The piping and heat exchanger are made out of Hastelloy. The MHD pressure drop
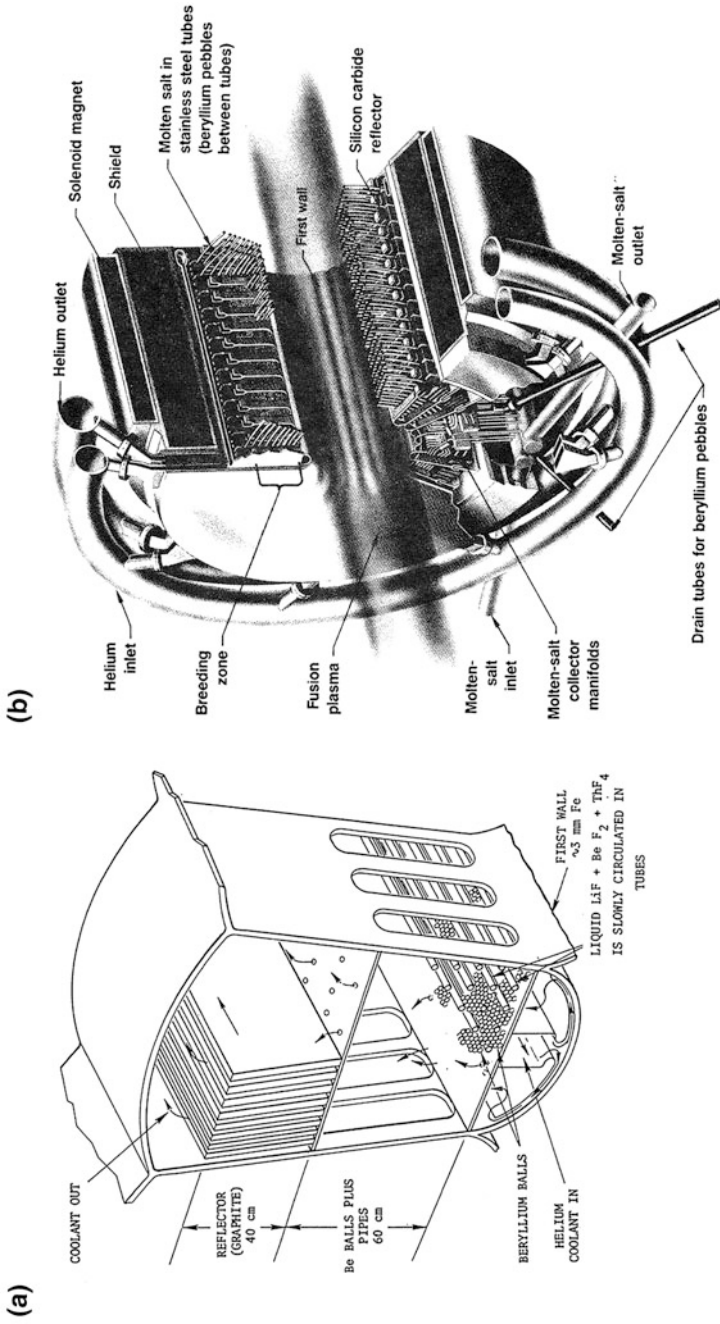
Fig. 14.14 Fission-suppressed blanket based on beryllium pebbles, showing the sub-module (**a**) and the module (**b**) (Moir et al. 1984a, b; 1985)

Table 14.10 Molten salt blanket parameters

$P_{nuclear}$	4,440 MW
P_{fusion}	3,000 MW
$P_{alpha\ particle}$	600 MW
$P_{blanket}$	3,840 MW
$P_{electric}$	1,380 MW
$P_{wall\ load}$	2 MW/m^2
Length of blanket	127 m
First wall radius	1.5 m
F_{net}^a	0.6
M^b	1.6
Fissile production	6,380 kg ^{233}U/year at 80 % capacity factor
Total cost	$4,870 M (1982$)

F_{net}^a is the fissile atoms bred/triton consumed
M^b is the energy released in the blanket per triton consumed divided by 14 MeV
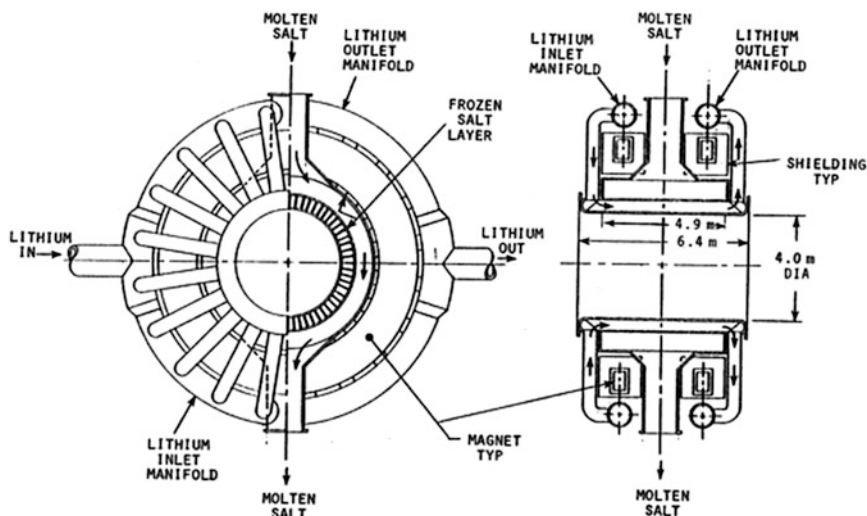
Fig. 14.15 Two zone lithium neutron multiplier blanket with a molten salt second zone for the breeding media

of the flowing lithium was found to be manageable ($\sim$0.7 MPa drop from the inlet to blanket) due to the low magnetic field ($\sim$3 T).

The ^{233}U produced by this blanket, containing the strong gamma emitting ^{232}U, could be used to fuel fission reactors without the isotope enrichment needed for ^{235}U. Reactors specially designed to burn separated wastes (such as actinides) from other reactors might also use this ^{233}U to compensate for their reactivity loss due to the waste products.

By this means fission reactors can do the "heavy lifting" of making power and burning wastes, and fusion reactors can do what they do best: breeding fissile material with fissioning suppressed in its blanket (except for neutron multiplication). The ideas further evolved with examples using liquid lithium as a neutron multiplier (Berwald et al. 1982), and versions with Pb were studied at the University of Wisconsin (Badger et al. 1975).

14.4.3 Gas-Cooled Designs: Fast-Fission Fuel Producers

Helium is chemically inert, which facilitates tritium removal, but its high required pressure (~ 60 atm) results in a significant amount of structural material. To contain the pressure, a cylindrical pressure-vessel concept was developed for the mirror reactor, Fig. 14.16.

The pressure vessel consists of a cylinder with a dome-shaped cap on the end facing the plasma. The inlet helium first passes over the lithium-containing tubes ("LiH pins") where the tritium is bred, then cools the first wall and finally passes over the fuel rods ("U_3Si pins"). In this example, the rods contained U_3Si, clad with Inconel 718. This design maximized Pu production, and non-uranium materials were minimized. The maximum power density was 500 W/cm^3 which gave a maximum fuel temperature of 900 °C. The helium pressure was 60 atm, the pressure drop was 1.5 atm, and the power consumed by the circulators was 3 % of the thermal power.

The pressure-cylinder concept in toroidal geometry for a pure fusion reactor is shown in Fig. 14.17.

Another helium-cooling concept is to embed coils of small diameter pressure tubes in the blanket, and transfer the heat from the fuel through a coupling medium such as liquid lithium or molten salt. One virtue of the tubing approach is the reduced probability of failure of welds because there are fewer welds. The tube concept has been studied by Mills (1974).

Heat transfer is limited with helium cooling, but fission-suppressed designs have a lower power density to be cooled and less afterheat, due to the reduced fission power density.

14.4.4 Liquid–Metal Blanket Designs

The excellent heat transfer properties of a liquid metal, along with its low pressure, results in low temperature drops and lower structural fractions. To minimize the pressure needed to force a liquid metal across magnetic fields, a special design of the coolant ducts is needed, including electrically insulated coatings. The slowing down of neutrons by the liquid–metal results in a minor loss of performance, which, relative to the helium-cooled case, is compensated for by the reduced
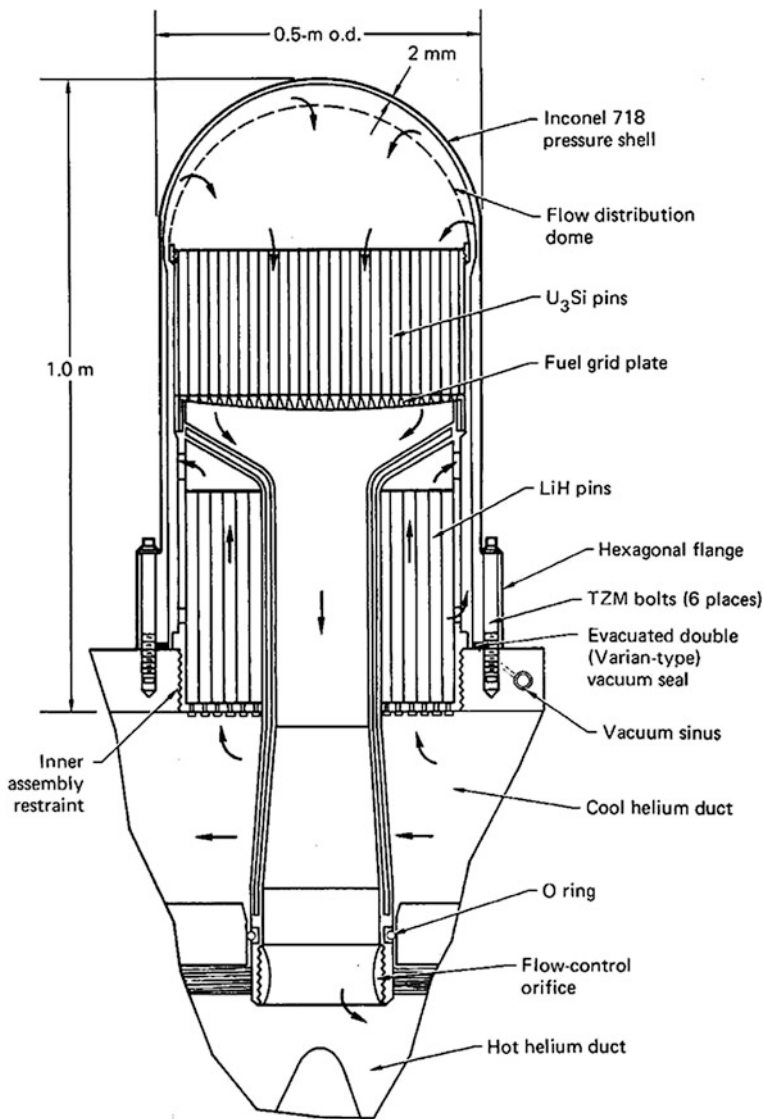
Fig. 14.16 Blanket module based on pressure-cylinder concept (Moir et al. 1975; Bender and Carlson 1978; and Moir 1981)

amount of structural material. Liquid–metal blankets have been designed for a pure fusion reactor (Badger et al. 1975) and for an inertial fusion concept (Bechtel Corp. 1977).

For discussion of the system economics of the fusion fuel producer and its satellite fission reactors see Moir (1981).

Fig. 14.17 Pressure-cylinder blanket assembly in toroidal geometry (Moir 1981)
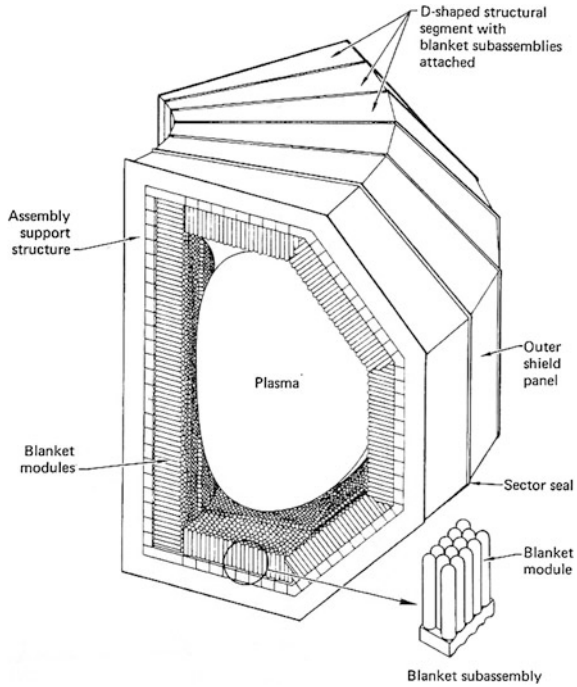
14.5 Blanket Designs for Waste Incineration

Some hybrids emphasize burning actinides from fission reactor spent fuel. The blanket can be kept subcritical at all times, in contrast to a fast fission reactor, where reactivity control is a safety issue. The harder neutron spectra from a 14 MeV neutron source means that more neutrons will cause fission, destroying the actinides (desirable), and fewer will be captured, producing higher atomic number transuranics (undesirable). Actinide wastes could be processed out of spent fuel and then be put in a fusion blanket in suitable form for incineration (fissioning). The revenues would come from both electrical power sales and waste disposal. It is desirable to estimate how many actinide atoms can be fissioned per fusion neutron.

The equations in this section ignore the thermal power contribution from re-emerging input energy, which was more accurately represented in Eq. (14.1).

Let M be the blanket energy gain for each 14 MeV neutron entering the blanket and F, the number of atoms fissioned for each 14 MeV neutron. Since the neutron power is 0.8 P_{fusion},

$$P_{th} = P_{fusion} \times 0.8M + 0.2P_{fusion} \quad M = \frac{P_{th} - 0.2P_{fusion}}{0.8P_{fusion}} \qquad (14.9)$$

Assuming that each neutron is absorbed in ^{6}Li, we find the fusion reactor thermal power to be

$$P_{th} = 14.06 \overset{n}{\text{MeV}} + 3.52 \overset{\alpha}{\text{MeV}} + 4.79 \overset{^6\text{Li}(n,\alpha)T}{\text{MeV}} = 22.37 \, \text{MeV} \tag{14.10}$$

In this pure fusion case

$$M = \frac{14.06 \, \text{MeV} + 4.79 \, \text{MeV}}{14.06 \, \text{MeV}} = 1.34 \tag{14.11}$$

For the hybrid reactor we assume that F atoms are fissioned per fusion event, releasing F × 200 MeV energy. Assuming that one neutron (per fusion neutron) is absorbed in ^{6}Li plus energy released by fission, the total thermal power is

$$P_{th} = P_{fusion} \times (0.8M + 0.2) = 14.06 \, \text{MeV} + 3.52 \, \text{MeV}$$
$$+ 4.79 \, \text{MeV} + F \times 200 \, \text{MeV}$$
$$(14.06 \, \text{MeV} + 3.52 \, \text{MeV}) \times (0.8M + 0.2) = 14.06 \, \text{MeV} + 3.52 \, \text{MeV}$$
$$+ 4.79 \, \text{MeV} + F \times 200 \, \text{MeV}$$

This equation uses definitions of M and F to relate them to each other. Solving for F, we find:

$$F = \frac{14.06 \, \text{MeV} \times M - 18.85 \, \text{MeV}}{200 \, \text{MeV}} \tag{14.12}$$

Let $\varepsilon = 1/(\text{number of fission-produced neutrons per fusion event})$. Then $\varepsilon = (\text{number of fusion neutrons})/(\text{number of fission neutrons})$

$$\varepsilon = \frac{1}{Fv} \tag{14.13}$$

where v = number of neutrons released per fission.

If the neutron multiplication factor k is large, then F will be large, and ε will be small. This corresponds to effective use of the fusion neutrons, but k must be kept well below 1.0 to avoid criticality of the blanket, even under accident conditions.

14.5.1 Hard Spectrum Sodium-Cooled, Minor-Actinide Burner (University of Texas)

The University of Texas waste-burner tokamak uses water-cooled copper coils. First the spent fuel wastes from an LWR are "burned" in another LWR, which destroys about 75 % of the transuranics. The 25 % remaining then goes to the fusion waste burner blanket (Kotschenreuther 2009). This blanket has a 25 cm thick zone around the outside of the tokamak toroidal magnet coils, cooled by liquid sodium. The input

power to sustain the plasma is 50 MW (which might consume 100 MWe at 50 % efficiency) and there is more power for the magnets. For 3,000 MW total thermal power, the fusion power varies from 100 MW dropping to 25 MW after 15 % of the transuranics fed are fissioned and rises to 100 MW after 50 % of the transuranics have been burned. The discharged fuel is then processed and fed back for another burn cycle repeatedly until less than 1 % of the remaining original transuranics remain. The 14 MeV fusion neutrons are multiplied in a lead region where they produce 0.6 extra neutrons (one being used to breed tritium).

The blanket energy is produced primarily by fission reactions. The fusion neutron power (80 % of the fusion power) is multiplied by fission and other reactions. This multiplication, M, varies from 38 to 150.

$$
\begin{aligned}
M &= \frac{P_{th} - 0.2P_{fusion}}{0.8P_{fusion}} = \frac{3{,}000\,\text{MW} - 0.2 \times 100\,\text{MW}}{0.8 \times 100\,\text{MW}} = 38 \\
M &= \frac{P_{th} - 0.2P_{fusion}}{0.8P_{fusion}} = \frac{3{,}000\,\text{MW} - 0.2 \times 25\,\text{MW}}{0.8 \times 25\,\text{MW}} = 150
\end{aligned}
\tag{14.14}
$$

and F varies as follows for two typical operating point during a burn cycle:

$$
\begin{aligned}
F &= \frac{14.06 \times 37.5 - 18.85\,\text{MeV}}{200\,\text{MeV}} = 2.54 \\
F &= \frac{14.06 \times 150 - 18.85\,\text{MeV}}{200\,\text{MeV}} = 10.45
\end{aligned}
\tag{14.15}
$$

The fission multiplication factor k_{eff} is reported to vary from 0.93 to 0.98. Then

$$
\begin{aligned}
\varepsilon &= \frac{1}{Fv} = \frac{1}{2.54 \times 2.8} = 0.14 \\
\varepsilon &= \frac{1}{Fv} = \frac{1}{10.45 \times 2.8} = 0.034
\end{aligned}
\tag{14.16}
$$

There are many more fission neutrons than fusion neutrons so this blanket is dominated by the fission process.

The small fraction of neutrons that are external supplied during the part of the burn cycle where k_{eff} is close to unity will require attention to criticality safety under abnormal conditions such as loss of coolant and reconfiguration into a more compact fuel arrangement. Use of sodium implies that water-cooling must be excluded in the tokamak systems for safety reasons.

Assuming M = 75 and F = 5.16 fissions, and estimating the leakage and (n, 2n) type reactions, we find the approximate neutron balance shown in Table 14.11.

A similar study assumes a fusion power of 150 MW, a k_{eff} of 0.93, an energy multiplication of 118, and the hybrid blanket would burn Pu and minor actinides from spent LWR fuel (Wu et al. 2006).

Table 14.11 Neutron sources and sinks for University of Tennessee example, average burn

Sources		Sinks	
D–T	1	(n, γ)	10.24
$(n, f)^a$	14.45	(n, f)	5.16
$(n, 2n$ etc.$)$	0.2	$^6Li(n, \alpha)T$	1.1
		Captures	0.3
		Leakage	0.05
Total	16.85	Total	16.85

^{a} $\nu = 2.8$

14.5.2 Hard Spectrum, Sodium Cooled, All Transuranics Burner (Georgia Tech University)

Another waste burner design is based on an ITER-like superconducting tokamak, shown in Fig. 14.18.

In this case all the transuranics from an LWR are burned in the hybrid. The blanket uses fast reactor metal fuel elements, sodium cooled. A burnup of 25 % per cycle is limited by fuel damage of 200 dpa. A fusion power varying from 180 to 240 MW results in 3,000 MW total thermal power. The criticality constant varies from 0.85 to 0.90 during the cycle. In this way one hybrid can burn up the transuranics from 3 to 5 LWRs of equal power.

$$M = \frac{P_{th} - 0.2P_{fusion}}{0.8P_{fusion}} = \frac{3,000\,\text{MW} - 0.2 \times 200\,\text{MW}}{0.8 \times 200\,\text{MW}} = 18.5 \tag{14.17}$$

$$F = \frac{14.06 \times 18.5 - 18.85\,\text{MeV}}{200\,\text{MeV}} = 1.21 \tag{14.18}$$
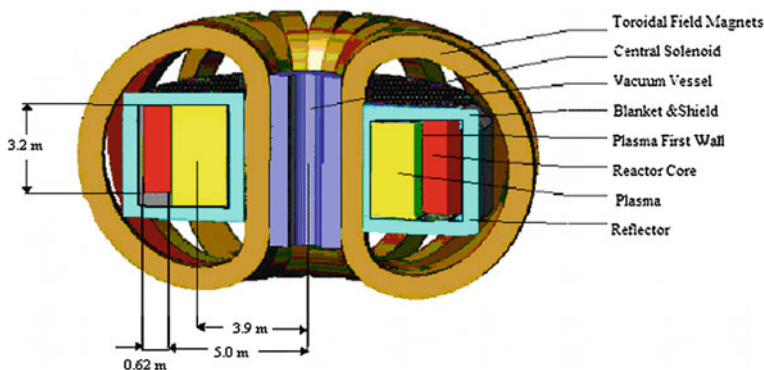
Fig. 14.18 Configuration of Subcritical Advanced Burner Reactor-(SABR) (Stacey 2008, 2009)

Table 14.12 Neutron sources and sinks for Georgia Tech example average burn, M = 18.5, F = 1.21

Sources		Sinks	
D–T	1	(n, γ)	2.05
$(n, f)^a$	3.51	(n, f)	1.21
$(n, 2n$ etc.$)$	0.2	$^6Li(n, \alpha)T$	1.1
		Captures	0.3
		Leakage	0.05
Total	4.71	Total	4.71

^{a} $\nu = 2.9$

$$\varepsilon = \frac{1}{F\nu} = \frac{1}{1.21 \times 2.9} = 0.28 \qquad (14.19)$$

This value of ε is larger than the prior example, showing that the fission process is a little less dominant, as also shown by the lower k_{eff} of 0.85–0.9. The neutron balance of this system is shown in Table 14.12.

14.5.3 Molten Salt Waste Burner, All Transuranics

Cheng (2005) has studied actinide burning with a blanket design where separated transuranics from light water reactors are fed to the fusion blanket as they are fissioned. The model has structures, a first wall, a fissioning zone and a reflector zone. In the fissioning zone, in the "hard spectra" case there is only molten salt with the dissolved actinides; and in the "soft spectra" case 50 % of the volume is taken up by beryllium that both multiplies neutrons and moderates them. After the initial inventory is burned and continuously replaced about three times a quasi-steady state is achieved.

Soft spectra case-steady state:

$$M = 13, \ F = 0.83, \ k_{eff} = 0.60, \quad \varepsilon = \frac{1}{F\nu} = \frac{1}{0.83 \times 2.6} = 0.46 \qquad (14.20)$$

Hard spectra case-steady state:

$$M = 8.6, \ F = 0.51, \ k_{eff} = 0.56, \quad \varepsilon = \frac{1}{F\nu} = \frac{1}{0.51 \times 2.7} = 0.73 \qquad (14.21)$$

These two cases show even less dominance of the fission process as is shown by the still lower k_{eff} values and larger values of ε.

A 3,000 MW_{fusion} plant with a neutron wall load of 1 MW/m^2 would burnup ~ 1 t/full power year of actinides with an inventory of 2.3 and 13 t for the soft and hard spectra cases for a fusion power of 230 and 350 MW_{fusion} respectively. Chemical attack of the beryllium by the molten salt should be prevented by coatings or by separate zones. Table 14.13 shows the neutron balance for these cases.

Table 14.13 Neutron sources and sinks for Molten Salt example

Sources		Sinks	
Average burn, Soft spectra, M = 13, F = 0.83			
D–T	1	(n, γ)	1.08
(n, f)	2.16	(n, f)	0.83
(n, 2n etc.)	0.2	^{6}Li(n, α)T	1.1
		Captures	0.3
		Leakage	0.05
Total	3.36	Total	3.36
Hard spectra, M = 8.6, F = 0.51			
D–T	1	(n, γ)	0.57
(n, f)	1.33	(n, f)	0.51
(n, 2n etc.)	0.2	^{6}Li(n, α)T	1.1
		Captures	0.3
		Leakage	0.05
Total	2.53	Total	2.53

14.5.4 Pu Waste Burning Molten Salt Inertial Fusion Reactor

An inertial fusion case was studied for the purpose of burning plutonium (Moir et al. 2009), where the blanket consists of about 50 % by volume beryllium and the remainder molten salt and some steel. The molten salt is steadily fed Pu (96 % ^{239}Pu, 6 % ^{240}Pu) at the rate of 1.3 t/year, which is the Pu burn rate, producing 4,000 MW of thermal power. The fusion power is 500 MW. The k_{eff} is 0.55, the inventory of all actinides is about 1 t. After a few years the system is in quasi-steady state. Processing at a slow rate was employed to prevent the valence +3 fission products (mostly rare-earth elements) from building up too much.

$$M = 9.8, \ F = 0.59, \ k_{eff} = 0.59, \quad \varepsilon = \frac{1}{Fv} = \frac{1}{0.59 \times 2.7} = 0.63 \quad (14.22)$$

The performance is very close to that of the Cheng case above with a soft spectra that also used beryllium. Apparently, a plutonium feed and a transuranic feed from LWR spent fuel give fairly similar results, as would be expected, since 90 % of LWR spend fuel transuranics are plutonium and only 10 % are Am and Cm.

Economic studies are needed to determine the value of burning fission actinide wastes in a fusion reactor, to find out how much such a machine can cost, and to assess the desirability of waste burning as a mission for fusion.

14.6 Blanket Designs for High Power Production

If the idea is to get the "best" performance out of a fusion plant whose power is limited to about 500 MW fusion power, then fission suppression is probably not optimal. Fast fission breeding blankets would probably yield a lower cost of

electricity (COE), but safety would be a major design issue. A relatively low power (~500 MWth) may be acceptable in a *pilot* hybrid plant, but a later commercial plant should have a higher power (≥3,000 MWth) to minimize the COE.

A 500 MWth fusion reactor with a fast-fission blanket can yield 3,000 MWth power and 1.5 t fissile fuel per year. However, A 2,400 MWth fusion reactor with a fission-suppressed blanket can yield 3,000 MW thermal and almost 7 t fissile fuel per year. Economic analysis shows that the fusion reactor with a fission-suppressed blanket would yield a lower net COE.

The fast-fission blanket designs of Lee (1976) if not processed often for fuel production, could produce large energy multiplication and go to high burnup, as shown in Fig. 14.13.

The high radiation damage rate limits fuel burnup, and the high afterheat power density is a safety concern. An extensive study of power production versus fuel production found that fuel production was favored over power production at modest powers (~1 GWe) but the economy of scale at high power (~3 GWe) favored power production (Tenney et al. 1978).

Recent studies of an inertial fusion neutron source, assuming no processing of spent fuel, were aimed at power production. With beryllium neutron multiplier over 50 % of initial heavy atoms fissioned before the solid fuel damage was limiting, because the beryllium reduced the neutron energies (Moses et al. 2009a, b), and $M \sim 6.5$.

A similar study, assuming molten salt fuel form and equal parts of uranium and thorium, gave a multiplication of 4.8 without beryllium (Moir et al. 2009b). A non-beryllium case with ^{238}U feed at the rate atoms fissioned achieved a multiplication $M \sim 2.3$ when steady state was reached (Cheng 2005).

14.7 Safety

This section supplements the previous discussion on Safety (Sect. 12.5). The issue of safety for hybrid fusion can be split into two separate discussions depending on whether one goes the route of a fission-suppressed or fast-fission hybrid fusion reactor. In the fission-suppressed case, after the fuel is extracted and diluted, it is either burned in conventional reactors such as light water reactors (LWR's) or in Generation-IV reactors (such as liquid metal, gas cooled high temperature or molten salt reactors). The safety issue here is the same as for those reactors, many of which have been running with continuously improving safety for several decades.

The presence of small amounts (as characteristic of a fission suppressed design) of fission products and actinides in the fusion reactor blanket and coolant circuit make these radioactive. If a large tokamak plasma like ITER disrupted, about a gigajoule could be suddenly released in a small volume. If the superconducting coils abnormally quenched and the protection circuitry failed, then more energy could be released, which could damage the magnet and possibly the blanket (For example, the Large Hadron Collider at CERN, Switzerland, suffered great damage in 2008 when a string of superconducting magnets quenched).

An inertial fusion reactor, on the other hand, has no large storage of energy in close proximity to the blanket other than the fusion yield of a few hundred MegaJoule in the blast chamber and possible chemical reactions if reactive coolants (such as lithium) are used.

The fast fission hybrids, as proposed for ITER (Rebut 2006), by the University of Texas (Kotschenreuther 2009), and by Georgia Tech (Stacey 2008) are all magnetic fusion configurations, with potential for plasma energy and magnet coil energy release. In these cases the fusion reactor sits inside a subcritical fission reactor. The fast fission hybrid has a much larger amount of actinides and radionuclides in the blanket than a fission-suppressed blanket. A fusion reactor accident might damage the blanket and release some radionuclides into the containment building. Thus, the fast-fission hybrid will have greater safety concerns than a fission-suppressed hybrid, because of its much larger radionuclide "source term", its much higher power density, and its greater afterheat. An exception could be a molten salt blanket with continuous online processing to remove fission products.

14.8 Nonproliferation

Any nuclear scheme, fission or fusion can be a proliferation risk if misused. To turn fertile material into fissile material (i.e. material with the potential to make nuclear weapons) one needs neutrons. The source of these neutrons can be either a fission reactor, a fusion reactor, or a spallation neutron source. More than 50 years of fusion research shows that fusion is difficult and expensive. A proliferator has simpler options, such as buying centrifuges to enrich uranium, breeding plutonium in a reactor, or stealing fissile materials or warheads. Thus it seems unlikely that any proliferator would choose to do so with fusion.

Nevertheless, once fusion reactors are built, safeguards against proliferation must be maintained. For pure fusion fertile material may be excluded from the blanket.

In fast-fission hybrid fusion, one has a very complex reactor, part fission, part fusion. Refueling must be done in a way that is proliferation resistant. For example, the developers of the Integral Fast Reactor (IFR) have developed "pyroprocessing", which can be done entirely in the reactor building with remote handling. All that emerges from the reactor during this step is the highly radioactive, intermediate Z fission fragments along with a very small amount of actinide waste that carries over in the reprocessing. There is no requirement to separate the pure plutonium. The plutonium and other actinides, mixed with fission products, can be reinserted into the reactor. During the reprocessing phase, no human could get near this material and survive. Any fast fission hybrid fusion reactor would have to use a similarly viable reprocessing method.

As regards the fission-suppressed hybrid fusion reactor, the fusion reactor itself has little proliferation danger. The final fission reactor, which burns the fuel that the fusion reactor produces, has the same proliferation risk as today's reactors do. The additional proliferation risk from fission suppressed hybrid fusion comes from

the reprocessing. This is the separation of the ^{239}Pu from the ^{238}U, or the ^{233}U from the ^{232}Th. At this point one is dealing with nearly pure fissile (i.e. bomb making) material. The separation and dilution of the fertile material must clearly be done under heavy guard and in a secure facility. We assume only isotopically dilute material is transported; if not, the transport must also be under heavy guard.

When U^{233} or ^{235}U is used in a power reactor it is usually diluted to about 3–5 % enrichment, and <20 % for a research reactor. For efficient weapons use much higher enrichments are needed, so the theft of low-enrichment uranium is not an immediate proliferation concern, because isotopic enrichment (using centrifuges, gaseous diffusion, etc.) is very difficult and expensive. Uranium fuel in which ^{239}Pu has been bred, on the other hand, is a great concern, because the plutonium can be separated chemically, which is much easier. Therefore, reprocessing involving plutonium must be done in a very secure facility, to prevent theft. Plutonium can be made somewhat proliferation-resistant if >7 % of ^{240}Pu can be produced by neutron absorption in ^{239}Pu. The ^{240}Pu makes the Pu unsuitable for weapons, because of its high spontaneous fission rate, which would make the fuel ignite prematurely and overheat before full compression (Lamarsh and Baratta 2001).

14.8.1 Proliferation Resistance from ^{232}U

We now consider further the nonproliferation aspects of ^{233}U and ^{232}U fuel. The thorium cycle is mentioned only in passing when normally discussing nuclear energy. This is due in part to the difficulty of starting the cycle since no fissile isotopes exist naturally with thorium as it does with uranium–plutonium (^{235}U exists in nature).

Diluting ^{233}U with ^{238}U to ∼5 % enrichment makes the fuel highly proliferation-resistant. Even before this dilution is done, the breeding of ^{233}U by fusion–fission hybrids also produces some ^{232}U, which makes weaponization of ^{233}U difficult. The 14 MeV neutrons facilitate the three threshold reactions leading to ^{232}U: ^{232}Th(n, 2n); ^{233}U(n, 2n); and ^{233}Pa(n, 2n) whose thresholds are over 6 MeV, Fig. 14.19.

While the 14 MeV *fusion* neutrons can produce much ^{232}U (>2.4 %), only a small fraction of *fission* neutrons are above the threshold energy, so in fission reactors ^{232}U/^{233}U ∼ 0.1 %). Additional information can be found in works by Holdren (1981) and by Kang and von Hipple (2001).

At doping levels ^{232}U/^{233}U = 2.4 %, the radiation dose rate at 1 m from 5 kg one year after chemical separation of daughter products is 1 Sv/h (100 rem/h) giving a fatal dose after only a few hours. This dose rate increases a factor of 3 after 10 years from separation, giving a fatal dose in a little over 1 h.

Immediately after chemical separation the heat generation rate from ^{232}U is 15 W/kg and increases to 130 W/kg after 10 years. The "shelf-life" of the high
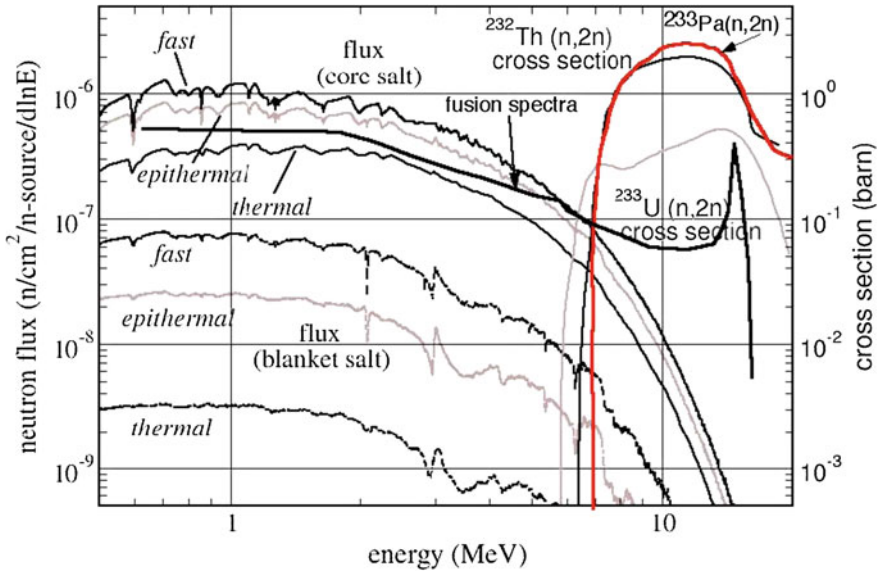
Fig. 14.19 Threshold cross sections for producing ^{232}U. The fusion neutron spectrum is superimposed but not to scale vertically [Le Brun et al. 2005]

explosive (HE) of a nuclear weapon owing to this radiation field would be well under one year. Thus, high ^{232}U concentrations would make it more difficult (but not impossible) to manufacture a weapon from ^{233}U (Moir 2012).

14.9 The Energy Park

The "Energy Park", shown in Fig. 14.20, could be a promising model for a sustainable world energy supply.

One fusion reactor would produce ^{233}U fuel for five external fission reactors, each producing 0.9 GWe. These reactors could be PWRs, BWRs, gas-cooled pebble beds, Generation-IV reactors, or other advanced reactors with passive safety features. A sixth reactor in the high security area would burn the plutonium that is generated in the other reactors.

Each reactor is fueled annually with about one metric ton of ^{233}U mixed in with about 24 metric tons of ^{238}U (Garwin and Charpak 2001). With just 4 % enrichment this is a highly proliferation resistant fuel. Each reactor produces annually about 750 kg of highly radioactive material with half-life $\leq$30 years, about 200 kg of plutonium and other actinides, and about 50 kg of much less radioactive material, such as ^{99}Tc with a 200,000 year half-life (Garwin 2001 and Refs therein). Except for the few hundred kg converted to actinides, the 24 metric tons of ^{238}U just "go along for the ride" during reprocessing.
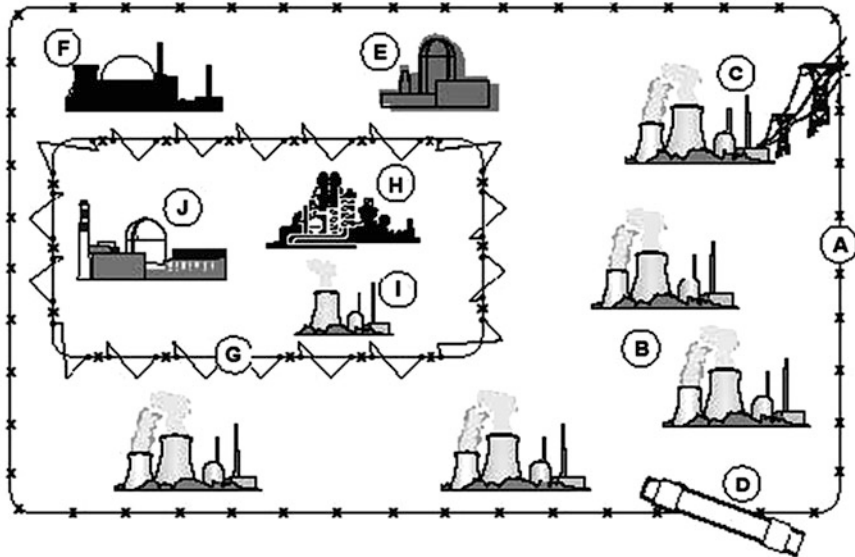
Fig. 14.20 The Energy Park: Inside a low security fence (*A*), 5,900 MWe LWR's (*B*), Electricity going out (*C*), hydrogen and/or liquid fuel pipeline (*D*), cooling pools for radiation products (*E*), hydrogen and/or liquid fuel factory (*F*). Inside a high security fence (*G*), unburned or undiluted actinides; the separation plant (*H*), the actinide burner (*I*), and the fusion reactor (*J*) (Manheimer 2005, 2006, 2009)

The reactors are supplied with fuel by a single fusion reactor that breeds ^{233}U from ^{232}Th and immediately dilutes this fissile fuel with ^{238}U into a subcritical mix. The fusion reactor is the size of the original Large ITER, and it is run in a fission-suppressed mode. Its 1.6 GW of neutron power produces about 13.5 GW worth of ^{233}U fuel, which is enough to run the five satellite fission reactors, which each generate 2.7 GWth. The fusion reactor itself produces about 2.4 GW of thermal power (including the exothermic reactions in the blanket) or about 0.8 GWe.

In the energy park, there could also be a hydrogen or liquid fuel manufacturing plant. It would use a part of the energy produced by the nuclear reactors to produce fuel for transportation, industry or home heating.

The waste from the fission reactors goes to a cooling pool to reduce its radioactivity. Then it goes to a reprocessing plant inside the high security fence where the uranium, plutonium, long, and short lived radio isotopes are separated out. The 5 LWR's each produce ~ 200 kg of plutonium and higher actinides yearly, so these fuel a sixth reactor of the same size that we call the "plutonium burner". This reactor could be for instance an Integral Fast Reactor (IFR) run at low conversion ratio. With its fast neutron spectrum it burns the actinides and produces electricity for the grid. Only one of the 7 reactors is a fast neutron reactor. This could be an advantage, since worldwide experience with fast reactors is much less than with thermal reactors (especially LWRs), and the cost of LWRs may be lower.

The radioisotopes in spent fuel are actinides and fission products. Standard chemical processes such as PUREX and UREX can extract virtually all (more than 99 %) of the uranium and actinides and can also separate the uranium from other actinides. If the long lived fission products can be economically separated out, and transmuted with fusion neutrons (Manheimer 2006), it might be more economically desirable to do so, rather than sending them to a geologic repository.

Many of the fission products can be separated chemically. Some of the isotopes could be used for beneficial purposes, such as medical diagnosis and therapy, industrial irradiations, sterilization of medical equipment, food preservation, and research. The remaining isotopes would go to sealed cooling pools or dry-cask storage, where they could remain secure until the radioactivity had decayed to a safe level, perhaps a few hundred years. Later, the few remaining long-lived isotopes could be separated and incinerated, or sent to a permanent repository. The volume to be stored in a repository could be a factor of 100 lower than without actinide incineration.

Thus, the beneficial uses of radioisotopes and the incineration of actinides could greatly ameliorate the radioactive waste problem.

The plutonium burner reactor does not need high neutron economy or high efficiency of electricity generation, because its primary purpose is to destroy plutonium, so less expensive materials could be used, but it would nevertheless generate substantial electrical power.

The plutonium burner, reprocessing plant, and possibly the fusion reactor would be in a highly secure area. The remainder of the park would be in a lower security area similar to today's nuclear plants (Fig. 14.20). The plutonium would travel just from the reprocessing plant to the burner, and there would be no long distance travel, unless the energy park served other off-site reactors.

Some facilities similar to this energy park exist today: the Kashiwazaki-Kariwa nuclear plant in north western Japan, and Bruce complex on Lake Huron, Canada. Each is a suite of seven nuclear reactors, with total capacity ~ 7 GWe. These could be modified to an "Energy Park" configuration by replacing one LWR with the fusion hybrid, replacing one LWR with the plutonium burner, and adding a reprocessing plant on site. Thus, the energy park concept is not far from existing multi-unit power plants.

Some LWRs could also help assure adequate tritium breeding, by irradiating lithium in the reactors. For example, the Department of Energy is starting production of tritium at the TVA Watts Barr nuclear facility. While burning $\sim$ one metric ton of nuclear fuel (about 4,000 mol), about 3 kg (1,000 mol) of tritium are produced. In other words, for every four nuclear reactions, one triton is produced.

One fusion neutron produces about 0.6 ^{233}U's. If all the LWR's are operated in this mode, a 10–15 % additional tritium resource could become available for the fusion reactor, so its blanket design requirements would be relaxed. The fusion reactors produce fuel for the LWR's, and the LWR's could provide some of the tritium fuel for the fusion reactor. There might be a small cost penalty, but no power penalty, for this symbiosis.

To summarize, there are one fusion hybrid reactor, six thermal fission reactors, and one plutonium burner reactor in the park, with a total power generation of about 6 GWe. Some of the electricity, hydrogen, or low-enriched ^{233}U fuel could be exported to other countries, who would return their spent fuel to the Energy Park. The park would reprocess its spent fuel, recycle uranium and plutonium fuels, incinerate most of the other actinides, provide some radioisotopes for beneficial uses, store the remaining fission products securely until they decay, and eliminate or greatly reduce the material requiring disposal in a repository. Thus, the Energy Park is a vision for a safe, sustainable, environmentally sound future world energy supply, which could power the world at 30 TW for thousands of years.

14.10 Problems

14.1. A fusion power plant is to produce a net power output of 50 MWe. The driver efficiency is 42 % and the energy conversion efficiency is 45 %. If Q = 17, what are the total electrical power generated and the recirculating power fraction?

14.2. ^{233}Th (half life 22.2 min) is destroyed by decay into protactinium ^{233}Pa and by neutron absorption with cross section 1,400 b (1 b = 10^{-28} m^2). If the neutron flux is 10^{18} m^{-2} s^{-1}, what fraction of the ^{233}Th atoms go to ^{234}Th instead of decaying into ^{233}Pa ?

14.3. (Similar to previous problem) Assuming that the absorption cross section of ^{233}Pa (half life 27 d) is 460 b and the flux is again 10^{18} m^{-2} s^{-1}, what fraction of ^{233}Pa becomes ^{234}Pa instead of decaying into ^{233}U ? This shows the need to use a low flux or to remove the ^{233}Pa from the reactor.

14.4. Assume that one neutron absorbed in the blanket generates k secondary neutrons by fission, k^2 neutrons in the next generation, etc., so the total number of neutrons resulting from one incident neutron is $1 + k + k^2 + k^3 + \cdots = (1 - k)^{-1}$ neutrons per incident neutron. If each fission releases 2.8 neutrons, then 200/2.8 = 71 MeV is associated with each fission neutron released. Estimate the approximate blanket energy gain factor for a blanket with k = 0.94.

14.5. Derive Eq. (14.1), taking into account the fact that input energy also comes out and can be converted into electricity.

14.11 Review Questions

1. Explain the meanings of the parameters in the equation $P_{net} = \eta_e(0.8M + 0.2 + 1/Q)P_f - P_f/(\eta_d Q)$

2. What can happen if Np and Pa are not removed from the reactor promptly?

3. About how many fast fission reactors does it take to breed fissile fuel for one LWR, and about how many fission reactors can be fueled by one hybrid reactor?

4. Why can a fusion reactor generate more neutrons in the blanket than 2 MeV neutrons from fission can?
5. How much fissile fuel is required to start up a fast fission reactor? A fusion reactor?
6. Name two disadvantages of hybrids relative to LMFBRs.
7. What are the three applications of hybrids?
8. What are the advantages of fission-suppressed hybrids over high-power hybrids?
9. What features should a hybrid reactor driver have?
10. About how many MWth and MWe have been produced in tokamaks for more than 2 s?
11. What tritium breeding reaction is endothermic?
12. What fraction of lithium is ^{6}Li?
13. How does the DD reaction rate compare with the DT reaction rate?
14. What is the threshold neutron energy for fission of ^{238}U? of ^{232}Th?
15. What is the meaning of η?
16. Why would UC and UO_2 perform less well neutronically than pure U fuel?
17. What are the advantages of molten salt fuel?
18. How can fast fission and thermal fission be suppressed? What are the benefits of suppression?
19. What are the benefits of having ^{232}U in the fuel?
20. How can a blanket be optimized for waste incineration?
21. What are the advantages and disadvantages of helium coolant?
22. Explain the parameters in the equation $\varepsilon = 1/Fv$. What is a typical value of v from fast fission?
23. How can we decide which is better, fission-suppressed fissile fuel breeder hybrid or a waste-incinerating hybrid?
24. What are the disadvantages of hybrids optimized for high power production?
25. What happened at CERN and how does it relate to large tokamak hybrids?
26. How do fission-suppressed hybrids and high-power fast fission hybrids compare with regard to safety? With regard to proliferation?
27. What ^{240}Pu fraction is desirable for nonproliferation?
28. How can ^{233}U be made proliferation resistant?
29. Describe an Energy Park, including numbers of reactors and secure areas.
30. What are the potential benefits of an Energy Park?
31. How could additional tritium be obtained in an Energy Park?

References

Argonne National Laboratory (1963) Reactor physics constants. Argonne National Laboratory report, p 23

Azechi H et al (2009) Plasma physics and laser development for the fast ignition realization experiment (FIREX) project. Nucl Fusion 49:104024

Badger et al (1975) UWMAK-II—a conceptual tokamak power reactor design. University of Wisconsin Rep. UWFDM-112

Barr W et al (1977) Engineering of beam direct conversion for a 120 kV 1 MW ion beam. In: Proceedings of 7th symposium on engineering problems of fusion research, October

Bechtel Corp (1977) Laser fusion–fission reactor systems study. U.S. ERDA Rep. UCRL-13796

Bender DJ, Carlson DA (1978) System model for analysis of the mirror fusion/fission reactor. Lawrence Livermore National Laboratory Report UCRL-52293.

Berwald DH et al (1982) Fission-suppressed hybrid reactor—the fusion breeder. Lawrence Livermore National Laboratory, Livermore, CA, UCID-19638

Bethe H (1979) The fusion hybrid, Physics Today, May

Blinkin LV, Novikov MV (1977) Optimal Symbiotic Molten-Salt Fission–Fusion/Fission System, I.V. Kurchatov Institute of Atomic Energy, preprint IAE-2819, Moscow, UCRL-Trans-11288

Campbell D (2001) The physics of the international tokamak experimental reactor, FEAT. Phys Plasmas 8:2041

Chang Y (2002) Advanced fast reactor: a next generation nuclear energy concept. Forum on physics and society, April

Chang Y (2009) Private communication

Cheng ET (2005) Performance characteristics of actinide-burning fusion power plants. Fusion Sci Technol 47:1219–1223

Fraser JS, Hoffman CRJ, Tunnicliffe PR (1973) The role of electricity produced neutrons in nuclear power generation. Chalk River Nuclear Laboratories Rep. AECL-4658

Freidberg JP, Kadak AC (2009) Fusion-fission hybrids revisited. Nat Phys 5:370

Garwin R, Charpak G (2001) Megawatts and megatons. Alfred Knopf, New York

Gibson A, The JET Team (1998) Deuterium-tritium plasmas in JET, behavior and implications. Phys Plasmas 5:1839

Greenspan E et al (1977) Natural uranium fueled light water moderated breeding hybrid power reactors—a feasibility study. Princeton Plasma Physics Laboratory Rep. PPPL-1444

Hawryluk R et al (1998) Fusion plasma experiments on TFTR: a 20 year retrospective. Phys Plasmas 5:1577

Hoffert M et al (2002) Advanced technology paths to global climate stability: energy for a greenhouse planet. Science 298:981

Holdren JP (1981) Fusion-fission hybrids: environmental aspects and their role in hybrid rationale. J Fusion Energy 1:197–210

Ide S, The JT-60 Team (2000) Latest progress in steady state plasma research on the Japan atomic energy research institute tokamak-60 upgrade. Phys Plasmas 7:1927

Isayamab A, The JT-60 Team (2005) Steady-state sustainment of high-β plasmas through stability control in Japan atomic energy research institute tokamak-60 upgrade. Phys Plasmas 12:056117

Ishida S, The JT-60 Team, The JFT-2M Group (2004) High-beta steady-state research and future directions on the Japan atomic energy research institute tokamak-60 upgrade and the Japan atomic energy research institute fusion torus-2 modified. Phys Plasmas 11:2532

Jassby D (1981) The fusion-supported decentralized nuclear energy system. J Fusion Energy 1:59

Kang J, von Hippel FN (2001) U-232 and the proliferation resistance of U-233 in spent fuel. Sci Glob Secur 9:1–32

Kelly J, Rose R (1981) The tokamak hybrid reactor. Nucl Eng Design 63:395

Koide Y, The JT 60 Team (1997) Progress in confinement and stability with plasma shape and profile control for steady-state operation in the Japan atomic energy research institute tokamak-60 upgrade. Phys Plasmas 4:1623

Kotschenreuther M, Valanju PM, Mahajan SM, Schneider EA (2009) Fusion-fission transmutation scheme-efficient destruction of nuclear waste. Fusion Eng Des 84:83–88

Kusama Y, The JT-60 Team (1999) Recent progress in high performance and steady-state experiments on the Japan atomic energy research institute tokamak-60 upgrade with W-shaped divertor. Phys Plasmas 6:1935

Lamarsh JR, Baratta AJ (2001) Introduction to nuclear engineering, 3rd edn. Prentice Hall, Upper
    Saddle River, NJ, p 227

Le Brun C, Mathieu L, Heuer D, Nuttin A (2005) Impact of the MSBR concept technology on
    long-lived radio-toxicity and proliferation resistance. Note LPSC 05-81, technical meeting on
    fissile material management strategies for sustainable nuclear energy, Vienna, Austria

Lee JD (1976) Blanket design for the mirror fusion/fission hybrid reactor, Fig. 10 burn results,
    p 27. In: Proceedings of US-USSR symposium on fusion-fission reactors, Lawrence
    Livermore Laboratory, Livermore, California LLL-ERDA, CONF-760733, 13–16 July 1976,
    p 272

Lee JD (1978) Private communications

Lee JD (1979). Private communications

Lee JD, Moir R (1981) Fission suppressed blankets for fissile fuel breeding fusion reactors.
    J Fusion Energy 1:299

Lee JD et al (1982) Feasibility study of a fission-suppressed tandem-mirror hybrid reactor.
    Lawrence Livermore National Laboratory, Livermore, CA, UCID-19327, p IV-1–IV-98

Lessor DL (1975) Neutron and alpha particle energy spectrum and angular distribution effects
    from beam-plasma D-T. Pacific Northwest Laboratories (USA) Rep. BNWL-B-409

Lidsky LM (1969) Fission-fusion symbiosis: general considerations and a specific example. In:
    Proceedings of british nuclear energy society conference on nuclear fusion reactors Culham
    Lab, Culham Laboratory Rep. (CLM-NFE), pp 41–53

Lidsky LM (1975) Review paper fission-fusion systems: hybrid, symbiotic and Augean. Nucl
    Fusion 15:151–173

Lidsky LM (1982) End product economics and fusion research program priorities. J Fusion
    Energy 2:269

Loarte A et al (2004) Characterization of pedestal parameters and ELM energy losses in JET and
    predictions for ITER. Phys Plasmas 11:2668

Manheimer W (1999) Back to the future, the historical, scientific, naval and environmental case
    for fission fusion. Fusion Tech 36:1

Manheimer W (2003) An alternate development path for magnetic fusion. J Fusion Energy
    20(4):131

Manheimer W (2005) The fusion hybrid as a key to sustainable development. J Fusion Energy
    23(4):223–235

Manheimer W (2006) Can fusion and fission breeding help civilization survive? J Fusion Energy
    25:121

Manheimer W (2009) Hybrid fusion: the only viable development path for tokamaks? J Fusion
    Energy 28:60

Maniscalco J et al (1984) The fusion breeder-an early application of nuclear fusion. Fusion Tech
    6:584

Mills RG (ed) (1974) A fusion power plant. Princeton Plasma Physics Laboratory Rep. MATT-
    1050

Moir RW (1981) The fusion-fission fuel factory. In: Teller E (ed) Fusion, vol 1, Part B, Chap. 15.
    Academic Press, NY

Moir RW (1982) The fusion breeder. J Fusion Energy 2:351

Moir RW et al (1975) Progress on the conceptual design of a mirror hybrid fusion/fission reactor.
    Lawrence Livermore Laboratory Report UCRL-51797:45

Moir RW et al (1984a) Helium-cooled molten salt fusion breeder. Lawrence Livermore National
    Laboratory, Livermore, CA, UCID-20153

Moir RW et al (1984b) Feasibility study of a fission-suppressed tokamak fusion breeder.
    Lawrence Livermore National Laboratory, Livermore, CA, UCID-20154

Moir RW et al (1985) Design of a helium-cooled molten salt fusion breeder. Fusion Technol
    8:465–473

Moir RW (1994) Direct energy conversion beam dump for a 1.6 MeV neutral beam for the
    international thermonuclear experimental reactor (ITER). Fusion Technol 15:129

Moir RW, Hagmann CA, Shaw HR (2009a) Pu from weapons burning in a molten salt version of LIFE. Lawrence Livermore National Laboratory report LLNL-TR-418362

Moir RW, Shaw HF, Caro A, Kaufman L, Latkowski JF, Powers J, Turchi PEA (2009b) Molten salt fuel version of laser inertial fusion fission energy (LIFE). Fusion Sci Technol 56:632–640

Moir RW (2012) Fission-suppressed fusion, thorium cycle breeder, and nonproliferation. Trans Fusion Sci Technol 61:243.

Moses EI et al (2009a) A sustainable nuclear fuel cycle based on laser inertial fusion energy. Fusion Sci Technol 56:547

Moses EI et al (2009b) A sustainable nuclear fuel cycle based on laser inertial fusion energy. Fusion Sci Technol 56:548–565

Najmabadi F, The ARIES Team (1997) Overview of the ARIES-RS reversed-shear tokamak power plant study. Fusion Eng Design 38:3

Obenschain S et al (2006) Pathway to a lower cost high repetition rate ignition facility. Phys Plasmas 13:056320

Plechaty et al (1976) Tabular and graphical presentation of 175 neutron group constants derived from the LLL evaluated neutron data library (ENDL), vol 16. Lawrence Livermore Laboratory Rep. UCRL-50400

Rebut PH (2006) From JET to reactor. Plasma Phys Controlled Fusion 48:B1

Rose R (1981) The case for the fusion hybrid. J Fusion Energy 1:185

Sakharov A (1990) Memoirs. Vintage Books, New York, p 142

Saltmarsh MJ, Grimes WR, Santor RT (1979) An optimization of the fission-fusion hybrid concept. Oak Ridge National Laboratory Report ONL/PPA-79/3

Shirai H, The JT-60 Team (1998) Recent experimental and analytic progress in the Japan atomic energy research institute tokamak-60 upgrade with W-shaped divertor configuration. Phys Plasmas 5:1712

Simpson J (1987) Outlook for the fusion hybrid and tritium breeding fusion reactors. National Academy Press, Washington DC

Stacey WM et al (2008) A TRU-Zr metal-fuel sodium-cooled fast subcritical advanced burner reactor. Nucl Technol 162:53

Stacey WM (2009) Georgia tech studies of sub-critical advanced burner reactors with a D-T fusion tokamak neutron source for the transmutation of spent nuclear fuel. J Fusion Energy 28:328

Takenaga H, The JT-60 Team (2001) Improved particle control for high integrated plasma performance in Japan atomic energy research institute tokamak-60 upgrade. Phys Plasmas 8:2217

Tenney F et al (1978) A systems study of tokamak fusion-fission reactors, PPPL-1450, p 544

Thumm M et al (2008) Progress in the 10 MW 140 GHz ECH system for the stellarator W7-X. IEEE Trans Plasma Sci 36:341

Wu Y, Zheng S, Zhu X, Wang W, Wang H, Liu S, Bai Y, Chen H, Hu L, Chen M, Huang Q, Huang D, Zhang S, Li J, Chu D, Jiang J, Song Y (2006) Conceptual design of the fusion-driven subcritical system FDS-I. Fusion Eng Des 81:1305–1311

Appendix A
Units

	Abbreviation	Measure of
Ampere	A	Current
Candela	cd	Luminous intensity
Kelvin	K	Temperature
Kilogram	kg	Mass
Metre	m	Length
Mole	mol	Amount of substance
Radian	rad	Plane angle
Second	s	Time
Steradian	sr	Solid angle

Derived units	Equal to	Measure of
Becquerel	$Bq = s^{-1}$	Radioactive decay
Coulomb	$C = A\text{-}s$	Charge
Farad	$F = A\text{-}s/V$	Capacitance
	$= C/V$	
	$= C^2/J$	
Gray	$Gy = J/kg$	Absorbed dose
Henry	$H = V\text{-}s/A$	Inductance
	$= J/A^2$	
	$= Wb/A$	
Hertz	$Hz = s^{-1}$	Frequency
Joule	$J = N\text{-}m$	Energy
	$= kg\text{-}m^2/s^2$	
	$= W\text{-}s$	
Newton	$N = kg\text{-}m/s^2$	Force
	$= J/m$	
Ohm	$\Omega = V/A$	Resistance
Pascal	$Pa = N/m^2$	Pressure or stress
	$= J/m^3$	

(continued)

Derived units	Equal to	Measure of
Sievert	Sv = J/kg	Dose equivalent
Tesla	T = Wb/m^2	Magnetic flux
	= V-s/m^2	Density
Volt	V = W/A	Voltage
	= J/C	
Watt	W = J/s	Power
	= V-A	
Weber	Wb = V-s	Magnetic flux

Prefixes					
10^{18}	Exa	E	10^{-2}	Centi	c
10^{15}	Peta	P	10^{-3}	Milli	m
10^{12}	Tera	T	10^{-6}	Micro	μ
10^{9}	Giga	G	10^{-9}	Nano	n
10^{6}	Mega	M	10^{-12}	Pico	p
10^{3}	kilo	k	10^{-15}	Femto	f

Energy	Joule
Btu (international)	1055.1
Calorie (international)	4.1868
Electron volt, eV	1.60219×10^{-19}
Kilo-electron-Volt, keV	1.60219×10^{-16}
Mega-electron-Volt, MeV	1.60219×10^{-13}
erg	10^{-7}
Foot-pound-force	1.3558
Kilowatt-hour	3.6000×10^{6}
Ton TNT	4.20×10^{9}
Tera-Watt-year, TWy	3.1536×10^{19}
Quad (Q) (10^{15} Btu)	1.055×10^{18}
Ton of coal (Bituminous)	2.95×10^{10}
Barrel of oil (42 US gallons)	6.2×10^{9}
Cubic metre natural gas (35.3 Ft^3)	3.85×10^{7}
Ton of oil (1,000 kg)	4.194×10^{10}
Cubic metre liquefied natural gas	2.01×10^{10}
Associated with atomic mass unit	1.4924×10^{-10}

Power	Watt
Btu/h (international)	0.29307
Horsepower, hp (550 ft-lb$_f$ /s)	745.7
Horsepower, hp (electrical)	746.0

Mass	Kilogram
Pound-mass (avoirdupois)	0.45359
Slug	14.594
Ton (metric)	1000.0
Ton (short)	907.18
Ton (long)	1016.0
Atomic mass unit, u	1.660566×10^{27}

Length	Metre
Angstrom Å	10^{-10}
Foot, ft	0.30480
Micron	10^{-6}
Inch	0.0254
Mil, 10^{-3} inch	2.540×10^{-5}
Mile (US statute)	1609.3
Mile (nautical)	1852.0
Yard	0.91440

Time	Seconds
Day	86,400
Year	3.1536×10^7
Month	2.628×10^6
Minute	60
Hour	3,600

Area	Square metres
Barn	10^{-28}
Square foot, ft^2	0.092903

Volume	Cubic metres
Cubic centimetre, cm^3	10^{-6}
Litre	10^{-3}
Cubic foot, ft^3	0.028317
Gallon (US liquid)	3.7854×10^{-3}

Velocity	Metres per second
Ft/s	0.30480
Ft/h	8.4667×10^{-5}
Mile/h (US statute)	0.44704

Force	Newtons
Dyne	10^{-5}
Pound-force	4.4482
Poundal	0.13826
Kilogram-force	9.80665

Density	Kilogram/m^3
Pound-mass/ft^3	16.0185
Gram/cm^3	1,000

Pressure or stress	Pascal
Atmosphere, 760 Torr	1.01325×10^5
Bar	10^5
Dyne/cm^2	0.100000
Foot of water	2.98893
Kilogram-force/mm^2	9.80665×10^6
Kilogram-force/cm^2	9.80665×10^4
Millimetre (Hg)	133.322
Torr	133.322
Pound-force/ft^2	47.880
Pound-force/in^2, psi	6894.76
ksi	6.89476×10^6

Temperature	Kelvin
Celsius, C	C + 273.15
Fahrenheit, F	(F + 459.67)/1.8
Rankine, R	R/1.8
eV	11604.85

Charge	Coulomb
Statcoulomb, esu	3.33564×10^{-10}
Faraday	9.6487×10^{4}

Current	Ampere
esu, current	3.3356×10^{-10}
emu, current	10.000

Electromotive force	Volt
Statvolt	299.79
emu of potential	10^{-8}

Magnetic flux	Weber
Maxwell	10^{-8}

Magnetic flux density	Tesla
Gauss	10^{-4}

Inductance	Henry
emu, inductance	10^{-9}
esu, inductance	8.98758×10^{11}

Magnetic field	Ampere/m
Oersted	79.577

Resistance	Ohm
emu, resistance	10^{-9}
esu, resistance	8.98758×10^{11}

Capacitance	Farad
emu, capacitance	10^{9}
esu, capacitance	1.11265×10^{-12}

Radioactivity	
Curie (decay rate)	3.7×10^{10} Bq
Roentgen (radiation dose)	2.57976×10^{4} C/kg
Rad (absorbed radiation dose)	0.01 Gy
rem ("Roentgen-equivalent-man")	(0.01) QF Gy
QF (quality factor)	1 for betas (electrons), X rays
	2–5 for thermal neutrons
	5–10 for fast neutrons
	(~ 10 MeV)
	10 for protons
	20 for alpha particles

Other	
Degree (angle)	0.0174533 radians
Btu/ft^2-h (heat flux)	3.152 W/m^2
Btu/ft^2-h-F (heat transfer coefficient)	5.674 W/m^2-K
Btu/ft-h-F (thermal conductivity)	1.731 W/m-K
Btu/lb-F (specific heat)	4187 J/kg-K

Appendix B
Constants

Nuclear masses (To find atomic masses, add Zm_e)

Atomic numeric Z	Mass numeric A	Particle	Mass (u)	Mass (kg)	Percent abundance
0	0	Electron, e	0.0005485801	9.109534×10^{-31}	
0	1	Neutron, n	1.00866452	1.674954×10^{-27}	
1	1	Proton, p, h	1.00727644	1.672649×10^{-27}	99.985
1	2	Deuteron, D, ^{2}H	2.013553	3.343468×10^{-27}	0.0153
1	3	Triton, T, ^{3}H	3.015501	5.007438×10^{-27}	
2	3	^{3}He	3.014933	5.006495×10^{-27}	0.00013
2	4	^{4}He, a	4.001503	6.44760×10^{-27}	99.99987
3	6	^{6}Li	6.013470	9.985764×10^{-27}	7.42
3	7	^{7}Li	7.014354	1.164780×10^{-26}	92.58
4	9	^{9}Be	9.009986	1.496168×10^{-26}	100
5	10	^{10}B	10.010757	1.662352×10^{-26}	19.78
5	11	^{11}B	11.018857	1.829754×10^{-26}	80.22
6	12	^{12}C	11.996709	1.992133×10^{-26}	98.89
6	13	^{13}C	13.000059	2.158746×10^{-26}	1.11

Other constants

Boltzmann constant	$k = 1.38066 \times 10^{-23}$ J/K
Speed of light in vacuum	$c = 2.99792 \times 10^{8}$ m/s
Electronic charge	$e = 1.60219 \times 10^{-19}$ C
Avogadro constant	$N_A = 6.02204 \times 10^{23}$
Planck constant	$h = 6.62618 \times 10^{-34}$ J-s
Stefan–Boltzmann constant	$\sigma = 5.67032 \times 10^{-8}$ W m^{-2} K^{-4}
Permittivity of free space	$\varepsilon_0 = 8.85419 \times 10^{-12}$ F/m
Permeability of free space	$\mu_0 = 4\pi \times 10^{-7}$ H/m
Energy associated with l u	$= 931.481$ MeV
Molecular density at l Pa, 273.15 K	$= 2.6516 \times 10^{20}$ molecules/m^3
Acceleration of gravity at sea level, 45° latitude	$g = 9.8062$ m/s^2

Appendix C
Error Function

Reference:

Abramowitz M, Stegun IA (1964) Handbook of mathematical functions, Chap 7. National Bureau of Standards. Appl Math Series 55, Washington, DC

$$\text{erf}(z) = \frac{2}{\sqrt{\pi}} \int\limits_{0}^{z} dy \ \exp(-y^2) \tag{C1}$$

$$\text{erf}(-z) = -\text{erf}(z) \tag{C2}$$

for small z:

$$\text{erf}(z) = \frac{2}{\sqrt{\pi}} \left(z - \frac{z^3}{3 \cdot 1!} + \frac{z^5}{5 \cdot 2!} - \frac{z^7}{7 \cdot 3!} + \frac{z^9}{9 \cdot 4!} - \dots \right) \tag{C3}$$

for large z:

$$\text{erf}(z) = 1 - \frac{e^{-Z^2}}{z\sqrt{\pi}} \left(1 - \frac{1}{2z^2} + \frac{1 \cdot 3}{(2z^2)^2} - \frac{1 \cdot 3 \cdot 5}{(2z^2)^3} + \dots \right) \tag{C4}$$

z	erf(z)
0	0
0.05	0.056372
0.10	0.112463
0.15	0.167996
0.20	0.222703
0.25	0.276326
0.30	0.328627
0.35	0.379382
0.40	0.428392
0.45	0.475482
0.50	0.520500
	(continued)

(continued)

z	erf(z)
0.55	0.563323
0.60	0.603856
0.65	0.642029
0.70	0.677801
0.75	0.711156
0.80	0.742101
0.85	0.770668
0.90	0.796908
0.95	0.820891
1.00	0.842701
1.05	0.862436
1.10	0.880205
1.15	0.896124
1.20	0.910314
1.25	0.922900
1.30	0.934008
1.35	0.943762
1.40	0.952285
1.45	0.959695
1.50	0.966105
1.55	0.971623
1.60	0.976348
1.65	0.980376
1.70	0.983790
1.75	0.986672
1.80	0.989091
1.85	0.991111
1.90	0.992790
1.95	0.994179
2.00	0.995322

Appendix D
Vector Relations

$\overrightarrow{A} = A_x\widehat{x} + A_y\widehat{y} + A_z\widehat{z}$, where $\widehat{x}$, $\widehat{y}$, and $\widehat{z}$ are unit vectors.

Scalar or dot product of two vectors: $\overrightarrow{A} \cdot \overrightarrow{B} = A_xB_x + A_yB_y + A_zB_z$.

Vector or cross product:

$$\overrightarrow{A} \times \overrightarrow{B} \equiv \begin{vmatrix} \widehat{x} & \widehat{y} & \widehat{z} \\ A_x & A_y & A_z \\ B_x & B_y & B_z \end{vmatrix}$$
$$= (A_yB_z - A_zB_y)\widehat{x} + (A_zB_x - A_xB_z)\widehat{y} + (A_xB_y - A_yB_x)\widehat{z}$$
$$= -\overrightarrow{B} \times \overrightarrow{A}$$

Differential operator Del: $\overrightarrow{\nabla} \equiv \widehat{x}\frac{\partial}{\partial x} + \widehat{y}\frac{\partial}{\partial y} + \widehat{z}\frac{\partial}{\partial z}$

Gradient of scalar: $\overrightarrow{\nabla}\phi \equiv (\partial\phi/\partial x)\widehat{x} + (\partial\phi/\partial y)\widehat{y} + (\partial\phi/\partial z)\widehat{z}$

Divergence of vector: $\overrightarrow{\nabla} \cdot \overrightarrow{A} = (\partial A_x/\partial x) + (\partial A_y/\partial y) + (\partial A_z/\partial z)$

Curl of vector:

$$\overrightarrow{\nabla} \times \overrightarrow{A} = \begin{vmatrix} \widehat{x} & \widehat{y} & \widehat{z} \\ \frac{\partial}{\partial x} & \frac{\partial}{\partial y} & \frac{\partial}{\partial z} \\ A_x & A_y & A_z \end{vmatrix} = [(\partial A_z/\partial y) - (\partial A_y/\partial z)]\widehat{x} + [(\partial A_x/\partial z)$$
$$- (\partial A_z/\partial x)]\widehat{y} + [(\partial A_y/\partial x) - (\partial A_x/\partial y)]\widehat{z}$$

Laplacian of scalar: $\nabla^2\phi \equiv (\partial^2\phi/\partial x^2) + (\partial^2\phi/\partial y^2) + (\partial^2\phi/\partial z^2)$

Laplacian of vector: $\nabla^2\overrightarrow{A} = \left(\frac{\partial^2 A_x}{\partial x^2} + \frac{\partial^2 A_x}{\partial y^2} + \frac{\partial^2 A_x}{\partial z^2}\right)\widehat{x} + \left(\frac{\partial^2 A_y}{\partial x^2} + \frac{\partial^2 A_y}{\partial y^2} + \frac{\partial^2 A_y}{\partial z^2}\right)\widehat{y}$
$$+ \left(\frac{\partial^2 A_z}{\partial x^2} + \frac{\partial^2 A_z}{\partial y^2} + \frac{\partial^2 A_z}{\partial z^2}\right)\widehat{z}$$

Theorems

Divergence theorem	$\int d\vec{x}\,\vec{\nabla}\cdot\vec{A} \underset{\text{volume}}{} = \int d\vec{S}\cdot\vec{A} \underset{\text{surface}}{}$
Stokes' theorem	$\int d\vec{S}\cdot\vec{\nabla}\times\vec{A} \underset{\text{surface}}{} = \oint d\vec{l}\cdot\vec{A} \underset{\text{boundary curve}}{}$
	$\int d\vec{x}\,\vec{\nabla}\times\vec{A} \underset{\text{volume}}{} = \int d\vec{S}\times\vec{A} \underset{\text{surface}}{}$
	$\int d\vec{S}\times\vec{\nabla}\phi \underset{\text{surface}}{} = \oint d\vec{l}\cdot\phi \underset{\text{boundary curve}}{}$

Identities

$$\vec{\nabla}p(\psi) = \frac{dp}{d\psi}\vec{\nabla}\psi$$

$$\vec{A}\cdot(\vec{B}\times\vec{C}) = \vec{B}\cdot(\vec{C}\times\vec{A}) = \vec{C}\cdot(\vec{A}\times\vec{B}) \equiv (\vec{A}\,\vec{B}\,\vec{C})$$

$$(\vec{A}\times\vec{B})\cdot(\vec{C}\times\vec{D}) = (\vec{A}\cdot\vec{C})(\vec{B}\cdot\vec{D}) - (\vec{A}\cdot\vec{D})(\vec{B}\cdot\vec{C})$$

$$\vec{A}\times(\vec{B}\times\vec{C}) = (\vec{A}\cdot\vec{C})\vec{B} - (\vec{A}\cdot\vec{B})\vec{C} = -(\vec{B}\times\vec{C})\times\vec{A}$$

$$(\vec{A}\times\vec{B})\times(\vec{C}\times\vec{D}) = (\vec{A}\,\vec{B}\,\vec{D})\vec{C} - (\vec{A}\,\vec{B}\,\vec{C})\vec{D} = (\vec{A}\,\vec{C}\,\vec{D})\vec{B} - (\vec{B}\,\vec{C}\,\vec{D})\vec{A}$$

$$\vec{\nabla}(\phi + \psi) = \vec{\nabla}\phi + \vec{\nabla}\psi$$

$$\vec{\nabla}\cdot(\vec{A} + \vec{B}) = \vec{\nabla}\cdot\vec{A} + \vec{\nabla}\cdot\vec{B}$$

$$\vec{\nabla}\times(\vec{A} + \vec{B}) = \vec{\nabla}\times\vec{A} + \vec{\nabla}\times\vec{B}$$

$$\vec{\nabla}(\phi\psi) = \phi\vec{\nabla}\psi + \psi\vec{\nabla}\phi$$

$$\vec{\nabla}\cdot(\phi\vec{A}) = \phi\vec{\nabla}\cdot\vec{A} + \vec{\nabla}\phi\cdot\vec{A}$$

$$\vec{\nabla}\times(\phi\vec{A}) = \phi\vec{\nabla}\times\vec{A} + \vec{\nabla}\phi\times\vec{A}$$

$$\vec{\nabla}\times\vec{\nabla}\phi = 0$$

$$\vec{\nabla}\cdot(\vec{\nabla}\times\vec{A}) = 0$$

$$\vec{\nabla}\cdot(\vec{A}\times\vec{B}) = \vec{B}\cdot(\vec{\nabla}\times\vec{A}) - \vec{A}\cdot(\vec{\nabla}\times\vec{B})$$

$$\vec{\nabla}\times(\vec{A}\times\vec{B}) = (\vec{B}\cdot\vec{\nabla})\vec{A} - (\vec{A}\cdot\vec{\nabla})\vec{B} + \vec{A}(\vec{\nabla}\cdot\vec{B}) - \vec{B}(\vec{\nabla}\cdot\vec{A})$$

$$(\vec{A}\cdot\vec{\nabla})\vec{B} \equiv A_x\frac{\partial\vec{B}}{\partial x} + A_y\frac{\partial\vec{B}}{\partial y} + A_z\frac{\partial\vec{B}}{\partial z}$$

$$\vec{\nabla}(\vec{A}\cdot\vec{B}) = (\vec{A}\cdot\vec{\nabla})\vec{B} + (\vec{B}\cdot\vec{\nabla})\vec{A} + \vec{A}\times(\vec{\nabla}\times\vec{B}) + \vec{B}\times(\vec{\nabla}\times\vec{A})$$

$$\vec{\nabla}\times(\vec{\nabla}\times\vec{A}) = \vec{\nabla}\cdot(\vec{\nabla}\cdot\vec{A}) - \nabla^2\vec{A}.$$

Cylindrical Geomentry

$$\vec{\nabla} = \hat{r}\frac{\partial}{\partial r} + \frac{\hat{\phi}}{r}\frac{\partial}{\partial \phi} + \hat{z}\frac{\partial}{\partial z}$$

$$\vec{\nabla}\psi = \hat{r}\frac{\partial \psi}{\partial r} + \frac{\hat{\phi}}{r}\frac{\partial \psi}{\partial \phi} + \hat{z}\frac{\partial \psi}{\partial z}$$

$$\vec{\nabla} \cdot \vec{A} = \frac{1}{r}\frac{\partial}{\partial r}(rA_r) + \frac{1}{r}\frac{\partial A_\phi}{\partial \phi} + \frac{\partial A_z}{\partial z}$$

$$\vec{\nabla} \times \vec{A} = \left(\frac{1}{r}\frac{\partial A_z}{\partial \phi} - \frac{\partial A_\phi}{\partial z}\right)\hat{r} + \left(\frac{\partial A_r}{\partial z} - \frac{\partial A_z}{\partial r}\right)\hat{\phi} + \left(\frac{1}{r}\frac{\partial}{\partial r}(rA_\phi) - \frac{1}{r}\frac{\partial A_r}{\partial \phi}\right)\hat{z}$$

$$\nabla^2\psi = \frac{1}{r}\frac{\partial}{\partial r}r\frac{\partial \psi}{\partial r} + \frac{1}{r^2}\frac{\partial^2 \psi}{\partial \phi^2} + \frac{\partial^2 \psi}{\partial z^2}$$

$$\nabla^2\vec{A} = \left[\nabla^2 A_r - \frac{1}{r^2}\left(A_r + 2\frac{\partial A_\phi}{\partial \phi}\right)\right]\hat{r} + \left[\nabla^2 A_\phi - \frac{1}{r^2}\left(A_\phi - 2\frac{\partial A_r}{\partial \phi}\right)\right]\hat{\phi} + \nabla^2 A_z\hat{z}$$

$$(\vec{A} \cdot \vec{\nabla})\vec{B} = \left[A_r\frac{\partial B_r}{\partial r} + \frac{A_\phi}{r}\frac{\partial B_r}{\partial \phi} + A_z\frac{\partial B_r}{\partial z} - \frac{1}{r}A_\phi B_\phi\right]\hat{r}$$

$$+ \left[A_r\frac{\partial B_\phi}{\partial r} + \frac{A_\phi}{r}\frac{\partial B_\phi}{\partial \phi} + A_z\frac{\partial B_\phi}{\partial z} + \frac{1}{r}A_\phi B_r\right]\hat{\phi}$$

$$+ \left[A_r\frac{\partial B_z}{\partial r} + \frac{A_\phi}{r}\frac{\partial B_z}{\partial \phi} + A_z\frac{\partial B_z}{\partial z}\right]\hat{z}$$

Appendix E
Abbreviations

ACT	Aggressive conservative tokamak	6
ALARA	As low as reasonably achievable	12
ARIES	Advanced Research, Innovation, and Evaluation Study	13
ARIES TNS	Advanced Research, Innovation, and Evaluation Study—The Next Step	7
ASDEX	Axisymmetric divertor experiment	5
AT	Advanced tokamak	13
ATC	Adiabatic toroidal compressor	5
ATJ	Type of graphite	6
BCS	Bardeen-cooper-schrieffer	4
BES	Beam emission spectroscopy	11
BHP	Biological hazard potential	12
BiSSCO	Developmental high-temperature superconductor (BI2Sr2CaCu2O8)	4
CAD	Computer aided design	6
CANDU	Canadian deuterium uranium	6
CAT	Computed axial tomography	11
CC	Correction coils	4
CCD	Charge-coupled device	11
CECE	Combined electrolysis catalytic exchange	12
CFC	Carbon fiber composite	2, 7
CHI	Coaxial helicity injection	5
CI	Clearance index	12
CICC	Cable in conduit conductor	4
CLAM	China low activation martensitic	13
CMOS	Complementary metal oxide semiconductor	8
COE	Cost of electricity	1
COL	Construction and operation license	13
COM	Center of mass	6
CORC	(A way of producing HTSC cable)	4
CS	Central solenoid	1
CS	Compact stellarator	6
CT	Compact toroid	7
CVD	Carbon vapor deposited	8
CW	Cold worked	8
CX	Charge exchange	11
CXRS	Charge exchange recombination spectroscopy	11

(continued)

DAC	Derived air concentration	12
DAGMC	Direct accelerated geometry monte carlo	6
DBTT	Ductile to brittle transition temperature	8
DCLL	Dual cooled lithium lead	6
DD	Deuterium-deuterium	1
DEMO	Demonstration power plant	1
DIII-D	Doublet three D tokamak at General Atomics Company	8
DiMES	Divertor materials evaluation system	11
DLL	Dual-cooled lithium lead	13
DNB	Diagnostic neutral beam	5
DOE	Department of energy	12
DPSSL	Diode pumped solid state laser	14
DT	Deuterium-tritium	1
DWT	Dual-cooled waste transmutation	13
EAST	Experimental advanced superconducting tokamak	4
EBW	Electron bernstein waves	11
ECA	Electron cyclotron absorption	11
ECCD	Electron cyclotron current drive	5
ECE	Electron cyclotron emission	11
ECH	Electron cyclotron heating	5
ECR	Electron cyclotron resonance	5
ECRH	Electron cyclotron resonance heating	1
ELM	Edge localized mode	4
ESS	European spallation source	8
ET	Event tree analysis	12
ETNF	Estimated time to next failure	3
EUROFER	A european RAFM steel	6
EUV	Extreme ultraviolet	11
F82H	A Japanese RAFM steel	6
FAME	Fusion and materials evaluation	6
FCI	Flow channel inserts	13
FDS	Fusion driven subcritical	13
FFHR	Force free helical reactor	6
FFRF	Fission-fusion research facility	13
FIR	Far infrared	11
FLIBE	Molten salt ($LiF + BeF_2$)	6
FLR	Fast linear reactor	3
FNSF	Fusion nuclear science facility	8
FRC	Field reversed configurations	1
FT	Fault tree analysis	12
FTF	Fusion test facility	14
FTU	Frascati tokamak upgrade	7
FW	First wall	6
FZK	Forschungszentrum Karlsruhe	2
HCLL	Helium cooled lithium lead	6

(continued)

HCPB	Helium-cooled pebble bed	6
HEMJ	Helium-cooled multi-jet	7
HHFC	High heat flux components	6
HIBP	Heavy ion beam probe	11
HIT-SI	Helicity injected torus-steady inductive	5
HTE	High-temperature electrolysis	6
HTL	High temperature liquid LiPb blanket	13
HTO	A tritiated water molecule	2
HTSC	High-temperature superconductors	2
HX	Heat rejection heat exchanger	6
HYLIFE	High yield lithium injection fusion energy	6
IAEA	International atomic energy agency	1
IBW	Ion bernstein wave	5
ICF	Inertial confinement fusion	7
ICR	Ion cyclotron resonance	5
ICRF	Ion cyclotron range of frequencies	5
ICRH	Ion cyclotron resonance heating	5
IDC	Interest during construction	13
IEA	International energy agency	1
IEC	Inertial electrostatic confinement	1
IEEE	Institute of electrical and electronics engineers	13
IFMIF	International fusion materials irradiation facility	1
IFR	Integral fast reactor	14
IHX	Intermediate heat exchanger	6
IR	Infrared	11
ISLA	International symposia on lithium applications for fusion devises	7
ITB	Internal transport barrier	5
ITER	International thermonuclear experimental reactor (now just called "ITER", pronounced "eater")	1
JAERI	Japan atomic energy research institute	5
JET	Joint European torus	13
JUDITH	A high heat flux facility in Germany	6
KIT	Karlsruhe institute of technology	4,7
KSTAR	Korea superconducting tokamak advanced reactor	8
LANL	Los Alamos National Laboratory	3
LBL	Lawrence Berkeley Laboratory	14
LCFS	Last closed flux surface	7,11
LFS	Low field side	5
LHCD	Lower hybrid current drive	5
LHD	Large helical device	1
LHR	Lower hybrid resonance	5
LIDAR	Light detection and raging	11
LIF	Laser induced fluorescence	11
LIFE	Laser inertial fusion engine	14
LINUS	Slow liner driven by compressed gas	3

(continued)

(continued)

LLNL	Lawrence Livermore National Laboratory	1
LMFBR	Liquid metal fast breeder reactor	14
LMJ	Laser MegaJoule	1
LOCA	Loss of coolant accident	12
LOFA	Loss of flow accident	12
LOS	Line of sight	11
LOSP	Loss of off-site power	13
LTE	Local thermodynamic equilibrium	11
LWR	Light water reactor	14
MAST	Meg-ampere spherical tokamak	1
MCF	Magnetic confinement fusion	2
MCP	Microchannel plate	11
MDT	Mean down time	13
MFTF	Mirror fusion test facility	4
MHD	Magnetohydrodynamic	1,11
MLM	Multilayer mirror	11
MPR	Magnetic proton recoil	11
MSE	Motional stark effect	7
MST	Madison symmetric torus	1
MTBF	Mean time between failures	13
MTF	Magnetized target fusion	1
MTTM	Mean time to maintain	13
MTTR	Mean time to repair	13
MTTR	Mean time to restore	13
NBI	Neutral beam injection	2,7
NDT	Nil ductility temperature	8
NIF	National ignition facility	1
NIFS	National Institute for Fusion Science	11
NITE	Nano-infiltration and transient eutectic-phase	8
NPA	Neutral particle analyzer	11
NRL	Naval research laboratory	14
NSTX	National spherical torus experiment	1
NTM	Neoclassical tearing mode	5
ODS	Oxide dispersion strengthened	6
OECD	Organization for economic cooperation and development	1
OFHC	Oxygen-free high thermal conductivity	6
ORE	Occupational radiation exposure	12
PCS	Plasma control system	7
PDE	Partial differential equation	7
PF	Poloidal field	1
PFC	Plasma facing components	7
PHA	Pulse-height-analysis	11
PISCIES	A plasma-wall interaction experiment at UCSD	6
PKA	Primary knock-on atom	7
PMT	Photomultiplier tube	11

(continued)

(continued)

PPCS	Power plant conceptual study	12,13
PPPL	Princeton Plasma Physics Laboratory	8
PSOL	Scrape-off layer power flow	7
PWR	Pressurized water reactor	12
RABiTS	A technique for fabricating HTSC	4
RAF	Reduced activation ferritic	2
RAFM	Reduced activation ferritic/martensitic	6,8
RDF	Reactor demonstration facility	7
REBCO	Name of a developmental high-temperature superconductor (REBa2Cu3O7)	4
RF	Radiofrequency	7
RFP	Reversed field pinches	1
RFX	Reversed field experiment	1
RIC	Radiation induced conductivity	11
RIED	Radiation induced electrical degradation	11
RIEMF	Radiation induced electromotive force	11
RITES	Radiation induced thermo-electric sensitivity	11
RNC	Radial neutron cameras	11
RRR	Residual resistivity ratio	10
RT	Real-time	7
RTAI	Real time application interface	7
RTNS-II	Rotating target neutron source-II	8
SA	Solution annealed	8
SABR	Subcritical advanced burner reactor	14
SAR	Safety analysis report	12
SI	System internationale	9
SLIDE	Solid/liquid diverter experiment	7
SLL	Quasistatic lithium-lead	13
SMBI	Supersonic molecular beam injection	7
SMES	Superconducting magnetic energy storage	3
SNR	Satisfactory signal-to-noise ratio	11
SOFIT	Short-flow-path-foam-in-tube	7
SOL	Scrape-off layer	7
SSPX	Sustained spheromak physics experiment	1
SXR	Soft X-ray	11
TAE	Toroidal Alfven eigenmode	5
TBM	Test blanket module	13
TBR	Tritium breeding ratio	6
TEMHD	Thermoelectric magnetohydrodynamic	7
TEXTOR	Tokamak experiment for technology oriented research	11
TF	Toroidal field	1
TFMC	Toroidal field model coil	4
TFTR	Tokamak fusion test reactor	7
TIEMF	Temperature induced electro-motive force	11
TIG	Tungsten-inert-gas	9
TLC	Tighten, lube, and clean	13

(continued)

(continued)

TRU	Transuranic	14
TS	Thomson scattering	11
TVTS	Television thomson scattering	11
UHR	Upper hybrid resonance	5
UREX	Uranium recovery by extraction	14
VDE	Vertical displacement event	6
VNC	Vertical neutron cameras	11
VPH	Volume phase holographic	11
VPI	Vacuum pressure impregnation	4
VUV	Vacuum ultraviolet	11
WCLL	Water cooled lithium lead	6
XCS	X-ray crystal spectroscopy	11
XIS	X-ray imaging system	11
YAG	Yttrium aluminum garnet	11
YBCO	Developmental high-temperature superconductor (YBa2Cu3O7)	4

Appendix F
Symbols Used in Equations

Latin letters	Meaning	Units	Section
a	Plasma edge radius	m	1.2
A	Magnetic vector potential	T m	3.1
a	R/2L parameter in RLC circuits	Ohm/H	3.3
A	Mass ratio M/m	–	6.10
a	(Alpha density)/(fuel ion density)	–	7.1
A	Constant	–	8.4
A	Constant	m^3	8.5
A	Atomic weight of atom	g/mole	8.6
A	Cross sectional area of tube	m^2	9.4
A	Excitation rate constant	W m^3	11.7
A	Availability	–	13.2
a, b	Inner radius	m	3.3
a, b	Dimensions of rectangular duct	m	9.1
A, A_1	Dimensionless coefficients	–	7.1
A_1	Constant	m^4	8.5
A_1, A_2	Constants	–	3.3
a_1/a_2	Ratio of minor radii of two reactors	–	13.4
a_p	Probability of return to plasma	–	7.7
a_v	Probability of entering vacuum duct	–	7.7
a_w	Probability of hitting walls	–	7.7
A_c	Area of copper	m^2	2.2
a_c	Coil radius	m	2.2
A_ϕ	Toroidal component of vector potential	T m	5.11
A_{kj}	Radiative decay rate of level k to level j	m^3/s	11.6
A_s	Constant	m^3	11.6
A_w	Area of water channel	m^2	3.9
B	Magnetic induction (commonly called "magnetic field")	T	1.2
B	Thickness of blanket + shield	m	1.2
B	Outer radius	m	3.3
B	L/2	m	3.9
B	$(m*/2kT*)^{1/2}$	s/m	5.2
b	Burgers vector		8.4
$B_\perp$	Component of b perpendicular to flow velocity	T	6.9
B_{c2}	Upper critical magnetic induction	T	4.1

(continued)

(continued)

Latin letters	Meaning	Units	Section
B_e	B value where melting occurs	T	3.4
B_k	Component of B in direction of propagation	T	11.8
B_o	B field at plasma axis R_o	T	5.8
B_p, B_θ	Poloidal magnetic induction	T	1.3
B_r	Radial magnetic field	T	3.1
B_t, B_ϕ	Toroidal magnetic induction	T	1.4
B_y	B value where yielding occurs	T	3.4
B_z	Axial magnetic field	T	2.2
$\widetilde{B}$	Fluctuating magnetic field	T	11.7
c	Speed of light in vacuum	m/s	1.2
C	Capacitance	F	3.3
c_v	Specific heat	J/kg K	3.4
C	Constant	s	5.2
C	Conductivity ratio	–	6.9
C	Hydrogen atom concentration	m^{-3}	8.5
C	Conductance	m^3/s	9.1
c	Thickness of coil	M	1.2
C, C_p	Specific heat	J/kg K	3.9
c_s	Ion sound speed	m/s	7.2
C_c	Total capital cost	$	13.3
C_D	Direct capital cost	$	13.3
C_f	Annual fuel costs	$	13.3
C_{kj}	Collisional excitation rate of level k to energy level j	m^3/s	11.6
C_{mol}	Conductance for molecular flow	m^3/s	9.1
$C_{o\&m}$	Annual cost of operations and maintenance	$	13.3
C_T	Trapped atom concentration	m^{-3}	8.5
C_t^m	Maximum concentration in traps	m^{-3}	8.5
C_{vis}	Conductance for viscous flow	m^3/s	9.1
D	Tube diameter	m	3.9
d	Filament diameter	m	4.3
d	Average height of obstacles	m	8.4
d	Groove spacing	m	11.6
D	Roots of equation	–	3.3
D	Diffusion coefficient	m^2/s	8.5
D_∞	Particle diffusion coefficient	m^2/s	7.5
$d\ell$	Differential length	m	2.2
dm/dt	Mass flow rate	kg/s	6.9
dn	Thickness of normal conductor	m	4.3
dN/dt	molecular flow rate	s^{-1}	9.1
dN/dx	Particle deposition per meter	m^{-1}	7.4
D_o	Constant in equation for D	m^2/s	8.5
dP/dt	Rate of change of pressure	Pa/s	9.1
dP_{ff}/dE	Bremsstrahlung radiation per unit energy	W m^{-3} eV^{-1}	11.6
dp_z/dr	Impurity pressure gradient	Pa/m	11.7

(continued)

(continued)

Latin letters	Meaning	Units	Section
ds	Thickness of superconductor	m	4.3
dx/dt	Wall thickness loss rate	m/s	8.6
E	Energy	J	1.2
E	Electric field	V/m	2.1
E	Projectile energy	J or MeV	8.1
E	W/W_{th}	–	8.6
E	Ion kinetic energy	J	11.4
$\tilde{E}$	Fluctuating electric field	V/m	11.7
E(k)	Elliptical integral	–	3.1
e_a, e_w	Emissivities of armor and wall	–	6.7
E_d	Activation energy for diffusion	J or eV	8.5, 12.2
E_{ll}	E component parallel to B	V/m	5.3
E_{n0}	Incident neutron energy	eV	11.5
E_{n1}	Scattered neutron energy	eV	11.5
E_o	Reference electric field	V/m	5.7
E_o	Injected particle energy per unit mass	eV/u	7.4
E_{p1}	Scattered proton energy	eV	11.5
E_r	Radial electric field	V/m	11.7
E_s	Activation energy for solution	J or eV	12.2
f	Friction factor	–	3.9, 6.9
f	(pellet atoms)/(fuel ions)	–	7.4
f	Ratio of thermal diffusivities	–	7.9
F	Atoms fissioned per fusion event	–	14.5
f(v)	Velocity distribution function	s/m	2.9
$f(\mathbf{x}, \mathbf{v}, t)$	Velocity distribution function	m^{-3}	6.10
f_α	Fraction of alpha energy retained in plasma	–	5.2
f_a	Alpha density fraction	–	7.1
f_{av}	Availability factor	–	13.3
f_b	Burnup fraction	–	12.2
f_{amp}	(Target heat flux width)/(midplane heat flux width)	–	7.2
f_c	Cyclotron frequency	Hz	2.3
f_{ce}	Electron cyclotron frequency	Hz	5.7
f_{ci}	Ion cyclotron frequency	Hz	5.7
F_{CR}	Fixed charge ratio	–	13.3
f_{ind}	Indirect cost multiplier	–	13.3
ϕ_j	Particle flux of species j	$m^{-2} s^{-1}$	8.6
$f_j(t)$	Failure probability of item j	–	3.8
f_{LH}	Lower hybrid frequency	Hz	5.7
f_{pe}	Electron plasma frequency	Hz	5.7
f_U	Upper hybrid frequency	Hz	5.7
f_z	Impurity fraction	–	2.9
G	Parameter in gas shielding model	–	7.4
$g(\alpha, \beta)$	Parameter in Bz equation	–	3.9
h	Planck constant	J s	4.1

(continued)

(continued)

Latin letters	Meaning	Units	Section
H	Magnetic field	A/m	4.1
H	Parameter in collision equations	–	5.2
h	Convective heat transfer coefficient	$W/m^2\ K$	6.7
h	Blister skin thickness	M	8.6
h	Enthalpy	J/kg	10.1
h	Distance from plasma center to a chord	m	11.8
h	8,760	h/year	13.3
$H_\perp$	Magnetic field perpendicular to ribbon	A/m	4.3
Ha	Hartmann number	–	6.9
H_{co}	Reference magnetic field	A/m	4.1
I	Current	A or MA	1.3
$\tilde{I}$	Intensity fluctuation	W/m^3	11.7
I	Radiation intensity	W	11.6
i	Annual interest rate	–	13.3
I_1, I_2	Current	A	11.2
I_{gun}	Plasma gun current	A	1.3
I_o	Initial current stored	A	3.5
I_{sat}	Saturation current	A	11.2
I_{tor}	Toroidal current	A	1.3
J	Current density	A/m^2	1.3
$J_\perp$	J component perpendicular to B		5.3
J_b	Bootstrap current density	A/m^2	5.11
J_{dif}	Diffusion flux	$m^{-2}\ s^{-1}$	12.2
J_{ll}	J component parallel to B	A/m^2	5.3
J_{rec}	Recombination flux	$m^{-2}\ s^{-1}$	12.2
Js	Filament current density	A/m^2	4.3
k	Constant	m^{-1}	1.3
k	Wave number	m^{-1}	2.9
k	Parameter of elliptical integral	–	3.1
K	Thermal conductivity	W/m K	3.4
K	Helicity	$T^2\ m^4$	5.11
k	Constant ~ 0.8	–	8.1
K	Recombination rate parameter	m^4/s	8.5
k	Boltzmann constant	J/K	9.1
K	Function of a and b	–	9.1
K	Surface recombination coefficient	m^4/s	12.2
K(k)	Elliptical integral	–	3.1
K(z)	Magnetic field distribution parameter	–	3.4
k_1	Constant	Pa m	9.1
k_{app}	Apparent mean thermal conductivity	W/K m	10.4
K_c	Fraction of p_c absorbed in walls	W/m^3	11.6
K_{cu}	Thermal conductivity of copper	W/m K	4.3
k_{eff}	Fission multiplication factor	–	14.5
k_L	Wave number of L wave	–	11.8

(continued)

(continued)

Latin letters	Meaning	Units	Section
$k_{\parallel}$	Wave vector component along B	m^{-1}	5.11
$k_{\perp}$	Wave vector component perpendicular to B	m^{-1}	5.11
Kn	Knudsen number	–	9.1
k_R	Wave number of R wave	–	11.8
K_S	Thermal conductivity of superconductor	W/m K	4.3
K_{sh}	Constant in inductance equation		3.3
L	Length	m	2.2
L	Inductance	H	3.3
L	Coulomb logarithm	–	5.2
ℓ	Length	m	3.3
ℓ	Characteristic length	m	3.4
ℓ	Length of tube section	m	9.4
L_c	Coolant channel length	m	6.9
L_c	Average spacing between obstacles	m	8.4
L_c	Height of mercury column	m	9.4
ℓ_c	Critical length for transpositions	m	4.3
L_s	Storage inductance	H	3.5
M	Molecular mass	kg	1.2
m	Mass of cooper pair	kg	4.1
m	Neutron mass	kg	6.10
M	Thermal stress parameter	W/m	6.8, 8.2
m	Mass of one gas molecule	kg	9.1
m	Spectral order number		11.6
M	Blanket energy gain factor		14.5
$\dot{m}$	Mass flow rate	kg/s	12.2
M	Target mass	kg	6.10
M	Mass of material	kg	10.1
m*	Mass of field particle	kg	5.2
M_1	Projectile mass	kg	8.1
m_1, m_2	Incident and target masses	kg	8.5
M_2	Target mass	kg	8.1
m_b	Beam ion mass	kg	11.7
m_{Li}	Lithium ion mass	kg	7.9
M_{Li}	Total mass of lithium in plasma	kg	7.9
m_t	Mass of tritium atom	kg	12.2
n	Plasma density	m^{-3}	1.2
N	Number of coils or of turns	–	2.2
N	Degrees of freedom	–	5.4
N	Refractive index	–	5.7
N	Number of data points	–	6.10
n	Harmonic number	–	11.6
n	Number of malfunctions repaired	–	13.2
n	Economy of scale exponent	–	13.4
n, m	Toroidal and poloidal mode numbers	–	11.3

(continued)

(continued)

Latin letters	Meaning	Units	Section
n_1	Fluctuating component of density	m^{-3}	5.7
n_1, n_2	Densities of species 1 and 2	m^{-3}	1.2
n_{20}	Plasma density in units of 10^{20} m^{-3}	–	5.2
n_A, n_B, n_C	Densities of a, b, c	m^{-3}	12.3
N_{av}	Avogadro number	–	1.2
n_b	Beam density	m^{-3}	5.6
n_{bo}	Initial beam density	m^{-3}	5.6
n_s	Atomic density of pellet	m^{-3}	7.4
n_c	Cutoff density	m^{-3}	11.8
n_e	Electron density	m^{-3}	1.2
n_{edge}	Plasma edge density	m^{-3}	7.9
N_f	Number of cycles to failure	–	8.3
n_i	Ion density	m^{-3}	1.2
n_j	Density of species j	m^{-3}	6.10
$\tilde{n}_j$	Fluctuating density of species j	m^{-3}	11.7
n_n	Gas density	m^{-3}	5.6
n_o	Uniform part of density	m^{-3}	5.7
N_o	Initial number of atoms	–	12.2
N_r	Random number	–	6.10
N_r	Plasma refractive index	–	11.6
n_s	Density of superconducting electrons	m^{-3}	4.1
Nu	Nusselt number	–	6.7
n_w	Wall atom density	m^{-3}	8.6
n_z	Impurity density	m^{-3}	1.2
P	Pressure	Pa	1.2
P	Power	W	3.9
P	Momentum	kg m/s	4.1
P	Vapor pressure	Pa	8.6
P	Pressure	Pa	9.4
$P(\psi, E)$	Scattering probability	–	6.10
P_1, P_2	Pressures at points 1 and 2	Pa	9.1
P_α	Alpha power density	W/m^3	5.2
P_{av}	Average pressure	Pa	9.1
P_b	Bremsstrahlung	W/m^3	11.6
P_α	Fusion product alpha power	W	7.7
P_{cx}	Power leaving plasma by charge exchange	W	7.7
P_{ext}	External heating power	W	7.7
P_{ion}	Power expended in ionization reactions	W	7.7
P_{SOL}	Power flowing into the scrape-off layer	W	7.2
P_c	Cyclotron radiation	W/m^3	11.6
P_{ch}	Power density of charge particles	W/m^3	6.15
P_{cond}	Conductive heat flow	W	10.4
P_{cr}	Critical pressure for blister formation	Pa	8.6
P_d	Dielectronic recombination	W/m^3	11.6

(continued)

(continued)

Latin letters	Meaning	Units	Section
P_{DD}	Power density of DD reactions	W/m^3	1.2
P_{DT}	Power density of DT reactions	W/m^3	1.2
P_E	Electrical power	W	1.2
P_e	Rated electrical power	MW	13.3
P_f	Fusion power	W	1.2
P_ϕ	Toroidal momentum	kg m/s	5.11
P_f	Fusion thermal power, including blanket	W	14.1
P_{fusion}	Thermal energy from fusion reactions	W	14.5
p_i	Ion pressure	Pa	5.4
P_{int}	Interaction probability	–	6.10
P_{in}	Input power	W	8.1
P_ℓ	Legendre polynomial	–	6.10
P_L	Line radiation	W/m^3	11.6
P_L	Power flow to limiter	W	7.7
P_n	Neutron power	W	8.1
P_{net}	Net electrical power output	W	14.1
p_o	Constant	Pa	8.6
P_{oh}	Ohmic heating power density	W/m^3	2.3
P_p	Pressure at the pump	Pa	9.1
P_r	Radiative recombination	W/m^3	11.6
Pr	Prandtl number	–	6.7
P_{rad}	Radiation power loss	W/m^3	11.6
P_{rej}	Heat rejection rate	W	13.4
P_{rf}	Radiofrequency power density	W/m^3	5.11
P_{th}	Thermal power	W	14.5
P_u	Ultimate pressure	Pa	9.1
P_w	Wall power flux	W/m^2	1.2
Q	Energy gain ratio	–	1.2
q	Charge	C	2.3
q	Maximum heat flux to coolant	W/m^2	4.3
Q	Helicity flux	T^2 m^5/s	5.11
q	Tokamak safety factor	–	7.6
Q	Throughput	Pa m^3/s	9.1
q''	Heat flux	W/m^2	6.8
q'''	Internal heat deposition	W/m^3	6.8
q*	Charge of field particle	C	5.2
Q_0	Constant leak rate	Pa m^3/s	9.1
q_{95}	Safety factor at the 95 % flux surface	–	7.2
q_{div}	Divertor heat flux	W/m^2	7.1
Q_L	Leak rate	Pa m^3/s	9.1
Q_z	Radiation power parameter	W-m^3	11.6
R	Major radius of torus	m	1.2
r	Radial coordinate	m	3.1
R	Resistance	Ohm	3.1

(continued)

(continued)

Latin letters	Meaning	Units	Section
R	Position of target nucleus	m	6.10
r	Position of neutron	m	6.10
r	Blister radius	m	8.6
R	Universal gas constant = 8.314	J/mole K	10.1
r(t)	Total failure rate	–	3.8
r_1, r_2	Inner and outer radii	m	3.9
R_1, R_2	Thermal resistances	m^2 K/W	6.7
R_B	Breeding ratio	–	12.2
R_L	Limiter reflection coefficient	–	7.7
R_m	Magnetic mirror ratio along B	–	7.5
r_p	Pellet radius	m	7.4
R_t	Major radius of the outer target	m	7.2
R_v	Vacuum duct reflection coefficient	–	7.7
R_w	Wall reflection coefficient	–	7.7
R_z	Impurity reflection coefficient	–	7.1
$\mathbf{r}_c$	Center of mass position vector	m	6.10
Re	Reynolds number	–	3.9
r_j	Failure rate of item j	–	3.8
r_n	Particle reflection coefficient	–	8.5
R_o	Major radius at plasma center	m	1.2
r_q	Reaction rate q	$m^{-3} s^{-1}$	6.10
R_r	Larger of electron and ion recycling coefficients	–	7.9
R_s	Resistance of one segment	Ohm	3.9
S	Surface area	m^2	1.2
S	Gap width	m	3.3
S	Standard deviation of sample	–	6.10
S	Source of implanted H atoms	$m^{-3} s^{-1}$	8.5
S	Solubility of gas in solid	$m^{-3} Pa^{-1/2}$	12.2
S_α	Sputtering rate by alphas	–	8.6
S_i	Fuel ion source per m^3	m^{-3}	7.4
s_ϕ	Magnetic flux skin depth	m	3.4
S_i	Sputtering rate by ions	–	7.1
S_j	Sputtering yield of species j	–	8.6
S_t	Pumping speed	m^3/s	9.1
S_z	Sputtering rate by other impurities	–	7.1
S_z	Ionization rate	m^3/s	11.6
T	Temperature	K or keV	1.2
t	Tube wall thickness	m	6.8
t	Energy deposition time	S	7.2
T	Target energy after collision	J or MeV	8.1
t	Time to form a monolayer	Pa	9.6
t	Thickness	m	11.3
T	Time interval	S	13.2
T*	Temperature of field particle	K or keV	5.2

(continued)

(continued)

Latin letters	Meaning	Units	Section
$T_\parallel$	Temperature parallel to B	J or keV	5.4
$T_\perp$	Temperature perpendicular to B	J or keV	5.4
$t_{1/2}$	Half-life of radioactive decay	S	12.2
T_{10}	Temperature in units of 10 kev	–	5.11
t_2	Doubling time	S	12.2
T_a	Armor temperature	K	6.7
T_c	Critical temperature	K	4.1
T_{dam}	T minus energy given to electrons	J or MeV	8.1
T_e	Electron temperature	J or keV	1.2
T_{ek}	Electron temperature in kev	keV	5.3
T_{el}	Energy given to electrons	J or MeV	8.1
T_f	Fluid temperature	K	6.7
T_{fa}	Adiabatic wall temperature	K	6.7
T_h, T_c	Hot and cold temperatures	K	2.4
T_i	Ion temperature	J or keV	1.2
T_i	Summation of repair times	s	13.2
T_{max}	Maximum final target energy	J or MeV	8.1
T_o	Temperature parameter	K	4.3
T_w	Wall temperature	K	6.7
T_z	Impurity temperature	J or keV	1.2
T_{fluct}	Fluctuating temperature	J or keV	11.7
u_{ez}	Z component of electron velocity	m/s	5.3
V	Volume	m^3	1.2
V	Velocity	m/s	1.2
V	Neutron velocity	m/s	6.10
V	Loop voltage	V	5.11
V	Target velocity	m/s	6.10
$v_\perp$	Velocity perpendicular to B	m/s	5.11
V_1, V_2	Voltages	V	11.2
$\mathbf{v}_b$	Beam velocity	m/s	11.7
V_c	Copper volume	m^2	2.2
V_c	Coolant flow velocity	m/s	6.9
v_c	Velocity of center of mass	m/s	6.10
v_ϕ	Toroidal velocity	m/s	2.9
v_ϕ	Toroidal rotation velocity	m/s	11.7
V_{fl}	Floating potential	V	11.2
$\tilde{v}_{j\parallel}$	Fluctuating velocity of species j	m/s	11.7
V_k	Ion velocity	m/s	11.4
v_{min}	Minimum speed to pass through	m/s	11.4
V_o	Initial voltage	V	3.3
v_{ph}	Phase velocity of wave	m/s	5.7
V_{pl}	Plasma potential	V	11.2
v_θ	Poloidal velocity	m/s	2.9
v_θ	Poloidal rotation velocity	m/s	11.7

(continued)

Latin letters	Meaning	Units	Section
v_R	Electron runaway velocity	m/s	5.11
v_T	Electron thermal speed	m/s	5.11
v_{th}	Molecular thermal velocity	m/s	9.1
W	Energy	J or keV	1.2
W	Incident ion energy	J or eV	8.6
W	Heat added	J	10.1
w	Width	m	11.3
W'_{DT}	Energy per DT reaction, including blanket energy gain	J or MeV	12.2
$W_\parallel$	Energy component parallel to B	J or keV	5.4
$W_\perp$	Energy component perpendicular to B	J or keV	5.4
W_1	Incident particle energy	J or MeV	8.5
W_B	Surface binding energy	J or eV	8.6
W_f	Final kinetic energy	J	11.7
W_i	Ion kinetic energy	J	5.4
W_o	Initial kinetic energy	J	11.7
W_{th}	Threshold energy	J or eV	8.6
X	$(m_* W/m T_*)^{1/2}$	–	5.2
X	$(\omega_{pe}/\omega)^2$	–	11.8
X	Parameter in decay equation	–	12.2
$\bar{x}$	Mean value of data	–	6.10
Y	Function of a and b	–	9.1
Y	ω_{ce}/ω	–	11.8
Y	Construction lead time	year	13.3
Y_j	Displacement in Y direction	m	11.4
z	Axial coordinate	m	3.1
Z	Impedance	s/m^3	9.1
$Z^{(z-1)*}$	Excited atom in charge state $(z-1)$	–	11.7
Z_1, Z_2	Incident and target charge numbers	–	8.5
Z_{eff}	Effective charge of plasma ions	–	5.3
Z_{jk}	Displacement in Z direction	m	11.4

Greek symbols

Symbols	Meaning	Units	Section
α	Absorption coefficient	m^{-1}	11.6
α	Angle between $\mathbf{v}_b$ and B_ϕ	rad	11.7
α	Parameter in pressure equation	s^{-1}	9.1
α	Parameter in transmutation equations	s^{-1}	12.3
α	Recombination rate	m^3/s	11.6
α	Sticking coefficient	–	8.6
α	Thermal expansion coefficient	K^{-1}	6.8, 7.6
α, β	Angles of incidence and diffraction	radian	11.6
α, β	Parameters in B_z equation	–	3.9
α, β, γ	Direction cosines of velocity vector	–	6.1

(continued)

(continued)

Greek symbols

Symbols	Meaning	Units	Section
α', β', γ'	Direction cosines after scattering	–	6.1
α_s	Stekly number	–	4.3
β	Parameter in maxwellian distribution	s^2/m^2	11.6
β	Ratio of plasma pressure to magnetic field pressure	–	1.2
Γ	Particle flux	$m^{-2}\,s^{-1}$	7.5
Γ_{beam}	Fuel influx from NBI or pellets	s^{-1}	7.9
Γ_{gas}	Gas influx	s^{-1}	7.9
Γ_z	Influx of particles with ionization state Z	$m^{-2}\,s^{-1}$	11.6
γ	Mass ratio	–	8.6
γ	(N + 2)/N	–	5.4
γ	Ratio of specific heats	–	6.7
γ	Relativistic factor	–	2.3
γ_m	Magnetic field pitch angle	rad	11.7
Δ	Energy gap	J or eV	4.1
Δ	Thickness of blanket + shield + coils	M	13.4
ΔE	Energy deposited on wall	J/m^2	7.2
ΔH	Heat of sublimation	J or eV	8.6
ΔM	Change of mass	kg	1.2
ΔT	Temperature difference	K or keV	3.9
Δp	Pressure drop	Pa	3.9
Δr	Difference of radii	–	3.2
Δr	Thickness of reflecting layer	m	11.8
$\Delta\varepsilon$	Cyclic strain	–	8.3
$\Delta\lambda_B$	Wavelength shift from Zeeman effect	m	11.7
$\Delta\lambda_e$	1/e width of broadened line	m	11.8
$\Delta\phi$	Change of phase angle	rad	11.8
$\Delta\phi_L$	Phase change of L wave	rad	11.8
$\Delta\phi_R$	Phase change of R wave	rad	11.8
$\Delta\omega$	Bandwidth of radiation	rad/s	11.6
δ	Skin depth	m	3.4
δ	Width characterizing outflow rate	m	7.9
$\delta\lambda$	Wavelength full width at half maximum intensity	m	11.6
$\delta\lambda_z$	Wavelength full width at half maximum intensity, Zeeman effect	m	11.6
ε	Error	–	6.1
ε	Kinetic energy	J	5.11
ε	Linhard reduced energy	–	8.5
ε	Nuclear excitation energy	J	6.1
ε	(Number of fusion neutrons)/(number of fission neutrons)	–	14.5
ε	Recirculating power fraction	–	13.4
ε_f	Fatigue strain parameter	–	8.3
ε_g	Grid transparency	–	11.4

(continued)

(continued)

Greek symbols			
Symbols	Meaning	Units	Section
ε_o	Permittivity of free space	F/m	2.2
$d\varepsilon/dt$	Strain rate	s^{-1}	8.4
ξ	Coherence length	m	4.1
η	Resistivity	Ohm m	2.2
η_{air}	Viscosity of air	Pa s	9.1
η_c	Carnot efficiency	–	2.4
η_d	Driver efficiency	–	14.1
η_e	Energy conversion efficiency	–	1.2
η_e	Thermal to electrical conversion efficiency	–	13.4
η_g	Generator efficiency	–	6.15
η_{he}	Heat engine efficiency	–	6.15
η_p	Pump efficiency	–	3.9
η_t	Thermal efficiency	–	6.15
η_x	Recuperator efficiency	–	6.15
$\eta_{\parallel}$	Resistivity parallel to B	Ohm m	5.3
$\eta_{\perp}$	Resistivity perpendicular to B	Ohm m	5.3
θ	Angle between k and B	rad	11.8
θ	Polar scattering angle	radian	6.1
θ	Scattering angle	radian	8.1
θ	Poloidal angle	rad	1.1
θ	Scattering angle	radian	8.1
θ	Dimensionless time	–	7.1
θ_D	Debye temperature	K	10.1
θ_{lim}	Maximum Rutherford scattering angle	rad	11.7
θ_p	Faraday rotation angle from plasma	rad	11.8
$\ln\Lambda$	Coulomb logarithm	-	5.11
λ	Component failure rate	s^{-1}	13.2
λ	(Copper volume)/(coil volume)	–	3.9
λ	DeBroglie wavelength	m	4.1
λ	Incident mean ion range	m	8.5
λ	Lattice parameter	m	8.5
λ	Mean free path	m	6.1, 9.1
λ	Radioactive decay constant	s^{-1}	12.2
λ	Thermal conductivity	W/m K	7.6
λ	Wavelength	m	5.7
λ_D	Debye length	m	11.8
λ_L	London penetration depth	m	4.1
λ_a	Attenuation length of beam	m	5.6
λ_{av}	Attenuation length at average n and T		5.6
λ_q	Power flux scale width	m	7.2
λ_o	Unshifted wavelength	m	11.7
λ_o	Wavelength from atom at rest	m	11.6

(continued)

Greek symbols			
Symbols	Meaning	Units	Section
λ^2	Sign determines density profile curvature	m^2	7.5
λ_φ	Failure rate parameter	–	3.8
μ	Bohr magneton	J/T	11.7
μ	Cosine of scattering angle	–	6.1
μ	Shear modulus	Pa	8.4
μ	True mean value	–	6.1
μ	Viscosity	Pa s	3.9
μ_o	Permeability of free space	H/m	1.2
ν	Kinematic viscosity	m^2/s	6.4
ν	Lattice vibration frequency	s^{-1}	8.5
ν	Neutrons released per fission	–	14.5
ν	Poisson ratio	–	6.8
ν_{eff}	Effective collision frequency	s^{-1}	5.3
ν_{ei}	Electron ion collision frequency	s^{-1}	5.3
ρ	Mass density	kg/m^3	1.2
ρ	Radial vector	m	3.1
ρ_i	Ion Larmor radius	m	11.7
ρ_m	Mass density	kg/m^3	3.9
Σ_{el}	Elastic scattering cross section	m^{-1}	6.1
Σ_{in}	Inelastic cross section	m^{-1}	6.1
Σ_ℓ	Legendre expansion coefficient	m^{-1}	6.1
Σ_t	Total macroscopic cross section	m^{-1}	6.1
Σ_γ	Radiative capture cross section	m^{-1}	6.1
Σ_{2n}	(n, 2n) cross section	m^{-1}	6.1
σ	Approximate total stress	Pa	6.8
σ	Cross section	m^2	1.2
σ	Stephan-Boltzmann constant	$W/m^2\ K^4$	6.7
σ	Stress	N/m^2	3.2
σ_j	Total cross section of species j	m^2	6.1
$\sigma(\psi, E)$	Scattering cross section	m^2	6.1
$\sigma_A,\ \sigma_B$	Cross sections for species A and B	m^2	12.3
σ_d	Desorption cross section	m^2	8.5
σ_h	Hoop stress	Pa	6.8
σ_{qj}	Cross section of species j for reaction q	m^2	6.1
σ_r	Recombination coefficient	m^2	7.5
σ_w	Tube wall conductivity	A/V m	6.9
$\sigma_{\bar{x}}$	Standard deviation of the mean	–	6.1
σ_y	Yield strength	Pa	6.8
σ_z	Axial stress	Pa	8.2
σ_θ	Azimuthal stress	Pa	8.2
σ_{o1}	Cross section for reionization of neutrals		5.6
σ_{1o}	Cross section for neutralization by charge exchange		5.6

(continued)

(continued)

Greek symbols			
Symbols	Meaning	Units	Section
$\langle \sigma v \rangle$	Reaction rate parameter	m^3/s	1.2
$\langle \sigma v \rangle_{DT}$	DT reaction rate parameter	m^3/s	5.2
τ	Characteristic time	s	3.4
τ	Confinement time	s	1.2
τ	Integration time	s	11.6
τ	Time constant for pressure change	s	9.1
τ_I	Temperature rise time	s	7.2
τ_i	Fuel ion confinement time	–	7.1
τ_i	Ion collision time	s	7.5
τ_i	Ion confinement time	s	7.9
τ_z	Impurity confinement time	–	7.1
τ_α	Alpha confinement time	–	7.1
τ_α	Alpha slowing down time	s	5.2
τ_{ll}	Ion parallel flow loss time	s	7.2
Φ_T	Toroidal magnetic flux	Wb	5.11
Φ_{el}	Electric potential	V	5.11
ϕ	Azimuthal scattering angle	radian	6.1
ϕ	Electrostatic potential	V	1.3
ϕ	Magnetic flux	Wb	4.1
ϕ	Neutron flux	m^{-2} s^{-1}	6.1
ϕ	Toroidal angle	Rad	1.1
ϕ_b	Bias grid potential	V	11.4
ϕ_c	Collector potential	V	11.4
ϕ_j	Particle flux of species j	m^{-2} s^{-1}	8.6
ϕ_n	Surface evaporation flux	m^{-2} s^{-1}	8.6
ϕ_o	Accelerating potential	V	11.7
ϕ_o	Fluxon	Wb	4.1
χ_e	Electron thermal diffusivity	m^2/s	7.9
χ_i	Ion thermal diffusivity	m^2/s	7.9
ψ	Scattering angle in COM system	radian	6.1
ψ_R	Radiation power parameter	–	6.15
Ω	Angle between the viewing sightline and B_ϕ	rad	11.7
$d\Omega'$	Differential solid angle	Sterad	6.1
ω	Angular frequency	rad/s	3.3
ω_c	Cyclotron frequency	rad/s	2.3
ω_{ce}	Electron cyclotron frequency	rad/s	5.7
ω_L	Lower hybrid frequency		5.7
ω_{pe}	Electron plasma frequency	rad/s	5.7
ω_{pi}	Ion plasma frequency	rad/s	5.7
ω_u	Upper hybrid frequency	rad/s	5.7

Appendix G
Answers to Problems

Kyung-Jin Kim

Chapter 1

1.1 Mass change $= \Delta M = (M_D + M_T - M_{He} - M_n)$
$$= (2.013553 + 3.015501 - 4.001503 - 1.008665 \text{ amu})$$
$$(1.660566 \times 10^{-27} \text{ kg/amu})$$

$$\text{Energy} = \Delta M \, c^2 = (3.13631 \times 10^{-27} \text{ kg})(2.99792 \times 10^8 \text{ m/s})^2$$
$$= 2.8188 \times 10^{-12} \text{ J}$$
$$= 17.593 \text{ MeV}$$

1.2

$$\text{Units } T^2/(\text{Henry/m}) = (V - s/m^2)^2/(V - s/A - m) = V - A - s/m^3 = J/m^3$$
$$= Pa$$

1.3

$$P_{dt} = 1/4 \, n^2 \, \langle \sigma v \rangle \, W_{DT} = 0.25 \, (4E40 \, \text{m}^{-3})(4.24E{-}22 \, \text{m}^3/\text{s}) \, (2.82E{-}12 \, \text{J})$$
$$= 12.0 \, \text{MW/m}^3$$

$$P_{cat} = 1/2 \, n^2 \, \langle \sigma v \rangle \, W_{cat} = 0.5 \, (4E40 \, \text{m}^{-3}) \, (5.16E{-}24 \text{m}^3/\text{s}) \, (3.46E{-}12 \, \text{J})$$
$$= 0.357 \, \text{MW/m}^3$$

Conclusion: DT has 34 times greater power density in this case. (Neither was at its optimum temperature).

1.4 $p = 2nT = 2\left(2.E20\,m^{-3}\right)(20\,keV)\,1.6022E-16\,J/keV = 1.28\,MPa$
$= 12.6\,atm$

$p = \beta B^2/2\mu_o \rightarrow B = (2\mu_o p/\beta)^{1/2} = (8\pi E-7 \times 1.28E6/0.06)^{1/2}$
$= 7.32T.$

1.5

Core volume $V = 2\pi R\pi a^2 = 2\pi^2 5\,m\,(2\,m)^2 = 395\,m^3$
Thermal power $= P_e/\eta_e = 1,000\,MWe/0.40 = 2,500\,MWth$

$$P_{core} = P_{th}/1.2 = 2,083\,MWth$$

$$P_{DT} = P_{core}/V = 5.27\,MW/m^3$$

$n = (4P_{DT}/\langle\sigma v\rangle\,W_{DT})^{1/2} = (4 \times 5.27E6/(2.65E-22 \times 2.82E-12))^{1/2}$
$= 1.67E20\,m^{-3}$

$p = 2nT = 2\,(1.67E20)\,15\,(1.602E-16) = 8.02E5\,Pa = 0.802\,MPa$

1.6 $$P_{DD} = (1/2)\,n^2\,\langle\sigma v\rangle\,W_{DD}$$

$$n = p/2T$$

$$P_{DD} = (1/2)(p/2T)^2\,\langle\sigma v\rangle\,W_{DD}$$

There is a broad maximum with the peak at about 17 keV.

T	$\langle\sigma v\rangle$	$\langle\sigma v\rangle/T^2$
1	1.52E−28	1.52E−28
1.5	1.38E−27	6.13E−28
2	5.42E−27	1.36E−27
3	2.95E−26	3.28E−27
4	8.47E−26	5.29E−27
5	1.77E−25	7.08E−27
6	3.09E−25	8.58E−27
8	6.90E−25	1.08E−26
10	1.21E−24	1.21E−26
15	2.97E−24	1.32E−26
20	5.16E−24	1.29E−26
25	7.60E−24	1.22E−26
30	1.02E−23	1.13E−26
40	1.55E−23	9.69E−27
50	2.08E−23	8.32E−27
60	2.60E−23	7.22E−27
80	3.60E−23	5.63E−27
100	4.55E−23	4.55E−27
150	6.75E−23	3.00E−27

1.7. $P_{cat} = 2 \times 10^{-7} p^2$ Eq. (1.12)
$p^2 = P_{cat}/2 \times 10^{-7} = (\beta B^2/2\mu_o)^2$
$B^4 = (P_{cat}/2 \times 10^{-7})(2\mu_o/\beta)^2 = 1.26 \times 10^4 \, T^4$
$\underline{B = 10.6 \, T.}$

Chapter 2

2.1 $E = 0.38 \, V/m$, $J = 9.5 \, MA/m^2$, $I = 2.7 \, MA$.
2.2 Eq. (2.8) $I = 2\pi RB/N\mu_o = 2\pi 1.5 * 2.2/16 * 4\pi 10^{-7} = 1.03 \times 10^6 \, A$

$$A_c = I/J = 1.03 \times 10^6/9 \times 10^6 = 0.114 \, m^2$$

$$V_c = 2\pi a_c A_c = 2\pi 0.7 * 0.114 = 0.501 \, m^3$$

$$P_c = \eta J^2 V_c = 2 \times 10^{-8} (9 \times 10^6)^2 0.501 = 8.12 \times 10^5 \, W \, per \, coil$$

Total for 16 coils is 13.0 MW.

2.3 $f_c = qB/2\pi m = 1.60 \times 10^{-19} 5/2\pi 3.34 \times 10^{-27} = 38.1 \, MHz$
2.4 $T_c = 30 + 273 = 303 \, K$

$$\eta = 0.6\eta_c \quad \eta_c = \eta/0.6 = 0.39/0.6 = 0.65$$

$$T_h \eta_c = T_h - T_c$$

$$T_h(1 - \eta_c) = T_c$$

$$T_h = T_c/(1 - \eta_c) = 303/0.35 = 866 \, K = 593 \, ^\circ C$$

Chapter 3

Pulsed magnets
3.1

(a) $R_{tot} = 1 \, m\Omega$, $L_{tot} = 16.6 \, nH$
(b) $I = 5.86E5 \, A$, $W = 721 \, J$, $W/W_o = 0.24$
(c) If current density were uniform, $B = 3.6 \, T$. For a long solenoid $B = 3.6 \, T$
(d) $D = 0.15 \, mm$, $B = \mu_o I/h = 2.1 \, T$

(e) P = 1.7 MPa, F = 2.84E5 N

(f) 42 cables

3.2 (Equations to be verified by the student).

3.3 $B = 0.7 t (10/0.6)^2 = 194$ T; $\tau \sim \sigma_o \mu_o l^2 = 50 \, \mu s$

$$p = B^2/2\mu_o = 194^2/8\pi10^{-7} = 1.5E10 \, Pa$$

Power density $= 8.1E-6p^2 = 1.8E15$ W/m^3.

3.4   ETNF $= 73$ shots

3.5 $I_{max} = 9.96E5$ A, $B_{max} = 6.1$ T

Water-cooled magnets

3.6 Eq. (3.66)

$P = r_1(900B)^2 = 0.05 (900 * 6)^2 = 1.46$ MW.

3.7 Eq. (3.29)

$s = (B^2/2\mu_o) (r_1/\Delta r + 1/3) = (16/8\pi10^{-7}) (1/0.2 + 0.333)$

$= 3.40 \times 10^7$ Pa

3.8 $g = 0.134$, $B = 1.07$ T

3.9 Maximize g in Table 3.3

$\beta = L/2r_1 = 2 \rightarrow L = 0.4$ m

$\alpha = r_2/r_1 = 3 \rightarrow r_2 = 0.3$ m

One pancake coil $N_{turns} = 2(r_2 - r_1)/a$

L_c = Length of conductor $= N_{turns}2\pi(r_2 + r_1)/2 = 2\pi(r_2^2 - r_1^2)/a$

$= 0.5027/a$

Try a = 0.0163, D = 0.0102 $\rightarrow L_c = 30.8$ m $\rightarrow I_{max} = 5{,}000$ A is OK

One-Coil resistance

$R_1 = hL_c/(a^2 - \pi D^2/4) = 2E-8 * 30.8/(0.0163^2$

$- 0.25 \pi 0.0102^2) = 0.003348$ Ohm

$N_{coils} = L/2a = 0.4/(2 * 0.0163) = 12.3$ coils. Use 13 coils.

$$R_{tot} = N_{coils}R_1 = 0.04352 \, Ohm$$

At I = 1,000 A, V = 44 V. Good impedance match to power supply.

$$P = IV = 44 \, kW.$$

$$\lambda = A_{cu}/A = (0.0163^2 - 0.25\pi\,0.0102^2)/0.0163^2 = 0.6925 = J/J_c$$

$$B_z = \lambda^{3/2}\mu_o g(\alpha, \beta)\,(P/\eta r_1)^{1/2}$$
$$= 0.6925^{3/2}\,4\pi10^{-7}\,0.142\,(44,000/(2E{-}8*0.1))^{1/2} = 0.48\,T.$$

3.10 $P_{seg} = 43.5/13 = 3.35\,kW$

$$dV/dt = P_{seg}/(C\rho_m\Delta T) = 3,350/(4182 \times 998 \times 60)$$
$$= 1.35E{-}5\,m^3/s \text{ per channel}$$

$$A = \pi D^2/4 = 8.17E{-}5\,m^2$$

$$v = (dV/dt)/A = 0.165\,m/s$$

$$Re = Dv\rho_m/\mu = (0.0102 \times 0.165 \times 998)/0.001002 = 1,676 \quad \text{laminar flow}$$

$$f = 64/Re = 0.0382$$

$$\Delta p = fL_c\rho_m v^2/2D = 0.0382 \times 30.8 \times 998 \times 0.165^2/(2 \times 0.00102)$$
$$= 1,567\,Pa$$

$$P_c = \Delta p\,(dV/dt)/\eta_p = 1,567 \times 1.35E{-}5/0.8 = 0.0264\,W \text{ per channel}$$

Total P = 0.34 W.

(Pumping power would be higher for small diameter tubes and long flow paths).

3.11 At r = 0.05 m, z = 0, $B_r = 0.052\,T$, $B_z = 0$

3.12 At r = 0, z = −0.05 m, $B_r = 0$, $B_z = 0.241\,T$

3.13 $B_z = 0.212\,T$
3.14 $B_r = 0.015\,T$, F = 82 N.

3.15

(a) 2 × 25 turns per pancake; L = 95 m
(b) $I_{max} = 870$ A, R = 0.0186 Ω; P = 14.0 kW per pancake;
(c) V = 1.46 m/s; $P_c = 30$ W;
(d) 23 pancakes;
(e) P = 0.32 MW; $B_z = 1.02$ T

3.16

v = 1.53 m/s; f = 0.033; P = 6540 W; R = 0.017 Ω; $I = (P/R)^{1/2} = 614$ A
From Fig. 3.37 I = 640 A.

3.17 $R = 2\pi r\eta/wt$; $P = (2\pi r\eta/wt)I^2$ per turn

$$v = I^2\eta/wtC\rho_m\Delta Td(1 - \pi/40).$$

Chapter 4

4.1 B $= 0.0052\,$T

4.2 $\xi = 6.5\,$nm

4.3 n $< (4qa^3/I^2\eta) = 21$

4.4 $\ell_c > 0.04\,$m, $T_o \approx 4$, $J_s \approx 2.5$E9,   dB/dt $\leq 0.066\,$T/s

4.5 $f(\alpha, \beta) = \beta \ln\{[\alpha + (\alpha^2 + \beta^2)^{1/2}]/[1 + (1 + \beta^2)^{1/2}]\}$

$$v(\ ) = 2\beta\pi(\alpha^2 - 1)$$

$$v(g, \beta) = 2\pi\beta\left\{[(g^2 - \beta^2)/2g]^2 - 1\right\}$$

$$g \equiv e^{f/\beta}[1 + (1 + \beta^2)^{1/2}]$$

$$V_{min} = 6.5\,\text{m}^3 \text{at } \beta = 0.8$$

$$IL_t = 1.3\text{E8 A m}$$

$$L = 1.6\,\text{m}, \quad r_2 = 1.52\,\text{m}$$

4.6 t $= 546\,$s $= 9.1\,$min

4.7 $\alpha_s = 45$

4.8 R $= 7.7$E-10Ω

Chapter 5

5.1 (a) P $= 0.45\,$MW/m^3 (b) P $= 0.014\,$MW/m^3

5.2 (a) $T_\parallel = 1\,$keV, $T_\perp = 3\,$keV

(b) $T_\parallel = T_\perp = 2.08\,$keV

5.3 $T_1/T_o = (B/B_o)^{4/5} \rightarrow T = 2.41\,$keV

5.4 $T_1/T_o = 1.35$

5.5 1.1 %

$W_o > 400\,$keV

5.6 $\eta_{D+} = 3\,\%$ Fig. 5.14

$\eta_{D-} = 60\,\%$

5.7 p $= 63\,$Pa

5.8 Beam divergence angle $= 0.9°$

1 MHz: couple to v_{ci} at B $\sim 0.13\,$T

5.9 100 MHz: couple to v_{LH} at B $\sim 0.24\,$T

10 GHz: couple to v_{ce} at B $\sim 0.36\,$T

5.10 The current drive required from each source is 0.5 $(1-0.64)$ $15\,\text{MA} = 2.7\,\text{MA}$

The input power is $2.7/(0.1 + 0.05) = 18\,\text{MW}$
Then $Q < 400/18 = 22$.

Chapter 6

6.1 $(1 - \eta)P\text{th} = 2.24\,\text{GWth}$
6.2 $q/A = 0.563\,\text{MW/m}^2$, $T_a = 2{,}000\,\text{K}$
6.3 $Nu = 63.9$, $T_s = 1{,}400\,\text{K}$
6.4 $(q/A)_{\text{max}} = 4.67\,\text{MW/m}^2$
    $\sigma_{\text{th}} = 97\,\text{MPa}$, $\sigma_h = 60\,\text{MPa}$
6.5 $P/q = f\rho_m v_c^3/8\eta_p(q/A) = 8.3\text{E}{-}5$
6.6 $v_c = 0.962\,\text{m/s}$, $C = 0.028$, $P = 148\,\text{kW}$.
6.7 (b) $P_4(\mu) = (1/8)\,(35\mu^4 - 30\,\mu_2 + 3)$
6.8 $a_\ell = [(2\ell + 1)/2] \int\limits_{-1}^{1} d\mu F(\mu)\, P\ell(\mu)$
6.9
    $\sigma_o(x, E' \rightarrow E) = S(x, E' \rightarrow E)(1 + b/3)$
    $\sigma_1(x, E' \rightarrow E) = S(x, E' \rightarrow E)(a)$
    $\sigma_2(x, E' \rightarrow E) = S(x, E' \rightarrow E)(2b/3)$
6.10
  $\lambda = 2.169$ cm
  $\ell_1 = 1.44$ cm
  $\alpha_o = 0$
  $\beta_o = 0.5$
  $\gamma_o = 0.866$
  $x_1 = x_o + \alpha_o\ell_1 = 0$
  $y_1 = y_o + \beta_o\ell_1 = 0.72$ cm
  $z_1 = z_o + \gamma_o\ell_1 = 1.247$ cm
  elastic scattering
  $\psi = 58.20°$
  $E' = 0.9705$ MeV
  $\theta = 56.6°$
  $\phi = 161.35°$
  $\alpha' = -0.267$, $\beta' = -0.4097$
  $\gamma' = 0.8722$
  $\ell_2 = 2.347$ cm
  $x_2 = x_1 + \alpha'\,\ell_2 = -0.627$ cm
  $y_2 = y_1 + \beta'\,\ell_2 = 0.241$ cm
  $z_2 = z_1 + \gamma'\,\ell_2 = 1.438$ cm
  both collisions are within the slab.

6.11 $N = 10^8$ histories.

6.12

$N = 10$, $\overline{X} = 198.7\,\text{g}$, $s = 14.7$

It is 90 % probable that $0.77 < s/\sigma < 1.65$, from which

$8.9 < \sigma < 19.1$

If we conservatively assume $\sigma = 19.1$, then

$$\sigma_{\overline{X}} = s/N^{1/2} = 6.0,$$

and it would be

61 % probable that $\mu = 198.7 \pm 6.0$

86 % probable that $\mu = 198.7 \pm 12.0$

90 % probable that $\mu = 198.7 \pm 18.0\ (\pm 3\ \sigma_{\overline{X}})$

If $N = 30$ and $s = 8.2$, then

It is 90 % probable that $0.84 < s/\sigma < 1.30$, from which

$6.3 < \sigma < 9.76$.

If we conservatively assume $s = 9.8$, then

$$\sigma_{\overline{X}} = s/N^{1/2} = 1.8$$

and it would be

61 % probable that $\mu = 196 \pm 1.8$

86 % probable that $\mu = 196 \pm 3.6$

90 % probable that $\mu = 196 \pm 5.4$

6.13 $N = 2.77 \times 10^4$ histories.

Chapter 7

7.1 $n_{Al}/n_i = 0.028$

$P_f/P_{fo} = 0.53$

Ignition prevented.

7.2 $A = 1.7E{-}3$

$F_a(\theta = 0.6) = 7.89E{-}4$

$F_\infty = 1.75E{-}3$

7.3 $c = 4.6 \times 10^{-5}$ m/s, $\langle \sigma v \rangle = 2.3 \times 10^{-14}$ m^{-3}/s $\lambda = 0.12$ m.

7.4 $Q = 2.01E5\ \text{Pa} - \text{m}^3/\text{s}$

$S_t = 1.E6\ \text{m}^3/\text{s}$

$A = 7{,}390\ \text{m}^2$

7.5 $u = -1.03E4$ m/s

$b_o = -48.3$ m^{-1}

$n_z(0)/n_{zw} = 0.050$

7.6 $a_p = 3/7$, $a_v + a_w = 4/7$, $R_\alpha = 0.801$, $f_\alpha = 0.106$
7.7 $Q = 4.4$
7.8 $G = 8.92E8$, $\ell/a = 0.58$, $\ell = 0.75$ m, $r_p = 3.7$ m

Chapter 8

8.1 $dx/dt = 0.98$ mm/year
8.2 $dn_{imp}/dt = 1.78E18$ atoms/m^2 s, $\Delta t = 0.112$ s
8.3 $p = 1.5 \times 10^{-5}$ Pa, $dx/dt = 0.08$ mm/year
8.4 $T_{max} = 1937$ K, $p_{max} = 0.1$ Pa
$\Delta n/S = 8.28 \times 10^{15}$ atoms/m^2 $\Delta x = 1.2 \times 10^{-13}$ m
8.5 92 MPa or 13,000 psi
8.6 41.8 dpa, 722 appm (He), 4,560 appm (Mn)
$\Delta V/V = 1.72$ %, $\Delta\ell/\ell = 0.57$ %
8.7 ~ 15 dpa
Parallel $\Delta\ell/\ell = -0.2$ %
Perpendicular $\Delta\ell/\ell = -2.4$ %
8.8 unattenuated fluence $= 4.4E27$ neutrons/m^2
Attenuation $\leq 7E{-}6$ needed
Damage to stabilizer may require more attenuation ($\sim 1.E{-}7$).

Chapter 9

9.1 $7.96E4$ N, $1.79E4$ lb$_f$, 8.94 t
9.2 $C_{eff} = 1.15E{-}3$ m^3/s, $t_2 = 2.28$ h
9.3

(a) $Q = 0.0589$ Pa m^3/s

(b) $v = 468$ m/s

(c) $dN/dt = 1.42E19$ air molecules/s

(d) viscous

(e) $C = 8.53$ m^3/s, $(p_2p_1) = 0.00691$ Pa
9.4 $5.08E{-}5$ Pa

9.5   (a) molecular flow

(b) $Q = 1.01\text{E}{-}3 \text{ Pa}{-}\text{m}^3/\text{s}$

(c) $dN/dt = 2.49\text{E}17 \text{ molecules/s}$

(d) $S_t = 0.505 \text{ m}^3/\text{s}$

9.6   (a) $Q = 7.92\text{E}{-}7 \text{ Pa m}^3/\text{s},\quad p = 5.29\text{E}{-}3 \text{ Pa}$

(b) $Q = 7.92\text{E}{-}7 \text{ Pa m}^3/\text{s},\quad p = 2.12\text{E}{-}4 \text{ Pa}$

(c) $Q = 7.92\text{E}{-}7 \text{ Pa m}^3/\text{s},\quad p = 1.61\text{E}{-}5 \text{ Pa}$

(d) $Q = 7.92\text{E}{-}7 \text{ Pa m}^3/\text{s},\quad p = 1.23\text{E}{-}5 \text{ Pa}$

9.7 $p(\infty) = p_u + p_L, \ p_L \equiv Q_o/\alpha V$
$\alpha V = S_1 C_1/(S_1 + C_1) + S_2 C_2/(S_2 P C_2)$

9.8 (a) $p(\infty) = 2.39\text{E}{-}4 \text{ Pa}$

(b) $p(\infty) = 1.10\text{E}{-}3 \text{ Pa}$

9.9 $Q_o = 1.33\text{E}{-}9 \text{ Pa m}^3/\text{s}$

9.10 $Q_{avg} = 8.68\text{E}{-}4 \text{ Pa m}^3/\text{s}$

9.11 Stainless steel chamber is safe for the vacuum chamber $t_{min}(\text{Al}) = 3.8 \text{ mm}$

9.12 $t = 32.0 \text{ h}$

9.13 No. True $p = 0.59 \text{ Torr}$, so the gage is a factor of 0.29 low
In argon a calibrated Pirani gage would read 0.38 Torr
but the given Pirani gage would read $0.29 (0.38) = 0.11 \text{ Torr}$.

Chapter 10

10.1   (a) $m = 578 \text{ kg per coil}$

(b) 25 W/coil

(c) 1.9 W/coil

(d) 3.9 W/coil, $A = 1.32 \text{ m}^2/\text{coil}$

10.2 From 300 K to 80 K, $W = 7.36\text{E}4 \text{ J}$ removed, to 0.46 L of liquid N_2
From 80 K to 4.2 K, $W = 6{,}000 \text{ J}$ removed, 2.21 L of liquid He
For 578 kg $\times$ 2 coils, this requires 532 L of LN_2 and 2,540 L of LHe

10.3 At input $= 1 \text{ kW}$, boil off $= 1{,}320 \text{ L/h}$. For Problem 10−1, boil off $= 81 \text{ L/h}$.

Chapter 11

11.1 Eq. (11.1) $T_e = 0.91$ eV Eq. (11.3) $n_i = 5.7E16$ m^{-3}

11.2 Eq. (11.8) $\partial B_n/\partial t = \phi/NA_c = 2$ V/$100\pi(0.0015)^2 = 2{,}800$ T/s

11.3 $J_z = (1/\mu_o)\partial Bp/\partial r = (B_{po}/\mu_o)(\partial/\partial r)(r/(a + r)) = B_{po}\, a/\mu_o(a + r)^2$

11.4 $B^2/2\mu_o + p = $ constant $\rightarrow dp/dt + (B/\mu_o)dB/dt = 0$

dB/dt = $(\mu_o/p)dp/dt = (4\pi E{-}7/3)$ (1.E4/0.005) = 0.84 T/s

$\phi = NA_c$ dB/dt = $100\pi 0.6^2$ 0.838 = 9.5 V

11.5 $N = (1/2)n^2 \langle\sigma v\rangle_{ddn}$ Vt

$\langle\sigma v\rangle_{ddn} = 2N/n^2 Vt = 2 \cdot E9/1 \cdot E42\ 0.01\ 2 \cdot E{-}6 = 1 \cdot E{-}25$ m^3/s$\rightarrow$

$\langle\sigma v\rangle_{dd} = 2.E25$ m^3/s

Interpolating in tablular data we find T = 5.2 keV.

11.6 $W_{++} = e(\phi_o + \phi)\rightarrow \phi = W_{++}/e{-}\phi_o = 9.3 - 10 = {-}0.7$ eV.

11.7 Eq. (11.41) $\rightarrow KT_i = 1.416E{-}17$ J $\rightarrow$ Ti = 88.4 eV

11.8 Eq. (11.42) $n = (\delta\lambda/A_s)^{3/2} = (2.E{-}9/2.0E{-}24)^{3/2} = 3.2E22$ m^{-3}

11.9 dP/dW = (P_b/T_e) exp $({-}W/T_e)$ Use two data points and divide equations:

$(dP/dW)_A/(dP/dW)_B = $ exp$((W_B/W_A)/T_e) = 100$

Solve for $T_e = 4$ keV/ln(100) = 0.87 keV

11.10 Eq. (11.85) $n = 3.55E14$ $\Delta\phi/\lambda_o\ell$ $\Delta\phi = 0.0628$ rad$\rightarrow$ n = 2.1E16 m^{-3}

11.11. N $\approx$ 9 fringes Eq. (11.85) $\Delta n = 2.23E15$ N/$\lambda_o\ell = 2.9E22$ m^{-3}

11.12. $v = c/\lambda = 8.9E11$ Hz, Eq. (11.74) $\theta_{rot} = 2.36E4$ $\ell nB_k/v^2 = 0.25$ rad.

Chapter 12

12.1 5.48 % will be He atoms

12.2 $t_2 = 1.46$ years; 14.5 kg/day

12.3 93 appm He.

12.4 $D = 1.92 \times 10^{-9}\,m^2/s$, $S = 1.45 \times 10^{21}\,atoms/m^2\,Pa^{1/2}$, $J_{dif} = 4.40 \times 10^{12}atoms/m^2 s$

$K = 7.08 \times 10^{-26}\,m^4/s$, $J_{rec} = 1.49 \times 10^{12}atoms/m^2\,s$ so flow is recombination limited.

$\lambda J_{rec}A = 5.33 \times 10^6\,Bq/s = 12.5\,Ci/day$.

12.6 1.18E8 Ci = 4.36E18 Bq.

Chapter 13

Reliability
13.1

$$\lambda = \frac{1 \text{ capacitor failure}}{300 \text{ capacitors} \ \times \ 2{,}000 \text{ pulses/year} \ \times \ 4 \text{ year}} = 4.2\text{E}{-}07 \text{ failure/pulse}$$

13.2

$$\lambda = (1 \text{ demand/year}) \ \times \ (1\text{E}{-}03 \text{ failure/demand}) \ = \ 1\text{E}{-}03 \text{ failure/year}$$

13.3

$$\lambda = \frac{2 \text{ detectors}}{4 \text{ detectors} \ \times \ 75 \text{ demands}} = 6.67\text{E}{-}03 \text{ failures/demand}$$

So yes, this type of detector head is adequate.

Availability
13.4 Assumptions:

The car does not have to be moving or its engine running to be available. The car may be ready and waiting at the mechanic garage but it is not being used and is unavailable to the driver until the driver pays and claims the car again.

$$Availability = \frac{uptime}{uptime \ + \ downtime} = \frac{8{,}760 \text{ h/year} \ - \ [3(1.5\text{ h}) \ + \ 9\text{ h} \ + \ 2\text{ h}]}{24 \text{ h/day} \ \times \ 365 \text{ days/year}}$$
$$= \frac{8{,}744.5 \text{ h/year}}{8{,}760 \text{ h/year}} = 0.998$$

13.5 Year 1   1,150 h/8,760 h   A = 0.131
     Year 2   3,873 h/8,760 h   A = 0.442
     Year 3   4,725 h/8,760 h   A = 0.539
     Year 4   6,856 h/8,760 h   A = 0.783
     Year 5   7,973 h/8,760 h   A = 0.910

$$5 \text{ year average} = \frac{0.131\text{ h} \ + \ 0.442\text{ h} \ + \ 0.539\text{ h} \ + \ 0.783\text{ h} \ + \ 0.910\text{ h}}{5 \text{ year}}$$
$$= 0.561 \text{ h/year}$$

Maintainability
13.6

$$Time\ to\ restore = 72\text{ h} \ + \ (24\text{ h} \ \times \ 3 \text{ workers}) \ + \ 2\text{ hr} \ + \ 1\text{ h} = 147\text{ h}$$

13.7

Inherent MTTR is without logistics or other times, just the active repair time.

$$MTTR = \frac{4\,h + 4\,h + 4\,h + 4\,h + 6\,h}{5\ \text{repairs}} = 4.4\,h/\text{repair}$$

Restore time includes 12-h warmup and 12-h re-cool time for each repair activity. No other times are given so assume spare parts are onsite in facility stores.

$$MDT = \frac{(12 + 4 + 12\,h) + (12 + 4 + 12\,h) + (12 + 4 + 12\,h) + (12 + 4 + 12\,h) + (12 + 6 + 12\,h)}{5\ \text{repairs}}$$

$$= 28.4\,h$$

Chapter 14

14.1 $P_f = P_{net}/(\eta_e + \eta_e/Q - 1/(\eta_d Q)) = 50/[0.45 + 0.45/17$
$\qquad - 1(0.42 * 17)] = 148.6\,\text{MWth}$

$P_{gross} = P_e = P_f(\eta_e + \eta_e/Q) = 148.6 * (0.45 + 0.45/17) = 70.8\,\text{MWe}$

Recirculating power fraction $= P_{recirculating}/P_{gross}$

$$= (P_{gross} - P_{net})/P_{gross} = (70.8 - 50)/70.8 = 0.294$$

14.2 $\lambda = \ln(2)/(22.2 \times 60) = 5.2 \times 10^{-4}\,s^{-1}$

Fraction $(234) = $ absorption$/($absorption $+$ decay$) = ns\phi/(ns\phi + \ln)$
$$= 1{,}400 \times 10^{-28}10^18/(1{,}400 \times 10^{-28}10^{18} + 5.2 \times 10^{-4})$$
$$= \underline{2.7 \times 10^{-4}}$$

14.3 $\lambda = \ln(2)/(27 \times 24 \times 3{,}600\,s) = 2.97 \times 10^{-7}\,s^{-1}$
Fraction $(^{234}Pa) = ns\phi/(ns\phi + \lambda n) = 460 \times 10^{-28}10^{18}/(460 \times 10^{-28}10^{18}$
$$+ 2.97 \times 10^{-7})$$
$$= 0.134$$

14.4

$M = ($energy per neutron absorbed in blanket$)/($fusion neutron energy$)$
$\quad = [71/(1 - 0.94)]/14.1 = \underline{84}.$

14.5 to be derived by student.

Index